

Nanostructure Science and Technology

*Series Editor:* David J. Lockwood

Hiroshi Yamashita

Hexing Li *Editors*

# Nanostructured Photocatalysts

Advanced Functional Materials

 Springer

# Nanostructure Science and Technology

More information about this series at <http://www.springer.com/series/6331>



Hiromi Yamashita • Hexing Li  
Editors

# Nanostructured Photocatalysts

Advanced Functional Materials

 Springer

*Editors*

Hiromi Yamashita  
Osaka University  
Osaka, Japan

Hexing Li  
Department of Chemistry  
Shanghai Normal University  
Shanghai, China

ISSN 1571-5744

ISSN 2197-7976 (electronic)

Nanostructure Science and Technology

ISBN 978-3-319-26077-8

ISBN 978-3-319-26079-2 (eBook)

DOI 10.1007/978-3-319-26079-2

Library of Congress Control Number: 2016931896

© Springer International Publishing Switzerland 2016

This work is subject to copyright. All rights are reserved by the Publisher, whether the whole or part of the material is concerned, specifically the rights of translation, reprinting, reuse of illustrations, recitation, broadcasting, reproduction on microfilms or in any other physical way, and transmission or information storage and retrieval, electronic adaptation, computer software, or by similar or dissimilar methodology now known or hereafter developed.

The use of general descriptive names, registered names, trademarks, service marks, etc. in this publication does not imply, even in the absence of a specific statement, that such names are exempt from the relevant protective laws and regulations and therefore free for general use.

The publisher, the authors and the editors are safe to assume that the advice and information in this book are believed to be true and accurate at the date of publication. Neither the publisher nor the authors or the editors give a warranty, express or implied, with respect to the material contained herein or for any errors or omissions that may have been made.

Printed on acid-free paper

This Springer imprint is published by Springer Nature  
The registered company is Springer International Publishing AG Switzerland

# Preface

Over the past few decades, research in photocatalysis has been very active and many applications using photocatalysts have been realized. Semiconductors such as  $\text{TiO}_2$  played an important role in these amazing developments. Modern nanotechnology has brought about a breakthrough to new functional materials. The combination of powerful spectroscopic techniques and advanced nanotechnology supports the understanding of the relation between nanostructure and mechanics of functions, and thus the development of new photocatalysts with attractive functionalities.

The design of photocatalysts is still a hot topic in scientific research and industrial application. This book summarizes the emergence of nanostructure controlled photocatalysts. These new photocatalysts open the possibility of efficient photocatalytic reactions under both UV light and visible-light irradiation, thus promising to make efficient use of sunlight. Many attractive and long-desired reactions can now be realized efficiently and selectively, including water splitting to produce hydrogen,  $\text{CO}_2$  fixation and conversion, selective organic synthesis, complete degradation of organic pollutants in air and water, and so forth.

While there are many books on semiconductor  $\text{TiO}_2$  photocatalysis, nanostructured photocatalysts are attractive beyond standard semiconductors and enable many novel uses of advanced  $\text{TiO}_2$  and MOF-based photocatalysts. Other new nanomaterials discussed in this book are Bi- and W-oxides, metal complexes, and porous nanomaterials. These can be synthesized using various subtle and skillful techniques and characterized by advanced spectroscopic analysis and other technologies. Many details of synthesis, characterization, and reaction applications of nanostructured photocatalysts are summarized.

The contributors to this book are leading researchers on photocatalysis. The editors thank the contributors for their attractive manuscripts, and the publisher for proposing a book on new materials related to energy and the environment. We sincerely hope this book provides a perspective on the varied ideas and approaches in photocatalyst design, and ultimately results in improvements in our way of life.

Osaka, Japan  
Shanghai, China

Hiromi Yamashita  
Hexing Li



# Contents

## Part I TiO<sub>2</sub> Photocatalysts with Unique Structures

- 1 Novel Titanium Oxide Materials Synthesized by Solvothermal and Supercritical Fluid Processes.....** 3  
Zhenfeng Bian, Yuning Huo, and Hexing Li
- 2 TiO<sub>2</sub>/Graphene Composites with Excellent Performance in Photocatalysis.....** 23  
Mingyang Xing, Bocheng Qiu, Xiao Li, and Jinlong Zhang
- 3 Controllable Synthesis and Photocatalytic Activities of TiO<sub>2</sub> Nanocrystals.....** 69  
Shuai Yuan, Yin Zhao, and Liyi Shi
- 4 Development of Visible Light Responsive Morphology Controlled TiO<sub>2</sub> Photocatalyst.....** 79  
Teruhisa Ohno
- 5 Development of Advanced Nanoarchitectures for Photocatalytic Treatment of NO<sub>x</sub>.....** 99  
Shuning Xiao, Dieqing Zhang, Guisheng Li, and Hexing Li
- 6 Preparation of TiO<sub>2</sub> Nanotubes-Based Electrophotocatalysts and Their Applications in Organic Pollutants Oxidation.....** 125  
Bo Tang, Meichuan Liu, and Guohua Zhao
- 7 Hollow Core–Shell Titania Photocatalysts for Selective Organic Synthesis.....** 137  
Sheela Chandren and Bunsho Ohtani
- 8 Design of Thin Film Photocatalysts Deposited on Rotating Disks for Degradation of Organic Dyes in Wastewater.....** 147  
Kan Li and Jinping Jia

## Part II Doped and Surface Modified TiO<sub>2</sub> Photocatalysts

- 9 Application of Metal Ion Implantation for the Design of Visible Light-Responsive Titanium Oxide Photocatalysts** ..... 173  
Hiromi Yamashita and Yuichi Ichihashi
- 10 Effect of F-Doping on the Photocatalytic Activity and Microstructures of Nanocrystalline TiO<sub>2</sub> Powders**..... 187  
Shengwei Liu and Jiaguo Yu
- 11 Photocatalytic Decomposition of NH<sub>3</sub> Over Fe-Doped TiO<sub>2</sub> Prepared by Solid-State Impregnation** ..... 201  
Yuichi Ichihashi, Atsushi Okemoto, Kazutaka Obata, Keita Taniya, and Satoru Nishiyama
- 12 Surface-Functionalized TiO<sub>2</sub> Photocatalyst Modified by the Interfacial Surface Complex (ISC)** ..... 211  
Shinya Higashimoto

## Part III Photocatalysts Supported on Unique Supports

- 13 Photocatalytic Properties of TiO<sub>2</sub>-Loaded Porous Silica with Hierarchical Macroporous and Mesoporous Architectures** ..... 229  
Takashi Kamegawa and Hiromi Yamashita
- 14 TiO<sub>2</sub> Photocatalyst Supported on Surface-Modified Silica Supports**..... 241  
Yasutaka Kuwahara, Xufan Qian, and Hiromi Yamashita
- 15 Photodegradation of Pollutants in Water over TiO<sub>2</sub> Supported on Molecular Sieves** ..... 259  
Albert Wan and Soofin Cheng
- 16 Plasmonic Photocatalysts: Preparation and Evaluation** ..... 281  
Atsuhiko Tanaka and Hiroshi Kominami

## Part IV Photocatalysts with Advanced Components

- 17 Nanostructured Elemental Photocatalysts: Development and Challenges** ..... 295  
Zhurui Shen and Jimmy C. Yu
- 18 Application of Layered Double Hydroxides (LDHs) in Photocatalysis**..... 313  
Shoji Iguchi, Kentaro Teramura, Saburo Hosokawa, and Tsunehiro Tanaka
- 19 Bismuth Oxyhalide Nano- and Microstructures: Morphology Modulation and Functionalization** ..... 325  
Ling Zhang and Wenzhong Wang

<b>20</b>	<b>Synthesis and Facet-Dependent Properties of Layered BiOCl Photocatalysts</b> .....	341
	Jie Li and Lizhi Zhang	
<b>21</b>	<b>Synthesis and Performance Enhancement for Bi<sub>2</sub>WO<sub>6</sub> as High-Activity Visible-Light-Driven Photocatalysts</b> .....	359
	Zhen Wei and Yongfa Zhu	
<b>22</b>	<b>Preparation and Characterization of Bismuth Tungstate Polycrystalline Flake-Ball Particles for Photocatalytic Reactions</b> .....	391
	Fumiaki Amano	
<b>23</b>	<b>Formation of BiOCl/Bi<sub>2</sub>O<sub>3</sub> and Related Materials for Efficient Visible-Light Photocatalysis</b> .....	405
	Sandipan Bera and Wan In Lee	
<b>24</b>	<b>Visible-Light-Responsive Photocatalysts and Photoelectrodes Using WO<sub>3</sub> Semiconductors for Degradation of Organics and Water Splitting</b> .....	429
	Kazuhiro Sayama	
<b>25</b>	<b>Z-Scheme Water Splitting into H<sub>2</sub> and O<sub>2</sub> Under Visible Light</b> .....	443
	Ryu Abe	
<b>Part V Metal Complex Photocatalysts</b>		
<b>26</b>	<b>Silica-Supported Metal Complex Photocatalysts</b> .....	465
	Kohsuke Mori and Hiromi Yamashita	
<b>27</b>	<b>Metal–Organic Framework (MOF) and Porous Coordination Polymer (PCP)-Based Photocatalysts</b> .....	479
	Yu Horiuchi, Takashi Toyao, and Masaya Matsuoka	
<b>28</b>	<b>Photocatalytic CO<sub>2</sub> Reduction to CO by ZIF-9/TiO<sub>2</sub></b> .....	491
	Sibo Wang and Xinchun Wang	
<b>29</b>	<b>Nanometal-Loaded Metal-Organic-Framework Photocatalysts</b> .....	507
	Meicheng Wen, Yasutaka Kuwahara, Kohsuke Mori, and Hiromi Yamashita	
<b>30</b>	<b>Metal-Organic Frameworks (MOFs) for Photocatalytic Organic Transformations</b> .....	523
	Dengrong Sun and Zhaohui Li	
	<b>Index</b> .....	537



# Contributors

**Ryu Abe** Department of Energy and Hydrocarbon Chemistry, Graduate School of Engineering, Kyoto University, Kyoto, Japan

**Fumiaki Amano** Department of Chemical and Environmental Engineering, Faculty of Environmental Engineering, The University of Kitakyushu, Kitakyushu, Japan

**Sandipan Bera** Department of Chemistry and Chemical Engineering, Inha University, Incheon, South Korea

**Zhenfeng Bian** Chinese Education Ministry Key Laboratory of Resource Chemistry, Shanghai Normal University, Shanghai, China

**Sheela Chandren** Universiti Teknologi Malaysia, Johor Bahru, Johor, Malaysia  
Institute of Catalysis, Hokkaido University, Sapporo, Japan

**Soofin Cheng** Department of Chemistry, National Taiwan University, Taipei, Taiwan

**Shinya Higashimoto** College of Engineering, Osaka Institute of Technology, Osaka, Japan

**Yu Horiuchi** Department of Applied Chemistry, Graduate School of Engineering, Osaka Prefecture University, Osaka, Japan

**Saburo Hosokawa** Department of Molecular Engineering, Graduate School of Engineering, Kyoto University, Kyoto, Japan

**Yuning Huo** Chinese Education Ministry Key Laboratory of Resource Chemistry, Shanghai Normal University, Shanghai, China

**Yuichi Ichihashi** Department of Chemical Science and Engineering, Graduate School of Engineering, Kobe University, Kobe, Japan

**Shoji Iguchi** Department of Molecular Engineering, Graduate School of Engineering, Kyoto University, Kyoto, Japan

**Jinping Jia** School of Environmental Science and Engineering, Shanghai Jiao Tong University, Shanghai, People's Republic of China

**Takashi Kamegawa** Nanoscience and Nanotechnology Research Center, Osaka Prefecture University, Osaka, Japan

Division of Materials and Manufacturing Science, Graduate School of Engineering, Osaka University, Osaka, Japan

**Hiroshi Kominami** Department of Applied Chemistry, Faculty of Science and Engineering, Kinki University, Osaka, Japan

**Yasutaka Kuwahara** Division of Materials and Manufacturing Science, Graduate School of Engineering, Osaka University, Osaka, Japan

Elements Strategy Initiative for Catalysts & Batteries Kyoto University (ESICB), Kyoto University, Katsura, Kyoto, Japan

**Wan In Lee** Department of Chemistry and Chemical Engineering, Inha University, Incheon, South Korea

**Kan Li** School of Environmental Science and Engineering, Shanghai Jiao Tong University, Shanghai, People's Republic of China

School of Materials Science and Engineering, Shanghai Jiao Tong University, Shanghai, People's Republic of China

**Guisheng Li** The Education Ministry Key Lab of Resource Chemistry, Shanghai Key Laboratory of Rare Earth Functional Materials, Department of Chemistry, Shanghai Normal University, Shanghai, China

**Hexing Li** The Education Ministry Key Lab of Resource Chemistry, Shanghai Key Laboratory of Rare Earth Functional Materials, Department of Chemistry, Shanghai Normal University, Shanghai, China

**Xiao Li** Key Laboratory for Advanced Materials and Institute of Fine Chemicals, East China University of Science and Technology, Shanghai, People's Republic of China

**Jie Li** Key Laboratory of Pesticide and Chemical Biology of Ministry of Education, Institute of Environmental Chemistry, College of Chemistry, Central China Normal University, Wuhan, People's Republic of China

**Zhaohui Li** Research Institute of Photocatalysis, State Key Laboratory of Photocatalysis on Energy and Environment, College of Chemistry, Fuzhou University, Fuzhou, China

**Meichuan Liu** Department of Chemistry, Shanghai Key Lab of Chemical Assessment and Sustainability, Tongji University, Shanghai, China

**Shengwei Liu** State Key Laboratory of Advanced Technology for Materials Synthesis and Processing, Wuhan University of Technology, Wuhan, China

**Masaya Matsuoka** Department of Applied Chemistry, Graduate School of Engineering, Osaka Prefecture University, Osaka, Japan

**Kohsuke Mori** Division of Materials and Manufacturing Science, Graduate School of Engineering, Osaka University, Osaka, Japan

Elements Strategy Initiative for Catalysts & Batteries Kyoto University (ESICB), Kyoto University, Katsura, Kyoto, Japan

**Satoru Nishiyama** Department of Chemical Science and Engineering, Graduate School of Engineering, Kobe University, Kobe, Japan

**Kazutaka Obata** Department of Chemical Science and Engineering, Graduate School of Engineering, Kobe University, Kobe, Japan

**Teruhisa Ohno** Applied Chemistry Section, Graduate School of Engineering, Kyushu Institute of Technology, Kitakyushu, Japan

**Bunsho Ohtani** Institute for Catalysis, Hokkaido University, Sapporo, Japan

**Atsushi Okemoto** Department of Chemical Science and Engineering, Graduate School of Engineering, Kobe University, Kobe, Japan

**Xufang Qian** Division of Materials and Manufacturing Science, Graduate School of Engineering, Osaka University, Osaka, Japan

**Bocheng Qiu** Key Laboratory for Advanced Materials and Institute of Fine Chemicals, East China University of Science and Technology, Shanghai, People's Republic of China

**Kazuhiro Sayama** Research Center for Photovoltaics (RCPV), National Institute of Advanced Industrial Science and Technology (AIST), Tsukuba, Japan

**Zhurui Shen** Department of Chemistry, Institute of Environment, Energy and Sustainability, The Chinese University of Hong Kong, Hong Kong, China

**Liyi Shi** Research Center of Nanoscience and Nanotechnology, Shanghai University, Shanghai, China

**Dengrong Sun** Research Institute of Photocatalysis, State Key Laboratory of Photocatalysis on Energy and Environment, College of Chemistry, Fuzhou University, Fuzhou, People's Republic of China

**Tsunehiro Tanaka** Department of Molecular Engineering, Graduate School of Engineering, Kyoto University, Kyoto, Japan

**Atsuhiko Tanaka** Department of Molecular Engineering, Graduate School of Engineering, Kyoto University, Kyoto, Japan

**Bo Tang** Department of Chemistry, Shanghai Key Lab of Chemical Assessment and Sustainability, Tongji University, Shanghai, China

**Keita Taniya** Department of Chemical Science and Engineering, Graduate School of Engineering, Kobe University, Kobe, Japan

**Kentaro Teramura** Department of Molecular Engineering, Graduate School of Engineering, Kyoto University, Kyoto, Japan

**Takashi Toyao** Department of Applied Chemistry, Graduate School of Engineering, Osaka Prefecture University, Osaka, Japan

**Albert Wan** Department of Chemistry, National Taiwan University, Taipei, Taiwan

**Wenzhong Wang** State Key Laboratory of High Performance Ceramics and Superfine Microstructures, Chinese Academy of Sciences, Shanghai Institute of Ceramics, Shanghai, People's Republic of China

**Sibo Wang** State Key Laboratory of Photocatalysis on Energy and Environment, College of Chemistry, Fuzhou University, Fuzhou, People's Republic of China

**Xinchen Wang** State Key Laboratory of Photocatalysis on Energy and Environment, College of Chemistry, Fuzhou University, Fuzhou, People's Republic of China

**Zhen Wei** Department of Chemistry, Tsinghua University, Beijing, China

**Meicheng Wen** Division of Materials and Manufacturing Science, Graduate School of Engineering, Osaka University, Osaka, Japan

**Shuning Xiao** The Education Ministry Key Lab of Resource Chemistry, Shanghai Key Laboratory of Rare Earth Functional Materials, Department of Chemistry, Shanghai Normal University, Shanghai, China

**Mingyang Xing** Key Laboratory for Advanced Materials and Institute of Fine Chemicals, East China University of Science and Technology, Shanghai, People's Republic of China

**Hiromi Yamashita** Division of Materials and Manufacturing Science, Graduate School of Engineering, Osaka University, Osaka, Japan

Elements Strategy Initiative for Catalysts & Batteries Kyoto University (ESICB), Kyoto University, Katsura, Kyoto, Japan

**Jimmy C. Yu** Department of Chemistry, Institute of Environment, Energy and Sustainability, The Chinese University of Hong Kong, Hong Kong, China

**Jianguo Yu** State Key Laboratory of Advanced Technology for Materials Synthesis and Processing, Wuhan University of Technology, Wuhan, China

**Shuai Yuan** Research Center of Nanoscience and Nanotechnology, Shanghai University, Shanghai, China

**Dieqing Zhang** The Education Ministry Key Lab of Resource Chemistry, Shanghai Key Laboratory of Rare Earth Functional Materials, Department of Chemistry, Shanghai Normal University, Shanghai, China

**Jinlong Zhang** Key Laboratory for Advanced Materials and Institute of Fine Chemicals, East China University of Science and Technology, Shanghai, People's Republic of China

**Lizhi Zhang** Key Laboratory of Pesticide and Chemical Biology of Ministry of Education, Institute of Environmental Chemistry, College of Chemistry, Central China Normal University, Wuhan, People's Republic of China

**Ling Zhang** State Key Laboratory of High Performance Ceramics and Superfine Microstructures, Chinese Academy of Sciences, Shanghai Institute of Ceramics, Shanghai, People's Republic of China

**Guohua Zhao** Department of Chemistry, Shanghai Key Lab of Chemical Assessment and Sustainability, Tongji University, Shanghai, China

**Yin Zhao** Research Center of Nanoscience and Nanotechnology, Shanghai University, Shanghai, China

**Yongfa Zhu** Department of Chemistry, Tsinghua University, Beijing, China



## About the Editors

**Hiromi Yamashita** has been a professor at Osaka University since 2004. He also has been a professor of Elements Strategy Initiative for Catalysts & Batteries (Kyoto University) since 2012. He received his Ph.D. degree from Kyoto University (supervisor: Prof. S. Yoshida) in 1987. He was an assistant professor at Tohoku University (with Profs. A. Tomita and T. Kyotani), an associate professor at Osaka Prefecture University (with Prof. M. Anpo), and an invited professor at University Pierre and Marie Curie (UPMC) (with Prof. M. Che). He was also a visiting research fellow at the Pennsylvania State University (with Prof. L.R. Radovic), University of Texas at Austin (with Prof. M.A. Fox), and California Institute of Technology (with Prof. M.E. Davis). He is now an editor of *Applied Catalysis B: Environmental* and an associate editor of *Journal of Photochemistry and Photobiology C: Photochemistry Reviews*. He has received awards from several societies such as the Catalysis Society of Japan, the Japanese Photochemistry Association, the Japan Petroleum Institute, and the Japan Institute of Metals and Materials. His research interests include the design of single-site photocatalysts and nanostructured catalysts.

**Hexing Li** received his Ph.D. degree from Fudan University in 1997 (Advised by Academician Jingfa Deng). He has been a professor at Shanghai Normal University since 1999. He is an invited professor of Shanghai University and a Ph.D. student advisor at East China Normal University and East China Science and Technology University. He is now an associate editor of *Applied Catalysis B: Environmental*. In addition, he is a director of both the Chinese Education Ministry Key Lab on Resource Chemistry and the International Joint Lab of Shanghai Normal University, Princeton University, and the National University of Singapore. He is also the vice-director of the Chinese Photochemistry and Photocatalysis Professional Committee. His research interests include the design of metal, organometal, and semiconductor nanomaterials for both thermo- and photocatalysis. He received Outstanding Youth Funding from NSFC and the first class of Nature Science Award from the Chinese Education Ministry.

**Part I**  
**TiO<sub>2</sub> Photocatalysts with Unique**  
**Structures**

# Chapter 1

## Novel Titanium Oxide Materials Synthesized by Solvothermal and Supercritical Fluid Processes

Zhenfeng Bian, Yuning Huo, and Hexing Li

### 1.1 Titanium Oxide Materials Synthesized by Solvothermal Methods

Solvothermal alcoholysis has received a large amount of interest in regard to synthesizing metal oxides because of the control over the particle size, shape, and crystal structure. The following alcoholysis reactions of  $Ti^{4+}$  illustrate the formation of  $TiO_2$  by capturing oxygen from the alcohol:



The structure of  $TiO_2$  will be easily controlled under slow alcoholysis process.  $TiO_2$  then nucleates into crystals with the alcohol as a template.  $TiO_2$  represents the most widely used semiconductor photocatalysts and photovoltaics, and its performances heavily governed by the physical and chemical properties such as surface area, particle size, micro/nanostructures, exposed crystal planes, and surface chemistry [1-6].

#### 1.1.1 $TiO_2$ Nanocrystals

Nanocrystalline anatase  $TiO_2$  photocatalysts are prepared by a facile solvothermal alcoholysis of  $TiCl_4$  with benzyl alcohol at low temperature (60 °C), followed by calcination at elevated temperatures from 300 to 800 °C [7]. During various

---

Z. Bian (✉) • Y. Huo • H. Li  
Chinese Education Ministry Key Laboratory of Resource Chemistry,  
Shanghai Normal University, 100 Guilin Road, Shanghai 200234, China  
e-mail: [bianzhenfeng@shnu.edu.cn](mailto:bianzhenfeng@shnu.edu.cn)

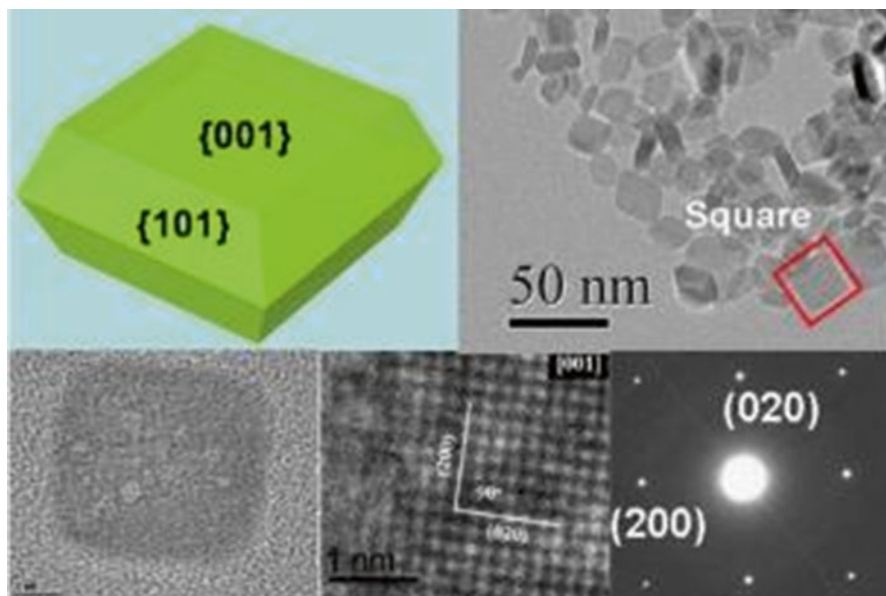


**Fig. 1.1** The model of the anatase TiO<sub>2</sub> decahedral nanocrystals with dominant {001} facets and representative HRTEM images and SAED patterns. Adapted from Ref. [9] with permission from The Royal Society of Chemistry

photocatalytic reactions, the as-synthesized TiO<sub>2</sub> nanocrystals exhibit high activity comparable to the commercially available Degussa P-25. The calcination temperature and time are crucial in determining the surface area, particle size, crystallinity, surface hydroxyl groups, and carbonaceous residues, which are strongly relative to the photocatalytic performance.

Furthermore, a new type of nanocrystalline mesostructured TiO<sub>2</sub> predominantly in the anatase phase with a high specific surface area up to 269 m<sup>2</sup>/g is prepared by an integrated solvothermal alcoholysis/UV-illumination techniques at low temperature (60 °C) [8]. This TiO<sub>2</sub> exhibits much higher activity than Degussa P-25 in photocatalytic degradation of acetone, which could be attributed to the enhanced crystallization degree and the formation of surface Ti-OH groups.

Anatase TiO<sub>2</sub> nanocrystals with dominant {001} facets are prepared by solvothermal alcoholysis of TiF<sub>4</sub> in either single alcohol or binary alcohols (Fig. 1.1) [9]. The smooth alcoholysis of TiF<sub>4</sub> and crystal growth of TiO<sub>2</sub> allows controllable synthesis of TiO<sub>2</sub> decahedral nanocrystals with uniform shape and particle size. The percentage of exposed {001} facets and the particle size could be adjusted by using different alcohols or changing the ratio of two alcohols. The high percentage of exposed {001} facets and the large surface area due to small particle size promote the activity under selective photocatalytic oxidation of toluene reaction.

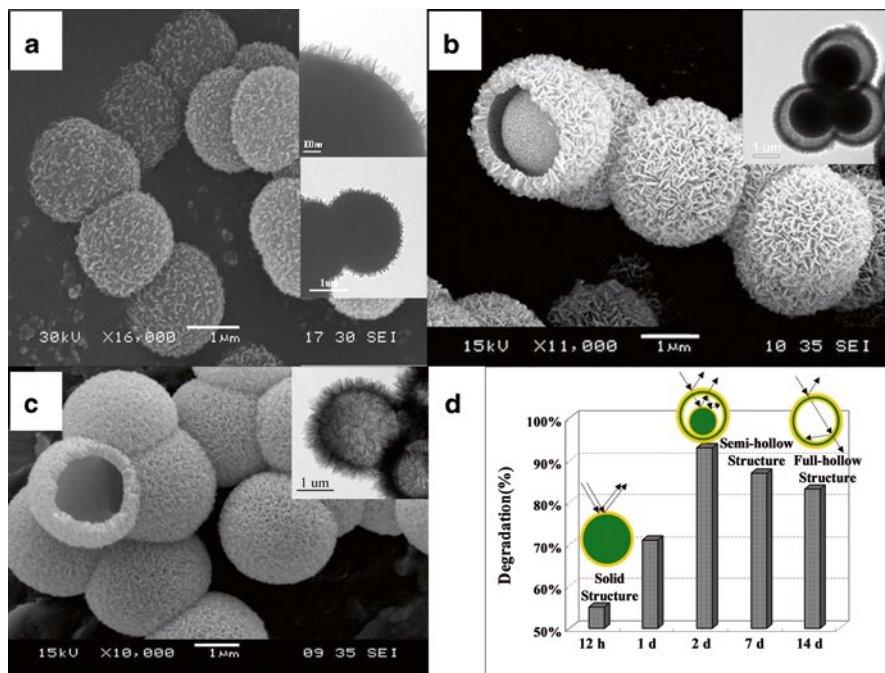


**Fig. 1.2** SEM and TEM (insets) images of the titania spheres synthesized for (a) 0.5, (b) 2, (c) 14 days and (d) phenol degradation efficiency under UV light irradiation. Adapted with permission from Ref. [18]. Copyright (2007) American Chemical Society

### 1.1.2 Micro/Nanostructured $\text{TiO}_2$

Morphology control of photocatalyst is important for their practical applications [10–13]. As an alternative, template free approaches based on different mechanisms have been developed to engineer photocatalyst nanostructure and morphology [14–17]. Hollow  $\text{TiO}_2$  microspheres are template-free synthesized by solvothermal alcoholysis  $\text{TiOSO}_4$  in the solution containing glycerol, alcohol, and ethyl ether [18]. Besides the morphology and size,  $\text{TiO}_2$  interior structure could be adjusted among solid, yolk–shell, and hollow depending on either the alcohol molecules (e.g., methanol, ethanol, and propanol) or the solvothermal alcoholysis reaction time.

Figure 1.2 reveals that small surface platelets (Fig. 1.2a) were formed after 12 h solvothermal alcoholysis and further grow into urchin like prickly surface with the increasing reaction time. The platelets formed shells on the solid cores, creating a core–shell structure (Fig. 1.2b). These cores shrink with the increasing reaction time, forming the yolk–shell structure with continuously reducing inner sphere size. The inner spheres finally disappeared after 14-day solvothermal alcoholysis, leading to hollow  $\text{TiO}_2$  microspheres (Fig. 1.2c). The yolk–shell structure allows multi-reflections of lights within chamber, leading to the enhanced light harvesting and

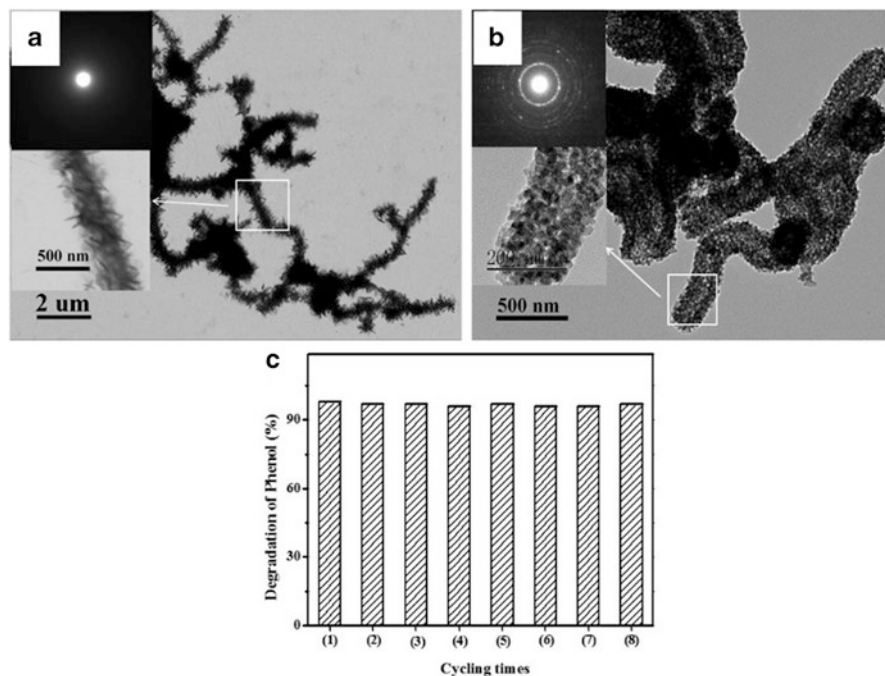


**Fig. 1.3** SEM and TEM images of the CNTs/TiO<sub>2</sub> before (a) and after (b) calcination at 500 °C (the inset is the SAED pattern) and recycling tests of phenol degradation for TiO<sub>2</sub>-NTs calcined at 500 °C (c). Adapted from Ref. [26] with permission from The Royal Society of Chemistry

thus the increased photocatalytic activity (Fig. 1.2d). Additionally, TiO<sub>2</sub> microspheres could be encapsulated between TiO<sub>2</sub> films and used as a scattering layer in dye-sensitized solar cells (DSSCs), which display increased cell efficiencies compared to those of pure TiO<sub>2</sub> films without any scattering layers [19]. This method can be further extended to other structure of TiO<sub>2</sub> including nanotextons and flower-like spheres and even non-TiO<sub>2</sub> materials like TiN, graphitized carbon, and MnO<sub>2</sub>.

TiO<sub>2</sub> nanotubes exhibit high photocatalytic activity owing to their unique three-dimensional structure, high surface area, and excellent electronic conductivity [20–23]. To date, TiO<sub>2</sub> nanotubes are mainly prepared by hydrothermally treating TiO<sub>2</sub> particles [24] or by anodic oxidation [25]. Solvothermal alcoholysis is an efficient method for preparing TiO<sub>2</sub> owing to the slow release of H<sub>2</sub>O, leading to a controllable hydrolysis and condensation process of Ti precursors, which facilitate the desired morphology and porous structure formation as well as the high crystallization degree of TiO<sub>2</sub> [18]. As shown in Fig. 1.3, well-defined mesoporous anatase TiO<sub>2</sub> nanotubes with high crystallization degree (TiO<sub>2</sub>-NTs) are prepared by solvothermal alcoholysis of TiOSO<sub>4</sub> in the presence of CNTs template, which exhibit high activity in photocatalytic phenol degradation [26].

To maximize the photocatalytic efficiency of TiO<sub>2</sub>, many efforts have been made to tailoring the nano/microstructures [27]. TiO<sub>2</sub> mesocrystal is a novel class of TiO<sub>2</sub>

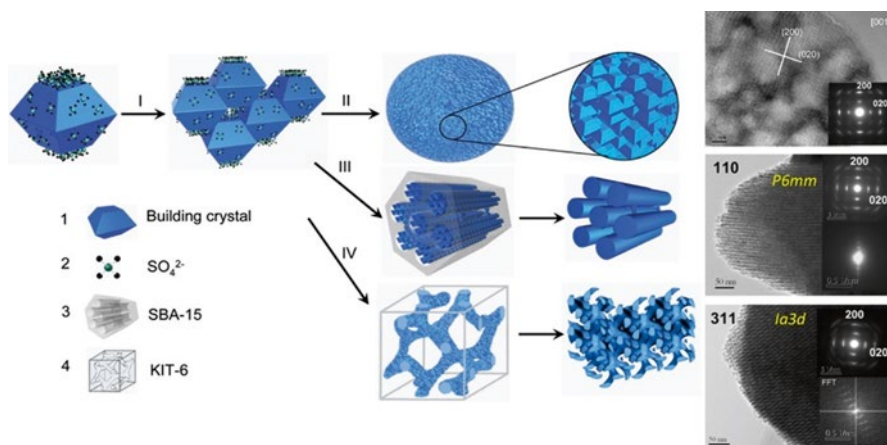


**Fig. 1.4** Schematic illustration of synthesis process of mesoporous single-crystal-like  $\text{TiO}_2$  (Step I–Step IV). Adapted with permission from Ref. [30]. Copyright (2011) WILEY-VCH Verlag GmbH & Co. KGaA, Weinheim

materials with advantages of single crystals and large specific surface area [28, 29]. High surface area and single crystalline anatase  $\text{TiO}_2$  with controlled mesoporous network and dominant (001) active facets are also prepared by solvothermal alcoholysis [30]. As shown in Fig. 1.4, the precursor solution containing  $\text{SO}_4^{2-}$  undergoes solvothermal alcoholysis reactions to generate  $\text{TiO}_2$  building crystals in which the (001) facets are preferably adsorbed by the  $\text{SO}_4^{2-}$ , followed by growth of the building crystals into crystal clusters and then into  $\text{TiO}_2$  crystals with the dominant (001) facets and disordered mesoporous networks originating from the voids among the building crystals. To construct an ordered mesoporous channels, the growth was confined within a scaffold with ordered pore channels, such as the silica containing 2D (SBA-15,  $P6mm$  space group) and 3D (KIT-6,  $Ia3d$  space group) ordered mesopores. Subsequent scaffold removal resulted in  $\text{TiO}_2$  crystals with replicated 2D or 3D ordered mesoporous structure, respectively. The pore volume and surface area of the crystals would be altered by using different solvents.

These single-crystal-like  $\text{TiO}_2$  mesocages exhibit superior activity and thermal stability over polycrystalline  $\text{TiO}_2$  or P-25 in liquid phase photocatalytic oxidation of toluene to benzaldehyde (Fig. 1.5a). During photocatalytic oxidation of large-sized cinnamyl alcohol into cinnamaldehyde, the  $\text{TiO}_2$  with 3D ordered mesopores shows higher activity than that with 2D ordered mesopores and other  $\text{TiO}_2$  photocatalysts (Fig. 1.5b).

Crystalline anatase  $\text{TiO}_2$  nanosheets are formed by using of benzyl alcohols in a solvothermal alcoholysis (Fig. 1.6). Firstly, the combination of benzyl alcohol and  $\text{TiF}_4$  produces an organic-enriched titanium precursor, followed by forming nanosheet anatase  $\text{TiO}_2$ . Directed self-assembly of these nanosheets results in the photonic  $\text{TiO}_2$ , which shows good potentials in photochemical processes, such as photovoltaics and photocatalysis. Moreover, by tuning the wavelength of the photonic band gap, it may create environmentally friendly and reflective coatings.

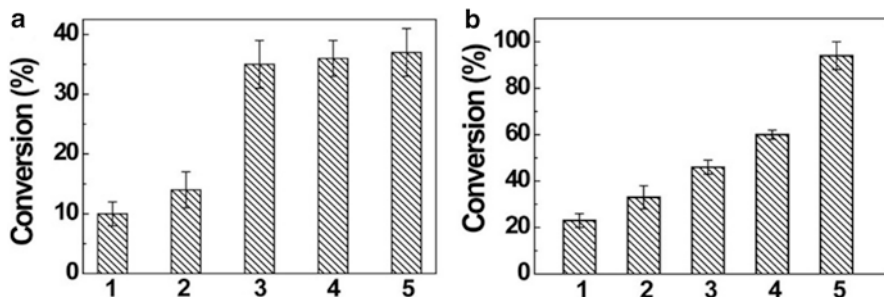


**Fig. 1.5** Photocatalytic conversions of the oxidations of toluene to benzaldehyde (a) and cinnamyl alcohol to cinnamaldehyde (b) in liquid phase in the presence of (1) commercial P-25, (2) polycrystalline TiO<sub>2</sub>, and single-crystal-like TiO<sub>2</sub> with (3) disordered, (4) ordered 2D, and (5) ordered 3D mesoporous structure. Adapted with permission from Ref. [30]. Copyright (2011) WILEY-VCH Verlag GmbH & Co. KGaA, Weinheim

### 1.1.3 Micro/Nanostructured TiO<sub>2</sub> with Dopants

Pristine TiO<sub>2</sub> could be activated only by UV lights due to its energy gap (3.0–3.2 eV) and thus, only less than 5 % solar light can be utilized. They also exhibit low quantum efficiency due to easy recombination between photoelectrons and holes. Modification of TiO<sub>2</sub> with heteroatoms, noble metals or other metal oxides is one of the promising ways to extend light absorption to the visible region and reduce the photoelectron–hole recombination.

Fe-doped nanocrystalline TiO<sub>2</sub> with a mesoporous structure (Fe/TiO<sub>2</sub>) was prepared via solvothermal alcoholysis, which could strengthen the incorporation of Fe-dopants into the TiO<sub>2</sub> network [32]. The Fe/TiO<sub>2</sub> displays spectral response in visible area owing to the formation of intermediate energy levels resulting from Fe-doping, which narrows the energy gap. Meanwhile, the Fe-dopants strongly interacting with TiO<sub>2</sub> also promote the photocatalytic activity owing to the inhibition of photoelectron–hole recombination.

Mesoporous Bi<sub>x</sub>Ti<sub>1-x</sub>O<sub>2</sub> microspheres with yolk–shell chamber are also prepared by solvothermal alcoholysis [33]. The cross-condensation between Ti-OH and Bi-OH ensures the complete incorporation of Bi-dopants into TiO<sub>2</sub> lattice, though Bi atom is bigger than Ti atom. Meanwhile, the aggregation of TiO<sub>2</sub> building clusters into microspheres, together with their subsequent reactions including dissolution and redeposition processes, results in the formation of hollow microspheres. The Bi-doping induces strong spectral response in visible region owing to the formation of intermediate energy levels to reduce the energy band gap. Meanwhile, the multiple reflections within hollow microsphere interior chamber promote the light harvesting and thus the photocatalytic activity.

Consecutive solvothermal and hydrothermal treatments are used to prepare yolk–shell Au/TiO<sub>2</sub> microspheres, in which the Au nanoparticles homogeneously encapsulated by the TiO<sub>2</sub> shells. Such process could be interpreted in terms of

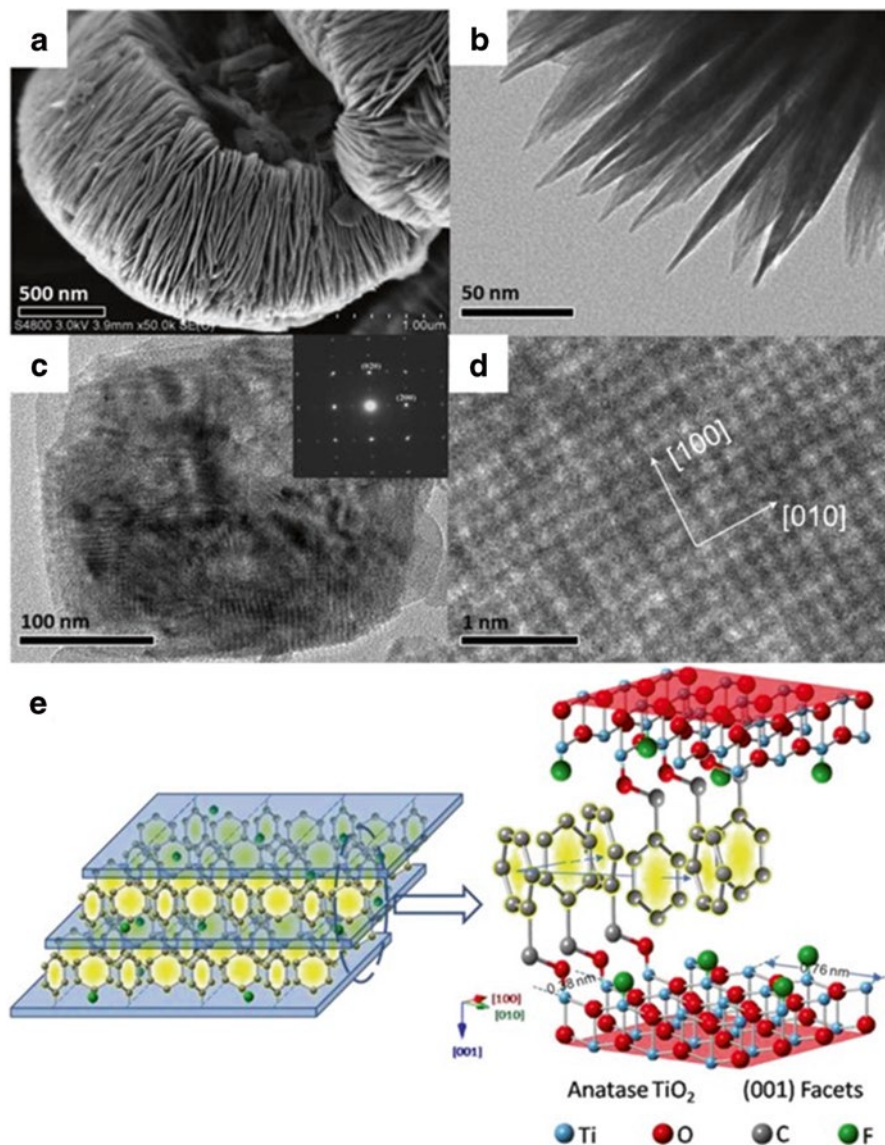


**Fig. 1.6** (a) SEM of layered structure obtained from the reaction of TiF<sub>4</sub> and benzyl alcohol. (b) TEM of the edge region of layered structure. (c) TEM of a thin section of the layered material. The inset is the small angle electron diffraction (SAED) of the nanoscale sheet of TiO<sub>2</sub>. (d) HRTEM image of a nanoscale sheet revealing the lattice planes of anatase TiO<sub>2</sub>. (e) Schematic representation of the layered structure with TiO<sub>2</sub> nanosheets held together through  $\pi$ -stacking between the layers. Adapted with permission from Ref. [31]. Copyright (2013) American Chemical Society

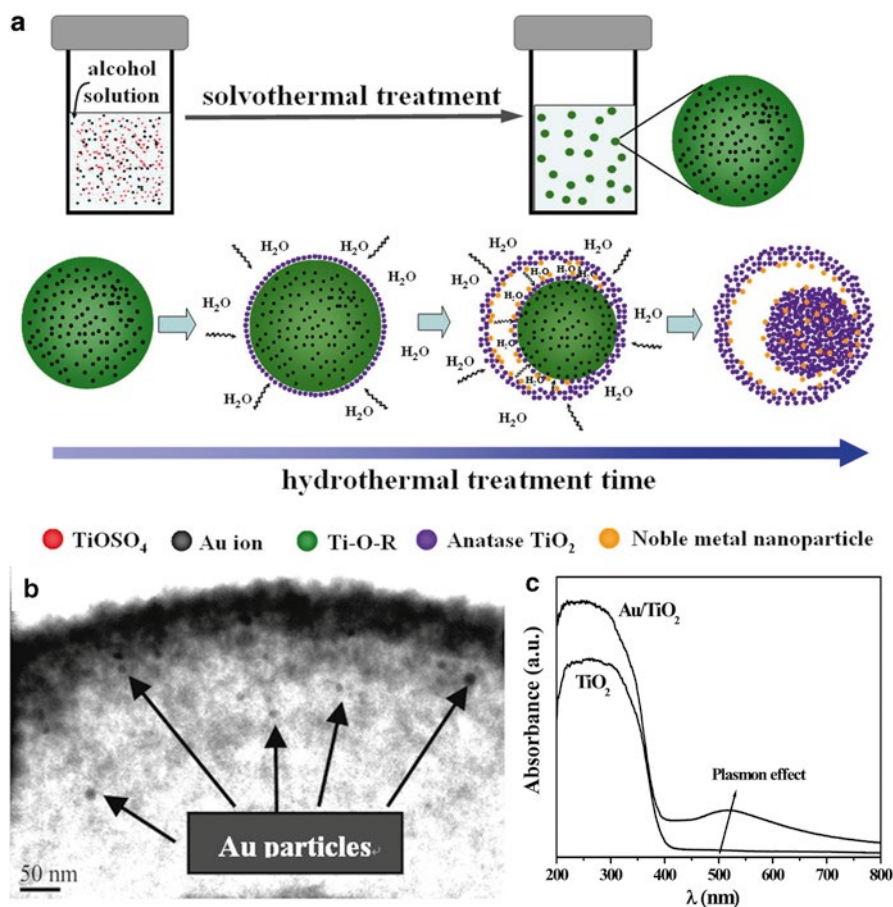


**Fig. 1.7** A proposed mechanism of encapsulating noble metal nanoparticles inside the core-shell TiO<sub>2</sub> microspheres (a); TEM pattern (b) and UV-Vis DRS (c) of Au/TiO<sub>2</sub>. Adapted from Ref. [35] with permission from The Royal Society of Chemistry

alcoholysis induced self-assembly, involving the aggregation of TiO<sub>2</sub> building clusters into spheres and their subsequent reaction, dissolution, and redeposition processes [34], together with the in situ Au<sup>3+</sup> reduction (Fig. 1.7a). Au nanoparticles are completely encapsulated by TiO<sub>2</sub> shells since the Ti<sup>4+</sup> is more easily hydrolyzed to construct a TiO<sub>2</sub> outer shell (Fig. 1.7b). The as-prepared Au/TiO<sub>2</sub> exhibits very high activity owing to enhanced light harvesting and the reduced recombination rate between photoelectrons and holes, corresponding to the high quantum efficiency (Fig. 1.7c) [35].

Flower-like Bi<sub>2</sub>O<sub>3</sub>/TiO<sub>2</sub> visible photocatalyst with surface enrichment of Bi<sub>2</sub>O<sub>3</sub> quantum dots is synthesized using a facile solvothermal alcoholysis, which exhibits much higher activity than either the Bi<sub>2</sub>O<sub>3</sub>/TiO<sub>2</sub> prepared by impregnation method or the powder Bi<sub>2</sub>O<sub>3</sub>/TiO<sub>2</sub> obtained by mechanically crushing the flower-like Bi<sub>2</sub>O<sub>3</sub>/TiO<sub>2</sub> [36]. The high activity could be attributed to the enhanced light absorbance via multiple

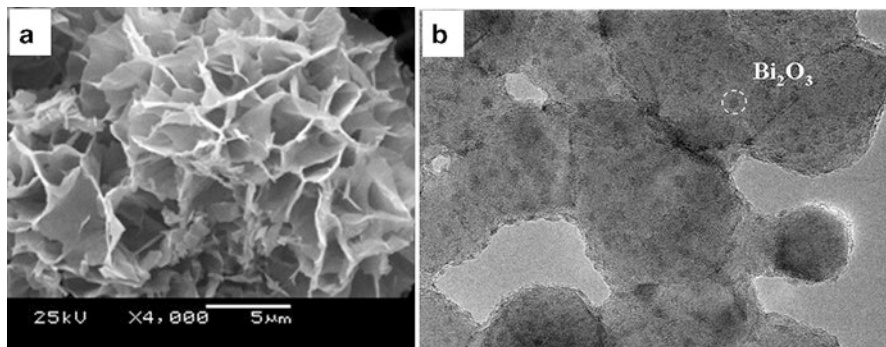


**Fig. 1.8** (a) SEM and (b) HRTEM images of the 3.3 % Bi<sub>2</sub>O<sub>3</sub>/TiO<sub>2</sub> sample. Adapted with permission from Ref. [36]. Copyright (2010) Elsevier B.V. All rights reserved

reflections within flower-like structure, the enhanced photosensitizing effect of Bi<sub>2</sub>O<sub>3</sub> quantum dots owing to their extremely small size strongly interacted with TiO<sub>2</sub>. Besides the high activity, the Bi<sub>2</sub>O<sub>3</sub>/TiO<sub>2</sub> also displays strong durability and could be reused for more than ten times, which could be attributed to both the high hydrothermal stability of the flower-like structure and the inhibition of Bi<sub>2</sub>O<sub>3</sub> leaching owing to its strong interaction with TiO<sub>2</sub> (Fig. 1.8).

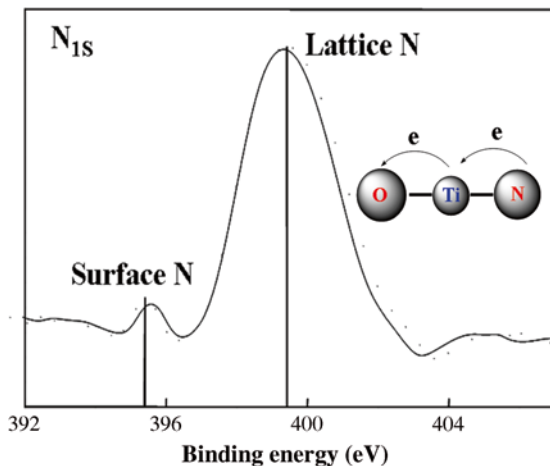
## 1.2 Supercritical Preparation of Doped TiO<sub>2</sub>

Doping TiO<sub>2</sub> with nitrogen [37–40], sulfur [41–43], fluorine [44, 45], carbon [46–48], and other elements has been frequently employed for achieving visible-light photocatalysts. Up to now, the doped TiO<sub>2</sub> photocatalysts are mainly synthesized through sol–gel route, chemical vapor deposition, spray pyrolysis, and ion implantation [49–54]. To ensure the incorporation of dopants into the TiO<sub>2</sub> lattice, all these processes should be conducted at high temperature, which inevitably limits dopant-loading and also lowers the surface area due to particle agglomeration and/or pore collapse [55, 56]. Preparation of doped TiO<sub>2</sub> photocatalysts under supercritical conditions could preserve the porous materials and high surface area in the precursor owing to the lack of surface tension [57]. Meanwhile, the high pressure and temperature under supercritical conditions may also enhance crystallization degree of anatase and promote the incorporation of dopants into the TiO<sub>2</sub> lattice [58, 59], leading to the high quantum efficiency.

### 1.2.1 N-Doped TiO<sub>2</sub>

The N-doped TiO<sub>2</sub> is prepared by treating TiO<sub>2</sub> gel precursor in NH<sub>3</sub>/EtOH fluid under supercritical conditions (SC), denoted as TiO<sub>2</sub>N(SC) [60]. Most N dopants in TiO<sub>2</sub>N(SC) are present in either O–Ti–N and/or N–Ti–N nitrides while only trace

**Fig. 1.9** XPS spectra of N1s in TiO<sub>2</sub>N(SC) sample (*inset* is plausible model of electron transfer)



are present in adsorbed N species (see XPS spectrum in Fig. 1.9). The TiO<sub>2</sub>N(SC) exhibits high activity owing to the high surface area, large pore volume, well-crystallized anatase, and strong absorbance of lights in a broad wavelength range. Furthermore, the electron-deficient nitrogen atoms in O–Ti–N nitrides could also account for the enhanced activity since it could inhibit the recombination between the photoelectrons and holes by capturing the photoelectrons.

### 1.2.2 S-Doped TiO<sub>2</sub>

S-doped TiO<sub>2</sub> is synthesized by treating the TiO<sub>2</sub> gel precursor under supercritical conditions in CS<sub>2</sub>/ethanol fluid [61]. The S-species incorporated into the TiO<sub>2</sub> network by forming S–Ti–O bonds (Scheme 1.1). As shown in Table 1.1, during liquid phase photocatalytic degradation of methylene blue (MB) under visible light irradiation (>420 nm), the as-prepared S-doped TiO<sub>2</sub> exhibits much higher activity than the undoped TiO<sub>2</sub> obtained via either supercritical treatment or direct calcinations. The activity of the S-doped TiO<sub>2</sub> strongly depends on the S-content and the maximum activity is achieved at S–Ti molar ratio of 1.8 %. Meanwhile, the S-doped TiO<sub>2</sub> shows higher activity than the N-doped TiO<sub>2</sub> obtained via supercritical treatment (Table 1.1). The promoting effects of both the supercritical treatment and S-modification on the photocatalytic activity are considered as the high surface, large porous channels, well-crystallized anatase, excellent thermal stability, and strong absorbance for visible lights, corresponding to the high quantum efficiency.

**Scheme 1.1** Plausible model of electron transfer in S–Ti–O bond

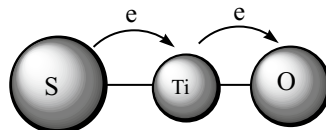


**Table 1.1** Structural parameters and photocatalytic activity of different samples

Sample	[CS <sub>2</sub> ] (M)	S <sub>BET</sub> (m <sup>2</sup> /g)	V <sub>p</sub> (cm <sup>3</sup> /g)	d <sub>p</sub> (nm)	Band gap (eV)	Degradation rate (%)
TiO <sub>2</sub> (DC)	0	21	0.031	5.7	3.2	7.0
TiO <sub>2</sub> (SC)	0	68	0.37	20	3.2	11.2
P25 TiO <sub>2</sub>	0	45	0.25	20	3.1	10.0
0.50 %TiO <sub>2</sub> -S(SC)	0.68	88	0.38	23	2.8	74.5
1.0 % TiO <sub>2</sub> -S(SC)	1.4	91	0.38	23	2.7	78.0
1.4 % TiO <sub>2</sub> -S(SC)	2.0	97	0.40	24	2.7	83.3
1.8 % TiO <sub>2</sub> -S(SC)	2.7	104	0.42	25	2.6	88.6
2.6 % TiO <sub>2</sub> -S(SC)	3.4	97	0.43	27	2.7	82.7
1.7 % TiO <sub>2</sub> -N(SC)	/	90	0.59	17	2.90	64.5

Reaction conditions: 0.050 g catalyst, 50 ml 0.01 g/l MB aqueous solution, three 150 W xenon lamps ( $\lambda > 420$  nm), 303 K, 3 h, 1000 rpm

### 1.2.3 N and F Co-doped TiO<sub>2</sub>

The N and F co-doped TiO<sub>2</sub> (TiO<sub>2-x-y</sub>N<sub>x</sub>F<sub>y</sub>) is prepared by treating the TiO<sub>2</sub> gel precursor in NH<sub>4</sub>F/ethanol fluid under supercritical conditions [62]. During the photocatalytic degradation of MB under visible light irradiation, the TiO<sub>2-x-y</sub>N<sub>x</sub>F<sub>y</sub> exhibits high activity owing to the synergetic promoting effects from the N- and F-dopants incorporated into the TiO<sub>2</sub> lattice via forming N–Ti–O and F–Ti–O bonds, corresponding to the enhanced surface acidic sites and spectral response in visible region (Fig. 1.10), together with the increased number of oxygen vacancies. Thus, the adsorption for both the reactant molecules and visible lights could be enhanced while the photoelectron–hole recombination rate could be reduced, leading to the enhanced quantum efficiency.

### 1.2.4 La-Doped TiO<sub>2</sub>

La-dopants exhibit significant improvement on both the photocatalytic activity and the thermal stability of TiO<sub>2</sub> [63, 64]. La-doped TiO<sub>2</sub> (La/TiO<sub>2</sub>) with optimum La/Ti molar ratio of 1.25 % is prepared by ultrasound-assisted sol–gel method, followed

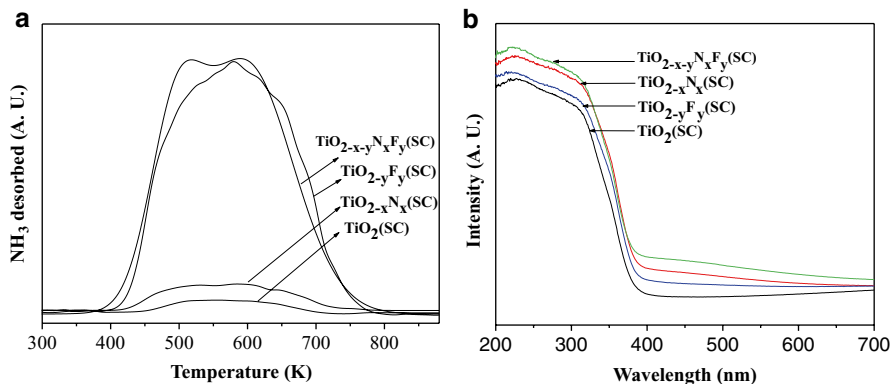


**Fig. 1.10** (a) NH<sub>3</sub>-TPD profiles of different samples and (b) UV-Vis DRS spectra of different samples

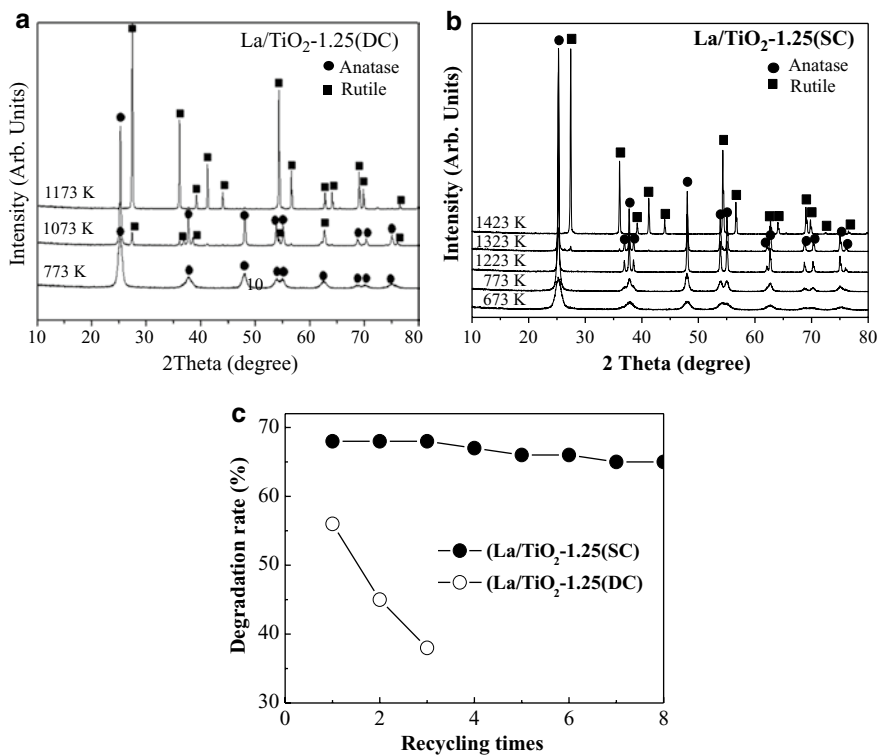


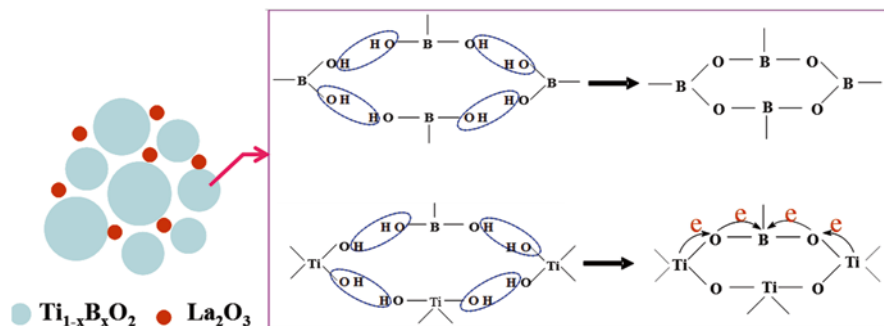
**Fig. 1.11** (a) XRD patterns of La/TiO<sub>2</sub>-1.25(DC) and (b) La/TiO<sub>2</sub>-1.25(SC) calcined at elevated temperatures. (c) Durability test. Reaction conditions: 0.050 g photocatalyst, 30 ml 0.10 g/l phenol aqueous solution, three 8 W lamps ( $\lambda=310$  nm), 303 K, 4 h, 1000 rpm

by supercritical drying the gel precursor in ethanol fluid [65]. Figure 1.11 reveals that the La/TiO<sub>2</sub>-1.25(SC) shows much higher thermal stability against the phase transformation from anatase to rutile than the La/TiO<sub>2</sub>-1.25(DC) obtained by direct calcinations since the presence of porous network structure achieved under

supercritical conditions might inhibit particle gathering. Meanwhile, the supercritical treatment might also strengthen the interaction between the La-dopants and the  $\text{TiO}_2$  network, leading to enhanced thermal stability. Figure 1.11 also shows that the  $\text{La}/\text{TiO}_2\text{-1.25(SC)}$  can be used repetitively for more than eight times without significant decrease in activity while the  $\text{La}/\text{TiO}_2\text{-1.25(DC)}$  loses 32 % activity even after being used for three times. According to ICP analysis, the deactivation of  $\text{La}/\text{TiO}_2\text{-1.25(DC)}$  is mainly attributed to the leaching off of the La-dopants (37.6 %). No significant leaching-off of La-dopants has been found in the  $\text{La}/\text{TiO}_2\text{-1.25(SC)}$  since supercritical treatment could enhance the interaction between  $\text{La}_2\text{O}_3$  and  $\text{TiO}_2$ .

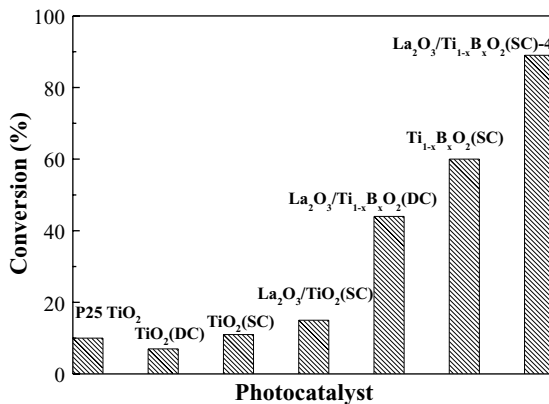
### 1.2.5 La and B Co-doped $\text{TiO}_2$

The supercritical treatment supplies a powerful way to incorporate B-dopants in the  $\text{TiO}_2$  lattice which is difficult to achieve via regular methods including sol-gel method. Herein, the  $\text{La}_2\text{O}_3/\text{Ti}_{1-x}\text{B}_x\text{O}_2$  is prepared under supercritical conditions in which the  $\text{La}_2\text{O}_3$  is present in a separate phase adsorbed by  $\text{TiO}_2$  while B-dopants are incorporated into  $\text{TiO}_2$  lattice via Ti-O-B bond (Scheme 1.2) [66]. During the degradation of MB under visible light irradiation, the as-prepared  $\text{La}_2\text{O}_3/\text{Ti}_{1-x}\text{B}_x\text{O}_2$  exhibits high activity (Fig. 1.12) owing to the synergetic promoting effects from



**Scheme 1.2** Formation of Ti-O-B bond and the electron transfer in  $\text{La}_2\text{O}_3/\text{Ti}_{1-x}\text{B}_x\text{O}_2(\text{SC})$  catalyst

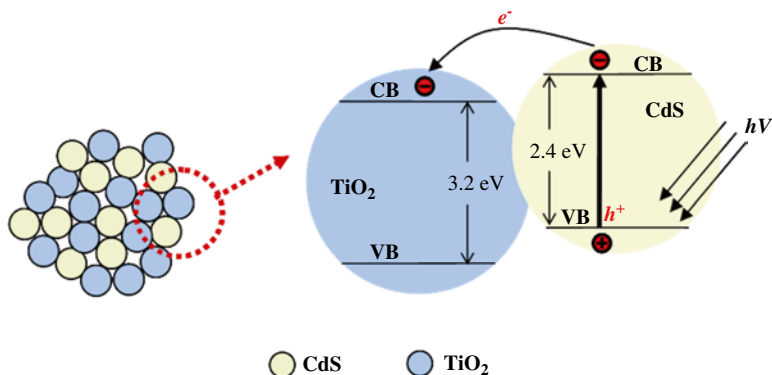
**Fig. 1.12** MB conversion rate of different photocatalysts. Reaction conditions: 0.050 g catalyst, 50 ml 0.010 g/l MB, three 150 W xenon lamps ( $\lambda > 420$  nm), 303 K, 3 h, 1000 rpm



the supercritical treatment, the  $\text{La}_2\text{O}_3$  and the B-dopant. The B-doping extended the light absorbance from UV to visible region owing to the formation of intermediate energy levels to narrow energy band gaps. While, the  $\text{La}_2\text{O}_3$  could enhance the surface area and also capture the photoelectrons to inhibit photoelectron–hole recombination. Furthermore, supercritical treatment results in the well crystallized anatase, the high surface area due to the presence of porous network structure, and the strong interactions of either the  $\text{La}_2\text{O}_3$  or the B-dopants with  $\text{TiO}_2$  which enhances the doping effect and also inhibits the dopant leaching during photocatalytic reactions.

### 1.2.6 $\text{TiO}_2$ –CdS Composite

The CdS distribution and its interaction with  $\text{TiO}_2$  play key roles in determining the photocatalytic performance of the CdS– $\text{TiO}_2$  [67, 68]. We prepare a CdS– $\text{TiO}_2$  composite by doping the  $\text{TiO}_2$  precursor with  $\text{Cd}^{2+}$  and in situ sulfurization in ethanol fluid containing  $\text{SC}(\text{NH}_3)_2$  under supercritical conditions [69]. The CdS acts as a photosensitizing agent in visible light area, while the  $\text{TiO}_2$  acts as an electron acceptor to separate the photoelectrons from holes in the CdS (Scheme 1.3). Under visible light irradiation, the as-prepared CdS– $\text{TiO}_2$  composite exhibits high activity in photocatalytic degradation of 4-chlorophenol (4-CP) owing to the high surface area, the high dispersion of CdS nanocrystals, and especially the strong interaction between CdS and  $\text{TiO}_2$  which greatly enhances the photosensitizing effect of CdS and also effectively inhibits the photoelectron–hole recombination. Meanwhile, the CdS– $\text{TiO}_2$  composite also displays strong durability since the strong CdS– $\text{TiO}_2$  interaction could efficiently protect the CdS from photo-corrosion and leaching off (see Fig. 1.13).



**Scheme 1.3** Illustration of electron transfer between CdS and  $\text{TiO}_2$  in the CdS– $\text{TiO}_2(\text{SC})$  composite

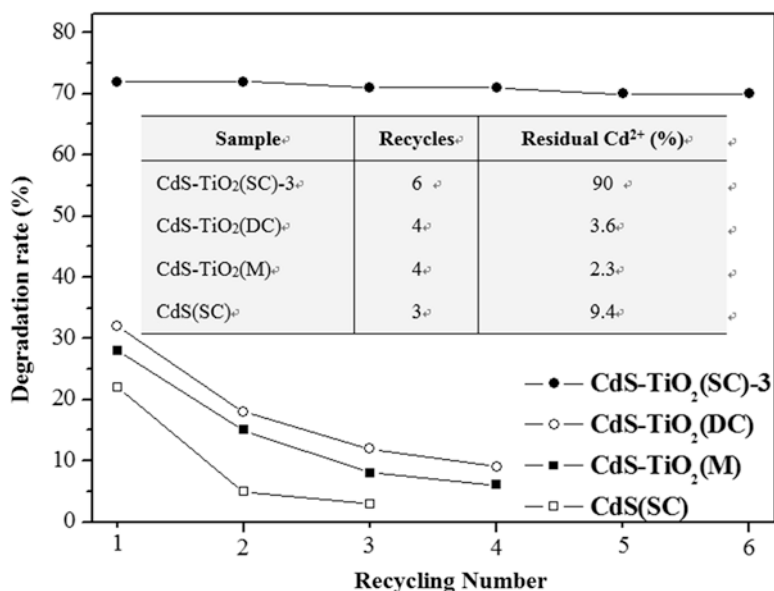


**Fig. 1.13** Recycling test of different photocatalysts and ICP analysis of residual Cd<sup>2+</sup> in used photocatalysts. Reaction conditions: 0.080 g photocatalyst, 50 ml 1.0×10<sup>-4</sup> M *p*-chlorophenol solution, a 500 W Xe lamp ( $\lambda > 420$  nm), 303 K, 6 h, 800 rpm

### 1.3 Conclusions

This chapter provides an overview of the solvothermal and supercritical fluid methods to synthesize pure and doped TiO<sub>2</sub> with hierarchical structure and morphologies. Their photocatalytic performances in mineralizing organic pollutants have been thoroughly examined, and the correlation of photocatalytic performance to either the structural or physical chemistry property has been explored based on the detailed characterizations and kinetic studies. The solvothermal alcoholysis supplies a platform to prepare TiO<sub>2</sub> and other oxide semiconductors with controllable structure and morphology owing to the smooth alcoholysis process, the structure-directing agent of alcohols, and the self-assembly induced by alcohol template. Meanwhile, the supercritical treatment offers a facile approach to prepare doped TiO<sub>2</sub> with uniform distribution of high-content dopants and the strong dopant-TiO<sub>2</sub> interaction, which could efficiently enhance the doping effect and inhibit the dopant leaching, leading to the enhanced photocatalytic activity and durability. We believe that, with the improvement and development of the above two technologies, new nanostructured materials could be synthesized, which may offer more opportunities for their applications in environmental cleaning, new energy production, energy storage, and drug delivery.

**Acknowledgement** This work was supported by NFSC (21261140333, 21237003, 21407106, 21207091, 21522703, 21577092), Shanghai government (14ZR1430800, 13SG44, 15520711300), and Program for Changjiang Scholars and Innovative Research Team in University (IRT1269) and International Joint Laboratory on Resource Chemistry (IJLRC). Research is also supported by The Program for Professor of Special Appointment (Eastern Scholar) at Shanghai Institutions of Higher Learning.

## References

1. Bach U, Lupo D, Comte P, Moser JE, Weissortel F, Salbeck J, Spreitzer H, Gratzel M (1998) Solid-state dye-sensitized mesoporous TiO<sub>2</sub> solar cells with high photon-to-electron conversion efficiencies. *Nature* 395:583–585
2. Chen C, Ma W, Zhao J (2010) Semiconductor-mediated photodegradation of pollutants under visible-light irradiation. *Chem Soc Rev* 39:4206–4219
3. Dai Y, Cobley CM, Zeng J, Sun Y, Xia Y (2009) Synthesis of anatase TiO<sub>2</sub> nanocrystals with exposed {001} facets. *Nano Lett* 9:2455–2459
4. Feng X, Shankar K, Varghese OK, Paulose M, Latempa TJ, Grimes CA (2008) Vertically aligned single crystal TiO<sub>2</sub> nanowire arrays grown directly on transparent conducting oxide coated glass: synthesis details and applications. *Nano Lett* 8:3781–3786
5. Liu G, Yang HG, Wang X, Cheng L, Pan J, Lu GQ, Cheng H-M (2009) Visible light responsive nitrogen doped anatase TiO<sub>2</sub> sheets with dominant {001} facets derived from TiN. *J Am Chem Soc* 131:12868–12869
6. Yang HG, Liu G, Qiao SZ, Sun CH, Jin YG, Smith SC, Zou J, Cheng HM, Lu GQ (2009) Solvothermal synthesis and photoreactivity of anatase TiO<sub>2</sub> nanosheets with dominant {001} facets. *J Am Chem Soc* 131:4078–4083
7. Zhu J, Yang J, Bian ZF, Ren H, Liu YM, Cao Y, Li HX, He HY, Fan KN (2007) Nanocrystalline anatase TiO<sub>2</sub> photocatalysts prepared via a facile low temperature nonhydrolytic sol-gel reaction of TiCl<sub>4</sub> and benzyl alcohol. *Appl Catal B* 76:82–91
8. Zhu H, Bian Z-F, Ren H, Liu Y-M, Cao Y, Li H-X, Dai W-L, He H-Y, Fan K-N (2007) An integrated low temperature approach to highly photoactive nanocrystalline mesostructured titania. *Catal Commun* 8:971–976
9. Zhu J, Wang S, Bian Z, Xie S, Cai C, Wang J, Yang H, Li H (2010) Solvothermally controllable synthesis of anatase TiO<sub>2</sub> nanocrystals with dominant {001} facets and enhanced photocatalytic activity. *CrystEngComm* 12:2219–2224
10. Caruso RA, Schattka JH, Greiner A (2001) Titanium dioxide tubes from sol-gel coating of electrospun polymer fibers. *Adv Mater* 13:1577–1579
11. Dinsmore AD, Hsu MF, Nikolaidis MG, Marquez M, Bausch AR, Weitz DA (2002) Colloidosomes: selectively permeable capsules composed of colloidal particles. *Science* 298:1006–1009
12. Mitchell DT, Lee SB, Trofin L, Li NC, Nevanen TK, Soderlund H, Martin CR (2002) Smart nanotubes for bioseparations and biocatalysis. *J Am Chem Soc* 124:11864–11865
13. Qi LM, Li J, Ma JM (2002) Biomimetic morphogenesis of calcium carbonate in mixed solutions of surfactants and double-hydrophilic block copolymers. *Adv Mater* 14:300–303
14. Afanasiev P, Bezverky I (2003) Genesis of vesicle-like and tubular morphologies in inorganic precipitates: amorphous Mo oxysulfides. *J Phys Chem B* 107:2678–2683
15. Guo CW, Cao Y, Xie SH, Dai WL, Fan KN (2003) Fabrication of mesoporous core-shell structured titania microspheres with hollow interiors. *Chem Commun* 6:700–701
16. Yang HG, Zeng HC (2004) Preparation of hollow anatase TiO<sub>2</sub> nanospheres via Ostwald ripening. *J Phys Chem B* 108:3492–3495
17. Yin YD, Rioux RM, Erdonmez CK, Hughes S, Somorjai GA, Alivisatos AP (2004) Formation of hollow nanocrystals through the nanoscale Kirkendall effect. *Science* 304:711–714

18. Li H, Bian Z, Zhu J, Zhang D, Li G, Huo Y, Li H, Lu Y (2007) Mesoporous titania spheres with tunable chamber structure and enhanced photocatalytic activity. *J Am Chem Soc* 129:8406–8407
19. Lv F, Xiao S, Zhu J, Li H (2014) Dye-sensitized solar cells with enhanced efficiency using hierarchical TiO<sub>2</sub> spheres as a scattering layer. *RSC Adv* 4:36206–36211
20. Gomathi A, Vivekchand SRC, Govindaraj A, Rao CNR (2005) Chemically bonded ceramic oxide coatings on carbon nanotubes and inorganic nanowires. *Adv Mater* 17:2757–2761
21. Shankar K, Basham JI, Allam NK, Varghese OK, Mor GK, Feng X, Paulose M, Seabold JA, Choi K-S, Grimes CA (2009) Recent advances in the use of TiO<sub>2</sub> nanotube and nanowire arrays for oxidative photoelectrochemistry. *J Phys Chem C* 113:6327–6359
22. Ohsaki Y, Masaki N, Kitamura T, Wada Y, Okamoto T, Sekino T, Niihara K, Yanagida S (2005) Dye-sensitized TiO<sub>2</sub> nanotube solar cells: fabrication and electronic characterization. *Phys Chem Chem Phys* 7:4157–4163
23. Tachikawa T, Tojo S, Fujitsuka M, Sekino T, Majima T (2006) Photoinduced charge separation in titania nanotubes. *J Phys Chem B* 110:14055–14059
24. Tsai CC, Teng HS (2004) Regulation of the physical characteristics of titania nanotube aggregates synthesized from hydrothermal treatment. *Chem Mater* 16:4352–4358
25. Chanmanee W, Watcharenwong A, Chenthamarakshan CR, Kajitvichyanukul P, de Tacconi NR, Rajeshwar K (2008) Formation and characterization of self-organized TiO<sub>2</sub> nanotube arrays by pulse anodization. *J Am Chem Soc* 130:965–974
26. Bian Z, Zhu J, Cao F, Huo Y, Lu Y, Li H (2010) Solvothermal synthesis of well-defined TiO<sub>2</sub> mesoporous nanotubes with enhanced photocatalytic activity. *Chem Commun* 46:8451–8453
27. Chen X, Mao SS (2007) Titanium dioxide nanomaterials: synthesis, properties, modifications, and applications. *Chem Rev* 107:2891–2959
28. Hong Z, Wei M, Lan T, Jiang L, Cao G (2012) Additive-free synthesis of unique TiO<sub>2</sub> mesocrystals with enhanced lithium-ion intercalation properties. *Energy Environ Sci* 5:5408–5413
29. Jiao W, Wang L, Liu G, Lu GQ, Cheng H-M (2012) Hollow anatase TiO<sub>2</sub> single crystals and mesocrystals with dominant {101} facets for improved photocatalysis activity and tuned reaction preference. *ACS Catal* 2:1854–1859
30. Bian Z, Zhu J, Wen J, Cao F, Huo Y, Qian X, Cao Y, Shen M, Li H, Lu Y (2011) Single-crystal-like titania mesocages. *Angew Chem Int Ed* 50:1105–1108
31. Zhu J, Wang J, Lv F, Xiao S, Nuckolls C, Li H (2013) Synthesis and self-assembly of photonic materials from nanocrystalline titania sheets. *J Am Chem Soc* 135:4719–4721
32. Zhu J, Ren J, Huo Y, Bian Z, Li H (2007) Nanocrystalline Fe/TiO<sub>2</sub> visible photocatalyst with a mesoporous structure prepared via a nonhydrolytic sol-gel route. *J Phys Chem C* 111:18965–18969
33. Bian Z, Ren J, Zhu J, Wang S, Lu Y, Li H (2009) Self-assembly of Bi<sub>x</sub>Ti<sub>1-x</sub>O<sub>2</sub> visible photocatalyst with core-shell structure and enhanced activity. *Appl Catal B* 89:577–582
34. Liu B, Zeng HC (2004) Fabrication of ZnO “dandelions” via a modified Kirkendall process. *J Am Chem Soc* 126:16744–16746
35. Bian Z, Zhu J, Cao F, Lu Y, Li H (2009) In situ encapsulation of Au nanoparticles in mesoporous core-shell TiO<sub>2</sub> microspheres with enhanced activity and durability. *Chem Commun* 25:3789–3791
36. Zhu J, Wang S, Wang J, Zhang D, Li H (2011) Highly active and durable Bi<sub>2</sub>O<sub>3</sub>/TiO<sub>2</sub> visible photocatalyst in flower-like spheres with surface-enriched Bi<sub>2</sub>O<sub>3</sub> quantum dots. *Appl Catal B* 102:120–125
37. Asahi R, Morikawa T, Ohwaki T et al (2001) Visible-light photocatalysis in nitrogen-doped titanium oxides. *Science* 293:269–271
38. Choi H, Antoniou MG, Pelaez M et al (2007) Mesoporous nitrogen-doped TiO<sub>2</sub> for the photocatalytic destruction of the cyanobacterial toxin microcystin-LR under visible light irradiation. *Environ Sci Technol* 41:7530–7535
39. Chen C, Bai H, Chang C (2007) Effect of plasma processing gas composition on the nitrogen-doping status and visible light photocatalysis of TiO<sub>2</sub>. *J Phys Chem C* 111:15228–15235

40. Kitano M, Funatsu K, Matsuoka M et al (2006) Preparation of nitrogen-substituted TiO<sub>2</sub> thin film photocatalysts by the radio frequency magnetron sputtering deposition method and their photocatalytic reactivity under visible light irradiation. *J Phys Chem B* 110:25266–25727
41. Tian FH, Liu CB (2006) DFT description on electronic structure and optical absorption properties of anionic S-doped anatase TiO<sub>2</sub>. *J Phys Chem B* 110:17866–17871
42. Wang J, Zhang Q, Yin S et al (2007) Raman spectroscopic analysis of sulphur-doped TiO<sub>2</sub> by co-grinding with TiS<sub>2</sub>. *J Phys Chem Solids* 68:189–192
43. Ho W, Yu JC, Lee S (2006) Low-temperature hydrothermal synthesis of S-doped TiO<sub>2</sub> with visible light photocatalytic activity. *J Solid State Chem* 179:1171–1176
44. Park JS, Choi W (2004) Enhanced remote photocatalytic oxidation on surface-fluorinated TiO<sub>2</sub>. *Langmuir* 20:11523–11527
45. Yu JC, Yu JG, Ho WK et al (2002) Effects of F-doping on the photocatalytic activity and microstructures of nanocrystalline TiO<sub>2</sub> powders. *Chem Mater* 14:3808–3816
46. Park JH, Kim S, Bard AJ (2006) Novel carbon-doped TiO<sub>2</sub> nanotube arrays with high aspect ratios for efficient solar water splitting. *Nano Lett* 6:24–28
47. Ren WJ, Ai ZH, Jia FL et al (2007) Low temperature preparation and visible light photocatalytic activity of mesoporous carbon-doped crystalline TiO<sub>2</sub>. *Appl Catal B* 69:138–144
48. Wu GS, Nishikawa T, Ohtani B et al (2007) Synthesis and characterization of carbon-doped TiO<sub>2</sub> nanostructures with enhanced visible light response. *Chem Mater* 19:4530–4537
49. Bacsa R, Kiwi J, Ohno T et al (2005) Preparation, testing and characterization of doped TiO<sub>2</sub> active in the peroxidation of biomolecules under visible light. *J Phys Chem B* 109:5994–6003
50. Chen XF, Wang XC, Hou YD et al (2008) The effect of postnitridation annealing on the surface property and photocatalytic performance of N-doped TiO<sub>2</sub> under visible light irradiation. *J Catal* 255:59–67
51. Guo Y, Zhang XW, Han GR (2006) Investigation of structure and properties of N-doped TiO<sub>2</sub> thin films grown by APCVD. *Mater Sci Eng B* 135:83–87
52. Li D, Haneda H, Hishita S et al (2005) Visible-light-driven N-F-codoped TiO<sub>2</sub> photocatalysts. 1. Synthesis by spray pyrolysis and surface characterization. *Chem Mater* 17:2588–2595
53. Li D, Haneda H, Hishita S, Ohashi N et al (2005) Fluorine-doped TiO<sub>2</sub> powders prepared by spray pyrolysis and their improved photocatalytic activity for decomposition of gas-phase acetaldehyde. *J Fluorine Chem* 126:69–77
54. Borras A, Lopez C, Rico V et al (2007) Effect of visible and UV illumination on the water contact angle of TiO<sub>2</sub> thin films with incorporated nitrogen. *J Phys Chem C* 111:1801–1808
55. Watanabe K, Menzel D, Nilius N et al (2006) Photochemistry on metal nanoparticles. *Chem Rev* 106:4301–4320
56. Thompson TL, Yates JT (2006) Surface science studies of the photoactivation of TiO<sub>2</sub>- new photochemical processes. *Chem Rev* 106:4428–4453
57. Gourinchas-Courtecuise V, Bocquet F, Chhor K et al (1996) Modeling of a continuous reactor for TiO<sub>2</sub> powder synthesis in a supercritical fluid - experimental validation. *J Supercritical Fluids* 9:222–226
58. An GM, Ma WH, Sun ZY et al (2007) Preparation of titania/carbon nanotube composites using supercritical ethanol and their photocatalytic activity for phenol degradation under visible light irradiation. *Carbon* 45:1795–1801
59. Aymonier C, Loppinet-Serani A, Reveron H et al (2006) Review of supercritical fluids in inorganic materials science. *J Supercritical Fluids* 38:242–251
60. Li HX, Li JX, Huo YN (2006) Highly active TiO<sub>2</sub>N photocatalysts prepared by treating precursors in NH<sub>3</sub>/EtOH fluid under supercritical conditions. *J Phys Chem B* 110:1559–1565
61. Li HX, Zhang XY, Huo YN et al (2007) Supercritical preparation of a highly active S-doped TiO<sub>2</sub> photocatalyst for methylene blue mineralization. *Environ Sci Technol* 41:4410–4414
62. Huo YN, Jin Y, Zhu J et al (2009) Highly active TiO<sub>2-x-y</sub>N<sub>x</sub>F<sub>y</sub> visible photocatalyst prepared under supercritical conditions in NH<sub>4</sub>F/EtOH fluid. *Appl Catal B* 89:543–550
63. Wu XH, Ding XB, Qin W et al (2006) Enhanced photo-catalytic activity of TiO<sub>2</sub> films with doped La prepared by micro-plasma oxidation method. *J Hazard Mater* 137:192–197

64. Yuan S, Sheng QR, Zhang JL et al (2005) Synthesis of  $\text{La}^{3+}$  doped mesoporous titania with highly crystallized walls. *Microporous Mesoporous Mater* 79:93–99
65. Huo YN, Zhu J, Li JX et al (2007) An active  $\text{La}/\text{TiO}_2$  photocatalyst prepared by ultrasonication-assisted sol-gel method followed by treatment under supercritical conditions. *J Mol Catal A* 278:237–243
66. Huo YN, Zhang XY, Jin Y et al (2008) Highly active  $\text{La}_2\text{O}_3/\text{Ti}_{1-x}\text{B}_x\text{O}_2$  visible light photocatalysts prepared under supercritical conditions. *Appl Catal B* 83:78–84
67. Yu J C, Wu L, Lin J et al (2003) Microemulsion-mediated solvothermal synthesis of nanosized CdS-sensitized  $\text{TiO}_2$  crystalline photocatalyst. *Chem Commun* 13:1552–1553
68. Wu L, Yu JC, Fu XZ (2006) Characterization and photocatalytic mechanism of nanosized CdS coupled  $\text{TiO}_2$  nanocrystals under visible light irradiation. *J Mol Catal A* 244:25–32
69. Huo YN, Yang XL, Zhu J et al (2011) Highly active and stable CdS- $\text{TiO}_2$  visible photocatalyst prepared by in-situ sulfurization under supercritical conditions. *Appl Catal B* 106:69–75

# Chapter 2

## TiO<sub>2</sub>/Graphene Composites with Excellent Performance in Photocatalysis

Mingyang Xing, Bocheng Qiu, Xiao Li, and Jinlong Zhang

### 2.1 Introduction

Since Fujishima and Honda in 1972 found that the TiO<sub>2</sub> electrodes could produce H<sub>2</sub> under light irradiation [1], TiO<sub>2</sub> has become one of the most promising oxide semiconductors which has been employed in diverse applications including air and waste water purifiers, solar energy cells and sensors [2–6]. The discovery of the phenomenon of photocatalytic splitting of water on TiO<sub>2</sub> electrodes indicates the coming of a new era of heterogeneous photocatalysis. Though TiO<sub>2</sub> has many advantages such as high photostability, non-toxicity, low cost, high activity, and so on [7–9], and its research in the field of photocatalysis also has made a great progress in recent years, TiO<sub>2</sub> applications in heterogeneous photocatalysis has many limitations that cannot be neglected. For instance, the photon flux of TiO<sub>2</sub> in the process of photoreaction under weaker light irradiation is very easy to be saturated, which will significantly reduce the energy efficiency of the whole process of waste water purification [10–17]. In addition, the largest application limitations of TiO<sub>2</sub> lies in the mismatching between its bandgap energy and the sunlight spectrum, that is, the TiO<sub>2</sub> can only absorb UV light less than 387 nm wavelength [18]. Thereby, TiO<sub>2</sub> photocatalytic technology can only effectively utilize less than 6 % of the energy derived from the sunlight incident to the earth's surface, which suggests its low potential of sustainable development in photocatalysis.

In order to overcome the abovementioned drawbacks, many modifications have been done on TiO<sub>2</sub> such as nonmetal doping [10, 19–22], metal doping [12, 14, 16, 23–27], semiconductor compound modification [28–35], and organic

---

M. Xing • B. Qiu • X. Li • J. Zhang (✉)

Key Laboratory for Advanced Materials and Institute of Fine Chemicals,  
East China University of Science and Technology,  
130 Meilong Road, Shanghai 200237, People's Republic of China  
e-mail: [jlzhang@ecust.edu.cn](mailto:jlzhang@ecust.edu.cn)

photosensitization [22, 36]. However, the traditional metal or nonmetal ions doped into  $\text{TiO}_2$  will lead to decrease of thermal stability of crystals, and introduce traps to capture the photogenerated carriers on the catalyst surface or in the bulk of catalysts, which can produce a large number of electron–hole recombination centers [16]. A visible light responsive carbon material introduced in  $\text{TiO}_2$  is considered as a useful way to improve its photocatalytic activity.

Compared with some other carbon materials such as nanotubes and fullerenes, graphene as a super star in the material science has attracted much more attention in the past several years, owing to its relative high surface area, excellent mechanical property, outstanding electronic conductivity, special photoelectrochemical property, and controllable bandgap [37–40]. These properties determine its large potential applications in electrochemistry and photocatalysis. On the other side, graphene can also potentially act as a support material, allowing semiconductor particles such as  $\text{TiO}_2$  to anchor on its surface. Recently, the application of graphene in the electrochemical modification on  $\text{TiO}_2$  has become a hot spot in the field of photocatalysis [41–46]. The compounding between graphene and  $\text{TiO}_2$  makes the successful connection between nanometer modules with excellent properties, greatly improving the transmission efficiency of optical carriers. Undoubtedly, the design and preparation of a series of new type of efficient  $\text{TiO}_2$ /graphene photocatalyst with an excellent performance is a new focus in photocatalysis for the degradation of organic pollutants and energy development.

In this chapter, we plan to give a short overview of the recent research progress of  $\text{TiO}_2$ /graphene in photocatalysis. The preparation, characterization and application of this functional composite are the major focus of the review. In addition to the traditional two dimensional (2D) graphene based composite, the burgeoning composite of three dimensional (3D) graphene composited with  $\text{TiO}_2$  is also the discussion focus, owing to its unique nature in photocatalysis.

## 2.2 Two Dimensional $\text{TiO}_2$ /Graphene Composite

Although the 2D-graphene has been widely used as a support for the preparation of semiconductor/graphene composites several decades ago, the  $\text{TiO}_2$ /graphene was firstly used in photocatalysis for photodegradation of methylene blue (MB) until 2009, which was reported by Li and his coworkers [47]. They successfully synthesized a chemically bonded  $\text{TiO}_2$ -graphene composite with 2D-graphene and nano-sized P25 by using a facile hydrothermal method. The reduction of graphene oxide and the loading of P25 on the surface of graphene could be achieved at the same time by a one-step hydrothermal process. The as-prepared  $\text{TiO}_2$ /graphene photocatalyst exhibited extending light absorption range, excellent adsorption of MB, and efficient photocatalytic activity, which was indeed rarely reported in other  $\text{TiO}_2$ /carbon materials at that time. From then on, many researchers have been reported many kinds of  $\text{TiO}_2$ /graphene composites by using different methods and used them in photocatalysis for the degradation of organic pollutants, water splitting, and  $\text{CO}_2$

photoreduction. We would like to summarize the research work on the 2D-structured TiO<sub>2</sub>/graphene photocatalysts, as shown in Table 2.1. The Table 2.1 includes the preparation methods, the characterization methods and the applications of 2D TiO<sub>2</sub>/graphene in photocatalysis. In the following sections, we will give the detail introduction and discussion of TiO<sub>2</sub>/graphene composites according to the Table 2.1.

## 2.2.1 Preparations

Chemical technology is an important method for the preparation of nanocomposites, which suggests some chemical reactions included in the process of preparation. According to the reports, the 2D-structured TiO<sub>2</sub>/graphene with varies morphologies could be synthesized by different methods, such as hydrothermal, mechanical mixing, pyrolysis, sol–gel, CVD, UV light irradiation, microwave, vacuum activation, and so on. In addition, some further modifications also could been done on these composites such as impurities doping to improve the visible light photocatalytic activity. Table 2.1 collects a summary of experimental details regarding the preparation of the composites together with some characterizations on their structural, textural, and chemical properties.

### 2.2.1.1 Hydrothermal

The hydrothermal method involves reactions under controlled temperature and/or pressure, and is usually performed in stainless steel autoclaves. When graphene oxide (GO)–TiO<sub>2</sub> composites are obtained by this method, GO is partially reduced yielding (reduced graphene oxide) RGO or GR, or in some cases, graphene sheets if some chemical reagent was added such as hydrazine and NaBH<sub>4</sub>. Additionally, changes in the crystalline phase or microstructure of TiO<sub>2</sub> are generally observed.

As we describe above, in 2009, Prof. Jinghong Li and his coworkers employed a simple hydrothermal method to successfully prepare a P25-graphene composite with excellent visible light photocatalytic activity [47]. One step hydrothermal treatment could achieve the loading of TiO<sub>2</sub> nanoparticles on the surface of graphene and the reduction of graphene oxide at one time. Liang et al. [48] used the GO as the substrates for the TiO<sub>2</sub> growth to obtain a TiO<sub>2</sub>/GO hybrid. Seen from the reaction scheme in Fig. 2.1a, the functional groups of hydroxyl and carboxyl on GO provided reactive and anchoring sites for nucleation and growth of nanomaterials. The authors described the reaction process as two steps. In the first step reaction, amorphous TiO<sub>2</sub> nanoparticles were coated on the surface of GO sheets by the hydrolysis of Ti(BuO)<sub>4</sub> with H<sub>2</sub>SO<sub>4</sub> in a EtOH/H<sub>2</sub>O mixed solvent at 80 °C, which was designed to slow down the hydrolysis reaction. This would lead to selective growth of TiO<sub>2</sub> on GO to eliminate the free growth of TiO<sub>2</sub> nanoparticles in the solution. Rapid hydrolysis occurred when only water was used as the solvent or in the absence of H<sub>2</sub>SO<sub>4</sub>, in which most of the TiO<sub>2</sub> particles grown in the solution

**Table 2.1** Summary of preparation of TiO<sub>2</sub>/graphene composites and applications in photocatalysis

Synthesis method	Type of catalyst	Precursor	Characterizations	Photocatalytic targets and light source	Ref.
Hydrothermal	P25-graphene	Distilled H <sub>2</sub> O + ethanol, P25, GO	TEM, XRD, FTIR, UV-DRS and EIS measurements	Methylene blue, UV and visible light ( $\lambda > 400$ nm)	[47]
	P25-GR	Distilled H <sub>2</sub> O + ethanol, P25, GO	TEM, XRD, ESR, UV-DRS	Benzene/Methylene blue, UV light (~254 nm) and visible light ( $\lambda > 400$ nm)	[46]
	Graphene/TiO <sub>2</sub>	Water/DMF, TiO <sub>2</sub> nanocrystals, GO	AFM, SEM, TEM, XRD	Methylene blue/Rhodamine B, UV light	[48]
	Graphene-TiO <sub>2</sub> NPs (spheres)	TiO <sub>2</sub> spheres, ethanol, 3-aminopropyl-trimethoxysilane (APTMS), GO	SEM, TEM, XRD, UV-DRS, AFM, Raman, Photocurrent measurement	Methylene blue, visible light ( $\lambda > 420$ nm)	[49]
	Ti <sup>3+</sup> -TiO <sub>2</sub> (nanorods)/B-graphene	TiO <sub>2</sub> nanorods, H <sub>2</sub> O, NaBH <sub>4</sub> , GO	FESEM, TEM, XRD, XPS	Simulated solar light and visible light ( $\lambda > 420$ nm)	[23]
	P25-RGO-hydrothermal serials	Distilled H <sub>2</sub> O + ethanol, P25, GO	XRD, XPS, TEM, FT-IR, Raman, UV-DRS	Photocatalytic H <sub>2</sub> evolution, 200 W Xe arc lamp	[50]
	TiO <sub>2</sub> /MG composites	Ti(OC <sub>4</sub> H <sub>9</sub> ) <sub>4</sub> , MoS <sub>2</sub> /graphene, ethanol + H <sub>2</sub> O,	TEM, Raman, SEM, XRD, BET, XPS, UV-DRS, photocurrent measurement	Photocatalytic H <sub>2</sub> evolution, UV light	[51]
	Graphene/TiO <sub>2</sub> composite	Distilled H <sub>2</sub> O + ethanol, TiO <sub>2</sub> nanosheets, GO	SEM, TEM, Raman, XRD, BET, XPS, UV-DRS, PL, Photocurrent measurement	Photocatalytic H <sub>2</sub> evolution, UV light	[52]
	Graphene@TiO <sub>2</sub> nanocomposites	(NH <sub>4</sub> ) <sub>2</sub> TiF <sub>6</sub> + distilled H <sub>2</sub> O	SEM, TEM, XRD, XPS, TGA, FT-IR,	Photocatalytic H <sub>2</sub> evolution, 300 W Xe arc lamp	[53]
	(rGO)-TiO <sub>2</sub> hybrid nanocrystals	TBT, EG, HAc, GO	TEM, XRD, FT-IR, Raman	CO <sub>2</sub> photoreduction, visible light (15 W energy-saving daylight bulb)	[54]
	TiO <sub>2</sub> -graphene 2D sandwich-like hybrid nanosheets	Binary ethylenediamine (En)/H <sub>2</sub> O, titanium (IV) (ammonium lactato) dihydroxybis, GO	TEM, XRD, XPS, UV-DRS, photocurrent measurements	CO <sub>2</sub> photoreduction, 300 W xenon arc lamp	[55]

Synthesis method	Type of catalyst	Precursor	Characterizations	Photocatalytic targets and light source	Ref.
Mechanical mixing	P25/GO/Pt hybrid photocatalysts	Distilled H <sub>2</sub> O + ethanol, Pt/P25, GO	TEM, XRD, XPS, TGA, FT-IR, Raman	Photocatalytic H <sub>2</sub> evolution, 300 W Xe arc lamp	[56]
	P25/B-GR	B-GR, P25, ultraphonic and vigorous stirring	TEM, XRD, XPS, photocurrent measurement	Methyl orange/CO <sub>2</sub> photoreduction, simulated solar light	[57]
	GO-TiO <sub>2</sub> NRCs	TiO <sub>2</sub> Nanorods, H <sub>2</sub> O + toluene	TEM, XRD, XPS, TGA, FT-IR, Raman, PL	Methylene blue, UV light irradiation ( $\lambda=254$ nm)	[58]
	P25/graphene composite	Distilled H <sub>2</sub> O, P25, GO (300 °C for 2 h under argon atmosphere)	FT-IR, TEM, UV-DRS, XPS, BET, photocurrent measurement	A 250 W high pressure mercury lamp ( $\lambda>400$ nm)	[59]
Pyrolysis method	G <sub>n</sub> -TiO <sub>2</sub> /MCM-41	2,3-Dihydroxynaphthalene (DN)-TiO <sub>2</sub> /MCM-41, heat treatment for carbonization at 1073 K under a N <sub>2</sub> flow	XRD, TEM, Raman, BET, UV-DRS	Degradation of 2-propanol, UV light	[60]
	Graphene oxide/TiO <sub>2</sub> composites	Sodium dodecylsulfate + H <sub>2</sub> O, TiCl <sub>3</sub> , Na <sub>2</sub> SO <sub>4</sub> , H <sub>2</sub> O <sub>2</sub> (90 °C)	TEM, XRD, XPS, AFM, Raman	Methyl orange, 1000 W xenon lamp ( $\lambda>400$ nm)	[42]
	TiO <sub>2</sub> /graphene composites	TiF <sub>4</sub> + H <sub>2</sub> O, (60 °C for 20 h)	XRD, TEM, TG-DTG, AFM, BET, XPS, Raman	Methyl orange, UV light	[61]

(continued)

**Table 2.1** (continued)

Synthesis method	Type of catalyst	Precursor	Characterizations	Photocatalytic targets and light source	Ref.
Sol-gel	Graphite oxide/TiO <sub>2</sub> composites	GO + (NH <sub>4</sub> ) <sub>2</sub> TiF <sub>6</sub> + H <sub>3</sub> BO <sub>3</sub> , heated at 60 °C, and then treated at 200 °C	SEM, TEM, XRD, XPS, TGA, AFM, BET, Raman, PL	Photocatalytic reduction of Cr(VI)/methyl orange, UV light	[62]
	Rutile TiO <sub>2</sub> -FGS hybrid materials	Graphene + sodium dodecyl sulfate + TiCl <sub>3</sub> + H <sub>2</sub> O <sub>2</sub> , heated at 90 °C, and calcined in static air at 400 °C	XRD, TEM, SEM, TGA		[43]
	Graphene Oxide/TiO <sub>2</sub> Composites	GO + sodium dodecylsulfate + TiCl <sub>3</sub> + Na <sub>2</sub> SO <sub>4</sub> + H <sub>2</sub> O <sub>2</sub> , heated at 90 °C, and calcined in the air at 400 °C	TEM, XRD, XPS, AFM, BET, Raman, UV-DRS	Methyl orange, 1000 W xenon lamp and a cutoff filter (>400 nm)	[42]
	TiO <sub>2</sub> -RGO	GO + H <sub>2</sub> O + TiF <sub>4</sub> , heated at 60 °C, + hydrazine hydrate, warmed to 100 °C and heated for 24 h	XRD, SEM, TEM, BET, TGA/DTA, Raman, DLS and Zeta potential measurement		[63]
	TiO <sub>2</sub> -graphene oxide	GO + sodium hydroxide, Ti(SO <sub>4</sub> ) <sub>2</sub> + H <sub>2</sub> SO <sub>4</sub> , heated at 80 °C	XRD, SEM, TEM, XPS, TGA	Methyl orange, UV light	[64]
	Graphene sheets (GSs) composites	TBOT + GO + ethanol + sodium borohydride, heated at 450 °C	XRD, Raman, TEM, XPS, UV-DRS	Photocatalytic H <sub>2</sub> evolution, UV-Vis light	[65]
UV light reduction	Nanosized GO-coated TiO <sub>2</sub> nanoparticles (NGOTs)	H <sub>2</sub> O, P25 + 200 W mercury lamp irradiation reduction	FT-IR, TEM, UV-DRS, Photoelectrochemical (PEC) measurements	Photocatalytic H <sub>2</sub> evolution, 300 W Xe arc lamp ( $\lambda > 320$ nm)	[66]
	TiO <sub>2</sub> -reduced graphene oxide	Ethanol + TiO <sub>2</sub> nanoparticles, 250 W high pressure Hg lamp	XRD, XPS, SEM, BET, UV-DRS	Photodecomposition of Sarin, Black light (150 W, center wavelength 364 nm)	[67]
	TiO <sub>2</sub> /graphene oxide sheets	Ethanol + TiO <sub>2</sub> nanoparticles, 110 mW/cm <sup>2</sup> mercury lamp (peak wavelengths at 275, 350, and 660 nm) irradiation	TEM, XPS, AFM, Raman		[68]
	RGO-TiO <sub>2</sub>	TiO <sub>2</sub> suspension + GO + methanol, purged with N <sub>2</sub> and exposed to UV-irradiation	SEM, TEM, UV-DRS	Photocatalytic degradation of 2,4-dichlorophenoxyacetic acid, UV light	[69]

Synthesis method	Type of catalyst	Precursor	Characterizations	Photocatalytic targets and light source	Ref.
Chemical vapor deposition (CVD)	Graphene-TiO <sub>2</sub> nanocomposites	Reactive magnetron sputtering	UV-DRS, AFM, XPS, Raman, PL	Methanol photooxidation, UV light	[70]
Microwave synthesis	TiO <sub>2</sub> -reduced graphene oxide composites	Tetrabutyl titanate + ethanol + acetic acid + H <sub>2</sub> O, heated at 500 °C, treated at 150 °C with microwave irradiation power of 150 W for 10 min	AFM, SEM, TEM, FTIR, XRD, PL	Photocatalytic reduction of Cr(VI), UV light	[71]
	CdS-TiO <sub>2</sub> -RGO	GO, CdCl <sub>2</sub> + Na <sub>2</sub> S + P25, an automated focused microwave system and irradiated at 150 °C under the power of 100 W for 10 min	SEM, TEM, BET, XRD, UV-DRS	Methyl orange, visible light ( $\lambda > 400$ nm)	[72]
	GO-TiO <sub>2</sub> hybrids (GTHs)	Tetra-n-butyl titanate + isopropyl alcohol + GO, nitric acid + urea, a domestic microwave oven	TEM, Raman, FTIR, PL, BET, XRD, UV-DRS	Methyl orange, UV light	[73]
Microwave-hydrothermal	Au-TiO <sub>2</sub> -graphene	Distilled H <sub>2</sub> O + ethanol, P25, GO, HAuCl <sub>4</sub> solution	SEM, TEM, BET, XPS, Raman, XRD, UV-DRS	Photocatalytic H <sub>2</sub> -production, Four low-power 420 nm LEDs (3 W)	[74]
Vacuum activation	Ti <sup>3+</sup> self-doped TiO <sub>2</sub> -graphene nanosheet composites	P25 + GO, heated in vacuum at 300 °C for 3 h	XRD, TEM, XPS, EPR, UV-DRS, IPCE	Methyl orange, visible light ( $\lambda > 420$ nm); Photocatalytic hydrogen evolution, , 300 W Xenon arc lamp light ( $\lambda > 400$ nm)	[75]

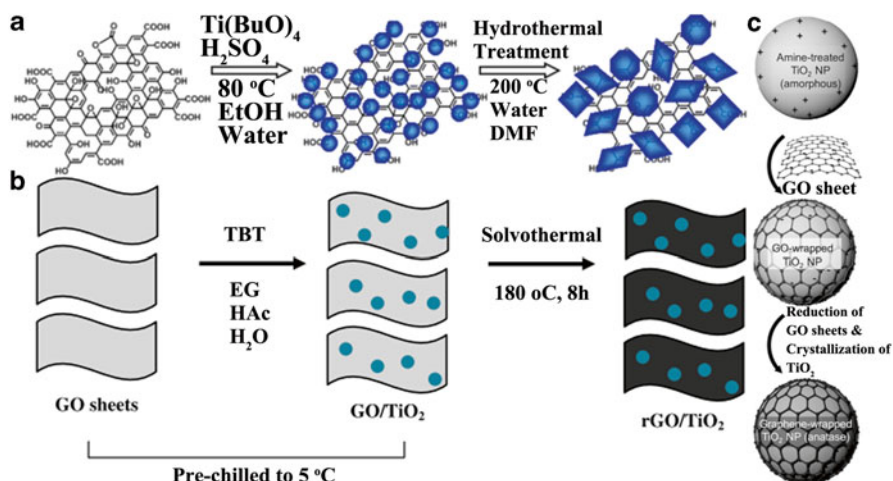


**Fig. 2.1** (a) Synthesis schemes of  $\text{TiO}_2$  nanocrystals on GO sheets [48]. Copyright 2010 Tsinghua University Press and Springer-Verlag Berlin Heidelberg. (b) Procedure for the synthesis of rGO- $\text{TiO}_2$  nanocomposites [54]. Copyright 2013 Tan et al. licensee Springer. (c) Synthesis steps of graphene-wrapped  $\text{TiO}_2$  NPs. Reproduced from Ref. [49] with permission of John Wiley & Sons, Inc.

rather than associated with GO was observed. In the second step, they carried out a hydrothermal treatment of the amorphous  $\text{TiO}_2/\text{GO}$  at 200 °C in a mixture of water/DMF, which induced the crystallization of the coating  $\text{TiO}_2$  on GO into anatase nanocrystals. Fan et al. [50] have done a comparison between  $\text{TiO}_2/\text{graphene}$  composites prepared by different technologies including UV-assisted photocatalytic reduction, hydrazine reduction, and hydrothermal method. They found the incorporation of RGO into P25 could be controlled by the preparation method, which significantly enhanced the photocatalytic activity of P25-RGO, and the composite prepared by the hydrothermal method exhibited the best performance of  $\text{H}_2$  evolution. Tan et al. [54] fabricated reduced graphene oxide (rGO)- $\text{TiO}_2$  hybrid nanocrystals through a hydrothermal method. Slow hydrolysis reaction was successfully attained through the use of ethylene glycol and acetic acid mixed solvents coupled with an additional cooling step. As shown in Fig. 2.1b, in the preparation, the TBT can be readily grafted onto the surface of GO through chemical adsorption at the molecular level, owing to the rich assortment of oxygen-containing groups, such as epoxide, hydroxyl, carbonyl, and carboxylic groups on graphene surface. EG and HAc were introduced into the mixture to co-control the hydrolysis rate of TBT. Furthermore, the mixtures were prechilled in an ice bath to further reduce the hydrolysis rate, which would hinder the agglomeration of the  $\text{TiO}_2$  nanoparticles on the graphene. During the hydrothermal process, the reduction of GO and the loading of  $\text{TiO}_2$  nanoparticles on the rGO surface were occurring simultaneously.

Besides to the  $\text{TiO}_2$  nanoparticles,  $\text{TiO}_2$  spheres were also compounded with the graphene by a hydrothermal method to prepare a core-shell like  $\text{TiO}_2/\text{graphene}$

composites by Park and his coworkers [49]. Schematic illustration of synthesis steps for graphene-wrapped anatase TiO<sub>2</sub> NPs are shown in Fig. 2.1c. Graphene-anatase TiO<sub>2</sub> hybrid NPs by wrapping amorphous TiO<sub>2</sub> NPs with GO was synthesized by using APTMS modified TiO<sub>2</sub> spheres as the precursor, followed by a one-step GO reduction and TiO<sub>2</sub> crystallization via a hydrothermal treatment. In this preparation, the key is that the surface of amorphous TiO<sub>2</sub> NPs was modified by the APTMS, which could ensure the wrapping of GO nanosheets on the TiO<sub>2</sub> spheres. The connection between TiO<sub>2</sub> and GO is an electrostatic interaction through the linker of APTMS.

The design and morphological control on crystal facets of anatase TiO<sub>2</sub> is considered as an effect way to optimize its photocatalytic performance. Hence, some researchers pay attention on the synthesis of graphene@TiO<sub>2</sub> single crystals exposed with high energy facets. For instance, Wang et al. [53] found a facile and simple method to synthesize graphene@TiO<sub>2</sub> nanocomposites with controlled crystal facets by a one-pot hydrothermal process. (NH<sub>4</sub>)<sub>2</sub>TiF<sub>6</sub> and GO were used as the starting materials. Graphene@TiO<sub>2</sub> composites with controlled crystal facets can be easily obtained by controlling the concentrations of (NH<sub>4</sub>)<sub>2</sub>TiF<sub>6</sub> in the precursor solutions and the reaction times.

Recently, molybdenum disulfide (MoS<sub>2</sub>) with a layered structure has been widely investigated as a promising electrocatalyst or cocatalyst instead of noble metals for the H<sub>2</sub> evolution [51, 76]. The introduction of MoS<sub>2</sub> in photocatalysis system of 2D-structured graphene/TiO<sub>2</sub> is also an interesting focus in the photocatalytic H<sub>2</sub> evolution. Xiang et al. [51] reported a new composite of TiO<sub>2</sub> nanocrystals grown in the layered MoS<sub>2</sub>/graphene hybrid prepared by a two-step hydrothermal method which could be used as a high-performance photocatalyst for the H<sub>2</sub> evolution. Sodium molybdate, thiourea, and graphene oxide were used as precursors of the MoS<sub>2</sub>/graphene hybrid and tetrabutylorthotitanate was used as the titanium precursor. The prepared composite displayed a synergistic effect between the MoS<sub>2</sub> and graphene components, which served as an electron collector and a source of active adsorption sites, respectively.

### 2.2.1.2 Mechanical Mixing

Seen from Table 2.1, among all the preparation methods, the simplest route involves mixing and sonication steps, owing to that the GO would be exfoliated when added to an aqueous or organic solution. Although the mixing method is very simple, in most cases the interaction between the two phases is very weak, since chemical bonding is not expected [77]. In our previous work, we designed ternary P25/GO/Pt hybrid photocatalysts which were prepared in different orders by employing different methods and using Degussa's TiO<sub>2</sub> (P25), GO, and chloroplatinic acid as precursors [56]. For instance, we prepared the (Pt/P25)+mGO and (Pt/mGO)+P25 by using the mechanical mixing method. A certain amount of Pt/P25 particles were dispersed into an aqueous suspension of GO, stirred for 24 h at room temperature,

centrifuged, washed and dried, which was denoted as (Pt/P25)+mGO, where “m” represents the quality ratio of GO/P25. 0.05 g chloroplatinic acid was dissolved into a solution containing GO, ethanol and deionized water, stirred for 30 min at room temperature, illuminated for 3 h. Then 0.5 g P25 was dispersed into the above mixture and stirred for 24 h at room temperature, centrifuged, washed and dried. The obtained catalyst was denoted as (Pt/mGO)+P25. Though there is absence a strong chemical bonding between  $\text{TiO}_2$  and GO by using a physical mixing technology, but the photogenerated electrons also can transfer from  $\text{TiO}_2$  to the GO owing to the intermolecular forces. In our investigation, the (Pt/mGO)+P25 gave a better photocatalytic activity than other catalysts prepared by different methods. After that, we continue to employ the simple mixing method to load the P25 nanoparticles on the surface of boron doped graphene nanosheets [57]. Firstly, the vacuum activation method was employed to prepare the boron doped graphene nanoribbons, and then the  $\text{TiO}_2$  was successfully embedded into the boron doped graphene nanosheets by a mechanical stirring and ultrasonic treatment. The loading of  $\text{TiO}_2$  on graphene surface gave a distinct pressure stress on the surface of graphene, which caused the rupture of C–C bonds close to Ti–O–C in B-GR nanoribbons, by a shear force from the ultraphonic treatment. The ultraphonic energy could cut some large-scaled graphene nanoribbons into smaller nanosheets.

Liu et al. [35] also prepared the self-assembled GO- $\text{TiO}_2$  nanorod composites by a mixing-like method at a low temperature. In the preparation, the  $\text{TiO}_2$  nanorods were stabilized by the oleic acid (OLA- $\text{TiO}_2$ ) which was hydrolysis at room temperature under the stirring for 24 h to ensure GO coordinated with Ti center on the surface of  $\text{TiO}_2$  nanorods. The self-assembly of  $\text{TiO}_2$  nanorods on the large GO sheets occurred in the water/toluene interface, as shown in Fig. 2.2a. The large GO sheets could act as an excellent supporter and stabilizer for the  $\text{TiO}_2$  nanorods, which is beneficial to the loading of  $\text{TiO}_2$  on the GO. They claimed that it was the first time the graphene- $\text{TiO}_2$  composites synthesized by a two-phase approach. This mixing-like procedure is facile and reproducible, which can be widely used in preparation of other nonpolar organic soluble nanocrytals on GO sheets.

In addition to the mixing at the room temperature, some other reports involved a mixing procedure at a high temperature for the crystallization of  $\text{TiO}_2$ . Yamashita and his coworkers reported that  $\text{TiO}_2$  nanoparticles supported on a mesoporous silica surface ( $\text{TiO}_2/\text{MCM-41}$ ) were selectively coated with graphene through the formation of surface complexes between  $\text{TiO}_2$  nanoparticles and 2, 3-dihydroxynaphthalene [60]. And then the complex was carbonization under  $\text{N}_2$  flow at a high temperature of 1073 K. Seen from Fig. 2.2b, the formation of DN- $\text{TiO}_2$  surface complexes presumably occurred through a previous reported similar process [78], that is, the dehydration between Ti-OH with the hydroxyl groups in DN. DN was used as a precursor of graphene which could be selectively anchored on  $\text{TiO}_2$  nanoparticles supported on MCM-41 through the formation of stable surface complexes. These complexes could be converted to graphene in the same places during the heat treatment in an inert atmosphere (Fig. 2.2b).

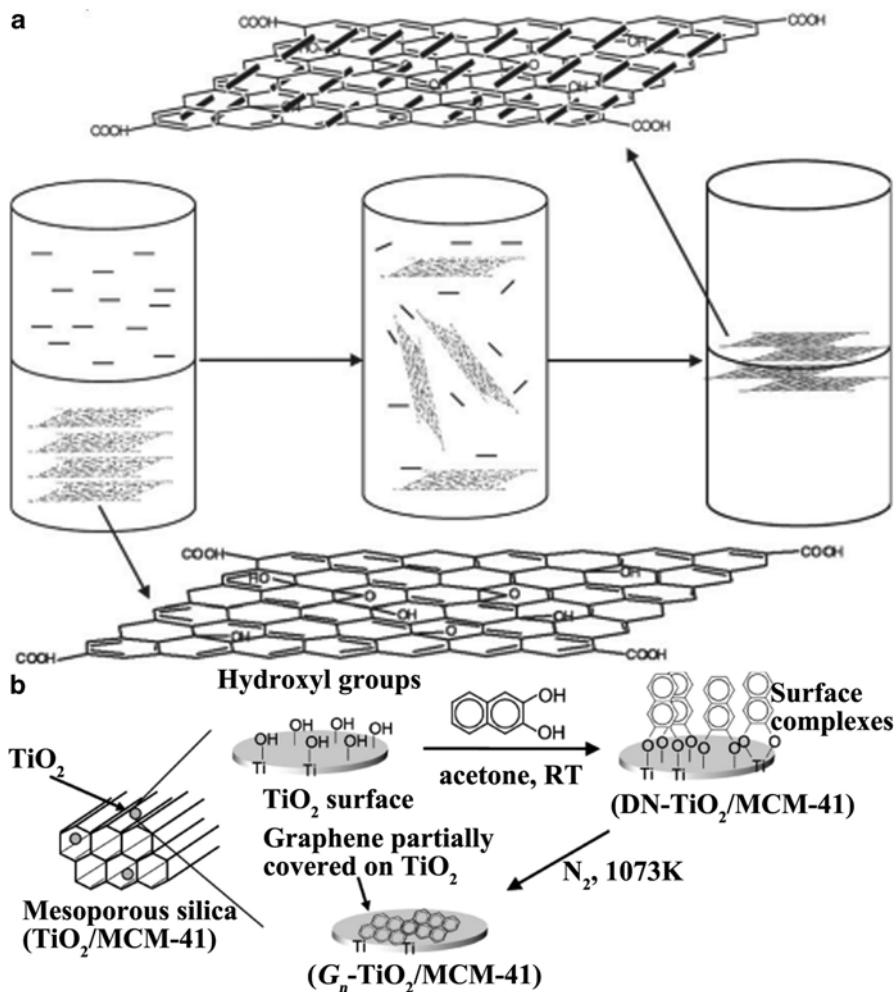


**Fig. 2.2** (a) Schematic presentation of self-assembly at the two-phase interface. Reproduced from Ref. [58] with permission of John Wiley & Sons, Inc. (b) Schematic diagram of the procedures for the preparation of G<sub>n</sub>-TiO<sub>2</sub>/MCM-41. Reprinted with permission from Ref. [60]. Copyright 2010 American Chemical Society

### 2.2.1.3 Sol-gel Method

Sol-gel is an advanced technology, which usually employs the compounds with high activity as the precursors. These raw materials are mixed in the liquid phase, and then the hydrolysis, and condensation reaction are occurring in the solution to form a stable system of transparent sol. After aging, colloidal particles in the sol aggregate slowly and form a three-dimensional network structure of the gel.

The solvent filled into the network structure of gel which losses the mobility. Gel was after drying and sintering to produce the nanomaterials. The sol-gel method has some advantages. For example, the reactants can be homogeneous mixing on the molecular level in a short time. In the sol-gel preparation process, some micro-elements can be easily and uniform quantitatively doped into the nanocomposites. Compared with the solid phase reaction, the involved chemical reaction is much easier occurring and always needs a relative low temperature.

Chen et al. [42] prepared the GO/TiO<sub>2</sub> composites by using TiCl<sub>3</sub> and GO as reactants through a sol-gel method. The authors found that the concentration of graphene oxide in starting solution played an important role in photoelectronic and photocatalytic activity of composites. Wang et al. [43] used anionic sulfate surfactants to assist the stabilization of graphene in aqueous solutions and facilitate the self-assembly of in situ grown nanocrystalline TiO<sub>2</sub> on the graphene by using a sol-gel method. The preparation process was schematically illustrated in Fig. 2.3. Firstly, the sulfate surfactant (i.e., sodium dodecyl sulfate) was dispersed on the graphene sheets and the titanium sources and solvents were mixed with the solution to obtain a sol after the stirring. And then the nucleation and condensation procedure resulted into the in situ crystallization of metal oxide precursors to produce the desired oxide phase and morphology. Lambert et al. [63] reported the TiO<sub>2</sub>-GO materials prepared via the hydrolysis of TiF<sub>4</sub> at 60 °C for 24 h in the presence of an aqueous dispersion of GO. The reaction proceeded to yield an insoluble material that was composed of TiO<sub>2</sub> and GO. These reactions were first performed on smaller scale by oven heating the TiF<sub>4</sub>-GO solutions in a beaker with no stirring and later in standard glassware with stirring to form a sol. The reaction proceeded to form a black/brown to gray gel/precipitate that was collected by centrifugation and washed with excess water, ethanol, and then dried. Zhang et al. [64] successfully synthesized the TiO<sub>2</sub>-GO intercalated composite at a low temperature (80 °C) by using graphite oxide and titanium sulfate (Ti(SO<sub>4</sub>)<sub>2</sub>) as the precursor and initial reactants. GO was firstly exfoliated by the NaOH and produced single and multilayered graphite oxide mixture, and then the [TiO]<sup>2+</sup> produced by the hydrolysis of Ti(SO<sub>4</sub>)<sub>2</sub> was diffused into the graphene oxide interlayer by the electrostatic attraction. It was obvious that the nucleation and

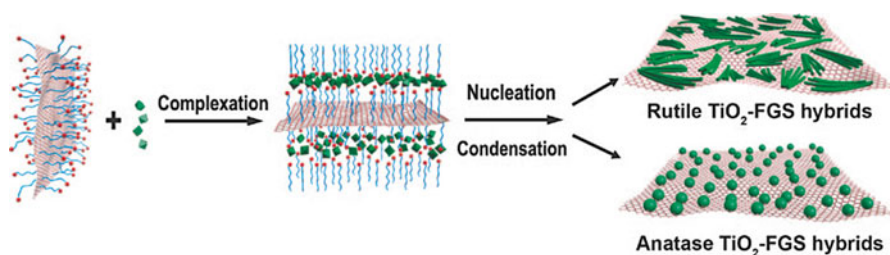


**Fig. 2.3** Anionic sulfate surfactant mediated stabilization of graphene and growth of self-assembled TiO<sub>2</sub>-FGS hybrid nanostructures. Reprinted with permission from Ref. [43]. Copyright 2009 American Chemical Society

growth of TiO<sub>2</sub> crystallites and the compounding between TiO<sub>2</sub> and graphene could take place at a low temperature by using a sol-gel method.

#### 2.2.1.4 UV Light Irradiation

In the preparation of TiO<sub>2</sub>/graphene composite, the reduction of graphene oxide is a very important process which determines the conductivity of graphene and the transfer efficiency of photogenerated electrons between TiO<sub>2</sub> and graphene. The reduction of graphene oxide is always achieved by a hydrothermal treatment at a high temperature in the presence of reductants, or direct heating the composite in the absence of air or in the inert gas atmosphere. Compared with the energy-extensive consumption of heating reduction procedure, the UV light irradiation method used for the reduction of GO is much more attractive owing to its low-energy consumption and manageable property.

Kim et al. [66] prepared the size-controlled nanographene oxides (NGOs <50 nm) by a two-step oxidation process, and then the NGOs were self-assembly compounded with the TiO<sub>2</sub> nanoparticles to form the core-shell like structures (Fig. 2.4a). A certain amount of P25 was added in the solution of NGOs solution, and then the mixture was aged under the stirring for overnight. In order to further improve the

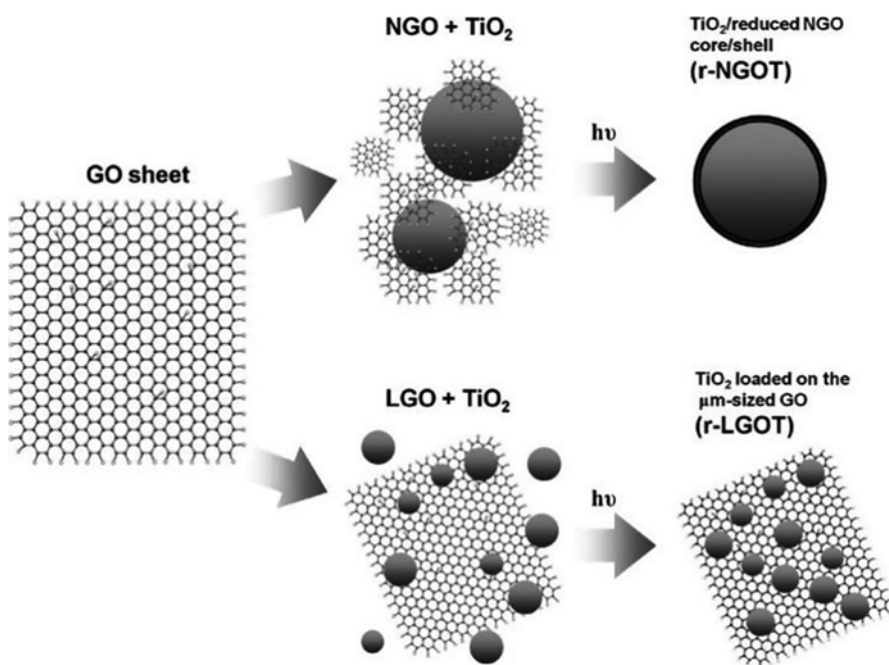


**Fig. 2.4** Illustration of the preparation procedure of r-NGOT and r-LGOT Reprinted with permission from Ref. [66]. Copyright 2012 American Chemical Society

reduction of the NGOs, a 200-W mercury lamp was used as the light source to reduce the NGOs for 30 min irradiation. Mohamed et al. [67] prepared the TiO<sub>2</sub>-reduced RGO composite by UV-assisted photocatalytic reduction of graphite oxide mixed with TiO<sub>2</sub> nanoparticles in the ethanol. The mixture was illuminated under a 250 W high pressure Hg lamp with the main wave crest at 254 nm for 24 h under ambient conditions and magnetic stirring. After UV irradiation, it was obvious that the color of suspension changed into grayish black, which indicated the successful reduction of graphene oxide sheets. Akhavan et al. [68] synthesized the composite of TiO<sub>2</sub> nanoparticles physically attached to the single-layer graphene oxide by a UV light assisted photoreduction method. It was found that the UV-assisted reduction of the graphene oxides by the TiO<sub>2</sub> nanoparticles was nearly completed after 2 h UV irradiation. However, the longer time irradiation would induce the decrease of the carbon content of the reduced graphene and the increase of the carbon defects on the graphene, indicating the presence of degradation of reduced graphene sheets by the TiO<sub>2</sub> nanoparticles in the UV-driven photocatalytic process.

### 2.2.1.5 Microwave Assisted Method

Although above mentioned preparation methods have many advantages in the synthesis of TiO<sub>2</sub>/graphene composite, all of them need take a long of reaction time. Microwave technology is a very simple and convenient approach applied in the reaction of organic synthesis, whose reaction speed can be up to dozens or even thousands of times faster than the conventional methods. It also can synthesize some complexes which are difficult to be created by the regular methods. Microwave technology is more and more widely used in the nanomaterial, pharmaceutical, and other chemical related research.

Liu et al. [71] reported the TiO<sub>2</sub>-RGO composites prepared via the microwave-assisted reduction of graphite oxide in a TiO<sub>2</sub> suspension by using a microwave synthesis system. Pu et al. [73] synthesized the GO-TiO<sub>2</sub> hybrids (GTHs) by a one-pot microwave-assistant combustion method. The precursor solution was heated on a hot plate at 100 °C to remove the solvent until a gel-like precursor was obtained. And then the precursor was introduced into a domestic microwave oven (700 W) and irradiated for different time, during which the combustion took place and black foam-like GTHs were obtained.

Some modifications to the microwave-assisted method have been introduced, including the use of impurities or semiconductors with the aim to improve the transfer efficiency of the photogenerated carriers among components. For instance, Wang et al. [74] fabricated the graphene based Au-TiO<sub>2</sub> photocatalysts by a simple, one-step microwave-assisted hydrothermal method, using Degussa P25 powder, graphene oxide and HAuCl<sub>4</sub> aqueous solution as the raw Au-TiO<sub>2</sub> photocatalysts. Lv et al. [72] prepared the CdS-TiO<sub>2</sub>-chemically reduced graphene oxide composites by using a microwave-assisted method for the reduction of GO in the CdS precursor solution with TiO<sub>2</sub> suspension. During the microwave reaction process,

positively charged Cd<sup>2+</sup> ions form complexes with TiO<sub>2</sub> nanoparticles and S<sup>2-</sup> from Na<sub>2</sub>S could move quickly to react with Cd<sup>2+</sup> producing uniform CdS nanoparticles compounded with TiO<sub>2</sub> under the microwave irradiation. Microwave-assisted method was a one-step procedure for the synthesis of CdS-TiO<sub>2</sub>-RGO composite, which would save a lot of time.

### 2.2.1.6 Other Methods

In addition to above mentioned methods, there are also some other methods which could be used in the preparation of TiO<sub>2</sub>/graphene composites, such as pyrolysis [42, 61], chemical vapor deposition [70] and vacuum activation methods [75]. Here, we want to give an introduction of vacuum activation for the preparation of TiO<sub>2</sub>/graphene composite.

As we all know that most of the traditional modification methods need a high temperature or complicated and expensive equipment, which can hardly be applied in industrial production and spread to other semiconductors [13]. Our previous research work has demonstrated that the low temperature vacuum activation technology is a low-cost and simple method to produce many oxygen vacancies in TiO<sub>2</sub> lattice and achieve the reduction of TiO<sub>2</sub> [15, 79, 80]. Recently, we successfully spread the vacuum activation method for the preparation of boron doped graphene nanoribbons [81]. Graphene oxides were mixed with the H<sub>3</sub>BO<sub>3</sub> which was used as the boron sources and reductent, and then the mixture was dried under a low temperature. The obtained powders were put into a vacuum tube furnace and heated at 300 °C for 3 h. In contrast to the hydrothermal method, the vacuum activation treatment could provide an anoxic environment, which is beneficial for the departing of oxygen atoms and the formation of lattice defects in the graphene. These defects make the graphene sheets fragile and readily attacked by boron atoms. Although the reason for the formation of graphene nanoribbons is unclear, we still gave an assumption for the formation mechanism of the nanoribbons. Before the vacuum activation, the H<sub>3</sub>BO<sub>3</sub> was connected to the graphene by the formation of B–O–C bonds. At the beginning of vacuum heating, the macro-residual stress on the B–O–C bonds induced rupture of the C–C bond. The juxtaposition of the buttressing C–O bond, combined with the departing force of the oxygen in the vacuum, distorts the β, γ-alkenes, making them more prone to the next attack by the boron oxides. The B–O groups tended to form a line on the carbon lattice, and the cooperative alignment induced rupture of the underlying C–C bonds. With the increase of the heating temperature and the heating time in the vacuum, the oxygen atoms began to depart from the skeleton to form the fully reduced graphene nanoribbons. Meanwhile, some of the absorbed boron atoms replaced the oxygen atoms in the defect sites to obtain the boron doped graphene nanoribbons.

Very recently, we continue to employ the vacuum activation in the preparation of graphene based composite. Ti<sup>3+</sup> self-doped TiO<sub>2</sub>-graphene photocatalyst was successfully prepared by a one-step vacuum activation which involved a relative lower temperature and was facile to be large-scaled reproduction [75]. Compared with

other traditional preparation methods, the vacuum activation exhibits a low temperature and low-costing, which can achieve the reduction of GO, the self-doping of  $\text{Ti}^{3+}$  in  $\text{TiO}_2$  and the loading of  $\text{TiO}_2$  nanoparticles on GR surface at the same time. In conclusion, considering the applications of simple vacuum activation method to prepare different kinds of photocatalysts with high photocatalytic activities, we anticipate our research to be a starting point for the synthesis of new materials with high photo-activity by a simple and cheap method.

## 2.2.2 Characterizations

### 2.2.2.1 Characterization for the Morphology of $\text{TiO}_2$ /Graphene Composite

To the binary composite, the micro-morphology is very important to reflect the compounding between the components. To the most reported 2D-structured  $\text{TiO}_2$ /graphene composite, the graphene shows a large-scale layer structure and plays the role of support. And the nanosized  $\text{TiO}_2$  particles are the role of major active component which are loading on the surface of graphene. The degree of dispersion of  $\text{TiO}_2$  nanoparticles on the graphene relates to the photocatalytic activity of composite. The TEM and SEM are considered as the most intuitive characterizations for the micro-morphology of  $\text{TiO}_2$ /graphene composite.

In the early stages, Zhang et al. [47] found that the  $\text{TiO}_2$  nanoparticles preferred to grow along the edge and wrinkles of the graphene sheets, according to the TEM image of P25-GR (Fig. 2.5a). Many carboxylic acid functional groups still remain along the edge and wrinkles after a hydrothermal treatment, which are beneficial to react with the surface hydroxyl groups on the surface of  $\text{TiO}_2$ , resulting in the firmly interaction between  $\text{TiO}_2$  and graphene. Xiang et al. [52] have done a comparison of TEM characterization between bare graphene and  $\text{TiO}_2$  nanosheets/graphene com-

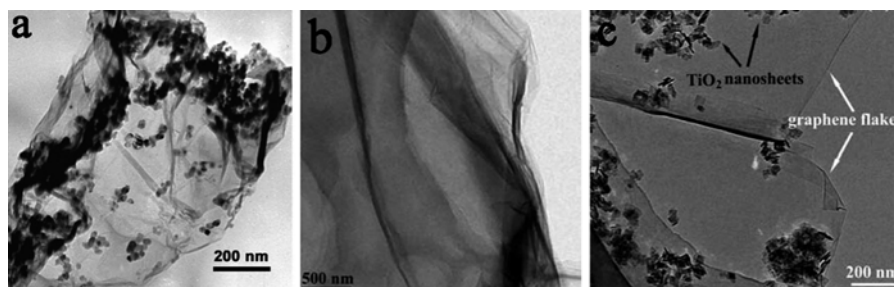


**Fig. 2.5** (a) Typical TEM image of P25-GR, with P25 loading on the surface of graphene and concentrating along the wrinkles. Reprinted with permission from Ref. [47]. Copyright 2010 American Chemical Society. TEM images of GO (b) and the G1.0 sample (c). Reproduced from Ref. [52] with permission of Royal Society of Chemistry

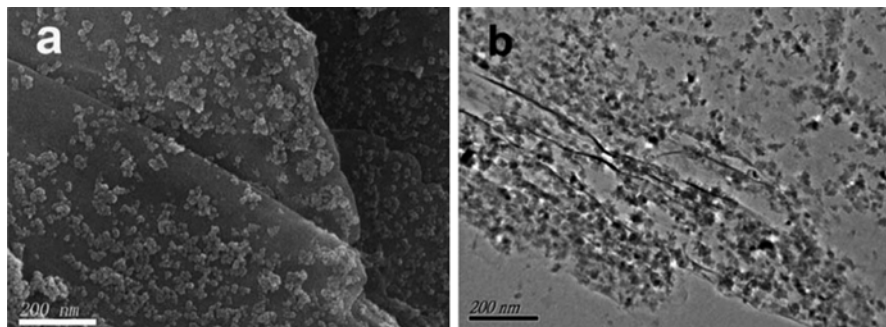


**Fig. 2.6** (a) SEM image of TiO<sub>2</sub>-G. (b) TEM image of TiO<sub>2</sub>-G. Reproduced from Ref. [82] with permission of Royal Society of Chemistry

posite, as shown in Fig. 2.5b,c. After the reduction, the reduced graphene remained the 2D-structured sheets with micrometer-long wrinkles after the hydrothermal treatment. The TiO<sub>2</sub> nanosheets with an average side size of 50–80 nm and a thickness of 6–8 nm were dispersed on the graphene sheets with face-to-face orientation, owing to the interaction between carboxylic acid functional groups on graphene and hydroxyl groups on TiO<sub>2</sub>.

Generally, if the TEM images give a well dispersion of TiO<sub>2</sub> on the graphene, the corresponding SEM images also provide a similar micro-morphology results which is always consistent with the TEM results. Wang et al. [82] prepared an interesting TiO<sub>2</sub>-decorated graphene nanohybrids by a hydrothermal method. The TEM and SEM images of TiO<sub>2</sub>-G all indicated that TiO<sub>2</sub>-G nanohybrids had several layers (Fig. 2.6), each of which exhibited TiO<sub>2</sub> NPs loading on the graphene surfaces. The individual TiO<sub>2</sub> NPs were well decorated on the surface of graphene with a wrinkled paper-like structure, and most TiO<sub>2</sub> NPs had diameters of 5–10 nm. Seen from the TEM images, the authors inferred that the TiO<sub>2</sub> nanoparticles were in situ growth on the surface of graphene, which would prevent the graphene sheets from the restacking.

Additionally, the controlling of size of graphene is also important to the micro-morphology of TiO<sub>2</sub>/graphene composite. Atomic Force Microscope (AFM) characterization is always used to detect the size of graphene sheets. Kim et al. [66] successfully achieved the controlling of graphene oxides by a two-step oxidation process. The AFM images and analysis results indicated that the thickness of NGOs varies in the range of 0.8–2.0 nm (Fig. 2.7), which indicated that some of the NGO sheets are stacked as double layers. The bottom parts in Fig. 2.7 showed the size distribution histograms of LGO and NGOs obtained from the AFM images, which showed a wide distribution of size (480–520 nm). The average sizes of NGO-100, NGO-200, and NGO-300 could be successively reduced to 164, 59, and 36 nm, respectively. Interestingly, all prepared NGOs showed much smaller average sizes and narrower size distributions compared to those for LGO.

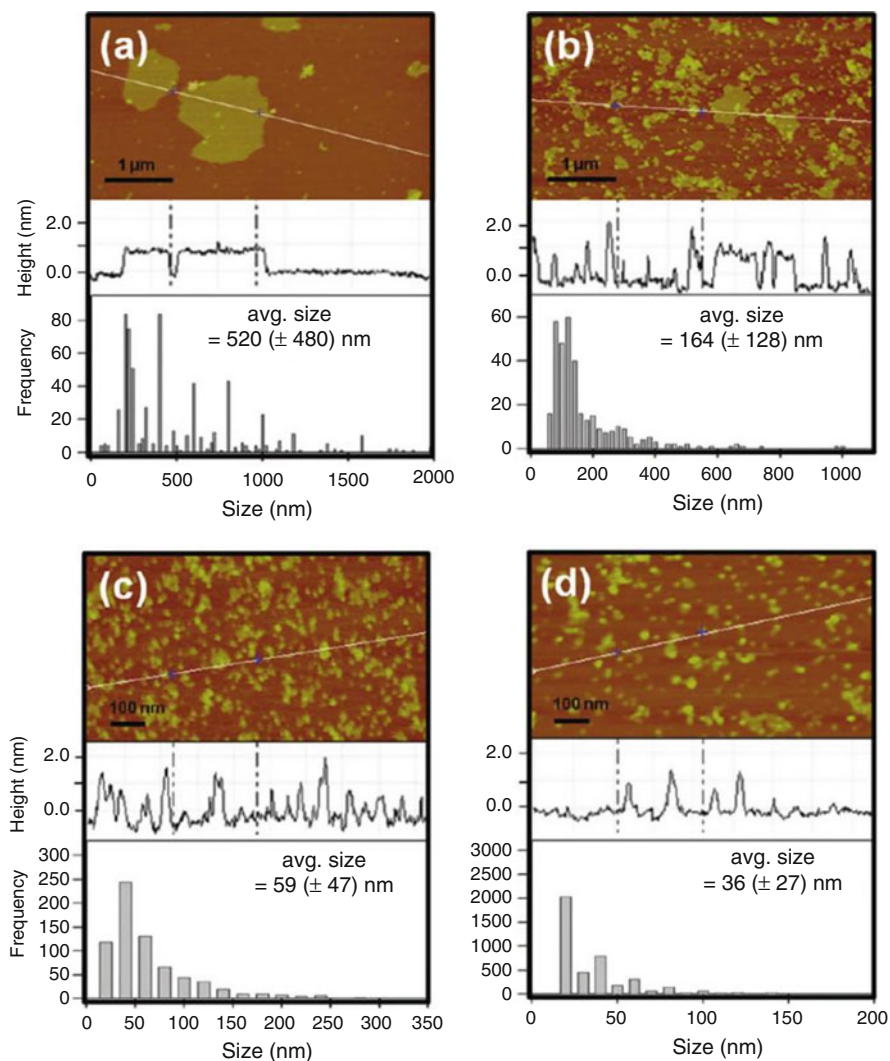


**Fig. 2.7** Tapping-mode AFM images (*top*) and the height cross-sectional profiles (*middle*) of (a) LGO, (b) NGO-100, (c) NGO-200, and (d) NGO-300. The size distribution histograms (*bottom*) were obtained by counting (frequency) from the AFM images. The average sizes of LGO, NGO-100, NGO-200, and NGO-300 are 520 (±480), 164 (±128), 59 (±47), and 36 (±27) nm, respectively Reprinted with permission from Ref. [66], Copyright 2012 American Chemical Society

### 2.2.2.2 Characterization for the Reduction of Graphene Oxides

Graphene is acknowledged as an ideal conductor which determines the transfer of photogenerated electrons from semiconductors to the graphene. However, the graphene oxide produced by the chemical methods is very difficult to completely

reduced, owing to the generation of defects in the skeleton of graphene during the chemical reduction process, resulting into the weaken of the transmission of light, the thermal conductivity and the electroconductivity. Hence, the “graphene” resulting from the chemical reduction of graphene oxides is difference from the “graphene” in a strict sense, though, the chemical redox method is still a popular technology used in the large-scaled preparation of graphene due to its low-cost and operability.

Now that the reduction of graphene oxides is so important to the photocatalytic activity of the TiO<sub>2</sub>/graphene composite, how to characterize the reduction degree of the graphene oxides in the composite? There are several characterizations for the investigation of the reduction of graphene oxides such as the XRD, Raman, XPS, and so on. There is a characteristic peak at 9.8° for the graphene oxides which is ascribed to the (001) interlayer spacing of 0.90 nm [52], as shown in Fig. 2.8a. Obviously, the peak at 9.8° disappeared to all the TiO<sub>2</sub>/graphene composites after a microwave-hydrothermal treatment, which indicated the successful reduction of

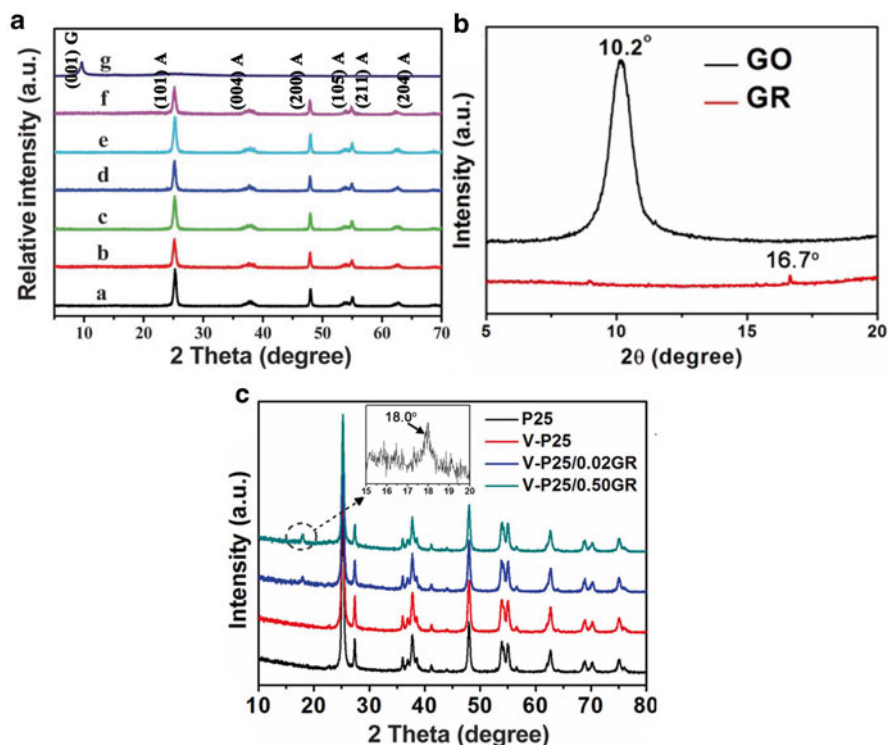


**Fig. 2.8** (a) XRD patterns of the TiO<sub>2</sub>/graphene composites (“g” is the XRD patterns of graphene oxide, and others are the XRD patterns of the composites). Reproduced from Ref. [52] with permission of Royal Society of Chemistry. (b) XRD patterns of the graphene oxide before and after vacuum activation Reprinted with permission from Ref. [75]. Copyright 2015 Macmillan (c) XRD patterns of the composites Reprinted with permission from Ref. [75]. Copyright 2015 Macmillan

graphene oxides by a chemical reduction treatment. The regular stacking of GO was destroyed by the reduction process under the microwave-hydrothermal conditions and could not be resolved by XRD. Our previous work demonstrated that the absence of a peak at  $10.2^\circ$  and the presence of another peak at  $16.7^\circ$  after the vacuum activation treatment also indicated the reduction of graphene oxides (Fig. 2.8b) [75]. The peak at a small angle of  $16.7^\circ$  is indicative of graphene with lower crystallinity and some defects induced by the vacuum activation [83]. Interestingly, the peak assigned to graphene changed from  $16.7^\circ$  to  $18.0^\circ$  after the loading of  $\text{TiO}_2$  nanoparticles. This shift may be resulted from the existence of chemical connection between  $\text{TiO}_2$  nanoparticles and GR surface carbon groups. The loading of  $\text{TiO}_2$  surface gave a distinct pressure stress on the graphene, which led to the characteristic peak of GR changing from  $16.7^\circ$  to  $18.0^\circ$ .

XPS characterization is another measurement to demonstrate the successful reduction of graphene oxides. Xiang et al. [52] found that the two characteristic peak of GO located at 287.0 eV in the C1s XPS spectrum of  $\text{TiO}_2$ /graphene composite was obvious decrease after the hydrothermal reduction, indicating the dam-

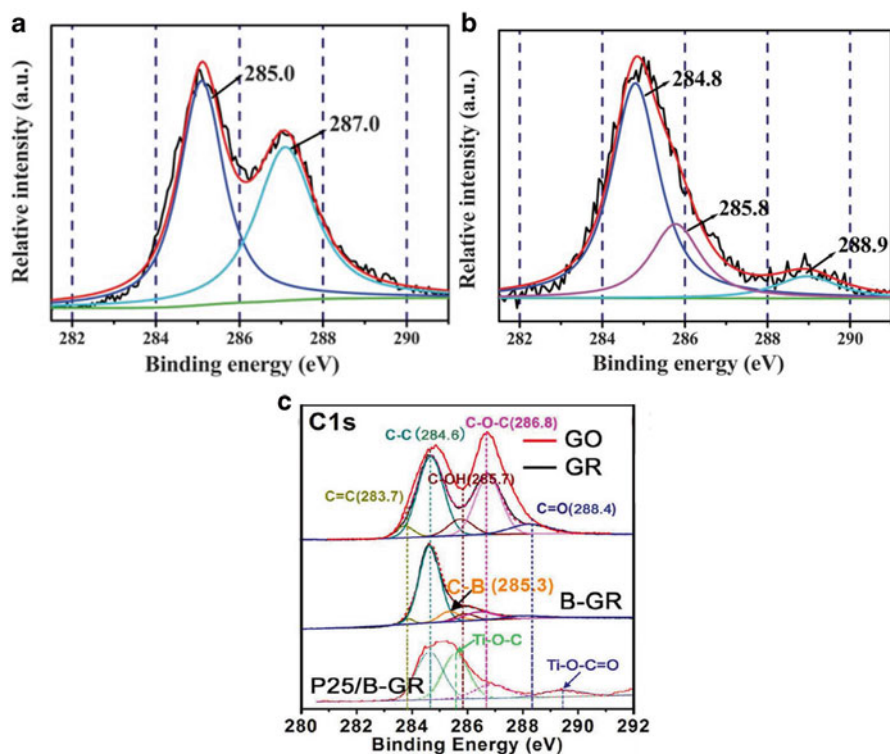


**Fig. 2.9** High-resolution XPS spectra of C1s for GO (a) and the G1.0 (b) sample. Reproduced from Ref. [52] with permission of Royal Society of Chemistry. (c) C1s XPS spectra for the GO, GR, B-GR and  $\text{TiO}_2$ /graphene composite Reprinted with permission from Ref. [57]. Copyright 2014 Macmillan

age of the oxygen-containing carbonaceous bands (C–OH) during the hydrothermal process (Fig. 2.9a, b). Our previous work also investigated the reduction of GO through the vacuum activation method [57]. Seen from the C1s XPS of GO, the peaks at 285.7, 286.8 and 288.4 eV were assigned to the C–OH, C–O–C, and C=O bonds (Fig. 2.9c). These oxidation groups in GO were breakage after a vacuum activation treatment, inducing the intensity decrease of the above mentioned peaks in Fig. 2.9c, which suggested the successful reduction of GO by a vacuum activation method.

In addition to the XRD and XPS, the Raman is another useful technology to detect the reduction of graphene oxides [49–51, 84]. Raman spectroscopy is a powerful nondestructive tool to characterize the crystalline quality of carbon. Xiang et al. [52] employed the Raman to investigate the reduction of graphene oxides in the TiO<sub>2</sub>/composites. The characteristic bands at 146, 397, 516, and 637 cm<sup>-1</sup> in Fig. 2.10 were corresponded to the  $E_{g(1)}$ ,  $B_{1g(1)}$ ,  $A_{1g} + B_{1g(2)}$ , and  $E_{g(2)}$  modes of anatase, respectively, and the peaks at 1354 and 1594 cm<sup>-1</sup> were ascribed to the D- and G-bands in GO, respectively. After the hydrothermal treatment, the G-bond and D-bond moved to 1342 and 1585 cm<sup>-1</sup> respectively, indicating the successful reduction of GO. Simultaneously, a further observation indicated that the TiO<sub>2</sub>/graphene composite showed an increased D/G intensity ratio in comparison to that of pure GO, also indicating the reduction of GO.

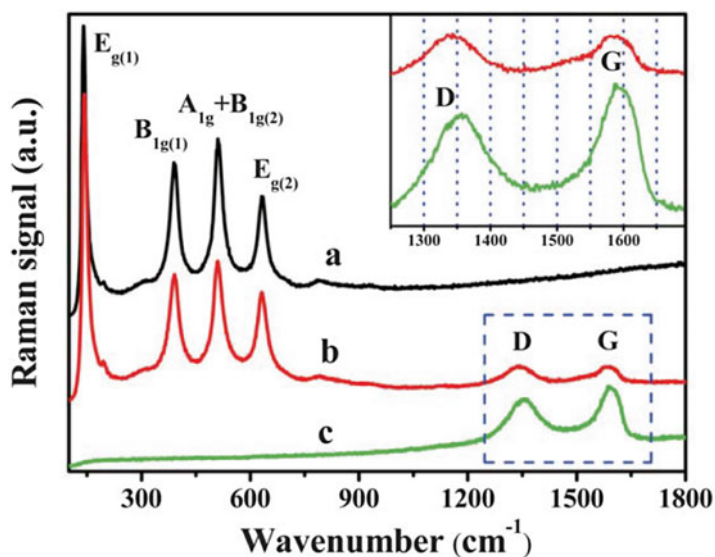


**Fig. 2.10** Raman spectra of the GO (a), G1.0 (b) and GO (c) samples. Reproduced from Ref. [52] with permission of Royal Society of Chemistry

### 2.2.2.3 Characterization for the Connection Between the Graphene and TiO<sub>2</sub>

To the TiO<sub>2</sub>/graphene composite, the connection between TiO<sub>2</sub> and graphene will make a great contribution to the chemical and physical properties of the composite, which determines its application in photocatalysis. Zhang et al. [47] investigated the connection between TiO<sub>2</sub> and graphene by using the FTIR characterization. Fig. 2.11a shows the FTIR spectra of TiO<sub>2</sub> and TiO<sub>2</sub>/graphene composite. The broad absorption at low frequency of <math>1000\text{ cm}^{-1}</math> was ascribed the vibration of Ti–O–Ti bonds in TiO<sub>2</sub>. After the introduction of graphene, the absorption peak corresponding to Ti–O–Ti shifted to higher wavenumbers, which was resulted from the combination of the vibration of Ti–O–Ti and Ti–O–C bonds. The results confirmed the formation of Ti–O–C bonds between TiO<sub>2</sub> and graphene during the hydrothermal reaction.

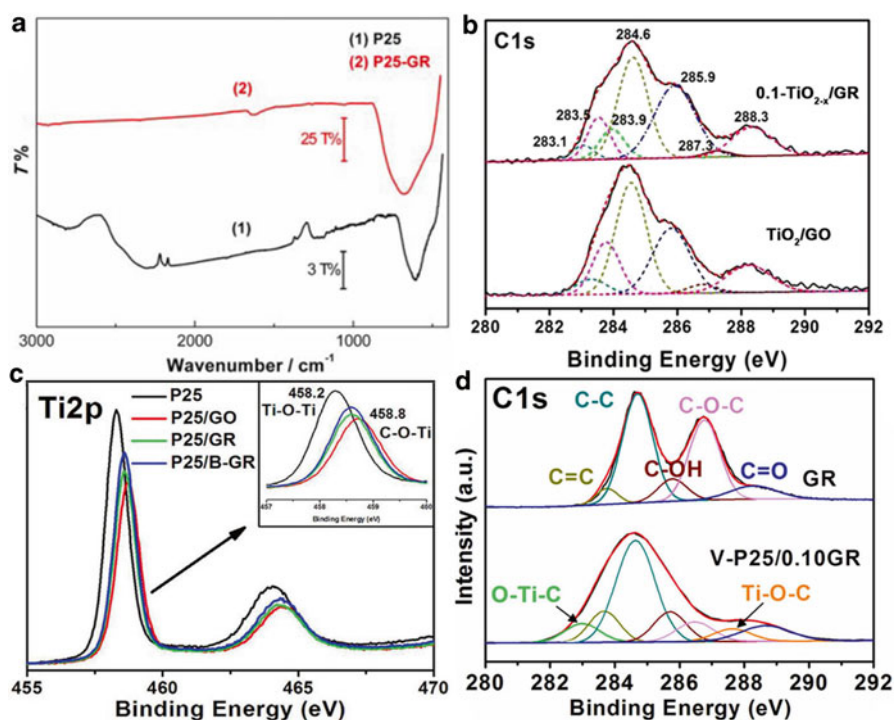


**Fig. 2.11** (a) FTIR spectra of (1) P25 and (2) P25-GR with different magnifications in the range of 3000–450  $\text{cm}^{-1}$  Reprinted with permission from Ref. [47]. Copyright 2010 American Chemical Society. (b) C1s XPS spectra for 0.1-TiO<sub>2-x</sub>/GR and TiO<sub>2</sub>/GO [23]. Copyright 2014 Rights Managed by Nature Publishing Group. (c) Ti2p XPS spectra for TiO<sub>2</sub> and TiO<sub>2</sub>/graphene composite [57]. Copyright 2014 Rights Managed by Nature Publishing Group. (d) C1s XPS spectra for the GR with and without P25 loading [75]. Copyright 2015 Rights Managed by Nature Publishing Group

In our investigation, the XPS measurement can also demonstrate the connection between TiO<sub>2</sub> and graphene in the TiO<sub>2</sub>/graphene composite. It was found that the presence of the peak at 283.1 eV in the C1s XPS spectrum was ascribed to the generation of Ti–O–C bond between TiO<sub>2</sub> and graphene (Fig. 2.11b) [23]. The Ti2p XPS spectra presented in Fig. 2.11c also demonstrated the generation of Ti–O–C structures [57]. The Ti2p 3/2 shifted from 458.2 to 458.8 eV after loading with B-GR, indicating that some Ti–O–Ti bonds were replaced by Ti–O–C owing to higher electronegativity of C than Ti. In addition to the Ti–O–C bond, our previous work found that the O–Ti–C bond also could be generated after a simple vacuum activation treatment [75]. The C1s XPS spectra suggested the existence of chemical binding between TiO<sub>2</sub> and GR (Fig. 2.11d). Compared with the blank GR, the two new peaks at 282.5 and 285.5 eV were ascribed to the O–Ti–C and Ti–O–C respectively, which indicated the chemical connection between TiO<sub>2</sub> and graphene.

#### 2.2.2.4 Characterization for the Electrochemical Property of the Composite

In order to investigate the electrochemical properties of TiO<sub>2</sub>/graphene composite, the photocurrent responses and EIS measurements are always carried out to characterize the electroconductivity of the composite. For instance, Zhang et al. [47] carried out the ESI measurement in the presence of a 2.5 mM K<sub>3</sub>[Fe(CN)<sub>6</sub>]/K<sub>4</sub>[Fe(CN)<sub>6</sub>] (1:1) mixture as a redox probe in 0.1 M KCl aqueous solution, and the ESI results are showed in Fig. 2.12a. The typical electrochemical impedance spectra were presented as Nyquist plots. It was noticeable that the semicircle of P25 in the plot became shorter with the introduction of graphene, which indicated a decrease in the solid state interface layer resistance and the charge transfer resistance on the surface. Obviously, both the electron-accepting and transporting properties of graphene in the composite could contribute to the suppression of charge recombination.

In order to investigate the light responsive property of TiO<sub>2</sub>/composite, the photoelectrochemical behaviors of the pure TiO<sub>2</sub> and TiO<sub>2</sub>/graphene composites are presented in Fig. 2.12b [85]. Under the UV light irradiation, the TiO<sub>2</sub>/graphene composites exhibited a much higher photocurrent density than pure TiO<sub>2</sub>. The authors classified that the improved photoresponse benefited from the introduction of graphene. With the extensive 2D p–p conjugation structure, graphene could accept the photogenerated electrons from TiO<sub>2</sub> and transfer them to the external circuit quickly. Lee et al. [49] found that the visible light also could induce a current signal on the TiO<sub>2</sub>/graphene composite as shown in Fig. 2.12c. A strong photocurrent response was observed for each switch-on/off event in the case of graphene-TiO<sub>2</sub> NPs, which confirmed high photo-activity of graphene-TiO<sub>2</sub> NPs under visible light irradiation. Additionally, our recent research work demonstrated that the P25/graphene composite could produce the electrons and exhibit a high photocurrent response under the simulated solar light irradiation (Fig. 2.12d) [57].

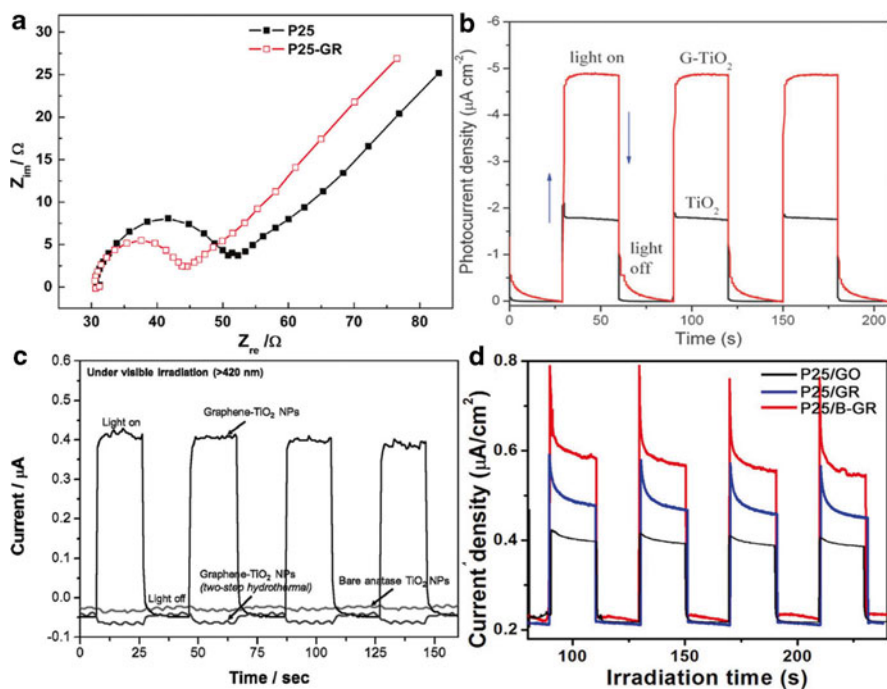


**Fig. 2.12** (a) EIS changes of P25 and P25-GR electrodes. Reprinted with permission from Ref. [47]. Copyright 2010 American Chemical Society. (b) Photocurrents of TiO<sub>2</sub> and G-TiO<sub>2</sub> composites under intermittent irradiation by an ultraviolet lamp at a bias potential of 0.2 V. Reproduced from Ref. [85] with permission of Royal Society of Chemistry. (c) Photocurrent responses of bare anatase TiO<sub>2</sub> NPs, graphene-TiO<sub>2</sub> NPs, and graphene-TiO<sub>2</sub> NPs under visible light irradiation ( $\lambda > 420$  nm). Reproduced from Ref. [49] with permission of John Wiley & Sons, Inc. (d) Transient photocurrent responses of P25/GO, P25/GR, and P25/B-GR in 0.5 M Na<sub>2</sub>SO<sub>4</sub> aqueous solution under solar irradiation [57]. Copyright 2014 Rights Managed by Nature Publishing Group

## 2.2.3 Applications in Photocatalysis

2D-structured TiO<sub>2</sub>/graphene composites have been widely used for the photodegradation of organic pollutants in recent years, but they have also been applied in many other fields, including hydrogen production and CO<sub>2</sub> photoreduction, which are related with the preservation of the environment. Hence, in this section, we would like to collect some information regarding the details of experiments performed for photocatalytic degradation of pollutants, as well as some of the other related applications in photocatalysis.

### 2.2.3.1 Photodegradation of Organic Pollutants

In this day and age, we are striving to develop the social productivity and improve the level of daily life, which inevitably causes serious damage to the environment and seriously threat to the human survival. Nowadays, water and air are considered

as the most valuable human resources which has attracted much more attention than before. Especially with the speeding up of the industrial process, a large amount of waste water and gas are directly discharged into the rivers and atmosphere, which will induce the accumulation of large amounts of toxic organic compounds in our daily lives and bring enormous threat to the human health. And in these organic pollutants, some compounds are very difficult to be degraded by the ordinary processing methods. The photocatalytic technology is an ideal method to degrade these organic compounds by using the inexhaustible solar light energy.

In 2009, Zhang et al. [47] prepared the P25/graphene composite by using a hydrothermal method, and firstly employed it for the photodegradation of MB. The authors said that three factors are crucial in photocatalysis, that is, adsorption of MB molecules, light absorption, and charge transportation and separation. The introduction

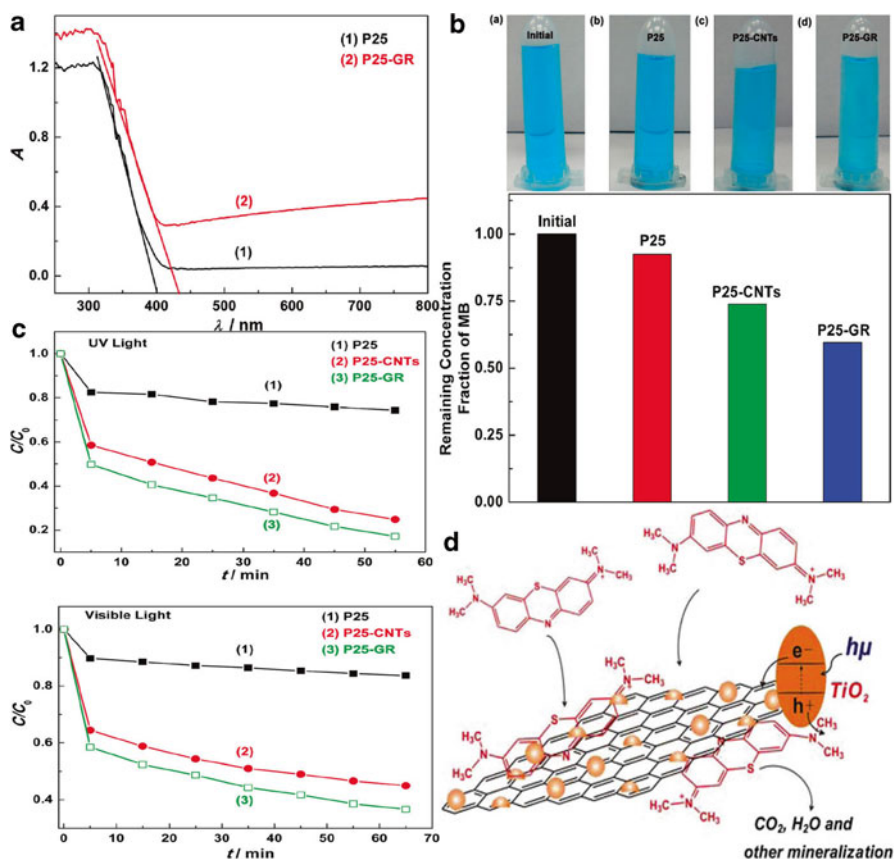


**Fig. 2.13** (a) Diffuse reflectance absorption spectra of (1) P25 and (2) P25-GR. (b) Bar plot showing the remaining methylene blue (MB) in solution. (c) Photodegradation of MB under UV light and visible light ( $\lambda > 400$  nm) over (1) P25, (2) P25-CNTs, and (3) P25-GR photocatalysts, respectively. (d) Schematic structure of P25-GR and tentative processes of photodegradation of methylene blue (MB) over P25-GR. Reprinted with permission from Ref. [47]. Copyright 2010 American Chemical Society

of graphene can satisfy these three factors at one time. As shown in Fig. 2.13a, the TiO<sub>2</sub>/graphene has an obvious enhancement visible light absorption compared with the pure P25. It was obvious that most dye molecules remained in the solution with bare P25 as the catalyst after equilibrium in the dark for 10 min, whereas a large amount of dye molecules was adsorbed on the surface of P25-GR. That means the TiO<sub>2</sub>/graphene composite had the highest adsorption data of the methylene blue among all the photocatalysts (Fig. 2.13b). Most importantly, the authors found that the TiO<sub>2</sub>/graphene also showed the highest photocatalytic activity for the degradation of MB both under the visible or UV light irradiation, as shown in Fig. 2.13c. In the TiO<sub>2</sub>/graphene photocatalytic system, the excited electrons of TiO<sub>2</sub> could transfer from the conduction band of TiO<sub>2</sub> to the graphene via a percolation mechanism. Graphene served as an acceptor of the generated electrons of P25 and effectively suppressed the electron and hole recombination, leaving more charge carriers to form reactive species and promote the degradation of dyes, as shown in Fig. 2.13d.

In our group we also chose some organic dyes as the simulated pollutant molecules to be photodegraded by the TiO<sub>2</sub>/graphene composites, such as methylene blue, methyl orange, and rhodamine B solutions. For instance, we successfully prepared the graphene nanoribbons and used it for the photodegradation of rhodamine B under the solar light irradiation [81]. It was found that the bandgap of the graphene could be adjusted by changing the morphology of graphene, and the nano-sized graphene exhibited a semiconductor property and showed a good photocatalytic activity for the first time. The prepared graphene nanoribbons continued to be used as the precursors to synthesize the nanocomposite of TiO<sub>2</sub> compounded with graphene nanoribbons by a facile ultrasonic-mechanical mixing method [57]. The prepared composite had an excellent performance for the photodegradation of methyl orange under the solar light irradiation. The outstanding transfer efficiency of photogenerated carriers induced by the nanosized compounding between TiO<sub>2</sub> and graphene were responsible for the enhancement photocatalytic activity.

In addition to the colored dyes, some colorless organic compounds also can be photodegraded by the graphene based photocatalysts. In our previous work, the Ti<sup>3+</sup> doped TiO<sub>2</sub> nanorods/boron doped graphene composite was prepared by a hydrothermal method and the synergistic effect on the visible light activity was investigated by the photodegradation of colorless phenol [23]. The TiO<sub>2</sub>/graphene composite showed a higher photodegradation of phenol than other photocatalysts, and the exposed (100) facets on TiO<sub>2</sub>, the self-doping of Ti<sup>3+</sup> and the boron doped in graphene were the reason for the excellent photocatalytic activity. Ng et al. [69] prepared the electrodes which consisted of TiO<sub>2</sub>/graphene nanocomposite. The graphene based electrodes had a significant activity for the complete photocatalytic decomposition of 2, 4-dichlorophenoxyacetic acid under the UV light irradiation. Kamegawa et al. [60] designed a composite of TiO<sub>2</sub> nanoparticles supported on a mesoporous silica surface (TiO<sub>2</sub>/MCM-41) which were selectively coated with graphene through the formation of surface complexes between TiO<sub>2</sub> nanoparticles and 2,3-dihydroxynaphthalene and following carbonization under N<sub>2</sub> flow. The selective graphene modification induced the enhanced photocatalytic activities of TiO<sub>2</sub>/MCM-41 for the decomposition of 2-propanol in water compared with unmodified

samples, owing to the appropriate adsorption properties of organics to transfer to the surface of TiO<sub>2</sub> nanoparticles.

### 2.2.3.2 Water Splitting

Water splitting is another important application of TiO<sub>2</sub>-based photocatalysis, due to the exhaustion of energy in the world. The hydrogen is regarded as the clean energy which is standing out in recent years owing to its low carbon consuming. Moreover, the first report on TiO<sub>2</sub> involved photocatalysis is also the application to water splitting for H<sub>2</sub> evolution [1]. Hence, the development for the photocatalytic water splitting on TiO<sub>2</sub>/graphene composite is very important in dealing with the energy shortage in the near future.

Fan et al. [50] developed a nanocomposite of TiO<sub>2</sub> and reduced graphene oxide as an efficient photocatalysts for the H<sub>2</sub> evolution. As an ideal conductor, graphene exhibited an excellent electron transfer capacity, leading to the enhancement of the lifetime of photogenerated electrons which is the key factor for the high photocatalytic water splitting activity of the TiO<sub>2</sub>/graphene composite. In order to further improve the electrons reduction capacity, Xiang et al. [52] prepared a TiO<sub>2</sub>/graphene composite exposed with (001) facets. The photogenerated electrons on (001) facet showed a relative higher reduction capacity than the electrons on the (101) facets, which combined with the high energy of graphene were responsible for the enhanced H<sub>2</sub> evolution of graphene modified TiO<sub>2</sub> nanosheets. Wang et al. [53] reported the synthesis of graphene@TiO<sub>2</sub> nanocomposites with controlled exposed crystal facets by a simple one-pot hydrothermal process. The prepared TiO<sub>2</sub>/graphene composite showed an enhanced photocatalytic H<sub>2</sub> evolution under the simulated solar light irradiation, owing to the exposed high reactive crystal facets and high dispersed TiO<sub>2</sub> nanocrystals on graphene.

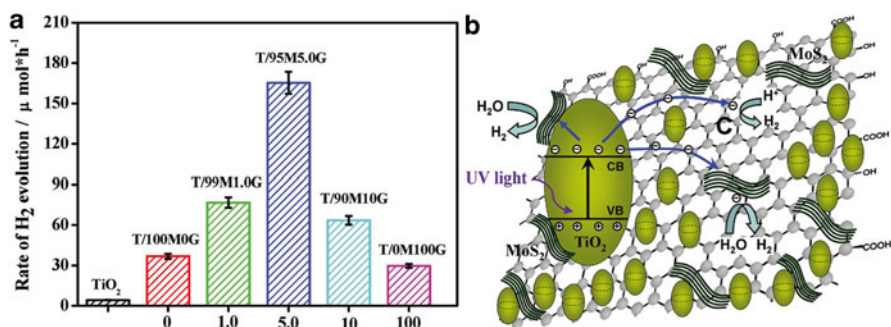


**Fig. 2.14** (a) Photocatalytic H<sub>2</sub> evolution of TiO<sub>2</sub>/MG composites. (b) Schematic illustration of the charge transfer in TiO<sub>2</sub>/MG composites. The proposed mechanism for the enhanced electron transfer in the TiO<sub>2</sub>/MG system under irradiation assumes that the photoexcited electrons are transferred from the CB of TiO<sub>2</sub> not only to MoS<sub>2</sub> nanosheets but also to the C atoms in graphene sheets, which can effectively reduce H<sup>+</sup> to produce H<sub>2</sub>. Reprinted with permission from Ref. [51]. Copyright 2012 American Chemical Society

In order to further improve the H<sub>2</sub> generation and decrease the cost of water splitting, MoS<sub>2</sub> is always used as the cocatalyst to replace the noble metals in the H<sub>2</sub> evolution photocatalysis. Xiang et al. [51] developed a new style composite material consisting of TiO<sub>2</sub> nanocrystals grown in the presence of a layered MoS<sub>2</sub>/graphene hybrid which was used as a high performance photocatalyst for the H<sub>2</sub> evolution (Fig. 2.14a). The TiO<sub>2</sub>/graphene composite showed high photocatalytic H<sub>2</sub> production activity with a rate as high as 165.3 μmol h<sup>-1</sup> for the sample containing 0.5 % MG hybrid cocatalyst consisting of 95 % MoS<sub>2</sub> and 5 % graphene. In the absence of noble metal of Pt, MoS<sub>2</sub> nanosheets in the hybrids could accept electrons and act as the active sites for the H<sub>2</sub> evolution, as shown in Fig. 2.14b. That because the fringe S in MoS<sub>2</sub> is always considered as an active site for the H<sub>2</sub> generation owing to its performance of the adsorption of hydrogens. The nanosized MoS<sub>2</sub> could further improve the H<sub>2</sub> generation due to the quantum-confinement effect. The authors concluded the advantages of using MoS<sub>2</sub> as the cocatalyst in the TiO<sub>2</sub>/graphene composite, including enhancement of charge separation, improvement of interfacial charge transfer, and an increase in the number of active adsorption sites and photocatalytic reaction centers.

### 2.2.3.3 CO<sub>2</sub> Photoreduction

With the intensification of the global greenhouse effect, CO<sub>2</sub> photoreduction become a hot research in the field of environment and energy. However, the traditional photocatalysts used for the reduction of CO<sub>2</sub> are still having a very low efficiency. Compared with some other carbon materials such as nanotubes and fullerenes, graphene has excellent conductive property, mechanical property, and chemical stability. Thereby, it is really urgency to design a new style graphene based photocatalyst for the CO<sub>2</sub> photoreduction.

Unfortunately, there is much less report on the CO<sub>2</sub> photoreduction compared with the reports on the organic pollutant photodegradation and water splitting on the TiO<sub>2</sub>/graphene composite, up to now. Tu et al. [55] fabricated the TiO<sub>2</sub>-graphene 2D sandwich-like hybrid nanosheets in a binary ethylenediamine (En)/H<sub>2</sub>O solvent by using an in situ simultaneous reduction hydrolysis technology. The high photocatalytic activity of G-TiO<sub>2</sub> hybrid was confirmed by photocatalytic reduction of CO<sub>2</sub> to valuable hydrocarbons (CH<sub>4</sub> and C<sub>2</sub>H<sub>6</sub>) in the presence of water vapor and without any noble metal cocatalysts (Fig. 2.15a). The enhanced conversion rate could be assigned to the well matching in the energy levels of d-orbital of TiO<sub>2</sub> and π-orbital of graphene. Moreover, the G-TiO<sub>2</sub> had chemical bond interactions and formed d-π electron orbital overlap. Under the UV light irradiation, the photogenerated electrons transferred from the TiO<sub>2</sub> to the graphene, which could reduce the CO<sub>2</sub> to generate the hydrocarbons, as shown in Fig. 2.15b. The synergistic effect of the surface-Ti<sup>3+</sup> sites and graphene favors the generation of C<sub>2</sub>H<sub>6</sub>, and the yield of the C<sub>2</sub>H<sub>6</sub> increases with the content of incorporated graphene.

In addition to the UV light, the visible light also could induce the photoreduction of CO<sub>2</sub> on the catalyst of TiO<sub>2</sub>/graphene composite. Tan et al. [54] successfully

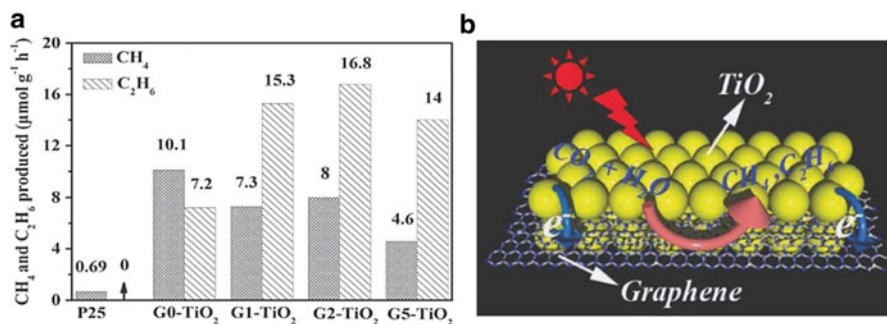


**Fig. 2.15** (a) Comparison of photocatalytic activity of samples G<sub>x</sub>-TiO<sub>2</sub> (x=0, 1, 2, 5) and P25. The molar ratio of C<sub>2</sub>H<sub>6</sub> to CH<sub>4</sub> increases from 0.71 (G<sub>0</sub>-TiO<sub>2</sub>), 2.09 (G<sub>1</sub>-TiO<sub>2</sub>), 2.10 (G<sub>2</sub>-TiO<sub>2</sub>), to 3.04 (G<sub>5</sub>-TiO<sub>2</sub>). (b) Schematic illustration of charge separation and transfer in G-TiO<sub>2</sub> system and photoreduction of CO<sub>2</sub> into CH<sub>4</sub> and C<sub>2</sub>H<sub>6</sub>. Reproduced from Ref. [55] with permission of John Wiley & Sons, Inc.

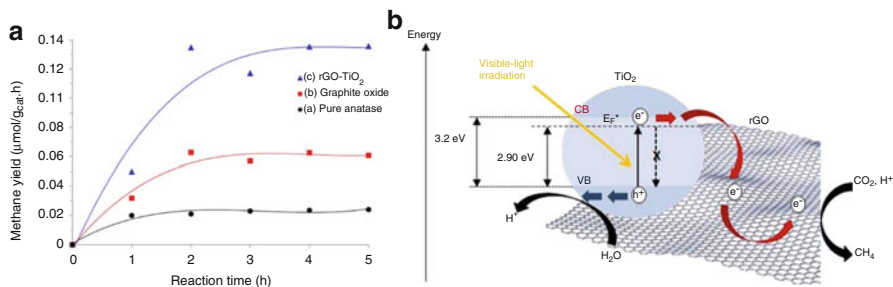


**Fig. 2.16** (a) Time dependence on photocatalytic formation rate of CH<sub>4</sub>. (b) Charge transfer and separation in rGO-TiO<sub>2</sub> composite. Schematic illustrating charge transfer and separation in the rGO-TiO<sub>2</sub> composite for photoreduction of CO<sub>2</sub> under visible light irradiation with introduction of a new energy level, E<sub>F</sub><sup>\*</sup>. Reprinted from Ref. [54]. Copyright 2013 Tan et al. licensee Springer

prepared the reduced graphene oxide (rGO)-TiO<sub>2</sub> hybrid nanocrystals through a novel and simple solvothermal synthetic route. The chemical bonds generated between TiO<sub>2</sub> and graphene could lead to the introduction of energy levels inside the bandgap of TiO<sub>2</sub> and narrow it from 3.2 to 2.9 eV, which was beneficial to the photoreduction of CO<sub>2</sub> under the visible light irradiation. Compared with the pure graphene oxide and the blank TiO<sub>2</sub>, the TiO<sub>2</sub>/graphene composite had the highest photoreduction efficiency of CO<sub>2</sub> in the visible light irradiation, as shown in Fig. 2.16a. The authors used the energy band theory to explain the reason of the photocatalytic activity of TiO<sub>2</sub>/graphene, and the corresponding schematic illustration are given in Fig. 2.16b. Generally, the overall mechanism of the CO<sub>2</sub> photoreduction process is a sequential combination of H<sub>2</sub>O oxidation and CO<sub>2</sub> reduction. Seen from Fig. 2.16b, the d orbital of TiO<sub>2</sub> and the π orbital of rGO matched well in energy levels, which induced a chemical bond interaction to form d-π electron orbital

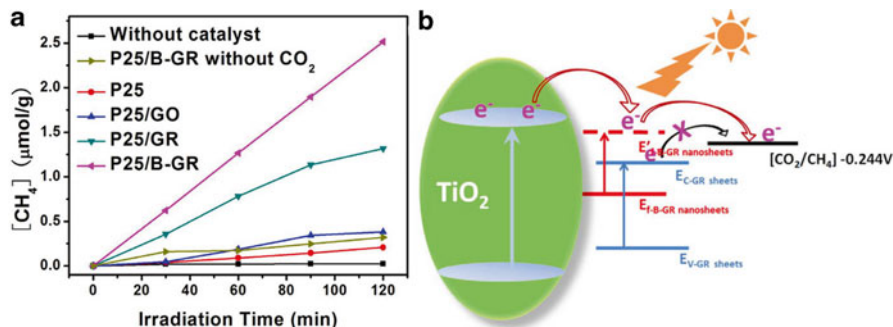


**Fig. 2.17** (a) Simulated solar light induced CO<sub>2</sub> reduction (The dark yellow line is the data of the blank photocatalytic test of P25/B-GR in the absence of CO<sub>2</sub>). (b) Schematic diagram of photo-generated electrons transfer between TiO<sub>2</sub> and graphene materials [57]. Copyright 2014 Rights Managed by Nature Publishing Group

overlap between TiO<sub>2</sub> and graphene. The CB flat band potential of TiO<sub>2</sub> is more negative than the reduction potential of CO<sub>2</sub>/CH<sub>4</sub>, indicating that the photogenerated electrons and holes on the irradiated rGO-TiO<sub>2</sub> composites could react with adsorbed CO<sub>2</sub> and H<sub>2</sub>O to produce CH<sub>4</sub> via an eight-electron reaction.

Our previous work also developed the application on the solar light-driven CO<sub>2</sub> photoreduction by using modified TiO<sub>2</sub>/graphene composite as the photocatalyst. Highly dispersed boron-doped graphene nanosheets loaded with TiO<sub>2</sub> nanoparticles were synthesized in our lab by using a simple mixing method [57]. The prepared P25/B-GR showed the higher CO<sub>2</sub> photoreduction capacity than other samples, as shown in Fig. 2.17a. Under the solar light irradiation, the photo-produced electrons of B-GR make its Fermi level ( $E'_{f-B-GR \text{ nanosheets}}$ ) being higher than the conduction band ( $E_{C-GR \text{ sheets}}$ ) of GR sheets (from  $E_{f-B-GR \text{ nanosheets}}$  to  $E'_{f-B-GR \text{ nanosheets}}$  in Fig. 2.17b). The level of  $E'_{f-B-GR \text{ nanosheets}}$  just falls in between the conduction band of TiO<sub>2</sub> and the relevant redox potentials of CO<sub>2</sub>/CH<sub>4</sub>, which is beneficial to the transfer of photo-generated electrons. Our results open the way to further implementation of graphene-based materials as photocatalysts that can be used in the photoreduction of CO<sub>2</sub> and photodegradation of other organic pollutants in the gas phase.

### 2.3 Three Dimensional TiO<sub>2</sub>/Graphene Composite

In addition to 2D-structured composites, the 3D-structured TiO<sub>2</sub>/graphene composites also attracted more attention in recent years. Compared with the 2D-structured graphene, 3D-graphene such as hydrogel or aerogel has some unique properties. For example, it has an ultra-light density, three-dimensional network structure, the appearance of the controllable morphology, controllable mechanical strength, excellent electrical conductivity, and strong adsorption performance for the gasoline and other organic compounds [86–88].

Since 2012, a versatile, ultralight, nitrogen (N) doped, three-dimensional (3D) graphene framework was successfully synthesized via a hydrothermal-calcination method by Qu and his coworkers for the first time [86], which has an excellent adsorption capacity of gasoline. The adsorption capacity could be as high as 200–600 times to its own weight for common pollution and organic solvents, much higher than that of the best carbonaceous sorbents reported previously. And then, Gao et al. [87] prepared the ultra-light graphene aerogel by a sol–gel and low-temperature freeze-drying technology, which had a record-breaking density of 0.16 mg cm<sup>-3</sup>. They found that the ultra-light aerogel not only had excellent electrical conductivity, but also exhibited the appearance of the controllable morphology and excellent performance of the adsorption of dyes and other organic pollutants.

To the 3D-graphene, the mechanical strength of the network structure is very important to spread its applications in the adsorption and photodegradation of organic pollutants. Most of the reported graphene aerogel and hydrogel are very fragile, which is difficult to undergo the stirring treatment during photocatalysis process. Hence, in order to improve the mechanical strength of 3D-graphene, Yu and his coworkers found that the adding of polyacrylamide (PAM) in the preparation of graphene hydrogel could greatly enhance the mechanical strength of the hydrogel [88]. The prepared GO/PAM hydrogels exhibited highly elastic and super-stretchable mechanical behavior, which was induced by the establishment of hydrogen-bonding interaction. This new nanocomposite would broaden the applications of hydrogels in the biomedical field and take us closer to artificial biotissues.

The abovementioned unique and outstanding performance of 3D-graphene determine that the composite of semiconductors compounded with the 3D-graphene has a broad application prospect in the field of environment protection and energy storage. To photocatalysis, TiO<sub>2</sub>-based materials are still the predominant photocatalyst owing to so many research focuses. Thus, in this section, we also give a simple summarization of the 3D-structured TiO<sub>2</sub>/graphene composites and applications in photocatalysis, as shown in Table 2.2.

### 2.3.1 Preparation

At first, we want to give a short introduction of the preparation of 3D-structured TiO<sub>2</sub>/graphene composites. Generally, there are three synthesized methods including the evaporation induced self-assembly, hydrothermal-freeze drying and thermal reduction for the preparation of TiO<sub>2</sub>/graphene hydrogen or aerogel.

The hydrothermal technology is still the main preparation method for the synthesis of 3D-structured TiO<sub>2</sub>/graphene composites, as shown in Table 2.2. Different from the preparation of 2D-structured TiO<sub>2</sub>/graphene by the hydrothermal method, the freeze drying after treatment plays an important role in the establishment of 3D-network structure during the hydrothermal process. A room temperature or high temperature drying will destroy the skeleton of 3D-graphene, resulting in the failure of formation of aerogel or hydrogel.

**Table 2.2** Summary of preparation of 3D-graphene-based composites and applications in photocatalysis

Synthesis method	Type of catalyst	Precursor	Characterizations	Photocatalytic targets and light source	Ref.
Hydrothermal-freeze drying	Titania/cellulose aerogels	TBOT, ethanol, anatase titania/cellulose (ATC aerogel)	SEM, TEM, XRD, XPS, TG-TA	Rhodamine B/methyl orange, A 100 W mercury lamp	[89]
	TiO <sub>2</sub> /GAs	Ti(SO <sub>4</sub> ) <sub>2</sub> +glucose+GO	SEM, TEM, BET, XPS, FTIR, TG-DTA, ESI measurement	Methyl orange, 300 W xenon lamp (with AM 1.5 air mass filter)	[84]
	TiO <sub>2</sub> -Graphene Hydrogel (TGH)	P25, GO	SEM, TEM, XRD, XPS, FTIR, BET, UV-DRS	Methylene blue, UV light	[90]
	MoS <sub>2</sub> /P25/graphene aerogel	P25 + MoS <sub>2</sub> nanosheets + GO	TEM, SEM, XRD, ESR, UV-DRS, PL	Photoelectrochemical (PEC) H <sub>2</sub> generation, a 350 W Xe arc lamp; methyl orange, UV light	[76]
Evaporation induced self-assembly	CdS/P25/graphene aerogels	P25 + CdS + GO	TEM, SEM, XRD, UV-DRS, Raman, Photocurrent and ESI measurements	Photoelectrochemical (PEC) H <sub>2</sub> Generation, A 150 W high-pressure xenon lamp with an AM 1.5 filter	[91]
	Hierarchical TiO <sub>2</sub> -SnO <sub>2</sub> -graphene aerogels	SnCl <sub>4</sub> ·5H <sub>2</sub> O+dimethylformamide (DMF)+GO+H <sub>2</sub> O, Ti(OBu) <sub>4</sub> +H <sub>2</sub> O	SEM, TEM, TGA, XRD		[92]
	P25-graphene hydrogels	P25 + GO evaporation at room temperature for 8 h	FESEM, XRD, FTIR, UV-DRS, Raman, BET	Methylene blue, UV light	[93]
Thermal reduction	Nanocomposite graphene hydrogel (NGH)	TiO <sub>2</sub> nanorods-Au nanoparticles, vitamin C, GO, heated to 90 °C	SEM, TEM, XRD, XPS, Raman, BET, UV-DRS, electrochemical impedance measurement	Photocatalytic H <sub>2</sub> production, UV/Visible light	[94]

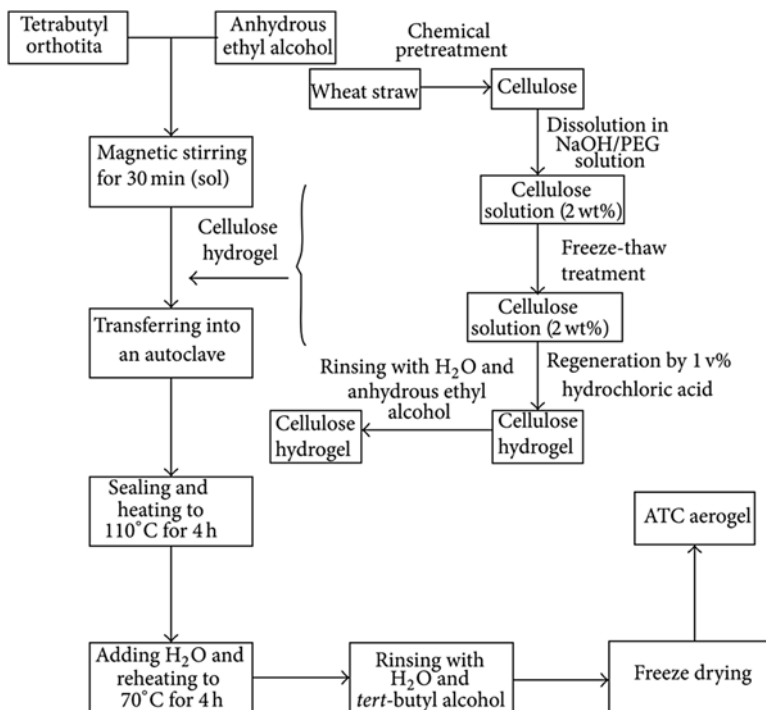


**Fig. 2.18** Diagram of the low-temperature hydrothermal preparation of ATC aerogel Reprinted with permission from Ref. [89]. Copyright Caichao Wan et al.

Wan et al. [89] developed a facile low-temperature hydrothermal method to prepare anatase titania/cellulose aerogels with strong photocatalytic activities. The involved low-temperature hydrothermal preparation of ATC aerogel is described in Fig. 2.18. All the precursors were mixed together and hydrothermal treated at 110 °C for 4 h. And then the mixture was reheated at 70 °C for another 4 h. After the freeze drying after treatment, the ATC aerogel was successfully obtained. Zhang et al. [90] also reported a new type of multifunctional TiO<sub>2</sub>-graphene nanocomposite hydrogel (TGH) by a similar one-pot hydrothermal approach and explored its environmental and energy applications as photocatalyst, reusable adsorbents, and supercapacitor. The graphene oxide was synthesized from graphite powder by the Hummer's method. The size of TGH could be freely adjusted by changing the volume of GO aqueous dispersion. The hydrothermal treatment could achieve the reduction of GO, the loading of TiO<sub>2</sub> on graphene, and the self-assembly of 3D-graphene at the same time.

Our recently research also found that the hydrothermal-freeze drying method is a very convenient technology to prepare the TiO<sub>2</sub>/GAs aerogel [84]. Very interestingly, we found that the addition of glucose during the hydrothermal treatment could achieve the in situ growth of TiO<sub>2</sub> nanocrystals with (001) facets on the surface of aerogel, which results into the highly dispersed TiO<sub>2</sub> nanocrystals on the

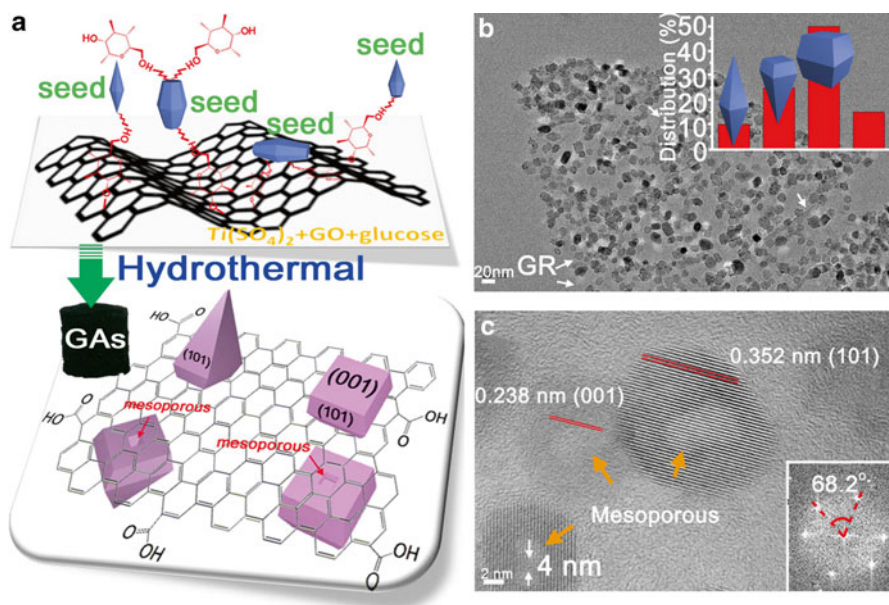


**Fig. 2.19** (a) Glucose-linked transformation pathway for in situ growth of  $\text{TiO}_2$  nanocrystals with (001) facets on the GAs surface. (b) TEM image for  $\text{TiO}_2/\text{GAs}$  (67 wt% of  $\text{TiO}_2$  in  $\text{TiO}_2/\text{GAs}$ ). Inset (b) is the corresponding morphology distribution of the  $\text{TiO}_2$  nanocrystals derived from 100 of  $\text{TiO}_2$  crystals in image (b). (c) HRTEM image for  $\text{TiO}_2/\text{GAs}$  (67 wt%). Inset (c) is the corresponding fast Fourier transform (FFT) pattern. Reprinted with permission from Ref. [84]. Copyright 2014 American Chemical Society

graphene and the strong interaction between  $\text{TiO}_2$  and graphene. As described in our report (Fig. 2.19),  $\text{Ti}(\text{SO}_4)_2$  was used as the titanium source to be first dissolved in an aqueous solution. The cultivation of  $\text{TiO}_2$  crystal seeds was necessary before a known amount of glucose being adsorbed on the seeds. During the hydrothermal process, large numbers of glucose molecules adsorbed onto the  $\text{TiO}_2$  (001) facets, generating nanosized seeds with exposed (001) facets owing to many hydroxyl groups on glucose. The hydroxyl groups at one end of glucose connected with GR, while the hydroxyl groups at the other end connected with the  $\text{TiO}_2$  facets. Thus, the hydroxyl groups enabled glucose to serve as the linker achieving the in situ growth of  $\text{TiO}_2$  nanocrystals on a GA surface.

In addition to prepare the  $\text{TiO}_2/\text{graphene}$  composites, the hydrothermal method also can be used to do some further modifications on the composites. For instance, the compounding of semiconductors such as  $\text{MoS}_2$ ,  $\text{SnO}_2$  or  $\text{CdS}$  on  $\text{TiO}_2/\text{graphene}$  composites. Han et al. [76] prepared a novel 3D-aerogel embedded with two types ( $\text{TiO}_2/\text{MoS}_2$ ) of functional nanomaterials via a facile one-pot hydrothermal process. During the hydrothermal process,  $\text{TiO}_2$  nanoparticles and  $\text{MoS}_2$  nanosheets were self-assembled into the 3D interconnected pores of aerogel, where the  $\text{TiO}_2$  nanoparticles decorated with the ultrathin  $\text{MoS}_2$  nanosheets were densely anchored onto the surface of graphene. The  $\text{MoS}_2$  could be used as the electron traps to enhance the

separation of photogenerated electrons and holes. In addition to the MoS<sub>2</sub>, they also synthesized the CdS/TiO<sub>2</sub>/graphene aerogel by the similar hydrothermal reaction [91]. During the hydrothermal reaction, the uniformly dispersed TiO<sub>2</sub> (P25) and CdS nanoparticles were loaded on the graphene sheets simultaneously, and the semiconductors were self-assembled into a 3D interconnected network aerogel. The precursor suspension gradually formed a network hydrogel and the P25 and CdS nanoparticles were loaded on the graphene support by one-step hydrothermal treatment. Finally, after cooling to the room temperature, a columnar hydrogel of 3D-graphene loaded with P25 and CdS was successfully obtained. Han et al. [92] also used the facile hydrothermal method to successfully synthesize the 3D structured TiO<sub>2</sub>-SnO<sub>2</sub>-graphene aerogels (TTGs). The synthesis procedure of TTGs is described in Fig. 2.20, which could be divided into three steps: (1) the stepwise hydrolysis of Sn<sup>4+</sup> and Ti<sup>4+</sup> to form the 2D-structured TiO<sub>2</sub>/SnO<sub>2</sub>/graphene composite; (2) the self-assembled of 2D-graphene based materials to form the 3D-structured graphene/semiconductors composite by a hydrothermal treatment. The generated graphene hydrogel contained TiO<sub>2</sub> and SnO<sub>2</sub> nanoparticles; (3) the last step is the freeze drying treatment. TTG could be obtained as a black monolith after the sublimation of water by the freeze drying of the hydrogel from step 2. It should be mentioned that the in situ reduction of GO in the hydrothermal process would decrease the oxygen content and improve the conductivity of the TTG.

As we discussed in Sect. 2.2, though the hydrothermal method is a simple and facile technology to prepare the nanocomposite materials, it always needs a relative higher synthesis temperature and much more expensive cost. Evaporation induced self-assembly technology is another method involving low energy consumption and operability, which has widely used in preparation of 3D-structured TiO<sub>2</sub>/graphene composite. Hou et al. [93] reported a room-temperature synthesis of chemically bonded TiO<sub>2</sub>-graphene composite hydrogels and applied them in the visible light-driven photocatalysis. Graphene oxide, P25 and other precursors were mixed together at room temperature, and then the mixture was ultrasonic for half an hour. After that, the 2D-composites were slow-evaporating solvent at room temperature

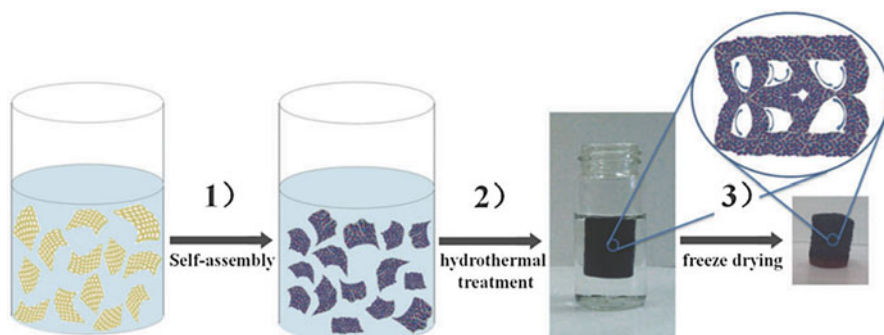
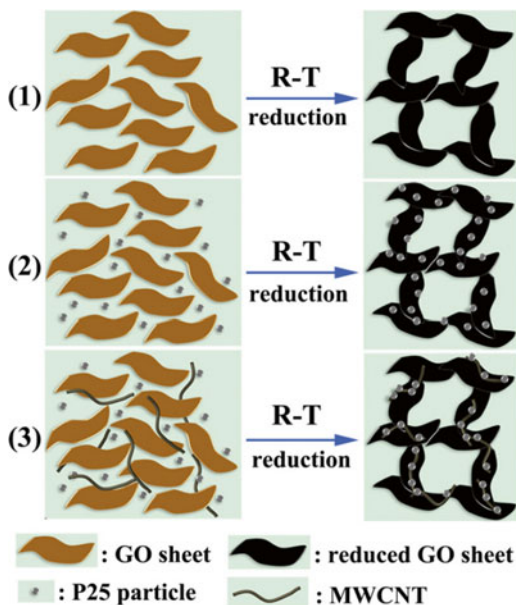


**Fig. 2.20** Schematic illustration of fabrication process for TTGs. Reproduced from Ref. [92] with permission of Royal Society of Chemistry

**Fig. 2.21** Diagrammatic sketches of formation for graphene hydrogels (1), P25-graphene hydrogels (2), and P25-MWCNTs-graphene hydrogels (3). R-T stands for room temperature. Reproduced from Ref. [93] with permission of Elsevier



for 8 h to obtain a hydrogels. The detailed diagrammatic sketches of the formation for different kinds of graphene-based hydrogels are illustrated in Fig. 2.21. With the reduction proceeding of the evaporation induced self-assembly process, the  $\pi$ -conjugated structures of reduced GO sheets were larger and larger which would increase the amount of  $\pi$ - $\pi$  stacking cross-links between graphene sheets. As a result, the partial overlapping or coalescing of flexible graphene sheets resulted into the construction of the 3D structures of hydrogels.

### 2.3.2 Characterizations

Very similar to the 2D-graphene, the XRD, Raman and XPS characterization are also always used to detect the reduction degree of the graphene oxides in the 3D-graphene based composite after a thermal reduction treatment, and the TEM, SEM are employed to detect the micro-morphology of the composite. For example, Zhang et al. [90] developed a new type of 3D-structured  $\text{TiO}_2$ /graphene composite hydrogels with multifunctions by using a facile one-step hydrothermal method. Seen from the Fig. 2.22, the composite had a 3D-block appearance (Fig. 2.22a), and the TEM image showed that the  $\text{TiO}_2$  nanoparticles are highly dispersed on the surface of graphene sheets (Fig. 2.22b). To the XRD and XPS analysis of 3D-structured  $\text{TiO}_2$ /graphene composite, the disappearing of the peak at  $10.4^\circ$  in the XRD patterns after a heat treatment indicated the successful reduction of GO (Fig. 2.22c), and the absence of characteristic peak of C-O and C=O in the C1s XPS spectra also suggested the reduction of GO during a hydrothermal process (Fig. 2.22d, e).

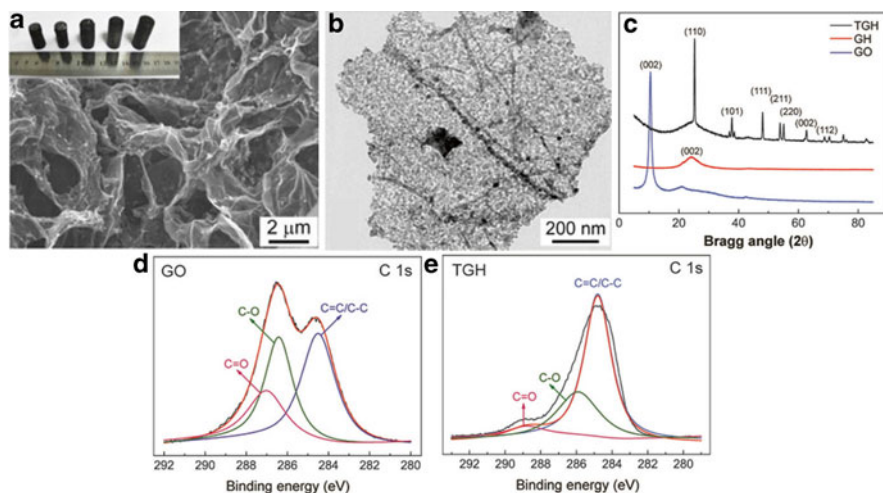


**Fig. 2.22** (a) Low-magnified SEM images of freeze-dried TGH, *inset* of (a) is the photograph of TGH with different ratios of TiO<sub>2</sub> to graphene at 180 °C for 2 h. (b) Low-magnified TEM images of freeze-dried TGH. (c) XRD patterns of TGH, GH, and GO; C1s XPS spectra of hydrogels before (d) and after (e) TiO<sub>2</sub> loading. Reprinted with permission from Ref. [90]. Copyright 2013 American Chemical Society

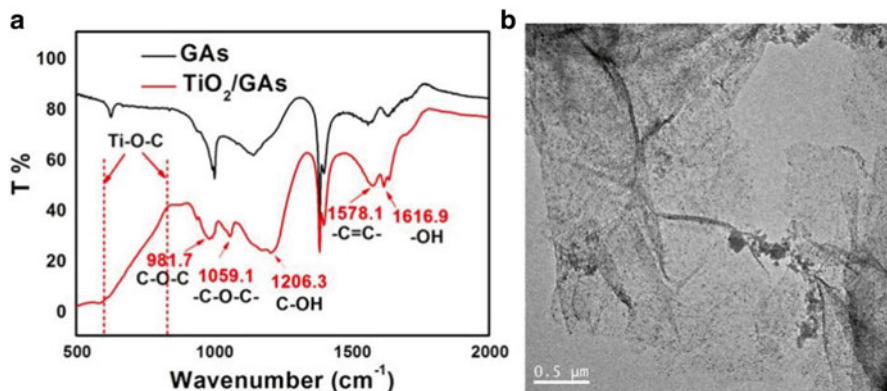


**Fig. 2.23** (a) FTIR spectra for GAS with and without TiO<sub>2</sub> nanocrystals (67 wt% TiO<sub>2</sub> on GAS); (b) TEM image for TiO<sub>2</sub>/GAS composite. Reprinted with permission from Ref. [84]. Copyright 2014 American Chemical Society

In our recent work, we used the FTIR characterization to investigate the connection between TiO<sub>2</sub> and graphene in the TiO<sub>2</sub>/GAS composite [84]. In the FTIR spectra of TiO<sub>2</sub>/GAS (Fig. 2.23a), the appearance of -C-O-C- signals resulted from the covalent linkage between the hydroxide radicals of GR and glucose. This reaction led to a new and very broad peak in the range of 600–800 cm<sup>-1</sup> belonging to the resulting Ti-O-C bond, indicating the interaction between the GA and TiO<sub>2</sub>. It was because of the formation of these chemical bonds to achieve the highly dispersed TiO<sub>2</sub> nanocrystals in situ growth on the 3D-structure graphene (Fig. 2.23b).

As we mention above, most of the reported graphene aerogels and hydrogels are very fragile, which are difficult to undergo stirring treatment during photocatalysis process, and thus, mechanical strength is another important characteristic for the  $\text{TiO}_2$ /graphene aerogels or hydrogels. In order to promote the mechanical strength of graphene hydrogels, Cong et al. [88] used polyacrylamide (PAM) as an additive to prepare a new kind of elastic GO/PAM hydrogel with exceptional mechanical strength by combining the characteristics of conventional double-network hydrogel and nanocomposite hydrogel, as shown in Fig. 2.24a. The authors explained that a  $\text{Ca}^{2+}$  coordination-induced GO nanosheet network and covalently cross-linked PAM network were intertwined by the hydrogen bonds between GO sheets and PAM chains, owing to the rich hydroxyl and epoxy groups on GO. The special interaction between ions-induced GO and PAM contributed to the dissipation of crack energy through unzipping and/or sliding of the weak crosslinks progressively or deforming the network conformation, which was responsible for the high toughness and good elasticity of the GO/PAM composite. Although the addition of organic polymer is beneficial to the mechanical strength of graphene hydrogels, the non-conducting high-molecular polymer may be harmful to the conductivity of the graphene which will hinder the application in photocatalysis. Hence, in our recent work, we employed glucose as a linker to synthesize mesoporous  $\text{TiO}_2$  nanocrystals grown in situ on graphene aerogels [84]. The prepared aerogels also had a good mechanical strength, as shown in Fig. 2.24e. The  $\text{TiO}_2$ /GAs prepared in the presence of glucose unfolded almost completely after removing the external pressure.

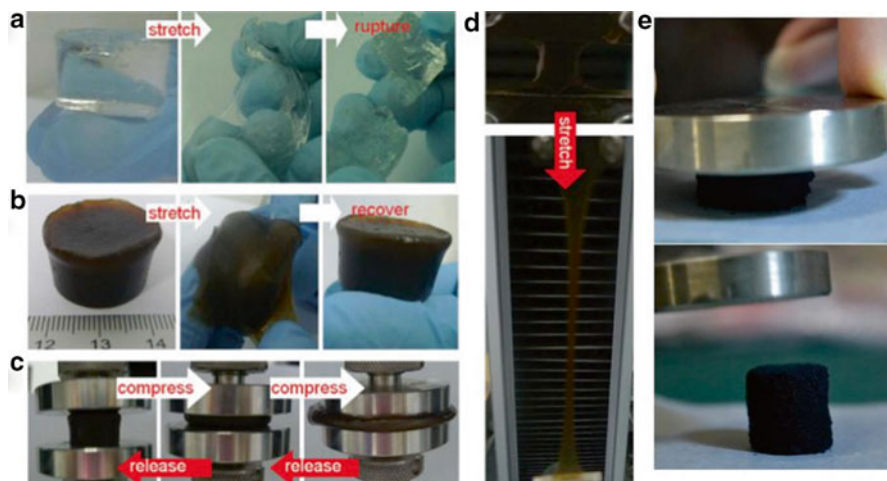


**Fig. 2.24** Photographs demonstrating the excellent mechanical behavior of GO/PAM hydrogels. PAM hydrogel is easily ruptured by stretching (a). The GO/PAM columnar hydrogels recover their initial shapes after stretching to an irregular film (b). After compression testing by  $>90\%$  (c). The GO/PAM hydrogel fixed to two clamps is stretched to 11 times its initial length in a tensile machine (d). Reproduced from Ref. [88] with permission of John Wiley & Sons, Inc. (e) The compressibility of  $\text{TiO}_2$ /GAs.  $\text{TiO}_2$ /GAs can be squeezed into a pellet under pressure. Once the external pressure is removed, the  $\text{TiO}_2$ /GAs unfolds almost completely. Reprinted with permission from Ref. [84]. Copyright 2014 American Chemical Society

### 2.3.3 Applications in Photocatalysis

Though 3D-structured graphene based materials have attracted much more attentions, but most of the applications focused on lithium ion battery rather than on photocatalysis. Seen from Table 2.2, Zhang et al. [90] developed a TiO<sub>2</sub>/graphene nanocomposite hydrogel (TGH) and explored its application in the photodegradation of methylene blue under the UV light irradiation. Compared with the pure graphene and blank TiO<sub>2</sub>, the TGH had an obvious enhanced photocatalytic activity. Our previous work also found that the TiO<sub>2</sub>/GAs exhibited a good adsorption capacity and photodegradation performance of methyl orange (Fig. 2.25a) [84]. Interestingly, our prepared aerogels had a good mechanical strength, indicating it was very easy for the recycle (Fig. 2.25b). The photocatalytic activity of TiO<sub>2</sub>/GAs was much more stable than other TiO<sub>2</sub>/graphene composites (Fig. 2.25a). In order to further improve the photocatalytic activity of the TiO<sub>2</sub>/graphene hydrogel, MoS<sub>2</sub> nanosheets were used as the cocatalyst to be loaded on the 3D-graphene [76]. Highly

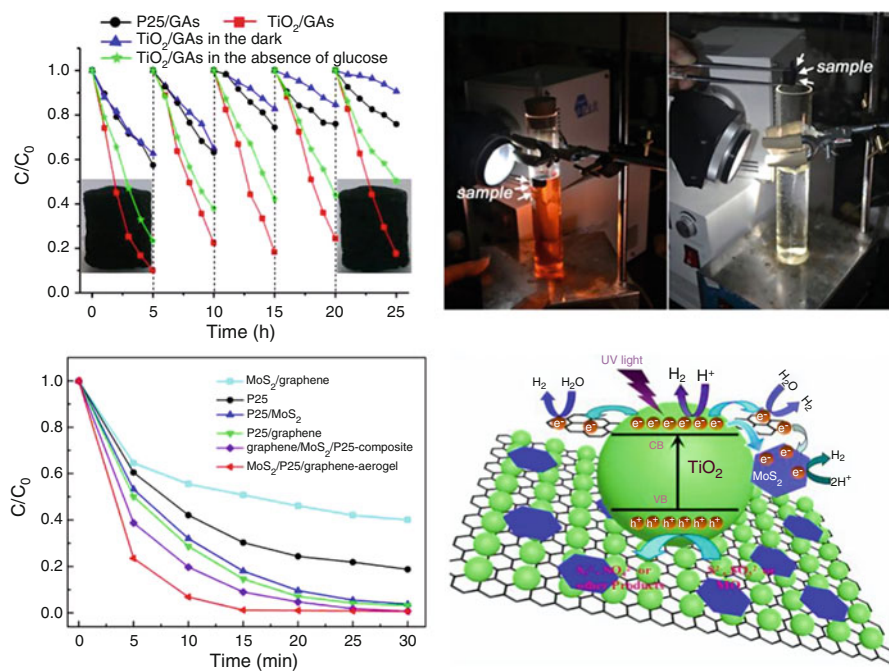


**Fig. 2.25** (a) Cycling photo-degradation of MO under simulated solar light irradiation (with an AM 1.5 air mass filter). (b) Pictures of photodegradation of MO under simulated solar light irradiation (with an AM 1.5 air mass filter). Reprinted with permission from Ref. [84]. Copyright 2014 American Chemical Society. (c) Photo-degradation of MO by different catalysts with a reaction time of 30 min under UV irradiation. (d) Illustration of the proposed reaction mechanism for hydrogen production and photo-degradation of MO over MoS<sub>2</sub>/P25/graphene-aerogel under UV irradiation. Reproduced from Ref. [76] with permission of Elsevier

dispersed  $\text{TiO}_2$  nanoparticles were densely anchored onto graphene nanosheets which were further decorated with the ultrathin  $\text{MoS}_2$  nanosheets. Compared with other photocatalysts such as P25,  $\text{P25}/\text{MoS}_2$ ,  $\text{P25}/\text{graphene}$ , and so on, the prepared 3D-structured  $\text{MoS}_2/\text{P25}/\text{graphene}$ -aerogel had the highest photocatalytic activity for the degradation of methyl orange among all the catalysts (Fig. 2.25c). The authors ascribed the superior photocatalytic activity of the ternary  $\text{MoS}_2/\text{P25}/\text{graphene}$  aerogel to three factors: (1) 3D-graphene porous network structure, excellent electroconductivity, and the maximization of accessible sites; (2) increasing active adsorption sites for the introduction of  $\text{MoS}_2$  nanosheets, (3) positive synergic effects among graphene,  $\text{MoS}_2$  nanosheets and  $\text{TiO}_2$  for decrease the recombination of photogenerated electrons and holes. Under the UV light irradiation, the introduced  $\text{MoS}_2$  could capture the photogenerated electrons from the conduction band of  $\text{TiO}_2$ , leading to the separation of electrons and holes (Fig. 2.25d).

In addition to the photodegradation of organic pollutants, the  $\text{TiO}_2/\text{graphene}$  hydrogels also could be used for the photocatalytic  $\text{H}_2$  evolution. Recently, Gao et al. [94] developed a 3D network of nanocomposite graphene hydrogel (NGH) materials. They demonstrated the practical applications of utilizing the NGH with water for the photocatalytic  $\text{H}_2$  production. Under UV–Visible light irradiation, the  $\text{TiO}_2$  nanorods and 2D-structured RGO- $\text{TiO}_2$  showed  $\sim 156$  and  $51 \mu\text{mol h}^{-1} \text{g}^{-1}$  of  $\text{H}_2$  generation respectively. RGO- $\text{TiO}_2$  gave a low  $\text{H}_2$  production due to the light shading of graphene induced by the incorporation of  $\text{TiO}_2$  nanorods between tightly packed/stacked 2D-graphene sheets. In contrast, by incorporating  $\text{TiO}_2$  nanorods into a 3D graphene with interconnected network pores, the photocatalytic activity was observed to increase to  $\sim 167$ – $242 \mu\text{mol h}^{-1} \text{g}^{-1}$ . By forming a 3D framework of NGH, a desirable porous structure were able to be created which would facilitate water absorption, and supply an open structure for the integration of  $\text{TiO}_2$  nanorods and Au nanoparticles for the charge generation and collection via interconnected highly conductive electrical pathways.

## 2.4 Conclusions and Prospective

Undoubtedly, graphene is an ideal support and conductor in photocatalysis, which can capture the photogenerated electrons from the  $\text{TiO}_2$  and transfer them to participating in the photocatalytic reactions. These electrons can also be stored in the  $\pi$ – $\pi$  network of the composites, which can not only reduce the graphene oxides by themselves but also shuttle to other metal particles deposited on the graphene layers. In that case, the introduction of graphene hinders the electron–hole recombination on  $\text{TiO}_2$  and further extends the absorption of light to the visible region.

However, most applications of  $\text{TiO}_2/\text{graphene}$  composites in photocatalysis concentrate on the laboratory conditions, and it is really difficult to achieve its industrial applications dealing with environmental issues. The poor dispersion of  $\text{TiO}_2$  on graphene, the low connection between  $\text{TiO}_2$  and graphene, the uncontrollable of micro-morphology of composite, and the difficult recycle for powders all hinder

industrial application of TiO<sub>2</sub>/graphene composite. Future works should be focused on the stability of TiO<sub>2</sub>/graphene composite as well as on its immobilization on appropriate substrates for operation of photoreactors in continuous mode, which is close to industrial application in environmental issues. Compare with the 2D-structured TiO<sub>2</sub>/graphene, we believe that the 3D-structured TiO<sub>2</sub>/graphene has relatively larger potential application in photocatalysis, owing to its strong adsorption capacity, excellent photocatalytic activity, and stable appearance. A serial of TiO<sub>2</sub>/graphene aerogels or hydrogels with strong mechanical strength arrangement together will exhibit an outstanding adsorption capacity and photocatalytic activity for organic pollutants. The block appearance of hydrogels can undergo strong stirring treatment and be very easy for recycle, which will decrease the cost and improve industrial applications.

**Acknowledgements** This work has been supported by National Nature Science Foundation of China (21577036, 21203062, 21377038, 21173077, 21237003), the National Basic Research Program of China (973 Program, 2013CB632403), the Research Fund for the Doctoral Program of Higher Education (20120074130001), the Fundamental Research Funds for the Central Universities (22A201514021), and the “Chenguang Program” supported by Shanghai Education Development Foundation and Shanghai Municipal Education Commission (14CG30).

## References

1. Fujishima A, Honda K (1972) Electrochemical photolysis of water at a semiconductor electrode. *Nature* 238:37–38
2. Bach U, Lupo D, Comte P, Moser JE, Weissortel F et al (1998) Solid-state dye-sensitized mesoporous TiO<sub>2</sub> solar cells with high photon-to-electron conversion efficiencies. *Nature* 395:583–585
3. Crossland EJW, Noel N, Sivaram V et al (2013) Mesoporous TiO<sub>2</sub> single crystals delivering enhanced mobility and optoelectronic device performance. *Nature* 495:215–219
4. O'Regan B, Gratzel M (1991) A low-cost, high-efficiency solar cell based on dye-sensitized colloidal TiO<sub>2</sub> films. *Nature* 353:737–740
5. Yang HG, Sun CH, Qiao SZ, Zou J, Liu G et al (2008) Anatase TiO<sub>2</sub> single crystals with a large percentage of reactive facets. *Nature* 453:638–641
6. Khan SUM, Al-Shahry M, Ingler WB (2002) Efficient photochemical water splitting by a chemically modified n-TiO<sub>2</sub>. *Science* 297:2243–2245
7. Linsebigler AL, Lu G, Yates JT (1995) Photocatalysis on TiO<sub>2</sub> surfaces: principles, mechanisms, and selected results. *Chem Rev* 95:735–758
8. Schneider J, Matsuoka M, Takeuchi M, Zhang J, Horiuchi Y, Anpo M, Bahnemann DW (2014) Understanding TiO<sub>2</sub> photocatalysis: mechanisms and materials. *Chem Rev* 114:9919–9986
9. Thompson TL, Yates JT (2006) Surface science studies of the photoactivation of TiO<sub>2</sub> new photochemical processes. *Chem Rev* 106:4428–4453
10. Xing M, Zhang J, Chen F (2009) New approaches to prepare nitrogen-doped TiO<sub>2</sub> photocatalysts and study on their photocatalytic activities in visible light. *Appl Catal B Environ* 89:563–569
11. Xing M, Zhang J, Chen F (2009) Photocatalytic performance of N-doped TiO<sub>2</sub> adsorbed with Fe<sup>3+</sup> ions under visible light by a redox treatment. *J Phys Chem C* 113:12848–12853
12. Xing MY, Wu YM, Zhang JL, Chen F (2010) Effect of synergy on the visible light activity of B, N and Fe Co-doped TiO<sub>2</sub> for the degradation of MO. *Nanoscale* 2:1233–1239

13. Xing M, Zhang J, Chen F, Tian B (2011) An economic method to prepare vacuum activated photocatalysts with high photo-activities and photo-sensitivities. *Chem Commun* 47:4947–4949
14. Xing MY, Qi DY, Zhang JL, Chen F (2011) One-step hydrothermal method to prepare carbon and lanthanum Co-doped TiO<sub>2</sub> nanocrystals with exposed {001} facets and their high UV and visible-light photocatalytic activity. *Chem Eur J* 17:11432–11436
15. Xing MY, Qi DY, Zhang JL, Chen F, Tian BZ, Bagwas S, Anpo M (2012) Super-hydrophobic fluorination mesoporous MCF/TiO<sub>2</sub> composite as a high-performance photocatalyst. *J Catal* 294:37–46
16. Xing MY, Fang WZ, Nasir M, Ma YF, Zhang JL, Anpo M (2013) Self-doped Ti<sup>3+</sup>-enhanced TiO<sub>2</sub> nanoparticles with a high-performance photocatalysis. *J Catal* 297:236–243
17. Xing MY, Yang BX, Yu H, Tian BZ, Bagwasi S, Zhang JL, Gongs XQ (2013) Enhanced photocatalysis by Au nanoparticle loading on TiO<sub>2</sub> single-crystal (001) and (110) facets. *J Phys Chem Lett* 4:3910–3917
18. Chen X, Mao SS (2007) Titanium dioxide nanomaterials: synthesis, properties, modifications, and applications. *Chem Rev* 107:2891–2959
19. Qi D, Xing M, Zhang J (2014) Hydrophobic carbon-doped TiO<sub>2</sub>/MCF-F composite as a high performance photocatalyst. *J Phys Chem C* 118:7329–7336
20. Cong Y, Chen F, Zhang J, Anpo M (2006) Carbon and nitrogen-codoped TiO<sub>2</sub> with high visible light photocatalytic activity. *Chem Lett* 35:800–801
21. Wu YM, Xing MY, Tian BZ, Zhang JL, Chen F (2010) Preparation of nitrogen and fluorine Co-doped mesoporous TiO<sub>2</sub> microspheres and photodegradation of acid orange 7 under visible light. *Chem Eng J* 162:710–717
22. Wu YM, Xing MY, Zhang JL (2011) Gel-hydrothermal synthesis of carbon and boron Co-doped TiO<sub>2</sub> and evaluating its photocatalytic activity. *J Hazard Mater* 192:368–373
23. Xing M, Li X, Zhang J (2014) Synergistic effect on the visible light activity of Ti<sup>3+</sup> doped TiO<sub>2</sub> nanorods/boron doped graphene composite. *Sci Rep* 4:5493
24. Yang P, Lu C, Hua N, Du Y (2002) Titanium dioxide nanoparticles Co-doped with Fe<sup>3+</sup> and Eu<sup>3+</sup> ions for photocatalysis. *Mater Lett* 57:794–801
25. Yu L, Yuan S, Shi LY, Zhao Y, Fang JH (2010) Synthesis of Cu<sup>2+</sup> doped mesoporous titania and investigation of its photocatalytic ability under visible light. *Microporous Mesoporous Mater* 134:108–114
26. Yuan XL, Zhang JL, Anpo M, He DN (2010) Synthesis of Fe<sup>3+</sup> doped ordered mesoporous TiO<sub>2</sub> with enhanced visible light photocatalytic activity and highly crystallized anatase wall. *Res Chem Intermed* 36:83–93
27. Cong Y, Zhang J, Chen F, Anpo M, He D (2007) Preparation, photocatalytic activity, and mechanism of nano-TiO<sub>2</sub> Co-doped with nitrogen and iron (III). *J Phys Chem C* 111:10618–10623
28. Chen XY, Lu DF, Lin SF (2012) Preparation and properties of sulfur-doped visible-light response S-TiO<sub>2</sub>/SiO<sub>2</sub> photocatalyst. *Chin J Catal* 33:993–999
29. Cheng C, Amini A, Zhu C, Xu Z et al (2014) Enhanced photocatalytic performance of TiO<sub>2</sub>-ZnO hybrid nanostructures. *Sci Rep* 4:4181
30. Dong F, Sun YJ, Fu M (2012) Enhanced visible light photocatalytic activity of V<sub>2</sub>O<sub>5</sub> cluster modified N-doped TiO<sub>2</sub> for degradation of toluene in Air. *Int J Photoenergy*. doi:10.1155/2012/569716
31. Dong RF, Tian BZ, Zhang JL, Wang TT, Tao QS, Bao SY et al (2013) AgBr@Ag/TiO<sub>2</sub> core-shell composite with excellent visible light photocatalytic activity and hydrothermal stability. *Catal Commun* 38:16–20
32. Driessen MD, Goodman AL, Miller TM et al (1998) Gas-phase photooxidation of trichloroethylene on TiO<sub>2</sub> and ZnO: influence of trichloroethylene pressure, oxygen pressure, and the photocatalyst surface on the product distribution. *J Phys Chem B* 102:549–556
33. Du X, Wang Y, Mu Y et al (2002) A new highly selective H<sub>2</sub> sensor based on TiO<sub>2</sub>/PtO-Pt dual-layer films. *Chem Mater* 14:3953–3957

34. Li W, Zhang M, Du Z, Ma Q, Jameel H, Chang H (2015) Photocatalytic degradation of lignin model compounds and kraft pine lignin by CdS/TiO<sub>2</sub> under visible light irradiation. *BioResources* 10(1):1245–1259
35. He CX, Tian BZ, Zhang JL (2010) Thermally stable SiO<sub>2</sub>-doped mesoporous anatase TiO<sub>2</sub> with large surface area and excellent photocatalytic activity. *J Colloid Interface Sci* 344:382–389
36. Liu Y, Xing M, Zhang J (2014) Ti<sup>3+</sup> and carbon Co-doped TiO<sub>2</sub> with improved visible light photocatalytic activity. *Chin J Catal* 35:1511–1519
37. Geim AK (2009) Graphene: status and prospects. *Science* 324:1530–1534
38. Li Z, Wang J, Liu X et al (2011) Electrostatic layer-by-layer self-assembly multilayer films based on graphene and manganese dioxide sheets as novel electrode materials for supercapacitors. *J Mater Chem* 21:3397–3403
39. Chen Z, Berciaud S, Nuckolls C, Heinz TF, Brus LE (2010) Energy transfer from individual semiconductor nanocrystals to graphene. *ACS Nano* 4:2964–2968
40. Rao CNR, Sood AK, Subrahmanyam KS, Govindaraj A (2009) Graphene: the new two-dimensional nanomaterial. *Angew Chem Int Ed* 48:7752–7777
41. Huang Q, Tian S, Zeng D et al (2013) Enhanced photocatalytic activity of chemically bonded TiO<sub>2</sub>/graphene composites based on the effective interfacial charge transfer through the C–Ti bond. *ACS Catal* 3:1477–1485
42. Chen C, Cai W, Long M et al (2010) Synthesis of visible-light responsive graphene oxide/TiO<sub>2</sub> composites with p/n heterojunction. *ACS Nano* 4:6425–6432
43. Wang D, Choi D, Li J et al (2009) Self-assembled TiO<sub>2</sub>/graphene hybrid nanostructures for enhanced Li-ion insertion. *ACS Nano* 3:907–914
44. Williams G, Seger B, Kamat PV (2008) TiO<sub>2</sub>-graphene nanocomposites UV-assisted photocatalytic reduction of graphene oxide. *ACS Nano* 2:1487–1491
45. Xin X, Zhou X, Wu J et al (2012) Scalable synthesis of TiO<sub>2</sub>/graphene nanostructured composite with high-rate performance for lithium ion batteries. *ACS Nano* 6:11035–11043
46. Zhang Y, Tang ZR, Fu X, Xu YJ (2010) TiO<sub>2</sub>-graphene nanocomposites for gas-phase photocatalytic degradation of volatile aromatic pollutant: is TiO<sub>2</sub>-graphene truly different from other TiO<sub>2</sub>-carbon composite materials? *ACS Nano* 4:7303–7314
47. Zhang H, Lv X, Li Y, Wang Y, Li J (2009) P25-graphene composite as a high performance photocatalyst. *ACS Nano* 4:380–386
48. Liang Y, Wang H, Chen Z, Dai H (2010) TiO<sub>2</sub> nanocrystals grown on graphene as advanced photocatalytic hybrid Materials. *Nano Res* 3:701–705
49. Lee JS, You KH, Park CB (2012) Highly photoactive, low bandgap TiO<sub>2</sub> nanoparticles wrapped by graphene. *Adv Mater* 24:1084–1088
50. Fan W, Lai Q, Zhang Q, Wang Y (2011) Nanocomposites of TiO<sub>2</sub> and reduced graphene oxide as efficient photocatalysts for hydrogen evolution. *J Phys Chem C* 115:10694–10701
51. Xiang Q, Yu J, Jaroniec M (2012) Synergetic effect of MoS<sub>2</sub> and graphene as cocatalysts for enhanced photocatalytic H<sub>2</sub> production activity of TiO<sub>2</sub> nanoparticles. *J Am Chem Soc* 134:6575–6578
52. Xiang Q, Yu J, Jaroniec M (2011) Enhanced photocatalytic H<sub>2</sub>-production activity of graphene-modified titania nanosheets. *Nanoscale* 3:3670–3678
53. Wang Z, Huang B, Dai Y et al (2012) Crystal facets controlled synthesis of graphene@TiO<sub>2</sub> nanocomposites by a one-pot hydrothermal process. *Cryst Eng Comm* 14:1687–1692
54. Tan LL, Ong WJ, Chai SP, Mohamed A (2013) Reduced graphene oxide-TiO<sub>2</sub> nanocomposite as a promising visible-light-active photocatalyst for the conversion of carbon dioxide. *Nanoscale Res Lett* 8:1–9
55. Tu W, Zhou Y, Liu Q et al (2013) An in situ simultaneous reduction-hydrolysis technique for fabrication of TiO<sub>2</sub>-graphene 2D sandwich-like hybrid nanosheets: graphene-promoted selectivity of photocatalytic-driven hydrogenation and coupling of CO<sub>2</sub> into methane and ethane. *Adv Funct Mater* 23:1743–1749
56. Zhang L, Xi Z, Xing M, Zhang J (2013) Effects of the preparation order of the ternary P25/GO/Pt hybrid photocatalysts on hydrogen production. *Int J Hydrogen Energ* 38:9169–9177

57. Xing M, Shen F, Qiu B, Zhang J (2014) Highly-dispersed boron-doped graphene nanosheets loaded with TiO<sub>2</sub> nanoparticles for enhancing CO<sub>2</sub> photoreduction. *Sci Rep* 4:6341–6346
58. Liu J, Bai H, Wang Y, Liu Z, Zhang X, Sun DD (2010) Self-assembling TiO<sub>2</sub> nanorods on large graphene oxide sheets at a two-phase interface and their anti-recombination in photocatalytic applications. *Adv Funct Mater* 20:4175–4181
59. Zhang Y, Pan C (2011) TiO<sub>2</sub>/graphene composite from thermal reaction of graphene oxide and its photocatalytic activity in visible light. *J Mater Sci* 46:2622–2626
60. Kamegawa T, Yamahana D, Yamashita H (2010) Graphene coating of TiO<sub>2</sub> nanoparticles loaded on mesoporous silica for enhancement of photocatalytic activity. *J Phys Chem C* 114:15049–15053
61. Zhang H, Xu P, Du G et al (2011) A facile one-step synthesis of TiO<sub>2</sub>/graphene composites for photodegradation of methyl orange. *Nano Res* 4:274–283
62. Jiang G, Lin Z, Chen C, Zhu L, Chang Q et al (2011) TiO<sub>2</sub> nanoparticles assembled on graphene oxide nanosheets with high photocatalytic activity for removal of pollutants. *Carbon* 49:2693–2701
63. Lambert TN, Chavez CA, Lu P et al (2009) Synthesis and characterization of titania/graphene nanocomposites. *J Phys Chem C* 113:19812–19823
64. Zhang Q, He Y, Chen X et al (2011) Structure and photocatalytic properties of TiO<sub>2</sub>-graphene oxide intercalated composite. *Chin Sci Bull* 56:331–339
65. Zhang XY, Li HP, Cui XL, Lin Y (2010) Graphene/TiO<sub>2</sub> nanocomposites: synthesis, characterization and application in hydrogen evolution from water photocatalytic splitting. *J Mater Chem* 20:2801–2806
66. Kim H, Moon G, Park Y, Choi W (2012) Solar photoconversion using graphene/TiO<sub>2</sub> composites: nanographene shell on TiO<sub>2</sub> core versus TiO<sub>2</sub> nanoparticles on graphene sheet. *J Phys Chem C* 116:1535–1543
67. Mohamed RM (2012) UV-assisted photocatalytic synthesis of TiO<sub>2</sub>-reduced graphene oxide with enhanced photocatalytic activity in decomposition of sarin in gas phase. *Desalina Water Treat* 50:147–156
68. Akhavan O, Abdolahad M, Esfandiari A, Mohatashamifar M (2010) Photodegradation of graphene oxide sheets by TiO<sub>2</sub> nanoparticles after a photocatalytic reduction. *J Phys Chem C* 114:12955–12959
69. Ng YH, Lightcap IV, Goodwin K, Matsumura M, Kamat PV (2010) To what extent do graphene scaffolds improve the photovoltaic and photocatalytic response of TiO<sub>2</sub> nanostructured films? *J Phys Chem Lett* 1:2222–2227
70. Sellappan R, Sun J, Galeckas A, Lindvall N et al (2013) Influence of graphene synthesizing techniques on the photocatalytic performance of graphene-TiO<sub>2</sub> nanocomposites. *Phys Chem Chem Phys* 15:15528–15537
71. Liu X, Pan L, Lv T, Zhu G et al (2011) Microwave-assisted synthesis of TiO<sub>2</sub>-reduced graphene oxide composites for the photocatalytic reduction of Cr(VI). *RSC Adv* 1:1245–1249
72. Lv T, Pan L, Liu X, Lu T et al (2012) One-step synthesis of CdS-TiO<sub>2</sub>-chemically reduced graphene oxide composites via microwave-assisted reaction for visible-light photocatalytic degradation of methyl orange. *Catal Sci Technol* 2:754–758
73. Pu X, Zhang D, Gao Y, Shao X, Ding G, Li S, Zhao S (2013) One-pot microwave-assisted combustion synthesis of graphene oxide-TiO<sub>2</sub> hybrids for photodegradation of methyl orange. *J Alloys Compd* 551:382–388
74. Wang Y, Yu J, Xiao W, Li Q (2014) Microwave-assisted hydrothermal synthesis of graphene based Au-TiO<sub>2</sub> photocatalysts for efficient visible-light hydrogen production. *J Mater Chem A* 2:3847–3855
75. Qiu B, Zhou Y, Ma Y, Yang X, Sheng W, Xing M, Zhang J (2015) Facile synthesis of the Ti<sup>3+</sup> self-doped TiO<sub>2</sub>-graphene nanosheet composites with enhanced photocatalysis. *Sci Rep* 5:8589–8591
76. Han W, Zang C, Huang Z et al (2014) Enhanced photocatalytic activities of three-dimensional graphene-Based aerogel embedding TiO<sub>2</sub> nanoparticles and loading MoS<sub>2</sub> nanosheets as co-catalyst. *Int J Hydrogen Energ* 39:19502–19512

77. Morales-Torres S, Pastrana-Martínez L, Figueiredo J, Faria J, Silva AT (2012) Design of graphene-based TiO<sub>2</sub> photocatalysts – a review. *Environ Sci Pollut Res* 19:3676–3687
78. Moser J, Punchedi S, Infelta PP, Graetzel M (1991) Surface complexation of colloidal semiconductors strongly enhances interfacial electron-transfer rates. *Langmuir* 7:3012–3018
79. Xing M, Zhang J, Qiu B, Tian B, Anpo M, Che M (2014) A brown mesoporous TiO<sub>2-x</sub>/MCF composite with an extremely high quantum yield of solar energy photocatalysis for H<sub>2</sub> evolution. *Small*. doi:10.1002/sml.201403056
80. Qiu B, Zhong C, Xing M, Zhang J (2015) Facile preparation of C-modified TiO<sub>2</sub> supported on MCF for high visible-light-driven photocatalysis. *RSC Adv* 5:17802–17808
81. Xing M, Fang W, Yang X, Tian B, Zhang J (2014) Highly-dispersed boron-doped graphene nanoribbons with enhancing conductibilities and photocatalysis. *Chem Commun* 136:5852–5855
82. Wang K, Li HN, Wu J et al (2011) TiO<sub>2</sub>-decorated graphene nanohybrids for fabricating an amperometric acetylcholinesterase biosensor. *Analyst* 136:3349–3354
83. Wu Y, Wang B, Ma Y et al (2010) Efficient and large-scale synthesis of few-layered graphene using an arc-discharge method and conductivity studies of the resulting films. *Nano Res* 3:661–669
84. Qiu B, Xing M, Zhang J (2014) Mesoporous TiO<sub>2</sub> nanocrystals grown in situ on graphene aerogels for high photocatalysis and lithium-ion batteries. *J Amer Chem Soc* 136:5852–5855
85. Zhou K, Zhu Y, Yang X, Jiang X, Li C (2011) Preparation of graphene-TiO<sub>2</sub> composites with enhanced photocatalytic activity. *New J Chem* 35:353–359
86. Zhao Y, Hu C, Hu Y, Cheng H, Shi G, Qu L (2012) A versatile, ultralight, nitrogen-doped graphene framework. *Angew Chem Int Ed* 51:11371–11375
87. Sun H, Xu Z, Gao C (2013) Multifunctional, ultra-flyweight, synergistically assembled carbon aerogels. *Adv Mater* 25:2554–2560
88. Cong HP, Wang P, Yu SH (2014) Highly elastic and superstretchable graphene oxide/polyacrylamide hydrogels. *Small* 10:448–453
89. Wan C, Lu Y JC, Sun Q, Li J (2014) A facile low-temperature hydrothermal method to prepare anatase titania/cellulose aerogels with strong photocatalytic activities for rhodamine B and methyl orange degradations. *J Nanomater*, Article ID 717016
90. Zhang Z, XiaoF GY, Wang S, Liu Y (2013) One-pot self-assembled three-dimensional TiO<sub>2</sub>-graphene hydrogel with improved adsorption capacities and photocatalytic and electrochemical activities. *ACS Appl Mater Interfaces* 5:2227–2233
91. Han W, Ren L, Gong L, Qi X et al (2013) Self-assembled three-dimensional graphene-based aerogel with embedded multifarious functional nanoparticles and its excellent photoelectrochemical activities. *ACS Sustain Chem Eng* 2:741–748
92. Han S, Jiang J, Huang Y, Tang Y, Cao J, Wu D, Feng X (2015) Hierarchical TiO<sub>2</sub>-SnO<sub>2</sub>-graphene aerogels for enhanced lithium storage. *Phys Chem Chem Phys* 17:1580–1584
93. Hou C, Zhang Q, Li Y, Wang H (2012) P25-graphene hydrogels: room-temperature synthesis and application for removal of methylene blue from aqueous solution. *J Hazard Mater* 205:229–235
94. Gao M, Peh CKN, Ong WL, Ho GW (2013) Green chemistry synthesis of a nanocomposite graphene hydrogel with three-dimensional nano-mesopores for photocatalytic H<sub>2</sub> production. *RSC Adv* 3:13169–13177

# Chapter 3

## Controllable Synthesis and Photocatalytic Activities of TiO<sub>2</sub> Nanocrystals

Shuai Yuan, Yin Zhao, and Liyi Shi

### 3.1 Introduction

TiO<sub>2</sub> nanocrystals with wide bandgap are considered to be the most potential photocatalysts. There are three TiO<sub>2</sub> crystal phases, i.e., rutile, anatase, and brookite in nature. Rutile is the thermodynamically stable form, whereas anatase and brookite are metastable. The photocatalytic properties of TiO<sub>2</sub> not only depend on crystal phase, crystallinity, but also on shape and size, etc. [1]. It is meaningful to find efficient synthetic methods for TiO<sub>2</sub> nanocrystals of controllable structures, and understand the structure–photocatalytic activity relationship.

Various synthetic methods have been developed to fabricate TiO<sub>2</sub> nanocrystals, such as sol–gel method [2], solvothermal (hydrothermal when water is used as solvent) method [3], and reverse micelle methods [4]. Among these methods, the solvothermal method normally has better controllability on size, shape, and crystallinity of the TiO<sub>2</sub> nanocrystal [5–7].

As illustrated in Fig. 3.1, the solvothermal processes are usually carried out in an autoclave lined with Teflon. Thus, crystal synthesis or crystal growth are carried out under high temperature and high pressure water conditions from substances which are insoluble in ordinary temperature and pressure (<100 °C, <1 atm). Usually, metal oxide nanocrystals with high crystallinity and dispersity could be obtained by solvothermal method at relative low temperature (<250 °C), because of avoidance of high-temperature calcination.

---

S. Yuan • Y. Zhao • L. Shi (✉)  
Research Center of Nanoscience and Nanotechnology, Shanghai University,  
99 Shangda Road, P.O. Box 111, Shanghai 200444, China  
e-mail: [shiliyi@shu.edu.cn](mailto:shiliyi@shu.edu.cn)

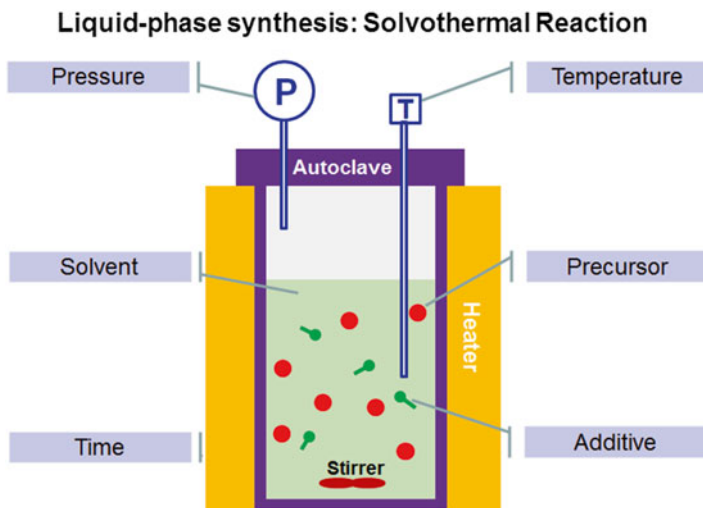


**Fig. 3.1** Scheme of the solvothermal reactor and reaction factor

Based on our previous work on controllable preparation of  $\text{TiO}_2$  nanocrystal [8–14], we summarize the solvothermal route using peroxotitanate solution to get  $\text{TiO}_2$  nanocrystals with controllable shape, size, and crystal phase and high dispersity.

## 3.2 Controllable Preparation and Photocatalytic Properties of $\text{TiO}_2$ Nanocrystals

The formation process of metal oxide nanocrystals in liquid phase can be divided into nucleation and crystal growth stages. Usually, there is no obvious boundary between the two stages [15]. During the solvothermal reaction process, the environment and reaction conditions will affect nucleation and crystal growth process. So it is flexible to adjust nanocrystal size, shape, and crystal phase by changing the factors illustrated in Fig. 3.1. Here, we focus on the effects of solvent and doping ions.

### 3.2.1 Effects of Solvents on Morphologies of $\text{TiO}_2$ Nanocrystals

It was reported that the (001) crystal face of anatase has higher photocatalytic activity than the other faces. However, the higher surface energy will drive (001) crystal face to progressively reduce. Yang et al. prepared  $\text{TiO}_2$  crystals with 64 % (001) face using  $\text{TiF}_4$  and HF as precursor and crystal face regulation agent, respectively.

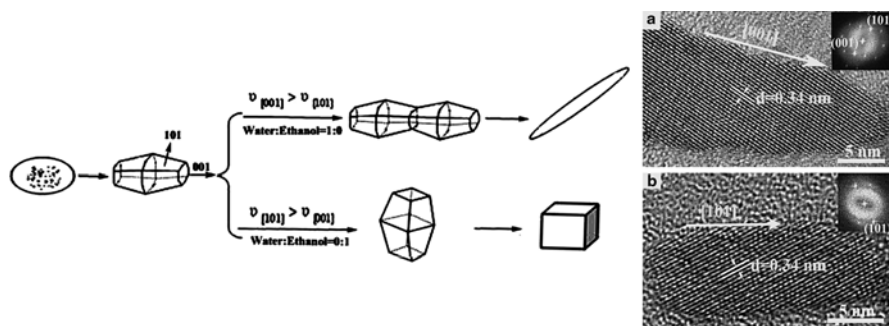


**Fig. 3.2** Growth schematic diagram of TiO<sub>2</sub> nanostructures in different solvent. Reprinted with permission from Ref. [9] copyright 2009 American Chemical Society

The F–Ti bond can reduce the surface energy of (001) face, making it more stable than (101) face. However, the fluoride has to be removed by high temperature calcination [16]. During the calcination process, the reconstruction of (001) face will inevitably happen. Moreover, the corrosivity of the TiF<sub>4</sub>–HF reaction system should be taken good care of.

The addition of surfactants in the hydrothermal reaction system is also an effective method to control the growth of nanocrystals by adjusting the surface energy. Lauric acid (LA), trioctylphosphine oxide (TOPO), quaternary ammonium hydrate (R<sub>3</sub>NOH, R=H, CH<sub>3</sub>, C<sub>2</sub>H<sub>5</sub>, C<sub>4</sub>H<sub>9</sub>, etc.) have been used to prepare TiO<sub>2</sub> nanocrystals with different shapes [17, 18]. However, there are considerable residual organic molecules on the TiO<sub>2</sub> surface. It is necessary to remove the residues by calcination. As a consequence, the growth and sintering of TiO<sub>2</sub> nanocrystals are inevitable.

Our group explored a facile route for the synthesis of controlled crystalline phase and morphology TiO<sub>2</sub> nanocrystal colloids from peroxotitanium acid (PTA) by solvothermal method [9]. This approach can give pure anatase by oxidizing amorphous titanium hydroxide precipitates using hydrogen peroxide, followed by the solvothermal treatment under low temperature and neutral pH condition. Colloidal TiO<sub>2</sub> nanocrystals with a diversity of well-defined morphologies and size-controlled nanoparticles have been successfully fabricated by adjusting the solvent of peroxotitanate complex solution.

As shown in Fig. 3.2, in the solvent mixture of alcohol and water, the alcohol molecule, such as ethanol, can strongly adsorb to the (001) plane, which depresses the growth rate along the [001] direction. As a result, the shape of TiO<sub>2</sub> nanocrystal transforms from “rectangular” to “rodlike” with increasing water–ethanol ratio. And the particle size increases from 9.0 to 47.0 nm with increasing water–ethanol ratio.

According to Fig. 3.3, the –O–O– bonds decomposed after solvothermal reaction. But there are organic molecule residues on the TiO<sub>2</sub> nanocrystal surface, which is confirmed by the C–H signal in FT-IR spectra of as-prepared TiO<sub>2</sub> samples. However, after the vacuum treatment at 40 °C, the organic molecules can be removed effectively, indicated by the disappearance of C–H peaks in FT-IR spectra.

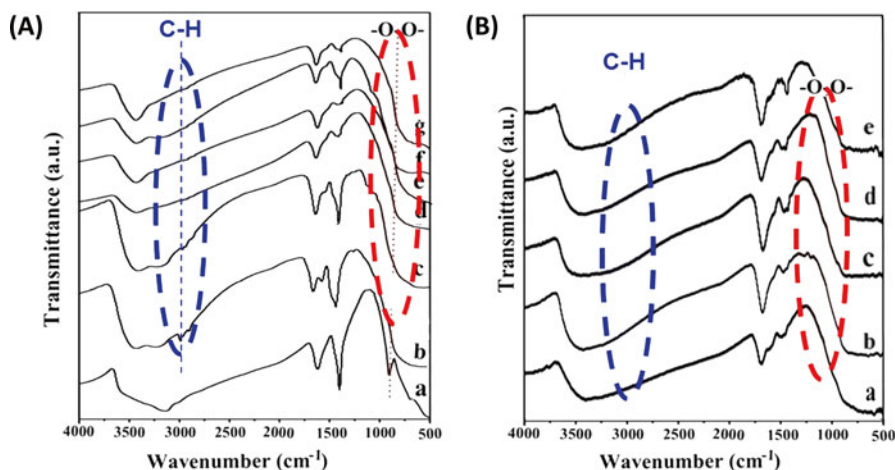


**Fig. 3.3** (A) FT-IR patterns of TiO<sub>2</sub> nanocrystals prepared in (a) H<sub>2</sub>O and (b) ethanol before solvothermal treatment and in (c) ethanol, (d) H<sub>2</sub>O–ethanol=1:4, (e) H<sub>2</sub>O–ethanol=1:1, (f) H<sub>2</sub>O–ethanol=4:1, and (g) H<sub>2</sub>O after solvothermal. Reprinted with permission from Ref. [9] copyright 2009 American Chemical Society; (B) TiO<sub>2</sub> nanocrystals prepared by solvothermal method in (a) ethanol, (b) H<sub>2</sub>O–ethanol=1:4, (c) H<sub>2</sub>O–ethanol=1:1, (d) H<sub>2</sub>O–ethanol=4:1, (e) H<sub>2</sub>O after removing the organic molecules adsorbed on surface by vacuum at 40 °C

**Table 3.1** The photocatalytic activities of TiO<sub>2</sub> nanocrystals before and after vacuum treatment at 313 K

Sample <sup>a</sup>	$T_W$	$T_{WE4}$	$T_{WE1}$	$T_{WE0.25}$	$T_E$
$V_{H_2O}:V_{ethanol}^b$	1:0	4:1	1:1	1:4	0:1
$D_{phenol}^c$ (%)	33.8	50.4	77.4	87.0	29.0
$D_{phenol}^d$ (%)	35.0	57.5	73.9	87.8	34.3

<sup>a</sup> $T_W$ ,  $T_{WE4}$ ,  $T_{WE1}$ ,  $T_{WE0.25}$ ,  $T_E$  represent samples prepared in the solvent of pure H<sub>2</sub>O, solvent mixture of H<sub>2</sub>O and ethanol=4:1, H<sub>2</sub>O and ethanol=1:1, H<sub>2</sub>O and ethanol=1:4, and pure ethanol

<sup>b</sup> $V$  is volume of solvent

<sup>c</sup> $D_{phenol}$  refers to the degrading efficiency of phenol on the as-prepared samples [9]

<sup>d</sup> $D_{phenol}$  refers to the degrading efficiency of phenol on the vacuum-treated samples

The photocatalytic activities of TiO<sub>2</sub> nanocrystals were evaluated by decomposing phenol under UV light irradiation. The TiO<sub>2</sub> particles prepared in the 1:4 water–ethanol solvent showed the highest activity due to its morphology [9]. Moreover, the photocatalytic activities of the vacuum treated sample show a slight improvement compared with the as-prepared samples, which should be attributed to cleaner surface (Table 3.1).

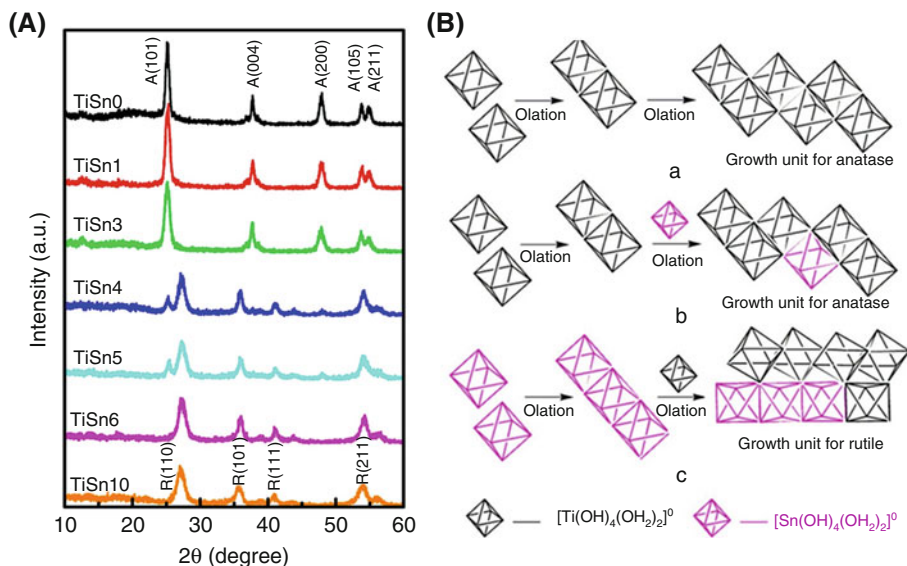


**Fig. 3.4** (A) XRD patterns of Ti<sub>1-x</sub>Sn<sub>x</sub>O<sub>2</sub> nanocrystal colloids. A anatase, R rutile; (B) Proposed reaction mechanism: (a) undoped anatase TiO<sub>2</sub> samples; (b) low level Sn<sup>4+</sup>-doped anatase Ti<sub>1-x</sub>Sn<sub>x</sub>O<sub>2</sub> samples; (c) high level Sn<sup>4+</sup>-doped rutile Ti<sub>1-x</sub>Sn<sub>x</sub>O<sub>2</sub> samples. Reprinted from Ref. [10] with permission from Elsevier

### 3.2.2 Effects of Dopants on Crystal Phase and Shape of TiO<sub>2</sub> Nanocrystals

Compared with anatase-type TiO<sub>2</sub>, rutile-type TiO<sub>2</sub> is thermally stable, of higher refractive index and has wider sunlight absorption range. In addition, there is synergistic effect between anatase and rutile TiO<sub>2</sub> on the photocatalytic properties [19]. However, it is difficult to prepare highly dispersed rutile TiO<sub>2</sub> nanocrystals by high-temperature calcination methods or conventional hydrothermal methods.

Based on our previous works, rutile-type TiO<sub>2</sub> nanocrystal colloids with small size (<10 nm) have been successfully synthesized from peroxo-metal-complex precursor by hydrothermal method in the presence of crystal phase-inducing agent Sn<sup>4+</sup> [10, 12]. As shown in Fig. 3.4A, the XRD pattern of undoped TiO<sub>2</sub> sample is indexed as anatase phase. With increasing Sn<sup>4+</sup> doping concentration, TiO<sub>2</sub> nanocrystals transferred from anatase to rutile gradually. Moreover, all diffraction peaks corresponding to SnO<sub>2</sub> are not present in the pattern of all samples [20]. Based on these results, it can be inferred that either Sn<sup>4+</sup> ion has been substituted into the crystal lattice sites of TiO<sub>2</sub> or SnO<sub>2</sub> exists as a highly dispersed polymeric form over the TiO<sub>2</sub> surface, which could not be detected by XRD.

The significant changes in the phase structure of Sn<sup>4+</sup> doped TiO<sub>2</sub> samples (Ti<sub>1-x</sub>Sn<sub>x</sub>O<sub>2</sub>) can be well explained by the addition of dopant Sn<sup>4+</sup> ion. The ionic radius of Sn<sup>4+</sup> is 0.069 nm, and it is likely to substitute Ti<sup>4+</sup> (with an ionic radius of 0.068 nm)

in the  $\text{TiO}_2$  lattice [21, 22]. Furthermore, both of them belong to the tetragonal crystal symmetry with the space group  $P42/mmm$ , and have very similar lattice parameters [23]. Therefore, the addition of  $\text{Sn}^{4+}$  into the reaction solution can assist the crystallization in rutile structure. Calculated by Scherrer formula, the anatase crystalline size gradually decreased from 16.1 to 9.8 nm with increasing  $\text{Sn}^{4+}$  content (from  $\text{TiSn0}$  to  $\text{TiSn3}$ ). After that, an obvious increase to 15.5 and 18.8 nm can be observed (samples  $\text{TiSn4}$  and  $\text{TiSn5}$ ). In the case of the rutile phase, the crystalline size slightly decreases from 8.0 to 7.0 nm with enhancing the  $\text{Sn}^{4+}$  doping levels from  $\text{TiSn4}$  to  $\text{TiSn10}$ . Generally,  $\text{Sn}^{4+}$  doping  $\text{TiO}_2$  can inhibit the growth of crystal grains due to the presence of  $\text{Ti-O-Sn}$  [24]. However, an interesting trend for anatase crystalline size, that is, a first decrease at low dopant level and an obvious increase at high dopant level is observed, which should be ascribed to the fact that the dopant  $\text{Sn}^{4+}$  concentrated in rutile and has a lower effect on anatase when two phases coexist [25]. This assumption can be confirmed from the experiment results that rutile crystals are smaller than anatase crystals in the case of coexistence of anatase and rutile phase samples. According to the report by Overstone and Yanagisawa, a critical particle size is required for anatase to rutile transformation [26]. However, a different trend is obtained in our work, which indicates rutile formation occurs through a different mechanism, favored by tin incorporation.

The growth of nanocrystals in hydrothermal solution occurring in the presence of  $\text{Sn}^{4+}$  ions could be illustrated by the scheme in Fig. 3.4B. Firstly, the peroxotitanium complex is a dinuclear of two  $\text{Ti}^{4+}$  ions coordinated by peroxide ligands. This dinuclear peroxotitanium complex slowly condenses to polynuclear anions. After being heated, the peroxy groups decompose and the monomer  $[\text{M}(\text{OH})_4(\text{OH}_2)_2]^0$  ( $\text{M}:\text{Ti}$  or  $\text{Sn}$ ) growing units are formed [27, 28]. In the case of low  $\text{Sn}^{4+}$  dopant level or undoped condition, octahedral  $[\text{Ti}(\text{OH})_4(\text{OH}_2)_2]^0$  is the dominant basic unit. When the basic unit octahedral  $[\text{Ti}(\text{OH})_4(\text{OH}_2)_2]^0$  joined together, sharing other edges leading to anatase has more chances than joining the opposite edge to form rutile (Fig. 3.4B, a and b) [29]. At high  $\text{Sn}^{4+}$  dopant level, the basic unit octahedral  $[\text{Sn}(\text{OH})_4(\text{OH}_2)_2]^0$  increases in the reaction medium. The more the  $[\text{Sn}(\text{OH})_4(\text{OH}_2)_2]^0$  exists, the more the rutile nuclei can be formed, which results in the  $[\text{Ti}(\text{OH})_4(\text{OH}_2)_2]^0$  units growing epitaxially on it (Fig. 3.4B, c) [30]. Thus, the addition of dopant  $\text{Sn}^{4+}$  affects the crystalline phase structure of the  $\text{Ti}_{1-x}\text{Sn}_x\text{O}_2$  samples. This possible growth mechanism was confirmed by XPS and ICP-AES analysis results, i.e., dopant  $\text{Sn}^{4+}$  tends more to form a nucleus and induces the formation of rutile at high doping concentration [10]. The effect of other dopants, such as  $\text{W}^{6+}$ , was also investigated. The results shows the doping concentration of  $\text{W}^{6+}$  only affects the morphology of  $\text{TiO}_2$ , and has no effect on crystal phase [14].

The photocatalytic activity of  $\text{Sn}^{4+}$  doped  $\text{TiO}_2$  nanocrystals was evaluated by the Fdegradation of phenol under UV light. The anatase nanocrystal with smaller size and larger surface area shows higher photocatalytic activity (Table 3.2).

**Table 3.2** Kinetic values for the phenol photodecomposition and photocatalytic ability results for Ti<sub>1-x</sub>Sn<sub>x</sub>O<sub>2</sub> nanocrystal colloids [10]

Sample <sup>a</sup>	Degradation of phenol (%) <sup>b</sup>	Apparent rate constant $k$ ( $h^{-1}$ )	Half-life $t_{1/2}$ (h)
TiSn0	21.0	0.0307	22.5
TiSn1	83.4	0.317	2.2
TiSn3	84.9	0.332	2.1
TiSn4	22.9	0.0367	18.9
TiSn5	17.2	0.0327	21.2
TiSn6	9.8	0.0148	46.7
TiSn10	42.6	0.0756	9.2

<sup>a</sup> TiSn0, TiSn1, etc. represent TiO<sub>2</sub>, Ti<sub>0.99</sub>Sn<sub>0.01</sub>O<sub>2</sub>, etc., respectively

<sup>b</sup> The samples were irradiated under UV light for 6 h

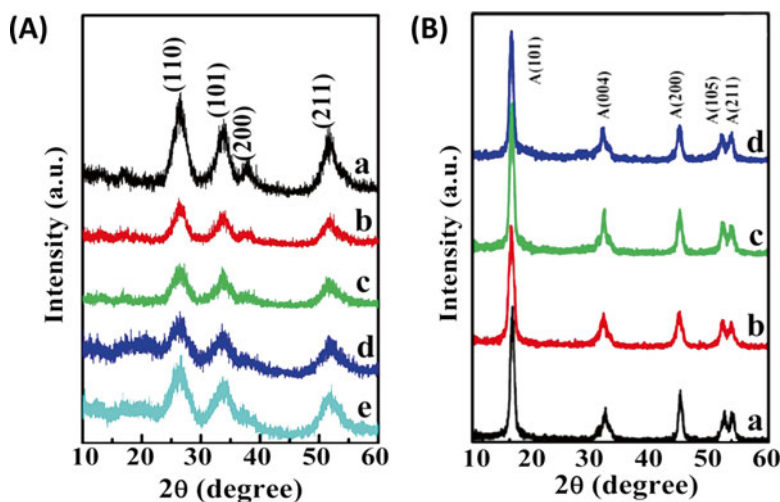


**Fig. 3.5** (A) XRD patterns of SnO<sub>2</sub> nanocrystals prepared in (a) H<sub>2</sub>O, (b) H<sub>2</sub>O–ethanol=4:1, (c) H<sub>2</sub>O–ethanol=1:4, (d) ethanol, and (e) 1-butanol. Reprinted from Ref. [12]; (B) XRD patterns of Sn<sup>4+</sup> doped TiO<sub>2</sub> nanocrystals prepared in 1-butanol: (a) TiO<sub>2</sub>, (b) Ti<sub>0.97</sub>Sn<sub>0.03</sub>O<sub>2</sub>, (c) Ti<sub>0.95</sub>Sn<sub>0.05</sub>O<sub>2</sub>, and (d) Ti<sub>0.90</sub>Sn<sub>0.10</sub>O<sub>2</sub>. Reprinted from Ref. [11] with permission from Elsevier

### 3.2.3 Synergetic Effects of Solvent and Dopants

To better understand the effect of solvent and Sn<sup>4+</sup> doping on crystal phase and morphology of TiO<sub>2</sub> nanocrystals, we further investigated the crystallinity of pure SnO<sub>2</sub> prepared in water, mixed water–ethanol solvent, ethanol, and 1-butanol, compared by XRD (Fig. 3.5A). The crystallinity of SnO<sub>2</sub> prepared in mixed water–alcohol or alcohol solvent is relatively poor compared with SnO<sub>2</sub> prepared in water. When using 1-butanol as reaction solvent, only anatase TiO<sub>2</sub> nanocrystal is obtained even

at high  $\text{Sn}^{4+}$  doping content (Fig. 3.5B), which may be due to the steric effects of alkyl chain of 1-butanol hindering the formation of rutile nuclei [11, 12]. As a result,  $\text{Sn}^{4+}$  doped anatase  $\text{TiO}_2$  can be obtained even in high  $\text{Sn}^{4+}$  doping concentration.

### 3.3 Summary

Crystal phase, size, and shape of  $\text{TiO}_2$  can be tuned by controlling the nucleation and crystal growth environment during solvothermal reaction. Here, we emphasize the effect of solvent and doping agent on crystal phase and morphology of  $\text{TiO}_2$  nanocrystals. One advantage of preparing  $\text{TiO}_2$  nanocrystals in a solvent mixture of alcohol and water by solvothermal method lies in that the small alcohol molecules adsorbed on the surface of as-prepared  $\text{TiO}_2$  nanocrystals can be removed easily by vacuum treatment at low temperature. As a consequence, the photocatalytic activity of  $\text{TiO}_2$  can be preserved by avoiding the high temperature calcination.

### References

1. Schneider J, Matsuoka M, Takeuchi M et al (2014) Understanding  $\text{TiO}_2$  photocatalysis: mechanisms and materials. *Chem Rev* 114(19):9919–9986
2. Leong KH, Monash P, Ibrahim S et al (2014) Solar photocatalytic activity of anatase  $\text{TiO}_2$  nanocrystals synthesized by non-hydrolytic sol–gel method. *Sol Energy* 101:321–332
3. Carlucci C, Xu H, Scremin BF et al (2014) Selective synthesis of  $\text{TiO}_2$  nanocrystals with morphology control with the microwave-solvothermal method. *CrystEngComm* 16:1817–1824
4. Stathatos E, Lianos P, Monte FD et al (1997) Formation of  $\text{TiO}_2$  nanoparticles in reverse micelles and their deposition as thin films on glass substrates. *Langmuir* 13(16):4295–4300
5. Li XL, Peng Q, Yi JX et al (2006) Near monodisperse  $\text{TiO}_2$  nanoparticles and nanorods. *Chem Eur J* 12:2383–2391
6. Dinh C-T, Nguyen T-D, Kleitz F et al (2009) Shape-controlled synthesis of highly crystalline titania nanocrystals. *ACS Nano* 3(11):3737–3743
7. Wen CZ, Jiang HB, Qiao SZ et al (2011) Synthesis of high-reactive facets dominated anatase  $\text{TiO}_2$ . *J Mater Chem* 21:7052–7061
8. Zhang M, Shi L, Yuan S et al (2009) Synthesis and photocatalytic properties of highly stable and neutral  $\text{TiO}_2/\text{SiO}_2$  hydrosol. *J Colloid Interface Sci* 330(1):113–118
9. Liao J, Shi L, Yuan S et al (2009) Solvothermal synthesis of  $\text{TiO}_2$  nanocrystal colloids from peroxotitanate complex solution and their photocatalytic activities. *J Phys Chem C* 113(43):18778–18783
10. Zhao Y, Liu J, Shi L et al (2010) Surfactant-free synthesis uniform  $\text{Ti}_{1-x}\text{Sn}_x\text{O}_2$  nanocrystal colloids and their photocatalytic performance. *Appl Catal B* 100(1–2):68–76
11. Zhao Y, Liu J, Shi L et al (2011) Solvothermal preparation of  $\text{Sn}^{4+}$  doped anatase  $\text{TiO}_2$  nanocrystals from peroxo-metal-complex and their photocatalytic activity. *Appl Catal B* 103(3–4):436–443
12. Liu J, Zhao Y, Shi L et al (2011) Solvothermal synthesis of crystalline phase and shape controlled  $\text{Sn}^{4+}$ -doped  $\text{TiO}_2$  nanocrystals: effects of reaction solvent. *ACS Appl Mater Interfaces* 3(4):1261–1268
13. Li W, Zhao Y, Yuan S et al (2012) Synthesis and characterization of highly dispersed  $\text{TiO}_2$  nanocrystal colloids by microwave-assisted hydrothermal method. *J Mater Sci* 47:7999–8006

14. Xu H, Liao J, Yuan S et al (2014) Tuning the morphology, stability and photocatalytic activity of TiO<sub>2</sub> nanocrystal colloids by tungsten doping. *Mater Res Bull* 51:326–331
15. Jun YW, Choi JS, Cheon J (2006) Shape control of semiconductor and metal oxide nanocrystal through nonhydrolytic colloidal routes. *Angew Chem Int Ed* 45(21):3414–3439
16. Yang HG, Sun CH, Qiao SZ et al (2008) Anatase TiO<sub>2</sub> single crystals with a large percentage of reactive facets. *Nature* 453:638–642
17. Jun YW, Casula MF, Sim JH et al (2003) Surfactant assisted elimination of a high energy facet as a means of controlling the shapes of TiO<sub>2</sub> nanocrystals. *J Am Chem Soc* 125(51):15981–15985
18. Chemseddine A, Moritz T (1999) Nanostructuring titania: control over nanocrystal structure, size, shape, and organization. *Eur J Inorg Chem* 1999(2):235–245
19. Yan MC, Chen F, Zhang JL et al (2005) Preparation of controllable crystalline titania and study on the photocatalytic properties. *J Phys Chem B* 109(18):8673–8678
20. Sensato FR, Custodio R, Longo E et al (2003) Electronic and structural properties of Sn<sub>x</sub>Ti<sub>1-x</sub>O<sub>2</sub> solid solutions: a periodic DFT study. *Catal Today* 85:145–152
21. Cao YQ, He T, Zhao LS et al (2009) Structure and phase transition behavior of Sn<sup>4+</sup>-doped TiO<sub>2</sub> nanoparticles. *J Phys Chem C* 113:18121–18124
22. Ovenstone J, Titler PJ, Withnall R et al (2001) A study of the effects of europium doping and calcination on the luminescence of titania phosphor materials. *J Phys Chem B* 105:7170–7177
23. Hirata T, Ishioka K, Kitajima M et al (1996) Concentration dependence of optical phonons in the TiO<sub>2</sub>-SnO<sub>2</sub> system. *Phys Rev B* 53:8442–8448
24. Sayilkan F, Asiltürk M, Kirazlı N (2009) Photocatalytic antibacterial performance of Sn<sup>4+</sup>-doped TiO<sub>2</sub> thin films on glass substrate. *J Hazard Mater* 162:1309–1316
25. Chinarro E, Moreno B, Jurado JR (2007) Combustion synthesis and EIS characterization of TiO<sub>2</sub>-SnO<sub>2</sub> system. *J Eur Ceram Soc* 27:3601–3604
26. Overstone J, Yanagisawa K (1999) Effect of hydrothermal treatment of amorphous titania on the phase change from anatase to rutile during calcination. *Chem Mater* 11:2770–2774
27. Muhlebach J, Muller K, Schwarzenbach G (1970) Peroxo complexes of titanium. *Inorg Chem* 9:2381–2390
28. Ichinose H, Terasaki M, Katsuki H (2001) Properties of peroxotitanium acid solution and peroxo-modified anatase sol derived from peroxotitanium hydrate. *J Sol-Gel Sci Technol* 22:33–40
29. Tian BZ, Chen F, Zhang JL et al (2006) Influences of acids and salts on the crystalline phase and morphology of TiO<sub>2</sub> prepared under ultrasound irradiation. *J Colloid Interface Sci* 303:142–148
30. Kumar KP, Fray DJ, Nair J et al (2007) Enhanced anatase-to-rutile phase transformation without exaggerated particle growth in nanostructured titania-tin oxide composites. *Scripta Mater* 57:771–774

# Chapter 4

## Development of Visible Light Responsive Morphology Controlled TiO<sub>2</sub> Photocatalyst

Teruhisa Ohno

### 4.1 Introduction and Abstract

TiO<sub>2</sub> has been intensively investigated or environmental clean up and solar light energy conversion in the past several decades because of stable physical-chemical properties, low cost and high activity [1–3]. TiO<sub>2</sub> has three crystal structures such as rutile, anatase, and brookite. Although Rutile TiO<sub>2</sub> with rather low photocatalytic activity, it has some advantages over anatase such as higher chemical stability and higher refractive index. It is of fundamental significance to explore mild synthetic techniques by which particle shapes, nano-scale morphologies, and crystallinity are well defined and controlled [3–5]. Moreover, surface chemistry of single crystalline rutile particles has been the subject of intensive studies because their chemical activity depends greatly on surface structures and exposed crystal faces [6].

It has been reported that well-crystallized faceted particles showed enhanced photocatalytic activity compared to normal spherical shaped particles with poor crystallinity [7]. Therefore, preparation of exposed crystal face-controlled TiO<sub>2</sub> nanoparticles has long been paid attention in order to develop a high active TiO<sub>2</sub> photocatalyst. Among several kinds of synthetic methods for TiO<sub>2</sub> nanoparticles, a hydrothermal treatment should be one of best candidate for TiO<sub>2</sub> syntheses because it directly produces well-morphology controlled TiO<sub>2</sub> nanoparticles using additives for exposing crystal faces under mild conditions. Recently, morphology controlled TiO<sub>2</sub> having anatase, rutile, and brookite phases can be prepared by using these techniques [8–13].

So many intensive efforts to improve the visible-light responsibility of TiO<sub>2</sub> photocatalyst involving impurity doping have been made in the last few decades [14–

---

T. Ohno (✉)

Applied Chemistry Section, Graduate School of Engineering, Kyushu Institute of Technology,  
1-1 Sensuicho, Tobata-ku, Kitakyushu, Fukuoka 804-8550, Japan  
e-mail: [tohno@che.kyutech.ac.jp](mailto:tohno@che.kyutech.ac.jp)

19]. However, impurity doping sometimes increase defects in  $\text{TiO}_2$  resulting in decrease of photocatalytic activity because the defects work as recombination centers [20, 21]. Recently, unique visible-light responsive  $\text{TiO}_2$  photocatalysts were developed by modification of metal compounds which work as a sensitizer for a visible light [22–26]. This is one of interesting method for visible light responsive  $\text{TiO}_2$  preparation without defects. However, back electron transfer between injected electrons from metal sensitizer in  $\text{TiO}_2$  bulk and oxidized metal ions on the surface of  $\text{TiO}_2$  may easily proceeded resulting in significant decrease in a photocatalytic activity under visible light. Therefore, it is necessary for new discovery for development metal compounds modified  $\text{TiO}_2$  showing visible light responsibility.

Our previous studies suggest that redox reaction proceed separately on specific exposed crystal faces of  $\text{TiO}_2$  [8–13]. This kind of preferential reaction was assigned by site-selective deposition of metal or metal oxide on the specific exposed crystal faces under photoexcitation [8–13].

As mentioned above, metal compounds modification on  $\text{TiO}_2$  surface for exhibiting visible light activity can be also applied to shape-controlled brookite and rutile  $\text{TiO}_2$  nanorod for remarkable improvement of photocatalytic activity under visible light. In this case, crystal face-selective metal compounds modification on exposed crystal face-controlled  $\text{TiO}_2$  nanorods having brookite and rutile phases can be achieved. The prepared brookite and rutile  $\text{TiO}_2$  nanorods by site-selective modification with metal compounds should be an ideal visible light responsive  $\text{TiO}_2$  photocatalyst because a remarkable suppression of back electron transfer from in the  $\text{TiO}_2$  injected by metal compounds sensitizer to oxidized metal compounds on the surface of  $\text{TiO}_2$  nanorod having brookite or rutile phase [13, 27].

In this manuscript, a preparation of the morphology controlled rutile and brookite  $\text{TiO}_2$  nanorod with exposed crystal faces by hydrothermal technique is summarized. The obtained rutile and brookite  $\text{TiO}_2$  nanorods showed high levels of activity for degradation of organic compounds compared to the activity levels of anatase fine particles (ST-01), which is one of the most famous commercially available photocatalyst developed for environmental clean up by the company in Japan. In addition, the technology of visible light responsive treatment for morphology controlled rutile and brookite  $\text{TiO}_2$  nanorod with exposed crystal faces by crystal face selective modification of metal compounds on rutile and brookite  $\text{TiO}_2$  nanorod is discussed. The metal ion modified rutile and brookite  $\text{TiO}_2$  nanorod shows much higher activity than conventional visible light responsive N-doped  $\text{TiO}_2$ , which is commercially available in Japan.

## 4.2 Morphology Controlled Rutile $\text{TiO}_2$ Nanorod with Exposed Crystal Faces

We prepared morphology-controlled rutile  $\text{TiO}_2$  nanorod by using with hydrothermal technique. Under our experimental conditions, rutile uniform  $\text{TiO}_2$  nanorods were obtained, and developed crystal faces were observed. The obtained rutile  $\text{TiO}_2$  nanorod showed high activity for degradation of acetaldehyde under UV irradiation compared to that of anatase fine particles (ST-01) which is commercially available

in Japan. The assignment and activity on the exposed crystal faced of rutile  $\text{TiO}_2$  nanorod was also investigated by TEM with SAED and photodeposition of metal compounds. From photodeposition of Pt and  $\text{PbO}_2$ , we suggest that the (110) face provides reductive sites and that the (111) face provides oxidative sites. The results suggested that the crystal faces facilitate the separation of electrons and holes, resulting in improvement of photocatalytic activity.

#### ***4.2.1 Experimental Details for Preparation and Activity Evaluation of Rutile $\text{TiO}_2$ Nanorod with Exposed Crystal Faces***

In a typical synthesis procedure, a chemical solution was put in a sealed Teflon-lined autoclave reactor containing aqueous solution of titanium trichloride ( $\text{TiCl}_3$ ) and sodium chloride (NaCl). The solutions were then put into a 200 °C oven for 48 h. The substrate was centrifuged and rinsed with deionized water and then dried in a vacuum oven. Samples are referred to as SH1 (NaCl 1 M), SH3 (NaCl 3 M), and SH5 (NaCl 5 M).

Reduction site and oxidation site on the exposed crystal faces of rutile  $\text{TiO}_2$  nanorod were assigned by photodeposition technique of Pt and  $\text{PbO}_2$ , respectively. Rutile  $\text{TiO}_2$  nanorod aqueous suspension (SH3) containing 2-propanol and hexachloroplatinic acid ( $\text{H}_2\text{PtCl}_6 \cdot 6\text{H}_2\text{O}$ ) was irradiated with a mercury UV lamp (light intensity:  $1.0 \text{ mW cm}^{-2}$ ).  $\text{N}_2$  gas was purged through the suspension prior to UV irradiation in order to remove oxygen. After irradiation, the color of the powder changed from white to gray silver, and the suspension was centrifuged and washed with distilled water. The collected powder (Pt loaded rutile  $\text{TiO}_2$  nanorod) was dried at 70 °C under reduced pressure for 24 h. Photodeposition of  $\text{PbO}_2$  on the oxidation site of rutile  $\text{TiO}_2$  nanorod performed by using same light source (mercury UV lamp, light intensity:  $1.0 \text{ mW cm}^{-2}$ ) as the case of photodeposition of Pt on the surface of rutile  $\text{TiO}_2$  nanorod. This reaction was carried out in an aqueous Pt loaded rutile  $\text{TiO}_2$  nanorod suspension containing  $\text{Pb}(\text{NO}_3)_2$  under aerated conditions according to the literature [8–13, 27]. After the reaction, the color of the powder changed from gray silver to brown, indicating that  $\text{PbO}_2$  had been deposited on the surface of rutile  $\text{TiO}_2$  nanorod. Pt and  $\text{PbO}_2$  particles deposited on rutile  $\text{TiO}_2$  nanorod were analyzed by SEM, EDX and TEM images.

The photocatalytic activity of  $\text{TiO}_2$  nanoparticles was evaluated by photodecomposition of acetaldehyde. The change in concentration of acetaldehyde and evolved  $\text{CO}_2$  as a function of irradiation time were analyzed. A Tedlar bag was used as the photoreactor vessel.  $\text{TiO}_2$  powder was spread on the bottom of a glass dish, and this was placed in the reaction vessel. Five hundred ppm of acetaldehyde was prepared in the vessel. The irradiation was conducted at room temperature after equilibrium between the gas and adsorbed acetaldehyde had been reached. The light source was a 500 W Xe-lamp. The light beam was passed through a UV-35 filter to cut off wavelength shorter than 350 nm. Fine stainless meshes were used as neutral density filters to adjust the irradiation intensity ( $10$  or  $30 \text{ mW cm}^{-2}$ ). After starting the irra-

diation, the decrease in acetaldehyde concentration and evolved  $\text{CO}_2$  concentration was measured using a gas chromatograph. ST-01 having an anatase phase fine  $\text{TiO}_2$  produced by Ishihara Sangyo CO. Ltd. and MT-600 having rutile phase produced by Teyca Co. Ltd. were usually used as a reference catalyst.

#### 4.2.2 Physical Properties Analyses and Photocatalytic Activities of Rutile $\text{TiO}_2$ Nanorod with Exposed Crystal Faces

XRD patterns of all the obtained particles were assigned to pure rutile phase and no other phases were detected. The mean grain size was determined from Scherrer's equation. The average crystallite sizes of the samples were found to be 66.0, 72.7, and 97.2 nm for samples SH1, SH3, and SH5, respectively. Figure 4.1 shows TEM images and selected area electron diffraction (SAED) patterns. TEM images (Fig. 4.1: SH1, SH3, and SH5) showed that the shape of the rod end changed from symmetric triangular tip to asymmetric triangular tip when the concentration of NaCl was increased. The SAED patterns of the exposed surface of the end of the rod and side surface of the rod are assigned to (111) and (110), respectively. The growth direction of the  $\text{TiO}_2$  rod is the (001) direction. In addition, (001) crystal faces are exposed gradually with increase in NaCl concentration. A spot pattern indicates a single crystalline nature of the rutile  $\text{TiO}_2$  nanorods.

Figure 4.2 shows photocatalytic evolution of  $\text{CO}_2$  by decomposition of acetaldehyde on reference  $\text{TiO}_2$  and SH1, SH3, and SH5 under UV light irradiation at the light intensity of  $10 \text{ mW cm}^{-2}$ . Photocatalytic activities of rutile  $\text{TiO}_2$  nanorods are higher than those of MT-600 and ST-01. Among the rutile  $\text{TiO}_2$  nanorods, SH5 showed the highest photocatalytic activity. The order of photocatalytic activities was  $\text{SH5} > \text{SH3} > \text{ST-01} > \text{SH1} > \text{MT-600B}$  as shown in Fig. 4.2. The separation of reaction site on the surface of rutile  $\text{TiO}_2$  nanorod might be one of important factor for its remarkable activity improvement because of suppression of back reaction on the surface of  $\text{TiO}_2$ . Moreover, it is expected that the efficiency of electron-hole separation should be enhanced because of the difference in the electronic band

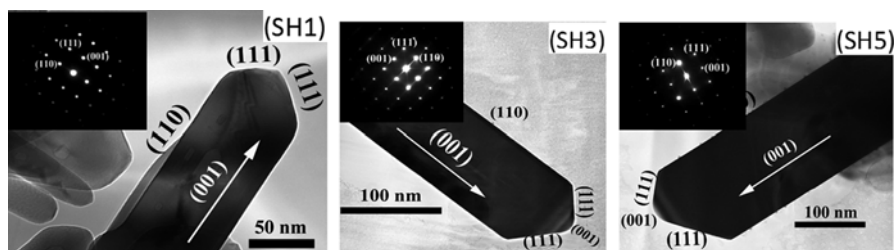
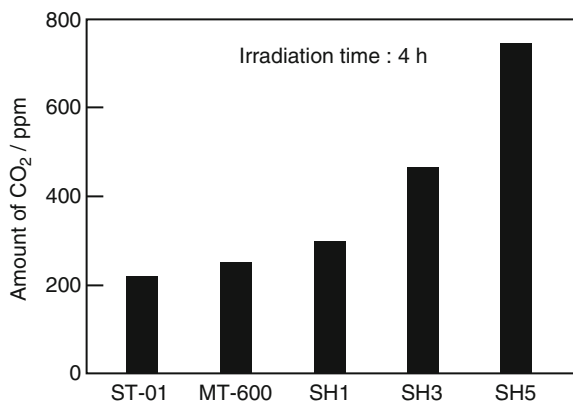
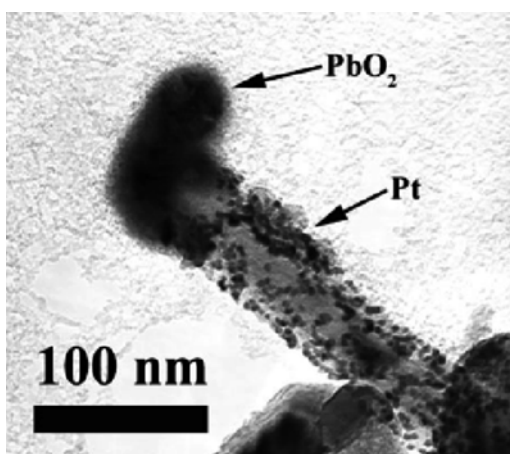


Fig. 4.1 TEM images and SAED patterns of SH1, SH3, and SH5

**Fig. 4.2** Amount of evolved  $\text{CO}_2$  as a result of decomposition of acetaldehyde on rutile  $\text{TiO}_2$  nanorod. (Light intensity:  $10 \text{ mW cm}^{-2}$ , irradiation time: 4 h, acetaldehyde: 500 ppm)



**Fig. 4.3** TEM image rutile  $\text{TiO}_2$  nanorod (SH3) on which Pt and  $\text{PbO}_2$  particles were deposited for reduction site and oxidation site, respectively. Reproduced from Ref. [9] with permission from Elsevier



structure between different crystals surfaces. Therefore, it is important to identify the actual reactive sites on the surface of rutile  $\text{TiO}_2$  nanorods.

Figure 4.3 shows TEM images of rutile  $\text{TiO}_2$  nanorods loaded with Pt for reduction site and  $\text{PbO}_2$  for oxidation site under UV irradiation, respectively. The deposited metals were analyzed by EDX (which is not shown here). Pt particles were deposited only on the (110) face. This result indicates that the reduction mainly proceeded on the (110) face of rutile  $\text{TiO}_2$  nanorods. The  $\text{PbO}_2$  particles were deposited on the (111) faces indicating that the (111) face provides the oxidation site for rutile  $\text{TiO}_2$  nanorods. Spatially separation of reaction sites on rutile  $\text{TiO}_2$  nanorods such as reduction and oxidation sites are considered to be very efficient for some kinds of photocatalytic reactions.

Different surface energy levels of the conduction and valence bands are expected for different crystal faces of  $\text{TiO}_2$  because of the atomic arrangements characteristic of these faces. The difference in the energy levels drives the electrons and holes to

different crystal faces, leading to separation of electrons and holes [8]. The effective separation of oxidation and reduction sites of rutile particles suggests that the electronic energy levels of the (110) face are lower than those of the (111) face as shown in Fig. 4.3 [28, 9]. Ohno et al. suggested that the isolation of oxidation or reduction site on the surface of  $\text{TiO}_2$  particles is large enough to drive the photocatalytic oxidation of water on rutile particles when suitable electron acceptors are added to the solution [8]. The effective separation of oxidation and reduction sites on the surface of rutile  $\text{TiO}_2$  particles should be important factor to obtain the high efficiency of some photocatalytic reactions because of suppression of back reaction on the surface of  $\text{TiO}_2$ . The large specific surface areas and small crystal sizes as well as high crystallinity of  $\text{TiO}_2$  might usually play important roles in the enhancement of photocatalytic activities. In addition, spatial separation of reaction sites on the photocatalyst nanoparticle by controlling exposed crystal surface of the rutile  $\text{TiO}_2$  nanorod is a more important factor for improvement of photocatalytic activity because a rutile  $\text{TiO}_2$  nanorod having a small surface area ( $10\text{--}30\text{ m}^2\text{ g}^{-1}$ ) showed a higher photocatalytic activity than that of ST-01 with a large surface area ( $300\text{ m}^2\text{ g}^{-1}$ ).

### 4.3 Visible Light Responsive Rutile $\text{TiO}_2$ Nanorod Modified with $\text{Fe}^{3+}$ Compounds on Exposed Crystal Face

Ohno et al. developed visible light responsive rutile  $\text{TiO}_2$  nanorod treated with  $\text{Fe}^{3+}$  ions [27]. Trivalent iron(III) ( $\text{Fe}^{3+}$ ) compounds were site-selectively loaded on  $\{111\}$  exposed crystal faces of rutile  $\text{TiO}_2$  nanorod by utilizing adsorption property of iron(III)/iron(II) ( $\text{Fe}^{3+}/\text{Fe}^{2+}$ ) ion. The  $\text{Fe}^{3+}$  compounds modified rutile  $\text{TiO}_2$  nanorod showed a remarkable high photocatalytic activity under visible-light irradiation because oxidation and reduction site-selectively proceed over  $\text{Fe}^{3+}$  ion modified on  $\{111\}$  faces and bare  $\text{TiO}_2$  surface on  $\{110\}$  faces, respectively. Double-beam photoacoustic spectroscopic analyses suggest that the high activity of the  $\text{TiO}_2$  with site-selective modification of  $\text{Fe}^{3+}$  ion is attributed to not only an efficient electron injection from  $\text{Fe}^{3+}$  ion but also an efficient reduction by injected electron on  $\{110\}$  faces.

#### 4.3.1 *Experimental Details for Preparation and Activity Evaluation of $\text{Fe}^{3+}$ Compounds Modified Rutile $\text{TiO}_2$ Nanorod*

Non-site-selective modification of  $\text{Fe}^{3+}$  compounds on the entire surface of rutile  $\text{TiO}_2$  nanorod is as follows. An aqueous suspension composed of rutile  $\text{TiO}_2$  nanorod and an aqueous solution of  $\text{Fe}(\text{NO}_3)_3$  was stirred under an aerated condition. After filtration, the residue was washed with deionized water several times until the ionic

conductivity of the supernatant was  $<10 \mu\text{S cm}^{-2}$  in order to achieve complete removal of  $\text{NO}_3^-$  ion. The obtained particles (non-site-selective  $\text{Fe}^{3+}$  compounds loaded rutile  $\text{TiO}_2$  nanorod) were dried under reduced pressure.

Preparation procedure of visible light responsive rutile  $\text{TiO}_2$  nanorod site-selective modified with  $\text{Fe}^{3+}$  compounds is as follows. An aqueous suspension composed of rutile  $\text{TiO}_2$  nanorod and an aqueous solution of  $\text{Fe}(\text{NO}_3)_3$  with ethanol was stirred under an aerated condition by bubbling  $\text{N}_2$  gas. Photo-reduction of  $\text{Fe}^{3+}$  loaded on reduction crystal face ( $\{110\}$  faces) of rutile  $\text{TiO}_2$  nanorod proceeded during UV irradiation with a 500-W super-high-pressure mercury lamp (light intensity :  $1.0 \text{ mW cm}^{-2}$ ).  $\text{Fe}^{2+}$  compounds on the surface of rutile  $\text{TiO}_2$  nanorod, which is generated by reduction of  $\text{Fe}^{3+}$ , were dissolved in aqueous phase. The supernatant and residue was separated by filtration immediately after the photoirradiation. The residue was washed with deionized water several times until the ionic conductivity of the supernatant was  $<10 \mu\text{S cm}^{-1}$ , and then the particles were dried under reduced pressure (Scheme 4.1).

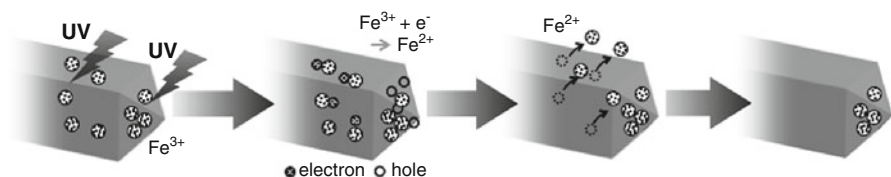
Photocatalytic activities of samples were evaluated by photocatalytic decomposition of acetaldehyde. The glass dish contained 100 mg samples was placed in a  $125 \text{ cm}^3$  Tedlar bag. Five hundred ppm of gaseous acetaldehyde was injected into the Tedlar bag, and photoirradiation was performed at room temperature after the acetaldehyde had reached adsorption equilibrium. The gaseous composition in the Tedlar bag was 79 % of  $\text{N}_2$ , 21 % of  $\text{O}_2$ ,  $<0.1$  ppm of  $\text{CO}_2$ , and 500 ppm of acetaldehyde, and relative humidity was ca. 30 %. A LED emitted light at a wavelength of ca. 455 nm ( $\pm 15$  nm) with an intensity of  $1.0 \text{ mW cm}^{-2}$ , was used for visible light irradiation. The concentrations of  $\text{CH}_3\text{CHO}$  and  $\text{CO}_2$  were estimated by gas chromatography.

In order to elucidate the electron transfer between rutile  $\text{TiO}_2$  nanorod and  $\text{Fe}^{3+}$  compounds loaded on the oxidation site of rutile  $\text{TiO}_2$  nanorod, double beam photoacoustic spectroscopy was used. A  $\text{TiO}_2$  sample was placed in a gas-exchangeable photoacoustic (PA) cell equipped with two valves for gas flow. The atmosphere was controlled by a flow of nitrogen containing ethanol vapor ( $\text{N}_2 + \text{EtOH}$ ) or artificial air containing ethanol vapor (air + EtOH). A LED emitting light at ca. 625 nm was used as a probe light, and the output intensity was modulated by a digital function generator at 80 Hz. A blue-LED (emitting light at ca. 470 nm,  $8.1 \text{ mW cm}^{-2}$ ) was also used as simultaneous continuous irradiation for photoexcitation. The PA signal acquired by a condenser microphone buried in the cell was amplified and monitored by a digital lock-in amplifier. Detailed setups of double-beam photoacoustic (DB-PA) spectroscopic measurements have been reported previously [29].

### **4.3.2 Physical Properties Analyses and Photocatalytic Activities of Visible Light Responsive Rutile $\text{TiO}_2$ Nanorod Modified with $\text{Fe}^{3+}$ Compounds**

The rutile  $\text{TiO}_2$  nanorod have been prepared according to our previous paper [9, 10]. The rutile  $\text{TiO}_2$  nanorods used in this paper have exposed crystal faces with  $\{110\}$  and  $\{111\}$ . The specific surface area of the bare rutile rod was  $34 \text{ m}^2 \text{ g}^{-1}$ .

Valence states of iron compounds on rutile  $\text{TiO}_2$  nanorod were confirmed to be trivalent state by XPS analyses. UV irradiation during  $\text{Fe}^{3+}$  modification decreased net amount of  $\text{Fe}^{3+}$  ion modified on the  $\text{TiO}_2$  surface while almost of  $\text{Fe}^{3+}$  ion was adsorbed on the  $\text{TiO}_2$  surface in dark. It is reported that  $\text{Fe}^{2+}$  ion hardly adsorb on  $\text{TiO}_2$  surface compared to  $\text{Fe}^{3+}$  compound [30]. Therefore,  $\text{Fe}^{2+}$  ion produced as a result of reduction of  $\text{Fe}^{3+}$  ion by photoexcited electron on reduction site of rutile  $\text{TiO}_2$  nanorod from  $\text{TiO}_2$  surface diffused into aqueous media. Our previous study suggested that reduction and oxidation on the rutile  $\text{TiO}_2$  nanorod proceed predominantly on  $\{110\}$  and  $\{111\}$  exposed crystal faces, respectively [22]. Therefore,  $\text{Fe}^{3+}$  ions are expected to mainly adsorb on  $\{111\}$  faces under UV irradiation because  $\text{Fe}^{3+}$  ion on  $\{110\}$  faces desorbs due to reduction of  $\text{Fe}^{3+}$  to  $\text{Fe}^{2+}$  (Scheme 4.1). Modification of  $\text{Fe}^{3+}$  ion induced color change from white to pale yellow as reported in previous study [26]. Figure 4.4 show UV–Vis spectra of bare and site-selective



**Scheme 4.1** Site selective modification on the shape controlled rutile rod with  $\{110\}$  and  $\{111\}$  exposed crystal faces

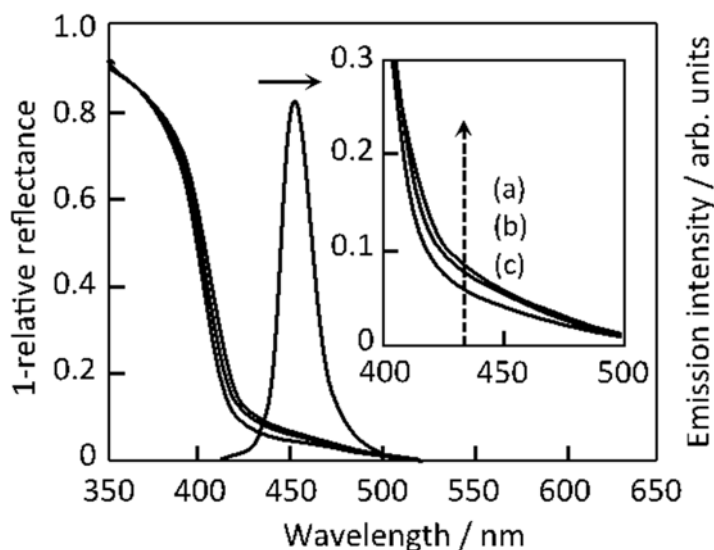


**Fig. 4.4** UV–Vis spectra of (a) non-site-selective  $\text{Fe}^{3+}$  modified rutile  $\text{TiO}_2$  nanorod, (b) site-selective  $\text{Fe}^{3+}$  modified rutile  $\text{TiO}_2$  nanorod, (c) rutile  $\text{TiO}_2$  nanorod without modification of  $\text{Fe}^{3+}$  compounds and emission spectrum of LED used for photocatalytic evaluation

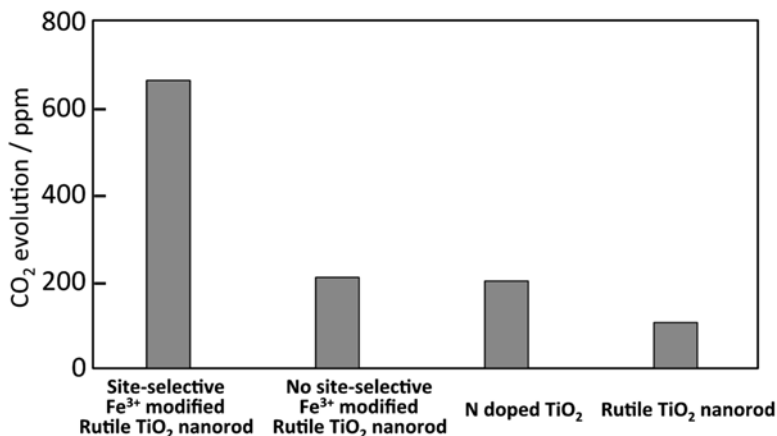


**Fig. 4.5** Amount of evolved CO<sub>2</sub> for acetaldehyde decomposition over Fe<sup>3+</sup> modified rutile TiO<sub>2</sub> nanorod, N-doped TiO<sub>2</sub>, and rutile TiO<sub>2</sub> nanorod under visible-light irradiation

Fe<sup>3+</sup> modified rutile TiO<sub>2</sub> nanorod, and non site-selective Fe<sup>3+</sup> modified rutile TiO<sub>2</sub> nanorod. In the wavelength region between 400 and 500 nm of DR spectra, a red shift of photoabsorption edge was observed. Photoabsorption was increased with an increase in the net amount of Fe<sup>3+</sup> ion adsorbed on the rutile TiO<sub>2</sub> nanorod.

Photocatalytic activity of Fe<sup>3+</sup>-modified rutile TiO<sub>2</sub> nanorod for decomposition of acetaldehyde was evaluated under visible light irradiation. Figure 4.5 shows amount of evolved CO<sub>2</sub> as a result of acetaldehyde degradation under visible-light irradiation for 24 h. Photocatalytic activity of Fe<sup>3+</sup>-modified rutile TiO<sub>2</sub> nanorod was higher than bare rutile TiO<sub>2</sub> nanorod and visible light responsive N-doped TiO<sub>2</sub> produced by Sumitomo Chemical Co. Ltd. Japan. This result indicates that Fe<sup>3+</sup> compound modification for rutile TiO<sub>2</sub> nanorod induce photocatalytic reaction under visible-light irradiation as follows [26]:

(1) photoexcited Fe<sup>3+</sup> compound loaded on rutile TiO<sub>2</sub> nanorod injected electrons into the conduction band of rutile TiO<sub>2</sub> nanorod and became an oxidized state of Fe<sup>3+</sup> (Fe<sup>4+</sup>), (2) injected electrons, which was trapped by Ti<sup>4+</sup> in the bulk resulting in generation of Ti<sup>3+</sup>, migrated to the surface of rutile TiO<sub>2</sub> nanorod and reduced oxygen species on the surface of rutile TiO<sub>2</sub> nanorod and (3) the oxidized state of Fe<sup>3+</sup> compound (Fe<sup>4+</sup>) oxidized acetaldehyde and go back to the initial state of metal ions compound (Fe<sup>3+</sup>). Site-selective modified Fe<sup>3+</sup> rutile TiO<sub>2</sub> nanorod showed higher photocatalytic activity than N-doped TiO<sub>2</sub> (N-TiO<sub>2</sub>; Sumitomo Chemical Co.), which is well-known as a conventional visible-light responsive TiO<sub>2</sub>. Moreover, photocatalytic activity of Fe<sup>3+</sup>-modified rutile TiO<sub>2</sub> showed dependence on its preparation method (Site-selective modified Fe<sup>3+</sup> rutile TiO<sub>2</sub> nanorod > No site-selective modified Fe<sup>3+</sup> rutile TiO<sub>2</sub> nanorod). The plausible reason for difference of photocatalytic activity should be site selectivity of Fe<sup>3+</sup> modification. In order to make clear it, following experiments were carried out.

Same modification method was applied to commercial rutile  $\text{TiO}_2$ , which has spherical shape without specific exposed crystal faces. Therefore, UV irradiation during  $\text{Fe}^{3+}$  modification is thought to induce no site-selective modification on the particle because redox reaction proceeds in the neighboring sites without being separated. Amounts of evolved  $\text{CO}_2$  evolution as a result of decomposition of acetaldehyde over site-selective and no site-selective  $\text{Fe}^{3+}$ -modified commercial rutile  $\text{TiO}_2$  are 495 and 500 ppm under visible light irradiation for 24 h. These two samples were prepared by different kind of modification method, but same net amount of  $\text{Fe}^{3+}$  compound was loaded on rutile between these samples by adjusting initial amount of  $\text{Fe}^{3+}$ . The photocatalytic activities of these samples are quite similar, regardless of the presence or absence of UV irradiation during  $\text{Fe}^{3+}$  modification. This indicates that the UV irradiation induced formation of same  $\text{Fe}^{3+}$  species for photocatalytic reaction as that no site-selective modification of  $\text{Fe}^{3+}$  on rutile  $\text{TiO}_2$  nanorod. Therefore, the reason for high activity of site-selective  $\text{Fe}^{3+}$  modified samples is that UV irradiation during  $\text{Fe}^{3+}$  modification induces site-selective  $\text{Fe}^{3+}$  compounds loading on rutile  $\text{TiO}_2$  nanorod.

Behavior of injected electron in  $\text{TiO}_2$  was observed by DB-PAS [29]. Figure 4.6 shows PA intensity for no site-selective  $\text{Fe}^{3+}$  modified rutile  $\text{TiO}_2$  nanorod, site-selective  $\text{Fe}^{3+}$  modified rutile  $\text{TiO}_2$  nanorod and bare  $\text{TiO}_2$  as a function of irradiation time of visible-light in the presence of  $\text{N}_2 + \text{EtOH}$ . PA intensity increased with visible-light irradiation because  $\text{Ti}^{4+}$  was reduced to  $\text{Ti}^{3+}$  by injected electrons from photoexcited  $\text{Fe}^{3+}$  compound loaded on rutile  $\text{TiO}_2$  nanorod. The saturation limit of PA intensity showed no dependence on  $\text{Fe}^{3+}$ -modification conditions. This is reasonable result because photoabsorption of these samples was not so different from each other as shown in Fig. 4.4. This indicates that the plausible factor may be efficiency of reduction on rutile  $\text{TiO}_2$  nanorod modified with  $\text{Fe}^{3+}$  by injected electron.

DB-PA measurements in the presence of oxygen were also carried out in order to elucidate the behavior of injected electrons in the rutile  $\text{TiO}_2$  nanorod. Figure 4.7 shows time-course curve of no site-selective  $\text{Fe}^{3+}$  modified rutile  $\text{TiO}_2$  nanorod, site-selective  $\text{Fe}^{3+}$  modified rutile  $\text{TiO}_2$  nanorod, and bare rutile  $\text{TiO}_2$  nanorod under

**Fig. 4.6** Time-course curves of PA signals of (a) no site-selective  $\text{Fe}^{3+}$  modified rutile  $\text{TiO}_2$  nanorod, (b) site-selective  $\text{Fe}^{3+}$  modified rutile  $\text{TiO}_2$  nanorod, and (c) bare rutile  $\text{TiO}_2$  nanorod under visible-light irradiation in the presence of  $\text{N}_2 + \text{EtOH}$

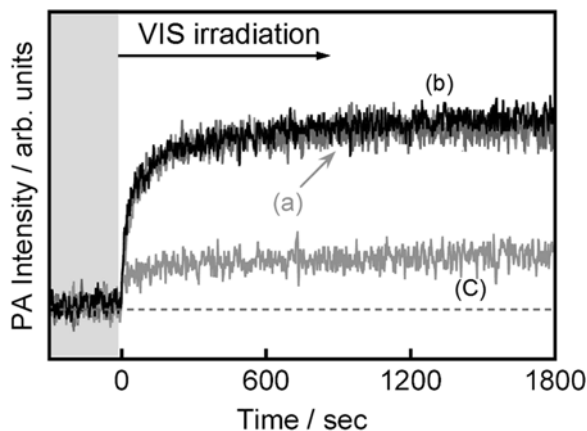
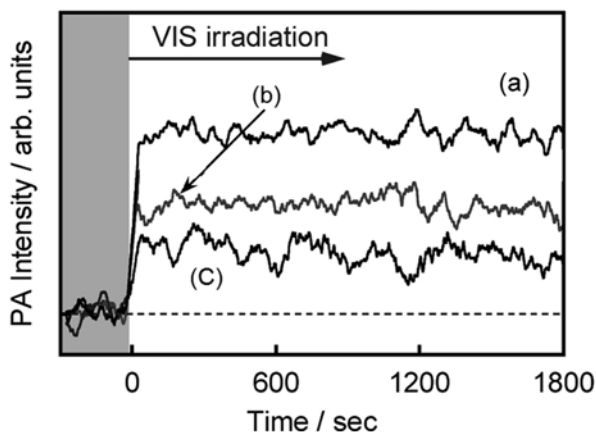


**Fig. 4.7** Time-course curves of PA signals with 50 points smoothing of (a) no site-selective  $\text{Fe}^{3+}$  modified rutile  $\text{TiO}_2$  nanorod, (b) site-selective  $\text{Fe}^{3+}$  modified rutile  $\text{TiO}_2$  nanorod, and (c) bare rutile  $\text{TiO}_2$  nanorod under visible-light irradiation in the presence of air + EtOH



visible-light irradiation in the presence of air + EtOH. PA intensity attributed to  $\text{Ti}^{3+}$  formation was largely decreased because an electron accumulation by injected electrons from excited state of  $\text{Fe}^{3+}$  was suppressed due to electron consumption by oxygen species on reduction site of rutile  $\text{TiO}_2$  nanorod. Steady-state value of PA intensity showed dependence on modification method (no site-selective  $\text{Fe}^{3+}$  modified rutile  $\text{TiO}_2$  nanorod > site-selective  $\text{Fe}^{3+}$  modified rutile  $\text{TiO}_2$  nanorod). This suggests that reduction efficiently proceeded on surface of site-selective  $\text{Fe}^{3+}$  modified rutile  $\text{TiO}_2$  nanorod is thought to be higher than that on no site-selective  $\text{Fe}^{3+}$  modified rutile  $\text{TiO}_2$  nanorod because an efficient consumption of injected electrons in rutile  $\text{TiO}_2$  nanorod by reduction of oxygen on  $\{110\}$  faces proceeded without retardation by site-selective coverage of  $\text{Fe}^{3+}$  ion on  $\{111\}$  face. The injected electron in the rutile  $\text{TiO}_2$  nanorod site-selective modification of  $\text{Fe}^{3+}$  ions is thought to be prevented from being trapped by oxidized  $\text{Fe}^{3+}$  ( $\text{Fe}^{4+}$ ) because the injected electrons should be efficiently consumed on  $\{110\}$  faces.

#### 4.4 Morphology Controlled Brookite $\text{TiO}_2$ Nanorod with Exposed Crystal Faces

Exposed crystal face-controlled brookite titanium(IV) oxide ( $\text{TiO}_2$ ) nanorods with various aspect ratios were prepared by a hydrothermal process with or without PVA or PVP as an aspect reagent. The nanorod-shaped brookite  $\text{TiO}_2$  had larger  $\{210\}$  and smaller  $\{212\}$  exposed crystal faces, which were assigned by TEM with the SAED technique. Their aspect ratios were greatly influenced by the addition of PVA or PVP as an aspect ratio control reagent to the reaction solution used in the hydrothermal treatment. The photocatalytic activity for decomposition of acetaldehyde increased with increase in the aspect ratio because the surface area ratio of  $\{210\}$  to  $\{212\}$  exposed crystal faces, which are attributed to reduction and oxidation sites, respectively, became more optimal.

#### **4.4.1 *Experimental Details for Preparation and Activity Evaluation of Brookite TiO<sub>2</sub> Nanorod With and Without Polymer as a Morphology Control Reagent***

Morphology-controlled brookite TiO<sub>2</sub> nanorods with {210} and {212} exposed crystal faces were prepared by hydrothermal synthesis [31–34].

The typical procedure for preparation of shape-controlled brookite TiO<sub>2</sub> nanorods is as follows. Amorphous titanium hydroxide particles were dispersed in 30 % hydrogen peroxide. Then 25 % ammonia and glycolic acid were added. After stirring the solution at ca. 60 °C for 6 h to remove the excess amount of hydrogen peroxide and ammonia, an orange gelled compound was obtained. The gelled compound was dispersed in deionized water and pH of the solution was adjusted to 10 by addition of ammonia. Then the volume of the solution was adjusted (50.0 cm<sup>3</sup>) by addition of deionized water, and the solution in a Teflon bottle sealed with a stainless jacket was heated at 200 °C for 48 h in an oven. After hydrothermal treatment, the residue was washed with deionized water until ionic conductivity of the supernatant was <10 μS cm<sup>-1</sup>. The particles were dried under reduced pressure at 60 °C for 12 h.

For controlling aspect ratio of brookite of TiO<sub>2</sub> nanorod, we modified the preparation procedure as follows. Amorphous titanium hydroxide particles were dispersed in 30 % hydrogen peroxide. Then 25 % ammonia and glycolic acid were added, and yellow peroxy titanate (PTA) solution was obtained. An aqueous solution containing an appropriate amount of PVA or PVP (5, 25, 50 mg) was added to the PTA solution. After stirring the solution at room temperature for 6 h to remove the excess amount of hydrogen peroxide and ammonia, an orange gelled compound was obtained. The gelled compound was dispersed in deionized water and pH of the solution was adjusted to 10 by addition of ammonia. Then the volume of the solution was adjusted (50.0 cm<sup>3</sup>) by addition of deionized water, and the solution in a Teflon bottle sealed with a stainless jacket was heated at 200 °C for 48 h in an oven. After hydrothermal treatment, the residue in the Teflon bottle was washed with milli-Q water until ionic conductivity of the supernatant was <10 μS cm<sup>-1</sup>. The particles were dried under reduced pressure at 60 °C for 12 h.

#### **4.4.2 *Procedure for Preparation of Brookite TiO<sub>2</sub> Nanorods Using Titanium Bis(Ammonium Lactate) Dihydroxide (TALH) as a Starting Material [31]***

Five milliliters of Titanium(IV) bis(ammonium lactate) dihydroxide (TALH) aqueous precursor (50 %) and an aqueous solution containing urea (7 M) were mixed and then deionized water was added to reach a final volume of 50 cm<sup>3</sup>. The resulting solution was transferred into a Teflon cup. The Teflon bottle sealed with a stainless jacket was heated at 230 °C for 48 h in an oven. The resulting powder was separated by centrifugation and washed with milli-Q water until ionic conductivity of the supernatant was <10 μS cm<sup>-1</sup>. The particles were dried under reduced pressure at 60 °C for 12 h.

#### 4.4.3 Physical Properties Analyses and Photocatalytic Activities of Brookite $\text{TiO}_2$ Nanorod with Exposed Crystal Faces

Figure 4.8 shows a TEM image of brookite  $\text{TiO}_2$  without a polymer. Brookite  $\text{TiO}_2$  nanorod with a length of 100 nm, width of 25 nm, and an aspect ratio of 2.7 was obtained. Relative surface area of the prepared brookite  $\text{TiO}_2$  nanorod was  $47 \text{ m}^2 \text{ g}^{-1}$ . Exposed crystal faces were analyzed by TEM and selected area electron diffraction (SAED) analysis and assigned to large  $\{212\}$  and small  $\{210\}$  exposed crystal faces (Fig. 4.8). Reactivity assignment of exposed  $\{210\}$  and  $\{212\}$  crystal faces of a brookite  $\text{TiO}_2$  nanorod were assigned to reduction and oxidation sites by photodeposition of  $\text{PbO}_2$  and Pt nanoparticles, respectively, according to the previously reported technique [9–11]. These results indicated that reduction and oxidation on the brookite  $\text{TiO}_2$  nanorod proceeds predominantly on  $\{210\}$  and  $\{212\}$  exposed crystal faces, respectively (not shown here). Therefore,  $\text{Fe}^{3+}$  ions are expected to mainly adsorb on  $\{212\}$  faces under UV irradiation because  $\text{Fe}^{3+}$  ions on  $\{210\}$  faces desorb due to reduction of  $\text{Fe}^{3+}$  to  $\text{Fe}^{2+}$  (Scheme 4.1). The  $\text{Fe}^{2+}$  ions were recovered as  $\text{Fe}^{3+}$  ions as a result of reoxidation by oxygen and/or positive holes on  $\{212\}$  faces.

TEM and SEM images of aspect ratio controlled brookite  $\text{TiO}_2$  by addition of the PVA polymer (Fig. 4.9). These results indicate that addition of 50 mg of PVA was sufficient to prepare brookite  $\text{TiO}_2$  particles with the smallest aspect ratio (Fig. 4.9). The aspect ratio (AR) and TEM images of the prepared samples were summarized in Fig. 4.10.

Photocatalytic activities of brookite  $\text{TiO}_2$  nanorod were evaluated by photocatalytic decomposition of toluene. One hundred milligrams of powder, which had complete extinction of incident radiation, was spread on a glass dish, and the glass dish was placed in a Tedlar bag. Five hundred parts per million of gaseous acetaldehyde or one hundred parts per million of gaseous toluene was injected into the Tedlar bag, and photoirradiation was performed at room temperature after the toluene had reached adsorption equilibrium. The gaseous composition in the Tedlar bag was 79 % of  $\text{N}_2$ , 21 % of  $\text{O}_2$ , <0.1 ppm of  $\text{CO}_2$ , and 100 ppm or 500 ppm of toluene,

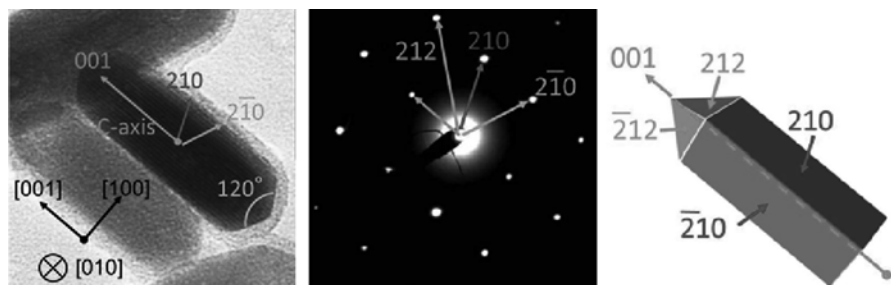
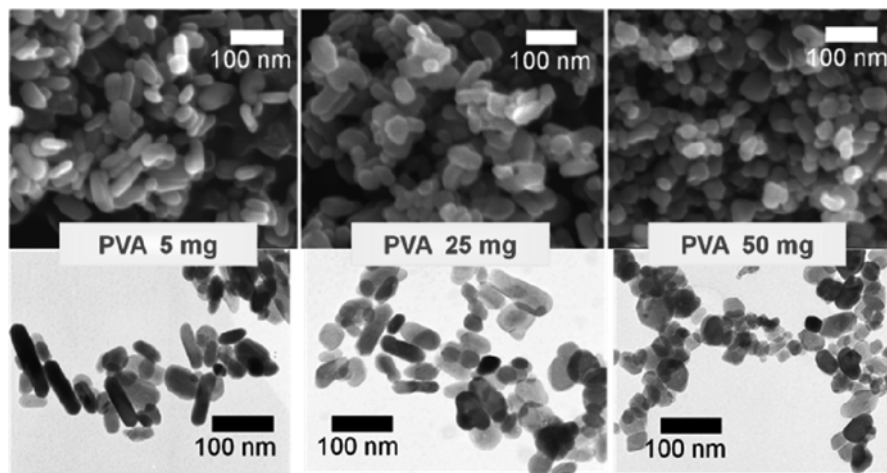
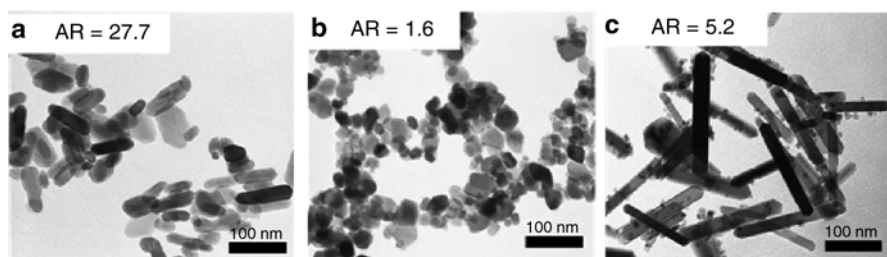


Fig. 4.8 SAED analysis of the prepared brookite  $\text{TiO}_2$  without a polymer



**Fig. 4.9** The influence on aspect ratio of brookite  $\text{TiO}_2$  nanorods by addition of PVA

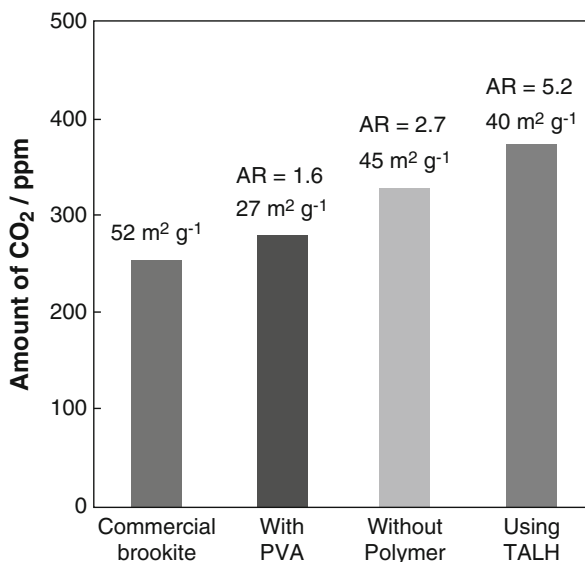


**Fig. 4.10** TEM image of the prepared brookite  $\text{TiO}_2$  nanorod with aspect ratio (AR): (a) Without a polymer, (b) With PVA (50 mg), (c) Using TALH as starting compound

and relative humidity was ca. 30 %. A light-emitting diode with a center wavelength of ca. 365 nm and an intensity of  $0.1 \text{ mW cm}^{-2}$ , was used as the light source. The concentrations of acetaldehyde and carbon dioxide ( $\text{CO}_2$ ) were estimated by gas chromatography (Shimadzu, GC-8A, FID detector) with a PEG-20 M 20 % Celite 545 packed glass column and by gas chromatography (Shimadzu, GC-9A, FID detector) with a TCP 20 % Uniport R packed column and a methanizer (GL Sciences, MT-221), respectively.

The photocatalytic activities of the prepared samples for decomposition of toluene were evaluated. Figure 4.11 shows  $\text{CO}_2$  evolution as a result of toluene decomposition over several kinds of brookite  $\text{TiO}_2$  under UV irradiation for 8 h by using LED at a wavelength of 365 nm. The amount of  $\text{CO}_2$  evolved varied greatly among the samples. The aspect ratio of a brookite  $\text{TiO}_2$  nanorod with specific exposed crystal faces is rather sensitive to photocatalytic activity for toluene decomposition. Toluene decomposition on a photoirradiated brookite  $\text{TiO}_2$  nanorod with a larger aspect ratio showed higher photocatalytic activity than brookite  $\text{TiO}_2$  nanorod with a

**Fig. 4.11** CO<sub>2</sub> evolution as a result of toluene decomposition over several kinds of prepared brookite TiO<sub>2</sub> under UV irradiation for 8 h by using an LED at a wavelength of 365 nm



smaller aspect ratio. This result suggested that photocatalytic toluene decomposition was drastically improved by controlling the ratio of exposed reduction sites to oxidation sites on the surface of the brookite TiO<sub>2</sub> nanorod. Under optimized conditions, reduction sites on the surface of the brookite TiO<sub>2</sub> nanorod should be predominantly exposed as shown in Fig. 4.11. These results indicated that reduction of oxygen on the surfaces of the reduction sites of a brookite TiO<sub>2</sub> nanorod might be the rate-determining step for toluene oxidation over a brookite TiO<sub>2</sub> nanorod under UV light.

#### 4.4.4 Non-Site-Selective and Site-Selective Fe<sup>3+</sup> Compounds Modification of Brookite TiO<sub>2</sub> Nanorod

For non-site-selective Fe<sup>3+</sup> compounds modification of brookite TiO<sub>2</sub> nanorod, an aqueous suspension containing shape-controlled brookite TiO<sub>2</sub> nanorods and an aqueous solution of iron(III) nitrate (Fe(NO<sub>3</sub>)<sub>3</sub>) was stirred for 6 h under an aerated condition. After stirring, the supernatant and residue were separated by filtration, and the residue was washed with deionized water several times until the ionic conductivity of the supernatant was <10 μS cm<sup>-1</sup> in order to remove NO<sub>3</sub><sup>-</sup> ions. The particles were then dried under reduced pressure.

For site-selective Fe<sup>3+</sup> compounds modification of brookite TiO<sub>2</sub> nanorod, an aqueous suspension containing each brookite TiO<sub>2</sub> and an aqueous solution of Fe(NO<sub>3</sub>)<sub>3</sub> with ethanol was stirred for 6 h under an aerated condition. The stirring was carried out under UV irradiation with a 500-W super-high-pressure mercury lamp (Ushio, SX-UI501UO), the light intensity of which was 1.0 mW cm<sup>-2</sup>. The

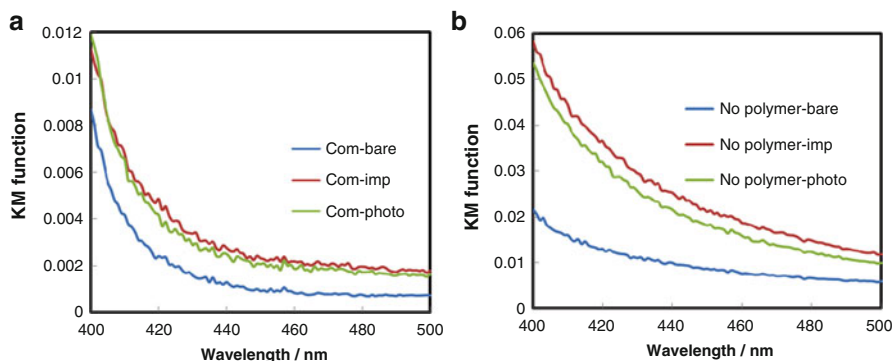


**Fig. 4.12** UV-Vis spectra of bare and  $\text{Fe}^{3+}$  (0.05 wt%)-modified brookite  $\text{TiO}_2$ : (a) commercial, (b) without a polymer

supernatant and residue were separated by filtration immediately after the 6 h of stirring. The residue was washed with deionized water several times until the ionic conductivity of the supernatant was  $<10 \mu\text{S cm}^{-1}$ , and then the particles were dried under reduced pressure.

A color of brookite  $\text{TiO}_2$  nanorod changed from white to pale yellow. Figure 4.12 shows UV-Vis spectra of bare and  $\text{Fe}^{3+}$ -modified  $\text{TiO}_2$ . Imp means non-site-selective  $\text{Fe}^{3+}$  compounds modification of brookite  $\text{TiO}_2$  and photo means site-selective  $\text{Fe}^{3+}$  compounds modification of brookite  $\text{TiO}_2$ . An increase in photoabsorption was observed in the wavelength region between 400 and 500 nm of DR spectra. Photoabsorption was increased with an increase in the net amount of  $\text{Fe}^{3+}$  compounds loaded on the brookite  $\text{TiO}_2$  nanorod.

Photocatalytic activities of samples were evaluated by photocatalytic decomposition of acetaldehyde. One hundred milligrams of powder, which had complete extinction of incident radiation, was spread on a glass dish, and the glass dish was placed in a  $125 \text{ cm}^3$  Tedlar bag (AS ONE Co. Ltd.). Five hundred parts per million of gaseous acetaldehyde was injected into the Tedlar bag, and photoirradiation was performed at room temperature after the acetaldehyde had reached adsorption equilibrium. The gaseous composition in the Tedlar bag was 79 % of  $\text{N}_2$ , 21 % of  $\text{O}_2$ ,  $<0.1$  ppm of  $\text{CO}_2$ , and 500 ppm of acetaldehyde, and relative humidity was ca. 30 %. A light-emitting diode (LED; Lumileds, Luxeon LXHL-NRR8), which emitted light at a wavelength of ca. 455 nm with an intensity of  $1.0 \text{ mW cm}^{-2}$ , was also used. The concentrations of acetaldehyde and carbon dioxide ( $\text{CO}_2$ ) were estimated by gas chromatography (Shimadzu, GC-8A, FID detector) with a PEG-20 M 20 % Celite 545 packed glass column and by gas chromatography (Shimadzu, GC-9A, FID detector) with a TCP 20 % Uniport R packed column and a methanizer (GL Sciences, MT-221), respectively.

Figure 4.13 shows dependence of the site-selective  $\text{Fe}^{3+}$  compounds modified brookite  $\text{TiO}_2$  on photocatalytic activity ( $\text{CO}_2$  evolution as a result of acetaldehyde degradation after 24 h of photoirradiation). Photocatalytic activity of the  $\text{Fe}^{3+}$ -

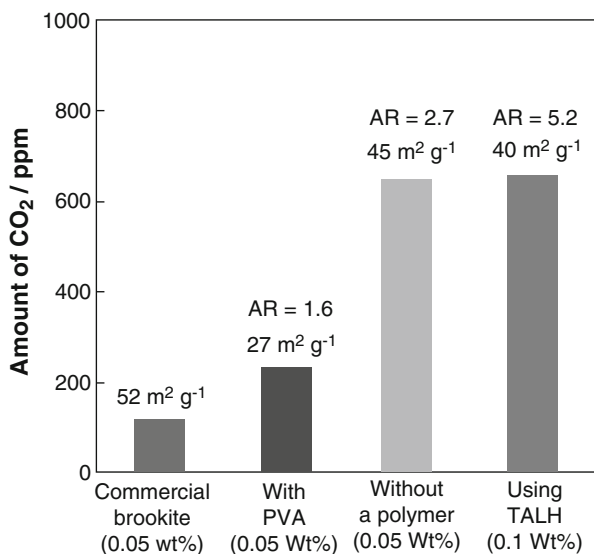


**Fig. 4.13**  $\text{CO}_2$  evolution as a result of acetaldehyde decomposition over several kinds of  $\text{Fe}^{3+}$ -modified brookite  $\text{TiO}_2$  under visible light irradiation for 24 h by using an LED at a wavelength of 455 nm

modified brookite  $\text{TiO}_2$  nanorod was much higher than that of  $\text{Fe}^{3+}$ -modified commercial spherical shaped brookite  $\text{TiO}_2$ . Under visible light irradiation, no photocatalytic activities of the brookite  $\text{TiO}_2$  nanorod and commercial brookite  $\text{TiO}_2$  nanoparticles without  $\text{Fe}^{3+}$  modification were observed for oxidation of acetaldehyde. This indicates that  $\text{Fe}^{3+}$  ions on the brookite  $\text{TiO}_2$  nanorod induced photocatalytic reaction under visible-light irradiation [26]. The amount of evolved  $\text{CO}_2$  over nitrogen-doped  $\text{TiO}_2$  (N- $\text{TiO}_2$ ; Sumitomo Chemical Co.) was about 180 ppm under the same experimental condition.  $\text{Fe}^{3+}$ -modified brookite  $\text{TiO}_2$  nanorod showed higher photocatalytic activity than that of N- $\text{TiO}_2$ .

Photocatalytic activity was increased by a  $\text{Fe}^{3+}$  modification because of the increase in visible light photoabsorption. On the other hand, an excess amount of  $\text{Fe}^{3+}$  modification decreased photocatalytic activity presumably due to a decrease of reduction sites by coverage of the  $\text{TiO}_2$  surface. Therefore, increase in photocatalytic activity of the site-selective  $\text{Fe}^{3+}$ -modified brookite  $\text{TiO}_2$  nanorod might be attributable to removal of an excess amount of  $\text{Fe}^{3+}$  compounds, which covered reduction sites on the surface of brookite  $\text{TiO}_2$  nanorod. In addition, a site-selective  $\text{Fe}^{3+}$  modified brookite  $\text{TiO}_2$  nanorod with a larger aspect ratio showed higher photocatalytic activity for acetaldehyde degradation than that of a brookite  $\text{TiO}_2$  nanorod site-selectively modified with  $\text{Fe}^{3+}$  compounds having a smaller aspect ratio. These results suggested that the rate-determining step of acetaldehyde oxidation under visible light might be oxygen reduction proceeded on the reduction site of brookite  $\text{TiO}_2$  nanorod. Therefore, a site-selective  $\text{Fe}^{3+}$  modified brookite  $\text{TiO}_2$  nanorod with a larger aspect ratio having a large reduction area showed the highest activity for acetaldehyde oxidation under visible light.

The same modification method was applied to commercial brookite  $\text{TiO}_2$ , which has a spherical shape without specific exposed crystal faces. Figure 4.13 shows the amount of  $\text{CO}_2$  evolution over site-selective  $\text{Fe}^{3+}$ -modified commercial brookite  $\text{TiO}_2$  nanoparticles under visible-light irradiation. The photocatalytic activity of  $\text{Fe}^{3+}$ -modified commercial brookite  $\text{TiO}_2$  is quite low comparing to that of site-selective  $\text{Fe}^{3+}$ -modified brookite  $\text{TiO}_2$  nanorod because UV irradiation during  $\text{Fe}^{3+}$  modification does not induce site-selective modification on the commercial brookite  $\text{TiO}_2$  nanoparticles because redox reaction proceeds in the neighboring sites without being separated.

## 4.5 Conclusions

We have demonstrated that the morphology of rutile and brookite  $\text{TiO}_2$  particles can be controlled by means of hydrothermal process with morphology controlled reagents. Addition of PVP and PVA to hydrothermal preparation process for brookite  $\text{TiO}_2$  nanorod reduces the aspect ratio of brookite  $\text{TiO}_2$  nanorod ( $AR \sim 1.6\text{--}5.2$ ). Each exposed crystal surface of rutile and brookite  $\text{TiO}_2$  nanorod shows different activities such as oxidation and reduction, respectively. The photocatalytic activities of rutile and brookite  $\text{TiO}_2$  nanorods show higher activity than that of commercially available anatase or brookite  $\text{TiO}_2$  fine particles which were commercially available in Japan. It was found that the photocatalytic activity depends on not relative surface area but surface structure of the  $\text{TiO}_2$  nanorods, suggesting that prevention of electron-hole pair recombination is one of important role during the photodegradation of organic compounds.

UV irradiation during  $\text{Fe}^{3+}$ -modification on shape-controlled rutile and brookite  $\text{TiO}_2$  nanorods showed high photocatalytic activity under visible-light irradiation because  $\text{Fe}^{3+}$  ion was site-selectively modified on  $\{111\}$  and  $\{212\}$  exposed crystal faces, respectively, and redox reactions were spatially separated. DB-PA analyses indicate that photocatalytic activity was determined by not efficiency of electron injection but efficiency of reduction by injected electron. The efficiency of reduction was influenced by site-selectivity of  $\text{Fe}^{3+}$ -modification on  $\{111\}$  faces because  $\text{Fe}^{3+}$  ion remained on  $\{110\}$  faces of  $\text{TiO}_2$  retard a reduction.

## References

1. Hoffmann MR, Martin ST, Choi WY, Bahnemann DW (1995) Environmental applications of semiconductor photocatalysis. *Chem Rev* 95:69–96
2. Choi W (2006) Pure and modified  $\text{TiO}_2$  photocatalysts and their environmental applications. *Catal Surv Asia* 10:16–28
3. Chen X, Mao SS (2007) Titanium dioxide nanomaterials: synthesis, properties, modifications, and applications. *Chem Rev* 107:2891–2959

4. Hosono E, Fujihara S, Kakiuchi K, Imai H (2004) Growth of submicrometer-scale rectangular parallelepiped rutile TiO<sub>2</sub> films in aqueous TiCl<sub>3</sub> solutions under hydrothermal conditions. *J Am Chem Soc* 126:7790–7791
5. Neale NR, Frank AJ (2007) Size and shape control of nanocrystallites in mesoporous TiO<sub>2</sub> films. *J Mater Chem* 17:3216–3221
6. Huang X, Pan C (2007) Large-scale synthesis of single-crystalline rutile TiO<sub>2</sub> nanorods via a one-step solution route. *J Cryst Growth* 306:117–122
7. Testino A, Bellobono IR, Buscaglia V, Canevali C, D'Arienzo M, Polizzi S, Scotti R, Morazzoni F (2007) Optimizing the photocatalytic properties of hydrothermal TiO<sub>2</sub> by the control of phase composition and particle morphology. A systematic approach. *J Am Chem Soc* 129:3564–3575
8. Ohno T, Sarukawa K, Matsumura M (2002) Crystal faces of rutile and anatase TiO<sub>2</sub> particles and their roles in photocatalytic reactions. *New J Chem* 26:1167–1170
9. Bae E, Murakami N, Ohno T (2009) Exposed crystal surface-controlled TiO<sub>2</sub> nanorods having rutile phase from TiCl<sub>3</sub> under hydrothermal conditions. *J Mol Catal A Chem* 300:72–79
10. Bae E, Ohno T (2009) Exposed crystal surface-controlled rutile TiO<sub>2</sub> nanorods prepared by hydrothermal treatment in the presence of poly(vinyl pyrrolidone). *Appl Catal B Environ* 91:634–639
11. Bae E, Murakami N, Nakamura M, Ohno T (2010) Effect of chemical etching by sulfuric acid or H<sub>2</sub>O<sub>2</sub>–NH<sub>3</sub> mixed solution on the photocatalytic activity of rutile TiO<sub>2</sub> nanorods. *Appl Catal A Gen* 380:48–54
12. Murakami N, Kurihara Y, Tsubota T, Ohno T (2009) Shape-controlled anatase titanium(IV) oxide particles prepared by hydrothermal treatment of peroxo titanate in the presence of polyvinyl alcohol. *J Phys Chem C* 113:3062–3069
13. Ohno T, Higo T, Saito H, Yuan S, Jin Z, Yang Y, Tsubota T (2015) Dependence of photocatalytic activity on aspect ratio of a brookite TiO<sub>2</sub> nanorod and drastic improvement in visible light responsibility of a brookite TiO<sub>2</sub> nanorod by site-selective modification of Fe<sup>3+</sup> on exposed faces. *J Mol Catal A Chem* 396:261–267
14. Sato S (1986) photocatalytic activity of nox-doped TiO<sub>2</sub> in the visible-light region. *Chem Phys Lett* 123:126–128
15. Asahi R, Morikawa T, Ohwaki T, Aoki K, Taga Y (2001) Visible-light photocatalysis in nitrogen-doped titanium oxides. *Science* 293:269–271
16. Umebayashi T, Yamaki T, Itoh H, Asai K (2002) Band gap narrowing of titanium dioxide by sulfur doping. *Appl Phys Lett* 81:454–456
17. Ohno T, Akiyoshi M, Umebayashi T, Asai K, Mitsui T, Matsumura M (2004) Preparation of S-doped TiO<sub>2</sub> photocatalysts and their photocatalytic activities under visible light. *Appl Catal A Gen* 265:115–121
18. Ohno T, Tsubota T, Nishijima K, Miyamoto Z (2004) Degradation of methylene blue on carbonate species-doped TiO<sub>2</sub> photocatalysts under visible light. *Chem Lett* 33:750–751
19. Irie H, Watanabe Y, Hashimoto K (2003) Carbon-doped anatase TiO<sub>2</sub> powders as a visible-light sensitive photocatalyst. *Chem Lett* 32:772–773
20. Serpone N, Lawless D (1994) Spectroscopic, photoconductivity, and photocatalytic studies of TiO<sub>2</sub> colloids – naked and with the lattice doped with Cr<sup>3+</sup>, Fe<sup>3+</sup>, and V<sup>5+</sup> cations. *Langmuir* 10:643–652
21. Ikeda S, Sugiyama N, Pal B, Marci G, Palmisano L, Noguchi H, Uosakid K, Ohtani B (2001) Photocatalytic activity of transition-metal-loaded titanium(IV) oxide powders suspended in aqueous solutions: Correlation with electron-hole recombination kinetics. *Phys Chem Chem Phys* 3:267–273
22. Kisch H, Zang L, Lange C, Maier WF, Antonius C, Meissner D (1998) Modified, amorphous titania – a hybrid semiconductor for detoxification and current generation by visible light. *Angew Chem Int Ed* 37:3034–3036
23. Zang L, Lange C, Abraham I, Storck S, Maier WF, Kisch H (1998) *J Phys Chem B* 102:10765–10771

24. Zang L, Lange C, Abraham I, Storck S, Maier WF, Kisch H (1998) Amorphous microporous titania modified with platinum(IV) chloride – a new type of hybrid photocatalyst for visible light detoxification. *J Phys Chem B* 102:10765–10771
25. Macyk W, Kisch H (2001) Photosensitization of crystalline and amorphous titanium dioxide by platinum(IV) chloride surface complexes. *Chem Eur J* 7:1862–1867
26. Murakami N, Chiyoya T, Tsubota T, Ohno T (2008) Switching redox site of photocatalytic reaction on titanium(IV) oxide particles modified with transition-metal ion controlled by irradiation wavelength. *Appl Catal A Gen* 348:148–152
27. Murakami N, Ono A, Nakamura M, Tsubota T, Ohno T (2010) Development of a visible-light-responsive rutile rod by site-selective modification of iron(III) ion on {111} exposed crystal faces. *Appl Catal A General* 97:115–119
28. Oliver PM, Watson GW, Kelsey ET, Parker SC (1997) Atomistic simulation of the surface structure of the TiO<sub>2</sub> polymorphs rutile and anatase. *J Mater Chem* 7:563–568
29. Murakami N, Mahaney OOP, Abe R, Torimoto T, Ohtani B (2007) Double-beam photoacoustic spectroscopic studies on transient absorption of titanium(IV) oxide photocatalyst powders. *J Phys Chem C* 111:11927–11935
30. Ohno T, Haga D, Fujihara K, Kaizaki K, Matsumura M (1997) Unique effects of iron(III) ions on photocatalytic and photoelectrochemical properties of titanium dioxide. *J Phys Chem B* 101:6415–6419
31. Kandiel TA, Feldhoff A, Robben L, Dillert R, Bahnemann DW (2010) Tailored titanium dioxide nanomaterials: anatase nanoparticles and brookite nanorods as highly active photocatalysts. *Chem Mat* 22:2050–2060
32. Kobayashi M, Tomita K, Petrykin V, Yin S, Sato T, Yoshimura M, Kakihana M (2007) Hydrothermal synthesis of nanosized titania photocatalysts using novel water-soluble titanium complexes. *Solid State Phenomena* 124–126:723–726
33. Zhang H, Banfield JF (2000) Understanding polymorphic phase transformation behavior during growth of nanocrystalline aggregates: insights from TiO<sub>2</sub>. *J Phys Chem B* 104:3481–3487
34. Kobayashi M, Petrykin V, Kakihana M, Tomita K (2009) Hydrothermal synthesis and photocatalytic activity of whisker-like rutile-type titanium dioxide. *J Am Ceram Soc* 92(S1): S21–S26

# Chapter 5

## Development of Advanced Nanoarchitectures for Photocatalytic Treatment of $\text{NO}_x$

Shuning Xiao, Dieqing Zhang, Guisheng Li, and Hexing Li

### 5.1 Introduction

With the rapid development of economy and science technology, the level of social industrialization is continuously increasing. Though the mankind have benefited from the industrial civilization, they still suffered from the energy shortage and environmental degradation. Owing to the industrial waste gas emission, air pollution is becoming one of the most difficult environmental issues to deal with [1–5]. As known, the polluted air includes various chemical compositions, including dust, toxic gases, greenhouse gases, and metal salts. Among them, nitrogen oxide ( $\text{NO}_x$ ) has proved as an important family of air polluting chemical compounds to human [6, 7]. Different routes, such as selective catalytic reduction [8–10], selective non-catalytic reduction [11–14], photocatalytic technologies [15–19], have been explored for removing  $\text{NO}_x$ . Among them, photocatalytic technology obtained lots of attentions owing to its preferred advantages, including simple operation, low cost, high efficiency, and strong durability [5]. In this chapter, we mainly focus on reviewing the latest development of advanced nanoarchitectures for photocatalytic treatment of  $\text{NO}_x$ .

#### 5.1.1 Generation Mechanism of $\text{NO}_x$

Nitrogen oxides ( $\text{NO}_x$ ) mainly comprise nitric oxide (NO), nitrous oxide ( $\text{N}_2\text{O}$ ), nitrogen dioxide ( $\text{NO}_2$ ), dinitrogen trioxide ( $\text{N}_2\text{O}_3$ ), dinitrogen tetroxide ( $\text{N}_2\text{O}_4$ ), dinitrogen pentoxide ( $\text{N}_2\text{O}_5$ ), and so on.  $\text{NO}_x$  generation contains two majority routes.

---

S. Xiao • D. Zhang • G. Li (✉) • H. Li

The Education Ministry Key Lab of Resource Chemistry, Shanghai Key Laboratory of Rare Earth Functional Materials, Department of Chemistry, Shanghai Normal University, 100 Guilin Road, Shanghai 200234, China  
e-mail: [liguisheng@shnu.edu.cn](mailto:liguisheng@shnu.edu.cn)

Natural emissions of  $\text{NO}_x$  mainly come from the decomposition of organic substances in the soil or in the ocean, geologic activities (including volcano eruption, earthquakes, and others), and lightning, natural fires [20, 21]. Anthropogenic emissions of  $\text{NO}_x$  mostly come from fossil fuel combustion processes, such as automobiles, aircraft, industrial, and internal combustion processes [22–24].

### 5.1.2 Physical and Chemical Properties of $\text{NO}_x$

NO accounts for about 95 vol.% of the initial  $\text{NO}_x$  emissions. After being emitted into the air, a series of reactions will occur between NO and  $\text{O}_2$  owing to the highly active chemical properties of NO. NO can be oxidized by oxygen into nitrogen dioxide, as shown in Eq. (5.1). Such reaction has been speculated as occurring via the ONOONO intermediate. In the presence of water, NO molecules could further react with oxygen to form nitrous acid ( $\text{HNO}_2$ ), as shown in Eq. (5.2). From the two reactions, one could see that the derivative products of NO in the presence of moisture atmosphere are corrosive and acidic. They may create tremendous harm to both environment and humans.



### 5.1.3 Hazard for Environment and Humans

$\text{NO}_x$  could not only pollute the atmospheric environment, but also cause harm to the health of humans directly or indirectly. The main hazards of  $\text{NO}_x$  were mainly listed in the following contents: [25, 26]

1. Threats to human and animal health. NO can be combined with the hemoglobin in the blood to generate nitroso-hemoglobin or nitroso-methemoglobin, so that the blood oxygen capacity decreased with hypoxia, convulsions and paralysis and other symptoms occurred.
2. Acid rain.  $\text{NO}_x$  could undergo some certain chemical reactions with other substances in the atmosphere to form acid chemicals in air with the formation of acid rain. Acid rain brings great harm to the environment and human life, such as destructing the root system of plants, damaging cell membranes of trees, undermining photosynthesis, corroding buildings, transport, and various historical monuments, and causing acidification of rivers and lakes resulting in death of a variety of aquatic life.
3. Photochemical smog. Under light irradiation,  $\text{NO}_x$  could react with hydrocarbons ( $\text{C}_x\text{H}_y$ ) and ozone to generate small organic particles, containing peroxide acetyl

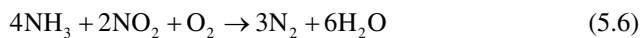
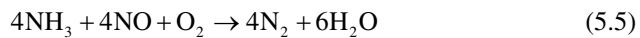
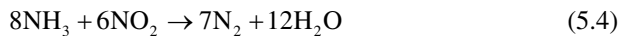
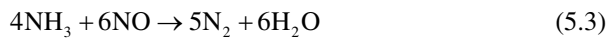
nitrate (PAN) and a variety of nitrogen-containing compounds. These small organic particles are so called photochemical smog, which can cause eyes mucous membrane irritation, headaches, respiratory disorders, chronic respiratory disease, pulmonary function abnormalities and other symptoms for human beings and animals.

4. Causing climate change and ozone hole.  $N_2O$ , as one type of  $NO_x$ , could cause the greenhouse effect, further leading to the global warming. Due to the highly active nature of N atoms,  $N_2O$  could release a single atom of nitrogen to react with ozone molecules, causing the destruction of the ozone layer.

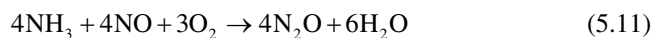
#### 5.1.4 Traditional Techniques for Removing $NO_x$

Based on the generation mechanism of  $NO_x$ , two types of routes were proposed for removing  $NO_x$  [27]. One is to utilize advanced low  $NO_x$  combustion technology to improve coal combustion process for reducing the emission of  $NO_x$  in thermal power industries. The other one is to purify the generated  $NO_x$  via eliminating them from the flue gas for the primary de- $NO_x$  treatment. To the case of low concentrated  $NO_x$ , secondary methods, including selective catalytic reduction (SCR) and selective non-catalytic reduction (SNCR) have been proposed for removing  $NO_x$  [28].

As the most widely used technology for de- $NO_x$  in industrial applications, SCR usually uses ammonia to reduce  $NO_x$  to the non-toxic and harmless nitrogen, released into the atmospheric environment [29–31]. In a typical SCR process, the flue  $NO_x$  gas is mixed with  $NH_3$ , and then the mixture goes through a catalytic bed to form  $N_2$  and water vapor, shown in the following reactions [32]:



In addition to the above reactions, other side reactions could occur as the reaction from (5.7) to (5.11).



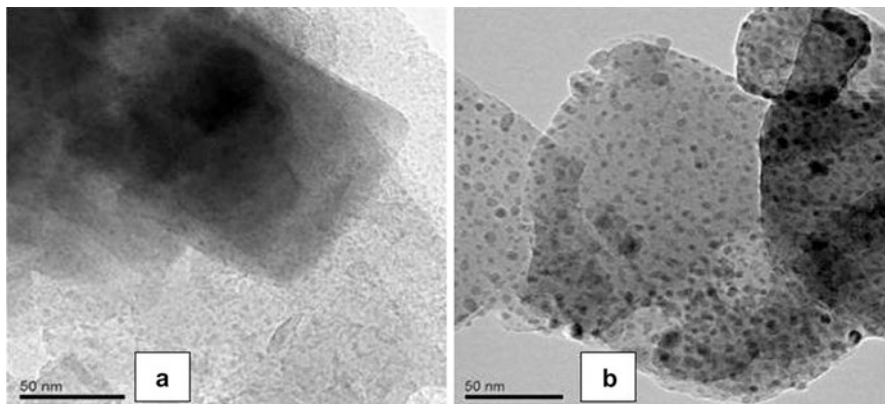


**Fig. 5.1** TEM images of Cu-CHA samples: (a) fresh and (b) aged at 800 °C for 120 h. Reprinted with permission from Ref. [9]. Copyright 2012 Elsevier

By selecting suitable catalysts, such as chromia [33], metal or metal alloys [34–36],  $\text{MnO}_x\text{-CeO}_x$  [37], and  $\text{V}_2\text{O}_5$  [38–40], these reactions can be performed in the range of 200–500 °C. For example, Cu-CHA zeolites have been proved effective for reducing NO at 500 °C. As shown in Fig. 5.1a, no Cu particles could be found in the fresh sample, which exhibited an excellent activity for reducing  $\text{NO}_x$ . This suggested that highly dispersed Cu species were the key to de- $\text{NO}_x$  reaction. However, the de- $\text{NO}_x$  reaction could be prohibited by increasing the size of Cu to about 10 nm upon heating the fresh sample at 800 °C shown in Fig. 5.1b [9]. It should be pointed out that ammonia gas could prefer to react with  $\text{NO}_x$ , rather than  $\text{O}_2$ , with the formation of  $\text{N}_2$  and  $\text{H}_2\text{O}$  [41, 42]. Under ideal conditions, SCR could achieve a high  $\text{NO}_x$  removal rate up to 90 %. Nevertheless, it still suffers some shortcomings, such as the secondary pollution owing to the inability to precisely control the amount of ammonia or release of ammonia [43, 44], expensive equipment like high-specification piping systems and reactors for inhibiting the high corrosion of liquid ammonia, and so on.

Compared SCR, selective non-catalytic reduction (SNCR) is a homogeneous method to remove  $\text{NO}_x$  at high temperature. In a typical SNCR process,  $\text{NO}_x$  reacts with amino containing reducing agent (such as ammonia, and urea) at about 700–1100 °C, producing  $\text{N}_2$  and  $\text{H}_2\text{O}$  [45–47]. The equipment of SNCR technology is simple and easy to operate, thus, such technology has been widely used in power industry for de- $\text{NO}_x$ . However, SNCR requires an extremely high temperature to drive the reactions between  $\text{NO}_x$  and ammonia attributing to the high energy barrier in the absence of catalysts. It should be acknowledged that SNCR is not an environmental route for treating  $\text{NO}_x$  owing to its high energy consumption.

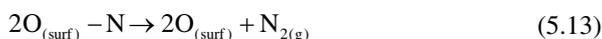
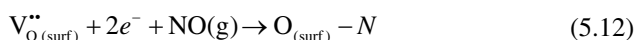
## 5.2 Photo-Reduction Techniques for NO<sub>x</sub> Removal

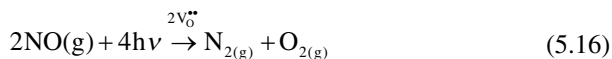
### 5.2.1 Photo-Selective Catalytic Reduction of NO<sub>x</sub>

As a secondary method to removing NO<sub>x</sub>, photo-selective catalytic reduction (PSCR) utilizes suitable reducing agents to convert NO<sub>x</sub> to N<sub>2</sub> with the aid of photocatalytic route under light irradiation in air. Such benign technique obtained lots of attention from the researchers owing to its room -temperature operation reaction and non-toxic product of nitrogen. To date, lots of works have been reported on the investigation of various reducing agents (NH<sub>3</sub>, CO and hydrocarbons) on the performance of PSCR for treating NO<sub>x</sub>. Cant et al. found that NO could be reduced to N<sub>2</sub> by NH<sub>3</sub> at room temperature on the surface of TiO<sub>2</sub> wafer under near ultraviolet illumination [48]. Sano et al. selected CH<sub>3</sub>OH as a reducing agent to selectively reduce N<sub>2</sub>O to N<sub>2</sub> by using Ag<sup>+</sup>/TiO<sub>2</sub> [49]. Besides, other types of photocatalysts, including TiO<sub>2</sub> loaded on ZSM-5 or MCM-41 and noble metal doped TiO<sub>2</sub>, were explored for reducing NO<sub>x</sub> to N<sub>2</sub> in the presence of reducing agents [50, 51]. However the requirement of reducing agents (NH<sub>3</sub>, CO and other hydrocarbons) greatly inhibits the practical application of PSCR technology.

### 5.2.2 Photocatalytic Reduction of NO<sub>x</sub>

For relieving the dependence on the reducing agents, it is highly required to realize the photocatalytic reduction of NO in the absence of reducing agents. Recently, Wu et al. reported the selective photoreduction of NO<sub>x</sub> to nitrogen by Fe<sup>3+</sup> doped nano-structured TiO<sub>2</sub> photocatalysts without using reducing agents. Though only about 1 % of NO<sub>x</sub> (10 ppb) could be reduced to N<sub>2</sub> by photocatalytic process, such improvement opens a door for realizing the photocatalytic reduction of NO<sub>x</sub> [52]. It was found that the introduced Fe<sup>3+</sup> ions could substitute part of Ti<sup>4+</sup> ions in the TiO<sub>2</sub> lattice with the formation of stable positively charged oxygen vacancies. These vacancies played an important role in both suppressing the conversion of NO to NO<sub>2</sub> and increasing the photoreduction of NO to N<sub>2</sub>. The possible mechanism of photocatalytic reduction of NO was proposed as following equations (Eq. 5.12–5.16). The oxygen vacancies (V<sub>o</sub><sup>••</sup>) could act as the active species for capturing the electrons and NO molecules for producing O<sub>(surf)</sub>-N bonds. Then, the surface O<sub>(surf)</sub>-N further disaggregated to N<sub>2</sub> and O<sub>2</sub> with exothermal through a surface vacancy diffusion mechanism.





Nevertheless, it should be pointed out that few developments have been achieved for improving the activity of photocatalytic reduction of  $\text{NO}_x$ . Recently, Huang et al. reported an approach to synthesize rutile  $\text{TiO}_2$ /titania nanotube composites (FESEM and TEM shown in Fig. 5.2). After  $\text{H}_2$ -thermal treatment, the composite materials exhibited nearly 100 % of NO conversion with 81.7 %  $\text{N}_2$  selectivity and 18.3 %  $\text{N}_2\text{O}$  selectivity under natural solar-light irradiation at extremely low pressure of 1

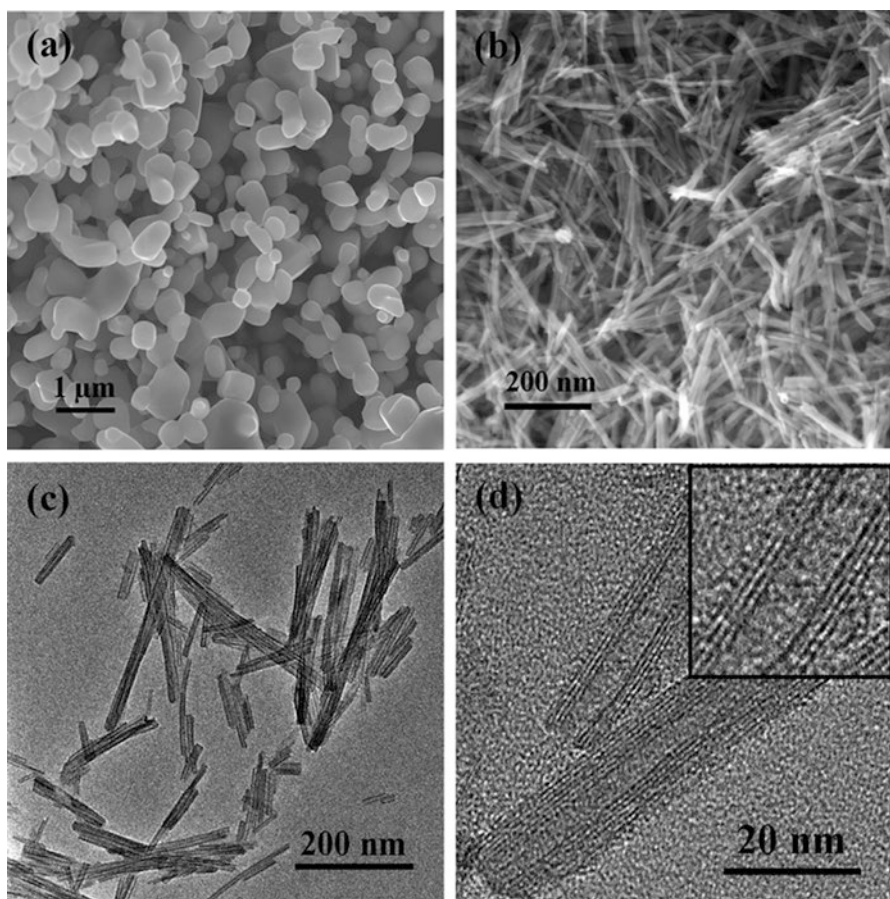


**Fig. 5.2** FE-SEM images of the rutile  $\text{TiO}_2$  precursor (a) and rutile/Tnt (b). TEM and HRTEM images of rutile/Tnt (c) and (d). Reprinted with permission from Ref. [53]. Copyright 2013 Elsevier

Torr [53]. Though NO molecules possess a high positive formation enthalpy ( $H_f=90.2$  kJ/mol), they become thermodynamically unstable in such a low pressure system. With the help of defect sites (oxygen vacancies), the NO molecules could be adsorbed on the catalyst surface, leading to a weakened activation barrier. Thus, photocatalysts could easily drive the reaction to decompose NO into  $N_2$  and  $O_2$  directly under light irradiation. However, it is worth to mention that although this approach shows a perfect de- $NO_x$  property, the extreme reaction conditions could only be operated in laboratory.

### 5.3 Photocatalytic Oxidation of $NO_x$

For oxidizing  $NO_x$ , lots of efforts have been done for improving the photocatalytic performance based on different ways including catalysts-fabrication, reactors-design, light harvesting, and so on. Among those, design and fabrication of highly efficient photocatalyst is considered to be the most effective and direct approach for improving the activity. Since 1972 Fujishima reported the photocatalytic phenomenon on the  $TiO_2$  electrode, titanium dioxide ( $TiO_2$ ) has become the most widely used photocatalyst in both photocatalytic oxidation and reduction reactions [54]. However,  $TiO_2$  can only work under UV light irradiation owing to its large band gap. This greatly prohibits its application in solar-light region. Therefore, it is required to tailor/modify  $TiO_2$ , and even to develop new photocatalysts for explore its application in longer-wavelength light region. Herein, the latest development of designing various advanced photocatalysts with nano-architecture was briefly reviewed to the case of photocatalytic oxidation of  $NO_x$ .

#### 5.3.1 $TiO_2$ -Based Photocatalysts

Among various semiconductors,  $TiO_2$  exhibits excellent properties, such as low cost, nontoxic, high stability and powerful light-induced abilities, for the oxidation of organic pollutants including VOCs, POPs,  $NO_x$  and dyes. As known,  $TiO_2$  exists in three crystal phases (anatase, rutile, and brookite), among which, brookite type of  $TiO_2$  is rarely utilized as a catalyst due to its unstable crystal structure during the reactions [55]. Both rutile and anatase  $TiO_2$  show excellent photocatalytic activities. Anatase  $TiO_2$  possess a band gap energy of 3.2 eV, slightly larger than the rutile of 3.1 eV, suggesting that rutile  $TiO_2$  can be excited under longer wavelength light than anatase  $TiO_2$ . However, the photocatalytic activity of anatase  $TiO_2$  is better than that of rutile  $TiO_2$ . This is attributed to the following reasons: (1) the lower conduction band of anatase could provide a strong adsorption of  $O_2$  molecules; (2) the more lattice defects in anatase  $TiO_2$  could produce oxygen vacancies to capture electron favoring the separation of photogenerated carriers; (3) the larger surface area of anatase  $TiO_2$  provides more active sites for catalysis.

Zhang et al. compared the photocatalytic performance for oxidizing NO of various TiO<sub>2</sub> photocatalysts with an average grain size from 0.02 to 1 μm. It was found that the anatase TiO<sub>2</sub> has exhibited a much higher activity for oxidizing NO than that of rutile TiO<sub>2</sub> [56]. This is because higher negative energies of the conduction band edge of anatase induced a reductive potential to more negative values. Besides, the surface -OH groups as well as the physical adsorbed H<sub>2</sub>O favors the formation of reactive OH radicals on the anatase of TiO<sub>2</sub>. For the pure anatase TiO<sub>2</sub>, both particle size and surfaces area are the two vital properties to affect the photocatalytic performances. Ohko et al. reported the fabrication of a photocatalytic film for treating NO via a spin coating route by using an anatase TiO<sub>2</sub> nanocrystals (ca. 20 nm) aqueous sol [57]. Matsuda investigated the size-effect of anatase TiO<sub>2</sub> on the photocatalytic activity for oxidizing NO under UV light irradiation [58]. The grain size of the TiO<sub>2</sub> ranged from 7 to 200 nm, The TiO<sub>2</sub> crystals, with an average size of 7 nm, possessed the highest activity for oxidizing NO with good stability owing to its large surface area and increased active sites. Recently, lots of research works proved that anatase TiO<sub>2</sub> single crystal, with various facets exposed, could exhibited different physicochemical properties, greatly affecting the oxidative/reductive capability of the catalysts during the photocatalytic reactions [59–64]. Both theoretical and experimental explores suggested that {001} of facets of anatase TiO<sub>2</sub> has a higher surface energy compared with the more stable {101} facets. The former is more effective for dissociative adsorption of reactant molecules, especially for the water [65–67]. Water molecules could be physically adsorbed and chemically dissociated on the {001} facets. However, the later only allows the physical adsorption of water molecules. As known, the adsorbed water can induce the formation of reactive OH radicals for further oxidizing NO during the photo-oxidation reactions [68–70].

Tian et al. found that highly reactive {001} facets of anatase TiO<sub>2</sub> exhibit much stronger NO adsorption capabilities than that of the thermally stable {101} facets, owing to active sites (coordinated oxygen (O<sub>2c</sub>) sites of (001) surface) for the NO chemisorption (see Fig. 5.3). On the {001} surface, NO molecules are easily to be

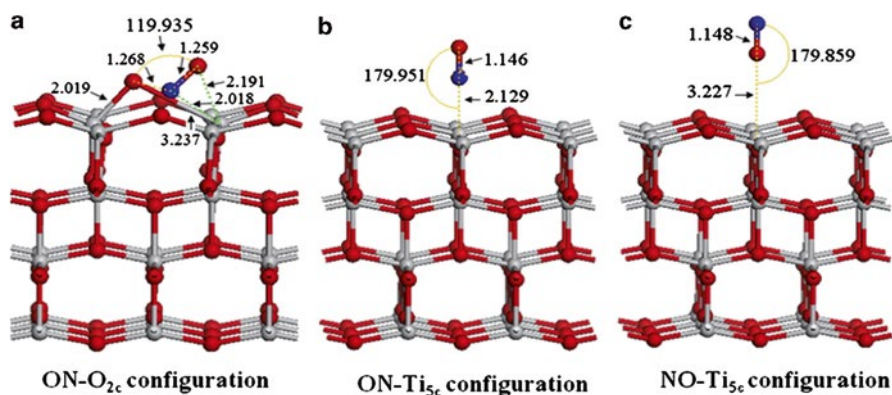


**Fig. 5.3** Optimized adsorption structures of NO on different sites of anatase TiO<sub>2</sub> (001) surface: (a) N end of NO toward the surface O<sub>2c</sub> (b) N end of NO toward the surface Ti<sub>5c</sub> (c) O end of NO toward the surface Ti<sub>5c</sub>. The Ti, O, and N atoms are in gray, red, and blue, respectively. Reprinted with permission from Ref. [71]. Copyright 2014 Elsevier

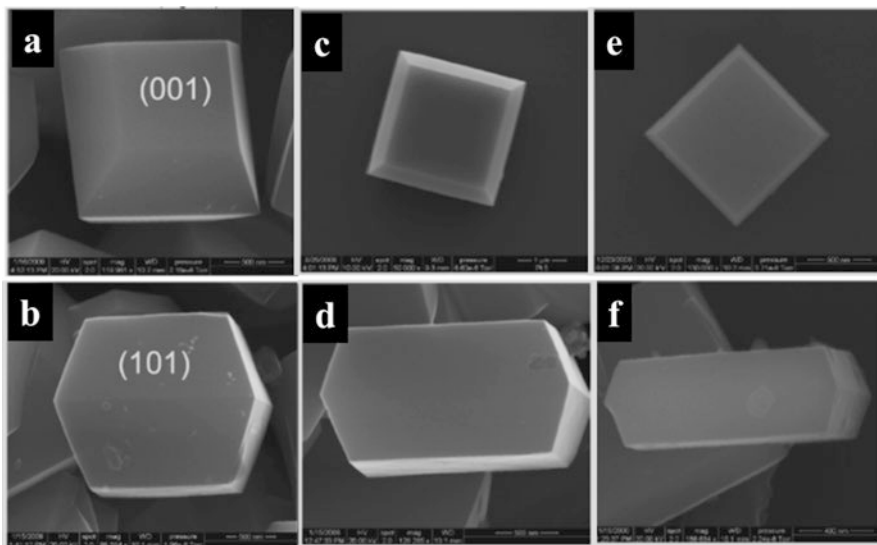


**Fig. 5.4** FESEM images of {001} facets exposed  $\text{TiO}_2$  with {001} facets percentage of (a, b) 27 %, (c, d) 39 %, and (e, f) 50 % prepared with 0.5, 1, and 2 mL of ionic liquid at 210 °C for 90 min, respectively. Reprinted with permission from Ref. [73]. Copyright 2010 American Chemical Society

oxidized into  $\text{NO}_2^-$  species. Such  $\text{NO}_2^-$  ions could be trapped efficiently by {001} surface, and further react with water or oxygen to form  $\text{HNO}_2$  or  $\text{HNO}_3$  [71]. Sofianou et al. reported that the nano and microstructures of anatase  $\text{TiO}_2$  with dominant {001} facets showed a higher activity of NO oxidation than commercial P25 owing to its high {001} facets exposed percentage and high surface area [72]. Zhang et al. reported a microwave-assisted process to synthesize micrometer-sized anatase  $\text{TiO}_2$  single-crystals with a large percentage of {001} reactive facets [73]. As shown in Fig. 5.4, the exposed percentage of {001} facets could be tuned from 27 to 50 % via controlling the concentrations of fluorine-rich ionic liquid (1-methyl-imidazolium tetrafluoroborate). Both the photocatalytic NO removal rate and the reaction kinetics were proportional to the percentages of {001} facets. It was interesting that larger micrometer-size anatase  $\text{TiO}_2$  single crystals with remarkable 80 % {001} reactive facets could be obtained via further increasing the concentration of ionic liquid [74]. The as-formed micrometer-size anatase  $\text{TiO}_2$  single crystals exhibited an enhanced NO oxidation activity and a high thermal stability up to 800 °C.

More recently, Wen et al. used sodium dodecyl benzene sulfonate (SDBS) as a surfactant for the fabrication of uniformed anatase single-crystal cubes with active {010} and {001} facets shown in Fig. 5.5a–d [75]. It was proved that SBDS could be perpendicularly anchor onto {010} plane to form electrostatic interaction between  $\text{Ti}_{5c}$  atoms and sulfonate anion, as shown in Fig. 5.5e. In addition, Fig. 5.5f exhibits the preferential absorption of SBDS on the {010} facets for stabilizing the {010} facets. Thus, high percentage of {010} facets exposed  $\text{TiO}_2$  could be achieved, producing a much higher NO removal rate than that of the sample with {001} facets exposure. Compared to anatase  $\text{TiO}_2$ , rutile  $\text{TiO}_2$ -based photocatalysts were seldom

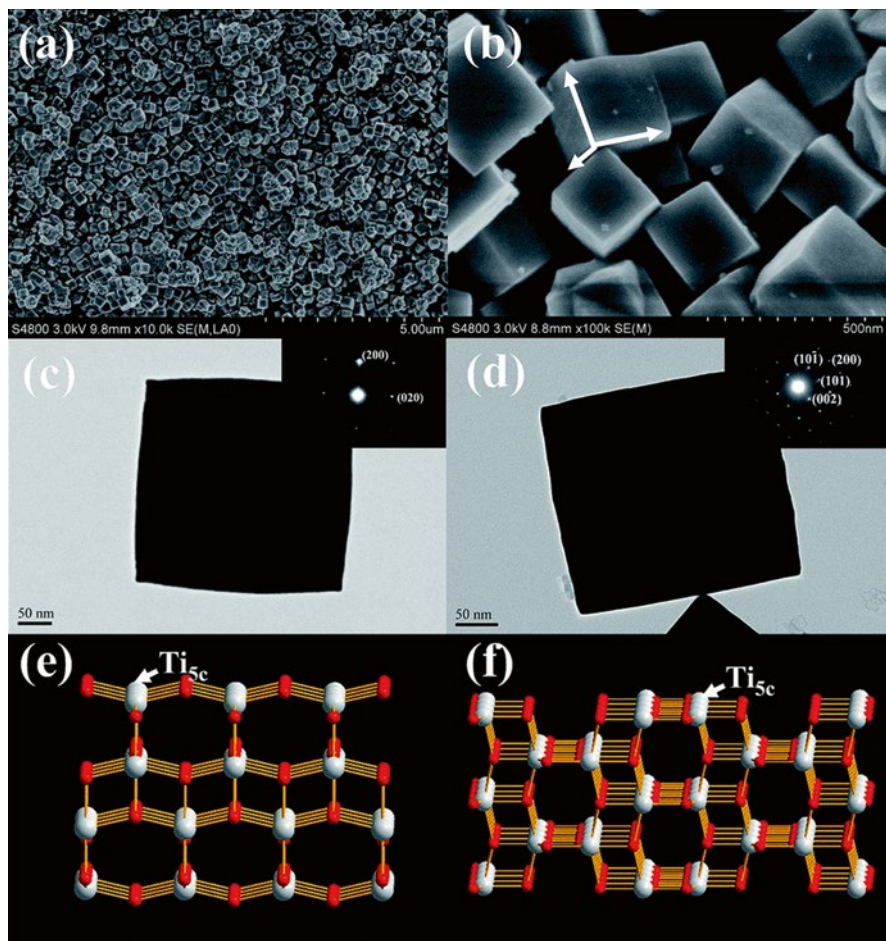


**Fig. 5.5** Low (a) and high (b) resolution FE-SEM images of the cubic anatase. (c, d) TEM images of two representative cubes, the insets are the corresponding SAED patterns. (e, f) Schematic of atomic structure of {001} and {010} facets; gray  $\text{Ti}^{4+}$ , red  $\text{O}^{2-}$ . Reference [75]-Reproduced by permission of The Royal Society of Chemistry (Color figure online)

reported to be utilized in the photocatalytic oxidation of NO. Zhang et al. explored a fast microwave synthetic route for obtaining 3D hierarchical rutile  $\text{TiO}_2$  nano-rod clusters with high NO photocatalytic oxidation activity [76].

### 5.3.2 Modified $\text{TiO}_2$ Photocatalysts

Because of the broad band gap of  $\text{TiO}_2$  (3.0 eV for the rutile and 3.2 eV for the anatase), the photocatalytic applications of  $\text{TiO}_2$  are still confined in the ultraviolet region [77–80]. For better utilization of the visible light (40–50 % of solar energy),

modifying  $\text{TiO}_2$  via doping or coupling, has been proved as effective way for extending the light-response region to longer wavelength. Chen et al. reviewed the modification of  $\text{TiO}_2$  with metal or non-metal atoms [77]. Obviously, modification could allow  $\text{TiO}_2$  to exhibit greatly enhanced photocatalytic performances owing to the following reasons: (1) Narrow band gap could be produced for altering the optical properties of  $\text{TiO}_2$  via doping other elements; (2) The formation of heterojunctions through coupling other low band-gap semiconductors could facilitate the electron-hole separation efficiency; (3) noble metal modification was favorable for improving the electron transfer rate and extending the light-response region to longer wavelength owing to the surface plasmon resonance (SPR) effect.

### 5.3.2.1 Metal Enhanced $\text{TiO}_2$ Photocatalysts

Metal modification could be realized by depositing metal clusters on the surface of  $\text{TiO}_2$  nanocrystals by various approaches, including impregnation reduction, surface sputtering, and photoreduction. Metal modification could alter the electronics division of the  $\text{TiO}_2$ . As known, the work function of metal (especially noble metal) is higher than that of  $\text{TiO}_2$ . Accordingly, the electron could migrate from  $\text{TiO}_2$  to the metal until their Fermi levels were equal. Thus, metal modification has been proved an efficient way to improve the surface properties of catalysts and to enhance the photocatalytic performances of  $\text{TiO}_2$ .

To date, various metals have been modified onto the surfaces or into the lattice framework of  $\text{TiO}_2$  for improving the photocatalytic activity for de- $\text{NO}_x$  [81–88]. Ishibai et al. found that  $\text{Pt}/\text{TiO}_2$  could be used as good candidate for oxidizing NO under both UV and visible light irradiation owing to the formation of Ti–O–Pt connection [89]. Huang et al. used an acid-catalyzed sol–gel method coupled with impregnation process to synthesize  $\text{PtO}_x$  modified  $\text{TiO}_2$  photocatalysts with enhanced visible-light activity and a lower  $\text{NO}_2$  selectivity for treating NO compared to pure  $\text{TiO}_2$  [90]. Except for Pt, metal Rh was proved to be more effective for enhancing the  $\text{NO}/\text{NO}_2$  to  $\text{NO}_3^-$  conversion rate of  $\text{TiO}_2$  than Pt owing to the strong  $\text{NO}_x$  adsorption capability of the composites of  $\text{Rh}/\text{TiO}_2$  [91]. It also suggested that doping  $\text{Pd}^{2+}$  into P25 could enhance the NO adsorption and prevent the recombination of photogenerated carriers, leading to the enhancement of de- $\text{NO}_x$  activity. However, both  $\text{Pd}^0$  and  $\text{PdO}$  showed almost no positive effect on photocatalytic NO removal [92, 93]. In addition, gold nanoparticles have been considered as a good noble metal with perfect plasmon resonance effects, thus coupling  $\text{TiO}_2$  with gold could be as one of the most promising cocatalysts to improve the photocatalytic efficiency via surface plasmon resonance effect [94–96].

Recently, Zhang et al. reported a novel Au- $\text{TiO}_2$  photocatalyst for photocatalytic oxidizing NO through coating Au nanoparticles onto rutile  $\text{TiO}_2$  nanorod bundles [97]. As shown in Fig. 5.6a–d, the rutile nanorods oriented crystal grew along the [001] direction and self-assembled to form nanorods bundles via a microwave-assisted hydrothermal approach. Au nanoparticles were deposited through in situ photo-reduction of  $\text{HAuCl}_4$  in aqueous solution. Fig. 5.6e displayed that the as-obtained composites could absorb the visible light centered at ca. 550 nm owing

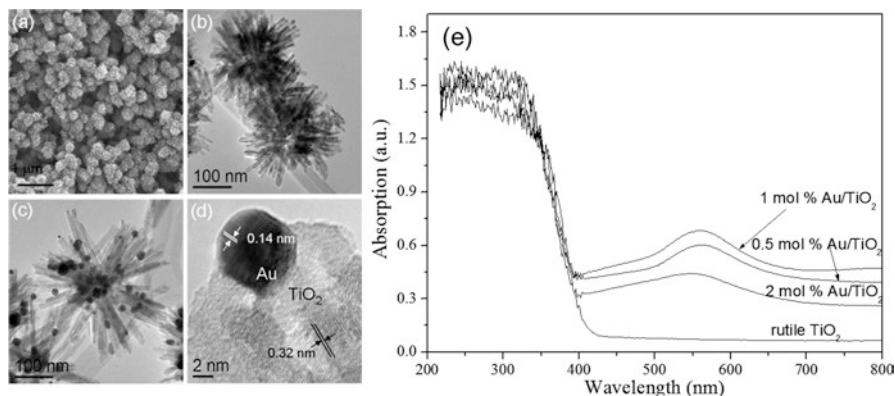


**Fig. 5.6** (a) FESEM and TEM images of rutile  $\text{TiO}_2$  and 1.0 mol%  $\text{Au/TiO}_2$ , (b) UV-Vis spectra of pure rutile  $\text{TiO}_2$  and  $\text{Au/TiO}_2$  with different Au loadings. Reprinted with permission from Ref. [97]. Copyright 2014 Elsevier

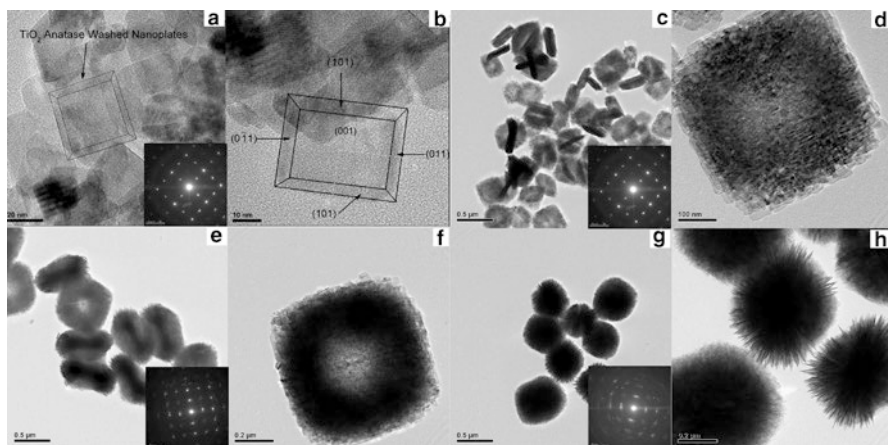


**Fig. 5.7** TEM micrographs of the pure  $\text{TiO}_2$  anatase nanoplates, in the insert corresponding SAED pattern (a, b), 2 at.%  $\text{Mg}^{2+}/\text{TiO}_2$ , in the insert corresponding SAED pattern (c, d), 5.1 at.%  $\text{Mg}^{2+}/\text{TiO}_2$  in the insert corresponding SAED pattern (e, f), 6.2 at.%  $\text{Mg}^{2+}/\text{TiO}_2$  anatase nanocrystals, in the insert corresponding SAED pattern (g, h). Reprinted with permission from Ref. [100]. Copyright 2014 Elsevier

to the surface plasmon resonance effect of Au nanoparticles. It was found that Au nanoparticles not only could contribute the SPR effect, but also could activate NO molecule via weakening the N-O bond through strong chemical adsorption.

Besides noble metals modification, transition metal ion can also be used to dope  $\text{TiO}_2$  for tuning the crystallinity degree or introducing the crystal lattice defects of  $\text{TiO}_2$ , thereby inhibiting the recombination of electron-hole pairs and prolonging the carriers lifetime [98, 99]. Sofianou et al. reported the  $\text{Mg}^{2+}$  doped anatase  $\text{TiO}_2$  nanocrystals with exposed {001} facets [100]. As shown in Fig. 5.7,

the morphologies of  $\text{TiO}_2$  nanocrystals could change from nano-sheets to sea-urchin liked structure via increasing the concentration of  $\text{Mg}^{2+}$ . DFT calculation indicated  $\text{Mg}^{2+}$  doping shifted the absorption edge of  $\text{TiO}_2$  to a lower energy, thus the de- $\text{NO}_x$  activity was greatly improved.  $\text{Mn}^{4+}$  ions were also chosen by the same group for enhancing the activity of anatase  $\text{TiO}_2$  with exposed  $\{001\}$  facets in photocatalytic NO oxidation [101].

### 5.3.2.2 Non-metal Modified $\text{TiO}_2$ Photocatalysts

Non-metal doping has also been utilized to improve the photocatalytic activity of  $\text{TiO}_2$ . Such route usually can narrow the band gap of  $\text{TiO}_2$  for absorbing visible light. Various non-metal modified  $\text{TiO}_2$  catalysts have been explored for visible-light driven applications [102–115]. Yin et al. fabricated N-doped  $\text{TiO}_2$  (anatase, rutile, and brookite types) by using  $\text{TiCl}_3$  and hexamethylenetetramine as precursors via a homogeneous precipitation solvothermal process [116]. Such N-doped  $\text{TiO}_2$  catalysts showed enhanced visible-light driven photocatalytic activity for de- $\text{NO}_x$  under both visible-light or UV-light irradiation. Upon further loading Fe or Pt on the surface of the as-obtained N-doped  $\text{TiO}_2$ , the de- $\text{NO}_x$  activity could be greatly enhanced under 390 nm UV light or 445 nm blue LED light irradiation [117]. Huang et al. fabricated carbon doped mesoporous  $\text{TiO}_2$  nanocrystals [118]. The oxygen sites in the  $\text{TiO}_2$  lattice were substituted by carbon atoms with the formation of C-Ti-O-C structures, allowing a strong light absorption in the visible region. The as-prepared C-doped mesoporous  $\text{TiO}_2$  showed a 25 % NO removal rate for treating the flow NO gas. Tseng et al. also proved that de- $\text{NO}_x$  activity by photocatalysis on different  $\text{TiO}_2$  phases (anatase, rutile, and brookite) could be improved by loading carbonaceous species on the surface  $\text{TiO}_2$  [119].

Ding et al. demonstrated an aerosol assisted flow route to the synthesis of B, N-codoped  $\text{TiO}_2$  photocatalysts with improved de- $\text{NO}_x$  activity under visible light irradiation [120]. Owing to the introduction of B and N into the  $\text{TiO}_2$  lattice with the formation of B–O–Ti and N–Ti–O bounds, a stable internal charge transfer between boron and nitrogen could reduce the photo-transition energy for  $\text{TiO}_2$  from the valence band to the conduction band, extending the photo-response to visible-light region. Meanwhile,  $\text{Ti}^{3+}$  ions could be generated through boron doping, with the formation of oxygen vacancies for trapping photogenerated electrons. Thus, the electron-hole separation efficiency could be well improved. Besides, it was also noted that hollow cavity could be produced for the as-obtained samples after doping boron, as shown in Fig. 5.8. Such hollow structure is favorable for supplying more reactive sites for photocatalytic reaction [63, 121, 122]. Because of the high visible-light response capability and hollow structures, the as-prepared hollow B, N-codoped  $\text{TiO}_2$  exhibited excellent photocatalytic performance for oxidizing NO.

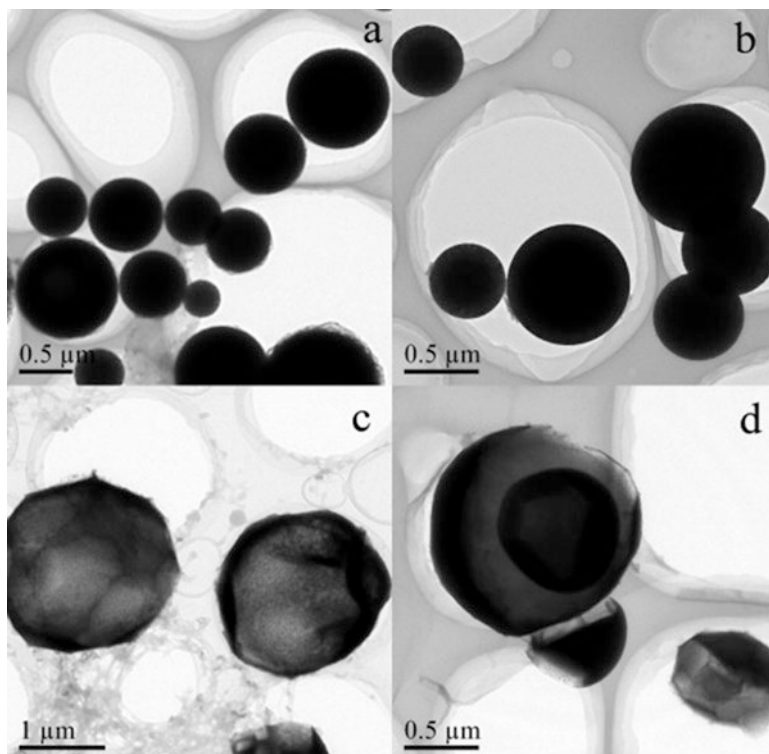


**Fig. 5.8** TEM images of the samples prepared by the aerosol-assisted flow synthetic method. (a) Pure  $\text{TiO}_2$ ; (b) N-doped  $\text{TiO}_2$ ; (c) B-doped  $\text{TiO}_2$ ; and (d) B, N-codoped  $\text{TiO}_2$ . Reprinted with permission from Ref. [120]. Copyright 2011 Elsevier

### 5.3.3 *Non-TiO<sub>2</sub>-Based Photocatalysts (Bismuth Based Photocatalysts)*

Physicochemical properties of photocatalysts play an important role for affecting the photocatalytic performances. Though  $\text{TiO}_2$ -based photocatalysts have been proved the most widely used candidates, their applications were still limited by its narrow spectral response range. Based on modification, both of visible-light capability and activity were proved, nevertheless, modifying  $\text{TiO}_2$  still suffers some shortcomings, such as low quantum efficiency, weakened reduction/oxidation capability of the conduction or valence band, and so on. It is highly required to seek other non- $\text{TiO}_2$  photocatalysts with stable crystal structure and superior electronic or photonic properties, allowing the super strong photocatalytic activities for treating  $\text{NO}_x$ . From the viewpoint of the electronic band structure of semiconductors, the valence band (VB) of bismuth-based composite oxides is composed of O 2p orbital, as well as the orbital hybridization of Bi 6s and O 2p. Such strong interaction

between Bi 6s and O 2p orbitals reduces its symmetry, resulting in the relevant dipole formation. These dipoles could narrow the band gaps, allowing a wide visible light response region. Meanwhile, the position of the valence band could be improved, thereby enhancing the oxidation capability and the mobility rate of the photogenerated holes. It should be also pointed out that Bi-based composite oxides always exist in a unique layered structure with a “two-dimensional” photocatalytic effect, allowing fast separation of the photo-induced electron and holes and better polarization of the related atoms during the photocatalytic process [123–125]. Besides, the halogen ions located between the layers of BiOX (X=Cl, Br, I) were easily to be substituted by other hybrid atoms. This could make it possible to alter the electro/photonic properties of the BiOX via doing routes. For these reasons, lots of bismuth-based photocatalysts have been reported, so far, for explore their photocatalytic applications.

### 5.3.3.1 BiOX (X=Cl, Br, I)

Zhang et al. compared the de-NO<sub>x</sub> activity of BiOCl, BiOBr, and BiOI 2D nano-plates. They found that BiOCl and BiOBr exhibited more remarkable activity than that of BiOI [126]. Among them, BiOBr showed the best performance in NO oxidation, attributing to the ultrathin nano-plates, layered structures, high surface area, and suitable band structure. Ai et al. reported a non-aqueous sol–gel approach to synthesize hierarchical BiOBr nano-plate microspheres with highly activity for indoor NO<sub>x</sub> removal with the aid of ethylene glycol and CTAB as the precursors [127]. As shown in Fig. 5.9, the as-prepared microspheres catalysts (average size of ca. 2–5 μm) were self-assembled with lots of interwoven nano-plates. Under UV–Visible light irradiation, the as-formed BiOBr microspheres exhibited a 45 % NO removal rate in 10 min, whereas the degradation of NO on bulk BiOBr reached merely 13 %. Moreover, the microsphere sample also showed an enhanced photocatalytic performance under visible light ( $\lambda > 420$  nm) irradiation. Compared to the bulk BiOBr, the high photocatalytic activity of the BiOBr microspheres was

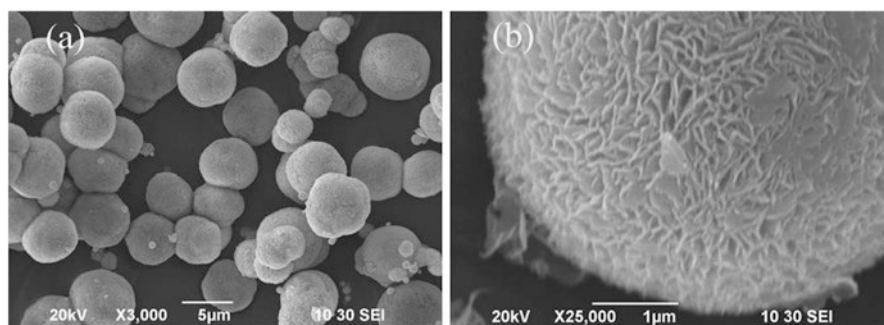


**Fig. 5.9** SEM images at low magnification (a) and high magnification (b) of BiOBr microspheres. Reprinted with permission from Ref. [127]. Copyright 2009 American Chemical Society

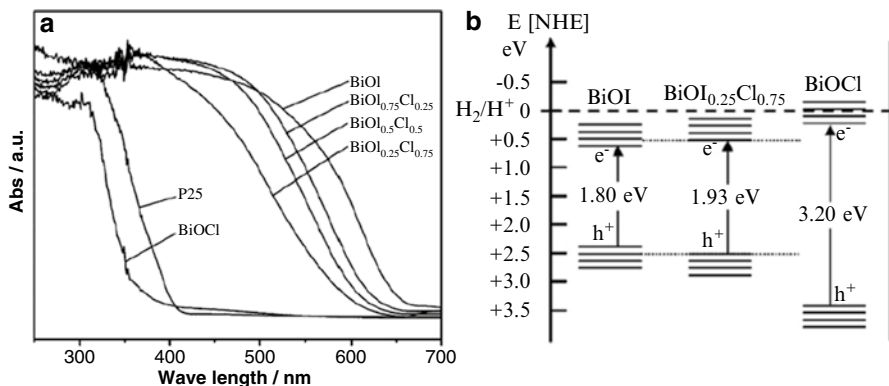


**Fig. 5.10** (a) UV-Vis DRS of as-prepared BiOI/BiOCl samples and (b) Schematic illustration of the band gap structures of BiOCl,  $\text{BiOI}_{0.75}\text{I}_{0.25}$ , and BiOI. Reprinted with permission from Ref. [129]. Copyright 2012 Elsevier

attributed to the hierarchical structure with a high surface area, allowing the diffusion of intermediates. The same group also loaded nano-sized BiOBr onto the surface of graphene sheets for enhancing the rates of charge transportation and separations via the strong chemical bonding between BiOBr and graphene, thus the visible light driven de- $\text{NO}_x$  activity was greatly improved [128].

Dong et al. prepared porous BiOCl/BiOI composite of nano-plates and micro-flowers hybrids under room temperature [129]. Figure 5.10a indicated that pure BiOCl can only absorb UV light with an absorption edge at 370 nm, and pure BiOI has a strong light absorbance in visible light region with an absorption edge at 670 nm. The absorption edge of the BiOCl/BiOI composites shifted monotonically to longer wavelengths upon introducing I to the BiOCl crystals. Therefore, the band gap of BiOCl was narrowed from 3.20 to 1.93 eV (for sample  $\text{BiOI}_{0.25}\text{Cl}_{0.75}$ ) via loading BiOI, as shown in Fig. 5.10b. Owing to the suitable band structures and large surface areas, such hierarchical BiOCl/BiOI hybrids exhibited enhanced visible-light driven activity in removal of NO in air, exceeding that of P25 and other Bi-based catalysts.

As known, among the BiOX ( $X=\text{Cl}, \text{Br}, \text{I}$ ) photocatalysts, BiOCl can only absorb UV light because of the band gap limitation. Thus, lots of studies were focused on doping hybrid atoms or coupling with other low band-gap semiconductors for BiOCl. However, these could bring derived disadvantages, such as inhibiting the charge or breaking down the lattice symmetry. Recently, Li et al. explored a strong photosensitized RhB-BiOCl system to treat  $\text{NO}_x$  and water pollution under visible-light irradiation under the help of the strong RhB self-sensitization effect on the {001} facets exposed BiOCl [130]. As shown in Fig. 5.11, {001} facets exposed BiOCl nanocrystals exhibited an enriched oxygen atom density, promoting the adsorption of cationic dye RhB and creating a rich oxygen vacancy state. Thus, the photogenerated electrons under visible light irradiation could migrate from the excited dye molecule to the conduction band of BiOCl, and further inject into the

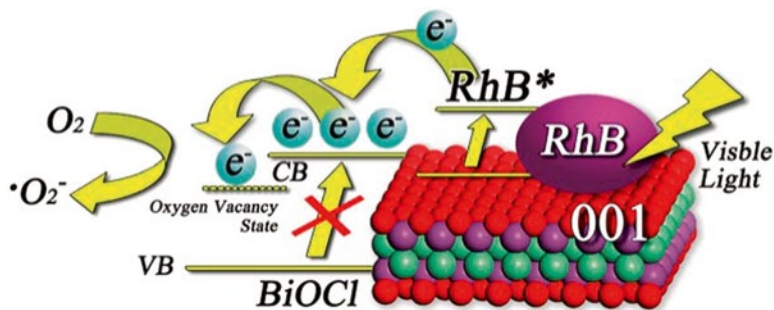
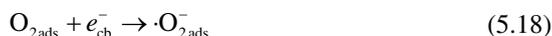


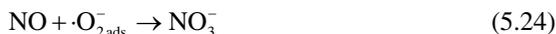
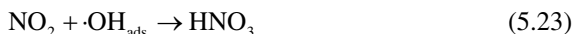
**Fig. 5.11** Possible mechanism of the RhB–BiOCl system. Reference [130]—Reproduced by permission of The Royal Society of Chemistry

oxygen vacancy state to produce  $\cdot\text{OH}^-$  and  $\cdot\text{O}_2^-$  radicals for oxidizing  $\text{NO}_x$ . It was interesting that such RhB–BiOCl hybrid system could continuous work for treating 4-chlorophenol at basic conditions ( $\text{pH} > 10$ ) while keeping RhB nearly unchanged owing to the fast electron transfer from 4-CP anions to RhB radicals ( $\text{RhB}^+$ ) with the regeneration of RhB molecules.

### 5.3.3.2 $\text{Bi}_2\text{WO}_6$

Among the bismuth based photocatalysts,  $\text{Bi}_2\text{WO}_6$ , is the simplest member of the Aurivillius family of layered perovskites. For the band gap structure, the valence band of  $\text{Bi}_2\text{WO}_6$  is determined by the hybridized Bi 6s orbitals and O 2p orbitals, while the conduction band is formed of W5d orbitals. Owing to its suitable band gaps,  $\text{Bi}_2\text{WO}_6$  has been widely utilized as an efficient catalyst for both photocatalytic degradation of pollutants and energy production under visible-light irradiation [131–135]. Huang et al. reported a ultrasonic spray pyrolysis route to the synthesis of porous  $\text{Bi}_2\text{WO}_6$  microsphere for photocatalytic NO oxidation [136]. Compared with bulk  $\text{Bi}_2\text{WO}_6$ , the porous  $\text{Bi}_2\text{WO}_6$  calcined at 600 °C showed an obvious blue shift with a absorption edge of about 450 nm, thus the de- $\text{NO}_x$  performance was also improved. Li et al. analyzed the photocatalytic NO oxidation mechanism by using  $\text{Bi}_2\text{WO}_6$  as catalyst [137]. Different from that of  $\text{TiO}_2$ , the valence band hole could not oxidize water to  $\cdot\text{OH}$  radicals because of the much more negative potential of  $\text{Bi}^{\text{V}}/\text{Bi}^{\text{III}}$  ( $E = +1.59$  eV) than that of  $\cdot\text{OH}/\text{OH}^-$  ( $E = +1.99$  eV). As a result, the main active species to oxidize NO was the photogenerated hole itself. It might exist small amount of  $\cdot\text{OH}$  radicals produced by other routes. And the reaction mechanism is shown in the following formula:





Zhou et al. studied the role of graphene on the band structure and interfacial interaction of  $\text{Bi}_2\text{WO}_6/\text{graphene}$  composites [138]. Based on the Mott–Schottky measurements, they found that the chemical interaction between  $\text{Bi}_2\text{WO}_6$  and graphene can contribute to a 0.34 eV downshift in Fermi level, which means photo-generated electrons can transfer from  $\text{Bi}_2\text{WO}_6$  to graphene easily once they were in contact with each other. To further illustrating the mechanism of photocatalytic oxidation of NO, the electron spin resonance (ESR) spin-trap technique was measure to track the active species during reactions. Figure 5.12a exhibits similar ESR signals for  $\text{Bi}_2\text{WO}_6$  and  $\text{Bi}_2\text{WO}_6/\text{graphene}$  suggesting the ability to generate  $\cdot\text{O}_2^-$  radicals was not enhanced by composting graphene. Figure 5.12b reveals that there is no typical signal with the characteristic intensity of 1:2:2:1 were observed for either sample which indicates that the  $\cdot\text{OH}$  could not be the dominant active species during the de- $\text{NO}_x$  reaction.

### 5.3.3.3 $\text{BiVO}_4$

Bismuth vanadate ( $\text{BiVO}_4$ ) is also an important multi-bismuth oxide with three main phase structures of tetragonal zircon, tetragonal scheelite, and monoclinic scheelite. Owing to the close relationship between phase structure and the photocatalytic

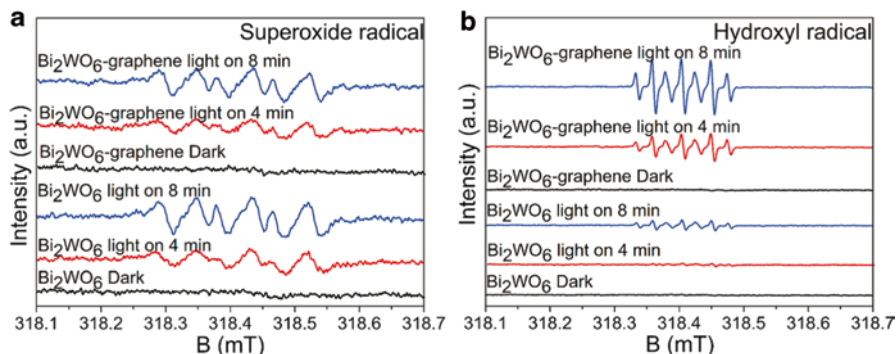


**Fig. 5.12** DMPO spin-trapping ESR spectra of  $\text{Bi}_2\text{WO}_6$  and  $\text{Bi}_2\text{WO}_6/\text{graphene}$  in methanol dispersion for  $\text{DMPO}\cdot\text{O}_2^-$  (a) and aqueous dispersion for  $\text{DMPO}\cdot\text{OH}\cdot$  (b). Reference [138]-Reproduced by permission of The Royal Society of Chemistry

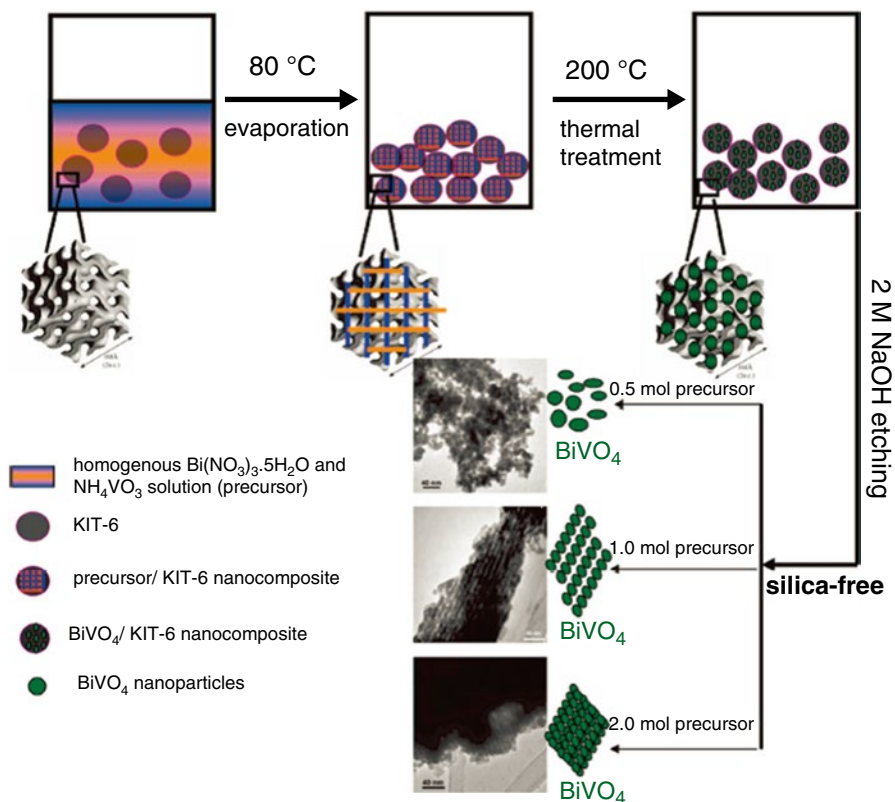


**Fig. 5.13** Proposed process for fabrication of mesoporous BiVO<sub>4</sub>. Reprinted with permission from Ref. [139]. Copyright 2008 American Chemical Society

activity of BiVO<sub>4</sub>, the monoclinic scheelite with a narrowing band gap of 2.4 eV shows a significantly higher visible light activity than the other two phases. Li et al. reported the ordered mesoporous BiVO<sub>4</sub> crystals obtained by a nanocasting route via choosing silica (KIT-6) as a template [139]. As shown in Fig. 5.13, the precursor is introduced into the silica (KIT-6) pores during the evaporation process to form a precursor/KIT-6 nanocomposite. BiVO<sub>4</sub> was crystallized inside the silica template to form an ordered *Ia3d* structure under heat treatment at 200 °C. Mesoporous BiVO<sub>4</sub> with large surface could be produced after removing silica by NaOH aqueous solution. The as-prepared mesoporous BiVO<sub>4</sub> exhibited a 3.5 times NO removal rate than the conventional BiVO<sub>4</sub> and a stable photoreaction cycling performance under visible-light irradiation. Ai et al. reported two morphologies of hierarchical BiVO<sub>4</sub> three-dimensional superstructures by a template-free hydrothermal process using ethylene glycol as solvent [140]. By adjusting the reaction time, microboats and microspheres BiVO<sub>4</sub> with excellent photocatalytic removal rate of NO<sub>x</sub> were obtained owing to their high visible-light adsorption capability, more electron-holes generated inside the crystal, and fast electron-migration to the surface of BiVO<sub>4</sub> crystals.

## 5.4 Summary and Future Outlooks

This chapter briefly reviews the latest development of the photocatalytic technology for treating  $\text{NO}_x$  via designing and fabricating novel photocatalytic semiconductor nanomaterials. Despite the tremendous efforts carried out to improve the de- $\text{NO}_x$  activity, many problems still challenge the researchers. Especially, few improvements have been achieved in the case of the photocatalytic reduction of  $\text{NO}_x$ . As known, the photocatalytic reduction of  $\text{NO}_x$  could be the only one accepted green technology for de- $\text{NO}_x$ , because its final product  $\text{N}_2$  is friendly to humans. Besides, there is still a long way to go for photocatalytic oxidation of NO oxidation to be applied in industries. Nevertheless, we still believe that the above issues could be resolved by further exploration of the design and fabrication of novel photocatalysts or reactors in relation to the oxidation/reduction of  $\text{NO}_x$ .

**Acknowledgements** This work was supported by the National Natural Science Foundation of China (NSFC 21477079, 21207090, 21237003, 21261140333), PCSIRT (IRT1269), Shanghai Government (14JC1402500, 11SG42, 15QA1403300h), the Doctoral Program of Higher Education (20123127120009), and Shanghai Normal University (DXL122 and S30406).

## References

1. Gaya UI, Abdullah AH (2008) Heterogeneous photocatalytic degradation of organic contaminants over titanium dioxide: a review of fundamentals, progress and problems. *J Photochem Photobio C* 9(1):1–12
2. Busca G, Berardinelli S, Resini C et al (2008) Technologies for the removal of phenol from fluid streams: a short review of recent developments. *J Hazard Mater* 160(2–3):265–288
3. Lee H, Choi W (2002) Photocatalytic oxidation of arsenite in  $\text{TiO}_2$  suspension: kinetics and mechanisms. *Environ Sci Technol* 36(17):3872–3878
4. Dalton JS, Janes PA, Jones NG et al (2002) Photocatalytic oxidation of  $\text{NO}_x$  gases using  $\text{TiO}_2$ : a surface spectroscopic approach. *Environ Pollut* 120(2):415–422
5. Lasek J, Yu Y-H, Wu JCS (2013) Removal of  $\text{NO}_x$  by photocatalytic processes. *J Photochem Photobio C* 14:29–52
6. Hoek G, Krishnan RM, Beelen R et al (2013) Long-term air pollution exposure and cardio-respiratory mortality: a review. *Environ Health* 12(1):43
7. Wang S, Hao J (2012) Air quality management in China: issues, challenges, and options. *J Environ Sci* 24(1):2–13
8. Yang QW, Li PF, Ren BN et al (2013) Study on the mechanism of SCR NO by Mn-Ce/CNTs catalyst at low-temperature. *Adv Mater Res* 773:645–648
9. Schmieg SJ, Oh SH, Kim CH et al (2012) Thermal durability of Cu-CHA  $\text{NH}_3$ -SCR catalysts for diesel NO<sub>x</sub> reduction. *Catal Today* 184(1):252–261
10. Colombo M, Nova I, Tronconi E (2012) Detailed kinetic modeling of the  $\text{NH}_3$ -NO/ $\text{NO}_2$  SCR reactions over a commercial Cu-zeolite catalyst for diesel exhausts after treatment. *Catal Today* 197(1):243–255
11. Møller J, Munk B, Crillessen K et al (2011) Life cycle assessment of selective non-catalytic reduction (SNCR) of nitrous oxides in a full-scale municipal solid waste incinerator. *Waste Manage (Oxford)* 31(6):1184–1193
12. Fan W, Zhu T, Sun Y et al (2014) Effects of gas compositions on  $\text{NO}_x$  reduction by selective non-catalytic reduction with ammonia in a simulated cement precalciner atmosphere. *Chemosphere* 113:182–187

13. Farcy B, Abou-Taouk A, Vervisch L et al (2014) Two approaches of chemistry downsizing for simulating selective non catalytic reduction DeNO<sub>x</sub> process. *Fuel* 118:291–299
14. S-I F, Song Q, Tang J-S et al (2014) Effect of CaO on the selective non-catalytic reduction deNO<sub>x</sub> process: experimental and kinetic study. *Chem Eng J* 249:252–259
15. Sano T, Tsutsui S, Koike K et al (2013) Activation of graphitic carbon nitride (gC<sub>3</sub>N<sub>4</sub>) by alkaline hydrothermal treatment for photocatalytic NO oxidation in gas phase. *J Mater Chem A* 1(21):6489–6496
16. Bianchi CL, Pirola C, Selli E et al (2012) Photocatalytic NO<sub>x</sub> abatement: the role of the material supporting the TiO<sub>2</sub> active layer. *J Hazard Mater* 211:203–207
17. Mitsionis A, Vaimakis T, Trapalis C et al (2011) Hydroxyapatite/titanium dioxide nanocomposites for controlled photocatalytic NO oxidation. *Appl Catal B* 106(3):398–404
18. Zhu W, Liu P, Xiao S et al (2015) Microwave-assisted synthesis of Ag-doped MOFs-like organotitanium polymer with high activity in visible-light driven photocatalytic NO oxidization. *Appl Catal B* 172:46–51
19. Yu YH, Pan YT, Wu YT et al (2011) Photocatalytic NO reduction with C<sub>3</sub>H<sub>8</sub> using a monolith photoreactor. *Catal Today* 174(1):141–147
20. Price C, Rind D (1994) Possible implications of global climate change on global lightning distributions and frequencies. *J Geophys Res* 99(D5):10823–10831, 1984–2012
21. Delmas R, Serça D, Jambert C (1997) Global inventory of NO<sub>x</sub> sources. *Nutr cycl agroecosys* 48(1–2):51–60
22. Benkovitz CM, Scholtz MT, Pacyna J et al (1996) Global gridded inventories of anthropogenic emissions of sulfur and nitrogen. *J Geophys Res* 101(D22):29239–29253, 1984–2012
23. Olivier J, Bouwman A, Van der Hoek K et al (1998) Global air emission inventories for anthropogenic sources of NO<sub>x</sub>, NH<sub>3</sub> and N<sub>2</sub>O in 1990. *Environ Pollut* 102(1):135–148
24. Lamsal L, Martin R, Padmanabhan A et al (2011) Application of satellite observations for timely updates to global anthropogenic NO<sub>x</sub> emission inventories. *Geophys Res Lett* 38(5)
25. Sadanaga Y, Matsumoto J, Kajii Y (2003) Photochemical reactions in the urban air: recent understandings of radical chemistry. *J Photochem Photobiol C* 4(1):85–104
26. Chen B, Hong C, Kan H (2004) Exposures and health outcomes from outdoor air pollutants in China. *Toxicology* 198(1):291–300
27. Normann F, Andersson K, Leckner B et al (2009) Emission control of nitrogen oxides in the oxy-fuel process. *Prog Energ Combust Sci* 35(5):385–397
28. Fang HL, DaCosta HF (2003) Urea thermolysis and NO<sub>x</sub> reduction with and without SCR catalysts. *Appl Catal B* 46(1):17–34
29. Kang M, Park ED, Kim JM et al (2007) Manganese oxide catalysts for NO<sub>x</sub> reduction with NH<sub>3</sub> at low temperatures. *Appl Catal A* 327(2):261–269
30. Wu Z, Jin R, Liu Y et al (2008) Ceria modified MnO<sub>x</sub>/TiO<sub>2</sub> as a superior catalyst for NO reduction with NH<sub>3</sub> at low-temperature. *Catal Commun* 9(13):2217–2220
31. Grossale A, Nova I, Tronconi E et al (2008) The chemistry of the NO/NO<sub>2</sub>–NH<sub>3</sub> “fast” SCR reaction over Fe-ZSM5 investigated by transient reaction analysis. *J Catal* 256(2):312–322
32. Roy S, Hegde MS, Madras G (2009) Catalysis for NO<sub>x</sub> abatement. *Appl Energy* 86(11):2283–2297
33. Schneider H, Scharf U, Wokaun A et al (1994) Chromia on titania: IV. Nature of active sites for selective catalytic reduction of NO by NH<sub>3</sub>. *J Catal* 146(2):545–556
34. Kwak JH, Tran D, Szanyi J et al (2012) The effect of copper loading on the selective catalytic reduction of nitric oxide by ammonia over Cu-SSZ-13. *Catal Lett* 142(3):295–301
35. Xue J, Wang X, Qi G et al (2013) Characterization of copper species over Cu/SAPO-34 in selective catalytic reduction of NO<sub>x</sub> with ammonia: relationships between active Cu sites and de-NO<sub>x</sub> performance at low temperature. *J Catal* 297:56–64
36. Hamill C, Burch R, Goguet A et al (2014) Evaluation and mechanistic investigation of a AuPd alloy catalyst for the hydrocarbon selective catalytic reduction (HC-SCR) of NO<sub>x</sub>. *Appl Catal B* 147:864–870
37. Shen B, Ma H, Yao Y (2012) Mn-CeO<sub>x</sub>/Ti-PILCs for selective catalytic reduction of NO with NH<sub>3</sub> at low temperature. *J Environ Sci* 24(3):499–506

38. Lu Z, Jiang L, Dai Q et al (2012) Low temperature selective catalytic reduction of NO in flue gas by V<sub>2</sub>O<sub>5</sub>/ACF. *Environ Sci Technol* 10:12
39. Li P, Liu Z, Li Q et al (2014) Multiple roles of SO<sub>2</sub> in selective catalytic reduction of NO by NH<sub>3</sub> over V<sub>2</sub>O<sub>5</sub>/AC catalyst. *Ind Eng Chem Res* 53(19):7910–7916
40. Chen L, Li J, Ge M (2009) Promotional effect of Ce-doped V<sub>2</sub>O<sub>5</sub>-WO<sub>3</sub>/TiO<sub>2</sub> with low vanadium loadings for selective catalytic reduction of NO<sub>x</sub> by NH<sub>3</sub>. *J Phys Chem C* 113(50):21177–21184
41. Kwak JH, Tonkyn RG, Kim DH et al (2010) Excellent activity and selectivity of Cu-SSZ-13 in the selective catalytic reduction of NO<sub>x</sub> with NH<sub>3</sub>. *J Catal* 275(2):187–190
42. Liu F, He H, Ding Y et al (2009) Effect of manganese substitution on the structure and activity of iron titanate catalyst for the selective catalytic reduction of NO with NH<sub>3</sub>. *Appl Catal B* 93(1–2):194–204
43. Devadas M, Kröcher O, Elsener M et al (2006) Influence of NO<sub>2</sub> on the selective catalytic reduction of NO with ammonia over Fe-ZSM5. *Appl Catal B* 67(3–4):187–196
44. Sjövall H, Olsson L, Fridell E et al (2006) Selective catalytic reduction of NO<sub>x</sub> with NH<sub>3</sub> over Cu-ZSM-5 – the effect of changing the gas composition. *Appl Catal B* 64(3–4):180–188
45. Tayyeb Javed M, Irfan N, Gibbs BM (2007) Control of combustion-generated nitrogen oxides by selective non-catalytic reduction. *J Environ Manag* 83(3):251–289
46. Mahmoudi S, Baeyens J, Seville JPK (2010) NO<sub>x</sub> formation and selective non-catalytic reduction (SNCR) in a fluidized bed combustor of biomass. *Biomass Bioenerg* 34(9):1393–1409
47. Lee GW, Shon BH, Yoo JG et al (2008) The influence of mixing between NH<sub>3</sub> and NO for a De-NO<sub>x</sub> reaction in the SNCR process. *J Ind Eng Chem* 14(4):457–467
48. Cant NW, Cole JR (1992) Photocatalysis of the reaction between ammonia and nitric oxide on TiO<sub>2</sub> surfaces. *J Catal* 134(1):317–330
49. Sano T, Negishi N, Mas D et al (2000) Photocatalytic decomposition of N<sub>2</sub>O on highly dispersed Ag<sup>+</sup> ions on TiO<sub>2</sub> prepared by photodeposition. *J Catal* 194(1):71–79
50. Hu Y, Martra G, Zhang J et al (2006) Characterization of the local structures of Ti-MCM-41 and their photocatalytic reactivity for the decomposition of NO into N<sub>2</sub> and O<sub>2</sub>. *J Phys Chem B* 110(4):1680–1685
51. Anpo M, Zhang SG, Mishima H et al (1997) Design of photocatalysts encapsulated within the zeolite framework and cavities for the decomposition of NO into N<sub>2</sub> and O<sub>2</sub> at normal temperature. *Catal Today* 39(3):159–168
52. Wu Q, van de Krol R (2012) Selective photoreduction of nitric oxide to nitrogen by nanostructured TiO<sub>2</sub> photocatalysts: role of oxygen vacancies and iron dopant. *J Am Chem Soc* 134(22):9369–9375
53. Huang KC, Chien SH (2013) Improved visible-light-driven photocatalytic activity of rutile/titania-nanotube composites prepared by microwave-assisted hydrothermal process. *Appl Catal B* 140–141:283–288
54. Fujishima A, Honda K (1972) Electrochemical photolysis of water at a semiconductor electrode. *Nature* 238(5358):37–38
55. Dambournet D, Belharouak I, Amine K (2009) Tailored preparation methods of TiO<sub>2</sub> anatase, rutile, brookite: mechanism of formation and electrochemical properties. *Chem Mater* 22(3):1173–1179
56. Zhang J, Ayusawa T, Minagawa M et al (2001) Investigations of TiO<sub>2</sub> photocatalysts for the decomposition of NO in the flow system: the role of pretreatment and reaction conditions in the photocatalytic efficiency. *J Catal* 198(1):1–8
57. Ohko Y, Nakamura Y, Negishi N et al (2009) Photocatalytic oxidation of nitrogen monoxide using TiO<sub>2</sub> thin films under continuous UV light illumination. *J Photochem Photobio A* 205(1):28–33
58. Matsuda S, Hatano H, Tsutsumi A (2001) Ultrafine particle fluidization and its application to photocatalytic NO<sub>x</sub> treatment. *Chem Eng J* 82(1–3):183–188
59. Yang HG, Sun CH, Qiao SZ et al (2008) Anatase TiO<sub>2</sub> single crystals with a large percentage of reactive facets. *Nature* 453(7195):638–641

60. Wu B, Guo C, Zheng N et al (2008) Nonaqueous production of nanostructured anatase with high-energy facets. *J Am Chem Soc* 130(51):17563–17567
61. Yang HG, Liu G, Qiao SZ et al (2009) Solvothermal synthesis and photoreactivity of anatase TiO<sub>2</sub> nanosheets with dominant {001} facets. *J Am Chem Soc* 131(11):4078–4083
62. Yu J, Xiang Q, Ran J et al (2010) One-step hydrothermal fabrication and photocatalytic activity of surface-fluorinated TiO<sub>2</sub> hollow microspheres and tabular anatase single microcrystals with high-energy facets. *CrystEngComm* 12(3):872–879
63. Liu S, Yu J, Jaroniec M (2010) Tunable photocatalytic selectivity of hollow TiO<sub>2</sub> microspheres composed of anatase polyhedra with exposed {001} facets. *J Am Chem Soc* 132(34):11914–11916
64. Xi G, Ye J (2010) Synthesis of bismuth vanadate nanoplates with exposed {001} facets and enhanced visible-light photocatalytic properties. *Chem Commun* 46(11):1893–1895
65. Hengerer R, Kavan L, Krtil P et al (2000) Orientation dependence of charge-transfer processes on TiO<sub>2</sub> (anatase) single crystals. *J Electrochem Soc* 147(4):1467–1472
66. Kamei M, Mitsunashi T (2000) Hydrophobic drawings on hydrophilic surfaces of single crystalline titanium dioxide: surface wettability control by mechanochemical treatment. *Surf Sci* 463(1):L609–L612
67. Vittadini A, Selloni A, Rotzinger F et al (1998) Structure and energetics of water adsorbed at TiO<sub>2</sub> anatase (101) and (001) surfaces. *Phys Rev Lett* 81(14):2954
68. Yang W, Li J, Wang Y et al (2011) A facile synthesis of anatase TiO<sub>2</sub> nanosheets-based hierarchical spheres with over 90%{001} facets for dye-sensitized solar cells. *Chem Commun* 47(6):1809–1811
69. Liu G, Sun C, Yang HG et al (2010) Nanosized anatase TiO<sub>2</sub> single crystals for enhanced photocatalytic activity. *Chem Commun* 46(5):755–757
70. Selloni A (2008) Crystal growth: anatase shows its reactive side. *Nat Mater* 7(8):613–615
71. Zhao W, Tian FH, Wang X et al (2014) Removal of nitric oxide by the highly reactive anatase TiO<sub>2</sub> (001) surface: a density functional theory study. *J Colloid Interface Sci* 430:18–23
72. Sofianou MV, Trapalis C, Psycharis V et al (2012) Study of TiO<sub>2</sub> anatase nano and microstructures with dominant {001} facets for NO oxidation. *Environ Sci Pollut Res* 19(9):3719–3726
73. Zhang D, Li G, Wang H et al (2010) Biocompatible anatase single-crystal photocatalysts with tunable percentage of reactive facets. *Cryst Growth Des* 10(3):1130–1137
74. Zhang D, Li G, Yang X et al (2009) A micrometer-size TiO<sub>2</sub> single-crystal photocatalyst with remarkable 80% level of reactive facets. *Chem Commun* 29:4381–4383
75. Wen M, Liu P, Xiao S et al (2015) Uniform anatase single-crystal cubes with high thermal stability fully enclosed by active {010} and {001} facets. *RSC Adv* 5(15):11029–11035
76. Zhang D, Li G, Wang F et al (2010) Green synthesis of a self-assembled rutile mesocrystalline photocatalyst. *CrystEngComm* 12(6):1759–1763
77. Chen X, Mao SS (2007) Titanium dioxide nanomaterials: synthesis, properties, modifications, and applications. *Chem Rev* 107(7):2891–2959
78. Chen X, Shen S, Guo L et al (2010) Semiconductor-based photocatalytic hydrogen generation. *Chem Rev* 110(11):6503–6570
79. Shankar K, Basham JI, Allam NK et al (2009) Recent advances in the use of TiO<sub>2</sub> nanotube and nanowire arrays for oxidative photoelectrochemistry. *J Phys Chem C* 113(16):6327–6359
80. Chen D, Huang F, Cheng YB et al (2009) Mesoporous anatase TiO<sub>2</sub> beads with high surface areas and controllable pore sizes: a superior candidate for high-performance dye-sensitized solar cells. *Adv Mater* 21(21):2206–2210
81. Yu J, Xiang Q, Zhou M (2009) Preparation, characterization and visible-light-driven photocatalytic activity of Fe-doped titania nanorods and first-principles study for electronic structures. *Appl Catal B* 90(3):595–602
82. Yang Y, Wang H, Li X et al (2009) Electrospun mesoporous W<sup>6+</sup>-doped TiO<sub>2</sub> thin films for efficient visible-light photocatalysis. *Mater Lett* 63(2):331–333
83. Tian B, Li C, Gu F et al (2009) Flame sprayed V-doped TiO<sub>2</sub> nanoparticles with enhanced photocatalytic activity under visible light irradiation. *Chem Eng J* 151(1):220–227

84. Tian BZ, Li CZ, Gu F et al (2009) Visible-light photocatalytic activity of Cr-doped TiO<sub>2</sub> nanoparticles synthesized by flame spray pyrolysis. *J Inorg Mater* 24:661–665
85. Lorret O, Francová D, Waldner G et al (2009) W-doped titania nanoparticles for UV and visible-light photocatalytic reactions. *Appl Catal B* 91(1):39–46
86. Li J, Xu J, Dai WL et al (2009) Direct hydro-alcohol thermal synthesis of special core–shell structured Fe-doped titania microspheres with extended visible light response and enhanced photoactivity. *Appl Catal B* 85(3):162–170
87. Lee H, Shin M, Lee M et al (2015) Photo-oxidation activities on Pd-doped TiO<sub>2</sub> nanoparticles: critical PdO formation effect. *Appl Catal B* 165:20–26
88. Wang W, Ye Y, Feng J et al (2015) Enhanced photoreversible color switching of redox dyes catalyzed by barium-doped TiO<sub>2</sub> nanocrystals. *Angew Chem Int Ed* 54(4):1321–1326
89. Ishibai Y, Sato J, Akita S et al (2007) Photocatalytic oxidation of NO<sub>x</sub> by Pt-modified TiO<sub>2</sub> under visible light irradiation. *J Photochem Photobio A* 188(1):106–111
90. Huang C-H, Wang IK, Lin Y-M et al (2010) Visible light photocatalytic degradation of nitric oxides on PtOx-modified TiO<sub>2</sub> via sol–gel and impregnation method. *J Mol Catal A Chem* 316(1–2):163–170
91. Hashimoto K, Sumida K, Kitano S et al (2009) Photo-oxidation of nitrogen oxide over titanium(IV) oxide modified with platinum or rhodium chlorides under irradiation of visible light or UV light. *Catal Today* 144(1–2):37–41
92. Wu Z, Sheng Z, Wang H et al (2009) Relationship between Pd oxidation states on TiO<sub>2</sub> and the photocatalytic oxidation behaviors of nitric oxide. *Chemosphere* 77(2):264–268
93. Sheng Z, Wu Z, Liu Y et al (2008) Gas-phase photocatalytic oxidation of NO over palladium modified TiO<sub>2</sub> catalysts. *Catal Commun* 9(9):1941–1944
94. Fang C, Jia H, Chang S et al (2014) (Gold core)/(titania shell) nanostructures for plasmon-enhanced photon harvesting and generation of reactive oxygen species. *Energ Environ Sci* 7(10):3431–3438
95. Wu L, Li F, Xu Y et al (2015) Plasmon-induced photoelectrocatalytic activity of Au nanoparticles enhanced TiO<sub>2</sub> nanotube arrays electrodes for environmental remediation. *Appl Catal B* 164:217–224
96. Seh ZW, Liu S, Low M et al (2012) Janus Au–TiO<sub>2</sub> photocatalysts with strong localization of plasmonic near-fields for efficient visible-light hydrogen generation. *Adv Mater* 24(17):2310–2314
97. Zhang D, Wen M, Zhang S et al (2014) Au nanoparticles enhanced rutile TiO<sub>2</sub> nanorod bundles with high visible-light photocatalytic performance for NO oxidation. *Appl Catal B* 147:610–616
98. Ieperuma OA, Tennakone K, Dissanayake WDDP (1990) Photocatalytic behaviour of metal doped titanium dioxide: studies on the photochemical synthesis of ammonia on Mg/TiO<sub>2</sub> catalyst systems. *Appl Catal* 62(1):L1–L5
99. Liu B, Chen HM, Liu C et al (2013) Large-scale synthesis of transition-metal-doped TiO<sub>2</sub> nanowires with controllable overpotential. *J Am Chem Soc* 135(27):9995–9998
100. Sofianou M-V, Tassi M, Boukos N et al (2014) Solvothermal synthesis and photocatalytic performance of Mg<sup>2+</sup>-doped anatase nanocrystals with exposed {001} facets. *Catal Today* 230:125–130
101. Sofianou MV, Tassi M, Psycharis V et al (2015) Solvothermal synthesis and photocatalytic performance of Mn<sup>4+</sup>-doped anatase nanoplates with exposed {001} facets. *Appl Catal B* 162:27–33
102. Xu J, Ao Y, Chen M (2009) Preparation of B-doped titania hollow sphere and its photocatalytic activity under visible light. *Mater Lett* 63(28):2442–2444
103. Park Y, Kim W, Park H et al (2009) Carbon-doped TiO<sub>2</sub> photocatalyst synthesized without using an external carbon precursor and the visible light activity. *Appl Catal B* 91(1):355–361
104. Tafen DN, Wang J, Wu N et al (2009) Visible light photocatalytic activity in nitrogen-doped TiO<sub>2</sub> nanobelts. *Appl Phys Lett* 94(9):093101–093101–093103
105. Lv Y, Yu L, Huang H et al (2009) Preparation of F-doped titania nanoparticles with a highly thermally stable anatase phase by alcoholysis of TiCl<sub>4</sub>. *Appl Surf Sci* 255(23):9548–9552

106. Xiang Q, Yu J, Wang W et al (2011) Nitrogen self-doped nanosized TiO<sub>2</sub> sheets with exposed {001} facets for enhanced visible-light photocatalytic activity. *Chem Commun* 47(24):6906–6908
107. Zhang Q, Lima DQ, Lee I et al (2011) A highly active titanium dioxide based visible-light photocatalyst with nonmetal doping and plasmonic metal decoration. *Angew Chem Int Ed* 50(31):7088–7092
108. Han C, Pelaez M, Likodimos V et al (2011) Innovative visible light-activated sulfur doped TiO<sub>2</sub> films for water treatment. *Appl Catal B* 107(1–2):77–87
109. Xiong Z, Zhao XS (2012) Nitrogen-doped titanate-anatase core–shell nanobelts with exposed {101} anatase facets and enhanced visible light photocatalytic activity. *J Am Chem Soc* 134(13):5754–5757
110. Wang DH, Jia L, Wu XL et al (2012) One-step hydrothermal synthesis of N-doped TiO<sub>2</sub>/C nanocomposites with high visible light photocatalytic activity. *Nanoscale* 4(2):576–584
111. Feng N, Zheng A, Wang Q et al (2011) Boron environments in B-doped and (B, N)-codoped TiO<sub>2</sub> photocatalysts: a combined solid-state NMR and theoretical calculation study. *J Phys Chem C* 115(6):2709–2719
112. Varley JB, Janotti A, Van de Walle CG (2011) Mechanism of visible-light photocatalysis in nitrogen-doped TiO<sub>2</sub>. *Adv Mater* 23(20):2343–2347
113. Devi LG, Kavitha R (2013) A review on non metal ion doped titania for the photocatalytic degradation of organic pollutants under UV/solar light: role of photogenerated charge carrier dynamics in enhancing the activity. *Appl Catal B* 140–141:559–587
114. Yang C, Wang Z, Lin T et al (2013) Core-shell nanostructured “black” rutile titania as excellent catalyst for hydrogen production enhanced by sulfur doping. *J Am Chem Soc* 135(47):17831–17838
115. Zhang YC, Yang M, Zhang G et al (2013) HNO<sub>3</sub>-involved one-step low temperature solvothermal synthesis of N-doped TiO<sub>2</sub> nanocrystals for efficient photocatalytic reduction of Cr(VI) in water. *Appl Catal B* 142–143:249–258
116. Yin S, Aita Y, Komatsu M et al (2005) Synthesis of excellent visible-light responsive TiO<sub>2</sub> – N photocatalyst by a homogeneous precipitation-solvothermal process. *J Mater Chem* 15(6):674–682
117. Yin S, Liu B, Zhang P et al (2008) Photocatalytic oxidation of NO<sub>x</sub> under visible LED light irradiation over nitrogen-doped titania particles with iron or platinum loading. *J Phys Chem C* 112(32):12425–12431
118. Huang Y, Ho W, Lee S et al (2008) Effect of carbon doping on the mesoporous structure of nanocrystalline titanium dioxide and its solar-light-driven photocatalytic degradation of NO<sub>x</sub>. *Langmuir* 24(7):3510–3516
119. Yao-Hsuan T, Chien-Sheng K, Chia-Hung H et al (2006) Visible-light-responsive nano-TiO<sub>2</sub> with mixed crystal lattice and its photocatalytic activity. *Nanotechnology* 17(10):2490
120. Ding X, Song X, Li P et al (2011) Efficient visible light driven photocatalytic removal of NO with aerosol flow synthesized B, N-codoped TiO<sub>2</sub> hollow spheres. *J Hazard Mater* 190(1–3):604–612
121. Yu J, Yu X (2008) Hydrothermal synthesis and photocatalytic activity of zinc oxide hollow spheres. *Environ Sci Technol* 42(13):4902–4907
122. Pan JH, Zhang X, Du AJ et al (2008) Self-etching reconstruction of hierarchically mesoporous F-TiO<sub>2</sub> hollow microspherical photocatalyst for concurrent membrane water purifications. *J Am Chem Soc* 130(34):11256–11257
123. Zhang KL, Liu CM, Huang FQ et al (2006) Study of the electronic structure and photocatalytic activity of the BiOCl photocatalyst. *Appl Catal B* 68(3–4):125–129
124. Lin X, Huang T, Huang F et al (2006) Photocatalytic activity of a bi-based oxychloride Bi<sub>3</sub>O<sub>4</sub>Cl. *J Phys Chem B* 110(48):24629–24634
125. Cheng H, Huang B, Yang K et al (2010) Facile template-free synthesis of Bi<sub>2</sub>O<sub>3</sub>CO<sub>3</sub> hierarchical microflowers and their associated photocatalytic activity. *ChemPhysChem* 11(10):2167–2173
126. Zhang W, Zhang Q, Dong F (2013) Visible-light photocatalytic removal of NO in air over BiOX (X=Cl, Br, I) single-crystal nanoplates prepared at room temperature. *Ind Eng Chem Res* 52(20):6740–6746

127. Ai Z, Ho W, Lee S et al (2009) Efficient photocatalytic removal of NO in indoor air with hierarchical bismuth oxybromide nanoplate microspheres under visible light. *Environ Sci Technol* 43(11):4143–4150
128. Ai Z, Ho W, Lee S (2011) Efficient visible light photocatalytic removal of NO with BiOBr-Graphene nanocomposites. *J Phys Chem C* 115(51):25330–25337
129. Dong F, Sun Y, Fu M et al (2012) Room temperature synthesis and highly enhanced visible light photocatalytic activity of porous BiOI/BiOCl composites nanoplates microflowers. *J Hazard Mater* 219–220:26–34
130. Li G, Jiang B, Xiao S et al (2014) An efficient dye-sensitized BiOCl photocatalyst for air and water purification under visible light irradiation. *Environ Sci Processes Impacts* 16(8):1975–1980
131. Fu H, Pan C, Yao W et al (2005) Visible-light-induced degradation of rhodamine B by nano-sized  $\text{Bi}_2\text{WO}_6$ . *J Phys Chem B* 109(47):22432–22439
132. Zhang C, Zhu Y (2005) Synthesis of square  $\text{Bi}_2\text{WO}_6$  nanoplates as high-activity visible-light-driven photocatalysts. *Chem Mater* 17(13):3537–3545
133. Zhang L, Wang W, Zhou L et al (2007)  $\text{Bi}_2\text{WO}_6$  nano-and microstructures: shape control and associated visible-light-driven photocatalytic activities. *Small* 3(9):1618–1625
134. Li Y, Liu J, Huang X et al (2007) Hydrothermal synthesis of  $\text{Bi}_2\text{WO}_6$  uniform hierarchical microspheres. *Crys Growth Des* 7(7):1350–1355
135. Wu J, Duan F, Zheng Y et al (2007) Synthesis of  $\text{Bi}_2\text{WO}_6$  nanoplate-built hierarchical nest-like structures with visible-light-induced photocatalytic activity. *J Phys Chem C* 111(34):12866–12871
136. Huang Y, Ai Z, Ho W et al (2010) Ultrasonic spray pyrolysis synthesis of porous  $\text{Bi}_2\text{WO}_6$  microspheres and their visible-light-induced photocatalytic removal of NO. *J Phys Chem C* 114(14):6342–6349
137. Li G, Zhang D, Yu JC et al (2010) An efficient bismuth tungstate visible-light-driven photocatalyst for breaking down nitric oxide. *Environ Sci Technol* 44(11):4276–4281
138. Zhou Y, Zhang X, Zhang Q et al (2014) Role of graphene on the band structure and interfacial interaction of  $\text{Bi}_2\text{WO}_6$ /graphene composites with enhanced photocatalytic oxidation of NO. *J Mater Chem A* 2(39):16623–16631
139. Li G, Zhang D, Yu JC (2008) Ordered mesoporous  $\text{BiVO}_4$  through nanocasting: a superior visible light-driven photocatalyst. *Chem Mater* 20(12):3983–3992
140. Ai Z, Lee S (2013) Morphology-dependent photocatalytic removal of NO by hierarchical  $\text{BiVO}_4$  microboats and microspheres under visible light. *Appl Surf Sci* 280:354–359

# Chapter 6

## Preparation of TiO<sub>2</sub> Nanotubes-Based Electrophotocatalysts and Their Applications in Organic Pollutants Oxidation

Bo Tang, Meichuan Liu, and Guohua Zhao

### 6.1 Introduction

Over the past few decades, TiO<sub>2</sub> has been widely used as the photocatalyst for the degradation of diverse undesirable organics, owing to its intrinsic merits such as nonphotocorrosion, nontoxicity, and distinct optical and electronic properties [1–4]. Compared with TiO<sub>2</sub> nanofilms, TiO<sub>2</sub> nanotube arrays (TiO<sub>2</sub> NTs) in situ grown on the surface of pure Ti sheet by electrochemical anodic oxidation method not only has larger specific surface area and higher surface energy, but also exhibits greater adsorption capacity, more active sites, and superior photocatalytic (PC) efficiency [5–7]. Due to its splendid PC performance, TiO<sub>2</sub> NTs has received considerable attention in the realm of photocatalysis. Nevertheless, the large band gap energy of TiO<sub>2</sub> (3.2 eV for anatase and 3.0 eV for rutile) confines its optical absorption in the ultraviolet part of the solar light [8], and the rapid recombination of photo-induced electrons and holes greatly lowers its quantum efficiency, leading to low photo-generated current, so that highly concentrated refractory contaminants, such as aromatic organics and pesticides, could not be effectively PC oxidized and degraded by simple TiO<sub>2</sub> NTs [9]. Therefore, it is essential to find out effective solutions to assist TiO<sub>2</sub> NTs in enhancing PC activity and improve degradation efficiency.

Electrocatalytic (EC) oxidation, as another advanced oxidation technology with distinguished catalytic characteristics, such as versatility, high energy efficiency, easy handling, and environmental compatibility, has also been widely adopted in wastewater treatment [10]. It has been well known that combining PC oxidation with EC oxidation might be a feasible way to develop novel advanced oxidation processes (AOPs). Therefore, an anodic bias voltage is generally applied on the TiO<sub>2</sub> NTs electrode in order to help overcome the rapid recombination of

---

B. Tang • M. Liu • G. Zhao (✉)

Department of Chemistry, Shanghai Key Lab of Chemical Assessment and Sustainability, Tongji University, 1239 Siping Road, Shanghai 200092, China  
e-mail: [g.zhao@tongji.edu.cn](mailto:g.zhao@tongji.edu.cn)

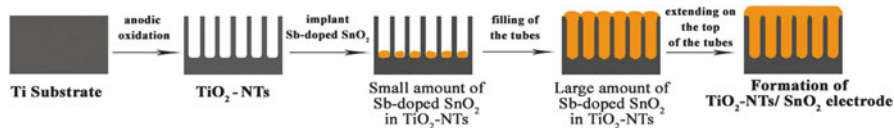
photo-produced electrons and holes, improving the photoelectric conversion efficiency [11]. However, considering the low conductivity and poor electrocatalytic performance of  $\text{TiO}_2$  NTs, it is not appropriate to be used individually as the electrode material. Nevertheless, in our previous works, we have recognized that  $\text{TiO}_2$  NTs can be served as an excellent microstructured tubular template [6]. Thus, combining photocatalyst  $\text{TiO}_2$  NTs with other PC or EC catalysts is a promising strategy to realize high PC and EC efficiency simultaneously. The present chapter mainly focuses on the reviews and discussions on some  $\text{TiO}_2$  NTs based unique microstructured electrodes with remarkable oxidation ability, strong stability and high electro-photocatalytic (EPC) efficiency, as well as their applications in organic pollutants degradation.

## 6.2 Ordered Stake Microstructured $\text{SnO}_2/\text{TiO}_2$ NTs [10, 12]

As one of the most suitable electrodes in degrading refractory organic pollutants, Sb-doped  $\text{SnO}_2$  electrode, which can be prepared easily and inexpensively, has excellent electrochemical oxidation ability toward the pollutants [13]. While due to the weak combination between Ti substrate and  $\text{SnO}_2$ , short service lifetime has become the main problem for commercial applications of Sb-doped  $\text{SnO}_2$  electrode.

Some novel approaches have been proposed to improve the electrochemical performance and stability of Sb-doped  $\text{SnO}_2$  electrode through design of its microstructure. Ordered stake microstructured  $\text{SnO}_2/\text{TiO}_2$  NTs is one of the typical examples. A schematic diagram of designing and preparing ordered stake microstructured  $\text{SnO}_2/\text{TiO}_2$  NTs electrode is shown in Scheme 6.1. Vertically aligned, well-ordered  $\text{TiO}_2$  NTs are firstly grown on the surface of Ti substrate by electrochemical anodic oxidation, and then Sb-doped  $\text{SnO}_2$  is loaded from the inside of  $\text{TiO}_2$  NTs to the top of it, leading an even coating of Sb-doped  $\text{SnO}_2$  on  $\text{TiO}_2$  NTs. Subsequently, a modified surfactant-assisted sol-gel method was adopted under vacuum environment to overcome the large surface tension of  $\text{TiO}_2$  NTs. As a result, the Sb-doped  $\text{SnO}_2$  was filled into Ti substrate and combined with  $\text{TiO}_2$  NTs forming an ordered stake microstructure. Such strategy is helpful to construct a consolidated bondage between the Ti substrate and Sb-doped  $\text{SnO}_2$  and is beneficial for the stability of  $\text{SnO}_2/\text{TiO}_2$  NTs. Additionally, owing to the large specific surface, space utilization, and three-dimensional microstructure of  $\text{TiO}_2$  NTs, the Sb-doped  $\text{SnO}_2$  loading amount will be increased significantly. Moreover, loading amount of per unit area under the restriction of the finite area is essential for the increment of electrochemical activity of  $\text{SnO}_2$  electrode. And the Sb-doped  $\text{SnO}_2$  particles are very likely to reach nanoscale and be highly dispersed because of the confining of  $\text{TiO}_2$  NTs once they embedded into the deep space of  $\text{TiO}_2$  NTs. Thus, the loading amount and active sites of Sb-doped  $\text{SnO}_2$  electrocatalysts can be increased significantly, which may further improve the electrochemical performance of the  $\text{SnO}_2/\text{TiO}_2$  NTs electrode.

Results show that the loading amount of Sb-doped  $\text{SnO}_2$  on a  $\text{SnO}_2/\text{TiO}_2$  NTs electrode is  $21.4 \text{ g m}^{-2}$ , which is more than two times of that on  $\text{SnO}_2/\text{Ti}$  electrode

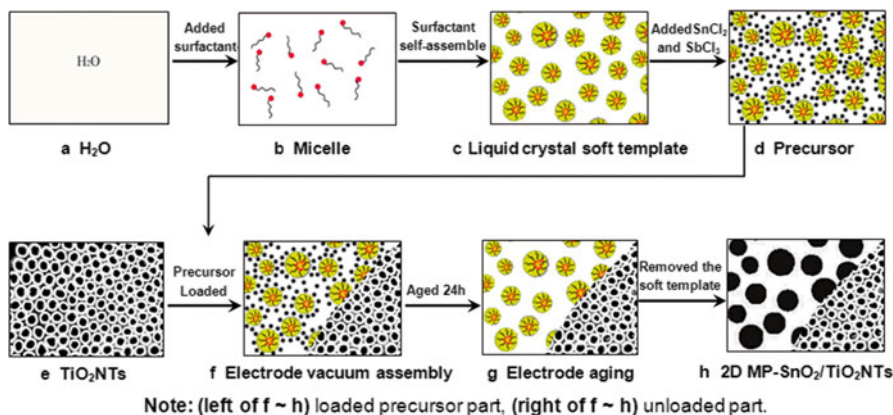


**Scheme 6.1** Schematic illustration for the growth of SnO<sub>2</sub>/TiO<sub>2</sub> NTs electrode [12]

(direct loading Sb-doped SnO<sub>2</sub> on the Ti substrate). The crystal lattice parameter of SnO<sub>2</sub> becomes smaller while that of TiO<sub>2</sub> gets larger, indicating the tighter combination between TiO<sub>2</sub> NTs and Sb-doped SnO<sub>2</sub>. As for electrochemical properties, the apparent rate constant ( $k_s$ ) of benzoic acid (BA) conversion on the SnO<sub>2</sub>/TiO<sub>2</sub> NTs electrode is  $(1.44 \pm 0.04) \times 10^{-4} \text{ s}^{-1}$  and that of SnO<sub>2</sub>/Ti is  $(1.01 \pm 0.03) \times 10^{-4} \text{ s}^{-1}$ . Furthermore, the initial instantaneous current efficiency of the degradation of BA on the SnO<sub>2</sub>/TiO<sub>2</sub> NTs electrode reaches 26.8 %, while it is only 13.3 % on the SnO<sub>2</sub>/Ti electrode. Compared with the PC properties of TiO<sub>2</sub> NTs, the band gap of SnO<sub>2</sub>/TiO<sub>2</sub> NTs decreases from 3.22 to 2.93 eV, and the photoconversion efficiency raises from 8.2 to 26.1 %. In the EPC aspect of BA, the current densities under 3.0 V were 4.0, 2.1, and 0.09 mA cm<sup>-2</sup> on the SnO<sub>2</sub>/TiO<sub>2</sub> NTs, SnO<sub>2</sub>/Ti, and TiO<sub>2</sub> NTs electrodes, respectively. The initial instantaneous current efficiency of the SnO<sub>2</sub>/TiO<sub>2</sub> NTs electrode increases to 100 %, much higher than 41.7 and 31.3 % on SnO<sub>2</sub>/Ti and TiO<sub>2</sub> NTs electrodes.  $k_s$  on SnO<sub>2</sub>/TiO<sub>2</sub> NTs is  $(5.26 \pm 0.16) \times 10^{-4} \text{ s}^{-1}$ , which is 3.2 times and 4.8 times than that of SnO<sub>2</sub>/Ti and TiO<sub>2</sub> NTs, respectively. The SnO<sub>2</sub>/TiO<sub>2</sub> NTs electrode has exhibited both excellent PC properties and excellent EC properties. After EPC degradation of BA on the electrode for 3.5 h, chemical oxygen demand (COD) removal is 100 %.

### 6.3 Sieve-Like Mp-SnO<sub>2</sub>/TiO<sub>2</sub> NTs [14]

As a good light transparent material, pure SnO<sub>2</sub> is usually used as the optical transparent electrode in the spectral electroanalysis. However, undoped pure SnO<sub>2</sub> is nonconductive. Sb is normally selected as the dopant to enhance its conductivity. Doping of trace amount of Sb has a cutoff effect on light. If the Sb-doped SnO<sub>2</sub> film is directly loaded on the TiO<sub>2</sub> NTs surface by simple methods, such as dipping or spin-coating, the UV absorption of TiO<sub>2</sub> NTs would decrease inevitably [15]. From such perspective, a novel electrode has been prepared by assembling sieve-like macroporous Sb-doped SnO<sub>2</sub> (Mp-SnO<sub>2</sub>) film on vertically aligned, well-ordered TiO<sub>2</sub> NTs through a block copolymer based soft template method. As illustrated by Scheme 6.2, micelles firstly generate in the surfactant solution, and then spontaneously grow into advanced homogeneous lyotropic liquid crystal (LC) with a columnar structure of high viscosity and transparent in appearance. Strong interaction between tin-antimony ions and the LC molecules is formed with the help of LC soft template. Subsequently, the controlled growth of SnO<sub>2</sub> on TiO<sub>2</sub> NTs is realized. These macropores ensure the light's source penetration through SnO<sub>2</sub> layer easily



**Scheme 6.2** Schematic illustration for the growth of the sieve-like Mp-SnO<sub>2</sub>/TiO<sub>2</sub> NTs electrode [14]

and illumination on the TiO<sub>2</sub> NTs directly. This leads to the superior PC and EC performances in the integrated electrophotocatalytic oxidation of refractory contaminations.

The pore size of the as-prepared Mp-SnO<sub>2</sub> ranges from 150 to 400 nm, and these macropores can increase the specific surface area and provide more active sites. Figure 6.1a demonstrates that the absorption band of the two SnO<sub>2</sub>/TiO<sub>2</sub> NTs catalysts exhibits a distinct red shift resulting from assembling of SnO<sub>2</sub>. Compared with the TiO<sub>2</sub> NTs, two SnO<sub>2</sub>/TiO<sub>2</sub> NTs have a better absorptive intensity in the long-wavelength range above 370 nm. As shown in Fig. 6.1b, the band gap of the Mp-SnO<sub>2</sub>/TiO<sub>2</sub> NTs is calculated to be 2.93 eV. The dark current density on the Mp-SnO<sub>2</sub>/TiO<sub>2</sub> NTs is 0.2 mA cm<sup>-2</sup>, whereas that on the TiO<sub>2</sub> NTs is only 0.01 mA cm<sup>-2</sup>, indicating that the conductivity of Mp-SnO<sub>2</sub>/TiO<sub>2</sub> NTs is increased by the assembling of the Sb doped SnO<sub>2</sub> electrocatalyst (Fig. 6.1c). Under the light irradiation of 365 nm, a high photoelectric conversion efficiency of 35.2 % can be obtained on Mp-SnO<sub>2</sub>/TiO<sub>2</sub> NTs, which is 3.1 times higher than that on TiO<sub>2</sub> NTs. The Mp-SnO<sub>2</sub>/TiO<sub>2</sub> NTs simultaneously possesses superior PC and EC performances. It displays excellent PEC synergistic oxidation ability in decreasing the toxicity of PNP. After 4 h, the PNP and TOC removal reaches 98 % and 91 %, respectively. Compared to conventional SnO<sub>2</sub>/Ti electrodes, the Mp-SnO<sub>2</sub>/TiO<sub>2</sub> NTs has demonstrated larger electrochemical surface absorption volume, smaller electrochemical impedance and lower reaction activation energy.

## 6.4 HOEP SnO<sub>2</sub>/TiO<sub>2</sub> NTs [16]

Generally, aromatic hydrocarbons have very high oxidation potentials, e.g., 2.8 V (vs. the saturated calomel electrode, SCE) for benzene, making it very difficult to use common electrodes with a low oxygen evolution potential (OEP) for their direct electrochemical oxidization [17]. And it is hard to achieve for a higher OEP than

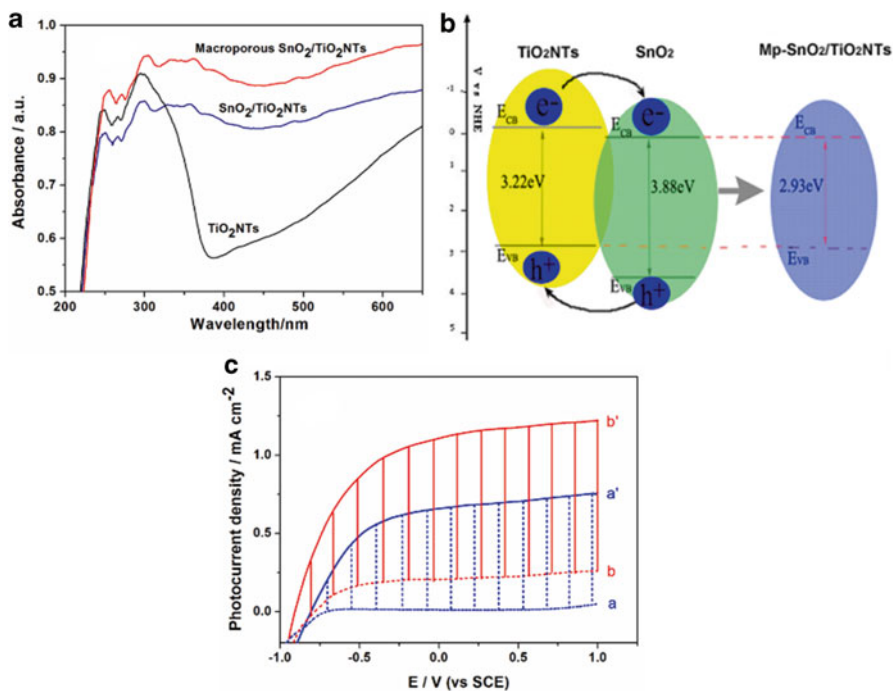
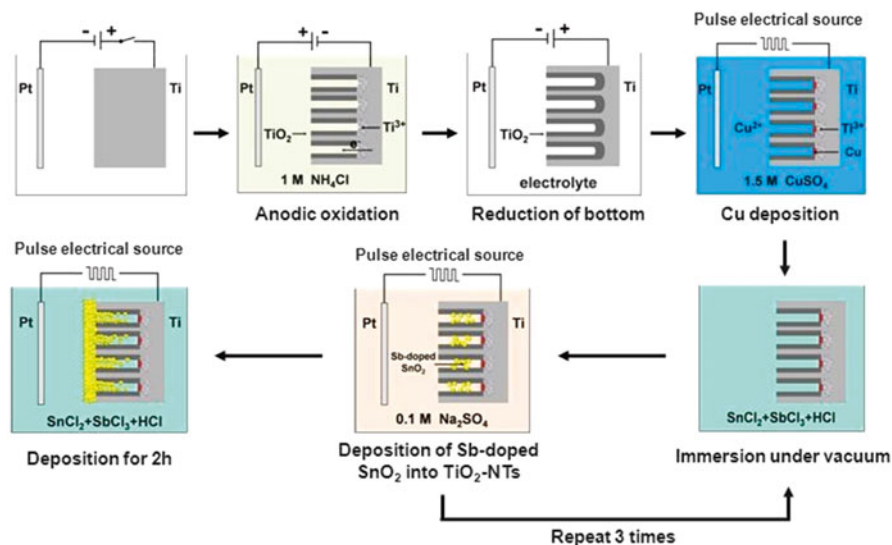


**Fig. 6.1** (a) UV vis DRS of Mp-SnO<sub>2</sub>/TiO<sub>2</sub> NTs, SnO<sub>2</sub>/TiO<sub>2</sub> NTs, and TiO<sub>2</sub> NTs. (b) Schematic illustration of the band-gap energy and charge separation of the Mp-SnO<sub>2</sub>/TiO<sub>2</sub> NTs electrode. (c) Photocurrent density versus bias potential (vs. SCE) at 365 nm in 1 M KOH solution: (a) TiO<sub>2</sub> NTs, dark; (a') TiO<sub>2</sub> NTs, light; (b) Mp-SnO<sub>2</sub>/TiO<sub>2</sub> NTs, dark; (b') Mp-SnO<sub>2</sub>/TiO<sub>2</sub> NTs, light [14]

2.0 V vs. SCE for the traditional Sb-doped SnO<sub>2</sub> anode achieved on a Ti substrate by the sol-gel method [18]. Thus, various efforts have been made to improve the OEP of the SnO<sub>2</sub> electrode by microstructure designing. In this light, the pulse electrodeposition method was applied for assembling SnO<sub>2</sub> into TiO<sub>2</sub> NTs, to obtain a high oxygen evolution potential (HOEP) SnO<sub>2</sub>/TiO<sub>2</sub> NTs electrode, as shown in Scheme 6.3. An intermediate layer with TiO<sub>2</sub> NTs formed on a Ti substrate by anodic oxidation has been fabricated. TiO<sub>2</sub> NTs were partially reduced at the bottom of TiO<sub>2</sub> NTs using the electrochemical method, and copper was deposited, which could enhance the combination between SnO<sub>2</sub> and the Ti substrate and the conductivity of the electrode. Besides, the intermediate layer was also favorable for the deposition of SnO<sub>2</sub> with copper particles serving as seeds.

Compared to the conventional Sb-doped SnO<sub>2</sub> electrode prepared by the sol-gel method, the proposed HOEP SnO<sub>2</sub>/TiO<sub>2</sub> NTs electrode [16] displays a higher crystallinity, a higher order degree of the atomic lattice, and a lower concentration of oxygen vacancies. The SEM image confirms that the surface of the HOEP SnO<sub>2</sub>/TiO<sub>2</sub> NTs electrode presents a three-dimensional structure consisting of Sb-doped SnO<sub>2</sub> nanoparticles with a certain microspherical structure, which may increase the specific area greatly and provide more active sites. The reaction activation energy

also decreases from  $11.67 \text{ kJ mol}^{-1}$  for the conventional  $\text{SnO}_2$  electrode to  $5.73 \text{ kJ mol}^{-1}$ . This HOEP  $\text{SnO}_2/\text{TiO}_2$  NTs electrode demonstrates superior electrochemical oxidation ability for fluorobenzene, which is highly stable and cannot even be degraded effectively on a BDD electrode with a strong oxidation capacity. As shown in Fig. 6.2a, the mineralization current efficiency (MCE) on HOEP  $\text{SnO}_2/\text{TiO}_2$  NTs ( $16.2\%$  at 1 h) is higher than that on BDD ( $8.03\%$ ) and conventional  $\text{SnO}_2$  ( $4.9\%$ ). At 4 h, the MCE values on HOEP  $\text{SnO}_2/\text{TiO}_2$  NTs, conventional  $\text{SnO}_2$ , and BDD are



**Scheme 6.3** Schematic illustration for the preparation of the HOEP  $\text{SnO}_2/\text{TiO}_2$  NTs electrode [16]

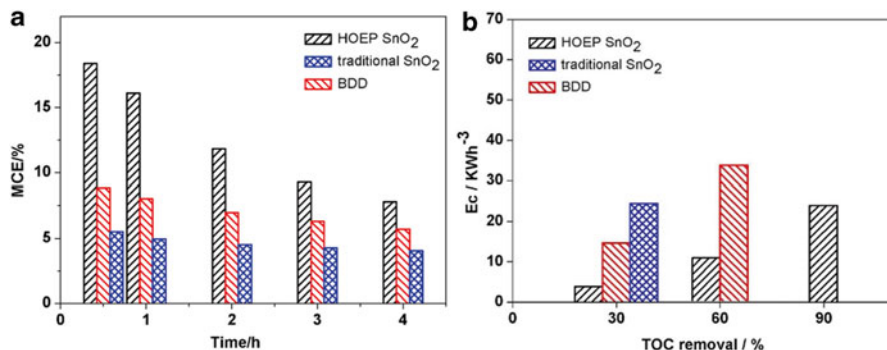


**Fig. 6.2** (a) Mineralization current efficiency (MCE) changes with time on the HOEP  $\text{SnO}_2$ , traditional  $\text{SnO}_2$ , and BDD electrodes. (b) Energy consumption changes with the total organic carbon (TOC) removal rate on the HOEP  $\text{SnO}_2$ , traditional  $\text{SnO}_2$ , and BDD electrodes [16]

7.8 %, 4.1 %, and 5.6 %, respectively. It can be seen from Fig. 6.2b that the HOEP SnO<sub>2</sub>/TiO<sub>2</sub> NTs consumes the lowest energy owing to its lower cell voltage than BDD and conventional SnO<sub>2</sub> (6.2, 9.3, and 7.3 V for HOEP SnO<sub>2</sub>/TiO<sub>2</sub> NTs, BDD, and conventional SnO<sub>2</sub>, respectively, at 20 mA cm<sup>-2</sup>). Compared to this, the energy consumption of BDD is about 3.1 times that of HOEP SnO<sub>2</sub>/TiO<sub>2</sub> NTs to reach TOC removal of 60 %.

## 6.5 Micro-grafted ZnO NRs/TiO<sub>2</sub> NTs [19]

As another promising heterogeneous photocatalyst, ZnO is also an excellent n-type semiconductor with good PC activity and exhibits comparable efficiency for the electrophotocatalytic oxidation of organic pollutants [20]. However, the photoelectric conversion efficiency of pure ZnO is relatively low due to its high recombination rate of the photo-generated electron-hole pairs and its limited light responding range. It is also reported that ZnO often suffers from severe photocorrosion when illuminated in water, which remarkably reduces its photostability and photoactivity [20, 21]. The nanosized coupling of TiO<sub>2</sub> and ZnO has attracted considerable interests in enhancing photo-generated charge separation as the heterojunction structure can inhibit the recombination of photo-generated electrons and holes to a certain degree [22]. Compared with nanoparticles and nanofilms, specific hexagonal-shaped crystalline, highly ordered, and vertically aligned 1D ZnO nanorods (NRs) can promote the PC activity to a large extent, which is beneficial for the PC degradation of aromatic pollutions in wastewater, such as chlorophenol and methyl orange [23]. It is expected to obtain higher surface area and more active sites when the two 1D ordered nanostructures are coupled in a suitable way with a controllable structure and appropriate amount, which may exhibit simultaneously high synergistic PC activity and special physical chemistry properties. On the bases of these discussions, a novel vertically grafted 1D ZnO NRs on the tops of TiO<sub>2</sub> NTs electrode was constructed [19]. By using the facile seed-induced hydrothermal synthesis route, ZnO NRs were grafted on vertically aligned TiO<sub>2</sub> NTs. These ZnO seeds have been demonstrated to be favorable for the growth of ZnO NRs (Figs. 6.3, 6.4, and 6.5).

As shown in Fig. 6.3, ZnO NRs grew as flowerlike clusters directly grafted on the tops of TiO<sub>2</sub> NTs, acting like a great quantity of lead wires, outstretching from the

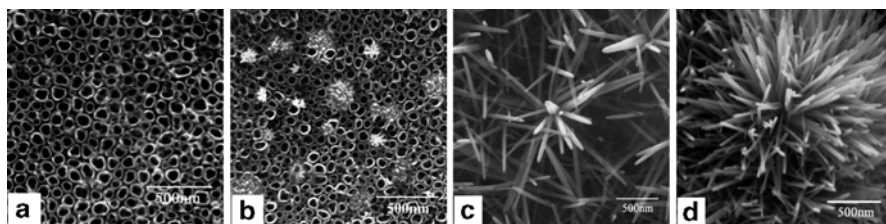


**Fig. 6.3** SEM images of as-prepared TiO<sub>2</sub> NTs (a) and ZnO NRs/TiO<sub>2</sub> NTs with different graft amount: (b) 0.23, (c) 0.65, (d) 0.98 mg cm<sup>-2</sup> [19]

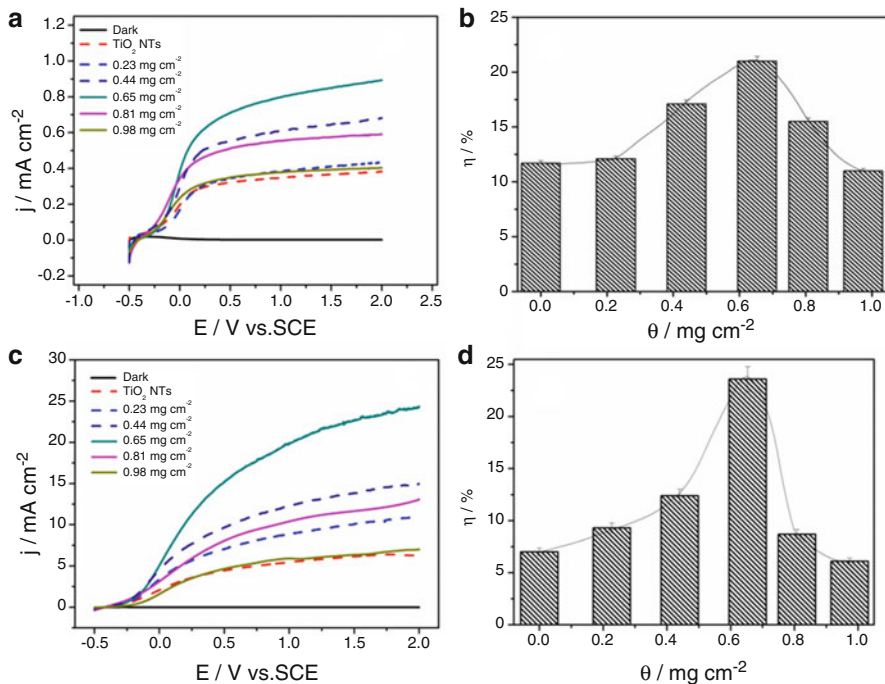


**Fig. 6.4** (a) Linear-sweep photovoltammograms of TiO<sub>2</sub> NTs and ZnO NRs/TiO<sub>2</sub> NTs with different graft amounts under the illumination of 254 nm UV light. (b) Photoelectric conversion efficiency of ZnO NRs/TiO<sub>2</sub> NTs with different graft amount under 254 nm UV light. (c) Linear-sweep photovoltammograms of TiO<sub>2</sub> NTs and ZnO NRs/TiO<sub>2</sub> NTs with different graft amounts under the illumination of 365 nm UV light. (d) Photoelectric conversion efficiency of ZnO NRs/TiO<sub>2</sub> NTs with different graft amount under 365 nm UV light. Photovoltammograms were all obtained at 50 mV/s [19]

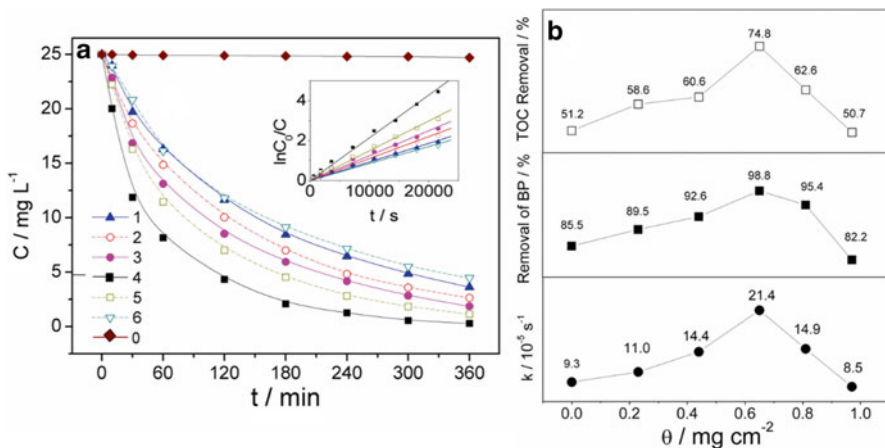
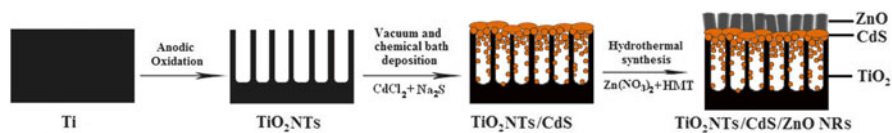


**Fig. 6.5** (a) Photolysis (0) and PEC removal of BPA on TiO<sub>2</sub> NTs (1) and ZnO NRs/TiO<sub>2</sub> NTs with different graft amount: (1) 0, (2) 0.23, (3) 0.44, (4) 0.65, (5) 0.81, and (6) 0.98 mg cm<sup>-2</sup>; inset: The relationship between the natural logarithm concentration of BPA and the time. (b) Calculated  $k$ , concentration removal percentage and TOC removal percentage of BPA on ZnONRs/TiO<sub>2</sub>NTs with different graft amounts [19]



**Scheme 6.4** Schematic illustration of the construction of a CdS/ZnO NRs /TiO<sub>2</sub> NTs photocatalyst [24]

trunk TiO<sub>2</sub> NTs. Thus, the grafted ZnO NRs could serve as several channels which are convenient for the transfer of the photo-generated electron and hole, providing a better charge separation, leading to a slight shift of the band gap absorption edges and changing the band gap energy ( $E_g$ ) consequently. Furthermore, the grafting amount would also alter the  $E_g$  to some extent. At an appropriate graft amount, ZnO NRs/TiO<sub>2</sub> NTs displayed broader optical absorption range and higher PC activity than pure TiO<sub>2</sub> NTs or ZnO NRs did. Under the illumination of 365 nm UV light, the photoelectric conversion efficiency was improved from 7.0 % of pure TiO<sub>2</sub> NTs to 23.6 % of ZnO NRs/TiO<sub>2</sub> NTs. In the electrophotocatalytic oxidation application, ZnO NRs/TiO<sub>2</sub> NTs presented higher degradation ability for bisphenol A (BPA). The kinetic constant was  $21.4 \times 10^{-5} \text{ s}^{-1}$ , about 2.3 times faster than that on pure TiO<sub>2</sub> NTs. Additionally, the stability of ZnO NRs was greatly improved with a stable BPA cyclic removal percentage as the received holes on ZnO NRs could keep ZnO from photocorrosion efficiently.

## 6.6 Encapsulated-Lidded CdS/ZnO NRs /TiO<sub>2</sub> NTs [24]

As above-mentioned, the predominant reason for unsatisfactory performances of TiO<sub>2</sub> NTs electrodes and photocatalysts is the large bandgap energy of TiO<sub>2</sub>, which limits its optical absorption within only the UV light region. Among various strategies for light harvesting, TiO<sub>2</sub> NTs decorated with narrow bandgap semiconductors have demonstrated splendid properties by virtue of enhanced visible light absorption, efficient charge carrier injection and transport in the ordered nanostructure [25]. CdS, as one of the most important II–VI semiconductors, has been widely utilized to modify TiO<sub>2</sub> for broadening its light spectrum to the visible region due to the fact that the photo-generated electrons of CdS could be injected into the conduction band of TiO<sub>2</sub> [26]. However, CdS suffers the critical drawback of photocorrosion like ZnO, which impedes its potential use in photocatalysis. Therefore, it is noted that a novel structure of encapsulated-lidded CdS/ZnO NRs/TiO<sub>2</sub> NTs provided a suitable model, which appears like “empty vessels with a big lid” [24]. It was fabricated by encapsulating the CdS NPs into the hollow shell of the TiO<sub>2</sub> NTs via a vacuum injection method and subsequently building a layer of ZnO NRs on the CdS/ TiO<sub>2</sub> NTs surface though hydrothermal synthesis, as illustrated in Scheme 6.4. The concentration of precursor was adjusted to approach the maximum ZnO coverage on the whole CdS/TiO<sub>2</sub> NTs surface. Thus, each nanotube is

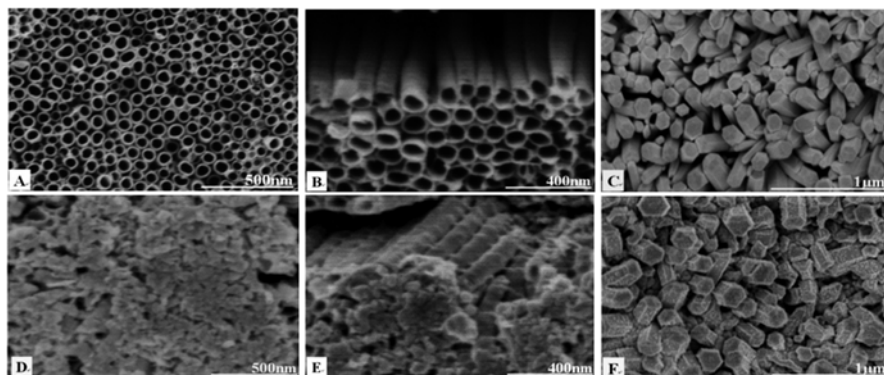


**Fig. 6.6** SEM images of the as-prepared photocatalysts: (a and b) top and side views of TiO<sub>2</sub> NTs; (c) ZnO NR/TiO<sub>2</sub> NTs; (d and e) top and side views of CdS/TiO<sub>2</sub> NTs; (f) CdS/ZnO NRs/TiO<sub>2</sub> NTs [24]

similar to an empty vessel, and the ZnO NR grows vertically on the top of nanotubes forming a thick layer as a big lid. In this conjunction, the ZnO NRs serve as favorable hole channels and receptors for the efficient separation of photoelectrons and holes. The microstructure of the as-prepared photocatalysts is confirmed by FE-SEM (Fig. 6.6).

After being sensitized by the CdS NPs, the absorption band edge of the obtained photocatalyst was evidently red-shifted to the visible region with the band gap reduced from its original 3.20 to 2.34 eV (Fig. 6.7). Photoelectric property tests demonstrated that the CdS/ZnO NRs/TiO<sub>2</sub> NTs kept a very high EPC activity in the both ultraviolet (UV) and visible region. The maximum photoelectric conversion efficiencies of CdS/ZnO NRs/TiO<sub>2</sub> NTs were 31.8 and 5.98 % under UV light (365 nm) and visible light (420–800 nm), respectively. In the EPC oxidation, CdS/ZnO NRs/TiO<sub>2</sub> NTs displayed a superior removal ability for methyl orange (MO) and a strong stability. The kinetic constants were  $1.77 \times 10^{-4} \text{ s}^{-1}$  under UV light, which was about 5.9 and 2.6 times of those on pure TiO<sub>2</sub> NTs and ZnO NRs/TiO<sub>2</sub> NTs. And it reached  $2.5 \times 10^{-4} \text{ s}^{-1}$  under visible light, 2.4 times of that on CdS/TiO<sub>2</sub> NTs.

## 6.7 Conclusion

In summary, series of modified TiO<sub>2</sub> NTs-based electrode with novel microstructures have been fabricated. By combining electrocatalysis technique, those particular microstructures succeeded in realizing efficient separation of photoelectrons and holes, and remarkable synergistic electrophotocatalytic oxidation ability was obtained as well. However, the exact structure–performance correlation is still unclear and demands further systematic investigation. A thorough and deep understanding of the precise degradation process on the surface of catalysts is essential for the design of other microstructures with enhanced EPC performances.

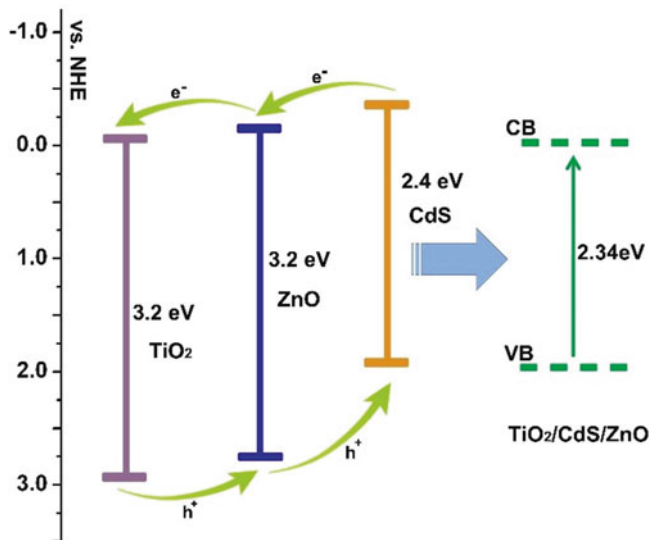


**Fig. 6.7** Schematic illustration of the band-gap energy and charge separation of the combined CdS/ZnO NRs/TiO<sub>2</sub> NTs photocatalyst [24]

Furthermore, new catalytic surface/interface structures and species in the assistance of electrocatalysis are definitely worth exploring, and their interdisciplinary applications in energy and environment has also attracted considerable attention.

**Acknowledgment** This work was financially supported by the National Natural Science Foundation of China (NSFC, No. 21477085, 21377092, 21277099, 21077077, and 20877058), 863 Program (2008AA06Z329) from the Ministry of Science, and Science and Technology Commission of Shanghai Municipality (14DZ2261100).

## References

- Beranek R, Tsuchiya H, Sugishima T, Macak JM, Taveira L, Fujimoto S, Kisch H, Schmuki P (2005) Enhancement and limits of the photoelectrochemical response from anodic TiO<sub>2</sub> nanotubes. *Appl Phys Lett* 87:3
- Chen X, Mao SS (2007) Titanium dioxide nanomaterials: synthesis, properties, modifications, and applications. *Chem Rev* 107:2891–2959
- Fujishima A, Zhang XT, Tryk DA (2008) TiO<sub>2</sub> photocatalysis and related surface phenomena. *Surf Sci Rep* 63:515–582
- Zhang YH, Tang ZR, Fu XZ, Xu YJ (2010) TiO<sub>2</sub>-graphene nanocomposites for gas-phase photocatalytic degradation of volatile aromatic pollutant: Is TiO<sub>2</sub>-graphene truly different from other TiO<sub>2</sub>-carbon composite materials? *ACS Nano* 4:7303–7314
- Kim JH, Zhu K, Yan YF, Perkins CL, Frank AJ (2010) Microstructure and pseudocapacitive properties of electrodes constructed of oriented NiO-TiO<sub>2</sub> nanotube arrays. *Nano Lett* 10:4099–4104
- Mohamed AER, Rohani S (2011) Modified TiO<sub>2</sub> nanotube arrays (TNTAs): progressive strategies towards visible light responsive photoanode, a review. *Energy Environ Sci* 4:1065–1086

7. Lee K, Mazare A, Schmuki P (2014) One-dimensional titanium dioxide nanomaterials: nanotubes. *Chem Rev* 114:9385–9454
8. Roy P, Berger S, Schmuki P (2011) TiO<sub>2</sub> nanotubes: synthesis and applications. *Angew Chem Int Ed Engl* 50:2904–2939
9. Liu Z, Zhang X, Nishimoto S, Jin M, Tryk DA, Murakami T, Fujishima A (2008) Highly ordered TiO<sub>2</sub> nanotube arrays with controllable length for photoelectrocatalytic degradation of phenol. *J Phys Chem C* 112:253–259
10. Li P, Zhao G, Cui X, Zhang Y, Tang Y (2009) Constructing stake structured TiO<sub>2</sub>-NTs/Sb-Doped SnO<sub>2</sub> electrode simultaneously with high electrocatalytic and photocatalytic performance for complete mineralization of refractory aromatic acid. *J Phys Chem C* 113:2375–2383
11. Shankar K, Basham JI, Allam NK, Varghese OK, Mor GK, Feng XJ, Paulose M, Seabold JA, Choi KS, Grimes CA (2009) Recent advances in the use of TiO<sub>2</sub> nanotube and nanowire arrays for oxidative photoelectrochemistry. *J Phys Chem C* 113:6327–6359
12. Zhao G, Cui X, Liu M, Li P, Zhang Y, Cao T, Li H, Lei Y, Liu L, Li D (2009) Electrochemical degradation of refractory pollutant using a novel microstructured TiO<sub>2</sub> nanotubes/Sb-doped SnO<sub>2</sub> electrode. *Environ Sci Technol* 43:1480–1486
13. Wiggins-Camacho JD, Stevenson KJ (2011) Indirect electrocatalytic degradation of cyanide at nitrogen-doped carbon nanotube electrodes. *Environ Sci Technol* 45:3650–3656
14. Chai S, Zhao G, Li P, Lei Y, Zhang Y-n, Li D (2011) Novel sieve-like SnO<sub>2</sub>/TiO<sub>2</sub> nanotubes with integrated photoelectrocatalysis: fabrication and application for efficient toxicity elimination of nitrophenol wastewater. *J Phys Chem C* 115:18261–18269
15. Leite ER, Bernardi MIB, Longo E, Varela JA, Paskocimas CA (2004) Enhanced electrical property of nanostructured Sb-doped SnO<sub>2</sub> thin film processed by soft chemical method. *Thin Solid Films* 449:67–72
16. Wu T, Zhao G, Lei Y, Li P (2011) Distinctive tin dioxide anode fabricated by pulse electrodeposition: high oxygen evolution potential and efficient electrochemical degradation of fluorobenzene. *J Phys Chem C* 115:3888–3898
17. Panizza M, Cerisola G (2009) Direct and mediated anodic oxidation of organic pollutants. *Chem Rev* 109:6541–6569
18. Zhu KJ, Zhang WC, Wang HF, Xiao ZL (2008) Electro-catalytic degradation of phenol organics with SnO<sub>2</sub>-Sb<sub>2</sub>O<sub>3</sub>/Ti electrodes. *Clean Soil Air Water* 36:97–102
19. Lei Y, Zhao G, Liu M, Zhang Z, Tong X, Cao T (2009) Fabrication, characterization, and photoelectrocatalytic application of ZnO nanorods grafted on vertically aligned TiO<sub>2</sub> nanotubes. *J Phys Chem C* 113:19067–19076
20. Xu TG, Zhang LW, Cheng HY, Zhu YF (2011) Significantly enhanced photocatalytic performance of ZnO via graphene hybridization and the mechanism study. *Appl Catal B Environ* 101:382–387
21. Chakrabarti S, Dutta BK (2004) Photocatalytic degradation of model textile dyes in wastewater using ZnO as semiconductor catalyst. *J Hazard Mater* 112:269–278
22. Yang GD, Yan ZF, Xiao TC (2012) Preparation and characterization of SnO<sub>2</sub>/ZnO/TiO<sub>2</sub> composite semiconductor with enhanced photocatalytic activity. *Appl Surf Sci* 258:8704–8712
23. Liu YB, Zhou BX, Bai J, Li JH, Zhang JL, Zheng Q, Zhu XY, Cai WM (2009) Efficient photochemical water splitting and organic pollutant degradation by highly ordered TiO<sub>2</sub> nanopore arrays. *Appl Catal B Environ* 89:142–148
24. Zhang YN, Zhao G, Lei Y, Li P, Li M, Jin Y, Lv B (2010) CdS-encapsulated TiO<sub>2</sub> nanotube arrays lidded with ZnO nanorod layers and their photoelectrocatalytic applications. *ChemPhysChem* 11:3491–3498
25. Sun WT, Yu Y, Pan HY, Gao XF, Chen Q, Peng LM (2008) CdS quantum dots sensitized TiO<sub>2</sub> nanotube-array photoelectrodes. *J Am Chem Soc* 130:1124–1125
26. Baker DR, Kamat PV (2009) Photosensitization of TiO<sub>2</sub> nanostructures with CdS quantum dots: particulate versus tubular support architectures. *Adv Funct Mater* 19:805–811

# Chapter 7

## Hollow Core–Shell Titania Photocatalysts for Selective Organic Synthesis

Sheela Chandren and Bunsho Ohtani

### 7.1 Introduction

Titania ( $\text{TiO}_2$ ) is by far the most widely investigated metal oxide, mainly because of its chemical stability, nontoxicity, and well-positioned valence and conduction bands [1, 2]. Three common  $\text{TiO}_2$  polymorphs exist in nature, which, in order of abundance, are rutile, anatase, and brookite. The rutile and anatase polymorphs are primarily used in photocatalysis. Both the rutile and anatase crystal structures comprise of distorted octahedra. In rutile, a slight distortion from orthorhombic geometry occurs, where the unit cell is stretched beyond a cubic shape. In anatase, the distortion of the cubic lattice is more significant, and thus, the resulting symmetry is less orthorhombic [3].  $\text{TiO}_2$ , in anatase form, exhibits a strong photocatalytic effect, which generates electron–hole pairs. As a result, the material can harvest photons in the near-UV region ( $<410$  nm) to provide strong oxidizing power to decompose organic molecules on the surface.

A wide range of other semiconductors and materials have been tested for photocatalytic activity [4]. In general, they have been found to be less active than  $\text{TiO}_2$ . Among the many applications of  $\text{TiO}_2$ -based materials are solar cells for the production of hydrogen [5], production of pigments and cosmetic products [6, 7] and preparation of anti-reflection coating materials [8]. Apart from that,  $\text{TiO}_2$  was also utilized in the design of electrodes for electrochemical processes [9], as component of thin film optical devices such as gas sensors [10] and bactericides [11].

---

S. Chandren

Universiti Teknologi Malaysia, Johor Bahru, Johor, Malaysia

Institute for Catalysis, Hokkaido University, Sapporo 001-0021, Japan

B. Ohtani (✉)

Institute for Catalysis, Hokkaido University, Sapporo 001-0021, Japan

e-mail: [ohtani@cat.hokudai.ac.jp](mailto:ohtani@cat.hokudai.ac.jp)

TiO<sub>2</sub>-based photocatalysts have also been successfully used in photocatalytic organic syntheses [12, 13], especially in the selective formation of useful and valuable organic cyclic compounds, for example, through the redox-combined synthesis of L-pipecolinic acid (L-PCA), a useful intermediate material for various fine chemicals [14]. In these syntheses reactions, the photocatalytic reaction is operated under deaerated conditions, in order to avoid undesirable excessive oxidation through the radical chain reaction with oxygen (O<sub>2</sub>) and to allow the use of an alternative electron acceptor [12, 15]. Apart from that, TiO<sub>2</sub> particles or isolated titanium oxide species that are distributed onto or into inorganic supports can also be used in selective organic syntheses [16, 17]. Among all the works carried out [18, 19], TiO<sub>2</sub> particles incorporated into porous substances is one of the most widely used methods to provide the selectivity. This method, however, tends to decrease the photocatalytic activity of the core TiO<sub>2</sub> due to the surface coverage of these substances.

The synthesis of a unique core-shell composite photocatalyst comprising commercially available TiO<sub>2</sub> particles encapsulated in a hollow silica (SiO<sub>2</sub>) shell (SiO<sub>2</sub>/void/TiO<sub>2</sub>) has been reported [20–23]. Besides showing the ability to decompose small substrates, this hollow core-shell material also exhibited the capacity to retain the intrinsic activity of original TiO<sub>2</sub> for small substrates due to the presence of a void space between the TiO<sub>2</sub> core and the hollow SiO<sub>2</sub> shell. This composite showed superior photocatalytic activity in methanol dehydration, decomposition of acetic acid [21] and photocatalytic redox-combined synthesis of L-pipecolinic acid (L-PCA) [22, 23]. In this chapter, the preparation of hollow core-shell TiO<sub>2</sub> with adjustable shell thickness and size of void space is explained. The applications of this composite in different photocatalytic reactions, with focus on selective organic synthesis, are also given. Modifications of the SiO<sub>2</sub> shell in order to control the microenvironment of the TiO<sub>2</sub> core are also discussed.

## 7.2 Hollow Core-Shell Structure with Titania Core and Silica Shell

Due to their potential unique and tunable physical properties, the preparation of inorganic hollow nanoparticles with controlled size, shape and hollow interior has sparked great interest [24]. These hollow core-shell composites are most often used in catalysis, pigment encapsulation, chromatography, controlled release of drugs, and gene therapy [25–29]. Despite the wide usage, efforts to increase their applications are still being explored by revising the properties of shell materials and by preparing better hollow structures, such as yolk-shell nanostructures [30], hollow spheres with controllable surface pores [31], pH or temperature-responsive hollow capsules [32, 33], and concentric hollow nanospheres [34].

For the preparation of hollow core-shell composite, a number of methods have been established. These preparation methods generally involve multistep and

require highly controlled and sensitive synthesis protocols to ensure complete coverage of core particles with the shell material [35]. Although various methods have been developed for the synthesis of hollow core–shell structures, such as precipitation [36], grafted polymerizations [37], sol–gel condensation [38], and layer-by-layer adsorption [39], it is still difficult to control the thickness and homogeneity of the coating. Here, a method of synthesizing hollow core–shell composite of titania core and silica shell with adjustable shell thickness and size of void space (hollowness) is highlighted. The surface of the core material was first coated with an appropriate primer to enhance interaction between the shell and the core.

### 7.2.1 Preparation of Hollow Core–Shell Composite of Titania Core and Silica Shell

In 2006, Ikeda et al. [40] reported the preparation of platinumized strontium titanate ( $\text{Pt-SrTiO}_3$ ) covered with hollow silica. The composite was prepared by double-layer winding of carbon and  $\text{SiO}_2$  layers on  $\text{Pt-SrTiO}_3$ , followed by heat treatment to remove the carbon layer. The surface was then partially modified with a fluoroalkylsilylation agent and the modified composite was able to stay at gas–water interface. This material was then used as photocatalyst for overall water splitting and showed higher efficiency than those of the conventional systems. The authors suggested that the superior photocatalytic activity might have been caused by the suppression of backward reaction. This system successfully proved that  $\text{TiO}_2$  could be modified to improve its selectivity, without decomposition of the modifiers themselves, and also the shielding of the active surface that causes the decrease in reaction rate, was also successfully prevented. The same principle can be applied to other photocatalyst in order to increase its selectivity and also photocatalytic activity.

The hollow core–shell composite photocatalyst which consisted of commercially available  $\text{TiO}_2$  particles incorporated in a hollow silica shell ( $\text{SiO}_2/\text{void}/\text{TiO}_2$ ) has been proven to possess size-selective properties in the photodecomposition of organic compounds;  $\text{SiO}_2/\text{void}/\text{TiO}_2$  showed photocatalytic activity for decomposition of small substrates retaining the activity of original bare  $\text{TiO}_2$ , while negligible activity for polymers was observed, i.e.,  $\text{SiO}_2/\text{void}/\text{TiO}_2$  exhibits molecular-size selectivity [20, 21]. Recently, the use of the  $\text{SiO}_2/\text{void}/\text{TiO}_2$  photocatalyst for the synthesis of L-pipecolic acid (L-PCA) was attempted, and another function of silica shell to improve stereoselectivity, instead of molecular-size selectivity [22, 23], have been found.

Ikeda et al. [41] reported that by varying the thickness of the  $\text{SiO}_2$  shell of the  $\text{SiO}_2/\text{void}/\text{TiO}_2$ , the photocatalytic activities for gas-phase photocatalytic reactions also varied. It was reported that with thicker shells, the rate of acetone decomposition was decreased. This is caused by the possible hindrance of substrate supply to the core- $\text{TiO}_2$  surface. However, the opposite was observed for the photodecompo-

sition of gaseous 2-propanol into carbon dioxide. The composite induced a higher-level activity when compared to the naked  $\text{TiO}_2$ . These results suggest that the thickness of the silica layer in the  $\text{SiO}_2/\text{void}/\text{TiO}_2$  plays an important role in the overall photocatalytic activity. The other significant point is that the effect of shell thickness has only been reported for gas-phase reactions and not for liquid phase. The other effect that was explored in the synthesis of this hollow core-shell composite is varying of the void-space thickness. Apart from the thickness of the silica shell, Chandren and Ohtani [22, 23] prepared  $\text{SiO}_2/\text{void}/\text{TiO}_2$  with different sizes of the void space. The authors reported that some remarkable photocatalytic characteristics were discovered, more specifically those related to the presence of the lateral silica shell. In order to study those above-mentioned aspects, the fabrication of  $\text{SiO}_2/\text{void}/\text{TiO}_2$  composites with varying void space and also shell thickness via the modification of the previously reported procedure, as shown in Fig. 7.1.

The first step was by modifying the  $\text{TiO}_2$  surface with amino groups, 3-aminopropyltrimethoxysilane (APS), in order to enhance interaction between  $\text{TiO}_2$  and the carbon source. Then a carbon layer was added by using aqueous glucose (glucose aq.) as the carbon source under hydrothermal conditions with agitation. The surface of the carbon-coated  $\text{TiO}_2$  was then modified with *N*-(2-aminoethyl)-3-aminopropyltrimethoxysilane (AEAPS). Following that, a  $\text{SiO}_2$  layer, using tetraethyl orthosilicate (TEOS) as the silica source, was coated followed by heat treatment to remove the carbon layer. The resulting  $\text{SiO}_2/\text{void}/\text{TiO}_2$  consists of agglomerated  $\text{TiO}_2$  encapsulated in porous  $\text{SiO}_2$ . The  $\text{TiO}_2$  and

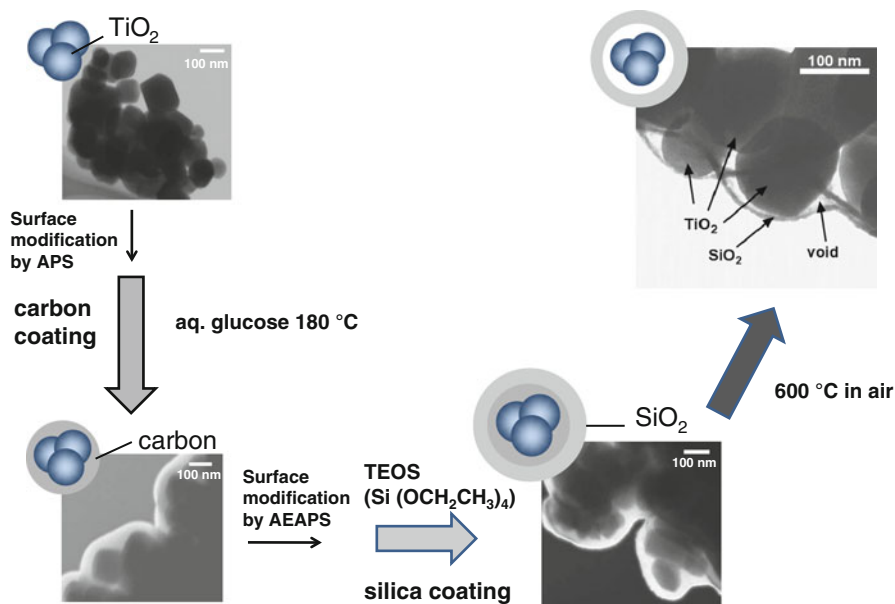


**Fig. 7.1** Schematic representation of the procedure for the preparation of  $\text{SiO}_2/\text{void}/\text{TiO}_2$ . SEM images taken in transmission mode

SiO<sub>2</sub> parts are separated by a void space and the size (thickness) of the void space are controlled by varying the concentration of glucose aq. Higher concentration of glucose resulted in larger (thicker) void space and vice versa. The thickness of the SiO<sub>2</sub> shell can also be varied by changing the silylation period; a thicker layer of SiO<sub>2</sub> shell is obtained with longer silylation period and vice versa. The SiO<sub>2</sub> shell was found to be porous and amorphous [22].

### 7.3 Hollow Core–Shell Composite of Titania Core and Silica Shell as a Photocatalyst for Selective Organic Synthesis

Titania with core–shell structure has been the subject of extensive research, due to its tunable surface properties, enhanced optical, electronic, and/or catalytic properties and its potential applications in many areas such as microelectronics, optoelectronics, optical devices, and catalysis [18, 19, 22]. One of the most interesting application is the use of hollow core–shell TiO<sub>2</sub> in selective organic synthesis. Here, the application of hollow core–shell composite of TiO<sub>2</sub> core and silica shell in the photocatalytic redox-combined synthesis of L-pipecolinic acid (L-PCA) will be discussed. The function of SiO<sub>2</sub> shell to improve stereoselectivity, instead of molecular-size selectivity, will be shown. As mentioned in the previous section, fabrication of an SiO<sub>2</sub>/void/TiO<sub>2</sub> composite was performed by varying the shell thickness and also size (thickness) of void spaces.

#### 7.3.1 Stereoselective Synthesis of L-Pipecolinic Acid from L-Lysine

One of the most essential compounds for the production of various medicines and/or biologically active chemical compounds is pipecolinic acid (PCA) [14]. One such example is a commercially available local anesthetic, L-N-propylpipecolinic acid 2,6-xylylidide, which is synthesized from L-(S)-PCA (L-PCA). Deaminocyclization of L-(S)-lysine (L-Lys) is the most preferable chemical process that is commonly used to obtain L-PCA due to several advantages [13]. Firstly, the starting material is optically pure, cheap and readily available, making it highly feasible. Secondly, this chemical process only releases ammonia as a by-product, when L-Lys is used as a source. It has been reported that the photoirradiation of deaerated aqueous solutions of L-Lys with suspended particulate semiconductor photocatalysts (TiO<sub>2</sub> or cadmium sulfide (CdS)) demonstrated the potential for one-step synthesis of L-PCA from L-Lys [13, 42, 43]. There is no requirement to protect the functional groups of L-Lys, and the photocatalytic synthesis proceeds under atmospheric pressure at room temperature.

The type of photocatalyst used is a key determining factor of optical purity of the product PCA (OP<sub>PCA</sub>). While TiO<sub>2</sub> photocatalysts yielded L-excess, its CdS counter-

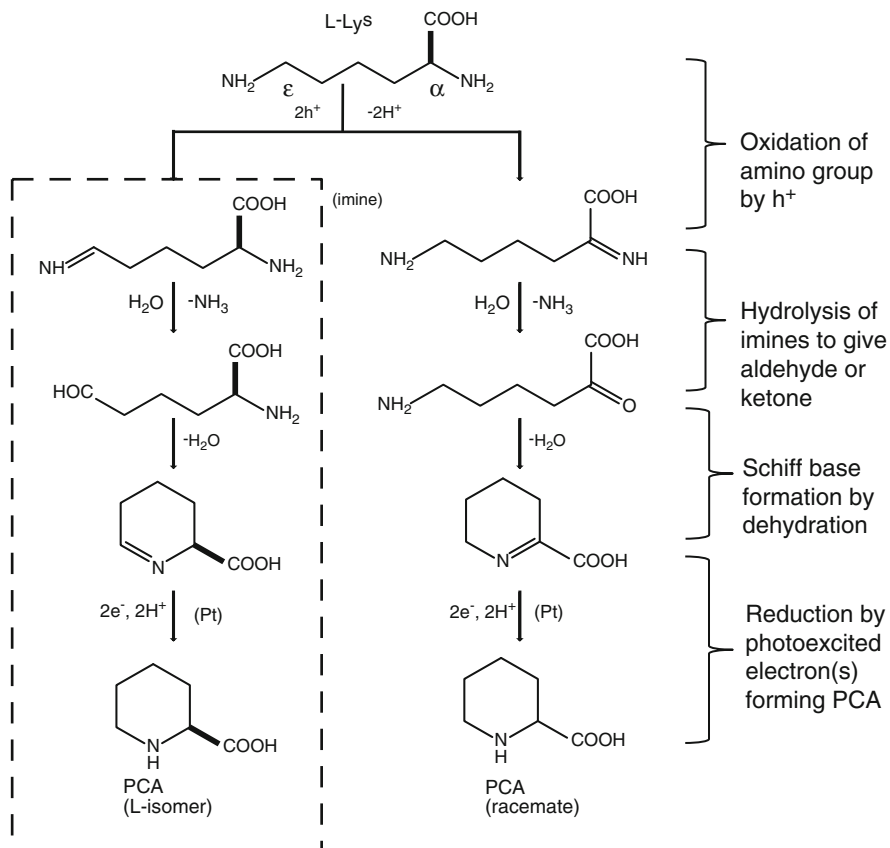


**Fig. 7.2** Proposed mechanism of the photocatalytic deaminocyclization of L-Lys on platinized  $\text{TiO}_2$  powders. The desired pathway that will yield L-PCA is shown in the *dotted box*

part gave almost racemic PCA [42]. This dependence is caused by the difference in position of attack by positive hole ( $h^+$ ) generated with photoexcitation of a photocatalyst (Fig. 7.2). Such selectivity in the oxidation position in L-Lys may depend on the micro-environment, in other words the environment surrounding the  $\text{TiO}_2$  instead of the whole reaction mixture, surface properties of a photocatalyst and potential of  $h^+$  to oxidize amino groups. Thus, a possible strategy for selective photocatalytic reaction with maintenance of a high rate would be to modify the surface and/or environment near the surface.

In solution, the  $\epsilon$ -amino group will be protonated, while the  $\alpha$ -amino group will remain in the neutral form because the basicity of  $\epsilon$ -amino group is higher than that of  $\alpha$ -amino group. Hence, to increase the oxidation of the  $\epsilon$ -amino group through the boxed pathway in Fig. 7.2, lower pH will be needed [22], since neutral amino groups undergo oxidation more easily compared with protonated amino groups. With lower pH, the  $\alpha$ -amino group will also be protonated, and when both amino

groups are in the protonated form, preferential oxidation of  $\epsilon$ -amino group occurs owing to lesser steric hindrance. The aforementioned ammonia released as the by-product of this reaction will, however, neutralize the acidic condition. And so, an acidic condition that will not be neutralized by the released ammonia is an important requirement to ensure the preferential oxidation of the  $\epsilon$ -amino group, which will result in PCA with high optical purity.

### 7.3.2 Stereoselective Synthesis of *L*-Pipicolinic Acid from *L*-Lysine by Hollow Core–Shell Composite of Titania Core and Silica Shell

In 2012, Chandren and Ohtani [22, 23] showed that by using platinumized hollow core–shell composite of commercially available  $\text{TiO}_2$  photocatalyst particles encapsulated in hollow  $\text{SiO}_2$  shells ( $\text{SiO}_2/\text{void}/\text{TiO}_2$ ), high photocatalytic performance for inducing selective production of *L*-PCA was achieved. The photocatalytic reaction was carried out by using different platinumized photocatalysts, such as commercial bare  $\text{TiO}_2$ , mechanically mixed  $\text{TiO}_2$  and  $\text{SiO}_2$ ,  $\text{TiO}_2$  directly covered with  $\text{SiO}_2$  and  $\text{SiO}_2/\text{void}/\text{TiO}_2$ . By using platinumized  $\text{SiO}_2/\text{void}/\text{TiO}_2$  as a photocatalyst, *L*-PCA was obtained from *L*-Lys maintaining high-level activity, comparable to that of the original bare  $\text{TiO}_2$ . The authors deduced that the high purity of obtained *L*-PCA was caused by the slightly acidic microenvironment of the core  $\text{TiO}_2$  surface induced by the  $\text{SiO}_2$  shells. Under the ordinary conditions without being immersed in aqueous solutions, the composite consists of  $\text{TiO}_2$  core that is encapsulated in a hollow  $\text{SiO}_2$  shell; the  $\text{SiO}_2$  shell is expected to be slightly shrunk and porous as exemplified in Fig. 7.3a. However, during the photocatalytic synthesis of PCA in the *L*-Lys aqueous solution, the shell may behave as a swollen-sponge and adsorbs water from the solution, providing acidic environment for the  $\text{TiO}_2$  core (Fig. 7.3b). This possible acidic

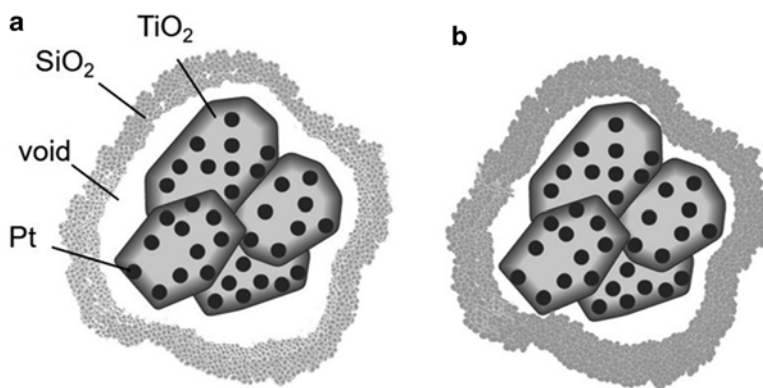


Fig. 7.3 The  $\text{SiO}_2/\text{void}/\text{TiO}_2$  in (a) ordinary dry condition and (b) an aqueous solution of *L*-Lys

microenvironment of the core  $\text{TiO}_2$  surface induced by the water-swollen  $\text{SiO}_2$  shell might lead to protonation of the  $\alpha$ -amino group (Fig. 7.2) to result in retardation of  $\alpha$ -route due to higher (more anodic) oxidation potential of the ammonium (protonated) form of amino groups in Lys. The appreciable acidity of the  $\text{SiO}_2$  shell close to, but not in contact with, the core  $\text{TiO}_2$  surface can account for the improved  $\text{OP}_{\text{PCA}}$  by promoting protonation of the  $\alpha$ -amino group in L-Lys. Therefore, by using  $\text{SiO}_2/\text{void}/\text{TiO}_2$  as the photocatalyst, no addition of any chemicals such as acid or a buffer solution is needed as the hollow core–shell composite provides an advantageous microenvironment for selective L-PCA synthesis.

## 7.4 Summary

Hollow core–shell titania photocatalysts can have different structures and morphologies. Numerous methods of synthesis of core–shell titania composites have already been reported in the literature. New techniques are also emerging in order to complete the coverage of core particle and homogeneous coating. These hollow core–shell composites have been widely investigated in material science and are exploited for a very wide range of applications. In this chapter, the focus was made on preparation of hollow core–shell particles of titania core encapsulated in silica shells ( $\text{SiO}_2/\text{void}/\text{TiO}_2$ ) for the use in the selective organic synthesis of L-pipecolinic acid from L-lysine. When platinumized  $\text{SiO}_2/\text{void}/\text{TiO}_2$  was used as a photocatalyst, L-pipecolinic acid from L-lysine was obtained, keeping high-level photocatalytic activity; comparable to that of the original bare  $\text{TiO}_2$ . This was caused by the slightly acidic microenvironment of the core  $\text{TiO}_2$  surface induced by the swollen  $\text{SiO}_2$  shells. This shows that the hollow core–shell particles are efficient for both size-selective and stereo-selective photocatalytic reactions. The study highlighted in this chapter may open a new direction of material chemistry for designing the microenvironment of photocatalyst surface to control reaction selectivity in organic synthesis, since the use of hollow core–shell photocatalysts in selective organic syntheses is still not fully explored.

## References

1. Wells RPK (2009) Oxide materials in photocatalytic processes. In: Metal oxide catalysis. Wiley-VCH, Weinheim, pp 755–769
2. Hashimoto K, Irie H, Fujishima A (2005)  $\text{TiO}_2$  photocatalysis: a historical overview and future prospects. *Jpn J Appl Phys* 1(44):8269–8285
3. Thompson TL, Yates JT (2006) Surface science studies of the photoactivation of  $\text{TiO}_2$ -new photochemical processes. *Chem Rev* 106:4428–4453
4. Fechete I, Wang Y, Védrine JC (2012) The past, present and future of heterogeneous catalysis. *Catal Today* 189:2–27

- Oregan B, Gratzel M (1991) A low-cost, high-efficiency solar-cell based on dye-sensitized colloidal TiO<sub>2</sub> films. *Nature* 353:737–740
- Tena MA, Mestre A, Garcia A, Sorli S, Monros G (2003) Synthesis of gray ceramic pigments with rutile structure from alkoxides. *J Sol-Gel Sci Technol* 26:813–816
- Jaroenworarluck A, Sunsaneeyametha W, Kosachan N, Stevens R (2006) Characteristics of silica-coated TiO<sub>2</sub> and its UV absorption for sunscreen cosmetic applications. *Surf Interface Anal* 38:473–477
- Wang R, Hashimoto K, Fujishima A, Chikuni M, Kojima E, Kitamura A, Shimohigoshi M, Watanabe T (2007) Light-induced amphiphilic surfaces. *Nature* 388:431–432
- Xiao P, Liu DW, Garcia BB, Sepehri S, Zhang YH, Cao GZ (2008) Electrochemical and photoelectrical properties of titania nanotube arrays annealed in different gases. *Sens Actuators B Chem* 134:367–372
- Hazra SK, Roy S, Basu S (2004) Growth of titanium dioxide thin films via a metallurgical route and characterizations for chemical gas sensors. *Mater Sci Eng B* 110:195–201
- Rodrigues CP, Ziolli RL, Guimaraes JR (2007) Inactivation of *Escherichia coli* in water by TiO<sub>2</sub>-assisted disinfection using solar light. *J Braz Chem Soc* 18:126–134
- Ohtani B, Pal B, Ikeda S (2003) Photocatalytic organic syntheses: selective cyclization of amino acids in aqueous suspensions. *Catal Surv Asia* 7:165–176
- Pal B, Ikeda S, Kominami H, Kera Y, Ohtani B (2003) Photocatalytic redox-combined synthesis of L-pipecolic acid from L-lysine by suspended titania particles: effect of noble metal loading on the selectivity and optical purity of the product. *J Catal* 217:152–159
- Bailey PD, Millwood PA, Smith PD (1998) Asymmetric routes to substituted piperidines. *Chem Commun* 6:633–640
- Shiraishi Y, Hirai T (2008) Selective organic transformations on titanium oxide-based photocatalysts. *J Photochem Photobiol C Photochem Rev* 9(4):157–170
- Xu YM, Langford CH (1997) Photoactivity of titanium dioxide supported on MCM41, zeolite X, and zeolite Y. *J Phys Chem B* 101(16):3115–3121
- Xamena F, Calza P, Lamberti C, Prestipino C, Damin A, Bordiga S (2003) Enhancement of the ETS-10 titanosilicate activity in the shape-selective photocatalytic degradation of large aromatic molecules by controlled defect production. *J Am Chem Soc* 125(8):2264–2271
- Ikeda S, Kowata Y, Ikeue K, Matsumura M, Ohtani B (2004) Asymmetrically modified titanium(IV) oxide particles having both hydrophobic and hydrophilic parts of their surfaces for liquid-liquid dual-phase photocatalytic reactions. *Appl Catal A Gen* 265(1):69–74
- Inumaru K, Kasahara T, Yasui M, Yamanaka S (2005) Direct nanocomposite of crystalline TiO<sub>2</sub> particles and mesoporous silica as a molecular selective and highly active photocatalyst. *Chem Commun* 16:2131–2133
- Ikeda S, Ikoma Y, Kobayashi H, Harada T, Torimoto T, Ohtani B (2007) Encapsulation of titanium(IV) oxide particles in hollow silica for size-selective photocatalytic reactions. *Chem Commun* 36:3753–3755
- Ikeda S, Kobayashi H, Ikoma Y, Harada T, Torimoto T, Ohtani B (2007) Size-selective photocatalytic reactions by titanium(IV) oxide coated with a hollow silica shell in aqueous solutions. *Phys Chem Chem Phys* 9:6319–6326
- Chandren S, Ohtani B (2012) Preparation, characterization and photocatalytic performance of titania particles encapsulated in hollow silica shells as an efficient photocatalyst for redox-combined stereoselective synthesis of L-pipecolic acid from L-lysine. *J Photochem Photobiol A* 246:50–59
- Chandren S, Ohtani B (2012) Preparation and reaction of titania particles encapsulated in hollow silica shells as an efficient photocatalyst for stereoselective synthesis of pipecolic acid. *Chem Lett* 41(7):677–679
- Liu X, Qiu G, Li X (2005) Shape-controlled synthesis and properties of uniform spinel cobalt oxide nanocubes. *Nanotechnology* 16:3035
- Templeton AC, Wuelfing WP, Murray RW (2000) Monolayer-protected cluster molecules. *Acc Chem Res* 33(1):27–36

26. Caruso F (2001) Nanoengineering of particle surfaces. *Adv Mater* 13(1):11–22
27. Xia Y, Gates B, Yin Y, Lu Y (2000) Monodispersed colloidal spheres: old materials with new applications. *Adv Mater* 12(10):693–713
28. Li ZZ, Wen LX, Shao L, Chen JF (2004) Fabrication of porous hollow silica nanoparticles and their applications in drug release control. *J Control Release* 98(2):245–254
29. Ohmori M, Matijević E (1993) Preparation and properties of uniform coated inorganic colloidal particles: 8. Silica on iron. *J Colloid Interface Sci* 60(2):288–292
30. Smith JN, Meadows J, Williams PA (1996) Adsorption of polyvinylpyrrolidone onto polystyrene latices and the effect on colloid stability. *Langmuir* 12(16):3773–3778
31. Chen D, Cao L, Huang F, Imperia P, Cheng Y-B, Caruso RA (2010) Synthesis of monodisperse mesoporous titania beads with controllable diameter, high surface areas, and variable pore diameters (14–23 nm). *J Am Chem Soc* 132(12):4438–4444
32. Kim S, Fisher B, Eisler H-J, Bawendi M (2003) Type-II quantum dots: CdTe/CdSe (core/shell) and CdSe/ZnTe (core/shell) heterostructures. *J Am Chem Soc* 125(38):11466–11467
33. Kalele SA, Ashtaputre SS, Hebalkar NY, Gosavi SW, Deobagkar DN, Deobagkar DD (2005) Optical detection of antibody using silica–silver core–shell particles. *Chem Phys Lett* 404(1–3):136–141
34. Kalele SA, Kundu AA, Gosavi SW, Deobagkar DN, Deobagkar DD, Kulkarni SK (2006) Rapid detection of *Escherichia coli* by using antibody-conjugated silver nanoshells. *Small* 2(3):335–338
35. Kalele S, Gosavi SW, Urban J, Kulkarni SK (2006) Nanoshell particles: synthesis, properties and applications. *Curr Sci* 91(8):1038–1052
36. Imhof A (2006) Preparation and characterization of titania-coated polystyrene spheres and hollow titania shells. *Langmuir* 17:3579–3585
37. Okaniwa M (1998) Synthesis of poly (tetrafluoroethylene)/poly(butadiene) core-shell particles and their graft copolymerization. *J Appl Polym Sci* 68:18–190
38. See KH, Mullins ME, Mills OP, Heiden PA (2005) A reactive core-shell nanoparticle approach to prepare hybrid nanocomposites: effects of processing variables. *Nanotechnology* 16:1950–1959
39. Caruso F, Caruso RA, Möhwald H (1999) Production of hollow microspheres from nanostructured composite particles. *Chem Mater* 1:3309–3314
40. Ikeda S, Hirao K, Ishino S, Matsumura M, Ohtani B (2006) Preparation of platinized strontium titanate covered with hollow silica and its activity for overall water splitting in a novel phase-boundary photocatalytic system. *Catal Today* 117(1–3):343–349
41. Ikeda S, Kobayashi H, Ikoma Y, Harada T, Yamazaki S, Matsumura M (2009) Structural effects of titanium(IV) oxide encapsulated in a hollow silica shell on photocatalytic activity for gas-phase decomposition of organics. *Appl Catal A Gen* 369:113–118
42. Ohtani B, Tsuru S, Nishimoto S, Kagiya T, Izawa K (1990) Photocatalytic one-step syntheses of cyclic imino acids by aqueous semiconductor suspensions. *J Org Chem* 55:5551–5553
43. Ohtani B, Kawaguchi J, Kozawa M, Nakaoka Y, Nosaka Y (1995) Titanium(IV) oxide photocatalyst of ultra-high activity for selective N-cyclization of an amino-acid in aqueous suspensions. *Chem Phys Lett* 242:315–319

# Chapter 8

## Design of Thin Film Photocatalysts Deposited on Rotating Disks for Degradation of Organic Dyes in Wastewater

Kan Li and Jinping Jia

### 8.1 PC Wastewater Treatment

Textile industry generates a large amount of wastewater daily. It is estimated that more than 15 % of the world dye production, about 400-t per day, is released into natural environment during synthesis, processing, and use [1]. Because such wastewater usually contains organic and inorganic compounds including dyes, pigments, oils, surfactants, and sizing agents, it has to be treated before discharge. In a typical process for industrial textile wastewater treatment, which includes initial physicochemical treatment such as iron–carbon internal electrolysis and coagulation, then followed by biological processes such as anaerobic and activated sludge treatment, not only the chemical oxygen demand (COD) in effluent can only be reduced to 300–500 mgO<sub>2</sub>L<sup>-1</sup>, which does not meet the discharge or reuse standards, but the color can also hardly be completely removed. Development of new textile wastewater post-treatment method thus is highly demanded.

Photocatalytic (PC) technique owns extremely strong oxidation activity and only requires photocatalyst and light, which has been widely researched in wastewater treatment [2–6], air purification [7–11], self-cleaning surface [12–15], anti fogging [16–18], fresh product storage [19–21], antibacterial materials [22–24], sensors [25–28], and energy generation (electricity [29–32] and hydrogen [33–36]). In a

---

K. Li

School of Environmental Science and Engineering, Shanghai Jiao Tong University,  
No. 800 Dong Chuan Road, Shanghai 200240, People's Republic of China

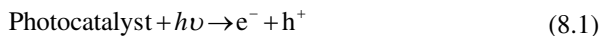
School of Materials Science and Engineering, Shanghai Jiao Tong University,  
No. 800 Dong Chuan Road, Shanghai 200240, People's Republic of China

J. Jia (✉)

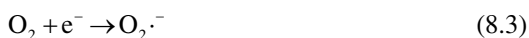
School of Environmental Science and Engineering, Shanghai Jiao Tong University,  
No. 800 Dong Chuan Road, Shanghai 200240, People's Republic of China

e-mail: [jjia@sjtu.edu.cn](mailto:jjia@sjtu.edu.cn)

typical PC wastewater treatment process, photocatalyst is first excited to generate electron ( $e^-$ ) and hole ( $h^+$ ) pairs by photon with the energy ( $h\nu$ ) of greater than or equal to the bandgap energy of photocatalyst:



The photo-generated electrons and holes can be used in a number of oxidation/reduction reactions. The most common is the formation of hydroxyl radical ( $\cdot\text{OH}$ ) and superoxide anion radical ( $\text{O}_2^{\cdot-}$ ) through the splitting of water and reaction with dissolved oxygen, respectively:



The  $\text{O}_2^{\cdot-}$  radical can be further protonated to form hydroperoxyl radical ( $\text{HO}_2^{\cdot}$ ) and  $\text{H}_2\text{O}_2$ . These radicals own strong oxidation activity and can be used to degrade a wide range of organic pollutants. So far, PC technique has been applied to various actual wastewater treatment including textile wastewater [37, 38], papermaking wastewater [39, 40], olive mill wastewater [41–43], petroleum refinery wastewater [44], and hospital wastewater [45]. However, this method still has limitation in current format. It is only effective for treating low concentration wastewater because more energy and much longer time are needed for higher concentration. Considering the fact that there are significant amount of non-biodegradable compounds existing in actual wastewaters, photocatalysis after biological process for post-treatment of actual wastewater is feasible.

Though large amount of works have been done on the synthesis of various photocatalysts with unique morphologies and high PC activities in the past few years, PC technique is still facing many bottlenecks before it can be really industrial applied in wastewater treatment. Paz presented a review of papers and patents on the applications of  $\text{TiO}_2$  photocatalysis for environmental purification in 2010 [46]. The statistic data were categorized according to water treatment, air treatment and self-cleaning surfaces. The number of publications in each of the categories increased monotonically and the research on air treatment and self-cleaning surfaces far lagged behind that on water treatment, which indicates that water treatment is still the subject of most of the scientific manuscripts on  $\text{TiO}_2$  photocatalysis. However Paz found that the number of patents on air treatment surpassed that of water treatment since year 1997, which indicates that for real industrial application, PC water treatment far lags behind air treatment. Ochiai et al. also reported the similar trend in the market growth of industries related to photocatalysis based on a survey by the Photocatalysis Industry Association of Japan in 2012 [47]. The market was categorized according to exterior, interior, road, cleanup, livingware, and others. More than half of the sales volume was occupied by “exterior” and “interior”, which are based on the self-cleaning concept on a titania-coated ceramic tile or glass. Recently, the sales volume of “cleanup” application involved in PC indoor

air-purifiers greatly increased, which indicates the increasing number of peoples who are interested in environmental issues such as sick house syndrome. On the other hand, the sales volume of PC water-purifiers which is involved in “other” application is actually much smaller than others.

In PC water treatment process, light utilization efficiency and light quantum yield play more important role than other ordinary chemical factors such as concentration, pH, temperature and pressure. Poor light utilization efficiency and low light quantum yield are the two main bottlenecks that influence PC degradation efficiency and restrict the application of PC technique in wastewater treatment. Besides these two factors, some other issues also need to be considered before application, such as the recovery and “light self-shielding effect” caused by powder photocatalyst, the utilization of visible light in solar energy and the complicated water qualities in different wastewaters. These bottlenecks will be analyzed in this chapter.

In order to solve or improve these bottlenecks, a rotating disk PC reactor has been developed by researchers. This reactor exhibits excellent PC performance due to its high light utilization efficiency and may have a broad application prospect. The rotating disk PC reactor and its latest research progresses will also be introduced in this chapter.

## 8.2 Bottlenecks Existing in PC Wastewater Treatment

### 8.2.1 Light Utilization Efficiency

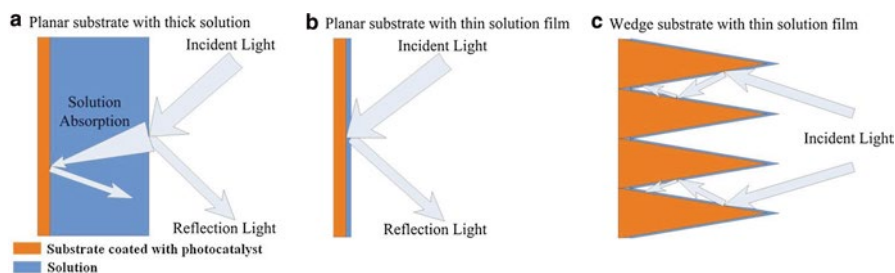
Because light loss always exists in a PC process, light utilization efficiency means the ratio between the light that absorbed by photocatalysts and the light that emitted from light source. First, there is no kind of material is absolute black body. When light irradiates on the surface of materials, part of light will be absorbed by materials while other part of light will reflect on the surface of materials. This reflection also happens on the surface of liquid, for example, the light will reflect on the surface of water and this reflection is especially significant for UV light. Second, solution and the organic compounds in solution also have strong light absorption, especially for the solution with high color and in the reactor with long optical path. According to Beer-Lambert law,

$$A = \epsilon bc \quad (8.4)$$

where  $A$  is the absorbance;  $b$  is the path length; and  $c$  is the molarity of solution. The absorbance, or radiation power loss due to solution absorption is in proportion to the thickness and concentration of solution. If more light was absorbed by solution, then less light can achieve on the surface of photocatalysts to excite them and start the PC reaction, which reduces the light utilization efficiency. The Data in Table 8.1 can confirm more directly that this light absorption by solution is very strong [48]. The transmittance ( $T$ , %), or the portion of light that can be used for photocatalytic

**Table 8.1** Transmittance ( $T$ , %) of 20 mg L<sup>-1</sup> Dye Solution at 254 nm. Reprinted from Ref. [48] with permission from Wiley

Solution	$T^a$ (%)	$T^b$ (%)	Solution	$T^a$ (%)	$T^b$ (%)
Acid Fuch sine 6B	25.3	2.1	Methylene Blue	18.2	0.9
Allura Red	10.7	0.2	Methyl Orange	19.8	2.1
Amaranth	16.2	0.6	Neutral Brown RL	23.1	2.4
Carmine	16.0	0.6	Neutral Bordeaux GRL	6.1	0.1
Direct Violet R	29.4	3.1	Neutral Orange RL	20.5	1.2
Weak Acid Green GS	18.9	0.9	Rhodamine B	17.0	0.8
Disperse Grey BR	25.4	2.2	Sunset Yellow	20.5	1.2
Food Lemon Yellow	16.5	1.1	Weak Acid Black BR	26.0	2.2

<sup>a</sup>In 1 cm quartz cell<sup>b</sup>In 4 cm quartz cell**Fig. 8.1** Schematic diagrams of light utilization in different PC water treatment processes. (a) The PC process with thick solution and planar substrate; (b) Thin film PC process with planar substrate; (c) Thin film PC process with light-harvesting substrate

degradation, of 20 mg L<sup>-1</sup> various dye solutions at 254 nm ranges from 6.1 to 29.4 % for 1 cm light path length, and only 3.1 to 0.1 % for 4 cm light path length. The dye concentration of 20 mg L<sup>-1</sup> (or lower concentration) is always used in laboratory scale experiments to test the performance of photocatalysts, but compares with real industrial wastewater, 20 mg L<sup>-1</sup> is in a very low concentration level. The transmittance and light utilization efficiency will be even lower with the increase of concentration.

According to the discussion above, as shown in Fig. 8.1a, the main light losses in PC wastewater treatment process can be summarized as light reflection, including the reflection on catalyst surface and on solution surface, and light absorption by solution. These light losses greatly influence the light utilization efficiency and restrict the real industrial application of photocatalysis, especially for the PC liquid phase reaction.

In order to reduce light loss caused by solution absorption, a thin film PC reactor can be used, in which a thin layer of aqueous solution covers the surface of immobilized photocatalyst during PC reaction (Fig. 8.2b). Various kinds of thin film PC reactors have been developed in the past few years, including rotating disk reactor

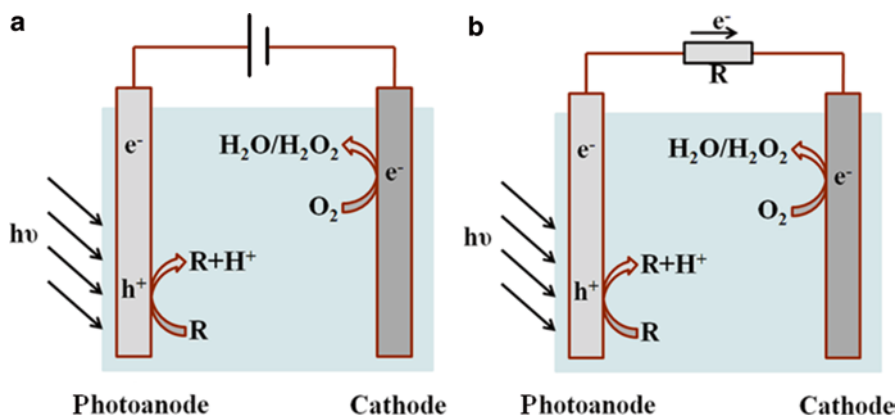


**Fig. 8.2** Schematic diagrams of (a) photoelectrocatalytic (PEC) system and (b) photo fuel cell (PFC) system

[49, 50], rotating drum reactor [51, 52], spinning disk reactor [53–55], inclined plate reactor [56, 57], and cascade reactor [58, 59]. These reactors have been proven to be effective for treating wastewater containing high concentration pollutants. A pilot plant with two thin film fixed bed reactors has already been built in Tunisia using solar energy to treat textile wastewater [60].

In order to reduce light loss caused by reflection, based on the thin film reactor, to change the planar structured substrate to a wedge or pyramid structured substrate (Fig. 8.1c) can not only enlarge surface area, but also enhance light utilization efficiency through multiple light reflections [61–63].

## 8.2.2 Light Quantum Yield

Light quantum yield is also very important for PC reaction. Though the photo-generated holes and electrons own strong oxidation and reduction activities, the electrons will easily recombine with the valence band holes in nanoseconds with simultaneous dissipation of heat energy in the absence of strong electron scavengers, resulting in a low light quantum yield.

The light quantum yield can be improved through integrating other active materials to form photocatalyst-based hetero-junction, such as photocatalyst-semiconductors [64–66], photocatalyst-noble metals [67–69], and photocatalyst-carbon materials [70–72]. These hetero-junctions can reduce the recombination rate by migrating electrons to the lower energy states and migrating holes to the opposite direction. Besides hetero-junction, a single cathode can also be connected with photoanode to transfer photo-generated electrons to cathode with or without the help of bias potential. When a bias potential is applied, it is a photoelectrocatalytic (PEC) process (Fig. 8.2a) [73, 74]. When there is no bias potential, with reasonable selection of

cathode material, photo-generated electrons can also transfer from photoanode to cathode spontaneously due to the potential existing between photo-excited anode and cathode (Fig. 8.2b). In this case, similar with a microbial fuel cell (MFC), it acts as a photo fuel cell (PFC) with a double benefit, the organic pollutants are degraded and the light and chemical energy are converted into electricity simultaneously in external circuit [75–77].

### 8.2.3 Other Problems Need To Be Considered

Poor light utilization efficiency and low light quantum yield are the two main factors that restrict the application of PC technique in wastewater treatment. Besides these, some other issues also need to be considered.

The immobilization of photocatalyst is required because large amount of powder photocatalyst not only causes “light self-shielding effect” to block incident light, but the recovering step from the solution is also inconvenient at large scale. In the pilot PC wastewater treatment plants with  $\text{TiO}_2$  powder suspended in slurry built in Germany and Spain, sedimentation tanks are needed [78, 79]. In sedimentation period, the best choice is change in pH of suspensions to the  $\text{pH}_{zpc}$  to achieve fast sedimentation of the catalyst. However, the pH needs to be adjusted by charge neutralization within the permitted disposal range after sedimentation. Furthermore, the small remaining fraction of catalyst still needs to be recovered by membrane micro-filtration to avoid the wash out of catalyst particles causing a non-acceptable secondary pollution related to the possible toxicity of nanoparticles. Though immobilization of photocatalyst can solve this problem, due to the small surface area and mass transfer limitation, compared to suspended system, immobilization of photocatalyst always results in a reduction in PC performance. In a thin film PC reactor, the mass transfer can be effectively improved, so the development of photocatalyst film with micro structures to obtain large surface area is important. Meanwhile, the mechanical strength of these micro structures should also be considered during long-term wastewater treatment.

Another issue should be considered is that as one of the most active photocatalysts,  $\text{TiO}_2$  can only be excited by UV irradiation that only occupies less than 5 % of the solar light due to its wide band gap. It is necessary to develop novel photocatalyst to utilize more visible light in solar energy.  $\text{TiO}_2$  has been doped with various non-metal and metal atoms (like S, I, Fe, La, and V) [80–82] or coupled with other catalysts with narrow band gap (like  $\text{CdS}/\text{TiO}_2$  and  $\text{Cu}_2\text{O}/\text{TiO}_2$ ) [64, 83] to extend its visible-light activity. Meanwhile, other non- $\text{TiO}_2$  photocatalysts with narrow band gap (like  $\text{Bi}_2\text{O}_3$ ,  $\text{WO}_3$ ,  $\text{CdS}$ , and  $\text{GaP}$ ) have also been widely investigated in recent years [84, 85]. Besides these, dye sensitization process is also a special way to utilize visible light [86, 87]. The dye adsorbed on the surface of photocatalyst can be excited by visible light to generate electrons. The electrons then inject from the excited dye to the conduction band of photocatalyst, where the electrons

were further scavenged by dissolved oxygen to yield  $O_2^{\cdot-}$  radical anions and oxidize dye molecules. In this process, photocatalyst does not need to be excited by visible light, but the existence of photocatalyst is a prerequisite because it plays the important role of electron carrier and acceptor. The increase in both the dye adsorption amount and strength can promote the electron transfer from the excited dye to catalyst.

At last, the wastewater qualities such as COD, color, pH, and inorganic anions will also influence PC activity and should be considered during PC wastewater treatment.

### 8.3 Rotating Disk PC Reactor

The rotating disk PC reactor is a thin solution film reactor that can effectively reduce light loss caused by solution absorption. The reactor is shown in Fig. 8.3 and is composed of three major components: a reactor vessel, a disk loaded with photocatalyst, and light source. The reactor system also includes a control system for rotating speed. The disk is arranged in the way that half of it is immersed in the solution and the other half is exposed to the open air. No catalyst-recovering step is needed due to the immobilization of catalyst. Furthermore, with the immobilization of catalyst on a metal disk, such as Ti, a bias potential can be applied to form PEC process to effectively separate photo-generated electrons and holes. More important is that when the disk is rotating, a thin solution film will form on the upper part of the disk, the incident light penetrates this thin film and irradiates on the surface of

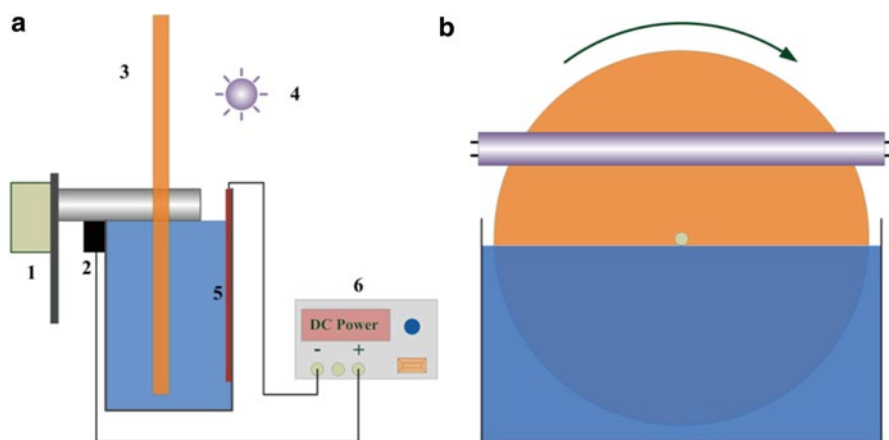
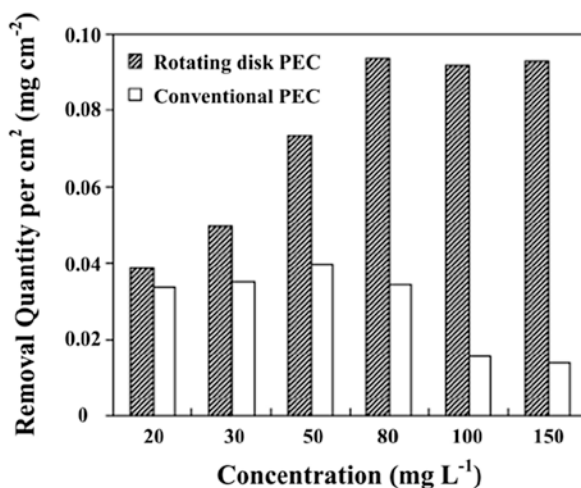


**Fig. 8.3** (a) Schematic diagram of the side view of rotating disk PEC reactor. (1) motor; (2) carbon brush; (3) photocatalytic disk; (4) light source; (5) cathode; (6) DC power supply. (b) The front view of rotating disk PEC reactor

photocatalyst directly, which significantly reduces the light loss caused by solution absorption and improves light utilization efficiency. The rotation of the disk also refreshes the thin solution film on the exposed side of the disk and promotes mass transfer of target compounds and dissolved oxygen in solution.

In comparison with conventional immersed PEC reactor, the rotating disk PEC reactor exhibited much better PC degradation efficiency, especially for dye solution with high concentration. Rhodamine B (RhB) solutions with concentrations ranging from 20 to 150 mg L<sup>-1</sup> were treated by us in a rotating disk PEC reactor and a conventional immersed PEC reactor (solution thickness was 1 cm), respectively [88]. In the investigated concentration range, rotating disk PEC reactor removed total color and TOC by 84–27 % and 48–7 % respectively in 1 h, which was much higher than 55–3 % and 30 % to nonobserved removal by conventional immersed PEC reactor under the same treatment conditions. High concentration will limit the conventional immersed PEC efficiency, which is a bottleneck problem preventing the PC technique from being industrialized. However, one of the significant advantages of rotating disk PEC is that its oxidation capacity increases with the increase of the solution concentration. Figure 8.4 shows the absolute quantity of RhB removed by each cm<sup>2</sup> disk surface area when rotating disk PEC reactor and conventional immersed PEC reactor were used to treat RhB solution at different concentration levels within 1 h. With RhB concentration increasing from 20 to 150 mg L<sup>-1</sup>, RhB removed by rotating disk PEC reactor increased steadily until it leveled off at 80 mg L<sup>-1</sup>, whereas the maximum amount of RhB removed by the conventional immersed PEC reactor was 50 mg L<sup>-1</sup>. Beyond that concentration, RhB removal decreased. The transmittance of the 50 mg L<sup>-1</sup> RhB solution was 0.23 %, and no transmittance was observed for the solution with RhB concentration of 80 mg L<sup>-1</sup> or higher. The radiation had been totally absorbed by the sample solution.

**Fig. 8.4** Absolute quantity of RhB removed by each cm<sup>2</sup> disk surface area using rotating disk PEC and conventional immersed PEC procedure to treat RhB solutions at different concentration levels [88]



In the rotating disk PEC reactor, rotating speed and bias potential are two main factors that influence PC performance. Firstly, rotating speed affects the thickness of solution film on disk. The thickness of solution film increases with increasing rotating speed [49, 88, 89]. However, the film is still in a thin level with high rotating speed and the influence of film thickness on light loss caused by rotating speed can be neglected. Secondly, rotating speed also affects mass transfer and dissolved oxygen concentration in solution. Because dissolved oxygen can react with photo-generated electrons to form  $O_2^{\cdot-}$ , better PC performance can be obtained with high dissolved oxygen concentration. It has been found that in a rotating disk reactor, even at very low rotating speed, the dissolved oxygen started to increase significantly [90]. As the rotating speed increased, the rate of dissolved oxygen increase was higher, resulting in reaching the saturation value of dissolved oxygen in a shorter time. At very high rotating speed, the dissolved oxygen reached saturation in less than 2 min.

Bias potential is another important parameter in rotating disk reactor because it facilitates separation of the photo-generated electrons and holes. PC performance improves with the increase of bias potential and usually less than 1 V bias potential is enough for a PEC process. Further increase in potential may have no improvement or even slight reduction in PC performance, which can be explained by more water oxidized by high potential. Because the potential needed in a PEC process is very low, a solar cell or a dye sensitization solar cell (DSSC) can be used as power supply to replace DC power. In latest researches, microbial fuel cell (MFC) and photo fuel cell (PFC) are also employed to apply potential [91, 92]. When a  $TiO_2/Ti-Pt$  PFC was employed as power supply, a bias potential between 0.6 and 0.75 V could be applied. The PC degradation efficiency of Reactive Brilliant Red X-3B (RBR) in the rotating disk reactor was significantly improved and the result was similar with that obtained by a 0.7 V DC power [92].

## 8.4 Photocatalyst Film in Rotating Disk Reactor

Photocatalyst film plays the most important role in a rotating disk PC reactor. Besides high UV or visible light PC activity, the film should also own large surface area and high mechanical strength for long-term performance.

In the past few years, large amount of powder photocatalysts with various morphologies and extremely large surface area have been synthesized [93–97]. One simple way to obtain photocatalyst film is to immobilize these powders on the rotating disk with the help of adhesive. This method has been successfully used in the preparation of photoanode in DSSC [98–100]. The film can be protected well during the usage because the DSSC is a sealed system. However, in wastewater treatment process, the powders will easily fall off. This is especially obvious in rotating disk reactor due to the interaction between solution and the film caused by the rotation of the disk. Eight different adhesives were tested by Dionysiou et al. for suitability to

immobilize three different  $\text{TiO}_2$  pellets, including irregular-shaped pellets, cylindrical pellets and spherical composite pellets, on the rotating disk support respectively [101].  $\text{TiO}_2$  pellet disintegration was observed in long-term performance in the best conditions, especially at high rotating speed.

$\text{TiO}_2$  film with high mechanical strength can be obtained using sol-gel method. Sol-gel solution with titania precursor is first dip-coated or spin-coated on the surface of rotating disk. Then after calcination, the sol-gel prepared  $\text{TiO}_2$  film can be obtained (Fig. 8.5a) [88]. Many researches have reported that the sol-gel prepared  $\text{TiO}_2$  film exhibited excellent stability and almost no  $\text{TiO}_2$  disintegration was observed in long-term performance [56, 88]. However, the surface area of sol-gel prepared  $\text{TiO}_2$  film is relatively small because there is no micro-structure on film surface. Researchers have found that the additive acid (including  $\text{HCl}$ ,  $\text{HNO}_3$  and  $\text{HF}$ ) in the sol greatly influences the final morphology of  $\text{TiO}_2$  film, and a coral-like  $\text{TiO}_2$  nanostructured film can be synthesized using the sol-gel method in the presence of  $\text{HF}$  [102]. But this film was only utilized in a DSSC, not in wastewater treatment.

$\text{TiO}_2$  nanotube film can be synthesized through anodization on a Ti substrate. The surface area (length and diameter of the tube) and mechanical strength of the nanotube film can be controlled by changing anodization conditions, such as voltage, time and electrolyte. Zhang et al. have applied a  $\text{TiO}_2$  nanotube film on a rotating disk PC reactor to treat RhB solution [103]. Compared with the result obtained by  $\text{TiO}_2$  nanoparticle disk, a significant in substrate removal efficiency of about 25–40 % was observed. However, it has been found that though  $\text{TiO}_2$  nanotube film processes larger surface area, there was no significant difference on PC performance between nanotube film and sol-gel prepared film when they were applied to degrade RhB in a thin film PC reactor [104]. The nanotube is blind pore architecture and the diameter is usually small (nano-level), the tube can be easily sealed by water and the air in tube can hardly move out, resulting in decreasing efficient surface area of  $\text{TiO}_2$  nanotube film. Meanwhile, the small sized nanotube is also not good for solution

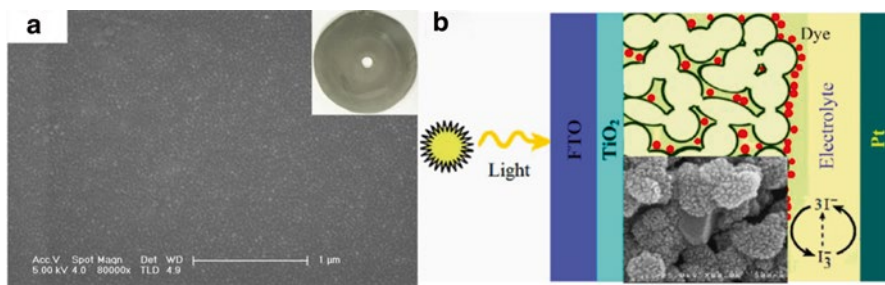


**Fig. 8.5** (a)  $\text{TiO}_2$  film rotating disk prepared by sol-gel method. Reprinted with permission from Ref. [88] Copyright 2008 American Chemical Society; (b) Coral-like  $\text{TiO}_2$  film prepared by sol-gel method and its application in DSSC. Reprinted with permission from Ref. [102] Copyright 2013 American Chemical Society

mass transfer. With changing electrolyte and controlling anodization time, different coral-like TiO<sub>2</sub> films can be obtained [105, 106]. Coral-like TiO<sub>2</sub> films could also be synthesized through anodization using H<sub>2</sub>SO<sub>4</sub> as electrolyte [105]. Compared with nanotube, coral-like structure owns better mass transfer, which results in larger photo generated current and better performance on the PC degradation of dye than nanotube TiO<sub>2</sub> film and flat TiO<sub>2</sub> film prepared by sol-gel method.

H<sub>2</sub>O<sub>2</sub> direct oxidation on a Ti substrate has also been employed by researchers to synthesize TiO<sub>2</sub> film with micro structures, such as TiO<sub>2</sub> nanorods film and flower-like TiO<sub>2</sub> film [107, 108]. Li et al. have synthesized flower-like TiO<sub>2</sub> film on a rotating disk surface using H<sub>2</sub>O<sub>2</sub> direct oxidation with the assistance of [Bmin]BF<sub>4</sub> ionic liquid [108]. The obtained film not only exhibited efficient decomposition of RhB, but was also stable on Ti substrate during the PC reaction in rotating disk reactor. The mesoporous structure may lead not only to well mass transfer, but also to enhancement of light harvesting and reactant adsorption. The UV adsorption on flower-like film is much higher than that on non-flower-like film.

The calcination temperature greatly influences the PC activity of the TiO<sub>2</sub> film. The PC performance on dye degradation enhanced with the calcination temperature increasing from 250 to 550 °C and dropped down at 650 °C. At 250 °C, TiO<sub>2</sub> is still amorphous. Anatase TiO<sub>2</sub> can be formed when the calcination temperature is higher than 350 °C and the best anatase TiO<sub>2</sub> is obtained at 550 °C. Then TiO<sub>2</sub> turns from anatase to rutile with calcination temperature further increasing to 650 °C. It has been reported that anatase TiO<sub>2</sub> owns better PC activity than rutile and amorphous TiO<sub>2</sub> [109]. However, in a PEC process, because Ti is always used as substrate, the resistance generated on Ti substrate surface caused by high temperature calcination should also be considered. It has been found that nearly no resistance (less than 0.3 Ω cm<sup>-2</sup>) existing on Ti substrate when the calcination temperature is lower than 450 °C, while 38,000 Ω cm<sup>-2</sup> resistance is measured when the Ti substrate is calcined at 550 °C and the Ti surface is almost non-conduction after calcination at 650 °C [92]. The existence of large resistance between TiO<sub>2</sub> and Ti substrate greatly influences the effect of bias potential in PEC system. Though the PC activity obtained by TiO<sub>2</sub>/Ti disk calcined at 550 °C is better than that obtained by disk calcined at 450 °C, the PEC activity of 550 °C calcined film is worse. The calcination temperature should be carefully optimized if a bias potential is applied in a rotating disk PC reactor.

In order to utilize visible light, Bi-based compounds films were synthesized and applied in rotating disk PC reactor. Bi<sub>2</sub>O<sub>3</sub> film with the band gap of 2.8 eV has been coated on Ti rotating disk by sol-gel method [110]. However, it does not exhibit very good PC performance on RhB removal under visible light due to the extremely fast recombination rate of photo-generated electrons and holes. Further modification of Bi<sub>2</sub>O<sub>3</sub> film is needed to improve its PC activity. Ordered macroporous Bi<sub>2</sub>O<sub>3</sub>/TiO<sub>2</sub> film coated on a rotating disk was prepared by sol-gel method in the presence of polystyrene (PS) microspheres as a template by Huo's group (Fig. 8.6) [111]. The film shows spectral response in visible light due to the low band gap energy of Bi<sub>2</sub>O<sub>3</sub> and enhancement of photo-generated electrons and holes separation due to the Bi<sub>2</sub>O<sub>3</sub>-TiO<sub>2</sub> hetero-junctions. Meanwhile, the ordered macroporous also promotes

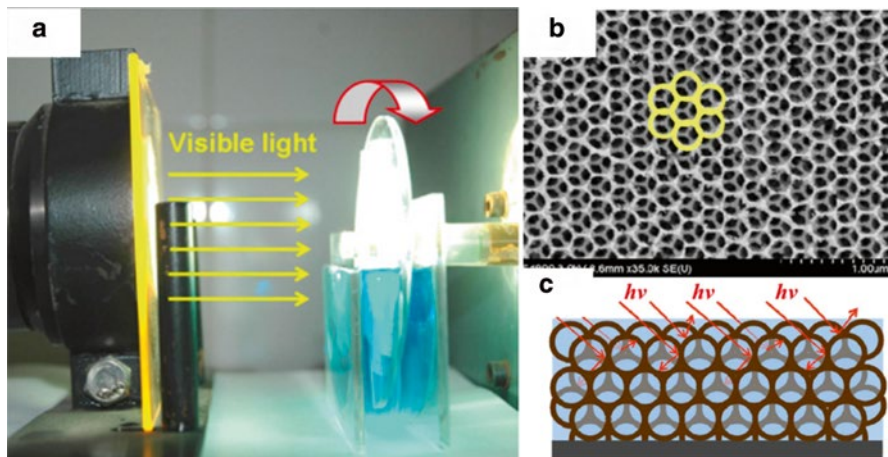


**Fig. 8.6** (a) Rotating disk PC reactor with  $\text{Bi}_2\text{O}_3/\text{TiO}_2$  film, (b) FESEM image of  $\text{Bi}_2\text{O}_3/\text{TiO}_2$  film, (c) light harvest in macropores of  $\text{Bi}_2\text{O}_3/\text{TiO}_2$  film. Reprinted from Ref. [111] with permission from Elsevier

mass transfer and light-harvesting via multiple reflections. The film exhibited high activity in aqueous visible-light-driven PC degradation of single and mixed dyes in the rotating disk PC reactor.

Using  $\text{Bi}_2\text{O}_3$  film as precursor to react with halogen ions in acidic condition, Li et al. have synthesized hierarchical structured  $\text{BiOX}$  ( $X=\text{Cl}, \text{Br}$ ) films on a rotating disk surface (Fig. 8.7a, b) [112, 113]. Compared with sol-gel prepared  $\text{TiO}_2$  film and  $\text{Bi}_2\text{O}_3$  film,  $\text{BiOX}$  film exhibited better RhB degradation efficiency under UV irradiation, which may be due to its large surface area. Because the band gap energy of  $\text{BiOCl}$  (3.2 eV) is wider than that of  $\text{BiOBr}$  (2.5 eV), the UV oxidation activity of  $\text{BiOCl}$  film is stronger than that of  $\text{BiOBr}$  film. Meanwhile, the  $\text{BiOX}$  film owns strong RhB adsorption capacity due to its unique hierarchical structure. RhB was also removed under visible light through dye sensitization process. Because the band gap energy of  $\text{BiOBr}$  film is suitable for visible light excitation, part of visible light can be utilized to excite  $\text{BiOBr}$  film to directly oxidize RhB, which resulted in better RhB removal of  $\text{BiOBr}$  film under visible light. Other dyes could also be degraded both under UV and visible light (Fig. 8.7c). However, because the  $\text{BiOX}$  film was negatively charged, cationic dyes such as RhB are much easier to adsorb than anionic dyes such as Methyl Orange (MO), resulting in different color removal efficiencies under visible light irradiation (Fig. 8.7d, e). Besides  $\text{Bi}_2\text{O}_3$  film, Bi film prepared by RF magnetron sputter or electrochemical reduction can also be employed as precursor to react with chloride ion to synthesize  $\text{BiOCl}$  film [114, 115]. However, as a new kind of photocatalytic material, the mechanical strength and the chemical stabilities including the influences of pH and inorganic ions in solution still need to be improved for these  $\text{BiOX}$  films.

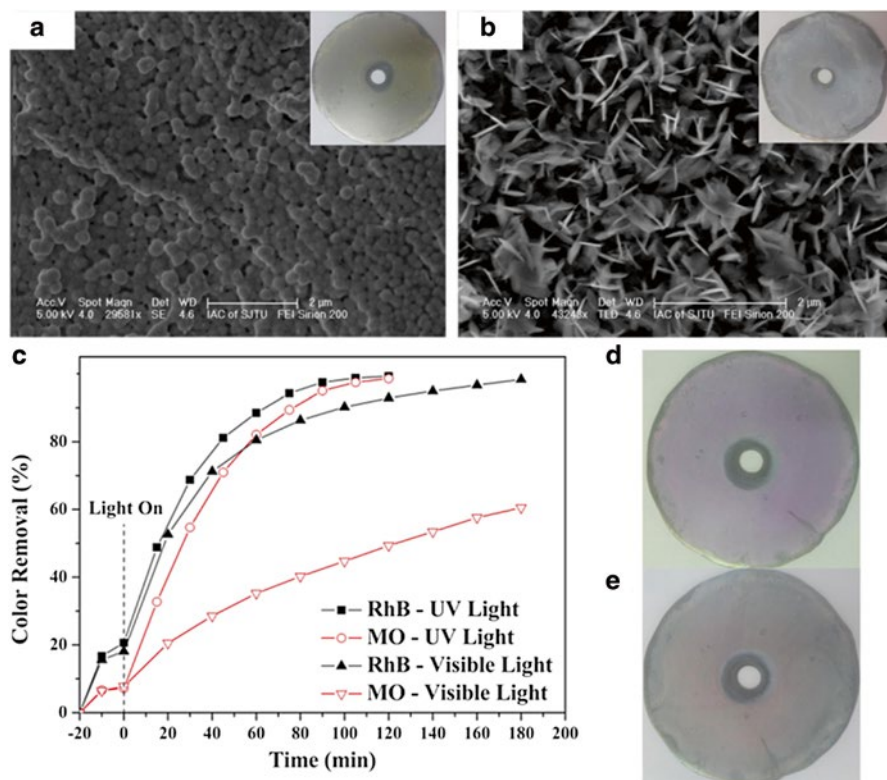


**Fig. 8.7** FESEM image of (a)  $\text{Bi}_2\text{O}_3$  film and (b)  $\text{BiOCl}$  film [112]; (c) Comparison of PC degradation of RhB and MO under UV and visible light irradiation in a  $\text{BiOBr}$  rotating disk reactor; Photographic images of (d) RhB and (e) MO adsorbed  $\text{BiOBr}$  film disks. Reprinted from Ref. [113] with permission from Elsevier

## 8.5 Macro Structure of the Rotating Disk

To change the planar structured rotating disk to a wedge structured disk can not only increase the illuminated area, but also recapture reflected photons (Fig. 8.8a, b). Comparing the incident light reflectivity on planar and wedge sol-gel prepared  $\text{TiO}_2/\text{Ti}$  disks (Fig. 8.8c), we have found that the reflectivity was more than 30 % on planar disk surface and it only less than 1 % on wedge disks [116]. It is also found that reflectivity may suffer with further decrease of width–height ratio. Meanwhile, disk surface also increases with the decrease of width–height ratio. Deep investigation in degradation of RhB with wedge and planar rotating disk reactor also finds that multiple reflections plays an important role in PC performance improvement. In addition, with decrease of width–height ratio, contribution from multiple reflections decreases and that from the enlarged surface area becomes more prominent. However, with decrease of width–height ratio, the angle between the neighboring

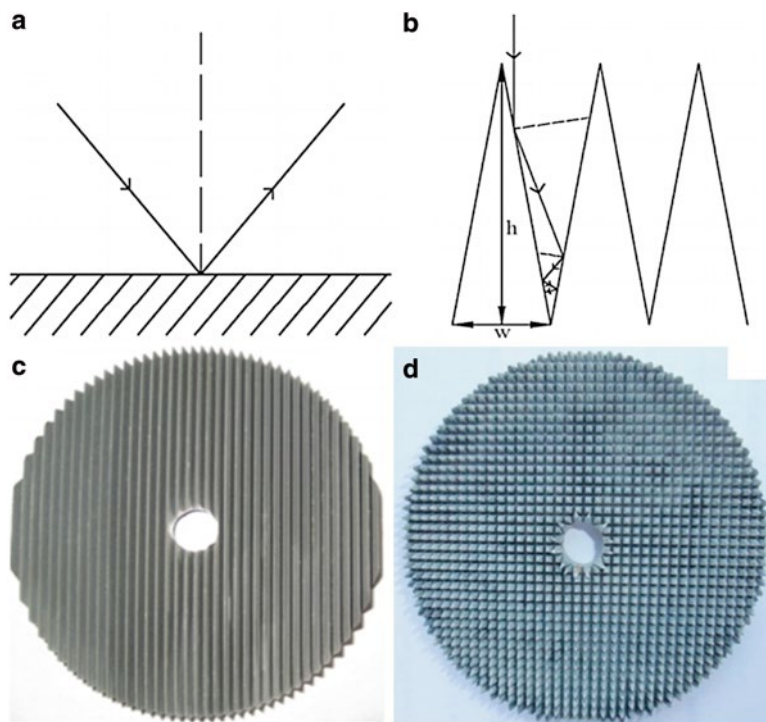


**Fig. 8.8** Schematic illustration of (a) single reflection on planar surface and (b) multiple reflections on sledge surface. Top views of (c) wedge and (d) pyramid rotating disks. Reproduced with permission from Ref. [116]. Copyright 201 American Chemical Society

wedge walls also decrease. For example, when the ratio is 1:4, the angle is only less than  $14^\circ$ . Such a small angle may hold-up solution among the gaps during disk rotation. This hold-up solution will greatly influence mass transfer and light absorption, resulting in slight decrease of RhB removal.

The pyramid disk has the same surface area as the wedge disk when they have the same width–height ratio, but exhibits stronger light-harvesting property (Fig. 8.8d). However, more solution will be hold-up in the narrow gaps between pyramids, especially for the pyramid with low width–height ratio. This greatly restricts mass transfer and light absorption, resulting in a worse PC performance than wedge disk [48].

Due to its high PC performance, the wedge structured rotating disk PC reactor was employed by researchers to post-treat actual textile wastewater collected after activated sludge treatment [117]. The COD content in effluent could be effectively reduced from  $380 \text{ mgO}_2 \text{ L}^{-1}$  to less than  $100 \text{ mgO}_2 \text{ L}^{-1}$  in 3 h treatment. Compared with planar disk, benefit from high light utilization efficiency, the wedge rotating disk reactor could compensate COD removal inhibition caused by the large amount of anions ( $\text{NO}_3^-$ ,  $\text{SO}_4^{2-}$ , and  $\text{Cl}^-$ ) existing in the wastewater. Meanwhile, these

**Table 8.2** Comparison of actual wastewater treatment with different UV PC reactors

Wastewater and initial COD	PC reactor	UV power (W)	COD removal	Ref
Textile wastewater, 380 mgO <sub>2</sub> L <sup>-1</sup>	Wedge rotating disk reactor, 50 ml	22	5 h, 85 %	[117]
Textile wastewater, 880 mgO <sub>2</sub> L <sup>-1</sup>	Wedge rotating disk reactor, 50 ml	22	6 h, 88 %	[117]
Textile wastewater, 380 mgO <sub>2</sub> L <sup>-1</sup>	Rotating disk reactor, 50 ml	22	5 h, 38 %	[117]
Textile wastewater, 880 mgO <sub>2</sub> L <sup>-1</sup>	Rotating disk reactor, 50 ml	22	6 h, 54 %	[117]
Olive mill wastewater, 1400 mgO <sub>2</sub> L <sup>-1</sup>	Inclined plate reactor, 300 ml	30	24 h, 38 %	[118]
Textile wastewater, 404 mgO <sub>2</sub> L <sup>-1</sup>	Cylindrical reactor, 350 ml	400	4 h, 40 %	[37]
Paper mill wastewater, 215 mgO <sub>2</sub> L <sup>-1</sup>	Cylindrical reactor, 350 ml	500	3 h, 80 %	[39]
Petroleum wastewater, 170–180 mgO <sub>2</sub> L <sup>-1</sup>	Cylindrical reactor, 850 ml	400	4 h, 90 %	[44]
Olive mill wastewater, 1000 mgO <sub>2</sub> L <sup>-1</sup>	Cylindrical reactor, 350 ml	400	3 h, 44 %	[119]

anions could be employed as electrolyte and a bias potential could be applied to further improve the PC performance. Table 8.2 shows the comparison of the result with the performances obtained by other types of PC reactors to treat actual wastewaters. For cylindrical reactor, due to absorption by solution, the UV power (more than 400 W) was much higher than that was used in the thin film PC reactor (less than 30 W). Compared to planar thin solution film reactor, COD removal efficiency obtained by the wedge rotating disk reactor was much higher and the treatment time was shorter.

## 8.6 Dual Rotating Disk PC Reactor

In order to enhance light quantum yield of photocatalyst film in rotating disk reactor, besides PEC process, a rotating disk cathode can also be connected with photoanode to fabricate dual rotating disk PC reactor. In this process, the photo-generated electrons can transfer to cathode spontaneously due to the potential existing between photo-excited photoanode and cathode. It is a very interesting system because with the change of cathode material, the potential between photoanode and cathode can be controlled. Then different electron reduction reactions can take place on cathode surface. As shown in Fig. 8.9, when a Cu disk was connect to a TiO<sub>2</sub>/Ti rotating disk to fabricate a TiO<sub>2</sub>/Ti-Cu dual rotating disk reactor, much better PC performance was obtained on dye degradation in comparison to that obtained by TiO<sub>2</sub>/Ti rotating disk PEC reactor [120]. Due to the Schottky barrier existing between TiO<sub>2</sub> and Cu

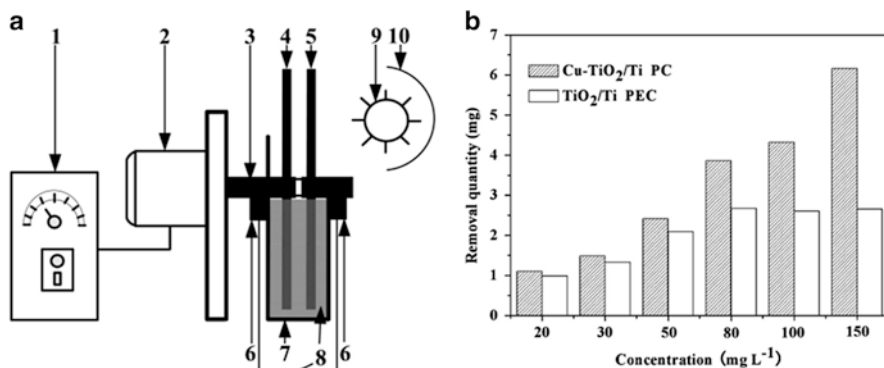


**Fig. 8.9** (a) Schematic diagram of TiO<sub>2</sub>/Ti-Cu dual rotating disks PC reactor. (1) speed controller; (2) motor; (3) axis; (4) Cu disk; (5) TiO<sub>2</sub>/Ti disk; (6) carbon brush; (7) reaction cell; (8) wastewater; (9) UV lamp; (10) aluminum foil; (b) Absolute quantity of RhB removed using TiO<sub>2</sub>/Ti PEC and TiO<sub>2</sub>/Ti-Cu PC procedures to treat RhB solutions at different concentration levels. Reproduced with permission from Ref. [120]. Copyright 2009 American Chemical Society

cathode, approximately 100 mV of potential and 10 μA of current were measured in external circuit during PC treatment. At this potential, O<sub>2</sub> double-electron reduction took place on Cu cathode to generate H<sub>2</sub>O<sub>2</sub>,



which improved dye degradation efficiency.

When noble metal, such as Pt is used as cathode, much larger potential can be obtained between photo-excited photoanode and cathode. It is reported that more than 0.6 V potential can be generated in a TiO<sub>2</sub>/Ti-Pt system [92]. At this potential, O<sub>2</sub> four-electron reduction takes place to form H<sub>2</sub>O instead of H<sub>2</sub>O<sub>2</sub> at Pt cathode



Then it is a dual rotating disk PFC to degrade organic pollutants and generate electricity simultaneously. For example, in a BiOBr/Ti-Pt rotating disk PFC, the open circuit voltage can achieve as large as 0.7–0.8 V [113]. Because O<sub>2</sub> four-electron reduction took place on cathode, the short circuit current detected in external circuit was also much larger than that detected in TiO<sub>2</sub>/Ti-Cu dual rotating disk reactor (Fig. 8.10a). Meanwhile, compared with BiOBr/Ti rotating disk reactor, the BiOBr/Ti-Pt rotating disk PFC can effectively improve the separation of photo-generated electrons and holes and enhance PC performance due to the large open circuit voltage generated (Fig. 8.10b).

To further enhance the potential between photoanode and cathode by changing the pH condition in anode and cathode cells, H<sub>2</sub> can also be generated on Pt cathode in the absence of O<sub>2</sub>



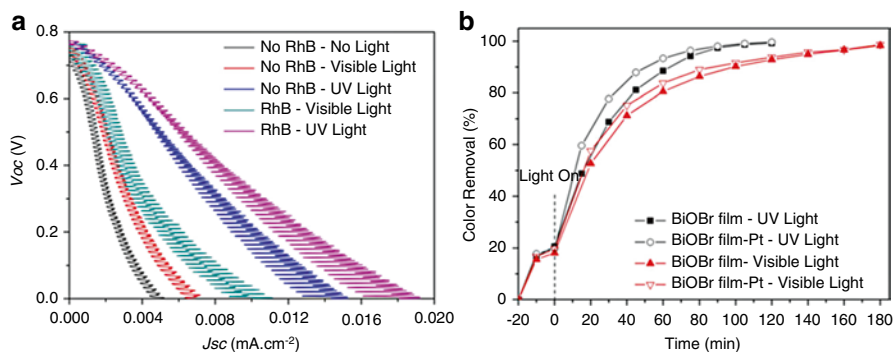


**Fig. 8.10** (a) Current–voltage (J–V) plots for BiOBr/Ti-Pt rotating disk PFC with and without RhB as “fuel” under UV and visible light irradiation. (b) Color removals of RhB in BiOBr/Ti rotating disk PC reactor and BiOBr/Ti-Pt rotating disk PFC. Reprinted from Ref. [109] with permission from Elsevier

A high efficient rotating disk PFC for simultaneous production of  $\text{H}_2$  and electricity with the degradation of high concentration dye wastewater was established in last year [121]. The hydrogen generation rate and the current obtained in this rotating disk PFC were ten times higher than that obtained in conventional immersed reactor.

## 8.7 Conclusion

In this chapter, the bottlenecks existing in PC wastewater treatment application are analyzed. Light reflection, including the reflection on catalyst surface and on solution surface, and light absorption by solution causes poor light utilization efficiency. Meanwhile, the recombination of photo-generated electrons and holes causes the low light quantum yield. Poor light utilization efficiency and low light quantum yield are the two main bottlenecks that restrict the application of PC technique in wastewater treatment. A rotating disk PC reactor is a kind of thin film reactor that can effectively reduce the light loss caused by solution adsorption. The latest developments of this reactor are also carefully introduced in this chapter, including the photocatalyst films, rotating disk macro structures and the utilization of photo-generated electrons. With these developments, the light utilization efficiency and light quantum yield can be enhanced to some extent. Though actual textile wastewater has already been post-treated in a wedge structured rotating disk PC reactor and good results were obtained, there are still some key issues need to be solved before this technique can be really applied in wastewater treatment. These issues include:

1. Development of photocatalyst film with large surface area, high light (both UV and visible light) utilization efficiency, and strong stability (both mechanical strength and chemical stability).
2. Model establishment of rotating disk reactor, including scale-up model, series–parallel connection model and continuous–static flow model. Because the wedge

disk exhibited a much better performance, this is especially important for wedge rotating disk PC reactor.

3. More efficient utilization of electrons in dual rotating disk PC reactor. This can not only improve PC performance, but can also generate useful power, such as electricity and  $H_2$ .

With the combination of high active photocatalyst and high efficient PC reactor, we believe that PC technique can be really applied in wastewater treatment in the near future.

**Acknowledgments** Financial supports from the Natural Science Foundation of China (Project No. 21477076, 51278295, and 20937003), China Postdoctoral Science Foundation (2015M581624) are gratefully acknowledged.

## References

1. Garcia JC, Oliveria JL, Silva AEC et al (2007) Comparative study of the degradation of real textile effluents by photocatalytic reactions involving UV/TiO<sub>2</sub>/H<sub>2</sub>O<sub>2</sub> and UV/Fe<sup>2+</sup>/H<sub>2</sub>O<sub>2</sub> systems. *J Hazard Mater* 147:105–110
2. Ahmed S, Rasul MG, Marten WN et al (2010) Heterogeneous photocatalytic degradation of phenols in wastewater: a review on current status and developments. *Desalination* 261:3–18
3. Ahmed S, Rasul MG, Brown R et al (2011) Influence of parameters on the heterogeneous photocatalytic degradation of pesticide and phenolic contaminants in wastewater: a short review. *J Environ Manage* 92:311–330
4. Chong MN, Jin B, Chow CWK et al (2010) Recent developments in photocatalytic water treatment technology: a review. *Water Res* 44:2997–3027
5. Konstantinou IK, Albanis TA (2004) TiO<sub>2</sub>-assisted photocatalytic degradation of azo dyes in aqueous solution: kinetic and mechanistic investigations: a review. *Appl Catal B Environ* 49:1–14
6. Akpan UG, Hameed BH (2009) Parameters affecting the photocatalytic degradation of dyes using TiO<sub>2</sub>-based photocatalysts: a review. *J Hazard Mater* 170:520–529
7. Zhao J, Yang X (2003) Photocatalytic oxidation for indoor air purification: a literature review. *Build Environ* 38:645–654
8. Mo J, Zhang Y, Xu Q et al (2009) Photocatalytic purification of volatile organic compounds in indoor air: a literature review. *Atmos Environ* 43:2229–2246
9. Chen H, Nanayakkara CE, Grassian VH (2012) Titanium dioxide photocatalysis in atmospheric chemistry. *Chem Rev* 112:5919–5948
10. Li D, Haneda H, Hishita S et al (2005) Visible-light-driven N-F-Codoped TiO<sub>2</sub> photocatalysts. 2. Optical characterization, photocatalysis, and potential application to air purification. *Chem Mater* 17:2596–2602
11. Wang S, Ang HM, Tade MO (2007) Volatile organic compounds in indoor environment and photocatalytic oxidation: state of the art. *Environ Int* 33:694–705
12. Chen J, Poon C (2009) Photocatalytic construction and building materials: from fundamentals to applications. *Build Environ* 44:1899–1906
13. Parkin IP, Palgrave RG (2005) Self-cleaning coating. *J Mater Chem* 15:1689–1695
14. Zhang L, Dillert R, Bahnemann D et al (2012) Photo-induced hydrophilicity and self-cleaning: models and reality. *Energy Environ Sci* 5:7491–7507
15. Euvananont C, Junin C, Inpor K et al (2008) TiO<sub>2</sub> optical coating layers for self-cleaning applications. *Ceram Int* 34:1067–1071

16. Tricoli A, Righettoni M, Pratsinis SE (2009) Anti-fogging nanofibrous SiO<sub>2</sub> and nanostructured SiO<sub>2</sub>-TiO<sub>2</sub> films made by rapid flame deposition and in situ annealing. *Langmuir* 25:12578–12584
17. Zhang H, Li Z, Liu L et al (2009) Mg<sup>2+</sup>/Na<sup>+</sup>-doped rutile TiO<sub>2</sub> nanofiber mats for high-speed and anti-fogged humidity sensors. *Talanta* 79:953–958
18. Lai Y, Tang Y, Gong J et al (2012) Transparent superhydrophobic/superhydrophilic TiO<sub>2</sub>-based coatings for self-cleaning and anti-fogging. *J Mater Chem* 22:7420–7426
19. Keller N, Ducamp M-N, Robert D et al (2013) Ethylene removal and fresh product storage: a challenge at the frontiers of chemistry. Toward an approach by photocatalytic oxidation. *Chem Rev* 113:5029–5070
20. Chawengkijwanich C, Hayata Y (2008) Development of TiO<sub>2</sub> powder-coated food packaging film and its ability to inactivate *Escherichia coli* in vitro and in actual tests. *Int J Food Microbiol* 123:288–292
21. Ye S, Tian Q, Song X et al (2009) Photoelectrocatalytic degradation of ethylene by a combination of TiO<sub>2</sub> and activated carbon felts. *J Photochem Photobiol A Chem* 208:27–35
22. Dastjerdi R, Montazer M (2010) A review on the application of inorganic nano-structured materials in the modification of textiles: focus on anti-microbial properties. *Colloid Surface B Biointerfaces* 79:5–18
23. Yu JC, Ho W, Lin J et al (2003) Photocatalytic activity, antibacterial effect, and photoinduced hydrophilicity of TiO<sub>2</sub> films coated on a stainless steel substrate. *Environ Sci Technol* 37:2296–2301
24. Fu G, Vary PS, Lin C-T (2005) Anatase TiO<sub>2</sub> nanocomposites for antimicrobial coatings. *J Phys Chem B* 109:8889–8898
25. Zhu Y, Shi J, Zhang Z et al (2002) Development of a gas sensor utilizing chemiluminescence on nanosized titanium dioxide. *Anal Chem* 74:120–124
26. Zheng Q, Zhou B, Bai J et al (2008) Self-organized TiO<sub>2</sub> nanotube array sensor for the determination of chemical oxygen demand. *Adv Mater* 20:1044–1049
27. Wang G, Wang Q, Lu W et al (2006) Photoelectrochemical study on charge transfer properties of TiO<sub>2</sub>-B nanowires with an application as humidity sensors. *J Phys Chem B* 110:22029–22034
28. Bao S-J, Li CM, Zang J-F et al (2008) New nanostructured TiO<sub>2</sub> for direct electrochemistry and glucose sensor applications. *Adv Funct Mater* 18:591–599
29. Hagfeldt A, Boschloo G, Sun L et al (2010) Dye-sensitized solar cells. *Chem Rev* 110:6595–6663
30. He H, Liu C, Dubois KD et al (2012) Enhanced charge separation in nanostructured TiO<sub>2</sub> materials for photocatalytic and photovoltaic applications. *Ind Eng Chem Res* 51:11841–11849
31. Mor GK, Shankar K, Paulose M et al (2006) Use of highly-ordered TiO<sub>2</sub> nanotube arrays in dye-sensitized solar cells. *Nano Lett* 6:215–218
32. Liu B, Aydil ES (2009) Growth of oriented single-crystalline rutile TiO<sub>2</sub> nanorods on transparent conducting substrates for dye-sensitized solar cells. *J Am Chem Soc* 131:3985–3990
33. Chen X, Shen S, Guo L et al (2010) Semiconductor-based photocatalytic hydrogen generation. *Chem Rev* 110:6503–6570
34. Ni M, Leung MKH, Leung DYC et al (2007) A review and recent developments in photocatalytic water-splitting using TiO<sub>2</sub> for hydrogen production. *Renew Sust Energ Rev* 11:401–425
35. Yu J, Qi L, Jaroniec M (2010) Hydrogen production by photocatalytic water splitting over Pt/TiO<sub>2</sub> nanosheets with exposed (001) facets. *J Phys Chem C* 114:13118–13125
36. Wang G, Wang H, Ling Y et al (2011) Hydrogen-treated TiO<sub>2</sub> nanowire arrays for photoelectrochemical water splitting. *Nano Lett* 11:3026–3033
37. Pekakis PA, Xekoukoulotakis NP, Mantzavinos D (2006) Treatment of textile dyehouse wastewater by TiO<sub>2</sub> photocatalysis. *Water Res* 40:1276–1286
38. Rao NN, Chaturvedi V, Puma GL (2012) Novel pebble bed photocatalytic reactor for solar treatment of textile wastewater. *Chem Eng J* 184:90–97

39. Yuan R, Guan R, Liu P et al (2007) Photocatalytic treatment of wastewater from paper mill by TiO<sub>2</sub> loaded on activated carbon fibers. *Colloid Surface A Physicochem Eng Aspects* 293:80–86
40. Ghaly MY, Jamil TS, El-Seesy IE et al (2011) Treatment of highly polluted paper mill wastewater by solar photocatalytic oxidation with synthesized nano TiO<sub>2</sub>. *Chem Eng J* 168:446–454
41. Baransi K, Dubowski Y, Sabbah I (2012) Synergetic effect between photocatalytic degradation and adsorption processes on the removal of phenolic compounds from olive mill wastewater. *Water Res* 46:789–798
42. Badawy MI, Gohary FE, Ghaly MY et al (2009) Enhancement of olive mill wastewater biodegradation by homogeneous and heterogeneous photocatalytic oxidation. *J Hazard Mater* 169:673–679
43. Ugurlu M, Karaoglu MH (2011) TiO<sub>2</sub> supported on sepiolite: preparation, structural and thermal characterization and catalytic behavior in photocatalytic treatment of phenol and lignin from olive mill wastewater. *Chem Eng J* 166:859–867
44. Saeni J, Nejati H (2007) Enhanced photocatalytic degradation of pollutants in petroleum refinery wastewater under mild conditions. *J Hazard Mater* 148:491–495
45. Chong MN, Jin B (2012) Photocatalytic treatment of high concentration carbamazepine in synthetic hospital wastewater. *J Hazard Mater* 199–200:135–142
46. Paz Y (2010) Application of TiO<sub>2</sub> photocatalysis for air treatment: patents' overview. *Appl Catal B Environ* 99:448–460
47. Ochiai T, Fujishima A (2012) Photoelectrochemical properties of TiO<sub>2</sub> photocatalyst and its applications for environmental purification. *J Photochem Photobiol C Photochem Rev* 13:247–262
48. Li K, Yang C, Wang Y et al (2012) A high-efficient rotating disk photoelectrocatalytic (PEC) reactor with macro light harvesting pyramid-surface electrode. *AIChE J* 58:2448–2455
49. Dionysiou DD, Balasubramanian G, Suidan MT et al (2000) Rotating disk photocatalytic reactor: development, characterization, and evaluation for the destruction of organic pollutants in water. *Water Res* 34:2927–2940
50. Dionysiou DD, Suidan MT, Baudin I et al (2002) Oxidation of organic contaminants in a rotating disk photocatalytic reactor: reaction kinetics in the liquid phase and the role of mass transfer based on the dimensionless Damköhler number. *Appl Catal B Environ* 38:1–16
51. Zhang L, Kanki T, Sano N et al (2001) Photocatalytic degradation of organic compounds in aqueous solution by a TiO<sub>2</sub>-coated rotating-drum reactor using solar light. *Sol Energy* 70:331–337
52. Damodar RA, Swaminathan T (2008) Performance evaluation of a continuous flow immobilized rotating tube photocatalytic reactor (IRTPR) immobilized with TiO<sub>2</sub> catalyst for azo dye degradation. *Chem Eng J* 144:59–66
53. Boiarkina I, Pedron S, Patterson DA (2011) An experimental and modeling investigation of the effect of the flow regime on the photocatalytic degradation of methylene blue on a thin film coated ultraviolet irradiated spinning disc reactor. *Appl Catal B Environ* 110:14–24
54. Boiarkina I, Norris S, Patterson DA (2013) The case for the photocatalytic spinning disc reactor as a process intensification technology: comparison to an annular reactor for the degradation of methylene blue. *Chem Eng J* 225:752–765
55. Boiarkina I, Norris S, Patterson DA (2013) Investigation into the effect of flow structure on the photocatalytic degradation of methylene blue dehydroabietic acid in a spinning disc reactor. *Chem Eng J* 222:159–171
56. Xu Y, Jia J, Zhong D et al (2009) Degradation of dye wastewater in a thin-film photoelectrocatalytic (PEC) reactor with slant-placed TiO<sub>2</sub>/Ti anode. *Chem Eng J* 150:302–307
57. Xu Y, Zhong D, Jia J et al (2013) Dual slant-placed electrodes thin-film photocatalytic reactor: enhanced dye degradation efficiency by self-generated electric field. *Chem Eng J* 225:138–143
58. Chan AHC, Chan CK, Barford JP et al (2003) Solar photocatalytic thin film cascade reactor for treatment of benzoic acid containing wastewater. *Water Res* 37:1125–1135

59. Stephan B, Ludovic L, Dominique W (2011) Modelling of a falling thin film deposited photocatalytic step reactor for water purification: pesticide treatment. *Chem Eng J* 169:216–225
60. Zayani G, Bousselmi L, Mhenni F et al (2009) Solar photocatalytic degradation of commercial textile azo dyes: performance of pilot plant scale thin film fixed-bed reactor. *Desalination* 246:344–352
61. Zhang Z, Anderson WA, Moo-Young M (2004) Experimental analysis of a corrugated plate photocatalytic reactor. *Chem Eng J* 99:145–152
62. Zhang L, Anderson WA, Zhang Z (2006) Development and modeling of a rotating disc photocatalytic reactor for wastewater treatment. *Chem Eng J* 121:125–134
63. Donaldson AA, Ye A, McEvoy JG et al (2013) Rotating corrugated photoreactor design: experimental and computational analysis of TiO<sub>2</sub>-based photocatalysis. *AIChE J* 59:560–570
64. Yang L, Luo S, Li Y et al (2010) High efficient photocatalytic degradation of p-nitrophenol on a unique Cu<sub>2</sub>O/TiO<sub>2</sub> p-n heterojunction network catalyst. *Environ Sci Technol* 44:7641–7646
65. Bessekhouad Y, Robert D, Weber J-V (2005) Photocatalytic activity of Cu<sub>2</sub>O/TiO<sub>2</sub>, Bi<sub>2</sub>O<sub>3</sub>/TiO<sub>2</sub> and ZnMn<sub>2</sub>O<sub>4</sub>/TiO<sub>2</sub> heterojunctions. *Catal Today* 101:315–321
66. Bessekhouad Y, Robert D, Weber JV (2004) Bi<sub>2</sub>S<sub>3</sub>/TiO<sub>2</sub> and CdS/TiO<sub>2</sub> heterojunctions as an available configuration for photocatalytic degradation of organic pollutant. *J Photochem Photobiol A Chem* 163:569–580
67. Yu J, Xiong J, Cheng B et al (2005) Fabrication and characterization of Ag-TiO<sub>2</sub> multiphase nanocomposite thin films with enhanced photocatalytic activity. *Appl Catal B Environ* 60:211–221
68. Sakthivel S, Shankar MV, Palanichamy M et al (2004) Enhancement of photocatalytic activity by metal deposition: characterization and photonic efficiency of Pt, Au and Pd deposited on TiO<sub>2</sub> catalyst. *Water Res* 38:3001–3008
69. Li FB, Li XZ (2002) The enhancement of photodegradation efficiency using Pt-TiO<sub>2</sub> catalyst. *Chemosphere* 48:1103–1111
70. Yu Y, Yu JC, Yu J-G et al (2005) Enhancement of photocatalytic activity of mesoporous TiO<sub>2</sub> by using carbon nanotubes. *Appl Catal A Gen* 289:186–196
71. Zhang L-W, Fu H-B, Zhu Y-F (2008) Efficient TiO<sub>2</sub> photocatalysts from surface hybridization of TiO<sub>2</sub> particles with graphite-like carbon. *Adv Funct Mater* 18:2180–2189
72. Zhou K, Zhu Y, Yang X et al (2011) Preparation of graphene-TiO<sub>2</sub> composites with enhanced photocatalytic activity. *New J Chem* 35:353–359
73. Kim DH, Anderson MA (1994) Photoelectrocatalytic degradation of formic acid using a porous TiO<sub>2</sub> thin-film electrode. *Environ Sci Technol* 28:479–483
74. Li XZ, Liu HS (2005) Development of an E-H<sub>2</sub>O<sub>2</sub>/TiO<sub>2</sub> photoelectrocatalytic oxidation system for water and wastewater treatment. *Environ Sci Technol* 39:4614–4620
75. Lianos P (2011) Production of electricity and hydrogen by photocatalytic degradation of organic wastes in a photoelectrochemical cell: the concept of the Photofuelcell: a review of a re-emerging research field. *J Hazard Mater* 185:575–590
76. Kaneko M, Nemoto J, Ueno H et al (2006) Photoelectrochemical reaction of biomass and bio-related compounds with nanoporous TiO<sub>2</sub> film photoanode and O<sub>2</sub>-reducing cathode. *Electrochem Commun* 8:336–340
77. Li K, Xu Y, He Y et al (2013) Photocatalytic fuel cell (PFC) and dye-photosensitization photocatalytic fuel cell (DSPFC) with BiOCl/Ti photoanode under UV and visible light irradiation. *Environ Sci Technol* 47:3490–3497
78. Bahnemann D (2004) Photocatalytic water treatment: solar energy applications. *Sol Energy* 77:445–459
79. Malato S, Fernández-Ibáñez P, Maldonado MI et al (2009) Decontamination and disinfection of water by solar photocatalysis: recent overview and trends. *Catal Today* 147:1–59
80. Cong Y, Tian BZ, Zhang JL et al (2011) Improving the thermal stability and photocatalytic activity of nanosized titanium dioxide via La<sup>3+</sup> and N co-doping. *Appl Catal B Environ* 101:376–381

81. Chang S, Liu W (2011) Surface doping is more beneficial than bulk doping to the photocatalytic activity of vanadium-doped TiO<sub>2</sub>. *Appl Catal B Environ* 101:333–342
82. Wang Y, Feng CX, Zhang JJ et al (2010) Enhanced visible light photocatalytic activity of N-doped TiO<sub>2</sub> in relation to single-electron-trapped oxygen vacancy and doped-nitrogen. *Appl Catal B Environ* 100:84–90
83. Huo YN, Yang XL, Zhu J et al (2011) Highly active and stable CdS-TiO<sub>2</sub> visible photocatalyst prepared by in situ sulfurization under supercritical conditions. *Appl Catal B Environ* 106:69–75
84. Prier CK, Rankic DA, MacMillan DWC (2013) Visible light photoredox catalysis with transition metal complexes: applications in organic synthesis. *Chem Rev* 113:5322–5363
85. Maeda K, Domen K (2010) Solid solution of GaN and ZnO as a stable photocatalyst for overall water splitting under visible light. *Chem Mater* 22:612–623
86. Wu T, Liu G, Zhao J et al (1998) Photoassisted degradation of dye pollutants. V. Self-photosensitized oxidative transformation of Rhodamine B under visible light irradiation in aqueous TiO<sub>2</sub> dispersions. *J Phys Chem B* 102:5845–5851
87. Zhao J, Wu T, Wu K et al (1998) Photoassisted degradation of dye pollutants. 3. Degradation of the cationic dye rhodamine B in aqueous anionic surfactant/TiO<sub>2</sub> dispersions under visible light irradiation: evidence for the need of substrate adsorption on TiO<sub>2</sub> particles. *Environ Sci Technol* 32:2394–2400
88. Xu Y, He Y, Cao X et al (2008) TiO<sub>2</sub>/Ti rotating disk photoelectrocatalytic (PEC) reactor: a combination of highly effective thin-film PEC and conventional PEC process on a single electrode. *Environ Sci Technol* 42:2612–2617
89. Zeevalkink JA, Kelderman P, Bouelhouwer C (1978) Liquid film thickness in a rotating disc gas-liquid contactor. *Water Res* 12:577–581
90. Dionysiou DD, Burbano AA, Suidan MT (2002) Effect of oxygen in a thin-film rotating disk photocatalytic reactor. *Environ Sci Technol* 36:3834–3843
91. Yuan S-J, Sheng G-P, Li W-W et al (2010) Degradation of organic pollutants in a photoelectrocatalytic system enhanced by a microbial fuel cell. *Environ Sci Technol* 44:5575–5580
92. Li K, Zhang H, Tang T et al (2014) Optimization and application of TiO<sub>2</sub>/Ti-Pt photo fuel cell (PFC) to effectively generate electricity and degrade organic pollutants simultaneously. *Water Res* 62:1–10
93. Tian G, Chen Y, Zhou W et al (2011) 3D hierarchical flower-like TiO<sub>2</sub> nanostructure: morphology control and its photocatalytic property. *CrystEngComm* 13:2994–3000
94. Nguyen-Phan T, Kim EJ, Hahn SH et al (2011) Synthesis of hierarchical rose bridal bouquet- and humming-top-like TiO<sub>2</sub> nanostructures and their shape-dependent degradation efficiency of dye. *J Colloid Interf Sci* 356:138–144
95. Wu X, Lu GQ, Wang L (2011) Shell-in-shell TiO<sub>2</sub> hollow spheres synthesized by one-pot hydrothermal method for dye-sensitized solar cell application. *Energy Environ Sci* 4:3565–3572
96. Yang M, Ma J, Zhang C et al (2005) General synthetic route toward functional hollow spheres with double-shelled structures. *Angew Chem Int Ed* 44:6727–6730
97. Cui Y, Liu L, Li B et al (2010) Fabrication of tunable core-shell structured TiO<sub>2</sub> mesoporous microspheres using linear polymer polyethylene glycol as templates. *J Phys Chem C* 114:2434–2439
98. Shao F, Sun J, Gao L et al (2011) Template-free synthesis of hierarchical TiO<sub>2</sub> structures and their application in dye-sensitized solar cells. *ACS Appl Mater Interfaces* 3:2148–2153
99. Zhao L, Li J, Shi Y et al (2013) Double light-scattering layer film based on TiO<sub>2</sub> hollow spheres and TiO<sub>2</sub> nanosheets: improved efficiency in dye-sensitized solar cells. *J Alloy Compd* 575:168–173
100. Fang WQ, Yang XH, Zhu H et al (2012) Yolk@shell anatase TiO<sub>2</sub> hierarchical microspheres with exposed {001} facets for high-performance dye sensitized solar cells. *J Mater Chem* 22:22082–22089

101. Dionysiou DD, Khodadoust AP, Kern AM et al (2000) Continuous-mode photocatalytic degradation of chlorinated phenols and pesticides in water using a bench-scale TiO<sub>2</sub> rotating disk reactor. *Appl Catal B Environ* 24:139–155
102. Bahramian A (2013) High conversion efficiency of dye-sensitized solar cells based on coral-like TiO<sub>2</sub> nanostructured films: synthesis and physical characterization. *Ind Eng Chem Res* 52:14837–14846
103. Zhang A, Zhou M, Han L et al (2011) The combination of rotating disk photocatalytic reactor and TiO<sub>2</sub> nanotube arrays for environmental pollutants removal. *J Hazard Mater* 186:1374–1383
104. Yao Y, Li K, Chen S et al (2012) Decolorization of rhodamine B in a thin-film photoelectrocatalytic (PEC) reactor with slant-placed TiO<sub>2</sub> nanotubes electrode. *Chem Eng J* 187:29–35
105. Mizukoshi Y, Ohtsu N, Masahashi N (2013) Structural and characteristic variation of anodic oxide on pure Ti with anodization duration. *Appl Surf Sci* 283:1018–1023
106. Hua X-S, Zhang Y-J, Ma N-H et al (2009) A new coral structure TiO<sub>2</sub>/Ti film electrode applied to photoelectrocatalytic degradation of Reactive Brilliant Red. *J Hazard Mater* 172:256–261
107. Wu J-M (2007) Photodegradation of rhodamine B in water assisted by titania nanorod thin films subjected to various thermal treatments. *Environ Sci Technol* 41:1723–1728
108. Li H, Zhang J, Chen X et al (2013) Ionic-liquid-assisted growth of flower-like TiO<sub>2</sub> film on Ti substrate with high photocatalytic activity. *J Mol Catal A Chem* 373:12–17
109. Zhu HY, Lan Y, Gao XP et al (2005) Phase transition between nanostructures of titanate and titanium dioxides via simple wet-chemical reactions. *J Am Chem Soc* 127:6730–6736
110. Li K, Yang C, Xu Y et al (2012) Effect of inorganic anions on rhodamine B removal under visible light irradiation using Bi<sub>2</sub>O<sub>3</sub>/Ti rotating disk reactor. *Chem Eng J* 211–212:208–215
111. Huo Y, Chen X, Zhang J et al (2014) Ordered macroporous Bi<sub>2</sub>O<sub>3</sub>/TiO<sub>2</sub> film coated on a rotating disk with enhanced photocatalytic activity under visible irradiation. *Appl Catal B Environ* 148–149:550–556
112. Li K, Tang Y, Xu Y et al (2013) A BiOCl film synthesis from Bi<sub>2</sub>O<sub>3</sub> film and its UV and visible light photocatalytic activity. *Appl Catal B Environ* 140–141:179–188
113. Li K, Zhang H, Tang Y et al (2015) Photocatalytic degradation and electricity generation in a rotating disk photo electrochemical cell over hierarchical structured BiOBr film. *Appl Catal B Environ* 164:82–91
114. Cao S, Guo C, Lv Y et al (2009) A novel BiOCl film with flowerlike hierarchical structures and its optical properties. *Nanotechnology* 20:275702
115. Zhang X, Liu X, Fan C et al (2013) A novel BiOCl thin film prepared by electrochemical method and its application in photocatalysis. *Appl Catal B Environ* 132–133:332–341
116. Li K, He Y, Xu Y et al (2011) Degradation of rhodamine B using an unconventional graded photoelectrode with wedge structure. *Environ Sci Technol* 45:7401–7407
117. Li K, Zhang H, He Y et al (2015) Novel wedge structured rotating disk photocatalytic reactor for post-treatment of actual textile wastewater. *Chem Eng J* 268:10–20
118. Costa JC, Alves MM (2013) Posttreatment of olive mill wastewater by immobilized TiO<sub>2</sub> photocatalysis. *Photochem Photobiol* 89:545–551
119. Chatzisyneon E, Stypas E, Bousios S et al (2008) Photocatalytic treatment of black table olive processing wastewater. *J Hazard Mater* 154:1090–1097
120. Xu Y, He Y, Jia J et al (2009) Cu-TiO<sub>2</sub>/Ti dual rotating disk photocatalytic (PC) reactor: dual electrode degradation facilitated by spontaneous electron transfer. *Environ Sci Technol* 43:6289–6294
121. Tang T, Li K, Ying D et al (2014) High efficient aqueous-film rotating disk photocatalytic fuel cell (RDPFC) with triple functions: cogeneration of hydrogen and electricity with dye degradation. *Int J Hydrogen Energy* 39:10258–10266

**Part II**  
**Doped and Surface Modified TiO<sub>2</sub>**  
**Photocatalysts**

# Chapter 9

## Application of Metal Ion Implantation for the Design of Visible Light-Responsive Titanium Oxide Photocatalysts

Hiroshi Yamashita and Yuichi Ichihashi

### 9.1 Metal Ion Implantation

The utilization of  $\text{TiO}_2$  semiconductor as photocatalyst has recently attracted a great deal of attention especially for various environmental applications [1–9]. Although  $\text{TiO}_2$  is known as one of the most stable and highly reactive photocatalysts, the new concept for the design of the unique photocatalytic system which can operate efficiently not only under UV light irradiation but also under visible light irradiation should be developed. Recently it has been successfully made the application of the ion beam technology using the accelerated metal ions to design the unique  $\text{TiO}_2$  photocatalyst realizing a breakthrough in the development of the efficient photocatalytic system and the utilization of solar light energy [3, 10–16]. Metal ions are the electronic charged atoms whose kinetic energies can be controlled by the acceleration of metal ions under the controlled electronic field. The ion beam techniques, such as an ion-implantation method and an ionized cluster beam (ICB) method, use the accelerated metal ion beam generated by applying these unique properties of metal ions. By these methods, the metal ions are accelerated in the electronic field and injected to the sample target as the ion beam (Fig. 9.1). These metal ions can have the interaction in the different manner with the sample target depending on their kinetic energy. In the case of the ion-implantation method, metal ions are

---

H. Yamashita (✉)

Division of Materials and Manufacturing Science, Graduate School of Engineering,  
Osaka University, Suita, Osaka, Japan

Elements Strategy Initiative for Catalysts & Batteries Kyoto University (ESICB),  
Kyoto University, Katsura, Kyoto, Japan

e-mail: [yamashita@mat.eng.osaka-u.ac.jp](mailto:yamashita@mat.eng.osaka-u.ac.jp)

Y. Ichihashi

Department of Chemical Science and Engineering, Graduate School of Engineering,  
Kobe University, Kobe, Hyogo, Japan

e-mail: [ichiy@kobe-u.ac.jp](mailto:ichiy@kobe-u.ac.jp)

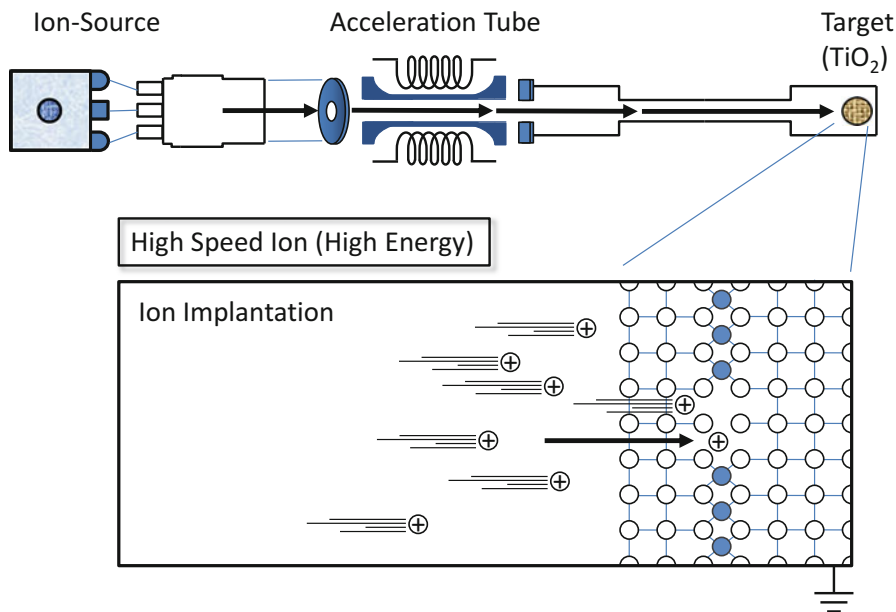


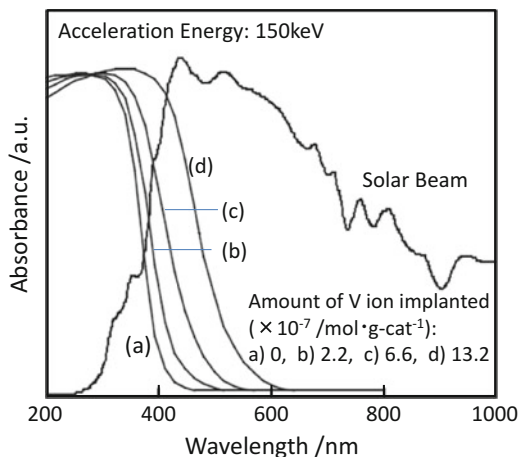
**Fig. 9.1** Schematic diagram of the ion beam techniques; metal ion implantation (high speed ion)

accelerated enough to have the high kinetic energy (50–200 keV) and can be implanted into the bulk of samples. On the other hand, the metal ions (ionized clusters) are accelerated to have the low kinetic energy (0.2–2 keV) in the ICB method and these ions are deposited to form the thin film on the top surface of sample. With these unique properties of the ion beam techniques, the well-defined semiconductor materials and thin films have been developed [17–19]. Recently, the applications of the ion-implantation method and the ICB method have been made to prepare the efficient  $\text{TiO}_2$  photocatalyst and realize the utilization of visible light. The photocatalytic properties of these unique  $\text{TiO}_2$  photocatalysts for the purification of water and air have been investigated.

## 9.2 Metal Ion-Implanted $\text{TiO}_2$ Semiconductor Powder

$\text{TiO}_2$  photocatalysts cannot absorb visible light and only make use of 3–5 % of the solar beams that reach the earth, necessitating the utilization of an ultraviolet light source. It is, therefore, necessary to develop a modified  $\text{TiO}_2$  photocatalytic system which can be applied under visible and/or solar light irradiation. Recently using the advanced metal ion-implantation technique, the visible light sensitive metal ion-implanted  $\text{TiO}_2$  can be developed [7–12]. As shown in Fig. 9.2, the absorption band of the  $\text{TiO}_2$  (anatase) implanted with V ions by the ion-implantation method with high acceleration energy (150 keV) and calcined in  $\text{O}_2$  at 725 K after ion

**Fig. 9.2** UV–VIS spectra of the TiO<sub>2</sub> (a) and the V ion-implanted TiO<sub>2</sub> (b–d) and the solar spectrum reaching on the earth



implantation has been found to shift to the visible light regions, the extent depending on the amount of V ions implanted. The V ions implanted within the bulk of TiO<sub>2</sub> can modify the electronic properties of the TiO<sub>2</sub> surface layer. The ion implantation with the other transition metal ions such as Cr, Mn, Fe, and Co is also effective to modify the properties of TiO<sub>2</sub> to make a large shift in the absorption band to the visible light region. It can be expected that photocatalytic reactions could be observed under visible light irradiation on these metal ion-implanted TiO<sub>2</sub> catalysts. On the other hand, metal ion (Cr, V) doped TiO<sub>2</sub> prepared chemically by the impregnation and the sol–gel method could make no shift in the adsorption band of TiO<sub>2</sub>. These modification of electronic properties of TiO<sub>2</sub> have made in different way depending on the methods of metal ion doping and the metal ion implantation is the only smart technique to realize the red-shift of the adsorption band of TiO<sub>2</sub> to the visible light regions.

The SIMS analysis on the depth concentration profile of the Cr ions in the Cr ion-implanted TiO<sub>2</sub> photocatalyst where ion implantation was performed at 150 keV indicated that the most Cr ions was implanted within the bulk of TiO<sub>2</sub> photocatalyst and the deeper the ions were implanted in the bulk of TiO<sub>2</sub> with the increase in the acceleration energy. Furthermore, XPS measurements of the catalysts did not show any evidence of the presence of Cr ions on the TiO<sub>2</sub> surface indicating that Cr ions are highly dispersed within the bulk of TiO<sub>2</sub> but not on the surface. The use of the metal ion-implantation method to modify the bulk electronic properties of TiO<sub>2</sub> photocatalysts without any change in the structure and properties of the top surface of the TiO<sub>2</sub> can be considered as one of the most significant advantages. Usually the chemical doped metal ions often works as electron–hole recombination centers to decrease the photocatalytic reactivity. Under UV light irradiation ( $\lambda < 380$  nm), the photocatalytic reactivity for the NO decomposition and the degradation of organic compounds on the metal ion-implanted TiO<sub>2</sub> is similar to the un-implanted original TiO<sub>2</sub> photocatalyst, indicating that the implanted metal ions do not work as the electron–hole recombination center in the metal ion-implanted photocatalysts.

**Fig. 9.3** Reaction time profiles of the photocatalytic decomposition of NO into  $N_2$  and  $N_2O$  on the Cr ion-implanted  $TiO_2$  photocatalyst prepared by the metal ion implantation under visible light ( $\lambda > 450$  nm) irradiation

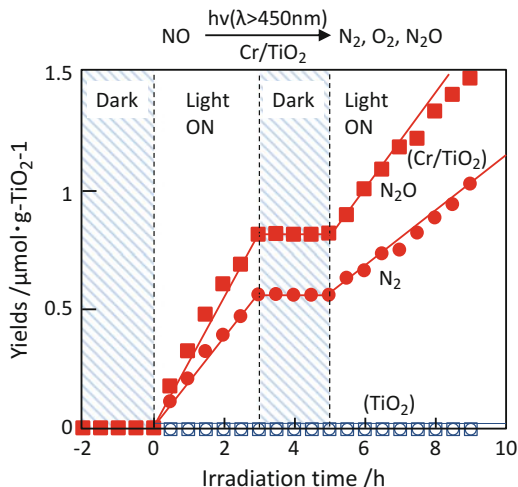
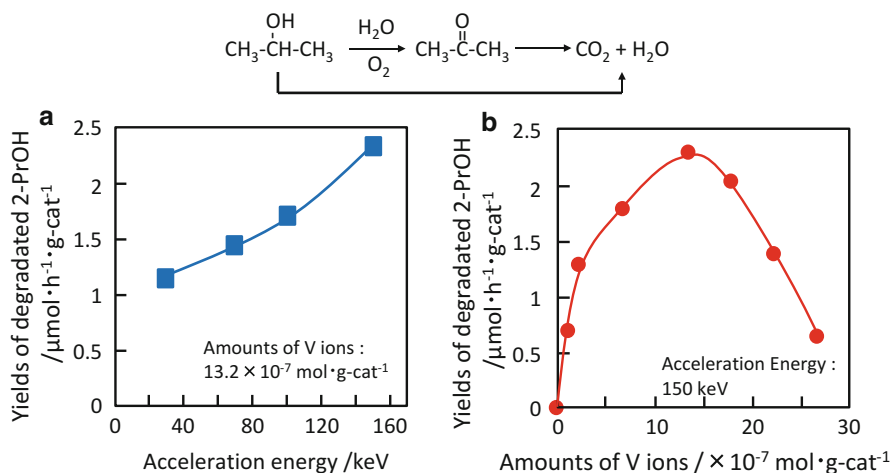


Figure 9.3 shows the time profiles of the photocatalytic decomposition of NO into  $N_2$ ,  $O_2$ , and  $N_2O$  on the Cr ion-implanted  $TiO_2$  catalysts under UV light irradiation ( $\lambda > 450$  nm). Visible light irradiation of the Cr ion-implanted  $TiO_2$  in the presence of NO at 275 K leads to the direct decomposition of NO into  $N_2$ ,  $O_2$ , and  $N_2O$  with a good linearity to the irradiation time. The liquid-phase photocatalytic degradation of 2-propanol diluted in water into acetone,  $CO_2$ , and  $H_2O$  also proceeded on the V ion-implanted  $TiO_2$  catalysts under visible light irradiation ( $\lambda > 450$  nm). Under the same conditions of visible light irradiation, these photocatalytic reactions do not proceed on the un-implanted original  $TiO_2$  photocatalyst. Thus, it can be seen that the implantation of metal ions is the determining factor in the use of visible light.

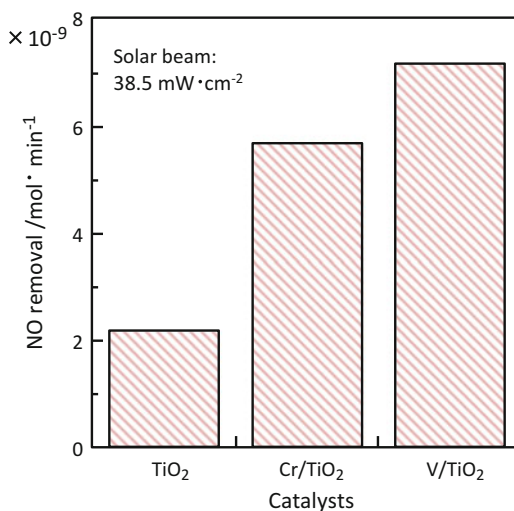
Figure 9.4a, b show the effect of the acceleration energy applied in the ion-implantation process and the amount of implanted metal ions on the photocatalytic reactivity for the NO decomposition on the V ion-implanted  $TiO_2$  photocatalyst under visible light irradiation. As shown in Fig. 9.4a, with the same amounts of V ion-implanted, the more efficient photocatalytic reactivity can be observed on the photocatalyst with V ions implanted with the higher acceleration energy within the range investigated. The metal ion implantation within the deeper bulk of  $TiO_2$  photocatalyst by the higher accelerated energy seems to be suitable to realize the more efficient photocatalytic reactivity under visible light irradiation. The results in Fig. 9.4b indicate that increasing the amounts of V ions implanted into the deep bulk of the  $TiO_2$  causes the increase in the photocatalytic reactivity under visible light irradiation having a maximum at around  $0.66 \mu\text{mol} \cdot \text{TiO}_2^{-1}$  and then decrease with excess amount of V ions implanted. These results indicate that there is an optimal condition in the depth and amount of implanted metal ions to achieve the efficient photocatalytic reactivity under visible light irradiation.

The field work experiments have been carried out to investigate the photocatalytic reactivity of the metal ion-implanted  $TiO_2$  photocatalyst under the outdoor solar



**Fig. 9.4** Effects of the acceleration energy (a) and the amount of implanted ions (b) on the reactivity of V ion-implanted  $\text{TiO}_2$  for the photocatalytic degradation of 2-propanol diluted in water

**Fig. 9.5** The photocatalytic decomposition on NO on the un-implanted original  $\text{TiO}_2$  and the V and Cr ion-implanted  $\text{TiO}_2$  photocatalysts under the outdoor solar beam irradiation



beam irradiation and the results for the photocatalytic decomposition of NO diluted in air atmosphere are shown in Fig. 9.5. Under outdoor solar beam irradiation, the Cr and V ion-implanted  $\text{TiO}_2$  photocatalysts show about three times higher photocatalytic reactivity than the un-implanted original  $\text{TiO}_2$  photocatalyst. These results clearly show that the application of the metal ion-implantation method can realize the photocatalytic system which can utilize visible and solar light energy efficiently.

### 9.3 Metal Ion-Implanted TiO<sub>2</sub> Thin Film

TiO<sub>2</sub> thin film prepared mainly by the sol–gel method have been utilized in many fields applying not only their photocatalytic properties but also antibacterial and superhydrophilic properties [7]. It has been desired to develop the TiO<sub>2</sub> thin film having the efficient photocatalytic reactivity and the high mechanical stability in being supported on various substrates in any desired forms. Using an ionized cluster beam (ICB) method with the low acceleration energy (0.2–2 keV), efficient TiO<sub>2</sub> thin film photocatalysts can be prepared on various types of substrates such as porous glass plate, activated carbon fiber, etc. under mild and dry conditions [12, 18, 19]. In the ICB method, the Ti cluster beam is produced by ejecting of the Ti vapor ionized by the electrons emitted from the ionization filament, and then the produced ionized clusters were accelerated by an accelerating electrode. Active TiO<sub>2</sub> thin films were produced by impingement of the ionized clusters and oxygen gas onto the support substrate. The advantages of using the ICB method are: (1) no contamination because of dry process in high vacuum; (2) production of highly crystalline films on various substrates without calcination; (3) well-controlled thickness.

Characterizations of these films by means of UV–VIS, XAFS, SEM, XRD, XPS techniques showed that the TiO<sub>2</sub> in transparent thin films having the well-crystallized structure mainly in the anatase phase could be formed on silica glass plate (PVG) by the ICB method. This TiO<sub>2</sub> thin film exhibited also the efficient reactivity for the photocatalytic decomposition of NO into N<sub>2</sub> and O<sub>2</sub> under UV irradiation, the photocatalytic properties and physical properties of the TiO<sub>2</sub> thin films are dependent on the film thickness and the higher reactivity can be observed on the thinner TiO<sub>2</sub> film. The TiO<sub>2</sub> thin film prepared on the silica glass plate exhibit higher photocatalytic reactivities than TiO<sub>2</sub> powder and catalysts prepared by the conventional impregnation method. Furthermore, UV irradiation of the TiO<sub>2</sub> thin film in a diluted aqueous solution of propanol, dichloroethane or phenol led to the efficient decomposition of these organic pollutants finally into CO<sub>2</sub>, H<sub>2</sub>O, and HCl. These results have clearly shown that the ICB method is useful in the preparation of transparent TiO<sub>2</sub> thin film having the efficient photocatalytic reactivity.

In order to improve the electronic properties of the TiO<sub>2</sub> thin film to absorb the visible light, metal ions (V or Cr ions) were implanted into the TiO<sub>2</sub> thin films at high energy acceleration (150 keV) using a metal ion implantation. As shown in Fig. 9.6, the UV–VIS absorption spectra of these metal ion-implanted TiO<sub>2</sub> thin films are found to shift toward visible light regions depending on the amount of metal ions implanted. They were found to exhibit an effective photocatalytic reactivity for the liquid-phase degradation of propanol diluted in water (Fig. 9.7) and the decomposition of NO into N<sub>2</sub> and O<sub>2</sub> at 295 K under visible light ( $\lambda > 450$  nm) irradiation, while the un-implanted original TiO<sub>2</sub> thin film cannot exhibit the reactivity. It has clearly demonstrated that the application of such ion beam techniques as the ICB method and the metal ion implantation can allow us to prepare the TiO<sub>2</sub> thin film which can work effectively under visible light irradiation.

**Fig. 9.6** UV–VIS spectra (transmittance) of the V ion-implanted TiO<sub>2</sub> thin film photocatalysts

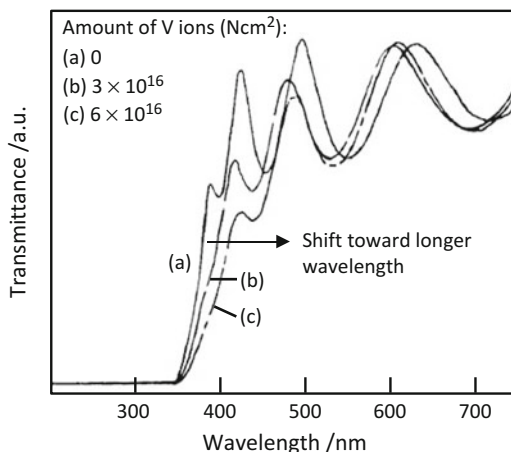
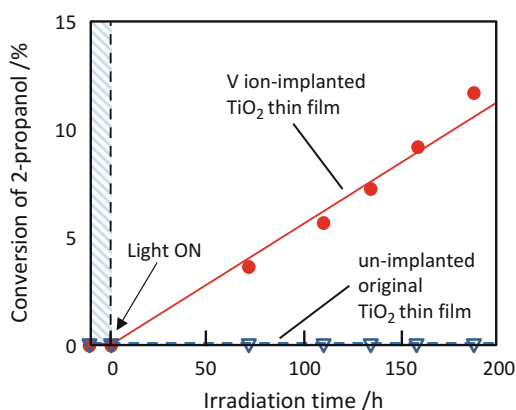


**Fig. 9.7** Reaction time profiles of photocatalytic degradation of 2-propanol on the V ion-implanted TiO<sub>2</sub> thin film photocatalysts under visible light irradiation ( $\lambda > 450$  nm)



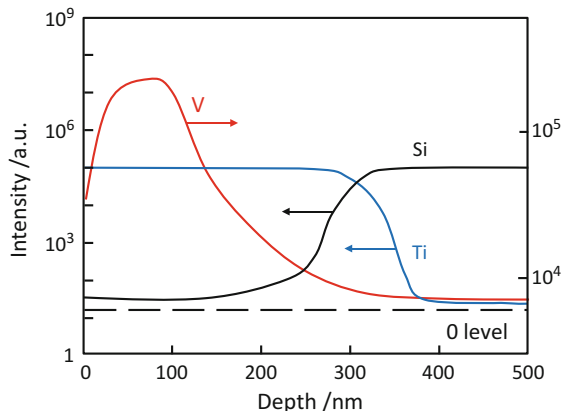
Using the transparent TiO<sub>2</sub> thin film which can operate under visible light and solar beam irradiation, the many innovative possibility can be opened to the environmental problems.

#### 9.4 Mechanism in the Metal Ion-Implanted TiO<sub>2</sub>

Metal ion implantation is very effective to modify TiO<sub>2</sub> semiconductor powder and thin film to absorb and utilize the visible light. The local structure of implanted metal ions and their role in the modification of the electronic state of TiO<sub>2</sub> have been investigated using various spectroscopic techniques.

Figure 9.8 shows the depth concentration profile of the V ions in the V ion-implanted TiO<sub>2</sub> thin film deposited on glass plate where ion implantation was

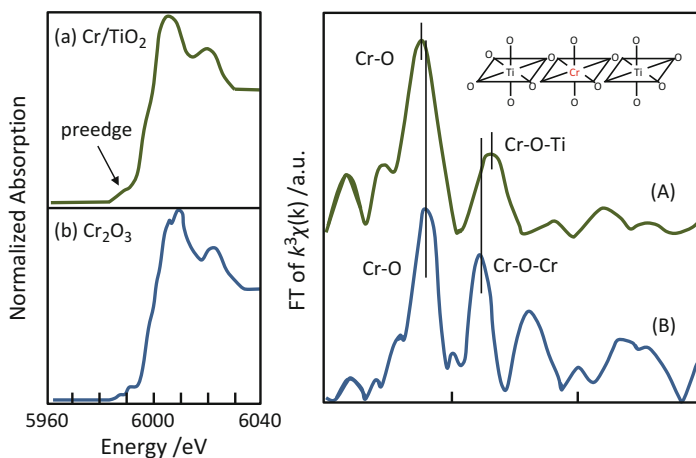
**Fig. 9.8** The depth concentration profile of V ions obtained from SIMS measurements with the V ion-implanted TiO<sub>2</sub> thin film



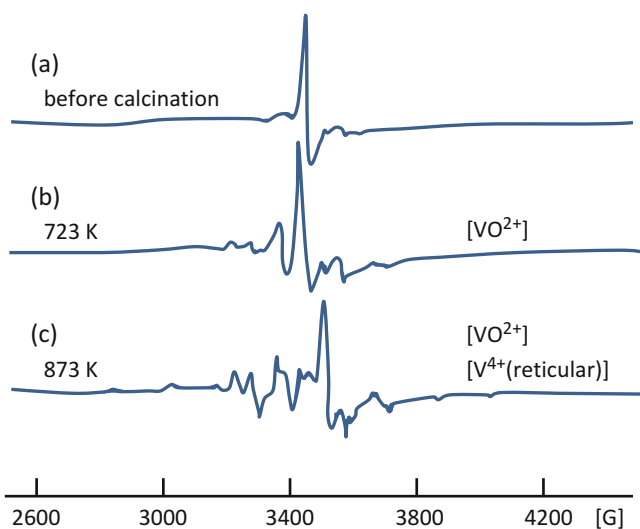
performed at 150 keV. The most V ions were implanted within the bulk of TiO<sub>2</sub> thin film and the deeper the ions were implanted in the bulk of TiO<sub>2</sub> with the increase in the acceleration energy. XPS measurements of the catalysts did not show any evidence of the presence of implanted metal ions on the TiO<sub>2</sub> surface indicating that implanted metal ions are highly dispersed within the bulk of TiO<sub>2</sub> but not on the top surface. The use of the metal ion implantation to modify the bulk electronic properties of TiO<sub>2</sub> without any change in the structure and properties of the top surface of the TiO<sub>2</sub> can be considered as one of the most significant advantages. On the other hand, metal ion (Cr, V) doped TiO<sub>2</sub> prepared chemically by the impregnation and the sol-gel method could make no shift in the adsorption band of TiO<sub>2</sub>. These modifications of electronic properties of TiO<sub>2</sub> have been made in different ways depending on the methods of metal ion doping and the metal ion implantation is the smartest technique to modify TiO<sub>2</sub> to absorb the visible light.

Figure 9.9 shows the XAFS (XANES and FT-EXAFS) spectra of the Cr ion-implanted TiO<sub>2</sub> thin film. The analysis of these spectra indicates that in the Cr ion-implanted TiO<sub>2</sub> the Cr ions are highly dispersed in the lattice of TiO<sub>2</sub> having octahedral coordination. These Cr ions are isolated and substituted with Ti<sup>4+</sup> ions in the lattice positions of the TiO<sub>2</sub>. On the other hand, the Cr-doped TiO<sub>2</sub> catalysts chemically prepared by the impregnation as well as the sol-gel method were found to have a mixture of the aggregated Cr-oxides having tetrahedral coordination similar to CrO<sub>3</sub> and octahedral coordination similar to Cr<sub>2</sub>O<sub>3</sub> [20, 21]. Figure 9.10 shows the ESR spectra of the V ion-implanted TiO<sub>2</sub> powder catalysts measured before and after calcination in O<sub>2</sub>. Distinct signals which can be assigned to the reticular V<sup>4+</sup> ions were detected only after calcination at around 723–823 K. These signals due to the reticular V<sup>4+</sup> ions have been observed only with the metal ion-implanted TiO<sub>2</sub> catalyst after the calcination which can exhibit the efficient red shift in their absorption band. On the other hand, the ESR signal assignable to the reticular V ion has never been observed with the V ion-doped TiO<sub>2</sub> prepared chemically by the impregnation as well as the sol-gel method.

These spectroscopic investigations suggest that the substitution of octahedrally coordinated Ti ions in bulk TiO<sub>2</sub> lattice with implanted metal ions is important to



**Fig. 9.9** XANES (*a, b*) and Fourier-transforms of EXAFS (*A, B*) of the Cr ion-implanted TiO<sub>2</sub> thin film after calcination at 723 K (*a, A*), and Cr<sub>2</sub>O<sub>3</sub> (*b, B*) as reference

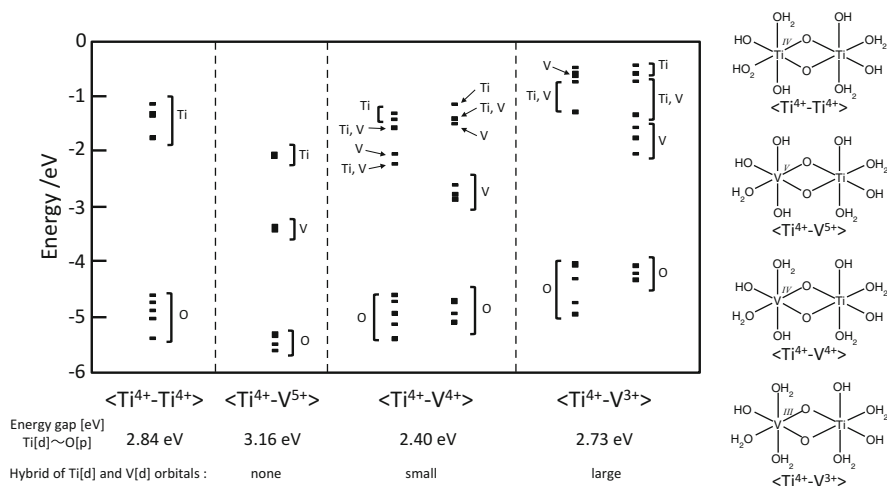


**Fig. 9.10** ESR spectra of the V ion-implanted TiO<sub>2</sub> photocatalysts before calcination (*a*) and after calcination in O<sub>2</sub> at 723 K (*b*) and 873 K (*c*)

modify TiO<sub>2</sub> to be able to adsorb visible light and operate as efficient photocatalyst under visible and/or solar light irradiation.

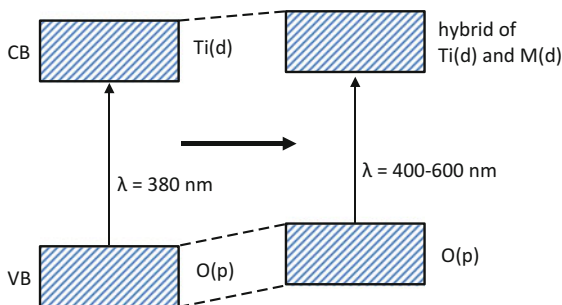
To prove this mechanism induced by the metal ion implantation, the theoretical approach using the *ab initio* molecular orbital calculation on the basis of the density functional theory method have been carried out. Because of the capacity of the calculation, the binuclear cluster models having the octahedral coordination similar to the coordination of TiO<sub>2</sub> have been applied. In these cluster models, the metal ions having the various electric charges (V<sup>5+</sup>, V<sup>4+</sup>, V<sup>3+</sup>) are substituted with Ti<sup>4+</sup> ion

octahedrally coordinated in the lattice position of  $\text{TiO}_2$  [14]. As shown in Fig. 9.11, the models having  $\text{V}^{4+}$  ion  $\langle \text{Ti}^{4+}-\text{V}^{4+} \rangle$  and  $\text{V}^{3+}$  ion  $\langle \text{Ti}^{4+}-\text{V}^{3+} \rangle$  can have the energy gap of  $\text{Ti(d)}-\text{O(d)}$  smaller than that of un-implanted pure Ti-oxide  $\langle \text{Ti}^{4+}-\text{Ti}^{4+} \rangle$ . With these models the overlap of  $\text{Ti(d)}$  and  $\text{V(d)}$  orbitals are observed. These results indicate that the mixing of the  $\text{Ti(d)}$  orbital of Ti-oxide and the metal(d) orbital of the implanted metal ions in the low electric charge is essential to decrease the energy gap between  $\text{Ti(d)}$  and  $\text{O(p)}$  orbitals of Ti-oxide. Considering this mechanism, it can be proposed that in the metal ion-implanted  $\text{TiO}_2$  the overlap of the conduction band due to  $\text{Ti(d)}$  of  $\text{TiO}_2$  and the metal (d) orbital of the implanted metal ions can decrease the band gap of  $\text{TiO}_2$  to enable to absorb the visible light (Fig. 9.12). The present results can indicate that the substitution of Ti ions with the isolated metal ions implanted into the lattice position of the bulk of  $\text{TiO}_2$  (Fig. 9.13) is the determining factor for the utilization of visible light and solar beam.



**Fig. 9.11** The energy level of higher-lying molecular orbital obtained by the ab initio molecular orbital calculations with the cluster models of the V ion-implanted  $\text{TiO}_2$  photocatalyst

**Fig. 9.12** Energy diagram of  $\text{TiO}_2$  and metal ion-implanted  $\text{TiO}_2$



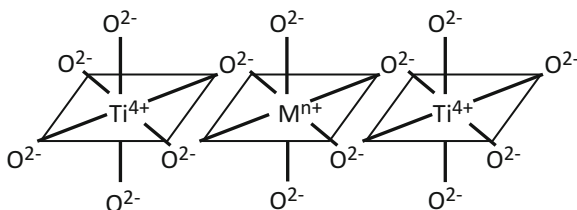


**Fig. 9.13** Local structure of metal ion-implanted  $\text{TiO}_2$ . Implanted metal ions  $\text{M}^{n+}$  ( $\text{Cr}^{3+} \sim \text{Cr}^{4+}$ ,  $\text{V}^{3+} \sim \text{V}^{4+}$ ) are highly dispersed and isolated in  $\text{TiO}_2$  matrix and substituted with octahedrally coordinated lattice  $\text{Ti}^{4+}$  with the low oxidized state

## 9.5 Metal Ion-Implanted Ti-Zeolite

Although  $\text{TiO}_2$  have the octahedral coordination, titanium oxide having the tetrahedral coordination (tetra-Ti-oxide) can be prepared in the silica matrix such as zeolite and mesoporous silica. Ti-containing zeolites (Ti-zeolites) with the tetrahedral coordinated Ti-oxide species showing unique reactivities for various photocatalytic reactions under UV-irradiation (220–260 nm) [22] are the good candidates as the efficient and selective photocatalysts. Although these tetrahedrally coordinated Ti-oxide species can exhibit the unique photocatalytic reactivity, they can only adsorb and utilize UV light at around 220–250 nm to form the charge transfer excited state as active species. It is also vital to develop the Ti-zeolites which can operate efficiently under visible light irradiation. The application of metal ion implantation to modify the Ti-zeolites is very interesting [23]. Recently it has been found that the metal ion implantation with V ions has been applied on the Ti-zeolites and Ti-containing mesoporous silica to design the photocatalysts which can operate under visible light irradiation.

The metal ion implantation with V ions on Ti-zeolites and Ti-containing mesoporous silica was carried at 150 eV. Figure 9.14 shows the effect of metal ion implantation on the diffuse reflectance UV–Vis absorption spectra of Ti-HMS mesoporous silica having the tetrahedrally coordinated Ti-oxide in the frameworks. As shown in Fig. 9.14, the V ion-implanted Ti-HMS can absorb the light at the longer wavelengths ( $\sim 450$  nm) while the original un-implanted Ti-HMS absorbs the UV light at the shorter than 300 nm. These results indicate that the metal ion implantation is effective to modify the Ti-HMS to absorb the visible light and exhibit the photocatalytic reaction under visible light irradiation (Fig. 9.15).

These metal ion-implanted Ti-zeolites (V/Ti-zeolite) and Ti-containing mesoporous silica (V/Ti-mesoporous silica) can show the efficient photocatalytic reactivity for various reactions such as NO decomposition and partial oxidation of hydrocarbons even under visible light irradiation in keeping the unique photocatalytic properties of the tetrahedrally coordinated Ti-oxide species. The investigations using XAFS analysis on the local structure of active sites and the molecular orbital calculations on the electronic structure of active sites have revealed that the direct coordination and interaction between the implanted metal ions and the tetrahedrally coordinated Ti-oxide species can modify the electronic state of the Ti-oxide species to absorb and utilize the visible light.

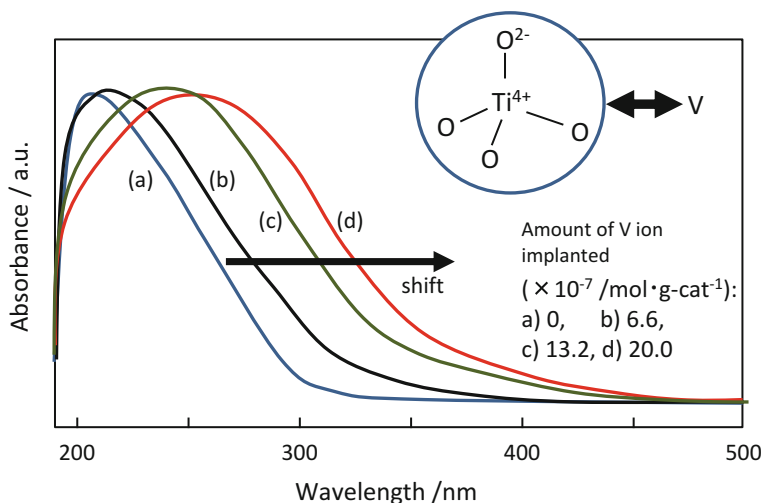
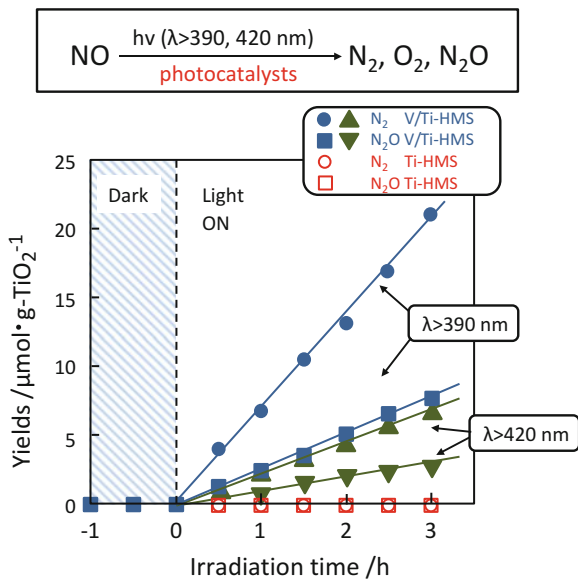


**Fig. 9.14** Diffuse reflectance UV-Vis absorption spectra of the V ion-implanted Ti-containing mesoporous silica (Ti-HMS)

**Fig. 9.15** Reaction time profiles of the photocatalytic decomposition of NO on Ti-HMC and V ion-implanted Ti-HMS under visible light irradiation ( $\lambda > 390$  nm, 420 nm). The amount of implanted V ion:  $2.0 \mu\text{mol/g-cat}$ . The yield of  $\text{N}_2$  (filled circle, filled triangle) and  $\text{N}_2\text{O}$  (filled square, filled inverted triangle) formation on V/Ti-HMS; the yield of  $\text{N}_2$  (circle) and  $\text{N}_2\text{O}$  (square) formation on Ti-HMS



**Acknowledgments** The author appreciate Profs. M. Anpo, M. Matsuoka, M. Takeuchi (Osaka Pref. Univ.), K. Ikeue (Kumamoto Univ.) for their fruitful discussions and useful advises on this investigations. The present work is supported by the Grant-in-Aid for Scientific Research (KAKENHI) from Ministry of Education, Culture, Sports, Science and Technology. The X-ray adsorption experiments were performed at the SPring-8 and KEK-PF.

## References

1. Qian X, Fuku K, Kuwahara Y, Lamegawa T, Mori K, Yamashita H (2014) Design and functionalization of photocatalytic systems within mesoporous silica. *ChemSusChem* 7:1528–1536
2. Kuwahara Y, Yamashita H (2011) Efficient photocatalytic degradation of organics diluted in water and air using TiO<sub>2</sub> designed with zeolites and mesoporous silica materials. *J Mater Chem* 21:2407–2416
3. Yamashita H, Anpo M (2004) Application of an ion beam technique for the design of visible light-sensitive, highly, efficient and highly selective photocatalysts: ion-implantation and ionized cluster beam methods. *Catal Surv Asia* 8:35–45
4. Yamashita H, Takeuchi M, Anpo M (2004) Visible-light-sensitive photocatalysts. In: Nalwa HS (ed) *Encyclopedia of nanoscience and nanotechnology*. American Scientific Publishers, New York, pp 640–654
5. Anpo M (ed) (2000) *Photofunctional zeolites: synthesis*. NOVA Science Publishers, Inc, New York
6. Anpo M, Che M (2000) Applications of photoluminescence techniques to the characterization of solid surfaces in relation to adsorption, catalysis and photocatalysis. *Adv Catal* 44:119–257
7. Fujishima A, Hashimoto K, Watanabe T (1998) TiO<sub>2</sub> photocatalysis. Bkc Inc, Tokyo
8. Heller A (1995) Chemistry and applications of photocatalytic oxidation of thin organic films. *Acc Chem Res* 28:503–508
9. Kamat PV (1993) Photochemistry on nonreactive and reactive semiconductor surfaces. *Chem Rev* 93:267–300
10. Anpo M, Ichihashi Y, Takeuchi M, Yamashita H (1999) Design and development of unique titanium oxide photocatalysts capable of operating under visible light irradiation by an advanced metal ion-implantation method. *Stud Surf Sci Catal* 121:104–105
11. Anpo M, Ichihashi Y, Takeuchi M, Yamashita H (1998) Design of unique titanium oxide photocatalysts by an advanced metal ion-implantation method and photocatalytic reactions under visible light irradiation. *Res Chem Intermed* 24:143–149
12. Takeuchi M, Yamashita H, Matsuoka M, Anpo M, Hirao T, Itoh N, Iwamoto N (2000) Photocatalytic decomposition of NO under visible light irradiation on the Cr ion-implanted TiO<sub>2</sub> thin film photocatalyst. *Catal Lett* 67:135–137
13. Yamashita H, Harada M, Misaka J, Takeuchi M, Ikeue K, Anpo M (2002) Photocatalytic degradation of propanol diluted in water under visible light irradiation using metal ion-implanted titanium dioxide photocatalysts. *Photochem Photobiol A Chem* 148:257–261
14. Yamashita H, Harada M, Misaka J, Takeuchi M, Ichihashi Y, Goto F, Ishida M, Sasaki T, Anpo M (2001) Application of ion beam techniques for preparation of metal ion-implanted TiO<sub>2</sub> thin film photocatalyst available under visible light irradiation: metal ion-implantation and ionized cluster beam method. *J Synchrotron Rad* 8:569–571
15. Yamashita H, Honda M, Harada M, Ichihashi Y, Anpo M, Hirao T, Itoh N, Iwamoto N (1998) Preparation of titanium oxide photocatalysts anchored on porous silica glass by a metal ion-implantation method and their photocatalytic reactivities for the degradation of 2-propanol diluted in water. *J Phys Chem B* 102:10707–10711

16. Yamashita H, Ichihashi Y, Takeuchi M, Kishiguchi S, Anpo M (1999) Characterization of metal ion-implanted titanium oxide photocatalysts operating under visible light irradiation. *J Synchrotron Rad* 6:451–452
17. Takeuchi M, Yamashita H, Matsuoka M, Anpo M (2000) Photocatalytic decomposition of NO on titanium oxide thin film photocatalysts prepared by an ionized cluster beam method. *Catal Lett* 66:185–187
18. Yamashita H, Harada M, Tanii A, Honda M, Takeuchi M, Ichihashi Y, Anpo M (2000) Preparation of efficient titanium oxide photocatalysts by an ionized cluster beam method and their application for the degradation of propanol diluted in water. *Stud Surf Sci Catal* 130:1931–1936
19. Yamashita H, Harada M, Tanii A, Honda M, Takeuchi M, Ichihashi Y, Anpo M, Iwamoto N, Itoh N, Hirao T (2000) Preparation of efficient titanium oxide photocatalysts by an ionized cluster beam (ICB) method and their photocatalytic reactivities for the purification of water. *Catal Today* 63:63–69
20. Yamashita H, Ariyuki M, Higashimoto S, Zhang SG, Chang JS, Park SE, Lee JM, Matsumura Y, Anpo M (1999) Characterization and photocatalytic reactivities of Cr-HMS mesoporous molecular sieves. *J Synchrotron Rad* 6:453–456
21. Yamashita H, Yoshizawa K, Ariyuki M, Higashimoto S, Che M, Anpo M (2001) Photocatalytic reactions on chromium containing mesoporous silica molecular sieves (Cr-HMS) under visible light irradiation: decomposition of NO and partial oxidation of propane. *Chem Commun* 435–436
22. Yamashita H, Anpo M (2003) Photocatalysis of the titanium oxide and chromium oxide species included within micro- and meso-porous zeolite materials: XAFS and photoluminescence studies. *Curr Opin Solid State Mater Sci* 7:471–481
23. Yamashita H, Kanazawa Y, Kida K, Anpo M (2005) Application of a metal ion-implantation for the preparation of visible-light sensitive zeolite photocatalyst: V ion-implanted Ti-containing HMS mesoporous molecular sieves. *Phys Scr T* 115:467–470

# Chapter 10

## Effect of F-Doping on the Photocatalytic Activity and Microstructures of Nanocrystalline TiO<sub>2</sub> Powders

Shengwei Liu and Jiaguo Yu

### 10.1 Introduction

In the past decades, it was demonstrated that F-doping of TiO<sub>2</sub> photocatalysts, involving either surface fluorination (surface doping) or lattice fluorine-doping (bulk doping), can be employed to modify significantly the multilevel microstructures and the photocatalytic performances [1, 2]. The crystallographic and textural structures can be largely modified by the mediating effects of added fluoride in the preparation of F-doped TiO<sub>2</sub> photocatalysts. Specifically, highly crystalline anatase phases TiO<sub>2</sub> nanocrystals with remarkable thermal stability are exclusively favored in the fluoride-mediated synthesis [3, 4]; especially, the metastable and reactive {001} facets of anatase TiO<sub>2</sub> crystals can be selectively stabilized by suitable high coverage of surface fluorine [5, 6]. In addition, porous polycrystalline anatase TiO<sub>2</sub> hollow microspheres can be also created by fluoride-mediated self-transformation processes [7, 8]. Surface fluorination of TiO<sub>2</sub> photocatalysts greatly modifies the surface characteristics, including surface charge, acidity, polarity, defects, etc., which are essential factors influencing the adsorption capacity and selectivity toward targeted molecules [9, 10]. Meanwhile, surface fluorination significantly modifies the interfacial charge transfer dynamics and mechanism, typically, preferential formation of surface-free mobile hydroxyl radicals [11, 12]. The lattice fluorine-doping significantly alters the localized electronic structures and surface defect states, giving rise to visible light photocatalytic activity [13, 14]. And, the effects of lattice fluorine-doping are more predominant when co-doping with other complementary elements is used [15, 16]. Notably, in the preparation of F-doped TiO<sub>2</sub> photocatalysts, the fluoride mediated structural control and the guest modification via surface/bulk doping can be achieved simultaneously, and the fluorination effects should be considered comprehensively.

---

S. Liu • J. Yu (✉)

State Key Laboratory of Advanced Technology for Materials Synthesis and Processing,  
Wuhan University of Technology, Wuhan, China  
e-mail: [jiaguoyu@yahoo.com](mailto:jiaguoyu@yahoo.com)

## 10.2 Fluoride-Mediated Synthesis of TiO<sub>2</sub> Nanocrystals and Hollow Microspheres

The two approaches for the preparation of F-doped TiO<sub>2</sub> photocatalysts are post-synthesis fluorination and in-situ fluorination [1]. The post-synthesis fluorination process is normally related to the Langmuir-type adsorption of fluoride on the surface of catalyst, which is largely dependent on the solution pH value. The in-situ fluorination process, involving fluoride mediated synthesis, is not only able to facilitate control the chemical nature of incorporated fluorine (including adsorbed fluoride and lattice-doped fluorine), but also enables the flexible fluoride-mediated crystal modification and organization, as shown in Fig. 10.1.

Fluoride-mediated synthesis can be used to control the phase, size, shape, and thermal stability of the resulting TiO<sub>2</sub> nanocrystals, which are all important factors influencing the photocatalytic processes and kinetics. It has been shown that fluoride-mediated solution synthesis facilitates the production of TiO<sub>2</sub> in the form of anatase [3, 4, 7, 17, 18]. For example, Yu et al. [4] demonstrated that the addition of NH<sub>4</sub>HF<sub>2</sub> exclusively inhibited the formation of brookite phase and favored the selective synthesis of anatase nanocrystals during hydrothermal hydrolysis of tetrabutyl orthotitanate (TBOT). The crystallization process of anatase phase from amorphous TiO<sub>2</sub> was postulated to take place via nonlinear spiral polycondensation of TiO<sub>6</sub> octahedra, in contrast to the linear polycondensation of these octahedral units as in the case of rutile evolution [19, 20]. The added fluoride into the synthesis system can be readily adsorbed on the surface of TiO<sub>6</sub> octahedra by electrostatic interactions and/or hydrogen bonding. The fluoride adsorption and/or complexation not only affect the reaction processes and dynamics but also exert steric hindrance on the arrangement of TiO<sub>6</sub> octahedra. In this regard, the surface fluorination inhibits linear condensation of TiO<sub>6</sub> octahedra and favors the spiral chain growth and structural evolution to anatase, which may be similar to the spatial effects by surface sulfation [19]. Meanwhile, the size and degree of crystallinity can be also significantly enlarged during the fluoride-mediated solution synthesis [3, 4, 7, 18]. It was proposed that fluoride ions promoted the dissolution and re-crystallization processes of metastable TiO<sub>2</sub> intermediates and facilitated the crystal growth and crystallization of anatase nanocrystals [21]. In addition, the thermal stability could be largely enhanced for the anatase crystals prepared via fluoride-mediated solution routes. Normally, the phase transformation from anatase to rutile is significantly inhibited upon calcination, and the phase transformation temperature is enlarged [3, 22]. For

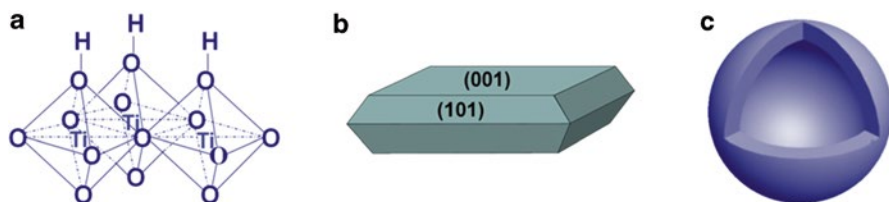


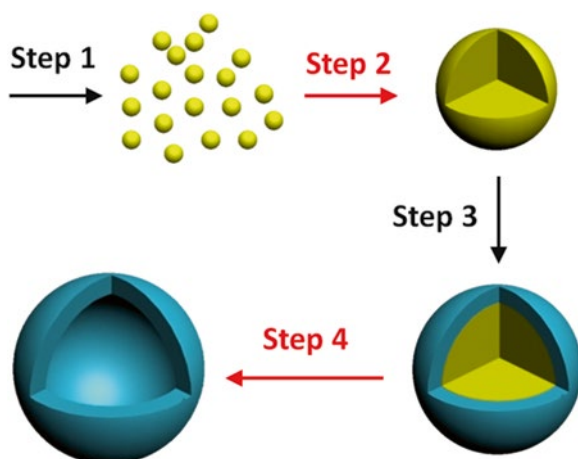
**Fig. 10.1** Fluoride mediated crystal modification and organization: (a) anatase-phase crystallization; (b) {001} facets stabilization; (c) inside-out hollowing

example, Lv et al. recently reported that  $\text{TiO}_2$  nanosheets showed a remarkable thermal stability against phase transition up to  $1100\text{ }^\circ\text{C}$  [23]. Owing to the higher degree of crystallinity and the protecting effects of surface adsorbed fluorine, the surface nucleation initiating the phase transition is significantly restricted with consequence of higher thermal stability. Notably, it is likely that the surface fluorination facilitates the crystal growth model changing from Ostwald ripening to oriented attachment [22]. Interestingly, the selective adsorption of fluorine on the anatase  $\{001\}$  facets during fluoride-mediated solution synthesis can be employed to modify the reaction dynamics and to stabilize the high-energy  $\{001\}$  facets [5, 6]. Lu et al. successfully synthesized anatase  $\text{TiO}_2$  crystals with high percentage (47 %) of  $\{001\}$  facets using HF as a capping agent under specific hydrothermal conditions [5]. This pioneering work has stimulated a great interest in the synthesis and assembly of anatase  $\text{TiO}_2$  crystals with dominant high-energy  $\{001\}$  facets and directed research efforts in this area towards increasing the percentage of the exposed  $\{001\}$  facets as well as the reduction of the particle size, and towards exploiting novel physicochemical properties and potential applications [6, 23–31]. Up to now, the percentage of  $\{001\}$  facets can approach 100 % and the thickness of anatase nanosheets can be as thin as 1.6 nm [25]. Note that, the  $\{001\}$  facets can be selectively etched by long-term/intensive F-complexing dissolution, especially, in acid solution [28].

The fluoride mediated solution synthesis has also been developed for one-pot template-free fabrication of  $\text{TiO}_2$  hollow microspheres, which is termed as fluoride mediated self-transformation (FMST) method by Yu et al. [7, 8]. Based on the FMST strategy, a simple hydrothermal treatment of  $\text{TiOSO}_4$  or  $\text{Ti}(\text{SO}_4)_2$  aqueous solution containing certain fluoride (e.g.,  $\text{NH}_4\text{F}$ ,  $\text{NH}_4\text{HF}_2$ ,  $\text{CF}_3\text{COOH}$ ) gave rise to fluorinated  $\text{TiO}_2$  porous hollow microspheres in high yield [7, 8, 18, 21, 32]. Typically, the hollow anatase  $\text{TiO}_2$  microspheres are composed of a porous shell of closely packed nanoparticles with a roughen exterior [7].

The basic formation processes are illustrated in Fig. 10.2 [7, 8, 18]. Firstly (*Step 1, rapid nucleation*), a rapid nucleation of metastable  $\text{TiO}_2$  nanoclusters occurs in the reaction solution due to high initial supersaturation. Secondly (*Step 2, directed*

**Fig. 10.2** Formation processes of hollow  $\text{TiO}_2$  microspheres by fluoride-mediated self-transformation (FMST) method



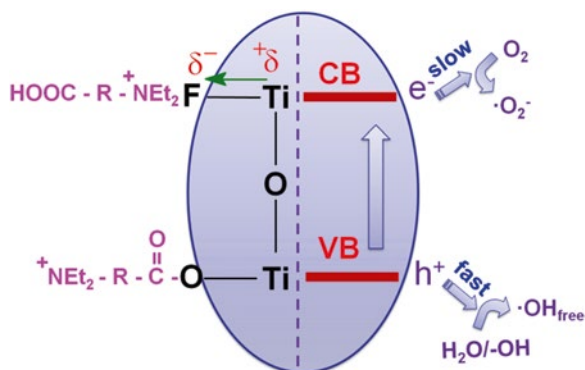
*self-assembly*), these incipient nanoclusters directionally organize into amorphous spherical aggregates in order to minimize the total Gibbs free energy. Thirdly (*Step 3, spontaneous coating*), as the supersaturation drops with time, heterogeneous nucleation of a crystalline thin shell occurs around the amorphous solid microparticles, forming an amorphous core @ crystalline shell structure. Finally (*Step 4, in situ self-transformation*), preferential dissolution of the amorphous core takes place along with concurrent deposition of a porous crystalline shell to produce hollow microspheres without significant alteration of the bulk particle morphology. As for the controllable synthesis of TiO<sub>2</sub> hollow microspheres, *Step 2* and *Step 4* are especially crucial. *Step 2* is related to the directed assembly process. Usually, after nucleation, three possible processes may occur, that is, directed assembly, random aggregation, and in-situ crystallization. If self-assembly process is out of control, in-situ crystallization and/or random aggregation prevails, dispersed nanoparticles and ill-shaped aggregates will be yielded as main products [8]. Only when directed assembly process is dominant, solid spheres are formed, and the hollowing process would be possible. As for the preparation of TiO<sub>2</sub> hollow spheres by hydrolysis of Ti(SO<sub>4</sub>)<sub>2</sub> with NH<sub>4</sub>F, the addition of urea benefits the tuning of nucleation dynamics and surface states of the elementary TiO<sub>2</sub> building blocks, and thus, promotes the assembly of primary nanoparticles into metastable solid microparticles [8]. As a result, uniform well-defined TiO<sub>2</sub> hollow spheres are dominantly produced. *Step 4* is related to the in-situ self-transformation process. After the assembly of primary nanoparticles into solid spheres, they are still not the most stable, a dissolution and recrystallization process will occur to achieve a more stable structure. If the dissolution occur selectively in the interior, and the dissolved matter can readily diffuse outside and re-crystallize on the surface, the hollow structure will be formed. The control experiments and time-dependent evolution processes confirm that the fluoride addition is crucial for the inside-out hollowing process [7, 18]. In the absence of fluoride, amorphous solid TiO<sub>2</sub> microspheres evolve only into the crystalline counterpart without a hollow formation. In contrast, formation of hollow spheres readily occurred after adding fluoride into the synthesis mixture. Moreover, the rate of the evolution process leading to hollow spheres could be enhanced by increasing molar ratio of fluorine to titanium. It is suggested that the strong complexing ability and fast diffusion ability of fluoride ions facilitates the selective interior dissolution and preferential external recrystallization of titania species.

The F-mediated preparation of titania hollow microspheres is very flexible in controlling the resulting multilevel microstructures, including structural parameters of both hollow spheres and their elemental building blocks, by changing experimental parameters such as reactants (titania precursors and fluoride), molar ratio of fluorine to titanium, hydrothermal temperature and time, catalyst, solvents and dopants, etc. [7, 8, 18, 21, 27, 32–37]. For example, the shape of shell-building nanoparticles can be tuned into faceted polyhedra with exposed high percentage of {001} facets, as a consequence of increasing ethanol amount in the mixture of solvents for the preparation of TiO<sub>2</sub> hollow spheres by hydrolysis of Ti(SO<sub>4</sub>)<sub>2</sub> with NH<sub>4</sub>F [27]. It was shown that the addition of ethanol facilitates the selective surface fluorination, consequently, reduces the surface energy and increases the percentage of exposed {001} facets.

### 10.3 Surface Fluorination Effects

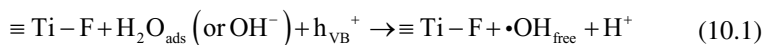
The surface fluorination of TiO<sub>2</sub> photocatalysts affects surface properties, including surface charge, surface acidity and polarity, etc., thus, it is expected that adsorption properties of fluorinated TiO<sub>2</sub> (F-TiO<sub>2</sub>) can be significantly altered by surface fluorination [9, 10]. Notably, the surface fluorination process and the resulting surface properties of TiO<sub>2</sub> are affected by the pH value, and thus, adsorption behavior on F-TiO<sub>2</sub> surface is also pH-dependent [10]. Generally, the surface fluorination may significantly reduce surface charge in acidic pH range, and thus adsorption of the positively charged organic pollutants is usually favored, while adsorption of negatively charged organic pollutant is normally inhibited. As a result of great influence over adsorption capacity, surface fluorination of TiO<sub>2</sub> photocatalyst affects the interfacial charge transfer rate and thus the photocatalytic reaction kinetics. Usually, a higher adsorption capacity results in higher photocatalytic activity. For example, Li et al. [38] demonstrated an almost linear relationship between the photocatalytic reaction rate and the adsorption capacity for adsorption and decomposition of acetaldehyde on F-TiO<sub>2</sub>. It was pointed out that adsorbed molecules may react more efficiently with surface bound photogenerated short-living active species, such as  $\cdot\text{OH}$  and  $h^+$  [27]. Moreover, TiO<sub>2</sub>-mediated photocatalytic degradation of dyes under visible irradiation is also favored by surface fluorination-enhanced dye adsorption. Zhao et al. demonstrated that the increase in the adsorption amount and the strength of N-alkyl-containing cationic dyes (such as RhB and MB) on F-TiO<sub>2</sub> promotes the electron transfer from the excited dyes to TiO<sub>2</sub>, enhancing their visible-light degradation rate [9]. In contrast, a suppressed adsorption of some anionic dyes (such as fluorescein and alizarin red) on F-TiO<sub>2</sub> retards their visible-light degradation [9]. Interestingly, surface fluorination of TiO<sub>2</sub> not only affects adsorption capacity, but also significantly affects the adsorption sites and modes of reactant molecules. As a consequence of the variation in adsorption sites and modes, the photocatalytic mechanisms may also be drastically changed by surface fluorination. Zhao et al. [9] observed that RhB preferentially anchors on pure TiO<sub>2</sub> through the carboxylic ( $-\text{COOH}$ ) group, leading to the direct cleavage of the RhB chromophore structure under visible irradiation, whereas, on F-TiO<sub>2</sub>, adsorption of this dye occurs via cationic moiety ( $-\text{NEt}_2$  group) and N-dealkylation predominates before destruction of the chromophore structure (Fig. 10.3).

**Fig. 10.3** Surface fluorination effects: modifying reactant adsorption capacity and mode (*left*); tuning charge transfer kinetic and mechanism (*right*).  $+\text{NEt}_2\text{-R-COOH}$  Rhodamine B molecule, CB conduction band, VB valence band



Otherwise, in special cases, an inhibited adsorption of some molecules, especially intermediates, on the surface fluorinated photocatalyst avoids the inactivation of the photocatalyst or formation of surface charge recombination centers [11, 39–41], maintaining the consecutive photocatalytic processes with high efficiency. For example,  $\text{H}_2\text{O}_2$  evolution during the photocatalytic degradation of formic acid is greatly enhanced on the surface fluorinated  $\text{TiO}_2$  as compared to pristine  $\text{TiO}_2$  [39, 40]. One important reason of this behavior is that the surface fluorination significantly inhibits the surface enrichment of  $\text{CO}_2^{\cdot-}$  radical anion produced during photocatalytic degradation of formic acid. The desorbed  $\text{CO}_2^{\cdot-}$  radical anion may react with dissolved  $\text{O}_2$  to significantly enhance the production of  $\text{H}_2\text{O}_2$ . Moreover, the photocatalytic selectivity of  $\text{TiO}_2$  photocatalyst can be also tuned by the inhibited adsorption of certain molecules due to the surface fluorination. For example, Liu et al. [27] demonstrated that the surface-clean hollow  $\text{TiO}_2$  spheres (surface fluoride removed by calcination at 600 °C) preferentially decomposes methylene blue (MB) in comparison to methyl orange (MO). In contrast, because the selective adsorption of MB is inhibited, the fluorinated hollow  $\text{TiO}_2$  spheres show preferential decomposition of MO over MB.

Notably, the enhanced adsorption on the F- $\text{TiO}_2$  surface (dependent on the specific pH range and the type of adsorbing species) is not the only possible factor that is responsible for the enhanced photocatalytic degradation of various species in the F- $\text{TiO}_2$  suspension. In some cases, the adsorption of certain reactant molecules is inhibited on F- $\text{TiO}_2$ , but their photocatalytic decomposition is still greatly enhanced. For example, Choi et al. demonstrated that, despite small adsorption of Acid Orange 7 (AO7) on F- $\text{TiO}_2$ , the photocatalytic degradation rate of AO7 in the F- $\text{TiO}_2$  suspension was also enhanced in comparison to that in the pure  $\text{TiO}_2$  suspension [41]. In this situation, Minero et al. [11] proposed that the surface fluorination of  $\text{TiO}_2$  promotes the production of mobile free OH radicals ( $\cdot\text{OH}_{\text{free}}$ , Eq. (10.1), Fig. 10.3) by activating adsorbed  $\text{H}_2\text{O}$  ( $\text{H}_2\text{O}_{\text{ads}}$ ), whereas most OH radicals generated on pure  $\text{TiO}_2$  surface prefer to remain adsorbed ( $\cdot\text{OH}_{\text{ads}}$ , Eq. (10.2)) [11, 12]:



It is expected the desorbed and free  $\cdot\text{OH}$  radicals are more reactive than the surface-bound  $\cdot\text{OH}$  due to the facile homogeneous photocatalytic reactions [42], and thus the photocatalytic decomposition rate of most organic pollutant in aqueous solution can be enhanced upon surface fluorination. Based on the kinetic analysis and competition experiments with different hydroxyl radical scavengers, it was shown that the degradation of phenol proceeds completely by free hydroxyl radicals on the surface fluorinated  $\text{TiO}_2$ , while for bare titania, about 10 % is due to direct hole oxidation and 90 % due to the adsorbed hydroxyl radicals [12]. Moreover, the generation of free hydroxyl radical on the F- $\text{TiO}_2$  surface is further supported by Mrowetz and Selli using DMPO-spin trap ESR technique [43] and by Yu et al. using terephthalic acid based photoluminescence technique [4]. Interestingly, the surface

fluorination effect is observed not only at  $\text{TiO}_2$ /water interface but also at  $\text{TiO}_2$ /air interface. Choi et al. [44] demonstrated that the enhanced diffusion of mobile OH radicals from the F- $\text{TiO}_2$  into air could enable the remote photocatalytic degradation of stearic acids.

Unfortunately, the surface fluorination-enhanced production of mobile free hydroxyl radicals in  $\text{TiO}_2$  suspensions is not universal, which cannot be observed for the photocatalytic oxidation of some molecules that are usually initiated by a direct hole transfer. Choi et al. [41] demonstrated that the photocatalytic degradation of dichloroacetate (DCA) is weaker on the F- $\text{TiO}_2$  as compared to pristine  $\text{TiO}_2$  at pH=4. It was shown that the photocatalytic degradation of DCA on  $\text{TiO}_2$  is mainly initiated by a direct hole transfer. As the DCA adsorption on  $\text{TiO}_2$  surface is inhibited by surface fluorination, the photodegradation rate is reduced because of unfavorable direct hole transfer. Not only reactant molecules affect the photocatalytic pathway and kinetics on the F- $\text{TiO}_2$ , but also the  $\text{TiO}_2$  photocatalyst itself affects the photocatalytic pathway and kinetics. Lv et al. [45, 46] showed that the dark adsorption of anionic Brilliant Red X3B is greatly reduced on both anatase and rutile  $\text{TiO}_2$  in the presence of fluoride, but interestingly, while the surface fluorination of anatase  $\text{TiO}_2$  enhanced significantly the photocatalytic degradation rate of X3B by more than two times at pH=3.0; however, the photocatalytic reactivity on rutile  $\text{TiO}_2$  was reduced to some extent after surface fluorination. It is implied that OH radical-mediated oxidation is preferred on anatase  $\text{TiO}_2$  and is enhanced on anatase F- $\text{TiO}_2$ , whereas the direct hole transfer-mediated oxidation is dominated on rutile  $\text{TiO}_2$  and is largely inhibited on rutile F- $\text{TiO}_2$  as a result of the hindered adsorption (or complexation).

It is noteworthy that the aforementioned photocatalytic oxidation mechanism is initiated through interfacial hole-transfer, either the direct hole transfer-mediated oxidation pathway or the OH-mediated oxidation pathway, which seems not require the participation of electron-activated  $\text{O}_2$  as an oxidant [47]. In fact, not only the hole transfer is affected by surface fluorination, but the electron transfer too. Choi et al. [41] inferred that the electron transfer kinetics is slower on F- $\text{TiO}_2$  than on pure  $\text{TiO}_2$ , based on the fact that the photocurrent collection in deaerated  $\text{TiO}_2$  suspensions was reduced in the presence of  $\text{F}^-$ , using either methyl viologen or ferric ions as electron transfer mediators (electron shuttles). It was assumed that a higher overpotential is required for electrons trapped on the surface of F- $\text{TiO}_2$  transferring to electron acceptors ( $\text{O}_2$ ) in the electrolyte solution. The surface  $\equiv\text{Ti}-\text{F}$  group seems to act as an electron-trapping site and to reduce interfacial electron transfer rates by tightly holding trapped electrons because of the strong electronegativity of fluorine [41, 48]. Such a presumption is confirmed by the inferior photocatalytic reduction reactivity of fluorinated photocatalysts [41].

Notably, although the interfacial electron transfer to  $\text{O}_2$  is retarded after surface fluorination, the charge recombination rate is still lower, as supported by electrochemical analyses [49]. It is possible that there is a stronger electron storage capacity on the surface of fluorinated  $\text{TiO}_2$  relative to pristine  $\text{TiO}_2$ . Electron storage in the surface  $\equiv\text{Ti}-\text{F}$  moiety, not only retards electron transfer (to  $\text{O}_2$ ), but also inhibits charge recombination that in turn significantly facilitates the interfacial hole transfer (to adsorbed  $\text{H}_2\text{O}$  or sur-

face hydroxyl) to give rise to free OH radicals (Fig. 10.3) [1, 4]. In this regard, the overall photocatalytic reactivity can be enhanced if the diminution in the recombination rate offsets the undesirable decrease in reactivity toward oxygen. Yu et al. showed that the modification of TiO<sub>2</sub> film with trifluoroacetic acid (TFA) results in superior photocatalytic activity, and proposed that the chemisorbed TFA can withdraw and enrich the photogenerated electrons and reduce the electron–hole recombination [32, 48].

The overall photocatalytic performance of F-TiO<sub>2</sub> could be further enhanced if electron transfer is improved. For instance, co-catalysts and ad-species promoting electron trapping and transfer give rise to synergistic effects on F-TiO<sub>2</sub> photocatalysts. For example, when the photocatalytic degradation of phenol in TiO<sub>2</sub>-F suspensions was performed in the presence of Cu<sup>2+</sup>, a synergistic increase in the photocatalyst activity was detected due to the efficient trapping of photogenerated electrons by Cu<sup>2+</sup> [50]. In line with this, the simultaneous modification of TiO<sub>2</sub> with platinum nanoparticles and fluoride [28, 47, 51] has been reported to be beneficial for both hydrogen production and organic pollutant degradation. For example, Yu et al. [28] showed that the deposition of Pt nanoparticles on F-TiO<sub>2</sub> nanosheets significantly enhanced the water splitting and production of H<sub>2</sub>, due to synergetic interaction of surface fluorine and Pt co-catalyst in promoting the interfacial electron transfer. Interestingly, in contrast to the negative surface fluorination effect on rutile as mentioned above, Xu et al. [45] demonstrated that in the presence of AgNO<sub>3</sub>, the fluoride-induced rate enhancement of photocatalytic phenol degradation could be also observed with rutile, as a result of the increased rate of scavenging the conduction band electrons.

In brief, the surface fluorination effects can be resumed as follows: (1) adsorption capacity and mode can be modified by surface fluorination, depending on the specific kind of molecules; (2) direct hole transfer is retarded by surface fluorination, while indirect hole transfer is enhanced by surface fluorination, originating from enhanced production of mobile free OH radicals; (3) surface electron storage is enhanced by fluorination, leading to retarded electron transfer but inhibited charge recombination. All these three aspects shall be comprehensively considered in understanding the unique photocatalytic redox properties of surface fluorinated photocatalysts (Fig. 10.3).

## 10.4 Lattice Fluorine Doping

In addition to the surface fluorination on TiO<sub>2</sub> photocatalysts, fluorine is also introduced into the lattice of TiO<sub>2</sub> host, for example, upon subsequent high-temperature calcination or using fluorine-containing titanium precursors (such as TiF<sub>4</sub>) [3, 14]. The localized energy levels (F 2p states) associated with lattice fluorine dopant in TiO<sub>2</sub> host residing below the valence band of TiO<sub>2</sub>, will not directly introduce localized states in the band gap [13]. Based on the EPR experiments coupled with DFT theoretical calculations, Giamello et al. [13] suggested that lattice fluorine doping induced the formation of reduced Ti<sup>3+</sup> centers, which highly localize the extra electron in the 3d orbital of titanium for charge compensation, introducing localized electronic states just below the bottom of the conduction band (Fig. 10.4a).

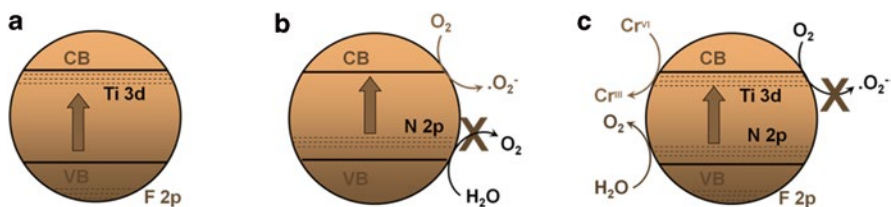


**Fig. 10.4** Band structures and photocatalytic redox abilities of F-doped TiO<sub>2</sub> (a); N-doped TiO<sub>2</sub> (b) and N/F-co-doped TiO<sub>2</sub> (c). CB conduction band, VB valence band

Amazingly, although localized electronic states in the band gaps and the visible light photocatalytic activity are introduced by lattice fluorine monodoping, commonly, no significant modification of the optical absorption in the visible light region is documented [13]. It was proposed that the surface defect states (oxygen vacancies) may introduce extrinsic surface absorption that cannot be recorded by absorption spectra, which is able to excite the charge carrier and trigger the surface photocatalytic reactions [38].

Significantly, the contribution from lattice doped fluorine is much more predominant when synergistically co-doped with other complementary elements. It has been demonstrated that various fluorine-involved co-doped TiO<sub>2</sub> systems, including metal/F-co-doped TiO<sub>2</sub> and nonmetal/F-co-doped TiO<sub>2</sub> [1, 15, 16, 36], exhibit improved visible light absorption and photocatalytic activity, compared to the pure or mono-doped ones. The synergetic effects of fluorine-based co-doping at least include 3 aspects. (1) *The complementary co-doping reduces the doping-associated energy cost and bulk defect density with consequence of higher doping level and thus stronger visible-light harvesting, smaller amount of recombination centers and thus faster charge mobility* [52]. For example, Zhao et al. [16] demonstrated that the amount of doped N in the N/F-TiO<sub>2</sub> (2.0 %) is much higher than that in N-TiO<sub>2</sub> (0.95 %) with the same N/Ti molar ratio of 3 in the synthesis system, but using NH<sub>4</sub>F and NH<sub>4</sub>Cl as dopants for N/F-TiO<sub>2</sub> and N-TiO<sub>2</sub> respectively. Accordingly, the absorption intensity in visible light region of the N/F-co-doped TiO<sub>2</sub> was observed to be much higher than that of the N-doped TiO<sub>2</sub> [16, 52], because the absorption intensity is normally proportional to the doping concentration. (2) *The synergetic codoping tunes the band structures (including CB and VB levels) with consequence of desired photocatalytic redox ability and selectivity*, which is well illustrated in Fig. 10.4c for N/F-co-doped TiO<sub>2</sub> system [16]. While the CB is essentially not altered, N-doping in TiO<sub>2</sub> results in the formation of N-derived localized states in the band gap above the VB (Fig. 10.4b) [16]. As a result, the oxidation power of the hole in the valence band ( $h_{\text{VB}}$ ) is reduced in the N-doped TiO<sub>2</sub>, which makes the oxidation reaction unfavorable [16]. Zhao et al. demonstrated that by a concomitant doping of fluorine, the position of N-derived localized states can be positively shifted towards VB, and consequently, the oxidation power and mobility of  $h_{\text{VB}}$  can be enhanced, which is confirmed by the experimentally observed blue-shifted light absorption, positive-shifted flat-band potential, as well as continuous

evolution of  $O_2$  by visible-light irradiation of  $AgNO_3$  aqueous solution in the N/F-co-doped  $TiO_2$  system [16]. More significantly, after N/F co-doping, the bottom of CB lowers down, and the reduction potential of CB electron is reduced to some extent that the one-electron  $O_2$  reduction become difficult [16]. Consequently, the competitive capture of CB electron by  $O_2$  is inhibited, and the selective reduction of toxic  $Cr^{VI}$  species in air without any sacrificial reagents is significantly enhanced in the N/F-co-doped  $TiO_2$  system under visible-light irradiation [16]. (3) *The co-doping would improve the thermal and photocatalytic stability.* For example, Yu et al. [22] recently showed that due to the shielding effect of surface fluorination, the phase transformations from anatase to rutile as well as removal of N-dopants during annealing were greatly inhibited. Such enhanced stabilizing effect on the phase structures and the nature of N-derived dopants is crucial for the superior photocatalytic performance. Moreover, the chemical structure evolution of doped nitrogen species upon annealing in air was experimentally recorded for the first time and correlated with the generation and annihilation of bulk oxygen deficiencies [22].

## 10.5 Conclusions and Outlooks

Modifying  $TiO_2$  photocatalysts by F-doping, starting from fluoride mediated structural control to the guest modification via surface/bulk doping, give rise to unique F-doping effects and exceptional photocatalytic performances. Note that, in most cases, both structural modification and surface/bulk fluorinations coexist, and consequently, the F-doping effects shall be comprehensively considered. For example, the unique geometrical and electronic properties associated with {001} facets are crucial for the charge separation and transfer occurring in photocatalytic redox processes, being a consequence of favored dissociative adsorption and spatial separation of redox sites [6]. Nevertheless, the synergetic effect between the exposed facets and surface fluorination shall not be ignored regarding facilitating adsorption and interfacial charge transfer [6, 30]. The structural advantages of porous hollow spherical architectures may enhance light harvesting by multi-reflection within cavity and facilitate surface reactant enrichment because of inside-out concentration variation [1, 7]. But, the contribution from surface/bulk fluorination and fluorine-promoted co-doping within hollow  $TiO_2$  microspheres in tuning light absorption and in inhibiting charge recombination shall not be underestimated [35, 36]. On the other hand, the specific effects of F-doping in tuning the multiple photocatalytic processes shall be understood taking account of the specific photocatalytic redox reaction occurred [1]. For example, as for the photocatalytic oxidation reactions, the surface fluorination effect depends not only on adsorption but also on the photocatalytic oxidation pathway of adsorbed molecules on  $TiO_2$ . If the surface fluorination enhances adsorption of molecules (usually, cationic and some polar molecules), normally, their photocatalytic oxidation can be enhanced by surface fluorination. Otherwise, if the surface fluorination inhibits adsorption of molecules (usually, anionic substrates and some nonpolar molecules), the surface fluorination effect is

dependent on the specific photocatalytic oxidation pathway of adsorbed molecules on  $\text{TiO}_2$ . When OH radical-mediated oxidation is preferred, the production of free hydroxyl radicals is enhanced by surface fluorination, and thus the photocatalytic oxidation can be enhanced by surface fluorination against inhibited adsorption, giving rise to overall positive surface fluorination effect. In contrast, as the direct hole transfer-mediated oxidation is dominated, the photocatalytic oxidation will be inhibited by surface fluorination in parallel with the hindered adsorption (or complexation) of molecules, resulting in a negative surface fluorination effect.

Overall, the special structural effects in combination with the unique surface/bulk fluorination effects afforded fluorinated  $\text{TiO}_2$  micro-/nanostructures as advanced photocatalysts with enhanced light harvesting ability, facilitated bulk diffusion and interfacial transfer of photoexcited electrons and holes, modified reactant adsorption capacity and mode, as well as controllable photoredox reaction mechanism and kinetics. Notably, the F-doping effects for non- $\text{TiO}_2$  photocatalysts are basically similar to those for  $\text{TiO}_2$ -based photocatalysts. The attractive photocatalytic properties of F-doped semiconductor photocatalysts endow them with superior performance in the environmental purification with respect to photocatalytic removal of organic pollutants and toxic metal ions in water and air, as well as in  $\text{H}_2$  production by photocatalytic water splitting [1, 2]. Nevertheless, there are still concerns about practical applications and mechanistic disagreements regarding fluorination effects of fluorinated photocatalysts. Although fluoride is highly stable towards photooxidation by VB hole owing to high oxidation potential of redox couple  $\text{F}^{\cdot}/\text{F}^- = 3.6 \text{ V}$  [41], the fluorinated photocatalyst is usually not stable. One detrimental limitation is that the fluoride adsorbed on the surface of semiconductor photocatalysts may be easily removed during their usage and can diffuse into the aqueous suspension, which affects the stability of fluorinated photocatalysts, the reproducibility of experimental results and the potential environmental impact of desorbing fluoride. Recently, Xu et al. [53] suggested that these drawbacks can be settled to great extent by fixing fluorine-containing minerals, such as fluorite or fluorapatite, on  $\text{TiO}_2$  (instead of the direct surface adsorption of fluoride ions), which may be more valuable for practical applications, due to the considerable positive surface fluorination effects and desirable recyclability. On the other hand, there might be contradiction in understanding of fluorination effects, which are likely associated with the coexistence of incorporated fluorine with different chemical species and in possible synergetic effects from all incorporated elements. Besides, the different routes and conditions employed for the preparation of fluorinated photocatalysts materials may result in different structures and not easily predictable properties.

## References

1. Liu SW, Yu JG, Cheng B et al (2012) Fluorinated semiconductor photocatalysts: tunable synthesis and unique properties. *Adv Colloid Interface Sci* 173:35–53
2. Lv KL, Cheng B, Yu JG et al (2012) Fluorine ions-mediated morphology control of anatase  $\text{TiO}_2$  with enhanced photocatalytic activity. *Phys Chem Chem Phys* 14:5349–5362

3. Yu JC, Yu JG, Ho W et al (2002) Effects of F-doping on the photocatalytic activity and microstructures of nanocrystalline TiO<sub>2</sub> powders. *Chem Mater* 14:3808–3816
4. Yu JG, Wang WG, Cheng B et al (2009) Enhancement of photocatalytic activity of mesoporous TiO<sub>2</sub> powders by hydrothermal surface fluorination treatment. *J Phys Chem C* 113:6743–6750
5. Yang HG, Sun CH, Qiao SZ et al (2008) Anatase TiO<sub>2</sub> single crystals with a large percentage of reactive facets. *Nature* 453(7195):638–641
6. Liu SW, Yu JG, Jaroniec M et al (2011) Anatase TiO<sub>2</sub> with dominant high-energy {001} facets: synthesis, properties, and applications. *Chem Mater* 23(18):4085–4093
7. Yu J, Liu S, Yu H (2007) Microstructures and photoactivity of mesoporous anatase hollow microspheres fabricated by fluoride-mediated self-transformation. *J Catal* 249(1):59–66
8. Liu S, Yu J, Mann S (2009) Spontaneous construction of photoactive hollow TiO<sub>2</sub> microspheres and chains. *Nanotechnology* 20:325606
9. Wang Q, Chen C, Zhao D (2008) Change of adsorption modes of dyes on fluorinated TiO<sub>2</sub> and its effect on photocatalytic degradation of dyes under visible irradiation. *Langmuir* 24:7338–7345
10. Kim J, Choi W, Park H (2010) Effects of TiO<sub>2</sub> surface fluorination on photocatalytic degradation of methylene blue and humic acid. *Res Chem Intermed* 36(2):127–140
11. Minero C, Mariella G, Maurino V et al (2000) Photocatalytic transformation of organic compounds in the presence of inorganic anions. 1. hydroxyl-mediated and direct electron-transfer reactions of phenol on a titanium dioxide-fluoride system. *Langmuir* 16:2632–2641
12. Minero C, Mariella G, Maurino V et al (2000) Photocatalytic transformation of organic compounds in the presence of inorganic ions. 2. competitive reactions of phenol and alcohols on a titanium dioxide-fluoride system. *Langmuir* 16(23):8964–8972
13. Czoska AM, Livraghi S, Chiesa M et al (2008) The nature of defects in fluorine-doped TiO<sub>2</sub>. *J Phys Chem C* 112(24):8951–8956
14. Ho W, Yu JC, Lee S (2006) Synthesis of hierarchical nanoporous F-doped TiO<sub>2</sub> spheres with visible light photocatalytic activity. *Chem Commun* 10:1115–1117
15. Chen C, Ma W, Zhao J (2010) Photocatalytic degradation of organic pollutants by co-doped TiO<sub>2</sub> under visible light irradiation. *Curr Org Chem* 14(7):630–644
16. Wang Q, Chen C, Ma W et al (2009) Pivotal role of fluorine in tuning band structure and visible-light photocatalytic activity of nitrogen-doped TiO<sub>2</sub>. *Chem Eur J* 15(19):4765–4769
17. Yu J, Dai G, Cheng B (2010) Effect of crystallization methods on morphology and photocatalytic activity of anodized TiO<sub>2</sub> nanotube array films. *J Phys Chem C* 114:19378–19385
18. Yu J, Zhang J (2010) A simple template-free approach to TiO<sub>2</sub> hollow spheres with enhanced photocatalytic activity. *Dalton Trans* 39(25):5860–5867
19. Yan MC, Chen F, Zhang JL et al (2005) Preparation of controllable crystalline titania and study on the photocatalytic properties. *J Phys Chem B* 109:8673–8678
20. Izumi F (2006) The polymorphic crystallization of titanium(IV) oxide under hydro-thermal conditions. II. The roles of inorganic anions in the nucleation of rutile and anatase from acid solutions. *Bull Chem Soc Jpn* 51(6):1771–1776
21. Yu J, Xiang Q, Ran J et al (2010) One-step hydrothermal fabrication and photocatalytic activity of surface-fluorinated TiO<sub>2</sub> hollow microspheres and tubular anatase single micro-crystals with high-energy facets. *CrystEngComm* 12(3):872–879
22. Liu S, Yu J, Wang W (2010) Effects of annealing on the microstructures and photoactivity of fluorinated N-doped TiO<sub>2</sub>. *Phys Chem Chem Phys* 12(38):12308–12315
23. Lv K, Xiang Q, Yu J (2011) Effect of calcination temperature on morphology and photocatalytic activity of anatase TiO<sub>2</sub> nanosheets with exposed {001} facets. *Appl Catal B Environ* 104(3-4):275–281
24. Liu G, Yu JC, Lu GQ et al (2011) Crystal facet engineering of semiconductor photocatalysts: motivations, advances and unique properties. *Chem Commun* 47(24):6763–6783

25. Fang WQ, Gong XQ, Yang HG (2011) On the unusual properties of anatase TiO<sub>2</sub> exposed by highly reactive facets. *J Phys Chem Lett* 2(7):725–734
26. Jiang ZY, Kuang Q, Xie ZX et al (2010) Syntheses and properties of micro/nanostructured crystallites with high-energy surfaces. *Adv Funct Mater* 20(21):3634–3645
27. Liu S, Yu J, Jaroniec M (2010) Tunable photocatalytic selectivity of hollow TiO<sub>2</sub> microspheres composed of anatase polyhedra with exposed {001} facets. *J Am Chem Soc* 132:11914–11916
28. Xiang Q, Yu J, Jaroniec M et al (2011) Tunable photocatalytic selectivity of TiO<sub>2</sub> films consisted of flower-like microspheres with exposed {001} facets. *Chem Commun* 47(15):4532–4534
29. Yu J, Qi L, Jaroniec M (2010) Hydrogen production by photocatalytic water splitting over Pt/TiO<sub>2</sub> nanosheets with exposed (001) facets. *J Phys Chem C* 114(34):13118–13125
30. Xiang Q, Lv K, Yu J (2010) Pivotal role of fluorine in enhanced photocatalytic activity of anatase TiO<sub>2</sub> nanosheets with dominant (0 0 1) facets for the photocatalytic degradation of acetone in air. *Appl Catal B Environ* 96(3-4):557–564
31. Yu JG, Low JX, Xiao W et al (2014) Enhanced photocatalytic CO<sub>2</sub>-reduction activity of anatase TiO<sub>2</sub> by coexposed {001} and {101} Facets. *J Am Chem Soc* 136(25):8839–8842
32. Yu J, Shi L (2010) One-pot hydrothermal synthesis and enhanced photocatalytic activity of trifluoroacetic acid modified TiO<sub>2</sub> hollow microspheres. *J Mol Catal A Chem* 326(1-2):8–14
33. Lv KL, Yu JG, Fan JJ et al (2011) Rugby-like anatase titania hollow nanoparticles with enhanced photocatalytic activity. *CrystEngComm* 13(23):7044–7048
34. Cai JH, Wang ZY, Lv KL et al (2013) Rapid synthesis of a TiO<sub>2</sub> hollow microsphere assembly from hollow nanoparticles with enhanced photocatalytic activity. *RSC Adv* 3(35):15273–15281
35. Xiang QJ, Yu JG, Cheng B et al (2010) Microwave-hydrothermal preparation and visible-light photoactivity of plasmonic photocatalyst Ag-TiO<sub>2</sub> nanocomposite hollow spheres. *Chem Asian J* 5(6):1466
36. Liu SW, Yu JG, Mann S (2009) Synergetic codoping in fluorinated Ti<sub>1-x</sub>Zr<sub>x</sub>O<sub>2</sub> hollow microspheres. *J Phys Chem C* 113(24):10712–10717
37. Yu JG, Liu SW, Zhou MH (2008) Enhanced photocatalytic activity of hollow anatase microspheres by Sn<sup>4+</sup> incorporation. *J Phys Chem C* 112(6):2050–2057
38. Li D, Haneda H, Hishita S et al (2005) Fluorine-doped TiO<sub>2</sub> powders prepared by spray pyrolysis and their improved photocatalytic activity for decomposition of gas-phase acetaldehyde. *J Fluor Chem* 126(1):69–77
39. Selli E, Mrowetz M (2006) H<sub>2</sub>O<sub>2</sub> evolution during the photocatalytic degradation of organic molecules on fluorinated TiO<sub>2</sub>. *New J Chem* 30(1):108–114
40. Maurino V, Minero C, Mariella G et al (2005) Sustained production of H<sub>2</sub>O<sub>2</sub> on irradiated TiO<sub>2</sub>- fluoride systems. *Chem Commun* 20:2627–2629
41. Park H, Choi W (2004) Effects of TiO<sub>2</sub> surface fluorination on photocatalytic reactions and photoelectrochemical behaviors. *J Phys Chem B* 108(13):4086–4093
42. Lv K, Xu Y (2006) Effects of polyoxometalate and fluoride on adsorption and photocatalytic degradation of organic dye X3B on TiO<sub>2</sub>: the difference in the production of reactive species. *J Phys Chem B* 110(12):6204–6212
43. Selli E, Mrowetz M (2005) Enhanced photocatalytic formation of hydroxyl radicals on fluorinated TiO<sub>2</sub>. *Phys Chem Chem Phys* 7:1100–1102
44. Park H, Choi W (2004) Enhanced remote photocatalytic oxidation on surface-fluorinated TiO<sub>2</sub>. *Langmuir* 20(26):11523–11527
45. Xu Y, Lv K, Xiong Z et al (2007) Rate enhancement and rate inhibition of phenol degradation over irradiated anatase and rutile TiO<sub>2</sub> on the addition of NaF: new insight into the mechanism. *J Phys Chem C* 111(51):19024–19032
46. Lv K, Li X, Deng K et al (2010) Effect of phase structures on the photocatalytic activity of surface fluorinated TiO<sub>2</sub>. *Appl Catal B Environ* 95(3-4):383–392

47. Kim J, Lee J, Choi W (2008) Synergic effect of simultaneous fluorination and platinization of TiO<sub>2</sub> surface on anoxic photocatalytic degradation of organic compounds. *Chem Commun* 6:756–758
48. Yu JC, Ho W, Yu J (2003) Effects of trifluoroacetic acid modification on the surface microstructures and photocatalytic activity of mesoporous TiO<sub>2</sub> thin Films. *Langmuir* 19(9):3889–3896
49. Monllor-Satoca D, Gomez R (2008) Electrochemical method for studying the kinetics of electron recombination and transfer reactions in heterogeneous photocatalysis: the effect of fluorination on TiO<sub>2</sub> nanoporous layers. *J Phys Chem C* 112(1):139–147
50. Wang N, Chen Z, Zhu L et al (2007) Synergistic effects of cupric and fluoride ions on photocatalytic degradation of phenol. *J Photochem Photobiol A Chem* 191(2):193–200
51. Liu G, Yang HG, Wang XW et al (2009) Enhanced photoactivity of oxygen-deficient anatase TiO<sub>2</sub> sheets with dominant {001} facets. *J Phys Chem C* 113(52):21784–21788
52. Di Valentin C, Finazzi E, Pacchioni G et al (2008) Density functional theory and electron paramagnetic resonance study on the effect of N-F codoping of TiO<sub>2</sub>. *Chem Mater* 20(1):3706–3714
53. Cong S, Xu Y (2011) Enhanced sorption and photodegradation of chlorophenol over fluoride-loaded TiO<sub>2</sub>. *J Hazard Mater* 192(2):485–489

# Chapter 11

## Photocatalytic Decomposition of NH<sub>3</sub> Over Fe-Doped TiO<sub>2</sub> Prepared by Solid-State Impregnation

Yuichi Ichihashi, Atsushi Okemoto, Kazutaka Obata, Keita Taniya, and Satoru Nishiyama

### 11.1 Introduction

Investigations using various kinds of titanium dioxide (TiO<sub>2</sub>), such as photo-splitting of water [1], photovoltaic devices [2], liquid solar cells [3], surface wettability conversion [4], degradation of pollutants and toxic materials [5–8], have been actively carried out. This wide applicability can be attributed to its nontoxicity, low cost, photostability, redox efficiency, and availability. However, the low efficiency of hydrogen production with TiO<sub>2</sub> is mainly due to its large bandgap (3.2 eV) located in the UV region of solar radiation, which accounts for only 3–5 % of the incoming solar energy [9, 10], rendering the overall process impractical. Therefore, some shifts in optical response from the UV to the visible range will have a profound positive effect on the photocatalytic efficiencies of TiO<sub>2</sub> materials [11–13]. TiO<sub>2</sub> doped with other low-cost 3d transition metals such as Fe and Cr [12–15] can extend its light absorption to the visible spectrum and improve the separation efficiency of photo-induced electrons and holes. Owing to the two main reasons stated above, TiO<sub>2</sub> doped with these low-cost metals can also display a higher photocatalytic activity of H<sub>2</sub> production than un-doped TiO<sub>2</sub> [14, 15].

As global energy needs continue to increase, fossil fuel resources are depleted, and serious environmental problems arise; modern society has been seeking new technologies to effectively address these issues [1, 16–18]. Hydrogen has been identified as a promising future energy carrier. There is much interest in finding ways to produce hydrogen from renewable energy supplies, such as solar and wind resources, to avoid the emission of greenhouse gases inevitably released by its production from fossil fuels. Photocatalytic water splitting using solar energy can contribute a

---

Y. Ichihashi (✉) • A. Okemoto • K. Obata • K. Taniya • S. Nishiyama  
Department of Chemical Science and Engineering, Graduate School of Engineering, Kobe University, 1-1 Rokkodai, Nada, Kobe 657-8501, Japan  
e-mail: [ichiy@kobe-u.ac.jp](mailto:ichiy@kobe-u.ac.jp)

solution to problems arising from environmental and energy issues related to hydrogen production [15, 19, 20]. However, water splitting cannot proceed without sacrificial carbon-containing materials such as methanol or ethanol.

The photodecomposition of ammonia is an anticipated methodology as hydrogen production processes implement these requirements [21–24]. The photocatalytic process proceeds at room temperature and atmospheric pressure by only using clean and inexhaustible light energy. Furthermore, ammonia has a number of advantages as a hydrogen storage carrier as follows: CO<sub>2</sub> is not exhausted in ammonia decomposition since it does not contain carbon. Ammonia can be easily transported and stored, as severe conditions are not necessary for its liquefaction. Hydrogen content percentage in one molecule (NH<sub>3</sub>: 17.6 %) is high in comparison with that in other hydrogen storage carriers such as liquefied petroleum gas (LPG). As mentioned above, this photocatalytic process has the possibility of contributing to the establishment of a hydrogen energy recycling-based society.

Until now the doping of Fe nano particles to TiO<sub>2</sub> photocatalyst by preparation method of a solid-state reaction had been successfully used to modify the electronic properties of TiO<sub>2</sub> semiconductor, so that in this chapter we focused our attention on the possibility of utilizing the hydrogen formation by the photocatalytic decomposition of ammonia under visible light irradiation.

## 11.2 Preparation and Characterization of TiO<sub>2</sub> Doped with Fe

Fe-doped TiO<sub>2</sub> photocatalyst (Fe-TiO<sub>2</sub>) was prepared by a solid-state reaction [25]. A mixture of starting materials consisting of TiO<sub>2</sub> (Degussa P25), Fe<sub>2</sub>O<sub>3</sub> (Nacalai Tesque) and H<sub>2</sub>O was evaporated to dryness in a hot water bath at 363 K. The mixture was calcined at 1273 K for 10 h in air. The obtained material was named Fe-TiO<sub>2</sub>. For comparison, Fe loaded on a TiO<sub>2</sub> photocatalyst (Fe/TiO<sub>2</sub>) was also prepared by the impregnation method with an aqueous solution of [Fe(NO<sub>3</sub>)<sub>3</sub>]·9H<sub>2</sub>O. TiO<sub>2</sub> calcined at 1273 K was added into an aqueous solution in which the precursor was dissolved. The solution was evaporated to dryness in a hot water bath at 353 K. The sample was dried and then calcined under air-flow at 723 K (Fe/TiO<sub>2</sub>). Platinization of Fe/TiO<sub>2</sub> (Pt loading: 0.5 wt%) was carried out using a photodeposition method involving the irradiation of an aqueous suspension of TiO<sub>2</sub> with a 500 W Xenon lamp for 2 h in the presence of methanol, H<sub>2</sub>O and H<sub>2</sub>PtCl<sub>6</sub> [26]. After irradiation, the filtered Pt/Fe-TiO<sub>2</sub> sample was washed with deionized water, and then freeze-dried. The obtained sample was designated as Pt/Fe-TiO<sub>2</sub>.

The photoluminescence (PL) properties of samples were measured with a fluorescence spectrometer (HITACHI F-7000) equipped with a 150 W Xenon lamp at 77 K. Diffuse reflection (DR) spectra were obtained using a UV–visible diffuse reflectance (UV–Vis-DR) spectrometer (HITACHI U-3210D) and were converted from reflection to absorption by the Kubelka–Munk method. Electron spin resonance

(ESR) signals from both  $\text{Fe}^{3+}$  and  $\text{Ti}^{4+}$  ions were recorded in the X-band at room temperature. ESR signals were registered by the lack of saturation in the field range of 30–550 mT.

The photocatalytic reaction was carried out in a quartz-glass batch reactor. The photocatalyst (40 mg) was suspended in 5 mL of ammonia aqueous solution (0.59 mol/L). The reactor was purged with an Ar gas flow for 15 min. The reaction solution was then stirred with a magnetic stirrer and irradiated with a 500 W Xenon lamp through a color filter (Hoya UV25 or L42) for 8 h. The gas phase products were analyzed by gas chromatography (Shimadzu GC-8A) equipped with a thermal conductivity detector using Ar carrier gas.

### 11.3 Unique Photocatalysis of $\text{TiO}_2$ Doped with Fe

UV–Vis-DR spectra of Fe- $\text{TiO}_2$ , Fe/ $\text{TiO}_2$ , and  $\text{TiO}_2$  are shown in Fig. 11.1. As made evident from the spectra, the light absorption edge of Fe- $\text{TiO}_2$  prepared by a solid-state reaction is remarkably red-shifted to the visible light range compared with both Fe/ $\text{TiO}_2$  prepared by an impregnation method and pure  $\text{TiO}_2$ . The red shift in the absorption edge of Fe- $\text{TiO}_2$  can be attributed to the excitation of 3d electrons of  $\text{Fe}^{3+}$  ions to the  $\text{TiO}_2$  conduction band (charge-transfer transition), i.e., the formation of impurity band [14]. Therefore, it is suggested that the substitution of Fe for  $\text{Ti}^{4+}$  leads to the effective utilization of irradiated light. Figure 11.2 shows the photoluminescence (PL) spectra of Pt/Fe- $\text{TiO}_2$ , Pt/Fe/ $\text{TiO}_2$ , and Pt/ $\text{TiO}_2$  excited by the light irradiation at wavelength of either 310 nm (a) or 500 nm (b). As shown in Fig. 11.2a, the photoluminescence peaks of all photocatalysts, which are excited by the light irradiation at wavelength of 310 nm, are observed at around 390 nm. These spectra are attributed to pure rutile  $\text{TiO}_2$ . The peak intensity of Pt/Fe- $\text{TiO}_2$  is lower than that of Pt/ $\text{TiO}_2$  and Pt/Fe/ $\text{TiO}_2$ . It is speculated that formation of the impurity band in Pt/Fe- $\text{TiO}_2$  leads to the quenching of luminescence intensity of pure  $\text{TiO}_2$  crystal. Figure 11.2b shows the luminescence spectra of Pt/Fe- $\text{TiO}_2$ , Pt/Fe/ $\text{TiO}_2$ , and Pt/ $\text{TiO}_2$  excited by the light irradiation at wavelength of 500 nm. Pt/Fe- $\text{TiO}_2$  photocatalyst exhibits an intense photoluminescence at around 564 nm, which is attributed to the formation of impurity band [27]. On the other hand, the photoluminescence intensities of Pt/ $\text{TiO}_2$  and Pt/Fe/ $\text{TiO}_2$  photocatalysts are quite weak. Therefore, it is suggested that Fe- $\text{TiO}_2$  photocatalyst prepared by a solid-state reaction forms an impurity band (see Fig. 11.3).

UV light irradiation of Pt/Fe- $\text{TiO}_2$  photocatalyst which is doped with Fe nano particles in titanium oxide by a solid-state reaction leads to the decomposition of ammonia to hydrogen and nitrogen in an aqueous solution at room temperature. Figure 11.4 shows the time profiles of  $\text{H}_2$  and  $\text{N}_2$  yields in the photocatalytic reaction of  $\text{NH}_3$  solution over Pt/Fe- $\text{TiO}_2$ . No formation of products is observed under dark conditions. The formation of hydrogen and nitrogen is observed as soon as the reaction solution is irradiated with UV light. The above results indicate that this reaction proceeds photocatalytically. Nitrogen and hydrogen are found to be produced

**Fig. 11.1** UV-Vis-DR spectra of Fe-TiO<sub>2</sub>, Fe/TiO<sub>2</sub>, and TiO<sub>2</sub> photocatalysts

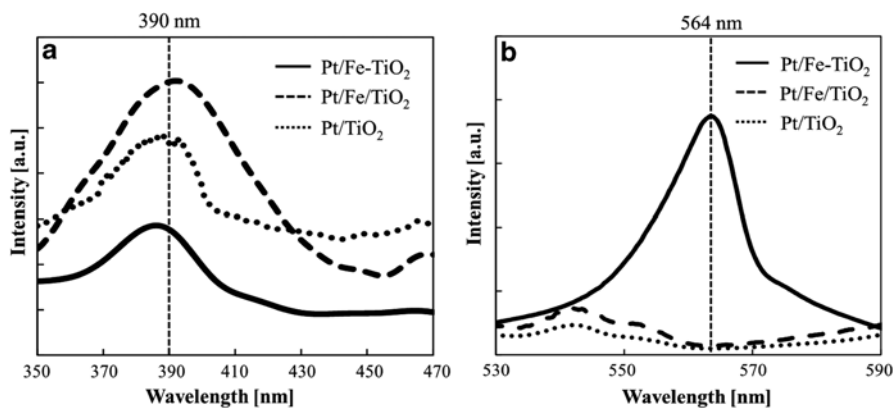
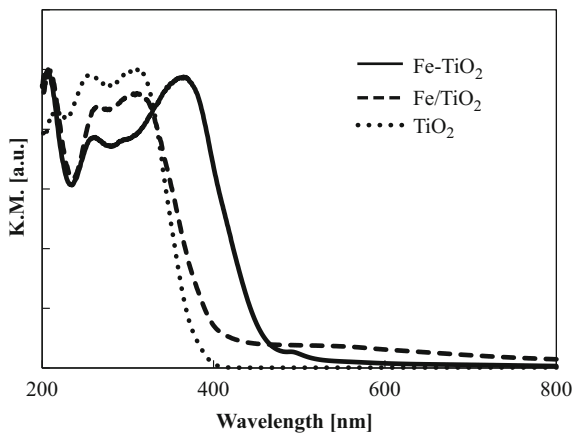


**Fig. 11.2** Photoluminescence spectra of Pt/TiO<sub>2</sub>, Pt/Fe/TiO<sub>2</sub>, and Pt/Fe-TiO<sub>2</sub>; excitation light: 310 nm (a) and 500 nm (b)

**Fig. 11.3** Schematic representation of impurity band in Fe-TiO<sub>2</sub> photocatalyst prepared by a solid-state reaction

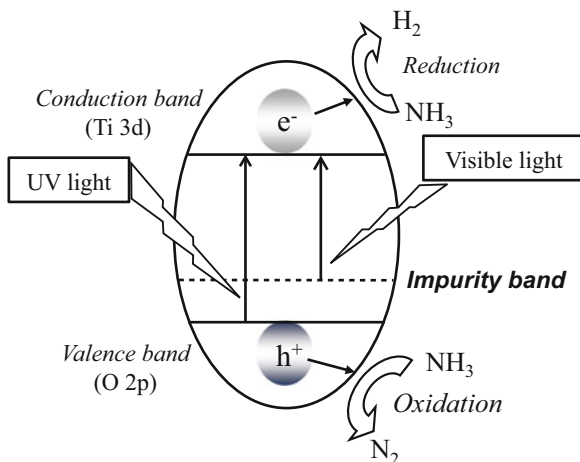


**Fig. 11.4** Time profiles of H<sub>2</sub> and N<sub>2</sub> yields for the photodecomposition of NH<sub>3</sub> aq. over Pt/Fe-TiO<sub>2</sub> under UV light irradiation ( $\lambda > 250$  nm)

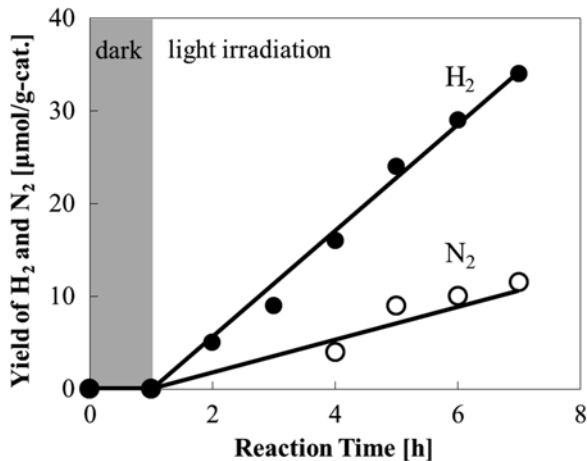


**Table 11.1** Photocatalytic yield of H<sub>2</sub> under various reaction conditions over Pt/TiO<sub>2</sub>, Pt/Fe/TiO<sub>2</sub>, and Pt/Fe-TiO<sub>2</sub> photocatalysts: Pt content; 0.5 wt%, Fe content; 1.0 wt%

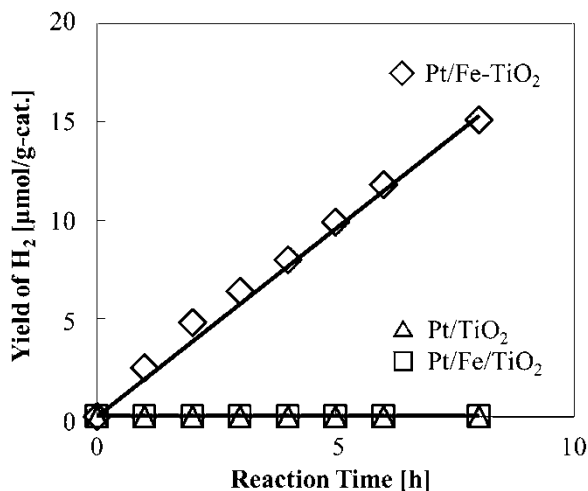
Entry	Catalyst	Reactant	Yield of H <sub>2</sub> [μmol/g-cat.]
1	Pt/TiO <sub>2</sub>	H <sub>2</sub> O	0
2	Pt/TiO <sub>2</sub>	NH <sub>3</sub> +H <sub>2</sub> O	18
3	Pt/Fe-TiO <sub>2</sub>	H <sub>2</sub> O	0
4	Pt/Fe-TiO <sub>2</sub>	NH <sub>3</sub> +H <sub>2</sub> O	27
5	Pt/Fe/TiO <sub>2</sub>	NH <sub>3</sub> +H <sub>2</sub> O	10

by the ratio of 1:3 until 7 h (see Fig. 11.4). It is seemed that nitrogen and hydrogen stoichiometrically produced from NH<sub>3</sub>. From the mass spectrometry by using the deuterium oxide (D<sub>2</sub>O), the photodecomposition of NH<sub>3</sub> in D<sub>2</sub>O solution caused not the formation of D<sub>2</sub>, but the formation of H<sub>2</sub>. Hence, hydrogen formation is established as being derived from the photodecomposition of ammonia.

Table 11.1 shows the photocatalytic H<sub>2</sub> evolution from an aqueous solution of NH<sub>3</sub> over Pt/Fe-TiO<sub>2</sub>, Pt/Fe/TiO<sub>2</sub>, and Pt/TiO<sub>2</sub> photocatalysts under UV light irradiation. In case of the reaction over Pt/TiO<sub>2</sub> and Pt/Fe-TiO<sub>2</sub> photocatalysts with only H<sub>2</sub>O as a reactant, the formation of H<sub>2</sub> is not observed (Entries 1, 3). On the other hand, the formation of hydrogen over all photocatalysts is observed by using an aqueous solution of NH<sub>3</sub> (Entries 2, 4, 5). Hence, it is found that NH<sub>3</sub> contributes to hydrogen formation. The photocatalytic activity of Pt/Fe-TiO<sub>2</sub> which is doped with Fe by a solid-state reaction is found to be higher than Pt/TiO<sub>2</sub> (Entries 2, 4). H<sub>2</sub> yield of Pt/Fe/TiO<sub>2</sub> photocatalyst prepared by impregnation method is also lower than that of Pt/Fe-TiO<sub>2</sub> (Entries 4, 5). As shown in Fig. 11.4 and Table 11.1, Pt/Fe-TiO<sub>2</sub> gives the highest yield of H<sub>2</sub> via NH<sub>3</sub> photodecomposition.

The decomposition of aqueous ammonia is carried out over Pt/Fe-TiO<sub>2</sub>, Pt/TiO<sub>2</sub>, and Pt/Fe/TiO<sub>2</sub> under visible light irradiation ( $\lambda > 420$  nm); the results are shown in Fig. 11.5. The visible light irradiation to Pt/Fe-TiO<sub>2</sub> in the presence of ammonia

**Fig. 11.5** Time profiles of  $H_2$  yields for the photodecomposition of  $NH_3$  aq. over Pt/TiO<sub>2</sub>, Pt/Fe/TiO<sub>2</sub>, and Pt/Fe-TiO<sub>2</sub> under visible light irradiation ( $\lambda > 420$  nm)



(a) Pt/TiO<sub>2</sub>

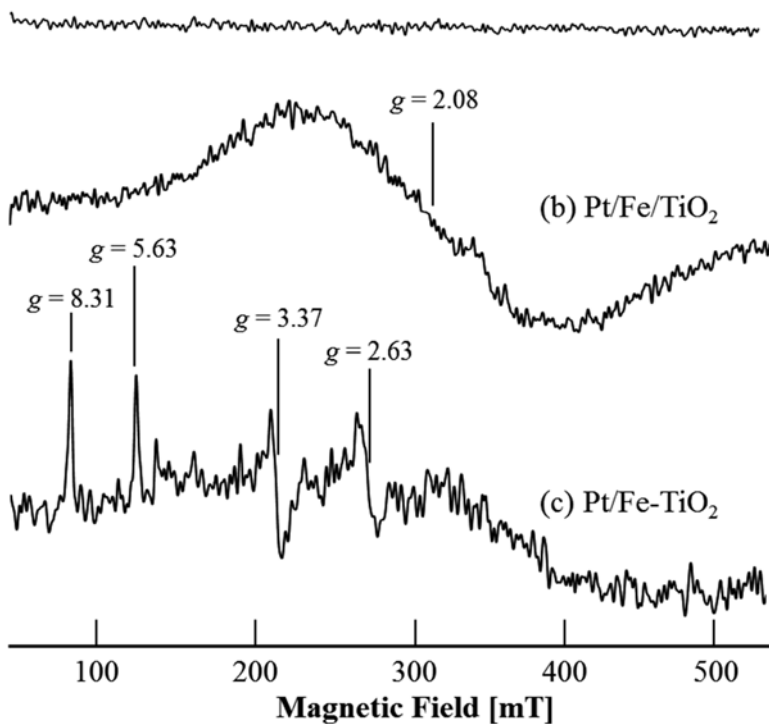


**Fig. 11.6** ESR spectra of Pt/TiO<sub>2</sub> (a), Pt/Fe/TiO<sub>2</sub> (b), and Pt/Fe-TiO<sub>2</sub> (c) photocatalysts

leads to the photocatalytic decomposition of  $\text{NH}_3$  and the evolution of  $\text{H}_2$ ; doping with Fe in  $\text{TiO}_2$  by a solid-state reaction is effective to utilize visible light. On the other hand, no evolution of  $\text{H}_2$  is observed over  $\text{Pt/TiO}_2$  and  $\text{Pt/Fe/TiO}_2$ . No effect attributed to Fe impregnation can be observed;  $\text{TiO}_2$  impregnated with Fe does not function as a photocatalyst under visible light.

ESR spectra of each photocatalyst are shown in Fig. 11.6. ESR spectroscopy is the technique for detecting and monitoring very low levels of transition metal ion dopants [28]. Figure 11.6 shows the ESR spectra of  $\text{Pt/TiO}_2$ ,  $\text{Pt/Fe/TiO}_2$ , and  $\text{Pt/Fe-TiO}_2$ . No peaks are observed in the spectrum of  $\text{Pt/TiO}_2$  (see Fig. 11.6a); it is obvious that peaks attributed to Pt and Ti atoms are not observed. The spectrum of  $\text{Pt/Fe/TiO}_2$  has a signal at  $g=2.08$ , which is assigned to the  $\text{Fe}^{3+}$  spin ( $S=5/2$ ) on the surface of  $\text{TiO}_2$  (Fig. 11.6b) [29, 30]. In addition, the spectrum of the  $\text{Pt/Fe-TiO}_2$  shown in Fig. 11.6c has signals present at  $g=2.63, 3.37, 5.63,$  and  $8.31$ , which are assigned to  $\text{Fe}^{3+}$  ions substituting for  $\text{Ti}^{4+}$  in the  $\text{TiO}_2$  rutile lattice [31]. The Fe dopant can be inserted into the  $\text{TiO}_2$  lattice as a Fe impurity band below the conduction band and above the valence band of  $\text{TiO}_2$ , creating an optical band gap [19, 32]. It has been reported that electrons in the valence band of  $\text{TiO}_2$  can firstly transfer to the Fe impurity band, and these electrons can then transfer from the impurity band to the conduction band through absorption of other photons. The excited electrons appear in the conduction band and holes in the valence band are subsequently formed [19]. Therefore, it is speculated that the substitution of  $\text{Ti}^{4+}$  with  $\text{Fe}^{3+}$  in  $\text{Fe-TiO}_2$  leads to the effective utilization of irradiated light owing to the presence of an Fe impurity band. As the results of XRD measurement of the  $\text{TiO}_2$  photocatalysts, only rutile  $\text{TiO}_2$  peaks were observed and no peak attributed to ferric oxide species on the surface of  $\text{TiO}_2$  could be observed. Thus, it is suggested that the dopant metals substituted for portions of the  $\text{Ti}^{4+}$  sites in  $\text{TiO}_2$  crystal do not effect a change in the  $\text{TiO}_2$  structure [25]. According to the above results obtained from UV-Vis, PL and ESR analyses, it is speculated that  $\text{TiO}_2$  has the ability to use not only UV light but also visible light by substituting  $\text{Fe}^{3+}$  for  $\text{Ti}^{4+}$  in its lattice.

## 11.4 Summary

Photocatalyst prepared by the loading of Pt on  $\text{Fe-TiO}_2$  is shown to effectively decompose aqueous  $\text{NH}_3$  to  $\text{H}_2$  and  $\text{N}_2$  under UV light irradiation at room temperature.  $\text{Pt/Fe-TiO}_2$  photocatalyst prepared by a solid-state reaction ( $\text{Pt/Fe-TiO}_2$ ) led to a higher activity than pure  $\text{TiO}_2$  photocatalysts ( $\text{Pt/TiO}_2$ ). And also,  $\text{Pt/Fe-TiO}_2$  effectively produced the hydrogen by the photocatalytic decomposition of  $\text{NH}_3$  solution under visible light irradiation. It was found from UV-Vis, ESR, and PL measurements that by substituting  $\text{Fe}^{3+}$  for  $\text{Ti}^{4+}$ , the resulting  $\text{Fe-TiO}_2$  catalyst material might allow for the effective utilization of irradiation light owing to the presence of a Fe impurity band, thereby leading to its higher activity.

## References

1. Fujishima A, Kudo K (1972) Electrochemical photolysis of water at a semiconductor electrode. *Nature* 238:37–38
2. Linsebigler AL, Lu G, Yates JT (1995) Photocatalysis on TiO<sub>2</sub> surfaces: principles, mechanisms, and selected results. *Chem Rev* 95:735–758
3. O'Regan B, Grätzel M (1991) A low-cost, high-efficiency solar cell based on dye-sensitized colloidal TiO<sub>2</sub> films. *Nature* 353:737–740
4. Wang R, Sakai N, Fujishima A, Watanabe T, Hashimoto K (1999) Studies of surface wettability conversion on TiO<sub>2</sub> single-crystal surfaces. *J Phys Chem B* 103:2188–2194
5. Rodriguez SM, Richter C, Galvez GB, Vincent M (1996) Photocatalytic degradation of industrial residual waters. *Sol Energy* 56:401–410
6. Irmak S, Kusvuran E, Erbatur O (2004) Degradation of 4-chloro-2-methylphenol in aqueous solution by UV irradiation in the presence of titanium dioxide. *Appl Catal B* 54:85–91
7. Azevedo EB, Neto FRA, Dezotti M (2004) Degradation of 4-chloro-2-methylphenol in aqueous solution by UV irradiation in the presence of titanium dioxide. *Appl Catal B* 54:165–173
8. Baran W, Makowski A, Wardas W (2008) The effect of UV radiation absorption of cationic and anionic dye solutions on their photocatalytic degradation in the presence TiO<sub>2</sub>. *Dyes Pigm* 76:226–230
9. Tang H, Prasad K, Sanjinés R, Schmid PE, Lévy F (1994) Electrical and optical properties of TiO<sub>2</sub> anatase thin films. *J Appl Phys* 75:2042–2047
10. Lindgren T, Mwabora JM, Avendaño E, Jonsson J, Hoel A, Granqvist CG (2003) Photoelectrochemical and optical properties of nitrogen doped titanium dioxide films prepared by reactive DC magnetron sputtering. *J Phys Chem B* 107:5709–5716
11. Asahi R, Morikawa T, Ohwaki T, Aoki K, Taga Y (2001) Visible-light photocatalysis in nitrogen-doped titanium oxides. *Science* 293:269–271
12. Anpo M, Ichihashi Y, Takeuchi M, Yamashita H (1998) Design of unique titanium oxide photocatalysts by an advanced metal ion-implantation method and photocatalytic reactions under visible light irradiation. *Res Chem Intermed* 24:143–149
13. Yamashita H, Ichihashi Y, Takeuchi M, Kishiguchi S, Anpo M (1999) Characterization of metal ion-implanted titanium oxide photocatalysts operating under visible light irradiation. *J Synchrotron Radiat* 6:451–452
14. Khan MA, Woo SI, Yang OB (2008) Hydrothermally stabilized Fe(III) doped titania active under visible light for water splitting reaction. *Int J Hydrog Energy* 33:5345–5351
15. Dholam R, Patel N, Adami M, Miotello A (2009) Hydrogen production by photocatalytic water-splitting using Cr- or Fe-doped TiO<sub>2</sub> composite thin films photocatalyst. *Int J Hydrog Energy* 34:5337–5346
16. Maeda K, Abe R, Domen K (2011) Role and function of ruthenium species as promoters with TaON-based photocatalysts for oxygen evolution in two-step water splitting under visible light. *J Phys Chem C* 115:3057–3064
17. Dorian JP, Franssen HT, Simbeck DR (2006) Global challenges in energy. *Energy Policy* 34:1984–1991
18. Mu Y, Zheng XJ, Yu HQ, Zhu RF (2006) Biological hydrogen production by anaerobic sludge at various temperatures. *Int J Hydrog Energy* 31:780–785
19. Sun T, Liu E, Fan J, Hu X, Wu F, Hou W, Yang Y, Kang L (2013) High photocatalytic activity of hydrogen production from water over Fe doped and Ag deposited anatase TiO<sub>2</sub> catalyst synthesized by solvothermal method. *Chem Eng J* 228:896–906
20. Momirlan M, Veziroglu TN (2002) Current status of hydrogen energy. *Renew Sustain Energy Rev* 6:141–179
21. Li QS, Domen K, Naito S, Onishi T, Tamaru K (1983) Photocatalytic synthesis and photodecomposition of ammonia over SrTiO<sub>3</sub> and BaTiO<sub>3</sub> based catalyts. *Chem Lett* 3:321–324

22. Kaneko M, Gokan N, Katakura N, Takei Y, Hoshino M (2005) Artificial photochemical nitrogen cycle to produce nitrogen and hydrogen from ammonia by platinumized  $\text{TiO}_2$  and its application to a photofuel cell. *Chem Commun* 2005:1625–1627
23. Maffei N, Pelletier L, Charland JP, McFarlan A (2005) An intermediate temperature direct ammonia fuel cell using a proton conducting electrolyte. *J Power Sources* 140:264–267
24. Pelletier L, McFarlan A, Maffei N (2005) Ammonia fuel cell using doped barium cerate proton conducting solid electrolytes. *J Power Sources* 145:262–265
25. Kato H, Kudo A (2002) Visible-light-response and photocatalytic activities of  $\text{TiO}_2$  and  $\text{SrTiO}_3$  photocatalysts codoped with antimony and chromium. *J Phys Chem B* 106:5029
26. Nemoto J, Gokan N, Ueno H, Kaneko M (2007) Photodecomposition of ammonia to dinitrogen and dihydrogen on platinumized  $\text{TiO}_2$  nanoparticles in an aqueous solution. *J Photochem Photobiol A* 185:295–300
27. Tang H, Berger H, Schmid PE, Levy F (1993) Photoluminescence in  $\text{TiO}_2$  anatase single crystals. *Solid State Commun* 87:847–850
28. Egerton TA, Harris E, Lawson EJ, Mile B, Rowlands CC (2001) An EPR study of diffusion of iron into rutile. *Phys Chem Chem Phys* 3:497
29. Ranjit KT, Viswanathan B (1997) Synthesis, characterisation and photocatalytic properties of iron doped  $\text{TiO}_2$  catalysts. *J Photochem Photobiol A* 108:79–84
30. Zhu J, Chen F, Zhang J, Chen H, Anpo M (2006)  $\text{Fe}^{3+}$ - $\text{TiO}_2$  photocatalysts prepared by combining sol-gel method with hydrothermal treatment and their characterization. *J Photochem Photobiol A* 180:196–204
31. Maksinov NG, Mikhailova IL, Anufrenko VF (1973) The EPR spectra and the state of  $\text{Fe}^{2+}$  ions in  $\text{TiO}_2$ . *Kinet Catal* 13:1162
32. Yalcin Y, Kilic M, Cinar Z (2010)  $\text{Fe}^{3+}$ -doped  $\text{TiO}_2$ : a combined experimental and computational approach to the evaluation of visible light activity. *Appl Catal B* 99:469–477

# Chapter 12

## Surface-Functionalized TiO<sub>2</sub> Photocatalyst Modified by the Interfacial Surface Complex (ISC)

Shinya Higashimoto

### 12.1 Introduction

TiO<sub>2</sub> photocatalysts are known to promote such photochemical reactions as the decomposition of volatile organic compounds (VOC), H<sub>2</sub> production from aqueous solutions, and selective transformation of organic compounds [1–6]. In general, TiO<sub>2</sub> photocatalysts operate by the band-gap excitation (3.0–3.2 eV) or more under UV-light irradiation which reaches only a few percent to the earth's surface. Therefore, the development of visible-light sensitive TiO<sub>2</sub> photocatalyst has been a great concern regarding the efficient utilization of solar light [7–10]. Figure 12.1 shows several strategies to design visible-light responsive TiO<sub>2</sub> photocatalysts: coupling of different semiconductors, doping with nitrogen and other elements [11–15], organic dye-sensitizer [16], plasmonic Au, Ag nanoparticles [17–20], metal doping or grafting with such metal ions as Fe<sup>3+</sup> and Cu<sup>2+</sup>, and interfacial surface complex (ISC) [21–32].

Recently, attention is paid to the ISC formed by the interaction of TiO<sub>2</sub> surface with such colorless organic compounds as amine [21, 22], phenol [23], and aromatic alcohol [24–30]. For example, the binaphthol-modified TiO<sub>2</sub> [31] and hydroxynaphthalene-modified TiO<sub>2</sub> photocatalysts exhibit hydrogen production from triethanolamine aqueous solutions and selective reduction of nitrobenzene into aminobenzene [32], respectively, under visible-light irradiation. Moreover, the ISC formed by the interaction of benzyl alcohol with TiO<sub>2</sub> surface was found to induce unique oxidations of benzyl alcohol into benzaldehyde under visible-light irradiation [24–30].

In this chapter, we review the visible-light responsive TiO<sub>2</sub> photocatalyst modified with the ISC, which exhibits selective oxidation of several aromatic alcohols under visible-light irradiation. It was confirmed that the origin of the visible-light response

---

S. Higashimoto (✉)  
College of Engineering, Osaka Institute of Technology,  
5-16-1 Omiya, Asahi-ku, Osaka 535-8585, Japan  
e-mail: [higashimoto@chem.oit.ac.jp](mailto:higashimoto@chem.oit.ac.jp)

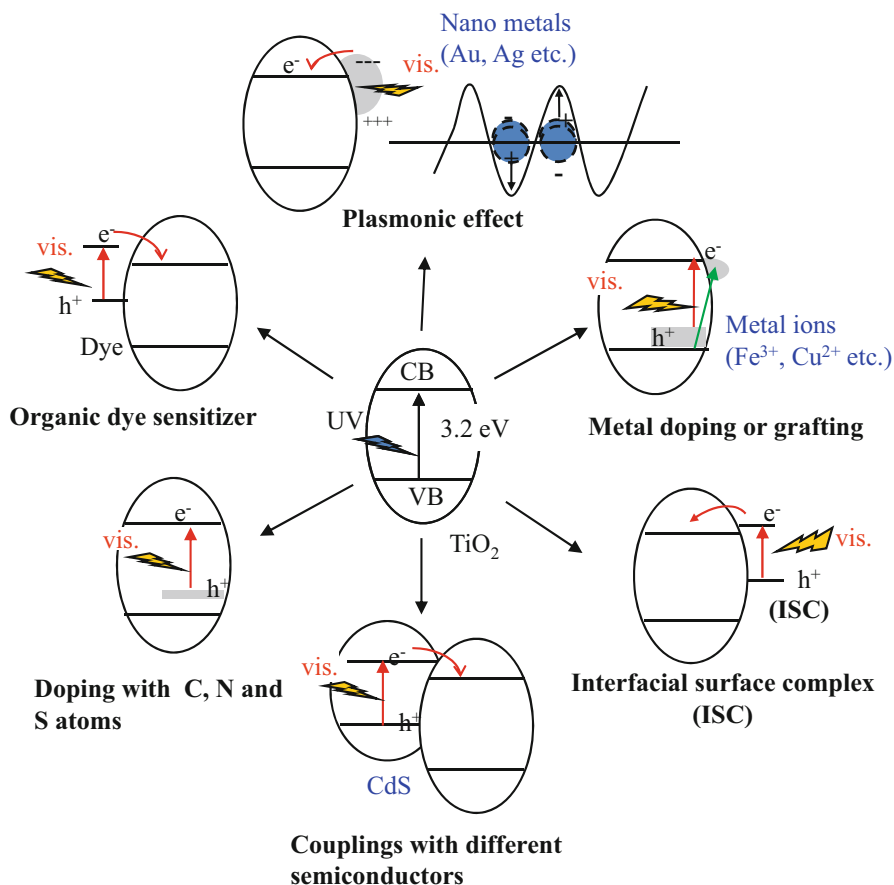


**Fig. 12.1** Several strategies to design visible-light responsive  $\text{TiO}_2$  photocatalysts

as well as reaction mechanisms was discussed by the combination of DFT calculations. Furthermore, the kinetics for the photocatalytic oxidation of benzylic alcohols substituted with electron-donating (ED) groups:  $-\text{OCH}_3$ ,  $-\text{CH}_3$ ,  $-\text{C}(\text{CH}_3)_3$ , and with electron-withdrawing (EW) groups:  $-\text{Cl}$ ,  $-\text{CF}_3$ , and  $-\text{NO}_2$ , were also mentioned.

## 12.2 Visible-Light Responsive $\text{TiO}_2$ Photocatalyst for Selective Oxidation of Benzyl Alcohol

### 12.2.1 Photocatalytic Reactions

Figure 12.2 shows the reaction time profiles for the oxidation of benzyl alcohol in an acetonitrile solution suspended with  $\text{TiO}_2$  photocatalyst in the presence of  $\text{O}_2$  under visible light irradiation ( $\lambda > 420$  nm). This reaction does not proceed without  $\text{TiO}_2$  or irradiation. It was observed that the amount of benzyl alcohol decreased with an increase in the

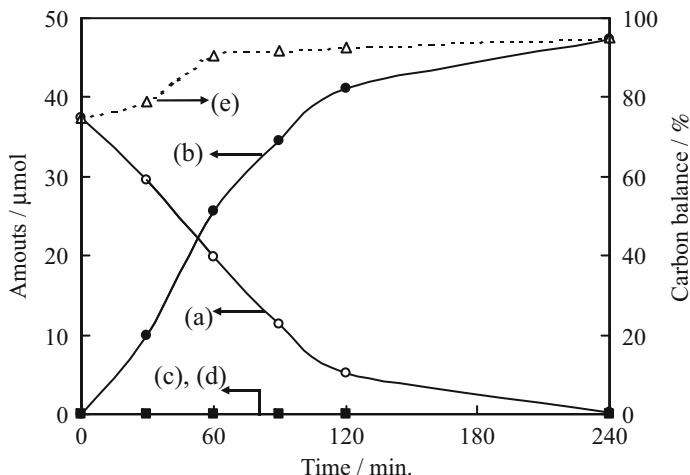


**Fig. 12.2** Photocatalytic oxidation of benzyl alcohol on TiO<sub>2</sub> under visible-light irradiation. The initial amount of benzyl alcohol added to the reaction cell was 50 μmol. Amounts of: (a) benzyl alcohol; (b) benzaldehyde; (c) benzoic acid; (d) CO<sub>2</sub>; and (e) percentage of total organic compounds evolved in solution are plotted

irradiation time, while the amounts of benzaldehyde increased. Neither oxidative products such as benzoic acid nor CO<sub>2</sub> were formed. The yield of benzaldehyde reached ca. 95 % and the carbon balance in the liquid phase was ca. 95 % after photo-irradiation for 240 min. It was observed that benzyl alcohol is adsorbed on TiO<sub>2</sub> more selectively than benzaldehyde, when a mixture of benzyl alcohol and benzaldehyde was exposed on TiO<sub>2</sub> under dark conditions. These results indicate that the interaction between benzaldehyde and TiO<sub>2</sub> is fairly weak. According to DFT calculations [29], the interaction of benzyl alcohol with the TiO<sub>2</sub> surface induced orbital mixing between the anti-bonding  $\pi$  molecular orbitals (MO) of a phenyl group and the O2p atomic orbitals (AOs) of TiO<sub>2</sub> in the band-gap region, while that of benzaldehyde did not induce orbital mixing. From these results, once benzaldehyde is produced by the oxidation of benzyl alcohol, benzaldehyde is immediately released into the bulk solution and it is not oxidized further to benzoic acid or CO<sub>2</sub>.

The photocatalytic activities for the oxidation of benzyl alcohol or  $\alpha$ ,  $\alpha$ -d<sub>2</sub> benzyl alcohol were investigated at 283–313 K [27]. The kinetic isotope effect (KIE) [ $=k_{C-H}/k_{C-D}$ ] was estimated to be  $\approx 4.0$  at 283 K and the activation energy was determined to be 19 kJ/mol. These results suggest that the process for the  $\alpha$ -deprotonation is the rate determining step (RDS) for the overall reaction.

### 12.2.2 Influence of Calcination Temperatures and Surface Treatment with HF of the TiO<sub>2</sub>

Physicochemical properties and photocatalytic activities on the TiO<sub>2</sub> photocatalysts as a function of the calcination temperatures are listed in Table 12.1. It was observed that all of the TiO<sub>2</sub> possess anatase structure by XRD analysis, and specific surface

**Table 12.1** Physicochemical properties and reaction rate constants for the TiO<sub>2</sub> photocatalysts as a function of the calcination temperature

Photocatalysts	$S$ (m <sup>2</sup> g <sup>-1</sup> ) <sup>a</sup>	$d$ (nm) <sup>b</sup>	$k/(s^{-1})$ <sup>c</sup>	Uptakes (μmol) <sup>d</sup>
Untreated TiO <sub>2</sub>	320	7.3	$2.1 \times 10^{-4}$	12.3
TiO <sub>2</sub> (673)	255	14.8	$1.0 \times 10^{-4}$	7.2
TiO <sub>2</sub> (773)	158	15.8	$5.8 \times 10^{-5}$	5.4
TiO <sub>2</sub> (873)	124	21.6	$3.1 \times 10^{-5}$	3.6
TiO <sub>2</sub> (973)	91	23.7	$1.0 \times 10^{-5}$	2.6

<sup>a</sup>Specific surface area ( $S$ )<sup>b</sup>Crystallite size ( $d$ )<sup>c</sup>Reaction rate constant ( $k$ ) for the oxidation of benzyl alcohol<sup>d</sup>Uptakes of benzyl alcohol within 1 h in the dark. Benzyl alcohol (50 μmol) was added to an acetonitrile solution suspended with TiO<sub>2</sub> (50 mg)

area decreases due to aggregation of TiO<sub>2</sub> particles, while the crystallite size increases with an increase in the calcination temperature of TiO<sub>2</sub>. On the other hand, the reaction rate constants ( $k$ ) as well as uptakes of benzyl alcohol on the TiO<sub>2</sub> in dark decrease as a function of calcinations temperatures. Therefore, it was considered that a decrease of the photocatalytic activities is attributed to a decrease of specific surface area of TiO<sub>2</sub> through aggregation of TiO<sub>2</sub> nanoparticles.

In order to clarify the contribution of the surface states of TiO<sub>2</sub> on the photocatalytic activities, the reactions were carried out on fluorinated TiO<sub>2</sub> (HF-TiO<sub>2</sub>) on which the surface OH was exchanged to fluoride by diluted HF aqueous solution [33]. From the XPS analysis [25], the surface state of HF-TiO<sub>2</sub> was confirmed that the F<sup>-</sup> ions are adsorbed on the TiO<sub>2</sub> surface possibly to form ≡Ti-F or ≡TiOF<sub>2</sub> [34]. Table 2 shows uptakes of benzyl alcohols on the HF-TiO<sub>2</sub> in the dark and photo-formed benzaldehyde after photocatalytic reaction. It was observed that the photocatalytic activity and adsorbability of benzyl alcohol decreased with an increase of HF added to TiO<sub>2</sub>. In particular, HF(50)-TiO<sub>2</sub> exhibited negligible photocatalytic activity, and almost all active sites are de-activated by the addition of F<sup>-</sup> ions. From these results, the active sites were estimated to be 3.4 nm<sup>-2</sup> on the TiO<sub>2</sub> surface. When the photo-oxidation of benzyl alcohol (10 mmol) on TiO<sub>2</sub> (50 mg) was performed under visible light irradiation, 2.2 mmol of benzaldehyde was produced after 36 h [24, 27]. Considering the density of active sites (3.4 nm<sup>-2</sup>), the turnover number (TON) and turnover frequency (TOF) was estimated to be ca. 24 and 0.7 h<sup>-1</sup>, respectively, suggesting that this reaction does, indeed, take place photocatalytically.

### 12.2.3 Identification of Active Sites and Formation of the Interfacial Surface Complex

Figure 12.3 shows FT-IR spectra of the untreated TiO<sub>2</sub>, TiO<sub>2</sub> heat-treated at different temperatures and TiO<sub>2</sub> modified with aq. HF. As shown in Fig. 12.3a, the untreated TiO<sub>2</sub> exhibits the unresolved IR band at ca. 3500–3700 cm<sup>-1</sup>, which are due to the

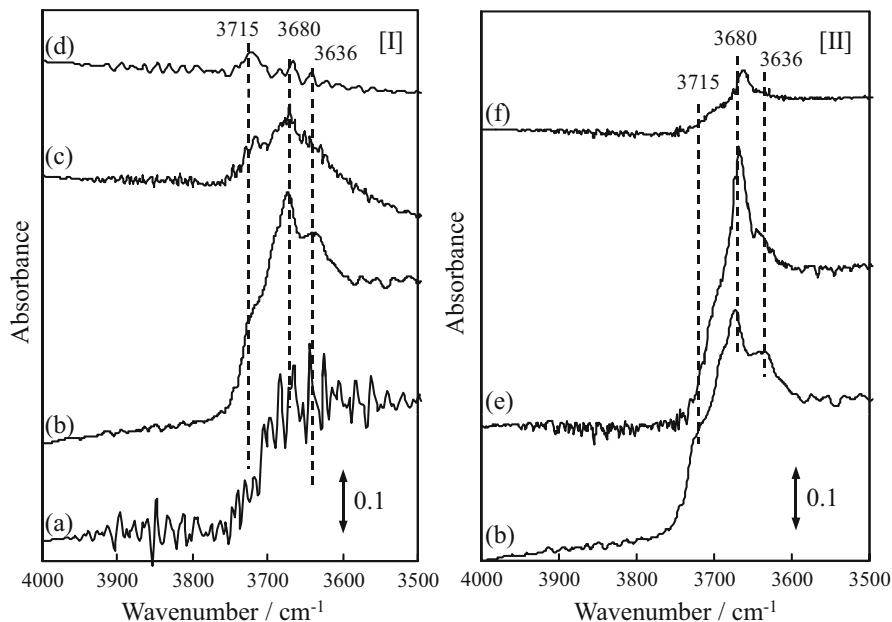
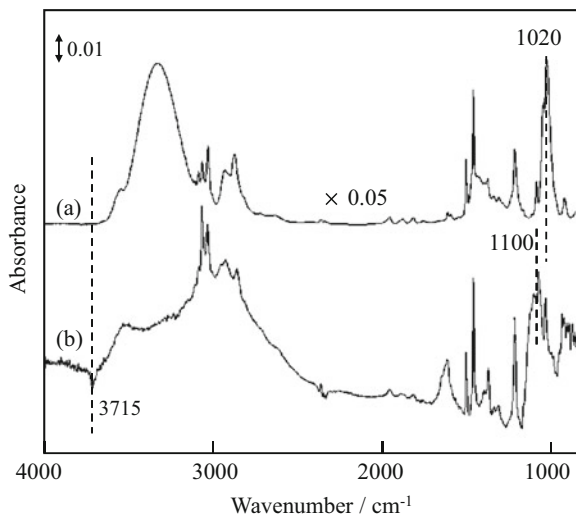


**Fig. 12.3** FT-IR spectra of (a) untreated TiO<sub>2</sub>; TiO<sub>2</sub> heat-treated at: (b) 673 K, (c) 773 K, (d) 873 K; (e) HF(50)-TiO<sub>2</sub>; and (f) HF(400)-TiO<sub>2</sub>. The spectra (e) and (f) were recorded after heat-treatment at 673 K

surface OH groups involving weakly adsorbed water molecules. When the TiO<sub>2</sub> was heat-treated at 673 K in O<sub>2</sub>, the IR bands at 3636, 3680, and 3715 cm<sup>-1</sup> were clearly observed (Fig. 12.3b). Upon calcination of TiO<sub>2</sub> at 773 K, the IR band at 3636 cm<sup>-1</sup> disappeared and the intensity of the bands at 3680 and 3715 cm<sup>-1</sup> decreased (Fig. 12.3c). Furthermore, the IR band at 3680 cm<sup>-1</sup> almost disappeared at 873 K, while that at 3715 cm<sup>-1</sup> is still observed (Fig. 12.3d). According to a previous report [35–37], the IR band at 3636 cm<sup>-1</sup> can be assigned to the physically adsorbed H<sub>2</sub>O on the surface, while the other type of OH groups were identified as follows: the band at 3680 cm<sup>-1</sup> corresponds to the adjacent OH groups interacting via weak hydrogen bonds (bridge OH groups bound to two other Ti sites), while the band at 3715 cm<sup>-1</sup> can be attributed to the terminal OH groups. As shown in Fig. 12.3e, the IR band at 3715 cm<sup>-1</sup> on the HF(50)-TiO<sub>2</sub> drastically decreased, while the significant change of the IR band at 3680 cm<sup>-1</sup> was not observed, compared with the TiO<sub>2</sub> untreated by HF. Furthermore, HF(400)-TiO<sub>2</sub> also showed a band at 3680 cm<sup>-1</sup> and its peak intensity was lower than that of HF(50)-TiO<sub>2</sub>, as shown in Fig. 12.3f. These results indicate that the terminal Ti-OH groups sensitively react with the appropriate amount of HF, while the bridge OH groups react with an excess of HF.

Moreover, the states of benzyl alcohol adsorbed on TiO<sub>2</sub> were analyzed by FT-IR spectroscopy and the results are shown in Fig. 12.4. It was observed that the IR band of the benzyl alcohol adsorbed on TiO<sub>2</sub> is essentially the same as that for the molecular benzyl alcohol by itself (Fig. 12.4a, b). However, the following unique features

**Fig. 12.4** FT-IR spectra of: (a) benzyl alcohol by itself; and (b) benzyl alcohol adsorbed on TiO<sub>2</sub>



caused by the interaction of benzyl alcohol with the TiO<sub>2</sub> surface are characteristic: (i) a remarkable downward negative band at 3715 cm<sup>-1</sup> attributed to the O-H stretching of the terminal OH group; (ii) a new band is appeared at ca. 1100 cm<sup>-1</sup>, which is attributed to the C-O stretching of the alkoxide species formed between TiO<sub>2</sub> and benzyl alcohol, while that of benzyl alcohol by itself is 1020 cm<sup>-1</sup>. These results indicate that C-O bond strength significantly increases, probably due to the formation of the ISC. Taking these results into consideration, the surface alkoxide species formed by the interaction of benzyl alcohol with the terminal OH groups as active sites, clearly plays a significant role in the photocatalytic reaction while the interaction with the bridge OH groups are inactive for the reaction.

### 12.2.4 Origin of the Visible-Light Responsive Photocatalysis

Figure 12.5a, b shows the UV-Vis spectra of the pure TiO<sub>2</sub> and the TiO<sub>2</sub> adsorbed with benzyl alcohol, respectively [27]. It was observed that the TiO<sub>2</sub> adsorbed with benzyl alcohol exhibits visible-light absorption, while the TiO<sub>2</sub> exhibits little visible light absorbance. The visible-light absorbance is not due to a direct band-gap excitation (3.1 eV) but to the excitation of the ISC formed by the interaction of TiO<sub>2</sub> with benzyl alcohol. On the other hand, neither methanol nor benzene-adsorbed TiO<sub>2</sub> exhibited absorption in the visible region, suggesting that the absorption in the visible region is unique on the benzyl alcohol-adsorbed TiO<sub>2</sub>.

The action spectrum was obtained in order to identify the photo-responsible center. The AQY at various wavelengths of irradiated light on the photocatalytic reaction is shown in Fig. 12.5c. The AQY plots form the action spectrum for the

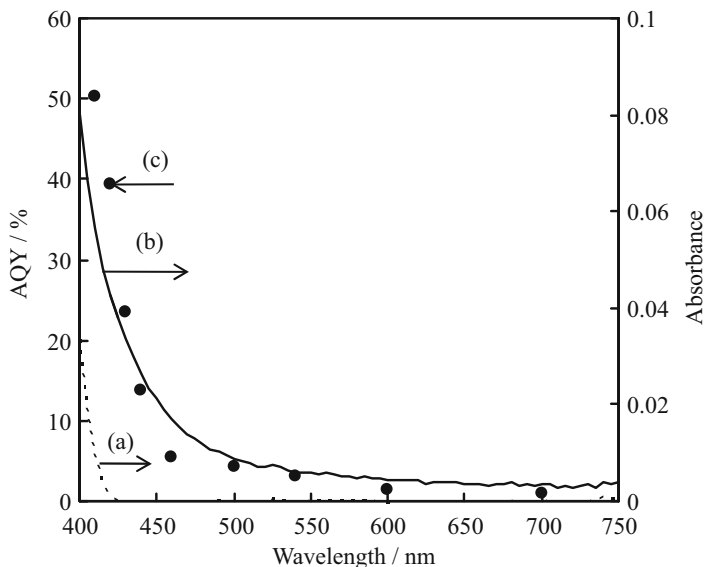


**Fig. 12.5** UV-Vis absorption spectra of: (a) untreated TiO<sub>2</sub>, (b) TiO<sub>2</sub> adsorbed with benzyl alcohol, and (c) quantum yields for the photocatalytic oxidation of benzyl alcohol into benzaldehyde on TiO<sub>2</sub>

photocatalytic reaction on TiO<sub>2</sub>, and are extended towards ca. 700 nm. These results show that the action spectrum is in good agreement with the photo-absorption of TiO<sub>2</sub>-adsorbed benzyl alcohol (Fig. 12.5b), indicating that the photo-excitation of the ISC by itself plays a significant role in the photo-oxidation of benzyl alcohol.

### 12.2.5 Electronic Structures of the ISC by DFT Calculations

The interaction of benzyl alcohol with TiO<sub>2</sub> surface was studied by DFT calculations [30]. It was confirmed that the interaction of benzyl alcohol with surface hydroxyl groups on the TiO<sub>2</sub> surface induce orbital mixing, and play a significant role in the formation of the alkoxide ([Ti]-O-CH<sub>2</sub>-ph) species. The optimized structure and its electron density contour maps of the alkoxide species are shown in Fig. 12.6. As shown in Fig. 12.6, the orbital #211 at -0.783 eV forms the valence band maximum (VBM) of TiO<sub>2</sub>, while #218 at +2.267 eV forms the conduction band minimum (CBM). One type of surface state ( $\alpha$ ) consisting of the orbitals (#212 to #215) originates with the alkoxide species hybridized with the O2p AOs in the VB of the TiO<sub>2</sub>. In particular, the orbitals (#214 and #215) extend to the PhCH<sub>2</sub>O-[Ti] bonding region, indicating that the O2p AOs in the alkoxide hybridizes with the Ti3d AOs by an electron-donating interaction. The energy gap

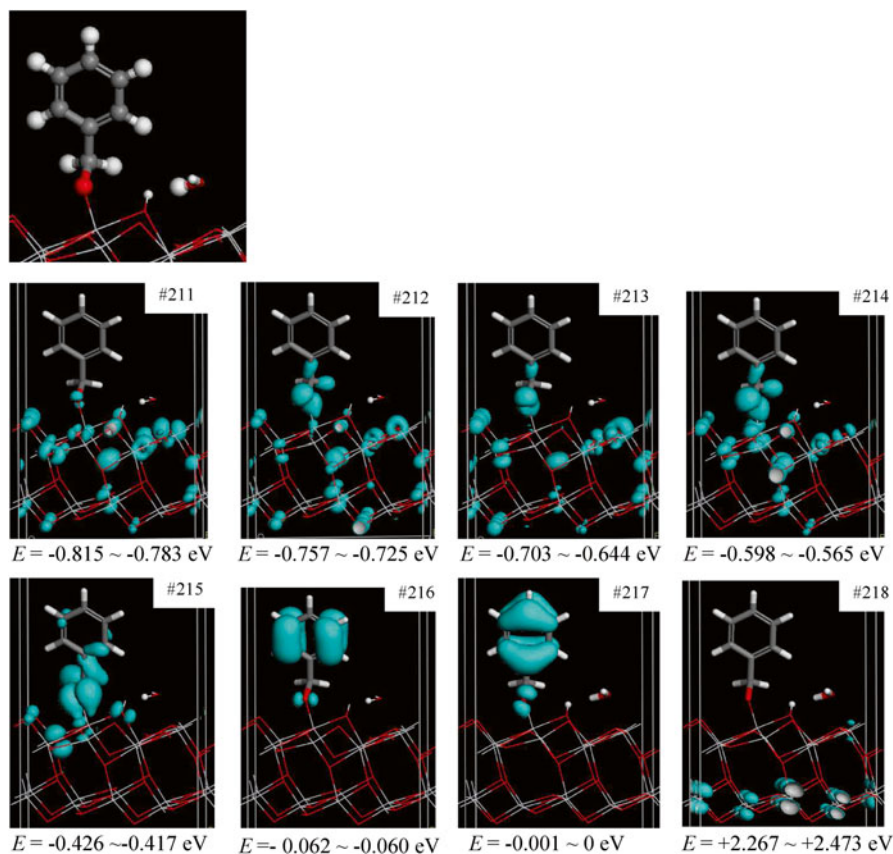
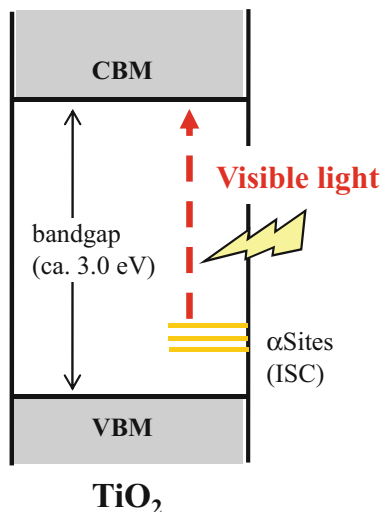


**Fig. 12.6** Optimized structure of the alkoxide species formed by the interaction of benzyl alcohol and  $\text{TiO}_2$  and its electron density contour maps

between #215 and #218 was estimated to be 2.68 eV. The other surface state ( $\beta$ ) consisting of the orbitals (#216 and #217) is localized within the phenyl ring. The energy gap between #217 (HOMO) and #218 (CBM) was estimated to be 2.27 eV. These calculations clearly demonstrate that two types of surface states ( $\alpha$  and  $\beta$ ) are created in the band-gap region. The surface states of  $\alpha$  and  $\beta$  are localized at 0.4 and 0.8 eV above the VBM, respectively. Here, if the photo-induced charge separation from the  $\beta$  to CBM takes place, the holes left on the phenyl groups cannot significantly oxidize methylene groups judging from the energy levels of the orbitals (#216 and #217). We can thus assume that the origin for the visible-light response in the  $\text{TiO}_2$ -alkoxide is mainly attributed to the excitation from the  $\alpha$  level to the CBM, which can lead to the charge separation, i.e., hole in alkoxide and electron in Ti site as shown in Fig. 12.7.

**Fig. 12.7** Possible electron transfers from the surface states to the CBM of the TiO<sub>2</sub> under visible-light irradiation



### 12.2.6 Reaction Mechanisms Behind the Selective Photocatalytic Oxidation of Benzyl Alcohol

From the experimental and theoretical studies by DFT calculations, one of the favorable reaction paths is depicted in Fig. 12.8. The TiO<sub>2</sub> surface involves terminal OH groups (Fig. 12.8i). When the benzyl alcohol interacts with Ti-OH, the alkoxide species is formed on a Ti site (Fig. 12.8ii). This interaction induces absorption in the visible light region which was assigned to the ligand-to-metal charge transfer (LMCT) of the ISC as shown in Fig. 12.8iii. Visible-light irradiation of the ISC produces holes (h<sup>+</sup>) and electrons (e<sup>-</sup>). Subsequently, the electrons are transferred to O<sub>2</sub> to form superoxide anions, which induce α-deprotonation from the benzyl alcohol by an assist of holes (Fig. 12.8iv). Such hydro-peroxide species would further induce the de-protonation from another benzyl alcohol to form benzaldehyde, accompanied by the regeneration of the surface terminal OH groups. The consecutive generation of the terminal OH groups would, thus, be one of the key-factors for the photocatalytic reaction. These reaction mechanisms were supported by DFT calculations.

### 12.2.7 Electronic Effects of the Substituted Groups on Several Photocatalytic Reactions

Photocatalytic reactions of benzyl alcohol and its derivatives into corresponding aldehydes were carried out on TiO<sub>2</sub> under visible light irradiation [24, 26]. As shown in Table 3, benzyl alcohol and its derivatives substituted by -OCH<sub>3</sub>, -Cl, -NO<sub>2</sub>, -CH<sub>3</sub>, -CF<sub>3</sub>, and -C(CH<sub>3</sub>)<sub>3</sub> groups were successfully converted to corresponding

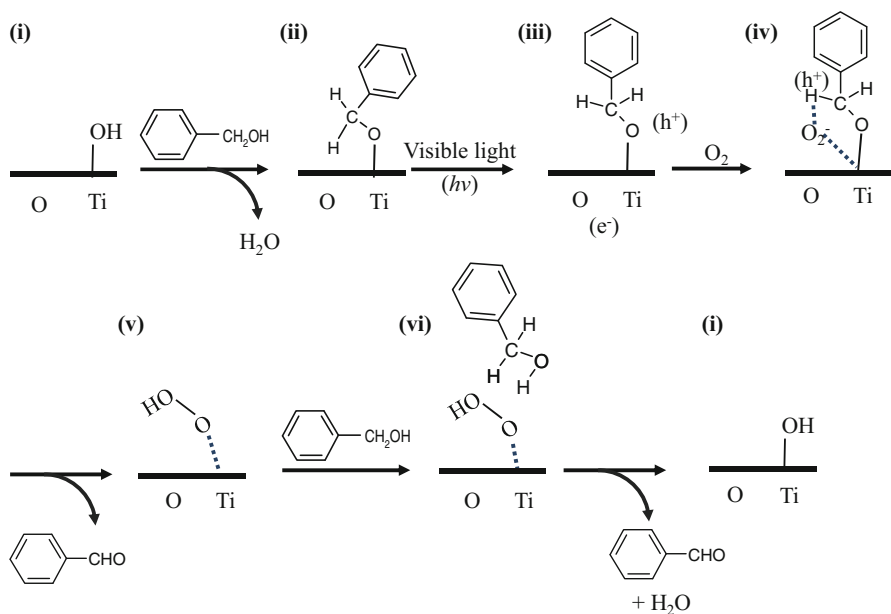


**Fig. 12.8** Reaction paths for the selective oxidation of benzyl alcohol in the presence of  $\text{O}_2$  on the  $\text{TiO}_2$  surface

aldehydes with a high conversion (>99 %) and high selectivity (>99 %) on  $\text{TiO}_2$ , while no other products were observed.

Electric effects of several substituted groups for benzylic alcohols on the photocatalytic activities were investigated. Figure 12.9 shows the relationship between the reaction rate constants ( $k$ ) and the oxidative potentials ( $E_A$ ) of several benzylic alcohols. It was observed that the photocatalytic activity was not governed by the Hammett rule, i.e., substitution with  $-\text{OCH}_3$ ,  $-\text{CH}_3$ ,  $-\text{C}(\text{CH}_3)_3$  (electron-donating groups) as well as with  $-\text{Cl}$ ,  $-\text{CF}_3$ , and  $-\text{NO}_2$  (electron-withdrawing groups) increased the photocatalytic activities. It is assumed that the photocatalytic activities are influenced by synergetic effects: oxidizability of benzylic alcohol to form radicals and their stabilities. That is, the lower the  $E_A$  of the benzylic alcohols are, the more efficiently they are oxidized into radical cations. Subsequently, further electron-elimination from radical cations is enhanced by the de-stabilized radicals, leading to efficient formation of corresponding benzaldehydes.

Figure 12.10 shows effects of the electronic properties by the *ortho*-, *meta*-, and *para*-orientations on the photocatalytic activities for the oxidation of benzylic alcohols substituted with: (a)  $-\text{OCH}_3$ , (b)  $-\text{CH}_3$ , (c)  $-\text{CF}_3$ , and (d)  $-\text{NO}_2$  into corresponding benzaldehydes. It was observed that methoxybenzaldehyde and methylbenzaldehyde in *meta*-orientation are photo-formed more efficiently than those in *ortho*- and *para*-orientation, while nitrobenzaldehyde and (trifluoromethyl)benzaldehyde in *ortho*- and *para*-orientation are formed more efficiently than those in *meta*-orientation.

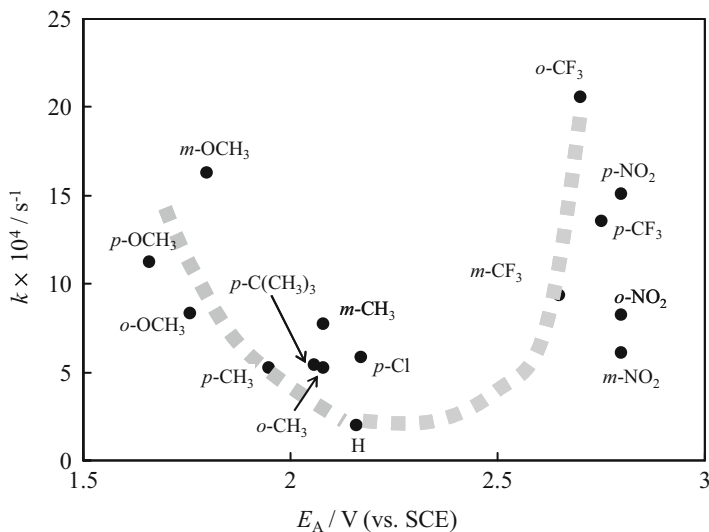


**Fig. 12.9** Relationship between the apparent reaction rate constants ( $k$ ) for the photocatalytic oxidation of benzylic alcohols and their oxidative potentials ( $E_A$ ). The substituents of the benzylic alcohols are shown in this figure

**Fig. 12.10** Apparent reaction rate constants ( $k$ ) for the photocatalytic oxidation of benzylic alcohols substituted with *ortho*-, *meta*-, and *para*-oriented (a)  $-\text{OCH}_3$ , (b)  $-\text{CH}_3$ , (c)  $-\text{CF}_3$ , and (d)  $-\text{NO}_2$  into corresponding aldehydes

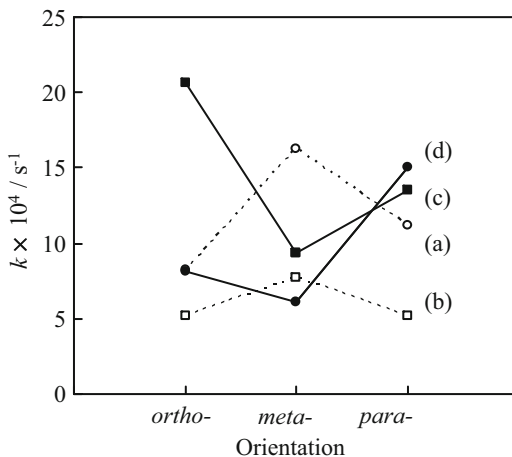
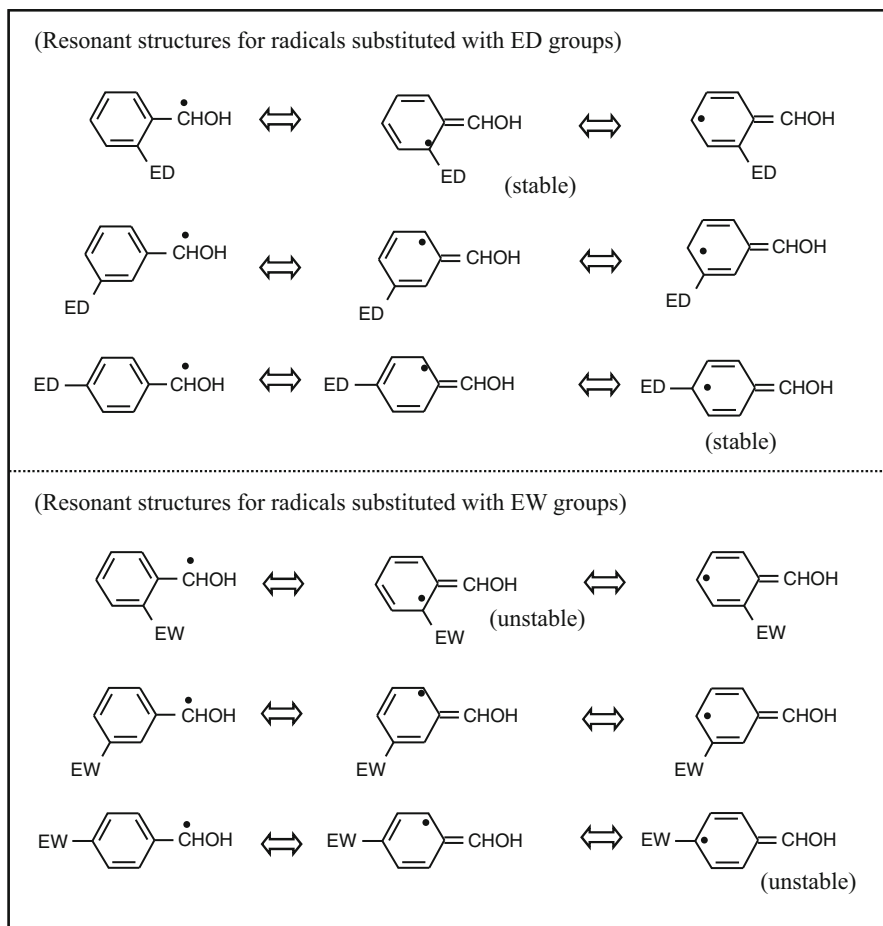


Figure 12.11 shows the resonant structures of the radicals substituted with ED and EW groups. The resonant structures of the radicals with ED groups were found to be more stabilized in *ortho*- and *para*-orientation than in *meta*-orientation, while those with EW were more de-stabilized in *ortho*- and *para*-orientation than in *meta*-orientation. The effect of the orientation on the photocatalytic activity could, thus, be clearly explained by the stability of the resonant structures of the benzylic alcohol radicals, i.e., the resonant structures of the radicals in *meta*-orientation for



**Fig. 12.11** Resonant structures of benzylic alcohol radicals substituted with ED and EW groups

benzyl alcohols substituted with ED groups and in *ortho*- and *para*-orientation for those with EW groups enhance destabilization, leading to further reactions to form corresponding aldehydes. From these results, photocatalytic activities for the oxidation of benzylic alcohols with different substituted groups are strongly influenced by both oxidizability of benzylic alcohols into radicals and their stabilities.

### 12.3 Conclusions

The selective photocatalytic oxidation of benzyl alcohol and its derivatives on  $\text{TiO}_2$  in the presence of  $\text{O}_2$  under visible light irradiation have been successfully demonstrated. Visible-light responses were attributed to the oxidation of the interfacial surface

complex formed by the interaction of benzylic alcohol with surface OH groups on the TiO<sub>2</sub>. It was also confirmed that the rate determining step is the dissociation process for the C-H bonding, which is assisted by the superoxide anion radicals.

Furthermore, it was indicated that the photocatalytic activity of the benzylic alcohols was promoted by phenyl-ring substitution with electron-releasing groups (-OCH<sub>3</sub>, -CH<sub>3</sub>, -C(CH<sub>3</sub>)<sub>3</sub>) as well as electron-withdrawing groups (-Cl, -CF<sub>3</sub>, and -NO<sub>2</sub>). These phenomena could be explained by the oxidizability of benzylic alcohol to form corresponding benzylic alcohol radical cations and their stability. It was, thus, demonstrated that the ISC formed on the TiO<sub>2</sub> exhibit unique photocatalytic oxidation of aromatic alcohols under visible light irradiation.

## References

1. Hoffman MR, Martin ST, Choi W, Bahnemann DW (1995) Environmental applications of semiconductor photocatalysis. *Chem Rev* 95:69–96
2. Fujishima A, Rao TN, Tryk DA (2000) Titanium dioxide photocatalysis. *J Photochem Photobiol C Photochem Rev* 1:1–21
3. Shiraishi Y, Hirai T (2008) Selective organic transformations on titanium oxide-based photocatalysts. *J Photochem Photobiol C Photochem Rev* 9:157–170
4. Palmisano G, García-López E, Marci G, Loddo V, Yurdakal S, Augugliaro V, Palmisano L (2010) Advances in selective conversions by heterogeneous photocatalysis. *Chem Commun* 46:7074–7089
5. Fox MA, Dulay MT (1993) Heterogeneous photocatalysis. *Chem Rev* 93:341–357
6. Schneider J, Matsuoka M, Takeuchi M, Zhang J, Horiuchi Y, Anpo M, Bahnemann DW (2014) Understanding TiO<sub>2</sub> photocatalysis: mechanisms and materials. *Chem Rev* 114:9919–9986
7. Ma Y, Wang X, Jia Y, Chen X, Han H, Li C (2014) Titanium dioxide-based nanomaterials for photocatalytic fuel generations. *Chem Rev* 114:9987–10043
8. Kudo A, Miseki Y (2009) Heterogeneous photocatalyst materials for water splitting. *Chem Soc Rev* 38:253–278
9. Asahi R, Morikawa T, Irie H, Ohwaki T (2014) Nitrogen-doped titanium dioxide as visible-light-sensitive photocatalyst: designs, developments, and prospects. *Chem Rev* 114:9824–9852
10. Lang X, Chen X, Zhao J (2014) Heterogeneous visible light photocatalysis for selective organic transformations. *Chem Soc Rev* 43:473–486
11. Asahi R, Morikawa T, Aoki K, Taga Y (2001) Visible-light photocatalysis in nitrogen-doped titanium oxides. *Science* 293:269–271
12. Sakthivel S, Kisch H (2003) Daylight photocatalysis by carbon-modified titanium dioxide. *Angew Chem Int Ed* 42:4908–4911
13. Ohno T, Akiyoshi M, Umebayashi T, Asai K, Mitui T, Matsumura M (2004) Preparation of S-doped TiO<sub>2</sub> photocatalysts and their photocatalytic activities under visible light. *Appl Catal A Gen* 265:115–121
14. Sakthivel S, Janczarek M, Kisch H (2004) Visible light activity and photoelectrochemical properties of nitrogen-doped TiO<sub>2</sub>. *J Phys Chem B* 108:19384–19387
15. Higashimoto S, Tanihata W, Nakagawa Y, Azuma M, Ohue H, Sakata Y (2008) Effective photocatalytic decomposition of VOC under visible-light irradiation on N-doped TiO<sub>2</sub> modified by vanadium species. *Appl Catal A Gen* 340:98–104
16. Zhang M, Chen CC, Ma WH, Zhao J (2008) Visible-light-induced aerobic oxidation of alcohols in a coupled photocatalytic system of dye-sensitized TiO<sub>2</sub> and TEMPO. *Angew Chem Int Ed* 47:9730–9733

17. Tian Y, Tatsuma T (2005) Mechanisms and applications of plasmon-induced charge separation at TiO<sub>2</sub> films loaded with gold nanoparticles. *J Am Chem Soc* 127:7632–7637
18. Kowalska E, Abe R, Ohtani B (2009) Visible light-induced photocatalytic reaction of gold-modified titanium(IV) oxide particles: action spectrum analysis. *Chem Commun* 2:241–243
19. Naya S, Kimura K, Tada H (2013) One-step selective aerobic oxidation of amines to imines by gold nanoparticle-loaded rutile titanium(IV) oxide plasmon photocatalyst. *ACS Catal* 3:10–13
20. Tanaka A, Nishino Y, Sakaguchi S, Yoshikawa T, Imamura K, Hashimoto K, Kominami H (2013) Functionalization of a plasmonic Au/TiO<sub>2</sub> photocatalyst with an Ag co-catalyst for quantitative reduction of nitrobenzene to aniline in 2-propanol suspensions under irradiation of visible light. *Chem Commun* 49:2551–2553
21. Lang X, Ma W, Zhao Y, Chen C, Ji H, Zhao J (2012) Visible-light-induced selective photocatalytic aerobic oxidation of amines into imines on TiO<sub>2</sub>. *Chem Eur J* 18:2624–2631
22. Higashimoto S, Hatada Y, Ishikawa R, Azuma M, Sakata Y, Kobayashi H (2013) Selective photocatalytic oxidation of benzyl amine by O<sub>2</sub> into N-benzylidenebenzylamine on TiO<sub>2</sub> using visible light. *Curr Org Chem* 17:2374–2381
23. Kim S, Choi W (2005) Visible-light-induced photocatalytic degradation of 4-chlorophenol and phenolic compounds in aqueous suspension of pure titania: demonstrating the existence of a surface-complex-mediated path. *J Phys Chem B* 109:5143–5149
24. Higashimoto S, Kitao N, Yoshida N, Sakura T, Azuma M, Ohue H, Sakata Y (2009) Selective photocatalytic oxidation of benzyl alcohol and its derivatives into corresponding aldehydes by molecular oxygen on titanium dioxide under visible light irradiation. *J Catal* 266:279–285
25. Higashimoto S, Okada K, Morisugi T, Azuma M, Ohue H, Kim T-H, Matsuoka M, Anpo M (2010) Effect of surface treatment on the selective photocatalytic oxidation of benzyl alcohol into benzaldehyde by O<sub>2</sub> on TiO<sub>2</sub> under visible light. *Top Catal* 53:578–583
26. Higashimoto S, Suetsugu N, Azuma M, Ohue H, Sakata Y (2010) Efficient and selective oxidation of benzyl alcohol by O<sub>2</sub> into corresponding aldehydes on a TiO<sub>2</sub> photocatalyst under visible light irradiation: effect of phenyl-ring substitution on the photocatalytic activity. *J Catal* 274:76–83
27. Higashimoto S, Okada K, Azuma M, Ohue H, Terai T, Sakata Y (2012) Characteristics of the charge transfer surface complex on titanium(IV) dioxide for the visible light induced chemo-selective oxidation of benzyl alcohol. *RSC Adv* 2:669–676
28. Higashimoto S, Shirai R, Osano Y, Azuma M, Ohue H, Sakata Y, Kobayashi H (2014) Influence of metal ions on the photocatalytic activity: selective oxidation of benzyl alcohol on iron (III) ion-modified TiO<sub>2</sub> using visible light. *J Catal* 311:137–143
29. Li R, Kobayashi H, Guo J, Fan J (2011) Visible-light induced high-yielding benzyl alcohol-to-benzaldehyde transformation over mesoporous crystalline TiO<sub>2</sub>: a self-adjustable photo-oxidation system with controllable hole-generation. *J Phys Chem C* 115:23408–23416
30. Kobayashi H, Higashimoto S (2015) DFT study on the reaction mechanisms behind the catalytic oxidation of benzyl alcohol into benzaldehyde by O<sub>2</sub> over anatase TiO<sub>2</sub> surfaces with hydroxyl groups: role of visible-light irradiation. *Appl Catal B Env* 170:135–143
31. Ikeda S, Abe C, Torimoto T, Ohtani B (2003) Photochemical hydrogen evolution from aqueous triethanolamine solutions sensitized by binaphthol-modified titanium(IV) oxide under visible-light irradiation. *J Photochem Photobiol A Chem* 160:61–67
32. Kamegawa T, Seto H, Matsuura S, Yamashita H (2012) Preparation of hydroxynaphthalene-modified TiO<sub>2</sub> via formation of surface complexes and their applications in the photocatalytic reduction of nitrobenzene under visible-light irradiation. *ACS Appl Mater Inter* 4:6635–6639
33. Minero C, Mariella G, Maurino V, Pelizzetti E (2000) Photocatalytic transformation of organic compounds in the presence of inorganic anions. 1. hydroxyl-mediated and direct electron-transfer reactions of phenol on a titanium dioxide–fluoride system. *Langmuir* 16:2632–2641
34. Liu G, Sun C, Yang HG, Smith SC, Wang L, Lu GQ, Cheng HM (2010) Nanosized anatase TiO<sub>2</sub> single crystals for enhanced photocatalytic activity. *Chem Commun* 46:755–757

35. Nosaka AY, Nishino J, Fujiwara T, Ikegami T, Yagi H, Akutsu H, Nosaka Y (2006) Effects of thermal treatments on the recovery of adsorbed water and photocatalytic activities of TiO<sub>2</sub> photocatalytic systems. *J Phys Chem B* 110:8380–8385
36. Parfitt GD (1976) The surface of titanium dioxide. *Prog Surf Membr Sci* 11:181–226
37. Deiana C, Fois E, Coluccia S, Martra G (2010) Surface structure of TiO<sub>2</sub> P25 nanoparticles: infrared study of hydroxy groups on coordinative defect sites. *J Phys Chem C* 114:21531–21538

**Part III**  
**Photocatalysts Supported on Unique**  
**Supports**

# Chapter 13

## Photocatalytic Properties of TiO<sub>2</sub>-Loaded Porous Silica with Hierarchical Macroporous and Mesoporous Architectures

Takashi Kamegawa and Hiromi Yamashita

### 13.1 Introduction

In modern society, the emission of toxic chemicals leads to air and water pollution issues on a global scale. The design of efficient systems is an important agenda for achieving safer and more comfortable life spaces. Titanium dioxide (TiO<sub>2</sub>) based photocatalysts have attracted considerable attentions owing to their high chemical stability, low cost, nontoxicity, and fascinating properties for dealing with the environmental problems [1–6]. Coating technologies of TiO<sub>2</sub>-based photocatalysts also open the way for design of photofunctional surface with additional functions such as self-cleaning effect and photoinduced superhydrophilicity [6–9]. In photocatalytic reaction process, photo-formed electron–hole pairs in TiO<sub>2</sub> play significant roles. Most organic compounds, i.e., volatile organic compounds (VOCs) such as acetaldehyde and toluene, dye molecules and endocrine disruptors, in air and water are removable through the total oxidation by proper utilization of TiO<sub>2</sub>-based photocatalysts under light irradiation from various light sources [5, 6, 10–14]. The efficient degradation of undesired organic compounds into CO<sub>2</sub> and H<sub>2</sub>O leads to the reduction of environmental burdens. TiO<sub>2</sub>-based photocatalysts also can be used for many

---

T. Kamegawa (✉)

Nanoscience and Nanotechnology Research Center, Osaka Prefecture University,  
1-2 Gakuencho, Nakaku, Sakai, Osaka 599-8570, Japan

Division of Materials and Manufacturing Science, Graduate School of Engineering,  
Osaka University, 2-1 Yamadaoka, Suita, Osaka 565-0871, Japan

e-mail: [t-kamegawa@21c.osakafu-u.ac.jp](mailto:t-kamegawa@21c.osakafu-u.ac.jp)

H. Yamashita

Division of Materials and Manufacturing Science, Graduate School of Engineering,  
Osaka University, 2-1 Yamadaoka, Suita, Osaka 565-0871, Japan

Elements Strategy Initiative for Catalysts & Batteries Kyoto University (ESICB),  
Kyoto University, Katsura, Kyoto, Japan

other purposes such as production of clean energies and fine chemicals under controlled conditions besides environmental purification [15–20].

On the other hand, recently, nanostructured materials have attracted considerable attentions owing to their specific functions based on their fascinating architectures in nanoscale. The construction of nanostructures leads to expand the inherent properties of materials in various applications. In the synthesis of siliceous materials except for zeolite and mesoporous silica, various types of nanostructures such as fibers, hollow spheres, core–shell, flakes, and tubes are realized by selecting of templates and controlling of preparation conditions [21–24]. Siliceous materials with three-dimensionally ordered macroporous (3DOM) structure are also synthesized by using spherical polymers as a hard template [25–34]. Macroporous architectures (pore diameter: greater than 50 nm) are relatively larger as compared to microporous (less than 2 nm) and mesoporous (2–50 nm) architectures, which are also expected to be a functional nanospace. Well known porous siliceous materials such as zeolite and mesoporous silica have been utilized as a platform for design of TiO<sub>2</sub>-based photocatalysts and still investigated on their adsorption assisted photocatalytic performance in environmental purification [33, 35–40]. To improve the photocatalytic activity of TiO<sub>2</sub> in the degradation of organic molecules, controlling of the adsorption capacity of organic molecules on TiO<sub>2</sub>-based photocatalysts has been investigated [36–40]. Photocatalytic reactions essentially occur on their surface, suggesting the importance of the adsorption process of organic molecules on TiO<sub>2</sub> and its surroundings. In this chapter, the differences in the TiO<sub>2</sub>-based photocatalysts designed by using porous silica with one or both types of pores, i.e., ordered mesopores and hierarchical macropores, are presented in relation to utilization of nanostructured materials as a platform in the design of high performance photocatalysts. Special attention has been focused on the roles of nanospace in macroporous scale as well as the relationships between the nano architecture and catalytic performance in photocatalytic purification of contaminated water under UV light irradiation.

## 13.2 Preparation of TiO<sub>2</sub>-Loaded Porous Silica Photocatalysts

Monodispersed poly(methyl methacrylate) (PMMA) spheres were synthesized in accordance with previous literatures [41]. PMMA colloidal crystal as a hard template for construction of macroporous structure was synthesized from the water dispersed solution of PMMA spheres through the self-assembling process (Fig. 13.1). PMMA colloidal crystals with close packed structure showed the opalescence depending on the particle size under fluorescent light. Synthesis of porous silica with one or both types of pores, i.e., ordered mesopores and hierarchical macropores, was carried out by applying a solvent evaporation method [31–34, 42]. Porous silica with hierarchical macroporous and mesoporous architectures

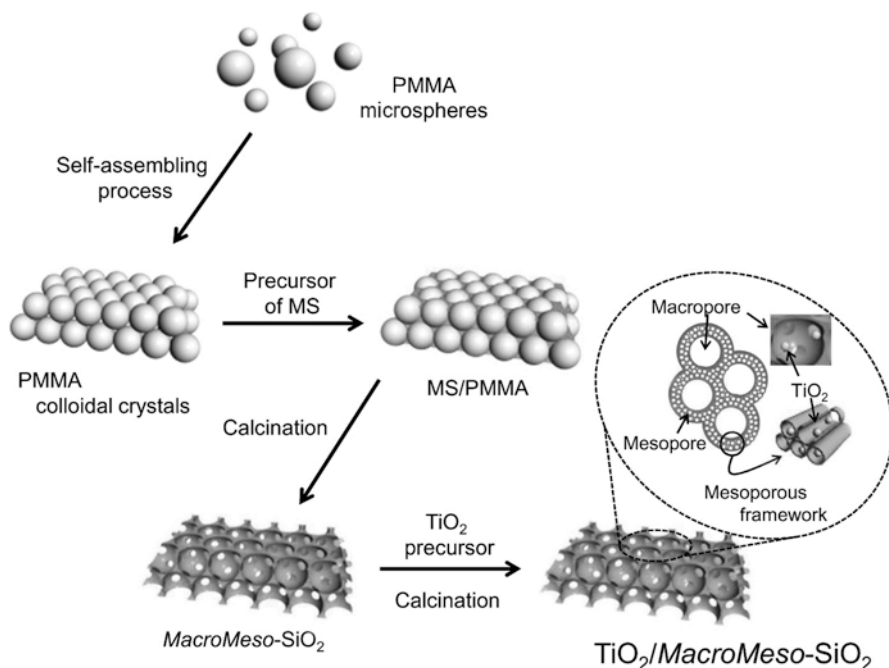


**Fig. 13.1** Schematic diagram of the procedures for the synthesis of TiO<sub>2</sub>/MacroMeso-SiO<sub>2</sub>

(MacroMeso-SiO<sub>2</sub>) was synthesized by using a same precursor solution for synthesis of mesoporous silica (Meso-SiO<sub>2</sub>) via a solvent evaporation process. The precursor solution, which contained tetramethoxysilane (Si source) and octadecyltrimethylammonium chloride (template for construction of mesopores), was prepared by a modified method reported earlier [31, 32, 42]. For preparation of MacroMeso-SiO<sub>2</sub>, precursor solution was slowly loaded with PMMA colloidal crystals by vacuum filtration methods using Buchner funnel [25–27]. The precursor solution of MacroMeso-SiO<sub>2</sub> was fully solidified in the interstitial space of assembled PMMA particles. The schematic illustration of the synthesis procedure is shown in Fig. 13.1. Meso-SiO<sub>2</sub> was prepared by spreading of a same precursor solution on poly(vinylidene chloride) sheet and drying at 298 K. Hierarchical macroporous silica (Macro-SiO<sub>2</sub>) was prepared by same procedures for synthesis of MacroMeso-SiO<sub>2</sub> without the addition of octadecyltrimethylammonium chloride in precursor solution. All samples were finally calcined in air at 823 K.

TiO<sub>2</sub> loadings on three types of porous silica supports (MacroMeso-SiO<sub>2</sub>, Meso-SiO<sub>2</sub>, and Macro-SiO<sub>2</sub>) were carried out by a simple impregnation method from 2-propanol solution of titanium isopropoxide (Ti source) [33]. After calcination at 773 K, each sample was denoted as TiO<sub>2</sub>/MacroMeso-SiO<sub>2</sub>, TiO<sub>2</sub>/Meso-SiO<sub>2</sub>, and TiO<sub>2</sub>/Macro-SiO<sub>2</sub> (TiO<sub>2</sub> content: 10 wt%). The schematic diagram of TiO<sub>2</sub>/MacroMeso-SiO<sub>2</sub> is also shown in Fig. 13.1.

### 13.3 Characterization of TiO<sub>2</sub>-Loaded Porous Silica Photocatalysts

The structure of PMMA particles used as a hard template and TiO<sub>2</sub>-loaded porous silica photocatalysts were investigated by SEM measurement. As shown in Fig. 13.2a, PMMA particles have an approximately spherical shape (diameter: ca. 360 nm) with a narrow size distribution. TiO<sub>2</sub>/*Meso*-SiO<sub>2</sub> had a dense powder form with a flat surface morphology (Fig. 13.2b). In line with the structure of PMMA colloidal crystal, uniform and well-ordered macroporous structure was clearly observed in SEM images of TiO<sub>2</sub>/*MacroMeso*-SiO<sub>2</sub> and TiO<sub>2</sub>/*Macro*-SiO<sub>2</sub> (Fig. 13.2c, d). The diameter of macropores was estimated to be about 300 nm and slightly smaller than the size of spherical PMMA particles. The shrinkage mainly occurred by condensation of the solidified silica precursor in the calcination process. About 20 % shrinkage in diameter was observed in both samples. The presence of interconnecting hierarchical macroporous networks was confirmed in the magnified SEM image of TiO<sub>2</sub>/*MacroMeso*-SiO<sub>2</sub> (Fig. 13.2c). The three round holes as a black dot on inside wall of each macropore were connected to the three neighboring macropores located on the downside of the wall.

Particle size is comparable in each sample, whereas the weight in same volume is a quite different by the presence of uniform and well-ordered macroporous architectures.

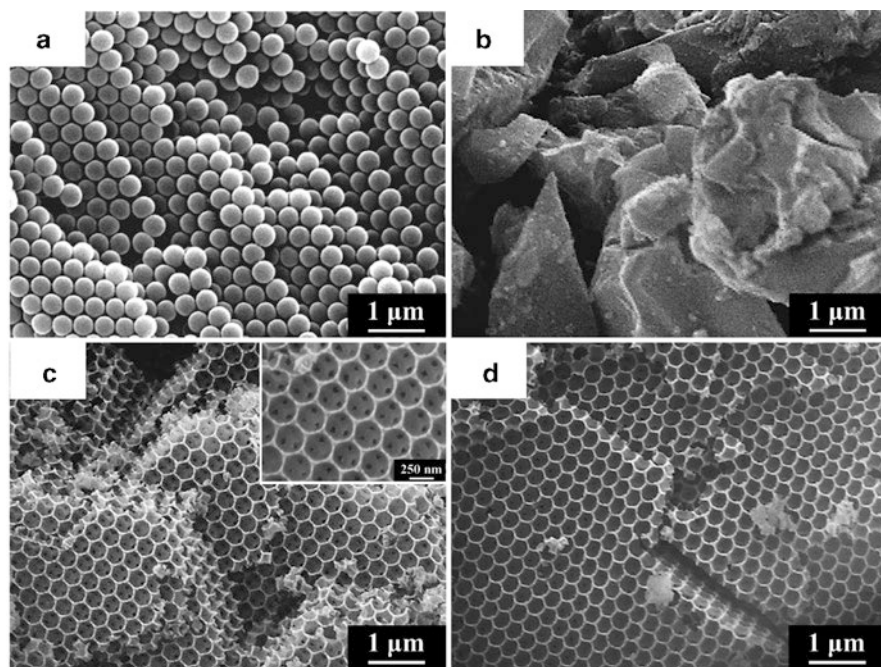


**Fig. 13.2** SEM images of (a) PMMA particles, (b) TiO<sub>2</sub>/*Meso*-SiO<sub>2</sub>, (c) TiO<sub>2</sub>/*MacroMeso*-SiO<sub>2</sub>, and (d) TiO<sub>2</sub>/*Macro*-SiO<sub>2</sub>

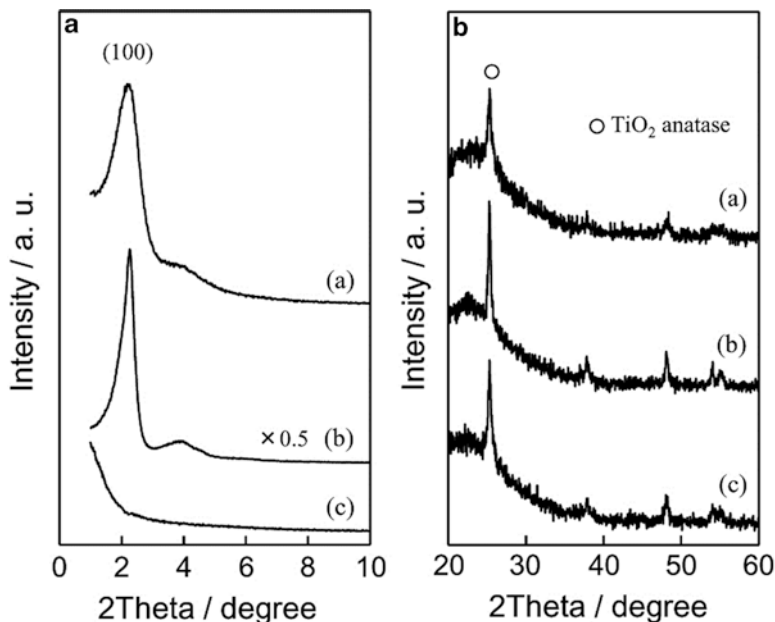


**Fig. 13.3** (A) Low-angle and (B) high-angle XRD patterns of TiO<sub>2</sub>-loaded porous silica photocatalysts ((a) TiO<sub>2</sub>/MacroMeso-SiO<sub>2</sub>, (b) TiO<sub>2</sub>/Meso-SiO<sub>2</sub>, and (c) TiO<sub>2</sub>/Macro-SiO<sub>2</sub>)

The hierarchical macroporous architectures of TiO<sub>2</sub>/MacroMeso-SiO<sub>2</sub> are consists of same component of TiO<sub>2</sub>/Meso-SiO<sub>2</sub>. The thickness of walls separating two neighboring macropores in TiO<sub>2</sub>/MacroMeso-SiO<sub>2</sub> was estimated to be about 50 nm, which is quite smaller than the particle size of TiO<sub>2</sub>/Meso-SiO<sub>2</sub>. TiO<sub>2</sub>/MacroMeso-SiO<sub>2</sub> has uniformly segmentalized structure of TiO<sub>2</sub>/Meso-SiO<sub>2</sub> by the construction of macroporous architectures. The BET surface area of samples was determined to be 865 m<sup>2</sup>/g (TiO<sub>2</sub>/MacroMeso-SiO<sub>2</sub>), 725 m<sup>2</sup>/g (TiO<sub>2</sub>/Meso-SiO<sub>2</sub>), and 85 m<sup>2</sup>/g (TiO<sub>2</sub>/Macro-SiO<sub>2</sub>), respectively. The construction of macroporous structure does not greatly contribute to increases of surface area. The relatively large surface area of TiO<sub>2</sub>/MacroMeso-SiO<sub>2</sub> mainly based on the presence of uniform mesoporous structure.

TiO<sub>2</sub>/MacroMeso-SiO<sub>2</sub> and TiO<sub>2</sub>/Meso-SiO<sub>2</sub> have XRD peaks in the small region ( $2\theta < 10^\circ$ ), showing the existence of a mesoporous structure (Fig. 13.3a). No diffraction peak was observed in the case of TiO<sub>2</sub>/Macro-SiO<sub>2</sub>. TiO<sub>2</sub>/MacroMeso-SiO<sub>2</sub> has broad and slightly weak diffraction peaks as compared to those of TiO<sub>2</sub>/Meso-SiO<sub>2</sub>, while the peaks are observed at almost same angles. As shown in Fig. 13.3b, wide angle XRD patterns ( $20^\circ < 2\theta < 60^\circ$ ) exhibited the characteristic diffraction peaks with a broad diffraction peak of the amorphous silica wall from  $2\theta = 20\text{--}30^\circ$ . The intensity of diffraction peak ( $2\theta = \text{ca. } 25^\circ$ ) due to the (101) reflection of TiO<sub>2</sub> anatase phase showed decreasing in the following order: TiO<sub>2</sub>/Meso-SiO<sub>2</sub> > TiO<sub>2</sub>/Macro-SiO<sub>2</sub> > TiO<sub>2</sub>/MacroMeso-SiO<sub>2</sub>, suggesting the formation of TiO<sub>2</sub> particles on Meso-SiO<sub>2</sub> with a high crystallinity in the series of samples.

The light absorption property of each sample was investigated by UV–Vis absorption measurements. The typical absorption was observed in the UV light region corresponding to the band gap energy of TiO<sub>2</sub> particles with small differences in each sample. The blue shifts of absorption spectrum were observed in comparison with the spectrum position of bulk TiO<sub>2</sub> powder with anatase structure. The absorption band edge of TiO<sub>2</sub> was obviously changed by the quantum-size effect. The shifts of absorption spectrum suggest that TiO<sub>2</sub> nanoparticles are successfully loaded on porous silica with dispersed state. The small differences in the band gap energy are caused by the particle size and crystallinity changes during the TiO<sub>2</sub> loading process on porous silica.

## 13.4 Photocatalytic Reactions on TiO<sub>2</sub>-Loaded Porous Silica Photocatalysts

### 13.4.1 Degradation of Phenol and Bisphenol A in Water

The degradation of phenol (PH) and bisphenol A (BPH) in water was carried out to investigate on the photocatalytic performance of TiO<sub>2</sub>-loaded porous silica photocatalysts under UV light irradiation. These two organic compounds are chosen as model of toxic and water soluble compounds having different molecular size (ca. 0.7 nm (PH) and 1.3 nm (BPH) in the long axis direction) [43, 44]. The differences in the adsorption capacity of PH were relatively small, while large difference was observed in the case of the adsorption capacity of BPH. As compared to other samples, TiO<sub>2</sub>/MacroMeso-SiO<sub>2</sub> exhibited good adsorption capabilities in both systems. Figure 13.4 shows relationship between the adsorption capacity on TiO<sub>2</sub>-loaded porous silica photocatalysts and the apparent rate constant in the degradation of PH in water under UV light irradiation. The apparent rate constant was analyzed by applying pseudo-first-order kinetics [45–47]. The relationship between concentration of each compound and reaction time can be represented as following Eq. (13.1):

$$\ln(C_0 / C) = k_n t \quad (13.1)$$

where  $k_n$  is the apparent rate constant,  $n$  is the kinds of compounds ( $n$ =PH and BPH),  $C_0$  is the initial concentration, and  $C$  is the concentration at a given UV light irradiation time. Under UV light irradiation, the amount of PH and BPH was gradually decreased in proportion to the reaction time.

The apparent rate constant follows the order of TiO<sub>2</sub>/Meso-SiO<sub>2</sub>>TiO<sub>2</sub>/Macro-SiO<sub>2</sub>>TiO<sub>2</sub>/MacroMeso-SiO<sub>2</sub> in the photocatalytic degradation of PH in water under UV light irradiation. As shown in Fig. 13.4, there are no relations with the adsorption capacity of PH on each sample. In the series of samples, TiO<sub>2</sub>/Meso-SiO<sub>2</sub> contains TiO<sub>2</sub> with a relatively high crystallinity. The order of apparent rate constant corresponds to a sequence of the crystallinity of TiO<sub>2</sub> on porous silica. The photocatalytic performance in the degradation of PH is affected to a large degree by the

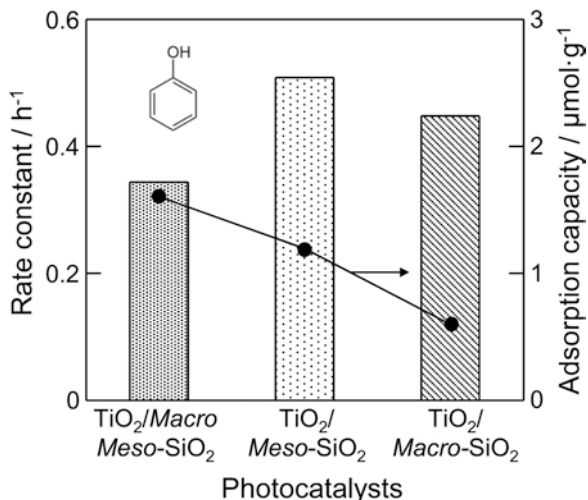


**Fig. 13.4** Relationship between the rate constant in the degradation of phenol (PH) in water under UV light irradiation and adsorption capacity on TiO<sub>2</sub>-loaded porous silica photocatalysts. Photocatalytic reactions were performed at 298 K in a Pyrex glass reaction vessel containing an aqueous PH solution (0.1 mmol/L, 10 mL) and each sample (10 mg). Adsorption capacity was also evaluated at 298 K in the following conditions: aqueous PH solution (0.1 mmol/L, 10 mL), sample (10 mg), and adsorption time (0.5 h)

crystallinity of TiO<sub>2</sub> on porous silica. The influences of diffusion limitation of PH in the photocatalytic performance are estimated to be small because of the small molecular size of PH as compared to the size of pores in each sample. Therefore, photocatalytic performance in the degradation of a relatively small PH was scarcely affected by the structural differences in porous silica used as a support of TiO<sub>2</sub> photocatalyst.

On the other hand, TiO<sub>2</sub>/MacroMeso-SiO<sub>2</sub> exhibited a higher photocatalytic performance than that on TiO<sub>2</sub>/Meso-SiO<sub>2</sub> and TiO<sub>2</sub>/Macro-SiO<sub>2</sub> in the degradation of BPH in water (Fig. 13.5). The apparent rate constant follows the order of TiO<sub>2</sub>/MacroMeso-SiO<sub>2</sub> > TiO<sub>2</sub>/Macro-SiO<sub>2</sub> > TiO<sub>2</sub>/Meso-SiO<sub>2</sub>.

The catalytic performance of porous materials is influenced by accessibility of compounds to the catalytically active site. The long diffusion path and small size of the pores adversely affect the catalytic performance of porous materials [31, 32, 48, 49]. BPH has relatively large molecular size in comparison with the molecular size of PH. Although the crystallinity of TiO<sub>2</sub> on Meso-SiO<sub>2</sub> was higher than that on MacroMeso-SiO<sub>2</sub> and Macro-SiO<sub>2</sub>, the opposite order was clearly observed in this reaction. Combined nanostructure of ordered mesoporous and hierarchical macroporous structures in TiO<sub>2</sub>/MacroMeso-SiO<sub>2</sub> was uniformly segmentalized structure of TiO<sub>2</sub>/Meso-SiO<sub>2</sub> by well-ordered macropores. This combined structure in TiO<sub>2</sub>/MacroMeso-SiO<sub>2</sub> realized formation of many mesopores apertures and a short mesoporous channel, which is advantageous in the degradation of a relatively large BPH in water. In addition to an abovementioned structural function, the higher

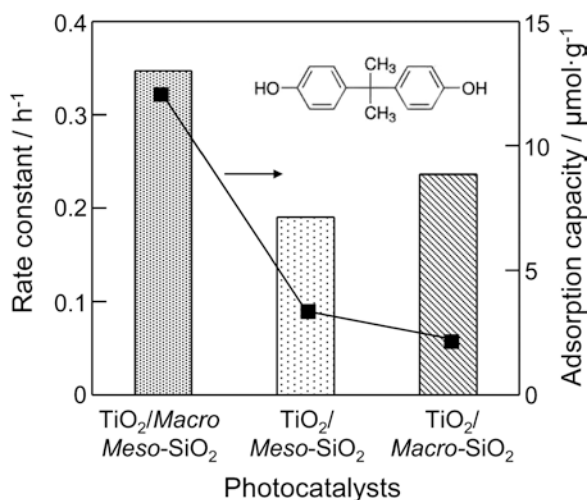


**Fig. 13.5** Relationship between the rate constant in the degradation of bisphenol A (BPH) in water under UV light irradiation and adsorption capacity on TiO<sub>2</sub>-loaded porous silica photocatalysts. Photocatalytic reaction was performed at 298 K in a Pyrex glass reaction vessel containing an aqueous BPH solution (0.1 mmol/L, 10 mL) and each sample (10 mg). Adsorption capacity was also evaluated at 298 K in the following conditions: aqueous BPH solution (0.1 mmol/L, 10 mL), sample (10 mg), and adsorption time (0.5 h)

photocatalytic performance of TiO<sub>2</sub>/MacroMeso-SiO<sub>2</sub> in comparison with that of TiO<sub>2</sub>/Macro-SiO<sub>2</sub> is also attributed to the differences in the adsorption capacity of BPH. The efficient adsorption process on TiO<sub>2</sub> and its surroundings is essential in photocatalytic reactions.

### 13.4.2 Decolorization of Methylene Blue in Water

The relation of adsorption capacity and photocatalytic performance of TiO<sub>2</sub>-loaded porous silica photocatalysts and bulk TiO<sub>2</sub> (P25) as a reference was investigated in the decolorization of methylene blue (MB) dye in water under UV light irradiation. MB is also a well-known soluble dye in water and used as a model contaminant of water in photocatalytic reaction tests. The size of MB is ca. 1.6 nm in the long axis direction [43, 44]. Figure 13.6 shows adsorption isotherms of MB on each sample. TiO<sub>2</sub>/MacroMeso-SiO<sub>2</sub> exhibited large increases at low MB concentration region, and then reached a plateau at relatively high MB concentration region. The equilibrium adsorption amount ( $Q_e$ ) was calculated by the following Eq. (13.2):

$$Q_e = (C_0 - C_e)V/m \quad (13.2)$$

where  $C_0$  is the initial concentration of MB solution (mg/L),  $C_e$  is the equilibrium concentration of MB (mg/L),  $V$  is the volume of solution, and  $m$  is the mass of

**Fig. 13.6** Adsorption isotherms of methylene blue (MB) on (a) TiO<sub>2</sub>/MacroMeso-SiO<sub>2</sub>, (b) TiO<sub>2</sub>/Meso-SiO<sub>2</sub>, (c) TiO<sub>2</sub>/Macro-SiO<sub>2</sub>, and (d) TiO<sub>2</sub> (P25). Adsorption tests of MB were carried out at 298 K under the following reaction conditions: aqueous MB solution (0–1.0 mmol/L, 10 mL), and adsorption time (0.5 h)

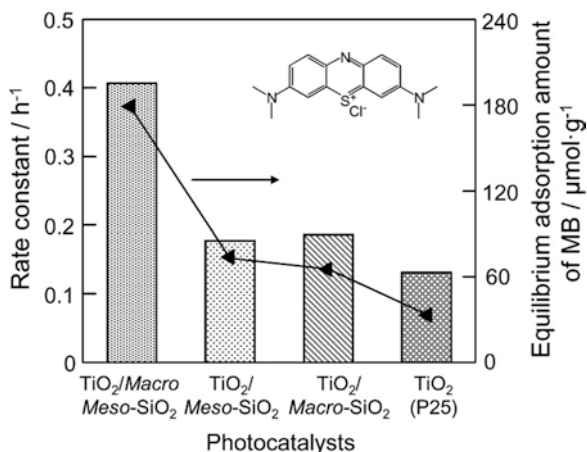
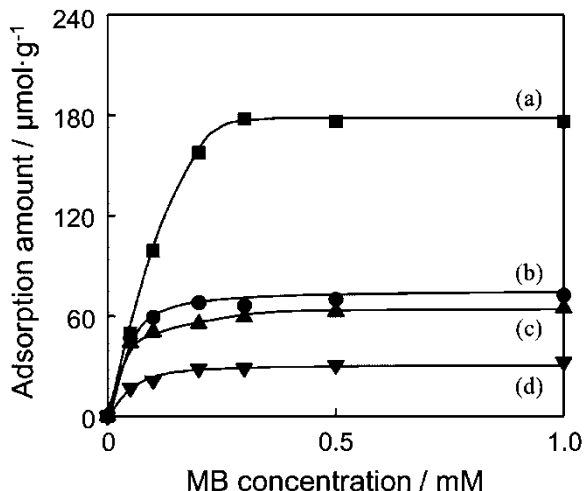


**Fig. 13.7** Relationship between the rate constant in the photocatalytic decolorization of methylene blue (MB) and equilibrium adsorption amount of MB diluted in water on TiO<sub>2</sub>-loaded porous silica photocatalysts and bulk TiO<sub>2</sub> (P25). Photocatalytic reactions were performed at 298 K in a quartz vessel containing an aqueous MB solution (0.1 mmol/L, 10 mL) and each sample (10 mg)

adsorbent. The equilibrium adsorption amount follows the order of TiO<sub>2</sub>/MacroMeso-SiO<sub>2</sub> ≫ TiO<sub>2</sub>/Meso-SiO<sub>2</sub> > TiO<sub>2</sub>/Macro-SiO<sub>2</sub> > TiO<sub>2</sub> (P25). By uses of combined structure of ordered mesoporous and hierarchical macroporous architectures, TiO<sub>2</sub>/MacroMeso-SiO<sub>2</sub> exhibited a good adsorption capacity of MB, which is quite higher than that of a series of evaluated samples.

Figure 13.7 shows relationship between the apparent rate constant in the photocatalytic decolorization of MB and equilibrium adsorption amount of MB diluted in water on each sample. Color of MB was gradually disappeared under

UV light irradiation. The color change was scarcely observed in the absence of photocatalysts as a blank test.  $\text{TiO}_2/\text{MacroMeso-SiO}_2$  showed much higher decolorization rate than  $\text{TiO}_2/\text{Meso-SiO}_2$  and  $\text{TiO}_2/\text{Macro-SiO}_2$ . The apparent rate constant ( $k_{\text{MB}}$ ) calculated by Eq. (13.1) was as follows:  $\text{TiO}_2/\text{MacroMeso-SiO}_2 \gg \text{TiO}_2/\text{Macro-SiO}_2 \approx \text{TiO}_2/\text{Meso-SiO}_2 > \text{TiO}_2$  (P25), where  $\text{TiO}_2/\text{Meso-SiO}_2$  and  $\text{TiO}_2/\text{Macro-SiO}_2$  showed similar photocatalytic activity. There are good relationships between the photocatalytic performance and adsorption capacity. These results indicated that macroporous structure has unique adsorption properties to condense MB molecules in water. Consequently,  $\text{TiO}_2/\text{MacroMeso-SiO}_2$  exhibited superior adsorption capacity and photocatalytic performance among these samples owing to the structural characteristics of  $\text{MacroMeso-SiO}_2$  in the dye enrichment and subsequent photocatalytic reaction process.

### 13.5 Conclusions

Porous siliceous materials, which contain one or both types of ordered mesopores and hierarchical macropores, were successfully synthesized by applying template strategies via a solvent evaporation process and used as a platform for design of  $\text{TiO}_2$ -loaded porous silica photocatalysts. The specific photocatalytic performance of  $\text{TiO}_2$  in water purification was realized through the utilization of combined nanospace of hierarchical macroporous and ordered mesoporous architectures. In particular, the unique adsorption properties of relatively large organic molecules led to the enhanced photocatalytic performance in water purification under UV light irradiation. These results suggested that the structure control of porous siliceous materials is one way to facilitate further progress and new applications in the related research fields.

### References

1. Fox MA, Dulay MT (1993) Heterogeneous photocatalysis. *Chem Rev* 93:341–357
2. Kamat PV (1993) Photochemistry on nonreactive and reactive (semiconductor) surfaces. *Chem Rev* 93:267–300
3. Hoffmann MR, Martin ST, Choi W, Bahnemann DW (1995) Environmental applications of semiconductor photocatalysis. *Chem Rev* 95:69–96
4. Chen X, Mao SS (2007) Titanium dioxide nanomaterials: synthesis, properties, modifications and applications. *Chem Rev* 107:2891–2959
5. Kuwahara Y, Kamegawa T, Mori K, Yamashita H (2010) Design of new functional Titanium oxide-based photocatalysts for degradation of organics diluted in water and air. *Curr Org Chem* 14:616–629
6. Fujishima A, Rao TN, Tryk DA (2000) Titanium dioxide photocatalysis. *J Photochem Photobiol C Photochem Rev* 1:1–21
7. Wang R, Hashimoto K, Fujishima A, Chikuni M, Kojima E, Kitamura A, Shimohigoshi M, Watanabe T (1997) Light-induced amphiphilic surfaces. *Nature* 388:431–432
8. Kamegawa T, Suzuki N, Yamashita H (2011) Design of macroporous  $\text{TiO}_2$  thin film photocatalysts with enhanced photofunctional properties. *Energy Environ Sci* 4:1411–1416

9. Kamegawa T, Shimizu Y, Yamashita H (2012) Superhydrophobic surfaces with photocatalytic self-cleaning properties by nanocomposite coating of TiO<sub>2</sub> and polytetrafluoroethylene. *Adv Mater* 24:3697–3700
10. Choi W, Termin A, Hoffmann MR (1994) The role of metal ion dopants in quantum-sized TiO<sub>2</sub>: correlation between photoreactivity and charge carrier recombination dynamics. *J Phys Chem* 98:13669–13679
11. Yamashita H, Harada M, Misaka M, Takeuchi M, Neppolian B, Anpo M (2003) Photocatalytic degradation of organic compounds diluted in water using visible light-responsive metal ion-implanted TiO<sub>2</sub> catalysts: Fe ion-implanted TiO<sub>2</sub>. *Catal Today* 84:191–196
12. Asahi R, Morikawa T, Ohwaki T, Aoki K, Taga Y (2001) Visible-light photocatalysis in nitrogen-doped titanium oxides. *Science* 293:269–271
13. Sakthivel S, Kisch H (2003) Daylight photocatalysis by carbon-modified titanium dioxide. *Angew Chem Int Ed* 42:4908–4911
14. Ohno T, Akiyoshi M, Umabayashi T, Asai K, Mitui T, Matsumura M (2004) Preparation of S-doped TiO<sub>2</sub> photocatalysts and their photocatalytic activities under visible light. *Appl Catal A Gen* 265:115–121
15. Fuku K, Kamegawa T, Mori K, Yamashita H (2012) Highly dispersed platinum nanoparticles on TiO<sub>2</sub> prepared by using the microwave-assisted deposition method: an efficient photocatalyst for the formation of H<sub>2</sub> and N<sub>2</sub> from aqueous NH<sub>3</sub>. *Chem Asian J* 7:1366–1371
16. Kamegawa T, Matsuura S, Seto H, Yamashita H (2013) A visible-light-harvesting assembly with a sulfocalixarene linker between dyes and a Pt-TiO<sub>2</sub> photocatalyst. *Angew Chem Int Ed* 52:916–919
17. Kominami H, Yamamoto S, Imamura K, Tanaka A, Hashimoto K (2014) Photocatalytic chemoselective reduction of epoxides to alkenes along with formation of ketones in alcoholic suspensions of silver-loaded titanium(IV) oxide at room temperature without the use of reducing gases. *Chem Commun* 50:4558–4560
18. Kamegawa T, Seto H, Matsuura S, Yamashita H (2012) Preparation of hydroxynaphthalene-modified TiO<sub>2</sub> via formation of surface complexes and their applications in the photocatalytic reduction of nitrobenzene under visible-light irradiation. *ACS Appl Mater Interfaces* 4:6635–6639
19. Lang X, Ma W, Chen C, Ji H, Zhao J (2014) Selective aerobic oxidation mediated by TiO<sub>2</sub> photocatalysis. *Acc Chem Res* 47:355–363
20. Palmisano G, García-López E, Marci G, Loddo V, Yurdakal S, Augugliaro V, Palmisano L (2010) Advances in selective conversions by heterogeneous photocatalysis. *Chem Commun* 46:7074–7089
21. Wang J, Zhang J, Asoo BY, Stucky GD (2003) Structure-selective synthesis of mesostructured/mesoporous silica nanofibers. *J Am Chem Soc* 125:13966–13967
22. Fowler CE, Khushalani D, Mann S (2001) Interfacial synthesis of hollow microspheres of mesostructured silica. *Chem Commun* 2028–2029
23. Okada S, Mori K, Kamegawa T, Che M, Yamashita H (2011) Active site design in a core-shell nanostructured catalyst for a one-pot oxidation reaction. *Chem Euro J* 17:9047–9051
24. Kamegawa T, Yamahana D, Seto H, Yamashita H (2013) Preparation of single-site Ti-containing mesoporous silica with a nanotube architecture and its enhanced catalytic activities. *J Mater Chem A* 1:891–897
25. Velev OD, Jede TA, Lobo RF, Lenhoff AM (1997) Porous silica via colloidal crystallization. *Nature* 389:447–448
26. Holland BT, Blanford CF, Stein A (1998) Synthesis of macroporous minerals with highly ordered three-dimensional arrays of spheroidal voids. *Science* 281:538–540
27. Stein A, Schrodin RC (2001) Colloidal crystal templating of three-dimensionally ordered macroporous solids: materials for photonics and beyond. *Curr Opin Solid State Mater Sci* 5:553–564
28. Li F, Wang Z, Ergang NS, Fyfe CA, Stein A (2007) Controlling the shape and alignment of mesopores by confinement in colloidal crystals: designer pathways to silica monoliths with hierarchical porosity. *Langmuir* 23:3996–4004

29. Xue C, Wang J, Tu B, Zhao D (2010) Hierarchically porous silica with ordered mesostructure from confinement self-assembly in skeleton scaffolds. *Chem Mater* 22:494–503
30. Stein A, Wilson BE, Rudisill SG (2013) Design and functionality of colloidal-crystal-templated materials - chemical applications of inverse opals. *Chem Soc Rev* 42:2763–2803
31. Kamegawa T, Suzuki N, Che M, Yamashita H (2011) Synthesis and unique catalytic performance of single-site Ti-containing hierarchical macroporous silica with mesoporous frameworks. *Langmuir* 27:2873–2879
32. Kamegawa T, Tanaka S, Seto H, Zhou D, Yamashita H (2013) Preparation of aluminum-containing mesoporous silica with hierarchical macroporous architecture and its enhanced catalytic activities. *Phys Chem Chem Phys* 15:13323–13328
33. Kamegawa T, Ishiguro Y, Seto H, Yamashita H (2015) Enhanced photocatalytic properties of TiO<sub>2</sub>-loaded porous silica with hierarchical macroporous and mesoporous architectures in water purification. *J Mater Chem A* 3:2323–2330
34. Kamegawa T, Ando T, Ishiguro Y, Yamashita H (2015) Hydroxylation of phenol on iron-containing mesoporous silica with hierarchical macroporous architecture. *Bull Chem Soc Jpn* 88:572–574
35. Inumaru K, Kasahara T, Yasui M, Yamanaka S (2005) Direct nanocomposite of crystalline TiO<sub>2</sub> particles and mesoporous silica as a molecular selective and highly active photocatalyst. *Chem Commun* 2131–2133
36. Kuwahara Y, Maki K, Matsumura Y, Kamegawa T, Mori K, Yamashita H (2009) Hydrophobic modification of a mesoporous silica surface using a fluorine-containing silylation agent and its application as an advantageous host material for the TiO<sub>2</sub> photocatalyst. *J Phys Chem C* 113:1552–1559
37. Kamegawa T, Yamahana D, Yamashita H (2010) Graphene coating of TiO<sub>2</sub> nanoparticles loaded on mesoporous silica for enhancement of activity photocatalytic. *J Phys Chem C* 114:15049–15053
38. Kamegawa T, Kido R, Yamahana D, Yamashita H (2013) Design of TiO<sub>2</sub>-zeolite composites with enhanced photocatalytic performances under irradiation of UV and visible light. *Micropor Mesopor Mater* 165:142–147
39. Qian XF, Kamegawa T, Mori K, Li HX, Yamashita H (2013) Calcium phosphate coatings incorporated in mesoporous TiO<sub>2</sub>/SBA-15 by a facile inner-pore sol-gel process toward enhanced adsorption-photocatalysis performances. *J Phys Chem C* 117:19544–19551
40. Qian XF, Fuku K, Kuwahara Y, Kamegawa T, Mori K, Yamashita H (2014) Design and functionalization of photocatalytic systems within mesoporous silica. *ChemSusChem* 7:1528–1536
41. Zou D, Ma S, Guan R, Park M, Sun L, Aklonis JJ, Salovey R (1992) Model filled polymers. V Synthesis of crosslinked monodisperse polymethacrylate beads. *J Polym Sci Part A Polym Chem* 30:137–144
42. Ogawa M (1996) A simple sol-gel route for the preparation of silica-surfactant mesostructured materials. *Chem Commun* 1149–1150
43. Berens AR (1997) Predicting the migration of endocrine disrupters from rigid plastics. *Polym Eng Sci* 37:391–395
44. Ocampo-Pérez R, Leyva-Ramos R, Sanchez-Polo M, Rivera-Utrilla J (2013) Role of pore volume and surface diffusion in the adsorption of aromatic compounds on activated carbon. *Adsorption* 19:945–957
45. Ding Z, Lu GQ, Greenfield PF (2000) Role of the crystallite phase of TiO<sub>2</sub> in heterogeneous photocatalysis for phenol oxidation in water. *J Phys Chem B* 104:4815–4820
46. Ohko Y, Ando I, Niwa C, Tatsuma T, Yamamura T, Nakashima T, Kubota Y, Fujishima A (2001) Degradation of bisphenol A in water by TiO<sub>2</sub> photocatalyst. *Environ Sci Technol* 35:2365–2368
47. Konstantinou IK, Albanis TA (2004) TiO<sub>2</sub>-assisted photocatalytic degradation of azo dyes in aqueous solution: kinetic and mechanistic investigations: a review. *Appl Catal B Environ* 49:1–14
48. Egeblad K, Christensen CH, Kustova M (2008) Templating mesoporous zeolites. *Chem Mater* 20:946–960
49. Choi M, Na K, Kim J, Sakamoto Y, Terasaki O, Ryoo R (2009) Stable single-unit-cell nanosheets of zeolite MFI as active and long-lived catalysts. *Nature* 461:246–249

# Chapter 14

## TiO<sub>2</sub> Photocatalyst Supported on Surface-Modified Silica Supports

Yasutaka Kuwahara, Xufan Qian, and Hiromi Yamashita

### 14.1 Introduction

Contamination of water and air with harmful organic compounds, especially resulting from industries, still remains a major pollution problem, since they are often responsible for disruption of ecosystems and illness in the human body. Current environmental regulations require treatment and stabilization of these hazardous constituents, and are anticipated to become more stringent in the future. To develop clean and safe chemical processes and materials contributing to this issue in accordance with the principles of “*green chemistry*” is obligation of our age, which should be undertaken with great urgency.

TiO<sub>2</sub> semiconductors have been recognized as a most promising photocatalyst for the decomposition of contaminated water and air, owing to suitable band gap energy for photo-induced redox reactions, mechanical and chemical stability, nontoxicity to the human body and environment, low cost, and convenience in preparation [1–4]. With these advantages, TiO<sub>2</sub> allows total oxidation of most organic compounds under ultraviolet (UV) light irradiation and convenient handling in environment and amenity spaces. Since the discovery of the photocatalytic properties of TiO<sub>2</sub>, applications in environmental cleanup, such as sterilization, antifouling and antibacterial coating, have been one of the most active areas in TiO<sub>2</sub> photocatalyst research, while

---

Y. Kuwahara (✉) • H. Yamashita (✉)

Division of Materials and Manufacturing Science, Graduate School of Engineering, Osaka University, 2-1 Yamadaoka, Suita, Osaka 565-0871, Japan

Elements Strategy Initiative for Catalysts & Batteries Kyoto University (ESICB), Kyoto University, Katsura, Kyoto 615-8520, Japan

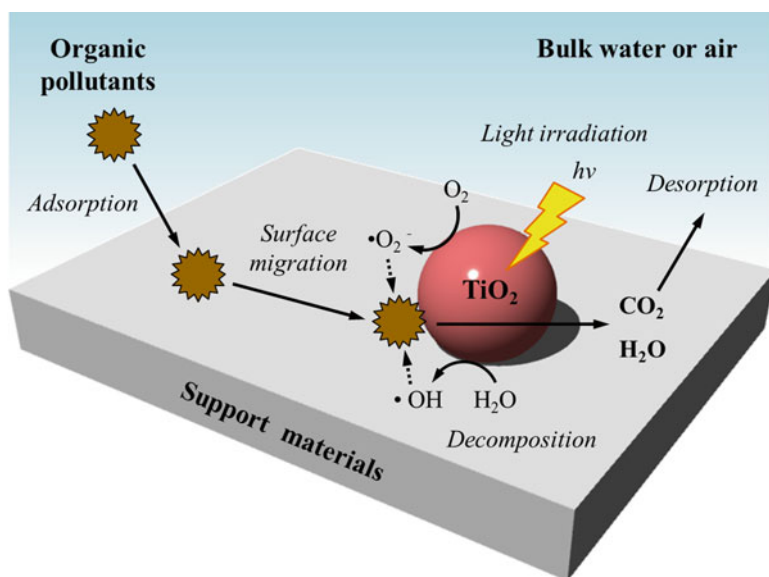
e-mail: [kuwahara@mat.eng.osaka-u.ac.jp](mailto:kuwahara@mat.eng.osaka-u.ac.jp); [yamashita@mat.eng.osaka-u.ac.jp](mailto:yamashita@mat.eng.osaka-u.ac.jp)

X. Qian

Division of Materials and Manufacturing Science, Graduate School of Engineering, Osaka University, 2-1 Yamadaoka, Suita, Osaka 565-0871, Japan

applications in solar energy conversion, energy storage, and green chemical synthesis have also been attracting increasing attention as well [5, 6]. Photocatalysis of  $\text{TiO}_2$  can provide adaptable and wide ranging solutions to environmental problems, now occurring on a global scale, because it occurs under environmentally-benign conditions using only light as an energy source. For further exploitation of its catalytic performance, remarkable developments in the fabrication of  $\text{TiO}_2$  photocatalyst have been made recently by introducing advanced preparation techniques. Among numerous researches dealing with  $\text{TiO}_2$  photocatalysts, significant efforts have been directed toward utilization of visible light by sensitization [7, 8], doping heteroatoms [9–12], and coupling with small band gap semiconductors [13] or plasmonic photocatalysts (e.g., Au, Ag, and Cu nanoparticles) [14], in addition to the improvement of the quantum efficiency by combining with small amounts of noble metals such as Pt and Ag for efficient charge separation [15]. Another huge concern is the morphological control (polyhedron, mesoporous oxides, hollow spheres, nano tubes, and thin films), since the photocatalytic efficiency of  $\text{TiO}_2$  is significantly influenced by its structural features such as crystal structure, exposed-facet, particle size, surface area, porosity, and other related factors [5, 16–19].

On the other hand, practical engineering applications of  $\text{TiO}_2$  photocatalysts require some solutions for the large-scale implementation. Due to the small particle size of  $\text{TiO}_2$  powder and solubility in aqueous medium,  $\text{TiO}_2$  particles need to be fixed on bulky support materials or to be blended with binder materials, so that the recovery from the treated water can be simplified. Furthermore, the concentration of



**Scheme 14.1** Schematic illustration of adsorption and oxidation kinetics of the organic pollutant on the surface of supported  $\text{TiO}_2$  photocatalytic system (so-called *Langmuir–Hinshelwood Mechanism*)

the organic compounds once discharged into water bodies such as rivers and sea areas is extremely lowered, making it difficult for them to be re-condensed and decomposed. Scheme 14.1 represents possible adsorption and oxidation kinetics of organic pollutant on supported TiO<sub>2</sub> photocatalytic system (so-called *Langmuir–Hinshelwood Mechanism*); The organic reactants diluted in aqueous medium or atmosphere are considered to be first adsorbed on the surface of the support where they migrate to the TiO<sub>2</sub> particles, and then are photocatalytically oxidized in the vicinity of TiO<sub>2</sub> by radical species such as hydroxyl radicals ( $\bullet\text{OH}$ ) and superoxide radical anions ( $\bullet\text{O}_2^-$ ) which are formed by the reaction of H<sub>2</sub>O and O<sub>2</sub> with photo-generated holes ( $h^+$ ) and electrons ( $e^-$ ), respectively. Thus, photodegradation reaction of organic contaminants essentially occurs in the adsorbed phase at the surface of TiO<sub>2</sub> and not in the solution, but TiO<sub>2</sub> itself has little affinity for hydrophobic organic molecules due to its surface polarity, so that preconcentration of organic reactants onto the TiO<sub>2</sub> surface is desirable for efficient photocatalytic degradation. These operational problems have led to a number of attempts to explore suitable supports for TiO<sub>2</sub>, for which mechanically and chemically stable bulky materials, e.g., silica (SiO<sub>2</sub>), alumina (Al<sub>2</sub>O<sub>3</sub>), silicon carbide (SiC) [20], silicon nitride (Si<sub>3</sub>N<sub>4</sub>) [21], and sorbents such as clays and activated carbons, have been suggested [22–24]. But unfortunately, TiO<sub>2</sub> supported on these traditional materials has been frequently reported to be less photoactive than the corresponding TiO<sub>2</sub> alone. This is because the nature of support materials influences not only the adsorption of organic reactants but also the crystallinity of TiO<sub>2</sub> photocatalyst. Hence, a good understanding of the physicochemical properties of support materials and the synergism between the supports and TiO<sub>2</sub> photocatalyst is of great importance to fabricate efficient photodegradation systems.

Recently, increasing attention has been directed to the use of ordered porous silicate materials, such as zeolites and mesoporous silicas with mean pore diameters of less than 50 nm, as hosts for TiO<sub>2</sub> photocatalyst. These nano-structured silicate materials have widely been used in chemical industries for many decades, as catalysts in petrochemical refining and chemical synthesis, sorbents in chromatographic and environmental applications, and hosts for biological applications [25, 26]. This is primarily because they offer many benefits, such as high chemical and mechanical stability, flexible morphology, tunable pore sizes, high surface area, adsorption and condensation properties, and environmental compatibility. In addition, they are transparent in the wide wavelength range including UV–visible light region, enabling them to act as host materials for photocatalysts. With these fascinating features, combination of these nano-porous silicate materials and TiO<sub>2</sub> photocatalyst provides advanced photocatalytic systems with prominent adsorption and condensation properties which enable photodegradation of organic pollutants diluted in air and water with high-efficiency. To date, a great deal of fundamental researches and engineering applications for this hybrid photocatalytic system have been reported; for example, environmental cleanup (de-NO<sub>x</sub>, deodorization, and water/air purification) and energy-conversion processes [27]. Current research has been focused on further improvement of their catalytic efficiencies by introducing advanced synthetic techniques [28]. Unlike the case of zeolite with restricted micro-

porous structures (<2 nm), mesoporous silica in particular has mesoporous structures (2–50 nm) available for accommodating bigger nanoparticles or metal clusters and amorphous silica frameworks with abundant surface-exposed silanol groups, which can be tailored via a postmodification. This merit can offer further opportunities in the development of efficient photodegradation systems within the space of nanopores.

In this chapter, we provide an overview of the recent development of TiO<sub>2</sub> photocatalyst supported on ordered nano-porous silicate materials with regard to environmental purification applications harnessing solar energy. In particular, we introduce the strategies for the design and functionalization of mesoporous-silica-based TiO<sub>2</sub> photocatalytic systems in terms of surface chemistry engineering, in which we put great emphasis on how the surface environment of the nano-spaces contributes to the photocatalytic efficiency of TiO<sub>2</sub>.

### 14.1.1 Zeolite-Supported TiO<sub>2</sub> Photocatalytic System

Among various supports for TiO<sub>2</sub> photocatalysts, zeolite is one of the leading candidates as compared to other conventional inorganic supports such as silica and alumina. Zeolites are aluminosilicate microporous materials consisting of cross-linkage of SiO<sub>4</sub><sup>4-</sup> and AlO<sub>4</sub><sup>5-</sup> tetrahedral units with pore diameters of less than 2 nm [25, 26]. The chemical formula of zeolite is in general expressed as M<sub>m</sub>[Al<sub>m</sub>Si<sub>n</sub>O<sub>2(m+n)</sub>]·xH<sub>2</sub>O, where M is an exchangeable cation (H<sup>+</sup>, Na<sup>+</sup>, K<sup>+</sup>, Ca<sup>2+</sup>, Mg<sup>2+</sup>, etc.) electrostatically trapped at the tetrahedral aluminum sites in the extraframework for the charge compensation, and it is well-known that these electrostatically polarized or unbalanced sites work as strong adsorption sites for polar molecules. For these reasons, zeolites have widely been used as useful cation-exchangers and adsorbents. The uniform pore distributions and relatively narrow channel sizes of zeolites endow them with a molecular sieving property toward the reactants and also offer large surface area available for adsorption.

Numerous kinds of naturally occurring and synthetic zeolites have been identified so far, the latter are formed by sol-gel and hydrothermal processes of silica-alumina gel in the presence of alkalis and structure directing agents (SDA). SDA-free zeolites such as A, X, MOR have been frequently used as commercially valuable zeolites. When using zeolites as supports for TiO<sub>2</sub> photocatalysts, their chemical composition, such as SiO<sub>2</sub>/Al<sub>2</sub>O<sub>3</sub> ratio and cation type, topology, and morphology (crystallinity, surface area, pore diameter, and particle size) need to be carefully selected, taking into account the nature of the support and the situations where the catalyst is used [29, 30]. Figure 14.1 shows the comparison of photocatalytic activities using TiO<sub>2</sub> photocatalysts supported on a various types of zeolites, including A-zeolite (LTA structure), X- and Y-zeolites (FAU structure) with different SiO<sub>2</sub>/Al<sub>2</sub>O<sub>3</sub> ratios from 2.5 to 200 as well as ZSM-5 zeolites (MFI structure) with SiO<sub>2</sub>/Al<sub>2</sub>O<sub>3</sub>=760, together with the corresponding water adsorption capacities and surface areas. Zeolites X and Y have topologically similar framework structures with a pore diameter of about 0.74 nm and with a supercage window of

about 1.3 nm, which are wider than that of LTA structure (0.41 nm) and MFI structure (0.55–0.51 nm). Note that TiO<sub>2</sub> particles were incorporated in zeolites by the conventional wet impregnation method using ammonium titanyl oxalate ((NH<sub>4</sub>)<sub>2</sub>[TiO(C<sub>2</sub>O<sub>4</sub>)<sub>2</sub>]·2H<sub>2</sub>O) as a titanium source and water as a medium to prepare fine TiO<sub>2</sub> particles within the zeolite micropores, and the TiO<sub>2</sub> content was empirically fixed to be 10 wt%. The photocatalytic activity was evaluated by the photocatalytic degradation of 2-propanol diluted in water under UV-light irradiation.

The results disclose that zeolites with higher SiO<sub>2</sub>/Al<sub>2</sub>O<sub>3</sub> ratios show higher photocatalytic activities, irrespective of the zeolite topologies or surface areas. More importantly, TiO<sub>2</sub> photocatalysts supported on high-silica zeolites, such as HY (200) and ZSM-5 (760), similarly exhibit photocatalytic activities higher than that of bulk TiO<sub>2</sub> powder (Evonik P25®), even though ZSM-5 zeolite has smaller surface area (ca. 400 m<sup>2</sup>/g) and narrower pore diameter (0.55–0.51 nm) compared to Y zeolite (ca. 700 m<sup>2</sup>/g and 0.74 nm). It has been well established that the variation of the SiO<sub>2</sub>/Al<sub>2</sub>O<sub>3</sub> ratio of the zeolite framework influences the hydrophilic–hydrophobic

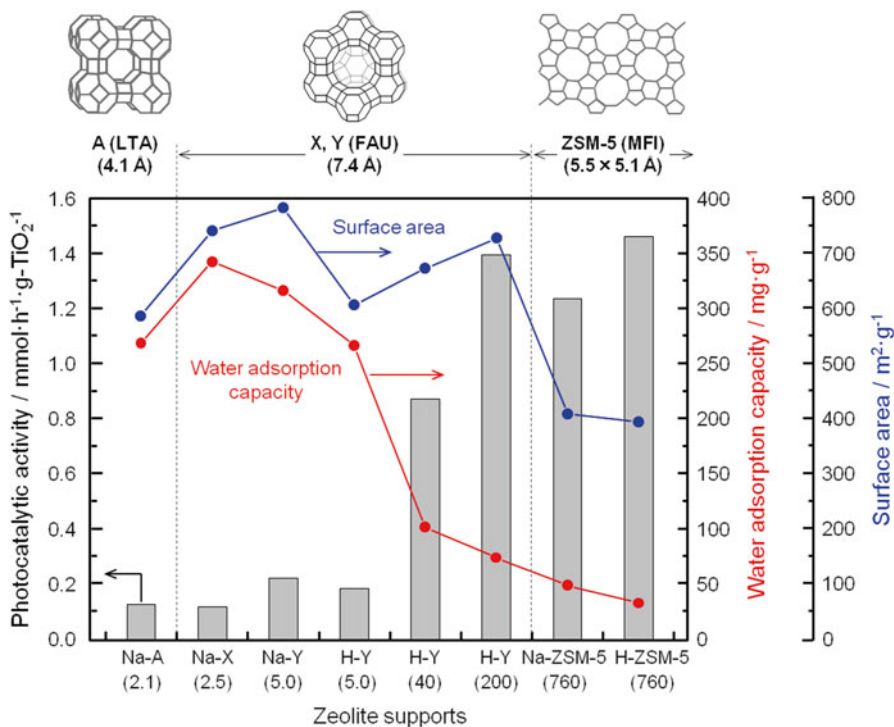


**Fig. 14.1** Comparison of photocatalytic activities of TiO<sub>2</sub> photocatalysts supported on various types of zeolites and their water adsorption capacities and surface areas. TiO<sub>2</sub> content of each catalyst was fixed to be 10 wt%, and the samples were calcined at 823 K in air for crystallization. Photocatalytic activities were determined by the photocatalytic degradation of 2-propanol diluted in water under UV-light irradiation ( $\lambda > 250$  nm). Reproduced by permission of The Royal Society of Chemistry [31]

character of zeolites, which consequently affects their sorptive properties [32, 33]. As summarized in Fig. 14.1, zeolites with higher  $\text{SiO}_2/\text{Al}_2\text{O}_3$  ratios show less water adsorption capacities, representing their intrinsic hydrophobic character, which is due to the reduced number of Al-related adsorption sites and the formation of electrostatically-neutral surface. This comparative study gives us a conclusion that, in the aqueous medium, the photocatalytic activity of the supported  $\text{TiO}_2$  is closely correlated with the surface hydrophilic–hydrophobic properties that arise from  $\text{SiO}_2/\text{Al}_2\text{O}_3$  ratio rather than other structural factors.

The above relationship can be explained in terms of adsorption kinetics of water molecules as they are the dominant species in aqueous medium, which can be well understood by water adsorption measurement. Generally, zeolites with low  $\text{SiO}_2/\text{Al}_2\text{O}_3$  ratio, e.g. NaY(5) and HY(5), show adsorption–desorption isotherms with steep increases in the amount of adsorbed water at very low vapor pressure region ( $p/p_0 < 0.1$ ) (Fig. 14.2), among those NaY(5) exhibits more steep increase even from extremely low pressure region. This is because the  $\text{Na}^+$  cations on the zeolite surface work as strong adsorption sites for water molecules via electrostatic interactions. As  $\text{SiO}_2/\text{Al}_2\text{O}_3$  ratio of zeolite increases, the adsorption isotherm shifts to the higher vapor pressure region, and high-silica zeolite, e.g. HY(810) synthesized via repeated dealumination treatment, shows little increase in the adsorbed amount of water up to  $p/p_0 = 0.8$ , suggesting a smaller interaction at the solid–water interface. Structurally considering, water molecules are strongly polarized due to the high electronegativity of the oxygen atom, which leads to strong interaction with cationic adsorption sites (e.g. alkali cations and  $\text{Al}^{3+}$  sites) rather than with neutral surfaces of siliceous zeolites. It is presumable that, in the hybrid photocatalytic systems, water molecules potentially act as an inhibitor, preferentially interacting with the cationic surface and interrupting the diffusion of inherently hydrophobic organic reactants, and thus result in lower photocatalytic efficiency [34]. This mechanism conversely indicates that the hydrophobic pore space provides efficient

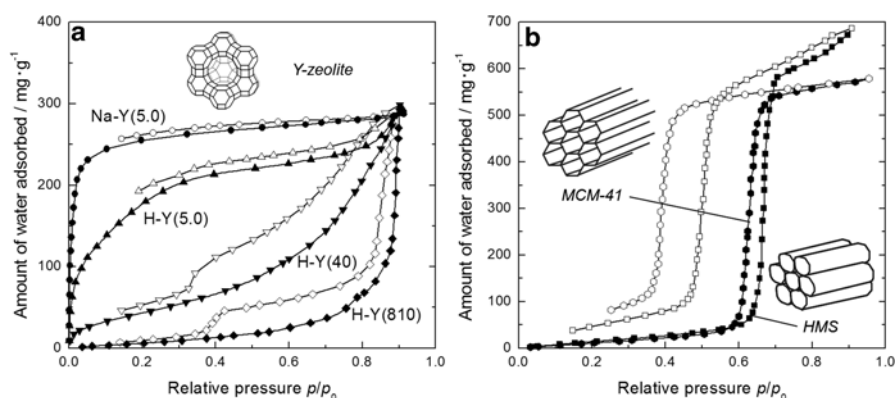


**Fig. 14.2** Water adsorption (filled) and desorption (open) isotherms of (a) Y-zeolites (NaY(5), HY(5), HY(40), HY(810)) and (b) mesoporous silicas (MCM-41 and HMS families) measured at 298 K. Adapted by permission of The Royal Society of Chemistry [31]

adsorption and transportation of organic reactants to the active TiO<sub>2</sub> sites, and thus improves the photocatalytic efficiency of TiO<sub>2</sub>.

On the other hand, mesoporous silicas (Fig. 14.2b) show little adsorption at low vapor pressure region, reflecting a weak interaction between water molecules and the silanol groups on the mesoporous silica surface. However, they exhibit rapid increase at around  $p/p_0=0.6$ , which corresponds to the capillary condensation of water molecules into the mesopores, and provide much larger water adsorption capacities than those of zeolites due to their larger pore volumes. Silanol groups existing on mesoporous silica surface by nature show hydrophilic property. At higher vapor pressure conditions, they preferentially trap and transfer water molecules into silica pores rather than organic compounds, thereby, photocatalytic activity of TiO<sub>2</sub> supported on mesoporous silica is unexpectedly suppressed in spite of its larger pore size.

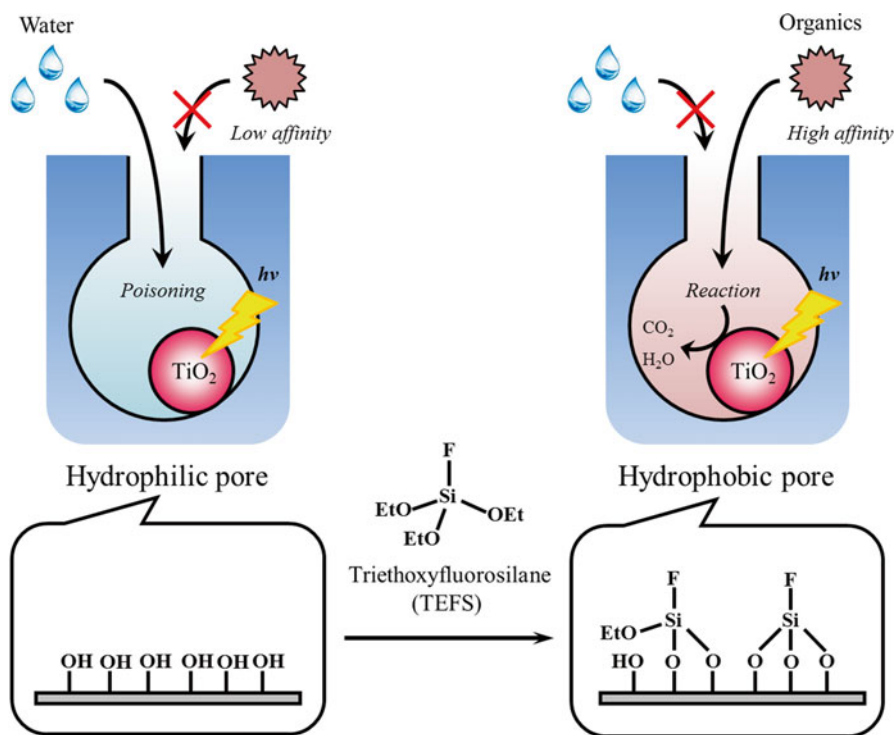
Thus, the surface of zeolite and mesoporous silica materials intrinsically shows hydrophilic character, which is insufficient to satisfy the requirements for TiO<sub>2</sub> support. Therefore, particular methodologies to improve surface hydrophobicity are required. In the case of zeolites, dealumination is one of the most convenient and widely-accepted techniques for the improvement of surface hydrophobicity. However, it is well-known that conventional SDA-free zeolites such as A, X, MOR with high-silica content cannot be directly synthesized due to the limitations of naturally-occurring Si/Al ratios. To obtain highly siliceous zeolites, it is necessary to perform a repeated dealumination treatment, in which the Al atoms are expelled from the zeolite framework by hydrothermal treatment, acid leaching, and chemical treatments [34]. Nevertheless, such repeated dealumination treatments under severe conditions sometimes afford zeolites with lots of deficient sites in the framework and intra-particle voids, leading to a decreased quality of zeolite structure.

### ***14.1.2 TiO<sub>2</sub> Photocatalyst Supported on Zeolites Hydrophobically Modified by Fluorine-Containing Silane Coupling Agent***

To improve the adsorption of organic compounds in the nanopore spaces, a surface modification technique using silane coupling agent has been proposed. Postmodification of the silica surface using silane coupling agent is one of the generalized methods for tailoring surface morphology and physicochemical properties for designing multi-functionalized surfaces on silicate materials, which allows them to be intelligent materials such as drug carriers, photosensors, sensitizers, solid catalysts, and advantageous supports for metal catalysts and biocatalysts [35, 36]. Surface modification is conventionally achieved by the condensation polymerization between silanol groups ( $\equiv\text{Si-OH}$ ) and organosilanes having hydrophobic functional groups (e.g. methyl, propyl, octyl, phenyl etc.), otherwise, creating new silicate layers over the support surface. However, the resulting organo-functionalized materials are thermally unstable; the organic functional groups are easily combusted and hydroxyl groups are regenerated to afford hydrophilic surface. Hence, deposition of

TiO<sub>2</sub> photocatalyst, which requires high calcination temperatures for crystallization of TiO<sub>2</sub>, on such organo-functionalized silica materials seems useless.

To this end, we prepared hydrophobic porous silicas using a fluorine-containing silane coupling agent, triethoxyfluorosilane (TEFS), instead of the conventional organosilane coupling agents [37]. Scheme 14.2 presents the main principles of surface modification in TiO<sub>2</sub>/porous silica photocatalytic systems. The merit of TEFS is to substitute surface hydroxyl groups with a heat-resistant ≡Si–F bond, otherwise, to cover the surface with a new silicate layer without significant blockage of micro/meso pores. For example, TEFS-modified zeolites showed lower water adsorption capacities in water adsorption measurement compared to the corresponding unmodified zeolites without significant loss of surface areas and pore volumes, verifying an improved hydrophobicity of zeolite surface by the TEFS modification (Fig. 14.3a). Furthermore, the modified zeolites were thermally stable up to 773 K, where the organic functional groups attached on silica surface are easily combusted. Therefore, this postmodification method can be an alternative route for fabricating hydrophobic silica materials while keeping its structure and thermal stability. The influence of the above modification on the photocatalytic activity of loaded TiO<sub>2</sub> was evaluated by the degradation of alcohol diluted in water and alde-



**Scheme 14.2** Illustration of TiO<sub>2</sub> photocatalysts supported on hydrophilic and hydrophobic pores and surface modification using triethoxyfluorosilane (TEFS) as a silylation agent

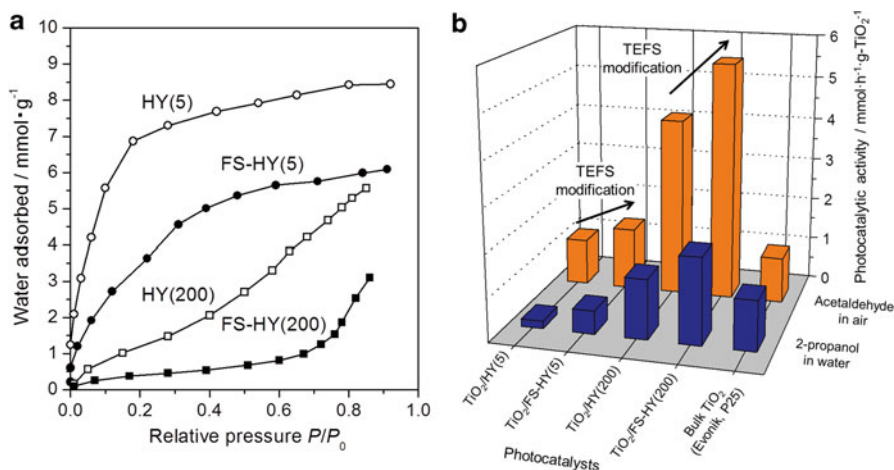


**Fig. 14.3** (a) Water adsorption isotherms of unmodified Y-zeolites (HY(5) and HY(200)) and TEFS-modified Y-zeolites (FS-HY(5) and FS-HY(200)) measured at 298 K. (b) Comparison of photocatalytic activities of TiO<sub>2</sub> photocatalysts supported on unmodified Y-zeolites and TEFS-modified Y-zeolites, together with that of commercial bulk TiO<sub>2</sub> (Evonik, P25<sup>®</sup>). Photocatalytic activities were determined by the photocatalytic degradation of 2-propanol diluted in water (2.6 mmol/L) and acetaldehyde diluted in air (1000 ppm) under UV-light irradiation ( $\lambda > 250$  nm). The TiO<sub>2</sub> content of each catalyst was fixed to be 10 wt%, and the samples were calcined at 823 K in air for crystallization

hyde in air under UV-light irradiation (Fig. 14.3b). As aforementioned, use of zeolites with higher SiO<sub>2</sub>/Al<sub>2</sub>O<sub>3</sub> ratio is effective for exploiting the photocatalytic performance of TiO<sub>2</sub>. In particular, the influence of zeolite support was more pronounced in the gaseous phase reactions rather than in liquid phase reactions, in which five times greater photocatalytic activity was obtained over zeolite-supported TiO<sub>2</sub> systems compared to bulk TiO<sub>2</sub> powder (Evonik, P25<sup>®</sup>) under optimum conditions. This is primarily because the diffusion of water molecules is less dominant in gaseous phase than in aqueous phase, and secondarily because zeolites are commonly known to have excellent adsorption properties particularly toward volatile organic compounds (VOCs) such as acetaldehyde and toluene etc. It is considered that the zeolite with inert siliceous surface facilitates the organic molecular transfer within pore spaces and contributes to the high catalytic efficiency of TiO<sub>2</sub>. As a matter of fact, TiO<sub>2</sub> supported on the hydrophobically modified zeolites exhibited much higher photocatalytic activities than those supported on the unmodified zeolites in both reactions. This is attributed to the high affinity of the zeolites with organic molecules as mentioned above, that is, the hydrophobic pores having smaller interaction with water molecules allows organic molecules smooth transportation and easy access to the TiO<sub>2</sub> active sites, resulting in higher photocatalytic efficiencies. Zeolites are very potent supports for TiO<sub>2</sub> photocatalysts, especially suited to adsorb and condense organic pollutants diluted in air, and the zeolites hydrophobically modified using TEFS can further improve the degradation efficiency of TiO<sub>2</sub> photocatalysts.

### 14.1.3 *TiO<sub>2</sub> Photocatalyst Supported on Mesoporous Silica Hydrophobically Modified by Fluorine-Containing Silane Coupling Agent*

One of the critical drawbacks of the TiO<sub>2</sub>/zeolite hybrid photocatalytic system is the limitation of adsorbable molecule size due to its narrow channel size (<2 nm). Mesoporous silica with larger pore sizes (2–50 nm) can offer much larger interior space which can accommodate larger organic molecules. With this pore size suitable for the uptake of larger molecules and with well-defined and unique structural features, the mesoporous silica is attractive for a range of applications in purification, environmental applications, fine chemistry, and biotechnology. Furthermore, tunable morphologies and fine connectivity of the pores may facilitate the mass transfer of organic reactants [38]. Thus, the mesoporous silica can be envisaged as an alternative support for TiO<sub>2</sub>, however, there still remains a critical problem, that is a high affinity with water molecules due to its hydrophilic surface nature (see Fig. 14.2b). Recent research on TiO<sub>2</sub>/mesoporous silica hybrids has aimed at the functionalization of pore surface by direct/post-synthetic modifications using a variety of organosilanes [35]. For example, Inumaru and coworkers grafted *n*-octyl groups onto the pore walls of TiO<sub>2</sub>/MCM-41 in which TiO<sub>2</sub> was highly dispersed in the mesopores [39]. They found that the *n*-octyl-grafted TiO<sub>2</sub>/MCM-41 efficiently decomposed dilute 4-nonylphenol polyethoxylate (NEPO), an endocrine disrupter, under UV-light irradiation, which outperformed the activity of commercial bulk TiO<sub>2</sub> catalyst under the same reaction conditions. The higher activity of *n*-octyl-grafted TiO<sub>2</sub>/MCM-41 was ascribed to the unique hydrophobic nano-space to selectively adsorb and condense low-concentrated NEPO molecules from water. This example suggests that the pore space of mesoporous silica can be hydrophobically tailored by removing surface hydroxyl groups or by replacing them by other functional groups through the postmodification techniques. With this view, we applied the surface modification technique using TEFS to the TiO<sub>2</sub>/mesoporous silica hybrid to fabricate an efficient photodegradation system [40], where HMS-type mesoporous silica with wormhole-like pore structure and pore diameter of ca. 2–3 nm was used as a representative mesoporous silica. Hydrophobic modification was performed by the same procedure as in the case of zeolite, followed by TiO<sub>2</sub> deposition using tetraisopropylorthotitanate (TPOT: Ti(OC<sub>3</sub>H<sub>7</sub>)<sub>4</sub>) as a titanium precursor. After grafting optimal amount of fluorine atoms, the water adsorption capacity dramatically decreased compared to that of pure HMS, while keeping most of its textural properties and thermal stability (Fig. 14.4a). This result indicates that the hydrophobic nano-space was successfully created by the coating of new silicate layer over the mesoporous silica surface.

The efficacy of the hydrophobic modification of mesoporous silica on adsorption and photocatalysis was evaluated by the photocatalytic degradation of 2-propanol and phenol diluted in water under UV-light irradiation. Phenol is one of the ideal model pollutants for photocatalytic studies since phenolic derivatives in aqueous solutions are commonly known to cause severe environmental problems in industry

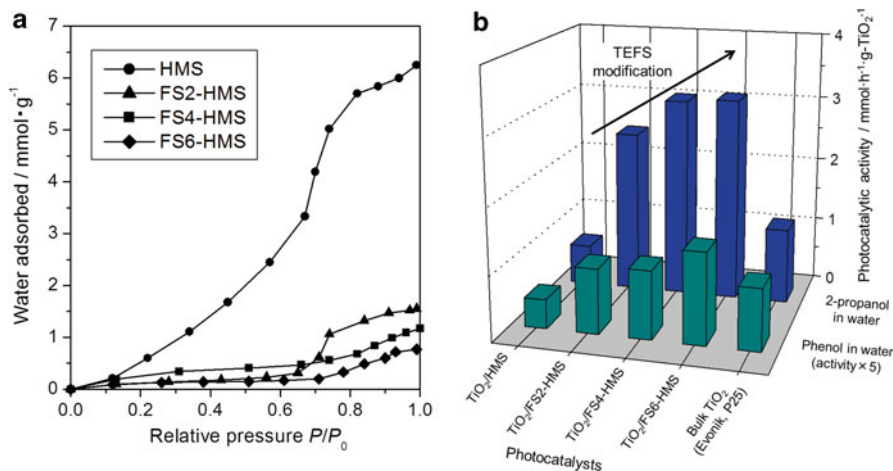


**Fig. 14.4** (a) Water adsorption isotherms of TEFS-modified HMS-type mesoporous silicas measured at 298 K. (b) Comparison of photocatalytic activities of TiO<sub>2</sub> photocatalysts supported on TEFS-modified HMS-type mesoporous silicas and commercial bulk TiO<sub>2</sub> (Evonik, P25<sup>®</sup>). Photocatalytic activities were determined by the photocatalytic degradation of 2-propanol in water (2.6 mmol/L) and phenol diluted in water (0.23 mmol/L) under UV-light irradiation ( $\lambda > 250$  nm). The TiO<sub>2</sub> content of each catalyst was fixed to be 10 wt%, and the samples were calcined at 823 K in air for crystallization

and agriculture, and these compounds are normally refractory and persistent toward biological treatment processes. As shown in Fig. 14.4b, TiO<sub>2</sub> photocatalysts supported on original HMS are rather less photoactive than commercial bulk TiO<sub>2</sub> powder (Evonik, P25<sup>®</sup>), however, a significant improvement of photocatalytic activity was observed in the TiO<sub>2</sub> photocatalysts supported on TEFS-modified HMS (FS $n$ -HMS ( $n=2, 4$ , and  $6$ ), where  $n$  corresponds to the molar ratio of TEFS per Si, 20, 40, and 60 mol%, respectively). Additional adsorption experiments under dark conditions revealed that the photocatalytic activities corresponded fairly well to the adsorbed amounts of organic molecules, proving that the adsorption property which arises from hydrophobicity of the support plays a vital role in determining the photocatalytic degradation rate. Surprisingly, TiO<sub>2</sub> supported on FS-HMS with an optimal fluorine content outperformed bulk TiO<sub>2</sub> photocatalyst under the same reaction conditions in both reactions. This noticeable improvement of photocatalytic activities is attributed to the multiple effects involving the surface hydrophobicity and retained mesopore structure.

Aside from this, in supported TiO<sub>2</sub> photocatalytic systems, well-defined nanoporous spaces of zeolites and mesoporous silica offer an unusual environment for TiO<sub>2</sub> particles and may alter physicochemical property of TiO<sub>2</sub>. Structurally considering, encapsulation of TiO<sub>2</sub> into the spatially restricted micro/mesopores of nanoporous silica would be effective in increasing the number of surface photoactive sites by the formation of highly-dispersed nano-size TiO<sub>2</sub> particles, and also improving adsorption towards organic molecules by enlarging surface area available for

adsorption. Furthermore, it has been reported that nano-size  $\text{TiO}_2$  particles show enhanced reactivities compared to bulk  $\text{TiO}_2$  due to the quantum size effects (changes in the valence and conduction band edges and spatial localization of the photogenerated electrons and holes) [27]. Meanwhile, such nano-size  $\text{TiO}_2$  particles require higher light energies for photoexcitation, consequently the absorbable light spectrum is limited (While bulk  $\text{TiO}_2$  absorbs UV-light with a wavelength shorter than 390 nm, the nano-size  $\text{TiO}_2$  particles created inside micro/mesopores generally have absorption band at  $\lambda < 360$  nm). Indeed, the hydrophobicity of supports is the most dominant factor responsible for determining the overall reactivity of  $\text{TiO}_2$  as noted above, however, these are a number of factors controlling the reactivity, all of which are most likely working simultaneously. For the design of efficient  $\text{TiO}_2$  photodegradation systems, optimal control of those factors to maximize the reactivity of  $\text{TiO}_2$  is clearly needed.

#### ***14.1.4 $\text{TiO}_2$ Photocatalyst Supported on Mesoporous Silica Modified with Calcium Phosphate***

As a result of the rapid increase of research in the preparation of nano-structured materials with new physicochemical properties, it is currently possible to create advanced supports with larger pore sizes and unique surface chemistry that will further improve photocatalytic efficiency of  $\text{TiO}_2$ , instead of the conventional zeolites and mesoporous silicas. Recently, we fabricated  $\text{TiO}_2$ /mesoporous silica photocatalytic system incorporating calcium phosphate (CaP) minerals on its surface [41]. Calcium phosphate (CaP) minerals, such as hydroxyapatite ( $\text{Ca}_{10}(\text{PO}_4)_6(\text{OH})_2$ , HAp), are the main inorganic constituents of human tissue. Moreover, the synthetic HAp with various nanostructures has widely been used as drug carriers, adsorbents for separation/purification of biomolecules, and catalysts supports owing to the good affinity for various organic molecules [42]. For the application in adsorption and catalysis, enlargement of available surface area of HAp is of great importance. Although numerous attempts have been performed to combine CaP minerals and silica component to fabricate intelligent nano-composites, most of the methods always suffer from the heterogeneous distribution of CaP components and phase separation due to the rapid growth and aggregation of CaP crystals. To this end, we synthesized CaP-coated  $\text{TiO}_2$ /mesoporous silica composite via a postmodification route, where as-prepared SBA-15 type mesoporous silica with larger pore size (ca. 7 nm) was used as a silica host because it offers much larger interior space that can accommodate CaP nano-crystals. The coating of CaP onto the SBA-15 silica surface was performed by a facile sol-gel process, which is favored in HAp coatings on many bulk artificial materials due to the chemical homogeneity and fine grain size of HAp crystals.

By increasing the content of CaP, the pore diameter of SBA-15 silica was reduced from 7.1 to 6.4 nm (Fig. 14.5), indicating the change of thickness of the CaP coating layer. The highly dispersed CaP phase effectively increased the amount of methy-

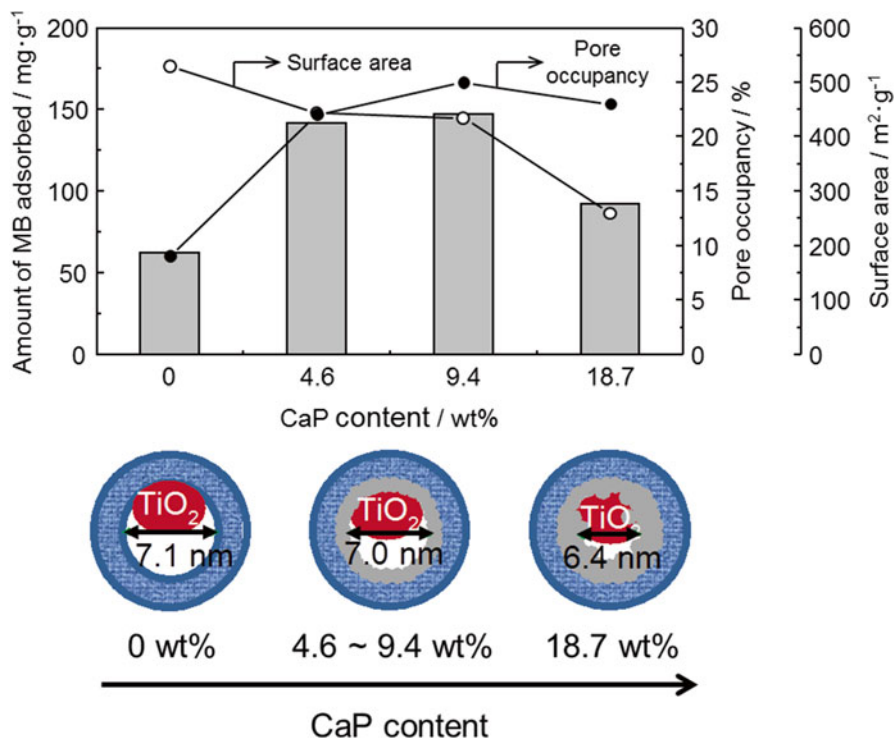


**Fig. 14.5** Adsorption capacities for methylene blue (MB) dye and estimated pore occupancy of adsorbed dye molecules on TiO<sub>2</sub>/SBA-15 hybrid photocatalysts with different weight percent of CaP (0–18.7 wt%), together with schematic illustrations of their pore size variations

lene blue (MB) molecules adsorbed from the aqueous solution. The main cause of this remarkable adsorption capacity is the high affinity of CaP phase toward MB rather than the surface area of the supports (Fig. 14.5). It is assumable that MB molecules with positively charged N-alkyl groups could be easily adsorbed on the surface of CaP with abundant PO<sub>4</sub><sup>3-</sup> groups through electrostatic interactions.

Evaluation of the photocatalytic performance under UV light irradiation made it clear that a moderate CaP coverage and high adsorption capacity were necessary for improving the photodegradation efficiency of TiO<sub>2</sub> (Fig. 14.6a). The photocatalytic efficiency of the CaP-coated TiO<sub>2</sub>/SBA-15 was higher than that of the physical mixture of CaP and TiO<sub>2</sub>/SBA-15, which also had an adsorption capacity identical to the composite sample. This phenomenon implies that the proximity of CaP (adsorption sites) and TiO<sub>2</sub> (photocatalytic sites) on nanoscale plays a crucial role for enhancing the photocatalytic degradation efficiency. It is deduced that the dye molecules are pre-adsorbed and enriched on the CaP adsorption sites, and the proximity of CaP and TiO<sub>2</sub> allows dye molecules to efficiently access to the TiO<sub>2</sub> active sites. Additionally, the MB enriched on the CaP adsorption sites could alleviate the

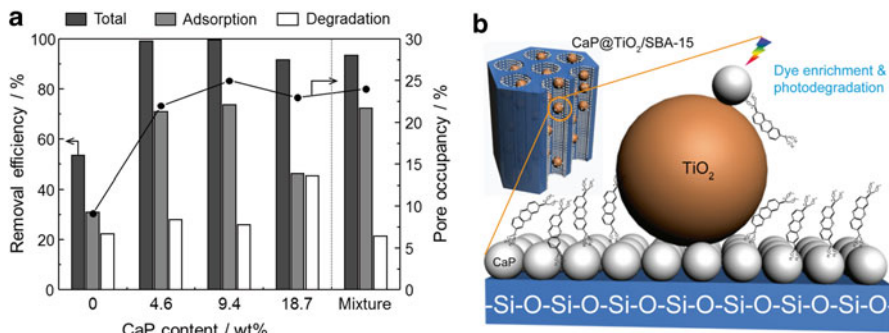


**Fig. 14.16** (a) Removal efficiency of MB by adsorption, photodegradation, and sum of them (total) on  $\text{TiO}_2/\text{SBA-15}$  hybrid photocatalysts modified with different amounts of CaP (0–18.7 wt%) and (b) schematic illustration of adsorption and photodegradation kinetics of MB dye on CaP-coated  $\text{TiO}_2/\text{SBA-15}$

over-coverage of MB molecules on  $\text{TiO}_2$  photoactive sites, which also facilitates the efficient absorption of photons from UV light (Fig. 14.6b).

### 14.1.5 Conclusions

In this chapter, we review strategies and recent developments in designing  $\text{TiO}_2$ -sorbent hybrid photocatalysts, especially those supported on ordered nano-porous silica materials including zeolites and mesoporous silicas, with the objective of fabricating efficient photodegradation systems toward organic compounds diluted in water and air. From a fundamental perspective, we also describe the basic features of zeolites and mesoporous silicas, adsorption kinetics on their surfaces, and the role of water molecules in catalysis. Our comprehensive studies demonstrated that adsorption plays a predominant role in photocatalysis in comparison with photoredox processes of  $\text{TiO}_2$ , and the adsorption and enrichment of organic pollutants strongly relies on the surface properties on the support materials such as hydrophilicity/hydrophobicity or surface charge. Therefore, surface-chemistry engineering is desirable for  $\text{TiO}_2$ /porous silica photocatalytic systems especially for the abatement of organic pollutants in water and air at low concentrations. In this regard, the use of porous silica materials with modified surfaces as hosts for  $\text{TiO}_2$  photocatalysts was proven to offer further opportunities to control the adsorption property for organic compounds, which led to improved photocatalytic efficiencies in water/gas purification [43]. Future studies of  $\text{TiO}_2$ /porous silica hybrid photocatalysts will involve optimization of structures of porous silica support, tailoring the nano-space with multifunctionalities, selective anchoring of specific functional groups on the support surfaces to give a molecularly recognizable synergistic effect, and their use in real environmental applications.

It can also be foreseen that new technologies to prepare nano-structured materials with unprecedented physicochemical and optical properties will emerge in the near future, which will bring us new concepts for designing hybrid photocatalytic systems. Continuous exploration of support materials suitable for TiO<sub>2</sub> photocatalyst and optimization of the photocatalytic efficiency will boost the utilization of TiO<sub>2</sub> as an environmental catalyst, which will further reduce the burden on the environment.

## References

1. Fujishima A, Honda K (1972) Electrochemical photolysis of water at a semiconductor electrode. *Nature* 238:37–38
2. Hoffmann MR, Martin ST, Choi W, Bahnemann DW (1995) Environmental applications of semiconductor photocatalysis. *Chem Rev* 95:69–96
3. Linsebigler AL, Lu G, Yates JT (1995) Photocatalysis on TiO<sub>2</sub> surfaces: principles, mechanisms, and selected results. *Chem Rev* 95:735–758
4. Fujishima A, Rao TN, Tryk DA (2000) Titanium dioxide photocatalysis. *J Photochem Photobiol C* 1:1–21
5. Chen X, Mao SS (2007) Titanium dioxide nanomaterials: synthesis, properties, modifications, and applications. *Chem Rev* 107:2891–2959
6. Kamat PV (2007) Meeting the clean energy demand: nanostructure architectures for solar energy conversion. *J Phys Chem C* 111:2834–2860
7. Kalyanasundaram K, Vlachopoulos N, Krishnan V, Monnier A, Graetzel M (1987) Sensitization of titanium dioxide in the visible light region using zinc porphyrins. *J Phys Chem* 91:2342–2347
8. O'Regan B, Grätzel M (1991) A low-cost, high-efficiency solar cell based on dye-sensitized colloidal TiO<sub>2</sub> films. *Nature* 353:737–740
9. Asahi R, Morikawa T, Ohwaki T, Aoki K, Taga Y (2001) Visible-light photocatalysis in nitrogen-doped titanium oxides. *Science* 293:269–271
10. Yamashita H, Harada M, Misaka J, Takeuchi M, Ikeue K, Anpo M (2002) Degradation of propanol diluted in water under visible light irradiation using metal ion-implanted titanium dioxide photocatalysts. *J Photochem Photobiol A* 148:257–261
11. Yamashita H, Anpo M (2004) Application of an ion beam technique for the design of visible light-sensitive, highly efficient and highly selective photocatalysts: ion-implantation and ionized cluster beam methods. *Catal Surv Asia* 8:35–45
12. Kamegawa T, Sonoda J, Sugimura K, Mori K, Yamashita H (2009) Degradation of isobutanol diluted in water over visible light sensitive vanadium doped TiO<sub>2</sub> photocatalyst. *J Alloys Compd* 486:685–688
13. Gopidas KR, Bohorquez M, Kamat PV (1990) Photophysical and photochemical aspects of coupled semiconductors: charge-transfer processes in colloidal cadmium sulfide-titania and cadmium sulfide-silver(I) iodide systems. *J Phys Chem* 94:6435–6440
14. Li H, Bian Z, Zhu J, Huo Y, Li H, Lu Y (2007) Mesoporous Au/TiO<sub>2</sub> nanocomposites with enhanced photocatalytic activity. *J Am Chem Soc* 129:4538–4539
15. Duonghong D, Borgarello E, Grätzel M (1981) Dynamics of light-induced water cleavage in colloidal systems. *J Am Chem Soc* 103:4685–4690
16. Li H, Bian Z, Zhu J, Zhang D, Li G, Huo Y, Li H, Lu Y (2007) Mesoporous titania spheres with tunable chamber structure and enhanced photocatalytic activity. *J Am Chem Soc* 129:8406–8407

17. Yuan S, Sheng Q, Zhang J, Yamashita H, He D (2008) Synthesis of thermally stable mesoporous TiO<sub>2</sub> and investigation of its photocatalytic activity. *Micropor Mesopor Mater* 110:501–507
18. Kamegawa T, Suzuki N, Yamashita H (2011) Design of macroporous TiO<sub>2</sub> thin film photocatalysts with enhanced photofunctional properties. *Energy Environ Sci* 4:1411
19. Kamegawa T, Shimizu Y, Yamashita H (2012) Superhydrophobic surfaces with photocatalytic self-cleaning properties by nanocomposite coating of TiO<sub>2</sub> and polytetrafluoroethylene. *Adv Mater* 24:3697–3700
20. Yamashita H, Nishida Y, Yuan S, Mori K, Narisawa M, Matsumura Y, Ohmichi T, Katayama I (2007) Design of TiO<sub>2</sub>-SiC photocatalyst using TiC-SiC nano-particles for degradation of 2-propanol diluted in water. *Catal Today* 120:163–167
21. Yamashita H, Nose H, Kuwahara Y, Nishida Y, Yuan S, Mori K (2008) TiO<sub>2</sub> photocatalyst loaded on hydrophobic Si<sub>3</sub>N<sub>4</sub> support for efficient degradation of organics diluted in water. *Appl Catal A* 350:164–168
22. Ooka C, Yoshida H, Horio M, Suzuki K, Hattori T (2003) Adsorptive and photocatalytic performance of TiO<sub>2</sub> pillared montmorillonite in degradation of endocrine disruptors having different hydrophobicity. *Appl Catal B* 41:313–321
23. Ooka C, Yoshida H, Suzuki K, Hattori T (2004) Highly hydrophobic TiO<sub>2</sub> pillared clay for photocatalytic degradation of organic compounds in water. *Micropor Mesopor Mater* 67:143–150
24. Kuwahara Y, Kamegawa T, Mori K, Yamashita H (2010) Design of new functional titanium oxide-based photocatalysts for degradation of organics diluted in water and air. *Curr Org Chem* 14:616–629
25. Arends IWCE, Sheldon RA, Wallau M, Schuchardt U (1997) Oxidative transformations of organic compounds mediated by redox molecular sieves. *Angew Chem Int Ed* 36:1144–1163
26. Hölderich W, Hesse M, Nümann F (1988) Zeolites: catalysts for organic syntheses. *Angew Chem Int Ed* 27:226–246
27. Yamashita H, Anpo M (2003) Local structures and photocatalytic reactivities of the titanium oxide and chromium oxide species incorporated within micro- and mesoporous zeolite materials: XAFS and photoluminescence studies. *Curr Opin Solid State Mater Sci* 7:471–481
28. Yamashita H, Mori K, Shironita S, Horiuchi Y (2008) Applications of single-site photocatalysts to the design of unique surface functional materials. *Catal Surv Asia* 12:88–100
29. Xu Y, Langford CH (1995) Enhanced photoactivity of a titanium(IV) oxide supported on ZSM5 and zeolite A at low coverage. *J Phys Chem* 99:11501–11507
30. Xu Y, Langford CH (1997) Photoactivity of titanium dioxide supported on MCM41, zeolite X, and zeolite Y. *J Phys Chem B* 101:3115–3121
31. Kuwahara Y, Yamashita H (2011) Efficient photocatalytic degradation of organics diluted in water and air using TiO<sub>2</sub> designed with zeolites and mesoporous silica materials. *J Mater Chem* 21:2407–2416
32. Chen NY (1976) Hydrophobic properties of zeolites. *J Phys Chem* 80:60–64
33. Stach H, Lohse U, Thamm H, Schirmer W (1986) Adsorption equilibria of hydrocarbons on highly dealuminated zeolites. *Zeolites* 6:74–90
34. Kuwahara Y, Aoyama J, Miyakubo K, Eguchi T, Kamegawa T, Mori K, Yamashita H (2012) TiO<sub>2</sub> photocatalyst for degradation of organic compounds in water and air supported on highly hydrophobic FAU zeolite: structural, sorptive, and photocatalytic studies. *J Catal* 285:223–234
35. Price PM, Clark JH, Macquarrie DJ (2000) Modified silicas for clean technology. *J Chem Soc Dalton Trans* 101–110
36. Descalzo AB, Martínez-Máñez R, Sancenón F, Hoffmann K, Rurack K (2006) The supramolecular chemistry of organic-inorganic hybrid materials. *Angew Chem Int Ed* 45:5924–5948
37. Kuwahara Y, Kamegawa T, Mori K, Yamashita H (2008) Fabrication of hydrophobic zeolites using triethoxyfluorosilane and their application as supports for TiO<sub>2</sub> photocatalysts. *Chem Commun* 39:4783–4785

38. Soler-Illia GJ, Sanchez C, Lebeau B, Patarin J (2002) Chemical strategies to design textured materials: from microporous and mesoporous oxides to nanonetworks and hierarchical structures. *Chem Rev* 102(11):4093–4138
39. Inumaru K, Kiyoto J, Yamanaka S (2000) Molecular selective adsorption of nonylphenol in aqueous solution by organo-functionalized mesoporous silica. *Chem Commun* 903–904
40. Kuwahara Y, Maki K, Matsumura Y, Kamegawa T, Mori K, Yamashita H (2009) Hydrophobic modification of a mesoporous silica surface using a fluorine-containing silylation agent and its application as an advantageous host material for the TiO<sub>2</sub> photocatalyst. *J Phys Chem C* 113:1552–1559
41. Qian XF, Kamegawa T, Mori K, Li HX, Yamashita H (2013) Calcium phosphate coatings incorporated in mesoporous TiO<sub>2</sub>/SBA-15 by a facile inner-pore sol-gel process toward enhanced adsorption-photocatalysis performances. *J Phys Chem C* 117:19544–19551
42. Kuwahara Y, Yamanishi T, Kamegawa T, Mori K, Yamashita H (2011) Enhancement in adsorption and catalytic activity of enzymes immobilized on phosphorus- and calcium-modified MCM-41. *J Phys Chem B* 115:10335–10345
43. Qian X, Fuku K, Kuwahara Y, Kamegawa T, Mori K, Yamashita H (2014) Design and functionalization of photocatalytic systems within mesoporous silica. *ChemSusChem* 7:1528–1536

# Chapter 15

## Photodegradation of Pollutants in Water over TiO<sub>2</sub> Supported on Molecular Sieves

Albert Wan and Soofin Cheng

### 15.1 Background

Photocatalysis is a promising method to effectively remove organic pollutants in water by utilizing semiconducting materials as photocatalysts and free solar energy [1, 2]. Through the process of photocatalytic degradation, organic pollutants can be decomposed or converted to harmless products such as CO<sub>2</sub>, H<sub>2</sub>O, and mineral acids [3–5]. Among different semiconductors, titanium dioxide (TiO<sub>2</sub>) is one of the most widely studied photocatalysts for water purification because of its nontoxicity, high adsorption ability, multifaceted electronic properties, low cost, and good thermal and photo-stability [6–9]. The band gap of TiO<sub>2</sub> is around 3.0–3.2 eV [10–12], which falls in the energy range of UV light. Thus through the absorption of photons with energy larger than the band gap of TiO<sub>2</sub>, electrons can be excited to its conduction band and holes are generated in the valence band. The excited charge carriers are highly reactive reducing and oxidizing agents, which can react with either water or oxygen to generate •OH radicals, and the latter are the key active species of photodegradation of organic pollutants in water [3, 13, 14]. However, the charge carriers may also be quenched by recombination [15, 16], by being trapped in metastable surface states [16, 17] or by reacting with pre-adsorbed species on the catalyst surface [4, 5, 16]. As a result, the catalytic activity of TiO<sub>2</sub> is limited. Therefore, a proper design of the catalyst to effectively utilize the generated charge carriers for photocatalytic reaction is highly desired. Recent studies have revealed that the photocatalytic activity of TiO<sub>2</sub> catalyst is markedly influenced by several factors, including the phase composition (rutile or anatase), crystallinity [18–20], numbers of surface hydroxyl group [21–23], surface area, and the size of TiO<sub>2</sub> particles [19, 24, 25].

---

A. Wan • S. Cheng (✉)

Department of Chemistry, National Taiwan University,  
No. 1, Roosevelt Road Section 4, Taipei 10617, Taiwan  
e-mail: [chem1031@ntu.edu.tw](mailto:chem1031@ntu.edu.tw)

Dispersion of  $\text{TiO}_2$  on supported materials has been reported to be an effective approach to increase the catalytic activity of  $\text{TiO}_2$  in photodegradation of pollutants. The surface area of  $\text{TiO}_2$  particles formed on supporting materials of high surface areas can be much larger than the unsupported one, and thus supported  $\text{TiO}_2$  can have higher adsorbates per unit area and higher photocatalytic reaction rate. Moreover, the adsorbates may also be adsorbed on the support and consequentially migrate to the active centers on  $\text{TiO}_2$  for further reaction. On the other hand, the recombination rate of electron–hole pairs for the supported  $\text{TiO}_2$  particles in micro or nano-scale has been reported to be much lower than the bulk  $\text{TiO}_2$  [26–28]. Another advantage of dispersing  $\text{TiO}_2$  on supporting materials is the possibility of recovering the catalysts in cost effective manners after the process of water purification. So far  $\text{TiO}_2$  has been successfully dispersed on glass [24, 29], stainless steel [30], alumina [25, 31], silica [32, 33], activated carbons [34–38], carbon nanotubes [39, 40], clays [21, 41], etc. Carbon and silica-based molecular sieves have also been utilized as supports for  $\text{TiO}_2$  catalysts. Both types of molecular sieves have high adsorption capabilities due to their extra large surface areas. Comparing to carbon molecular sieves, silica molecular sieves have higher ordered pores and much better chemical stability in general. Moreover, the synthesis of ordered mesoporous carbon materials is more complicated and often requires structural replication utilizing mesoporous silica as templates. In this chapter, the preparation methods of  $\text{TiO}_2$  supporting on different types of silica-based molecular sieves and the resulting structures are demonstrated. The catalytic performances of these catalysts for photodegradation of organic pollutants in water are also discussed.

## 15.2 Methods of Dispersing $\text{TiO}_2$ on Silica Molecular Sieves

Preparation of  $\text{TiO}_2$  dispersed on different types of silica molecular sieves has been carried out by using various methods. Impregnation is the most common method of preparing supported  $\text{TiO}_2$  catalysts [42–50]. In a typical procedure, Ti-source (e.g.,  $\text{Ti}(\text{OEt})_4$ ) is added to the support powders of porous  $\text{SiO}_2$  while stirring and is subsequently hydrolyzed on the silica surface. Calcination treatment is normally conducted in the end to remove the solvent and residues of the precursors. Typically the crystallinity of  $\text{TiO}_2$  particles can be retained on the supporting materials through this process.

Another widely used preparation method is coprecipitation of  $\text{SiO}_2$  and  $\text{TiO}_2$  via a sol–gel process that allows the precursors of both oxide species to be hydrolyzed simultaneously in the presence of surfactants as structural directing agents for the formation of porous  $\text{SiO}_2$  [27, 30, 51–55]. Through this process, Ti was reported to be mainly incorporated into the silica framework when the Ti content is low (Si/Ti molar ratio >20). The mesoporous silica materials with low Ti contents prepared by using coprecipitation typically generated  $\text{TiO}_2$  particles with poor crystallinity and their photocatalytic activities usually were not significantly higher than unsupported  $\text{TiO}_2$ .

Deposition of TiO<sub>2</sub> nanoparticles onto the support of mesoporous SiO<sub>2</sub> through electrostatic interaction between the particles and the support has been carried out [49]. By mixing the synthesized TiO<sub>2</sub> nanoparticles and mesoporous SiO<sub>2</sub> in an aqueous solution and controlling its pH, positively charged TiO<sub>2</sub> and negatively charged SiO<sub>2</sub> can interact with each other electrostatically. Another reported method also mixes TiO<sub>2</sub> nanoparticles and molecular sieves in a solvent. However, the solvent was removed by evaporation and the samples were cleaned through calcination treatment [38, 56, 57].

Encapsulation of TiO<sub>2</sub> nanoparticles in mesoporous SiO<sub>2</sub> through a one-pot synthesis has been developed and reported [58]. In this method, TiO<sub>2</sub> nanoparticles were first prepared by hydrolyzing the titania precursor Ti-source (e.g., titanium tetraisopropoxide, TTIP) in the reverse micelle microemulsion. The mixture of the nanoparticles and the microemulsion were then added in the pore-directing micelle consisted of silica precursor and surfactant, followed by hydrothermal treatment. By using this method, the TiO<sub>2</sub> nanoparticles were ensured to be incorporated inside the pores of mesoporous SiO<sub>2</sub> and retain their crystallinities.

### 15.3 Types of Pollutants and Their Analysis Methods

The molecular sieves supported TiO<sub>2</sub> have been applied to the photodegradation of various organic pollutants in water. Methylene blue (MB), methylene orange (MO) and their derivatives are good examples of recalcitrant azo dyes and alkaline organic pollutants that are nonbiodegradable, and have been commonly used as model compounds for photocatalytic degradation [38, 43, 45, 48, 49, 58, 65]. MB and MO are widely used for textile dyeing, paper printing and other industrial applications, and are difficult to be removed through conventional process of waste water treatment. These two azo dyes are durable under UV exposure and are more easily investigated because of their relatively slow photodegradation processes.

Several compounds which have been widely used as pesticides may contaminate environment and threaten the health of human being. 2,4-Dichlorophenoxyacetic acid (2,4-D) is one of the most commonly used pesticides and is known as a growth inhibitor of plants and also an endocrine disrupter [59]. 2,4-D can be easily translocated within the plants after being absorbed because of its polar nature, and can accumulate and consequently inhibit the growth of the plants [60]. Because of its low tendency of being absorbed by soil, the residues of 2,4-D have been reported to exist in ground water and have the potential of contaminate drinking water [61]. Propoxur (2-(1-methylethoxy)phenylmethyl carbamate) is another commonly used pesticide for controlling household agricultural pests and is known to be an acetylcholinesterase inhibitor that causes nerve related symptoms of weakness and paralysis [62]. The residues of propoxur are increasingly detected within soil and wastewater because of its massive usage [63, 64]. The photodegradation of aromatic pollutants such as benzene, monochlorobenzene (MCB), 1,2-dichlorobenzene (DCB), and phenol have also been studied because of their existence in industrial waste and their volatility allowing them to access to the environment easily [50, 58, 65].

The photodegradation of the pollutants in water can be quantified by measuring the concentrations of the pollutants before and after the photocatalytic reaction. Typically, the catalyst was suspended and mixed with the pollutant in water under stirring for a period of time in dark prior to the photocatalytic reaction, in order to measure the amount of the pollutant adsorbed by the catalyst. The solution was then irradiated by UV light for another period of time and was analyzed to determine the amount of the pollutant that was decomposed by the photodegradation [38, 43, 45, 48, 49, 58, 65]. For dye pollutants, their concentrations are usually determined by spectrophotometric method. However, the types of products after the photodegradation process cannot be determined through this method. Another way to ensure complete mineralization of the organic pollutants is to direct the outlet gases of the reactor through a bubbling trap of saturated  $\text{Ba}(\text{OH})_2$  solution and determine the yield of  $\text{CO}_2$  in the photocatalytic reaction based on the weight of  $\text{BaCO}_3$  precipitate [50, 58]. The conversion of the pollutant during the reaction can be back-calculated from the  $\text{CO}_2$  yield. On the other hand, the products remained in the aqueous solution can be analyzed by using gas chromatography (GC) [50, 58].

## 15.4 Performance of $\text{TiO}_2$ Deposited on Molecular Sieves in Photodegradation of Organic Pollutants in Water

Molecular sieves have been widely used as the supporting materials because of their well-defined pore structure/size, good (hydro)thermal stability, and very large surface area [66–69]. Zeolites and mesoporous silica materials are most commonly used supports. Nevertheless, clays and silica with hierarchical macro and mesopores are also studied. The catalytic performances of these catalysts in photodegradation of organic pollutants in water are discussed.

### 15.4.1 Zeolites

Zeolites are [microporous aluminosilicate](#) containing ordered pore structures and crystalline framework. They are commonly used as commercial [adsorbents](#) and catalysts [66, 70]. Zeolites are used as supporting materials of photocatalysts in the wastewater treatment because of its unique uniform pore structures, photochemical and thermal stability, large surface area, and transparency to UV-visible light irradiation. Zeolites are capable of adsorbing organic compounds effectively through van der Waals force with silica lattice, and via electrostatic interactions and  $\pi$ – $\pi$  interactions with extra-framework cations [71]. The adsorption ability of zeolites may benefit the supported catalysts by bringing more organic compounds to the active sites of  $\text{TiO}_2$ . In addition, zeolites may stabilize the organic intermediates generated on  $\text{TiO}_2$  in the cavities and therefore may minimize electron–hole recombination and favor the photocatalytic reaction [72].

Deposition of TiO<sub>2</sub> nanoparticles on HY, H $\beta$  zeolites and ZSM-5 (Si/Al ratios of 3, 5, and 53, respectively) and the photocatalytic performance of these catalysts for photocatalytic degradation of 2,4-dichlorophenoxyacetic acid (2,4-D) in aqueous solution have been reported by Murugesan et al. [57]. The catalysts of TiO<sub>2</sub> dispersed on the zeolitic supports were prepared by mixing TiO<sub>2</sub> and the zeolites in acetone, followed by filtration and calcination. The results of BET measurements reveal that increasing the loading of TiO<sub>2</sub> on HY, H $\beta$  zeolites and HZSM-5 decreases the surface area of the catalysts possibly resulted from the blocking of zeolite pores by TiO<sub>2</sub> particles. The order of abilities of the catalysts to adsorb 2,4-D were found to be HY > H $\beta$  > HZSM-5. The adsorption abilities of the catalysts is in accordance to the number of protonic sites, where 2,4-D molecules are expected to have more affinity due to their polarity in nature. Moreover, the relative photonic efficiencies ( $\zeta_r$ ) of these supported catalysts were measured using phenol as a reference reactant (see Eq. (15.1)).

$$\zeta_r = \frac{k_s}{k} \quad (15.1)$$

where  $k_s$  is the initial rate of phenol degradation over supported TiO<sub>2</sub> and  $k$  is the initial rate of phenol degradation over the standard TiO<sub>2</sub> photocatalyst (Degussa P-25) which is commercially available. The measured values of  $\zeta_r$  for catalysts of TiO<sub>2</sub> dispersed on HY, H $\beta$ , and HZSM-5 were all greater than 1, indicating the photocatalytic efficiencies of TiO<sub>2</sub> can be improved by the zeolitic supports. Mineralization studies reveal that the photocatalytic degradation of 2,4-D over catalysts of 1 wt% TiO<sub>2</sub> dispersed on HY, H $\beta$ , and HZSM-5 were all more efficient than bare TiO<sub>2</sub>. The same group also investigated the photodegradation of propoxur (2-(1-methylethoxy)phenylmethyl carbamate) over TiO<sub>2</sub> supported on H $\beta$  zeolite [73]. The TiO<sub>2</sub>/H $\beta$  catalyst was found to be more efficient than bare TiO<sub>2</sub> in photodegradation of propoxur, attributing to the higher adsorption capacity of propoxur (20 mmol g<sup>-1</sup>) in TiO<sub>2</sub>/H $\beta$  compared to that of bare TiO<sub>2</sub> (5.5 mmol g<sup>-1</sup>).

Guo et al. [45] reported the dispersion of TiO<sub>2</sub> on the external surface of Na<sup>+</sup>-exchanged ZSM-5 (NaZSM-5) using a sol-gel process, in which Ti(OBu)<sub>4</sub> was hydrolyzed in an absolute ethanol-diethanolamine solution containing NaZSM-5 powders. The photocatalytic performance of the TiO<sub>2</sub>/NaZSM-5 catalyst was tested via the photodegradation of methylene orange (MO) dye. The photocatalytic activities of TiO<sub>2</sub>/NaZSM-5 catalysts with different contents of Na<sup>+</sup> were found to be higher than that of bare TiO<sub>2</sub> (Fig. 15.1). The high activities of TiO<sub>2</sub>/NaZSM-5 catalysts were attributed to the reversible adsorption of MO molecules at the medium-strong acidic sites of zeolitic supports. In other words, the strong acidic sites on ZSM-5 would contribute to strongly adsorbed dye molecules, which were not transferable to the photocatalytically active TiO<sub>2</sub> centers. Increasing the Na<sup>+</sup> content in the zeolites was found to decrease the strong acid sites of the support and reduced the strongly adsorbed MO. Oppositely, the amount of reversibly adsorbed MO on the medium-strong acid sites was increased and the photocatalytic activities of the catalysts was enhanced. However, when the content of Na<sup>+</sup> was too high (>1.3 wt%), both strong and medium-strong acid sites of the support are suppressed and

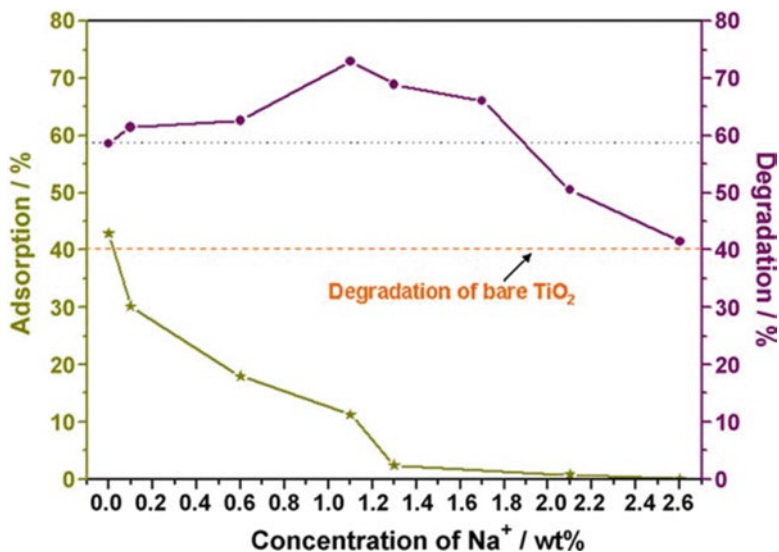


**Fig. 15.1** Effect of Na<sup>+</sup> contents on the adsorption and degradation of MO over TiO<sub>2</sub>/NaHZSM-5 nano-composites. Adapted from Ref. [45]

the adsorption of MO was negligible. When the Na<sup>+</sup> loading were further increased to 2.6 %, the photocatalytic activity of NaZSM-5 supported TiO<sub>2</sub> catalyst was the same as that of bare TiO<sub>2</sub>.

The preparation of thin films with commercial TiO<sub>2</sub> nanoparticles (Degussa P25) and HZSM-5 using acrylic emulsion as binders has been reported by Boule et al. [65] The photocatalytic degradation of phenol in aqueous solution has been investigated. The thin films containing HZSM-5 was found to be more active than the films without HZSM-5. They concluded that larger amount of phenol can be adsorbed by HZSM-5 on the thin films and can further react with the reactive species of TiO<sub>2</sub> nanoparticles. The presence of zeolites also reduces the reactive charge carriers that react with the polymer support and thus increases the stability of the thin films under long exposure period of UV light.

The photocatalysis of TiO<sub>2</sub> nanoparticles deposited on natural zeolite (clinoptilolite) has been studied by Jiang et al. [56]. Natural zeolites have the advantages of cheap and easy availability, comparing to the synthetic zeolites. The TiO<sub>2</sub> particles dispersed on the zeolite were prepared by hydrolysis of the precursor of TiO<sub>2</sub>, Ti(OC<sub>4</sub>H<sub>9</sub>)<sub>4</sub>, in ethanol containing the natural zeolite with acidic aqueous solution. The size of TiO<sub>2</sub> particles (~80 nm) were much larger than the pore size of the zeolites (0.4–0.7 nm) and thus were dispersed on the external surfaces of the zeolites without incorporating into their pores. The results of XRD measurements for the sample showed only the diffraction peaks of zeolites and no diffraction peaks of rutile or anatase crystalline phase of TiO<sub>2</sub>, indicating that the TiO<sub>2</sub> loading was small and the TiO<sub>2</sub> particles were smaller than the detection limit of XRD (~2 nm). The formation of Ti-O-Si and Ti-O-Al bonds between TiO<sub>2</sub> and the zeolite was verified

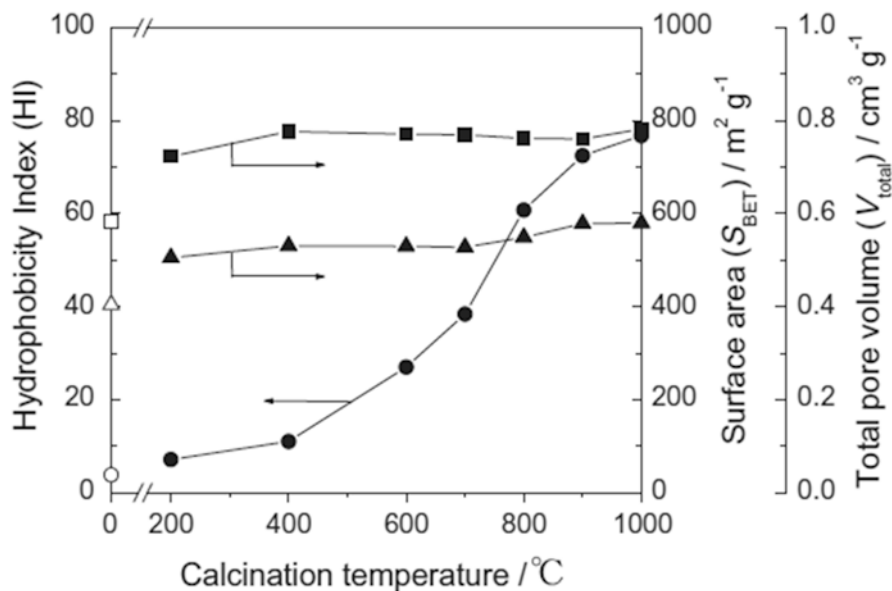


**Fig. 15.2** The HI values (filled circle), surface area (filled square), and total pore volume (filled triangle) of TiO<sub>2</sub> dispersed on zeolites as a function of calcination temperature. Open symbols correspond to HY zeolite precursor with HI=5.8. Adapted from Ref. [46]

by FT-IR analysis. The TiO<sub>2</sub>/zeolite was found to exhibit higher photocatalytic activity than pure TiO<sub>2</sub> in the degradation of MB. The higher activity of TiO<sub>2</sub>/zeolite was attributed to the good adsorption capability of the zeolitic support.

Highly hydrophobic FAU zeolites were prepared and used as the support materials of TiO<sub>2</sub> photocatalysts by Yamashita et al. [46] The degree of hydrophobicity of the zeolite was estimated by the adsorption measurements using water and toluene and was defined as the weight ratio of the adsorbed toluene and water (hydrophobicity index  $HI = X_{\text{toluene}}/X_{\text{water}}$ ). Highly hydrophobic zeolites with  $HI > 60$  were obtained by leaching the Al in zeolites with mineral acids ( $>2.0$  N) to reduce the Al content to  $<0.21$  mmol g<sup>-1</sup>. The results of TG, FT-IR, and <sup>29</sup>Si MAS NMR analyses revealed that the hydrophobicity of the dealuminated zeolites was further enhanced by calcination due to the healing of silanol defect sites through dehydroxylation condensation and the formation of refined silica surface with fewer adsorption sites. The degree of hydrophobicity of the zeolite was found to be correlated to the calcination temperature (Fig. 15.2). The photocatalytic activity of TiO<sub>2</sub> dispersed on zeolitic supports with different degrees of hydrophobicity were studied by the degradation of 2-propanol in water and acetaldehyde in air under UV irradiation. The degradation rate was found to follow the pseudo-first-order kinetics and the first-order rate constant ( $k$ ) was used as an indicator of the activity of the catalyst:

$$-\ln\left(\frac{C}{C_0}\right) = kt \quad (15.2)$$

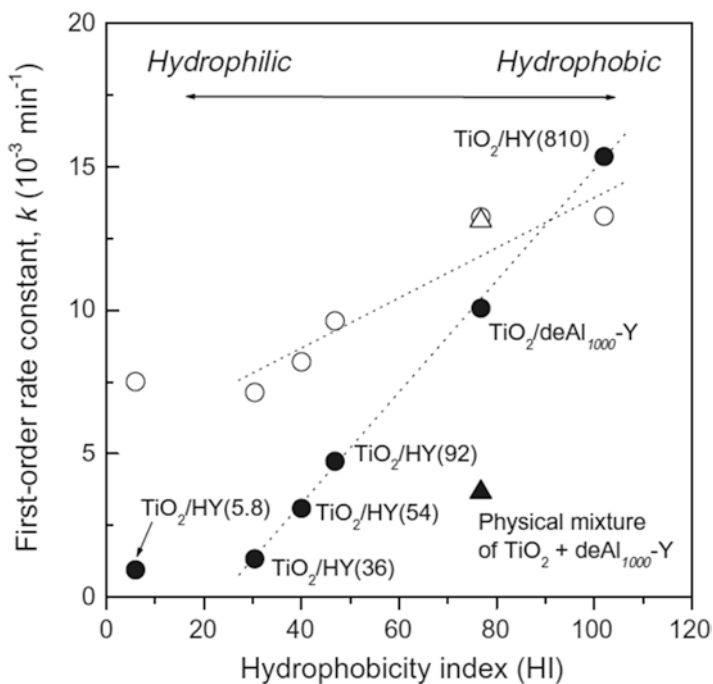


**Fig. 15.3** The correlation between the rate constant ( $k$ ) in photocatalytic degradation and HI values of zeolite supports. *Filled circles*: photodegradation of 2-propanol in water; *open circles*: photodegradation of acetaldehyde in air. Adapted from Ref. [46]

where  $C_0$  and  $C$  are the initial concentration and the concentration of MB at time  $t$ , respectively, and  $k$  is the rate constant. The photocatalytic activities for degradation of both 2-propanol in water and acetaldehyde in air were improved significantly when the hydrophobicity of zeolite was enhanced (Fig. 15.3). For example, when HI of the zeolitic supports was enhanced from 6.0 to 102, the  $k$  value of the supported TiO<sub>2</sub> catalysts increased from  $0.95 \times 10^{-3}$  to  $15.4 \times 10^{-3} \text{ min}^{-1}$  ( $k = 3.69 \text{ min}^{-1}$  for unsupported TiO<sub>2</sub> powder) in the photodegradation of 2-propanol. The improvement of the photoactivity was attributed to high diffusivity of organic molecules within the microchannels of the hydrophobic zeolite and thus high accessibility of the molecules to the TiO<sub>2</sub> active sites.

### 15.4.2 Mesoporous SiO<sub>2</sub>

Supporting TiO<sub>2</sub> on mesoporous SiO<sub>2</sub> materials for photocatalytic reaction has attracted great attention due to their high surface area ( $\sim 600$ – $1000 \text{ m}^2 \text{ g}^{-1}$ ), controllable and large pore size (2–30 nm) and pore volume ( $0.6$ – $2.5 \text{ cm}^3 \text{ g}^{-1}$ ), narrow distribution of the pore dimension, and good stability of these materials [40–42].

Moreover, because of the relatively large pore size of mesoporous SiO<sub>2</sub>, comparing to zeolites, TiO<sub>2</sub> particles may be able to incorporate within the pores and are expected to less aggregate during the photocatalytic reactions. Same as zeolites, the large surface area of the mesoporous SiO<sub>2</sub> materials may effectively adsorb organic pollutants in water and enhanced the photocatalytic efficiency of the TiO<sub>2</sub> catalyst. Two mesoporous silica materials were popularly used as the TiO<sub>2</sub> supports, namely, SBA-15 and MCM-41. Both have the 2-D hexagonal pore structures, while SBA-15 has larger pore diameters and thicker walls than MCM-41 (>6 nm vs. 2 nm in pore diameter and >3 nm vs. 1 nm in wall thickness).

### 15.4.3 SBA-15

Titanium-containing SBA-15 has been prepared by using a direct synthesis method in acidic solution under hydrothermal conditions by Zhao et al. [44]. The characterization results using XRD, UV-Vis spectroscopy and NMR revealed that Ti ions were incorporated within the silica framework of SBA-15 and anatase TiO<sub>2</sub> clusters were formed on the external surface of SBA-15 particles when Ti loading was higher than a Ti/Si molar ratio of 0.023. The photocatalytic activities of the catalysts were tested by measuring the decomposition of Orange II in aqueous solution. Both Ti ions and anatase TiO<sub>2</sub> clusters were found to be active for the photocatalytic reaction. The photocatalytic activity was improved when the external TiO<sub>2</sub> particles were increased by increasing the Ti/Si ratio of the catalyst (from 0.023 to 0.091). However, the photocatalytic activity decreased when the Ti/Si ratio was too high (more than 0.091) because of the aggregation of TiO<sub>2</sub> particles.

### 15.4.4 MCM-41

The TiO<sub>2</sub> nanoparticles were deposited on MCM-41 and the photocatalytic activity was compared with those deposited on NaY and Na-mordenite zeolites by Cheng et al. [50] using impregnation method. The characterization results of XRD and FT-IR measurements revealed that TiO<sub>2</sub> on these porous supports were crystallized as anatase structures, and the particle size increased with TiO<sub>2</sub> loading. The total surface areas of the supported catalysts determined by BET measurements were found to decrease with TiO<sub>2</sub> loading possibly because of the pore blocking by TiO<sub>2</sub> particles (Table 15.1). Furthermore, the absorption peak of TiO<sub>2</sub> in the UV-Vis spectra blue-shifted as the size of TiO<sub>2</sub> decreased, indicating the increase of band gap energy. The change of band gap energy with the size of TiO<sub>2</sub> is consistent with the "particle size quantization effect" [74, 75]. The photocatalytic activities of these supported TiO<sub>2</sub> and commercially available unsupported TiO<sub>2</sub> catalysts were studied by measuring the yield of CO<sub>2</sub> generated from the degradation of different aromatic pollutants, including benzene, monochlorobenzene (MCB), 1,2-dichlorobenzene

**Table 15.1** BET surface area, particle size and bandgap values of commercial and supported TiO<sub>2</sub>. Adapted from Ref. [50]

Catalyst (TiO <sub>2</sub> loading)	Surface area (m <sup>2</sup> /g)	TiO <sub>2</sub> particle diameter (nm) <sup>a</sup>	Band gap (eV)
NaY support			
0	851	–	–
5 %	716	–	3.25
10 %	658	–	3.23
20 %	596	20.7	3.19
30 %	532	21.2	3.17
45 %	400	22.0	3.15
60 %	276	27.3	3.13
Na-mordenite support			
0 %	383	–	–
5 %	364	–	3.26
10 %	348	–	3.23
20 %	324	–	3.20
30 %	253	30.9	3.19
45 %	231	39.8	3.15
60 %	148	52.1	3.11
MCM-41 support			
0 %	1009	–	–
2 %	997	–	3.23
5 %	954	–	3.22
10 %	891	–	3.19
20 %	811	4.5	3.18
30 %	701	5.6	3.15
Commercial TiO <sub>2</sub>			
Anatase	34	62.7	3.09
Rutile	6	64.7	2.86
p-25	54	–	3.04

<sup>a</sup>Determined by Scherrer's equation with the (1 1 0) peaks on XRD patterns for anatase and rutile, respectively

(DCB), and phenol. Interestingly, the degradation efficiency was strongly influenced by the volatility and the hydrophilicity of the pollutants. Among the pollutants, phenol was found to have the highest degradation efficiency likely because of its nucleophilicity which facilitates the molecule to react with •OH radicals. For volatile molecules such as benzene and MCB, the pollutants partially dissipated into gas flow and the CO<sub>2</sub> yields were lower. The dissipation of volatile pollutants over supported TiO<sub>2</sub> was much lower than the unsupported TiO<sub>2</sub>, implying the good adsorption capabilities for volatile molecules of molecular sieves. The molecular sieves enhance the mineralization efficiency possibly by transferring the organic adsorbates on the support to the TiO<sub>2</sub> crystalline for further decomposition reaction. Moreover, the dissipation of pollutants was less significant over the catalysts with larger total surface area in general due to their higher adsorption capabilities.

**Table 15.2** The results of photodegradation of different aromatic pollutants in water. Adapted from Ref. [50]

Catalyst (TiO <sub>2</sub> loading)	Benzene		MCB		DCB	Phenol
	CO <sub>2</sub> yield (%)	Dis. (%) <sup>a</sup>	CO <sub>2</sub> yield (%)	Dis. (%)	CO <sub>2</sub> yield (%)	CO <sub>2</sub> yield (%)
<b>Na Y support</b>						
5 %	23.7	5.6	27.1	1.0	30.9	43.3
10 %	30.8	9.5	33.8	1.2	44.7	49.4
20 %	35.8	10.9	37.5	2.1	52.2	53.7
30 %	39.4	9.9	46.4	2.4	61.1	69.0
45 %	37.2	13.7	40.6	5.8	53.1	62.5
60 %	16.9	17.9	32.1	7.5	35.1	46.6
<b>Na-mordenite support</b>						
5 %	21.0	17.3	32.4	2.2	34.8	31.8
10 %	29.7	15.1	34.7	2.8	44.5	61.5
20 %	31.8	9.3	45.2	4.1	57.2	68.9
30 %	36.5	8.6	36.2	5.2	53.3	66.2
45 %	30.7	18.3	31.0	4.7	45.8	60.1
60 %	12.8	22.1	19.9	4.8	42.7	47.3
<b>MCM-41 support</b>						
2 %	25.0	7.6	37.8	0.6	43.6	57.4
5 %	31.1	5.8	44.3	0.7	51.4	65.9
10 %	33.1	5.9	51.4	0.7	69.1	78.3
20 %	29.1	8.3	38.9	1.4	60.5	63.5
30 %	27.0	16.0	36.8	4.2	41.2	39.9
<b>Commercial TiO<sub>2</sub></b>						
Anatase	25.0	30.2	38.0	5.9	41.9	78.0
Rutile	17.6	26.2	18.0	18.0	11.7	26.9
P-25	36.6	–	–	–	–	~100

<sup>a</sup>Dis. dissipation to the gas phase

For the molecular sieve-supported TiO<sub>2</sub> catalysts, the photocatalytic activities were found to be correlated to the hydrophilicities of the supports and the pollutants. For example, the surface hydrophilicity of MCM-41 due to the OH groups present on its surface facilitates the adsorption of polar or hydrophilic pollutants. As a result, the catalyst of TiO<sub>2</sub>/MCM-41 was found to have the highest photocatalytic activity for the degradation of MCB, DCB and phenol, but have lower activity than TiO<sub>2</sub>/NaY for the photodegradation of benzene, which is nonpolar and hydrophobic in nature, even though the surface area at the same TiO<sub>2</sub> loading was higher (Table 15.2). Furthermore, there is an optimal loading of TiO<sub>2</sub> dispersed on different types of supports in order to obtain the highest photodegradation activities of these catalysts. The requirement of the loading optimization of TiO<sub>2</sub> can be explained as a result of the particle size effect, in which fast electron–hole recombination was proposed to occur on the surface of small TiO<sub>2</sub> particles or in the bulk of large TiO<sub>2</sub> particles [22].

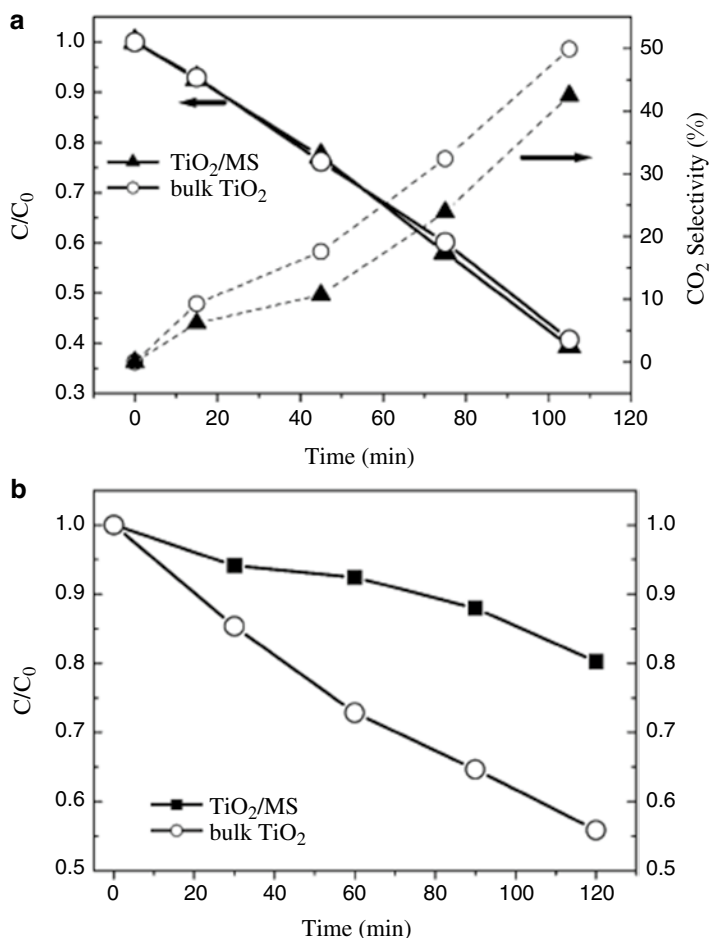


**Fig. 15.4** Photo-degradation rates of TiO<sub>2</sub>/MS in comparison to those of bulk anatase TiO<sub>2</sub> (based on the same 0.01 g TiO<sub>2</sub> content) for (a) phenol and (b) lipase with 300 nm UV illumination. Adapted from Ref. [58]

An one-pot synthesis method has been developed to encapsulate nano-sized TiO<sub>2</sub> particles in mesoporous SiO<sub>2</sub> (MS) materials [58]. In this method, the TiO<sub>2</sub> particles were incorporated in the pore-directing micelles during the cooperative assembly of silica precursor and surfactant. The results of XRD, TEM, and N<sub>2</sub> sorption measurements confirmed the formation of TiO<sub>2</sub> particles within the mesopores of the MS materials and the retention of their anatase crystallinity. The catalytic activity of TiO<sub>2</sub>/MS for photodegradation of phenol was similar to that of bulk anatase and was lower for the degradation of porcine pancreatic lipase than the bulk TiO<sub>2</sub> (Fig. 15.4), revealing that most TiO<sub>2</sub> particles of the TiO<sub>2</sub>/MS catalyst were located within the mesopores of MS and large molecules which could not enter the pores would not be photodegraded. The encapsulated nano-sized TiO<sub>2</sub> particles in mesoporous SiO<sub>2</sub> materials are applicable as photocatalytic active materials in textiles [58, 76, 77].

**Table 15.3** Adsorptive ability of the catalysts for MB. Adapted from Ref. [42]

Sample	Initial concentration (mg L <sup>-1</sup> )	Conc. after 5 min (mg L <sup>-1</sup> )	Conc. after 60 min (mg L <sup>-1</sup> )
TiO <sub>2</sub>	30	30	29
TPA-TiO <sub>2</sub>	30	5	4
MCM-41	30	22	12
TiO <sub>2</sub> /MCM-41	30	24	17
Ti-MCM-41	30	23	14
TT-MCM-41	30	3	0

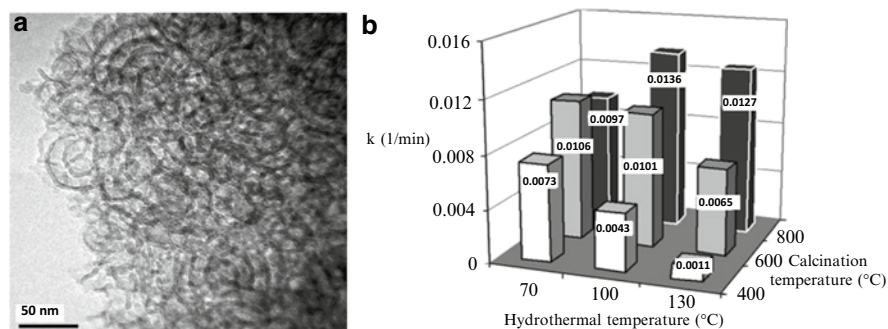
Catalysts of tungstophosphoric acid (TPA) modified TiO<sub>2</sub> nanoparticles incorporated in MCM-41 were prepared and their photocatalytic performance were studied by Zanjanchi et al. [42]. The TPA modified TiO<sub>2</sub> (TPA-TiO<sub>2</sub>) particles have been synthesized using a sol-gel method and have been loaded on MCM-41 using impregnation method. For comparison, Ti containing MCM-41 was also prepared by using an isomorphous substitution synthesis method, in which the Ti precursor (titanium tetraisopropoxide) was added during the synthesis of MCM-41. The results of XRD measurements revealed that after incorporating TPA into TiO<sub>2</sub> particles, the crystallinity of the particles remained the anatase-phase of TiO<sub>2</sub> without forming any TPA crystalline phase. The adsorption abilities and photocatalytic activities of the supported and bare TiO<sub>2</sub> were tested on MB (Table 15.3). The MB adsorption abilities of TPA-TiO<sub>2</sub> particles and TPA-TiO<sub>2</sub>/MCM-41 were found to be much higher than the catalysts without TPA. The adsorption of MB on unsupported TiO<sub>2</sub> was not significant because of its small surface area. The greater MB adsorption abilities of TPA containing catalysts were attributed to the change of zeta potential which is known to be lower with the presence of acidic species. As a result, the surfaces of the catalysts were negatively charged and could adsorb the cationic dye molecules (MB<sup>+</sup>) effectively. Moreover, the photocatalytic activities of the catalysts were studied through the photodegradation of MB in aqueous solution containing hydrogen peroxide. The results show that TPA-TiO<sub>2</sub>/MCM-41 is the most efficient catalyst for the removal of MB among different materials even though its surface area (450 m<sup>2</sup> g<sup>-1</sup>) was smaller than TiO<sub>2</sub>/MCM-41 (590 m<sup>2</sup> g<sup>-1</sup>) and Ti/MCM-41 (750 m<sup>2</sup> g<sup>-1</sup>) (Table 15.4). The strong adsorptive capability of TPA-TiO<sub>2</sub>/MCM-41 due to the presence of TPA was considered to be the main reason for its superior photocatalytic activity.

#### 15.4.5 Other Types of Molecular Sieves

Mazinani et al. deposited TiO<sub>2</sub> nanoparticles within the pores of wormhole-like mesoporous SiO<sub>2</sub>, which was prepared by adding hexane into the HCl solution containing the silica precursor (TEOS) and the P123 surfactant during the hydrothermal process (Fig. 15.5a) [48]. The deposition of TiO<sub>2</sub> nanoparticles was conducted by

**Table 15.4** Adsorption and photocatalytic ability of prepared catalysts, bare TiO<sub>2</sub>, and MCM-41 for the removal of MB. Adapted from Ref. [42]

Catalyst	Conversion (%) (5 min)	Conversion (%) (15 min)
TiO <sub>2</sub>	0.7	3.0
MCM-41	9.0	44
TiO <sub>2</sub> -/MCM-41	20	43
Ti-MCM-41	24	47
TPA-TiO <sub>2</sub>	83	93
TT-MCM-41	90	100

**Fig. 15.5** (a) TEM image of wormhole-like mesoporous SiO<sub>2</sub>. (b) Effect of hydrothermal temperature and calcination temperature on photocatalytic rate constant. Adapted from Ref. [48]

mixing the particles with the mesoporous materials in aqueous solution, in which the pH was controlled (to be 3) to generate electrostatic interaction between positively charged TiO<sub>2</sub> particles and negatively charged SiO<sub>2</sub> materials. The BET and BJH measurements revealed the reduction of surface area and pore size of the mesoporous materials after the loading of TiO<sub>2</sub> particles. The photocatalytic activities of the TiO<sub>2</sub> nanoparticles incorporated in the wormhole-like mesoporous SiO<sub>2</sub> were investigated by measuring the degradation of MB in aqueous solution under UV irradiation. The rate of photodegradation of MB followed pseudo-first-order kinetics (Eq. (15.2)). The surface area of the catalyst and the crystallinity of TiO<sub>2</sub> particles within the mesopores of the support were found to be influenced by the temperature of the hydrothermal process and the post-calcination, respectively. The surface area of the catalyst was found to be lower when the temperature of the hydrothermal process was higher (from 70 to 130 °C). On the other hand, the XRD results reveal that TiO<sub>2</sub> particles became more crystalline (all in anatase phase) when the calcination temperature was higher (from 400 to 600 °C). In photodegradation of MB, the photocatalytic efficiency (expressed in rate constant  $k$ ) was found to be proportional to the surface area and crystallinity of TiO<sub>2</sub> particles (Fig. 15.5b). However, when the calcination temperature was higher than >600 °C, the surface area and the photocatalytic activity of the catalysts decreased because of the collapse of the pores and the growth of TiO<sub>2</sub> particles at high temperature.

The TiO<sub>2</sub> nanoparticles were loaded on the silica-clay (SC) composite prepared with mineral montmorillonite (MMT) and TEOS under hydrothermal conditions [41]. MMT is a widely used clay material composed of aluminosilicate layers with fine crystalline structures. The thick pore walls and fine crystalline of MMT layers were expected to benefit the thermal stability of the catalyst. Two different types of surfactants, cetyltrimethyl ammonium bromide (CTAB) and polyethylene glycol (PEG) were utilized for the synthesis of the SC in order to generate micro-mesopores (<4 nm) and relatively large mesopores (4–25 nm), respectively. The XRD results showed no rutile or anatase peaks of crystalline TiO<sub>2</sub> after dispersing TiO<sub>2</sub> particles on SC, possibly because of the small loading of TiO<sub>2</sub>. The photocatalytic activity of TiO<sub>2</sub>/SC was studied by the degradation of MO in aqueous solution under UV irradiation. The rate of photocatalytic degradation of MO over TiO<sub>2</sub>/SC was obtained by applying pseudo-first-order kinetics (Eq. (15.2)), and was higher than the degradation of MO using unsupported TiO<sub>2</sub>. The efficiency of photodegradation of TiO<sub>2</sub>/SC under natural solar irradiation was also tested. Up to 94 % of MO was removed after 8 h of solar irradiation.

Supporting materials of porous SiO<sub>2</sub> with hierarchical macro and mesopores (MacroMeso-SiO<sub>2</sub>) were prepared by Yamashita et al. [47] by using a solvent evaporation method, in which poly(methyl methacrylate) (PMMA) spheres were used as templates for generating macropores during the synthesis of mesoporous SiO<sub>2</sub>. For comparison, mesoporous silica (Meso-SiO<sub>2</sub>) and macroporous silica (Macro-SiO<sub>2</sub>) were also synthesized utilizing PMMA as templates and loaded with TiO<sub>2</sub> by an impregnation method. The results of BET measurements show that the surface area of TiO<sub>2</sub>/MacroMeso-SiO<sub>2</sub> (865 m<sup>2</sup>g<sup>-1</sup>) was larger than TiO<sub>2</sub>/Meso-SiO<sub>2</sub> (725 m<sup>2</sup>g<sup>-1</sup>) and TiO<sub>2</sub>/Macro-SiO<sub>2</sub> (85 m<sup>2</sup>g<sup>-1</sup>). The relatively large surface area of TiO<sub>2</sub>/MacroMeso-SiO<sub>2</sub> was attributed to the uniform mesoporous structure present in the support. The results of XRD, XANES, EXAFS, and SEM characterization verified the well-ordered two dimensional hexagonal mesoporous structures of TiO<sub>2</sub>/MacroMeso-SiO<sub>2</sub> and TiO<sub>2</sub>/Meso-SiO<sub>2</sub>, and reveal that TiO<sub>2</sub> particles formed on Meso-SiO<sub>2</sub> had slightly higher anatase crystallinity than the particles on MacroMeso-SiO<sub>2</sub> and Macro-SiO<sub>2</sub>. Moreover, all supported TiO<sub>2</sub> particles showed blue shifts in the absorption spectra compared to unsupported anatase TiO<sub>2</sub> powders due to the quantum-size effect [57, 72]. The photocatalytic performance of the supported TiO<sub>2</sub> were investigated in degradation of phenol and bisphenol in water. The adsorption capabilities of TiO<sub>2</sub>/MacroMeso-SiO<sub>2</sub> for both phenol and bisphenol were found to be better compared to TiO<sub>2</sub>/Meso-SiO<sub>2</sub> and TiO<sub>2</sub>/Macro-SiO<sub>2</sub>. Under UV irradiation, the apparent rate constants of photodegradation of phenol and bisphenol over the supported TiO<sub>2</sub> catalysts were obtained by applying pseudo-first-order kinetics (Eq. (15.2)). The apparent rate constants followed the order of TiO<sub>2</sub>/Meso-SiO<sub>2</sub> (0.51 h<sup>-1</sup>) > TiO<sub>2</sub>/Macro-SiO<sub>2</sub> (0.45 h<sup>-1</sup>) > TiO<sub>2</sub>/MacroMeso-SiO<sub>2</sub> (0.34 h<sup>-1</sup>) for the photodegradation of phenol, and TiO<sub>2</sub>/MacroMeso-SiO<sub>2</sub> (0.35 h<sup>-1</sup>) > TiO<sub>2</sub>/Macro-SiO<sub>2</sub> (0.24 h<sup>-1</sup>) > TiO<sub>2</sub>/Meso-SiO<sub>2</sub> (0.19 h<sup>-1</sup>) for the photodegradation of bisphenol. The results indicated that in the case of phenol, the diffusion limitation influenced by the structures of the supports was small and the photocatalytic activities were mainly affected by the degree of TiO<sub>2</sub> crystallinity. The reduction

of recombination probability of  $\text{TiO}_2$  with good crystallinity has been reported to enhance the photocatalytic reaction [78, 79]. On the other hand, the diffusion limitation of bisphenol, which is relatively large compared to the size of mesopores, plays a vital role in the photocatalytic reaction. The hierarchical macro and mesoporous structures of the support of  $\text{TiO}_2/\text{MacroMeso-SiO}_2$  formed many mesoporous apertures which effectively improved the accessibility of bisphenol to  $\text{TiO}_2$  and consequently enhanced its photocatalytic performance. Furthermore,  $\text{TiO}_2/\text{MacroMeso-SiO}_2$  also exhibited the highest adsorption capability and decolorization activity for MB among the catalysts.

## 15.5 Conclusions

The photocatalytic activity of supported  $\text{TiO}_2$  can be significantly enhanced by the molecular sieves as the supporting materials including zeolites, macro and mesoporous  $\text{SiO}_2$ , and clays, as summarized in Table 15.5. The enhancement of the activity is mainly attributed to the larger surface areas of the catalysts (more active sites of  $\text{TiO}_2$ ) and the higher adsorption capabilities to organic molecules of the supported  $\text{TiO}_2$  in most of the cases. The adsorption ability of the catalysts can be influenced by the affinity between the supporting materials or  $\text{TiO}_2$  to the organic molecules and can be controlled by changing the chemical composition of the catalysts. For example, enhancing the acidity of  $\text{TiO}_2$  nanoparticles by forming the composite of  $\text{TiO}_2$  with acidic species, and increasing the acidic sites and the hydrophobicity of the supporting materials have been demonstrated to improve the photocatalytic performance of the catalyst promisingly. Moreover, optimization of  $\text{TiO}_2$  loading, which in turn affecting the size of  $\text{TiO}_2$  particles, was found to be crucial to maximize the photocatalytic activity of the catalyst.

On the other hand, there are few drawbacks of utilizing catalysts of  $\text{TiO}_2$  loaded on molecular sieves that can potentially limit their applications in industrial water purification. Deposition of  $\text{TiO}_2$  nanoparticles on zeolitic supports typically results in the particles dispersed on the external surface of the zeolites since the pore size of zeolites is much smaller than the particles. Aggregation of the particles may occur during long UV-exposure due to the lack of supporting frameworks surrounding the particles. The  $\text{TiO}_2$  nanoparticles incorporated in mesoporous  $\text{SiO}_2$  could be more stable and show great enhancement of photocatalytic activity to the degradation of small molecules, but the activity for large molecules can suffer from diffusion problem. Another challenge is that  $\text{TiO}_2$  only absorbed light energy within UV region to generate reactive charge-hole carriers due to its large band gap. Dispersion of  $\text{TiO}_2$  particles on molecular sieves typically blue-shifts its absorption because of the particle-size quantization effect and makes the particles less effective to absorb and convert solar energy to charge carriers for photodegradation process. Nevertheless, the system of  $\text{TiO}_2$  supporting on molecular sieves has been proven to be a good platform for studying the correlation of catalytic performance to the chemical composition, crystallinity, and the size effect of the catalyst for photodegradation of pollutants in water.

**Table 15.5** Summary of the photocatalytic activities of TiO<sub>2</sub> supporting on different types of molecular sieves

Supporting materials	TiO <sub>2</sub> loading	Surface area (m <sup>2</sup> g <sup>-1</sup> )	Method of loading	Crystalline phase	Pollutants (concentration)	Enhancement factor <sup>m</sup>	Ref
HY zeolites	1 wt% <sup>b</sup>	605	Dry from suspension	Anatase, rutile	2,4-D (200 mg L <sup>-1</sup> )	1.8	[72]
H $\beta$ zeolites	1 wt% <sup>b</sup>	545	Dry from suspension	NA	2,4-D (200 mg L <sup>-1</sup> )	1.6	[72]
HZSM-5	1 wt% <sup>b</sup>	341	Dry from suspension	NA	2,4-D (200 mg L <sup>-1</sup> )	1.3	[72]
H $\beta$ zeolites	7 wt% <sup>b</sup>	499	Dry from suspension	Anatase, rutile	Propoxur (300 mg L <sup>-1</sup> )	1.5	[57]
NaZSM-5	9 wt%	364 <sup>c</sup>	Sol-gel	Anatase	MO (20 mg L <sup>-1</sup> )	1.9	[73]
HZSM-5 <sup>d</sup>	25 wt%	NA	Spray technique	Anatase	Phenol (0.1 mM)	2.5	[65]
Clinoptilolite	5 wt%	NA	Impregnation	No	MO (4–40 mg L <sup>-1</sup> )	~1.4 <sup>e</sup>	[56]
FAU zeolites	10 wt%	705	Impregnation	Anatase	2-propanol (2.6 mmol L <sup>-1</sup> )	~4.2 <sup>f</sup>	[46]
NaY zeolites	30 wt% <sup>b</sup>	532	Impregnation	Anatase	Various compounds <sup>g</sup>	~1.6 <sup>h</sup>	[50]
Na-mordenite	20 wt% <sup>b</sup>	324	Impregnation	Anatase	Various compounds <sup>g</sup>	~1.5 <sup>h</sup>	[50]
SBA-15	6.9 wt%	828	Impregnation	Anatase	Orange II (50 ppm)	~7	[44]
MCM-41	NA	590	Impregnation	Anatase	MB (30 mg L <sup>-1</sup> )	~14	[42]
MCM-41	10 wt% <sup>b</sup>	891	Impregnation	Anatase	Various compounds <sup>g</sup>	~1.5 <sup>h</sup>	[50]
MCM-41 (Ti) <sup>y</sup>	NA	750	Isomorphous substitution	No	MB (30 mg L <sup>-1</sup> )	~16	[42]
MCM-41 (TPA) <sup>k</sup>	NA	450	Dry from suspension	Anatase	MB (30 mg L <sup>-1</sup> )	~33	[42]
MS SiO <sub>2</sub>	12 wt%	645	One-pot synthesis	Anatase	Various compounds <sup>l</sup>	~1.5 <sup>m</sup>	[58]

(continued)

Table 15.5 (continued)

Supporting materials	TiO <sub>2</sub> loading	Surface area (m <sup>2</sup> g <sup>-1</sup> )	Method of loading	Crystalline phase	Pollutants (concentration)	Enhancement factor <sup>m</sup>	Ref
WL-MS SiO <sub>2</sub> <sup>n</sup>	NA	408	electrostatic interaction	Anatase	MB (40 mg L <sup>-1</sup> )	~2.2	[48]
Silicon-clay <sup>o</sup>	4.66 wt%	420	Dry from suspension	No	MO (20 mg L <sup>-1</sup> )	~1.5	[41]
MacroMeso-SiO <sub>2</sub>	10 wt%	865	Impregnation	Anatase	Various compounds <sup>p</sup>	~2.9	[47]

<sup>a</sup>Compared with the photocatalytic activity of unsupported TiO<sub>2</sub>

<sup>b</sup>The optimal loading for the best photocatalytic performance for the catalysts

<sup>c</sup>Only the surface area of the support without TiO<sub>2</sub> was indicated in the paper

<sup>d</sup>TiO<sub>2</sub> particles and HZSM-5 were blended with acrylic emulsion to form thin films

<sup>e</sup>This value depends on the initial concentration of MO

<sup>f</sup>This value depends on the hydrophobicity of the zeolite

<sup>g</sup>The pollutants investigated in this study include 0.5 mM of benzene, MCB, DCB, or phenol in aqueous solution

<sup>h</sup>In case of the pollutant of benzene in aqueous solution

<sup>i</sup>The dye solution contained 0.05 mol L<sup>-1</sup> of H<sub>2</sub>O<sub>2</sub>

<sup>j</sup>Ti containing MCM-41

<sup>k</sup>TiO<sub>2</sub> particles were modified with TPA prior to the deposition on MCM-41

<sup>l</sup>The pollutants investigated in this study include 0.6 mM of phenol or 120 mM porcine pancreatic lipase in aqueous solution

<sup>m</sup>This is the value for the photodegradation of phenol. The value was ~1 for lipase

<sup>n</sup>Wormhole-like mesoporous SiO<sub>2</sub>

<sup>o</sup>The silicon-clay contained micro-mesoporous structure

<sup>p</sup>The pollutants investigated in this study include 0.1 mmol L<sup>-1</sup> of phenol or bisphenol in aqueous solution

## References

1. Pan JH, Dou HQ, Xiong ZG, Xu C, Ma JZ, Zhao XS (2010) Porous photocatalysts for advanced water purifications. *J Mater Chem* 20:4512–4528
2. Zhao DY, Jaroniec M, Hsiao BS (2010) Editorial for themed issue on “advanced materials in water treatments”. *J Mater Chem* 20:4476–4477
3. Hoffman A, Carraway ER, Hoffman M (1994) Photocatalytic production of H<sub>2</sub>O<sub>2</sub> and organic peroxides on quantum sized semiconductor colloids. *Environ Sci Technol* 28:776–785
4. Pelaez M, Nicholas TN, Suresh C et al (2012) A review on the visible light active titanium dioxide photocatalysts for environmental applications. *Appl Catal B Environ* 125:331–349
5. Emilio CA, Litter MI, Kunst M, Bouchard M, Colbeau-Justin C (2006) Phenol photodegradation on platinumized-TiO<sub>2</sub> photocatalysts related to charge-carrier dynamics. *Langmuir* 22:3606–3613
6. Hoffmann MR, Martin ST, Choi W, Bahnemann DW (1995) Environmental applications of semiconductor photocatalysis. *Chem Rev* 95:69–96
7. Wang Y, Huang Y, Ho W, Zhang L, Zou Z, Lee S (2009) Biomolecule-controlled hydrothermal synthesis of C-N-S-tridoped TiO<sub>2</sub> nanocrystalline photocatalysts for NO removal under simulated solar light irradiation. *J Hazard Mater* 169:77–87
8. Su C, Tseng C-M, Chen L-F, You B-H, Hsu B-C, Chen S-S (2006) Sol-hydrothermal preparation and photocatalysis of titanium dioxide. *Thin Solid Films* 498:259–265
9. Zhao J, Wu T, Wu K, Oikawa K, Hidaka H, Serpone N (1998) Photoassisted degradation of dye pollutants. 3. Degradation of the cationic dye rhodamine B in aqueous anionic surfactant/TiO<sub>2</sub> dispersions under visible light irradiation: evidence for the need of substrate adsorption on TiO<sub>2</sub> particles. *Environ Sci Technol* 32:2394–2400
10. Asahi R, Taga Y, Mannstadt W, Freeman AJ (2000) Electronic and optical properties of anatase TiO<sub>2</sub>. *Phys Rev B* 61:7459–7465
11. Amtout A, Leonelli R (1995) Optical properties of rutile near its fundamental band gap. *Phys Rev B* 51:6842–6851
12. Koelsch M, Cassaignon S, Thanh Minh CT, Guillemoles J-F, Jolivet J-P (2004) Electrochemical comparative study of titania (anatase, brookite and rutile) nanoparticles synthesized in aqueous medium. *Thin Solid Films* 451:86–92
13. Al-Ekabi H, Serpone N, Pelizzetti E, Minero C (1989) Kinetic studies in heterogeneous photocatalysis. 2. Titania-mediated degradation of 4-chlorophenol alone and in a three-component mixture of 4-chlorophenol, 2,4-dichlorophenol, and 2,4,5-trichlorophenol in air-equilibrated aqueous media. *Langmuir* 5:250–255
14. Turchi CS, Ollis DF (1989) Mixed reactant photocatalysis - intermediates and mutual rate inhibition. *J Catal* 119:483–496
15. Tachikawa T, Fujitsuka M, Majima T (2007) Mechanistic insight into the TiO<sub>2</sub> photocatalytic reactions: design of new photocatalysts. *J Phys Chem C* 111:5259–5275
16. Choi W, Termin A, Hoffmann MR (1994) The role of metal ion dopants in quantum-sized TiO<sub>2</sub>: correlation between photoreactivity and charge carrier recombination dynamics. *J Phys Chem B* 98:13669–13679
17. Gomathi Devi L, Kavitha R (2013) A review on non metal ion doped titania for the photocatalytic degradation of organic pollutants under UV/solar light: role of photogenerated charge carrier dynamics in enhancing the activity. *Appl Catal B Environ* 140:559–587
18. Nishimoto SI, Ohtani B, Kajiwarra H, Kagiya T (1985) Correlation of the crystal structure of titanium dioxide prepared from titanium tetra-2-propoxide with the photocatalytic activity for redox reactions in aqueous propan-2-ol and silver salt solutions. *J Chem Soc Faraday Trans 1* 81:61–68
19. Tanaka K, Hisanaga T, Rivera AP (1993) Photocatalytic purification and treatment of water and air. Elsevier, Amsterdam
20. Fox MA, Dulay MT (1993) Heterogeneous photocatalysis. *Chem Rev* 95:341–357
21. Tran TH, Nosaka AY, Nosaka Y (2006) Adsorption and photocatalytic decomposition of amino acids in TiO<sub>2</sub> photocatalytic systems. *J Phys Chem B* 110:25525–25531

22. Oosawa Y, Grätzel M (1988) Effect of surface hydroxyl density on photocatalytic oxygen generation in aqueous TiO<sub>2</sub> suspensions. *J Chem Soc Faraday Trans 1*(84):197–205
23. Wang J, Liu X, Li R et al (2012) TiO<sub>2</sub> nanoparticles with increased surface hydroxyl groups and their improved photocatalytic activity. *Catal Commun* 19:96–99
24. Yoneyama H, Yamanaka S, Haga S (1989) Photocatalytic activities of microcrystalline TiO<sub>2</sub> incorporated in sheet silicates of clay. *J Phys Chem* 83:4833–4837
25. Zhang Z, Wang CC, Zakaria R, Ying J (1998) Role of particle size in nanocrystalline TiO<sub>2</sub>-based. Photocatalysis. *J Phys Chem B* 102:10871–10878
26. Ooka C, Yoshida H, Horio M, Suzuki K, Hattori T (2003) Adsorptive and photocatalytic performance of TiO<sub>2</sub> pillared montmorillonite in degradation of endocrine disruptors having different hydrophobicity. *Appl Catal B Environ* 41:313–321
27. Wu C, Tzeng L, Kuo Y, Shu CH (2002) Enhancement of the photocatalytic activity of TiO<sub>2</sub> film via surface modification of the substrate. *Appl Catal A Gen* 226:199–211
28. Sakthivel S, Shankar MV, Palanichamy M, Arabindoo B, Murugesan V (2002) Photocatalytic degradation of leather dye: comparative study of TiO<sub>2</sub> supported on alumina and glass beads. *J Photochem Photobiol A* 148:153–159
29. Nam H-J, Amemiya T, Murabayashi M, Itoh K (2004) Photocatalytic activity of sol–gel TiO<sub>2</sub> thin films on various kinds of glass substrates: the effects of Na<sup>+</sup> and primary particle size. *J Phys Chem B* 108:8254–8259
30. Chen Y, Dionysiou DD (2005) Effect of calcination temperature on the photocatalytic activity and adhesion of TiO<sub>2</sub> films prepared by the P-25 powder-modified sol-gel method. *J Mol Catal A* 244:73–82
31. Takeda N, Torimoto T, Sampath S, Kuwabata S, Yoneyama H (1995) Effect of inert supports for titanium dioxide loading on enhancement of photodecomposition rate of gaseous propionaldehyde. *J Phys Chem* 99:9986–9991
32. Sato S (1988) Effects of surface modification with silicon oxides on the photochemical properties of powdered titania. *Langmuir* 4:1156–1159
33. Anderson C, Bard AJ (1995) An improved photocatalyst of TiO<sub>2</sub>/SiO<sub>2</sub> prepared by a sol-gel synthesis. *J Phys Chem* 99:9822–9825
34. Yoneyama H, Torimoto T (2000) Titanium dioxide/adsorbent hybrid photocatalysts for photo-destruction of organic substances of dilute concentrations. *Catal Today* 58:133–140
35. Shi J, Zheng J, Wu P, Ji X (2008) Immobilization of TiO<sub>2</sub> films on activated carbon fiber and their photocatalytic degradation properties for dye compounds with different molecular size. *Catal Commun* 9:1846–1850
36. Takeda N, Iwata N, Torimoto T, Yoneyama H (1998) Influence of carbon black as an absorbent used in TiO<sub>2</sub> photocatalyst films on photodegradation behaviors of propylamide. *J Catal* 177:240–246
37. Matos J, Laine J, Herrmann JM (1998) Synergy effect in the photocatalytic degradation of phenol on a suspended mixture of titania and activated carbon. *Appl Catal B Environ* 18:281–291
38. Ao CH, Lee SC (2004) Combination effect of activated carbon with TiO<sub>2</sub> for the photodegradation of binary pollutants at typical indoor air level. *J Photochem Photobiol A Chem* 161:131–140
39. Yu Y, Yu JC, Chan C-Y et al (2005) Enhancement of adsorption and photocatalytic activity of TiO<sub>2</sub> by using carbon nanotubes for the treatment of azo dye. *Appl Catal B Environ* 61:1–11
40. Liu B, Zeng HC (2008) Carbon nanotubes supported mesoporous mesocrystals of anatase TiO<sub>2</sub>. *Chem Mater* 20:2711–2718
41. Li F, Jiang Y, Xia M et al (2009) A high-stability silica–clay composite: synthesis, characterization and combination with TiO<sub>2</sub> as a novel photocatalyst for azo dye. *J Hazard Mater* 165:1219–1223
42. Zanjanchi MA, Golmojeh H, Arvand M (2009) Enhanced adsorptive and photocatalytic achievements in removal of methylene blue by incorporating tungstophosphoric acid–TiO<sub>2</sub> into MCM-41. *J Hazard Mater* 169:233–239

43. Wittmann G, Demeestere K, Dombi A, Dewulf J, Langenhove HV (2005) Preparation, structural characterization and photocatalytic activity of mesoporous Ti-silicates. *Appl Catal B Environ* 61:47–57
44. Li G, Zhao XS (2006) Characterization and photocatalytic properties of titanium-containing mesoporous SBA-15. *Ind Eng Chem Res* 45:3569–3573
45. Guo P, Wang P, Guo H (2009) TiO<sub>2</sub>/Na-HZSM-5 nano-composite photocatalyst: reversible adsorption by acid sites promotes photocatalytic decomposition of methyl orange. *Appl Catal B Environ* 90:677–687
46. Kuwahara Y, Aoyama J, Miyakubo K et al (2012) TiO<sub>2</sub> photocatalyst for degradation of organic compounds in water and air supported on highly hydrophobic FAU zeolite: structural, sorptive, and photocatalytic studies. *J Catal* 285:223–234
47. Kamegawa T, Ishiguro Y, Seto H, Yamashita H (2015) Enhanced photocatalytic properties of TiO<sub>2</sub>-loaded porous silica with hierarchical macroporous and mesoporous architectures in water purification. *J Mater Chem A* 3:2323–2330
48. Mazinani B, Beitollahi A, Masrom AK et al (2012) Characterization and evaluation of the photocatalytic properties of wormhole-like mesoporous silica incorporating TiO<sub>2</sub>, prepared using different hydrothermal and calcination temperatures. *Res Chem Intermed* 38: 1733–1742
49. Jang JS, Choi SH, Kim HG, Lee JS (2008) Location and state of Pt in platinumized CdS/TiO<sub>2</sub>. *J Phys Chem C* 112:17200–17205
50. Hsien Y-H, Chang C-F, Chen Y-H, Cheng S (2001) Photodegradation of aromatic pollutants in water over TiO<sub>2</sub> supported on molecular sieves. *Appl Catal B Environ* 31:241–249
51. Tanev PT, Chibwe M, Pinnavaia TJ (1994) Titanium-containing mesoporous molecular sieves for catalytic oxidation of aromatic compounds. *Nature* 368:321–323
52. Koyano KA, Tatsumi T (1997) Synthesis of titanium-containing MCM-41. *Micro Mater* 10:259–271
53. Grieken RV, Mariscal R (2000) Surface modified amorphous titanosilicate catalysts for liquid phase epoxidation. *Catal Today* 61:49–54
54. Chen Y, Han X, Bao X (2004) Direct synthesis, characterization and catalytic activity of titanium-substituted SBA-15 mesoporous molecular sieves. *Appl Catal A Gen* 273:185–191
55. Kang M, Park MS (2004) Synthesis of high concentration titanium-incorporated nanoporous silicates (Ti-NPS) and their photocatalytic performance for toluene oxidation. *Appl Catal B Environ* 53:195–205
56. Li F, Jiang Y, Yu L et al (2005) Surface effect of natural zeolite (clinoptilolite) on the photocatalytic activity of TiO<sub>2</sub>. *Appl Surf Sci* 252:1410–1416
57. Shankar MV, Anandan S, Venkatachalam N, Arabindoo B, Murugesan V (2006) Fine route for an efficient removal of 2,4-dichlorophenoxyacetic acid (2,4-D) by zeolite-supported TiO<sub>2</sub>. *Chemosphere* 63:1014–1021
58. Lee YC, Cheng S (2006) One-pot synthesis and photocatalysis of encapsulated TiO<sub>2</sub> in mesoporous SiO<sub>2</sub>. *J Chin Chem Soc* 53:1355–1361
59. Colborn T, Vom Saal FS, Soto AM (1993) Developmental effects of endocrine disrupting chemicals in wildlife and humans. *Env Imp Ass Rev* 14:469–489
60. Pichat J, D'Oliveria JC, Maffre JF, Mas D (1993) Destruction of 2,4-D in water by TiO<sub>2</sub>-UV, H<sub>2</sub>O<sub>2</sub>-UV, or direct photolysis. In: Ollis DF, Al-Ekabi H (eds) *Photocatalytic purification and treatment of water and air*. Elsevier, Amsterdam, pp 683–687
61. Keith LH (1998) Environmental endocrine disruptors. *Pure Appl Chem* 70:2319–2326
62. Sun L, Lee HK (2003) Stability studies of propoxur herbicide in environmental water samples by liquid chromatography-atmospheric pressure chemical ionization ion-trap mass spectrometry. *J Chromatogr A* 1014:153–163
63. Stanley CW, Thorton JS (1972) Gas-chromatographic method for residues of Baygon and its major metabolite in animal tissues and milk. *J Agric Food Chem* 20:1269–1273
64. de la Guardia M, Khalaf KD, Carbonell V, Rubio AM (1995) Clean analytical method for the determination of propoxur. *Anal Chim Acta* 308:462–468

65. Noorjahan M, Durga Kumari V, Subrahmanyam M, Boule P (2004) A novel and efficient photocatalyst: TiO<sub>2</sub>-HZSM-5 combinate thin film. *Appl Catal B Environ* 47:209–213
66. Corma A (1997) From microporous to mesoporous molecular sieve materials and their use in catalysis. *Chem Rev* 97:2373–2420
67. Kresge CT, Leonowicz ME, Beck JS (1992) Ordered mesoporous molecular sieves synthesized by a liquid-crystal template mechanism. *Nature* 359:710–712
68. Beck JS, Higgins JB, Schlenker JL (1992) A new family of mesoporous molecular sieves prepared with liquid crystal templates. *J Am Chem Soc* 114:10834–110843
69. Schlenker D, Stucky GD (1998) Nonionic Triblock and Star Diblock Copolymer and oligomeric surfactant syntheses of highly ordered, hydrothermally stable, mesoporous silica structures. *J Am Chem Soc* 120:6024–6036
70. Auerbach SM, Carrado KA, Dutta PT (2005) *Handbook of zeolite science and technology*. Marcel Dekker, New York
71. Tayade RJ, Kulkarni RG, Jasra RV (2007) Enhanced photocatalytic activity of TiO<sub>2</sub>-coated NaY and HY zeolites for the degradation of methylene blue in water. *Ind Eng Chem Res* 46:369–376
72. Sankaraman S, Yoon KB, Yabe T, Kochi JK (1991) Control of back electron transfer from charge-transfer ion pairs by zeolite supercages. *J Am Chem Soc* 113:1419–1421
73. Mahalakshmi M, Vishnu Priya S, Banumathi A, Palanichamy M, Murugesan V (2009) Photocatalytic degradation of aqueous propoxur solution using TiO<sub>2</sub> and H $\beta$  zeolite-supported TiO<sub>2</sub>. *J Hazard Mater* 161:336–343
74. Anpo M, Shima T, Kodama S (1987) Photocatalytic hydrogenation of propyne with water on small-particle titania: size quantization effects and reaction intermediates. *J Phys Chem* 91:4305–4310
75. Hagfeldt A, Gratzel M (1995) Light-Induced redox reactions in nanocrystalline systems. *Chem Rev* 95:49–68
76. Yeber MC, Rodriguez J, Freer J (2000) Photocatalytic degradation of cellulose bleaching effluent by supported TiO<sub>2</sub> and ZnO. *Chemosphere* 41:1193–1197
77. Lei Q, Hinestroza JP (2004) Application of nanotechnology for high performance textiles. *J Text Apparel Technol Manag* 4:1–7
78. Furube A, Asahi T, Masuhara H, Yamashita H, Anpo M (1999) Charge carrier dynamics of standard TiO<sub>2</sub> catalysts revealed by femtosecond diffuse reflectance spectroscopy. *J Phys Chem B* 103:3120–3127
79. Kominami H, Murakami S, Kato J, Kera Y, Ohtani B (2002) Correlation between some physical properties of titanium dioxide particles and their photocatalytic activity for some probe reactions in aqueous systems. *J Phys Chem B* 106:10501

# Chapter 16

## Plasmonic Photocatalysts: Preparation and Evaluation

Atsuhiko Tanaka and Hiroshi Kominami

### 16.1 Introduction

In classical chemistry, gold (Au) has been treated as an inert material. However, Au nanoparticles (2–5 nm) on metal oxides exhibited high activities for many reactions [1]. Colloidal Au nanoparticles have attracted much attention due to their bright and fascinating color. They show wine-red color and are mostly used in stained glass windows of cathedrals and churches. An absorption band results when the incident photon frequency is resonant with the collective oscillation of the conduction band electrons and is known as surface plasmon resonance (SPR). Phenomena of SPR are most commonly observed when Cu, Ag, and Au are used. The resonance frequency of SPR is strongly dependent on the size, shape, interparticle interactions, dielectric properties, and local environment of the nanoparticles. Recently, plasmonic metal nanoparticles have been applied not only to stained glass but also to chemical sensors and biosensors [2], surface-enhanced Raman scattering (SERS) [3], fluorescence enhancement [4], and photocurrent enhancement in photovoltaic cells [5]. Tatsuma et al. found that charge separation is photoinduced at the interface between a plasmonic metal nanoparticle and a semiconductor such as TiO<sub>2</sub> [6]. The plasmon-induced charge separation can be applied to photovoltaic cells and photocatalysis if stable nanoparticles such as Au are used.

---

A. Tanaka

Department of Molecular Engineering, Graduate School of Engineering, Kyoto University, Kyoto daigaku Katsura, Nishikyo-ku, Kyoto 615-8510, Japan

H. Kominami (✉)

Department of Applied Chemistry, Faculty of Science and Engineering, Kinki University, Kowakae, Higashiosaka, Osaka 577-8502, Japan

e-mail: [hiro@apch.kindai.ac.jp](mailto:hiro@apch.kindai.ac.jp)

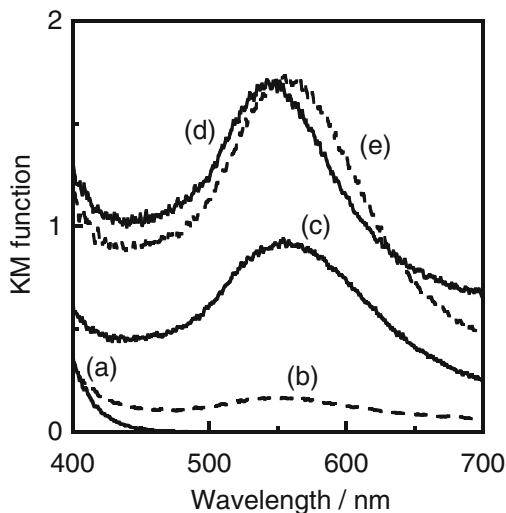
The SPR of Au nanoparticles has been applied to a visible light-responding photocatalyst; however, there are limited reports on applications of SPR-induced photoabsorption to chemical reactions, that is, oxidation of organic substrates, selective oxidation reaction, H<sub>2</sub> formation, and reduction of organic compounds. In the case of oxidation of organic substrates, Kowalska et al. reported oxidation of 2-propanol over Au/TiO<sub>2</sub> samples [7, 8]. They concluded from action spectrum analysis that the photoinduced oxidation of 2-propanol was driven by the SPR of Au particles. In the case of selective oxidation, Naya et al. reported selective conversion of alcohols to carbonyl compounds and amines to imines [9, 10]. They concluded that Au/rutile TiO<sub>2</sub> exhibited much higher activity than that of Au/anatase TiO<sub>2</sub> in selective oxidations. Shiraishi et al. reported that Au/P25 promoted efficient aerobic oxidation [11]. They concluded that this photocatalysis is promoted via plasmon activation of Au particles by visible light followed by consecutive electron transfer in the Au/rutile/anatase contact site. In the case of H<sub>2</sub> formation, Silva et al. reported H<sub>2</sub> formation from various substrates such as methanol and EDTA over Au/TiO<sub>2</sub> [12]. Yoshida et al. reported that Au nanorods/TiO<sub>2</sub> exhibited much higher activity for H<sub>2</sub> formation than did Au spherical particles/TiO<sub>2</sub> [13]. In the case of reduction of organic compounds, Ke et al. reported reduction of nitrobenzene, azobenzene, acetophenone, and styrene oxide over Au on various metal oxides including CeO<sub>2</sub>, TiO<sub>2</sub>, ZrO<sub>2</sub>, Al<sub>2</sub>O<sub>3</sub>, and zeolite Y [14]. In most of the above papers, samples were prepared by photodeposition method and there are few papers reporting another method for preparation of plasmonic photocatalysts. In the course of our studies on photocatalysts responding to visible light, we developed various methods for preparation of Au plasmonic photocatalysts. In this chapter, we introduce some of them and results of photoinduced chemical reactions over the prepared samples under irradiation of visible light.

## 16.2 Photodeposition Method

### 16.2.1 Preparation

The CeO<sub>2</sub> powder (198 mg) was suspended in water (10 cm<sup>3</sup>) in a test tube and the test tube was sealed with a rubber septum under argon (Ar). Aqueous solutions of citric acid (30 μmol) and tetrachloroauric acid (as 2 mg Au) were injected into the sealed test tube and then photoirradiated at  $\lambda > 300$  nm by a 400-W high-pressure mercury arc (Eiko-sha, Osaka) under Ar with magnetic stirring in a water bath continuously kept at 298 K. The Au source was reduced by photogenerated electrons, and Au metal was deposited on CeO<sub>2</sub> particles, resulting in the formation of Au/CeO<sub>2</sub>. Analysis of the liquid phase after the photodeposition revealed that the Au source was almost completely (>99.9 %) deposited as Au metal on the CeO<sub>2</sub> particles. The resultant powder was washed repeatedly with distilled water and then dried at 310 K overnight under air.

**Fig. 16.1** Effect of Au loading amounts on light absorption; (a) CeO<sub>2</sub>, (b) 0.1 wt% Au/CeO<sub>2</sub>, (c) 0.5 wt% Au/CeO<sub>2</sub>, (d) 1 wt% Au/CeO<sub>2</sub>, and (e) 2 wt% Au/CeO<sub>2</sub>



### 16.2.2 Characterization

The effect of Au loading on the absorption due to the SPR of Au loaded on CeO<sub>2</sub> is shown in Fig. 16.1. Although CeO<sub>2</sub> exhibited only an absorption at  $\lambda < 425$  nm due to the band-gap excitation, another strong photoabsorption was observed in the spectrum of Au/CeO<sub>2</sub> at around 550 nm, which was attributed to the SPR of the supported Au nanoparticles. The photoabsorption at 550 nm increased with increase in the loading amount of Au on CeO<sub>2</sub> and tended to be saturated at high loadings.

### 16.2.3 Mineralization of Organic Acid [15, 16]

To elucidate the applicability of Au/CeO<sub>2</sub>, mineralization of formic acid, oxalic acid, and acetic acid in aqueous solutions was examined under irradiation of visible light from a Xe lamp with an O-54 cutfilter at 298 K. In all cases, CO<sub>2</sub> was evolved just after irradiation of visible light and the amount of CO<sub>2</sub> increased linearly with irradiation time just before saturation at 100  $\mu$ mol, which corresponded to the initial amount of carbon (100  $\mu$ mol). The small apparent activation energy (2.4 kJ mol<sup>-1</sup>) and action spectrum in the mineralization of formic acid indicate that the rate determining step in mineralization of formic acid in the irradiated Au/CeO<sub>2</sub> system was different from the thermal activation process and that this mineralization involved a photoinduced step by the SPR of Au supported on CeO<sub>2</sub>. The Au/CeO<sub>2</sub> samples mineralized formic acid even under irradiation of green LED (center wavelength=530 nm). Apparent quantum efficiency (AQE) of formic acid mineralization increased with decrease in the intensity of the green light and reached 4.7 % at 0.4 mW cm<sup>-2</sup>.

### 16.2.4 Selective Oxidation of Organic Compounds [17]

Au/CeO<sub>2</sub> oxidized aromatic alcohols to corresponding aldehydes almost quantitatively in an aqueous suspension under irradiation of green light in the presence of O<sub>2</sub> [17]. Three blank reactions of benzyl alcohol at 298 K: (1) dark reaction in the presence of Au/CeO<sub>2</sub>; (2) photocatalytic reaction by bare CeO<sub>2</sub>, and (3) photochemical reaction, gave no or only a trace amount of benzaldehyde. From the results of these blank tests, it can be concluded that Au, CeO<sub>2</sub>, and visible light irradiation are indispensable for oxidation of benzyl alcohol to benzaldehyde. The following reaction mechanism is generally accepted as the mechanism of oxidation of an organic compound in the presence of O<sub>2</sub>: (1) incident photons are absorbed by Au particles through their SPR excitation, (2) electrons may be injected from Au particles into the conduction band of semiconductors supporting Au particles, (3) the resultant electron-deficient Au can oxidize organic compounds to be recovered to the original metallic state, and (4) electrons in the conduction band are consumed for reduction of O<sub>2</sub>.

## 16.3 Multistep Photodeposition [18]

### 16.3.1 Preparation

Bare CeO<sub>2</sub> powder (198 mg) was suspended in water (10 cm<sup>3</sup>) in a test tube, and the test tube was sealed with a rubber septum under argon (Ar). An aqueous solution of tetrachloroauric acid (HAuCl<sub>4</sub>) was injected into the sealed test tube and then photoirradiated at  $\lambda > 300$  nm by a 400-W high-pressure mercury arc (Eiko-sha, Osaka, Japan) under Ar with magnetic stirring in a water bath continuously kept at 298 K. The Au source was reduced by photogenerated electrons in the conduction band of CeO<sub>2</sub>, and Au metal was deposited on CeO<sub>2</sub> particles, resulting in the formation of Au/CeO<sub>2</sub>. This photodeposition of Au was repeated several times to obtain an Au/CeO<sub>2</sub> sample having a desired Au content. This photodeposition method is called the multistep (MS) photodeposition method and, hereafter, a sample prepared by the MS photodeposition method is designated as MS-Au(X)/CeO<sub>2</sub>, where X means total Au content. The amount of Au loaded per a single deposition in MS photodeposition was generally 0.5 wt%, and an MS-Au(1.0)/CeO<sub>2</sub> sample was prepared by performing the photodeposition two times. The MS photodeposition method can be used flexibly, e.g., an MS-Au(1.0)/CeO<sub>2</sub> sample can also be prepared by first 0.50 wt% Au loading followed by 0.10 wt% loading five times ( $1.0 = 0.50 + 0.10 \times 5$ ). General photodeposition method described in Sect. 16.2 in which all of the HAuCl<sub>4</sub> solution containing the desired amount of Au was injected, defined here as the single-step (SS) photodeposition method, was used for comparison with the MS photodeposition method, and a sample prepared by the SS photodeposition method is designated as SS-Au(X)/CeO<sub>2</sub>. It was confirmed that the Au source was also almost completely (>99.9 %) deposited as Au on the CeO<sub>2</sub> particles.

### 16.3.2 Characterization

The morphology of Au/CeO<sub>2</sub> particles was observed under TEM operated at 300 kV. Figure 16.2 shows TEM photographs of SS and MS-Au(1.0)/CeO<sub>2</sub> samples, respectively. In both cases, fine Au nanoparticles were observed within relatively sharp distributions. The average particle sizes of SS- and MS-Au(1.0)/CeO<sub>2</sub> samples were determined to be 59 and 92 nm with standard deviations of 4.9 and 8.0 nm, respectively. These results indicate that the size of Au nanoparticles loaded on CeO<sub>2</sub> is strongly affected by the type of photodeposition method and that there is a tendency for larger Au nanoparticles to be formed by the MS photodeposition method.

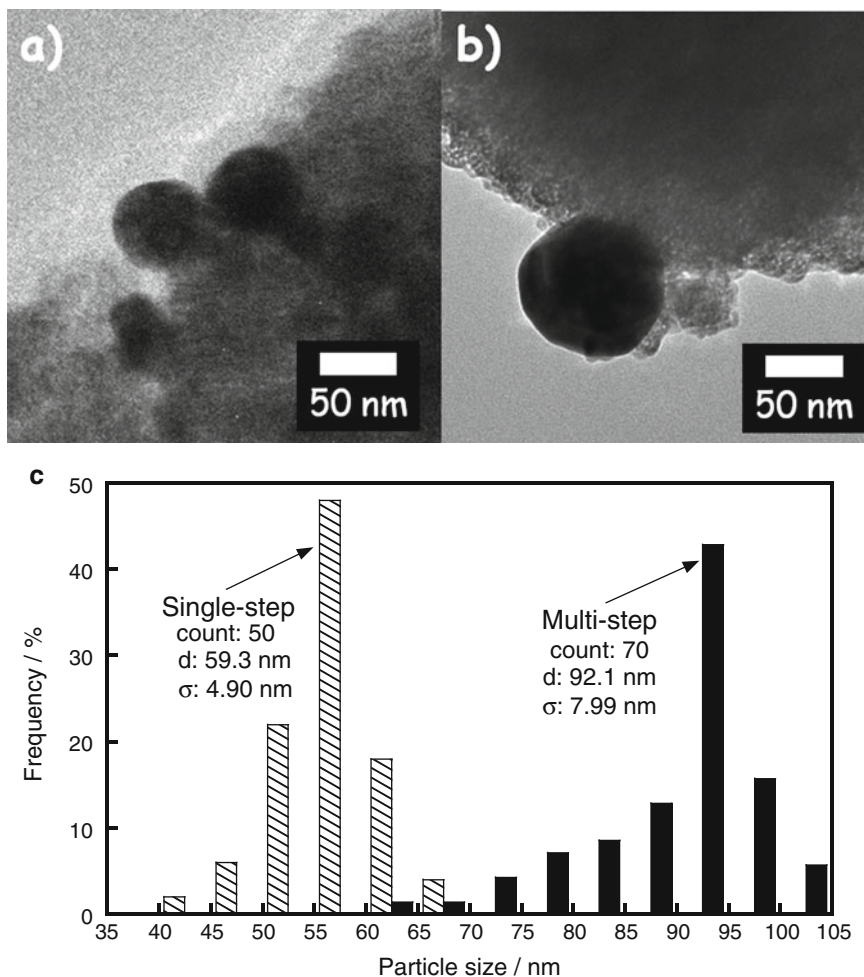


**Fig. 16.2** TEM images of (a) SS-Au(1.0)/CeO<sub>2</sub>, (b) MS-Au(1.0)/CeO<sub>2</sub>, and (c) size distributions of Au particles of SS- and MS-Au/CeO<sub>2</sub> samples

**Fig. 16.3** Absorption spectra of SS-Au(1.0)/CeO<sub>2</sub> (broken line) and MS-Au(1.0)/CeO<sub>2</sub> (solid line), and light intensity of visible light irradiated to reaction systems from a green LED (right axis)

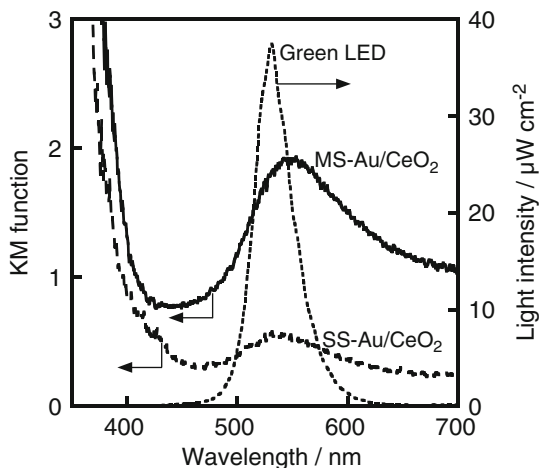
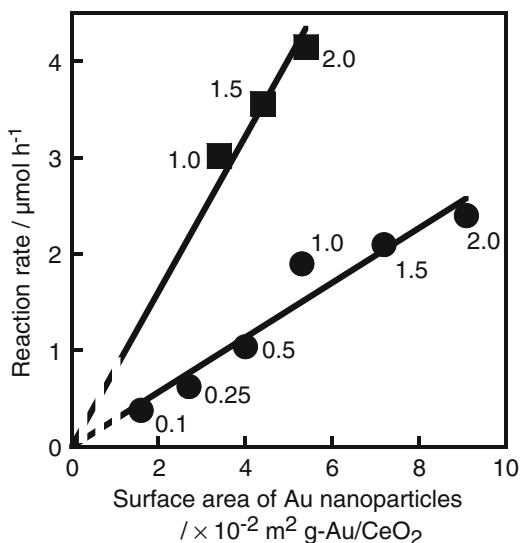


Figure 16.3 shows photoabsorption spectra of MS- and SS-Au(1.0)/CeO<sub>2</sub> samples. Strong photoabsorption was observed in both spectra at around 550 nm, and the strong photoabsorption was attributed to the SPR of the supported Au nanoparticles. It should be noted that MS-Au(1.0)/CeO<sub>2</sub> samples exhibited photoabsorption much stronger than that of SS-Au(1.0)/CeO<sub>2</sub> samples, although the amounts of Au (X) were the same. This result suggests that the intensity of photoabsorption due to the SPR of Au was affected by the size of Au nanoparticles. Similar results have been obtained in plasmonic Au/TiO<sub>2</sub> photocatalysts [19] and unsupported Au nanoparticles [20]. In the latter case, Shimizu et al. [20] reported that such observed features coincide with the prediction of the Mie theory. As also shown in Fig. 16.3, the photoabsorption property of Au/CeO<sub>2</sub> samples matched the wavelength of light emitted from a green LED.

### 16.3.3 Selective Oxidation of Organic Compounds

Photocatalytic oxidation of benzyl alcohol in aqueous suspensions of SS- and MS-Au(X)/CeO<sub>2</sub> samples having various values of X was examined using a green LED as the light source, and their rates of benzaldehyde formation were plotted against their external surface area of Au particles ( $S_{Au}$ ) (Fig. 16.4). Linear correlations between the rate and  $S_{Au}$  were observed in both SS- and MS-Au(X)/CeO<sub>2</sub> samples. It should be noted that the slopes of the plots were different, and MS-Au(X)/CeO<sub>2</sub> samples showed a slope larger than that of SS-Au(X)/CeO<sub>2</sub> samples. These results suggest that the external surface area of Au loaded on CeO<sub>2</sub> and the intensity of photoabsorption due to the SPR of Au nanoparticles are important factors controlling the photocatalytic activity of Au/CeO<sub>2</sub> regardless of the type of photodeposition method [18].

**Fig. 16.4** Effect of external surface area of Au nanoparticles of SS-Au(X)/CeO<sub>2</sub> (circles) and MS-Au(X)/CeO<sub>2</sub> (squares) on the rate of benzaldehyde formation from aqueous solutions of benzyl alcohol in the presence of O<sub>2</sub> under irradiation of visible light from a green LED (1.7 mW cm<sup>-2</sup>). Values in the figure are contents of Au (X)



## 16.4 Colloid Photodeposition Method [21]

### 16.4.1 Preparation

#### 16.4.1.1 Preparation of Colloidal Au Nanoparticles

Colloidal Au nanoparticles were prepared using the method reported by Frens [22]. To 750 cm<sup>3</sup> of an aqueous tetrachloroauric acid (HAuCl<sub>4</sub>) solution (0.49 mmol dm<sup>-3</sup>), 100 cm<sup>3</sup> of an aqueous solution containing sodium citrate (39 mol dm<sup>-3</sup>) was added. The solution was heated and boiled for 1 h. After the color of the solution had changed from deep blue to deep red, the solution was boiled for a further 30 min. After cooling the solution to room temperature, Amberlite MB-1 (ORGANO, 60 cm<sup>3</sup>) was added to remove excess sodium citrate. After 1-h treatment, MB-1 was removed from the solution using a glass filter.

#### 16.4.1.2 Loading of Au Particles on TiO<sub>2</sub>

Preparation of TiO<sub>2</sub> having 1.0 wt% Au as a typical sample is described. A TiO<sub>2</sub> sample (168 mg) was suspended in 20 cm<sup>3</sup> of an aqueous solution of colloidal Au nanoparticles (0.085 mg cm<sup>-3</sup>) in a test tube, and the test tube was sealed with a rubber septum under Ar. An aqueous solution of oxalic acid (50 μmol) was injected into the sealed test tube. The mixture was photoirradiated at  $\lambda > 300 \text{ nm}$  by a 400 W high-pressure mercury arc under Ar with magnetic stirring in a water bath continuously kept at 298 K. The resultant powder was washed repeatedly with distilled water and then dried at 310 K overnight under air. This preparation method is called the colloid photodeposition (CP) method.

### 16.4.2 Characterization

Figure 16.5 shows TEM photographs of Au(X)/TiO<sub>2</sub> samples (X=0.1, 0.5, 1.0, and 2.0). The average diameter of Au particles of Au(1.0)/TiO<sub>2</sub> was determined to be 12.7 nm, which is in good agreement with the average diameter (12.8 nm) of original colloidal Au nanoparticles before Au loading. Similar results were obtained for Au(X)/TiO<sub>2</sub> samples with larger X. It should be noted that the average particle size was not changed even though the amount of Au loading was increased up to 2.0 wt% as shown in Fig. 16.6a. On the other hand, the average diameter of Au nanoparticles of Au(X)/TiO<sub>2</sub> samples prepared by the SS photodeposition method increased with increase in X as shown in Fig. 16.6b. These results indicate that only the number of Au nanoparticles increased with increase in the amount of Au loading when the CP method was used and that effect(s) of the size of Au nanoparticle can be

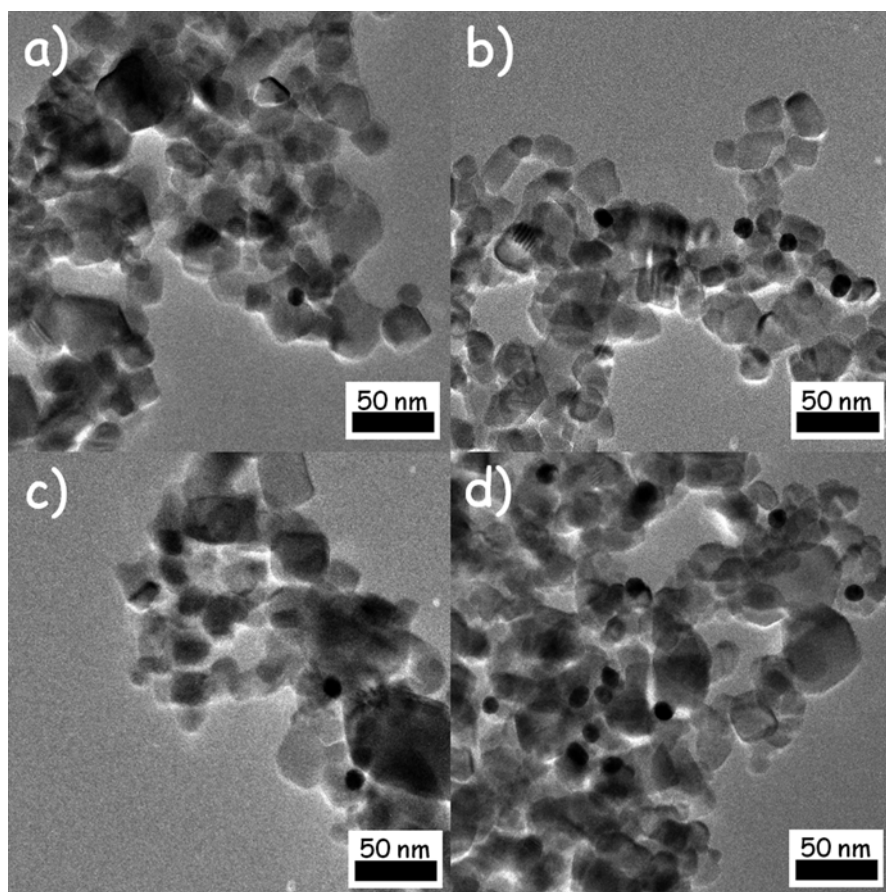


**Fig. 16.5** TEM images of Au(X)/TiO<sub>2</sub>(P25) samples (X= (a) 0.1, (b) 0.5, (c) 1.0, and (d) 2.0) prepared by the CP method

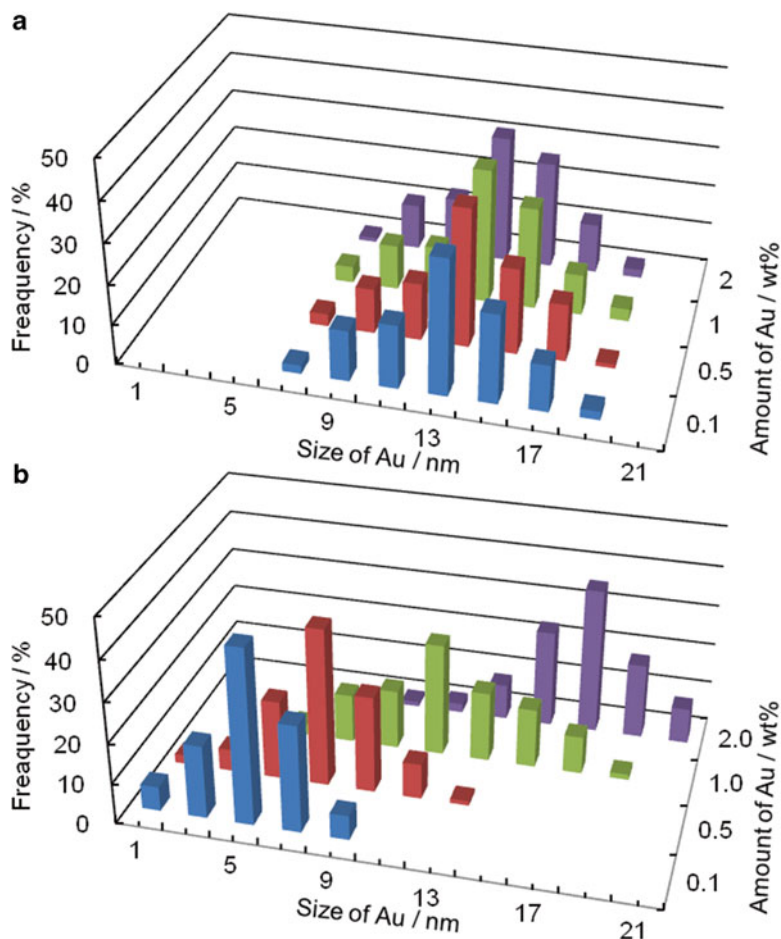


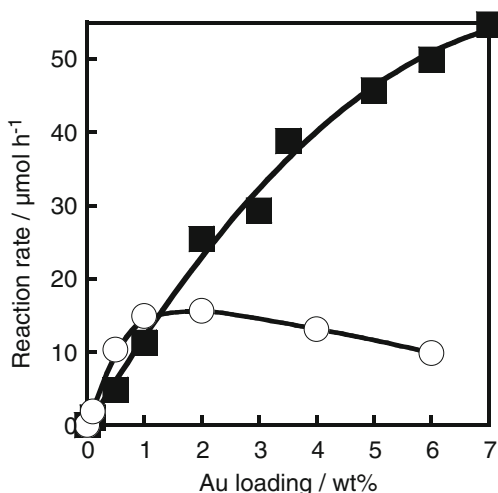
**Fig. 16.6** Effect of Au loading amounts (X) on distribution of Au nanoparticles of Au(X)/TiO<sub>2</sub> samples prepared by (a) CP method and (b) SS photodeposition method

ruled out in discussion about SPR-induced photoabsorption and photocatalytic activities of Au(X)/TiO<sub>2</sub> samples prepared by the CP method with different amounts of Au loading.

### 16.4.3 Mineralization of Organic Acid

Reaction rate of each Au(X)/TiO<sub>2</sub> prepared by the CP method was calculated and the effect of the amount of Au (X) on the rate of CO<sub>2</sub> evolution is shown in Fig. 16.7. The rate of CO<sub>2</sub> evolution increased almost linearly with increase in the amount of Au loading up to X=3.5. Very large reaction rates were obtained in the

**Fig. 16.7** Effect of Au loading amounts ( $X$ ) on the rate of evolution of  $\text{CO}_2$  from formic acid in aqueous suspensions of  $\text{Au}(X)/\text{TiO}_2$  samples prepared by CP method (squares) and SS photodeposition method (circles) under irradiation of visible light



samples with  $X > 5$ , although the rate tended to be saturated against the increase in  $X$ . These results show that activity of  $\text{Au}/\text{TiO}_2$  plasmonic photocatalysts can be controlled simply by the amount of Au loading using the CP method. For comparison,  $\text{Au}/\text{TiO}_2$  samples with various Au contents were prepared by the SS photodeposition method. The activities of  $\text{Au}(X)/\text{TiO}_2$  samples prepared by this method with  $X=0.5$  and  $1.0$  were slightly larger than those of  $\text{Au}/\text{TiO}_2$  with the same  $X$  prepared by the CP method as shown in Fig. 16.7; however, the reaction rate of  $\text{Au}(X)/\text{TiO}_2$  prepared by the SS photodeposition method was saturated even at  $X=1.0$  and further increase in  $X$  decreased activities. This behavior was in contrast to the reaction rate of  $\text{Au}(X)/\text{TiO}_2$  prepared by the CP method, which increased until at least  $X=7.0$ . These results indicate that the SS photodeposition method might be useful for preparation of  $\text{Au}/\text{TiO}_2$  with small Au contents; however, this method cannot be applied for preparation of  $\text{Au}/\text{TiO}_2$  with large amounts of Au loading.

## 16.5 Summary

In this chapter, preparation of plasmonic photocatalysts by various methods and use of these materials for several photoinduced reactions under irradiation of visible light.  $\text{Au}/\text{CeO}_2$  oxidized aromatic alcohols to corresponding aldehydes almost quantitatively in an aqueous suspension under irradiation of green light in the presence of  $\text{O}_2$ . The properties and performance of  $\text{Au}/\text{CeO}_2$  can be improved by using the multistep photodeposition method. Results obtained suggest that the external surface area of Au loaded on  $\text{CeO}_2$  and the intensity of photoabsorption due to the SPR of Au nanoparticles are important factors controlling the photocatalytic activity of  $\text{Au}/\text{CeO}_2$ . We also developed colloid photodeposition (CP) method for

preparation of Au/TiO<sub>2</sub>, in which the average diameter of Au particles was in good agreement with the average diameter of original colloidal Au nanoparticles before Au loading. Only the number of Au nanoparticles increased with increase in the amount of Au loading when the CP method was used and effect(s) of the size of Au nanoparticle can be ruled out in discussion about SPR-photoabsorption and photocatalytic activities of Au/TiO<sub>2</sub> samples prepared by the CP method with different amounts of Au loading.

## References

1. Takei T, Akita T, Nakamura I, Fujitani T, Okumura M, Okazaki K, Huang J, Ishida T, Haruta M (2012) Heterogeneous catalysis by gold. *Adv Catal* 55:1–126
2. Stewart ME, Anderton CR, Thompson LB, Maria J, Gray SK, Rogers JA, Nuzzo RG (2008) Nanostructured plasmonic sensors. *Chem Rev* 108:494–521
3. Stiles PL, Dieringer JA, Shah NC, Van Duyne RP (2008) Surface-enhanced Raman spectroscopy. *Annu Rev Anal Chem* 1:601–626
4. Lakowicz JR, Ray K, Chowdhury M, Szymanski H, Fu Y, Zhang J, Nowaczyk K (2008) Plasmon-controlled fluorescence: a new paradigm in fluorescence spectroscopy. *Analyst* 133:1308–1346
5. Atwater HA, Polman A (2010) Plasmonics for improved photovoltaic devices. *Nat Mater* 9:205–213
6. Tian Y, Tatsuma T (2005) Mechanisms and applications of plasmon-induced charge separation at TiO<sub>2</sub> films loaded with gold nanoparticles. *J Am Chem Soc* 127:7632–7637
7. Kowalska E, Abe R, Ohtani B (2009) Visible light-induced photocatalytic reaction of gold-modified titanium(IV) oxide particles: action spectrum analysis. *Chem Commun* 241–243
8. Kowalska E, Mahaney OOP, Abe R, Ohtani B (2010) Visible-light-induced photocatalysis through surface plasmon excitation of gold on titania surfaces. *Phys Chem Chem Phys* 12:2344–2355
9. Kimura K, Naya S, Jin-nouchi Y, Tada H (2012) TiO<sub>2</sub> crystal form-dependence of the Au/TiO<sub>2</sub> plasmon photocatalyst's activity. *J Phys Chem C* 116:7111–7117
10. Naya S, Kimura K, Tada H (2013) One-step selective aerobic oxidation of amines to imines by gold nanoparticle-loaded rutile titanium(IV) oxide plasmon photocatalyst. *ACS Catal* 3:10–13
11. Tsukamoto D, Shiraishi Y, Sugano Y, Ichikawa S, Tanaka S, Hirai T (2012) Gold nanoparticles located at the interface of anatase/rutile TiO<sub>2</sub> particles as active plasmonic photocatalysts for aerobic oxidation. *J Am Chem Soc* 134:6309–6315
12. Silva CG, Juarez R, Marino T, Molinari R, Garcia H (2011) Influence of excitation wavelength (UV or visible light) on the photocatalytic activity of titania containing gold nanoparticles for the generation of hydrogen or oxygen from water. *J Am Chem Soc* 133:595–602
13. Yuzawa H, Yoshida T, Yoshida H (2012) Gold nanoparticles on titanium oxide effective for photocatalytic hydrogen formation under visible light. *Appl Catal B* 115:294–302
14. Ke X, Sarina S, Zhao J, Zhang X, Chang J, Zhu H (2012) Tuning the reduction power of supported gold nanoparticle photocatalysts for selective reductions by manipulating the wavelength of visible light irradiation. *Chem Commun* 48:3509–3511
15. Kominami H, Tanaka A, Hashimoto K (2010) Mineralization of organic acids in aqueous suspensions of gold nanoparticles supported on cerium(IV) oxide powder under visible light irradiation. *Chem Commun* 46:1287–1289
16. Kominami H, Tanaka A, Hashimoto K (2011) Gold nanoparticles supported on cerium(IV) oxide powder for mineralization of organic acids in aqueous suspensions under irradiation of visible light of  $\lambda = 530$  nm. *Appl Catal A* 397:121–126

17. Tanaka A, Hashimoto K, Kominami H (2011) Selective photocatalytic oxidation of aromatic alcohols to aldehydes in an aqueous suspension of gold nanoparticles supported on cerium(IV) oxide under irradiation of green light. *Chem Commun* 47:10446–10448
18. Tanaka A, Hashimoto K, Kominami H (2012) Preparation of Au/CeO<sub>2</sub> exhibiting strong surface plasmon resonance effective for selective or chemoselective oxidation of alcohols to aldehydes or ketones in aqueous suspensions under irradiation by green light. *J Am Chem Soc* 134:14526–14533
19. Tanaka A, Sakaguchi S, Hashimoto K, Kominami H (2012) Preparation of Au/TiO<sub>2</sub> exhibiting strong surface plasmon resonance effective for photoinduced hydrogen formation from organic and inorganic compounds under irradiation of visible light. *Catal Sci Technol* 2:907–909
20. Shimizu T, Teranishi T, Hasegawa S, Miyake M (2003) Size evolution of alkanethiol-protected gold nanoparticles by heat treatment in the solid state. *J Phys Chem B* 107:2719–2724
21. Tanaka A, Ogino A, Iwaki M, Hashimoto K, Ohnuma A, Amano F, Ohtani B, Kominami H (2012) Gold-titanium(IV) oxide plasmonic photocatalysts prepared by a colloid-photodeposition method: correlation between physical properties and photocatalytic activities. *Langmuir* 28:13105–13111
22. Frens G (1973) Controlled nucleation for the regulation of the particle size in monodisperse gold suspensions. *Nat Phys Sci* 241:20–22

**Part IV**  
**Photocatalysts with Advanced Components**

# Chapter 17

## Nanostructured Elemental Photocatalysts: Development and Challenges

Zhurui Shen and Jimmy C. Yu

### 17.1 Introduction

In 1972, Fujishima and Honda found photocatalytic water splitting on the TiO<sub>2</sub> electrodes [1]. Since then, photocatalysis has attracted great attention due to its potential in environmental remediation and energy applications [2, 3]. Photocatalysis is based on the unique electronic structure of semiconductors, which consist of a filled valence band (VB) and an empty conduction band (CB). When the semiconductor absorbs the photons with energy higher than its band gap energy ( $E_g$ ), the electrons will be excited from the VB to its CB, leaving holes in the VB. Then the photoexcited electrons/holes will migrate to the surface of semiconductor. Except some combined electrons/holes, they will initiate the chemical reduction or oxidation reactions. Therefore, most of the photocatalysts are semiconductor compounds which can be triggered by solar light. To date, several hundreds of photocatalysts have been developed, and most of them are transition metal-based compounds. They can be sorted into oxides (e.g. TiO<sub>2</sub>) [4], sulfides (e.g. CdS) [5], nitrides (e.g. Ta<sub>3</sub>N<sub>5</sub>) [6], and oxynitrides (e.g. BaNbO<sub>2</sub>N) [7]. According to the crystal category, these photocatalysts are mainly ionic crystals. Their conduction bands are dominantly consisting of anion orbit states (e.g. O 2p), while their valence bands are dominantly consisting of metal orbit states (e.g. Ti 3d) [8]. This special electronic structure can crucially affect their photocatalytic activities, because it determines the light absorption range, electron/holes transfer and separation, etc., for the photocatalysts.

Recently, besides these widely studied photocatalysts, simple elemental photocatalysts have been studied and attracted the arising attention, such as silicon (Si) [9–12], selenium (Se) [13, 14], red phosphorus (P) [15–18], sulfur (S) [19–24],

---

Z. Shen • J.C. Yu (✉)

Department of Chemistry, Institute of Environment, Energy and Sustainability, The Chinese University of Hong Kong, Shatin, New Territories, Hong Kong, China  
e-mail: [jimyu@cuhk.edu.hk](mailto:jimyu@cuhk.edu.hk)

boron (B) [25], and bismuth (Bi) [26–29]. Most of them are composed of high abundant elements, cost-effective and visible light active. These advances make them a kind of promising photocatalysts especially in the industrial applications. Moreover, their crystal structures are quite different from the well-known ionic crystal photocatalysts, and they can be mainly classified into covalent crystals (e.g. Si, B) and molecular crystals (e.g. Se, P, S). This structural characteristic for elemental photocatalysts brings them special electronic structure, and thus some unexpected results can be envisaged in the investigation for elemental photocatalysts.

Si was the first case of elemental photocatalyst found in 1979 [30]. Its activity was proved in photoelectrochemical (PEC) H<sub>2</sub> evolution from a water-soluble organic reagent. For solar-driven photocatalysis without a bias, there have been a few examples in the past decades. However, they were mainly focusing on the degradation of organic agents [9, 10, 13, 14, 31, 32]. Until very recently, visible-light-driven (VLD) water splitting over red P (Hittorf phase) has been reported for the first time [15]. The mechanism for its activity was explained by multiple experimental methods and theoretical calculations. Photocatalytic water splitting was proved energetically possible due to proper energy levels of its CB and VB. This contribution inspired further study of novel elemental photocatalysts, e.g. S, B, red P allotropes, and Bi [17–29]. Bi is the latest found elemental photocatalyst [26–29]. Unlike others, it is not a semiconductor in its bulk form. But its photoexcited hot electrons/holes (surface plasmon resonance, SPR) can also initiate the chemical reactions. Although the study of elemental photocatalysts is still in its infancy, the continuous efforts will expand the scope of photocatalysis and greatly benefit the seeking of unknown photocatalysts.

Similar with traditional photocatalysts, the growing of elemental photocatalysts is also promoted by the nanoscience. For example, decreasing the particle size can efficiently improve the photocatalytic activity of sulfur [19]. Therefore, this chapter is intended to give a systematic and updated review of nanostructured elemental photocatalysts. It consists of two major sections. The first section mainly contains the preparation, characterization, and reactions of nanostructured elemental semiconductor photocatalysts (Si, Se, P, S, and B). The second section is a brief review about the semimetal Bi photocatalyst. Finally, from the viewpoint of nanoscience, we discuss the ideas and considerations of developing more efficient elemental photocatalysts.

## 17.2 Development of Elemental Semiconductor Photocatalysts

### 17.2.1 Silicon

*Silicon (Si)* is the second most abundant element on the earth (more than 25 % molar ratio). Elemental Si mainly exists in two allotropes, one is amorphous Si, and the other is crystalline Si with diamond cubic structure. Cubic Si is a kind of excellent semiconductor, which is widely used in electronic industry and solar cells [33]. It

has an indirect band gap of 1.1 eV and can absorb the solar light up to 1100 nm. These advances make Si a very promising photocatalyst. In fact, the Si photoelectrode has been used to generate H<sub>2</sub> from organic reagent early in 1979 [30].

As a photocatalyst, bulk Si has two apparent shortcomings [8]. First, the energy edges of its CB and VB slightly mismatch with the redox level of water. Second, the silicon is unstable in aqueous solution, and it can react with water to form an oxide layer. Nanoscaling method can be used to increase the energy difference between its band edges and redox levels of water. Therefore, Si nanostructures (e.g. Si nanowires array) have been prepared and widely used in the photoelectrochemical (PEC) water splitting [33]. Besides the quantum size effect, the bias applied in PEC process can also overcome the problem of its energy levels. However, nanostructured Si is even less stable than its bulk counterpart in the aqueous solution. Thus, several protective layers (e.g. TiO<sub>2</sub> coating [34]) have been developed to suppress its reaction with water [34, 35]. These contents can be found in detail in several review papers [33, 36, 37]. Herein, we mainly introduce the development of Si photocatalyst in powder forms without a bias.

In 1982, Golovanova et al. reported the photocatalytic decomposition of CCl<sub>4</sub> on a Si surface [31]. One year later, Taniguchi et al. have achieved the hydrogen production from aqueous ethanol using a surface-modified Si powder photocatalysts, where polypyrrole and Ag were deposited [32]. Recently, with the growing of nanoscience, Si-based nanostructured photocatalysts have attracted increasing interest. Several methods have been developed to prepare Si quantum dots (QDs)/nanowires. These mainly include: polyoxometalate-assisted electrochemical method [9], oxide-assisted growth, [38], and the vapor–liquid–solid method [39]. For example, Kang et al. found that 1–2 nm Si QDs show an excellent photocatalytic activity for CO<sub>2</sub> reduction and methyl red degradation, while 3–4 nm Si QDs as photocatalysts are only effective for the selective oxidation of benzene [9] (Fig. 17.1). This difference can be ascribed to the larger electrons/holes pair energy of 1–2 nm Si QDs than that of 3–4 nm Si QDs. While Shao et al. treated the Si nanowires using HF acid, which resulted in hydrogen terminated (partially fluorine terminated) on their surface [10]. These HF-treated Si nanowires were used as photocatalyst for Rhodamine B (RhB) degradation. They displayed obvious activity especially using noble metal as the cocatalyst. Moreover, the hydrogen/fluorine-terminated surface prohibited their oxidation by water. Thus, they showed a satisfied stability in the aqueous solution for 1 week. This work offered a useful method to increase the stability of nanostructured Si photocatalyst.

In the previous study, making a porous structure was proved effective to increase the activity and stability of Si photoelectrodes. It can decrease the electrons/holes recombination due to its high surface area and small wall thickness. Moreover, it can also suppress the formation of oxide layer on the Si/electrolyte interface. Recently, Quan and his coworkers used porous Si in photocatalysis without a bias for the first time [11]. Via the electro-assisted chemical etching, the as-prepared Si showed a bimodal porous structure consisting of macropores (~1.2 μm) and nanopores (~5 nm). Its band gap was increased to 2.2 eV, which is 1.0 eV larger than that of bulk Si. The Mott–Schottky experiment further indicated that this difference

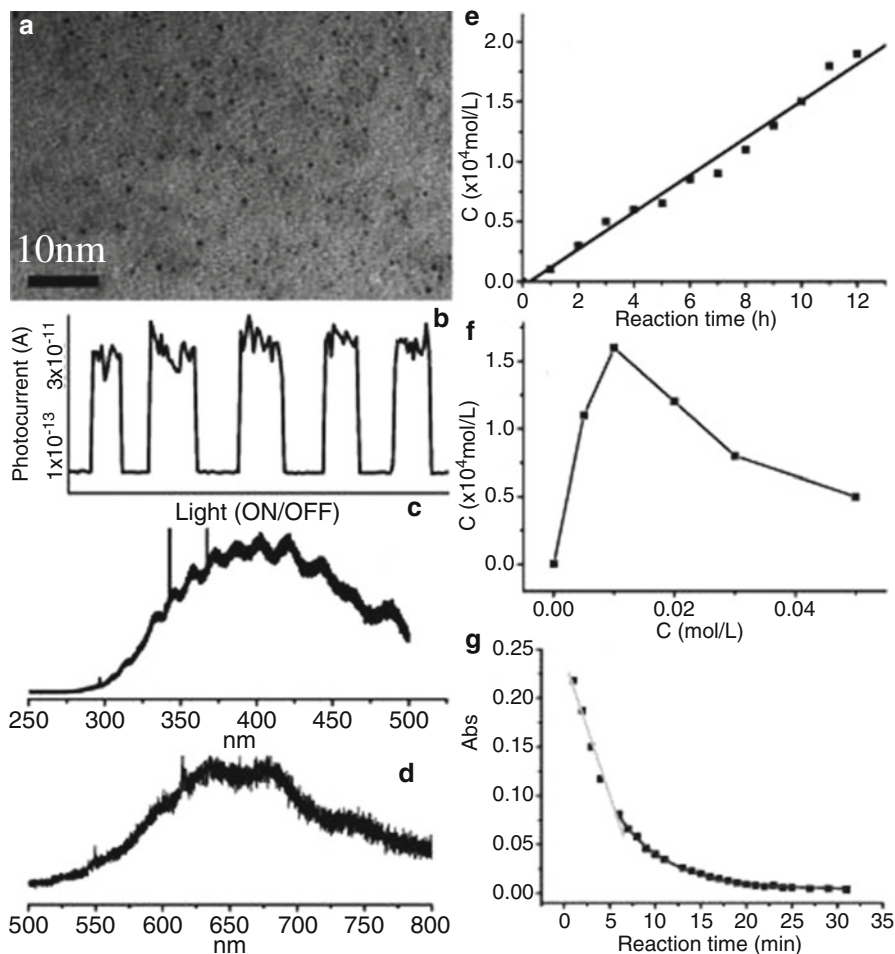


**Fig. 17.1** (a) TEM images of SiQDs and (b) photoresponse of SiQDs film; PL spectra of (c) 1–2 nm and (d) 3–4 nm SiQDs, respectively; (e) product ( $\text{CH}_2\text{O}/\text{HCOOH}$ ) concentration versus reaction time; (f) reduction rate or ( $\text{CH}_2\text{O}/\text{HCOOH}$ ) concentration (reaction time 12 h) versus  $[\text{CO}_3^{2-}]$ ; (g) methyl red concentration versus reaction time. Reprinted with permission from Ref. [9]. Copyright 2007, American Chemical Society

came from a more positive VB. Therefore, the hierarchical porous Si showed an excellent photocatalytic oxidation of phenol under visible light irradiation. Furthermore, this hierarchical porous Si showed much better stability than a macroporous counterpart. Another interesting porous Si photocatalyst was reported by Wang's group in 2014 [12] (Fig. 17.2). Typically, the  $\text{SiCl}_4$  in toluene was reduced by a NaK alloy in the glove box filled with Argon. After cleaning the excess NaK alloy, the raw product was heated in a furnace at certain temperature. Then, DI water was used to wash the salt by-product and resulted in a nanoporous Si with crystalline walls. The nanoporous Si had a high surface area. For example, a sample

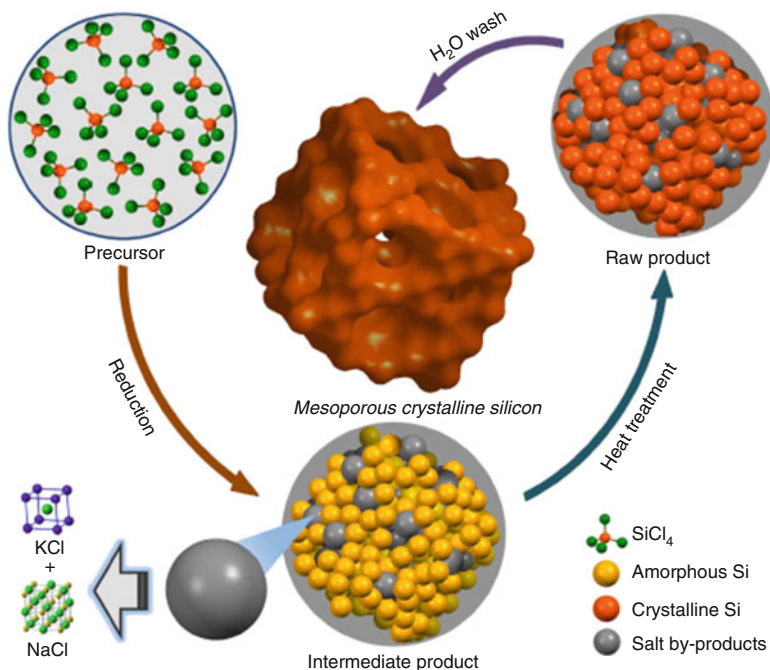


**Fig. 17.2** Scheme of the synthesis route of mPSi. The pictures of the intermediate product and raw product are schematic illustrations that do not exactly reflect the real structures. Reprinted with permission from Ref. [12]. Copyright 2014, Nature Publishing Group

heating at 600 °C (“mPSi-600”) showed a surface area of 497 m<sup>2</sup>/g. The mPSi-600 sample showed a band gap of 1.63 eV. After removing the surface oxide layer, it displayed a high H<sub>2</sub> evolution rate under visible light irradiation without cocatalyst. However, its dark reaction with water was also heavy. After 55 h of cyclic operation, it still showed an acceptable photocatalytic H<sub>2</sub> evolution rate (400 μmol H<sub>2</sub> h<sup>-1</sup> g<sup>-1</sup>). This result further evidenced the great potential of Si as a VLD photocatalyst.

### 17.2.2 Selenium

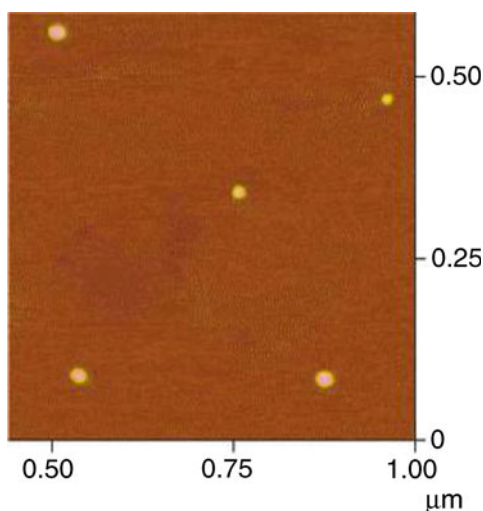
*Elemental Selenium (Se)* exists in six allotropes, including amorphous phase, monoclinic phase ( $\alpha/\beta/\gamma$ ), trigonal phase (grey), and Se gel. Amorphous Se (brick-red color) consists of random chains of 100 % twofold coordinated Se atoms, and crystalline trigonal Se and monoclinic Se are composed of infinite helical chains and Se<sub>8</sub> rings, respectively [40]. Amorphous Se has a band gap of 1.99 eV at room temperature, which decreases linearly as a function of elevated temperature toward that of the crystalline Se [41]. Amorphous Se powder can crystallize at 200 °C in vacuum. Then it has a band gap of 1.83 eV, which is identical to that of crystalline Se.

Elemental Se (especially the trigonal phase) has an excellent photoconductivity, thus it is widely used in solar cells, rectifiers, photographic exposure meters, xerography, and solid-state light sensing. However, there have been few reports on its photocatalytic applications.

The first example of Se photocatalyst was reported by Oak Ridge National Laboratory (U.S.A.) in 2004 [13] (Fig. 17.3). Uniform amorphous Se nanoparticles (ca. 25 nm) were prepared by reduction of aqueous selenious acid with freshly prepared ice-cold  $\text{NaBH}_4$ . The experiment was conducted at ambient conditions, and TX-100 was added to stabilize the Se nanoparticles. These Se nanoparticles can realize photocatalytic decoloration of methyl blue (MB) under the irradiation of UV light. Bulk amorphous Se was also tested, but it did not exhibit obvious photocatalytic activity. The reason can be ascribed to the energy mismatch of its CB or VB level for the photocatalysis.

Another example of Se photocatalyst was reported in 2011, and the photocatalytic activity of trigonal Se was proved for the first time [14]. Single crystalline Se nanorods were prepared via a polymer-assisted chemical reduction method. Typically, sodium salt of carboxymethyl cellulose and  $\text{SeO}_2$  were dissolved in the dilute NaOH solution. Then  $\text{NaBH}_4$  solution was then added dropwise to reduce the  $\text{SeO}_2$  to Se nanorods at 25 °C. The as-prepared Se nanorods were indexed to the trigonal phase, and proved to be single crystalline by HRTEM analysis. In the photocatalytic degradation for MB, it displayed an excellent activity under irradiation of UV light. Recycling test also suggested its high stability in a long-term photocatalytic experiment. Moreover, the Se nanorods showed an interesting “memory effect” during photocatalysis. After turning off the light, the degradation of MB can continue for a while. The ESR test evidenced that hydroxyl radicals could be attained without the irradiation.

**Fig. 17.3** AFM images of selenium nanoparticle stabilized in TX-100 micelle. Reprinted with permission from Ref. [13]. Copyright 2004, American Chemical Society



As a promising photocatalyst, the study of elemental Se is limited. The aforementioned work only reported its photocatalytic activity in the degradation of organic dyes. Other applications such as water splitting, CO<sub>2</sub> reduction, or bacterial killing are still lacking. Moreover, the nanostructured Se can also be combined with other well-known photocatalysts. This may lead to the improvement of photocatalytic activity for the whole composite.

### 17.2.3 Red Phosphorus

*Elemental phosphorus (P)* can exist in several forms including the white (P<sub>4</sub>), black, and red allotropes. Red P is the most abundant and easily available [42]. It is stable under ambient conditions and eco-friendly due to its nontoxicity [43]. Red P can be further classified into five allotropes. One is in amorphous phase, which is the most versatile and widely used in industry and our daily life. While the other four are in crystalline forms, they are type II (hexagonal), type III (unstable), type IV (fibrous phase), and type V (Hittorf phase) [44, 45]. The preparation of red allotropes using solution-based method has rarely been reported, because the high valence P (e.g. P<sup>5+</sup>, P<sup>3+</sup>) can hardly be reduced in the solution. Therefore, the high temperature gas–solid processes have become the main methods to obtain the red P. The commercial amorphous red P is mainly produced from the calcium (III) phosphate mineral. This reaction is conducted at more than 1000 °C and using coke as the reducing agent. The crystalline red allotropes are mainly produced by heating white P or amorphous red P in a sealed device assisting by catalysts (e.g. lead) [44, 45].

The red P allotropes displayed colors from blood red (amorphous) to dark red (fibrous type), corresponding to the slightly different light absorption edge from ~680 to ~720 nm [15–18]. This is very attractive for photocatalytic solar energy conversion. The photocatalytic activity of red P was first reported in our group [15] (Fig. 17.4). The amorphous red P was sealed in a vacuum tube furnace and heated to 450 °C for 12 h. The as-prepared products were microparticles coating with a layer of Hittorf phase (monoclinic) P nanorods. It was found that crystalline Hittorf red P can realize hydrogen evolution from a mixture of water and methanol under visible light irradiation. Moreover, it can also split water for the nearly stoichiometric evolution of H<sub>2</sub> and O<sub>2</sub>. In addition, it is also photocatalytic active for generating hydroxyl radicals. To elucidate its photocatalytic activity, the bands structure was calculated based on the coordination data of Hittorf red P. The calculated band gap is ca. 1.8 eV, and the reduction level of H<sup>+</sup>/H<sub>2</sub> lies within the band gap. Notably, the crystalline red P showed nearly two times of H<sub>2</sub> evolution rate compared with that of amorphous one, although the later has a 20 nm wider light absorption. Besides its less surface defects, this can be mainly ascribed to its nanorods morphology, which offered a higher surface to volume ratio and thus a lower recombination rate of electron/holes.

Red P is a typical molecular crystal. It is composed of P<sub>21</sub> molecular chains linked by van der Waals forces [45]. This structural characteristic brings red P a low

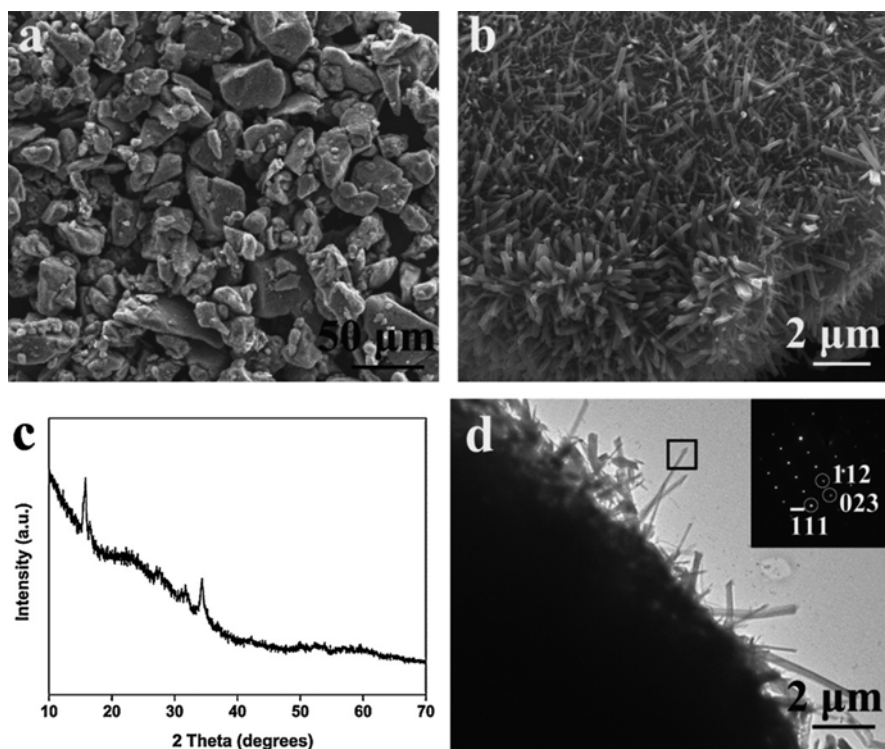


**Fig. 17.4** (a, b) SEM images, (c) a typical XRD pattern, and (d) TEM image (inset is ED patterns of marked square region) of crystalline red phosphorus. Reprinted with permission from Ref. [15]. Copyright 2012, Elsevier Ltd

conductivity and a high recombination rate of electrons/holes. Thus it suffers a relative low photocatalytic  $H_2$  evolution rate. To overcome this problem, we designed two kinds of nanostructured heterojunction to facilitate the charge carriers separation and transfer. One is the hierarchical microspheres assembled by  $YPO_4$  nanosheet/amorphous red P [16], and the other is the black P nanoparticle/amorphous red P composite [17].

The  $YPO_4$  nanosheet/amorphous red P microspheres were prepared via a facile hydrothermal method [17]. The starting materials were amorphous red P and  $YCl_3$  in aqueous solution. With the hydrothermal treatment, the  $YPO_4$  nanosheet/amorphous red P composite can be obtained by the reaction of red P, water, and  $YCl_3$ . Based on the time-dependent experiments, the formation process of the  $YPO_4$  nanosheet/amorphous red P composite can be demonstrated as follows. The solid red P microspheres firstly emerged from red P particles, which may be ascribed to the synergetic effect of the shear stress from water and the reaction between  $YCl_3$  and P. Then with gradual growth of the  $YPO_4$  nanosheet, a hollow interior was formed in the red P microsphere following the Kirkendall effect. Finally, the  $YPO_4$  nanosheet/amorphous red P hollow microspheres were produced after consumption

of  $\text{YCl}_3$ . The VLD photocatalysis experiments showed that the  $\text{YPO}_4$  nanosheet/amorphous red P hollow microspheres had enhanced photocatalytic  $\text{H}_2$  evolution rate than both of the components. A 55 wt%  $\text{YPO}_4$  composite was the best, which showed 6 times of  $\text{H}_2$  evolution rate than that of pure amorphous red P. The band structures analysis showed that the  $\text{YPO}_4$  had more negative CB and VB than those of red P. Thus the photoexcited holes can transfer from the VB of red P to the VB of  $\text{YPO}_4$ . This makes a better charge separation and transfer in the  $\text{YPO}_4$  nanosheet/amorphous red P composite.

The black P/red P heterojunction was prepared by an in-situ mechanical milling method [17]. During this process, the black P nanoparticles can be produced from the amorphous red P. By selecting the milling rate and time, composites with different weight percent of black P can be obtained (estimated by TGA analysis). Among them, the 50 wt% black P/red P composite displayed the best photocatalytic activity for VLD degradation of RhB dyes. The dynamic calculations showed that its apparent reaction rate was nearly three times compared with that of pure red P. Moreover, this value was comparable with that of CdS, a well-known VLD photocatalyst. The DFT calculation was then performed to explore the band structures of black P and red P. Results showed that the CB of red P is more negative than that of black P. Thus the photoexcited electrons can transfer from the CB of red P to the CB of black P, and more photoexcited holes can avoid recombination and involve in the reactions with organic dyes.

The aforementioned work efficiently improved the photocatalytic activity of red P via making the nanoscale heterojunctions. However, the amorphous red P still suffers from its excess defects on the surface, which are the electrons/holes trapping sites. Therefore, we decreased the size of crystalline red P allotropes and evaluated their photocatalytic activity [18] (Fig. 17.5). Similar work has scarcely been reported before, and a few examples usually used the high toxic agents. To overcome this drawback, we performed the fabrication using red P as the starting material and without any catalyst. Certain vacuum ( $-0.03$  to  $-0.09$  MPa) at  $550^\circ\text{C}$  was set in the sealed reaction tube to help the sublimation of red P. While a silicon wafer was placed in the tube to assist the growth of crystalline red P. Then after gradual cooling, high purity fibrous phase P submicron fibers were grown on the silicon wafer. In the VLD photocatalytic degradation of RhB, it displayed better than the amorphous P nanoparticles. By altering the growth wafer, type II phase red P nanorods were also fabricated. Interestingly, it displayed a much lower photocatalytic activity than that of fibrous red P, although they had the similar surface area and light absorption range. The reason might be ascribed to their difference in crystalline structures.

These results showed that crystalline red P might be better candidate than amorphous red P due to their less defects on the surface. However, simple methods and large-scale preparation for crystalline red P are great challenges. Moreover, even in the crystalline forms, the red P still affords a low conductivity. As a result, to construct the nanoscale heterojunction might be effective to improve the photocatalytic activity of red P. Additionally, combine red P with high conductivity materials (e.g. graphene) might also be useful to improve its activity.

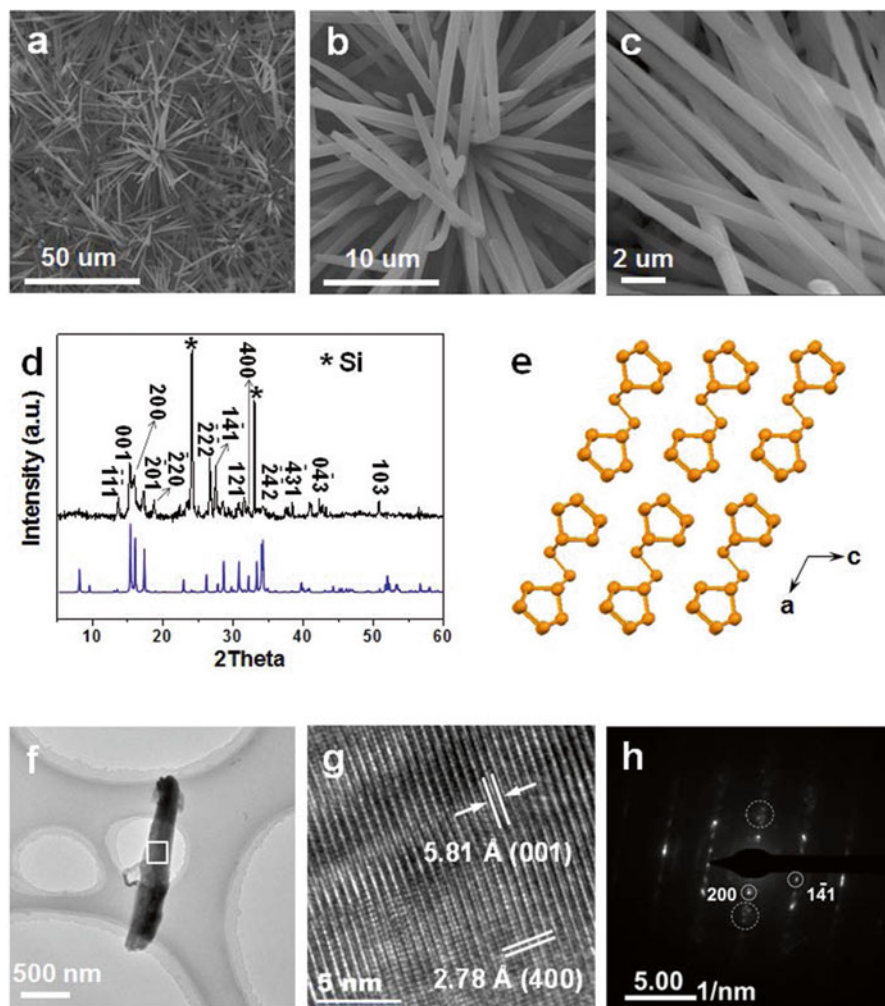


**Fig. 17.5** (a–c) Representative SEM images, (d) XRD patterns, the blue curve was the simulated pattern based on the crystallographic data, (e) atomic structure, and (f–h) TEM, HRTEM, and SAED analysis of fibrous phosphorus submicron fibers obtained at  $-0.06$  MPa, 100 mg red phosphorus, and  $550$  °C. Reprinted with permission from Ref. [18]. Copyright 2014, Royal Society of Chemistry

### 17.2.4 Sulfur

*Elemental sulfur* (S) has more than 30 solid allotropes [46]. As the molecular crystal, they were mainly composed of unbranched cyclic molecules sizes ranging from 6 to 20. These cyclic molecules stacked via van der Waals forces and formed different crystalline structures. Among them, the  $S_8$  cyclic molecules are the most stable configuration at standard temperature and pressure (STP) [46]. It can crystallize to

form three solid allotropes: orthorhombic  $\alpha$ -S, monoclinic  $\beta$ -S, and  $\gamma$ -S. The bulk  $\alpha$ -S is very abundant and can exist naturally on the earth. In 2012, Liu et al. investigated the electronic structure and photocatalytic activities of  $\alpha$ -S for the first time [19]. Bulk  $\alpha$ -S powder has a band gap of  $\sim 2.79$  eV and suitable CB and VB levels for photocatalysis ( $\sim -0.4$  eV vs. NHE,  $\sim 2.39$  eV vs. NHE). It can generate hydroxyl radicals under UV and visible light irradiation. Thus the organic dyes can be photocatalytic degradation in the presence of  $\alpha$ -S particles. Moreover, after making  $\alpha$ -S as a photoanode, it displayed apparent photoelectrochemical water splitting activity. However, due to its bad conductivity, the electrons/holes recombination is heavy in the S particles. This characteristic greatly decreased its photocatalytic activity. To overcome this drawback, they decreased the size of S by mechanical milling. The smaller size gives rise to a larger surface to volume ratio and suppresses the recombination of electrons/holes. Therefore, the mechanical milled S showed much enhanced photocatalytic activity in RhB degradation than its bulk counterpart.

Besides the high recombination rate of electrons/holes, another problem for S is its bad hydrophilic property. To solve these problems, several methods have been reported recently, such as combining S with graphene [20] or with graphene/g-C<sub>3</sub>N<sub>4</sub> [21], fabricating S/In<sub>2</sub>O<sub>3</sub> heterojunction [22] or preparing the S-copolymer nanofibers [23].

Hu et al. have prepared a kind of S nanoparticles/graphene composite using Na<sub>2</sub>S and Na<sub>2</sub>SO<sub>3</sub> as the S sources [20]. Na<sub>2</sub>S and Na<sub>2</sub>SO<sub>3</sub> can adsorb on the surface of graphene, and then reacted with each other to form S nanoparticles ( $< 0.3$   $\mu\text{m}$ ) under acidic condition. The as-prepared S/graphene composite can facilitate the charge separation and transfer. Moreover, graphene increased the hydrophilic property of the composite. Thus it displayed much better photocatalytic activity in the degradation of MB than that of pure S.

Our group has prepared graphene (RGO) and g-C<sub>3</sub>N<sub>4</sub> (CN) nanosheet co-wrapped S submicron particles as a new member of elemental S photocatalysts [21]. As shown in Fig. 17.6, two distinctive structures were fabricated by wrapping RGO and CN sheets in different orders. In the preparation, Triton X-100 was used as a capping agent for sulfur particles to introduce hydrophilic groups onto the surface and to limit the size of sulfur particles to the submicrometer region. The GO sheets were finally reduced to RGO sheets by the photochemical technique. The graphene/g-C<sub>3</sub>N<sub>4</sub> nanosheet can effectively improve the hydrophilic property of the composite. In addition, this special structure can also facilitate the charge separation and transfer. Therefore, both of the co-wrapped S particles displayed much better in photocatalytic bacteria disinfection than the pure S.

Chen et al. have prepared an S/In<sub>2</sub>O<sub>3</sub> core-shell heterojunction by a simple mechanical milling method [22]. Typically, commercial S and In<sub>2</sub>O<sub>3</sub> nanoparticles were mixed with certain DI water and milled at 400 rounds/min for 3 h. After that, the hydrophilic In<sub>2</sub>O<sub>3</sub> nanoparticles can anchor on the surface of S particles, and greatly improved the hydrophilic property of the composite. Additionally, the band alignment between S and In<sub>2</sub>O<sub>3</sub> can facilitate the charge separation and transfer. Therefore, the S/In<sub>2</sub>O<sub>3</sub> heterojunction showed nearly 14 times of apparent reaction rate compared with that of pure S in the photocatalytic degradation of MB.

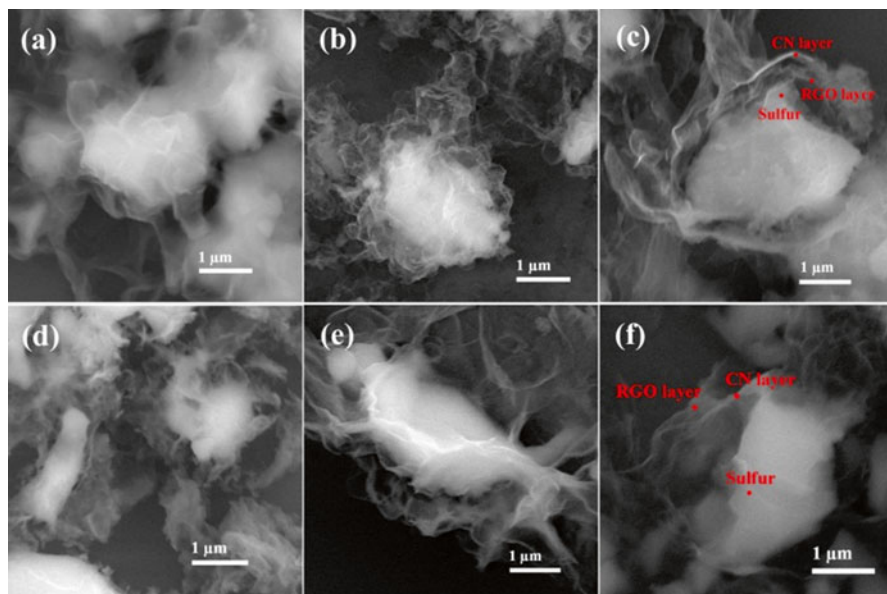


**Fig. 17.6** Scanning electron microscopy (SEM) images of (a)  $\text{RGOS}_s$ , (b)  $\text{CNRGOS}_s$ , (c) cross section of  $\text{CNRGOS}_s$  microspheres, (d)  $\text{CNS}_s$ , (e)  $\text{RGO/CNS}_s$ , and (f) cross section of  $\text{RGO/CNS}_s$  microspheres. Reprinted with permission from Ref. [21]. Copyright 2013, American Chemical Society

Zhang and his coworkers have prepared a kind of unique S-copolymer nanofibers using a hard template method [23]. With S and 1, 3-diisopropenylbenzene (DIB) as the starting materials, bulk S copolymers were firstly synthesized by a copolymerized method. Then, AAO membranes were used as templates for the preparation of copolymer nanowires with different content of S. The as-prepared nanofibers had a uniform length and diameter, and the S was homogenously distributed. After making them into photoanodes, the best S-copolymer nanofibers displayed about fivefold photocurrent compared with that of pure S under visible light irradiation. The authors ascribed this enhancement to the incorporation of DIB and the small size of the copolymer. The former decreased the band gap and thus improved the absorption of visible light. While the later increased the surface to volume ratio and thus improve the charge separation/transfer.

In addition, a kind of interesting S quantum dots (QDs) has been prepared very recently [24] (Fig. 17.7). By oxidation of CdS QDs with  $\text{HNO}_3$ , S QDs with average size of 1.6 nm was formed in a water/oil system. It can well disperse in the water due to abundant oxidized S species on the surface. The S QDs itself did not have photocatalytic activity. However, it can decorate on the surface of  $\text{TiO}_2$ , and bring a 193 times enhancement of photocatalytic activity in water splitting.

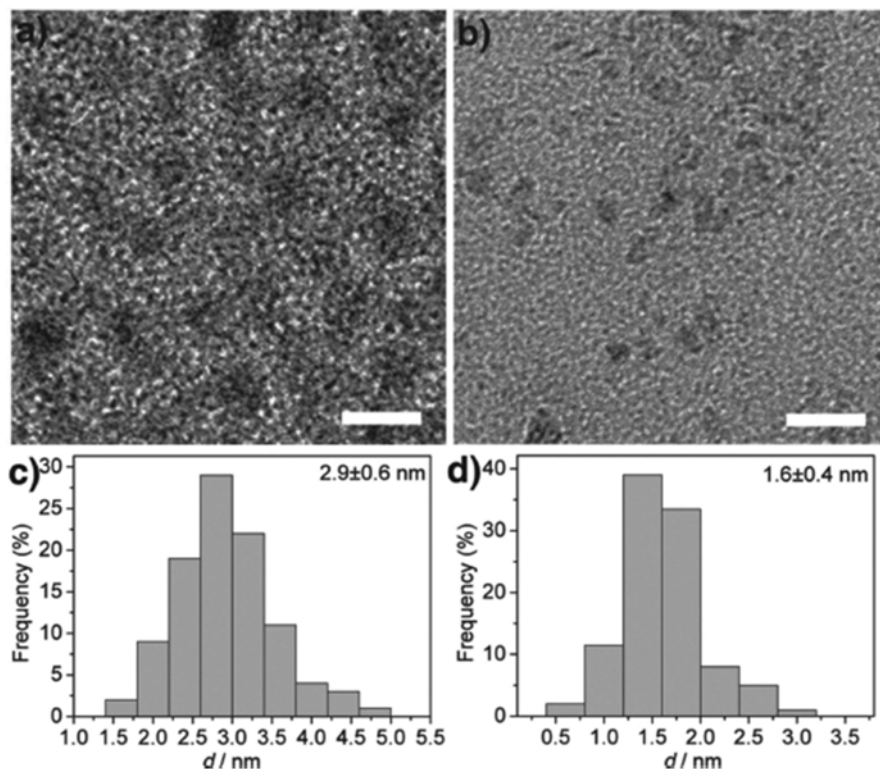


**Fig. 17.7** (a) TEM image of a large number of CdS QDs. (b) TEM image of S QDs obtained from CdS QDs. (c) Size distribution of CdS QDs. (d) Size distribution of S QDs obtained from CdS QDs. Scale bars in (a, b) are 5 nm. Reprinted with permission from Ref. [24]. Copyright 2014, Wiley-VCH

### 17.2.5 Boron

*Boron (B)* has attracted wide interest due to its interesting properties, such as light weight, high strength, high hardness, high melting point, and high chemical resistance. The pure elemental B was obtained early in 1909 [47]. It has at least 17 polymorphs (including B-rich compounds) as a result of electron-deficient bonding [48]. All polymorphs contain  $B_{12}$  icosahedral clusters as a basic building block. Amongst,  $\alpha$ -tetragonal,  $\alpha$ -rhombohedral,  $\beta$ -tetragonal, and  $\beta$ -rhombohedral B crystals are the four main forms under ambient conditions. These crystals can be classified as the covalent crystals.

Experimentally,  $\beta$ -rhombohedral B is the most thermodynamically stable form. In 2013, Liu and his coworkers studied the electronic structure and photocatalytic activities of  $\beta$ -rhombohedral B for the first time [25]. The submicron-sized  $\beta$ -rhombohedral B particles showed an attractive narrow band gap of 1.66 eV. It can generate hydroxyl radicals linearly under visible light irradiation. HRTEM image

showed a thin layer of amorphous oxide coating on the surface of B. After cleaning this layer by  $H_2$  reduction, its photocatalytic activity increased up to 2.2 times. However, the photocatalytic activity of  $\beta$ -rhombohedral B is very weak, even worse than other reported elemental photocatalyst such as Se, P, and S [13–24]. This can be mainly ascribed to its low conductivity at ambient condition. Considering other advances of B such as high abundance, high stability, and visible light response, it is meaningful to further study the elemental B photocatalyst.

### 17.3 Developments of Bismuth Photocatalyst (Semimetal)

*Elemental bismuth (Bi)*, in its bulk form (rhombohedral phase), is a typical semimetal. It has a low abundance on the earth, even less than the silver. However, the elemental Bi has two unique physical properties [26–29]. First, it shows a morphology-dependent surface plasmonic resonance (SPR) in the range of 220–280 nm. Second, after decreasing its size smaller than ca. 50 nm, it will transform from a semimetal to a semiconductor. Recently, based on these two points, elemental Bi has been studied as a promising photocatalyst.

The first example of elemental Bi photocatalyst was reported by Chen et al. in 2013 [26]. Via a PVP-assisted chemical reduction, uniform Bi nanospheres (solid/hollow) were prepared from  $Bi^{3+}$  solution. It has an average diameter from ~240 to 110 nm depending on the concentration of PVP. These Bi nanospheres showed obvious photocatalytic activity for reduction of Cr (VI) under both UV and visible light. Among them, the 110 nm Bi nanospheres with a hollow interior was the best. Its UV–Vis diffuse reflectance spectrum showed two main absorption peaks. One is centered at ca. 280 nm, which can be ascribed to its SPR effect. The other is centered at ca. 390 nm, which was realized as a characteristic of semiconductor.

Thereafter, Zhou et al. have prepared a Bi film using the electrochemical method. The as-prepared Bi film exhibited semimetallic behavior [27]. This was evidenced by the temperature dependence electrical resistivity measurements. Under UV light irradiation, it can generate hydroxyl radicals, which was detected by the ESR. Moreover, the Bi film showed an obvious photocatalytic activity for oxidation of NO under UV light irradiation (37.7 % removal after 30 min). To elucidate the photocatalytic mechanism, a DFT calculation toward its band structure was performed. This result further proved that it was a semimetal with an overlapped CB and VB. Dong et al. also reported a kind of semimetal Bi photocatalyst [28]. The as-prepared Bi particles had a single crystalline nature and the size of 100–200 nm. They can effectively remove the NO under UV light irradiation. Moreover, it displayed an interesting “memory effect” for photocatalysis after turning off the light. An SPR-related mechanism was demonstrated to illustrate its activity.

These results showed that the elemental Bi was a promising photocatalyst. However, its activity was relative low due to the high recombination rate of electrons/holes. Recently, Jiao and his coworkers fabricated a kind of Bi–Ag alloy nanospheres toward the improved activity [29] (Fig. 17.8). The Bi–Ag alloy nanospheres were well dispersed with an average size of 52 nm. Its UV–Vis reflectance

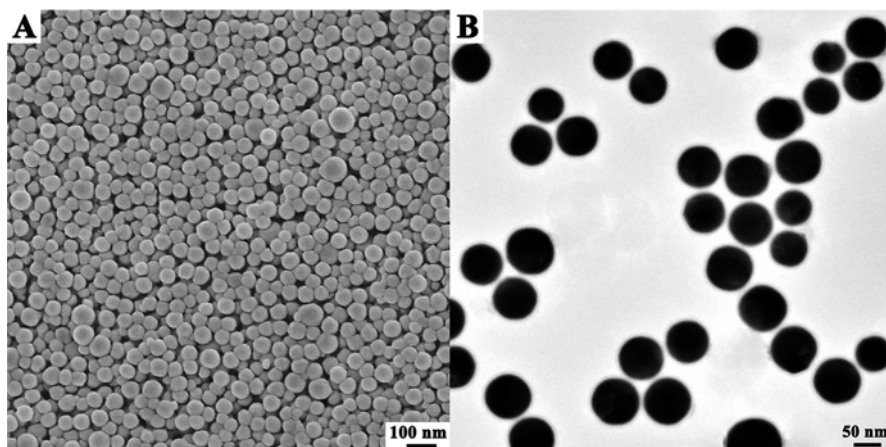


**Fig. 17.8** (a) SEM and (b) TEM images of BiAg alloy nanoparticles. Reprinted with permission from Ref. [29]. Copyright 2014, American Chemical Society

spectrum mainly displayed the characteristic of Ag. Under UV–Visible light irradiation, it showed a fourfold of photocurrent response compared with that of pure Bi nanospheres. Furthermore, an apparent  $H_2$  evolution was observed for the first time using elemental Bi nanospheres. The enhancement of activity was ascribed to the addition of Ag, which facilitate the charge separation and transfer in the alloy.

## 17.4 Outlook and Conclusions

In summary, nanoscience has effectively promoted the development of elemental photocatalysts. Morphology and crystal facet control may offer opportunities for the fabrication of more efficient photocatalytic materials. For example, most elemental photocatalysts reported in the literature are 0-dimension (0-D) nanoparticles (or nanospheres) and 1-D nanofibers/nanorods (or submicron fibers). Future research efforts should be focused on 3-D hierarchical assembly, particularly those with highly porous structures. 2-D nanosheets and nanoplates are also worth exploring because of their large surface area and distinctive electronic property. Recently, exposing highly active crystal facet has attracted great attention for traditional photocatalysts such as  $TiO_2$  [49, 50]. This is a great challenge for the elemental photocatalysts considering the complex procedures involved in the preparation of crystalline red P and other elements. More efficient preparation methods for crystalline elemental photocatalysts would need to be developed to initiate crystal facet control studies. Another limitation of elemental photocatalysts (maybe except Si) is their low conductivity and high recombination rate of electrons/holes. To overcome this problem, it may be useful to design and fabricate heterostructures. These include the p–n junction and the heterophase junction of same elements or composites with graphene or noble metals.

## References

1. Fujishima A, Honda K (1972) Electrochemical photolysis of water at a semiconductor electrode. *Nature* 238:37–38
2. Kudo A, Miseki Y (2009) Heterogeneous photocatalyst materials for water splitting. *Chem Soc Rev* 38:253–278
3. Chen XB, Shen SH, Guo LJ et al (2010) Semiconductor-based photocatalytic hydrogen generation. *Chem Rev* 110:6503–6570
4. Yu S, Yun HJ, Kim YH et al (2014) Carbon-doped TiO<sub>2</sub> nanoparticles wrapped with nanographene as a high performance photocatalyst for phenol degradation under visible light irradiation. *Appl Catal B Environ* 144:893–899
5. Jia L, Wang D, Huang Y et al (2011) Highly durable N-doped graphene/CdS nanocomposites with enhanced photocatalytic hydrogen evolution from water under visible light irradiation. *J Phys Chem C* 115:11466–11473
6. Su ZX, Wang L, Grigorescu S et al (2014) Hydrothermal growth of highly oriented single crystalline Ta<sub>2</sub>O<sub>5</sub> nanorod arrays and their conversion to Ta<sub>3</sub>N<sub>5</sub> for efficient solar driven water splitting. *Chem Comm* 50:15561–15564
7. Hisatomi T, Katayama C, Moriya Y et al (2013) Photocatalytic oxygen evolution using BaNbO<sub>2</sub>N modified with cobalt oxide under photoexcitation up to 740 nm. *Energ Environ Sci* 12:3595–3599
8. Liu G, Niu P, Cheng HM (2013) Visible-light-active elemental photocatalysts. *ChemPhysChem* 14:885–892
9. Kang ZH, Tsang CHA, Wong NB et al (2007) Silicon quantum dots: a general photocatalyst for reduction, decomposition, and selective oxidation reactions. *J Am Chem Soc* 129:12090–12091
10. Shao MW, Cheng L, Zhang XH et al (2009) Excellent photocatalysis of HF-treated silicon nanowires. *J Am Chem Soc* 131:17738–17739
11. Su JY, Yu HT, Quan X et al (2013) Hierarchically porous silicon with significantly improved photocatalytic oxidation capability for phenol degradation. *Appl Catal B Environ* 138–139:427–433
12. Dai F, Zai JT, Yi R et al (2014) Bottom-up synthesis of high surface area mesoporous crystalline silicon and evaluation of its hydrogen evolution performance. *Nat Comm* 5:3605
13. Nath S, Ghosh SK, Panigahi S et al (2004) Synthesis of selenium nanoparticle and its photocatalytic application for decolorization of methylene blue under UV irradiation. *Langmuir* 20:7880–7883
14. Chiou YD, Hsu YJ (2011) Room-temperature synthesis of single-crystalline Se nanorods with remarkable photocatalytic properties. *Appl Catal B Environ* 105:211–219
15. Wang F, Ng WKH, Yu JC et al (2012) Red phosphorus: an elemental photocatalyst for hydrogen formation from water. *Appl Catal B Environ* 111–112:409–414
16. Wang F, Li CH, Li YC et al (2012) Hierarchical P/YPO<sub>4</sub> microsphere for photocatalytic hydrogen production from water under visible light irradiation. *Appl Catal B Environ* 119–120:267–272
17. Shen ZR, Sun ST, Wang WJ et al (2015) A black–red phosphorus heterostructure for efficient visible-light-driven photocatalysis. *J Mater Chem A* 3:3285–3289
18. Shen ZR, Hu ZF, Wang WJ et al (2014) Crystalline phosphorus fibers: controllable synthesis and visible-light-driven photocatalytic activity. *Nanoscale* 6:14163–14167
19. Liu G, Niu P, Yin LC et al (2012) Alpha-sulfur crystals as a visible-light-active photocatalyst. *J Am Chem Soc* 134:9070–9073
20. Hu CY, Zheng SZ, Lian CJ et al (2014) One-step synthesis of a sulfur–graphene composite with enhanced photocatalytic performance. *Appl Surf Sci* 314:266–272
21. Wang WJ, Yu JC, Xia DH et al (2013) Graphene and g-C<sub>3</sub>N<sub>4</sub> nanosheets cocrapped elemental  $\alpha$ -sulfur as a novel metal-free heterojunction photocatalyst for bacterial inactivation under visible-light. *Environ Sci Technol* 47:8724–8732

22. Meng SG, Cao ZS, Fu XL et al (2015) Fabrication of hydrophilic S/In<sub>2</sub>O<sub>3</sub> core-shell nanocomposite for enhancement of photocatalytic performance under visible light irradiation. *Appl Surf Sci* 315:188–197
23. Zhuo SF, Huang Y, Liu CB et al (2014) Sulfur copolymer nanowires with enhanced visible-light photoresponse. *Chem Comm* 50:11208–11210
24. Li SX, Chen DJ, Zheng FY et al (2014) Water-soluble and lowly toxic sulphur quantum dots. *Adv Funct Mater* 24:7133–7138
25. Liu G, Yin LG, Niu P et al (2013) Visible-light-responsive  $\beta$ -rhombohedral boron photocatalysts. *Angew Chem Int Ed* 52:6242–6245
26. Qin F, Wang RM, Li GF et al (2013) Highly efficient photocatalytic reduction of Cr(VI) by bismuth hollow nanospheres. *Catal Comm* 42:14–19
27. Zhang Q, Zhou Y, Wang F et al (2014) From semiconductors to semimetals: bismuth as a photocatalyst for NO oxidation in air. *J Mater Chem A* 2:11065–11072
28. Dong F, Xiong T, Sun YJ et al (2014) A semimetal bismuth element as a direct plasmonic photocatalyst. *Chem Comm* 50:10386–10389
29. Jiao ZB, Zhang Y, Ouyang SX et al (2014) BiAg alloy nanospheres: a new photocatalyst for H<sub>2</sub> evolution from water splitting. *ACS Appl Mater Interfaces* 6:19488–19493
30. Bookbinder DC, Lewis NS, Bradley MG et al (1979) Photoelectrochemical reduction of N,N'-dimethyl-4,4'-bipyridinium in aqueous media at p-type silicon: sustained photogeneration of a species capable of evolving hydrogen. *J Am Chem Soc* 101:7721–7723
31. Golovanova GF, Petrov AS, Silaev EA (1982) Photocatalytic decomposition of CCl<sub>4</sub> on a silicon surface. *Kinet Catal* 23:1084–1087
32. Taniguchi Y, Yoneyama H, Tamura H (1983) Hydrogen evolution on surface-modified silicon powder photocatalysis in aqueous ethanol solutions. *Chem Lett* 3:269–272
33. Wang YL, Wang TY, Da PM et al (2013) Silicon nanowires for biosensing, energy storage, and conversion. *Adv Mater* 25:5177–5195
34. Chen YW, Prange JD, Duhnen S et al (2011) Atomic layer-deposited tunnel oxide stabilizes silicon photoanodes for water oxidation. *Nat Mater* 10:539–544
35. Jun K, Lee YS, Buonassisi T et al (2012) High photocurrent in silicon photoanodes catalyzed by iron oxide thin films for water oxidation. *Angew Chem Int Ed* 51:423–427
36. Peng KQ, Wang X, Li L et al (2013) Silicon nanowires for advanced energy conversion and storage. *Nano Today* 8:75–97
37. Levine A, Yuan GB, Xie J et al (2010) Preparations and energetic applications of Si nanowires. *Sci Adv Mater* 2:463–473
38. Chen ZH, Tang YB, Liu Y et al (2009) Dye degradation induced by hydrogen-terminated silicon nanowires under ultrasonic agitations. *J Appl Phys* 105:034307
39. Verplanck N, Galopin E, Camart JC et al (2007) Reversible electrowetting on superhydrophobic silicon nanowires. *Nano Lett* 7:813–817
40. Benkheldir ML (2006) Defect levels in the amorphous selenium bandgap (PhD thesis), Katholieke Universiteit Leuven
41. Bhatnagar AK, Venugopal Reddy K, Srivastava V (1985) Optical-energy gap of amorphous selenium-effect of annealing. *J Phys D* 18:L149–L153
42. Roth WL, Dewitt TW, Smith AJ (1947) Polymorphism of red phosphorus. *J Am Chem Soc* 69:2881–2885
43. Young JA (2004) Red phosphorus. *J Chem Educ* 81:945
44. Ruck M, Hoppe D, Wahl B et al (2005) Fibrous red phosphorus. *Angew Chem Int Ed* 44:7616–7619
45. Winchester RAL, Whitby M, Shaffer MSP (2009) Synthesis of pure phosphorus nanostructures. *Angew Chem Int Ed* 48:3616–3621
46. Stuedel R, Eckert B (2003) Solid sulfur allotropes. *Top Curr Chem* 230:1–79
47. Eremets MI, Struzhkin VV, Mao HK et al (2001) Superconductivity in boron. *Science* 293:272–274

48. Oganov AR, Chen JH, Gatti C et al (2009) Ionic high-pressure form of elemental boron. *Nature* 457:863–867
49. Yang HG, Sun CH, Qiao SZ et al (2008) Anatase TiO<sub>2</sub> single crystals with a large percentage of reactive facets. *Nature* 453:638–641
50. Liu G, Yu JC, Lu GQ et al (2011) Crystal facet engineering of semiconductor photocatalysts: motivations, advances and unique properties. *Chem Comm* 47:6763–6783

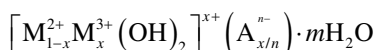
# Chapter 18

## Application of Layered Double Hydroxides (LDHs) in Photocatalysis

Shoji Iguchi, Kentaro Teramura, Saburo Hosokawa, and Tsunehiro Tanaka

### 18.1 Fundamentals of Layered Double Hydroxides (LDHs)

Layered double hydroxides (LDHs), also called hydrotalcite-like compounds, are natural and/or synthetic anionic clay materials. The term LDH was coined in the early works of Feithnecht, who named them “Doppelschichtstrukturen” (i.e., double layer structures), presuming a structure with intercalated hydroxide layers. This hypothesis was refuted many years later on the basis of single-crystal X-ray diffraction (XRD) analysis, which showed that LDHs consist of positively charged two-dimensional (2D) sheets, with all the cations located in the same layer, and the charge-compensating anions and water molecules in the interlayer region (Fig. 18.1) [1, 2]. It is known that the parent material of these anionic clays is the natural mineral hydrotalcite, which has the formula  $\text{Mg}_6\text{Al}_2(\text{OH})_{16}\text{CO}_3 \cdot 4\text{H}_2\text{O}$ . The general formula of LDHs is

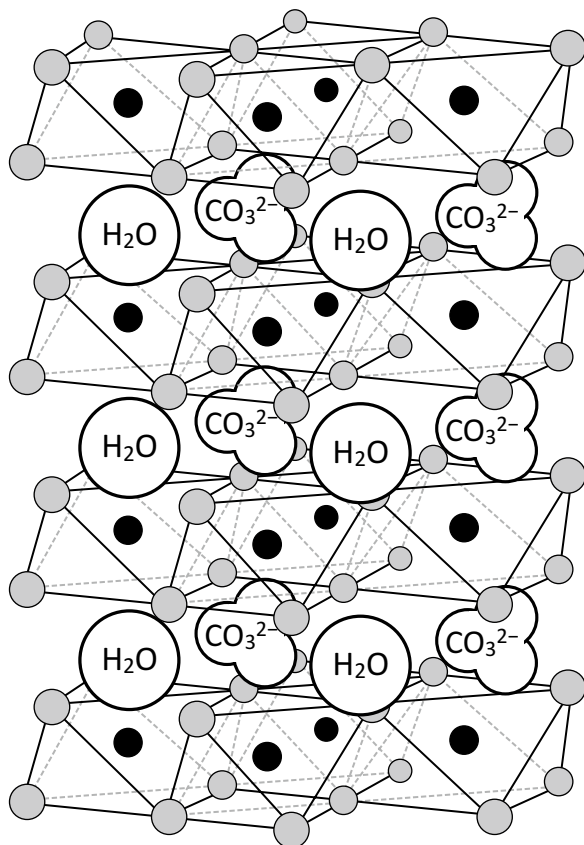


where  $\text{M}^{2+}$  and  $\text{M}^{3+}$  are divalent and trivalent cations, respectively;  $x$  represents the molar ratio of  $\text{M}^{3+}/(\text{M}^{2+} + \text{M}^{3+})$ , whereas  $\text{A}^{n-}$  is the interlayer anion of valence  $n$ . The natures of  $\text{M}^{2+}$ ,  $\text{M}^{3+}$ ,  $x$ , and  $\text{A}^{n-}$  might vary over a wide range, thus giving rise to a large number of isostructural materials, with variegated physical and chemical properties. The value of  $x$  to form a pure LDH phase is reported to range from 0.2 to 0.4. When the  $x$  value is outside of this range, hydroxides or other compounds are formed as impurity phases. The divalent cations ( $\text{M}^{2+} = \text{Fe}^{2+}$ ,  $\text{Co}^{2+}$ ,  $\text{Ni}^{2+}$ ,  $\text{Cu}^{2+}$ ,  $\text{Zn}^{2+}$ ,  $\text{Mn}^{2+}$ ,  $\text{Cd}^{2+}$ , and  $\text{Ca}^{2+}$ ) and the trivalent cations ( $\text{M}^{3+} = \text{Co}^{3+}$ ,  $\text{Fe}^{3+}$ ,  $\text{Mn}^{3+}$ ,  $\text{Ga}^{3+}$ ,  $\text{Cr}^{3+}$ ,  $\text{In}^{3+}$ ,  $\text{V}^{3+}$ ,  $\text{Y}^{3+}$ ,  $\text{La}^{3+}$ ) form LDHs through fully or partially replacing  $\text{Mg}^{2+}$  or  $\text{Al}^{3+}$  of the brucite-like layer of

---

S. Iguchi • K. Teramura (✉) • S. Hosokawa • T. Tanaka (✉)  
Department of Molecular Engineering, Graduate School of Engineering, Kyoto University,  
Kyotodaigaku Katsura, Nishikyo-ku, Kyoto 615-8510, Japan  
e-mail: [teramura@moleng.kyoto-u.ac.jp](mailto:teramura@moleng.kyoto-u.ac.jp); [tanakat@moleng.kyoto-u.ac.jp](mailto:tanakat@moleng.kyoto-u.ac.jp)

**Fig. 18.1** Schematic representation of the structure of LDHs containing  $\text{CO}_3^{2-}$  as interlayer anions



hydroxalcite [3]. In addition, tetravalent cations, such as  $\text{Ti}^{4+}$  [4],  $\text{Zr}^{4+}$  [5], and  $\text{Sn}^{4+}$  [6], also incorporate into the brucite-like layer, whereas some evidences reveal that  $\text{M}^{4+}$  cations form amorphous oxide particles instead of incorporating in the brucite-like layer. Multi-metal cations can be simultaneously incorporated into the brucite-like layer to prepare multi-component LDHs, provided  $x$  is in the correct range. The most common anion found in naturally occurring LDHs is carbonate ( $\text{CO}_3^{2-}$ ), which shows a high affinity for the interlayer in a series of LDHs. In fact, various kinds of charge-compensating anions may be incorporated into the interlayer, namely inorganic anions ( $\text{NO}_3^-$ ,  $\text{SO}_4^{2-}$ , halides, oxyanions, silicates, etc.), polyoxometalate anions ( $\text{Mo}_7\text{O}_{24}^{6-}$ ,  $\text{W}_7\text{O}_{24}^{6-}$ ,  $\text{V}_{10}\text{O}_{28}^{6-}$ ,  $\text{PMo}_{12}\text{O}_{40}^{3-}$ ,  $\text{PW}_{12}\text{O}_{40}^{3-}$ , etc.), complex anions (porphyrin complexes, phthalocyanine complexes,  $\text{Fe}(\text{CN})_6^{4-}/\text{Fe}(\text{CN})_6^{3-}$ ), and organic anions (carboxylates, dicarboxylates, alkylsulfates, alkanesulfates, etc.) [3].

LDHs are widely used as basic materials for  $\text{CO}_2$  capture and storage [7], removal of organic and inorganic anions from the aqueous solution [8–10], and base-catalyzed reactions [11]. Ebitani et al. reported that Mg–Al LDHs catalyze the aldol condensation of carbonyl compounds in an aqueous solution because their surface base sites show the property of high water tolerance [12], indicating that basic sites of LDHs and their derivatives may function in the presence of water.

## 18.2 Preparation

As reviewed by Reichle [13] and Cavani et al. [1], various preparation methods of LDHs have been developed. The optimum conditions, e.g., atmosphere, temperature, pH during the precipitation, concentration of precursor solution, aging procedure, etc., should be chosen in accordance with the kinds of metal components constituting the hydroxide sheets.

*Co-precipitation method:* LDHs are traditionally synthesized by co-precipitation from aqueous solution. The most common procedure is the constant-pH co-precipitation process, wherein the mixed aqueous solution of the metal components and the base solution (normally, an aqueous solution of NaOH) are added simultaneously to an aqueous solution of  $\text{Na}_2\text{CO}_3$  to maintain the suspension at a stable pH. In the so-called variable pH co-precipitation process, LDHs containing  $\text{CO}_3^{2-}$  as interlayer anions are prepared by gradually adding the aqueous solution containing the metal cations to the aqueous solution of  $\text{Na}_2\text{CO}_3$  until the suspension reaches a specified pH. As necessary, the aqueous solution of NaOH is then used to maintain the pH until the precipitation is completed. In both processes, the resulting suspension is stirred at a certain temperature as an aging for varying periods of time, and then collected by filtration. The filter cake is washed with pure water and is then dried [14].

*Hydrothermal synthesis:* Hydrothermal treatment is usually applied to obtain well-crystallized LDHs with large platelets. Homogeneous co-precipitation method under hydrothermal conditions is an advanced technique to synthesize well-defined LDH particles. Ogawa et al., for example, reported the following procedure: an aqueous solution containing urea and salts of the metal components mixed in a certain ratio were transferred into an autoclave and heated at 393 K for 24 h. After cooling to room temperature, the solid precipitate was collected and washed with deionized water. The pH of the solution changed from 3.4 to 8.4 during the course of the reaction, through the hydrolysis of urea [15]. We synthesized various kinds of LDHs via co-precipitation method combined with hydrothermal treatment as follows: after constant pH co-precipitation process at room temperature, the resulting suspension is transferred to a stainless steel autoclave with an inner Teflon vessel, and aged under hydrothermal conditions at 383 K. The resultant solid is collected by filtration and washed with 1.0 L of ultrapure water, and then dried at 383 K in air [16].

*Rehydration:* Since atmospheric  $\text{CO}_2$  is incorporated into the structure of LDH with high affinity, most synthesized LDHs contain  $\text{CO}_3^{2-}$  as interlayer anions or as surface-adsorbed species. The rehydration process (also called the reconstruction process), based on the “memory effect,” is necessary to obtain carbonate-free LDHs. As-prepared LDH is calcined at over 773 K in air or in an inert gas atmosphere to produce the mixed oxide via decomposition of its characteristic layered structure. The resulting mixed oxide is immersed in decarbonated water at room temperature for several hours under an inert gas atmosphere to yield rehydrated LDH, during which the layer structures of the hydroxide sheets are reconstructed and the charge-compensating  $\text{CO}_3^{2-}$  anions are replaced by  $\text{OH}^-$  anions [17]. Medina et al. argued that the rehydrated Mg–Al LDH that have active hydroxyl groups located near the edges of the platelets exhibits high performance in aldol condensations [18].

### 18.3 Characterization

**XRD patterns:** The most common technique for characterizing LDH structures is XRD. However, as the materials are often poorly crystallized, the diffraction patterns are broad and asymmetric, and hence difficult to analyze. The sharp diffraction peaks at low angle are assigned to the (003) and (006) phase reflections. These peaks are related to intervals of each hydroxide sheet and the distance from the hydroxide sheets to the interlayer anions, respectively, indicating that corresponding peaks are influenced by the interlayer anion size, the ratio of  $M^{2+}/M^{3+}$ , and the degree of hydration. The other intense peak around  $2\theta=60^\circ$  is indexed as a (110) phase with respect to the hexagonal axes. This reflection is independent of the kind of layer stacking and can therefore be utilized for the calculation of the parameter  $a$  as  $2d_{(110)}$ . The value of  $a$  should depend on the nature of the metal cations of the hydroxide sheets (the ionic radii of the cations) and the ratio of the metal components (Fig. 18.2a) [1].

**Fourier-transform Infrared (FT-IR) spectroscopy:** FT-IR spectroscopy is useful in identifying the presence of interlayer anions of LDHs and their derivatives. Information can be obtained about the type of bonds formed by the anions and their orientations. The adsorption at  $3500\text{--}3600\text{ cm}^{-1}$  is attributed to the hydrogen bonding stretching vibration of the OH group of the hydroxide sheets. A shoulder may be present at  $\sim 3000\text{ cm}^{-1}$ , assigned to hydrogen bonding between  $\text{H}_2\text{O}$  and the interlayer anions. The intensity and the position of this band depend on the type of anions and the amount of water in the interlayer. The main absorption bands corresponding to interlayer anions are observed between  $1000$  and  $1800\text{ cm}^{-1}$ . The peak due to vibration of the interlayer carbonates (chelating or bridging bidentate) appeared at  $1370\text{ cm}^{-1}$ . The vibration at  $1515\text{ cm}^{-1}$  is ascribed to a reduction in the symmetry, caused by monodentate carbonates interacting with  $\text{Mg}^{2+}$  [1, 18]. Medina et al., in the case of Mg–Al LDH, noticed that a significant amount of carbonates remain after the calcination/rehydration process due to the high affinity of carbonates to LDHs [18].

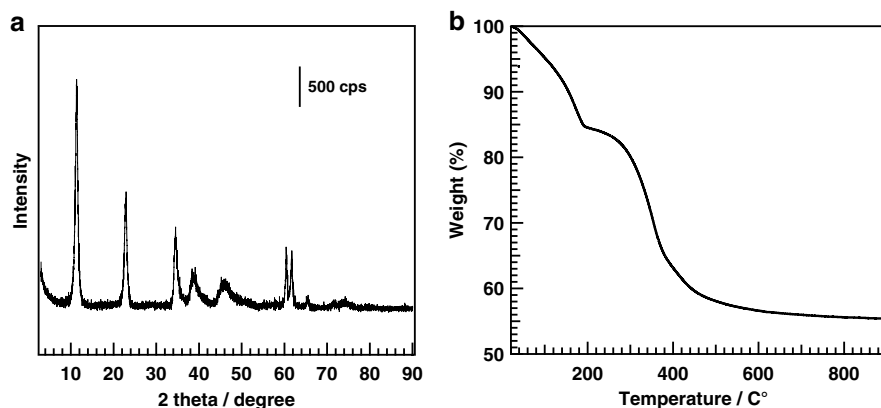


**Fig. 18.2** (a) XRD pattern of Mg–Al LDH measured by using  $\text{Cu K}\alpha$  radiation, (b) TG curve of Mg–Al LDH. Both of them are the original data from the authors of this chapter

*Thermogravimetry:* Their thermal behavior reflects many features of LDHs, such as the ratio of  $M^{2+}/M^{3+}$ , kinds of interlayer anions, and degree of hydration. LDHs exhibit characteristic two-step weight loss with increasing temperature in the TG curve. The first step, at less than 500 K, is due to desorption of water molecules present on the surface and in the interlayer without the decomposition of the layered structure. The second step, above 500 K, is caused by collapse of the layered structure accompanied by the dehydration of hydroxyl groups and desorption of the charge-compensating interlayer anions (Fig. 18.2b).

In addition, the densities and strengths of basic sites in LDHs and their derivatives are determined by temperature-programmed desorption (TPD) profiles combined with the results of FT-IR spectra and the thermogravimetric profiles. Scanning electron microscopy (SEM) images typically reveal the morphology of the synthesized LDHs. The characteristic layered structures and the platelet morphology are clearly observed.

## 18.4 Application to Photocatalytic Reactions

### 18.4.1 Degradation of Organic Compounds

The photocatalytic elimination of toxic organic pollutants using visible light has been extensively studied for two decades. From the perspectives of environmental concerns and energy shortages, it is necessary to develop a novel photocatalyst, which can effectively utilize renewable and clean solar energy. Although the band edge of  $TiO_2$ -based materials (such as  $TiO_{2-x}N_x$ ) significantly shifts toward the visible region, their photoelectronic transition efficiencies are low due to inherent light absorption properties of these materials. Aiming to obtain a novel photocatalyst with large surface area and high crystallinity, ordered layer photocatalysts have been paid great attentions [19].

Zn-containing LDHs (Zn-M LDHs) are widely used as photocatalysts for the degradation of organic compounds. Shao et al. reported that as-prepared Zn-Ti LDH, with a low band gap of ca. 3.1 eV exhibited significant photocatalytic activity for the degradation of Methylene blue under visible light irradiation; a level of activity was much higher than those of ZnO and  $TiO_2$ . Furthermore, Zn-Ti LDH is stable through five repeated application cycles with nearly constant photodecomposition percentage, indicating that Zn-Ti LDH does not deactivate during the photocatalytic process [20]. Xia et al. demonstrated the photocatalytic degradation of Rhodamine B (RB) under visible light irradiation using a series of Zn-M LDH (M=Al, Fe, Ti, and FeTi). The degradation rates of RB for all four of the LDHs are over 50 % after the photoirradiation for 60 min, in the following order: Zn-Ti  $\approx$  Zn-Al > Zn-Fe-Ti > Zn-Fe LDHs. Thermal regeneration of the Zn-Ti LDH utilized for RB degradation was feasible for at least three cycles, indicating that the structural stability of this material is sufficient to use it repeatedly as a photocatalyst for the degradation of RB [21]. In addition, various Zn-M LDHs, such as Zn-Cr [22],

Ag-loaded Zn–Cr [23], Pt-loaded Zn–Ti [24], Zn–Bi [25], and Mg–Zn–In LDH [19] have been reported as photocatalysts for the decomposition of organic compounds. On the other hand, metal oxides/LDH composites have been also reported to show similar activity for these photocatalytic reactions. Valente et al. presented the preparation of CeO<sub>2</sub> supported by Mg–Al LDH and their photocatalytic activities for the degradation of phenol and phenol-derivatives [26]. The photocatalytic systems for the degradation of organic dyes and compounds using TiO<sub>2</sub>/Mg–Al LDH [27], ZnO/Mg–Al LDH [28], SnO<sub>2</sub>/Mg–Al LDH [29], Fe<sub>3</sub>O<sub>4</sub>/Zn–Cr LDH [30], and (W<sub>7</sub>O<sub>24</sub>)<sup>6-</sup>-intercalated Mg–Al LDH [31] were also demonstrated.

### 18.4.2 Water Splitting

Since Honda and Fujishima found the photoelectrochemical water-splitting system using TiO<sub>2</sub> as a photoanode, various inorganic materials have been applied to catalyze the photocatalytic splitting of water. As brucite-like hydroxide sheets of LDHs can incorporate various kinds of metal cations to achieve the characteristic light absorption properties, some LDHs have recently attracted attention for their potential as new visible-light-responsive photocatalysts. LDHs are sometimes fabricated via a homogeneous precipitation method using urea and/or other amine compounds, as mentioned above. Organic residues cannot be removed by the mild heat treatment that enables LDHs to maintain their characteristic layered structure. Hence, it should be noted that such organic contaminants might influence photocatalytic activities.

García et al. reported that semiconductor materials based on three kinds of Zn<sup>2+</sup>-containing LDHs (Zn–Cr, Zn–Ti, and Zn–Ce LDH) show photocatalytic activity for O<sub>2</sub> evolution from water under visible light irradiation, in the presence of AgNO<sub>3</sub> as a sacrificial reagent. As shown in Fig. 18.3, a certain amount of O<sub>2</sub> was evolved under visible light irradiation using Zn–Cr LDH as the photocatalyst; furthermore, once the photocatalytic reaction rate tends to slow down, addition of AgNO<sub>3</sub> reactivates the formation of O<sub>2</sub>. It is indicated that the reason for the cessation in O<sub>2</sub> evolution is the lack of the sacrificial reagent, and not deactivation or corrosion of the catalyst. It should also be noted that the overall efficiency of the Zn–Cr LDH for O<sub>2</sub> generation under visible light irradiation is 1.6 times higher than that of a WO<sub>3</sub> photocatalyst under the same reaction conditions [4]. Wei et al. published a visible-light-responsive photocatalyst fabricated by anchoring Ni–Ti LDH to the surface of reduced graphene oxide sheets (RGO) that displays good activity for the photocatalytic O<sub>2</sub> evolution. The generation rates of O<sub>2</sub> over Ni–Ti LDH/RGO composites are much larger compared to bare Ni–Ti LDH and RGO, respectively; that is, the combination of Ni–Ti LDH and RGO significantly enhances the photocatalytic activity [32].

Wei et al. also reported a photocatalytic H<sub>2</sub> production system using various LDHs as photocatalysts that contain highly dispersed TiO<sub>6</sub> units. Ni–Ti, Zn–Ti, and Mg–Al–Ti LDH show photocatalytic activity for H<sub>2</sub> evolution using lactic acid as a sacrificial electron donor. In particular, Zn–Ti LDH, which contains highly dispersed TiO<sub>6</sub> units, displays a production rate 18 times higher than that of K<sub>2</sub>Ti<sub>4</sub>O<sub>9</sub>, which

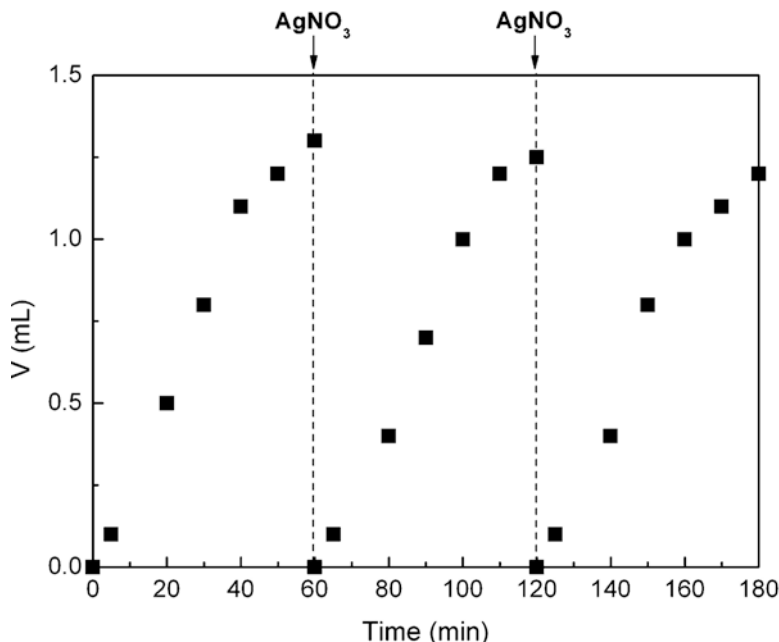


**Fig. 18.3** Volume of O<sub>2</sub> formed vs. irradiation time in three consecutive cycles in which additional amounts of AgNO<sub>3</sub> have been added every 60 min. Reprinted with permission from Journal of the American Chemical Society, 2009, *131*, 13833. Copyright (2009) American Chemical Society

contains highly aggregated TiO<sub>6</sub> octahedra [33]. On the other hand, Xu et al. demonstrated photocatalytic H<sub>2</sub> evolution with Rose bengal (RBdye) and Pt nanoparticles (photosensitizers) fixed on Mg–Al LDH (co-catalyst). A self-assembled RBdye–LDH–Pt system produces H<sub>2</sub> from water that contains Triethanolamine (TEOA) as a sacrificial reagent; the amount is a few times greater than that of the RBdye–Pt (without LDH) system. Pt nanoparticles on Mg–Al LDH can be used repeatedly, and the total turnover number after six runs for the RBdye–LDH–Pt system is calculated to be 304, based on Pt. Photocatalytic water splitting has many advantages: (1) immobilizing the dye photosensitizer for suppressed self-quenching, (2) close arrangement between photosensitizer molecules and co-catalyst nanoparticles for efficient electron transfer, (3) formation of well-dispersed co-catalyst nanoparticles on the support surface, and (4) easy recycling of the expensive co-catalyst [34].

### 18.4.3 CO<sub>2</sub> Conversion

Photocatalytic conversion of CO<sub>2</sub> to valuable compounds is one of the promising methods to create a sustainable carbon-cycling system. The CO<sub>2</sub> molecules adsorbed on the surface of photocatalysts should be converted into active species that can be

easily reduced by photogenerated electrons. Therefore, solid base materials are suitable candidates to construct the photocatalytic system for CO<sub>2</sub> conversion [35]. In the last 5 years, several research groups have demonstrated the photocatalytic conversion of CO<sub>2</sub> using synthetic LDHs. Izumi et al. reported that Cu<sup>2+</sup>-containing LDH photocatalysts show activity for CO<sub>2</sub> conversion using H<sub>2</sub> as the reductant, and CO and methanol are evolved as the reduction products of CO<sub>2</sub>. In their system, [Zn<sub>3</sub>Ga(OH)<sub>8</sub>]<sub>2</sub>[Cu(OH)<sub>4</sub>]<sub>2</sub>·*m*H<sub>2</sub>O and [Zn<sub>1.5</sub>Cu<sub>1.5</sub>Ga(OH)<sub>8</sub>]<sub>2</sub>(CO<sub>3</sub>)<sub>2</sub>·*m*H<sub>2</sub>O are used as photocatalysts, and the former shows higher activity than the latter for methanol formation as the reduction product of CO<sub>2</sub>. Cu<sup>2+</sup> species, in the interlayer for the former and in the inlayer for the latter, are considered active sites for CO<sub>2</sub> conversion under the irradiation [36–38]. Katsumata et al. also exhibited that noble-metal (Pt, Pd, and Au)-loaded Zn–Cr LDHs are active for the photocatalytic conversion of CO<sub>2</sub> to CO under UV irradiation. Since CO is not detected under visible light irradiation, it is concluded that photocatalytic conversion of CO<sub>2</sub> does not occur by absorption of the 410- and 570-nm peaks attributed to *d*–*d* transition [39].

We have published papers concerned with the photocatalytic system using various kinds of LDHs for CO<sub>2</sub> conversion. We reported a series of synthetic M<sup>2+</sup>–M<sup>3+</sup> LDHs (M<sup>2+</sup> = Mg<sup>2+</sup>, Ni<sup>2+</sup>, and Zn<sup>2+</sup>; M<sup>3+</sup> = Al<sup>3+</sup>, Ga<sup>3+</sup>, and In<sup>3+</sup>) that show activity toward the photocatalytic conversion of CO<sub>2</sub> in water [40]. As shown in Fig. 18.4, the use of Ni–Al LDH as a photocatalyst enabled us to achieve maximum conversion of CO<sub>2</sub> to CO with high selectivity, because it produces less H<sub>2</sub> as a reduction product of H<sup>+</sup> derived from water than other LDHs [16]. On the other hand, other LDHs such as Mg–In LDH and Ni–In LDH, both of which contain In<sup>3+</sup> as a triva-

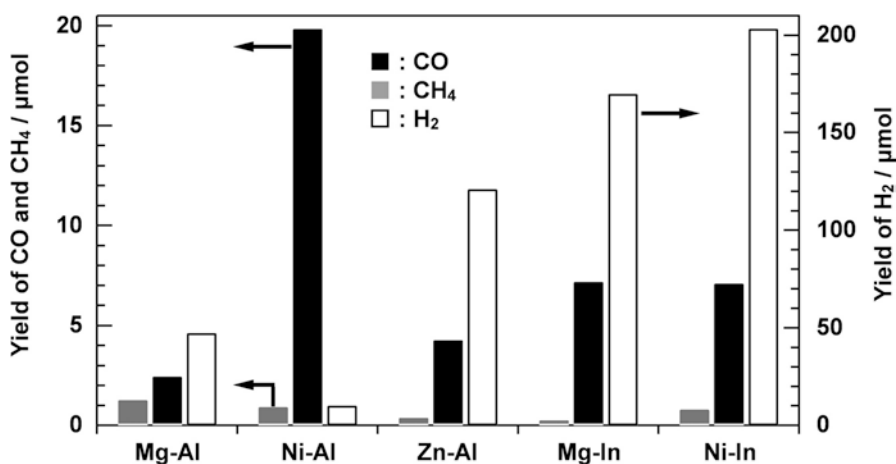


**Fig. 18.4** The amount of products evolved in the photocatalytic conversion of CO<sub>2</sub> in H<sub>2</sub>O over various M<sup>2+</sup>–M<sup>3+</sup> LDH after 8 h of photoirradiation. Black bar: CO, gray bar: CH<sub>4</sub>, white bar: H<sub>2</sub>, M<sup>2+</sup>/M<sup>3+</sup> = 3, photocatalyst weight: 500 mg, CO<sub>2</sub>: 7.7 mmol, H<sub>2</sub>O: 350 mL, light source: 400 W Hg lamp. Reprinted from *Catalysis Today*, 251, Shoji Iguchi, Kentaro Teramura, Saburo Hosokawa, and Tsunehiro Tanaka, Photocatalytic conversion of CO<sub>2</sub> in an aqueous solution using various kinds of layered double hydroxides, 140, Copyright (2015), with permission from Elsevier

lent cation, increase the  $H_2$  production, a less preferable condition. This led us to conclude that Ni–Al LDHs offer suitable surface properties for selective photocatalytic conversion of  $CO_2$  in water. In addition, we found that the addition of NaCl into the reaction solution obviously improved the photocatalytic conversion of  $CO_2$  to CO. More than twice amount of CO was evolved in an aqueous solution of NaCl (0.1 M) after 8 h of photoirradiation as compared to that in a pure water. Simultaneously, the addition of NaCl suppressed the  $H_2$  formation as a reduction product of  $H^+$ . Accordingly, the selectivity toward CO evolution was advanced by the addition of NaCl to the reaction solution. Furthermore, NaCl was no exception as an additive, and that other chloride salts such as KCl, CsCl,  $MgCl_2$ , and  $CaCl_2$  influenced the selectivity toward CO evolution to a similar extent, indicating that the presence of  $Cl^-$  in the reaction solution promoted the photocatalytic conversion of  $CO_2$  regardless of the nature of the counter cation. The products CO,  $H_2$ , and HClO are formed under photoirradiation as a reduction product of  $CO_2$  and  $H^+$ , and as an oxidation product of  $Cl^-$ , respectively. It should be possible to detect HClO selectively by using a *N,N'*-dimethyl-*p*-phenylenediamine (DPD) test due to the strong oxidation power of HClO. We conclude that the photogenerated holes during the photocatalytic reaction oxidize the reducing agent  $Cl^-$  to  $Cl_2$ , which is immediately converted into HClO in the presence of water [41].

## References

1. Cavani F, Trifirò F, Vaccari A (1991) Hydrotalcite-type anionic clays: preparation, properties and applications. *Catal Today* 11:173–301
2. Hoyo CD (2007) Layered double hydroxides and human health: an overview. *Appl Clay Sci* 36:103–121
3. Xu ZP, Zhang J, Adebajo MO, Zhang H, Zhou C (2011) Catalytic applications of layered double hydroxides and derivatives. *Appl Clay Sci* 53:139–150
4. Silva CG, Bouizi Y, Fornés V, García H (2009) Layered double hydroxides as highly efficient photocatalysts for visible light oxygen generation from water. *J Am Chem Soc* 131:13833–13839
5. Saber O (2007) Preparation and characterization of a new nano layered material, Co–Zr LDH. *J Mater Sci* 42:9905–9912
6. Saber O, Tagaya H (2003) Preparation and intercalation reaction of Zn–Sn LDH and Zn–Al–Sn LDH. *J Porous Mater* 10:83–91
7. Ram Reddy MK, Xu ZP, Lu GQ, Diniz da Costa JC (2006) Layered double hydroxide for  $CO_2$  capture: structure evolution and regeneration. *Ind Eng Chem Res* 45:7504–7509
8. Goh KH, Lim TT, Dong Z (2008) Application of layered double hydroxides for removal of oxyanions: a review. *Wat Res* 42:1343–1368
9. Das J, Patra BS, Baliarsingh N, Parida KM (2006) Adsorption of phosphate by layered double hydroxides in aqueous solutions. *Appl Clay Sci* 32:252–260
10. Goswamee RL, Sengupta P, Bhattacharyya KG, Dutta DK (1998) Adsorption of Cr (VI) in layered double hydroxides. *Appl Clay Sci* 13:21–34
11. Sels BF, De Vos DE, Jacobs PA (2001) Hydrotalcite-like anionic clays in catalytic organic reactions. *Catal Rev* 43:443–488
12. Ebitani K, Motokura K, Mori K, Mizugaki T, Kaneda K (2006) Reconstructed hydrotalcite as a highly active heterogeneous base catalyst for carbon–carbon bond formations in the presence of water. *J Org Chem* 71:5440–5447

13. Reichle WT (1986) Synthesis of anionic clay minerals (mixed metal hydroxides, hydrotalcite). *Solid State Ionics* 22:135–141
14. Evans DG, Duan X (2006) Preparation of layered double hydroxides and their applications as additives in polymers, as precursors to magnetic materials and in biology and medicine. *Chem Commun* 42:485–496
15. Ogawa M, Kaiho H (2002) Homogeneous precipitation of uniform hydrotalcite particles. *Langmuir* 18:4240–4242
16. Iguchi S, Teramura K, Hosokawa S, Tanaka T (2014) Photocatalytic conversion of CO<sub>2</sub> in an aqueous solution using various kinds of layered double hydroxides. *Catal Today*. doi:[10.1016/j.cattod.2014.09.005](https://doi.org/10.1016/j.cattod.2014.09.005)
17. Xu C, Gao Y, Liu X, Xin R, Wang Z (2013) Hydrotalcite reconstructed by *in situ* rehydration as a highly active solid base catalyst and its application in aldol condensations. *RSC Adv* 3:793–801
18. Abelló S, Medina F, Tichit D, Pérez-Ramírez J, Groen JC, Sueiras JE, Salagre P, Cesteros Y (2005) *Chem Eur J* 11:728–739
19. Huang L, Chu S, Wang J, Kong F, Luo L, Wang Y, Zou Z (2013) Novel visible light driven Mg–Zn–In ternary layered materials for photocatalytic degradation of methylene blue. *Catal Today* 212:81–88
20. Shao M, Han J, Wei M, Evans DG, Duan X (2011) The synthesis of hierarchical Zn–Ti layered double hydroxide for efficient visible-light photocatalysis. *Chem Eng J* 168:519–524
21. Xia SJ, Liu FX, Ni ZM, Xue JL, Qian PP (2013) Layered double hydroxides as efficient photocatalysts for visible-light degradation of Rhodamine B. *J Colloid Interface Sci* 405:195–200
22. Mohapatra L, Parida KM (2012) Zn–Cr layered double hydroxide: visible light responsive photocatalyst for photocatalytic degradation of organic pollutants. *Sep Purif Technol* 91:73–80
23. Sun J, Zhang Y, Cheng J, Fan H, Zhu J, Wang X, Ai S (2014) Synthesis of Ag/AgCl/Zn–Cr LDHs composite with enhanced visible-light photocatalytic performance. *J Mol Catal A Chem* 382:146–153
24. Chen G, Qian S, Tu X, Wei X, Zou J, Leng L, Luo S (2014) Enhancement photocatalytic degradation of rhodamine B on nanoPtintercalated Zn–Ti layered double hydroxides. *Appl Surf Sci* 293:345–351
25. Mohapatra L, Parida KM (2014) Dramatic activities of vanadate intercalated bismuth doped LDH for solar light photocatalysis. *Phys Chem Chem Phys* 16:16985–16996
26. Valente JS, Tzompantzi F, Prince J (2011) Highly efficient photocatalytic elimination of phenol and chlorinated phenols by CeO<sub>2</sub>/MgAl layered double hydroxides. *Appl Catal B Environ* 102:276–285
27. Paušová Š, Krýsa J, Jirkovský J, Mailhot G, Prevot V (2012) Photocatalytic behavior of nano-sized TiO<sub>2</sub> immobilized on layered double hydroxides by delamination/restacking process. *Environ Sci Pollut Res* 19:3709–3718
28. Yuan S, Li Y, Zhang Q, Wang H (2009) ZnO nanorods decorated calcined Mg–Al layered double hydroxides as photocatalysts with a high adsorptive capacity. *Colloids Surf A* 348:76–81
29. Dvininov E, Ignat M, Barvinschi P, Smithers MA, Popovici E (2010) New SnO<sub>2</sub>/MgAl-layered double hydroxide composites as photocatalysts for cationic dyes bleaching. *J Hazard Mater* 177:150–158
30. Chen D, Li Y, Zhang J, Zhou JZ, Guo Y, Liu H (2012) Magnetic Fe<sub>3</sub>O<sub>4</sub>/ZnCr-layered double hydroxide composite with enhanced adsorption and photocatalytic activity. *Chem Eng J* 185–186:120–126
31. Guo Y, Li D, Hu C, Wang C, Wang Y, Wang E, Zhou Y, Feng S (2001) Photocatalytic degradation of aqueous organochlorine pesticide on the layered double hydroxide pillared by Paratungstate A ion, Mg<sub>12</sub>Al<sub>6</sub>(OH)<sub>36</sub>(W<sub>7</sub>O<sub>24</sub>)·4H<sub>2</sub>O. *Appl Catal B Environ* 30:337–349
32. Li B, Zhao Y, Zhang S, Gao W, Wei M (2013) Visible-light-responsive photocatalysts toward water oxidation based on NiTi-layered double hydroxide/reduced graphene oxide composite materials. *ACS Appl Mater Interfaces* 5:10233–10239

33. Zhao Y, Chen P, Zhang B, Su DS, Zhang S, Tian L, Lu J, Li Z, Cao X, Wang B, Wei M, Evans DG, Duan X (2012) Highly dispersed  $\text{TiO}_6$  units in a layered double hydroxide for water splitting. *Chem Eur J* 18:11949–11958
34. Hong J, Wang Y, Pan J, Zhong Z, Xu R (2011) Self-assembled dye-layered double hydroxide-Pt nanoparticles: a novel  $\text{H}_2$  evolution system with remarkably enhanced stability. *Nanoscale* 3:4655–4661
35. Teramura K, Tanaka T, Ishikawa H, Kohno Y, Funabiki T (2004) Photocatalytic reduction of  $\text{CO}_2$  to CO in the presence of  $\text{H}_2$  or  $\text{CH}_4$  as a reductant over MgO. *J Phys Chem B* 108:346–354
36. Ahmed N, Shibata Y, Taniguchi T, Izumi Y (2011) Photocatalytic conversion of carbon dioxide into methanol using zinc–copper–M(III) (M=aluminum, gallium) layered double hydroxides. *J Catal* 279:123–135
37. Morikawa M, Ahmed N, Yoshida Y, Izumi Y (2014) Photoconversion of carbon dioxide in zinc–copper–gallium layered double hydroxides: the kinetics to hydrogen carbonate and further to CO/methanol. *Appl Catal B Environ* 144:561–569
38. Morikawa M, Ogura Y, Ahmed N, Kawamura S, Mikami G, Okamoto S, Izumi Y (2014) Photocatalytic conversion of carbon dioxide into methanol in reverse fuel cells with tungsten oxide and layered double hydroxide photocatalysts for solar fuel generation. *Catal Sci Technol* 4:1644–1651
39. Katsumata K, Sakai K, Ikeda K, Carja G, Matsushita N, Okada K (2013) Preparation and photocatalytic reduction of  $\text{CO}_2$  on noble metal (Pt, Pd, Au) loaded Zn–Cr layered double hydroxides. *Mater Lett* 107:138–140
40. Teramura K, Iguchi S, Mizuno Y, Shishido T, Tanaka T (2012) Photocatalytic conversion of  $\text{CO}_2$  in water over layered double hydroxides. *Angew Chem Int Ed* 51:8008–8011
41. Iguchi S, Teramura K, Hosokawa S, Tanaka T (2015) Effect of the chloride ion as a hole scavenger on the photocatalytic conversion of  $\text{CO}_2$  in an aqueous solution over Ni–Al layered double hydroxides. *Phys Chem Chem Phys* 17:17995–18003

# Chapter 19

## Bismuth Oxyhalide Nano- and Microstructures: Morphology Modulation and Functionalization

Ling Zhang and Wenzhong Wang

### 19.1 Introduction

Simple layered semiconductors with Sillén structures are considered as one of the most potential photocatalysts to meet the requirements of environmental and energy technologies driven by solar energy. Specially, bismuth oxyhalide nanomaterials BiOX (X=Cl, Br, and I) have received more and more interests as promising photocatalysts because their unique layered structures endow them with fascinating physicochemical properties and suitable band structure, as well as their high chemical and optical stability, nontoxicity, low cost, and corrosion resistance [1–3].

Compounds with these structures can be described as resulting from the intergrowth of PbO-type blocks ( $\text{Bi}_2\text{O}_2$ )<sup>2+</sup> and one (the simplest X1 structure), two and even three layers of halide ions X<sup>-</sup> (i.e., Bi-based oxychlorides such as BiOCl and Bi<sub>3</sub>O<sub>4</sub>Cl). The layered [X–Bi–O–Bi–X] slices stacked together by the nonbonding interaction (van der Waals force) through the halogen atoms along the *c*-axis. The internal static electric fields between [ $\text{Bi}_2\text{O}_2$ ]<sup>2+</sup> and the anionic halogen layers are believed to induce the efficient separation of the photogenerated electron–hole pairs, which favor the photocatalytic activity of the catalysts [4]. In addition, a bismuth center is surrounded by four oxygen and four halogen atoms in each [X–Bi–O–Bi–X] layer, which thus generate an asymmetric decahedral geometry. The strong intralayer covalent bonding and the weak interlayer van der Waals interaction give rise to highly anisotropic structural, electrical, optical, and mechanical properties, which endow BiOX with promising potential applications for photocatalysis.

---

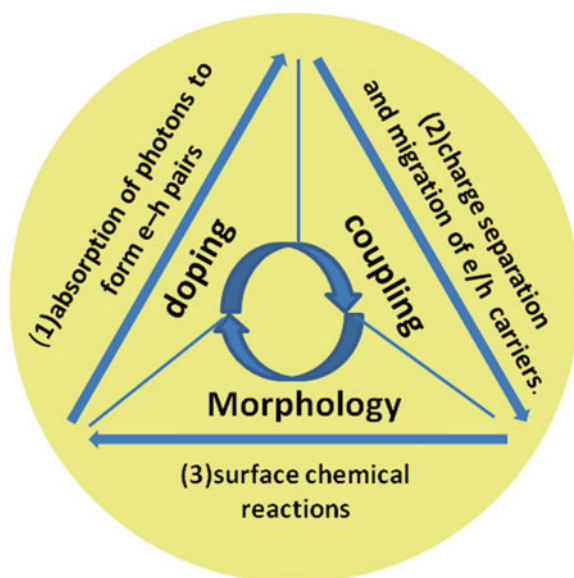
L. Zhang • W. Wang (✉)

State Key Laboratory of High Performance Ceramics and Superfine Microstructures,  
Chinese Academy of Sciences, Shanghai Institute of Ceramics, 1295 Dingxi Road,  
Shanghai 200050, People's Republic of China  
e-mail: [wzwang@mail.sic.ac.cn](mailto:wzwang@mail.sic.ac.cn)

The photocatalytic activity is closely related to the mobility of the photogenerated charge carriers and the positions of the conduction band (CB) and valence band (VB) in the photocatalyst. In 2008, Wang et al. reported that the band gaps of the sheet-shaped BiOX compounds were 3.44, 2.76, and 1.85 eV, respectively [5]. It is noted that with increasing atomic numbers, the indirect band gaps of BiOX become narrower, which is relative with their photocatalytic activity. In bismuth oxyhalide photocatalysts, the VB is commonly composed of O 2p, X np, and Bi 6s hybrid orbitals, whereas the CB consists of Bi 6p. It was found that the Bi 6s orbital is largely dispersed, which favors the mobility of photoinduced holes in the VB and is beneficial to the oxidation reaction. Thus, oxidation by the holes is a main feature of BiOX in photocatalysis considering the position of VB.

As mentioned above, the oxidizability is an important factor for photocatalysis, but it is not the only factor. As shown in Fig. 19.1, the main processes in a photocatalytic reaction could be summarized as follows: (1) the first step is absorption of photons to form electron–hole pairs; (2) the second step consists of charge separation and migration of photogenerated carriers; (3) the final step involves the surface chemical reactions. The photocatalysis of semiconductors is a complicated process, which is affected by electron structure, crystal structure, defects, size and surface morphology, etc. The nanoscale catalysts not only possess the advantage of large surface areas, but also present new physical and chemical properties due to the smaller size. Smaller particle sizes mean shorter distances for photogenerated carriers to migrate before reaching surface reaction sites, which improves the photocatalytic performance. However, smaller particle sizes also imply that the electron–hole pairs are conned to a smaller space and, therefore, should be more likely to collide and recombine. As a result, electron–hole recombination increases inversely with

**Fig. 19.1** Correlation of morphology modulation, doping, and coupling of semiconductors for photocatalytic process



particle volume [6]. Clearly the size of an individual particle must be chosen as a compromise between the positive influence of having more reactive sites and the negative influence of increased recombination. In addition, for quantum-sized photocatalyst, the band gap would be changed due to the quantum confinement effect, which in turn affected its photocatalytic activity. Therefore, morphology modulation, including shape, size, surface area, and dimensionality control, has always been of great importance for both scientific research and industrial applications.

Apart from the effects from size and shape, the catalytic property can also be tuned by varying the composition of the photocatalyst. Most of single-component catalysts are incapable for practical photocatalysis technology applications due to the wide band gap which only respond to UV light or suffer to fast combination of carriers [7]. Thus, it is necessary to fabricate hybrid photocatalysts to overcome these limitations. The hybrid photocatalysts are usually fabricated by ion doping or coupling with other active components. The hybrid photocatalysts integrate the synergistic effects of the individual species, endowing to increase light harvesting, prolong lifetime of carriers, thus to enhance the catalytic performance. The interrelationship among the key factors in morphology modulation, doping, and coupling of semiconductors for photocatalysis is illustrated schematically in Fig. 19.1.

In this feature chapter, we focus on the research of BiOX nanomaterials for efficient photocatalytic applications, which can be classified into two classes: morphology modulation and functional structural design. It may give us insight into the essence of structure and photocatalytic property. In addition, we highlight some crucial issues in the development of BiOX for environmental protection, and also give tentative suggestions on further increasing their photocatalytic performance.

## 19.2 Morphology Modulation

### 19.2.1 1D Nanostructure

One-dimensional (1D) nanostructures can efficiently scatter incident light to improve solar energy conversion and storage. However, the 1D BiOX nanostructure is unusual except by the hard templates method since their highly anisotropic layered structures tend to grow into nanoplate/sheet with 2D feature. Hard templates involving anodic aluminum oxide (AAO) [8] and electrospinning method [9] have also been employed to prepare BiOCl nanofibers/nanowire arrays, which displayed efficient photocatalytic performance in the degradation of organic dyes. As shown in Fig. 19.2a, the electrospinning method was applied to synthesize BiOCl nanofibers with diameters ranging from 80 to 140 nm by thermal treatments of the polyacrylonitrile (PAN) template at 500 °C for 10 h [9]. It is worth to note that BiOCl nanowire was also synthesized by combining wet etch (top-down) with liquid phase crystal growth (bottom-up) process [10]. The formation mechanism of such ordered BiOCl hierarchical structure is considered to be mainly originated from the highly preferred growth, which is governed by the lattice match between (110) facet of BiOCl and (220) or (002) facet of  $\beta$ - $\text{Bi}_2\text{O}_3$ .

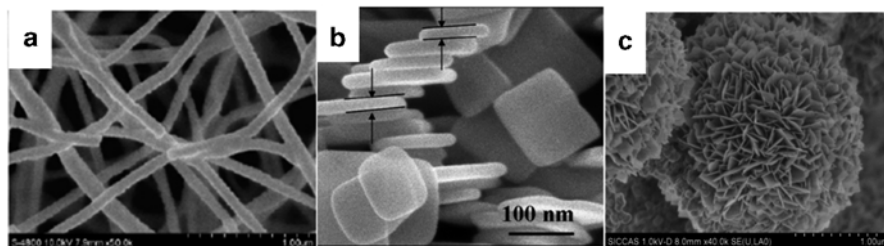


**Fig. 19.2** SEM images of the prepared (a) BiOCl nanofibers; (b) BiOCl nanoplates; (c) BiOCl microstructure. Reproduced from Ref. [9] with permission of The Royal Society of chemistry and Ref. [16] with permission of Elsevier

It is a different story in other bismuth-based oxyhalides that belong to the Sillén family expressed by bismuth oxide-based fluorite-like layers,  $[\text{Bi}_2\text{O}_2]^{2+}$ , inter-grown with multiple halide layers. The 1D nanostructure was formed due to its intrinsic monoclinic or orthorhombic crystal structure. For example,  $\text{Bi}_5\text{O}_7\text{I}$  nanobelts with length of 7–25  $\mu\text{m}$  and width of 0.3–1  $\mu\text{m}$  were prepared by a hydrothermal method in our group [11]. The  $[\text{Bi}_5\text{O}_7]^+$  and  $\text{I}^-$  slices are orderly piled up one-by-one along the  $c$ -axis into the unique layered structure. Permanent static electric fields between  $[\text{Bi}_5\text{O}_7]^+$  and  $\text{I}^-$  layers may work as the accelerators for the separation of electron–hole pairs under photoexcitation and may favor the highly photocatalytic efficiency of  $\text{Bi}_5\text{O}_7\text{I}$ . Recently, Ye et al. found that  $\text{Bi}_5\text{O}_7\text{I}$  rods showed considerably higher photocatalytic activity in degrading dyes than  $\text{Bi}_5\text{O}_7\text{I}$  sheets [12]. The shape-dependent photocatalytic activity could result from synergetic and internal electric field effects simultaneously.

### 19.2.2 2D Intrinsic Layered Nanostructure

Among various architectures, two-dimensional (2D) nanosheets with thickness generally below 100 nm are of great promise for highly efficient photocatalysis [13]. The 2D nanosheets usually prepared by exfoliation of a layered compound with a homogeneous ultrathin thickness has a lateral dimension of several hundred nanometers to several micrometers. Specifically, such 2D nanostructures easily arise from intrinsic lamellar structures, which are built by the interlaminated weak van der Waals force or electrostatic force [14]. BiOX compounds, as typical intrinsic layered photocatalysts, have a layer structure characterized by  $[\text{Bi}_2\text{O}_2]^{2+}$  slabs interleaved by double slabs of halogen atoms. The intrinsic layer structure led to the formation of nanoplates, nanosheets, and nanoflakes of BiOX compounds. It is believed that the strong internal static electric fields perpendicular to the  $[\text{X}]$  layer and the  $[\text{Bi}_2\text{O}_2]^{2+}$  layer enable the effective separation of the photoinduced electron–hole pairs, and then enhance the photocatalytic activity of BiOX.

Among numerous synthetic methodologies exploited for the preparation of 2D BiOX nanomaterials, using cetyltrimethylammonium oxyhalide is a facile way to prepare 2D nanosheet, which acted not only as a template but also as a Cl<sup>-</sup>/Br<sup>-</sup> source. In 2009, our research group reported that lamellar BiOBr was synthesized by a hydrothermal route using cetyltrimethylammonium bromine (CTAB) as the soft template for the successive growth of grains [15]. After ultrasonic treatment, the CTAB molecules with quantified concentration may turn into the lamellar structure. With increasing the concentration of CTAB which supplied the Br<sup>-</sup> source, the size of the BiOBr plate increased. BiOCl nanoplates, square-like in morphology with a size of about 50–100 nm and thickness about 30 nm (as shown in Fig. 19.2b), were prepared by a hydrothermal route using mannitol as the surfactant [16]. In addition, ultrathin BiOCl nanosheets with almost fully exposed active (001) facets have been prepared by using both mannitol and PVP as the surfactant in a hydrothermal reaction [17]. The ultrathin BiOCl nanosheets showed more excellent activity in degrading the RhB dye in aqueous solution.

Recently, a green and facile method had been reported by Li et al. to prepare black BiOCl nanoplates [18]. White BiOCl sample with a thickness of about 200 nm turned to be thinner with the Fe reduction. The as-prepared black sample exhibited a broad absorption covering the whole visible light region. Methyl orange (MO) photocatalytic degradation experiments showed that the black sample exhibited higher photocatalytic activity than the pristine BiOCl under visible light irradiation.

### 19.2.3 3D Assembled Hierarchical Architectures

Nanomaterials have been documented with exceptional properties in optics, electronics, magnetics, and catalysis compared with their bulk companions. In the past decades, considerable effort has been focused on the synthesis and characterization of nanocrystalline structures with tunable size and morphology. However, photocatalyst on nanoscale brings difficulties for the separation and recycling of these materials for industrial usage. Assembling the nanostructures into the desired hierarchical architectures is of great importance not only for fabricating functional nanodevices but also for paving the way from the nano- to macroscopic world. Furthermore, in comparison with 1D and 2D nanostructures, 3D hierarchical nano-/microstructures are more attractive for solar energy storage and conversion, which improved light harvesting, shortened diffusion pathways, faster interfacial charge separation, and more reactive sites, thus enhancing their photocatalytic efficiencies.

Electrospinning technique has been recently developed for the synthesis of nanofibrous. The fibrous membrane composed of nanofibers exhibits large surface area and porous structures, which makes it a very promising morphology for photocatalysis. BiOX (X=Cl, I) nanoplates were grown on the surface of the carbon nanotubes composite obtained by centrifugal spinning, forming a hierarchical structure by ionic layer adsorption and reaction method [19, 20]. The photocatalytic tests show that BiOCl and BiOI/carbon nanofiber compositions possessed good photocatalytic properties with regard to decomposing MO under a sunlight simulator lamp.

Hydro-/solvothermal routes are other important ways to obtain the assembled hierarchical architectures, especially, which carried out in the ethylene glycol (EG)/water or other organic solvents. Zhang et al. reported BiOX hierarchical microspheres prepared by solvothermal process in the presence of EG [21]. These hierarchical microspheres are composed of 2D nanoplates by self-assembly. EG was thought to play an important role in assembling 2D nanoplates into the 3D hierarchical microspheres. The photocatalytic activity had been evaluated by the degradation of the MO solution under visible light irradiation. The BiOI sample exhibited the best photocatalytic performance with the order of BiOI > BiOBr > BiOCl. It is worth to note that the photocatalytic performance of BiOX microspheres is different compared with the BiOX nanoplates (BiOBr > BiOCl > BiOI) reported by Wang et al. [5]

Recently, our group has developed a microemulsion route to synthesize uniform BiOCl and BiOBr microspheres in the presence of 2-methoxyethanol/water/EG solvent [22, 23]. The BiOCl and BiOBr microspheres with diameters in the range of 1–2  $\mu\text{m}$  are built by numerous interlaced 2D nanosheets with thickness of  $\sim 10$  nm (as shown in Fig. 19.2c). Under UV–visible light irradiation, the as-prepared BiOX microspheres displayed superior photocatalytic activity in the degradation of RhB dye and reduction of  $\text{CO}_2$ . Interestingly, the selective generation of oxygen vacancies on the {001} facets of BiOX nanosheets was thought as the main reason for the high photocatalytic activity of these photocatalysts. The oxygen vacancies on the {001} facets of BiOCl nanosheets were effectively regenerated by light irradiation, and also responsible for the efficient utilization of visible light to activate molecular oxygen to initiate the redox reaction on the surface of the photocatalyst.

## 19.3 Functional Structural Design

BiOCl is a wide band gap semiconductor that only responds to UV light, although it shows excellent photocatalytic activity for environmental remediation. In view of solar energy utilization, the overall photocatalytic efficiency is still low and far from practical application under sunlight irradiation. Searching for a photocatalyst that can harvest wide spectrum of solar light and can achieve efficient solar energy conversion undoubtedly remains an urgent challenge. In order to enhance the solar light harvesting and charge separation, many modification methods, such as doping, sensitization, coupling and so on, have successfully improved the efficiency of solar energy conversion [24].

### 19.3.1 Doping

Doping plays an indispensable role in modifying the properties of photoelectric materials. In photocatalysis, doping, mainly including metal ions and nonmetal doping have been intensively investigated since the nitrogen-doped  $\text{TiO}_2$  reported in

2001 [25]. In addition, for BiOX, self-doping and alloyed BiOX were easy to realize due to the valence-skipping feature of Bi atom and unlimited solubility among the halide atoms.

However, these dopants played different roles in the bismuth oxyhalides with different properties of induced doping ions. Widening or narrowing of the absorption spectrum, surface chemical state, the locations of the dopants, and induced defect states were key factors to affect the performance of the photocatalysts, which were discussed below on the basis of both the previous literature and our own recent work.

### 19.3.1.1 Self-Doping

The semiconductor photocatalysts induced with oxygen vacancies can absorb visible light and display excellent visible light photocatalytic activity [17, 26, 27]. The improved trapping of electrons to inhibit electron–hole recombination and the decreased band gap to enhance visible light harvesting are the benefits of self-doping of lower charged metal ions (Fig. 19.3a). Generally, the oxygen vacancies were engendered in difficult processes such as annealing in a reducing atmosphere. Interestingly, the black BiOCl with oxygen vacancies was easy to obtain under UV light irradiation [28] or by the Fe reduction in aqueous solution [29]. The low bond energy and long bond length of the Bi–O bond lead to produce oxygen vacancies. The as-prepared black BiOCl sample showed 20 times higher visible light photocatalytic activity than white BiOCl in RhB degradation. The trapping experiment showed that the superoxide radical ( $\cdot\text{O}_2^-$ ) and holes ( $h^+$ ) were the main active species in aqueous solution under visible light irradiation. In the last year, Zhang et al. reported that the oxygen vacancies on the (001) surface of BiOCl preferred to reduce molecular oxygen to  $\cdot\text{O}_2^-$  through one-electron transfer, while the oxygen vacancies on the (010) surface favored the formation of  $\text{O}_2^{2-}$  via two-electron transfer [30].

Our research group found reproducible photo-induced oxygen vacancies on the (001) facet of the BiOCl nanosheet [31]. These photo-induced defects not only enhanced the trap capability for  $\text{CO}_2$ , but also enhanced the efficiency of separation



**Fig. 19.3** Four proposed schemes illuminating the possible origin of visible light absorption and enhanced photocatalytic activity in doped BiOX: (a) self-doping: introduction of defect states below conduction band (CB); (b) alloyed effect: introduction of hybridization of the halogen np states on the top of valence band (VB); (c) nonmetal doping: introduction of impurity level above valence band; (d) metal doping: introduction of localized energy levels above valence band

of electron–hole pairs, which resulted in the photocatalytic CO<sub>2</sub> reduction under the simulated solar light. The CO<sub>2</sub> photo-reduction process on the BiOCl nanoplates was accompanying with process of formation and regeneration of oxygen vacancy defects under the UV–Vis light irradiated.

### 19.3.1.2 Alloyed Bismuth Oxyhalides

The bismuth oxide halides belong to the p-block semiconductors family and have band structures and dispersion relations that can be engineered by modulating the stoichiometry of the halogen elements [32, 33]. Therefore, tailoring the electronic structures of these alloyed photocatalysts to maximize their photocatalytic activities is feasible because it has been reported that there is unlimited solubility among them (as shown in Fig. 19.3b).

Recently, BiOCl<sub>x</sub>Br<sub>1-x</sub>, BiOI<sub>x</sub>Cl<sub>1-x</sub>, and BiOBr<sub>x</sub>I<sub>1-x</sub> have been synthesized [33–37], and all the alloyed compounds have been found to be more active than the corresponding pure forms. For example, although the band gap energies were in line with increasing the  $x$  value the activity of the BiOCl<sub>0.5</sub>Br<sub>0.5</sub> was the highest. Thus, it may be concluded that the light absorption and the competitive photooxidation power reach their optimal value at  $x=0.5$ . The photogenerated hole is the main reactive species in the presented system to remove aqueous RhB under visible light irradiation. This experimental result supported the theory computations that oxygen vacancies, which are energetically more favorable in alloyed BiOXs, could act as capture centers for excited electrons and, consequently, improve the separation of the electron–hole pairs [38]. Therefore, the alloying effect in BiOXs brings about a substantially lower electron–hole recombination rate and, accordingly, a much higher photocatalytic performances.

### 19.3.1.3 Nonmetal Doping

Layered BiOCl with open structure has a unique advantage in facilitating homogeneous doping [2]. The dopant at the atomic level in the whole of doped semiconductor matrix will not change the crystal structure of the semiconductor. Thus, homogeneous nonmetal doping in layered BiOCl possesses an extended band-to-band visible light absorption edge (as shown in Fig. 19.3c) [39–41]. For example, an obvious red shift in the absorption edge and an enhanced absorption in the visible light range were observed in the C-doped BiOCl hierarchical structures, which have been synthesized through a facile method using polyacrylamide (PAM) as both chelating and doping agents [42]. The C-doped BiOCl exhibited much higher photocatalytic activity than the pure one in the degradation of MO dye and colorless phenol contaminant under ultraviolet light irradiation but the absorption of the contaminants on the surface of C-doped BiOCl can be ignored in the photocatalysis. It was proposed that the enhanced degradation activity of C-doped BiOCl was due to the impurity energy levels above the VB of BiOCl. The impurity energy levels

can cause the shifting of the absorption edge to higher wavelengths and increase the lifetime of charge carriers. Thus, the photocatalytic activity would be improved by both the inhibition of recombination of photo-induced charge carriers and the effective usage of light source.

Recently, Fan et al. based on the density functional theory reported that the impurity energy levels in the nonmetal-doped BiOCl are mainly contributed by the np states of doping elements which can make the red shift of photoabsorption band edge into the visible light region [43]. It is worth to note that, among the B, C, N, Si, P, S-doped BiOCl system, the impurity levels of S-doped BiOCl system located in the top of valence band are difficult to produce recombination center of photon-generated carriers, which can result in narrowing BiOCl band gap and the red shift of light-responding scope. Therefore, the S-doped BiOCl system will be an appropriate path to enhance the photocatalytic activity of BiOCl.

#### 19.3.1.4 Metal Doping

For TiO<sub>2</sub>-based photocatalysts, transition metal doping by the wet-chemistry route will generally result in recombination centers in the band and thus less photocatalytic activity. Liu et al. thought the transition metal dopants existed as their oxide clusters instead of transition metal atoms within the surface/subsurface of doped matrices due to the differences in crystal nucleation ability and crystal structure between dopants and matrices (as shown in Fig. 19.3d) [44]. However, the metal ions doping in the BiOCl seems feasible to form the homogeneous dopants due to its layered and opened crystal structure. For instance, an absorption edge steeply lies about 378 nm for the pristine BiOCl, whereas Mn-doped BiOCl exhibits red shifts of absorption edge and significant enhancement of light absorption at 400–600 nm, which clearly indicates the presence of additional energy levels (Mn<sup>2+</sup>/Mn<sup>3+</sup>) of the transition metal ions into the forbidden gap of BiOCl [45]. Therefore, the absorption edge shifting toward higher wavelengths for the Mn-doped BiOCl should come from the electronic transition from the dopant energy level (Mn<sup>2+</sup>/Mn<sup>3+</sup>) to the conduction band of BiOCl. The increased photocatalytic activity in the degradation of malachite green dye by Mn-doped BiOCl might result from the increase of lifetime of photogenerated carriers due to scavenging of electrons by Mn, and enhancing surface absorption of the dyes by charging the particle surface.

In addition, Fe-doped and Fe, Nb-codoped BiOCl samples were obtained via the wet-chemistry routes [46–48]. Both doped samples show enhanced photocatalytic performance to degrade the RhB dyes since the doping of Fe<sup>3+</sup> could effectively increase the absorption of the photocatalysts. Fan et al. found that Mn-doped BiOCl with oxygen vacancy could narrow the band gap and extend the optical absorption to visible, red, and infrared light region based on density functional theory (DFT) + U calculations [49].

Rare earth ion dopant is another important metal-doping type to enhance the photocatalytic performance. The wide band gap of BiOCl could provide an optical window and the inherent quenching effects of rare earths, and importantly Bi could

be a more favorable cation for rare earth ion dopant emission. Li et al. observed high multiphoton-upconversion emission of  $\text{Er}^{3+}$  ions in the Er-doped BiOCl or Er/Yb-codoped BiOCl microcrystals under 980 nm excitation [50]. It was found that an isolated impurity energy band emerged in the middle of the band gap. Furthermore, Eu doping enhances the internal electric fields of BiOX and makes the variation of band gaps [50]. Eu doping makes BiOCl have stronger reducing activity, owing to the bottom of the conduction band of Eu-doped BiOCl being more negative. The theory findings could well explain the experimental observations in our group work:  $\text{Er}^{3+}$  and  $\text{Yb}^{3+}$ -doped  $\text{Bi}_5\text{O}_7\text{I}$  photocatalyst shows improved visible photocatalytic activity than the  $\text{Bi}_5\text{O}_7\text{I}$  photocatalyst [51].

### 19.3.2 Sensitizer Modifying

Sensitization of a wide band-gap semiconductor photocatalyst via chemisorbed or physisorbed photosensitizers can extend the spectrum applications from UV light to the full spectrum (as shown in Fig. 19.4a). Recently, researchers are intensively investigating photochemical water splitting based on the dye-sensitized oxide semiconductors [52–55]. The organization of dye molecules into assemblies could promote long-lived charge separation, and catalysis of the electrolysis reactions, in particular the four-electron oxidation of water. For example, our group employed phthalocyanine copper (CuPc) to photosensitize BiOCl via one-pot liquid loading [22]. The prepared BiOCl/CuPc has strong visible light absorption (500–800 nm) and displays 76 and 142 times photocurrent intensity higher than that of a bare BiOCl electrode under simulated solar light and the LED of 410 nm, respectively. Especially, in a methanol– $\text{H}_2\text{O}$ –RhB system, overall water splitting was realized on the BiOCl/CuPc hybrid. This may provide a prospective method for solar energy storage and conversion, though the activity is very low up to now.

### 19.3.3 Co-catalyst Modified Bismuth Oxyhalides

Generally, the photocatalytic reaction involves three steps: (1) the photocatalyst absorbs photon energy higher than the band-gap energy of the material and generates photoexcited electron–hole pairs, (2) the photoexcited carriers separate and migrate to the surface without recombination, and (3) adsorbed species are reduced and oxidized by the photogenerated electrons, holes, and active species. The first step is strongly dependent on the structural and electronic properties of the photocatalyst, while the latter two steps are adjusted and prompted by additional catalysts (called co-catalyst). Therefore, it is important to fabricate a photocatalytic system with the appropriate co-catalyst for solar energy conversion (as shown in Fig. 19.4b, c). By the photochemical labeling experiments, Au, Ag and Pt nanoparticles and  $\text{PbO}_2$ ,  $\text{MnO}_x$  were easily deposited on the surface of semiconductor photocatalysts

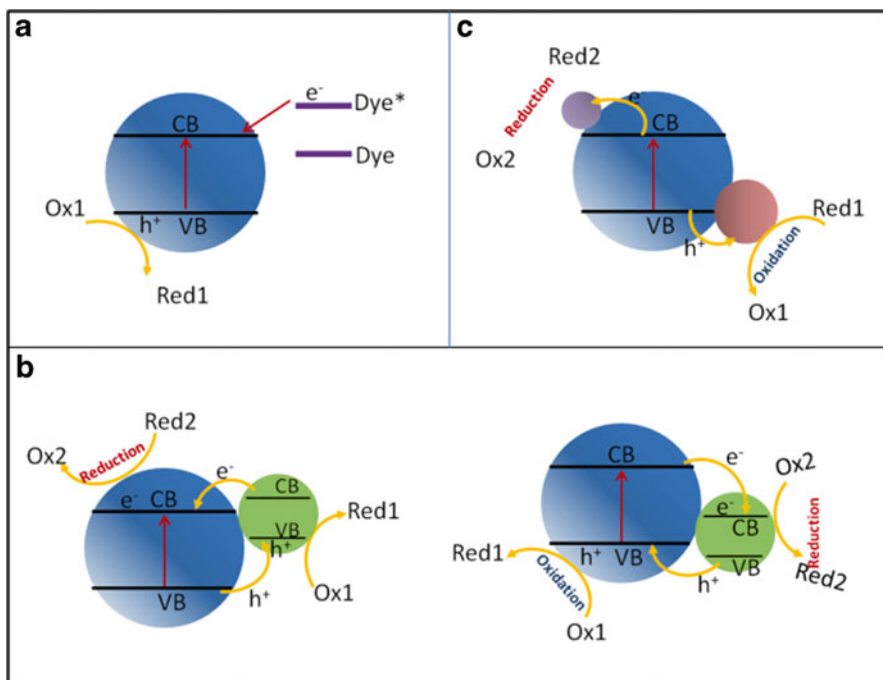


**Fig. 19.4** Photocatalytic mechanisms in functional coupled photocatalyst materials

[56]. The metal nanoparticles have been thought as deriving electron-type co-catalyst and the metal oxide as deriving hole-type co-catalyst. Recently, our group prepared BiOCl@Au/MnO<sub>x</sub> photocatalysts by the photo-deposition method [57]. The overall water splitting reaction was observed in the photocatalyst based on the driving force of the co-catalysts deposited on different facets. The oxygen and hydrogen evolution rate of the BiOCl@Au/MnO<sub>x</sub> sample was stability during a 30 h irradiation, though the evolution of H<sub>2</sub> was much smaller than that of O<sub>2</sub> in the photocatalysis. It was interpreted that photo-induced holes were the main active species of BiOX photocatalysts. Thus, the selective deposition of redox co-catalysts on the different facets of a single crystal, and efficient charge separation between different facets should be promising and intriguing for designing highly efficient solar energy conversion photocatalysts.

In addition, by coupling with semiconductors with suitable band gaps, the as-formed BiOCl/narrow band gap semiconductor composites could expand their photoabsorption into visible light range. Binary composites, such as WO<sub>3</sub>/BiOCl, NaBiO<sub>3</sub>/BiOCl, BiOCl/Bi<sub>2</sub>O<sub>3</sub>, BiOCl/BiOBr, and BiOI/BiOCl, have been prepared and have been proved to be efficient visible light-driven photocatalysts [58–65].

Furthermore, n–p heterostructure (built from n-type TiO<sub>2</sub> (anatase) and p-type BiOCl) as a model photoanode nanostructure for efficient PEC water splitting process had been reported by Shi et al. [66]. Due to the distinctive energy band structures of the two semiconductors, photo-induced carriers can transfer between

the BiOCl and TiO<sub>2</sub>, prompting the separation of electrons and holes. On the other hand, due to the different property of p-type and n-type semiconductors, the self-field formed in the interface between BiOCl layer and TiO<sub>2</sub> layer was helpful for efficient electron–hole transfer in the PEC water splitting.

### 19.3.4 Magnetic Functional

Magnetic supports for the photocatalysts could overcome the limitation of separation from the liquid phase thus the powder photocatalysts could be effectively recycled by applying an external magnetic field, which attracted increasing attention because of their scientific and technological importance in the environmental purification, especially in waste water treatment. Our group reported a highly efficient Fe<sub>3</sub>O<sub>4</sub>/BiOCl magnetic photocatalyst with special coupled nanostructure (as shown in Fig. 19.5) [67]. The Fe<sub>3</sub>O<sub>4</sub> nanoparticles inlaid with the BiOCl nanoflake, the interface with fewer defects are responsible for holding the high photocatalytic activity of BiOCl. As a comparison, the photocatalytic activities of most other magnetic photocatalysts with core-shell structure were dramatically decreased because of the introduction of the magnetic Fe<sub>3</sub>O<sub>4</sub> core.

Our group has also prepared another Fe<sub>3</sub>O<sub>4</sub>@SiO<sub>2</sub>/BiOCl magnetic photocatalyst [23]. The photo-induced electron from the conduction of BiOCl could not transfer to the Fe<sub>3</sub>O<sub>4</sub> core due to the inner layer of SiO<sub>2</sub>, which means the photocatalytic activity was kept in this magnetic photocatalyst. The photocatalytic elimination of 2,2-bis (4-hydroxyphenyl) propane (BPA) by BiOBr@SiO<sub>2</sub>@Fe<sub>3</sub>O<sub>4</sub> under the irradiation of different light sources was investigated. More importantly, the experi-

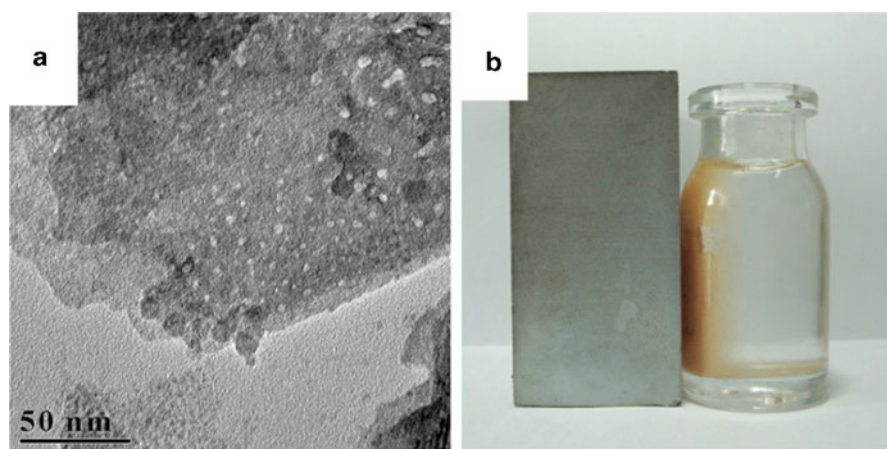


**Fig. 19.5** (a) TEM image of Fe<sub>3</sub>O<sub>4</sub>/BiOCl nanocomposite flakes; (b) a photograph showing magnetic recycle of the Fe<sub>3</sub>O<sub>4</sub>/BiOCl magnetic photocatalyst

mental results showed that only one main intermediate was detected during the photocatalytic degradation process. Direct oxidation by the photogenerated holes and partly due to  $\cdot\text{OH}$  oxidation is proposed to be the reason for the complete and fast removal of BPA.

## 19.4 Summary and Future Perspectives

This review focuses on research progress of the morphology modulation and functionalization of the nano- and micro-bismuth oxyhalide photocatalysts. The high photocatalytic activity mainly originates from the intrinsic layered structure no matter what morphology of the photocatalysts are. However, the efficiency of separation and transfer of the photogenerated carriers is relative with its morphology structure: the shorter transfer distance along with the internal electric field, the higher photo-activity of the bismuth oxyhalide photocatalysts since the carriers were speeded up via the internal electric field [56]. Furthermore, heterojunction construction will modulate the composition to increase internal electric field, then enhancing the photocatalytic activity of bismuth oxyhalides. These research works may offer guidance for the design and construction of high-performance bismuth oxyhalide photocatalysts. Although those strategies have increased the photocatalytic activity of bismuth oxyhalide, the state-of-the-art bismuth oxyhalide photocatalysts cannot satisfy many requirements of solar energy conversion and applications. We still need to keep an eye on the fundamental theory and some key issues in engineering the layered structure-mediated properties of bismuth oxyhalide photocatalysts. Some questions and future directions include as follows:

1. Previous investigations on the crystal structure and morphology of BiOX crystal-lites showed that they usually grow in the form of platelets with  $\{001\}$  facet exposed. The oxygen vacancies in these facets were easy to obtain under UV light irradiation. The photo-induced defect on the  $[\text{Bi}_2\text{O}_2]^{2+}$  slab can trap the photogenerated electrons at the defect sites. The changed charge density in the surface would alter the internal electric field (IEF) intensity and initiate structural rearrangement, which is proved crucial to impact their photocatalytic activity. Therefore, more strategies should be developed to modulate the surface charge then to enhance the internal electric field, which is advantageous for enhancing the efficiency of the photo-generated carriers.
2. The bismuth oxyhalide, due to its special electronic structure, is a significant class of oxidative photocatalyst. Most of the reports on BiOX photocatalysts are focused on the decomposition of liquid organic pollutants so far. BiOX are rarely used in the energy photocatalysis field, such as water splitting and  $\text{CO}_2$  photoreduction. It should be extended to utilizing BiOX photocatalysts in reducing photocatalytic reactions by upshifting the CB of the BiOX. Some key issues associated with the transfer of photo-induced electrons accelerated by the internal electric field were thought as key factors to govern the physicochemical properties and thus reducibility reaction.

## References

1. Cheng H, Huang B, Dai Y (2014) Engineering BiOX (X=Cl, Br, I) nanostructures for highly efficient photocatalytic applications. *Nanoscale* 6:2009–2026
2. Li J, Yu Y, Zhang L et al (2014) Bismuth oxyhalide nanomaterials: layered structures meet photocatalysis. *Nanoscale* 6:8473–8488
3. Ye L, Su Y, Jin X et al (2014) Recent advances in BiOX (X=Cl, Br and I) photocatalysts: synthesis, modification, facet effects and mechanisms. *Environ Sci Nano* 1:90–112
4. Zhang KL, Liu CM, Huang FQ et al (2006) Study of the electronic structure and photocatalytic activity of the BiOCl photocatalyst. *Appl Catal B* 68:125–129
5. An HZ, Du Y, Wang TM et al (2008) Photocatalytic properties of BiOX (X=Cl, Br, and I). *Rare Metals* 27:243–250
6. Osterloh FE et al (2013) Inorganic nanostructures for photoelectrochemical and photocatalytic water splitting. *Chem Soc Rev* 42:2294–2320
7. Marschall R et al (2014) Semiconductor composites: strategies for enhancing charge carrier separation to improve photocatalytic activity. *Adv Funct Mater* 24:2421–2440
8. Wu SJ, Wang C, Cui YF et al (2010) Synthesis and photocatalytic properties of BiOCl nanowire arrays. *Mater Lett* 64:115–118
9. Wang C, Shao C, Liu Y et al (2008) Photocatalytic properties BiOCl and Bi<sub>2</sub>O<sub>3</sub> nanofibers prepared by electrospinning. *Scr Mater* 59:332–335
10. Tian Y, Guo CF, Guo YJ et al (2012) BiOCl nanowire with hierarchical structure and its Raman features. *Appl Surf Sci* 258:1949–1954
11. Sun SM, Wang WZ, Zhang L et al (2009) Visible light-induced efficient contaminant removal by Bi<sub>5</sub>O<sub>7</sub>I. *Environ Sci Tech* 43:2005–2010
12. Su YR, Wang H, Ye LQ et al (2014) Shape-dependent photocatalytic activity of Bi<sub>5</sub>O<sub>7</sub>I caused by facets synergetic and internal electric field effects. *Rsc Adv* 4:65056–65064
13. Sun Y, Gao S, Xie Y et al (2014) Atomically-thick two-dimensional crystals: electronic structure regulation and energy device construction. *Chem Soc Rev* 43:530–546
14. Ida S, Ishihara T et al (2014) Recent progress in two-dimensional oxide photocatalysts for water splitting. *J Phys Chem Lett* 5:2533–2542
15. Shang M, Wang WZ, Zhang L et al (2009) Preparation of BiOBr lamellar structure with high photocatalytic activity by CTAB as Br source and template. *J Hazard Mater* 167:803–809
16. Xiong J, Cheng G, Li G et al (2011) Well-crystallized square-like 2D BiOCl nanoplates: mannitol-assisted hydrothermal synthesis and improved visible-light-driven photocatalytic performance. *RSC Adv* 1:1542–1553
17. Guan M, Xiao C, Zhang J et al (2013) Vacancy associates promoting solar-driven photocatalytic activity of ultrathin bismuth oxychloride nanosheets. *J Am Chem Soc* 135:10411–10417
18. Li Y, Li C, Zhang Z et al (2014) Black BiOCl with disorder surface structure prepared by Fe reduction and the enhanced photocatalytic activity. *Solid State Sci* 34:107–112
19. Jiang Z, Huang B, Lou Z et al (2014) Immobilization of BiOX (X=Cl, Br) on activated carbon fibers as recycled photocatalysts. *Dalton Trans* 43:8170–8173
20. Weng BC, Xu FH, Xu JG et al (2014) Hierarchical structures constructed by BiOX (X=Cl, I) nanosheets on CNTs/carbon composite fibers for improved photocatalytic degradation of methyl orange. *J Nano Res* 16:2766
21. Zhang X, Ai ZH, Jia FL et al (2008) Generalized one-pot synthesis, characterization, and photocatalytic activity of hierarchical BiOX (X=Cl, Br, I) nanoplate microspheres. *J Phys Chem C* 112:747–753
22. Zhang L, Wang WZ, Sun SM et al (2013) Water splitting from dye wastewater: a case study of BiOCl/copper(II) phthalocyanine composite photocatalyst. *Appl Catal B* 132:315–320
23. Zhang L, Wang WZ, Sun SM et al (2014) Elimination of BPA endocrine disruptor by magnetic BiOBr@SiO<sub>2</sub>@Fe<sub>3</sub>O<sub>4</sub> photocatalyst. *Appl Catal B* 148:164–169
24. Jing LQ, Zhou W, Tian GH et al (2013) Surface tuning for oxide-based nanomaterials as efficient photocatalysts. *Chem Soc Rev* 42:9509–9549

25. Asahi R, Morikawa T, Ohwaki T et al (2001) Visible-light photocatalysis in nitrogen-doped titanium oxides. *Science* 293:269–271
26. Ganduglia-Pirovano MV, Hofmann A, Sauer J et al (2007) Oxygen vacancies in transition metal and rare earth oxides: current state of understanding and remaining challenges. *Surf Sci Rep* 62:219–270
27. Ye L, Deng K, Xu F et al (2012) Increasing visible-light absorption for photocatalysis with black BiOCl. *Phys Chem Chem Phys* 14:82–85
28. Ye L, Zan L, Tian L et al (2011) The {001} facets-dependent high photoactivity of BiOCl nanosheets. *Chem Commun* 47:6951–6953
29. Sarwan B, Pare B, Acharya AD et al (2014) The effect of oxygen vacancies on the photocatalytic activity of BiOCl nanocrystals prepared by hydrolysis and UV light irradiation. *Mater Sci Semicond Process* 25:89–97
30. Li H, Shi J, Zhao K et al (2014) Sustainable molecular oxygen activation with oxygen vacancies on the {001} facets of BiOCl nanosheets under solar light. *Nanoscale* 6:14168–14173
31. Zhang L, Wang W, Jiang D et al (2014) Photoreduction of CO<sub>2</sub> on BiOCl nanoplates with the assistance of photoinduced oxygen vacancies. *Nano Res* 8:821–831
32. Gnayem H, Sasson Y et al (2013) Hierarchical nanostructured 3D flowerlike BiOCl<sub>x</sub>Br<sub>1-x</sub> semiconductors with exceptional visible light photocatalytic activity. *Acs Catal* 3:861
33. Ren KX, Liu J, Liang J et al (2013) Synthesis of the bismuth oxyhalide solid solutions with tunable band gap and photocatalytic activities. *Dalton Trans* 42:9706–9712
34. Shenawi-Khalil S, Uvarov V, Kritsman Y, Sasson Y et al (2011) A new family of BiO(Cl<sub>x</sub>Br<sub>1-x</sub>) visible light sensitive photocatalysts. *Catal Commun* 12:1136–1141
35. Gnayem H, Sasson Y et al (2013) Hierarchical nanostructured 3D flowerlike BiOCl<sub>x</sub>Br<sub>1-x</sub> semiconductors with exceptional visible light photocatalytic activity. *Acs Catal* 3:186–191
36. Lester Y, Avisar D, Gnayem H et al (2014) Demonstrating a new BiOCl<sub>0.875</sub>Br<sub>0.125</sub> photocatalyst to degrade pharmaceuticals under solar irradiation. *Water Air Soil Pollut* 225:2132
37. Na Y, Kim YI, Cho DW et al (2014) Adsorption/photocatalytic performances of hierarchical flowerlike BiOBr<sub>x</sub>Cl<sub>1-x</sub> nanostructures for methyl orange, Rhodamine B and methylene blue. *Mater Sci Semicond Process* 27:181–190
38. Zhang H, Liu L, Zhou Z et al (2012) Towards better photocatalysts: first-principles studies of the alloying effects on the photocatalytic activities of bismuth oxyhalides under visible light. *Phys Chem Chem Phys* 14:1286–1292
39. Li X, Jiang G, Wei Z et al (2013) One-pot solvothermal preparation of S-doped BiOBr microspheres for efficient visible-light induced photocatalysis. *MRS Commun* 3:219–224
40. Jiang G, Li X, Wei Z et al (2014) Immobilization of N, S-codoped BiOBr on glass fibers for photocatalytic degradation of rhodamine B. *Powder Tech* 261:170–175
41. Jiang G, Li X, Wei Z et al (2014) Growth of N-doped BiOBr nanosheets on carbon fibers for photocatalytic degradation of organic pollutants under visible light irradiation. *Powder Tech* 260:84–89
42. Yu J, Wei B, Zhu L et al (2013) Flowerlike C-doped BiOCl nanostructures: facile wet chemical fabrication and enhanced UV photocatalytic properties. *Appl Surf Sci* 284:497–502
43. Wang Y, Zhang XC, Zhao LJ et al (2014) First principles calculations on electronic structures and optical absorption properties of nonmetal doped BiOCl. *Chem J Chin Univ* 35:2624–2631
44. Liu G, Wang L, Yang HG et al (2010) Titania-based photocatalysts – crystal growth, doping and heterostructuring. *J Mater Chem* 20:831–843
45. Pare B, Sarwan B, Jonnalagadda SB et al (2011) Photocatalytic mineralization study of malachite green on the surface of Mn-doped BiOCl activated by visible light under ambient condition. *Appl Surf Sci* 258:247–253
46. Xia J, Xu L, Zhang J et al (2013) Improved visible light photocatalytic properties of Fe/BiOCl microspheres synthesized via self-doped reactable ionic liquids. *CrystEngComm* 15:10132–10141
47. Jiang G, Wang X, Wei Z et al (2013) Photocatalytic properties of hierarchical structures based on Fe-doped BiOBr hollow microspheres. *J Mater Chem A* 1:2406–2410

48. Nussbaum M, Shaham-Waldmann N, Paz Y et al (2014) Synergistic photocatalytic effect in Fe, Nb-doped BiOCl. *J Photochem Photobio A* 290:11–21
49. Wang C, Qiu H, Inoue T et al (2014) Electronic structure calculations of I and Mn doped BiOCl with modified Becke–Johnson potential. *Comput Mater Sci* 85:138–141
50. Zhao ZY, Dai WW et al (2014) Structural, electronic, and optical properties of Eu-Doped BiOX (X=F, Cl, Br, I): a DFT+U study. *Inorg Chem* 53:13001–13011
51. Zhang L, Wang WZ, Sun SM et al (2012) Photocatalytic activity of Er<sup>3+</sup>, Yb<sup>3+</sup> doped Bi<sub>5</sub>O<sub>7</sub>I. *Catal Commun* 26:88–92
52. Wang L, Shang J, Hao WC et al (2014) A dye-sensitized visible light photocatalyst-Bi<sub>24</sub>O<sub>31</sub>Cl<sub>10</sub>. *Sci Rep* 4:7384
53. Li GS, Jiang B, Xiao SN et al (2014) An efficient dye-sensitized BiOCl photocatalyst for air and water purification under visible light irradiation. *Environ Sci Process Impacts* 16:1975–1980
54. Luz A, Conradt J, Wolff M et al (2013) p-DSSCs with BiOCl and BiOBr semiconductor and polybromide electrolyte. *Solid State Sci* 19:172–177
55. Ye L, Gong C, Liu J et al (2012) Bi<sub>n</sub>(Tu)<sub>x</sub>Cl<sub>3n</sub>: a novel sensitizer and its enhancement of BiOCl nanosheets' photocatalytic activity. *J Mater Chem* 22:8354–8360
56. Li L, Salvador PA, Rohrer GS et al (2014) Photocatalysts with internal electric fields. *Nanoscale* 6:24–42
57. Zhang L, Wang WZ, Sun SM et al (2015) Selective transport of electron and hole among {001} and {110} facets of BiOCl for pure water splitting. *Appl Catal B* 162:470–474
58. Chakraborty AK, Rawal SB, Han SY et al (2011) Enhancement of visible-light photocatalytic efficiency of BiOCl/Bi<sub>2</sub>O<sub>3</sub> by surface modification with WO<sub>3</sub>. *Appl Catal A* 407:217–223
59. Shamaila S, Sajjad AKL, Chen F et al (2011) WO<sub>3</sub>/BiOCl, a novel heterojunction as visible light photocatalyst. *J Colloid Interface Sci* 356:465–472
60. Yu CL, Chen JC, Zhou WQ et al (2015) Grinding calcination preparation of WO<sub>3</sub>/BiOCl heterostructures with enhanced visible light photocatalytic activity. *Mater Res Innovations* 19:54–59
61. Chang XF, Yu G, Huang J et al (2010) Enhancement of photocatalytic activity over NaBiO<sub>3</sub>/BiOCl composite prepared by an in situ formation strategy. *Catal Today* 153:193–199
62. Chai SY, Kim YJ, Jung MH, Chakraborty AK, Jung D, Lee WI et al (2009) Heterojunctioned BiOCl/Bi<sub>2</sub>O<sub>3</sub>, a new visible light photocatalyst. *J Catal* 262:144–149
63. Zhang J, Xia JX, Yin S et al (2013) Improvement of visible light photocatalytic activity over flower-like BiOCl/BiOBr microspheres synthesized by reactable ionic liquids. *Colloids Surf A* 420:89–95
64. Dong F, Sun YJ, Fu M et al (2012) Room temperature synthesis and highly enhanced visible light photocatalytic activity of porous BiOI/BiOCl composites nanoplates microflowers. *J Hazard Mater* 219:26–34
65. Xiao X, Hao R, Liang M et al (2012) One-pot solvothermal synthesis of three-dimensional (3D) BiOI/BiOCl composites with enhanced visible-light photocatalytic activities for the degradation of bisphenol-A. *J Hazard Mater* 233:122–130
66. Fan WQ, Yu XQ, Song SY et al (2014) Fabrication of TiO<sub>2</sub>-BiOCl double-layer nanostructure arrays for photoelectrochemical water splitting. *CrystEngComm* 16:820–825
67. Zhang L, Wang WZ, Zhou L et al (2009) Fe<sub>3</sub>O<sub>4</sub> coupled BiOCl: a highly efficient magnetic photocatalyst. *Appl Catal B* 90:458–462

# Chapter 20

## Synthesis and Facet-Dependent Properties of Layered BiOCl Photocatalysts

Jie Li and Lizhi Zhang

### 20.1 Introduction

Bismuth oxychloride (BiOCl) is a layered material that consists of [Cl–Bi–O<sub>2</sub>–Bi–Cl] monolayers stacked together by van der Waals interaction between neighboring halogen atoms along the *c*-axis [1–3]. In its each [Cl–Bi–O<sub>2</sub>–Bi–Cl] monolayer of structural unit, a bismuth center coordinates with four oxygen and four halogen atoms to create an asymmetric decahedral geometry. The intriguing layered characteristics, featuring the strong intralayer covalent bonding within the [Bi<sub>2</sub>O<sub>2</sub>] layers and the weak interlayer van der Waals interaction between halogen double slabs, endow BiOCl with outstanding electrical, magnetic, optical, chemical, mechanical and catalytic properties and thus as a promising candidate for many applications. Its early-stage applications mainly involved cosmetic use, pharmaceutical design, ferroelectric study, and selective oxidation catalysis [4–6]. Despite these advances in its applications, BiOCl still could not effectively attract considerable research attention until the pioneering exploration of its photocatalysis application in 2006, when Huang et al. synthesized BiOCl nanoplates via thermal-assisted hydrolysis of BiCl<sub>3</sub> in excessive concentrated hydrochloric acid and demonstrated their superior photoactivity on degrading methyl orange (MO) dye, even better than the benchmark photocatalyst (commercial TiO<sub>2</sub> P25) [7]. This striking photoactivity of BiOCl coupling with its facile synthesis encouraged extensive research enthusiasm on exploring the potential photocatalytic properties of layered BiOCl. The subsequent research endeavors were mainly focused on optimizing the photoreactivity by

---

J. Li • L. Zhang (✉)

Key Laboratory of Pesticide and Chemical Biology of Ministry of Education, Institute of Environmental Chemistry, College of Chemistry, Central China Normal University, 152 Luoyu Road, Wuhan 430079, People's Republic of China  
e-mail: [zhanglz@mail.cnu.edu.cn](mailto:zhanglz@mail.cnu.edu.cn)

designing and fabricating various functional nanostructures including nanosheets, nanobelts, nanofibers, nanowires, nanoflowers, and hollow nanostructure, and also by introducing the well-known strategies including surface functionalization, doping, plasmon modification, and heterojunction construction [8–40]. Although the research field of BiOCl photocatalysis currently appears to be in its heydays, there is little progress on understanding its photocatalytic mechanism, especially the relationship between the layered structure and photocatalytic properties.

Our recent work on facet-controllable synthesis of BiOCl provides an avenue to tackle this challenge, as the as-synthesized BiOCl nanosheets with {001} and {010} facet exposure can serve as a platform to understand the photocatalysis mechanism of layered BiOCl [2, 3]. The selective exposure of dominated facet in BiOCl was achieved by a facile hydrothermal route, depending on the pH value of surrounding environment. When the pH value of growth environment changed from 1–4 to 6–8, the dominated facet on BiOCl surface varied correspondingly from {001} to {010}. Using these two faceted BiOCl, we for the first time unveiled several facet-dependent properties of BiOCl, including facet-dependent photocatalytic activities, facet-dependent molecular oxygen activation, facet-dependent oxygen vacancy engineering, facet-dependent doping, and facet-dependent selective silver deposition, which provided in-depth insights into the structure–property relationship [2, 3, 41–44]. On basis of experimental and theoretical mechanistic explorations, we concluded that these facet-dependent properties were attributed to its layered structure, which determined the photoreactivity of BiOCl via the following three-layered structure-related characteristics. The first one is the strong capability of the layered structure to induce internal electric fields, which can boost the charge separation and thus enhance the photoactivity. This is because the nonuniform charge distribution between  $[\text{Bi}_2\text{O}_2]$  and halogen slices in the nanosheets would polarize the related atoms and orbitals to form internal electric fields along the crystal orientation perpendicular to the [Cl] and  $[\text{Bi}_2\text{O}_2]$  layers [42]. The internal electric fields induced by the unique layered structure would promote the photoinduced charge separation and transfer from the bulk to the surface, which are beneficial to the subsequent photocatalytic reactions on the surface [7]. We highlighted the advantage of the preferential {001} facet exposure in BiOCl to make use of internal electric fields to enhance the photoactivity, and also demonstrated that more {001} facet exposure could induce the generation of stronger internal electric field, which favored the photo-generated charge separation and transfer, and thus enhance the photoreactivity [2, 42]. The second one is the facile generation of oxygen vacancies on the BiOCl {001} facet upon UV irradiation or heating in reductive nonaqueous solvents [3, 43–46]. Compared with nonlayered materials that have strong bonds in three dimension, layered counterparts form strong bonds only within its two-dimensional structural unit [47–49]. The huge differences in the strain between two-dimensional in-plane and three-dimensional direction remarkably activate the surface-exposed atoms of the layered structure, leading to their easy escape from mother crystals when subjected to the external thermal, electric, or light energy. The termination of oxygen atoms on BiOCl {001} facet enables the generation of oxygen vacancies on the {001} facet upon UV irradiation or heating in reductive nonaqueous solvents [3,

43, 44]. The generated oxygen vacancies can modulate the band structure to increase the light harvesting and the charge transfer, and also lower surface catalytic reaction barriers to activate gas molecules such as  $O_2$  and  $CO_2$  [50–52]. The third one is the open channel existing between the neighboring [Cl–Bi–O<sub>2</sub>–Bi–Cl] monolayers, which enables the intercalation of foreign molecules to create unexpected properties. A prototypical example was methyl orange intercalation-mediated superior photosensitization activity of {010}-faceted BiOCl nanosheets under visible light, in which the dominated {010} facet enriched with the open channels favored the adsorption of methyl orange and thereby the injection of electrons generated from methyl orange onto BiOCl [2]. Recently, we demonstrated that the open channel of BiOCl facilitated the implantation of carbonaceous species of dopant precursors into shallow lattice and their subsequent diffusion in bulk lattice to ultimately realize a high concentration of carbon dopants in BiOCl, which correspondingly promote its photoreactivity for solar-to-hydrogen conversion [41].

In this chapter, we first summarize the synthesis strategies of layered BiOCl, with a primary focus on the most commonly used hydrothermal and solvothermal routes. Next, we review the facet-dependent photocatalytic properties of BiOCl, including facet-dependent photocatalytic activities, facet-dependent molecular oxygen activation, facet-dependent carbon doping, and facet-dependent selective silver deposition. Finally, we would like to share our future plans in the field of BiOCl photocatalysis.

## 20.2 Synthesis of Layered BiOCl

To synthesize BiOCl, many bismuth-containing compounds, such as  $Bi(NO_3)_3$ ,  $NaBiO_3$ , and  $Bi_2O_3$ , were employed as bismuth sources, while the most intensively used chlorine sources were  $K(Na)Cl$ , hexadecyltrimethylammonium chloride (CTAC), chlorine-containing acid, and ionic liquid [15–26]. In addition,  $BiCl_3$  could act as both the bismuth and chlorine sources to prepare BiOCl via the hydrolysis [40]. Recently, many liquid-phase strategies were developed for the synthesis of nanostructured BiOCl because of their facile operation and powerful manufacturing ability to design various nanoarchitectures. Of these liquid-phase strategies, the two most often used ones were hydrothermal and solvothermal syntheses. In this section, we will summarize the recent progress on the hydrothermal and solvothermal syntheses of layered BiOCl.

### 20.2.1 Hydrothermal Route

Hydrothermal synthesis of BiOCl is usually realized by simply placing the mixed aqueous solution of bismuth and chlorine sources in a thermal-treated sealed vessel, where the auto-generated pressure upon heating enables the enhancement of the

solubility and the reactivity of reactant precursors to drive the chemical reactions that are unable to proceed at ambient conditions [53]. Moreover, adjusting the thermodynamic and kinetic parameters of these synthetic systems, such as the concentrations of reactant precursors, reaction time, the temperature of thermal treatment, ensures the fine tuning of size, shape, uniformity, dimensionality, crystal phase and exposed crystal facet of as-synthesized nanostructured BiOCl in a precisely controllable manner. To date, by using this well-established hydrothermal method, many BiOCl nanostructures have been successfully realized, such as nanosheets, nanobelts, nanofibers, nanowires, nanoflowers, and hollow nanostructure [8–40]

Among these nanostructures, two-dimensional nanosheet is the most easily formed structural motif of hydrothermally synthesized BiOCl. A typical example is the hydrothermal processing of  $\text{Bi}(\text{NO}_3)_3$  and KCl dispersed in aqueous solution to yield two-dimensional BiOCl nanosheets with {001} facet exposure. At the beginning of this hydrothermal reaction, two  $\text{Bi}^{3+}$  cations are inclined to react with two  $\text{H}_2\text{O}$  to yield one  $(\text{Bi}_2\text{O}_2)^{2+}$  and two  $\text{H}^+$ . Then, the coulomb coupling force between the negative  $\text{Cl}^-$  anions and the positive  $(\text{Bi}_2\text{O}_2)^{2+}$  cations directs their oriented assembly to form tiny crystalline nucleus of  $\text{Cl}-\text{Bi}-\text{O}_2-\text{Bi}-\text{Cl}$ , within which the Bi and O interact via covalent bonds. Despite the higher surface energy of {001} facet than the {010} counterpart, the twinborn  $\text{H}^+$  ions serve as a capping agent to selectively bond onto the surface-terminated oxygen atoms of {001} facet, guiding the assembly of  $\text{Cl}-\text{Bi}-\text{O}_2-\text{Bi}-\text{Cl}$  nucleus within their two-dimensional in-plane other than along the  $c$ -axis. The corresponding characterizations demonstrated that the formed nanosheet had ca. 80 % {001} facet exposure (Fig. 20.1) [2].

Over a long period of time, the breakthrough in synthesizing BiOCl nanosheets exposed with non-{001} facets was not made until our success in 2012 [3]. We increased the pH value of growth environment by adding  $\text{OH}^-$  ions into the precursor solution to decrease the  $\text{H}^+$  ions concentration and thus weaken the binding interaction between  $\text{H}^+$  ions and terminated oxygen of (001) surface. After the effect of  $\text{H}^+$  ions was eliminated, the assembly of  $\text{Cl}-\text{Bi}-\text{O}_2-\text{Bi}-\text{Cl}$  nucleus was driven totally by the decrease of total surface energy of crystals, leading to their stack along the  $c$ -axis and thereby the preferential growth of the {010}-faceted surface, as revealed by Fig. 20.2. Thus, we selectively exposed {001} and {010} facets of BiOCl nanosheet by tuning the pH value of hydrothermal reaction. The different surface atomic structures of these two faceted nanosheets bring a series of miraculous facet-dependent properties to BiOCl, which help to uncover the layered structure–property relationship.

### 20.2.2 Solvothermal Synthesis

The solvothermal approach is a special case of the hydrothermal route that uses organic solvent instead of water as the reaction medium [53]. The properties of the employed solvent, such as polarity, viscosity, and softness, usually impose remarkable influences on the reactivity, shapes, sizes, and phases of the final samples [54].

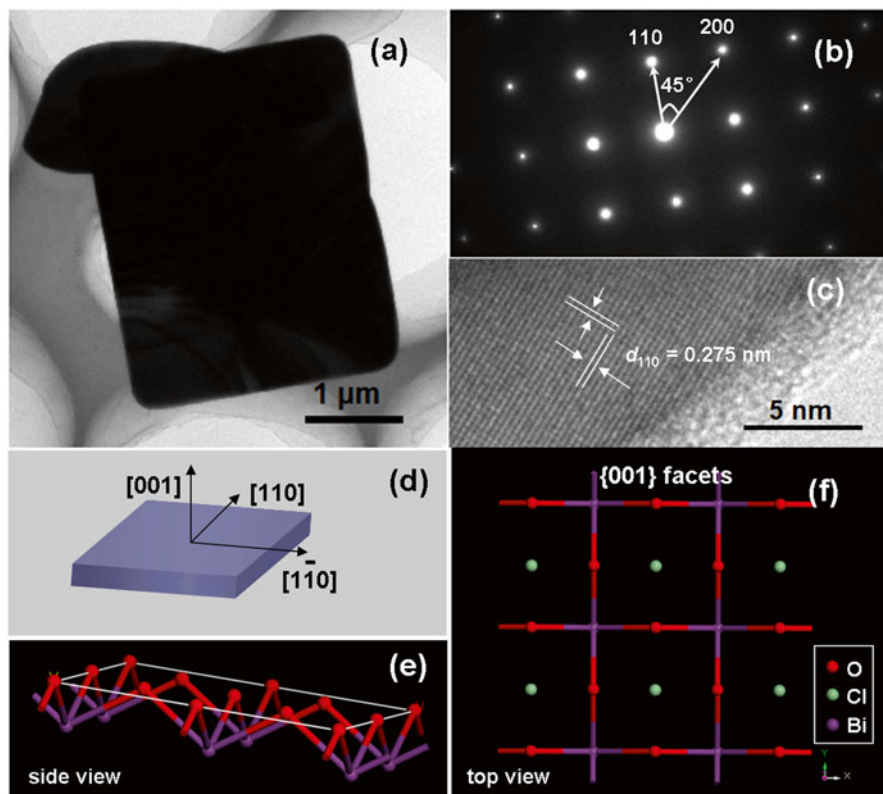


**Fig. 20.1** (a) Transmission electron microscopy (HRTEM) image, (b) Selected-area electron diffraction (SAED) pattern, and (c) high-resolution transmission electron microscopy (HRTEM) image of the {001} facet-dominant BiOCl nanosheet (named as BOC-001). (d) Schematic illustration of the crystal orientation of the nanosheet. The atomic structures of the {001} facets: (e) side view and (f) top view

During solvothermal synthesis of BiOCl, solvent molecules are prone to interact with the layered structure to create favorable functional architectures, such as hierarchical 3-D microspheres assembled by 2-D nanosheets and surface oxygen vacancy, which are difficult to achieve by hydrothermal route.

### 20.2.2.1 Hierarchical 3-D Microspheres Assembled by 2-D Nanosheets

It is known that the challenge of fabricating the nanostructures of BiOCl in a desired fashion is to slow down its fast nucleation rate in aqueous solutions. Solvothermal synthesis is a prospective alternative to solve this issue, because solvent molecules are capable of binding with bismuth precursors to yield bismuth-containing coordination compounds, slowing the  $\text{Bi}^{3+}$  releasing rate and thus controlling the growth rate of

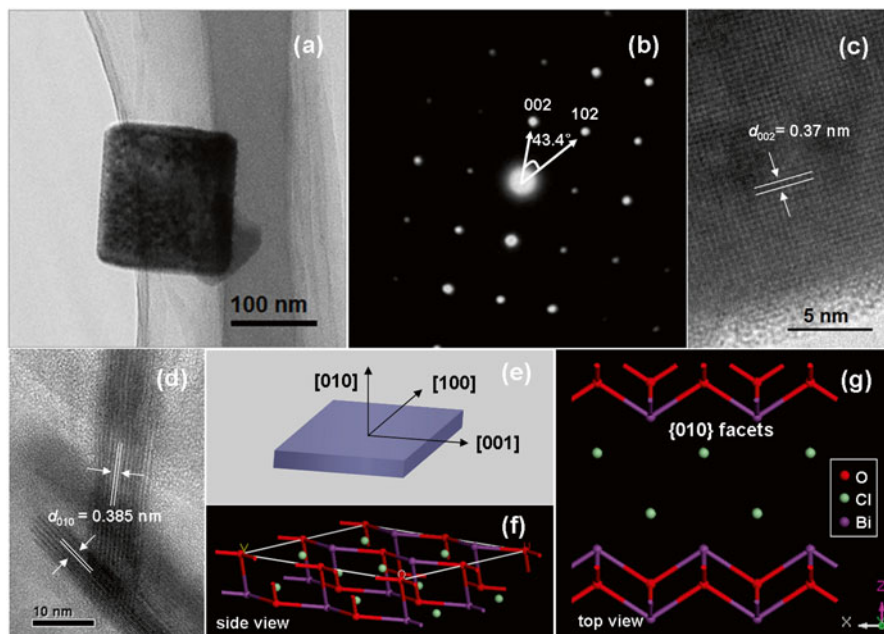


**Fig. 20.2** (a) TEM image, (b) SAED pattern, (c, d) HRTEM image of the {010} facet-dominant BiOCl nanosheet (named as BOC-010). (e) Schematic illustration of the crystal orientation of the nanosheet. The atomic structures of the {010} facets: (f) side view and (g) top view

BiOCl crystals. Additionally, the greater viscosity of solvent can control the supply rate and mobility of building blocks to favor the lower energy configuration interface and subsequently direct their perfectly oriented assemblies to generate a wide range of nanostructures. Our group first used ethylene glycol as the reaction solvent to fabricate 3-D hierarchical BiOCl microspheres assembled with 2-D nanosheets with high photoactivity [55]. During the growth process,  $\text{Bi}(\text{NO}_3)_3$  first coordinated with ethylene glycol to yield alkoxide complexes to control the releasing rate of  $\text{Bi}^{3+}$  cations, thereby leading to the lower growth rate of  $\text{X-Bi-O}_2\text{-Bi-X}$  nucleation, which were favorable for the Ostwald-ripening mediated formation of 2-D ultrathin building blocks. Subsequently, the strong viscosity of ethylene glycol and the Kirkendall effect upon heating favored the stack of tiny crystalline nucleus of  $\text{X-Bi-O}_2\text{-Bi-X}$  to yield a preliminary 3-D configuration, and thus directed the oriented assembly of building blocks to ultimately produce loose microspheres assembled with 2-D nanoplates.

### 20.2.2.2 Oxygen Vacancy Engineering

A distinct characteristic in solvothermally synthesized BiOCl is oxygen vacancy on its layered structure surface. Our group for the first time reported this interesting phenomenon by using ethylene glycol as the solvent [43, 44, 56]. As ethylene glycol was prone to react with oxygen atoms exposed on the oxide surface to yield oxygen

vacancies, we demonstrated that the (001) surfaces of BiOCl featuring high density of oxygen atoms favored the reaction between ethylene glycol and the terminated oxygen, and thus concluded the formation of oxygen vacancies was originated from the unique property of ethylene glycol and the surface characteristic of BiOCl nanoplates. Our proposed mechanism was as follows. Ethylene glycol reacted with the oxygen exposed on BiOCl surface to extract some surface oxygen atoms, resulting in the generation of oxygen vacancies. The generation of oxygen vacancies was also accompanied with the emergence of organic by-products via a successive reaction between ethylene glycol and surface terminated oxygen, which was confirmed by the GC-MS analysis. We also found that, by tuning the concentration of bismuth and chlorine sources in ethylene glycol, the oxygen vacancy amounts could be adjusted in a controllable manner (Fig. 20.3).

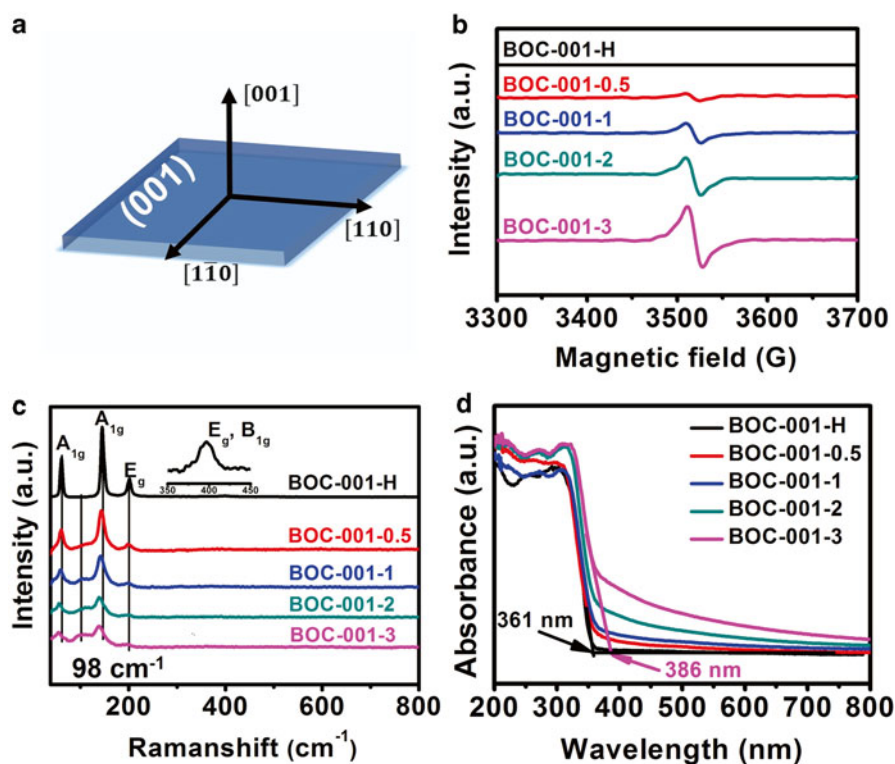


**Fig. 20.3** (a) Schematic illustration of the crystal orientation of the BiOCl single-crystalline nanosheet with {001} facets exposed. (b) Low-temperature electron paramagnetic resonance spectra, (c) Raman spectra, and (d) UV-Vis absorption spectra of the as-prepared BiOCl photocatalysts, which were called as BOC-001- $x$  ( $x=0.5, 1, 2,$  and  $3$ , which represented the millimole quantities of the bismuth precursor). For comparison, we annealed BOC-001-3 in the air at 300 °C to obtain a reference photocatalyst without OVs, which was denoted as BOC-001-H. No oxygen vacancy was observed in BOC-001-H, whereas for other samples, the concentration of oxygen vacancies increased with increasing the value of  $x$

## 20.3 Facet-Dependent Properties

Besides its facile generation of oxygen vacancies on the {001} facet, BiOCl possesses unique layered structure-mediated fascinating physicochemical properties and suitable band structure enabling fast charge transport and suitable redox potential, as well as its apparent merits including nontoxicity, elemental abundance, and good chemical stability [1]. These favorable properties provoke massive research endeavors on designing functional architectures by adopting the newly emerging nano-synthetic technologies, and also on improving photocatalytic activity by introducing the well-known strategies including surface functionalization, doping, plasmon modification, and heterojunction construction [8–40]. Although BiOCl has experienced an explosive development on the synthesis methods and photocatalysis applications, understanding of its fundamental photocatalysis mechanism, such as layered structure–photoreactivity relationship, has lagged behind largely because of the long-term lack of suitable experimental models.

It is known that photocatalytic reactions usually takes place on the surfaces of semiconductors, and the photocatalytic performance is largely dependent on the surface properties of semiconductors [1]. Therefore, the gap between the layered structure and the photoreactivity in BiOCl can be bridged with BiOCl nanosheets of different facet exposures as the experimental models for mechanistic investigation. Owing to the highly distinct surface atomic structures of {001} and {010} facets, BiOCl nanosheets exhibited interesting facet-dependent properties including facet-dependent photocatalytic activities, facet-dependent molecular oxygen activation, facet-dependent doping behaviors, and facet-dependent selective silver deposition [2, 3, 41–44], which are presented in the following section.

### 20.3.1 Facet-Dependent Photocatalytic Activities

Inspired by the success in realizing the facet-controllable synthesis of BiOCl, our group carried out the pioneering explorations on facet-dependent properties of BiOCl, which began with the facet-dependent photocatalytic activities. Regarding its wide band gap (3.4 eV), we first examined the UV light-driven activity of faceted BiOCl nanosheets toward pollutant degradation [2]. UV light irradiation endowed {001}-faceted BiOCl nanosheets with higher direct semiconductor photoexcitation activity than {010}-faceted counterparts (Fig. 20.4). This was because that BiOCl possessed a unique layered structure characterized by  $[\text{Bi}_2\text{O}_2]$  slabs interleaved with  $[\text{Cl}]$  slabs. The strong intralayer covalent bonding within  $[\text{Bi}_2\text{O}_2]$  slabs and the weak interlayer van der Waals interaction between double chlorine slabs resulted in the nonuniform charge distribution between  $[\text{Bi}_2\text{O}_2]$  and chlorine slices, which polarized the related atoms and orbitals to induce the formation of internal electric field (IEF) along the crystal orientation perpendicular to the  $[\text{Bi}_2\text{O}_2]$  and chlorine layers. The IEF induced by the unique layered structure could facilitate the separation and

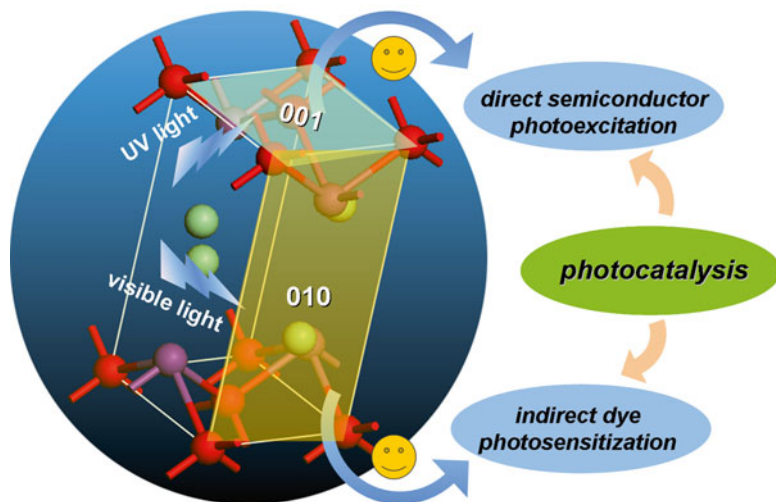


**Fig. 20.4** Schematic illustration of facet-dependent photoreactivity of BiOCl single-crystalline nanosheets

transfer of photogenerated charge carrier, thus favorable for the enhancement of photocatalytic performance.

Although BiOCl cannot absorb visible light, it can be photosensitized by dye molecules to initiate indirect photocatalysis [2]. In order to gain more insights into BiOCl photocatalysis mechanism, we further explored the visible-light-activated catalysis over faceted BiOCl with using MO as both the photosensitizer and the model pollutant. Different from the observation under UV light, {010} facet-dominant BiOCl nanosheets irradiated by visible light displayed superior indirect dye photosensitization activity. This was because the larger surface area and open channel characteristic of BiOCl nanosheets with exposed {010} facets could enhance the adsorption capacity of methyl orange molecules and provide more contact sites between the photocatalyst and dye molecules, facilitating more efficient electron injection from the photoexcited dye into the conduction band of the catalyst, favorable for the indirect dye photosensitization process. These findings not only provide facet-level insights into the relationship between the layered structure and the photoreactivity in BiOCl, but also provided effective guidance for the design and fabrication of highly efficient BiOCl-based photocatalyst.

### 20.3.2 Facet-Dependent Molecular Oxygen Activation

Although the facet-dependent photocatalytic activities of BiOCl nanosheets toward pollution degradation have been clarified, the first step of this photochemical reaction, especially the interaction between molecular oxygen and layered structure

surface of BiOCl during photocatalysis process, remains unexplored. It is necessary to clarify these processes because the activation of molecular oxygen by photogenerated electrons can yield reactive oxygen species (ROS), such as  $\cdot\text{O}_2^-$ ,  $\text{H}_2\text{O}_2$ , and  $\cdot\text{OH}$ , to facilitate pollution degradation, and also inhibit the recombination of photoinduced electrons and holes to enhance the lifetime of carriers [1, 3]. In addition, exploring the molecular oxygen activation on the surface of BiOCl is also driven by our limited knowledge on molecular oxygen activation mechanism, as the molecular oxygen activation is mainly focused on  $\text{TiO}_2$  photocatalysis. Obviously, BiOCl is an ideal platform to achieve this goal, because it can easily generate oxygen vacancies on its layered structure surface upon UV light irradiation or heating in reductive nonaqueous solvents [3, 43–46]. These surface oxygen vacancies favor oxygen adsorption and subsequent oxygen activation. These events, however, are difficult to occur on  $\text{TiO}_2$  because of its surface structures usually going against oxygen vacancy formation under mild conditions.

We first computationally simulated the molecular oxygen activation processes over {001} and {010} facet-dominant BiOCl nanosheets by calculating the density of states (DOS) and charge density difference with the first-principles calculations [3]. Theoretical calculation results revealed that molecular oxygen adsorbed onto the oxygen vacancy sites of {001} facet favored the formation of an end-on structure by interacting with the two nearest sublayer Bi atoms and thus extracting one electron from redistributed surface charges to generate  $\cdot\text{O}_2^-$ . On the {010} facet,  $\text{O}_2$  adsorbed on the oxygen vacancy site, combining three neighboring Bi atoms to form a complex bridge-on configuration that promotes the simultaneous transfer of two electrons to adsorbed  $\text{O}_2$  and then generates  $\cdot\text{O}_2^{2-}$  species (Fig. 20.4). Obviously, these results suggested that the molecular oxygen activation pathways on BiOCl surface were highly dependent on the surface atomic structures associated with the facet exposure.

To confirm these theoretical calculation results, we monitored the photocatalytic formation of ROS generation on the UV light-irradiated BOC-001 and BOC-010 surface by using electron spin resonance (ESR) techniques to probe the signal of  $\cdot\text{O}_2^{2-}$  and photoluminescence approach to detect the amount of  $\text{H}_2\text{O}_2$ , respectively [3]. The ESR spectra of BOC-001 and BOC-010 both gave a strong four-line ESR signal with the relative intensities of 1:2:2:1. The addition of SOD as the scavenger of  $\cdot\text{O}_2^-$  led to the more remarkable decrease in the ESR signal intensity of BOC-001 in comparison with that of BOC-010, indicating that the amount of  $\cdot\text{O}_2^-$  generated by BOC-001 was much more than that generated by BOC-010. In addition, more  $\text{H}_2\text{O}_2$  was generated in the presence of BOC-010. On the basis of theoretical calculations and experimental results, we proposed their molecular oxygen activation mechanisms as follows. Under UV light irradiation, the surfaces of BOC-001 and BOC-010 yielded oxygen vacancies with different structural configuration because of their distinct surface atomic arrangement. Subsequently, the (001) surface of BiOCl preferred to reduce  $\text{O}_2$  to  $\cdot\text{O}_2^-$  through one-electron transfer, while the (010) surface favored the formation of  $\cdot\text{O}_2^{2-}$  via two-electron transfer (Fig. 20.5). These findings provide atomic-level insight into the photocatalysis mechanism, which deepen our understanding of photocatalytic reaction process for developing

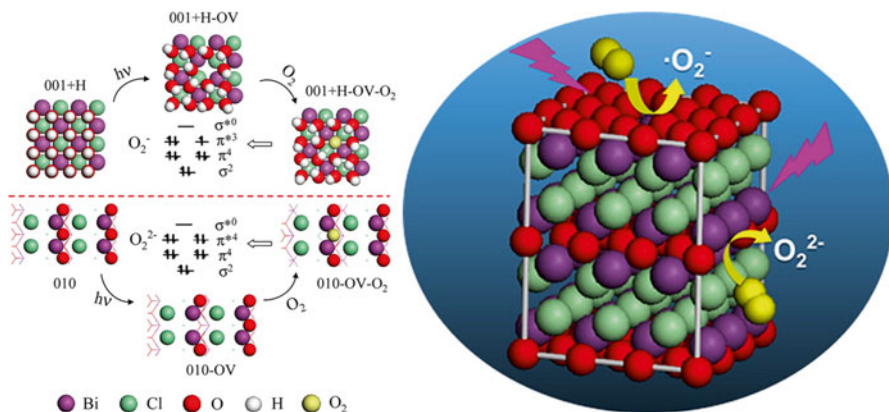


**Fig. 20.5** Proposed molecular oxygen activation processes on the {001} and {010} facets of BiOCl nanosheet surfaces

highly active photocatalysts, and also allow us to selectively manipulate the reaction processes via switching the molecular oxygen activation pathways.

### 20.3.3 Facet-Dependent Carbon Doping

Although BiOCl demonstrates superior photoactivity, even better than commercial P25, wide band-gap BiOCl can work, via direct semiconductor photoexcitation, only in ultraviolet region that covers 4 % solar spectrum, which limit its further applications.

We recently developed a homogeneous carbon doping strategy comprised of pre-hydrothermal carbonization processing and subsequent thermal treatment to increase solar absorption of BiOCl [41]. The first-step hydrothermal processing was found to be the key for this carbon doping strategy because of its ability to implant carbonaceous species into the shallow lattice of BiOCl. This hydrothermal reaction was carried out by only introducing the glucose as a carbon source into the synthetic system of the aforementioned faceted BiOCl nanosheets with maintaining other synthetic parameters unchanged. When bismuth nitrate and glucose were dissolved in the aqueous solution, glucose would coordinate with  $\text{Bi}^{3+}$  ions to generate alkoxides complexes, which reacted with chlorine ions immediately to generate tiny  $\text{X-Bi-O}_2\text{-Bi-X}$  crystalline nuclei wrapped with carbon-containing organic ligands under hydrothermal reaction condition. Subsequently, Ostwald ripening governed the growth of these crystalline nuclei and some key parameters such as surrounding pH, solution viscosity, and reaction temperature directed their oriented assembly into BiOCl intermediates, while the agglomeration of these crystalline nuclei would yield BiOCl nanocrystals implanted by carbon-chain-like species in their interior. With the proceeding of hydrothermal reaction, the carbon-chain-like species on the

surface of BiOCl would be carbonized into surface-modified carbonaceous species, while carbon atoms in alkoxide complexes coordinated with Bi in the inner of BiOCl were gradually substituted with Cl and/or O of BiOCl. On the other hand, these carbon-chain-like species at deep lattice of BiOCl was expelled outside the lattice of BiOCl because of the lattice self-purification effect. However, the increasing carbonaceous species coverage on the BiOCl surface would gradually block the escape of carbon-chain-like species, resulting in their residual within the shallow lattice of BiOCl. At the same time, the carbonization of these residual carbon-chain-like species occurred, producing the carbonaceous species located in the shallow lattice of BiOCl. It should be noted that, although {001}- and {010}-faceted BiOCl nanosheets underwent the same carbonization process described above, their facet-related surface atomic structures largely regulated the adsorption modes. In the case of {010} facet, the implanted carbonaceous species were prone to interact with oxygen atoms to form C–O and C=O bonds, because of the oxygen-terminated nature of BiOCl {001} facet and the strong affinity of carbonaceous species to oxygen atom (Fig. 20.6). Whereas, for {010} facet, the open channel along [010] orientation provided large accommodation space for the intercalation of carbonaceous species, resulting in the sandwich-like intercalation of carbonaceous species in the shallow lattice.

It is known that BiOCl crystallizes into unique layered structures consisting of [Cl–Bi–O<sub>2</sub>–Bi–Cl] slices stacked together by the van der Waals interaction between the halogen atoms along the *c*-axis [1]. Obviously, compared to the strong covalent binding between Bi and O, the weak van der Waals interaction of Cl favored its substitution by carbon energetically. When these carbon-modified BiOCl nanosheets were subjected to calcination in air, thermal treatment provided sufficient energy to trigger the decomposition of carbonaceous species into carbon dopant and simultaneously overcome the energy and space barrier for the subsequent substitution of lattice chlorine atoms with carbon atoms. For the {001} facet-dominating BiOCl nanosheets, dopant precursor was mainly close to the inner lattice oxygen of {001} facet and the carbon atoms must first traverse [Bi<sub>2</sub>O<sub>2</sub>] layers to subsequently substitute for chlorine. The strong covalent binding between Bi and O as well as their highly dense arrangement in [Bi<sub>2</sub>O<sub>2</sub>] layers would strongly inhibit the diffu-

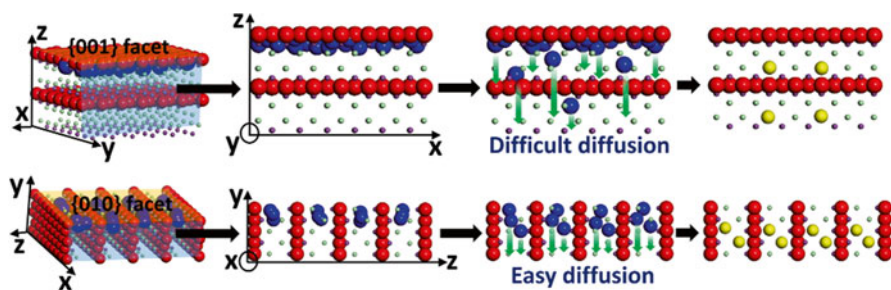
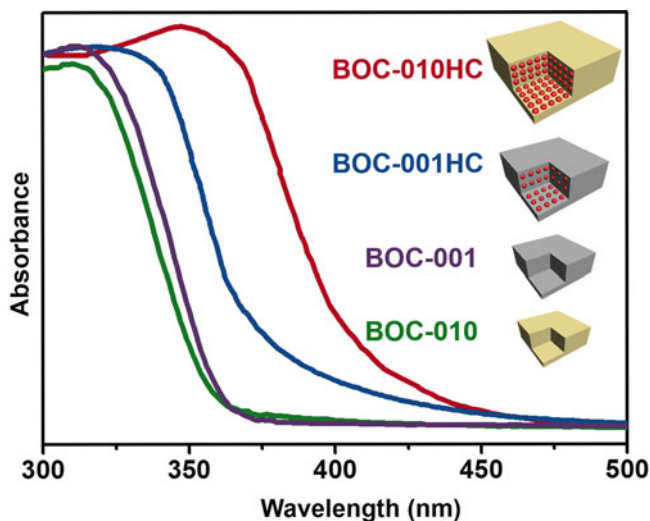


Fig. 20.6 Schematic illustration of the detailed carbon doping process of {001}- and {010}-faceted BiOCl

sion of carbon dopant, resulting in a low dopant concentration of 0.51 %. In contrast, the {010} facet-dominating nanosheets enabled 2.98 % carbon dopants to be homogeneously incorporated. This was because the open channels of {010}-faceted BiOCl could provide expedite diffusion pathway for the facile transfer of carbon dopant to the substitution sites. Meanwhile, the weak van der Waals interaction among the chlorine atoms along [010] crystal orientation favored the carbon dopant diffusion and the subsequent chlorine substitution by carbon. With this homogeneous carbon doping strategy, the intrinsic absorption edges were shifted from 365 and 360 nm to 380 and 430 nm for BiOCl with exposed {001} or {010} facet, respectively, as shown in Fig. 20.7. This study sheds light on the underlying doping mechanism to enrich fundamental theory of doping chemistry. These mechanistic insights establish a proof-of-concept strategy to guide the incorporation of other dopants in BiOCl lattice, and also open up new opportunities for the design and synthesis of high-performance doped BiOCl photocatalysts.

### 20.3.4 Facet-Dependent Selective Silver Deposition

Another promising route to extend the absorption of BiOCl to the visible light region is to construct plasmonic photocatalysis system by modifying BiOCl with visible-light-responsive plasmonic metal nanoparticles, which enable a coherent oscillation of the free electrons in resonance with the electrical field of the incoming electromagnetic irradiation to form so-called local surface plasmon resonance



**Fig. 20.7** UV-visible absorption spectra of pristine (called as BOC-001 and BOC-010) and carbon-doped BiOCl (called as BOC-001HC and BOC-010HC) with exposed {001} and {010} facet

(LSPR) [43, 56]. We developed a rapid microwave-assisted nonaqueous method to achieve this goal and observed an interesting selective deposition of silver onto the  $\{001\}$  facets of BiOCl, regardless of  $\{001\}$  or  $\{010\}$  facets as the dominant surface [43]. After the microwave heating of BiOCl nanosheets in ethylene glycol containing AgNO<sub>3</sub> for 10 min, numerous Ag nanocubes with size up to 200 nm emerged on the  $\{001\}$  facets of BOC-001 SCNSs (Fig. 20.8a, b), whereas no Ag nanocrystals was observed on the  $\{010\}$  facets of BOC-010 SCNSs. Surprisingly, plenty of Ag nanoparticles still appeared on the lateral  $\{001\}$  facets of BOC-010 SCNSs (Fig. 20.8c, d), although BOC-010 SCNSs were enclosed by a small fraction of  $\{001\}$  facets. Subsequent time-dependent synthesis experiments revealed that the  $\{001\}$  facets enabled much faster rate of silver nucleation than the  $\{010\}$  facets. These results demonstrated that the key for selective silver deposition on BiOCl was the  $\{001\}$  facet exposure, whose exposure percentages directly determined the efficiency of silver deposition (Fig. 20.8e).

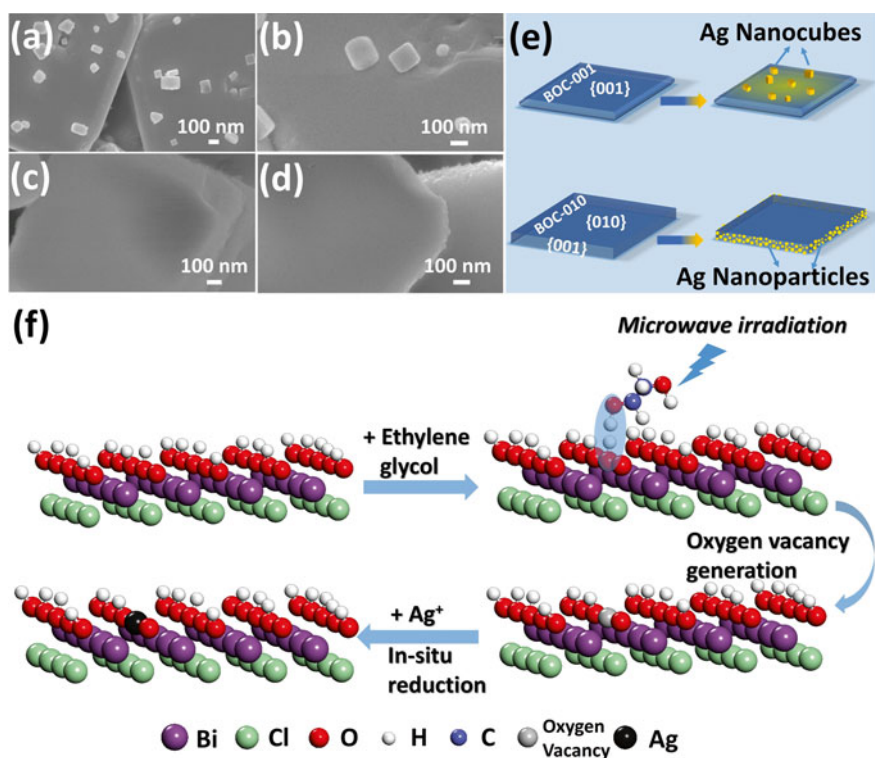


**Fig. 20.8** Scanning electron microscopy (SEM) images of (a) Ag-BOC-001 and (b) silver nanocubes on the top  $\{001\}$  facet of BOC-001; (c) SEM images of the Ag-BOC-010 nanosheets and (d) silver nanoparticles on the lateral  $\{001\}$  facet of BOC-010; (e) schematic illustration of the silver deposition on the  $\{001\}$  facets of BOC-001 and BOC-010; (f) possible pathway of the in situ reduction and deposition of Ag on the  $\{001\}$  facets of BiOCl in ethylene glycol under microwave irradiation

Our previous theoretical calculation demonstrated that hydrogen adsorbed {001} facets of BiOCl stabilized the surface-terminated oxygen atoms, leading to the formation of surface hydroxyl groups, while the {010} facets were free of adsorbed hydrogen [3]. We subsequently confirmed the existence of the surface hydroxyl groups on the {001} facet enriched with high density surface oxygen atoms by using in situ diffuse reflectance Fourier transform infrared (FTIR) spectroscopy, as evidenced by the much stronger signals of surface hydroxyl groups at  $3560\text{ cm}^{-1}$  of BOC-001 SCNSs relative to that of BOC-010 SCNS. In view of these results, we clarified the mechanism of facet-dependent selective silver deposition as follows (Fig. 20.8f). Compared with the {010} facets of BiOCl, its {001} facets possess a higher density of surface terminated oxygen atoms. Under microwave irradiation, ethylene glycol could react with the {001} facets of BiOCl to remove the surface oxygen atoms and then eliminate surface hydroxyl groups, simultaneously resulting in oxygen vacancies selectively formed in the {001} facets. Once the silver ions reached the electron-rich oxygen vacancies, they were immediately reduced by the oxygen vacancies and then nucleated on the {001} facets, accompanying with the quenching of oxygen vacancies and the appearance of tight interfaces between the Ag and BiOCl surface. After nucleation, nanosized silver would further grow into nanocubes or nanoparticles on the {001} facets of BiOCl via the hot ethylene glycol-induced silver ions reduction. The selective silver deposition onto the surface terminated oxygen atoms of the {001} facet endowed the as-prepared Ag/BiOCl composites with excellent catalytic activity for both Cr(VI) reduction and sodium pentachlorophenol oxidation under visible light. These results strongly demonstrate that the in situ deposition of plasmonic metal mediated by oxygen vacancies is a promising approach to construct high-performance metal/semiconductor plasma photocatalysts with improved interface engineering, and that the clarified relationship between the facet exposure and metal deposition preferences may serve as a versatile principle to craft desired plasmonic architectures.

## 20.4 Conclusion Remarks and Perspectives

Layered BiOCl photocatalysis is becoming a hot research topic because of its promising facile liquid-phase synthesis and high photoreactivity for potential energy and environmental applications. As attracted by these fascinating features, extensive research efforts have been dedicated to manufacturing various BiOCl nanostructures. These efforts culminated in the facet-controllable synthesis of BiOCl nanosheets with interesting facet-dependent properties, affording avenues to understanding the underlying layered BiOCl photocatalysis mechanism. These insightful explorations highlight the importance of BiOCl layered structure in determining its photocatalytic activity. Finally, we would like to share our future plans in the field of BiOCl photocatalysis. First, we hope to overcome the intrinsic drawback of BiOCl wide band-gap feature by modifying the band structure, such as doping and composition engineering. Second, we will construct more functional architectures

for better understanding the layered structure–photoreactivity relationship. Third, we plan to employ in situ observations based on advanced material characterization and theoretical calculations to advance further developments in this exciting field of layered BiOCl photocatalysis.

**Acknowledgments** This work was supported by the National Natural Science Funds for Distinguished Young Scholars (Grant 21425728), the National Basic Research Program of China (973 Program) (Grant 2013CB632402), the National Science Foundation of China (Grants 21177048, and 51472100), and the Key Project of Natural Science Foundation of Hubei Province (Grant 2013CFA114).

## References

1. Li J, Yu Y, Zhang LZ (2014) Bismuth oxyhalide nanomaterials: layered structures meet photocatalysis. *Nanoscale* 6:8473–8488
2. Jiang J, Zhao K, Xiao XY, Zhang LZ (2012) Synthesis and facet-dependent photoreactivity of BiOCl single-crystalline nanosheets. *J Am Chem Soc* 134:4473–4476
3. Zhao K, Zhang LZ, Wang JJ, Li QX, He WW, Yin JJ (2013) Surface structure-dependent molecular oxygen activation of BiOCl single-crystalline nanosheets. *J Am Chem Soc* 135:15750–15753
4. Maile FJ, Pfaff G, Reynders P (2005) Effect pigments – past, present and future. *Prog Org Coat* 54:150–163
5. Kijima N, Matano K, Saito M, Oikawa T, Konishi T, Yasuda H, Sato T, Yoshimura Y (2001) Oxidative catalytic cracking of n-butane to lower alkenes over layered BiOCl catalyst. *Appl Catal A* 206:237–244
6. Briand GG, Burford N (1999) Bismuth compounds and preparations with biological or medicinal relevance. *Chem Rev* 99:2601–2658
7. Zhang KL, Liu CM, Huang FQ, Zheng C, Wang WD (2006) Study of the electronic structure and photocatalytic activity of the BiOCl photocatalyst. *Appl Catal B* 68:125–129
8. Cheng HF, Huang BB, Dai Y (2014) Engineering BiOX (X=Cl, Br, I) nanostructures for highly efficient photocatalytic applications. *Nanoscale* 6:2009–2016
9. Ye LQ, Su YR, Jin XL, Xie HQ, Zhang C (2014) Recent advances on BiOX (X=Cl, Br and I) photocatalysts synthesis, modification, facet effect and mechanisms. *Environ Sci Nano* 1:90–112
10. Cheng HF, Huang BB et al (2012) A controlled anion exchange strategy to synthesize Bi<sub>2</sub>S<sub>3</sub> nanocrystals-BiOCl hybrid architectures with efficient visible light photoactivity. *Chem Commun* 48:97–99
11. Mu QH, Zhang QH et al (2012) Facile growth of vertically aligned BiOCl nanosheet arrays on conductive glass substrate with high photocatalytic properties. *J Mater Chem* 22:16851–16857
12. Shang M, Wang WZ, Zhang L (2009) Preparation of BiOBr lamellar structure with high photocatalytic activity by CTAB as Br source and template. *J Hazard Mater* 167:803–809
13. Lei YQ, Wang GH et al (2009) Synthesis, characterization and assembly of BiOCl nanostructure and their photocatalytic properties. *CrystEngComm* 11:1857–1862
14. Xiong JY, Chen G et al (2011) Well-crystallized square-like 2D BiOCl nanoplates: mannitol-assisted hydrothermal synthesis and improved visible-light-driven photocatalytic performance. *RSC Adv* 1:1542–1553
15. Ma JM, Liu XD et al (2010) Ionothermal synthesis of BiOCl nanostructures via a long-chain ionic liquid precursor route. *Cryst Growth Des* 10:2522–2527

16. Deng H, Wang JW et al (2005) Controlled hydrothermal synthesis of bismuth oxyhalide nanobelts and nanotubes. *Chem Eur J* 11:6519–6524
17. Wang C, Shao C et al (2008) Photocatalytic properties BiOCl and Bi<sub>2</sub>O<sub>3</sub> nanofibers prepared by electrospinning. *Scr Mater* 59:332–335
18. Wu SJ, Wang C et al (2010) Synthesis and photocatalytic properties of BiOCl nanowire arrays. *Mater Lett* 64:115–118
19. Geng J, Hou WH et al (2005) One-dimensional BiPO<sub>4</sub> nanorods and two-dimensional BiOCl lamellae : fast low-temperature sonochemical synthesis, characterization, and growth mechanism. *Inorg Chem* 44:8503–8509
20. Peng HL, Chan CK et al (2009) Shape evolution of layer-structured bismuth oxychloride nanostructures via low-temperature chemical vapor transport. *Chem Mater* 21:247–252
21. Zhang J, Shi FJ et al (2008) Self-assembled 3-D architectures of BiOBr as a visible light-driven photocatalyst. *Chem Mater* 20:2937–2941
22. Xiong JY, Jiao ZB et al (2013) Facile and rapid oxidation fabrication of BiOCl hierarchical nanostructures with enhanced photocatalytic properties. *Chem Eur J* 19:9472–9475
23. Song JM, Mao CJ et al (2010) Hierarchical structured bismuth oxychlorides self-assembly from nanoplates to nanoflowers via a solvothermal route and their photocatalytic properties. *CrystEngComm* 12:3875–3881
24. Xiao X, Zhang WD (2010) Facile synthesis of nanostructured BiOI microspheres with high visible light-induced photocatalytic activity. *J Mater Chem* 20:5866–5870
25. Chen YJ, Wen M, Wu QS (2011) Stepwise blossoming of BiOBr nanoplate-assembled microflowers and their visible-light photocatalytic activities. *CrystEngComm* 13:3035–3039
26. Zhu LP, Liao GH et al (2010) Self-assembled 3D BiOCl hierarchitectures: tunable synthesis and characterization. *CrystEngComm* 12:3791–3796
27. Zhang K, Liang J et al (2012) BiOCl submicrocrystals induced by citric acid and their high photocatalytic activities. *Cryst Growth Des* 12:793–803
28. Cheng HF, Huang BB et al (2011) One-pot miniemulsion-mediated route to BiOBr hollow microspheres with highly efficient photocatalytic activity. *Chem Eur J* 17:8039–8043
29. Feng YC, Li L et al (2011) Synthesis of mesoporous BiOBr 3D microspheres and their photodecomposition for toluene. *J Hazard Mater* 192:538–544
30. Zhang DQ, Wen MC et al (2012) Ionothermal synthesis of hierarchical BiOBr microspheres for water treatment. *J Hazard Mater* 211:104–111
31. Hao R, Xiao X et al (2012) Efficient adsorption and visible-light photocatalytic degradation of tetracycline hydrochloride using mesoporous BiOI microspheres. *J Hazard Mater* 209:137–145
32. Huo YN, Zhang J et al (2012) Solvothermal synthesis of flower-like BiOBr microspheres with highly visible-light photocatalytic performances. *Appl Catal B* 111:334–341
33. Cheng HF, Huang BB et al (2012) An anion exchange approach to Bi<sub>2</sub>WO<sub>6</sub> hollow microspheres with efficient visible light photocatalytic reduction of CO<sub>2</sub> to methanol. *Chem Commun* 48:9729–9731
34. Xiong JY, Chen G et al (2013) Tunable BiOCl hierarchical nanostructures for high-efficient photocatalysis under visible light irradiation. *Chem Eng J* 220:228–236
35. Peng SJ, Li LL et al (2013) Controlled synthesis of BiOCl hierarchical self-assemblies with highly efficient photocatalytic properties. *Chem Asian J* 8:258–268
36. Ren KX, Zhang K et al (2012) Controllable synthesis of hollow-flower-like BiOI microspheres and highly efficient adsorption and photocatalytic activity. *CrystEngComm* 14:4384–4390
37. Xia JX, Yin S et al (2011) Self-assembly and enhanced photocatalytic properties of BiOI hollow microspheres via a reactable ionic liquid. *Langmuir* 27:1200–1206
38. Henle J, Simon P et al (2007) Nanosized BiOX (X=Cl, Br, I) particles synthesized in reverse microemulsions. *Chem Mater* 19:366–373
39. Xia JX, Yin S et al (2011) Improved visible light photocatalytic activity of sphere-like BiOBr hollow and porous structures synthesized via a reactable ionic liquid. *Dalton Trans* 40:5249–5258

40. Zhang K, Zhang DQ et al (2012) A novel nanoreactor framework of iodine-incorporated BiOCl core-shell structure enhanced light-harvesting system for photocatalysis. *CrystEngComm* 14:700–707
41. Li J, Zhao K, Yu Y, Zhang LZ (2015) Facet-level mechanistic insights into general homogeneous carbon doping for enhanced solar-to-hydrogen conversion. *Adv Funct Mater.* doi:[10.1002/adfm.201404178](https://doi.org/10.1002/adfm.201404178)
42. Li J, Zhang LZ, Li YJ, Yu Y (2014) Synthesis and internal electric field dependent photoreactivity of Bi<sub>3</sub>O<sub>4</sub>Cl single-crystalline nanosheets with high {001} facet exposure percentages. *Nanoscale* 6:167–171
43. Li H, Zhang LZ (2014) Oxygen vacancies induced selective silver deposition on the {001} facets of BiOCl single-crystalline nanosheets for enhanced Cr(VI) and sodium pentachlorophenate removal under visible light. *Nanoscale* 6:7805–7810
44. Li H, Shi JG, Zhao K, Zhang LZ (2014) Sustainable molecular oxygen activation with oxygen vacancies on the {001} facets of BiOCl nanosheets under solar light. *Nanoscale* 6:14168–14173
45. Ye LQ, Zan L et al (2011) The {001} facets-dependent high photoactivity of BiOCl nanosheets. *Chem Commun* 47:6951–6953
46. Ye LQ, Deng KJ et al (2012) Increasing visible-light absorption for photocatalysis with black BiOCl. *Phys Chem Chem Phys* 14:82–85
47. Coleman JN, Lotya M et al (2011) Two-dimensional nanosheets produced by liquid exfoliation of layered materials. *Science* 331:568–571
48. Nicolosi V, Chhowalla M, Kanatzidis MG, Strano MS, Coleman JN (2013) Liquid exfoliation of layered materials. *Science* 340:1226419
49. Chhowalla M, Shin HS (2013) The chemistry of two-dimensional layered transition metal dichalcogenide nanosheets. *Nat Chem* 5:263–275
50. Zhang L, Wang WZ et al (2015) Photoreduction of CO<sub>2</sub> on BiOCl nanoplates with the assistance of photoinduced oxygen vacancies. *Nano Res* 8:821–831
51. Pan XY, Yang MQ, Fu XZ, Zhang N, Xu YJ (2013) Defective TiO<sub>2</sub> with oxygen vacancies: synthesis, properties and photocatalytic applications. *Nanoscale* 5:3601–3614
52. Guan ML, Xiao C et al (2013) Vacancy associates promoting solar-driven photocatalytic activity of ultrathin bismuth oxychloride nanosheets. *J Am Chem Soc* 135:10411–10417
53. Zhuang ZB, Peng Q, Li YD (2011) Controlled synthesis of semiconductor nanostructures in the liquid phase. *Chem Soc Rev* 40:5492–5513
54. Gao MR, Xu YF et al (2013) Nanostructured metal chalcogenides: synthesis, modification, and applications in energy conversion and storage devices. *Chem Soc Rev* 42:2986–3017
55. Zhang X, Ai ZH, Jia FL, Zhang LZ (2008) Generalized one-pot synthesis, characterization, and photocatalytic activity of hierarchical BiOX (X=Cl, Br, I) nanoplate microspheres. *J Phys Chem C* 112:747–753
56. Jiang J, Zhang LZ et al (2013) Self-doping and surface plasmon modification induced visible light photocatalysis of BiOCl. *Nanoscale* 5:10573–10581

# Chapter 21

## Synthesis and Performance Enhancement for $\text{Bi}_2\text{WO}_6$ as High-Activity Visible-Light-Driven Photocatalysts

Zhen Wei and Yongfa Zhu

### 21.1 Introduction

One of the major problems in photocatalysis applications is the use efficiency of visible light is low. In order to utilize solar energy more efficiently, researchers modified the common photocatalysts by dye-sensitization, ion doping, compositing with other visible-light photocatalysts. On the other hand, researchers try to develop new types of efficient visible-light photocatalysts. Tungstate semiconductor materials have unique structures as well as physical and chemical properties. These properties made them have a promising prospect such as using as magnetic devices, scintillating materials, corrosion inhibitors, and catalysts [1, 2]. Up to now,  $\text{Bi}_2\text{WO}_6$  is a kind of visible-light photocatalysts which were widely studied. In 1999, Akihiko Kudo et al. first reported the photocatalytic activity of splitting water by  $\text{Bi}_2\text{WO}_6$  under irradiation with  $\text{AgNO}_3$  as the sacrifice agent [3]. Zou and Ye et al. reported  $\text{Bi}_2\text{WO}_6$  could degrade  $\text{CHCl}_3$  and  $\text{CH}_3\text{CHO}$  efficiently under light with the wavelength longer than 440 nm [4].

The advantages of  $\text{Bi}_2\text{WO}_6$  photocatalysts are a good response of UV-visible light, a good stability, a low cost, and environmental friendly properties while the disadvantage is the quantum efficiency is low under visible light which is well worth further studying.

---

Z. Wei • Y. Zhu (✉)

Department of Chemistry, Tsinghua University, Beijing 100084, China  
e-mail: [zhuyf@tsinghua.edu.cn](mailto:zhuyf@tsinghua.edu.cn)

## 21.2 Physical Properties of $\text{Bi}_2\text{WO}_6$ Related to the Photocatalytic Activity

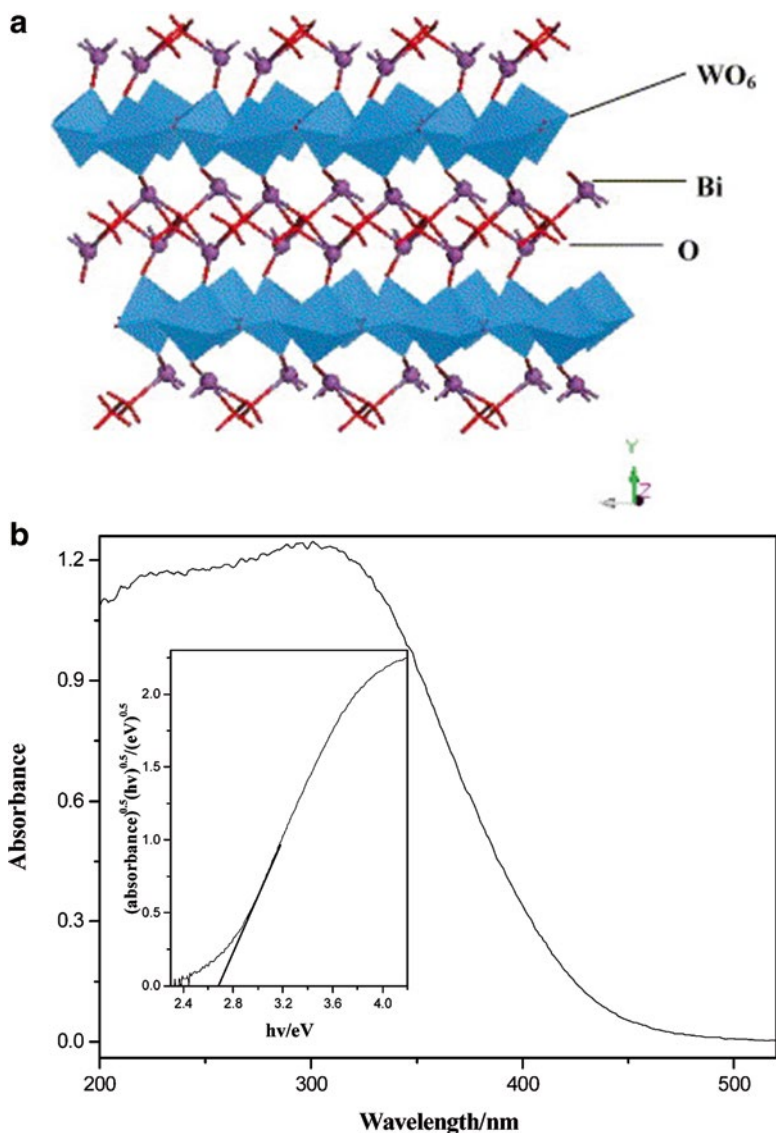
### 21.2.1 Crystal Form

$\text{Bi}_2\text{WO}_6$  is one of the simplest Aurivillius-type oxides with orthorhombic system, Pca21 space group [5]. The perovskite crystal structure of  $\text{Bi}_2\text{WO}_6$  is presented in Fig. 21.1a. The crystal has a layered structure with corner-shared  $\text{WO}_6$ .  $\text{Bi}_2\text{O}_2$  layers are sandwiched between  $\text{WO}_6$  octahedral layers along the c-axis direction [6, 7].

### 21.2.2 Band Gap and Band Structure of $\text{Bi}_2\text{WO}_6$

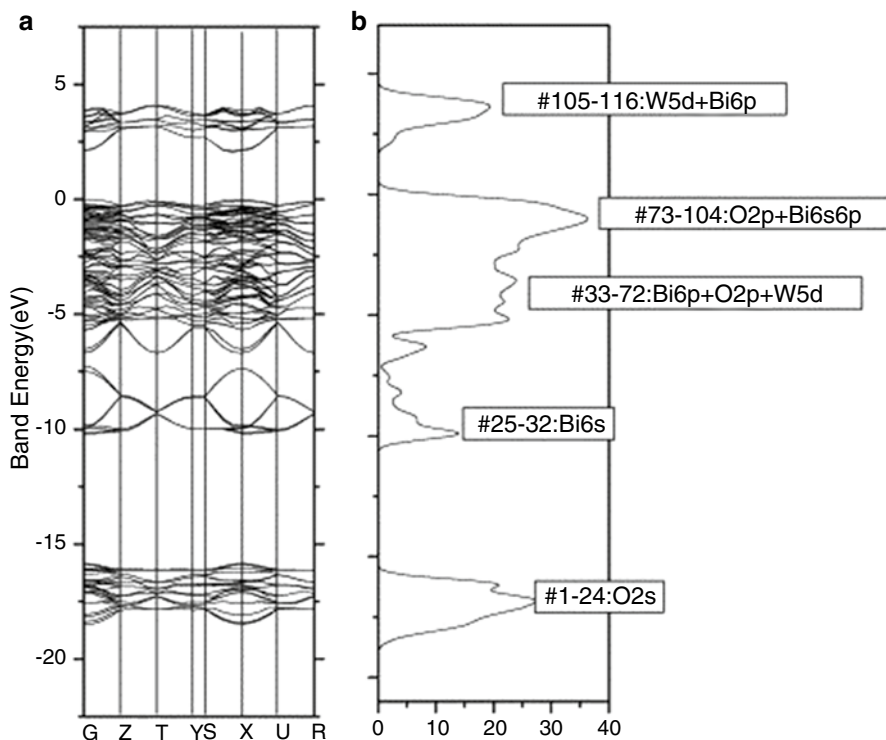
UV-visible diffuse reflectance spectroscopy (Fig. 21.1b) shows that the band gap energy of  $\text{Bi}_2\text{WO}_6$  is about 2.7 eV [8]. It presented the photoabsorption properties from the UV light region to visible light shorter than 470 nm [8]. The color of the oxide is yellowish, as predicted from their photoabsorption spectrum. The electronic structure of  $\text{Bi}_2\text{WO}_6$  was investigated by DFT calculations by several groups [8–10]. The calculated conduction and valence band-edge of  $\text{Bi}_2\text{WO}_6$  is 3.183 and 0.543 eV, respectively [11]. Figure 21.2 shows a typical electronic structure of  $\text{Bi}_2\text{WO}_6$ . The highest occupied molecular orbital levels were composed of the hybrid orbitals of O 2p and Bi 6s, while the lowest unoccupied molecular orbital levels were composed of the W 5d orbitals. The band structure indicates that charge transfer upon photoexcitation occurs from the O 2p+Bi 6s hybrid orbitals to the empty W 5d orbitals. This transition occurs because the 6s electrons usually occur at a lower energy than the charge-transfer transition in  $\text{WO}_6^{6-}$ . The valence band of  $\text{Bi}_2\text{WO}_6$  was composed of O 2p and Bi 6s orbitals, which is similar to that of  $\text{BiVO}_4$ . The considerable visible-light absorption of  $\text{Bi}_2\text{WO}_6$  is thus attributed to the transition from Bi 6s to the W 5d orbital.

Figure 21.3 shows the density contour maps of orbitals with the highest occupied molecular orbital (HOMO) and the lowest unoccupied molecular orbital (LUMO). HOMO shows the p orbital of the O atom and the s and p orbitals of the Bi atom, indicating that the orbitals are composed of the O 2p and Bi 6s orbitals. LUMO is mainly formed by the W 5d orbital, but O 2p mix into to some degree. This mixing is rather common for metal oxide semiconductors including  $d^{10}$  elements [12, 13]. The band gap of  $\text{Bi}_2\text{WO}_6$  was estimated to be 1.63 eV. Generally, the band gap calculated by DFT was smaller than that obtained by experiment, which is frequently pointed out as a common feature of DFT calculations [14]. The band gap becomes narrower and the considerable absorption extends up to the visible region, which could be due to the transition from the hybrid orbitals of Bi 6s and O 2p to the W 5d orbitals. Photooxidation of the pollutant over  $\text{Bi}_2\text{WO}_6$  photocatalyst occurs as a result of contributions from the photoexcited holes in the VB consisting of the O 2p and Bi 6s hybrid orbitals.



**Fig. 21.1** (a) Schematic crystal structure of  $\text{Bi}_2\text{WO}_6$  photocatalyst, (b) UV-Vis diffuse reflectance spectra of  $\text{Bi}_2\text{WO}_6$ . Reprinted from [6] and [8] with permission from Elsevier

The high photoactivity of  $\text{Bi}_2\text{WO}_6$  catalyst could be attributed to the  $\text{WO}_6$  layered structure, which is beneficial to the electron transfer to the surface of the photocatalyst along the layered network. Dipole moment of  $\text{WO}_6$ -distorted octahedra structure is in favor of photogenerated carriers separating. It has been reported that a series of layered structure compounds showed high activity for water splitting under irradiation, and of the layered structure was found to promote the charge carries



**Fig. 21.2** Energy band diagram (a) and density of states (b) for  $\text{Bi}_2\text{WO}_6$  calculated by the DFT method. Reprinted from [6] with permission from Elsevier

generation and separation [15]. For example, Kudo et al. [16] found that layered metal oxide semiconductor particles could evolve hydrogen much more easily than other compounds because the photogenerated electron–hole pairs can move effectively to the surface.

### 21.3 Controlled Synthesis and Morphology of $\text{Bi}_2\text{WO}_6$

The photocatalyst of  $\text{Bi}_2\text{WO}_6$  has a lot of preparation methods, such as: solid state reaction, liquid precipitation, hydrothermal method, ultrasonic synthesis, solvothermal method, and microwave hydrothermal method. We have reported a simple hydrothermal method to synthesize  $\text{Bi}_2\text{WO}_6$  nanoplates with square laminar morphologies for the first time [6–8].

$\text{Bi}_2\text{WO}_6$  nanoplates were synthesized through a hydrothermal process. Crystal diffraction peaks were seen when the temperature was no less than 120 °C [7]. Morphologies of  $\text{Bi}_2\text{WO}_6$  synthesized by the hydrothermal method were characterized by transmission electron microscope (TEM), as shown in Fig. 21.4. The whole process of the nanoplates growth was obtained by morphology observation of time

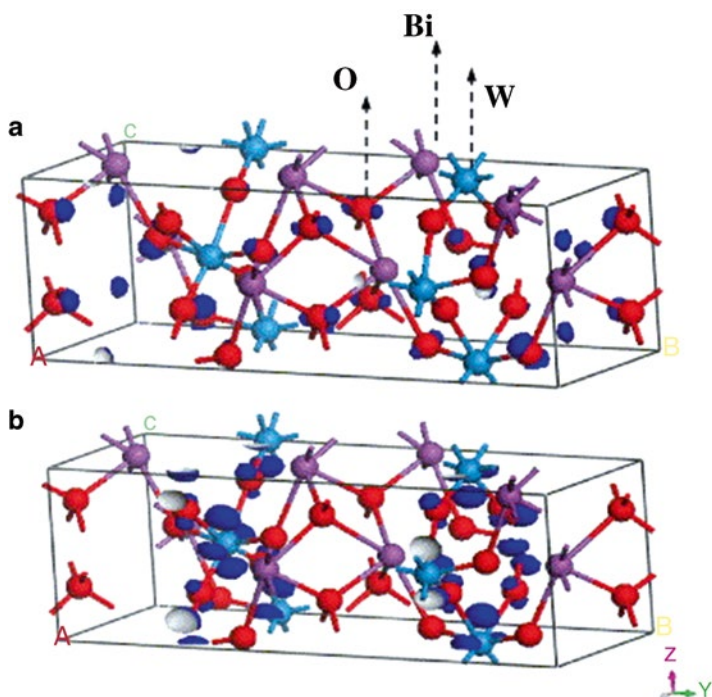


**Fig. 21.3** Density contour maps for HOMOs (a) and LUMOs (b) of  $\text{Bi}_2\text{WO}_6$ . Reprinted from [6] with permission from Elsevier

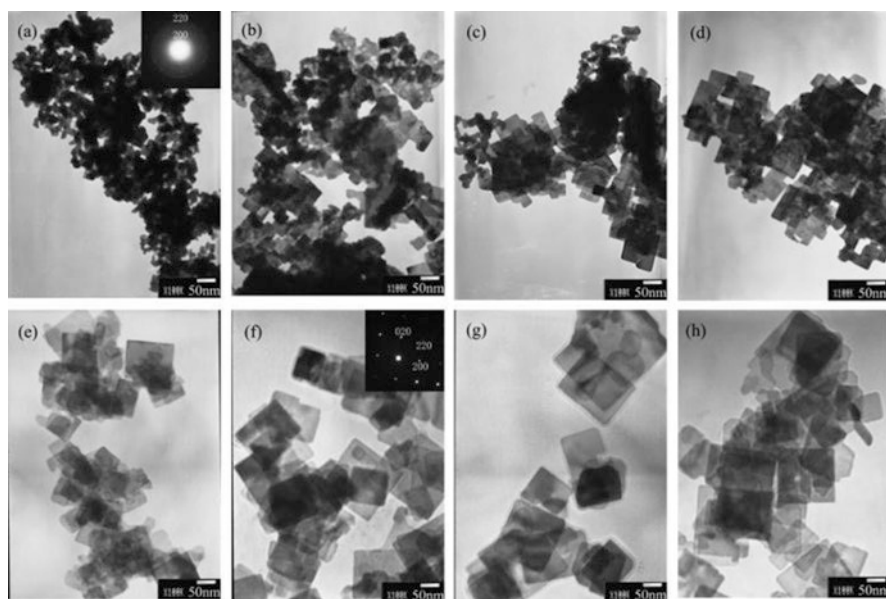


**Fig. 21.4** Morphologies of time series samples treated at  $160\text{ }^\circ\text{C}$ : (a) 2, (b) 4, (c) 8, (d) 12, (e) 16, (f) 20, (g) 24, and (h) 36 h. Reprinted with permission from [7]. Copyright 2005 American Chemical Society

series samples. For 20 h treatment, good-quality nanoplates could be obtained. The nanoplates grow preferentially along the (001) plane according to the indexed select electron diffraction pattern [7]. The thickness of the nanoplates was about 5 nm corresponding to three repeating units, i.e., ( $3 \times 1.6$  nm) 4.8 nm according to HRTEM. The schematic crystal structure of  $\text{Bi}_2\text{WO}_6$  is presented in Fig. 21.1a [6, 7].

The formation mechanism of the  $\text{Bi}_2\text{WO}_6$  nanoplates was displayed in Fig. 21.5 [7]. At the beginning, tiny crystalline nuclei were formed in a supersaturated medium. Then the crystal growth followed. Due to the energy difference in solubility between the large particles and the smaller particles, larger particles grew as small particles vanished. In early stages, an examination of the intermediate samples showed a coexistence of a small laminar structure and irregular crystalline nuclei. As the reaction continued, irregular nanoparticles vanished as larger nanoplates formed. The chains of octahedral-W usually play an important role in the high intrinsic anisotropic growth in various tungstates because the facets which are perpendicular to these chains are composed of highly distorted octahedral tungsten with dangling bonds. These facets usually have high chemical potential. It is believed that two-dimensional growth occurs only if the chemical potential of two surfaces is much higher than the others. The chains of octahedral-W equally existed along the *a*- and *b*-axes, indicating that the (200) and (020) facets have much higher chemical potentials than other facets. This structural feature will make the (200) and (020) facets very sensitive to the surrounding conditions. The anisotropic growth will happen when enough foreign energy input overcomes the reaction barrier. Finally the morphologies of the samples are plate-like, as observed in TEM images.

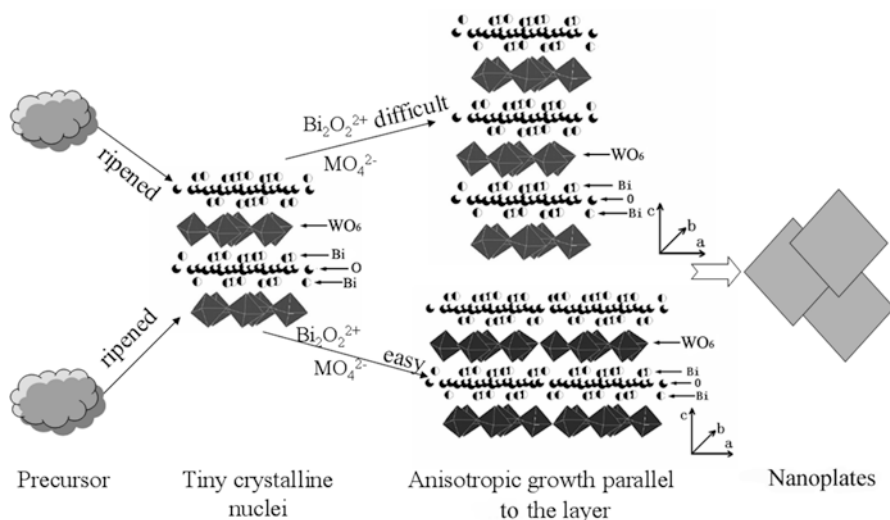


**Fig. 21.5** Growth mechanism of the nanoplates. Reprinted with permission from [7]. Copyright 2005 American Chemical Society

Yan and coworkers [17] have controlled the synthesis of  $\text{Bi}_2\text{WO}_6$  nanostructures via  $\text{Na}_2\text{SO}_4$ -assisted hydrothermal method by simply adjusting the reaction time and pH value (Fig. 21.6). Four typical  $\text{Bi}_2\text{WO}_6$  nanostructures were obtained, namely nest-like nanostructures assembled by nanoplates (NNS-ANPs), rod-like nanostructures assembled by nanoplates (RNS-ANPs), quantum dots-modified nanoplates (QDs-NPs), and smooth-surfaced nanoplates (SSNPs). The formation of  $\text{Bi}_2\text{WO}_6$  NNS-ANPs, SSNPs, and QDs-NPs follows a multistep growth pattern while the formation of  $\text{Bi}_2\text{WO}_6$  RNS-ANPs follows the classical Ostwald ripening pattern. The difference may stem from the combined effects of inorganic salts, pH, crystallization rate, and microenvironments of the hydrothermal reaction. Photocatalytic degradation results show that the degradation ratios (DRs) of three-dimensional structures are higher than those of two-dimensional structures, and surface QDs play key roles in enhancing the DRs of QDs-NPs. The PL spectra indicate that the morphology-dependent photocatalytic activities of different  $\text{Bi}_2\text{WO}_6$  nanostructures are mainly from the different charge-separation ability.

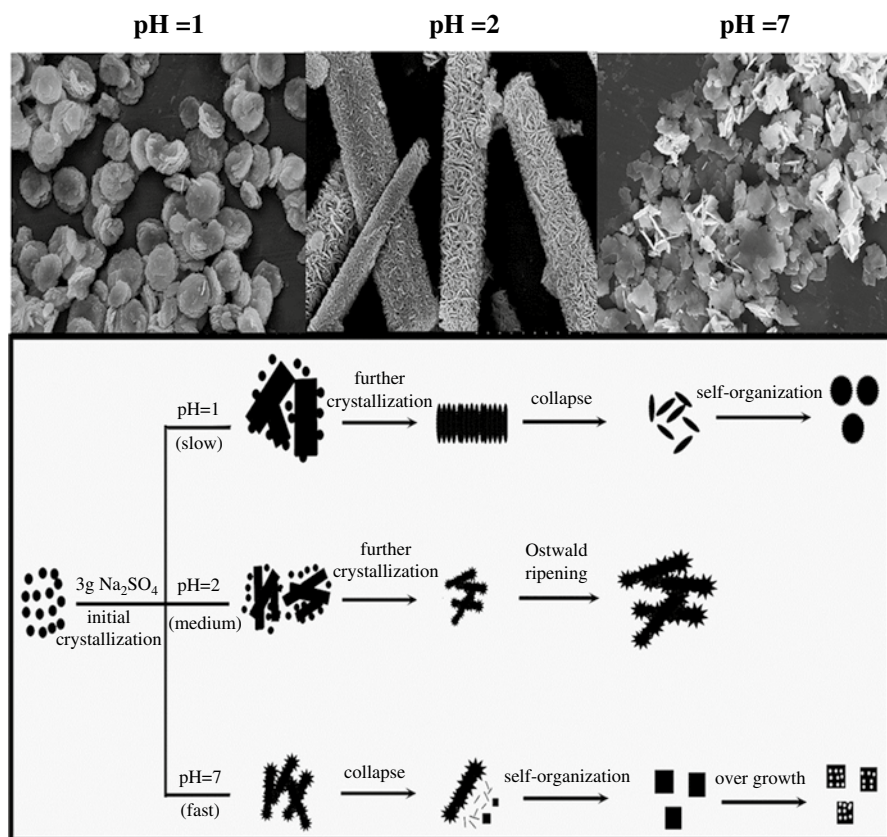


**Fig. 21.6** SEM images of  $\text{Bi}_2\text{WO}_6$  NNS-ANPs, SSNPs, and QDs-NPs (*upper*). Possible formation mechanism of  $\text{Bi}_2\text{WO}_6$  nanostructures (*lower*). Reprinted with permission from [17]. Copyright 2013 American Chemical Society

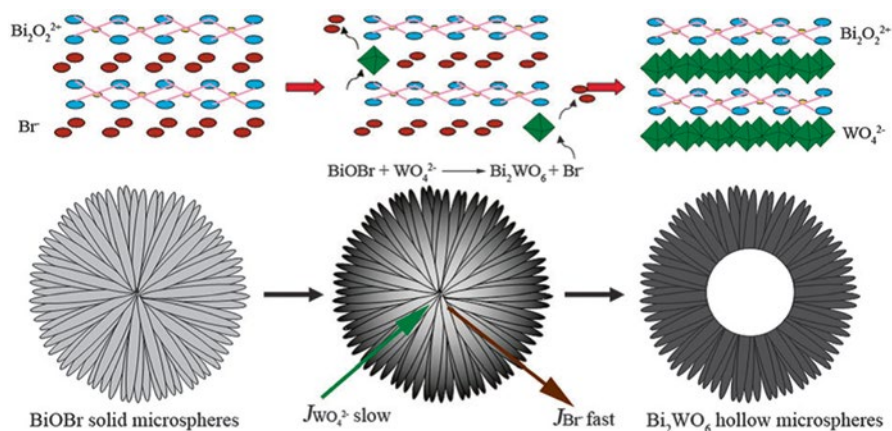


**Fig. 21.7** Schematic illustration of the anion exchange strategy: from BiOBr solid microspheres to Bi<sub>2</sub>WO<sub>6</sub> HMSs via the Kirkendall effect. Reprinted from [18] with permission of the Royal Society of Chemistry

Cheng and coworkers [18] have explored the anion exchange strategy to synthesize Bi<sub>2</sub>WO<sub>6</sub> hollow microspheres (HMSs). The chemical transformation from BiOBr solid microspheres into Bi<sub>2</sub>WO<sub>6</sub> HMSs was achieved by the microscale Kirkendall effect, as shown in Fig. 21.7. The Bi<sub>2</sub>WO<sub>6</sub> (HMSs) have a large surface area (23.8 m<sup>2</sup> g<sup>-1</sup>) and high CO<sub>2</sub> adsorption capacity. The HMSs display a high visible-light photocatalytic conversion efficiency of CO<sub>2</sub> into methanol without the aid of co-catalyst.

## 21.4 Photodegradation Process and Mechanism of Bi<sub>2</sub>WO<sub>6</sub>

Bi<sub>2</sub>WO<sub>6</sub> nanostructures were found to show high activity in organic compound degradation under visible light irradiation [7]. Some factors involved in the Bi<sub>2</sub>WO<sub>6</sub> photocatalysis process, including surface area, crystallization, hierarchical architecture, etc., have been extensively studied [7, 19, 20].

Among Bi<sub>2</sub>WO<sub>6</sub> nanoplate samples, only the sample prepared at 120 °C showed lower activities than the (solid state reaction) SSR sample. That sample is not highly crystallized, which is confirmed by the XRD result and TEM image. A lot of defects could act as an electron–hole recombination center. The activity increased with the hydrothermal process temperature. It has been reported by Amano et al. [21] that the photocatalytic activity of amorphous Bi<sub>2</sub>WO<sub>6</sub> was negligible due to the fast recombination of charge carriers and crystallization which provided a red shift of the photoabsorption edge and marked increase in the lifetime of photoexcited electrons, resulting in an increase in absorbed photons and photocatalytic reaction efficiency. The highest activity was obtained at 200 °C. When the temperature further increased, the activities decreased. It is mainly attributed to a worse

crystalline phase and is consistent with the XRD and TEM results. The  $\text{Bi}_2\text{WO}_6$  nanoplate prepared at  $200^\circ\text{C}$  shows a photocatalytic activity three times higher than that of the SSR sample [7].

The photocatalytic activity of  $\text{Bi}_2\text{WO}_6$  was found to be closely related with the pH value of the solution [8]. The solid particles were gained from the acidic suspension (pH 4.70) by a simple filtration and then observed by XRD. It was found that  $\text{Bi}_2\text{WO}_6$  was unstable in acidic solution. It could completely transform to  $\text{H}_2\text{WO}_4$  and  $\text{Bi}_2\text{O}_3$ , which is the reason that  $\text{Bi}_2\text{WO}_6$  has a poor catalytic activity in acidic solution.

Fu and coworkers [8] explored the mechanism of  $\text{Bi}_2\text{WO}_6$  photodegradation of RhB. 5,5-Dimethyl-1-pyrroline-*N*-oxide (DMPO) spin-trapping electron paramagnetic resonance (EPR) spectroscopy was conducted to monitor the active radicals that form during the photodegraded process. There were no signals when the RhB/ $\text{Bi}_2\text{WO}_6$  suspension was irradiated (Fig. 21.8). However, in the case of RhB/ $\text{TiO}_2$ , a spectrum displaying signals with characteristic intensity 1:2:2:1 for DMPO–OH adducts was obtained, indicating that the  $\cdot\text{OH}$  radical was formed. In another experiment, it was found that the addition of 2-propanol, a well-known scavenger of  $\cdot\text{OH}$  radicals, into the photoreaction system did not cause the apparent changes in the degradation rate of RhB. This indicates that the free  $\cdot\text{OH}$  radicals could not be the main active oxygen species in this photochemical process.

Meanwhile,  $\text{Bi}_2\text{WO}_6$  catalyst also showed the activity when the light wavelength was much longer than 490 nm, where it absorb poorly the light radiation. It is well known that RhB can absorb visible light in the range 400–600 nm, which is attributed to the ground state and the excited state of the dye. RhB is the main material absorbing light irradiation when  $\lambda > 490$  nm. So, it is postulated that the RhB photodegradation is attributed to the photosensitized process [22, 23]. When  $\lambda > 490$  nm, RhB is only the light absorbing species. From the dye-excited state, an electron is injected into the CB of  $\text{Bi}_2\text{WO}_6$  where it is captured by the surface adsorbed  $\text{O}_2$  to produce  $\text{O}_2^{\cdot-}$ , and the dye cation radicals are decomposed subsequently via attack by oxygen active species. The reaction possibly includes the following [6, 8]:

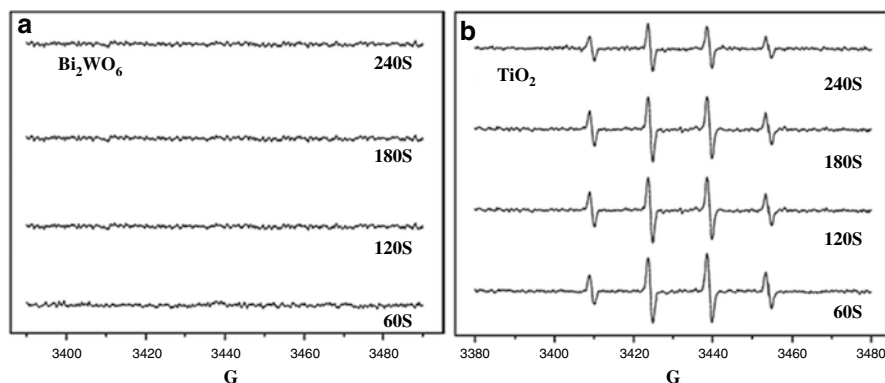
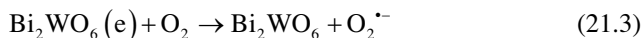


**Fig. 21.8** ESR signals of the DMPO–OH adducts as a function of light illumination time. Reprinted from [8] with permission from Elsevier



Sheng and coworkers [24] compared the difference photocatalytic activities of  $\text{Bi}_2\text{WO}_6$  and  $\text{WO}_3$  under visible light by using phenol degradation as a model reaction. They have proposed that the observed organic degradation over the irradiated  $\text{Bi}_2\text{WO}_6$  in aerated aqueous solution is due to the production of  $\cdot\text{OH}$  and  $\text{H}_2\text{O}_2$ . The valence band hole of  $\text{Bi}_2\text{WO}_6$  could oxidize water to produce  $\cdot\text{OH}$  and its conduction band electron could reduce  $\text{O}_2$  to produce  $\text{H}_2\text{O}_2$  in the photocatalytic reaction (Fig. 21.9). However, the two-electron reduction of  $\text{O}_2$  is usually slower than the one-electron reduction of  $\text{O}_2$ , which would limit application of  $\text{Bi}_2\text{WO}_6$  for environmental use. Further effort is needed for improvement of the catalyst photocatalytic activity of  $\text{Bi}_2\text{WO}_6$ .

Stability of a photocatalyst is very important from the viewpoint of practical application. The doped  $\text{TiO}_2$  photocatalysts sometimes suffer from photocorrosion and instability. The stability of  $\text{Bi}_2\text{WO}_6$  as a visible-light-driven photocatalyst is studied [8]. After five recycles for the photodegradation of RhB, the catalyst did not exhibit any significant loss of activity, confirming  $\text{Bi}_2\text{WO}_6$  is not photocorroded during the photocatalytic oxidation of the pollutant molecules. XRD analysis of the sample also showed that the crystal structure of the photocatalyst was not changed after the photocatalytic reaction.

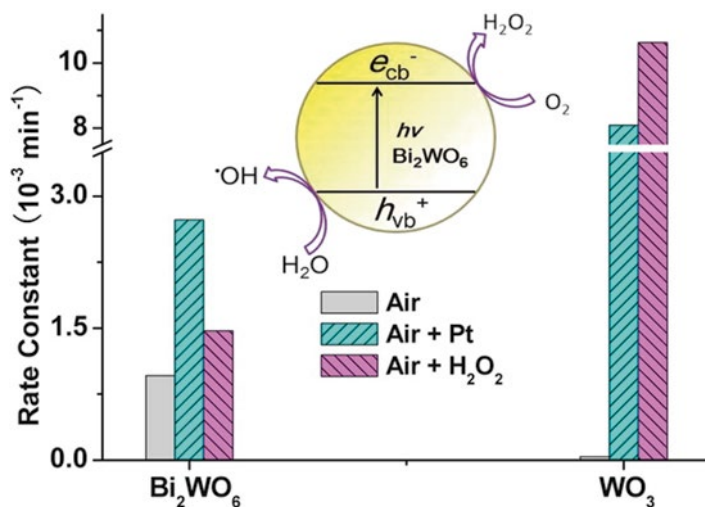


**Fig. 21.9** Phenol degradation under visible light in the aerated aqueous suspensions of  $\text{Bi}_2\text{WO}_6$  and  $\text{WO}_3$ , mechanism of photocatalytic activity of  $\text{Bi}_2\text{WO}_6$  (inset). Reprinted with permission from [24]. Copyright 2014 American Chemical Society

## 21.5 Enhanced Degradation by Combining Electro-Oxidation and Photocatalysis

Photoelectrocatalytic (PEC) oxidation has been proved to be an efficient way of degrading organic contaminants in aqueous solutions [25, 26]. In this process, the charge recombination is prevented by low electrical bias potential applied between the anode and the cathode; the electrochemical degradation of target contaminants is usually avoided. Electrochemical techniques have been extensively studied due to them degrade organic contaminants high efficiency and environmental compatibility [27, 28]. The main problem hindering the large-scale application in wastewater treatment is the high electric energy consumption mainly due to the side reaction of oxygen evolution [29]. Moreover, electrode passivation is susceptible because of electropolymerization and fouling as summarized in the literature [27, 30], which decreases the electro-oxidation efficiency. It is known that O<sub>2</sub> is beneficial for the photocatalytic degradation of organic contaminants because it can act as a scavenger of photogenerated electrons. Moreover, the photocatalytic reaction occurring on the photoanode surface could induce the formation of active radicals, which may activate the electrode. Attributed to the advantage of electro-oxidation and photocatalysis are complementary, a system that employs them both seems a worthwhile endeavor.

We have prepared the Bi<sub>2</sub>WO<sub>6</sub> nanoflake film electrode onto indium–tin oxide (ITO) glass via electrostatic self-assembly deposition (ESD) according to the method described in the literature [31]. The Bi<sub>2</sub>WO<sub>6</sub> nanoflake film exhibits photocatalytic activities toward degrading (4-chlorophenol) 4-CP under visible light irradiation. The removal efficiency of 4-CP can be increased by applying a bias potential to the Bi<sub>2</sub>WO<sub>6</sub> nanoflake film electrode. Moreover, a synergetic effect was observed in the degradation of 4-CP by the combination of electro-oxidation and photocatalysis [32].

Photocatalysis, electrochemical degradation, and PEC degradation of 4-CP at the bias potential of 2.0 V were performed, respectively [32]. The variation of relative concentration of 4-CP as a function of reaction time is shown in Fig. 21.10. It is clear that 4-CP can be photocatalytically degraded by using the Bi<sub>2</sub>WO<sub>6</sub> nanoflake film electrode; it can also be degraded via the electro-oxidation process with a bias potential of 2.0 V. Clearly, the degradation rate of 4-CP was the largest under the PEC process with the same bias potential. The pseudo-first kinetic constant of 4-CP for the PEC process is larger than the sum of the kinetic constant of electrochemical or photocatalytic process. A similar conclusion can be drawn by considering the reduction of TOC content. At the potential of 2.0 V, after 12 h reaction, the individual electrochemical degradation and photocatalysis permit TOC reduction of 25 and 20 %, respectively, while the combined PEC process leads to a TOC reduction of 65 %. Thus, it is reasonable to conclude that a sort of synergetic effect occurs during the PEC degradation of 4-CP.

The effect of the bias potential on the PEC degradation rate of 4-CP was further investigated [32]. As shown in Fig. 21.11, the degradation rate of 4-CP increases gradually as external potential increases. The influence of applied bias potential on 4-CP degradation was more significant at higher potential than that at lower potential.

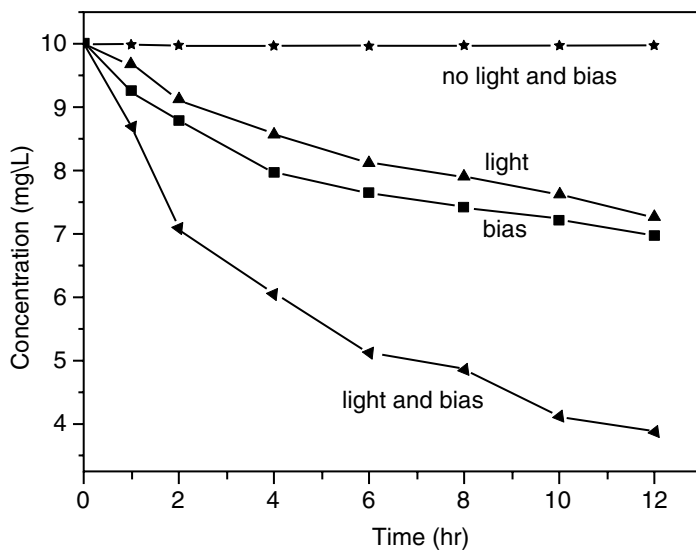


**Fig. 21.10** Variation of 4-CP concentration under various conditions with initial concentration =  $10 \text{ mg L}^{-1}$ , applied bias potential =  $2 \text{ V}$ , and light intensity =  $150 \text{ mA cm}^{-2}$ . Reprinted from [32] with permission from Elsevier

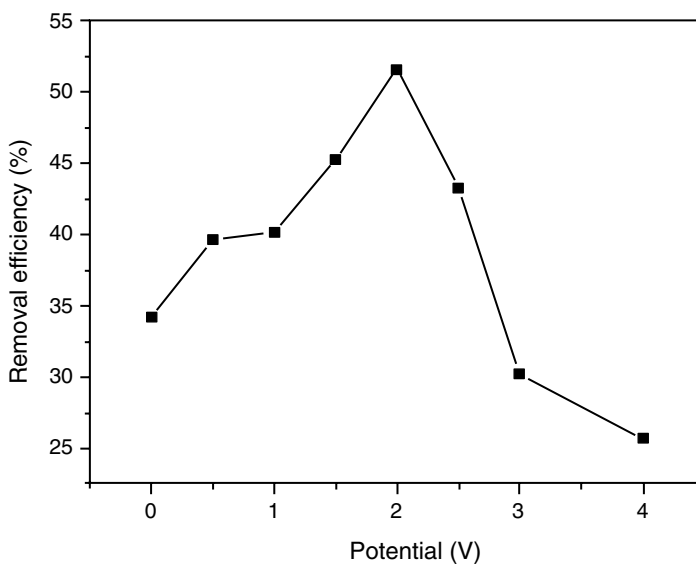


**Fig. 21.11** The effect of the bias potential on 4-CP removal efficiency with initial concentration of  $10 \text{ mg L}^{-1}$ , reaction time =  $8 \text{ h}$ . Reprinted from [32] with permission from Elsevier

The application of potentials greater than the Bi<sub>2</sub>WO<sub>6</sub> flat band potential across a photoelectrode increases the concentration of photogenerated holes or hydroxyl radicals on the surface. As a result, as the potential increases, the rate of 4-CP degradation increases, until most of the photogenerated electrons are removed. Further increase of the applied potential beyond the redox potential of 4-CP improves the degradation largely. In this case, the degradation of 4-CP was carried out by the combination of electro-oxidation and photocatalysis. However, with a bias potential greater than 2.0 V, the synergetic effect decreases gradually. A similar phenomenon was observed in our work on ZnWO<sub>4</sub> [33], and the explanation has been presented in detail. The overpotential for the oxygen evolution reaction increases with the current density. Thus, when the bias potential exceeds 2.0 V, most of the ·OH radicals formed further react to form oxygen. To further explore the reason, the electrode surface was analyzed by X-ray photoelectron spectroscopy (XPS). It was found that the deposited film can be formed on the electrode surface during the electrochemical and PEC degradation. The faster original oxidation of organic compounds at higher potential leads to the formation of more intermediates, deposited on the electrode surface, blocking further access of organic compounds and slowing the degradation.

## 21.6 Enhancement of the Performance of Bi<sub>2</sub>WO<sub>6</sub> by Doping or Substitution

A major limitation of achieving high photocatalytic efficiency in semiconductor systems is the quick recombination of charge carriers. Recombination, which has faster kinetics than surface redox reactions, is a major drawback as it reduces the quantum efficiency of photocatalysis. Therefore, ways to minimize the recombination rate are important if we are interested in maximizing the photocatalysis efficiency. For this purpose, fluorinated TiO<sub>2</sub> has been investigated in relation to doping (TiO<sub>2-x</sub>F<sub>x</sub>) or surface complexation (F-TiO<sub>2</sub>) [34–38]. Fluorinated Bi<sub>2</sub>WO<sub>6</sub> and fluorine-substituted Bi<sub>2</sub>WO<sub>6</sub> have been studied by our group recently [39, 40].

### 21.6.1 Doping by F

F-Bi<sub>2</sub>WO<sub>6</sub> catalyst was synthesized by a simple hydrothermal process [39]. It was found that the interaction of F<sup>-</sup> with the surface Bi<sup>3+</sup> ion prohibited the enlargement of the crystal nuclei. Each sample showed a monotonic increase in the BET surface area with increasing  $R_F$  (represents the molar ratio of F<sup>-</sup>). The absorption onsets of the samples were red-shifted apparently, when  $R_F$  increased from 0.2 to 0.6. The difference of the absorbance edges could arise from the fluorination of the Bi<sub>2</sub>WO<sub>6</sub> catalyst. Fluorinated Bi<sub>2</sub>WO<sub>6</sub> presented the enhanced photoactivity for the RhB degradation under simulative sunlight, which could be a synergetic effect of the

surface fluorination and the doping of crystal lattice. As shown in Fig. 21.12, in the case of the  $\text{Bi}_2\text{WO}_6$  catalyst, the absorption maximum of the suspension decreased by 92 % in the presence of  $\text{Bi}_2\text{WO}_6$  catalyst after irradiation for 300 min, and the band shifted from 553 to 515 nm. However, after irradiation for 210 min, ca. 98 % of RhB was degraded in the F- $\text{Bi}_2\text{WO}_6$  system and the spectral maximum shifted somewhat from 553 to 500 nm. In the F- $\text{Bi}_2\text{WO}_6$  system, five intermediates, namely, *N,N*-diethyl-*N'*-ethylrhodamine, *N,N*-diethylrhodamine, *N*-ethyl-*N'*-ethylrhodamine, *N*-ethylrhodamine, and RhB were thus identified, whereas the first three intermediates could only be identified in the case of the  $\text{Bi}_2\text{WO}_6$  system. This result indicated that more RhB molecules were degraded via the deethylation process in the F- $\text{Bi}_2\text{WO}_6$  system. It was proposed that the F<sup>-</sup>-containing function on the catalyst surface could serve as an electron-trapping site and enhance interfacial electron-transfer rates by tightly holding trapped electrons.

Fluorine-substituted samples  $\text{Bi}_2\text{WO}_6-x\text{F}_{2x}$  were prepared by a two-step process [40]. It was found that F<sup>-</sup> substitution could change the original coordination around

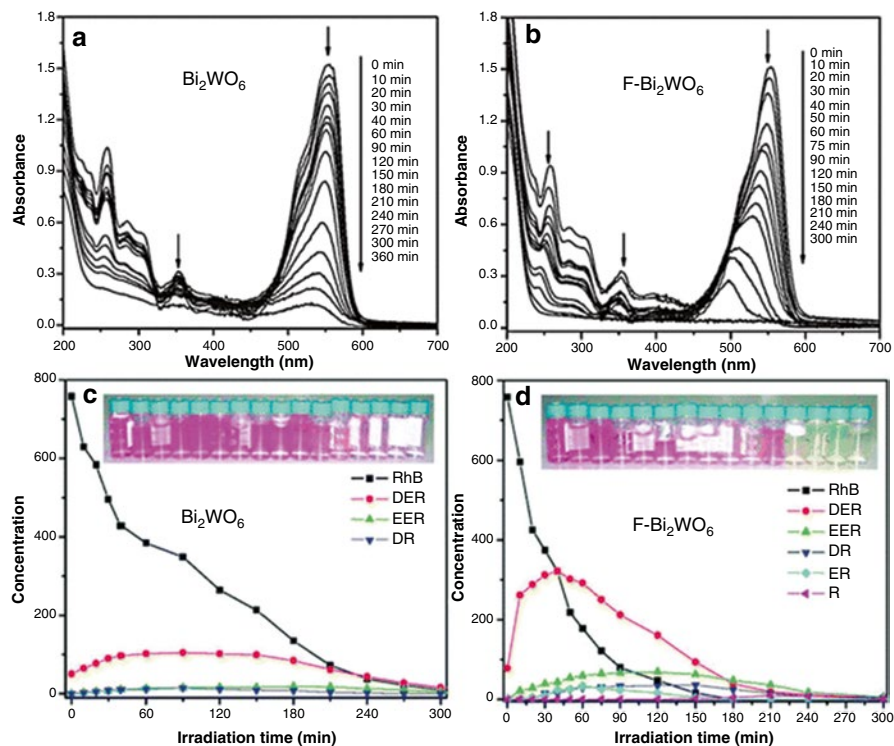


**Fig. 21.12** UV-visible spectral changes of RhB over the catalysts (a)  $\text{Bi}_2\text{WO}_6$  and (b) F- $\text{Bi}_2\text{WO}_6$ . Variations in the distribution of the intermediate products in the corresponding suspensions, (c)  $\text{Bi}_2\text{WO}_6$  and (d) F- $\text{Bi}_2\text{WO}_6$ . The concentrations of the *N*-dealkylated intermediates were determined by the corresponding peak areas gained from the HPLC technique. Reprinted with permission from [39] Copyright 2008 American Chemical Society

the W and Bi atoms. Compared with Bi<sub>2</sub>WO<sub>6</sub>, the photocatalytic activity of Bi<sub>2</sub>WO<sub>6-x</sub>F<sub>2x</sub> calcinated at 573 K increased about two times. The enhanced photocatalytic activity came from the following: (1) the mobility of photoexcited charge carriers in the valence and conduction bands was increased. Based on the DFT theoretical calculations [40], the valence bandwidth of Bi<sub>2</sub>WO<sub>6-x</sub>F<sub>2x</sub> was wider than that of Bi<sub>2</sub>WO<sub>6</sub> because the F 2p orbitals contributed to the valence band formation (Fig. 21.13). Consequently, the calculation results suggested that the wider and more dispersed bands of Bi<sub>2</sub>WO<sub>6-x</sub>F<sub>2x</sub> would increase the mobility of photoexcited charge carriers in the valence and conduction bands. Impedance spectra of Bi<sub>2</sub>WO<sub>6-x</sub>F<sub>2x</sub> showed a smaller arc radius of the EIS Nyquist plot, indicating that photogenerated electron–hole pairs were easily separated and transferred to the surface of the Bi<sub>2</sub>WO<sub>6-x</sub>F<sub>2x</sub> sample. (2) Bi<sub>2</sub>WO<sub>6-x</sub>F<sub>2x</sub> had a stronger oxidation power, which could induce the OH<sup>•</sup> radicals to take part in the photooxidation process. The ability of a semiconductor to photooxidate the adsorbed species on its surface is governed by the positions of its conduction band minimum (CBM) and valence band maximum (VBM) with respect to the redox potentials of the adsorbate, and thus, the photocatalytic ability of Bi<sub>2</sub>WO<sub>6</sub> is determined to a great extent by the positions of its CBM and VBM. The CBM and VBM of Bi<sub>2</sub>WO<sub>6-x</sub>F<sub>2x</sub> were lowered from those of Bi<sub>2</sub>WO<sub>6</sub> by 0.90 and 0.79 eV, respectively. The lowering of the VBM indicated that Bi<sub>2</sub>WO<sub>6-x</sub>F<sub>2x</sub> had a stronger oxidation power (Fig. 21.14).

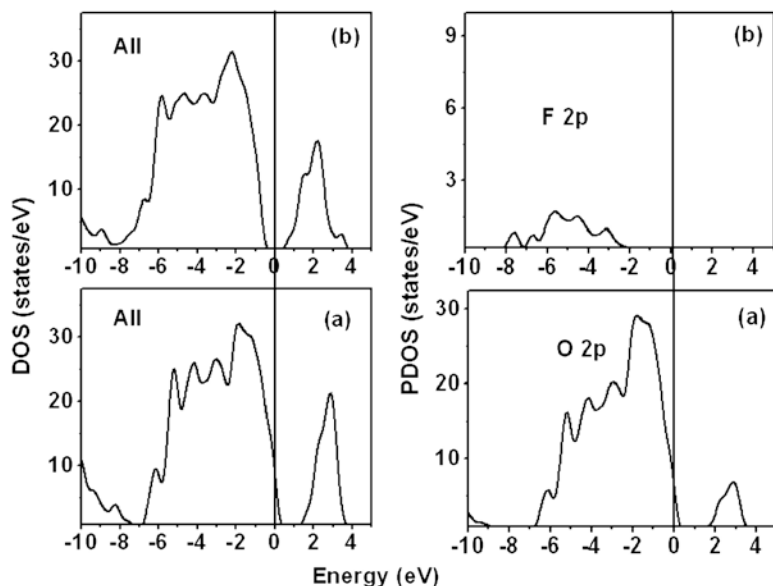


**Fig. 21.13** Total and partial DOS plots (left and right panels, respectively) calculated for (a) Bi<sub>2</sub>WO<sub>6</sub> and (b) Bi<sub>2</sub>WO<sub>6-x</sub>F<sub>2x</sub>. Reprinted with permission from [40]. Copyright 2009 American Chemical Society

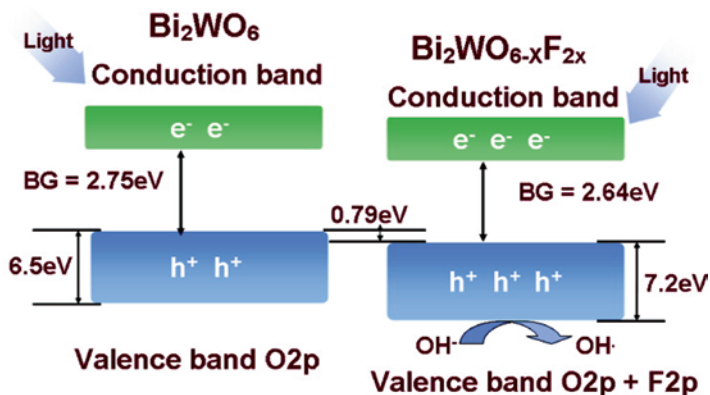


**Fig. 21.14** The mechanism of enhanced  $\text{Bi}_2\text{WO}_{6-x}\text{F}_{2x}$  photocatalytic activity. Reprinted with permission from [40]. Copyright 2009 American Chemical Society

### 21.6.2 Doping by F and Ce

Huang and coworkers [41] have studied Ce and F codoped  $\text{Bi}_2\text{WO}_6$ . F–Ce– $\text{Bi}_2\text{WO}_6$  nanoplates were successfully prepared by a facile one-step hydrothermal route. XPS results confirmed the coexistence of  $\text{Ce}^{3+}$ ,  $\text{Ce}^{4+}$ , and  $\text{F}^-$  species in  $\text{Bi}_2\text{WO}_6$ . Under visible light irradiation, F–Ce– $\text{Bi}_2\text{WO}_6$  exhibits a much higher photocatalytic activity for degradation of RhB than all other doping samples, including pure  $\text{Bi}_2\text{WO}_6$ , Ce– $\text{Bi}_2\text{WO}_6$ , and F– $\text{Bi}_2\text{WO}_6$ . Based on the results of active species trapping measurements, photogenerated holes ( $h^+$ ) and superoxide radicals ( $\cdot\text{O}_2^-$ ) playing a crucial role in photodegradation of RhB over F–Ce– $\text{Bi}_2\text{WO}_6$ , the photocatalytic mechanism was proposed (Fig. 21.15). The observed remarkably improved photocatalytic activity should be resulted from the synergistic effect of the codoping of Ce and F, in which the  $\text{Ce}^{3+}/\text{Ce}^{4+}$  redox couple acts as an electron scavenger and F narrowed the optical band gap enhancing the visible-light absorption. This synergistic effect effectively promotes the separation and transfer of photogenerated charge carriers and simultaneously depresses the recombination of holes ( $h^+$ ) and electrons ( $e^-$ ), resulting in the high photocatalytic performance. Their work could not only provide a better understanding of the synergistic effect of Ce and F comodification but also be beneficial for to the design of high-performance semiconductor photocatalysts.

### 21.6.3 Substitution by Others

Recent studies have shown that substitution of the M site ( $\text{A}_x\text{M}_y\text{O}_z$ ) with other metal ions could considerably improve the catalytic activity [42]. The substitution of M sites might induce a slight modification of crystal structure due to the different ion

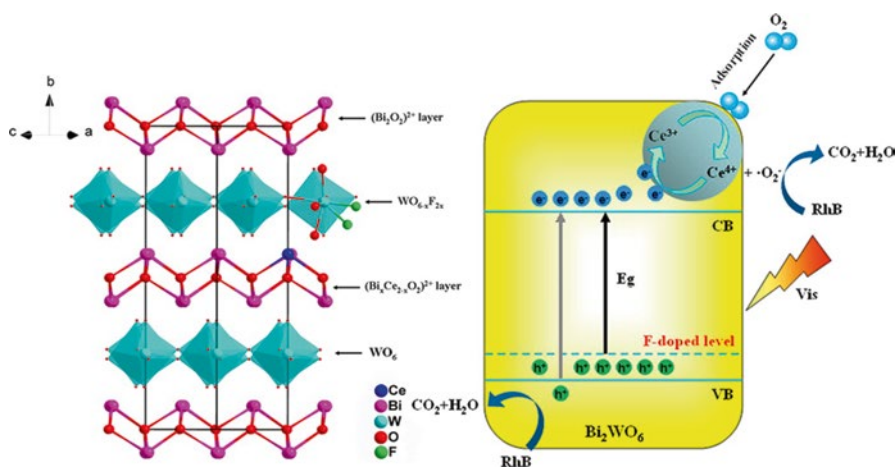


**Fig. 21.15** Crystal structure of F–Ce– $\text{Bi}_2\text{WO}_6$  and schematic diagrams of the photodegradation of RhB over F–Ce– $\text{Bi}_2\text{WO}_6$  under visible light irradiation. Reprinted with permission from [41]. Copyright 2014 American Chemical Society

radii, resulting in dramatic influence on the mobility of the charge carrier and change in the photocatalytic and photo-physical properties. Therefore, from the viewpoint of developing highly efficient  $\text{Bi}_2\text{WO}_6$  photocatalysts with wider optical response in the visible spectral range, the substitution of W sites in  $\text{Bi}_2\text{WO}_6$  with Mo has been further studied [10].  $\text{Bi}_2\text{Mo}_x\text{W}_{1-x}\text{O}_6$  solid solutions with adjustable band gaps were prepared by Yu's group via hydrothermal treatments; the visible-light-induced photocatalytic activity of  $\text{Bi}_2\text{WO}_6$  was found to be improved with certain extent of Mo substitution [43].

Phase-pure  $\text{Bi}_2\text{Mo}_x\text{W}_{1-x}\text{O}_6$  ( $0 \leq x \leq 1$ ) photocatalysts were also synthesized via a hydrothermal method [10]. The as-prepared  $\text{Bi}_2\text{Mo}_x\text{W}_{1-x}\text{O}_6$  photocatalysts had an Aurivillius crystal structure and showed special anisotropic growth. The optical absorption spectra of  $\text{Bi}_2\text{Mo}_x\text{W}_{1-x}\text{O}_6$  were red-shifted monotonically as the value of  $x$  increased. Based on theoretical calculations, as shown in Fig. 21.16, the introduction of Mo atom into  $\text{Bi}_2\text{WO}_6$  could reduce the conduction band level of  $\text{Bi}_2\text{WO}_6$ , so the band gap energy was reduced. The curvature of the conduction band became smaller with an increase of Mo content due to the different electronegativities of Mo 4d and W 5d. The mobility of the electronic carrier is reported to be proportional to the reciprocal effective mass of carrier that is in proportion to the curvature [42]. The photocatalytic activities determined by rhodamine B degradation under visible light irradiation ( $\lambda > 420$  nm) of  $\text{Bi}_2\text{Mo}_x\text{W}_{1-x}\text{O}_6$  photocatalysts were significantly improved as compared with that of  $\text{Bi}_2\text{MoO}_6$ . The higher efficiency of  $\text{Bi}_2\text{WO}_6$  was attributed to more effective photoelectron transfer in the conduction band with larger curvature. The photocatalytic activities under visible light irradiation ( $\lambda > 450$  nm) of  $\text{Bi}_2\text{Mo}_x\text{W}_{1-x}\text{O}_6$  photocatalysts were much higher than that of  $\text{Bi}_2\text{WO}_6$  [10].

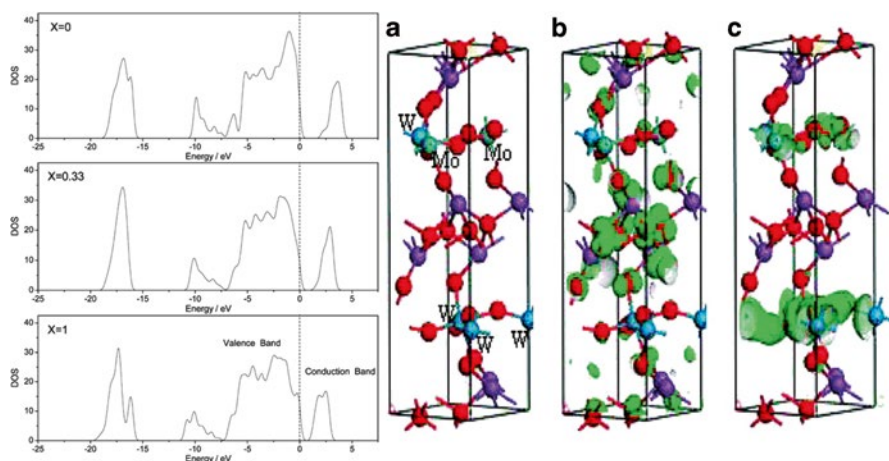


**Fig. 21.16** The evolution of electronic structure with the increased amount of Mo substitution and (a) the optimized model of Mo-doped  $\text{Bi}_2\text{WO}_6$ ; (b) electron density contour map for the top of the valence band (HOMO); (c) electron density contour map for the bottom of the conduction band (LUMO). Purple, blue, and red balls represent Bi, W, and O atoms, respectively. Reprinted with permission from [10]. Copyright 2011 American Chemical Society

## 21.7 Enhancement of the Activity by Modification

A major limitation to achieve high photocatalytic efficiency is the quick recombination of photo-generated charge carriers. Recombination has faster kinetics than surface redox reactions and greatly reduces the quantum efficiency of photocatalysis. Therefore, to enhance the photocatalytic efficiency, it is essential to retard the recombination of the charge carriers. Many works have been devoted to reduce the recombination of charge carriers by coupling the photocatalysts with other materials, such as noble metals [44, 45], semiconductors [46, 47], carbon nanotube [48], etc. Our group has developed conjugative  $\pi$  structure material hybridized semiconductors as efficient photocatalysts, such as  $\text{C}_{60}$  [49–51], polyaniline [52, 53], graphite-like carbon [54, 55], graphene [56–58], and graphene-like carbon nitride [59–61]. The hybridization of photocatalyst with conjugative  $\pi$  structure material possessing good electrical conductivity could reduce the recombination of charge carriers, and increase the photocatalytic efficiency. Besides, heterojunction structure between a photocatalyst and a narrow band gap semiconductor with matched band potentials may also improve the charge separation efficiency and extend the spectral responsive range [62, 63].

### 21.7.1 Surface Hybridization with C<sub>60</sub>

Concerning the high photocatalytic activity of nanosized Bi<sub>2</sub>WO<sub>6</sub>, it is expected that the visible photoactivity of Bi<sub>2</sub>WO<sub>6</sub> for degradation of dye can be enhanced via synergetic effect of C<sub>60</sub> and Bi<sub>2</sub>WO<sub>6</sub>. C<sub>60</sub>-modified Bi<sub>2</sub>WO<sub>6</sub> photocatalyst is obtained by chemically adsorbing C<sub>60</sub> on the surface of Bi<sub>2</sub>WO<sub>6</sub>. The photodegradation results of dyes over C<sub>60</sub>-modified Bi<sub>2</sub>WO<sub>6</sub> under visible light irradiation and solar (simulated by a Xenon lamp) show that the photocatalytic activity can be significantly enhanced. It is postulated that the enhanced photoactivity of C<sub>60</sub>-modified Bi<sub>2</sub>WO<sub>6</sub> catalysts results from high migration efficiency of photoinduced electron–hole pairs [51].

The existence of C<sub>60</sub> was confirmed by HRTEM and the diffuse-reflection spectra (DRS) of C<sub>60</sub>-modified Bi<sub>2</sub>WO<sub>6</sub> [51]. With the loading of C<sub>60</sub>, C<sub>60</sub>/Bi<sub>2</sub>WO<sub>6</sub> displayed the same absorption edge as Bi<sub>2</sub>WO<sub>6</sub> (Fig. 21.17a). However, the samples exhibited a greater light attenuation throughout the visible wavelengths consistent with the gray color of the catalyst. The absorption intensity increased rapidly with C<sub>60</sub>/Bi<sub>2</sub>WO<sub>6</sub> from 0.65 to 1.25 %, but the increment was small from 1.25 to 3.0 %. Considering the diameter of C<sub>60</sub> (0.71 nm) and the BET surface area of Bi<sub>2</sub>WO<sub>6</sub> (8.68 m<sup>2</sup> g<sup>-1</sup>), it can be estimated that the weight ratio is about 2.0 % with a nearly compact C<sub>60</sub> monolayer coverage on Bi<sub>2</sub>WO<sub>6</sub>. The actual concentration of C<sub>60</sub> absorbed on the surface of Bi<sub>2</sub>WO<sub>6</sub> could be even less than 2.0 % because C<sub>60</sub> can only occupy the active absorption site. The absorption intensity remained almost unchanged when the ratio of C<sub>60</sub>/Bi<sub>2</sub>WO<sub>6</sub> increased from 1.25 to 2.0 %, indicating that C<sub>60</sub> may aggregate to form a cluster on the surface of a Bi<sub>2</sub>WO<sub>6</sub> nanosheet when the weight ratio of C<sub>60</sub>/Bi<sub>2</sub>WO<sub>6</sub> was above 2.0 %.

The photocatalytic activity of the C<sub>60</sub>/Bi<sub>2</sub>WO<sub>6</sub> sample was evaluated by the degradation of MB in aqueous solution [51]. Figure 21.17b shows the photocatalytic degradation curve of normalized MB as a function of time. All the modified Bi<sub>2</sub>WO<sub>6</sub> samples exhibited higher photocatalytic activities than pure Bi<sub>2</sub>WO<sub>6</sub>. The optimal loading amount of C<sub>60</sub> on Bi<sub>2</sub>WO<sub>6</sub> for increasing the photocatalytic activity was 1.25 %. As mentioned in the result of diffuse reflection spectra, C<sub>60</sub> tended to aggregate on the surface of Bi<sub>2</sub>WO<sub>6</sub> when the mass ratio of C<sub>60</sub> is above 1.25 %, which resulted in the slower transmission of the photoinduced electrons. 1.25 % C<sub>60</sub> and Bi<sub>2</sub>WO<sub>6</sub> mechanical mixture as a reference was prepared by mere stirring. The photocatalytic activity of Bi<sub>2</sub>WO<sub>6</sub> modified by C<sub>60</sub> was enhanced by about 4 times compared with that of the Bi<sub>2</sub>WO<sub>6</sub> sample.

Electrochemical impedance spectroscopy (EIS) and photocurrent generation were used to investigate the photogenerated charge separation process on a ITO/Bi<sub>2</sub>WO<sub>6</sub> film and a ITO/Bi<sub>2</sub>WO<sub>6</sub>/C<sub>60</sub> film [51]. The arc radius on the EIS Nyquist plot of the ITO/Bi<sub>2</sub>WO<sub>6</sub>/C<sub>60</sub> film was smaller than that of the ITO/Bi<sub>2</sub>WO<sub>6</sub> film sample, which meant that an effective separation of photogenerated electron–hole pairs and fast interfacial charge transfer to the electron donor/electron acceptor occurred as suggested [55]. The photocurrent increased about two times after being modified by C<sub>60</sub>, suggesting the improvement of separation efficiency and inhibition of recombination of photoinduced electron–hole pairs.

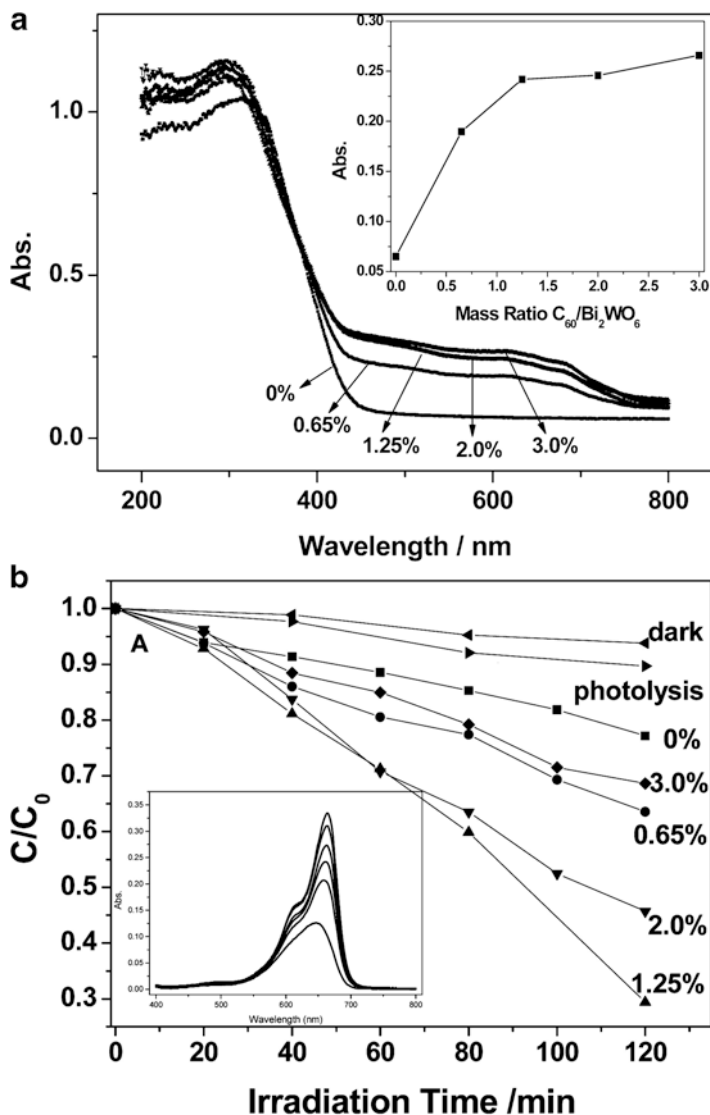


**Fig. 21.17** (a) UV-Vis DR spectra of  $Bi_2WO_6$  and  $C_{60}/Bi_2WO_6$  samples with various mass ratios. Inset: changes of absorbance (600 nm) as a function of mass ratio  $C_{60}/Bi_2WO_6$ . (b) Photocatalytic degradation of MB by  $C_{60}$ -modified  $Bi_2WO_6$  and  $Bi_2WO_6$  under visible light irradiation ( $\lambda > 420$  nm). Reprinted with permission from [Environ. Sci. Technol. 2007, 41, 6234–6239]. Copyright 2007 American Chemical Society. [51]

The mechanism of the enhancement of photocatalytic activity and photocurrent generation via  $C_{60}$  surface hybridization was thus proposed by Zhu and coworkers [51]. The schematic of photocatalytic mechanism is shown in Fig. 21.18. The reason should be closely attributed to the interaction between  $Bi_2WO_6$  and  $C_{60}$  which increased the photogenerated electron mobility in  $Bi_2WO_6$ . The  $C_{60}$  molecule was

**Fig. 21.18** Possible pathway of the photoelectron transfer excited by visible irradiation including the photocatalytic process for  $\text{C}_{60}$ -modified  $\text{Bi}_2\text{WO}_6$ . Reprinted with permission from [51]. Copyright 2007 American Chemical Society



mainly covered on the surface of  $\text{Bi}_2\text{WO}_6$ .  $\text{C}_{60}$  acted as an electron shuttle that could effectively transfer the photoelectrons from the conduction band of  $\text{Bi}_2\text{WO}_6$  after being illuminated under visible light irradiation. The delocalized conjugated  $\pi$  structure of  $\text{C}_{60}$  made it easier to transfer the photoinduced electrons. Accordingly, the photogenerated electrons in the modified  $\text{Bi}_2\text{WO}_6$  photocatalyst could easily migrate from the inner region to the surface to take part in the surface reaction.

### 21.7.2 Hybridization with Graphene

Yang and coworkers [58] synthesized the  $\text{Bi}_2\text{WO}_6$ -reduced graphene oxide (BWO-RGO) composite via electrostatic self-assembly. The positively charged BWO assembled with negatively charged GO sheets and then the composited GO was reduced via the hydrothermal treatment. The close interfacial contact and strong electronic interaction between BWO and RGO are achieved by this facile and efficient self-assembly route.

Photocatalytic degradation of pollutant bisphenol A, selective oxidation of benzyl alcohol, removal of heavy metal ion  $\text{Cr(VI)}$ , and selective reduction of 4-nitrophenol are selected as the probe reactions to investigate the photocatalytic activities of as-obtained BWO-RGO nanocomposites. The experimental results demonstrate the photocatalytic redox activities of BWO-RGO composites are predominantly dependent on the energy levels of photoinduced electrons or holes. In particular, the upshift of the valence band and conduction band edge of catalysts induced by the electronic interaction between BWO and RGO has an inconsistent influence on the photocatalytic reduction and oxidation reactions, respectively. As a result, the photocatalytic activity of reduction reactions is significantly enhanced, owing to the synergetic effect of the upshift of conduction band edge and the improved separation of photogenerated electrons/holes, while the oxidation ability of BWO-RGO nanocomposite is improved to a slight extent compared with bare BWO. The energy levels of photogenerated carriers should be the origins accounting for the different enhancement of photocatalytic activities for the different reactions (Fig. 21.19).

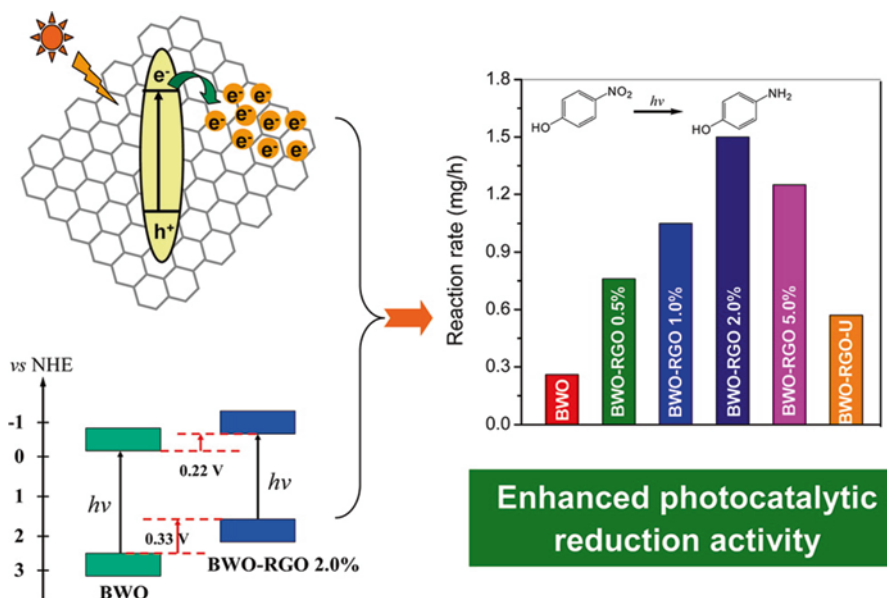


**Fig. 21.19** The mechanism of RGO enhanced of BWO photocatalytic reduction activity. Reprinted with permission from [58]. Copyright 2015 American Chemical Society

### 21.7.3 Hybridization with Graphene-Like Carbon Nitride

Graphite-like  $C_3N_4$  (denoted as  $C_3N_4$ ) possesses a very high thermal and chemical stability and has attracted extensive attention due to its outstanding mechanical, electrical, thermal, and optical properties [64]. We have for the first time reported a  $C_3N_4$ -hybridized  $Bi_2WO_6$  photocatalyst fabricated by a chemisorption method [61].

As can be seen from Fig. 21.20A, the  $Bi_2WO_6$  crystals prepared by the hydrothermal process are sheet-shaped and the average size of a  $Bi_2WO_6$  nanosheet was about 60 nm. There was no change of lattice structure of  $Bi_2WO_6$  after  $C_3N_4$  was adsorbed on the surface and the outer boundary was obviously different from the  $Bi_2WO_6$  core. The thickness of the  $C_3N_4$  layer coated on the  $C_3N_4/Bi_2WO_6$ -2 % sample was estimated to be 0.372 nm, which was close to the scale of monolayer  $C_3N_4$  (about 0.325 nm) [65]. Therefore, it can be estimated that the absorbed  $C_3N_4$  layer on the surface of  $C_3N_4/Bi_2WO_6$ -2 % was an approximately monolayer structure.

After hybridization with  $C_3N_4$ , the photocatalytic activity of  $Bi_2WO_6$  was obviously enhanced. A  $C_3N_4/Bi_2WO_6$  photocatalyst hybridized with monolayer  $C_3N_4$  exhibited the highest photocatalytic activity which was 68.9 % higher than that of pure  $Bi_2WO_6$ . The enhanced photocatalytic activity of the  $C_3N_4/Bi_2WO_6$  photocatalysts could be attributed to the synergetic effect between  $C_3N_4$  and  $Bi_2WO_6$ .

The conduction band (CB) and valence band (VB) potentials of the  $Bi_2WO_6$  are shown in Fig. 21.20B.  $Bi_2WO_6$  can absorb visible light to produce photogenerated electron-hole pairs. Since the VB position of  $Bi_2WO_6$  (+2.94 eV) was lower than the

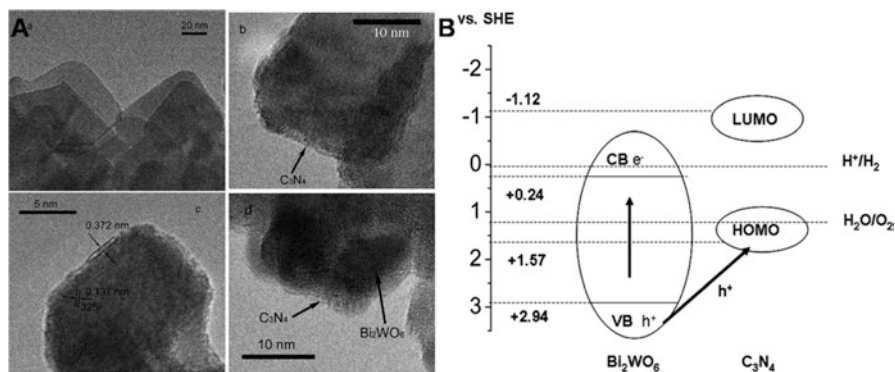


**Fig. 21.20** (A) TEM and HRTEM images of  $\text{Bi}_2\text{WO}_6$  and  $\text{C}_3\text{N}_4/\text{Bi}_2\text{WO}_6$  photocatalysts: (a)  $\text{Bi}_2\text{WO}_6$ , (b)  $\text{C}_3\text{N}_4/\text{Bi}_2\text{WO}_6$ , (c)  $\text{C}_3\text{N}_4/\text{Bi}_2\text{WO}_6$ -2 %, (d)  $\text{C}_3\text{N}_4/\text{Bi}_2\text{WO}_6$ -8 %. (B) Schematic drawing illustrating the mechanism of charge separation and photocatalytic activity over a  $\text{C}_3\text{N}_4/\text{Bi}_2\text{WO}_6$  photocatalyst under irradiation. Reprinted from [61] with permission of the Royal Society of Chemistry

highest occupied molecular orbital (HOMO) of  $\text{C}_3\text{N}_4$  (+1.57 eV), the photogenerated holes on  $\text{Bi}_2\text{WO}_6$  could transfer easily to  $\text{C}_3\text{N}_4$  via the well developed interface. Thus, the charge recombination could be effectively suppressed, leaving more hole charge carriers and enhancing the photocatalytic activity.

### 21.7.4 Heterojunction

Constructing heterojunctions between  $\text{Bi}_2\text{WO}_6$  and another semiconductor or noble metal is an effective way to enhance the activity. The photogenerated  $e^-$  and  $h^+$  can be efficiently separated at the interface through the heterojunctions. Zhang and coworkers [63] designed  $\text{Bi}_2\text{S}_3/\text{Bi}_2\text{WO}_6$  composite photocatalyst, which has a wide photoabsorption until 800 nm and exhibits significantly enhanced photocatalytic activity for phenol degradation under visible light irradiation. Xu and Ren found Cu and Ag composited with  $\text{Bi}_2\text{WO}_6$  enhanced its photocatalytic activity [66, 67]

In contrast, more studies focus on traditional photocatalyst of  $\text{TiO}_2$  and  $\text{Bi}_2\text{WO}_6$  heterogeneous system. Tian and coworkers [62] synthesized the oxygen vacancies of the  $\text{Bi}_2\text{WO}_6$  nanosheets by a simple hydrothermal-co-precipitation method. The broad spectrum photocatalyst,  $\text{Bi}_2\text{WO}_6$ - $\text{TiO}_2$  nanobelt heterostructures are obtained by assembling  $\text{Bi}_2\text{WO}_6$  nanocrystals on  $\text{TiO}_2$  nanobelts. Both  $\text{Bi}_2\text{WO}_6$  nanosheets and  $\text{Bi}_2\text{WO}_6$ - $\text{TiO}_2$  nanobelt have very broad visible and near-infrared absorption band (Fig. 21.21e), which can attribute to the oxygen vacancies. The 72-atom super cell of  $\text{Bi}_2\text{WO}_6$  has three oxygen vacancies after calculation. The oxygen vacancies of  $\text{Bi}_2\text{WO}_6$  can act to raise the Fermi level and reduce the band edge, allowing for interband transitions and carrier creation under near-infrared excitation.

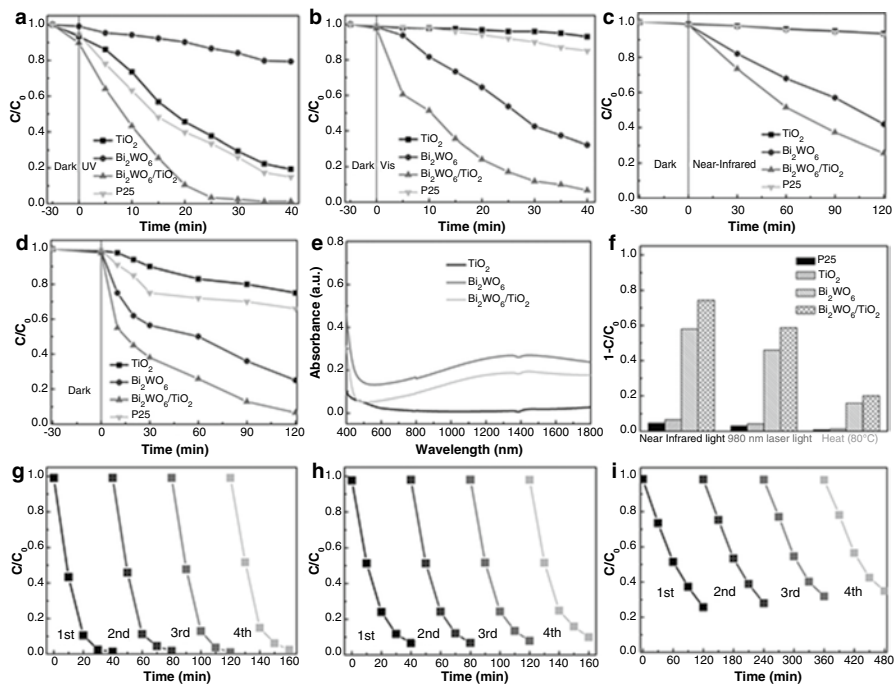


**Fig. 21.21** Photocatalytic degradation of MO in the presence of P25, TiO<sub>2</sub> nanobelts, Bi<sub>2</sub>WO<sub>6</sub> nanosheets, and Bi<sub>2</sub>WO<sub>6</sub>/TiO<sub>2</sub> nanobelt heterostructures under (a) UV light, (b) visible light, (c) near-infrared light, and (d) simulated sunlight irradiation; (e) the experimental visible and near-infrared absorption spectrum of TiO<sub>2</sub> nanobelts, Bi<sub>2</sub>WO<sub>6</sub> nanosheets, and Bi<sub>2</sub>WO<sub>6</sub>/TiO<sub>2</sub> nanobelt heterostructures; (f) Photocatalytic degradation of MO in the presence of P25, TiO<sub>2</sub> nanobelts, Bi<sub>2</sub>WO<sub>6</sub> nanosheets, and Bi<sub>2</sub>WO<sub>6</sub>/TiO<sub>2</sub> nanobelt heterostructures under near-infrared light irradiation, 980 nm laser light irradiation, and heat at 80 °C in the dark for 120 min; irradiation-time dependence of photocatalytic degradation of MO aqueous solution over Bi<sub>2</sub>WO<sub>6</sub>/TiO<sub>2</sub> nanobelt heterostructures (14 wt% Bi<sub>2</sub>WO<sub>6</sub>) during repeated photooxidation experiments under (g) UV light, (h) visible light, and (i) near-infrared light irradiation. Reprinted from [62] with permission from John Wiley & Sons

Bi<sub>2</sub>WO<sub>6</sub>/TiO<sub>2</sub> nanobelt heterostructures possess enhanced UV light, visible light, near-infrared light, and simulated sunlight photocatalytic activities compared with Bi<sub>2</sub>WO<sub>6</sub> nanosheets (Fig. 21.21a–d). The thermocatalytic reference experiment at 80 °C in the dark confirm that the near-infrared photocatalytic property of Bi<sub>2</sub>WO<sub>6</sub> nanosheets and Bi<sub>2</sub>WO<sub>6</sub>/TiO<sub>2</sub> nanobelt heterostructures is attributed to the photocatalysis reaction, not near-infrared light causes photochemical reaction or temperature effect (Fig. 21.22f). Similar with Bi<sub>2</sub>WO<sub>6</sub> nanosheets, the Bi<sub>2</sub>WO<sub>6</sub>/TiO<sub>2</sub> nanobelt heterostructures also exhibit the stable photocatalytic performance under UV, visible, and near-infrared light irradiation (Fig. 21.22g–i). The efficiency photocatalytic of Bi<sub>2</sub>WO<sub>6</sub>/TiO<sub>2</sub> nanobelt heterostructures will be better ways to take advantage of solar energy in the future.

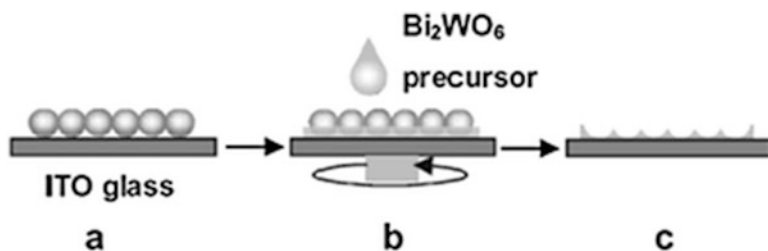


**Fig. 21.22** Schematic illustration for the preparation of  $\text{Bi}_2\text{WO}_6$ -ordered porous films: (a) a packed carbon sphere monolayer on ITO glass; (b) infiltration of  $\text{Bi}_2\text{WO}_6$  precursor by spin coating; (c) removal of carbon spheres by heating in air. Reprinted from [72] with permission from John Wiley & Sons

## 21.8 Synthesis of $\text{Bi}_2\text{WO}_6$ Porous Films with Enhanced Activity

Novel visible-light-driven photocatalysts are primarily synthesized by high-temperature ceramic methods and usually utilized as suspended powders. The limitations of low photocatalytic efficiency and laborious recollection of powders restricted their applications considerably. The preparation of macroporous and mesoporous films has been proposed as a method to increase the effective surface area of photocatalysts, which would allow for increased light absorption and improve photocatalytic performance [68–70]. Macroporous and mesoporous structures would presumably have a photocatalytic activity similar to nanoparticles but would not require the high maintenance costs associated with nanoparticles.

Compared with single-metal oxide porous films, there are two difficulties in the preparation of ternary metal oxide porous films. One is how to choose the precursors of the ternary metal oxide. The cations of the starting sol solution must be homogeneously mixed on the molecular scale in order to obtain porous ternary metal oxides with pure phases, otherwise, the samples obtained will contain secondary phases. The other problem is the porous structure is easy to collapse upon high temperature treatment. However, high calcination temperatures are usually necessary for the crystallization of ternary metal oxides [71].

We have developed a method by combining the evaporation-induced self-assembly method and the amorphous complex precursor method to obtain the  $\text{Bi}_2\text{WO}_6$  porous films (Fig. 21.22) [72]. From the viewpoint of developing an economical, preferentially solution-based route to porous ternary metal oxide films, an amorphous complex precursor was prepared and utilized instead of metal alkoxides. The homogenous amorphous complex precursor is produced by complexation between diethylenetriaminepenta-acetic acid and the low cost metal oxides or salts. The high viscosity of the precursor makes it suitable for preparation of the complex oxide films by a dip-coating or spin-coating technique. Mono-disperse carbon spheres of about 300 and 400 nm were synthesized according to the reported procedure [73, 74], and a packed carbon sphere

monolayer was generated on an ITO glass by vertical deposition [75] of the carbon spheres in ethanol. The spin-coating infiltration method was employed to achieve a homogeneous infiltration of the precursor. Finally, the carbon spheres were removed from the film by heating in air.

Figure 21.23 shows the scanning electron microscope (SEM) images of the carbon sphere monolayer array and  $\text{Bi}_2\text{WO}_6$  porous film synthesized with different sizes of carbon spheres and concentration of precursor. The average size of the open pores increased from 290 to 320 nm as the diameter of the carbon sphere template increased. All samples underwent shrinkage of the pore during calcination. As noted from the SEM images, the thickness of the  $\text{Bi}_2\text{WO}_6$  walls could be adjusted by changing the concentration of the  $\text{Bi}_2\text{WO}_6$  complex precursor. Furthermore, we can readily adjust the size of the pore by changing the diameter of carbon spheres, which could be easily realized by changing the hydrothermal temperature or time.

The photocatalytic decomposition rate of methylene blue (MB) over porous films was found to be more than twice faster than nonporous samples under visible light. The photoelectrochemical measurements show that an enhanced photocurrent is

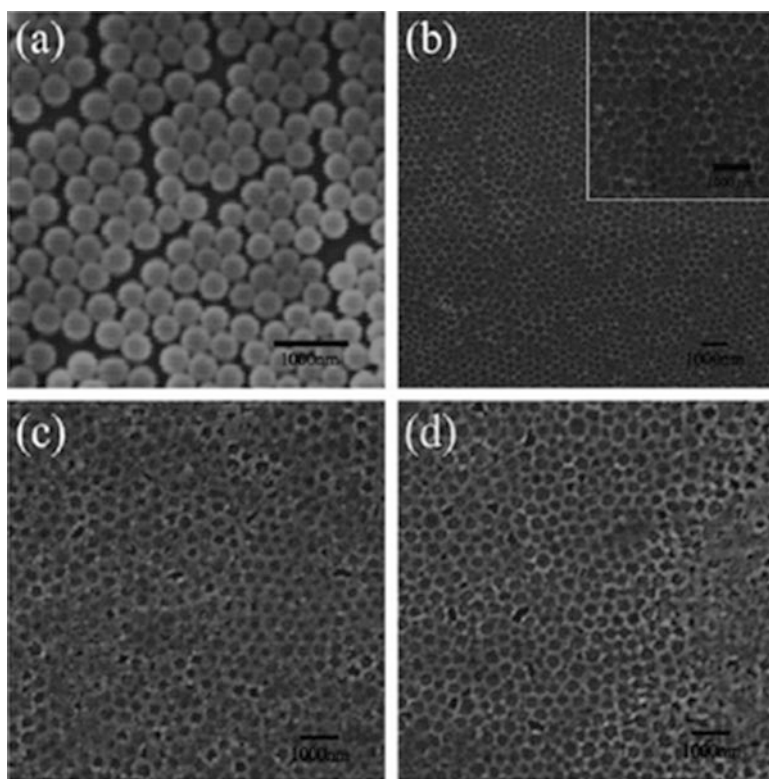


**Fig. 21.23** SEM images of the carbon sphere template (a), and as-prepared  $\text{Bi}_2\text{WO}_6$  porous films under different conditions (b–d). Reprinted with permission from [72] with permission from John Wiley & Sons

obtained essentially over the entire potential range for the porous  $\text{Bi}_2\text{WO}_6$  film (Fig. 21.24). It is interesting to note that there was a fivefold difference in the slope (photocurrent vs. potential) between the two films. The slope corresponds to the inverse resistance of contact between the working electrode material and the electrolyte [76]. The slope is strongly related to the texture of the film. In the case of porous  $\text{Bi}_2\text{WO}_6$  films, due to the much larger electrolyte exposed area, a much larger part of the structure is affected by the field of the Schottky junction at the semiconductor electrolyte interface. Thus the drift of photogenerated carriers within the Schottky space charge layer width becomes a key factor of the porous structure. Due to the much smaller distance from the place the charge carriers were generated in the  $\text{Bi}_2\text{WO}_6$  to the interface between the  $\text{Bi}_2\text{WO}_6$  and the electrolyte solution, the efficiency of the charge carrier transportation was higher in the porous  $\text{Bi}_2\text{WO}_6$  film than in the nonporous film, and an effective separation of the charge carriers could be anticipated [72].

Most recently, Wang and coworkers have successfully fabricated ordered mesoporous  $\text{Bi}_2\text{WO}_6$  via a hard-templated (SBA-15) nanocasting method (Fig. 21.25) [77]. The mesoporous  $\text{Bi}_2\text{WO}_6$  samples exhibit excellent photocatalytic degradation of

**Fig. 21.24** The potentiodynamic scans under chopped illumination for porous and nonporous  $\text{Bi}_2\text{WO}_6$  films. Electrolyte: 0.1 M  $\text{Na}_2\text{SO}_4$ , reference electrode: saturated calomel electrode (SCE). Reprinted with permission from [72] with permission from John Wiley & Sons

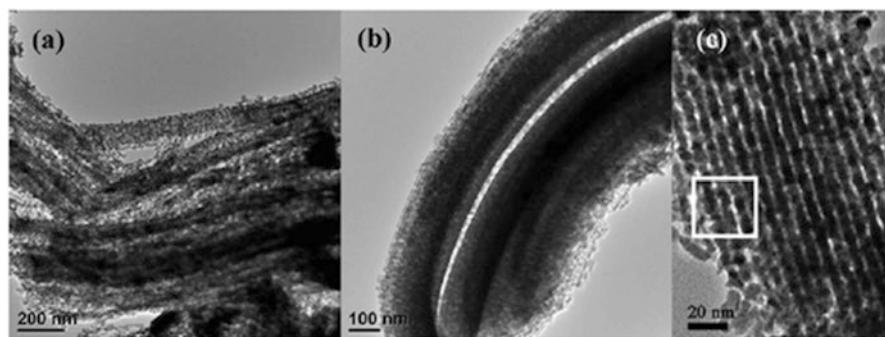
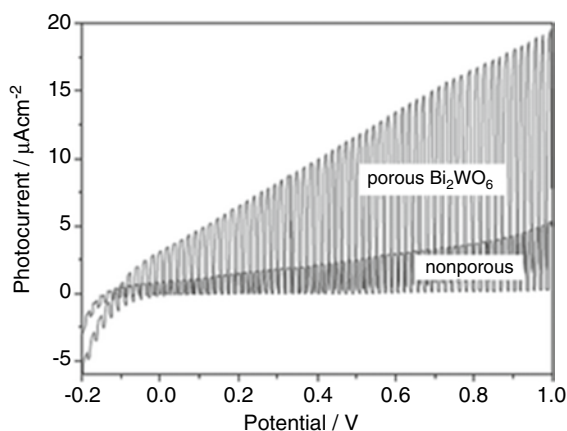


**Fig. 21.25** TEM images of mesoporous  $\text{Bi}_2\text{WO}_6$  prepared with SBA-15 as a hard template. Reprinted from [77] with permission from Elsevier

phenol under visible light irradiation. Compared with a reference nanoscale  $\text{Bi}_2\text{WO}_6$  sample, the mesoporous sample shows a much higher photocatalytic activity under the same conditions. The enhanced photocatalytic performance can be attributed to the higher BET surface area, as well as a negative shift of conduction band and a faster charge transfer in the mesoporous sample.

## 21.9 Concluding Remarks

$\text{Bi}_2\text{WO}_6$  has attracted widespread attention as a high-activity visible-light-driven photocatalyst and shows great potential. In order to improve its specific surface area and recyclability, solve narrow visible response range, and decrease the photo-generated carriers recombination rate, researchers have taken a series of effective measures, such as  $\text{Bi}_2\text{WO}_6$  hierarchical superstructures, photoelectrocatalytic, doping or substitution, surface hybridization with  $\pi$ -conjugated materials or construct heterojunctions, and forming porous films. But the cognition of preparation—structure—performance is not deep enough. There are large study space in controlled synthesis with different crystal faces exposed and the oxygen vacancies of  $\text{Bi}_2\text{WO}_6$ . The band gap adjustment of  $\text{Bi}_2\text{WO}_6$  and interfacial states of its heterostructures should be strengthened. And theoretical calculation would assist to understand in-depth the photocatalytic mechanism, which would be helpful in the improvement of existing photocatalysts and designing novel visible-light responsive photocatalyst.

## References

1. Nagirnyi V, Kirm M, Kotlov A, Lushchik A, Jönsson L (2003) Separation of excitonic and electron–hole processes in metal tungstates. *J Lumin* 102:597–603
2. Yu SH, Liu B, Mo MS, Huang JH, Liu XM, Qian YT (2003) General synthesis of single-crystal tungstate nanorods/nanowires: a facile – low-temperature solution approach. *Adv Funct Mater* 13:639–647
3. Kudo A, Hiji S (1999)  $\text{H}_2$  or  $\text{O}_2$  evolution from aqueous solutions on layered oxide photocatalysts consisting of  $\text{Bi}^{3+}$  with 6s (2) configuration and d (0) transition metal ions. *Chem Lett* 1999:1103–1104
4. Tang J, Zou Z, Ye J (2004) Photocatalytic decomposition of organic contaminants by  $\text{Bi}_2\text{WO}_6$  under visible light irradiation. *Catal Lett* 92:53–56
5. Ricote J, Pardo L, Castro A, Millan P (2001) Study of the process of mechanochemical activation to obtain Aurivillius oxides with  $n=1$ . *J Solid State Chem* 160:54–61
6. Fu H, Zhang L, Yao W, Zhu Y (2006) Photocatalytic properties of nanosized  $\text{Bi}_2\text{WO}_6$  catalysts synthesized via a hydrothermal process. *Appl Catal Environ* 66:100–110
7. Zhang C, Zhu Y (2005) Synthesis of square  $\text{Bi}_2\text{WO}_6$  nanoplates as high-activity visible-light-driven photocatalysts. *Chem Mater* 17:3537–3545
8. Fu H, Pan C, Yao W, Zhu Y (2005) Visible-light-induced degradation of rhodamine B by nanosized  $\text{Bi}_2\text{WO}_6$ . *J Phys Chem B* 109:22432–22439
9. Shimodaira Y, Kato H, Kobayashi H, Kudo A (2006) Photophysical properties and photocatalytic activities of bismuth molybdates under visible light irradiation. *J Phys Chem B* 110:17790–17797
10. Zhang L, Man Y, Zhu Y (2011) Effects of Mo replacement on the structure and visible-light-induced photocatalytic performances of  $\text{Bi}_2\text{WO}_6$  photocatalyst. *ACS Catalysis* 1:841–848

11. Xiao Q, Zhang J, Xiao C, Tan X (2008) Photocatalytic degradation of methylene blue over Co<sub>3</sub>O<sub>4</sub>/Bi<sub>2</sub>WO<sub>6</sub> composite under visible light irradiation. *Catal Comm* 9:1247–1253
12. Kato H, Kudo A (1998) New tantalate photocatalysts for water decomposition into H<sub>2</sub> and O<sub>2</sub>. *Chem Phys Lett* 295:487–492
13. Tang J, Zou Z, Ye J (2004) Efficient photocatalytic decomposition of organic contaminants over CaBi<sub>2</sub>O<sub>4</sub> under visible-light irradiation. *Angew Chem Int Ed* 43:4463–4466
14. Kudo A, Kato H, Nakagawa S (2000) Water splitting into H<sub>2</sub> and O<sub>2</sub> on new Sr<sub>2</sub>M<sub>2</sub>O<sub>7</sub> (M= Nb and Ta) photocatalysts with layered perovskite structures: factors affecting the photocatalytic activity. *J Phys Chem B* 104:571–575
15. Lei Z, You W, Liu M, Zhou G, Takata T, Hara M, Domen K, Li C (2003) Photocatalytic water reduction under visible light on a novel ZnIn<sub>2</sub>S<sub>4</sub> catalyst synthesized by hydrothermal method. *Chem Commun* 2142–2143
16. Kudo A, Omori K, Kato H (1999) A novel aqueous process for preparation of crystal form-controlled and highly crystalline BiVO<sub>4</sub> powder from layered vanadates at room temperature and its photocatalytic and photophysical properties. *J Am Chem Soc* 121:11459–11467
17. Yan Y, Wu Y, Yan Y, Guan W, Shi W (2013) Inorganic-salt-assisted morphological evolution and visible-light-driven photocatalytic performance of Bi<sub>2</sub>WO<sub>6</sub> nanostructures. *J Phys Chem C* 117:20017–20028
18. Cheng H, Huang B, Liu Y, Wang Z, Qin X, Zhang X, Dai Y (2012) An anion exchange approach to Bi<sub>2</sub>WO<sub>6</sub> hollow microspheres with efficient visible light photocatalytic reduction of CO<sub>2</sub> to methanol. *Chem Commun* 48:9729–9731
19. Amano F, Nogami K, Ohtani B (2009) Visible light-responsive bismuth tungstate photocatalysts: effects of hierarchical architecture on photocatalytic activity. *J Phys Chem C* 113:1536–1542
20. Amano F, Nogami K, Tanaka M, Ohtani B (2010) Correlation between surface area and photocatalytic activity for acetaldehyde decomposition over bismuth tungstate particles with a hierarchical structure. *Langmuir* 26:7174–7180
21. Amano F, Yamakata A, Nogami K, Osawa M, Ohtani B (2008) Visible light responsive pristine metal oxide photocatalyst: enhancement of activity by crystallization under hydrothermal treatment. *J Am Chem Soc* 130:17650–17651
22. Chen C, Li X, Ma W, Zhao J, Hidaka H, Serpone N (2002) Effect of transition metal ions on the TiO<sub>2</sub>-assisted photodegradation of dyes under visible irradiation: a probe for the interfacial electron transfer process and reaction mechanism. *J Phys Chem B* 106:318–324
23. Wong C, Chu W (2003) The hydrogen peroxide-assisted photocatalytic degradation of alachlor in TiO<sub>2</sub> suspensions. *Environ Sci Technol* 37:2310–2316
24. Sheng J, Li X, Xu Y (2014) Generation of H<sub>2</sub>O<sub>2</sub> and OH radicals on Bi<sub>2</sub>WO<sub>6</sub> for phenol degradation under visible light. *ACS Catalysis* 4:732–737
25. Christensen P, Curtis T, Egerton T, Kosa S, Tinlin J (2003) Photoelectrocatalytic and photocatalytic disinfection of *E. coli* suspensions by titanium dioxide. *Appl Catal Environ* 41:371–386
26. Xu Y, He Y, Cao X, Zhong D, Jia J (2008) TiO<sub>2</sub>/Ti rotating disk photoelectrocatalytic (PEC) reactor: a combination of highly effective thin-film PEC and conventional PEC processes on a single electrode. *Environ Sci Technol* 42:2612–2617
27. Muna GW, Tasheva N, Swain GM (2004) Electro-oxidation and amperometric detection of chlorinated phenols at boron-doped diamond electrodes: a comparison of microcrystalline and nanocrystalline thin films. *Environ Sci Technol* 38:3674–3682
28. Vlyssides A, Barampouti EM, Mai S, Arapoglou D, Kotronarou A (2004) Degradation of methylparathion in aqueous solution by electrochemical oxidation. *Environ Sci Technol* 38:6125–6131
29. Chen G (2004) Electrochemical technologies in wastewater treatment. *Sep Purif Technol* 38:11–41
30. Marselli B, Garcia-Gomez J, Michaud P-A, Rodrigo M, Comminellis C (2003) Electrogeneration of hydroxyl radicals on boron-doped diamond electrodes. *J Electrochem Soc* 150:D79–D83
31. Caruso F, Möhwald H (1999) Protein multilayer formation on colloids through a stepwise self-assembly technique. *J Am Chem Soc* 121:6039–6046

32. Zhao X, Xu T, Yao W, Zhang C, Zhu Y (2007) Photoelectrocatalytic degradation of 4-chlorophenol at Bi<sub>2</sub>WO<sub>6</sub> nanoflake film electrode under visible light irradiation. *Appl Catal Environ* 72:92–97
33. Zhao X, Zhu Y (2006) Synergetic degradation of rhodamine B at a porous ZnWO<sub>4</sub> film electrode by combined electro-oxidation and photocatalysis. *Environ Sci Technol* 40:3367–3372
34. Balek V, Li D, Šubrt J, Večerníková E, Hishita S, Mitsunashi T, Haneda H (2007) Characterization of nitrogen and fluorine co-doped titania photocatalyst: effect of temperature on microstructure and surface activity properties. *J Phys Chem Solid* 68:770–774
35. Li D, Haneda H, Hishita S, Ohashi N, Labhsetwar NK (2005) Fluorine-doped TiO<sub>2</sub> powders prepared by spray pyrolysis and their improved photocatalytic activity for decomposition of gas-phase acetaldehyde. *J Fluorine Chem* 126:69–77
36. Xiang Q, Lv K, Yu J (2010) Pivotal role of fluorine in enhanced photocatalytic activity of anatase TiO<sub>2</sub> nanosheets with dominant (001) facets for the photocatalytic degradation of acetone in air. *Appl Catal Environ* 96:557–564
37. Yu J, Xiang Q, Ran J, Mann S (2010) One-step hydrothermal fabrication and photocatalytic activity of surface-fluorinated TiO<sub>2</sub> hollow microspheres and tubular anatase single microcrystals with high-energy facets. *CrystEngComm* 12:872–879
38. Yu JC, Yu J, Ho W, Jiang Z, Zhang L (2002) Effects of F-doping on the photocatalytic activity and microstructures of nanocrystalline TiO<sub>2</sub> powders. *Chem Mater* 14:3808–3816
39. Fu H, Zhang S, Xu T, Zhu Y, Chen J (2008) Photocatalytic degradation of RhB by fluorinated Bi<sub>2</sub>WO<sub>6</sub> and distributions of the intermediate products. *Environ Sci Technol* 42:2085–2091
40. Shi R, Huang G, Lin J, Zhu Y (2009) Photocatalytic activity enhancement for Bi<sub>2</sub>WO<sub>6</sub> by fluorine substitution. *J Phys Chem C* 113:19633–19638
41. Huang H, Liu K, Chen K, Zhang Y, Zhang Y, Wang S (2014) Ce and F comodification on the crystal structure and enhanced photocatalytic activity of Bi<sub>2</sub>WO<sub>6</sub> photocatalyst under visible light irradiation. *J Phys Chem C* 118:14379–14387
42. Zhang L, Fu H, Zhang C, Zhu Y (2008) Effects of Ta<sup>5+</sup> substitution on the structure and photocatalytic behavior of the Ca<sub>2</sub>Nb<sub>2</sub>O<sub>7</sub> photocatalyst. *J Phys Chem C* 112:3126–3133
43. Zhou L, Yu M, Yang J, Wang Y, Yu C (2010) Nanosheet-based Bi<sub>2</sub>Mo<sub>x</sub>W<sub>1-x</sub>O<sub>6</sub> solid solutions with adjustable band gaps and enhanced visible-light-driven photocatalytic activities. *J Phys Chem C* 114:18812–18818
44. Hirakawa T, Kamat PV (2005) Charge separation and catalytic activity of Ag@TiO<sub>2</sub> core-shell composite clusters under UV-irradiation. *J Am Chem Soc* 127:3928–3934
45. Subramanian V, Wolf EE, Kamat PV (2004) Catalysis with TiO<sub>2</sub>/gold nanocomposites. Effect of metal particle size on the Fermi level equilibration. *J Am Chem Soc* 126:4943–4950
46. Elder S, Cot F, Su Y, Heald S, Tyryshkin A, Bowman M, Gao Y, Joly A, Balmer M, Kolwaite AC (2000) The discovery and study of nanocrystalline TiO<sub>2</sub>-(MoO<sub>3</sub>) core-shell materials. *J Am Chem Soc* 122:5138–5146
47. Tatsuma T, Saitoh S, Ngaotakanwivat P, Ohko Y, Fujishima A (2002) Energy storage of TiO<sub>2</sub>-WO<sub>3</sub> photocatalysis systems in the gas phase. *Langmuir* 18:7777–7779
48. Woan K, Pyrgiotakis G, Sigmund W (2009) Photocatalytic carbon-nanotube-TiO<sub>2</sub> composites. *Adv Mater* 21:2233–2239
49. Fu H, Xu T, Zhu S, Zhu Y (2008) Photocorrosion inhibition and enhancement of photocatalytic activity for ZnO via hybridization with C<sub>60</sub>. *Environ Sci Technol* 42:8064–8069
50. Zhang L, Wang Y, Xu T, Zhu S, Zhu Y (2010) Surface hybridization effect of C<sub>60</sub> molecules on TiO<sub>2</sub> and enhancement of the photocatalytic activity. *J Mol Catal A Chem* 331:7–14
51. Zhu S, Xu T, Fu H, Zhao J, Zhu Y (2007) Synergetic effect of Bi<sub>2</sub>WO<sub>6</sub> photocatalyst with C<sub>60</sub> and enhanced photoactivity under visible irradiation. *Environ Sci Technol* 41:6234–6239
52. Zhang H, Zong R, Zhao J, Zhu Y (2008) Dramatic visible photocatalytic degradation performances due to synergetic effect of TiO<sub>2</sub> with PANI. *Environ Sci Technol* 42:3803–3807
53. Zhang H, Zong R, Zhu Y (2009) Photocorrosion inhibition and photoactivity enhancement for zinc oxide via hybridization with monolayer polyaniline. *J Phys Chem C* 113:4605–4611
54. Zhang L, Cheng H, Zong R, Zhu Y (2009) Photocorrosion suppression of ZnO nanoparticles via hybridization with graphite-like carbon and enhanced photocatalytic activity. *J Phys Chem C* 113:2368–2374

55. Zhang LW, Fu HB, Zhu YF (2008) Efficient TiO<sub>2</sub> photocatalysts from surface hybridization of TiO<sub>2</sub> particles with graphite-like carbon. *Adv Funct Mater* 18:2180–2189
56. Sun S, Wang W, Zhang L (2013) Bi<sub>2</sub>WO<sub>6</sub> quantum dots decorated reduced graphene oxide: improved charge separation and enhanced photoconversion efficiency. *J Phys Chem C* 117:9113–9120
57. Xu T, Zhang L, Cheng H, Zhu Y (2011) Significantly enhanced photocatalytic performance of ZnO via graphene hybridization and the mechanism study. *Appl Catal Environ* 101:382–387
58. Yang J, Wang X, Zhao X, Dai J, Mo S (2015) Synthesis of uniform Bi<sub>2</sub>WO<sub>6</sub>-reduced graphene oxide nanocomposites with significantly enhanced photocatalytic reduction activity. *J Phys Chem C*
59. Li M, Zhang L, Fan X, Zhou Y, Wu M, Shi J (2015) Highly selective CO<sub>2</sub> photoreduction to CO over g-C<sub>3</sub>N<sub>4</sub>/Bi<sub>2</sub>WO<sub>6</sub> composites under visible light. *J Mater Chem A*
60. Tian Y, Chang B, Lu J, Fu J, Xi F, Dong X (2013) Hydrothermal synthesis of graphitic carbon nitride–Bi<sub>2</sub>WO<sub>6</sub> heterojunctions with enhanced visible light photocatalytic activities. *ACS Appl Mater Interfaces* 5:7079–7085
61. Wang Y, Bai X, Pan C, He J, Zhu Y (2012) Enhancement of photocatalytic activity of Bi<sub>2</sub>WO<sub>6</sub> hybridized with graphite-like C<sub>3</sub>N<sub>4</sub>. *J Mater Chem* 22:11568–11573
62. Tian J, Sang Y, Yu G, Jiang H, Mu X, Liu H (2013) A Bi<sub>2</sub>WO<sub>6</sub>-based hybrid photocatalyst with broad spectrum photocatalytic properties under UV, visible, and near-infrared irradiation. *Adv Mater* 25:5075–5080
63. Zhang Z, Wang W, Wang L, Sun S (2012) Enhancement of visible-light photocatalysis by coupling with narrow-band-gap semiconductor: a case study on Bi<sub>2</sub>S<sub>3</sub>/Bi<sub>2</sub>WO<sub>6</sub>. *ACS Appl Mater Interfaces* 4:593–597
64. Hu J, Cheng W, Huang S, Wu D, Xie Z (2006) First-principles modeling of nonlinear optical properties of C<sub>3</sub>N<sub>4</sub> polymorphs. *Appl Phys Lett* 89:261117–261117-3
65. Yan S, Lv S, Li Z, Zou Z (2010) Organic–inorganic composite photocatalyst of gC<sub>3</sub>N<sub>4</sub> and TaON with improved visible light photocatalytic activities. *Dalton Trans* 39:1488–1491
66. Ren J, Wang W, Sun S, Zhang L, Chang J (2009) Enhanced photocatalytic activity of Bi<sub>2</sub>WO<sub>6</sub> loaded with Ag nanoparticles under visible light irradiation. *Appl Catal Environ* 92:50–55
67. Xu J, Wang W, Gao E, Ren J, Wang L (2011) Bi<sub>2</sub>WO<sub>6</sub>/CuO: a novel coupled system with enhanced photocatalytic activity by Fenton-like synergistic effect. *Catal Comm* 12:834–838
68. Pan JH, Lee WI (2006) Preparation of highly ordered cubic mesoporous WO<sub>3</sub>/TiO<sub>2</sub> films and their photocatalytic properties. *Chem Mater* 18:847–853
69. Zhang L, Zhu Y, He Y, Li W, Sun H (2003) Preparation and performances of mesoporous TiO<sub>2</sub> film photocatalyst supported on stainless steel. *Appl Catal Environ* 40:287–292
70. Zukulova M, Zukal A, Kavan L, Nazeeruddin MK, Liska P, Grätzel M (2005) Organized mesoporous TiO<sub>2</sub> films exhibiting greatly enhanced performance in dye-sensitized solar cells. *Nano Lett* 5:1789–1792
71. Orilall MC, Abrams NM, Lee J, DiSalvo FJ, Wiesner U (2008) Highly crystalline inverse opal transition metal oxides via a combined assembly of soft and hard chemistries. *J Am Chem Soc* 130:8882–8883
72. Zhang LW, Wang YJ, Cheng HY, Yao WQ, Zhu YF (2009) Synthesis of porous Bi<sub>2</sub>WO<sub>6</sub> thin films as efficient visible-light-active photocatalysts. *Adv Mater* 21:1286–1290
73. Sun X, Li Y (2004) Colloidal carbon spheres and their core/shell structures with noble-metal nanoparticles. *Angew Chem Int Ed* 43:597–601
74. Sun X, Li Y (2004) Ga<sub>2</sub>O<sub>3</sub> and GaN semiconductor hollow spheres. *Angew Chem Int Ed* 43:3827–3831
75. Jiang P, Bertone J, Hwang K, Colvin V (1999) Single-crystal colloidal multilayers of controlled thickness. *Chem Mater* 11:2132–2140
76. Yang B, Zhang Y, Drabarek E, Barnes PR, Luca V (2007) Enhanced photoelectrochemical activity of sol-gel tungsten trioxide films through textural control. *Chem Mater* 19:5664–5672
77. Sun S, Wang W, Xu J, Wang L, Zhang Z (2011) Highly efficient photocatalytic oxidation of phenol over ordered mesoporous Bi<sub>2</sub>WO<sub>6</sub>. *Appl Catal Environ* 106:559–564

# Chapter 22

## Preparation and Characterization of Bismuth Tungstate Polycrystalline Flake-Ball Particles for Photocatalytic Reactions

Fumiaki Amano

### 22.1 Introduction

Preparations of hierarchical architectures by assembling nanomaterials of low-dimensional morphologies as building blocks have attracted much attention because of their expected novel properties and functions depending on the size, shape, orientation, alignment, or dimensionality. The hierarchical architectures exhibit characteristics of both nanometer-sized and micrometer-sized structures. Therefore, many research efforts have been devoted on the preparation of hierarchical architectures by assembling nanomaterials with anisotropic structures, such as one-dimensional (1D) and two-dimensional (2D) shapes.

Controlled solution-growth routes have often been used as bottom-up technology for anisotropic crystal growth of nanomaterials to construct hierarchical architectures. Hydrothermal preparation is one of the suitable methods for production of hierarchical architectures since the preparation conditions, such as temperature, composition of the precursor, and addition of structure-directing agents, are easily tunable. The addition of structure-directing agents such as surfactants and polymers is an effective method to control anisotropic crystal growth, which is generally achieved by a selective adsorption of the additives on specific sites suppressing isotropic crystal growth.

It has been reported that a hydrothermal condition promotes anisotropic crystal growth of bismuth tungstate ( $\text{Bi}_2\text{WO}_6$ ) and formation of nanometer-sized square-shaped 2D structures (nanoplates) [1–4]. Figure 22.1 shows the layered crystal structure of  $\text{Bi}_2\text{WO}_6$ , the mineral name of which is Russellite, in an orthorhombic

---

F. Amano (✉)

Department of Chemical and Environmental Engineering, Faculty of Environmental Engineering, The University of Kitakyushu,  
1-1 Hibikino, Wakamatsu-ku, Kitakyushu, Fukuoka 808-0135, Japan  
e-mail: [amano@kitakyu-u.ac.jp](mailto:amano@kitakyu-u.ac.jp)

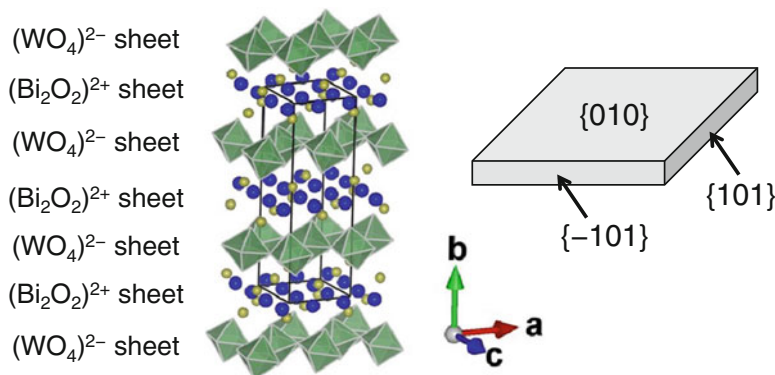


**Fig. 22.1** Crystal structure and square-shaped laminar plate of Bi<sub>2</sub>WO<sub>6</sub>

crystal system [5]. The bismuth-layered compounds of Aurivillius family are represented by a general formula of (Bi<sub>2</sub>O<sub>2</sub>) (A<sub>m-1</sub>B<sub>m</sub><sup>VI</sup>O<sub>3m+1</sub>). Bi<sub>2</sub>WO<sub>6</sub> is the  $m = 1$  member of the family (Bi<sub>2</sub>O<sub>2</sub>) (B<sub>m</sub><sup>VI</sup>O<sub>3m+1</sub>) of cation-deficient Aurivillius phases (B = W and Mo). Up to now Bi<sub>2</sub>WO<sub>6</sub>, Bi<sub>2</sub>MoO<sub>6</sub>, and Bi<sub>2</sub>W<sub>2</sub>O<sub>9</sub> have been identified as belonging to the cation-deficient bismuth-layered compounds [6]. The crystal of Bi<sub>2</sub>WO<sub>6</sub> is composed of accumulated layers of corner-sharing WO<sub>6</sub> octahedral (WO<sub>4</sub>)<sup>2-</sup> sheets and bismuth oxide (Bi<sub>2</sub>O<sub>2</sub>)<sup>2+</sup> sheets. The fabrication of Bi<sub>2</sub>WO<sub>6</sub> under hydrothermal conditions is a suitable method for promoting anisotropic crystal growth and producing square-shaped 2D nanostructures having a basal plane of (010) of an orthorhombic crystal system [2]. The (010) crystal plane-selective growth would result in the production of Bi<sub>2</sub>WO<sub>6</sub> nanoplates.

Bi<sub>2</sub>WO<sub>6</sub> and Bi<sub>2</sub>MoO<sub>6</sub> powders are yellow or yellow-green in color, and have attracted a great deal of attention as visible-light-responsive photocatalysts [2–4, 7–15]. The band gap was estimated to be 2.6–2.8 eV from their onset of the absorption edge in the diffuse reflectance UV–Visible spectra. The top of the valence band (VB) consists of O 2p and Bi 6s orbitals [3, 4]. The bottom of the conduction band (CB) consists of W 5d orbitals with a small contribution of Bi 6p orbitals. The interband transition from the O 2p and Bi 6s orbitals to the empty W 5d orbitals provides the visible-light absorption of Bi<sub>2</sub>WO<sub>6</sub>. In contrast, the contribution of the Bi 6s orbitals to the valence band formation is not observed for Bi<sub>2</sub>MoO<sub>6</sub> [13]. The visible-light absorption of Bi<sub>2</sub>MoO<sub>6</sub> is due to the transition from the O 2p orbitals to the CB derived from the primary Mo 4d orbitals.

Kudo et al. found the visible-light-induced photocatalytic activity of Bi<sub>2</sub>WO<sub>6</sub> for O<sub>2</sub> evolution by water oxidation in the presence of electron acceptor [7]. Ye et al. reported that Bi<sub>2</sub>WO<sub>6</sub> could induce not only photocatalytic O<sub>2</sub> evolution from water but also photocatalytic oxidative decomposition of organic compounds such as acetaldehyde (CH<sub>3</sub>CHO) and trichloromethane (CHCl<sub>3</sub>) under visible light irradiation [8]. Bi<sub>2</sub>WO<sub>6</sub> nanoplates prepared by the hydrothermal reaction method have been reported to induce degradation of organic pollutants, such as formaldehyde (CH<sub>3</sub>CHO), rhodamine B, and chlorophenol under visible light irradiation [2, 4, 9–12]. It has also been reported that hydrothermally prepared Bi<sub>2</sub>WO<sub>6</sub> particles with

square laminar shape or micrometer-sized spherical polycrystalline shape induce photocatalytic degradation of organic pollutants under visible-light irradiation [14–18].

While hydrothermal preparation of  $\text{Bi}_2\text{WO}_6$  photocatalysts have been reported by several groups, physical properties and structural characteristics affecting their photocatalytic efficiency have not been characterized in detail. Evaluation of major factors influencing photocatalytic activity of  $\text{Bi}_2\text{WO}_6$  is important for the development of new types of visible-light-responsive photocatalyst materials, such as highly active structure-controlled photocatalysts.

In this chapter, overview is given of preparation and characterization of  $\text{Bi}_2\text{WO}_6$  photocatalysts with micrometer-sized spherical assemblies of 2D flakes, which are composed of square-shaped nanoplates. The particles are prepared by a facile hydrothermal reaction without using any surfactants and polymers as structure-directing agents. The crystal growth mechanism of the spherical assemblies of polycrystalline 2D flakes is discussed to control hierarchical architectures composed of nanostructures and micrometer-sized structures. The hierarchical polycrystalline particles of “flake-ball” shape exhibit relatively high photocatalytic activity for oxidative decomposition of organic compounds under UV light irradiation and even under visible light irradiation (ca. 8 % apparent quantum efficiency at 400 nm for  $\text{CH}_3\text{CHO}$  decomposition) [14, 15, 19, 20]. The effect of specific surface area and crystallinity on such high activity is discussed based on the physical properties and structural characteristics obtained for the  $\text{Bi}_2\text{WO}_6$  flake-ball particles. The crucial roles of the morphological control in both nanostructures and microstructures are reviewed in terms of photocatalysis applications.

## 22.2 Preparation of $\text{Bi}_2\text{WO}_6$ Flake-Ball Particles

Zhu et al. have reported that  $\text{Bi}_2\text{WO}_6$  nanoplates with square laminar morphologies are synthesized by hydrothermal treatment at 160 °C for 20 h or 200 °C for 12 h [2]. The square nanoplates grew larger and thinner with an increase of the hydrothermal reaction temperature. The length of the edge could reach 200 nm and the thickness was about 5 nm. The  $\text{Bi}_2\text{WO}_6$  nanoplates are reported to exhibit activity for photodecolorization and photodegradation of rhodamine B under visible light irradiation [2–4].

One-pot hydrothermal preparations of  $\text{Bi}_2\text{WO}_6$  hierarchical architectures have been reported by several research groups. Huang et al. and Xie et al. reported a hydrothermal synthesis of micrometer-sized spherical polycrystalline particles of  $\text{Bi}_2\text{WO}_6$  composed of a number of plate-like nanomaterials using poly(vinyl pyrrolidone) (PVP) and triblock copolymer as a structure-directing agent [17, 18, 21]. Wang et al. and Amano et al. have reported the preparation of such  $\text{Bi}_2\text{WO}_6$  particles with a “flake-ball” shape by a facile hydrothermal reaction without any polymer, surfactant, and template in an aqueous solution of low pH value [16, 19, 20].

The  $\text{Bi}_2\text{WO}_6$  flake-ball particles were prepared by a hydrothermal reaction of sodium tungstate ( $\text{Na}_2\text{WO}_4$ ) and bismuth nitrate ( $\text{Bi}(\text{NO}_3)_3$ ) at 170 °C in an aqueous medium without addition of structure-directing agents [19, 20]. A 30-mL aqueous

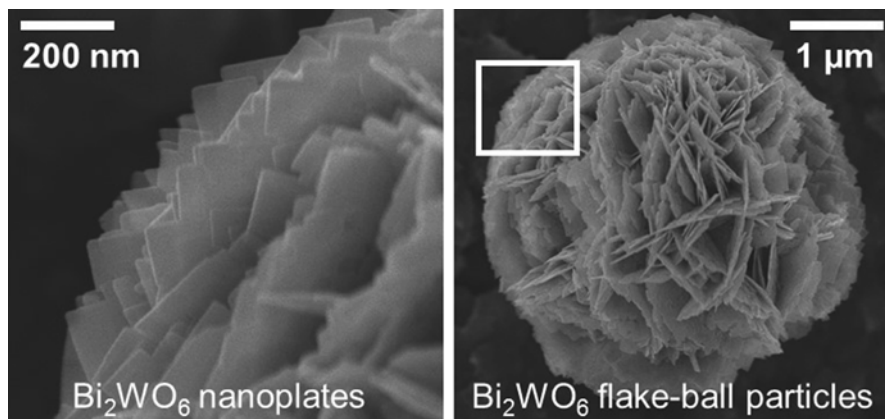


**Fig. 22.2** FE-SEM images of Bi<sub>2</sub>WO<sub>6</sub> flake-ball particles

solution of Na<sub>2</sub>WO<sub>4</sub> (2.75 mmol) was added dropwise to a mixture of Bi(NO<sub>3</sub>)<sub>3</sub> (pentahydrate, 99.9 %, 5.0 mmol) and water (20 mL) with vigorous magnetic stirring. The white slurry was stirred for an additional 10 min and then sonicated for 20 min at ambient temperature under ambient air. The suspension was strongly acidic (pH 1.2) due to hydrolysis of Bi(NO<sub>3</sub>)<sub>3</sub>. After pouring into a 100-mL Teflon-lined autoclave, water was added to ca. 80 % of the capacity of the autoclave. Hydrothermal reaction was performed at 433 K for 20 h under self-generated pressure. After cooling to room temperature, the yellowish white precipitate was collected by centrifugation, washed with 50 mL of water three times, and dried in an oven at 393 K.

Figure 22.2 shows the field-emission type scanning electron microscopy (FE-SEM) images of the Bi<sub>2</sub>WO<sub>6</sub> flake-ball particles with an average diameter of 3–4 μm. An enlarged view showed that each particle has ball-like shape consisting of an assembly of 2D flakes radiating in all directions. A high magnification image shows that the flakes are composed of square-shaped nanoplates with lateral sizes of a few hundreds of nanometers and thicknesses of 20–35 nm. The Bi<sub>2</sub>WO<sub>6</sub> flake-ball particles have hierarchical structure: the primary structure is a layered Bi<sub>2</sub>WO<sub>6</sub> crystal of alternate stacking of a (Bi<sub>2</sub>O<sub>2</sub>)<sup>2+</sup> layer and WO<sub>6</sub> octahedron. The secondary structure is the polycrystalline flakes of accumulated layered crystallites, which are assembled to flake-ball spherical particles as a tertiary structure.

### 22.3 Mechanism of Production of the Bi<sub>2</sub>WO<sub>6</sub> Flake-Ball Particles

Figure 22.3 shows a plausible process of the formation of Bi<sub>2</sub>WO<sub>6</sub> flake-ball particles via anisotropic growth of poorly crystallized 2D flakes from cores [19]. The mechanism of flake-ball particle formation has two stages: diffusion-limited

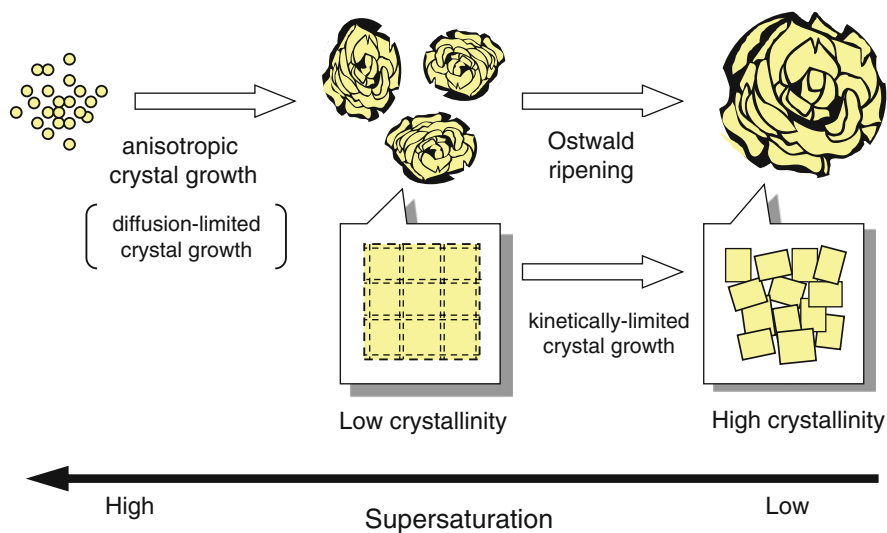


Fig. 22.3 Crystal growth mechanism of  $\text{Bi}_2\text{WO}_6$  flake-ball particles

anisotropic crystal growth and Ostwald ripening process with kinetically limited crystal growth, depending on the concentration of dissolved precursor changes during crystallization.

The flake-ball particles are produced through crystal plane-selective growth starting from cores, not through aggregation of nanoplates produced independently. Such anisotropic crystal growth is generally achieved by a selective adsorption of structure-directing agents on specific sites suppressing isotropic crystal growth. However, no structure-directing agents are added in this preparation method. Strongly acidic aqueous media and 10 % excess amount of the tungsten precursor were indispensable conditions for the flake-ball particle formation in relatively high yield [19]. This condition is found to be useful for the crystal plane-selective growth. In addition, in the case of low concentrations of the starting materials ( $\text{Na}_2\text{WO}_4$  and  $\text{Bi}(\text{NO}_3)_3$ ), a mixture of less crystallized nanoparticles and aggregated nanoplates were obtained instead of flake-ball particles. It is well known that a diffusion-limited growth condition, such as high supersaturation, is needed for the formation of polycrystalline aggregates with a multi-branching form. Therefore, the reason that poorly crystallized  $\text{Bi}_2\text{WO}_6$  2D flakes is grown from cores was concluded to high concentration of the precursors in feed solution.

The formation of 2D flakes composed of poorly crystallized  $\text{Bi}_2\text{WO}_6$  particles decreases the concentration of the precursors. Then, further growth of flake-ball particles progress through the Ostwald ripening process, in which smaller particles disappear due to their high solubility and crystallize to larger particles again (Gibbs–Thomson effect). Minimization of the surface free energy is a driving force for the formation of spherical-shaped particles. Further reaction resulted in increase in crystallite size as well as improvement in crystallinity of the nanoplates in polycrys-

talline 2D flakes. It is known that polyhedron-shaped single crystal is grown in the conditions of low supersaturation because kinetically limited crystal growth is favored [22]. Thus, the crystallinity of nanoplates gradually increased during the Ostwald ripening process.

## 22.4 Photocatalytic Activity of $\text{Bi}_2\text{WO}_6$ Flake-Ball Particles

The development of visible light-responsive photocatalysts is needed for the effective use of light energy. Semiconductor photocatalytic reactions can be classified into two research fields by consideration of the free energy change of reactions ( $\Delta_r G$ ) [23]. Photocatalytic water splitting to produce  $\text{H}_2$  is defined as the light energy conversion to chemical energy, since  $\Delta_r G > 0$ . Photocatalytic oxidative decomposition of organic compounds into  $\text{CO}_2$  can be considered as the energy-saving technology, since the reaction is thermodynamically possible ( $\Delta_r G < 0$ ). To achieve photocatalytic water splitting, band edges of CB and VB of a semiconductor photocatalyst must be located at a potential more negative than that for  $\text{H}_2$  evolution, 0 V vs. standard hydrogen electrode (SHE), and a potential more positive than that for water oxidation, +1.23 V vs. SHE, respectively. For oxidative decomposition of organic compounds, thermodynamic requirements are expected to be less severe than those for water splitting, because  $\Delta_r G < 0$ . However, in general, the CB edge must be more negative than the potential for one electron reduction of molecular oxygen to produce superoxide anion ( $\text{O}_2^{\cdot-}$ , -0.28 V vs. SHE) or hydroperoxy radical ( $\text{HO}_2^{\cdot}$ , -0.05 V vs. SHE). This is because the rates of multiple-electron reduction of  $\text{O}_2$  to produce hydrogen peroxide ( $\text{H}_2\text{O}_2$ ) and water are kinetically very slow.

The VB edges of simple metal oxides, which are generally composed of O 2p orbitals, are usually located at around +3.0 V vs. SHE, indicating that it is impossible to develop photocatalysts of simple metal oxides simultaneously exhibiting a narrow band gap (<3.0 eV) and CB edge more negative than SHE [24]. One of the strategies to overcome this problem is surface modification of narrow band gap photocatalysts, e.g.,  $\text{WO}_3$  with co-catalysts promoting multi-electron reduction of  $\text{O}_2$  [25, 26]. Another strategy is creation of an electron donor level near the VB edge of a wide band gap photocatalyst or a new VB composed of orbitals with energy higher than that of the O 2p orbitals.  $\text{Bi}_2\text{WO}_6$  is one of the photocatalysts in the latter case. Contribution of the Bi 6s orbitals to the VB has been reported for  $\text{Bi}_2\text{WO}_6$  crystals based on calculation using a density functional theory [3, 4]. This would provide both a negative CB edge required for one-electron reduction of  $\text{O}_2$  and a narrow band gap of 2.6–2.8 eV to absorb the violet part of visible light.

Visible light-induced degradation of organic dyes in water using  $\text{Bi}_2\text{WO}_6$  crystallites has been reported elsewhere [3, 4, 10, 12, 16, 17]. However, decolorization of dyes in an aqueous solution might not be appropriate as a test reaction for visible-light-driven photocatalysts, because of (1) possible participation of a dye-sensitized process in decolorization, (2) molar amount of dye smaller than that of a photocatalyst, and (3) incomplete decomposition of dye molecules [27].

The  $\text{Bi}_2\text{WO}_6$  flake-ball particles exhibit relatively high photocatalytic efficiency for mineralization of oxidative decomposition of gaseous  $\text{CH}_3\text{CHO}$  in air under UV irradiation and even under visible light irradiation ( $\lambda > 400$  nm) [14]. The apparent quantum efficiency at 400-nm irradiation was reported to be ca. 8 %. The band gap energy estimated from the absorption edge of a diffuse reflectance spectrum was ca. 2.8 eV for the  $\text{Bi}_2\text{WO}_6$  flake-ball particles. Since the onset of action spectrum, which is the photocatalytic activity plotted against wavelength of light, was located at 440 nm, the visible-light-induced degradation of  $\text{CH}_3\text{CHO}$  is assignable to be induced by interband photoexcitation of  $\text{Bi}_2\text{WO}_6$ . A control experiment indicates that the photocatalytic activity of  $\text{TiO}_2$  (Evonik Degussa P25) was negligible in this reaction condition under visible light. Complete oxidative decomposition of  $\text{CH}_3\text{CHO}$  over the  $\text{Bi}_2\text{WO}_6$  flake-ball particles was proved by the twofold larger yield of  $\text{CO}_2$  (60  $\mu\text{mol}$ ) than the amount of  $\text{CH}_3\text{CHO}$  in the feed (30  $\mu\text{mol}$ ),  $\text{CH}_3\text{CHO} + 5/2\text{O}_2 \rightarrow 2\text{CO}_2 + 2\text{H}_2\text{O}$ . The  $\text{Bi}_2\text{WO}_6$  flake-ball particles could be used repeatedly without deactivation, indicating that the visible-light-induced reaction was “photocatalytic.”

It is reported that the photocatalytic activity for  $\text{CH}_3\text{CHO}$  decomposition was proportional to the specific surface area when the  $\text{Bi}_2\text{WO}_6$  flake-ball particles exhibited similar crystalline content [28]. This proportional relation could be explained by the results showing that the initial rate of  $\text{CH}_3\text{CHO}$  decomposition was expressed by first-order kinetics with respect to the amount of surface-adsorbed  $\text{CH}_3\text{CHO}$ . The  $\text{Bi}_2\text{WO}_6$  flake-ball particles prepared under similar conditions except for preparation temperature in the range of 433–493 K exhibit similar hierarchical architecture, secondary particle size, crystalline shape, exposed crystalline lattice planes, and crystalline content. However, their specific surface areas were different owing to the increase in the thickness of crystalline nanoplates with increasing preparation temperature. The capacity for reactant adsorption is proportional to the specific surface area because the flake-ball particles exhibit exposed  $\text{Bi}_2\text{WO}_6$  (010) surfaces, which guarantee similar adsorption equilibrium constant  $K_a$ , and a cross-sectional adsorption area of a  $\text{CH}_3\text{CHO}$  molecule adsorbed on the surface (0.36  $\text{nm}^2$ ) [28]. Thus, the structure-controlled preparation of metal oxide particles enables the elucidation of the effect of only specific surface area on the photocatalytic efficiency.

## 22.5 Separation of $\text{Bi}_2\text{WO}_6$ Flake-Ball Particles from Water

Micrometer-sized photocatalyst allows easy and fast separation of the particles from liquid solution [19]. Figure 22.4 shows particle size distributions measured by a laser diffraction/scattering method of the  $\text{Bi}_2\text{WO}_6$  flake-ball particles suspended in water. The flake-ball particles show high dispersion in water and a relatively uniform diameter. The mean diameter was calculated to be 3.9  $\mu\text{m}$ , which is consistent with the estimation from FE-SEM analysis (3–4  $\mu\text{m}$ ). The  $\text{Bi}_2\text{WO}_6$  flake-ball particles are readily separated from a solution by sedimentation due to the micrometer-sized structure. Recovery of the powders from water seems to be a critical issue when ultrafine photocatalyst powders are used in aqueous systems. The  $\text{Bi}_2\text{WO}_6$  flake-ball particles were precipitated from an aqueous suspension in less than 1 h,

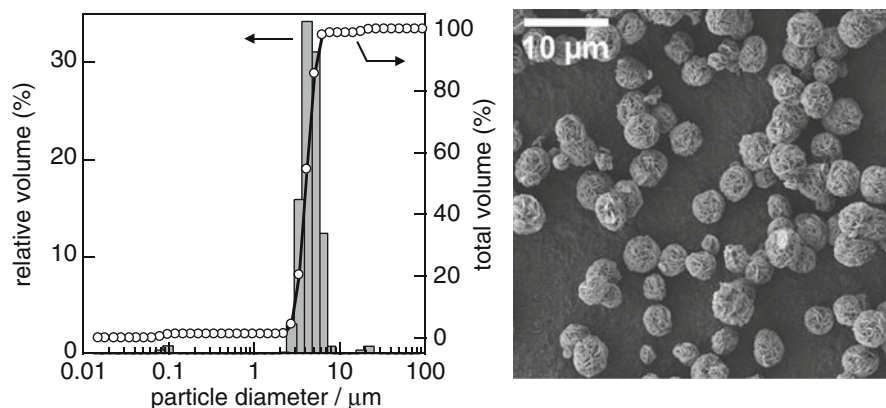


Fig. 22.4 Particle size distribution of  $\text{Bi}_2\text{WO}_6$  flake-ball particles

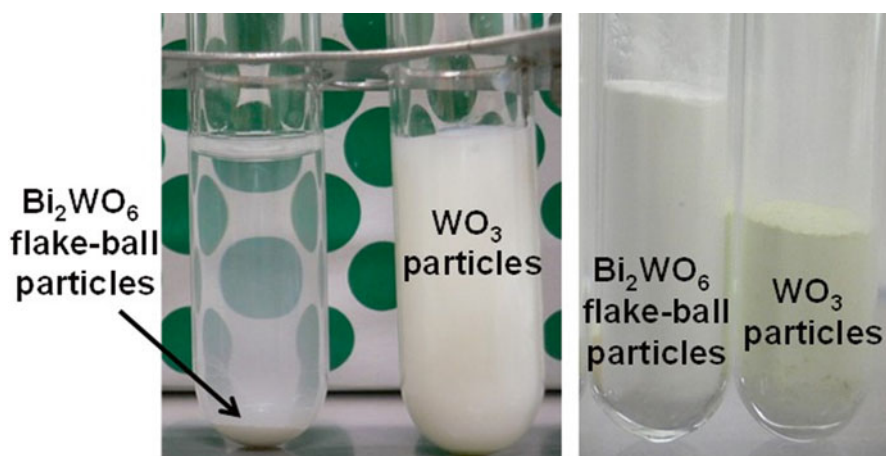


Fig. 22.5 Sedimentation of  $\text{Bi}_2\text{WO}_6$  flake-ball particles and  $\text{WO}_3$  particles in aqueous suspensions for 1 h and their powders

while a suspension of the fine powders of  $\text{TiO}_2$  and  $\text{WO}_3$  was unclear after 1 h as shown in Fig. 22.5. It should be noted that the flake-ball structure was unchanged during the photocatalytic reaction in aqueous solution with magnetic stirring as observed by FE-SEM images of samples collected after photocatalytic reaction. Thus, the photocatalysts with hierarchical architectures is beneficial for practical use in water purification system because of the feasible separation by sedimentation and filtration.

The  $\text{Bi}_2\text{WO}_6$  flake-ball particles show low bulk density owing to the large pore volumes attributed to the void spaces between 2D flakes. The analysis of pore volume distribution with the Barret–Joyner–Halenda (BJH) method indicates the presence of meso and macro pores, which are attributable to the spaces between

nanoplates and between 2D flakes, respectively. The large pore volume would facilitate mass transport of the reactant molecules. The rate of diffusion of reactant and products is very important in photocatalytic applications. It is revealed that control of the hierarchical assemblies of 2D nanostructures resulted in large surface area and large pore volume.

## 22.6 Light-Harvesting Effect of the $\text{Bi}_2\text{WO}_6$ Flake-Ball Particles

Enhanced photoabsorption improves the photocatalytic efficiency. The light harvesting effect has been reported for hierarchical micrometer-sized spherical particles such as jingle-bell structure and hollow structure [29]. The multiple reflection and scattering of light within the interior cavities increases the opportunity of photoabsorption processes and thus the optical path length, leading to more efficient light harvesting.

Figure 22.6 shows diffuse reflectance UV–Visible spectra of the  $\text{Bi}_2\text{WO}_6$  flake-ball particles before and after grinding in an agate mortar [15]. The photoabsorption at around 330–410 nm was decreased by a result of distraction of the spherical flake-ball shape by the grinding. Therefore, the decrease of photoabsorption is attributable to the reduction of multi-reflection and scattering due to the change in micrometer-scaled morphology. This indicates that the hierarchical architecture of flake-ball particles enhanced photoabsorption near the UV region of  $\text{Bi}_2\text{WO}_6$  photocatalysts. Yu et al. have also found such enhancement of optical absorbance for the  $\text{Bi}_2\text{WO}_6$  flake-ball particles, which they call flower-like assemblies, prepared by

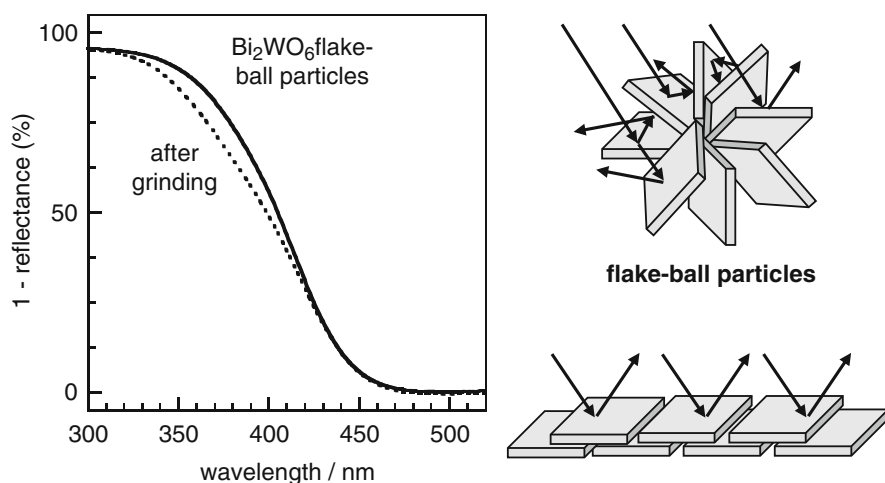


**Fig. 22.6** Diffuse reflectance UV–Visible spectra of  $\text{Bi}_2\text{WO}_6$  flake-ball particles before and after grinding in a mortar

hydrothermal reaction in the presence of poly(sodium 4-styrenesulfonate) [30]. This light-harvesting effect would be related to multi-reflection and scattering of light within the spaces between nanoplates and between polycrystalline 2D flakes, allowing increase of the optical path length.

The light-harvesting effect on the photocatalytic efficiency was investigated using  $\text{Bi}_2\text{WO}_6$  flake-ball particles before and after grinding [15]. However, the effect was negligible on photocatalytic activity in the conditions used for the photocatalytic reaction, and this seems reasonable considering the small change in photoabsorption in the whole range of wavelengths.

## 22.7 Photoexcited Electron Dynamics of the $\text{Bi}_2\text{WO}_6$ Flake-Ball Particles

Photocatalytic efficiency significantly depends on the kinetics of photoexcited carriers. Transient absorption spectroscopy has been used to study the generation of photoexcited charge carriers, relaxation to trapping sites, recombination of electrons and holes, and charge transfer to reactant molecules over photocatalysts such as  $\text{TiO}_2$  [31–33]. While the transient spectra in visible wavelength region are overlapped by surface-trapped holes, surface-trapped electrons, and electrons in bulk, the transient spectra in infrared (IR) region is simply assignable to electrons in the CB of semiconductor photocatalysts. Recent studies using transient IR absorption spectroscopy have shown that photocatalytic efficiencies under steady-state irradiation are related to the dynamics of photoexcited electrons in the time range of microseconds to milliseconds rather than ultrafast processes in the range of femtoseconds to picoseconds [34, 35].

The study of transient IR absorption spectroscopy indicates that crystallization of amorphous  $\text{Bi}_2\text{WO}_6$  enhanced the density of long-lived photoexcited electrons and the photocatalytic efficiency for oxidative decomposition of  $\text{CH}_3\text{CHO}$  to  $\text{CO}_2$  [14]. For well-crystallized  $\text{Bi}_2\text{WO}_6$  photocatalysts, the photocatalytic efficiency was increased in proportion to the specific surface area because of the increase in adsorbed amount of  $\text{CH}_3\text{CHO}$  [28].

Figure 22.7 shows the decay profiles of transient IR absorption at  $2000\text{ cm}^{-1}$  observed on a timescale of 0–100  $\mu\text{s}$  after pulse photoexcitation for the  $\text{Bi}_2\text{WO}_6$  flake-ball particles prepared at various hydrothermal reaction temperatures [35]. Rapid buildups of IR absorption were due to generation of photoexcited electrons in the CB. The decay of the signal is attributed to recombination of the photoexcited electrons with positive holes. Gradual increase in crystalline content with hydrothermal reaction temperatures increased the number of photoexcited electrons remaining in the sub-millisecond range and enhanced the photocatalytic efficiency of the  $\text{Bi}_2\text{WO}_6$  flake-ball particles. The photocatalytic activity of  $\text{Bi}_2\text{WO}_6$  for decomposition of  $\text{CH}_3\text{COOH}$  in water was significantly enhanced by the addition of electron acceptors compared to that in the case of  $\text{O}_2$  as a sole electron acceptor.

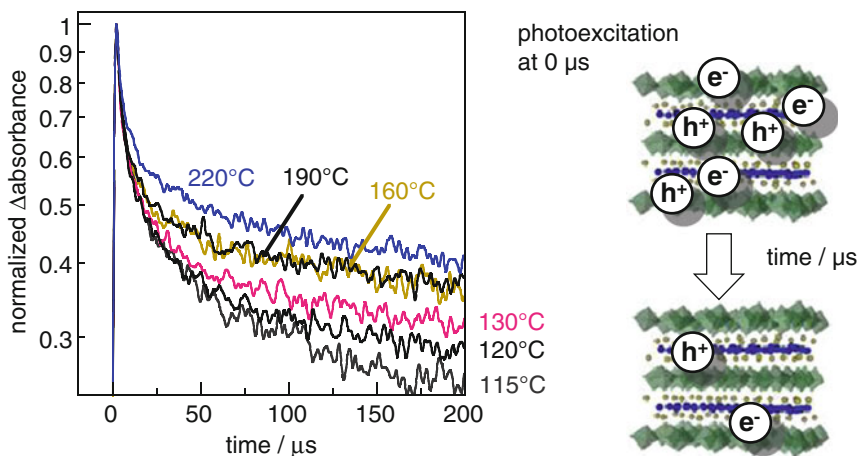


**Fig. 22.7** Transient IR absorption probed at  $2000\text{ cm}^{-1}$  of  $\text{Bi}_2\text{WO}_6$  flake-ball particles prepared at various hydrothermal reaction temperatures (photoexcitation by 355-nm laser pulse)

This result suggests that the rate of electron transfer to  $\text{O}_2$  is slow over  $\text{Bi}_2\text{WO}_6$  photocatalysts, and therefore the lifetime of the photoexcited electrons remaining in the sub-millisecond range is an important factor deciding the photocatalytic efficiency. Actually, electron transfer to  $\text{O}_2$  over the  $\text{Bi}_2\text{WO}_6$  surface occurred in the time range of  $200\ \mu\text{s}$  to a few milliseconds [35]. These findings clearly show that kinetics of  $\text{O}_2$  reduction plays crucial roles in determining the efficiency of  $\text{Bi}_2\text{WO}_6$  photocatalysts under specific reaction conditions. Thus, the knowledge of photoexcited carrier dynamics is indispensable to design highly active photocatalyst materials.

## 22.8 Conclusions and Outlook

This chapter overview the properties of the  $\text{Bi}_2\text{WO}_6$  flake-ball particles, which are micrometer-sized spherical assemblies of polycrystalline 2D flakes comprised of square-shaped nanoplates, for photocatalytic reactions. The  $\text{Bi}_2\text{WO}_6$  flake-ball particles exhibit a high level of photocatalytic activity owing to the nanoplate structure both with large specific surface area and high crystallinity. The photocatalytic efficiency increased proportionally to the increase of specific surface area for well-crystallized  $\text{Bi}_2\text{WO}_6$  particles. The micrometer-sized hierarchical architecture of flake-ball particles is found to be beneficial in practical use for oxidative decomposition of organic pollutants to  $\text{CO}_2$ , for example, in water purification systems because of the light-harvesting effect, large pore volume, and feasible separation from suspensions by sedimentation and filtration.

Much attention has been focused on  $\text{Bi}_2\text{WO}_6$  and the composite materials as visible-light-responsive photocatalysts. However, the absorption of  $\text{Bi}_2\text{WO}_6$  is not sufficient in a wide range of visible light. The onset wavelength of action spectrum was located at 440 nm, and this wavelength corresponds to the band gap energy of 2.8 eV. Therefore, band gap narrowing is necessary to improve the photocatalytic performance under visible light irradiation. The quantum efficiency also has room for further improvement. Recently, tungsten-rich flake-ball particles have been reported to exhibit a high level of visible-light-responsive activity due to the narrow band gap (2.70 eV) and large specific surface area ( $48 \text{ m}^2 \text{ g}^{-1}$ ) compared to those of the conventional  $\text{Bi}_2\text{WO}_6$  flake-ball particles (2.82 eV and  $19 \text{ m}^2 \text{ g}^{-1}$ ) [36]. Such development of new photocatalysts should be advanced based on the knowledge and information about physical properties and structural characteristics affecting their photocatalytic efficiency.

## References

1. Shi YH, Feng SH, Cao CS (2000) Hydrothermal synthesis and characterization of  $\text{Bi}_2\text{MoO}_6$  and  $\text{Bi}_2\text{WO}_6$ . *Mater Lett* 44:215–218
2. Zhang C, Zhu YF (2005) Synthesis of square  $\text{Bi}_2\text{WO}_6$  nanoplates as high-activity visible-light-driven photocatalysts. *Chem Mater* 17:3537–3545
3. Fu HB, Pan CS, Yao WQ, Zhu YF (2005) Visible-light-induced degradation of rhodamine B by nanosized  $\text{Bi}_2\text{WO}_6$ . *J Phys Chem B* 109:22432–22439
4. Fu HB, Zhang LW, Yao WQ, Zhu YF (2006) Photocatalytic properties of nanosized  $\text{Bi}_2\text{WO}_6$  catalysts synthesized via a hydrothermal process. *Appl Catal B* 66:100–110
5. Knight KS (1992) The crystal structure of russellite; a re-determination using neutron powder diffraction of synthetic  $\text{Bi}_2\text{WO}_6$ . *Mineral Mag* 56:399–409
6. Champarnaud-Mesjard JC, Frit B, Watanabe A (1999) Crystal structure of  $\text{Bi}_2\text{W}_2\text{O}_8$ , the  $n=2$  member of the homologous series  $(\text{Bi}_2\text{O}_2)\text{B}_n\text{VO}_{3n+1}$  of cation-deficient Aurivillius phases. *J Mater Chem* 9:1319–1322
7. Kudo A, Hijii S (1999)  $\text{H}_2$  or  $\text{O}_2$  evolution from aqueous solutions on layered oxide photocatalysts consisting of  $\text{Bi}^{3+}$  with  $6s^2$  configuration and  $d^0$  transition metal ions. *Chem Lett* 28:1103–1104
8. Tang JW, Zou ZG, Ye JH (2004) Photocatalytic decomposition of organic contaminants by  $\text{Bi}_2\text{WO}_6$  under visible light irradiation. *Catal Lett* 92:53–56
9. Yu JG, Xiong JF, Cheng B, Yu Y, Wang JB (2005) Hydrothermal preparation and visible-light photocatalytic activity of  $\text{Bi}_2\text{WO}_6$  powders. *J Solid State Chem* 178:1968–1972
10. Zhang S, Zhang C, Man Y, Zhu Y (2006) Visible-light-driven photocatalyst of  $\text{Bi}_2\text{WO}_6$  nanoparticles prepared via amorphous complex precursor and photocatalytic properties. *J Solid State Chem* 179:62–69
11. Zhao X, Xu T, Yao W, Zhang C, Zhu Y (2007) Photoelectrocatalytic degradation of 4-chlorophenol at  $\text{Bi}_2\text{WO}_6$  nanoflake film electrode under visible light irradiation. *Appl Catal Environ* 72:92–97
12. Shang M, Wang WZ, Sun SM, Zhou L, Zhang L (2008)  $\text{Bi}_2\text{WO}_6$  nanocrystals with high photocatalytic activities under visible light. *J Phys Chem C* 112:10407–10411
13. Shimodaira Y, Kato H, Kobayashi H, Kudo A (2006) Photophysical properties and photocatalytic activities of bismuth molybdates under visible light irradiation. *J Phys Chem B* 110:17790–17797

14. Amano F, Yamakata A, Nogami K, Osawa M, Ohtani B (2008) Visible light responsive pristine metal oxide photocatalyst: enhancement of activity by crystallization under hydrothermal treatment. *J Am Chem Soc* 130:17650–17651
15. Amano F, Nogami K, Ohtani B (2009) Visible light-responsive bismuth tungstate photocatalysts: effects of hierarchical architecture on photocatalytic activity. *J Phys Chem C* 113:1536–1542
16. Zhang LH, Wang WZ, Chen ZG, Zhou L, Xu HL, Zhu W (2007) Fabrication of flower-like  $\text{Bi}_2\text{WO}_6$  superstructures as high performance visible-light driven photocatalysts. *J Mater Chem* 17:2526–2532
17. Zhang LS, Wang WZ, Zhou L, Xu HL (2007)  $\text{Bi}_2\text{WO}_6$  nano- and microstructures: shape control and associated visible-light-driven photocatalytic activities. *Small* 3:1618–1625
18. Wu J, Duan F, Zheng Y, Xie Y (2007) Synthesis of  $\text{Bi}_2\text{WO}_6$  nanoplate-built hierarchical nest-like structures with visible-light-induced photocatalytic activity. *J Phys Chem C* 111:12866–12871
19. Amano F, Nogami K, Abe R, Ohtani B (2008) Preparation and characterization of bismuth tungstate polycrystalline flake-ball particles for photocatalytic reactions. *J Phys Chem C* 112:9320–9326
20. Amano F, Nogami K, Abe R, Ohtani B (2007) Facile hydrothermal preparation and photocatalytic activity of bismuth tungstate polycrystalline flake-ball particles. *Chem Lett* 36:1314–1315
21. Li YY, Liu JP, Huang XT, Li GY (2007) Hydrothermal synthesis of  $\text{Bi}_2\text{WO}_6$  uniform hierarchical microspheres. *Cryst Growth Des* 7:1350–1355
22. Imai H, Oaki Y, Kotachi A (2006) A biomimetic approach for hierarchically structured inorganic crystals through self-organization. *Bull Chem Soc Jpn* 79:1834–1851
23. Bard AJ (1980) Photoelectrochemistry. *Science* 207:139–144
24. Scaife DE (1980) Oxide semiconductors in photoelectrochemical conversion of solar-energy. *Sol Energ* 25:41–54
25. Abe R, Takami H, Murakami N, Ohtani B (2008) Pristine simple oxides as visible light driven photocatalysts: highly efficient decomposition of organic compounds over platinum-loaded tungsten oxide. *J Am Chem Soc* 130:7780–7781
26. Arai T, Horiguchi M, Yanagida M, Gunji T, Sugihara H, Sayama K (2009) Reaction mechanism and activity of  $\text{WO}_3$ -catalyzed photodegradation of organic substances promoted by a  $\text{CuO}$  cocatalyst. *J Phys Chem C* 113:6602–6609
27. Ohtani B (2008) Preparing articles on photocatalysis – beyond the illusions, misconceptions, and speculation. *Chem Lett* 37:217–229
28. Amano F, Nogami K, Tanaka M, Ohtani B (2010) Correlation between surface area and photocatalytic activity for acetaldehyde decomposition over bismuth tungstate particles with a hierarchical structure. *Langmuir* 26:7174–7180
29. Li HX, Bian ZF, Zhu J, Zhang DQ, Li GS, Huo YN, Li H, Lu YF (2007) Mesoporous titania spheres with tunable chamber structure and enhanced photocatalytic activity. *J Am Chem Soc* 129:8406–8407
30. Liu SW, Yu JG (2008) Cooperative self-construction and enhanced optical absorption of nanoplates-assembled hierarchical  $\text{Bi}_2\text{WO}_6$  flowers. *J Solid State Chem* 181:1048–1055
31. Yamakata A, Ishibashi T, Onishi H (2003) Kinetics of the photocatalytic water-splitting reaction on  $\text{TiO}_2$  and  $\text{Pt/TiO}_2$  studied by time-resolved infrared absorption spectroscopy. *J Mol Catal* 199:85–94
32. Tamaki Y, Furube A, Murai M, Hara K, Katoh R, Tachiya M (2007) Dynamics of efficient electron-hole separation in  $\text{TiO}_2$  nanoparticles revealed by femtosecond transient absorption spectroscopy under the weak-excitation condition. *Phys Chem Chem Phys* 9:1453–1460
33. Tamaki Y, Hara K, Katoh R, Tachiya M, Furube A (2009) Femtosecond visible-to-IR spectroscopy of  $\text{TiO}_2$  nanocrystalline films: elucidation of the electron mobility before deep trapping. *J Phys Chem C* 113:11741–11746

34. Yamakata A, Ishibashi T, Kato H, Kudo A, Onishi H (2003) Photodynamics of NaTaO<sub>3</sub> catalysts for efficient water splitting. *J Phys Chem B* 107:14383–14387
35. Amano F, Yamakata A, Nogami K, Osawa M, Ohtani B (2011) Effect of photoexcited electron dynamics on photocatalytic efficiency of bismuth tungstate. *J Phys Chem C* 115:16598–16605
36. Amano F, Nogami K, Ohtani B (2012) Enhanced photocatalytic activity of bismuth-tungsten mixed oxides for oxidative decomposition of acetaldehyde under visible light irradiation. *Catal Commun* 20:12–16

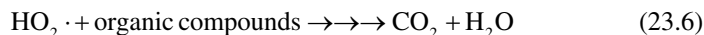
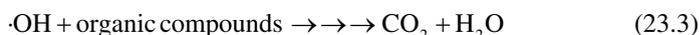
# Chapter 23

## Formation of BiOCl/Bi<sub>2</sub>O<sub>3</sub> and Related Materials for Efficient Visible-Light Photocatalysis

Sandipan Bera and Wan In Lee

### 23.1 Design of Visible-Light Photocatalysts Decomposing Organic Pollutants

Photocatalytic degradation of organic pollutant present in air and water has been accepted as an environmentally benign process for the treatment of pollutions in air and water. Many oxide semiconductors such as TiO<sub>2</sub>, ZnO, WO<sub>3</sub>, SnO<sub>2</sub>, and others have been applied as photocatalytic reactions [1–10]. The holes in the valence band (VB) of photocatalysts are generally used for various oxidation reactions, as shown in Eqs. (23.1)–(23.3). In addition, the electrons in the conduction band (CB) can also induce several oxidation reactions, as described in Eqs. (23.4)–(23.6).



---

S. Bera • W.I. Lee (✉)

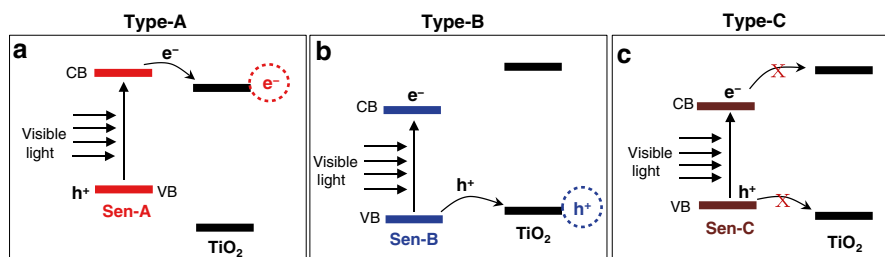
Department of Chemistry and Chemical Engineering, Inha University,  
Yonghyun, Nam-ku, Incheon 402-751, South Korea  
e-mail: [wain@inha.ac.kr](mailto:wain@inha.ac.kr)

TiO<sub>2</sub> has been known as the most efficient photocatalyst among various semiconductors due to its unique characteristics in band position, charge mobility, surface structure, chemical stability, and others [11–13]. Because of its large band gap ( $E_g=3.2$  eV), however, TiO<sub>2</sub> can utilize only the photons in the wavelength shorter than 380 nm, which occupies 4–5 % of the solar spectrum. Therefore, development of photocatalysts functional under visible light is indispensable in order to be able to utilize the major portion of the solar spectrum and to realize indoor application of photocatalysts.

Thus far, the major strategies for developing a visible-light photocatalyst are modification of the TiO<sub>2</sub> band gap by doping [14–26], or development of new semiconductor materials capable of absorbing visible light. Recently, several new photocatalytic semiconductors, including BiVO<sub>4</sub> [27, 28], Bi<sub>2</sub>WO<sub>6</sub> [29], CaBi<sub>2</sub>O<sub>4</sub> [30], PbBi<sub>2</sub>Nb<sub>2</sub>O<sub>9</sub> [31], Bi<sub>4</sub>Ti<sub>3</sub>O<sub>12</sub> [32], and others [33, 34], have been developed, but their photocatalytic efficiencies need to be further improved for practical applications. Another strategy to extend the light absorption property of TiO<sub>2</sub> is formation of heterojunction between TiO<sub>2</sub> and narrow band gap semiconductors [35–40]. So far, variety of coupled semiconductor systems, including CdS/TiO<sub>2</sub> [41], CdSe/TiO<sub>2</sub> [42], WO<sub>3</sub>/WS<sub>2</sub> [43], CdS/AgI [44], and others, have been designed and applied to the oxidation reactions under visible light. Recently, several oxide-based coupled systems such as Bi<sub>2</sub>O<sub>3</sub>/SrTiO<sub>3</sub> [45], Cu<sub>2</sub>O/TiO<sub>2</sub>, Bi<sub>2</sub>O<sub>3</sub>/TiO<sub>2</sub>, ZnMn<sub>2</sub>O<sub>4</sub>/TiO<sub>2</sub> [46, 47], and TiO<sub>2</sub>/Ti<sub>2</sub>O<sub>3</sub> [48] have also been reported to show visible-light photocatalytic activities. In most of the cases however, their catalytic activities are not significantly high, and the photocatalytic mechanism for those systems has not been systematically investigated thus far.

Recently, Lee et al. classified the TiO<sub>2</sub>-based composites according to the relative energy band positions between TiO<sub>2</sub> and narrow band gap sensitizers [49]. As shown in Scheme 23.1, the heterojunction structures are classified as three types.

In the Type-A heterojunction system, the excited electrons of the sensitizers by visible-light irradiation are transported to the TiO<sub>2</sub> CB. Those electrons in TiO<sub>2</sub> CB are then transferred to O<sub>2</sub> to form ·O<sub>2</sub><sup>-</sup> radicals and further converted to HO<sub>2</sub>· by reacting with proton, as described in Eqs. (23.4)–(23.6). Even though HO<sub>2</sub>· is not as strong as ·OH in regarding to oxidation ability, it is able to induce the complete mineralization of organic compounds [50, 51]. They can also be used for the decomposition of



**Scheme 23.1** Classification of sensitizer/TiO<sub>2</sub> heterojunction structures according to the relative energy band locations

organic pollutant, but the complete mineralization to CO<sub>2</sub> is not efficient, because the hole, regarded to be stronger oxidant, is not generated in the VB of TiO<sub>2</sub>.

In the Type-B heterojunction system, the electrons in the sensitizer VB are excited to its CB under visible-light irradiation. The generated holes in the sensitizer VB will be transported voluntarily to that of TiO<sub>2</sub>. By this inter-semiconductor hole-transport mechanism, holes are generated on the TiO<sub>2</sub> VB, followed by formation of ·OH radicals through the equations of (23.1)–(23.3). Then the generated ·OH radicals can completely decompose the organic compounds to CO<sub>2</sub> and H<sub>2</sub>O.

In the Type-C heterojunction system, the electrons in the sensitizer VB are excited to its CB under visible-light irradiation, but the photogenerated electrons and holes cannot be transported to TiO<sub>2</sub> CB and VB, respectively, since the energy level of sensitizer lies in-between the CB and VB of TiO<sub>2</sub>. Thus the coupling of these two semiconductors will not bring any synergetic effect in charge separations. As a result, the composites belonging to the Type-C heterojunction may not show appreciable visible-light photocatalytic activity.

Recently, bismuth oxychloride (BiOCl) has been known as potential photocatalyst in decomposing organic pollutants, due to its particular crystallographic structure, electronic properties, and chemical stability [52, 53]. Zhang et al. reported that BiOCl exhibited more efficient photocatalytic performance than Degussa P25 in decomposing methyl orange under UV illumination [54]. Thus far there have been various attempts to tailor BiOCl nanostructures with different morphologies including microspheres, microflowers, microplates, and nanoplates which exhibit enhanced photocatalytic properties in degradation of organic dyes [55–59]. Several studies have also been performed in investigating the facet-dependent photocatalytic activities of BiOCl, and it was found that the {001} facet of BiOCl reveals relatively higher photocatalytic activities [60–62]. For instance, Guan et al. reported that ultrathin BiOCl nanosheets with {001} facet exhibits much higher photocatalytic activity than conventional BiOCl structures [63]. However, its potential as environmental photocatalyst is restricted due to its large band gap (3.40 eV), which absorbs less than ~4 % of the whole solar spectrum. To achieve visible-light photocatalytic activity, doping of cations and/or anions into BiOCl lattice [64–73], or formation of BiOCl-based heterostructures with metals or narrow band gap semiconductors [74–100], have also been investigated.

BiOCl belongs to the family of main group multicomponent metal oxyhalides V–VI–VII, an important class of ternary compounds because of unique and excellent electrical, magnetic, optical, luminescent, and catalytic properties [52–64]. BiOCl is a tetragonal layered structure consisting of [Cl–Bi–O–Bi–Cl] sheets stacked together by non-bonding interaction through the Cl atoms along the c-axis, as shown in Fig. 23.1. It is also the simplest member of Sillén family expressed by [M<sub>2</sub>O<sub>2</sub>][Cl<sub>m</sub>] or [M<sub>3</sub>O<sub>4</sub>][Cl<sub>m</sub>](*m* = 1–3). The strong internal static electric fields perpendicular to the Cl layer and the bismuth oxide-based fluorite-like layer enable the effective separation of the photoinduced electron–hole pairs, which may result in enhanced photocatalytic activity. Moreover, BiOCl, a semiconductor with an indirect-transition band gap, makes the electrons excited to its CB through a certain *k*-space distance, reducing the recombination probability of photo-excited charge carriers.

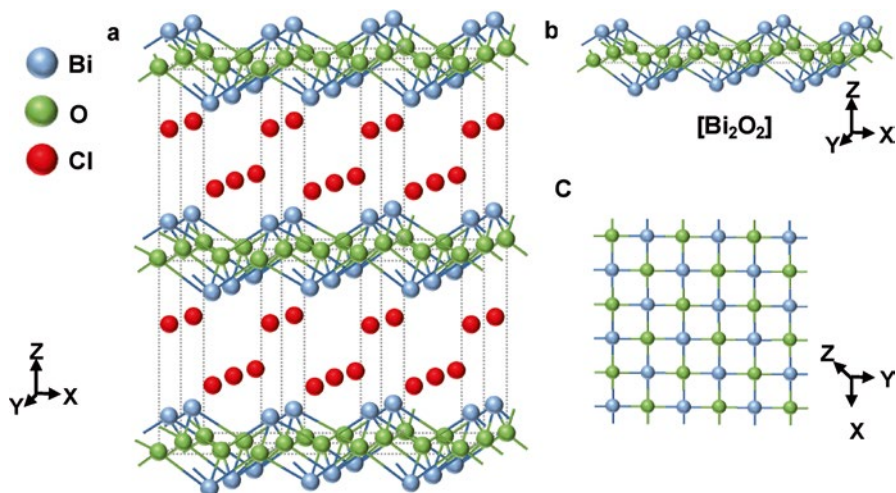
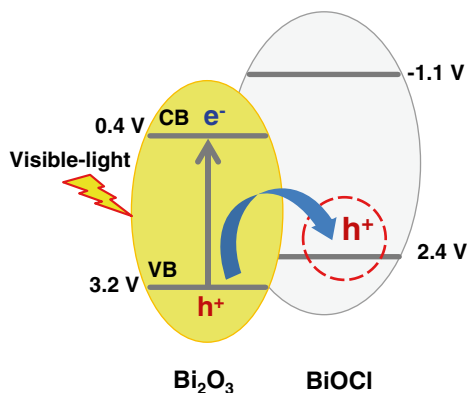


**Fig. 23.1** Schematic representation of the crystal structure of BiOCl (a) and three-dimensional projection of  $[\text{Bi}_2\text{O}_2]^{2+}$  layers along with the [010] (b) and [001] (c) direction, respectively

In the present chapter, BiOCl is coupled with visible-light-absorbing semiconductors such as  $\text{Bi}_2\text{O}_3$  or  $\text{Bi}_3\text{O}_4\text{Cl}$  to achieve visible-light photocatalytic activity. In principle, BiOCl/ $\text{Bi}_2\text{O}_3$  and BiOCl/ $\text{Bi}_3\text{O}_4\text{Cl}$  heterojunction designed in this work belongs to the Type-B heterojunction structure. It is considered for these heterojunction systems that BiOCl works as a main photocatalyst, while the  $\text{Bi}_2\text{O}_3$  or  $\text{Bi}_3\text{O}_4\text{Cl}$  play a role as a sensitizer absorbing visible light. As described in Scheme 23.2, for the BiOCl/ $\text{Bi}_2\text{O}_3$  composite, the VB level of  $\text{Bi}_2\text{O}_3$  is lower by 0.7 V than that of BiOCl. For the BiOCl/ $\text{Bi}_3\text{O}_4\text{Cl}$  composite, the exact energy band location of  $\text{Bi}_3\text{O}_4\text{Cl}$  has not been reported thus far, but its VB position is estimated from the data for  $\text{Bi}_2\text{O}_3$  and BiOCl. VB of  $\text{Bi}_2\text{O}_3$  originates from O 2p, whereas that of BiOCl mainly comes from Cl 3p. It is also deduced that the increase of Cl component in the bismuth oxychloride family raises the VB level. Therefore, the VB level of  $\text{Bi}_3\text{O}_4\text{Cl}$  will be located in the middle of that of  $\text{Bi}_2\text{O}_3$  and BiOCl, suggesting that the VB level of  $\text{Bi}_3\text{O}_4\text{Cl}$  is lower than that of BiOCl. In this regard, BiOCl/ $\text{Bi}_3\text{O}_4\text{Cl}$  is considered to be a Type-B heterojunction. With irradiation of visible light, the electrons in the VB of sensitizer are excited to its CB. Thereby the VB of sensitizer is rendered partially vacant, and the electrons in the VB of BiOCl can be transferred to that of  $\text{Bi}_2\text{O}_3$  or  $\text{Bi}_3\text{O}_4\text{Cl}$ . As a result, holes are generated in the VB of BiOCl, and these initiate photocatalytic oxidation reactions.

The objective of this chapter is to discuss two BiOCl-based heterojunction photocatalysts such as  $\text{Bi}_2\text{O}_3/\text{BiOCl}$  [100] and  $\text{Bi}_3\text{O}_4\text{Cl}/\text{BiOCl}$  [101]. In addition, photocatalytic activity and photostability of  $\text{Bi}_2\text{O}_3/\text{BiOCl}$  composite can be significantly enhanced by modifying its surface with molecular  $\text{WO}_3$  [102].

**Scheme 23.2** Schematic diagram for the charge flow occurring in BiOCl/Bi<sub>2</sub>O<sub>3</sub> (or BiOCl/Bi<sub>3</sub>O<sub>4</sub>Cl) composite under visible-light irradiation



## 23.2 Preparation of Materials and Measurements of Photocatalytic Activities

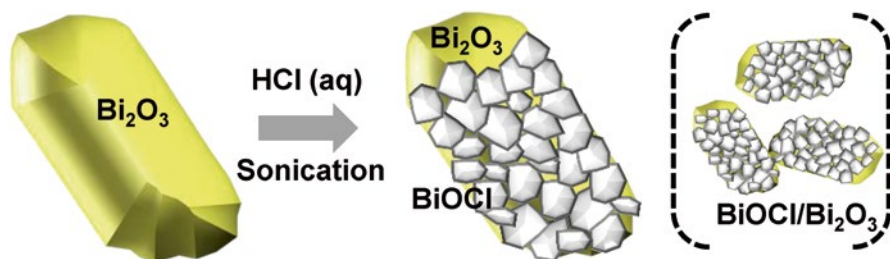
### 23.2.1 Preparation BiOCl/Bi<sub>2</sub>O<sub>3</sub> and Surface Modification with WO<sub>3</sub>

Bismuth(III) oxide powder (99.9 %, Aldrich Chemical Co.) was dispersed in 10 mL ethanol, stoichiometric amount of the concentrated HCl was then added dropwise while the solution was vigorously stirred. The resultant suspension was stirred for 3 h and sonicated for 1 h at room temperature. After treatment with HCl, the yellowish color of Bi<sub>2</sub>O<sub>3</sub> is gradually changed to white, suggesting that the surface of the Bi<sub>2</sub>O<sub>3</sub> particle is converted to BiOCl, as illustrated in Scheme 23.3. The obtained white precipitates were washed several times with ethanol and heat-treated at 300 °C for 1 h. The relative ratio of BiOCl in BiOCl/Bi<sub>2</sub>O<sub>3</sub> can be controlled by adjusting the amount of HCl added. Typically, a composite of 85 mol% BiOCl and 15 mol% Bi<sub>2</sub>O<sub>3</sub> (denoted as 85/15 BiOCl/Bi<sub>2</sub>O<sub>3</sub>) was synthesized by adding 2.0 equivalents of HCl to Bi<sub>2</sub>O<sub>3</sub>, and 55/45 BiOCl/Bi<sub>2</sub>O<sub>3</sub> was prepared by adding 1.8 equivalents of HCl.

For the modification of BiOCl/Bi<sub>2</sub>O<sub>3</sub> surface with WO<sub>3</sub>, 1.0 g of the as-prepared 85/15 BiOCl/Bi<sub>2</sub>O<sub>3</sub> (BiOCl:Bi<sub>2</sub>O<sub>3</sub>=85:15 in molarity) was suspended in 40 mL of 14.0 M aqueous NH<sub>4</sub>OH solution containing stoichiometric amounts of H<sub>2</sub>WO<sub>4</sub> (Aldrich). It was then dried slowly in a water bath by stirring at 65 °C. During this procedure, the surface of the BiOCl/Bi<sub>2</sub>O<sub>3</sub>, was covered uniformly with W-species. The collected sample was then dried at 100 °C for 4 h, and subsequently heat-treated at 220 °C for 2 h.

### 23.2.2 Preparation of BiOCl/Bi<sub>3</sub>O<sub>4</sub>Cl

Bi(NO<sub>3</sub>)<sub>3</sub>·5H<sub>2</sub>O (0.01 mol) was dissolved in 200 mL 1.0 M HNO<sub>3</sub> aqueous solution under magnetic stirring. By the subsequent addition of 10 mL 6.0 M hydrochloric acid to this solution, a white precipitate was formed immediately. After gentle



**Scheme 23.3** Preparation principle of BiOCl/Bi<sub>2</sub>O<sub>3</sub> heterojunction

stirring for 2 h, the precipitate was collected by centrifugation and washed by deionized water three times. Finally, the white powdered BiOCl was obtained by drying the precipitate at 100 °C for 24 h.

Bi<sub>3</sub>O<sub>4</sub>Cl powder with pale-yellow color was then synthesized by the solid-state reaction with Bi<sub>2</sub>O<sub>3</sub> and BiOCl. 0.010 mol BiOCl powder obtained by the above procedure and 0.010 mol Bi<sub>2</sub>O<sub>3</sub> (Aldrich) were mixed in a mortar, and subsequently annealed at 700 °C for 6 h. The crystallographic phase and purity of the Bi<sub>3</sub>O<sub>4</sub>Cl samples were identified by XRD.

The as-prepared 0.010 mol Bi<sub>3</sub>O<sub>4</sub>Cl powder was suspended in 100 mL ethanol, and the stoichiometric amounts of 6.0 M aqueous HCl were added at room temperature, to convert Bi<sub>3</sub>O<sub>4</sub>Cl partially to BiOCl. The composition of BiOCl was determined by the added molarity of HCl. Typically, for the formation of 47/53 BiOCl/Bi<sub>3</sub>O<sub>4</sub>Cl (47 % of BiOCl and 53 % of Bi<sub>3</sub>O<sub>4</sub>Cl), 7.0 mL of HCl was added. After a vigorous stirring for 3 h, the prepared BiOCl/Bi<sub>3</sub>O<sub>4</sub>Cl in ethanol solution was centrifuged and washed with ethanol several times. Finally, the composites were dried overnight at 100 °C.

### 23.2.3 Measurement of Photocatalytic Activities

Photocatalytic activities of the prepared catalysts under visible light were evaluated by the following two methods. First, the visible-light photocatalytic activity was evaluated by monitoring decomposition of 2-propanol (IP) in gas phase. The BiOCl/Bi<sub>2</sub>O<sub>3</sub>, BiOCl/Bi<sub>3</sub>O<sub>4</sub>Cl, and other photocatalytic samples were prepared as a form of particulate film. That is, the aqueous colloidal suspension containing 50 μmol of each photocatalytic sample was dropped and spread uniformly onto a 2.5 × 2.5 cm<sup>2</sup> Pyrex glass, and subsequently dried at 60 °C for 1 h. The whole area of the photocatalytic films was irradiated by a 300 W Xe lamp through a double mounted UV cut-off filter (<420 nm, Oriel), and then through a water filter to remove IR spectrum. The power of visible light irradiated to the photocatalytic sample was 0.5 W/cm<sup>2</sup>. The gas reactor system used for this photocatalytic reaction has been described elsewhere [36]. After evacuating the reactor, 0.08 μL of IP mixed in 1.6 μL of water

was added to the 200 mL gastight reactor. Then the initial concentration of gaseous IP in the reactor was kept to 117 ppm in volume (ppmv). Thus the ultimate concentration of CO<sub>2</sub> evolved will be 351 ppmv when the whole IP is completely decomposed, as shown in Eq. (23.7).



The total pressure of the reactor was then controlled to 700 Torr by filling with oxygen gas. After a certain time of irradiation, 0.5 mL of the gas sample was automatically picked up from the reactor, and sent to a gas chromatograph (Agilent Technologies, Model 6890N). For the detection of CO<sub>2</sub>, a methanizer was installed between the GC column outlet and the FID detector.

Second, visible-light photocatalytic activity was also evaluated by monitoring decomposition of 1,4-terephthalic acid (TPA) or salicylic acid (SA) in aqueous solution. Fifty micromole BiOCl/Bi<sub>2</sub>O<sub>3</sub> (or BiOCl/Bi<sub>3</sub>O<sub>4</sub>Cl) composites were suspended in 50 mL of 50 μM TPA (or SA) aqueous solution by magnetic stirring. The remnant TPA or SA concentrations after visible-light irradiation were analyzed from their characteristic absorption peaks detected by the UV–Vis spectrophotometer (Perkin–Elmer Lambda 40).

### 23.3 Characterization of BiOCl/Bi<sub>2</sub>O<sub>3</sub> and BiOCl/Bi<sub>3</sub>O<sub>4</sub>Cl

BiOCl/Bi<sub>2</sub>O<sub>3</sub> composites were formed by partially converting the Bi<sub>2</sub>O<sub>3</sub> in BiOCl, as shown in Scheme 23.3. As a result BiOCl/Bi<sub>2</sub>O<sub>3</sub> is a core-shell-like structure consisting of a BiOCl shell and a Bi<sub>2</sub>O<sub>3</sub> core. The initial Bi<sub>2</sub>O<sub>3</sub> was a rod-like structure with a diameter of 1–2 μm, as shown in Fig. 23.2a. By adding HCl, the surface of Bi<sub>2</sub>O<sub>3</sub> was converted to BiOCl/Bi<sub>2</sub>O<sub>3</sub>, and its shape was gradually changed with the increase of BiOCl content. By increasing the added amounts of HCl, the BiOCl phase is initially formed as a granular structure on the surface of the Bi<sub>2</sub>O<sub>3</sub> rods and it is then collapsed to form primary nanoparticles, as shown in Fig. 23.2b, c (85/15 BiOCl/Bi<sub>2</sub>O<sub>3</sub>). By addition of excessive HCl, the tablet-shaped pure BiOCl particles with a diameter of about 200 nm were formed (Fig. 23.2d).

The XRD patterns for BiOCl/Bi<sub>2</sub>O<sub>3</sub> composites with molar ratios of 100/0, 85/15, 55/45, 40/60, and 0/100 are illustrated in Fig. 23.2e. Pure Bi<sub>2</sub>O<sub>3</sub> and BiOCl were the monoclinic α-phase and tetragonal phase [100], respectively. With the increase of BiOCl component in BiOCl/Bi<sub>2</sub>O<sub>3</sub> composites, the intensity of (120) peak at 27.42°, which is identified as the main peak of the remnant Bi<sub>2</sub>O<sub>3</sub> phase, was gradually decreased, whereas that of the (101) peak at 25.86° inherent from the BiOCl phase was increased. No other phases were found in BiOCl/Bi<sub>2</sub>O<sub>3</sub> composites, suggesting that there is no appreciable chemical reaction between BiOCl and Bi<sub>2</sub>O<sub>3</sub>. The BiOCl/Bi<sub>2</sub>O<sub>3</sub> samples were annealed up to 450 °C in air, but the crystallinity of neither the BiOCl nor the Bi<sub>2</sub>O<sub>3</sub> was noticeably changed.

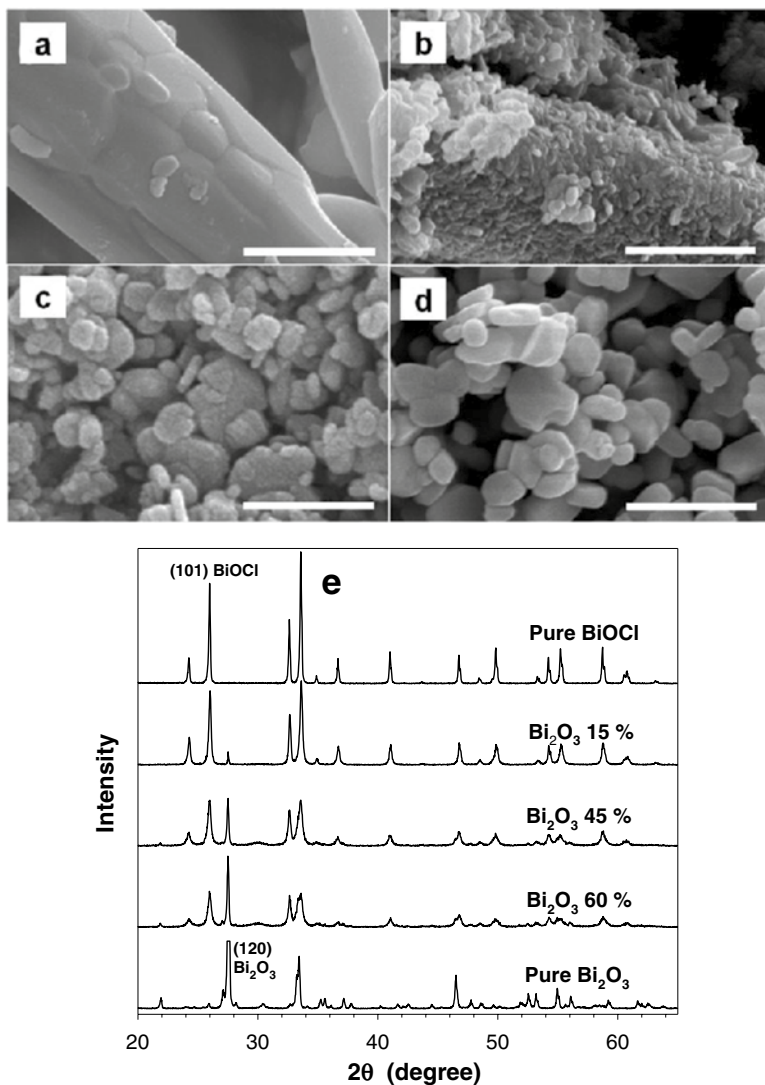


**Fig. 23.2** SEM images of pure  $\text{Bi}_2\text{O}_3$  (a), 40/60  $\text{BiOCl}/\text{Bi}_2\text{O}_3$  (b), 85/15  $\text{BiOCl}/\text{Bi}_2\text{O}_3$  (c), and pure  $\text{BiOCl}$  (d). Each scale bar is 1  $\mu\text{m}$ . X-ray diffraction patterns of  $\text{Bi}_2\text{O}_3$ ,  $\text{BiOCl}$ , and several  $\text{BiOCl}/\text{Bi}_2\text{O}_3$  in different compositions (e)

In preparing  $\text{BiOCl}/\text{Bi}_3\text{O}_4\text{Cl}$  composites, a three-step synthetic strategy was applied. Firstly, the  $\text{BiOCl}$  powder was formed by the reaction of  $\text{Bi}(\text{NO}_3)_3 \cdot 5\text{H}_2\text{O}$  and  $\text{HCl}$  at ambient condition. Secondly, the crystallized  $\text{Bi}_3\text{O}_4\text{Cl}$  with pale-yellow color was synthesized by the solid-state reaction with  $\text{Bi}_2\text{O}_3$  and  $\text{BiOCl}$  at 700  $^\circ\text{C}$ . Finally,  $\text{BiOCl}/\text{Bi}_3\text{O}_4\text{Cl}$  composites were prepared by treating  $\text{Bi}_3\text{O}_4\text{Cl}$  with the

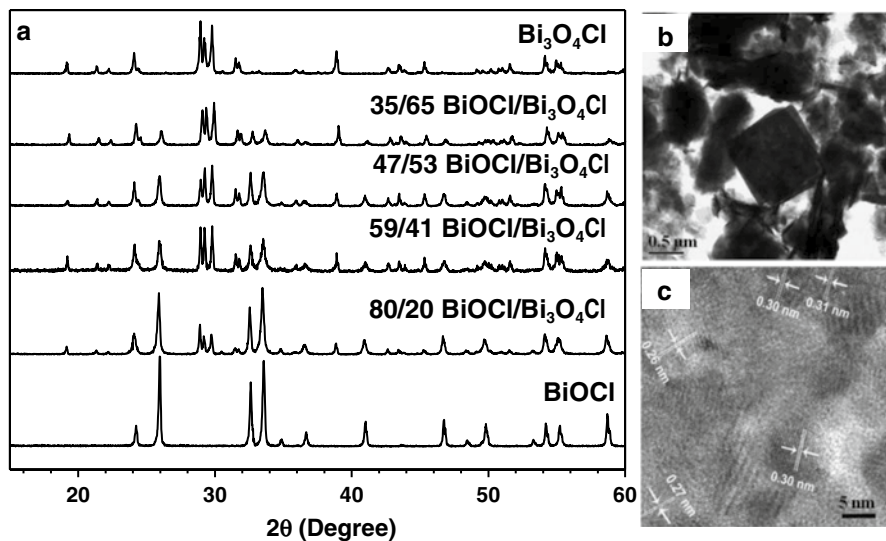


**Fig. 23.3** XRD patterns for the synthesized BiOCl, Bi<sub>3</sub>O<sub>4</sub>Cl, and the several BiOCl/Bi<sub>3</sub>O<sub>4</sub>Cl composites (a). Low (b) and high (c) magnification TEM images for the 47/53 BiOCl/Bi<sub>3</sub>O<sub>4</sub>Cl composite

stoichiometric amounts of aqueous HCl at room temperature. Transition of Bi<sub>3</sub>O<sub>4</sub>Cl color from pale yellow to white indicates the formation of BiOCl over the surface of Bi<sub>3</sub>O<sub>4</sub>Cl.

The crystallographic phases and compositions of the as-prepared BiOCl, Bi<sub>3</sub>O<sub>4</sub>Cl, and several BiOCl/Bi<sub>3</sub>O<sub>4</sub>Cl composites were analyzed by XRD. As shown in Fig. 23.3, the BiOCl prepared at the initial step is in the pure and highly crystallized phase. For the Bi<sub>3</sub>O<sub>4</sub>Cl derived from the solid-state reaction of BiOCl and Bi<sub>2</sub>O<sub>3</sub> at 700 °C, all the diffraction peaks corresponded to the monoclinic phase (I2/a space group, JCPDS: 86-2221) [101]. In the several BiOCl/Bi<sub>3</sub>O<sub>4</sub>Cl composites, both the tetragonal BiOCl and monoclinic Bi<sub>3</sub>O<sub>4</sub>Cl phases appeared, but other impurity phases were not detected at all. With increasing the molarity of HCl in the reaction of Bi<sub>3</sub>O<sub>4</sub>Cl and HCl, intensities of the characteristic BiOCl peaks were increased, whereas those of Bi<sub>3</sub>O<sub>4</sub>Cl were decreased. The relative compositions of BiOCl and Bi<sub>3</sub>O<sub>4</sub>Cl can be determined by analyzing the integrated areas of the main XRD peaks for both phases. Herein, the (011) peak of BiOCl and (114) peak of Bi<sub>3</sub>O<sub>4</sub>Cl were used to estimate the relative composition of the BiOCl/Bi<sub>3</sub>O<sub>4</sub>Cl composites.

The structure of the 47/53 BiOCl/Bi<sub>3</sub>O<sub>4</sub>Cl was examined by TEM, as shown in Fig. 23.3b, c. The shape and size of the composite is not uniform, while its average size is about 1 μm. It is considered that BiOCl occupies the surface of 47/53 BiOCl/

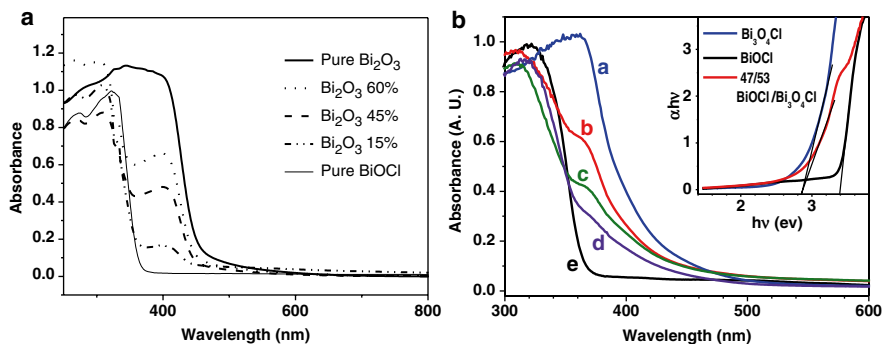


**Fig. 23.4** Diffuse reflectance spectra of several BiOCl/Bi<sub>2</sub>O<sub>3</sub> (a) and BiOCl/Bi<sub>3</sub>O<sub>4</sub>Cl composites (b) in different compositions. In (b), a denotes bare Bi<sub>3</sub>O<sub>4</sub>Cl, b denotes 47/53 BiOCl/Bi<sub>3</sub>O<sub>4</sub>Cl, c denotes 59/41 BiOCl/Bi<sub>3</sub>O<sub>4</sub>Cl, d denotes 80/20 BiOCl/Bi<sub>3</sub>O<sub>4</sub>Cl, and e denotes bare BiOCl. Plots of  $\alpha h\nu$  vs. irradiated light energy in eV were shown in the inset.  $a$ ,  $h$ , and  $\nu$  are absorption coefficient, Planck constant, and light frequency, respectively

Bi<sub>3</sub>O<sub>4</sub>Cl, because the surface will have higher opportunity to react with the added HCl [101]. High-resolution TEM image in Fig. 23.3c also suggests that the Bi<sub>3</sub>O<sub>4</sub>Cl nano-grains are embedded in the BiOCl matrix. The lattice spacings of 0.30 and 0.31 nm correspond to the (114) and (006) plane of the monoclinic Bi<sub>3</sub>O<sub>4</sub>Cl, whereas those of 0.26 and 0.27 nm can be indexed as (012) and (110) planes of the tetragonal BiOCl crystal. This clearly indicates that a tight heterojunction has been formed between BiOCl and Bi<sub>3</sub>O<sub>4</sub>Cl in a nano-size level.

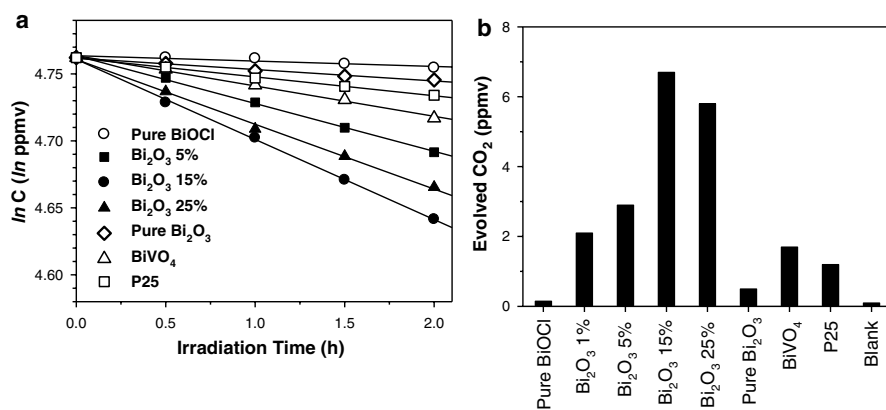
Optical properties of BiOCl/Bi<sub>2</sub>O<sub>3</sub>, BiOCl/Bi<sub>3</sub>O<sub>4</sub>Cl, and related materials were analyzed by UV–Visible diffuse reflectance spectra (DRS). Figure 23.4a indicates DRS of BiOCl, Bi<sub>2</sub>O<sub>3</sub>, and BiOCl/Bi<sub>2</sub>O<sub>3</sub> in several compositions. The band gaps ( $E_g$ ) of the BiOCl and Bi<sub>2</sub>O<sub>3</sub>, determined by extrapolation to the zero absorption coefficient, were 3.6 and 2.8 eV, respectively, corresponding to the results of the previous reports [54]. For BiOCl/Bi<sub>2</sub>O<sub>3</sub> composites, the absorbances in the 370–440 nm range gradually decrease, as Bi<sub>2</sub>O<sub>3</sub> component decreases. Therefore, those absorbance values could be used to estimate relative concentration of BiOCl and Bi<sub>2</sub>O<sub>3</sub> in the composites by applying Beer–Lambert’s law. Figure 23.4b shows DRS of the as-prepared BiOCl, Bi<sub>3</sub>O<sub>4</sub>Cl, and several BiOCl/Bi<sub>3</sub>O<sub>4</sub>Cl composites with different concentration of Bi<sub>3</sub>O<sub>4</sub>Cl. The band gaps of BiOCl and Bi<sub>3</sub>O<sub>4</sub>Cl were 3.4 and 2.85 eV, respectively, corresponding to the previous reports [100, 101, 103]. The BiOCl/Bi<sub>3</sub>O<sub>4</sub>Cl composites showed the dual absorption edges at 360 and 435 nm, indicating the presence of BiOCl and Bi<sub>3</sub>O<sub>4</sub>Cl. The absorbance in the 370–430 nm range gradually increased, as the component of Bi<sub>3</sub>O<sub>4</sub>Cl phase increased in the BiOCl/Bi<sub>3</sub>O<sub>4</sub>Cl composite.

## 23.4 Photocatalytic Properties Under Visible-Light

Photocatalytic activities of the prepared composites were evaluated under an irradiation of visible light ( $\lambda \geq 420$  nm). First of all, gaseous IP was utilized as a model compound. It has been well known that IP first decomposes to acetone, and then finally mineralized to CO<sub>2</sub>. The decomposition of gaseous IP approximated the first-order kinetics. That is, the photocatalytic reaction is simply described by  $-d[c]/dt = k[c]$ , where  $[c]$  is the concentration of IP, and  $k$  denotes the degradation rate constant.

The removal of IP as a function of irradiation time is described in Fig. 23.5a. The BiOCl/Bi<sub>2</sub>O<sub>3</sub> composites demonstrated notably high photocatalytic activities over a wide composition range, whereas the individual BiOCl and Bi<sub>2</sub>O<sub>3</sub> showed a negligible efficiency. The calculated degradation rate constants ( $K_{IP}$ ) in decomposing IP with several photocatalytic samples are shown in Table 23.1. Especially, the 85/15 BiOCl/Bi<sub>2</sub>O<sub>3</sub> revealed the highest decomposition rate. That is,  $K_{IP}$  of the 85/15 BiOCl/Bi<sub>2</sub>O<sub>3</sub> was 4.3 times that of Degussa P25. BET surface areas of the prepared photocatalysts are also given in Table 23.1. The surface areas of the BiOCl/Bi<sub>2</sub>O<sub>3</sub> composites were much smaller than that of Degussa P25, and this seems to be caused by considerably larger particle size. For the comparison of conversion efficiency per unit catalytic surface area, a parameter of  $K_{IP}/A$ , where  $A$  is the surface area of the photocatalyst applied to the catalytic reaction, was determined, as shown in Table 23.1. The  $K_{IP}/A$  of the 85/15 BiOCl/Bi<sub>2</sub>O<sub>3</sub> was 9.6 times as high as that of P25.

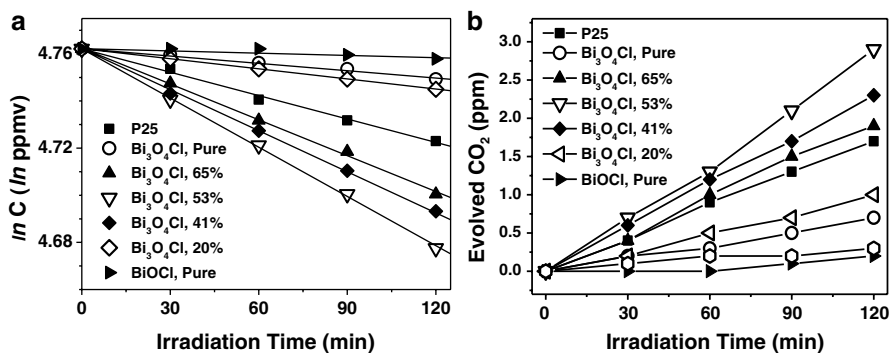
Figure 23.5b describes the evolution of CO<sub>2</sub> as a function of irradiation time. The trend of CO<sub>2</sub> evolution, according to relative composition in the BiOCl/Bi<sub>2</sub>O<sub>3</sub> composites, was very close to that of the IP removal. The highest photocatalytic activity was observed from the 85/15 BiOCl/Bi<sub>2</sub>O<sub>3</sub> composite. That is, the evolved CO<sub>2</sub> after 2 h irradiation was 6.7 ppm, which was 5.7 times that of P25.



**Fig. 23.5** Photocatalytic removal of gaseous IP vs. irradiation time (a), and CO<sub>2</sub> evolved in 2 h (b) under visible-light irradiation ( $\geq 420$  nm)

**Table 23.1** Surface areas and degradation rate constants of various visible-light photocatalysts in decomposing gaseous IP and aqueous TPA

Photocatalytic samples	BET surface area (m <sup>2</sup> /g)	2-Propanol (IP)		1,4-Terephthalic acid (TPA)	
		$K_{IP}$ (h <sup>-1</sup> )	$K_{IP}/A$ (h <sup>-1</sup> m <sup>-1</sup> )	$K_{TA}$ (h <sup>-1</sup> )	$K_{TA}/A$ (h <sup>-1</sup> m <sup>-1</sup> )
BiOCl	4.03	0.0034	0.075	0.0010	0.020
95/5 BiOCl/Bi <sub>2</sub> O <sub>3</sub>	5.14	0.0357	0.513	0.0640	0.919
85/15 BiOCl/Bi <sub>2</sub> O <sub>3</sub>	6.85	0.0603	0.602	0.0952	0.951
75/25 BiOCl/Bi <sub>2</sub> O <sub>3</sub>	7.29	0.0484	0.426	0.0895	0.788
Bi <sub>2</sub> O <sub>3</sub>	2.25	0.0085	0.163	0.0040	0.076
BiVO <sub>4</sub>	7.21	0.0226	0.193	0.0267	0.228
Degussa P25	56.0	0.0141	0.063	0.0081	0.036

**Fig. 23.6** Photocatalytic removal of gaseous IP (a) and CO<sub>2</sub> evolved (b) with the BiOCl, Bi<sub>3</sub>O<sub>4</sub>Cl, and the several BiOCl/Bi<sub>3</sub>O<sub>4</sub>Cl composites under visible-light irradiation ( $\lambda \geq 420$  nm)

As shown in Fig. 23.6a, the BiOCl/Bi<sub>3</sub>O<sub>4</sub>Cl composites also exhibited considerable enhancement in the photocatalytic removal of IP, whereas the end-members showed the negligible efficiency. Especially, 47/53 BiOCl/Bi<sub>3</sub>O<sub>4</sub>Cl demonstrated the highest catalytic efficiency. After 2 h of visible-light ( $\lambda \geq 420$  nm) irradiation,  $K_{IP}$  of the 47/53 BiOCl/Bi<sub>3</sub>O<sub>4</sub>Cl composite was 6.6 times that of Bi<sub>3</sub>O<sub>4</sub>Cl, and 2.1 times that of Degussa P25. The BET surface areas of BiOCl and Bi<sub>3</sub>O<sub>4</sub>Cl were determined to be 3.82 and 3.19 m<sup>2</sup>/g, respectively, while that of 47/53 BiOCl/Bi<sub>3</sub>O<sub>4</sub>Cl was 3.45 m<sup>2</sup>/g. The measured surface area of 47/53 BiOCl/Bi<sub>3</sub>O<sub>4</sub>Cl was less than 1/10 that of the Degussa P25 TiO<sub>2</sub> (47 m<sup>2</sup>/g), but its photocatalytic efficiency was more than twice, suggesting that the achieved photocatalytic activity is noticeably high.

In evolution of CO<sub>2</sub>, the similar trend was also observed, as shown in Fig. 23.6b. It was found that the CO<sub>2</sub> evolved in 2 h of the visible irradiation with 47/53 BiOCl/Bi<sub>3</sub>O<sub>4</sub>Cl was ~4 times that with pure Bi<sub>3</sub>O<sub>4</sub>Cl, and 1.7 times that with Degussa P25.

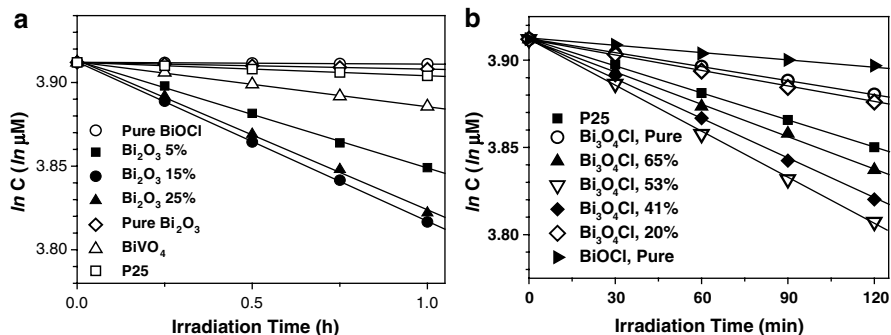


**Fig. 23.7** Photocatalytic removal of aqueous TPA with BiOCl/Bi<sub>2</sub>O<sub>3</sub> in different compositions (a) and aqueous SA with BiOCl/Bi<sub>3</sub>O<sub>4</sub>Cl in different compositions (b) under visible-light irradiation ( $\lambda \geq 420$  nm)

The photocatalytic activity of BiOCl/Bi<sub>2</sub>O<sub>3</sub> and BiOCl/Bi<sub>3</sub>O<sub>4</sub>Cl in different compositions was evaluated according to the removal of TPA and SA, respectively, which are dissolved in aqueous solution. The remnant TPA or SA after the irradiation of visible light ( $\geq 420$  nm) was analyzed from its characteristic absorption peak by UV–Visible spectroscopy. With approximating the photocatalytic degradation of TPA as the first-order kinetics, the plots of  $\ln C$  vs. irradiation time for several catalytic samples are shown in Fig. 23.7. The overall decomposition trend in aqueous solution was quite similar as that of the reaction in gas phase. The 85/15 BiOCl/Bi<sub>2</sub>O<sub>3</sub> and of 47/53 BiOCl/Bi<sub>3</sub>O<sub>4</sub>Cl showed the optimized photocatalytic activity. As shown in Fig. 23.7 and Table 23.1,  $k_{TA}$  (the degradation rate constant of TPA) of the 85/15 BiOCl/Bi<sub>2</sub>O<sub>3</sub> is 10.5 times that of P25 and 3.6 times that of BiVO<sub>4</sub>.

### 23.5 WO<sub>3</sub> Modification of BiOCl/Bi<sub>2</sub>O<sub>3</sub> Surface

Herein, we found that BiOCl/Bi<sub>2</sub>O<sub>3</sub> is a potential photocatalytic system working under visible light. However, this system has a few drawbacks as a photocatalyst. That is, BiOCl does not show sufficient photostability under UV light irradiation, and the adsorption affinity of organic molecules on its surface is not as efficient as that of several other oxides such as TiO<sub>2</sub>, ZnO, WO<sub>3</sub> or SnO<sub>2</sub>. To overcome these drawbacks, WO<sub>3</sub> was introduced on the surface of BiOCl/Bi<sub>2</sub>O<sub>3</sub> composite. The WO<sub>3</sub> on the surface of BiOCl/Bi<sub>2</sub>O<sub>3</sub> can increase adsorption affinity of organic molecules by the increase of surface acidity. Moreover, the coverage of WO<sub>3</sub> can protect BiOCl/Bi<sub>2</sub>O<sub>3</sub> system from photocorrosion.

The surface of tightly interconnected heterojunction structure of 85/15 BiOCl/Bi<sub>2</sub>O<sub>3</sub> was modified with various amounts of tungsten oxide for further improvement of visible-light photocatalytic activity. The shapes of the BiOCl/Bi<sub>2</sub>O<sub>3</sub> particles were not changed by the tungsten oxide loading. In order to estimate the

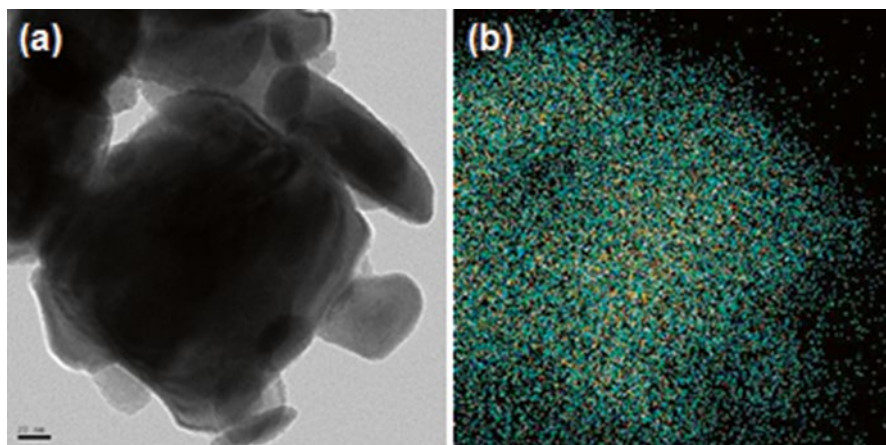


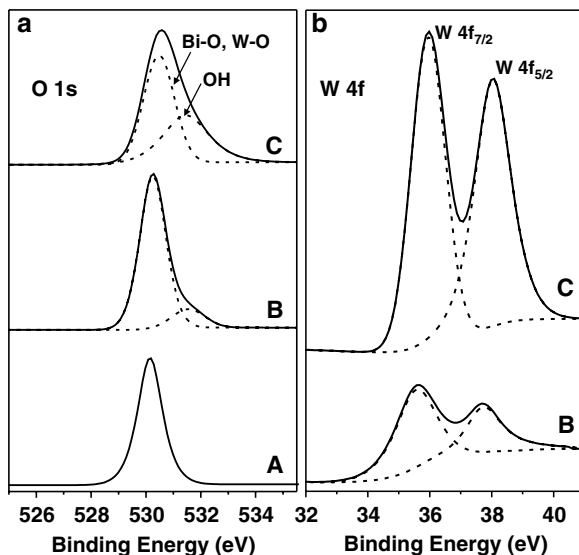
**Fig. 23.8** TEM images of 0.6 %  $\text{WO}_3/\text{BiOCl}/\text{Bi}_2\text{O}_3$  (a) and its tungsten-mapping image (b)

coverage of tungsten oxide over the surface of  $\text{BiOCl}/\text{Bi}_2\text{O}_3$ , TEM image of the 0.6 %  $\text{WO}_3/\text{BiOCl}/\text{Bi}_2\text{O}_3$  and the tungsten-mapping image for the corresponding sample are shown in Fig. 23.8. The tungsten-mapping image is the same as the original shape of 0.6 %  $\text{WO}_3/\text{BiOCl}/\text{Bi}_2\text{O}_3$  particle, clearly indicating that the tungsten oxide is uniformly distributed over the entire surface of  $\text{BiOCl}/\text{Bi}_2\text{O}_3$ .

XPS survey scans were performed to analyze the chemical compositions and oxidation states of the surfaces of the  $\text{WO}_3/\text{BiOCl}/\text{Bi}_2\text{O}_3$  composites. Figure 23.9 shows the high-resolution XPS spectra of O and W, which were taken from the surface of the bare  $\text{BiOCl}/\text{Bi}_2\text{O}_3$ , 0.6 %  $\text{WO}_3/\text{BiOCl}/\text{Bi}_2\text{O}_3$ , and 4 %  $\text{WO}_3/\text{BiOCl}/\text{Bi}_2\text{O}_3$  composites. As indicated in Fig. 23.9a, the O 1s band was considerably modified by the tungsten oxide loading. In the case of bare  $\text{BiOCl}/\text{Bi}_2\text{O}_3$ , the peak at 530.1 eV was assigned to the O 1s band of the  $\text{BiOCl}$  occupying the surface of  $\text{BiOCl}/\text{Bi}_2\text{O}_3$ . Contrastingly, O 1s peak of the  $\text{WO}_3/\text{BiOCl}/\text{Bi}_2\text{O}_3$  composites was considerably broader, and thus fitted with two peaks. The O 1s peak at ~530 eV contained contributions from both the  $\text{BiOCl}$  and  $\text{WO}_3$ , which have similar binding energies. The additional O 1s peak at 531.5 eV originated from the presence of –OH group or water molecule on the surface of  $\text{WO}_3/\text{BiOCl}/\text{Bi}_2\text{O}_3$ . With an increase in the concentration of W-species from 0.6 to 4.0 mol%, its intensity was enhanced considerably, indicating clearly that the tungsten oxide present on the surface of the  $\text{BiOCl}/\text{Bi}_2\text{O}_3$  contained considerable amounts of hydroxyl groups and/or surface-adsorbed water molecules. Figure 23.9b shows the W 4f XPS peaks for the 0.6 %  $\text{WO}_3/\text{BiOCl}/\text{Bi}_2\text{O}_3$  and 4 %  $\text{WO}_3/\text{BiOCl}/\text{Bi}_2\text{O}_3$  composites. The peaks with binding energies of 35.65 and 37.71 eV were assigned to W 4f<sub>7/2</sub> and W 4f<sub>5/2</sub>, respectively, which energies are typical for  $\text{W}^{6+}$  species. Hence it is deduced that the majority of W-species present in  $\text{WO}_3/\text{BiOCl}/\text{Bi}_2\text{O}_3$  are  $\text{WO}_3$  and that the detected –OH groups originate from adsorbed  $\text{OH}^-$  ions and/or  $\text{H}_2\text{O}$  on the surface of  $\text{WO}_3$ .

Comparing with the bare  $\text{BiOCl}/\text{Bi}_2\text{O}_3$ ,  $\text{WO}_3/\text{BiOCl}/\text{Bi}_2\text{O}_3$  composites exhibited a remarkably higher photocatalytic activity in removing IP under visible-light irradiation, whereas Degussa P25 or  $\text{WO}_3$  showed negligible efficiency. Among the

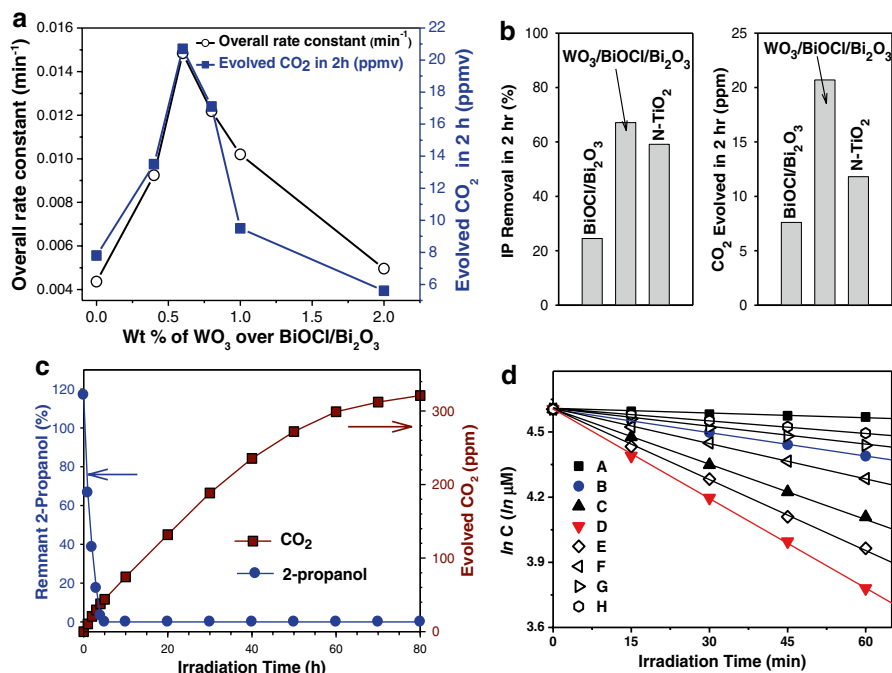
**Fig. 23.9** High-resolution XPS spectra and simulated Gaussian line shapes of O 1s (a) and W 4f (b) taken on the surface of bare BiOCl/Bi<sub>2</sub>O<sub>3</sub> and several WO<sub>3</sub>/BiOCl/Bi<sub>2</sub>O<sub>3</sub>. (A) Bare BiOCl/Bi<sub>2</sub>O<sub>3</sub>, (B) 0.6 % WO<sub>3</sub>/BiOCl/Bi<sub>2</sub>O<sub>3</sub>, (C) 4.0 % WO<sub>3</sub>/BiOCl/Bi<sub>2</sub>O<sub>3</sub>



WO<sub>3</sub>/BiOCl/Bi<sub>2</sub>O<sub>3</sub> composites, the 0.6 % WO<sub>3</sub>-loaded sample exhibited the highest efficiency. Its *k* was 4.0 times that of the bare BiOCl/Bi<sub>2</sub>O<sub>3</sub> and more than 20 times that of Degussa P25, as shown in Fig. 23.10a. In the evolution of CO<sub>2</sub>, a similar trend was observed (Fig. 23.10a). The CO<sub>2</sub> evolved with 0.6 % WO<sub>3</sub>/BiOCl/Bi<sub>2</sub>O<sub>3</sub> under 2 h visible-light irradiation was 2.7 times the amount with bare BiOCl/Bi<sub>2</sub>O<sub>3</sub> and 12.2 times that with Degussa P25. Comparing with typical N-doped TiO<sub>2</sub>, the prepared 0.6 % WO<sub>3</sub>/BiOCl/Bi<sub>2</sub>O<sub>3</sub> demonstrated 1.3 times the efficiency in removing IP, and 1.7 times the efficiency in evolving CO<sub>2</sub>, as shown in Fig. 23.10b. Figure 23.10c plots the trends of IP decomposition and CO<sub>2</sub> evolution with 0.6 % WO<sub>3</sub>/BiOCl/Bi<sub>2</sub>O<sub>3</sub> under long-term visible-light irradiation. In 4 h, the IP, with an initial concentration of 117 ppmv, was completely removed. In 60 h the amount of evolved CO<sub>2</sub> was 311 ppmv, which is ~90 % of the theoretical value (351 ppm), suggesting that this photocatalytic system can completely decompose IP to CO<sub>2</sub>. The decomposition trend of the aqueous TPA is quite similar to that of the gaseous IP, as shown in Fig. 23.10d.

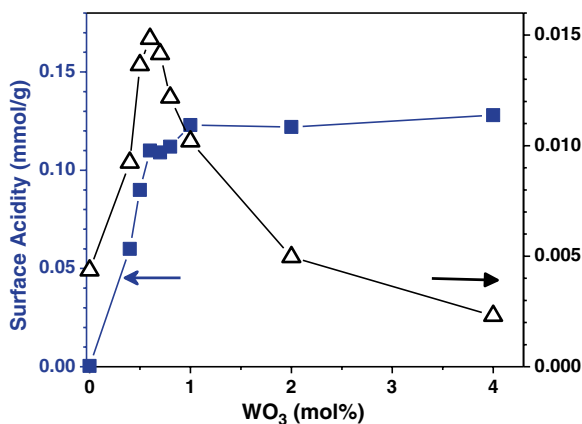
With increasing WO<sub>3</sub> loading, the visible-light photocatalytic activity of WO<sub>3</sub>/BiOCl/Bi<sub>2</sub>O<sub>3</sub> gradually increased, maximizing at 0.6 mol%. With further increases of WO<sub>3</sub>, photocatalytic activity was decreased sharply. The determined *k* of the 0.6 % WO<sub>3</sub>/BiOCl/Bi<sub>2</sub>O<sub>3</sub> was 3.8 times that of the bare BiOCl/Bi<sub>2</sub>O<sub>3</sub> and ~22 times that of Degussa P25.

Figure 23.11 also illustrates the trend of the photocatalytic activity in decomposing TPA as a function of WO<sub>3</sub> composition. Interestingly, the photocatalytic activity was maximized by introducing the 0.6 mol% concentration of WO<sub>3</sub>, at which the surface acidity just reaches its plateau. This suggests that the visible-light photocatalytic activity of WO<sub>3</sub>/BiOCl/Bi<sub>2</sub>O<sub>3</sub> is maximized at the very point that the entire surface of BiOCl is covered with molecular WO<sub>3</sub>-species. Further increases of WO<sub>3</sub> component sharply decreased the photocatalytic activity. The role of WO<sub>3</sub>, then, is



**Fig. 23.10** (a) Photocatalytic activity of WO<sub>3</sub>/BiOCl/Bi<sub>2</sub>O<sub>3</sub> as a function of WO<sub>3</sub> composition in decomposing gaseous IP and evolving CO<sub>2</sub>. (b) Photocatalytic efficiency of N-doped TiO<sub>2</sub> and 0.6 % WO<sub>3</sub>/BiOCl/Bi<sub>2</sub>O<sub>3</sub> in removing IP and in evolving CO<sub>2</sub>. (c) Trends of IP decomposition and CO<sub>2</sub> evolution with 0.6 % WO<sub>3</sub>/BiOCl/Bi<sub>2</sub>O<sub>3</sub> under long-term visible-light irradiation. (d) Photocatalytic removal of aqueous TPA vs. irradiation time. (A) Degussa P25, (B) bare BiOCl/Bi<sub>2</sub>O<sub>3</sub>, (C) 0.4 % WO<sub>3</sub>/BiOCl/Bi<sub>2</sub>O<sub>3</sub>, (D) 0.6 % WO<sub>3</sub>/BiOCl/Bi<sub>2</sub>O<sub>3</sub>, (E) 0.8 % WO<sub>3</sub>/BiOCl/Bi<sub>2</sub>O<sub>3</sub>, (F) 1.0 % WO<sub>3</sub>/BiOCl/Bi<sub>2</sub>O<sub>3</sub>, (G) 2.0 % WO<sub>3</sub>/BiOCl/Bi<sub>2</sub>O<sub>3</sub>, (H) 4.0 % WO<sub>3</sub>/BiOCl/Bi<sub>2</sub>O<sub>3</sub>, (I) WO<sub>3</sub>. 300 W Xe lamp through a UV cut-off filter ( $\lambda < 420$  nm, Oriol) and a water filter was used as a visible-light source

**Fig. 23.11** Surface acidity and photocatalytic activity of WO<sub>3</sub>/BiOCl/Bi<sub>2</sub>O<sub>3</sub> composites in removing TPA as a function of WO<sub>3</sub> concentration



to improve the adsorption affinity of BiOCl/Bi<sub>2</sub>O<sub>3</sub> toward OH<sup>-</sup>, H<sub>2</sub>O, and organic species. However, excessive loading onto the BiOCl/Bi<sub>2</sub>O<sub>3</sub> surface is detrimental to the photocatalytic reaction, due to screening of the photocatalytic sites formed on the BiOCl surface. The BET surface area of the samples was not appreciably changed by the introduction of WO<sub>3</sub>. The surface area of the bare Bi<sub>2</sub>O<sub>3</sub>/BiOCl composite was 7.58 m<sup>2</sup>/g, whereas that of WO<sub>3</sub>/BiOCl/Bi<sub>2</sub>O<sub>3</sub> composite containing 0.4–2.0 mol% of WO<sub>3</sub> was 7.68–8.20 m<sup>2</sup>/g. This suggests that the enhancement of photocatalytic activity was not caused by the increase in surface area.

Previously, it was reported that the monolayer coverage of WO<sub>3</sub> on the surface of TiO<sub>2</sub> greatly improves the photocatalytic activity under UV irradiation [104]. The coverage of WO<sub>3</sub> on the TiO<sub>2</sub> surface induces an increase in surface acidity and thereby increases the adsorption of organic compounds, which mechanism has been reported to be a major factor in enhancing the photocatalytic oxidation reaction [104, 105]. In those studies, a 3 mol% of WO<sub>3</sub> was required to achieve monolayer coverage over the entire surface of TiO<sub>2</sub> (Degussa P25 with surface area of ~50 m<sup>2</sup>/g). In the present study, the optimum amount of WO<sub>3</sub> on BiOCl/Bi<sub>2</sub>O<sub>3</sub> having a surface area of 7.68 m<sup>2</sup>/g was 0.6 mol%. Interestingly, the required amounts of WO<sub>3</sub> per unit surface area for these two photocatalysts are quite similar. Therefore, it is deduced that the molecular WO<sub>3</sub>-species cover the BiOCl/Bi<sub>2</sub>O<sub>3</sub> surface to a monolayer thickness in 0.6 mol% WO<sub>3</sub>/BiOCl/Bi<sub>2</sub>O<sub>3</sub>.

It was reported that the BiOCl can be damaged by UV irradiation. In the present study we also observed that the BiOCl/Bi<sub>2</sub>O<sub>3</sub> system could be slightly damaged even under visible light, but the WO<sub>3</sub> coverage greatly extended its stability [102]. To test the photochemical stability in decomposing gaseous IP during the photocatalytic reactions, pure BiOCl/Bi<sub>2</sub>O<sub>3</sub> and 0.6 % WO<sub>3</sub>/BiOCl/Bi<sub>2</sub>O<sub>3</sub> composites were reused five times. After each photocatalytic reaction, the reaction chamber was evacuated and the fresh reactant gas was refilled, the photocatalytic film remaining in the reaction chamber. Figure 23.12a, b show that the bare BiOCl/Bi<sub>2</sub>O<sub>3</sub> reused five times exhibited appreciably lower photocatalytic efficiency than the initial one, in both the decomposition of IP and the evolution of CO<sub>2</sub>. However, under the same

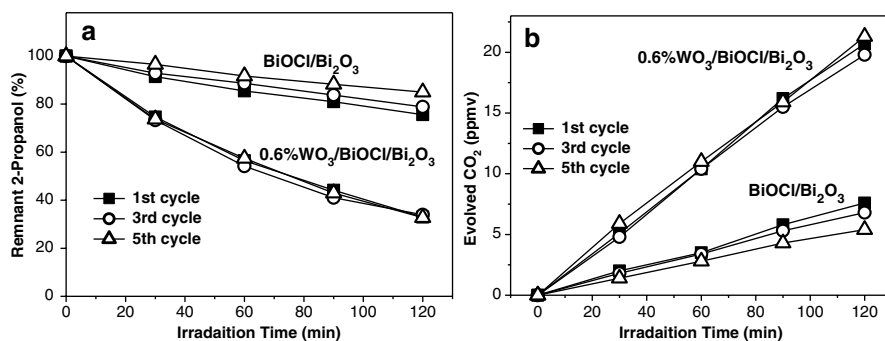


**Fig. 23.12** Cyclic photodegradation of gaseous IP (a) and evolution of CO<sub>2</sub> (b) under visible light ( $\geq 420$  nm) by repeated use of the bare BiOCl/Bi<sub>2</sub>O<sub>3</sub> and 0.6 % WO<sub>3</sub>/BiOCl/Bi<sub>2</sub>O<sub>3</sub>

experimental condition, the reused 0.6 %  $\text{WO}_3/\text{BiOCl}/\text{Bi}_2\text{O}_3$  showed no appreciable change in photocatalytic efficiency. This is clear evidence of the extended chemical stability of  $\text{WO}_3/\text{BiOCl}/\text{Bi}_2\text{O}_3$ . It is obvious that the  $\text{WO}_3$  monolayer protects the  $\text{BiOCl}/\text{Bi}_2\text{O}_3$  from chemical damage during the photocatalytic reaction.

## 23.6 Concluding Remarks

This chapter discussed the two heterojunction structures based on BiOCl, namely,  $\text{BiOCl}/\text{Bi}_2\text{O}_3$  and  $\text{BiOCl}/\text{Bi}_3\text{O}_4\text{Cl}$ , which are regarded to be promising systems in decomposing organic pollutants under visible light. In these heterojunction systems, it is considered that BiOCl works as a main photocatalyst, while the  $\text{Bi}_2\text{O}_3$  or  $\text{Bi}_3\text{O}_4\text{Cl}$  play a role as a sensitizer absorbing visible light. Working mechanism in these photocatalytic system is based on the hole transfer from the VB of  $\text{Bi}_2\text{O}_3$  or  $\text{Bi}_3\text{O}_4\text{Cl}$  to that of BiOCl. Moreover, we found that modification of  $\text{BiOCl}/\text{Bi}_2\text{O}_3$  surface with molecular  $\text{WO}_3$  species significantly increases the photostability as well as catalytic efficiency of the  $\text{BiOCl}/\text{Bi}_2\text{O}_3$  system. Monolayer coverage of  $\text{WO}_3$  not only increases the adsorption affinity of organic species, but also to protect the  $\text{BiOCl}/\text{Bi}_2\text{O}_3$  from chemical damage during the photocatalytic reaction. The achieved photocatalytic activity of  $\text{WO}_3/\text{BiOCl}/\text{Bi}_2\text{O}_3$  was 1.7 times that of typical N-doped  $\text{TiO}_2$ . We believe that the photocatalytic activity can be further enhanced by applying the nanosized BiOCl. More attention is necessary for the BiOCl-related photocatalytic system.

**Acknowledgments** This work was supported by the Korea Center for Artificial Photosynthesis (KCAP) funded by the Minister of Science, ICT and Future Planning (MSIP) through the National Research Foundation (NRF) of Korea (2009-0093884), and Basic Science Research Program through NRF funded by the Ministry of Education (NRF-2015R1D1A1A01057390).

## References

1. Fujishima A, Honda K (1972) Electrochemical photolysis of water at a semiconductor electrode. *Nature* 238:37–38
2. Turchi CS, Ollis DF (1990) Photocatalytic degradation of organic water contaminants: mechanisms involving hydroxyl radical attack. *J Catal* 122:178–192
3. Zhang H, Chen G, Bahnemann DJ (2009) Photoelectrocatalytic materials for environmental applications. *Mater Chem* 19:5089–5121
4. Muller HD, Steinbach F (1970) Decomposition of isopropyl alcohol photosensitized by zinc oxide. *Nature* 225:728–729
5. Dunkle SS, Helmich RJ, Suslick KS (2009)  $\text{BiVO}_4$  as a visible-light photocatalyst prepared by ultrasonic spray pyrolysis. *J Phys Chem C* 113:11980–11983
6. Wenjie L, Da P, Zhang Y, Wang Y, Lin X, Gong X, Zheng G (2014)  $\text{WO}_3$  nanoflakes for enhanced photoelectrochemical conversion. *ACS Nano* 8:11770–11777
7. Guan M, Zhao X, Duan L, Cao M, Guo W, Liu J, Zhang W (2013) Controlled synthesis of  $\text{SnO}_2$  nanostructures with different morphologies and the influence on photocatalysis properties. *J Appl Phys* 114:114302–114307

8. Yuan H, Xu J (2010) Preparation, characterization and photocatalytic activity of nanometer SnO<sub>2</sub>. *Int J Chem Eng Appl* 1:241–246
9. Hernandez-Alonso MD, Fresno F, Sareza S, Coronado JM (2009) Development of alternative photocatalysts to TiO<sub>2</sub>: challenges and opportunities. *Energy Environ Sci* 2:1231–1257
10. Hoffmann MR, Martin ST, Choi W, Bahnemann DW (1995) Environmental applications of semiconductor photocatalysis. *Chem Rev* 95:69–96
11. Ou Y, Lin J, Fang S, Liao D (2007) Study on the preparation of ultrafine mesoporous TiO<sub>2</sub> with controllable crystalline phase and its photocatalytic activities. *Catal Commun* 8:936–940
12. Palmisano G, Augugliaro V, Pagliaro M, Palmisano L (2007) Photocatalysis: a promising route for 21st century organic chemistry. *Chem Commun* 43:3425–3437
13. Chen CC, Ma WH, Zhao JC (2010) Semiconductor-mediated photodegradation of pollutants under visible-light irradiation. *Chem Soc Rev* 39:4206–4219
14. Wang J, Tafen DN, Lewis JP, Hong ZL, Manivannan A, Zhi MJ, Li M, Wu NQ (2009) Origin of photocatalytic activity of nitrogen-doped TiO<sub>2</sub> nanobelts. *J Am Chem Soc* 131:12290–12297
15. In S, Orlov A, Berg R, Garcia F, Pedrosa-Jimenez S, Tikhov MS, Wright DS, Lambert RM (2007) Effective visible light-activated B-doped and B, N-codoped TiO<sub>2</sub> photocatalysts. *J Am Chem Soc* 129:13790–13791
16. Borgarello E, Kiwi J, Gratzel M, Pelizzetti E, Visca M (1982) Visible light induced water cleavage in colloidal solutions of chromium-doped titanium dioxide particles. *J Am Chem Soc* 104:2996–3002
17. Nakhate GG, Nikama VS, Kanadea KG, Arbujb S, Kaleb BB, Baegc JO (2010) Hydrothermally derived nanosized Ni-doped TiO<sub>2</sub>: a visible light driven photocatalyst for methylene blue degradation. *Mater Chem Phys* 124:976–981
18. Klosek S, Raftery D (2001) Visible light driven V-doped TiO<sub>2</sub> photocatalyst and its photo-oxidation of ethanol. *J Phys Chem B* 105:2815–2819
19. Choi W, Termin A, Hoffmann MR (1994) The role of metal ion dopants in quantum-sized TiO<sub>2</sub>: correlation between photoreactivity and charge carrier recombination dynamics. *J Phys Chem* 98:13669–13679
20. Bouras P, Stathatos E, Lianos P (2007) Pure versus metal-ion-doped nanocrystalline titania for photocatalysis. *Appl Catal B* 73:51–59
21. Peng B, Meng X, Tang F, Ren X, Chen D, Ren J (2009) General synthesis and optical properties of monodisperse multifunctional metal-ion-doped TiO<sub>2</sub> hollow particles. *J Phys Chem C* 113:20240–20245
22. Asahi R, Morikawa T, Ohwaki T, Aoki K, Taga Y (2001) Visible-light photocatalysis in nitrogen-doped titanium oxides. *Science* 293:269–271
23. Tachikawa T, Tojo S, Kawai K, Endo M, Fujitsuka M, Ohno T, Nishijima K, Miyamoto Z, Majima T (2004) Photocatalytic oxidation reactivity of holes in the sulfur- and carbon-doped TiO<sub>2</sub> powders studied by time-resolved diffuse reflectance spectroscopy. *J Phys Chem B* 108:19299–19306
24. Dong F, Wang H, Wu Z (2009) One-step “green” synthetic approach for mesoporous C-doped titanium dioxide with efficient visible light photocatalytic activity. *J Phys Chem C* 113:16717–16723
25. Yu JC, Ho W, Yu J, Yip H, Wong PK, Zhao J (2005) Efficient visible-light-induced photocatalytic disinfection on sulfur-doped nanocrystalline titania. *J Environ Sci Technol* 39:1175–1179
26. Stengl V, Houskova V, Bakardjieva S, Murafa N (2010) Photocatalytic activity of boron-modified titania under UV and visible-light illumination. *ACS Appl Mater Interfaces* 2:575–580
27. Hernandez-Alonso MD, Fresno F, Sareza S, Coronado JM (2009) Development of alternative photocatalysts to TiO<sub>2</sub>: challenges and opportunities. *Energy Environ Sci* 2:1231–1257
28. Dunkle SS, Helmich RJ, Suslick KS (2009) BiVO<sub>4</sub> as a visible-light photocatalyst prepared by ultrasonic spray pyrolysis. *J Phys Chem C* 113:11980–11983

29. Yanhui Z, Yi-Jun X (2014)  $\text{Bi}_2\text{WO}_6$ : a highly chemoselective visible light photocatalyst toward aerobic oxidation of benzylic alcohols in water. *RSC Adv* 4:2904–2910
30. Tang J, Zou Z, Ye J (2004) Efficient photocatalytic decomposition of organic contaminants over  $\text{CaBi}_2\text{O}_4$  under visible-light irradiation. *Angew Chem Int Ed* 43:4463–4466
31. Dong HG, Hwang W, Lee JS (2004) An undoped, single-phase oxide photocatalyst working under visible light. *J Am Chem Soc* 126:8912–8913
32. He H, Yin J, Li Y, Zhang Y, Qiu H, Xu J, Xu T, Wang C (2014) Size controllable synthesis of single-crystal ferroelectric  $\text{Bi}_4\text{Ti}_3\text{O}_{12}$  nanosheet dominated with  $\{001\}$  facets toward enhanced visible-light-driven photocatalytic activities. *Appl Catal B* 156–157:35–43
33. Liu B, Fang Y, Li Z, Xu S (2015) Visible-light nanostructured photocatalysts – a review. *J Nanosci Nanotechnol* 15:889–920
34. Gusain M, Rawat P, Nagarajan R (2014) Soft chemical synthesis of  $\text{Ag}_3\text{SbS}_3$  with efficient and recyclable visible light photocatalytic properties. *Mater Res Bull* 60:872–875
35. Bessekhouad Y, Chaoui N, Trzpit M, Ghazzal N, Robert D, Weber JV (2006) UV–vis versus visible degradation of acid orange II in a coupled  $\text{CdS}/\text{TiO}_2$  semiconductors suspension. *J Photochem Photobiol A* 183:218–224
36. Bera S, Rawal SB, Kim HJ, Lee WI (2014) Novel coupled structures of  $\text{FeWO}_4/\text{TiO}_2$  and  $\text{FeWO}_4/\text{TiO}_2/\text{CdS}$  designed for highly efficient visible-light photocatalysis. *ACS Appl Mater Interfaces* 6:9654–9663
37. Kim YJ, Gao B, Han SY, Jung MH, Chakraborty AK, Ko TG, Lee CM, Lee WI (2009) Heterojunction of  $\text{FeTiO}_3$  nanodisc and  $\text{TiO}_2$  nanoparticle for a novel visible light photocatalyst. *J Phys Chem C* 113:19179–19184
38. Rawal SB, Chakraborty AK, Kim YJ, Kim HJ, Lee WI (2012) Double-heterojunction structure of  $\text{Sb}_x\text{Sn}_{1-x}\text{O}_2/\text{TiO}_2/\text{CdSe}$  for efficient decomposition of gaseous 2-propanol under visible-light irradiation. *RSC Adv* 2:622–630
39. Rawal SB, Sang SD, Lee WI (2012) Novel  $\text{Ag}_3\text{PO}_4/\text{TiO}_2$  composites for efficient decomposition of gaseous 2-propanol under visible-light irradiation. *Catal Commun* 17:131–135
40. Rawal SB, Bera S, Lee WI (2012) Visible-light photocatalytic properties of  $\text{W}_{18}\text{O}_{49}/\text{TiO}_2$  and  $\text{WO}_3/\text{TiO}_2$  heterocomposites. *Catal Lett* 142:1482–1488
41. Kim JC, Choi J, Lee YB, Hong JH, Lee JI, Yang JW, Lee WI, Hur NH (2006) Enhanced photocatalytic activity in composites of  $\text{TiO}_2$  nanotubes and  $\text{CdS}$  nanoparticles. *Chem Commun* 48:5024–5026
42. Zhang M, Xu Y, Lv J, Yang L, Jiang X, He G, Song X, Sun Z (2014) Capability of coupled  $\text{CdSe}/\text{TiO}_2$  heterogeneous structure for photocatalytic degradation and photoconductivity. *Nanoscale Res Lett* 9:1–7
43. Paola AD, Palmisano L, Venezia AM, Augugliaro V (2009) Coupled semiconductor systems for photocatalysis. Preparation and characterization of polycrystalline mixed  $\text{WO}_3/\text{WS}_2$  powders. *J Phys Chem B* 103:8236–8244
44. Gopidas KR, Bohorquez M, Kamat PV (1990) Photophysical and photochemical aspects of coupled semiconductors. Charge-transfer processes in colloidal  $\text{CdS}-\text{TiO}_2$ , and  $\text{CdS}-\text{AgI}$  systems. *J Phys Chem* 94:6435–6440
45. Zhang H, Ouyang S, Li Z, Liu L, Yu T, Ye J, Zou Z (2006) Preparation, characterization and photocatalytic activity of polycrystalline  $\text{Bi}_2\text{O}_3/\text{SrTiO}_3$  composite powders. *J Phys Chem Solids* 67:2501–2505
46. Zhang J, Zhu H, Zheng S, Pan F, Wang T (2009)  $\text{TiO}_2$  film/ $\text{Cu}_2\text{O}$  microgrid heterojunction with photocatalytic activity under solar light irradiation. *ACS Appl Mater Interfaces* 1:2111–2114
47. Bessekhouad Y, Robert D, Weber JV (2005) Photocatalytic activity of  $\text{Cu}_2\text{O}/\text{TiO}_2$ ,  $\text{Bi}_2\text{O}_3/\text{TiO}_2$  and  $\text{ZnMn}_2\text{O}_4/\text{TiO}_2$  heterojunctions. *Catal Today* 101:315–321
48. Liu H, Yang W, Ma Y, Yao J (2006) Extended visible light response of binary  $\text{TiO}_2-\text{Ti}_2\text{O}_3$  photocatalyst prepared by a photo-assisted sol–gel method. *Appl Catal A* 299:218–223
49. Rawal SB, Bera S, Lee D, Jang DJ, Lee WI (2013) Design of visible-light photocatalysts by coupling of narrow bandgap semiconductors and  $\text{TiO}_2$ : effect of their relative energy band positions on the photocatalytic efficiency. *Catal Sci Technol* 3:1822–1830

50. Agrios AG, Pichat P (2005) State of the art and perspectives on materials and applications of photocatalysis over TiO<sub>2</sub>. *J Appl Electrochem* 35:655–663
51. Gaya UI, Abdullah AH (2008) Heterogeneous photocatalytic degradation of organic contaminants over titanium dioxide: a review of fundamentals, progress and problems. *J Photochem Photobiol C* 9:1–12
52. Wang C, Shao C, Liuc Y, Zhang L (2008) Photocatalytic properties BiOCl and Bi<sub>2</sub>O<sub>3</sub> nanofibers prepared by electrospinning. *Scr Mater* 59:332–335
53. Ye L, Su Y, Jin X, Xie H, Zhang C (2014) Recent advances in BiOX (X = Cl, Br and I) photocatalysts: synthesis, modification, facet effects and mechanisms. *Environ Sci Nano* 1:90–112
54. Zhang KL, Liu CM, Huang FQ, Zheng C, Wang WD (2006) Study of the electronic structure and photocatalytic activity of the BiOCl photocatalyst. *Appl Catal B* 68:125–129
55. Xiong ZG, Zhao XS (2012) Nitrogen-doped titanate-anatase core-shell nanobelts with exposed {101} anatase facets and enhanced visible light photocatalytic activity. *J Am Chem Soc* 134:5754–5757
56. Hao H, Xu Y, Liu P, Zhang G (2015) BiOCl nanostructures with different morphologies: tunable synthesis and visible-light-driven photocatalytic properties. *Chin Chem Lett* 26:133–136
57. Gao X, Zhang X, Wang Y, Peng S, Yue B, Fan C (2015) Rapid synthesis of hierarchical BiOCl microspheres for efficient photocatalytic degradation of carbamazepine under simulated solar irradiation. *Chem Eng J* 263:419–426
58. Cheng G, Xiong Z, Stadler FJ (2013) Facile template-free and fast refluxing synthesis of 3D desertrose-like BiOCl nanoarchitectures with superior photocatalytic activity. *New J Chem* 37:3207–3213
59. Sarwan B, Pare B, Acharya AD (2014) The effect of oxygen vacancies on the photocatalytic activity of BiOCl nanocrystals prepared by hydrolysis and UV light irradiation. *Mater Sci Semicond Process* 25:89–97
60. Weng S, Pei Z, Zheng Z, Hu J, Liu P (2013) Exciton-free, nonsensitized degradation of 2-naphthol by facet-dependent BiOCl under visible light: novel evidence of surface-state photocatalysis. *ACS Appl Mater Interfaces* 5:12380–12386
61. Cui Z, Mi L, Zeng D (2013) Oriented attachment growth of BiOCl nanosheets with exposed {110} facets and photocatalytic activity of the hierarchical nanostructures. *J Alloys Compd* 549:70–76
62. Li L, Zhang M, Liu Y, Zhang X (2014) Hierarchical assembly of BiOCl nanosheets onto bicrystalline TiO<sub>2</sub> nanofiber: enhanced photocatalytic activity based on photoinduced interfacial charge transfer. *J Colloid Interface Sci* 435:26–33
63. Guan M, Xiao C, Zhang J, Fan S, An R, Cheng Q, Xie J, Zhou M, Ye B, Xie Y (2013) Vacancy associates promoting solar-driven photocatalytic activity of ultrathin bismuth oxychloride nanosheets. *J Am Chem Soc* 135:10411–10417
64. Xie F, Mao X, Fan C, Wang Y (2014) Facile preparation of Sn-doped BiOCl photocatalyst with enhanced photocatalytic activity for benzoic acid and rhodamine B degradation. *Mater Sci Semicond Process* 27:380–389
65. Li Y, Li C, Zhang Z, Zhang Y, Sun X, Si H, Zhang J (2014) Black BiOCl with disorder surface structure prepared by Fe reduction and the enhanced photocatalytic activity. *Solid State Sci* 34:107–112
66. Nussbaum M, Shaham-Waldmann N, Paz Y (2014) Synergistic photocatalytic effect in Fe, Nb-doped BiOCl. *J Photochem Photobiol A* 290:11–21
67. Xie F, Mao X, Fan C, Wang Y (2014) Facile preparation of Sn-Doped BiOCl photocatalyst with enhanced photocatalytic activity for benzoic acid and rhodamine B degradation. *Mater Sci Semicond Process* 27:380–389
68. Pu F, Lu X, Xia Y, Huang W, Liz Z (2014) Preparation of surface-sulfurized nanoflake-like BiOCl layered semiconductor films with interbedded S<sup>2-</sup> for enhanced photoelectrochemical performances. *J Electrochem Soc* 161:H269–H275

69. Kim WJ, Pradhan D, Min B, Sohn Y (2014) Adsorption/photocatalytic activity and fundamental natures of BiOCl and BiOCl<sub>x</sub>I<sub>1-x</sub> prepared in water and ethylene glycol environments, and Ag and Au-doping effects. *Appl Catal B* 147:711–725
70. Xia J, Xu L, Zhang J, Yin S, Li H, Xu H, Di J (2013) Improved visible light photocatalytic properties of Fe/BiOCl microspheres synthesized via self-doped reactable ionic liquids. *Cryst Eng Comm* 15:10132–10141
71. Yu J, Wei B, Zhu L, Gao H, Sun W, Xu L (2013) Flowerlike C-doped BiOCl nanostructures: facile wet chemical fabrication and enhanced UV photocatalytic properties. *Appl Surf Sci* 284:497–502
72. Zhang X, Zhao L, Fan C, Liang Z, Han P (2012) First-principles investigation of impurity concentration influence on bonding behavior, electronic structure and visible light absorption for Mn-doped BiOCl photocatalyst. *Physica B* 407:4416–4424
73. Parea B, Sarwana B, Jonnalagadda SB (2011) Photocatalytic mineralization study of malachite green on the surface of Mn-doped BiOCl activated by visible light under ambient condition. *Appl Surf Sci* 258:247–253
74. Lin H, Ding L, Pei Z, Zhou Y, Long J, Deng W, Wang X (2014) Au deposited BiOCl with different facets: on determination of the facet-induced transfer preference of charge carriers and the different plasmonic activity. *Appl Catal B* 160–161:98–105
75. Gao Y, Wang L, Li Z, Li C, Cao X, Zhou A, Hu Q (2014) Microwave-assisted synthesis of flower-like Ag-BiOCl nanocomposite with enhanced visible-light photocatalytic activity. *Mater Lett* 136:295–297
76. Hu J, Xu G, Wang J, Lv J, Zhang X, Zheng Z, Xie T, Wu Y (2014) Photocatalytic properties of Bi/BiOCl heterojunctions synthesized using an in-situ reduction method. *New J Chem* 38:4913–4921
77. Yu Y, Cao C, Liu H, Li P, Wei F, Jiang Y, Song W (2014) A Bi/BiOCl heterojunction photocatalyst with enhanced electron-hole separation and excellent visible light photodegrading activity. *J Mater Chem A* 2:1677–1681
78. Lin H, Ding L, Pei Z, Zhou Y, Long J, Deng W, Wang X (2014) Au deposited BiOCl with different facets: on determination of the facet-induced transfer preference of charge carriers and the different plasmonic activity. *Appl Catal B* 160–161:98–105
79. Zuo Y, Wang C, Sun Y, Cheng J (2015) Preparation and photocatalytic properties of BiOCl/Bi<sub>2</sub>MoO<sub>6</sub> composite photocatalyst. *Mater Lett* 139:149–152
80. Yue D, Chen D, Wang Z, Ding H, Zong R, Zhu Y (2014) Enhancement of visible photocatalytic performances of a Bi<sub>2</sub>MoO<sub>6</sub>-BiOCl nanocomposite with plate-on-plate heterojunction structure. *Phys Chem Chem Phys* 16:26314–26321
81. Yang W, Wen Y, Zeng D, Wang Q, Chen R, Wang W, Shan B (2014) Interfacial charge transfer and enhanced photocatalytic performance for the heterojunction WO<sub>3</sub>/BiOCl: first-principles study. *J Mater Chem A* 2:20770–20775
82. Li N, Jin Y, Hua X, Wang K, Xu K, Chen M, Teng F (2014) Uniform Fe<sub>2</sub>O<sub>3</sub> nanocubes on BiOCl nanosheets and its improved photocatalytic activity. *J Mol Catal A Chem* 395:428–433
83. Mao X, Fan C, Wang Y, Wang Y, Zhang X (2014) RhB-sensitized effect on the enhancement of photocatalytic activity of BiOCl toward bisphenol-A under visible light irradiation. *Appl Surf Sci* 317:517–525
84. Shia S, Gondal MA, Rashid SG, Qic Q, Al-Saadid AA, Yamani ZH, Suia Y, Xue Q, Shena K (2014) Synthesis of g-C<sub>3</sub>N<sub>4</sub>/BiOCl<sub>1-x</sub>Br<sub>1-x</sub> hybrid photocatalysts and the photoactivity enhancement driven by visible light. *Colloids Surf A* 461:202–211
85. Guerrero M, Altube A, García-Lecina E, Rossinyol E, Baró MD, Pellicer E, Sort J (2014) Facile in situ synthesis of BiOCl nanoplates stacked to highly porous TiO<sub>2</sub>: a synergistic combination for environmental remediation. *ACS Appl Mater Interfaces* 6:13994–14000
86. Ao Y, Tang H, Wang P, Wang C (2014) Deposition of Ag@AgCl onto two dimensional square-like BiOCl nanoplates for high visible-light photocatalytic activity. *Mater Lett* 131:74–77

87. Cheng J, Wang C, Cui Y, Sun Y, Zuo Y, Wang T (2014) Large improvement of visible-light driven photocatalytic property in AgCl nanoparticles modified black BiOCl microsphere. *Mater Lett* 127:28–31
88. Huang Z, Song J, Pan L, Jia X, Li Z, Zou J, Zhangab X, Wangab L (2014) W<sub>18</sub>O<sub>49</sub> nanowire alignments with a BiOCl shell as an efficient photocatalyst. *Nanoscale* 6:8865–9972
89. Lu H, Xu L, Wei B, Zhang M, Gao H, Sun W (2014) Enhanced photosensitization process induced by the p–n junction of Bi<sub>2</sub>O<sub>2</sub>CO<sub>3</sub>/BiOCl heterojunctions on the degradation of rhodamine B. *Appl Surf Sci* 303:360–366
90. Li N, Hua X, Wang K, Jin Y, Xu J, Chen M, Teng F (2014) In-situ synthesis of uniform Fe<sub>2</sub>O<sub>3</sub>/BiOCl p/n heterojunctions and improved photodegradation properties for mixture dyes. *Dalton Trans* 43:13742–13750
91. Li G, Jiang B, Xiao S, Lian Z, Zhang D, Yu JC, Li H (2014) An efficient dye-sensitized BiOCl photocatalyst for air and water purification under visible light irradiation. *Environ Sci Processes Impacts* 16:1975–1980
92. Tana C, Zhua G, Hojamberdiev M, Okada K, Liang J, Luo X, Liu P, Liu Y (2014) Co<sub>3</sub>O<sub>4</sub> nanoparticles-loaded BiOCl nanoplates with the dominant{001} facets: efficient photodegradation of organic dyes under visible light. *Appl Catal B* 152–153:425–436
93. Zhanga X, Guob T, Wanga X, Wanga Y, Fana C, Zhang H (2014) Facile composition-controlled preparation and photocatalytic application of BiOCl/Bi<sub>2</sub>O<sub>2</sub>CO<sub>3</sub> nanosheets. *Appl Catal B* 150–151:486–495
94. Tan C, Zhu G, Hojamberdiev M, Xu C, Liang J, Luo P, Liu Y (2013) Room temperature synthesis and photocatalytic activity of magnetically recoverable Fe<sub>3</sub>O<sub>4</sub>/BiOCl nanocomposite photocatalysts. *J Clust Sci* 24:1115–1126
95. Zhang J, Xia J, Yin S, Li H, Xu H, He M, Huang L, Zhang Q (2013) Improvement of visible light photocatalytic activity over flower-like BiOCl/BiOBr microspheres synthesized by reactable ionic liquids. *Colloids Surf A* 420:89–95
96. Xiao X, Hao R, Liang M, Zuo X, Nan J, Li L, Zhang W (2012) One-pot solvothermal synthesis of three-dimensional (3D) BiOI/BiOCl composites with enhanced visible-light photocatalytic activities for the degradation of bisphenol-A. *J Hazard Mater* 233–234:122–130
97. Cao J, Xu B, Lin H, Luo B, Chen S (2012) Novel Bi<sub>2</sub>S<sub>3</sub>-sensitized BiOCl with highly visible light photocatalytic activity for the removal of rhodamine B. *Catal Commun* 26:204–208
98. Cheng H, Huang B, Qin X, Zhanga X, Daib Y (2012) A controlled anion exchange strategy to synthesize Bi<sub>2</sub>S<sub>3</sub> nanocrystals/BiOCl hybrid architectures with efficient visible light photoactivity. *Chem Commun* 48:97–99
99. Zhu G, Hojamberdiev M, Katsumata K, Matsushita N, Okada K, Liu P, Zhou J, Liu Y (2014) Synthesis of heterostructured In<sub>2</sub>O<sub>3</sub>/BiOCl powders and their visible-light-driven photocatalytic activity for the degradation of rhodamine B. *Adv Powder Technol* 25:1292–1303
100. Chai SY, Kim YJ, Jung MH, Chakraborty AK, Jung D, Lee WI (2009) Heterojunctioned BiOCl/Bi<sub>2</sub>O<sub>3</sub>, a new visible light photocatalyst. *J Catal* 262:144–149
101. Gao B, Chakraborty AK, Yang JM, Lee WI (2010) Visible-light photocatalytic activity of BiOCl/Bi<sub>3</sub>O<sub>4</sub>Cl nanocomposites. *Bull Korean Chem Soc* 31:1941–1944
102. Chakraborty AK, Rawal SB, Han SY, Chai SY, Lee WI (2011) Enhancement of visible-light photocatalytic efficiency of BiOCl/Bi<sub>2</sub>O<sub>3</sub> by surface modification with WO<sub>3</sub>. *Appl Catal A* 407:217–223
103. Lin XP, Huang T, Huang FQ, Wang WD, Shi JL (2006) Photocatalytic activity of a bi-based oxychloride Bi<sub>3</sub>O<sub>4</sub>Cl. *J Phys Chem B* 110:24629–24634
104. Kwon YT, Song KY, Lee WI, Choi GJ, Do YR (2000) Photocatalytic behavior of WO<sub>3</sub>-loaded TiO<sub>2</sub> in an oxidation reaction. *J Catal* 191:192–199
105. Chakraborty AK, Chai SY, Lee WI (2008) Photocatalytic behavior of WO<sub>3</sub>/TiO<sub>2</sub> in decomposing volatile aldehydes. *Bull Korean Chem Soc* 29:494–496

# Chapter 24

## Visible-Light-Responsive Photocatalysts and Photoelectrodes Using $\text{WO}_3$ Semiconductors for Degradation of Organics and Water Splitting

Kazuhiro Sayama

### 24.1 Introduction

Visible-light-responsive photocatalysts have been extensively investigated for indoor or in-vehicle applications. Conventional  $\text{TiO}_2$  photocatalysts are responsive in the UV region and hence cannot be utilized under fluorescent light through acrylic plate, LED light, or sunlight through UV-cut glass, as the intensity of UV is negligible. However, there are large total photon numbers in the visible region from these light sources, and therefore the activity of visible-light-responsive photocatalysts is high compared with that of  $\text{TiO}_2$ . The development of new visible-light-responsive photocatalysts is challenging. Various  $\text{TiO}_2$  photocatalysts doped with anions (N, C, S) or transition metals have been developed; however, the photocatalytic activities of these complicated composites are not sufficient for practical use. On the other hand, tungsten oxide ( $\text{WO}_3$ ) is a visible-light-responsive photocatalyst, which absorbs light up to ca. 480 nm, as shown in Fig. 24.1. Compared with mixed metal oxides and doped oxides,  $\text{WO}_3$  is easy to prepare, modify, and coat onto substrates. The absorption coefficient of  $\text{WO}_3$  is very high due to the direct photon transition, and the amount of absorbed photons under fluorescent and sunlight is 10 and 3 times higher than that of  $\text{TiO}_2$ , respectively. The charge recombination in undoped  $\text{WO}_3$  is much higher than in doped semiconductors.  $\text{WO}_3$  also is non-toxic and is stable in acidic and oxidative conditions. Considering these advantages,  $\text{WO}_3$  semiconductors are of interest for further studies for use as photocatalysts. Figure 24.2 shows the band potentials of  $\text{WO}_3$  and  $\text{TiO}_2$ , and the redox potentials of the  $\text{O}_2$  reduction for the degradation of organic compounds and for water splitting. We have to always consider the relation of these potentials and the photocatalytic activity. The valence band potential of  $\text{WO}_3$  is almost the same as that of  $\text{TiO}_2$ ;

---

K. Sayama (✉)

Research Center for Photovoltaics (RCPV), National Institute of Advanced Industrial Science and Technology (AIST), Central 5, 1-1-1 Higashi, Tsukuba, Ibaraki 305-8565, Japan  
e-mail: [k.sayama@aist.go.jp](mailto:k.sayama@aist.go.jp)

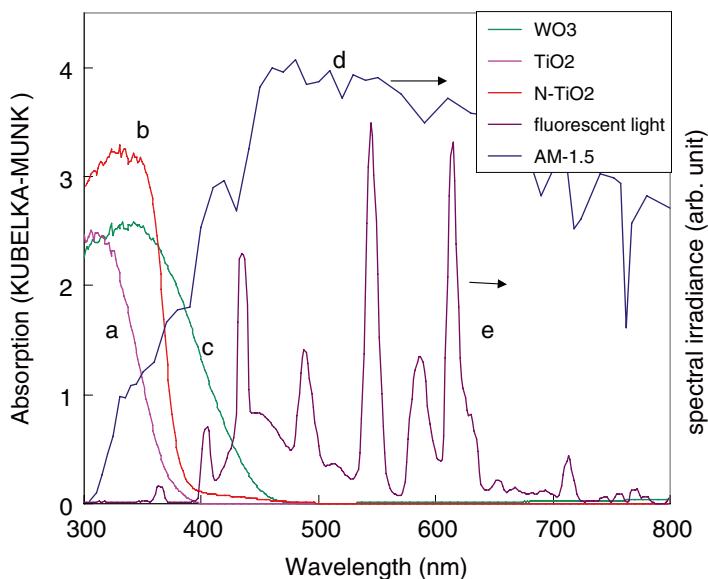


**Fig. 24.1** Absorption spectra of various semiconductors. (a)  $\text{TiO}_2$ , (b) N-doped  $\text{TiO}_2$ , (c)  $\text{WO}_3$ , (d) solar light, and (e) fluorescent light

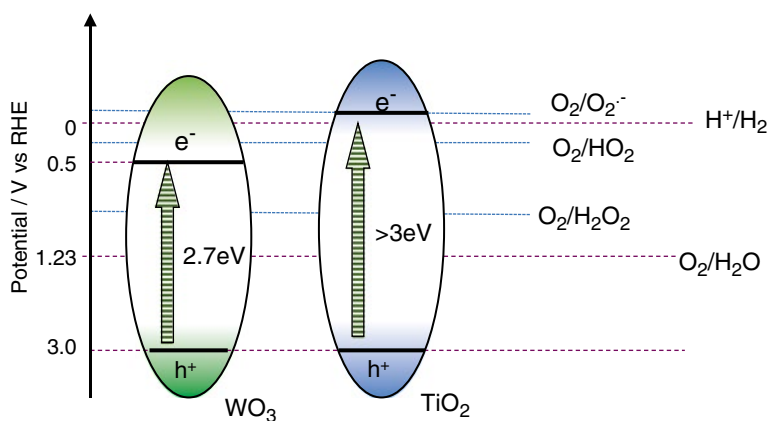


**Fig. 24.2** The band potentials of  $\text{WO}_3$  and  $\text{TiO}_2$ , and the redox potentials of the  $\text{O}_2$  reduction for degradation of organic compounds and for water splitting

therefore, the oxidation ability of holes at the valence band potential of  $\text{WO}_3$  is almost the same as that of  $\text{TiO}_2$ . It is suggested that most organic compounds can be oxidized into  $\text{CO}_2$  and water can be oxidized into  $\text{O}_2$ . However, these reactions are not efficient due to the limitation of the reduction reaction. The conduction band potential of  $\text{WO}_3$  is around 0.5 V RHE. For  $\text{WO}_3$ , the reduction of water into  $\text{H}_2$  cannot occur, and the  $\text{O}_2$  reduction is very slow.

In this chapter, the development of various  $\text{WO}_3$  photocatalysts for degradation of various organic compounds and for water splitting is reported. Moreover,  $\text{WO}_3$  particles have been used to fabricate porous and nanocrystalline photoelectrodes for water splitting. The charge separation of  $e^-$  and  $h^+$  occurs in the semiconductor nanoparticles; therefore, the nanocrystalline photoelectrodes are called photocatalytic photoelectrodes. The development of various  $\text{WO}_3$  nanocrystalline photoelectrodes with other semiconductors such as  $\text{BiVO}_4$  is also reported.

## 24.2 $\text{WO}_3$ Photocatalysts for Environmental Applications

### 24.2.1 Degradation of Various Organic Compounds

Various  $\text{TiO}_2$  photocatalysts have been developed, but very few reports exist concerning the degradation of organic substances over  $\text{WO}_3$  photocatalysts before 2007 [1–3]. Perhaps this is because the photocatalytic activity of  $\text{WO}_3$  toward organic substances is very low without suitable co-catalysts. Furthermore, the complete oxidation of organic substances to produce  $\text{CO}_2$  (complete mineralization) over these  $\text{WO}_3$  photocatalysts has not been investigated. Since 2007, it has been reported that the activity of  $\text{WO}_3$  photocatalysts for the complete oxidation of VOCs (volatile organic compounds) could be improved significantly in the presence of suitable co-catalysts such as Pt, Pd, and Cu compounds, as well as  $\text{Cu}^{2+}$  ions [4–13]. Figure 24.3 shows the degradation of various organic compounds into  $\text{CO}_2$  over  $\text{CuO-WO}_3$ ,  $\text{WO}_3$ , and  $\text{CuO}$ . The photocatalytic activity of complete oxidation into  $\text{CO}_2$  over  $\text{WO}_3$  was significantly improved by  $\text{CuO}$  loading as a co-catalyst.

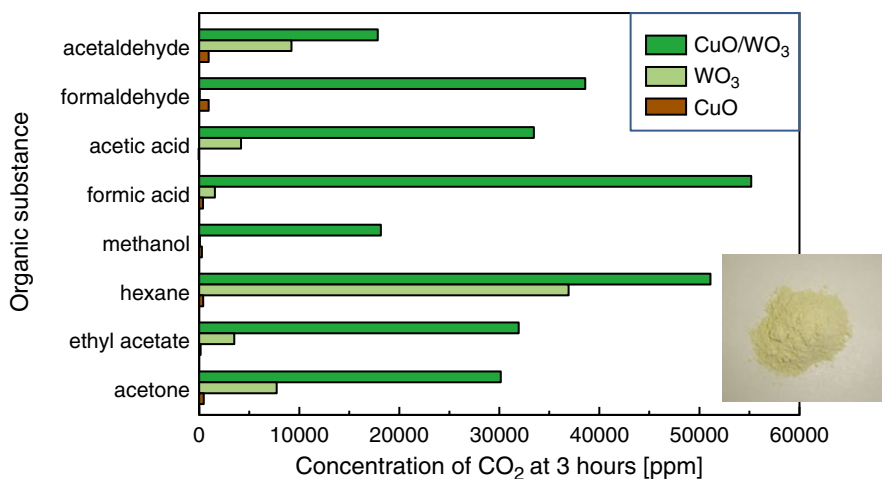
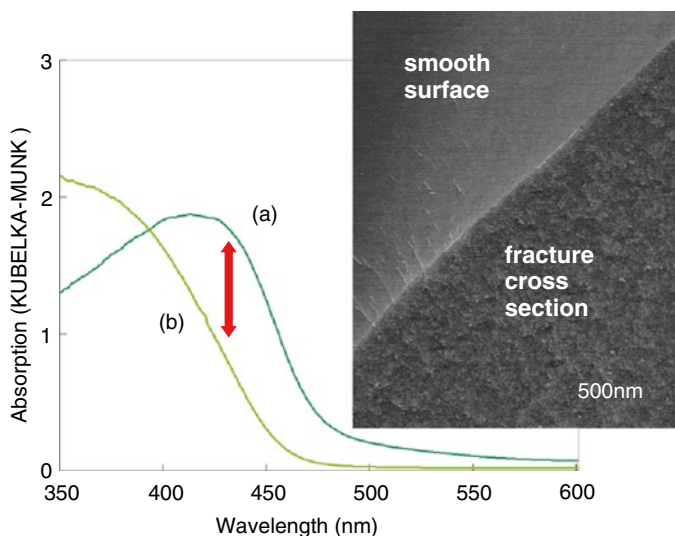


Fig. 24.3 Degradation of various organic compounds into  $\text{CO}_2$

Most of the reported  $\text{WO}_3$  photocatalyst studies to date have employed commercially available  $\text{WO}_3$  powders. The surface areas of most of these commercialized  $\text{WO}_3$  powders are very low (3–7  $\text{m}^2/\text{g}$ ) compared with the surface area of typical  $\text{TiO}_2$  photocatalysts (tens to hundreds of  $\text{m}^2/\text{g}$ ). Surface area is generally one of the most important factors affecting photocatalytic activity. We investigated various methods of preparing  $\text{WO}_3$  semiconductors with different surface areas with the aim of improving photocatalytic activity and clarifying the relation between the activity and the surface area of  $\text{WO}_3$ . During this investigation, we found that  $\text{WO}_3$  prepared from amorphous peroxo-tungstic acid (PA) showed higher activity than other  $\text{WO}_3$  for the degradation of various organic compounds, and this  $\text{WO}_3$  powder exhibited high absorption over the visible light region [14].

$\text{WO}_3(\text{PA})$  was prepared from W metal and  $\text{H}_2\text{O}_2$ . W metal powder was completely dissolved in aqueous  $\text{H}_2\text{O}_2$  in a glass beaker, and the transparent colorless solution was evaporated quickly on a hot stir plate. The white powder remaining in the beaker after evaporation was crystalline peroxo-tungstic acid,  $[\text{WO}_2(\text{O}_2)\text{H}_2\text{O}]_n\text{H}_2\text{O}$ . This powder was dissolved in hot water on a hot stir plate, where the solution temperature was kept at ca. 343 K for 90 min to age the solution. The colorless solution became orange during this aging treatment and then gradually evaporated. During evaporation, the viscosity of the orange solution increased, and  $\text{O}_2$  gas bubbles were observed in the viscous gel. As these  $\text{O}_2$  bubbles burst, an amorphous orange peroxo-tungstic acid powder evolved from the gel,  $\text{WO}_3 \cdot x\text{H}_2\text{O}_2 \cdot y\text{H}_2\text{O}$ . This amorphous powder is referred to as a-PA. There were many bubbles with sizes from a few  $\mu\text{m}$  to 200  $\mu\text{m}$  within the mass of the amorphous powder.  $\text{WO}_3(\text{PA})$  powder was then prepared by calcination (standard: 573 K) of the a-PA powder in air for 30 min. The agglomerate of a-PA powder shattered during the calcination due to escaping gasses, resulting in a fine powder of  $\text{WO}_3(\text{PA})$  which was used without any additional milling.

The photocatalytic activity for  $\text{CO}_2$  formation from hexane over  $\text{WO}_3(\text{PA})$  was over three times higher than measured for over commercial and home-made  $\text{WO}_3$ .  $\text{WO}_3(\text{PA})$  had a unique light absorption spectrum compared with the other  $\text{WO}_3$  samples (Fig. 24.4). Except for  $\text{WO}_3(\text{PA})$ , the absorption spectra of all the home-made and commercial  $\text{WO}_3$  powders decreased monotonously from the ultraviolet (UV) region to 480 nm. In contrast, for  $\text{WO}_3(\text{PA})$ , the absorption between 400 and 500 nm increased substantially, suggesting that the absorption band was red-shifted. Beneath the smooth surface of  $\text{WO}_3(\text{PA})$ , many particles of 30–40 nm diameter were observed, as shown in the SEM image of a fracture cross-section (Fig. 24.4). We propose that some non-uniform small hollows (low density areas) created by desorbing  $\text{H}_2\text{O}$  and  $\text{O}_2$  gases from the solid a-PA during heating or some aggregates (high density areas) of tightly packed primary particles might be present inside the  $\text{WO}_3(\text{PA})$  particles. The mechanism of strong light absorption of the  $\text{WO}_3(\text{PA})$  is depicted in Fig. 24.5. The surface of common  $\text{WO}_3$  powder was rougher than a few hundred nanometers, owing to random aggregates of the primary particles. The diffuse reflection is known to reach a maximum when the particle size of aggregates or surface roughness is similar to the incident light wavelength, due to Mie scattering. Therefore, powders with surface roughness values of a few hundred nanometers



**Fig. 24.4** Absorption spectra of (a)  $\text{WO}_3(\text{PA})$  and (b) typical  $\text{WO}_3$ . Insert is SEM photograph of  $\text{WO}_3(\text{PA})$

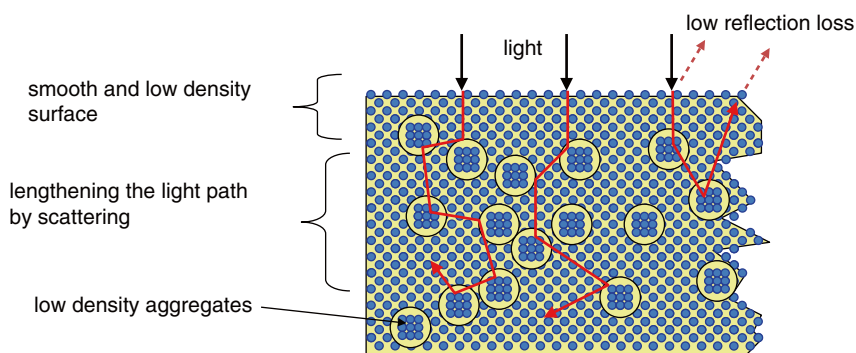


**Fig. 24.5** Mechanism of strong light absorption by the structure in  $\text{WO}_3(\text{PA})$

showed large reflectance. Moreover, the surface porosity of the  $\text{WO}_3(\text{PA})$  powder might also have contributed to decreased reflection, because the apparent density and the apparent refractive index decreased, and the large difference of refractive index at the interface with air was reduced. The reflection might be reduced at a smooth and porous surface, like  $\text{WO}_3(\text{PA})$ . Additionally, some structures beneath the transparent surface of  $\text{WO}_3(\text{PA})$  were observed with the optical microscope. This result suggests that structures such as aggregates and hollows had different refractive indices, and that the incident light was refracted at the interface of these structures within the  $\text{WO}_3$  matrix. Therefore, the light absorption might be improved simply by the lengthening of the absorption path, owing to the refraction inside the  $\text{WO}_3(\text{PA})$  powder.

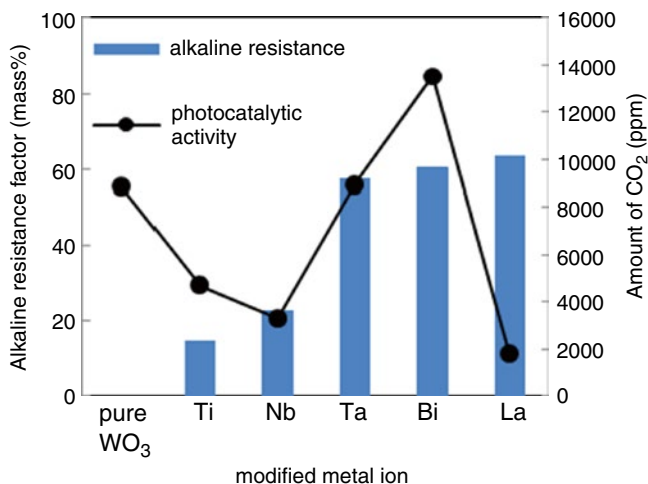


**Fig. 24.6** Alkali resistance factor of M-WO<sub>3</sub> in 1 M NaOH solution and the amount of CO<sub>2</sub> generation by CH<sub>3</sub>CHO degradation over Pt/M-WO<sub>3</sub>

### 24.2.2 Improving the Stability of Nanostructured WO<sub>3</sub> in Alkaline Solutions

WO<sub>3</sub> easily dissolves in an alkaline solution, limiting its practical application as a catalyst material. For example, kitchen and bathroom facilities and windows are frequently cleaned using strong alkaline detergents (pH: 13–14, typically around 0.1 M NaOH solution), and water splitting is often performed in an electrochemical cell with an alkaline electrolyte. Therefore, improving the stability of WO<sub>3</sub> in an alkaline environment is necessary. To this end, we prepared WO<sub>3</sub> photocatalyst powders modified with small amounts of various metal compounds, and we found that WO<sub>3</sub> modified with Bi showed not only very high alkaline resistance but also excellent photocatalytic activity [15]. The alkaline resistance factor of M-WO<sub>3</sub> (M=Ti, Nb, Ta, Bi, or La) in 1 M NaOH solution for 24 h and the amount of CO<sub>2</sub> generation from the degradation of CH<sub>3</sub>CHO over Pt/M-WO<sub>3</sub> powders are shown in Fig. 24.6. The catalyst powders were prepared using an impregnation method and sintered at 773 K. Bi-WO<sub>3</sub> was prepared from a Bi(NO<sub>3</sub>)<sub>3</sub> aqueous solution. The alkaline resistance factor (mass %) was defined as the ratio of the amount of remaining catalyst powder after NaOH immersion to the amount of catalyst before immersion. Pure WO<sub>3</sub> was completely dissolved in 1 M NaOH in a short time. Conversely, the alkaline resistance factor was improved by modification with other metal compounds. Ta, Bi, and La were particularly effective in improving WO<sub>3</sub> resistance when compared with Ti and Nb. Moreover, we found that the photocatalytic activity of WO<sub>3</sub> was enhanced by the modification of Bi, while it decreased with the addition of the other metals.

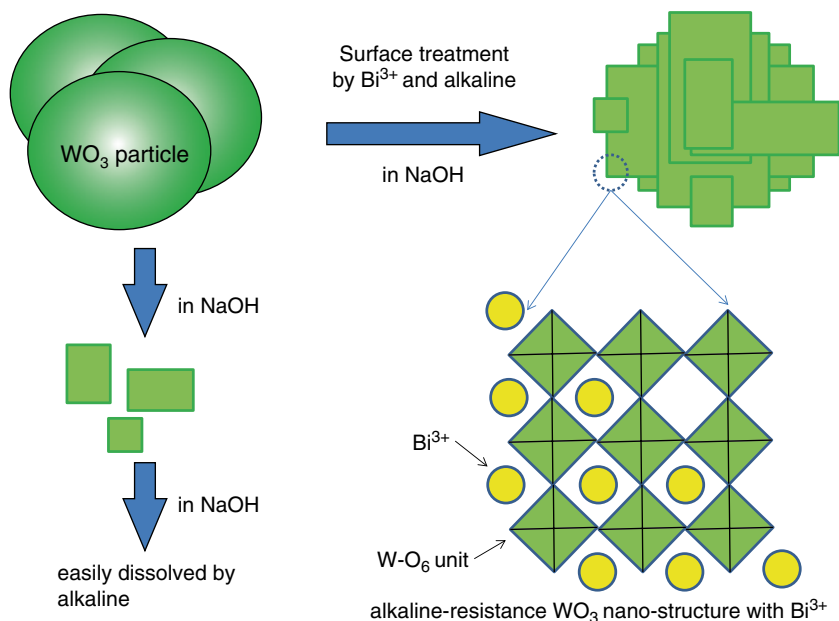


**Fig. 24.7** Dissolution reaction with  $\text{Bi}^{3+}$  ion and  $\text{NaOH}$

Before immersion in the  $\text{NaOH}$  solution, the  $\text{Bi-WO}_3$  particles were round with diameters around 200 nm, similar to pure  $\text{WO}_3$ . In contrast, the morphology of the  $\text{Bi-WO}_3$  particles after immersion in the alkaline solution exhibited angular particles with smooth terraces and step edges (Fig. 24.7). According to the results of the alkaline resistance cycle tests, it appeared that the angular particles formed during corrosion in the  $\text{NaOH}$  solution whereas they were stable under alkaline conditions. After pure  $\text{WO}_3$  was immersed in  $\text{NaOH}$  for a short time, we also observed some  $\text{WO}_3$  particles with terrace and step-like features. We also measured lattice fringe spacings from high-resolution transmission electron microscopy (HRTEM) images of  $\text{Bi-WO}_3$  before and after immersion. The bulk lattice fringes were parallel and perpendicular and the spacing values were 3.78–3.88 Å, which corresponds to the (200), (020), and (002) planes of monoclinic  $\text{WO}_3$ . As for the angular  $\text{Bi-WO}_3$ , most lattice spacing close to the terrace surface (2–4 nm) were larger (~4.0 Å) than that of the bulk. It was difficult through XRD analyses to reliably calculate the lattice expansion as the measurement accuracy was too low.

The rounded  $\text{Bi-WO}_3$  particles partially dissolved in  $\text{NaOH}$  resulting in shape changes. The lattice fringe of the terrace surface was larger than the bulk lattice spacings, suggesting that only the  $\text{WO}_3$  surface was intercalated by  $\text{Bi}^{3+}$ . It seems that surface modification by  $\text{Bi}^{3+}$  did not make  $\text{WO}_3$  stable in an alkaline solution. The particles stabilized in the alkaline solution showed angular structures, and it appears that the  $\text{Bi}^{3+}$  intercalated with specific crystal planes gave very high resistance to strong alkaline conditions. We observed that these specific crystal planes

are (200), (020), and (002), which are the most closely packed planes. As for the dissolution of  $\text{WO}_3$  in alkaline solutions, low coordination number W–O bonds are more easily dissolved than those with a high coordination number. It was observed that pure  $\text{WO}_3$  produced terraced structures during alkaline corrosion. This result supports our explanation. Hence, we are proposing the following mechanism for the angular particles of Bi- $\text{WO}_3$  in alkaline solutions. During dissolution in NaOH, the closest packed surface gradually appears and  $\text{Bi}^{3+}$  ions on the  $\text{WO}_3$  surfaces intercalate and stabilize the close-packed plane. As a result of these processes, the terrace and step-like structures are formed.

## 24.3 Solar Energy Conversion Using $\text{WO}_3$

### 24.3.1 Water Oxidation Over $\text{WO}_3$ Photocatalyst Using Redox Mediators

In the past 30 years, the direct water-splitting reaction using semiconductor photocatalyst powders to split water molecules into  $\text{H}_2$  and  $\text{O}_2$  has been intensively investigated as a potential solar energy conversion system. The reaction mechanisms of photocatalytic water splitting by conventional one- and two-step photoexcitation using reversible redox mediators, such as natural photosynthesis (Z-scheme reaction), are shown in Fig. 24.8. However, the quantum efficiencies (QE) of these reactions under visible light are low (<5.9 %). In addition, these systems have serious disadvantages: the simultaneous formation of  $\text{H}_2$  and  $\text{O}_2$  (an explosive gas mixture) and the need for a transparent, gastight photocatalytic reactor to accumulate  $\text{H}_2$  gas on a large scale. During photosynthesis, the oxidation of water into  $\text{O}_2$  and the reduction of reversible redox mediators occur, where the total Gibbs free energy increases ( $\Delta G > 0$ ). The photocatalytic reduction of redox mediators with positive  $\Delta G$ , instead of  $\text{H}_2$  formation, is also an attractive artificial photosynthesis reaction,

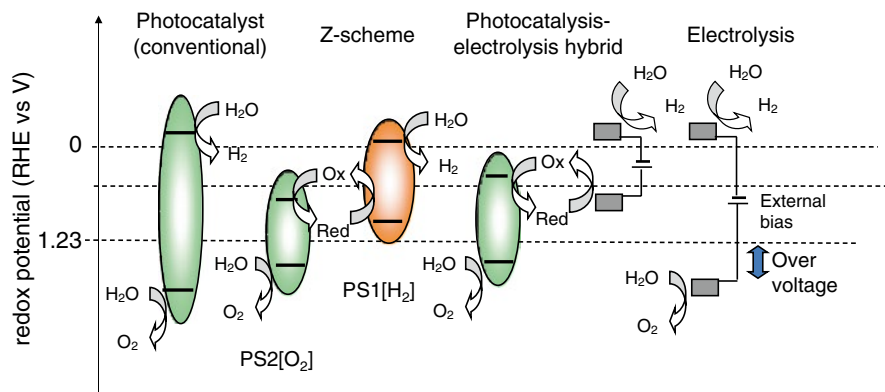
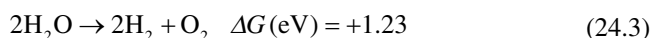


Fig. 24.8 Various hydrogen production technologies from water and their potential

because the accumulation of reduced redox mediators and the separation from O<sub>2</sub> gas are easier. A photocatalysis–electrolysis hybrid system using a reversible redox mediator [8, 16] is a practical water splitting system, where PS1[H<sub>2</sub>] in Fig. 24.8 is replaced by electrolysis, as pure H<sub>2</sub> is available on the counter-electrode, and a large area for H<sub>2</sub> accumulation over the photocatalysis pool is not needed. From the standpoint of stability, cost, and minimizing side-reactions, the Fe<sup>3+</sup>/Fe<sup>2+</sup> system is an excellent redox mediator. The Δ*G* is positive under acid conditions for both reactions (24.1) and (24.2).



Total (24.1)+(24.2)



Owing to the low redox potential and the low over-potential of the Fe<sup>2+</sup> oxidation, efficient H<sub>2</sub> production could be successfully achieved using Fe<sup>2+</sup> in an electrolysis pilot plant under a high current density with low applied bias <0.8 V. Conversely, the applied bias of water splitting in a conventional electrolysis is generally more than 1.6 V due to the high over-potential for O<sub>2</sub> formation. There is a possibility that the production costs of H<sub>2</sub> by electrolysis will be reduced significantly if Fe<sup>2+</sup> is efficiently produced from Fe<sup>3+</sup> by photocatalysis. Fe<sup>2+</sup> can be produced efficiently over a WO<sub>3</sub> photocatalyst under visible light using sacrificial electron donors such as organic compounds [8]. However, the photocatalytic activity of Fe<sup>2+</sup> and O<sub>2</sub> formation without sacrificial electron donors is very low.

We investigated Cs-modification of WO<sub>3</sub> on photocatalytic O<sub>2</sub> evolution and Fe<sup>3+</sup> ion reduction over WO<sub>3</sub> under visible light irradiation [17, 18].

The WO<sub>3</sub> powder was first thermally treated in air at 973 K to improve its crystallinity. Some metal salts such as alkali, alkaline earth, and transition-metal salts were used for the surface modification of the WO<sub>3</sub> photocatalyst. Then, these catalysts were stirred in H<sub>2</sub>SO<sub>4</sub> or FeSO<sub>4</sub> aqueous solutions for 30 min to facilitate ion exchange.

The round shape of the WO<sub>3</sub> particles changed, and many crystal facets appeared after impregnation of the cesium-containing aqueous solutions, as shown in Fig. 24.9. The surface was covered by thin Cs-tungstate layers (ca. 2 nm in thickness). Cation exchange was possible at the plane surfaces of the Cs-modified WO<sub>3</sub>. The photocatalytic activity of Cs-modified WO<sub>3</sub> was improved by ion exchange between Cs<sup>+</sup> and H<sup>+</sup> or Fe<sup>2+</sup> (partially); 10 times more than that of WO<sub>3</sub> without any treatment (Fig. 24.10). The optimized WO<sub>3</sub> showed a QE more than 50 times higher (31 % at 420 nm) than that reported previously under visible light, and showed the highest solar-to-chemical energy conversion efficiency ( $\eta_{\text{sun}}=0.38\%$ ) among all powder photocatalyst systems reported previously. This  $\eta_{\text{sun}}$  value is comparable to the solar-to-product energy conversion efficiencies of natural plant photosynthesis for biomass energy.

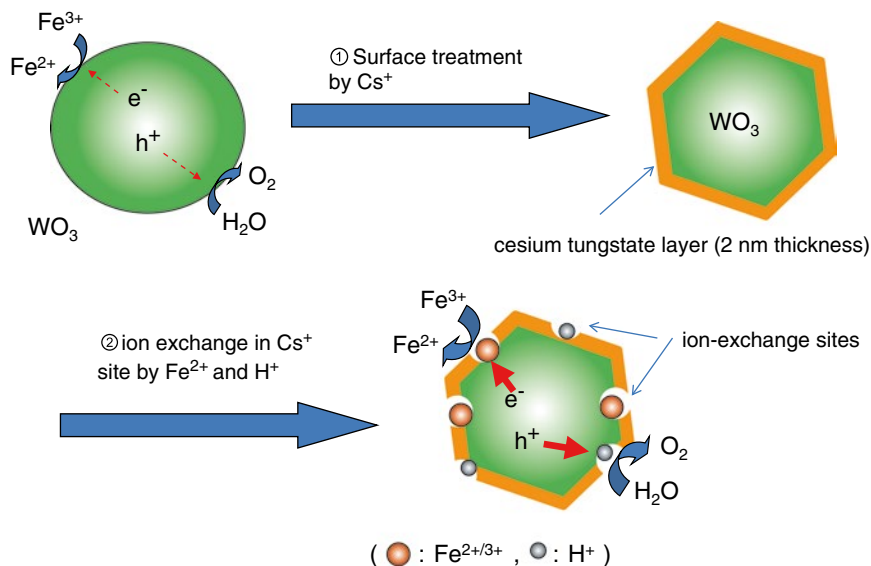


Fig. 24.9 Speculated reaction mechanism on  $\text{Cs}^+$  ion treatment

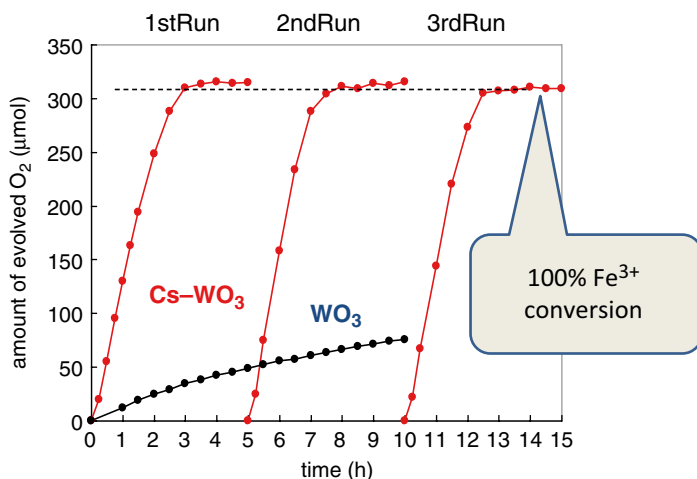
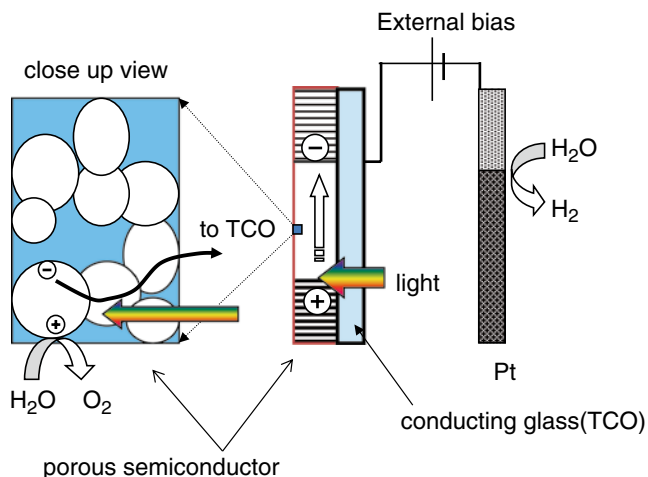


Fig. 24.10 Time course of  $\text{O}_2$  evolution in  $\text{Fe}^{3+}$ -containing aqueous solution

### 24.3.2 Water Oxidation Using Nanostructured Photoelectrodes

Since the report of the Honda–Fujishima effect using  $\text{TiO}_2$  illuminated with UV light [19], various photoelectrodes using oxide semiconductors have been widely investigated for solar hydrogen production systems. To increase the solar energy conversion efficiency, effective utilization of visible light over a wide wavelength range



**Fig. 24.11** Porous and nanocrystalline oxide semiconductor films on conducting glass photoelectrodes

is necessary. Note that oxide semiconductors have many advantages; for example, they are generally stable, are suitable for O<sub>2</sub> evolution, and are produced easily compared to non-oxide semiconductors. Moreover, most oxide semiconductors are n-type; therefore, H<sub>2</sub> gas collection at the counter electrode is easier compared to the large area photoelectrode of p-type semiconductors. However, the efficiencies of various conventional oxide semiconductor electrodes, such as single crystals or sintered pellets, are very low in the visible light region, even when a high external bias is applied.

It was reported that a nanocrystalline WO<sub>3</sub> thin film on a conducting glass electrode showed an excellent incident photon-to-current conversion efficiency (IPCE; >75 %) for water decomposition under visible light [20, 21]. The nanocrystalline WO<sub>3</sub> film was prepared by spreading a colloidal solution of WO<sub>3</sub> on a conducting glass and then firing it at high temperature. It is worth mentioning that high IPCEs were obtained with these simple wet processes, although many defects in the porous film electrodes may be present. Figure 24.11 depicts the porous structure of these nanocrystalline thin-film photoelectrodes. Porous thin-film photoelectrodes have the advantage that the diffusion length of the holes in the valence band formed by the band-gap photoexcitation is significantly shorter compared to the length scale of conventional thick photoelectrodes. The electrolyte solution can penetrate the porous structure and infiltrate the entire nanocrystalline semiconductor film. Hence, holes generated within the nanoparticles have only a short distance to travel to the semiconductor–electrolyte interface. Porous thin-film photoelectrodes are a few micrometers thick or less, whereas conventional photoelectrodes are at least a few hundred micrometers thick. Furthermore, the distance the electrons need to travel into the conducting plate is also shorter when the sample is irradiated through the conducting glass. Therefore, this type of electrode could have increased IPCE values.

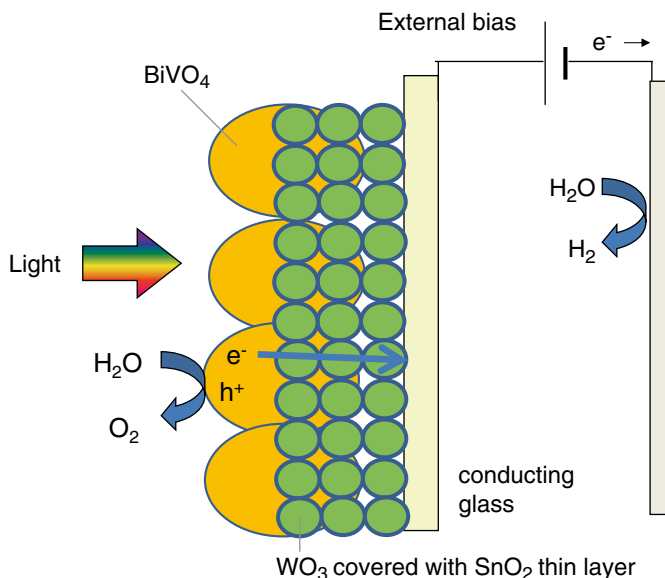


**Fig. 24.12** Mechanism of  $\text{WO}_3/\text{SnO}_2/\text{BiVO}_4$  photoelectrode

For porous photoelectrodes, charge separation occurs in the nanoparticles, while it occurs at the space charge layer of a conventional thick photoelectrode. The charge separation mechanism of the porous photoelectrodes is similar to that of a powder photocatalyst, as charge separation occurs in the small particles in both cases. Therefore, the porous photoelectrodes are sometimes called “photocatalyst electrodes.”

We have succeeded in greatly improving the efficiency of nanocrystalline  $\text{WO}_3$  and  $\text{BiVO}_4$  composite photoelectrodes (Figs. 24.12 and 24.13) using a highly concentrated carbonate aqueous electrolyte solution [22–24]. The precursor solutions of each oxide semiconductor were coated on a F-doped  $\text{SnO}_2$  (FTO) conductive glass substrate using a spin coater and then calcined at 773 K for 30 min for each coating. Initially, a  $\text{WO}_3$  layer was coated on FTO glass with subsequent multiple coatings of  $\text{BiVO}_4$  on top. For  $\text{WO}_3$ , 1.4 M peroxotungstic acid was used to deposit the film. In the case of  $\text{BiVO}_4$ , bismuth oxide and vanadium oxide materials from Enhanced Metal Organic Decomposition (Symetrix Co.) were mixed with a Bi:V ratio of 1:1 and then diluted with butyl acetate. The light-harvesting efficiency and photocurrent were significantly improved by the structure of the double-stacked photoelectrodes that trapped the light. The photocurrent was increased by the addition of an optimized  $\text{SnO}_2$  intermediate layer. A decreased resistance at the  $\text{BiVO}_4$  composite electrodes was observed in comparison to the bare  $\text{BiVO}_4$ . In the  $\text{BiVO}_4/\text{SnO}_2/\text{WO}_3$  photoelectrode, the highest IPCE was 53 % at 420 nm. The  $\text{H}_2$  and  $\text{O}_2$  were evolved stoichiometrically. The maximum value of the applied bias photon-to-current efficiency was 1.35 %.

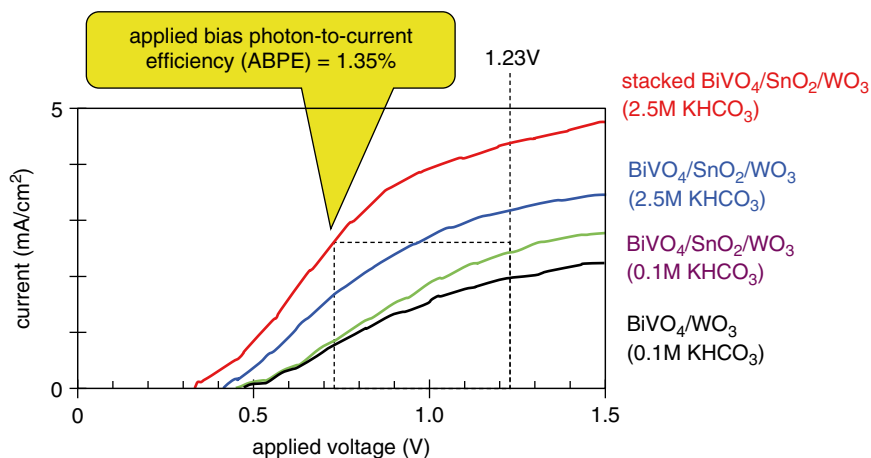


Fig. 24.13 Photocurrent–voltage properties on various photoanodes in  $\text{KHCO}_3$  aqueous solution

## 24.4 Conclusion

$\text{WO}_3$ -based photocatalysts have many advantages: high absorption in the visible light region by direct band-gap photoexcitation, strong hole oxidation ability for the complete degradation of organics into  $\text{CO}_2$ , easy preparation and coating on substrates, a non-toxic oxide, stability in acidic and oxidative conditions, and antibacterial activity under dark conditions.  $\text{Bi-WO}_3$  was stable in basic conditions up to  $\text{pH}=14$ . We hope that  $\text{WO}_3$  photocatalysts will be used in various practical applications for both environmental and energy applications.

## References

1. Kim KG, Jeong ED, Borse PH, Jeon S, Yong K, Lee JS, Li W, Oh SH (2006) Photocatalytic Ohmic layered nanocomposite for efficient utilization of visible light photons. *Appl Phys Lett* 89:064101–064103
2. Vinodgopal K, Bedja I, Hotchandani S, Kamat PV (1994) A photocatalytic approach for the decolorization of textile azo dyes in colloidal semiconductor suspensions. *Langmuir* 10:1767–1771
3. Sclafani A, Palmisano L, Marci G, Venezia AM (1998) Influence of platinum on catalytic activity of polycrystalline  $\text{WO}_3$  employed for phenol photodegradation in aqueous suspension. *Sol Energy Mat Sol Cells* 51:203–219
4. Abe R, Takami H, Murakami N, Ohtani B (2008) Pristine simple oxides as visible light driven photocatalysts: highly efficient decomposition of organic compounds over platinum-loaded tungsten oxide. *J Am Chem Soc* 130:7780–7781
5. Arai T, Horiguchi M, Yanagida M, Gunji T, Sugihara H, Sayama K (2008) Complete oxidation of acetaldehyde and toluene over a  $\text{Pd}/\text{WO}_3$  photocatalyst under fluorescentor visible-light irradiation. *Chem Commun* 2008:5565–5567. doi:10.1039/B811657A

6. Arai T, Yanagida M, Konishi Y, Iwasaki Y, Sugihara H, Sayama K (2007) Efficient complete oxidation of acetaldehyde into CO<sub>2</sub> over CuBi<sub>2</sub>O<sub>4</sub>/WO<sub>3</sub> composite photocatalyst under visible and UV light irradiation. *J Phys Chem C* 111:7574–7577
7. Arai T, Yanagida M, Konishi Y, Iwasaki Y, Sugihara H, Sayama K (2008) Promotion effect of CuO co-catalyst on WO<sub>3</sub>-catalyzed photodegradation of organic substances. *Cat Commun* 9:1254–1258
8. Arai T, Yanagida M, Konishi Y, Sugihara H, Sayama K (2008) Utilization of Fe<sup>3+</sup>/Fe<sup>2+</sup> redox for the photodegradation of organic substances over WO<sub>3</sub> photocatalyst and for H<sub>2</sub> production from the electrolysis of water. *Electrochemistry* 76:128–131
9. Arai T, Yanagida M, Konishi Y, Ikura A, Iwasaki Y, Sugihara H, Sayama K (2008) The enhancement of WO<sub>3</sub> catalyzed photodegradation of organic substances utilizing the redox cycle of copper ions. *Appl Catal B Environ* 84:42–47
10. Irie H, Miura S, Kamiya K, Hashimoto K (2008) Efficient visible light-sensitive photocatalysts: grafting Cu(II) ions onto TiO<sub>2</sub> and WO<sub>3</sub> photocatalysts. *Chem Phys Lett* 457:202–205
11. Zhao Z, Miyauchi M (2008) Nanoporous-walled tungsten oxide nanotubes as highly active visible-light-driven photocatalysts. *Angewandte Chemie Int Edit* 47:7051–7055
12. Sadakane M, Sasaki K, Kunioku H, Ohtani B, Ueda W, Abe R (2008) Tungsten oxide having high photocatalyst activity. *Chem Commun* 2008:6552–6554
13. Arai T, Horiguchi M, Yanagida M, Gunji T, Sugihara H, Sayama K (2009) Reaction mechanism and activity of WO<sub>3</sub>-catalyzed photodegradation of organic substances promoted by a CuO cocatalyst. *J Phys Chem C* 113:6602–6609
14. Sayama K, Hayashi H, Arai T, Yanagida M, Gunji T, Sugihara H (2010) Highly active WO<sub>3</sub> semiconductor photocatalyst prepared from amorphous peroxo-tungstic acid for the degradation of various organic compounds. *Appl Catal B* 94:150–157
15. Wada M, Wang N, Konishi Y, Miseki Y, Gunji T, Sayama K (2013) Angular Bi<sup>3+</sup>-WO<sub>3</sub> with significant alkali resistance and efficient photocatalytic activity. *Chem Lett* 42:395–397
16. Sayama K, Arakawa H, Okabe K, Kusama H (1998) Jpn Patent 3198298, 2001; U.S. Patent 09/028495
17. Miseki Y, Kusama H, Sugihara H, Sayama K (2010) Cs-modified WO<sub>3</sub> photocatalyst showing efficient solar energy conversion for O<sub>2</sub> production and Fe(III) ion reduction under visible light. *J Phys Chem Lett* 1:1196–1200
18. Miseki Y, Sayama K (2014) High-efficiency water oxidation and energy storage utilizing various reversible redox mediators under visible light over surface-modified WO<sub>3</sub>. *RSC Adv* 4:8308–8316
19. Fujishima A, Honda K (1972) Electrochemical photolysis of water at a semiconductor electrode. *Nature* 238:37–38
20. Santato C, Ulmann M, Augustynski J (2001) Photoelectrochemical properties of nanostructured tungsten trioxide films. *J Phys Chem B* 105:936–940
21. Santato C, Odziemkowski M, Ulmann M, Augustynski J (2001) Crystallographically oriented mesoporous WO<sub>3</sub> films: synthesis, characterization, and applications. *J Am Chem Soc* 123:10639–10649
22. Saito R, Miseki Y, Sayama K (2012) Highly efficient photoelectrochemical water splitting using a thin film photoanode of BiVO<sub>4</sub>/SnO<sub>2</sub>/WO<sub>3</sub> multi-composite in a carbonate electrolyte. *Chem Commun* 48:3833–3835
23. Saito R, Miseki Y, Sayama K (2013) Photoanode characteristics of multi-layer composite BiVO<sub>4</sub> thin film in a concentrated carbonate electrolyte solution for water splitting. *J Photochem Photobiol A Chem* 258:58–60
24. Fujimoto I, Wang N, Saito R, Miseki Y, Gunji T, Sayama K (2014) WO<sub>3</sub>/BiVO<sub>4</sub> composite photoelectrode prepared by improved auto-combustion method for highly efficient water splitting. *Int J Hydrogen Energ* 39:2454–2461

# Chapter 25

## Z-Scheme Water Splitting into H<sub>2</sub> and O<sub>2</sub> Under Visible Light

Ryu Abe

### 25.1 Semiconductor Photocatalysts for Solar Hydrogen Production

Photoinduced water splitting into H<sub>2</sub> and O<sub>2</sub> using semiconductor materials has recently been a cutting-edge research area due to the growing expectation for clean and direct production of H<sub>2</sub> from water by harvesting abundant solar light energy. After the report of pioneering work on photoelectrochemical water splitting using a single crystalline titania (TiO<sub>2</sub>) photoanode in 1972 [1], many researchers have intensively studied water splitting using semiconductor photoelectrodes or photocatalysts [2, 3]. As for photocatalytic water splitting using heterogeneous semiconductor particles, more than 100 photocatalytic systems have been already reported to be active for “overall” water splitting (i.e., simultaneous and stoichiometric generation of H<sub>2</sub> and O<sub>2</sub> from water). However, most of them function only under ultraviolet (UV) light ( $\lambda < 400$  nm) owing to the large band gaps of semiconductor materials [4, 5]. Even if all the photons in UV region (ca. 5 % of the total) were absorbed by a photocatalyst and ideally consumed for water splitting with 100 % of quantum efficiency, the maximum solar energy conversion efficiency for H<sub>2</sub> production would be only 2 %. Even this ideal value cannot far exceed the conversion efficiencies of photosynthesis in green plants under normal environmental conditions. Since nearly half of the solar energy incident on the Earth’s surface lies in the visible region ( $400 < \lambda < 800$  nm), it is essential to use visible light for realizing practically high H<sub>2</sub> production efficiency. For example, the utilization of visible light up to 600 nm can drastically improve the maximum solar energy conversion efficiency up to 16 %; a further extension up to 800 nm would give an ideal value

---

R. Abe (✉)

Department of Energy and Hydrocarbon Chemistry, Graduate School of Engineering,  
Kyoto University, A2 Kyoto University Katsura, Nishigyo-ku, Kyoto 615-8510, Japan  
e-mail: [ryu-abe@scl.kyoto-u.ac.jp](mailto:ryu-abe@scl.kyoto-u.ac.jp)

of 32 %, while the occurrence of recombination (between photoexcited electrons and holes) and/or backward electron transfers will undoubtedly lower the final conversion efficiency from the ideal values to some extent. The effective utilization of visible light is thus indispensable for achieving practically high efficiency of  $\text{H}_2$  production based on photocatalytic water splitting. Despite many years of intensive effort by researchers around the world, the overall water splitting under visible light had not been achieved for more than 30 years: until our first report in 2001 [6].

## 25.2 Difficulties in Achieving Water Splitting Using Visible Light

When a semiconductor material is used as heterogeneous photocatalyst for water splitting, the conduction band (CB) minimum of semiconductor must be more negative than the water reduction potential (0 V vs. SHE) to produce  $\text{H}_2$ , and at the same time the valence band (VB) maximum must be more positive than the water oxidation potential (+1.23 V vs. SHE) to produce  $\text{O}_2$  (see Fig. 25.1). Additionally, the semiconductor material must be stable in the reaction solutions (aqueous media in most cases), not only chemically but also photochemically (i.e., under irradiation). Metal oxide semiconductors are generally stable against photocorrosion and have thus been extensively studied as heterogeneous photocatalysts. However, Scaife pointed out in 1980 that it is intrinsically difficult to develop a metal oxide semiconductor photocatalyst that has both a sufficiently negative CB minimum for  $\text{H}_2$  production and a narrow band gap (i.e., <3.0 eV) allowing visible light absorption. This is due to the highly positive levels of VB maximum (at ca. +3.0 V vs. SHE) that are dominantly formed by the O 2p orbital [7]. Indeed, most of visible-light-responsive metal oxides, such as tungsten oxide ( $\text{WO}_3$ ) or iron oxide ( $\text{Fe}_2\text{O}_3$ ), cannot produce  $\text{H}_2$  from water, due to the insufficient energy of photoexcited electrons generated in

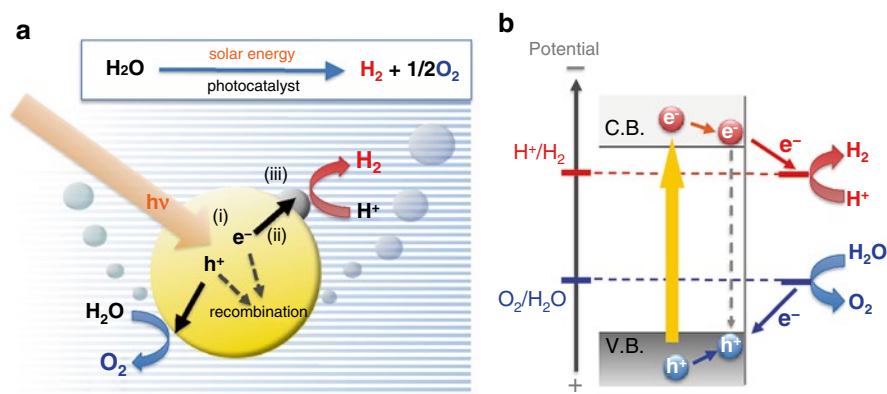


**Fig. 25.1** Schematic illustration of water splitting over semiconductor photocatalyst

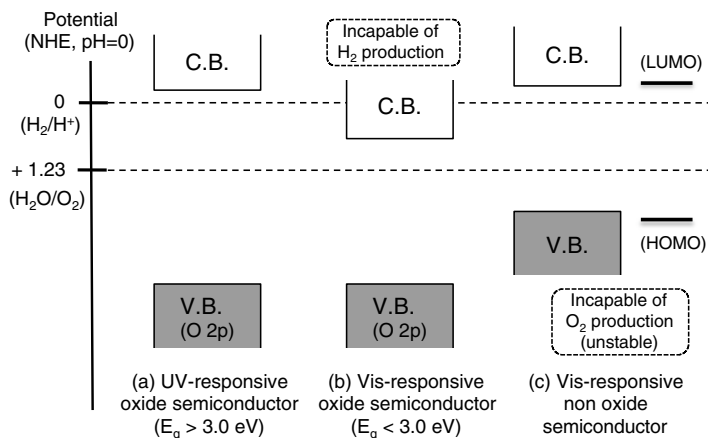


**Fig. 25.2** Band energy levels of various semiconductors

the CB minimums (Fig. 25.2). Although some of non-oxide semiconductors, such as organic dyes, metal complexes, sulfides, and nitrides, possess appropriate band levels for water splitting as well as narrow band gaps allowing under visible light absorption, they are generally unstable and readily deactivated through photocorrosion or self-oxidation by holes (or positive charge) generated in the materials themselves, rather than  $O_2$  evolution. For example, cadmium sulfide (CdS) had been regarded as one of the promising materials for visible-light-induced water splitting. However, it was revealed that the photogenerated holes in CdS preferentially oxidize the  $S^{2-}$  anions themselves, in place of  $H_2O$  molecules, in the absence of strong sacrificial electron donor, resulting in the elusion of  $Cd^{2+}$  cations along with oxidized species of  $S^{2-}$  (e.g.,  $SO_4^{2-}$ ). As briefly described above, there is only a few stable semiconductors having both a visible light absorption capability and sufficient band levels for water splitting; except for quite rare artificially created semiconductors such as GaN:ZnO solid solutions [8, 9]. Thus, the achieving efficient water splitting by visible light remains challenging.

### 25.3 Introduction of Two-Step Photoexcitation (Z-Scheme) Mechanism Toward Photocatalytic Water Splitting Under Visible Light

One of the promising approaches for achieving water splitting using visible light is to apply a two-step photoexcitation mechanism between two different photocatalysts [10], which was inspired by the Z-scheme mechanism of natural photosynthesis in green plants. In this system, the total reaction is broken up into two stages: reactions on a  $H_2$ -evolving photocatalyst and those on an  $O_2$ -evolving photocatalyst; these two photocatalysts are combined using a shuttle redox mediator (Red/Ox) in the

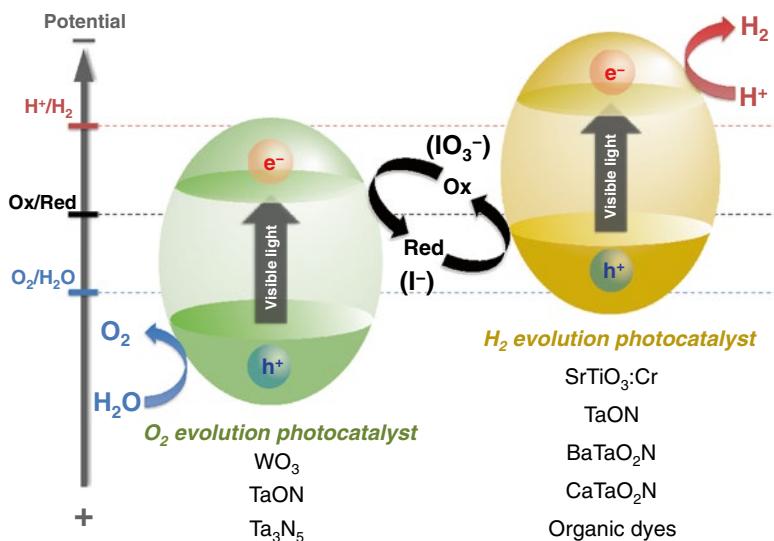


**Fig. 25.3** Overview of water splitting of a Z-scheme photocatalysis with an iodate ( $\text{IO}_3^-$ ) and iodide ( $\text{I}^-$ ) ion redox couple

solution, as illustrated in Fig. 25.3. Over a  $\text{H}_2$ -evolving photocatalyst, the photoexcited electrons in the CB reduce water to  $\text{H}_2$  and the holes generated in the VB oxidize a reductant (Red) to an oxidant (Ox). On the other hand, the Ox produced is reduced back to the Red by photoexcited electrons generated on the  $\text{O}_2$ -evolving photocatalyst, where the holes oxidize water to  $\text{O}_2$ . Introduction of this two-step photoexcitation mechanism can lower the energy required for each photocatalysis, allowing visible light to be utilized more efficiently than in conventional water-splitting systems. For example, visible-light-responsive oxides such as  $\text{WO}_3$  can be used as an  $\text{O}_2$ -evolving photocatalysts if they can reduce an appropriate Ox to a Red. Similarly, some non-oxide semiconductors (e.g., sulfides, oxynitrides, and dyes) can be used as  $\text{H}_2$ -evolving photocatalysts if they can oxidize an appropriate Red to an Ox.

In such systems with redox mediator, however, backward reactions readily proceed on the respective photocatalysis processes and consequently suppress the desired gas ( $\text{H}_2$  or  $\text{O}_2$ ) evolution (see Fig. 25.4). For example, on the  $\text{H}_2$ -evolving photocatalyst, the reduction of Ox to Red (indicated by the broken lines in Fig. 25.4), which is a thermodynamically advantageous backward reaction, tends to proceed preferentially over the water reduction to  $\text{H}_2$ . In contrast, the oxidation of Red to Ox preferentially proceeds by the photogenerated holes on the  $\text{O}_2$  evolving photocatalysts, suppressing  $\text{O}_2$  evolution consequently. Furthermore, it is much more difficult to achieve simultaneous evolution of  $\text{H}_2$  and  $\text{O}_2$  in two-step water-splitting systems in which the two different photocatalysts coexist in an aqueous solution containing both Red and Ox, because the two reactions have different favorable redox concentrations. For example, a high concentration of Red is favorable for the  $\text{H}_2$  evolution

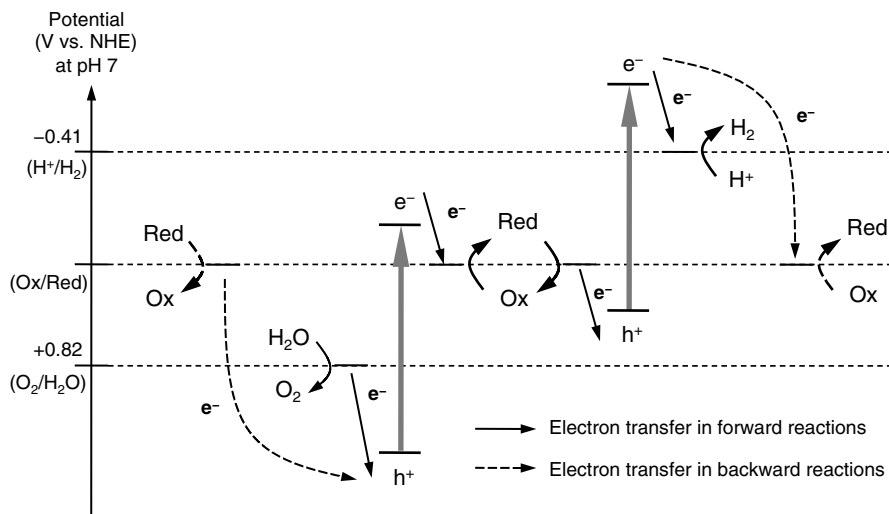


**Fig. 25.4** Forward and backward reactions in the two-step photoexcitation system

photocatalyst, but it causes a significant backward reaction (i.e., reoxidation of Red to Ox) over O<sub>2</sub> evolution photocatalysts, which suppresses O<sub>2</sub> evolution. On the other hand, a high concentration of Ox, which is desirable for the O<sub>2</sub> evolution photocatalyst, reduces the H<sub>2</sub> evolution rate. To realize a Z-scheme water splitting, it is thus necessary to develop a photocatalytic system that has a high selectivity for the forward reactions (H<sub>2</sub> or O<sub>2</sub> evolution, indicated by the solid lines in Fig. 25.4). Rational design of “nanostructured” reaction sites, as well as utilization of unique adsorption property of redox ions, was demonstrated to be the effective way for suppressing such backward reactions on photocatalysts, which will be introduced in subsequent chapters.

## 25.4 Z-Scheme Water-splitting Systems Using Two Different Photocatalysts in the Presence of Iodate/Iodide (IO<sub>3</sub><sup>-</sup>/I<sup>-</sup>) Redox Couple as Electron Shuttle

We demonstrated water splitting under visible light for the first time in 2001 using a Z-scheme photocatalytic system that consists of SrTiO<sub>3</sub> doped with Cr and Ta (denoted as SrTiO<sub>3</sub>:Cr/Ta) as H<sub>2</sub>-evolving photocatalyst, WO<sub>3</sub> as O<sub>2</sub>-evolving photocatalyst, and iodate/iodide (IO<sub>3</sub><sup>-</sup>/I<sup>-</sup>) redox couple as electron shuttle [6]. Prior to that, Z-scheme photocatalytic water splitting had been demonstrated using a combination of Pt-loaded anatase TiO<sub>2</sub> and bare rutile TiO<sub>2</sub> photocatalysts in the presence of IO<sub>3</sub><sup>-</sup>/I<sup>-</sup> shuttle redox [11]. Although this system could operate only under UV light ( $\lambda < 400$  nm) due to the large band gaps of the TiO<sub>2</sub> photocatalysts, it has constructed

a path to achieve water splitting under visible light. The key was controlling the reactivity of electrons and holes with a redox mediator ( $\text{IO}_3^-$  and  $\text{I}^-$  anions) and water molecules, by taking advantage of unique adsorption properties of these anions on the surface of photocatalysts [12–14].

### 25.4.1 Selective Water Oxidation on $\text{WO}_3$ Photocatalyst Using $\text{IO}_3^-$ as Electron Acceptor Under Visible Light Irradiation

As mentioned above, it was quite difficult to achieve simultaneous evolution of  $\text{H}_2$  and  $\text{O}_2$  in two-step water-splitting systems (Z-scheme) due to the preferential occurrence of undesirable backward reactions of the redox mediator, which suppress the desired forward reactions ( $\text{H}_2$  and  $\text{O}_2$  evolutions). Although some combinations of a photocatalyst and a redox mediator have been demonstrated to generate either  $\text{H}_2$  or  $\text{O}_2$  under UV or visible light irradiation, the gas evolution readily terminated during the reaction due to the backward reaction in most cases. However, we found that efficient and selective  $\text{O}_2$  evolution could proceed over rutile  $\text{TiO}_2$  and  $\text{PtO}_x$ -loaded  $\text{WO}_3$  photocatalysts in an aqueous solution containing  $\text{IO}_3^-$  anions as electron acceptors (Ox) according to the following reactions [6, 12–14]:

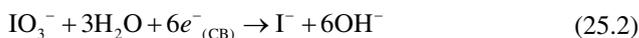
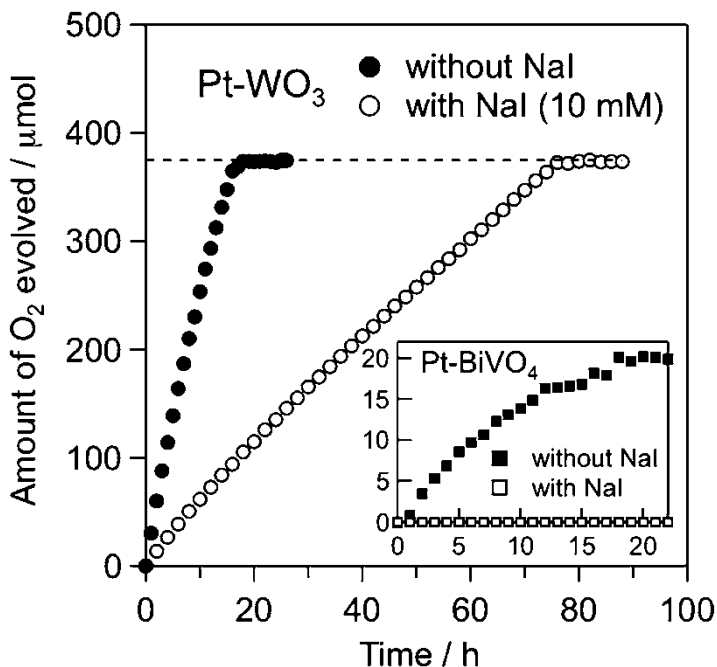
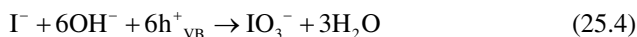


Figure 25.5, for example, shows the time courses of  $\text{O}_2$  evolution on  $\text{PtO}_x$ - $\text{WO}_3$  photocatalyst suspended in an aqueous solution of  $\text{NaIO}_3$  under visible light irradiation ( $\lambda > 410$  nm, 300 W Xe lamp with L-42 cut-off filter), along with those on  $\text{PtO}_x$ - $\text{BiVO}_4$  photocatalyst (inset). The  $\text{O}_2$  evolution on  $\text{PtO}_x$ - $\text{WO}_3$  photocatalyst proceeded at an almost constant rate and continued until the total amount of  $\text{O}_2$  reached 375  $\mu\text{mol}$ . The amount of evolved  $\text{O}_2$  (375  $\mu\text{mol}$ ) agrees with the stoichiometric value (obtained from Eqs. 25.2 and 25.3) expected from the amount of  $\text{IO}_3^-$  (250  $\mu\text{mol}$ ) added to the solution before irradiation. Interestingly, the  $\text{O}_2$  evolution on  $\text{PtO}_x$ - $\text{WO}_3$  proceeded with a constant rate even when the reaction was initiated in the coexistence of considerable amount of  $\text{NaI}$  (10 mM), ten times higher than that of  $\text{NaIO}_3$  (1 mM). Such behavior of  $\text{PtO}_x$ - $\text{WO}_3$  (and rutile  $\text{TiO}_2$ ) is quite unique from a thermodynamic viewpoint. The oxidation of water, which is thermodynamically less favorable than the oxidation of  $\text{I}^-$ , proceeded preferentially over these photocatalysts even in the presence of considerable amount of  $\text{I}^-$ . On the other hand, the addition of a certain amount of  $\text{I}^-$  to the solution completely suppressed  $\text{O}_2$  evolution over  $\text{PtO}_x$ - $\text{BiVO}_4$  photocatalysts (see inset of Fig. 25.5, for example), indicating the preferential occurrence of backward reaction (oxidation of  $\text{I}^-$ ) in place of  $\text{O}_2$  evolution.



**Fig. 25.5** Time course of photocatalytic O<sub>2</sub> evolution over PtO<sub>x</sub>(0.5 wt%)/WO<sub>3</sub> and PtO<sub>x</sub>(0.5 wt%)/BiVO<sub>4</sub> (inset) suspended in an aqueous solution (250 mL, pH 6.5 without adjustment) containing only NaIO<sub>3</sub> (0.25 mmol) or containing both NaIO<sub>3</sub> (0.25 mmol) and NaI (2.5 mmol)

The unique selectivity of the PtO<sub>x</sub>-WO<sub>3</sub> (as well as rutile TiO<sub>2</sub>) for O<sub>2</sub> evolution can be reasonably explained by the different adsorption properties of IO<sub>3</sub><sup>-</sup> and I<sup>-</sup> anions on the photocatalyst surfaces [14]. Interestingly, IO<sub>3</sub><sup>-</sup> ions exclusively adsorb on the surface of WO<sub>3</sub> particles as clearly seen in Fig. 25.6a; no adsorption of I<sup>-</sup> ions was observed (below the detection limit). The facile adsorption of IO<sub>3</sub><sup>-</sup> anions undoubtedly facilitate the reduction of IO<sub>3</sub><sup>-</sup> into I<sup>-</sup> by the photoexcited electrons on WO<sub>3</sub> (dominantly on the PtO<sub>x</sub> cocatalysts and/or the interfaces with WO<sub>3</sub>). Meanwhile, photogenerated holes can preferentially react with H<sub>2</sub>O molecules to produce O<sub>2</sub> on the bare surface of WO<sub>3</sub> because the rate of I<sup>-</sup> oxidation, which competes with water oxidation, is low due to the negligible adsorptivity of I<sup>-</sup> ions on the surface of WO<sub>3</sub>, as illustrated in Fig. 25.7a. In contrast, both IO<sub>3</sub><sup>-</sup> and I<sup>-</sup> ions adsorbed on the surface of BiVO<sub>4</sub> particles (see Fig. 25.6b), while IO<sub>3</sub><sup>-</sup> showed a higher adsorptivity than I<sup>-</sup> at higher concentrations. The appreciable adsorption of I<sup>-</sup> anions on BiVO<sub>4</sub> particles is undoubtedly responsible for the preferential oxidation of I<sup>-</sup> to IO<sub>3</sub><sup>-</sup> (or I<sub>3</sub><sup>-</sup>), which is thermodynamically more favorable than water oxidation, by photogenerated holes and for completely suppressing oxidation of water to O<sub>2</sub>, as depicted in Fig. 25.7b.



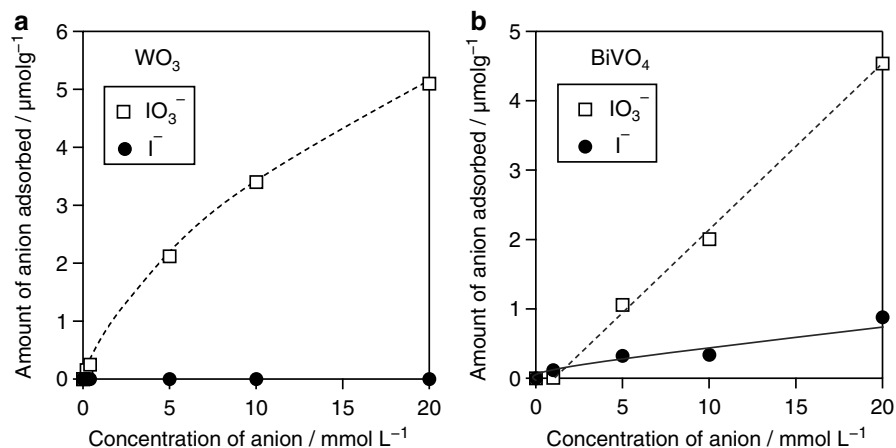


Fig. 25.6 Adsorption properties of iodate ( $\text{IO}_3^-$ ) and iodide ( $\text{I}^-$ ) anions on  $\text{WO}_3$  and  $\text{BiVO}_4$  powders

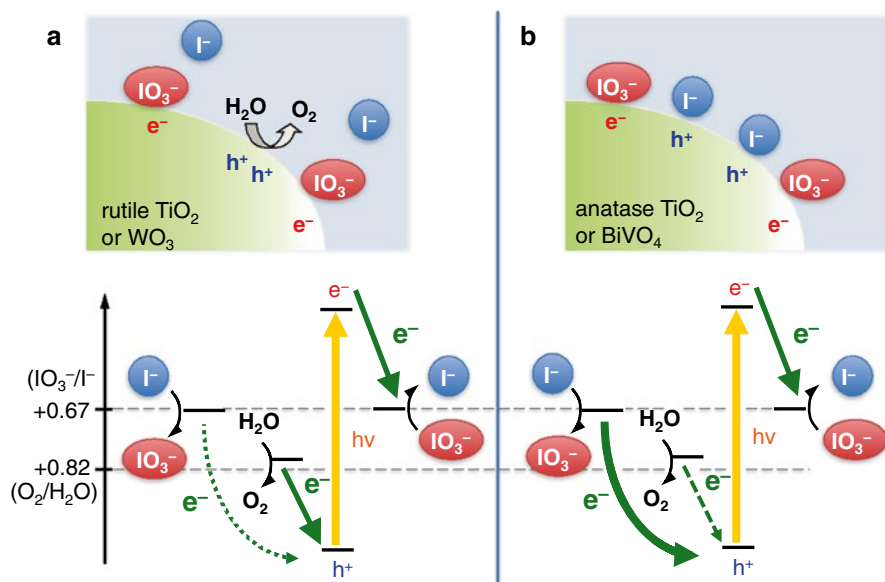
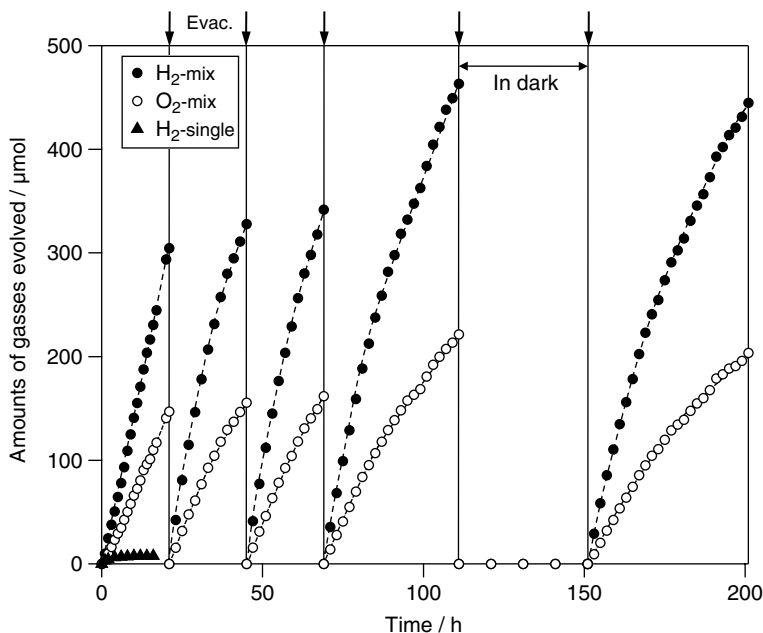


Fig. 25.7 Schematic illustration of photocatalytic reactions of iodate ( $\text{IO}_3^-$ ) and iodide ( $\text{I}^-$ ) anions

The different reactivity of anatase and rutile  $\text{TiO}_2$  samples was also reasonably explained by the adsorption properties of  $\text{IO}_3^-$  and  $\text{I}^-$  anions on them. The rutile  $\text{TiO}_2$  samples that exclusively adsorbed  $\text{IO}_3^-$  were able to generate  $\text{O}_2$  efficiently even in the coexistence of  $\text{IO}_3^-$  and  $\text{I}^-$ , whereas the anatase ones could not due to the significant occurrence of backward reaction (preferential oxidation of  $\text{I}^-$  instead of water).

### 25.4.2 Simultaneous Evolution of H<sub>2</sub> and O<sub>2</sub> Under Visible Light Irradiation Using a Combinations of SrTiO<sub>3</sub>:Cr/Ta and WO<sub>3</sub> Photocatalysts

Based on the above results on the selective O<sub>2</sub> evolution using rutile TiO<sub>2</sub> and PtO<sub>x</sub>-WO<sub>3</sub> photocatalysts with IO<sub>3</sub><sup>-</sup>/I<sup>-</sup> redox couple, we first constructed UV-responsive Z-scheme water-splitting systems by employing Pt-loaded anatase TiO<sub>2</sub> as H<sub>2</sub>-evolving photocatalysts, which was able to generate H<sub>2</sub> in the presence of I<sup>-</sup> electron donor accompanied by production of IO<sub>3</sub><sup>-</sup> (or I<sub>3</sub><sup>-</sup>, depending on pH of solution) under UV light [11, 12, 14]. A visible-light-driven water-splitting system was then constructed by employing the same strategy. A strontium titanate co-doped with Cr and Ta (SrTiO<sub>3</sub>:Cr/Ta [15] was found to be active for both H<sub>2</sub> and IO<sub>3</sub><sup>-</sup> production from an aqueous NaI solution under visible light irradiation ( $\lambda > 410$  nm). Although the single use of Pt-SrTiO<sub>3</sub>:Cr/Ta photocatalyst resulted in significant decrease in H<sub>2</sub> evolution rate with irradiation time due to the backward reaction (re-reduction of IO<sub>3</sub><sup>-</sup> to I<sup>-</sup> by photoexcited electrons), the combination of Pt-SrTiO<sub>3</sub>:Cr/Ta with PtO<sub>x</sub>-WO<sub>3</sub> photocatalysts afforded simultaneous evolution of H<sub>2</sub> and O<sub>2</sub> (initial H<sub>2</sub> rate: 16  $\mu\text{mol h}^{-1}$ , initial O<sub>2</sub> rate: 8  $\mu\text{mol h}^{-1}$ ) from an aqueous NaI solution under visible light irradiation ( $\lambda > 410$  nm), as shown in Fig. 25.8.



**Fig. 25.8** Time course of photocatalytic evolution of H<sub>2</sub> and O<sub>2</sub> using a mixture of Pt(0.3 wt%)/SrTiO<sub>3</sub> (Cr, Ta 4 mol% doped) and Pt(0.5 wt%)/WO<sub>3</sub> photocatalysts suspended in 5 mM of NaI aqueous solution (pH 6.5 without adjustment) under visible light irradiation ( $\lambda > 420$  nm). Triangles indicate H<sub>2</sub> evolution using Pt/SrTiO<sub>3</sub>:Cr/Ta alone

The reaction proceeded with no noticeable deactivation, even for long irradiation times. The total amount of H<sub>2</sub> gas evolved reached ca. 1.9 mmol, exceeding the stoichiometric amounts of the photocatalysts (SrTiO<sub>3</sub>:Cr/Ta: 1.1 mmol, WO<sub>3</sub>: 1.4 mmol) and I<sup>-</sup> (1.25 mmol) in the solution. No gas evolution was observed in the absence of redox. These results demonstrate that overall water splitting proceeds by a two-step photoexcitation (Z-scheme) mechanism combined with a redox cycle between IO<sub>3</sub><sup>-</sup> and I<sup>-</sup>. The first step involves reduction of water to H<sub>2</sub> and oxidation of I<sup>-</sup> to IO<sub>3</sub><sup>-</sup> over Pt-SrTiO<sub>3</sub>:Cr/Ta photocatalyst, while the second step involves reduction of IO<sub>3</sub><sup>-</sup> to I<sup>-</sup> and oxidation of water to O<sub>2</sub> over PtO<sub>x</sub>-WO<sub>3</sub> photocatalyst. This was the first demonstration of water splitting into H<sub>2</sub> and O<sub>2</sub> under visible light irradiation. It represents one of the most important technical breakthroughs in the field of photocatalytic water splitting.

### 25.4.3 Application of Tantalum Oxynitrides as H<sub>2</sub> Evolution Photocatalysts

As described above, photocatalytic water splitting under visible light was successfully demonstrated by using a doped oxide, SrTiO<sub>3</sub>:Cr/Ta, as the H<sub>2</sub>-evolving photocatalyst together with WO<sub>3</sub>. However, few metal oxide semiconductors have both a high visible light absorption and a sufficiently high potential for H<sub>2</sub> evolution, because of the highly positive valence bands formed by O 2p orbitals [7], as described in a previous section. Domen et al. have reported that some metal oxynitride (e.g., TaON, BaTaO<sub>2</sub>N, and LaTiO<sub>2</sub>N) or nitride (e.g., Ta<sub>3</sub>N<sub>5</sub>) powder photocatalysts exhibit activity for H<sub>2</sub> production from water in the presence of a sacrificial electron donor such as methanol under visible light irradiation [16]. Because N 2p orbitals have higher energy levels than O 2p orbitals, the VB maximums of metal oxynitrides and nitrides become more negative than that of the corresponding metal oxides. For example, the potential energies of the VB maximums increase in the order Ta<sub>2</sub>O<sub>5</sub> (3.6 V) < TaON (2.0 V) < Ta<sub>3</sub>N<sub>5</sub> (1.6 V vs. SHE), with increased contribution of N 2p orbitals [17]. On the other hand, the CB of these (oxy)nitrides (TaON and Ta<sub>3</sub>N<sub>5</sub>) consist of predominantly empty orbitals of tantalum, resulting in the similar CB minimums to those of the corresponding metal oxide (Ta<sub>2</sub>O<sub>5</sub>) in the range -0.3 to -0.5 V (vs. SHE), which are sufficient for H<sub>2</sub> production. In 2005, we demonstrated water splitting under visible light using tantalum oxynitride (TaON) as a H<sub>2</sub>-evolving photocatalyst in the presence of an IO<sub>3</sub><sup>-</sup>/I<sup>-</sup> shuttle redox mediator, combined with PtO<sub>x</sub>-WO<sub>3</sub> photocatalyst [13, 18]. Then, we also demonstrated water splitting using a series of mixed oxynitrides ATaO<sub>2</sub>N (A = Ca, Sr, Ba) as H<sub>2</sub>-evolving photocatalysts [19, 20]. These mixed tantalum oxynitrides with the perovskite structure can absorb wider range of visible light than others (WO<sub>3</sub> and TaON) as shown in Fig. 25.9, in which the absorption edges of ATaO<sub>2</sub>N shift to longer wavelengths with increasing ionic radius of A<sup>2+</sup> (Ca<sup>2+</sup>: 1.34 Å; Sr<sup>2+</sup>: 1.44 Å; Ba<sup>2+</sup>: 1.61 Å). The Pt-BaTaO<sub>2</sub>N photocatalyst was indeed demonstrated to be photoactive at wavelengths up to 660 nm for H<sub>2</sub> production in Z-scheme system with IO<sub>3</sub><sup>-</sup>/I<sup>-</sup> redox. It

**Fig. 25.9** Diffused reflectance spectra of various (oxy)nitrides and WO<sub>3</sub>

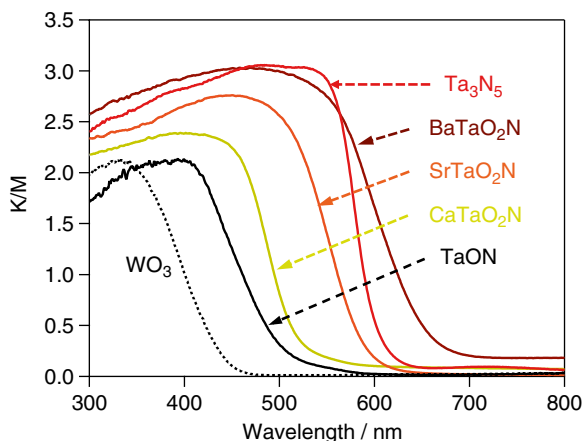
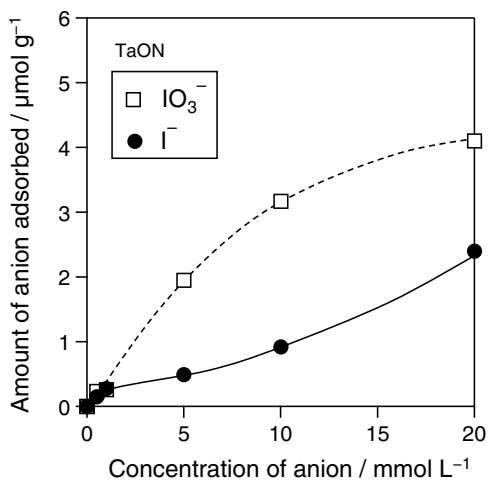


**Fig. 25.10** Adsorption properties of iodate (IO<sub>3</sub><sup>-</sup>) and iodide (I<sup>-</sup>) anions on TaON photocatalyst powder



represented the first example of a water-splitting system that effectively utilizes visible light at wavelengths longer than 600 nm for H<sub>2</sub> evolution.

A further advantage of this system is that the instability of (oxy)nitride materials can be greatly reduced. Some (oxy)nitride materials have been reported to be deactivated through self-oxidative decomposition, whereby nitrogen anions (N<sup>3-</sup>) are oxidized to N<sub>2</sub> by photogenerated holes:



It was confirmed that I<sup>-</sup> ions readily adsorb on the surface of TaON particles as seen in Fig. 25.10, for example. The appreciable adsorption of I<sup>-</sup> ions on TaON enabled the efficient oxidation of I<sup>-</sup> by the photogenerated holes on the TaON photocatalyst and effectively suppressed self-oxidative deactivation of TaON.

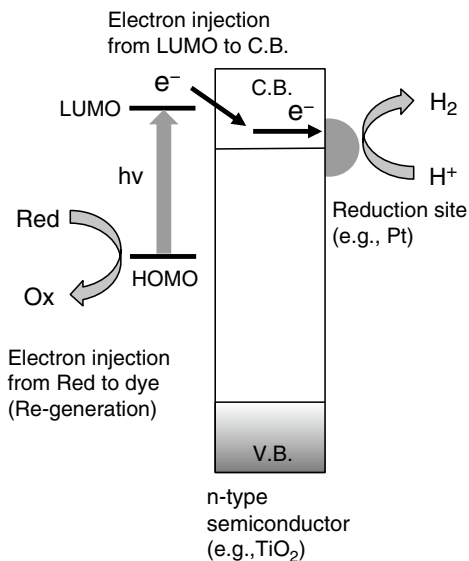
Although the primitive TaON-based Z-scheme system showed a low apparent quantum yield (ca. 0.4 % at 420 nm) [13, 18], an appropriate modification of TaON surface with  $\text{ZrO}_2$  species significantly increased the apparent quantum yield up to 6.3 % at 420 nm [21]. This high performance was explained by the suppression of electron–hole recombination in  $\text{ZrO}_2/\text{TaON}$ , which results from moderation of the n-type semiconducting character of TaON by the formation of a composite with  $\text{ZrO}_2$ . Although (oxy)nitrides have previously been considered to have relatively low efficiency for  $\text{H}_2$  evolution, predominantly due to the high concentration of anion defects generated in the preparation procedure (high temperature treatment in  $\text{NH}_3$  stream), these results suggested a possibility that appropriate surface modification of them will be an effective strategy for achieving efficient water splitting using metal oxynitride photocatalysts.

#### **25.4.4 Application of Surface-Modified Tantalum (Oxy)nitrides to $\text{O}_2$ Evolution Part**

Surface-modified (oxy)nitrides such as  $\text{RuO}_2\text{-TaON}$  and  $\text{Ir/TiO}_2\text{-Ta}_3\text{N}_5$  can also be used as  $\text{O}_2$  photocatalysts in a Z-scheme with an  $\text{IO}_3^-/\Gamma^-$  redox mediator. Because  $\Gamma^-$  anions react preferentially with photogenerated holes over TaON, the  $\text{O}_2$  evolution over the bare TaON photocatalyst was completely suppressed even with a small amount of  $\Gamma^-$ . Thus,  $\text{O}_2$ -evolving cocatalysts such as  $\text{RuO}_2$  and  $\text{IrO}_2$  were loaded on the TaON surface to modify the selectivity of holes to oxidation of water. The loading of the  $\text{RuO}_2$  cocatalyst on TaON was found to enhance  $\text{O}_2$  evolution in the presence of the electron donor  $\Gamma^-$ , which enabled the  $\text{RuO}_2\text{-TaON}$  photocatalyst to be used as an  $\text{O}_2$  photocatalyst in combination with  $\text{Pt-TaON}$  [22]. Structural analyses and (photo)electrochemical measurements revealed that the activity of  $\text{RuO}_2\text{-TaON}$  photocatalyst is strongly dependent on the generation of optimally dispersed  $\text{RuO}_2$  nanoparticles, which simultaneously promote both the reduction of  $\text{IO}_3^-$  and oxidation of water [23]. Modification of  $\text{Ta}_3\text{N}_5$  by Ir metal and rutile  $\text{TiO}_2$  particles also enhanced  $\text{O}_2$  evolution [24]. The combinations ( $\text{Pt-TaON}$ )–( $\text{RuO}_2\text{-TaON}$ ) and ( $\text{Pt-ZrO}_2/\text{TaON}$ )–( $\text{IrTiO}_2/\text{Ta}_3\text{N}_5$ ) permitted water splitting over a wider wavelength range of visible light (TaON: 500 nm,  $\text{Ta}_3\text{N}_5$ : 600 nm) than systems using  $\text{WO}_3$  (absorption edge of 450 nm) as the  $\text{O}_2$  photocatalyst.

We have recently demonstrated that the loading of nanoparticulate  $\text{IrO}_x$  or  $\text{CoO}_x$  cocatalysts on tantalum oxynitride photoanodes significantly improves both the photocurrent and the stability for photoelectrochemical water oxidation [25–27]. Especially, highly dispersed  $\text{CoO}_x$  nanoparticles on the porous TaON photoanodes were proven to efficiently scavenge photogenerated holes and effectively suppress the self-oxidative deactivation of the TaON surface, affording stable photocurrent corresponding to  $\text{O}_2$  evolution for long time [26]. We also demonstrated that the co-loading of  $\text{RhO}_x$  and  $\text{CoO}_x$  nanoparticles further enhanced photocurrent, as well as stability, on  $\text{BaTaO}_2\text{N}$  photoanodes, along with an obvious negative shift of onset potential for water oxidation, while sole loading resulted in a lower photocurrent or

**Fig. 25.11** Conceptual scheme of H<sub>2</sub> production over dye-sensitized n-type semiconductor



insufficient stability [27]. It was strongly suggested that the RhO<sub>x</sub> species acted as a facilitator of hole transfer between the BaTaO<sub>2</sub>N surface and CoO<sub>x</sub>, whereas water oxidation dominantly proceeded on the water oxidation cocatalyst CoO<sub>x</sub>. These results demonstrated the potential of metal (oxy)nitride semiconductors as stable and efficient photoanodes and/or photocatalysts by applying appropriate surface modifications with functional nanoparticles.

## 25.5 Robust Dye Sensitized Semiconductor with Nanostructured Reaction Site as H<sub>2</sub> Evolution Photocatalyst for Z-Scheme Water-Splitting System

Although water splitting under visible light has been achieved using various pairs of photocatalysts in the presence of an electron mediator IO<sub>3</sub><sup>-</sup>/I<sup>-</sup>, there are still a limited number of suitable photocatalysts, primarily due to the difficulty in tuning the band levels of inorganic (particularly oxide) semiconductor materials. On the other hand, it is relatively easy to fine tune the energy levels (HOMO and LUMO) of organic materials such as dye molecules, as has been demonstrated for dye-sensitized solar cells. Studies on dye-sensitized solar cells have revealed that various organic dyes possess both a sufficiently negative LUMO for electron injection to the conduction band of TiO<sub>2</sub> and a sufficiently positive HOMO to oxidize I<sup>-</sup> to I<sub>3</sub><sup>-</sup> in an organic solvent such as acetonitrile. Thus, dye-sensitized n-type semiconductors (e.g., TiO<sub>2</sub>) appear to be a promising H<sub>2</sub>-evolving photocatalyst with I<sub>3</sub><sup>-</sup>/I<sup>-</sup> redox couple. However, the instability of the oxidized states of conventional organic

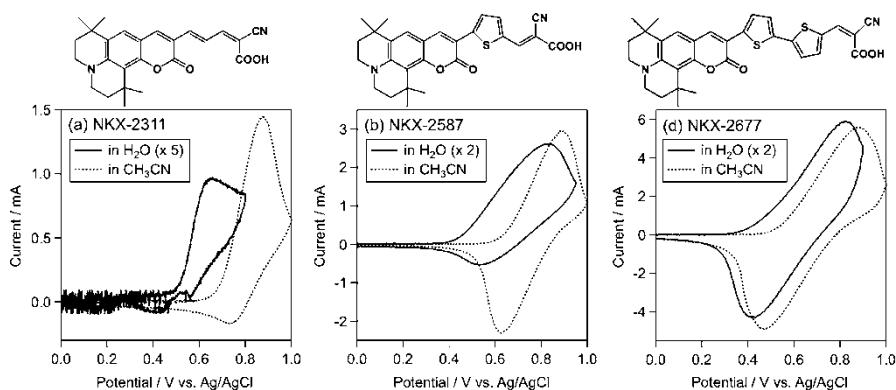


**Fig. 25.12** CV curves of coumarin dyes absorbed on a porous TiO<sub>2</sub> electrode in a dehydrated acetonitrile (AN) or aqueous solution containing 0.1 M of LiClO<sub>4</sub> as a supporting electrolyte: the scan rate was 100 mV s<sup>-1</sup>. Ag/AgCl in saturated aqueous NaCl solution and Ag/Ag<sup>+</sup> in 0.01 M AgNO<sub>3</sub> acetonitrile solution were used as a reference electrode in aqueous and AN solutions, respectively

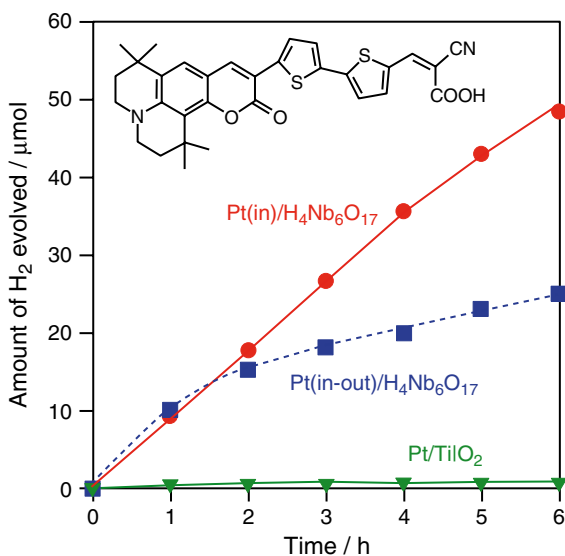
dye molecules in water have been making it difficult to achieve steady H<sub>2</sub> production with reversible electron donor such as I<sup>-</sup>. Figure 25.11 depicts the H<sub>2</sub> production processes over a dye-sensitized n-type semiconductor. An electron is excited from HOMO to LUMO by light absorption, injected into the conduction band of the semiconductor, and then consumed for H<sub>2</sub> production at a reduction site such as a Pt cocatalyst. The oxidized state of the dye, radical species in the most cases, can be regenerated to the ground state if it accepts an electron from an appropriate electron donor (Red). However, it has been proven that the lifetime of such radical species in aqueous solutions is generally too short to be regenerated by electron injection from reversible electron donors such as I<sup>-</sup>, resulting in irreversible reaction with water molecules to form inactive species.

As a simple but effective solution, we have demonstrated that the introduction of an oligothiophene moiety between the donor and acceptor parts of organic dyes drastically improved the stability of their oxidized species in water [28, 29]. For example, Fig. 25.12 shows the C–V profiles of coumarin dyes in water and in a dehydrated AN solution. In all cases, a current peak was observed when an anodic potential of over +0.4 V (vs. reference) was applied, which indicates oxidation of the dye molecule (S) to an oxidized state (S<sup>+</sup>). On the other hand, the reduction behavior strongly depended on the structure of the dye molecule. For NKX-2311, which does not have a thiophene ring, the reduction current peak was much lower than the oxidation peak even in AN and no reduction peak was observed in water. Although reversible behavior was observed for NKX-2587 in AN, the reduction current peak was much lower than the oxidation peak in water. These results indicate that the oxidized state of these dyes (NKX-2311 and NKX-2587) reacted with H<sub>2</sub>O molecules irreversibly and formed inactive species. On the other hand, a reversible current peak was observed in NKX-2677 during reverse cathodic scanning in both solvents, indicating that, even in water, the oxidized state (S<sup>+</sup>) has a relatively

long lifetime and can be reduced back to its original state by accepting an electron during sweeping of the cathode potential. Based on the molecular structures of the coumarin dyes examined, it is concluded that thiophene moieties (especially oligothiophene, which has two or more thiophene rings) play a significant role in stabilizing the oxidized states of the dyes in water. Kato et al. have examined the effect of light irradiation on the dyes adsorbed on nanocrystalline TiO<sub>2</sub> films under ambient conditions and found that dyes (not just coumarin dyes) containing an oligothiophene moiety are more stable than those without an oligothiophene moiety [30]. Transient absorption spectroscopy strongly implies that the positive charge in such dyes is located on the oligothiophene moiety. Therefore, the most likely explanation for the necessity of an oligothiophene moiety in the water-splitting reaction with I<sub>3</sub><sup>-</sup>/I<sup>-</sup> redox is that the positive charge of the oxidized dye is delocalized over the oligothiophene moiety reducing its reactivity toward H<sub>2</sub>O, while it can accept an electron from an I<sup>-</sup> anion thereby regenerating the original ground state of the dye. Indeed, the coumarin and carbazole dyes having oligothiophene moiety were demonstrated to generate H<sub>2</sub> stably from an aqueous potassium iodide (KI) solution under visible light irradiation, accompanied by stoichiometric production of I<sub>3</sub><sup>-</sup> in the solution as an oxidation product of I<sup>-</sup>, when combined with appropriate n-type semiconductors [28, 29].

“Nanostructured” reduction sites were successfully introduced to control the reaction selectivity of electrons and thus achieve steady water splitting on the dye-sensitized systems. As shown in Fig. 25.13 for example, H<sub>2</sub> evolution over NKX-2677-adsorbed Pt/TiO<sub>2</sub> terminated rapidly due to a significant backward reaction (reduction of I<sub>3</sub><sup>-</sup> to I<sup>-</sup>) on the Pt particles. In order to achieve steady H<sub>2</sub>, an internally platinized layered niobate, Pt(in)/H<sub>4</sub>Nb<sub>6</sub>O<sub>17</sub>, was applied as an n-type semiconductor instead of Pt/TiO<sub>2</sub>. As shown in Fig. 25.13, H<sub>2</sub> evolution proceeded with

**Fig. 25.13** Time courses of photocatalytic H<sub>2</sub> evolution under visible light ( $\lambda > 410$  nm) on NKX-2677 dye-adsorbed Pt(in)/H<sub>4</sub>Nb<sub>6</sub>O<sub>17</sub>, Pt(in-out)/H<sub>4</sub>Nb<sub>6</sub>O<sub>17</sub>, and Pt/TiO<sub>2</sub> photocatalysts suspended in 0.1 M aqueous KI solution (pH~6.5, without adjustment)



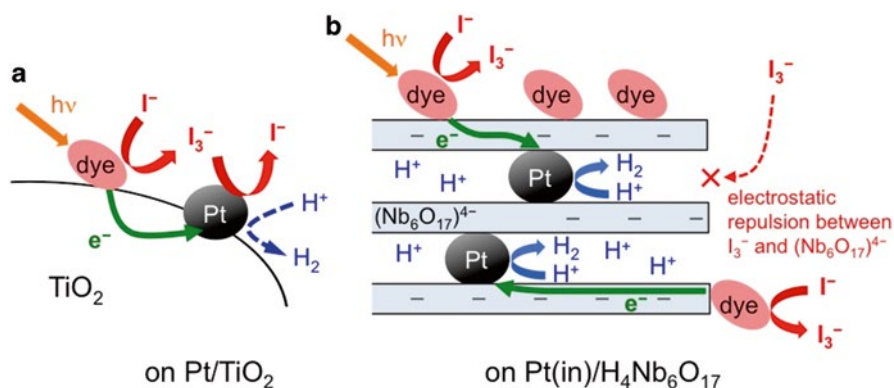


**Fig. 25.14** Conceptual schemes for suppression of backward reaction using nanostructured layered semiconductors

a steady rate over NKX-2677-adsorbed Pt(in)/H<sub>4</sub>Nb<sub>6</sub>O<sub>17</sub> from an aqueous solution containing I<sup>-</sup> electron donor under visible light irradiation. Since I<sub>3</sub><sup>-</sup> anions are unable to access the Pt particles inside due to the electrostatic repulsion between the anionic I<sub>3</sub><sup>-</sup> and the negatively charged (Nb<sub>6</sub>O<sub>17</sub>)<sup>4-</sup> layers, the backward reduction of I<sub>3</sub><sup>-</sup> to I<sup>-</sup> can be effectively suppressed (see Fig. 25.14). When Pt cocatalysts were loaded both in the interlayers and on the outlayers of H<sub>4</sub>Nb<sub>6</sub>O<sub>17</sub> [Pt(in-out)/H<sub>4</sub>Nb<sub>6</sub>O<sub>17</sub>], the rate of H<sub>2</sub> evolution gradually decreased, undoubtedly due to the occurrence of backward reduction of I<sub>3</sub><sup>-</sup> on the outer Pt particles. As shown in Fig. 25.15, the combination of NKX-2677-adsorbed Pt(in)/H<sub>4</sub>Nb<sub>6</sub>O<sub>17</sub> and IrO<sub>2</sub>-Pt/WO<sub>3</sub> resulted in simultaneous evolution of H<sub>2</sub> and O<sub>2</sub> in an almost stoichiometric ratio. The reaction proceeded without appreciable deactivation even after photoirradiation for 48 h. The total amount of evolved H<sub>2</sub> (ca. 116 μmol) exceeded the amount of dye molecules adsorbed on Pt/H<sub>4</sub>Nb<sub>6</sub>O<sub>17</sub> (ca. 0.55 μmol). On the other hand, the rate of gas evolution using NKX-2587 (which has one thiophene ring) decreased drastically with increasing irradiation time, as Fig. 25.14 shows. In the case of the NKX-2311 dye, which has no thiophene ring, only a small amount of H<sub>2</sub> was evolved during the initial period. These results again indicate that the oligothiophene moiety plays an essential role in stabilizing dye molecules during photocatalytic water splitting.

## 25.6 Concluding Remarks

A novel photocatalytic system that splits water into H<sub>2</sub> and O<sub>2</sub> was realized using a two-step photoexcitation system composed of a shuttle redox couple and two different semiconductor photocatalysts. We have first demonstrated water splitting based on the two-step photoexcitation process under UV light by using Pt-loaded anatase TiO<sub>2</sub> as the H<sub>2</sub> photocatalyst together with rutile TiO<sub>2</sub> for O<sub>2</sub> evolution in the presence of IO<sub>3</sub><sup>-</sup>/I<sup>-</sup> redox mediator. Although this system operates only under UV light ( $\lambda < 400$  nm)

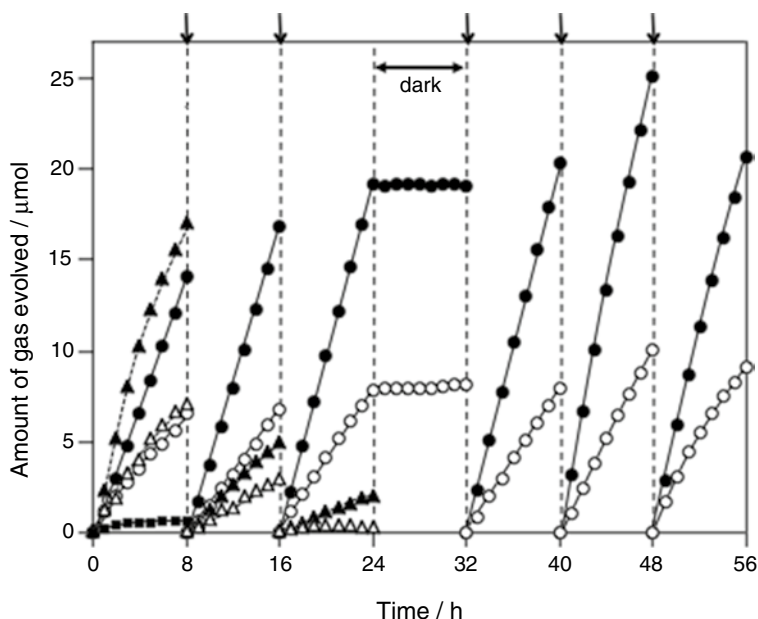


**Fig. 25.15** Time courses of photocatalytic evolution of H<sub>2</sub> (closed) and O<sub>2</sub> (open) using a mixture of coumarin dye-sensitized (circles: NKX2677, triangles: NKX 2587, square: NKX2311) Pt/H<sub>4</sub>Nb<sub>6</sub>O<sub>17</sub> (50 mg) and IrO<sub>2</sub>-Pt/WO<sub>3</sub> (100 mg) suspended in a 5 mM of KI aqueous solution under visible light ( $\lambda > 400$  nm). Arrows indicate evacuation of gas phase

due to the large band gap of the TiO<sub>2</sub> photocatalysts, it opened the way to achieve water splitting under visible light. The key was controlling the reactivity of electrons and holes with a redox mediator (IO<sub>3</sub><sup>-</sup> and I<sup>-</sup> anions) and water molecules. We have then achieved overall water splitting using various visible-light-responsive photocatalysts, such as SrTiO<sub>3</sub> doped with Cr, tantalum oxynitrides (TaON or BaTaO<sub>2</sub>N), and organic dyes, which work as H<sub>2</sub> evolution photocatalysts, combined with tungsten oxide (WO<sub>3</sub>) for O<sub>2</sub> evolution in the presence of a shuttle redox mediator such as iodate/iodide (IO<sub>3</sub><sup>-</sup>/I<sup>-</sup>) or triiodide/iodide (I<sub>3</sub><sup>-</sup>/I<sup>-</sup>). Although photocatalytic water splitting using visible light had been regarded as a kind of “dream reaction” for long time, it has indeed been demonstrated in several heterogeneous photocatalytic systems over the last decade. Although the introduction of Z-scheme water-splitting systems has significantly extended the available wavelengths (~700 nm for H<sub>2</sub> evolution and ~600 nm for O<sub>2</sub> evolution), the quantum efficiency (~6 %) is still too low to achieve practically high efficiency for H<sub>2</sub> production. New strategies for achieving efficient separation of electrons and holes in powdered semiconductor photocatalysts are highly desirable. Another technical challenge is the construction of a system that can generate H<sub>2</sub> separately from O<sub>2</sub> to minimize the danger of explosions. The Z-scheme photocatalytic systems have the potential to be used in such separated water-splitting systems. Such an achievement will help solve global energy and environmental problems toward the realization of a sustainable society.

## References

1. Fujishima A, Honda K (1972) Electro photolysis of water at a semiconductor electrode. *Nature* 238:37–38
2. Kudo A, Miseki Y (2009) Heterogeneous photocatalyst materials for water splitting. *Chem Soc Rev* 38:253–278
3. Abe R (2010) Recent progress on photocatalytic and photoelectrochemical water splitting under visible light irradiation. *J Photochem Photobiol C Photochem Rev* 11:179–209
4. Domen K, Naito S, Soma M, Onishi T, Tamaru K (1980) Photocatalytic decomposition of water vapor on an NiO–SrTiO<sub>3</sub> catalyst. *J Chem Soc Chem Commun* 1980:543–554
5. Kato K, Asakura K, Kudo A (2001) Highly efficient water splitting into H<sub>2</sub> and O<sub>2</sub> over lanthanum-doped NaTaO<sub>3</sub> photocatalysts with high crystallinity and surface nanostructure. *J Am Chem Soc* 125:3082–3089
6. Sayama K, Mukasa K, Abe R, Abe Y, Arakawa H (2001) Stoichiometric water splitting into H<sub>2</sub> and O<sub>2</sub> using a mixture of two different photocatalysts and an IO<sub>3</sub><sup>-</sup>/I<sup>-</sup> shuttle redox mediator under visible light irradiation. *Chem Commun* 2001:2416–2417
7. Scaife DE (1980) Oxide semiconductors in photoelectrochemical conversion of solar energy. *Sol Energ* 25:41–54
8. Maeda K, Takata T, Hara M, Saito N, Inoue Y, Kobayashi H, Domen K (2005) GaN:ZnO solid solution as a photocatalyst for visible-light-driven overall water splitting. *J Am Chem Soc* 127:8286–8287
9. Maeda K, Teramura K, Lu D, Takata T, Saito N, Inoue Y, Domen K (2006) Photocatalyst releasing hydrogen from water. *Nature* 440(295)
10. Bard AJ (1979) Photoelectrochemistry and heterogeneous photocatalysis at semiconductors. *J Photochem* 10:59–75
11. Abe R, Sayama K, Domen K, Arakawa H (2001) A new type of water splitting system composed of two different TiO<sub>2</sub> photocatalysts (anatase and rutile) and IO<sub>3</sub><sup>-</sup>/I<sup>-</sup> shuttle redox mediator. *Chem Phys Lett* 344:339–344
12. Abe R, Sayama K, Sugihara H (2005) Development of new photocatalytic water splitting into H<sub>2</sub> and O<sub>2</sub> using two different semiconductor photocatalysts and a shuttle redox mediator IO<sub>3</sub><sup>-</sup>/I<sup>-</sup>. *J Phys Chem B* 109:16052–16061
13. Abe R, Higashi M, Domen K (2011) Overall water splitting under visible light through two-step photoexcitation between TaON and WO<sub>3</sub> in the presence of an iodate/iodide shuttle redox mediator. *ChemSusChem* 4:228–237
14. Abe R (2011) Development of a new system for photocatalytic water splitting into H<sub>2</sub> and O<sub>2</sub> under visible light irradiation. *Bull Chem Soc Jpn* 84:1000–1030, Award account
15. Ishii T, Kato H, Kudo A (2004) H<sub>2</sub> evolution from an aqueous methanol solution on SrTiO<sub>3</sub> photocatalysts codoped with chromium and tantalum ions under visible light irradiation. *J Photochem Photobiol A Chem* 163:181–186
16. Hitoki G, Takata T, Kondo JN, Hara M, Kobayashi H, Domen K (2002) (Oxy)nitrides as new photocatalysts for water splitting under visible light irradiation. *Electrochemistry* 70:463–465
17. Chun WJ, Ishikawa A, Fujisawa H, Takata T, Kondo JN, Hara M, Kawai M, Matsumoto Y, Domen K (2003) Conduction and valence band positions of Ta<sub>2</sub>O<sub>5</sub>, TaON, and Ta<sub>3</sub>N<sub>5</sub> by UPS and electrochemical methods. *J Phys Chem B* 107:1798–1803
18. Abe R, Takata T, Sugihara H, Domen K (2005) Photocatalytic overall water splitting under visible light irradiation by TaON and WO<sub>3</sub> with an IO<sub>3</sub><sup>-</sup>/I<sup>-</sup> shuttle redox mediator. *Chem Commun* 2005:3829–3831
19. Higashi M, Abe R, Teramura K, Takata T, Ohtani B, Domen K (2008) Two step water splitting into H<sub>2</sub> and O<sub>2</sub> under visible light by ATaO<sub>2</sub>N (A=Ca, Sr, Ba) and WO<sub>3</sub> with IO<sub>3</sub><sup>-</sup>/I<sup>-</sup> shuttle redox mediator. *Chem Phys Lett* 452:120–123
20. Higashi M, Abe R, Takata T, Domen K (2009) Photocatalytic overall water splitting under visible light using ATaO<sub>2</sub>N (A=Ca, Sr, Ba) and WO<sub>3</sub> in a IO<sub>3</sub><sup>-</sup>/I<sup>-</sup> shuttle redox mediated system. *Chem Mater* 21:1543–1549

21. Maeda K, Higashi M, Lu D, Abe R, Domen K (2010) Efficient nonsacrificial water splitting through two-step photoexcitation by visible light using a modified oxynitride as a hydrogen evolution photocatalyst. *J Am Chem Soc* 132:5858–5868
22. Higashi M, Abe R, Ishikawa A, Takata T, Ohtani B, Domen K (2008) Z-scheme overall water splitting on modified-TaON photocatalysts under visible light ( $\lambda < 500$  nm). *Chem Lett* 37:138–139
23. Maeda K, Abe R, Domen K (2011) Role and function of ruthenium species as promoters with TaON-based photocatalysts for oxygen evolution in two-step water splitting under visible light. *J Phys Chem C* 115:3057–3064
24. Tabata M, Maeda K, Higashi M, Lu D, Takata T, Abe R, Domen K (2010) Modified Ta<sub>3</sub>N<sub>5</sub> powder as a photocatalyst for O<sub>2</sub> evolution in a two-step water splitting system with an iodate/iodide shuttle redox mediator under visible light. *Langmuir* 26:9161–9165
25. Abe R, Higashi M, Domen K (2010) Facile fabrication of an efficient oxynitride TaON photoanode for overall water splitting into H<sub>2</sub> and O<sub>2</sub> under visible light irradiation. *J Am Chem Soc* 132:11828–11829
26. Higashi M, Domen K, Abe R (2012) Highly stable water splitting on oxynitride TaON photoanode system under visible light irradiation. *J Am Chem Soc* 134:6968–6971
27. Higashi M, Domen K, Abe R (2013) Fabrication of an efficient BaTaO<sub>2</sub>N photoanode harvesting a wide range of visible light for water splitting. *J Am Chem Soc* 135:10238–10241
28. Abe R, Shinmei K, Hara K, Ohtani B (2009) Robust dye-sensitized overall water splitting system with two-step photoexcitation of coumarin dyes and metal oxide semiconductors. *Chem Commun* 2009:3577–3579
29. Abe R, Shinmei K, Koumura N, Hara K, Ohtani B (2013) Visible-light-induced water splitting based on two-step photoexcitation between dye-sensitized layered niobate and tungsten oxide photocatalysts in the presence of triiodide/iodide shuttle redox mediator. *J Am Chem Soc* 135:16872–16884
30. Katoh R, Furube A, Mori S, Miyashita M, Sunahara K, Koumura N, Hara K (2009) Highly stable sensitizer dyes for dye-sensitized solar cells: role of the oligothiophene moiety. *Energ Environ Sci* 2:542–546

**Part V**  
**Metal Complex Photocatalysts**

# Chapter 26

## Silica-Supported Metal Complex Photocatalysts

Kohsuke Mori and Hiromi Yamashita

### 26.1 Introduction

The hybridization of guest metal complexes with inorganic matrices, such as clays, zeolites, and mesoporous materials, has been extensively investigated in the drive to construct functional inorganic–organic devices [1]. Such materials often exhibit unexpected physicochemical properties that are induced by both steric and electrostatic constraints within the restricted void spaces as well as nature of the functional groups on the host surface. In the field of optical application, the good optical transparency of silica materials in the visible region provides great potentials as host materials [2, 3]. There have been numerous reports utilizing zeolites as promising supports that can host small molecules and micron-scale photonic band-gap materials within their restricted supercages (ca. 1.3 nm) [4]. On the other hand, the use of mesoporous silicas with uniform channels (2–50 nm) is of particularly interest, which can be easily tailored to afford preferred characteristics by anchoring functional groups to the surface or doping metal atoms into the silica framework [5, 6]. Additionally, the high surface areas as well as pore volumes facilitate the opportunity of doping large size molecules while being capable of a high concentration.

Investigations into emissive  $d^6$  or  $d^8$  metal complexes, exemplified by Ru(II) and Pt(II), have been numerous due to their potential capacity for application in chemical sensing, solar energy conversion, and photocatalysis [7, 8]. More recently, Ir(III) complexes have been the subject of much study with regard to their application in electrophosphorescent organic light-emitting diodes (OLEDs) [9]. For these

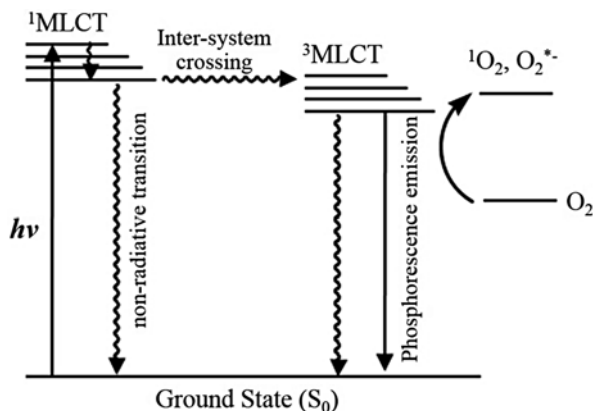
---

K. Mori (✉) • H. Yamashita

Division of Materials and Manufacturing Science, Graduate School of Engineering,  
Osaka University, 2-1 Yamadaoka, Suita, Osaka 565-0871, Japan

Elements Strategy Initiative for Catalysts and Batteries Kyoto University,  
ESICB, Kyoto University, Katsura, Kyoto 615-8520, Japan  
e-mail: [mori@mat.eng.osaka-u.ac.jp](mailto:mori@mat.eng.osaka-u.ac.jp); [yamashita@mat.eng.osaka-u.ac.jp](mailto:yamashita@mat.eng.osaka-u.ac.jp)

**Fig. 26.1** Simplified energy diagram of emissive  $d^6$  or  $d^8$  metal complexes



complexes, the absorption of visible light is known to lead to an excited singlet metal to ligand charge transfer ( $^1MLCT$ ), which is then transferred to a triplet  $MLCT$  ( $^3MLCT$ ) by intersystem crossing [10, 11]. In the absence of  $O_2$ , the excited  $^3MLCT$  exhibits a phosphorescence emission, while potentially active oxygen species such as singlet oxygen ( $^1O_2$ ) and superoxide anion ( $O_2^{*-}$ ) are generated by energy and/or electron transfer reactions from the excited  $^3MLCT$  to  $O_2$  (Fig. 26.1) [12]. It may be assumed that the enhanced excitation rate and quantum efficiency of the metal complexes increase the energy and/or electron transfer to  $O_2$ , which eventually enhances the photooxidation activity.

This part reviews recent studies on new luminescent hybrid photocatalysts developed by encapsulating or anchoring various metal complexes within the pores of zeolites and mesoporous silica materials. The resulting materials can exhibit unique physicochemical properties and photocatalytic abilities in the selective photooxidation using  $O_2$ - and  $H_2$ -evolving reaction in aqueous media controlled by the state of guest molecules as well as nature of host materials. The exploitation of host–guest interactions within the restricted pore arrangement is expected to confer new and more effective types of reactivity on the guest molecules.

## 26.2 Encapsulation of $Ru(bpy)_3^{2+}$ Within the Supercage of Zeolite Y

Partial substitution of  $Al^{3+}$  ions for  $Si^{4+}$  ions at the lattice positions of zeolites results in a network that bears a net negative charge. The negative charge is compensated by the extra framework alkali metal cations (i.e.  $Li^+$ ,  $Na^+$ ,  $K^+$ ,  $Rb^+$ , and  $Cs^+$ ). Physicochemical characteristics, such as electrostatic potential and electric field within the cage, spin-orbit coupling parameter, and space available for guest molecules within the supercage, are well controlled by charge-compensating alkali metal cations (Table 26.1) [13]. Since the estimated diameter of the  $Ru(bpy)_3^{2+}$  (bpy: bipyridine) complex was too large ( $\sim 1.2$  nm) for direct exchange through the zeolite

**Table 26.1** Compositions and characteristics of the zeolites Y including alkali metal cations

Zeolite	Unit cell composition	Ionic radius of alkali cation (Å)	Space volume of cavity (Å <sup>3</sup> )	Electrostatic field (V Å <sup>-1</sup> )	BET surface area (m <sup>2</sup> g <sup>-1</sup> )
Li <sup>+</sup> -Y	Li <sub>18</sub> Na <sub>37</sub> Al <sub>55</sub> Si <sub>137</sub> O <sub>384</sub>	0.68	834	2.1	729
Na <sup>+</sup> -Y	Na <sub>55</sub> Al <sub>55</sub> Si <sub>137</sub> O <sub>384</sub>	0.97	827	1.3	697
K <sup>+</sup> -Y	K <sub>46</sub> Na <sub>9</sub> Al <sub>55</sub> Si <sub>137</sub> O <sub>384</sub>	1.33	807	1.0	659
Rb <sup>+</sup> -Y	Rb <sub>35</sub> Na <sub>20</sub> Al <sub>55</sub> Si <sub>137</sub> O <sub>384</sub>	1.55	796	0.8	567
Cs <sup>+</sup> -Y	Cs <sub>35</sub> Na <sub>20</sub> Al <sub>55</sub> Si <sub>137</sub> O <sub>384</sub>	1.70	781	0.6	518

lattice apertures, a procedure for in situ synthesis of the complex was adopted. The supercages of the alkali metal cation-exchanged zeolite Y were doped with Ru ions and, subsequently, with the ligand bpy through the windows connected to the supercage, giving a series of Ru(bpy)<sub>3</sub><sup>2+</sup>@M-Y (M=Li<sup>+</sup>, Na<sup>+</sup>, K<sup>+</sup>, Rb<sup>+</sup>, and Cs<sup>+</sup>) [14]. The estimated diameter of Ru(bpy)<sub>3</sub><sup>2+</sup> is ~1.2 nm, and therefore this complex would occupy most of the volume of the zeolite Y supercage (~1.3 nm). This occupancy would ensure close proximity of the periphery of the bipyridine ligands to the zeolite framework, the therefore permit a full investigation examining the effect of the interactions between the two species.

As expected, remarkable decreases in BET surface area and BJH pore volume were also observed as the size of the alkali metal cations increased. TG analysis of the Ru(bpy)<sub>3</sub><sup>2+</sup>@Na<sup>+</sup>-Y sample indicated that the ratio of Ru ions to the estimated number of bpy ligands was ca. 1:3. An empirically derived relationship between the relative peak intensities of the 220 and 311 reflections in the XRD pattern confirms the formation of a large metal complex ion in the supercage of faujasite-type zeolites [15]. The UV-Vis spectrum of the Ru(bpy)<sub>3</sub><sup>2+</sup>@Na<sup>+</sup>-Y complex exhibits a slight blue shift of the MLCT band (450 nm) and significant broadening of the  $\pi$ - $\pi^*$  transition band in comparison with Ru(bpy)<sub>3</sub>Cl<sub>2</sub> in an aqueous solution, which can be attributed to the interaction between Ru(bpy)<sub>3</sub><sup>2+</sup> and the zeolite framework.

In the Ru K-edge XANES spectra, the encapsulated Ru ions within zeolite supercages appear to be in an electron-deficient state when compared to free Ru(bpy)<sub>3</sub>Cl<sub>2</sub>. Additionally, the electron density of the Ru atoms slightly increased as the ionic radius of the alkali metal cations increased. In the FT-EXAFS spectra, the first peaks of Ru(bpy)<sub>3</sub><sup>2+</sup>@M-Y, which are attributable to a Ru-N bond, are slightly shifted toward shorter interatomic distances. Curve-fitting analysis showed the average Ru-N distances decreased as the size of the alkali metal cations increased. This observation suggests that the encapsulated Ru(bpy)<sub>3</sub><sup>2+</sup> complexes may undergo strong shrinking and distortion within the zeolite cavity because of the steric constraints imposed by the limited void space.

The luminescence spectra of the <sup>3</sup>MLCT excited state of Ru(bpy)<sub>3</sub><sup>2+</sup>@M-Y were successfully observed at 77 K in the absence of O<sub>2</sub>. Interestingly, the intensity of the emission increased as the size of the alkali metal cations decreased. Additionally, luminescence maxima were slightly blue shifted in the order: free Ru(bpy)<sub>3</sub><sup>2+</sup> in an aqueous solution (599 nm) > Ru(bpy)<sub>3</sub><sup>2+</sup>@Na<sup>+</sup>-Y (585 nm) > Ru(bpy)<sub>3</sub><sup>2+</sup>@Cs<sup>+</sup>-Y

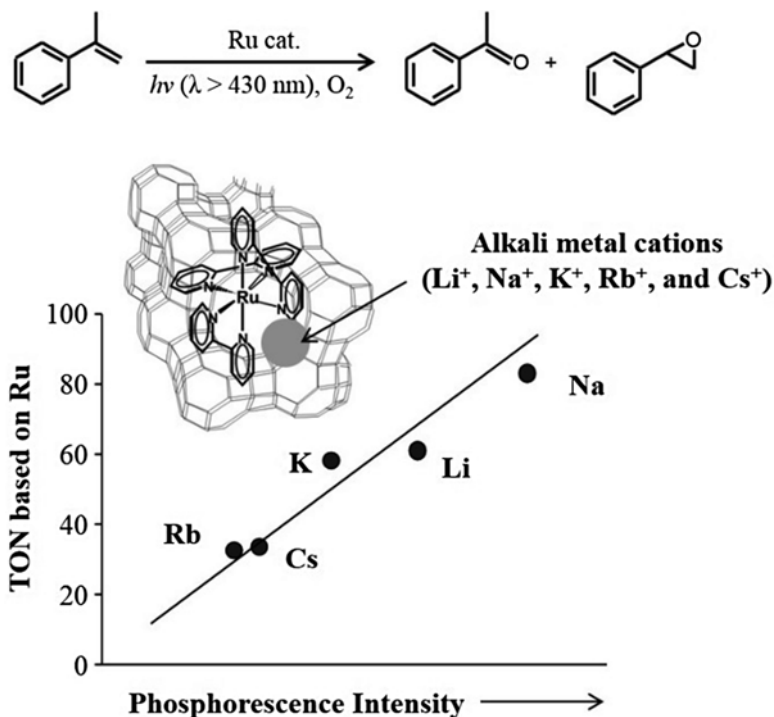


**Fig. 26.2** Relationship between phosphorescence intensity and photocatalytic activity of  $\text{Ru}(\text{bpy})_3^{2+}@\text{M}^+-\text{Y}$  ( $\text{Li}^+$ ,  $\text{Na}^+$ ,  $\text{K}^+$ ,  $\text{Rb}^+$ ,  $\text{Cs}^+$ ) zeolites

(579 nm). This phenomenon is known as “rigidochromism,” in which a reduction in relaxation as a result of a more rigid state causes the spectral blue shifts. The  $\text{Ru}(\text{bpy})_3^{2+}@\text{Cs}^+-\text{Y}$  emitted light of shorter wavelength compared to the  $\text{Ru}(\text{bpy})_3^{2+}@\text{Na}^+-\text{Y}$  complex and this reveals that the  $\text{Cs}^+-\text{Y}$  zeolite provides a less flexible microenvironment because of the larger ionic radius.

It was found that the encapsulation of  $\text{Ru}(\text{bpy})_3^{2+}$  within zeolite Y cages allows selective transformation of  $\alpha$ -methylstyrene to acetophenone under visible-light irradiation ( $\lambda > 430$  nm) and in the presence of molecular oxygen ( $\text{O}_2$ ) at room temperature. The total TON increased as the size of the alkali metal cations, viz.  $\text{Li}^+ > \text{Na}^+ > \text{K}^+ > \text{Rb}^+ > \text{Cs}^+$ , decreased. This tendency is corroborated with increasing intensity of the luminescence emission of the lowest  $^3\text{MLCT}$  state (Fig. 26.2). In this case, the major product obtained was acetophenone (>90 % selectivity) via  $\text{C}=\text{C}$  bond cleavage. The formation of the corresponding dimers was avoided. This highly selective photooxidation is in marked contrast to the reaction using a homogeneous  $\text{Ru}(\text{bpy})_3^{2+}$  complex, in which acetophenone, epoxide, and ene products were formed in 49, 29, and 22 % selectivity, respectively. Moreover, dissociated bpy ligands and/or the oxidized bpy species were detected in the homogeneous solution after the reaction. Such photodegradation was insignificant when the

$\text{Ru}(\text{bpy})_3^{2+}$  complex was contained within the rigid zeolite cavities. These results indicate that the zeolite not only acts as a support but provides a promising micro-environment which allows strict steric control of the reaction intermediate.

The efficient quenching of the photoluminescence by the addition of  $\text{O}_2$  indicates that the  $\text{Ru}(\text{bpy})_3^{2+}$  complex encapsulated within zeolite cavity easily interacts with  $\text{O}_2$  in its  $^3\text{MLCT}$  state. Stern–Volmer equation can be obtained for the quenching of the photoluminescence with  $\text{O}_2$ . As expected,  $\text{Ru}(\text{bpy})_3^{2+}@\text{Na}^+\text{-Y}$  gave a quenching rate constant of 0.018, which is larger than 0.005 observed with  $\text{Ru}(\text{bpy})_3^{2+}@\text{Rb}^+\text{-Y}$ . This result corresponds to an increase in photooxidation ability as well as photoluminescence intensity. Conclusively, this study unambiguously demonstrated that zeolites provide a method for controlling photocatalytic activities associated with the electronic configuration of the lowest triplet state of  $\text{Ru}(\text{bpy})_3^{2+}$  by varying the exchangeable alkali metal cations. The encapsulation of  $\text{Fe}(\text{bpy})_3^{2+}$  complexes within the alkali metal cation-exchanged zeolite Y has also been previously reported [4, 16]. Several parameters, such as the intensity of the MLCT band, the electron density of the Fe atoms, the average distances of the Fe–N bonds, and photooxidation abilities, were found to be systematically altered as the alkali metal cation was changed from  $\text{Li}^+$  to  $\text{Cs}^+$ .

### 26.3 $\text{Ru}(\text{bpy})_3^{2+}$ Complex Anchored Onto Silica-Coated Silver Nanoparticles

The unique phenomenon of localized surface plasmon resonance (LSPR) induced by Ag and Au nanoparticles (NPs) has attracted considerable attention because of the great potential to develop sensors for molecular recognition and nano-optical devices [17, 18]. In the vicinity of the metal surface, the local electromagnetic field is dramatically enhanced, as are Raman scattering and fluorescence processes of surface-anchored dye molecules [19]. This fascinating phenomenon has also made it possible to enhance photocurrent generation on polymer nanosheets incorporating dyes and to increase the absorption coefficient in dye-sensitized solar cells.

As mentioned in the above section, intensity of the photoluminescence emission of the encapsulated  $\text{Ru}(\text{bpy})_3^{2+}$  and photooxidation activity using  $\text{O}_2$  are correlated with each other, and the photocatalysts having high emission ability exhibit the enhanced photocatalytic activity. Based on this result, it can be theoretically expected that the enhanced local electromagnetic field near the Ag NPs could boost the excitation rate and quantum efficiency of  $\text{Ru}(\text{bpy})_3^{2+}$ , thus increasing the energy and/or electron transfer to  $\text{O}_2$ , which ultimately enhances the photooxidation activity. In order to verify this hypothesis, novel core-shell type photocatalyst was designed, in which  $\text{Ru}(\text{bpy})_3^{2+}$  complex was anchored onto the surface of Ag NPs coated with a sufficiently thin  $\text{SiO}_2$  layer ( $\text{Ru}(\text{bpy})_3^{2+}/\text{Ag}@\text{SiO}_2$ ) (Fig. 26.3) [20].

TEM images of the NPs showed a spherical form with an average particle size of 58 nm. The thickness of the  $\text{SiO}_2$  layer was determined to be about 2–3 nm based on

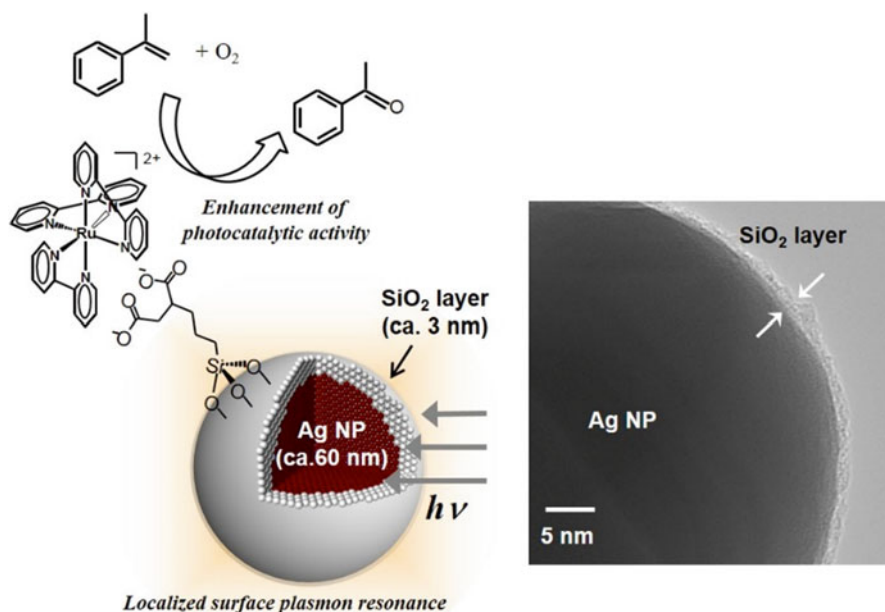


**Fig. 26.3** Illustration of surface structure and HR-TEM image of  $\text{Ru}(\text{bpy})_3^{2+}/\text{Ag}@\text{SiO}_2$

HR-TEM images. The Ru K-edge XANES spectrum was quite similar to that observed for the free  $\text{Ru}(\text{bpy})_3^{2+}$ . In comparison,  $\text{Ru}(\text{bpy})_3^{2+}/\text{Au}@\text{SiO}_2$  (average Au diameter: 58 nm, thickness of the  $\text{SiO}_2$  layer: 3 nm), colloidal  $\text{SiO}_2$  NPs without Ag (average diameter: 55 nm), and Ag NPs without the thin  $\text{SiO}_2$  layer (average diameter: 51 nm) were also synthesized.

As expected, the phosphorescence emission intensity of the  $\text{Ru}(\text{bpy})_3^{2+}$  dye associated with  $\text{Ag}@\text{SiO}_2$  is enhanced under degassing conditions at room temperature [12], which is twice as large as that of the sample without Ag NPs. The Ag core NPs are more advantageous than Au core NPs in the enhancement of the phosphorescence emission intensity, while the Ag NPs without a  $\text{SiO}_2$  layer exhibit marked quenching of the excited  $\text{Ru}(\text{bpy})_3^{2+}$  dye [13]. The  $\text{Ru}(\text{bpy})_3^{2+}/\text{Ag}@\text{SiO}_2$  system was found to be an effective photocatalyst for the selective oxidation of styrene derivatives under visible-light irradiation ( $\lambda > 400$  nm) in the presence of  $\text{O}_2$  at room temperature. The turnover numbers (TON) based on Ru content approached up to 860 in the oxidation of  $\alpha$ -methyl styrene, which is larger than that of the  $\text{Ru}(\text{bpy})_3^{2+}/\text{SiO}_2$  system by a factor of ca. 2. The  $\text{Ru}(\text{bpy})_3^{2+}/\text{Au}@\text{SiO}_2$  showed a slight enhancement of photocatalytic activity, but the Ag core NPs are also proven to be more advantageous than Au core NPs. The use of the Ag NPs without the  $\text{SiO}_2$  layer deactivated the photoinduced oxidation ability to a significant extent. Similar phenomena were observed in the oxidation of 1-methyl-1-cyclohexene. This tendency is consistent with increased phosphorescence emission from the lowest  $^3\text{MLCT}$  state (Fig. 26.4).

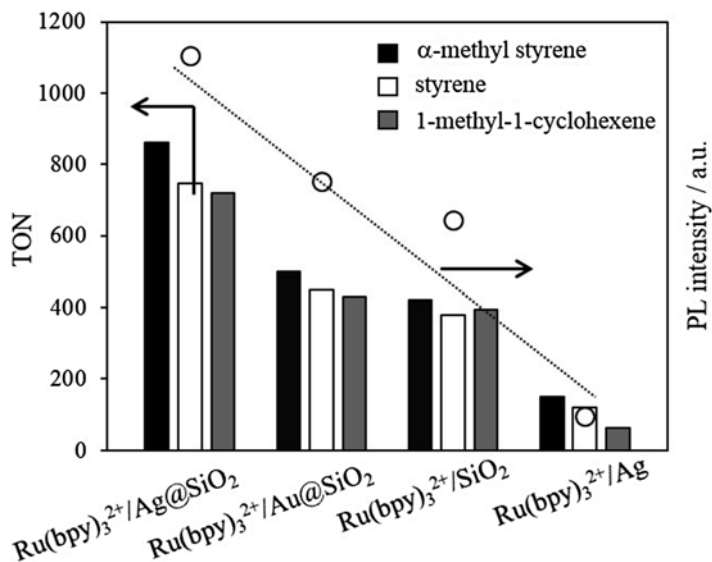


**Fig. 26.4** Relationship between TON for the photocatalytic oxidation using O<sub>2</sub> and photoluminescence intensity

The present study has demonstrated that interaction with the LSPR of Ag NPs can enhance the photocatalytic activity of a dye complex anchored to the surface. The importance of the thin SiO<sub>2</sub> layer is also confirmed. It is known that the electromagnetic field enhanced by the LSPR excitation is localized to the surface between the metal and the dielectric with a roughly exponentially decaying strength in space [21]. The SiO<sub>2</sub> layer, therefore, not only offers chemical inertness and transparency, but also provides a spacer to limit quenching via energy transfer with the core Ag NPs to optimize the LSPR effect. The importance of the use of Ag core is also evidenced. One possible explanation is that the surface plasmon from Au NPs (~550 nm) does not couple to the excitation wavelength of Ru complex dye (MLCT band at 450 nm), while the plasmon resonance frequency generated on Ag NPs (around 400 nm) may closely matched excitation frequency of the dye to offer reasonable enhancement.

## 26.4 Anchoring of Pt(tpy)Cl Complex Onto Mesoporous Silica

The photoluminescence from square-planar d<sup>8</sup> Pt(II) complexes, exemplified by [Pt(tpy)Cl]Cl (tpy: 2,2':6',2''-terpyridine), originates from some of lowest triplet excited states, including MLCT and metal-metal-to-ligand charge-transfer (MMLCT) excited states [22]. A low-lying MMLCT excited state appears in

non-covalent dimers and aggregates with short Pt $\cdots$ Pt separation ( $<3.5$  Å), and the resulting emission is observed at longer wavelengths than those of unimolecular  $^3\text{MLCT}$  emissions. Based on these characteristics, new inorganic–organic hybrid photocatalysts are developed by anchoring the [Pt(tpy)Cl]Cl complex to mesoporous silica hosts [23–25]. The choice of this [Pt(tpy)Cl]Cl complex for evaluation of host–guest interactions was motivated by the easy control of the interaction between each Pt complexes by varying the amount of Pt loadings, which allows the detailed investigation of the effect of spatial distribution of the Pt complex in the mesoporous channel on the phosphorescence emission and photocatalytic activities.

The mesoporous silica MCM-48, which consists of a uniform array of 3D-connected tubular pores, was employed as a host material, whose surface was modified with (3-aminopropyl)trimethoxysilane (APTMS). The [Pt(tpy)Cl]Cl complex was anchored to generate a new Pt–N bond via the loss of HCl, affording Pt(tpy)/MCM-48 samples with different Pt loadings (Pt: 0.2, 0.4, 0.8, 1.2, and 2.4 wt%). The estimated diameter of the [Pt(tpy)Cl]Cl complex (ca. 0.9 nm) is less than half that of the MCM-48 channel (2.5 nm). Therefore, the Pt precursors should diffuse to a sufficient extent to form surface-attached complexes that are homogeneously distributed across the channel under this loading level.

In the Pt L<sub>III</sub>-edge FT-EXAFS spectra, the peak due to the Pd–Cl bond, which was observed at around 1.8 Å in the original [Pt(tpy)Cl]Cl complex, entirely disappeared after reaction with APTMS-modified MCM-48 to generate the new Pt–N bond accompanied by elimination of the Pt–Cl bond. It is notable that the samples with high Pt loadings exhibit the additional peak at around 3.5 Å, which may be ascribed to the short non-covalent Pt $\cdots$ Pt interactions. The UV–Vis absorption bands of Pt(tpy)/MCM-48 are in good agreement with those of the free complex. At high Pt loading, there are additional long-wavelength absorption features at around 510 nm that are not present in the dilute solutions. This band is assigned to a MMLCT [ $d\sigma^*(\text{Pt})-\pi^*(\text{terpyridine})$ ] excited state that originates from relatively short Pt $\cdots$ Pt separations ( $<3.5$  Å) observed in dimers and aggregates [26]. Although the [Pt(tpy)Cl]Cl complex is luminescent in 77 K, Pt(tpy)/MCM-48 showed strong luminescence at room temperature. The peak intensity near 530 nm due to  $^3\text{MLCT}$  transitions is maximum at 0.4 wt% and further increase of the Pt loading resulted in a significant decrease in emission intensity. On the other hand, a new emission appeared at around 620 nm ascribed to the  $^3\text{MMLCT}$  transition, which showed the highest intensity at 2.4 wt% Pt loading. These results clearly evidenced that the Pt complex of the anchored systems exists in isolated form without aggregation at low loading level, whereas average separation between adjacent Pt complexes becomes smaller and the contribution of aggregation becomes dominant with increased Pt loading.

The potential photocatalytic activity of the anchored Pt complexes was first evaluated in the selective oxidation of styrene derivatives in the presence of molecular oxygen at room temperature. Here, 0.4 wt% Pt loading acts as the most efficient catalyst for the photooxidation, and the TON increases in the order of  $2.4 < 1.2 < 0.8 < 0.2 < 0.4$  wt%. This tendency corresponds to the increasing intensity of the luminescence emission due to the  $^3\text{MLCT}$  states (Fig. 26.5). In the absence of

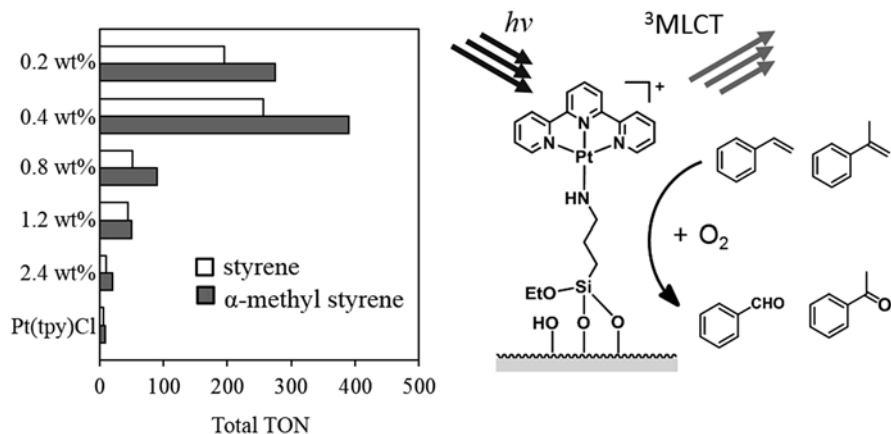


**Fig. 26.5** Effect of Pt loading amount in the Pt(tpy) complex anchored on MCM-48 mesoporous silica for photocatalytic oxidation of styrene derivatives in the presence of  $O_2$

$O_2$ , the excited  $^3MLCT$  states exhibit phosphorescence emission, while potentially active oxygen species such as  $^1O_2$  and  $O_2^{*-}$  are generated by energy and/or electron transfer reactions from the excited triplet state to  $O_2$ . It can be expected that the enhanced excitation rate and quantum efficiency of the anchored Pt complex increases the energy and/or electron transfer to  $O_2$ , which ultimately enhances the photooxidation activity.

Next,  $H_2$ -evolution in aqueous media in the presence of EDTA under visible-light irradiation ( $\lambda > 420$  nm) was performed. It should be noted that the photocatalytic activity significantly varies according to the amount of Pt loadings; no  $H_2$ -evolution occur to any significant extent at less than 0.4 wt% Pt loadings, while photocatalytic activity gradually increased at more than 0.8 wt% Pt loadings (Fig. 26.6). This behavior is sharp contrast to the photocatalytic oxidation using  $O_2$ , but is in good accordance with the increasing intensity of the luminescence emission due to the  $^3MMLCT$  states. Significantly, the maximum activity obtained by 2.4 wt% Pt loading is higher than that of the homogeneous counterparts under identical conditions.

The classical molecule-based photocatalytic  $H_2$ -evolution system consists of multi-components including EDTA (sacrificial electron donor),  $Ru(bpy)_3^{2+}$  (bpy = 2,2'-bipyridine) (photosensitizer), methylviologen ( $MV^{2+}$ , electron relay), and colloidal Pt ( $H_2$ -evolving catalyst) [27]. It is noteworthy that our photocatalytic system is a single component in which the anchored Pt complexes at high Pt loadings possess bifunctionality capable of visible-light photosensitization associated with the  $^3MMLCT$  excited states and hydrogenic activation to evolve  $H_2$  without an electron relay. The formation of the Pt complexes with close proximity is crucial because short-lived emissive  $^3MMLCT$  excited states act as more suitable photosensitizer compared to that from long-lived  $^3MLCT$  transitions. The favorable formation of the postulated hydride-diplatinum(II, III) intermediate by cooperative

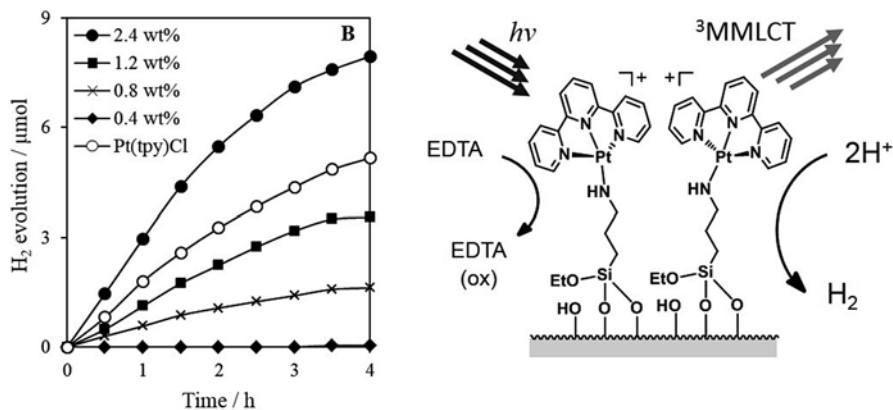


**Fig. 26.6** Effect of Pt loading amount in the Pt(tpy) complex anchored on MCM-48 for photocatalytic  $\text{H}_2$  production from an aqueous solution

action of adjacent Pt complexes also account for high photocatalytic activity at high Pt loadings.

*Vide supra*, MCM-48 consists of a uniform array of 3D-connected tubular pores. MCM-41 has a one-dimensional, hexagonally ordered, unconnected, but regular cylindrical pore structure. SBA-15 exhibits a regular one-dimensional array of tubular channels connected through lateral connections. Beside its large hexagonal channels ranging from 5 to 30 nm in diameter, SBA-15 has thicker pore walls (3–6 nm) than MCM-41. Additionally, this molecular sieve often exhibits surface roughness including a certain amount of disordered micropores and small mesopores. Such differences in the pore dimensions and structures of these materials make it possible to investigate the effect of nanoconfinement on anchored guest molecules.

Interestingly, the emission intensities vary according to the type of mesoporous silica materials; the intensity near 530 nm due to  $^3\text{MLCT}$  transitions increased in the order of  $\text{MCM-41} < \text{SBA-15} < \text{MCM-48}$  at 0.4 wt% Pt loading. At 2.4 wt% Pt loading, the emission at longer wavelength ascribed to the  $^3\text{MMLCT}$  transition also varies in the same order at 0.4 wt% Pt loading. The emission spectra are dependent on the ligand field strength, the redox properties of the metal and ligands, and the intrinsic properties of the ligands. Therefore, a slight change in the surroundings of the Pt complex, such as pore dimension and structure, significantly influences the orbital nature of the excited state. In this case, small hexagonal channels of MCM-48 (2.5 nm) and MCM-41 (2.6 nm) compared to SBA-15 (6.3 nm) may lead to much shorter Pt...Pt interactions owing to the  $\pi$ - $\pi$  stacking between terpyridine ligands. With respect to the emission lifetime, slightly shorter lifetime can be observed in the case of MCM-41 for both  $^3\text{MLCT}$  and  $^3\text{MMLCT}$  transition states, which may be attributable to the increase of nonradiative process within the one dimensional and small hexagonal channel structure of MCM-41.

As expected, the type of mesoporous silica material employed has a significant influence on the photocatalytic activities. The total TON in the aerobic photooxidation of styrene derivatives using the samples with 0.4 wt% Pt loading increases in the order of MCM-41 < SBA-15 < MCM-48. This tendency corresponds to the increasing intensity of the luminescence emission due to the  $^3\text{MLCT}$  states. As mentioned earlier, a similar phenomenon was observed by varying the Pt loading amounts in the MCM-48. It can be concluded that the anchored Pt complex with high emission intensity due to  $^3\text{MLCT}$  transitions increases the energy and/or electron transfer to  $\text{O}_2$ , which eventually enhances the photooxidation activity.

## 26.5 Summary and Outlook

This chapter deals with three types of new photocatalysts designed by hybridization of metal complexes with silica-based materials, which successfully showed unanticipated physicochemical properties as well as photocatalytic activity that are induced by both steric and electrostatic constraints within the restricted rigid spaces. The integration with other host materials, such as zirconium phosphate ( $\text{Zr}(\text{HPO}_4)_2 \cdot \text{H}_2\text{O}$ ) [28], layered niobate ( $\text{K}_4\text{Nb}_6\text{O}_{17}$ ) [29, 30], and ion exchange resins [31, 32], has also been intensively pursued by us in order to construct functional supramolecular materials. The design of effective photocatalysts for the synthesis of specialty chemicals under solar light irradiation is an essential and stimulating mission. Additionally, the effort toward environmentally friendly artificial photosynthetic methods,  $\text{H}_2$  production system driven by solar light radiation in an aqueous medium, has been desirable in the past decade. We expect that our design strategy combined with the advantages of metal complexes and inorganic supports can be further applied to the development of a wide range of functionalized photocatalysts aiming at environmentally benign chemical processes.

## References

1. Descalzo AB, Martínez-Máñez R, Sancenón F, Hoffmann K, Rurack K (2006) The supramolecular chemistry of organic–inorganic hybrid materials. *Angew Chem Int Ed* 45:5924–5948
2. Yamashita H, Mori K (2007) Applications of single-site photocatalysts implanted within the silica matrixes of zeolite and mesoporous silica. *Chem Lett* 36:348–353
3. Yamashita H, Mori K, Shironita S, Horiuchi Y (2008) Applications of single-site photocatalysts to the design of unique surface functional materials. *Catal Surv Asia* 12:88–100
4. Mori K, Kagohara K, Yamashita H (2008) Synthesis of tris(2,2'-bipyridine)iron(II) complexes in zeolite Y cages: influence of exchanged alkali metal cations on physicochemical properties and catalytic activity. *J Phys Chem C* 112:2593–2600
5. Wight AP, Davis ME (2002) Design and preparation of organic–inorganic hybrid catalysts. *Chem Rev* 102:3589–3614
6. Qian X, Fuku K, Kuwahara Y, Kamegawa T, Mori K, Yamashita H (2014) Design and functionalization of photocatalytic systems within mesoporous silica. *ChemSusChem* 7:1528–1536

7. Dearmond MK, Myrick ML (1989) The life and times of [Ru(bpy)<sub>3</sub>]<sup>2+</sup>-localized orbitals and other strange occurrences. *Acc Chem Res* 22:364–370
8. McMillin DR, Moore JJ (2002) Luminescence that lasts from Pt(trpy)Cl<sup>+</sup> derivatives (trpy=2,2':6',2''-terpyridine). *Coord Chem Rev* 229:113–121
9. Schubert US, Ulbricht C, Beyer B, Friebe C, Winter A (2009) Recent developments in the application of phosphorescent iridium(III) complex systems. *Adv Mater* 21:4418–4441
10. Hager GD, Crosby GA (1975) Charge-transfer excited states of ruthenium(II) complexes. I. Quantum yield and decay measurements. *J Am Chem Soc* 97:7031–7037
11. Mori K, Tottori M, Watanabe K, Che M, Yamashita H (2011) Photoinduced aerobic oxidation driven by phosphorescence Ir(III) complex anchored to mesoporous silica. *J Phys Chem C* 115:21358–21362
12. Juris A, Balzani V, Barigelli F, Campagna S, Belser P, Vonzelewsky A (1988) Ru(II) Ppyridine complexes – photophysics, photochemistry, electrochemistry, and chemiluminescence. *Coord Chem Rev* 84:85–277
13. Ramamurthy V, Eaton DF, Caspar JV (1992) Photochemical and photophysical studies of organic molecules included within zeolites. *Acc Chem Res* 25:299–307
14. Mori K, Kawashima M, Kagohara K, Yamashita H (2008) Influence of exchanged alkali metal cations within zeolite Y cages on spectroscopic and photooxidation properties of the incorporated tris(2,2'-bipyridine)ruthenium(II) complexes. *J Phys Chem C* 112:19449–19455
15. Quayle WH, Lunsford JH (1982) Tris(2,2'-bipyridine)ruthenium(III) in zeolite Y: characterization and reduction on exposure to water. *Inorg Chem* 21:97–103
16. Martis M, Mori K, Yamashita H (2014) Control of physicochemical properties and catalytic activity of tris(2,2[prime or minute]-bipyridine)iron(ii) encapsulated within the zeolite Y cavity by alkaline earth metal cations. *Dalton Trans* 43:1132–1138
17. Fuku K, Hayashi R, Takakura S, Kamegawa T, Mori K, Yamashita H (2013) The synthesis of size- and color-controlled silver nanoparticles by using microwave heating and their enhanced catalytic activity by localized surface plasmon resonance. *Angew Chem Int Ed* 52:7446–7450
18. Haes AJ, Van Duyne RP (2002) A nanoscale optical biosensor: sensitivity and selectivity of an approach based on the localized surface plasmon resonance spectroscopy of triangular silver nanoparticles. *J Am Chem Soc* 124:10596–10604
19. Horiuchi Y, Shimada M, Kamegawa T, Mori K, Yamashita H (2009) Size-controlled synthesis of silver nanoparticles on Ti-containing mesoporous silica thin film and photoluminescence enhancement of rhodamine 6G dyes by surface plasmon resonance. *J Mater Chem* 19:6745–6749
20. Mori K, Kawashima M, Che M, Yamashita H (2010) Enhancement of the photoinduced oxidation activity of a ruthenium(II) complex anchored on silica-coated silver nanoparticles by localized surface plasmon resonance. *Angew Chem Int Ed* 49:8598–8601, S8598/1–S8598/4
21. Kerker M (1985) The optics of colloidal silver: something old and something new. *J Colloid Inter Sci* 105:297–314
22. Miskowski VM, Houlding VH (1989) Electronic spectra and photophysics of platinum(II) complexes with.alpha.-diimine ligands. Solid-state effects. 1. Monomers and ligand.pi. dimers. *Inorg Chem* 28:1529–1533
23. Mori K, Watanabe K, Kawashima M, Che M, Yamashita H (2011) Anchoring of Pt(II) pyridyl complex to mesoporous silica materials: enhanced photoluminescence emission at room temperature and photooxidation activity using molecular oxygen. *J Phys Chem C* 115:1044–1050
24. Mori K, Watanabe K, Fuku K, Yamashita H (2012) Photoluminescence emission and photoinduced hydrogen production driven by Pt<sup>II</sup> pyridyl complexes anchored onto mesoporous silica. *Chem Eur J* 18:415–418
25. Mori K, Watanabe K, Terai Y, Fujiwara Y, Yamashita H (2012) Hybrid mesoporous-silica materials functionalized by Pt<sup>II</sup> complexes: correlation between the spatial distribution of the active center, photoluminescence emission, and photocatalytic activity. *Chem Eur J* 18:11371–11378

26. Kobayashi K, Sato H, Kishi S, Kato M, Ishizaka S, Kitamura N, Yamagishi A (2004) Spectroscopic evidence for Pt–Pt interaction in a langmuir-blodgett film of an amphiphilic platinum(II) complex. *J Phys Chem B* 108:18665–18669
27. Kalyanasundaram K, Kiwi J, Grätzel M (1978) Hydrogen evolution from water by visible light, a homogeneous three component test system for redox catalysis. *Helv Chim Acta* 61:2720–2730
28. Mori K, Aoyama J, Kawashima M, Yamashita H (2014) Visible-light driven H<sub>2</sub> production utilizing iridium and rhodium complexes intercalated into a zirconium phosphate layered matrix. *Dalton Trans* 43:10541–10547
29. Mori K, Ogawa S, Martis M, Yamashita H (2012) Intercalation of Pt(II) terpyridine complexes into layered K<sub>4</sub>Nb<sub>6</sub>O<sub>17</sub> and visible-light-driven photocatalytic production of H<sub>2</sub>. *J Phys Chem C* 116:18873–18877
30. Kawashima M, Mori K, Aoyama J, Yamashita H (2014) Synthesis and characterization of Ir and Rh complexes supported on layered K<sub>4</sub>Nb<sub>6</sub>O<sub>17</sub> as a heterogeneous photocatalyst for visible-light-induced hydrogen evolution. *Bull Chem Soc Jpn* 87:874–881
31. Mori K, Kakudo H, Yamashita H (2014) Creation of nickel-based active species within a macroreticular acidic resin: a noble-metal-free heterogeneous catalyst for visible-light-driven H<sub>2</sub> evolution from water. *ACS Catal* 4:4129–4135
32. Mori K, Kubota Y, Yamashita H (2013) Iridium and rhodium complexes within a macroreticular acidic resin: a heterogeneous photocatalyst for visible-light driven H<sub>2</sub> production without an electron mediator. *Chem Asian J* 8:3207–3213

# Chapter 27

## Metal–Organic Framework (MOF) and Porous Coordination Polymer (PCP)- Based Photocatalysts

Yu Horiuchi, Takashi Toyao, and Masaya Matsuoka

### 27.1 Introduction

Metal–organic frameworks (MOFs) also called porous coordination polymers (PCPs) have emerged as a new class of organic–inorganic hybrid materials [1–4]. MOFs are built by linking organic ligands to metal ions or metal-oxo clusters as nodes and possess three-dimensional porous network structures, as displayed in Fig. 27.1. One important feature of MOFs is extremely high porosity, attributable to the thin pore wall assembled by a single organic molecule. Taking advantage of the porous nature, MOFs have been largely applied to adsorbents [5–11], catalysts [12–17], sensors [18–20], drug delivery systems [21–23], and so on. Additionally, their designability coming from various combinations of organic bridging ligands and metal nodes also stimulates motivations in researchers toward the development of MOF-based highly functional materials. Appropriate choice of organic bridging ligands and metal nodes allows for the fine tuning of topology and surface functionality of MOFs. In particular, recently, much effort has been devoted to the exploration of the possibility to utilize MOFs as platforms for the integration of different functional molecular components to achieve light harvesting and to drive various photocatalytic reactions [24, 25]. We induct in this chapter recent progress of the development of MOF-based photocatalysts for visible-light-induced photocatalytic reactions and a one-pot sequential reaction.

---

Y. Horiuchi (✉) • T. Toyao • M. Matsuoka  
Department of Applied Chemistry, Graduate School of Engineering, Osaka Prefecture  
University, 1-1, Gakuen-cho, Nakaku, Sakai, Osaka 599-8531, Japan  
e-mail: [horiiuchi@chem.osakafu-u.ac.jp](mailto:horiiuchi@chem.osakafu-u.ac.jp)

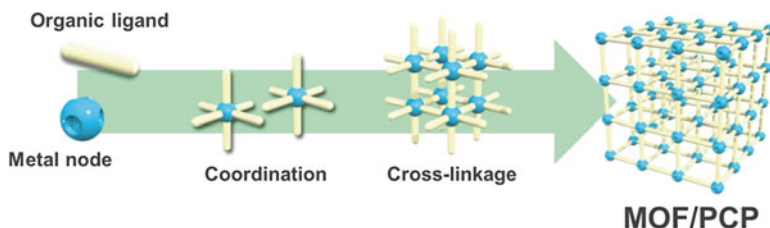


Fig. 27.1 Schematic illustration of the formation of MOF/PCP

## 27.2 MOF Photocatalysts with Light-Harvesting Organic Bridging Ligands

In recent years, research fields on photocatalysts are rapidly expanding in an effort to develop environmentally benign reaction systems including water splitting [26–30]. However, one of the typical photocatalysts,  $\text{TiO}_2$ , operates only under the UV light, which accounts for only 3–5 % of the solar spectrum. The development of visible-light-responsive photocatalysts should effect efficient utilization of solar light. In the context of application of MOFs to visible-light-responsive photocatalysts, MOFs exhibit significant flexibility in terms of framework design. The utilization of light-harvesting organic bridging ligand will achieve the accurate design of absorption characteristics of MOF photocatalysts.

Lin and co-workers have observed that Pt-loaded Zr-based MOFs consisting of a light-harvesting Ir complex as the bridging ligand act as hydrogen evolution photocatalysts under visible-light irradiation [31]. In this photocatalytic system, the reaction occurs through the light absorption by the Ir complex and the following electron injection into Pt nanoparticles. Moreover, recently, there has been intensive interest in semiconducting properties of MOFs. Garcia et al. and Majima et al. independently reported that light irradiation to MOF-5 induces phenomena of electron transfer from the photo-excited organic bridging ligands to the zinc-oxo clusters [32, 33]. This process takes place in photocatalytic reactions and photoluminescence in MOF-5 and is named linker-to-cluster charge transfer (LCCT). Garcia et al. also described that a Zr-based MOF is effective for hydrogen evolution reaction under irradiation with 370 nm light [34]. In this line, Li and co-workers described the successful tuning of the absorption of a Ti-based MOF by using a visible-light-active organic bridging ligand, 2-aminoterephthalic acid (2-ATA), and its application to visible-light-promoted photocatalytic  $\text{CO}_2$  reduction in acetonitrile solution to form formate anion [35]. Subsequently, Matsuoka et al. discovered the same MOF consisting titanium-oxo clusters and 2-ATA organic bridging ligands (Ti-MOF- $\text{NH}_2$ ) behaves as an effective photocatalyst for hydrogen evolution from water medium under visible-light irradiation [36]. The observations made in this investigation are described below.

The visible-light-responsive MOF photocatalyst, Ti-MOF- $\text{NH}_2$ , was prepared by a solvothermal method in DMF at 423 K from tetrapropyl orthotitanate as a titanium-oxo cluster source and 2-aminoterephthalic acid as an organic bridging

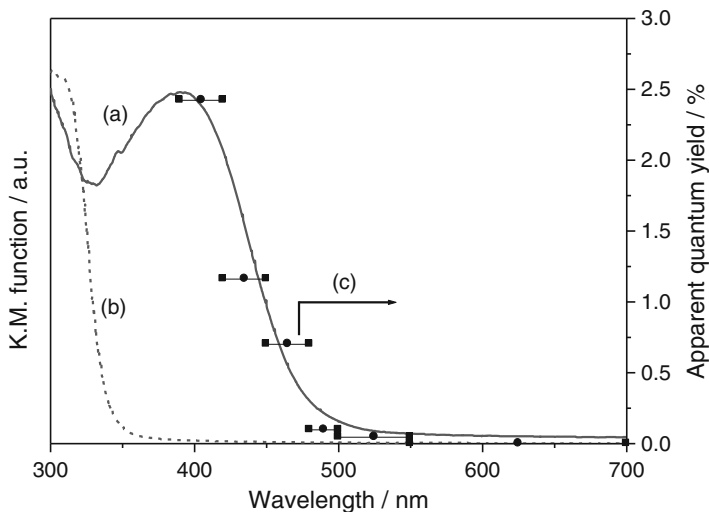
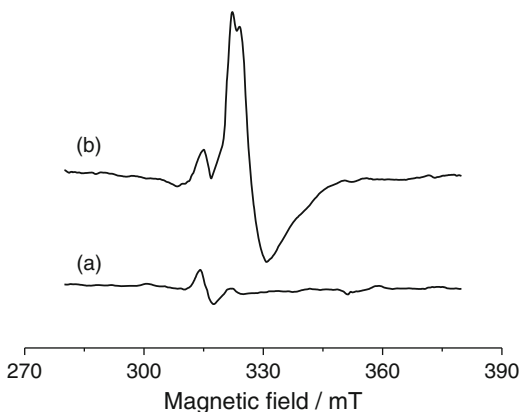


**Fig. 27.2** (a, b) DRUV–Vis spectra of (a) Ti-MOF-NH<sub>2</sub> and (b) MIL-125, and (c) irradiation wavelength dependence of apparent quantum yields for hydrogen evolution reaction over Pt-loaded Ti-MOF-NH<sub>2</sub>

ligand. After the solvothermal treatment for 48 h, the formed precipitate was separated by filtration, washed repeatedly with DMF, and dried at room temperature overnight. Finally, the obtained powder sample was dried under vacuum for 1 h to remove the residual organic bridging ligands, yielding Ti-MOF-NH<sub>2</sub> as yellow powder. The synthesized Ti-MOF-NH<sub>2</sub> exhibited visible-light absorption bands up to around 500 nm as can be seen in its diffuse reflectance UV–Vis (DRUV–Vis) spectrum shown in Fig. 27.2a. On the other hand, conventional Ti-based MOF (MIL-125) prepared by using terephthalic acid did not show absorption in the visible light region (Fig. 27.2b). When hydrogen evolution reaction was performed with Ti-MOF-NH<sub>2</sub> as a photocatalyst, the reaction proceeded efficiently under visible-light irradiation conditions in the presence of triethanolamine (TEOA) as sacrificial electron donors. Moreover, Pt loading was found to lead to the enhancement of photocatalytic activity of Ti-MOF-NH<sub>2</sub>. By contrast, no reaction occurred over MIL-125 and Pt-loaded MIL-125 under the same reaction condition.

The wavelength dependence of photocatalytic activity of Pt-loaded Ti-MOF-NH<sub>2</sub> revealed that the maximum wavelength available for the hydrogen evolution reaction was 500 nm (see Fig. 27.2c). Furthermore, apparent quantum yield response was observed to depend strongly on wavelength and showed good parallel relationship with the absorption spectrum of Ti-MOF-NH<sub>2</sub>. This finding indicated that photocatalytic reaction on Ti-MOF-NH<sub>2</sub> under visible-light irradiation conditions originates from absorption by its organic bridging ligand, 2-ATA. Subsequently, electron transfer from the organic bridging ligand to titanium-oxo cluster was confirmed by ESR measurements. For the measurements, a suspension containing Ti-MOF-NH<sub>2</sub>, TEOA, and water was degassed under vacuum at 77 K and irradiated with visible

**Fig. 27.3** ESR spectra of Ti-MOF-NH<sub>2</sub> before (a) and after (b) visible-light irradiation



light ( $\lambda > 420$  nm) for 3 h at room temperature. The ESR spectra were then obtained at 77 K. As shown in Fig. 27.3, typical signals corresponding to paramagnetic Ti<sup>3+</sup> centers in a distorted rhombic oxygen ligand field were observed in the spectrum of Ti-MOF-NH<sub>2</sub> after visible-light irradiation, which could not be seen in the spectrum before irradiation. These results are explained by the electron transfer from organic bridging ligands to titanium-oxo clusters and the reduction of Ti<sup>4+</sup> species to Ti<sup>3+</sup> species there. The observations made by the wavelength-dependent investigations and ESR measurements clearly demonstrated that the hydrogen evolution reaction in this Ti-MOF-NH<sub>2</sub>-based photocatalytic process proceeds through the light absorption by its organic bridging ligands and the following electron transfer to the catalytically active titanium-oxo clusters, that is, the LCCT mechanism.

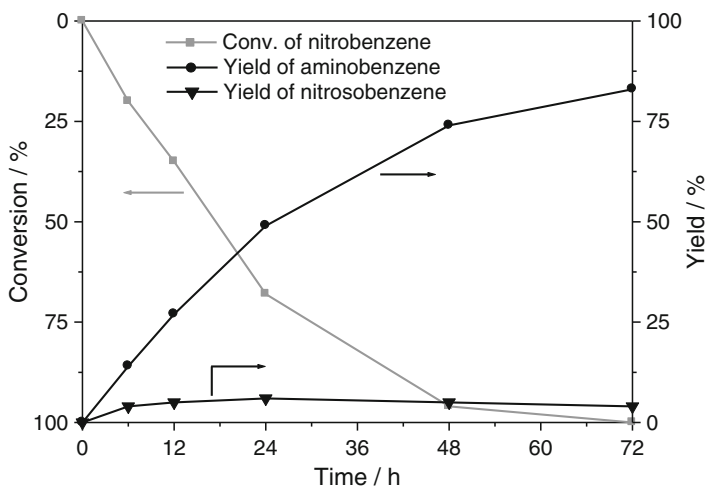


**Fig. 27.4** Time course plots of photocatalytic reduction of nitrobenzene over Pt-loaded Ti-MOF-NH<sub>2</sub> under visible-light irradiation ( $\lambda > 420$  nm) in the presence of TEOA

Pt-loaded Ti-MOF-NH<sub>2</sub> is also applicable to photocatalytic reduction of nitrobenzene to aminobenzene [37]. Figure 27.4 shows the time course plots for the photocatalytic reduction reaction over Pt-loaded Ti-MOF-NH<sub>2</sub> in acetonitrile solution in the presence of TEOA as electron donors under visible-light irradiation ( $\lambda > 420$  nm). The selective production of aminobenzene over Ti-MOF-NH<sub>2</sub> was found to take place along with the consumption of nitrobenzene under visible-light irradiation although nitrosobenzene was slightly obtained as an intermediate product of the reaction. Additionally, the Pt-loaded Ti-MOF-NH<sub>2</sub> photocatalyst could be recycled at least three times without significant loss of its activity and selectivity.

### 27.3 Accurate Design of MOF Photocatalysts for Improved Reactivity

By using 2-ATA organic bridging ligand, new visible-light-responsive MOF-based photocatalysts have been developed as described above. However, in this system, there are limitations in terms of utilizable ranges of irradiation wavelength and sacrificial electron donors. The photocatalytic reaction using up to 500 nm light is not enough for efficient utilization of solar light. Also, the Ti-MOF-NH<sub>2</sub> photocatalyst cannot promote the reaction in the presence of sacrificial electron donors, such as ethylenediaminetetraacetic acid (EDTA) and methanol, other than TEOA. In consideration of the LCCT mechanism, these barriers to the attainment of environmentally benign photocatalytic reaction systems are caused by characteristics of the 2-ATA organic bridging ligand where both light absorption and oxidation of sacrificial electron donors occur. In this sense, highly desirable is the design of new bridging ligands that possess wide absorption and a low highest occupied molecular orbital (HOMO) level. We introduce herein the track of the development of a new visible-light-responsive MOF photocatalyst containing a Ru complex as a bridging ligand initiated by design of the bridging ligand [38].

Firstly, DRUV–Vis and cyclic voltammetry (CV) measurements were carried out in order to gain an insight into HOMO–LUMO levels of bridging ligands. The obtained results revealed that bis(4'-(4-carboxyphenyl)-terpyridine)Ru(II) complex (denoted as Ru(tpy)<sub>2</sub>) has the potential to act as an effective bridging ligand. The DRUV–Vis spectrum of Ru(tpy)<sub>2</sub> exhibited wide absorption bands in the visible region up to 620 nm. Moreover, CV curves that were observed in CH<sub>2</sub>Cl<sub>2</sub> with 0.1 M tetrabutylammonium perchlorate as supporting electrolytes indicated that the HOMO level of Ru(tpy)<sub>2</sub> is lower than that of 2-ATA. From these results, energy diagrams of HOMO–LUMO levels of Ru(tpy)<sub>2</sub> and 2-ATA were determined and are summarized in Fig. 27.5. The thus-obtained HOMO–LUMO levels show that utilization of the Ru(tpy)<sub>2</sub> bridging ligand is expected to expand utilizable range of wavelength and sacrificial electron donor.

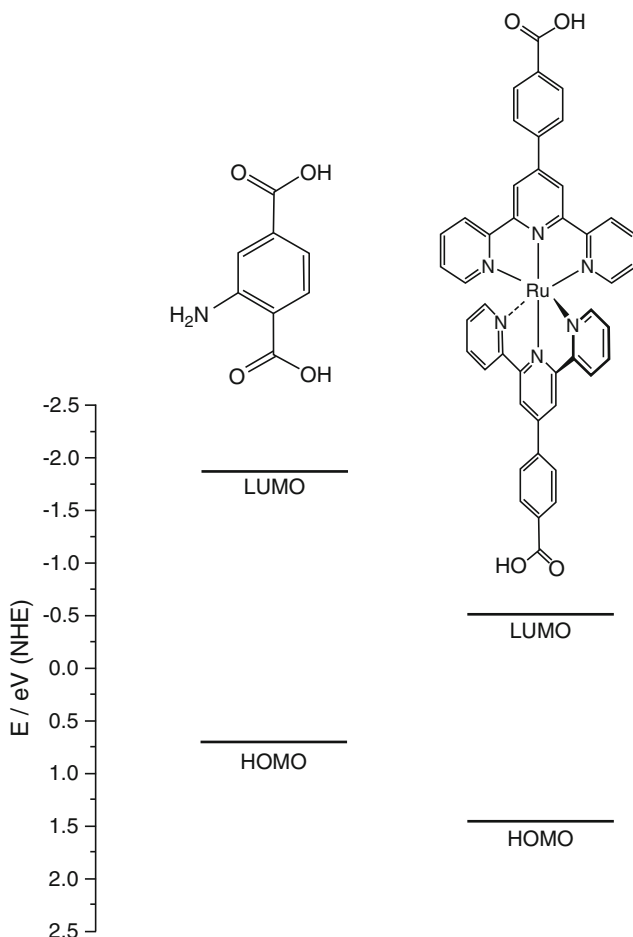


**Fig. 27.5** Energy diagrams of HOMO-LUMO levels of Ru(tpy)<sub>2</sub> and 2-ATA

Subsequently, in accordance with above investigations, new Ti-based MOF was prepared by using Ru(tpy)<sub>2</sub> as a bridging ligand (Ti-MOF-Ru(tpy)<sub>2</sub>) and applied to photocatalytic hydrogen evolution reaction. As shown in Fig. 27.6, hydrogen evolution was achieved over Ti-MOF-Ru(tpy)<sub>2</sub> in the presence of TEOA as sacrificial electron donors under visible-light irradiation with a wavelength range up to 620 nm. For this reaction, Pt nanoparticles as co-catalysts were deposited in-situ on Ti-MOF-Ru(tpy)<sub>2</sub> by adding H<sub>2</sub>PtCl<sub>6</sub> into the reaction solution. The expansion of utilizable wavelength range is due to an LCCT phenomenon that originates the Ru(tpy)<sub>2</sub> bridging ligand with wide visible-light absorption characteristics. Moreover, as expected, Ti-MOF-Ru(tpy)<sub>2</sub> was able to promote the photocatalytic hydrogen evolution reaction under visible-light irradiation ( $\lambda > 420$  nm) when using EDTA or methanol as a sacrificial electron donor in place of TEOA. These findings proved that the inspection of accurate combination of metal-oxo clusters and bridging ligands will enable us to develop more efficient MOF photocatalysts.

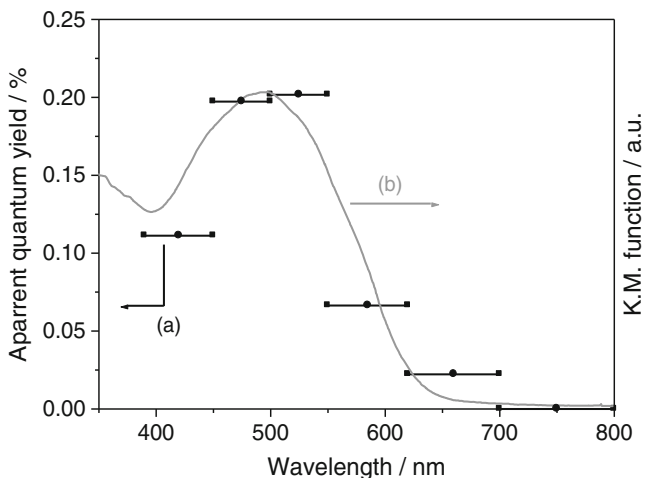
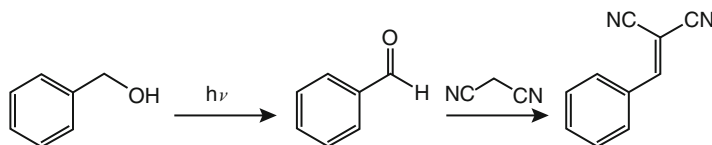


**Fig. 27.6** (a) Irradiation wavelength dependence of apparent quantum yields for hydrogen evolution reaction over Ti-MOF-Ru(tpy)<sub>2</sub> in the presence of TEOA and H<sub>2</sub>PtCl<sub>6</sub> and (b) DRUV-Vis spectrum of Ti-MOF-Ru(tpy)<sub>2</sub>

## 27.4 One-Pot Synthetic Process Based on MOF Photocatalysts

Recently, great attention has been paid to one-pot reactions in the light of green chemistry [39–42]. Green chemistry is a concept to produce chemical products with a consideration for inherently environmentally and ecologically benign materials in order to attain sustainable development. In industrial processes, most fine chemicals are synthesized via multistep reactions. As a consequence, the loss of products during each purification step reduces the overall efficiency of the synthetic process dramatically, and the production of a large amount of chemical wastes is also inevitable during the purification steps. The one-pot reaction is considered to be a promising approach to overcome these obstacles; however, industrial applications of the one-pot reaction processes are limited due to the difficulties in the material design with well-controlled isolated catalytic centers to promote each reaction step efficiently. The utilization of the designability of MOFs will enable us to develop new catalytic systems for the achievement of one-pot reactions. In this line, Matsuoka et al. developed a new one-pot chemical conversion system based on the photocatalytic ability and basicity of a bifunctional MOF [43]. The bifunctional MOF consists of zirconium-oxo clusters and 2-ATA organic bridging ligand (Zr-MOF-NH<sub>2</sub>) and can promote one-pot sequential photocatalytic oxidation and Knoevenagel condensation reactions.

Zr-MOF-NH<sub>2</sub> was prepared by a solvothermal method. A mixture of ZrCl<sub>4</sub>, 2-ATA, ion-exchanged water, and DMF was subjected to solvothermal conditions in a Teflon-lined stainless-steel autoclave at 393 K for 24 h. The synthesized Zr-MOF-NH<sub>2</sub> was applied to the one-pot reaction consisting of photocatalytic oxidation and Knoevenagel condensation (Scheme 27.1). The reaction was performed in *p*-xylene solution in the presence of benzyl alcohol and malononitrile under UV-light irradiation at 363 K. As



**Scheme 27.1** One-pot sequential photocatalytic oxidation and Knoevenagel condensation reaction

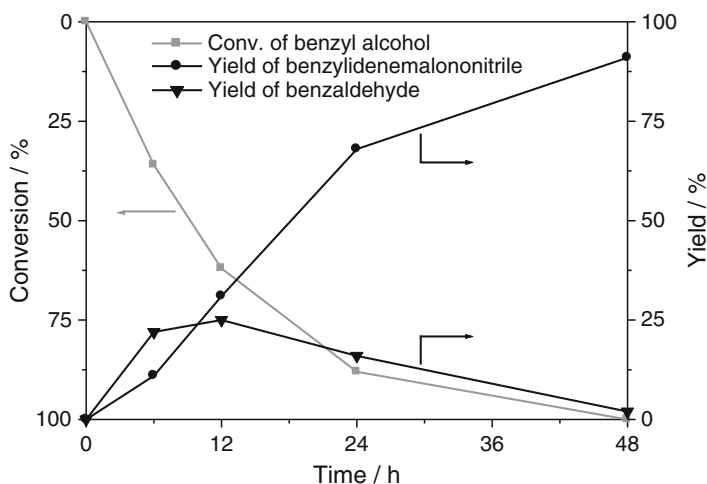


**Fig. 27.7** Time course plots of one-pot sequential photocatalytic oxidation and Knoevenagel condensation reaction over Zr-MOF-NH<sub>2</sub> under UV-light irradiation at 363 K

shown in Fig. 27.7, benzylidenemalononitrile was efficiently produced over Zr-MOF-NH<sub>2</sub> via a pathway involving initial formation of benzaldehyde. This finding clearly indicates that Zr-MOF-NH<sub>2</sub> behaves as a bifunctional catalyst.

The inspection of time course of the former process, photocatalytic oxidation of benzyl alcohol to produce benzaldehyde, demonstrated that zirconium-oxo clusters in Zr-MOF-NH<sub>2</sub> play an important role for the photocatalytic reaction. Under UV-light irradiation, photocatalytic oxidation effectively proceeded over Zr-MOF without amino groups prepared by using terephthalic acid organic bridging ligand as well as over Zr-MOF-NH<sub>2</sub>, while Al-MOF-NH<sub>2</sub> build from aluminum-oxo clusters and 2-ATA organic bridging ligands did not promote the reaction. In addition, no reaction occurred over Zr-MOF-NH<sub>2</sub> and Zr-MOF under dark conditions. The presence of zirconium-oxo clusters was thus found to be required for the progression of photocatalytic oxidation of benzyl alcohol to produce benzaldehyde. On the other hand, the amino groups in Zr-MOF-NH<sub>2</sub> acted as basic sites for the promotion of the latter Knoevenagel condensation to produce benzylidenemalononitrile. The reaction rates of Knoevenagel condensation over Zr-MOF-NH<sub>2</sub> and Al-MOF-NH<sub>2</sub> were largely higher than that of Zr-MOF. However, Knoevenagel condensation progressed over Zr-MOF moderately. This would be due to Lewis acidic properties

derived from the coordinatively unsaturated metal sites in Zr-MOF. In general, Knoevenagel condensation is known to be promoted not only by base catalysts but also by Lewis acid catalysts. The results obtained from the above effort demonstrated that Zr-MOF-NH<sub>2</sub> possesses bifunctional properties that play effective roles for respective photocatalytic oxidation and Knoevenagel condensation reactions.

## 27.5 Summary

In summary, this chapter highlights the rational design of photocatalyst materials based on designability of MOF. The development of visible-light-responsive Ti-based MOF photocatalysts has been achieved by using 2-ATA as a light-harvesting organic bridging ligand, in place of the conventional terephthalic acid. In this photocatalytic system, the reaction proceeds through the light absorption by its organic bridging ligand and the following electron transfer to the catalytically active titanium-oxo cluster. Moreover, appropriate choice of bridging ligands was found to lead to the improvement of photocatalytic performances of Ti-based MOF. The wide absorption and low HOMO levels of bridging ligands are effective for the expansion of utilizable ranges of wavelength and sacrificial reagents in photocatalytic reaction, respectively. Subsequently, the development of a novel one-pot reaction system utilizing a bifunctional MOF photocatalyst was described. The integration of the photocatalytic ability of zirconium-oxo clusters and basicity of 2-ATA allows for the progression of one-pot sequential photocatalytic oxidation and Knoevenagel condensation reaction over a single MOF material. These observations revealed the effectiveness of catalyst design through the utilization of the flexibility in terms of the combination of bridging ligands and metal nodes in MOFs and offer new guidelines for future development of highly functional MOF catalysts.

## References

1. Yaghi OM, Li G, Li H (1995) Selective binding and removal of guests in a microporous metal-organic framework. *Nature* 378:703–706
2. Kondo M, Yoshitomi T, Matsuzaka H et al (1997) Three-dimensional framework with channeling cavities for small molecules: {[M<sub>2</sub>(4, 4'-bpy)<sub>3</sub>(NO<sub>3</sub>)<sub>4</sub>]·xH<sub>2</sub>O}<sub>n</sub> (M=Co, Ni, Zn). *Angew Chem Int Ed Engl* 36:1725–1727
3. Yaghi OM, O'Keeffe M, Ockwig NW et al (2003) Reticular synthesis and the design of new materials. *Nature* 423:705–714
4. Kitagawa S, Kitaura R, Noro S-i (2004) Functional porous coordination polymers. *Angew Chem Int Ed* 43:2334–2375
5. Eddaoudi M, Kim J, Rosi N et al (2002) Systematic design of pore size and functionality in isorecticular MOFs and their application in methane storage. *Science* 295:469–472
6. Rosi NL, Eckert J, Eddaoudi M et al (2003) Hydrogen storage in microporous metal-organic frameworks. *Science* 300:1127–1129
7. Matsuda R, Kitaura R, Kitagawa S et al (2005) Highly controlled acetylene accommodation in a metal-organic microporous material. *Nature* 436:238–241

8. Li JR, Kuppler RJ, Zhou HC (2009) Selective gas adsorption and separation in metal-organic frameworks. *Chem Soc Rev* 38:1477–1504
9. Sumida K, Rogow DL, Mason JA et al (2012) Carbon dioxide capture in metal-organic frameworks. *Chem Rev* 112:724–781
10. Sakata Y, Furukawa S, Kondo M et al (2013) Shape-memory nanopores induced in coordination frameworks by crystal downsizing. *Science* 339:193–196
11. Sato H, Kosaka W, Matsuda R et al (2014) Self-accelerating CO sorption in a soft nanoporous crystal. *Science* 343:167–170
12. Wu CD, Hu A, Zhang L et al (2005) Homochiral porous metal-organic framework for highly enantioselective heterogeneous asymmetric catalysis. *J Am Chem Soc* 127:8940–8941
13. Lee J, Farha OK, Roberts J et al (2009) Metal-organic framework materials as catalysts. *Chem Soc Rev* 38:1450–1459
14. Furrusseng D, Aguado S, Pinel C (2009) Metal-organic frameworks: opportunities for catalysis. *Angew Chem Int Ed* 48:7502–7513
15. Corma A, Garcia H, Xamena F (2010) Engineering metal organic frameworks for heterogeneous catalysis. *Chem Rev* 110:4606–4655
16. Saito M, Toyao T, Ueda K et al (2013) Effect of pore sizes on catalytic activities of arenetricarbonyl metal complexes constructed within Zr-based MOFs. *Dalton Trans* 42:9444–9447
17. Horiuchi Y, Toyao T, Fujiwaki M et al (2015) Zeolitic imidazolate frameworks as heterogeneous catalysts for a one-pot P-C bond formation reaction via Knoevenagel condensation and phospho-Michael addition. *RSC Adv* 5:24687–24690
18. Lan A, Li K, Wu H et al (2009) A luminescent microporous metal-organic framework for the fast and reversible detection of high explosives. *Angew Chem Int Ed* 48:2334–2338
19. Chen BL, Wang LB, Xiao YQ et al (2009) A luminescent metal-organic framework with Lewis basic pyridyl sites for the sensing of metal ions. *Angew Chem Int Ed* 48:500–503
20. Kreno LE, Leong K, Farha OK et al (2012) Metal-organic framework materials as chemical sensors. *Chem Rev* 112:1105–1125
21. Horcajada P, Serre C, Vallet-Regi M et al (2006) Metal-organic frameworks as efficient materials for drug delivery. *Angew Chem Int Ed* 45:5974–5978
22. Horcajada P, Serre C, Maurin G et al (2008) Flexible porous metal-organic frameworks for a controlled drug delivery. *J Am Chem Soc* 130:6774–6780
23. Horcajada P, Chalati T, Serre C et al (2010) Porous metal-organic-framework nanoscale carriers as a potential platform for drug delivery and imaging. *Nat Mater* 9:172–178
24. Wang J-L, Wang C, Lin W (2012) Metal-organic frameworks for light harvesting and photocatalysis. *ACS Catal* 2:2630–2640
25. Nasalevich MA, van der Veen M, Kapteijn F et al (2014) Metal-organic frameworks as heterogeneous photocatalysts: advantages and challenges. *CrystEngComm* 16:4919–4926
26. Maeda K, Teramura K, Lu D et al (2006) Photocatalyst releasing hydrogen from water. *Nature* 440:295
27. Kudo A, Miseki Y (2009) Heterogeneous photocatalyst materials for water splitting. *Chem Soc Rev* 38:253–278
28. Maeda K, Domen K (2010) Photocatalytic water splitting: recent progress and future challenges. *J Phys Chem Lett* 1:2655–2661
29. Horiuchi Y, Toyao T, Takeuchi M et al (2013) Recent advances in visible-light-responsive photocatalysts for hydrogen production and solar energy conversion – from semiconducting TiO<sub>2</sub> to MOF/PCP photocatalysts. *Phys Chem Chem Phys* 15:13243–13253
30. Schneider J, Matsuoka M, Takeuchi M et al (2014) Understanding TiO<sub>2</sub> photocatalysis: mechanisms and materials. *Chem Rev* 114:9919–9986
31. Wang C, deKrafft KE, Lin W (2012) Pt nanoparticles@photoactive metal-organic frameworks: efficient hydrogen evolution via synergistic photoexcitation and electron injection. *J Am Chem Soc* 134:7211–7214
32. Alvaro M, Carbonell E, Ferrer B et al (2007) Semiconductor behavior of a metal-organic framework (MOF). *Chem Eur J* 13:5106–5112

33. Tachikawa T, Choi JR, Fujitsuka M et al (2008) Photoinduced charge-transfer processes on MOF-5 nanoparticles: elucidating differences between metal-organic frameworks and semiconductor metal oxides. *J Phys Chem C* 112:14090–14101
34. Gomes Silva C, Luz I, Llabrés i Xamena FX et al (2010) Water stable Zr–benzenedicarboxylate metal–organic frameworks as photocatalysts for hydrogen generation. *Chem Eur J* 16:11133–11138
35. Fu Y, Sun D, Chen Y et al (2012) An amine-functionalized titanium metal–organic framework photocatalyst with visible-light-induced activity for CO<sub>2</sub> reduction. *Angew Chem Int Ed* 51:3364–3367
36. Horiuchi Y, Toyao T, Saito M et al (2012) Visible-light-promoted photocatalytic hydrogen production by using an amino-functionalized Ti(IV) metal–organic framework. *J Phys Chem C* 116:20848–20853
37. Toyao T, Saito M, Horiuchi Y et al (2013) Efficient hydrogen production and photocatalytic reduction of nitrobenzene over a visible-light-responsive metal–organic framework photocatalyst. *Catal Sci Technol* 3:2092–2097
38. Toyao T, Saito M, Dohshi S et al (2014) Development of a Ru complex-incorporated MOF photocatalyst for hydrogen production under visible-light irradiation. *Chem Commun* 50:6779–6781
39. Hall N (1994) Chemists clean up synthesis with one-pot reactions. *Science* 266:32–34
40. Wasilke J-C, Obrey SJ, Baker RT et al (2005) Concurrent tandem catalysis. *Chem Rev* 105:1001–1020
41. Motokura K, Fujita N, Mori K et al (2005) An acidic layered clay is combined with a basic layered clay for one-pot sequential reactions. *J Am Chem Soc* 127:9674–9675
42. Toyao T, Fujiwaki M, Horiuchi Y et al (2013) Application of an amino-functionalised metal-organic framework: an approach to a one-pot acid-base reaction. *RSC Adv* 3:21582–21587
43. Toyao T, Saito M, Horiuchi Y et al (2014) Development of a novel one-pot reaction system utilizing a bifunctional Zr-based metal-organic framework. *Catal Sci Technol* 4:625–628

# Chapter 28

## Photocatalytic CO<sub>2</sub> Reduction to CO by ZIF-9/TiO<sub>2</sub>

Sibo Wang and Xinchun Wang

### 28.1 Introduction

Carbon monoxide is an important feedstock in C1 synthetic chemistry including the well-known Fischer-Tropsch route for hydrocarbon production from syngas (CO+H<sub>2</sub>) [1–3], and the commercialized Cativa (or Monsanto) process to produce acetic acid [4]. Industrially, CO is mainly produced from the gas reforming of CH<sub>4</sub> with CO<sub>2</sub>, which is a highly energy-intensive technology. Due to the large-scale requirement of CO in industries, it would be of paramount importance to produce CO from the direct conversion of CO<sub>2</sub> as an abundant and easily available carbon feedstock by renewable and eco-friendly energy, which would consequently reduce the ever-increasing atmospheric CO<sub>2</sub> concentration associated with the worldwide climate changes and the notorious greenhouse effect. Solar-driven semiconductor-mediated photocatalysis is always recognized as the most ideal solution for directly converting CO<sub>2</sub> into CO in a sustainable and carbon-neutral manner [5–7]. However, because of the intrinsic thermodynamic stability and kinetic inertness of linear CO<sub>2</sub> molecules, up to now, it still imposes significant challenges to operate this promising chemical CO<sub>2</sub>-to-CO transformation under low-temperature and -pressure conditions.

To accomplish efficient CO<sub>2</sub> conversion by photocatalysis under benign conditions, it is crucial to develop catalysts and/or cocatalysts that exhibit high activity and selectivity for CO<sub>2</sub> reduction upon light illumination. A great deal of effort has therefore been dedicated to explore active photocatalysts and cocatalysts, coupled with their combinations to establish chemical systems for CO<sub>2</sub> fixation with desired yield and selectivity [8–10]. Semiconductor materials such as TiO<sub>2</sub> [11], ZrO<sub>2</sub> [12],

---

S. Wang • X. Wang (✉)

State Key Laboratory of Photocatalysis on Energy and Environment, College of Chemistry,  
Fuzhou University, Fuzhou 350002, People's Republic of China  
e-mail: [xcwang@fzu.edu.cn](mailto:xcwang@fzu.edu.cn)

MgO [13], ZnO [14], CdS [15], CeO<sub>2</sub> [16], Ga<sub>2</sub>O<sub>3</sub> [17], and Ta<sub>2</sub>O<sub>5</sub> [18] have been developed as photocatalysts for the chemical conversion of CO<sub>2</sub>. Amongst them, thanks to the high photostability, low cost, availability, and nontoxicity, TiO<sub>2</sub> is regarded as one of the most convenient candidates for running photocatalytic CO<sub>2</sub> reduction catalysis [19–22]. But, a big obstacle that is inevitably encountered in utilizing TiO<sub>2</sub> in photocatalysis is the high recombination rate of the photogenerated electron-hole pairs, which fundamentally limits the catalytic efficiency of CO<sub>2</sub> transformation reactions [11, 23]. Cocatalysts are thus intensively applied in CO<sub>2</sub> photoreduction systems, as cocatalysts can promote the transport of photoexcited electrons as well as lower the activation energy or overpotential for CO<sub>2</sub> reduction catalysis [9]. Thus, exploiting and using suitable cocatalysts in CO<sub>2</sub> conversion system is a key to the catalytic efficiency [9, 24].

Noble metals (e.g., Au, Ag, Ru, Rh, Ir, and Pt) are extensively used as cocatalysts in CO<sub>2</sub> conversion systems [24–32]. However, the low abundance and the high cost of these noble metals seriously limit the practical applications of these noble-metal-containing CO<sub>2</sub> fixation systems. Alternatively, transition metal ions with multiple redox states and organic ligands are also a recommended choice of cofactors to immediately transfer the excited electrons for photoredox catalysis [33–41]. These facts offer great potential for the design of materials that can be assembled rationally from transition metal ions and organic ligands in a metal-organic fashion to act as non-noble-metal cocatalysts for the photocatalytic reduction of CO<sub>2</sub> under ambient conditions.

Metal-organic frameworks (MOFs) are interesting type of porous crystalline materials fabricated by metal ions (or clusters) and organic ligands [42–45]. MOFs feature with larger internal surfaces, uniform but controllable cavities together with flexible tenability in composition, structure, and functionality. Among the variety of MOFs, zeolitic imidazolate frameworks (ZIFs) are a particular subfamily that are constructed by tetrahedral transition metal ions and imidazolate linkers [46, 47]. ZIFs hold high chemical and thermal stabilities [48], and importantly have shown great opportunities for use in CO<sub>2</sub> capture/adsorption [49–51]. For example, the cobalt-containing zeolitic imidazolate framework (named as ZIF-9) shows very interesting CO<sub>2</sub> adsorption behavior: it presents small CO<sub>2</sub> uptake at low pressure, but exhibits remarkably improved CO<sub>2</sub> adsorption at higher pressure while still adsorbing negligible amounts of other gases such as N<sub>2</sub> and CH<sub>4</sub> [52–55]. ZIF-9 is assembled by cobalt ions tetrahedrally coordinated by four nitrogen atoms in the 1, 3-positions of benzimidazole ligands, thus establishing an infinite three-dimensional porous metal-organic networks. ZIF-9 thus features the combined catalytic redox functions of both cobalt and imidazolate entities in its harmonious chemical environments, which renders it a very promising candidate for use in CO<sub>2</sub> reduction applications.

In the previous works, we developed the ZIF-9 as an effective and stable cocatalyst for the photocatalytic reduction of CO<sub>2</sub> by the cooperation with several molecular and solid-state visible light harvesters under mild reaction conditions, such as

Ru-dye, CdS, and g-C<sub>3</sub>N<sub>4</sub> [56–58]. The ZIF-9 cocatalyst demonstrated multifunctional functions in supporting CO<sub>2</sub> photofixation catalysis, namely it not only promotes the adsorption and activation of CO<sub>2</sub>, but also facilitates the transportation of photo-triggered electrons. In this chapter, we demonstrate that the cocatalytic capability of ZIF-9 can further be extended to a CO<sub>2</sub> reduction system employing the star photocatalyst TiO<sub>2</sub> as a light sensitizer under simulated sunlight irradiation. Although TiO<sub>2</sub> is only a UV-active photocatalyst, the studies during the past 40 years has focused on the successful translation of TiO<sub>2</sub> into visible light-responsive photocatalysts by a number of physical and chemical tools. Thus, a natural next step as stimulated by this work is the merging of the ZIF-9 with modified TiO<sub>2</sub> photocatalysts for visible light-induced CO<sub>2</sub> photofixation in a sustainable manner. In the constructed hybrid chemical system, ZIF-9 effectively cocatalyzed the CO<sub>2</sub>-to-CO transformation reaction, and preserved its structure stability under the photocatalytic conditions.

## 28.2 Experimental

### 28.2.1 Materials, Synthesis, and Analysis

The chemical reagents used for sample synthesis and photocatalytic reactions including Co(NO<sub>3</sub>)<sub>2</sub>·6H<sub>2</sub>O, benzimidazole (H-PhIm), *N,N*-dimethylformamide (DMF), methanol, dichloromethane (DCM), triethanolamine (TEOA), and acetonitrile (MeCN) were purchased from Alfa Aesar. 2,2'-Bipyridine (bpy) was supplied by Sigma. TiO<sub>2</sub> (P25) was obtained from Degussa in a nanoporous powder formed by a mixture of anatase and rutile. All the chemicals were used as received without further purification. Carbon dioxide gas, supplied by Fuzhou Lianzhong Industrial Gases Co., Ltd, is super grade purity (99.999 %). The <sup>13</sup>CO<sub>2</sub> is of 97 % purity grade. The ZIF-9 sample was synthesized and fully characterized as reported in our previous works [56, 59].

Gas chromatographic analysis was carried out on an Agilent 7820A gas chromatography system (thermal conductivity detector, TCD; TD-01 packed column; argon as the carrier gas; oven temperature, 50 °C; inlet temperature, 120 °C; detector temperature, 200 °C). Gas chromatography mass spectrometry (GC-MS, HP 5973-Agilent 6890) was used to analyze the products of the <sup>13</sup>CO<sub>2</sub> isotopic experiment and to determine whether other potential products were generated in the liquid phase using helium as the carrier gas.

Photocurrent measurements were performed with a CHI Electrochemical System in the mixture of MeCN and H<sub>2</sub>O (v/v = 3/2) without any bias potential. A graphite rod and an Ag/AgCl (3 M KCl) electrode were used as the counter electrode and reference electrode, respectively. The working electrodes (indium-tin oxide, ITO) were irradiated from the back side to minimize the influence of the semiconductor layer.

### 28.2.2 Photocatalytic Tests

The CO<sub>2</sub> photocatalytic reduction reactions were performed in a Schlenk flask (80 ml) under an atmospheric pressure of CO<sub>2</sub>, and the reaction temperature was kept at 30 °C controlled by a flow of circulating cooling water. In the reaction system, TiO<sub>2</sub> (20 mg) and ZIF-9 (4 μmol) powder were dispersed in the reaction solution containing solvent (5 ml, H<sub>2</sub>O/MeCN=3), TEOA (1 ml), and bpy (10 mg). The reaction system was subjected to vacuum degassing and then backfilling with pure CO<sub>2</sub>. The process was repeated three times, and in the last cycle the reactor was backfilled with pure CO<sub>2</sub> (1 atm partial pressure). Then, the reaction system used a 300 W Xe lamp (without light filter) as the light source and energetically stirred by a magnetic stirrer during the reactions. After the reaction, the produced gas was analyzed and quantified by Agilent 7820A gas chromatography.

### 28.3 Results and Discussion

As can be seen in Table 28.1, a large amount of CO (28.7 μmol) and a small evolution of H<sub>2</sub> (6.9 μmol) together with a high selectivity for CO formation (80.6 %) were produced from the TiO<sub>2</sub>- and ZIF-9-based hybrid system (entry 1), after photoirradiation by the simulated sunlight for 1 h under the mild reaction conditions (30 °C, 1 atm CO<sub>2</sub>). The results demonstrated the high CO<sub>2</sub>-to-CO conversion efficiency

**Table 28.1** Investigations on the CO<sub>2</sub> photochemical reduction system under various reaction conditions<sup>a</sup>

Entry	CO (μmol)	H <sub>2</sub> (μmol)	CO+H <sub>2</sub> (μmol)	Sel. <sub>CO</sub> <sup>b</sup> (%)
1	28.7	6.9	35.6	80.6
2 <sup>c</sup>	n.d. <sup>d</sup>	n.d.	/	/
3 <sup>e</sup>	n.d.	n.d.	/	/
4 <sup>f</sup>	n.d.	0.3	0.3	0
5 <sup>g</sup>	0.5	0.9	1.4	35.7
6 <sup>h</sup>	n.d.	n.d.	/	/
7 <sup>i</sup>	n.d.	0.2	0.2	0
8 <sup>j</sup>	19.6	5.6	25.2	77.8

<sup>a</sup>Reaction conditions: TiO<sub>2</sub> (20 mg), ZIF-9 (4 μmol), TEOA (1 ml), solvent (5 ml, H<sub>2</sub>O/MeCN=2/3), bpy (10 mg), 30 °C, 1 atm CO<sub>2</sub>, 1 h

<sup>b</sup>Sel.<sub>CO</sub>=mol(CO)/mol(CO+H<sub>2</sub>)

<sup>c</sup>Without TiO<sub>2</sub>

<sup>d</sup>Not detectable

<sup>e</sup>In the dark

<sup>f</sup>Without ZIF-9

<sup>g</sup>Without TEOA

<sup>h</sup>Without bpy

<sup>i</sup>Using N<sub>2</sub> to replace CO<sub>2</sub>

<sup>j</sup>Using Co<sup>2+</sup> to replace ZIF-9

by the cooperative catalysis of TiO<sub>2</sub> and ZIF-9, acting as a photocatalyst and a cocatalyst, respectively. The observed catalytic performance of the CO<sub>2</sub> photoreduction catalysis was closely related to the multiple processes mainly including electron transfer, and CO<sub>2</sub> adsorption/activation.

To further explore the essence of the constructed heterogeneous CO<sub>2</sub> conversion system, several negative experiments were performed. Firstly, with the light harvester TiO<sub>2</sub> absented from the reaction system, it was unable to produce any CO or H<sub>2</sub> (entry 2, Table 28.1) under otherwise identical conditions. This observation revealed that light sensitization of the TiO<sub>2</sub> semiconductor, creating photoexcited electrons for subsequent photoredox reactions, is responsible for the initiation of CO<sub>2</sub> photoreduction catalysis. The photocatalytic nature of the reaction was further confirmed by the fact that no reaction occurred when the reaction was conducted in the dark (entry 3, Table 28.1). Secondly, once ZIF-9 was removed from the system, the evolution of CO was completely terminated but only with a tiny amount of H<sub>2</sub> generated (entry 4, Table 28.1), which thus demonstrated the cocatalyst character of ZIF-9 for CO<sub>2</sub> photoreduction catalysis over its unique metal-organic architecture, by merging the redox functions of cobalt to promote electron transfers and the characteristics of imidazolate-based entities for CO<sub>2</sub> activation [60]. Controlled experiment revealed that when using Co<sup>2+</sup> ion as a homogeneous cocatalyst for the system, the CO<sub>2</sub> reduction reaction also occurred (entry 8, Table 28.1). But, the catalytic efficiency was much weaker than that of ZIF-9 cocatalyst. This observation however strongly emphasized the significance of soft imidazolate-based entities in the ZIF-9 metal-organic architectures for the activation of CO<sub>2</sub> [60–62]. This is no surprise because imidazolate-based entities have been well employed as precursors of functional organic compounds for CO<sub>2</sub> capture and activation, such as ionic liquids and carbene. All the abovementioned findings highlighted that the superior cocatalytic performance of ZIF-9 for CO<sub>2</sub> reduction catalysis is originated from the synergy of cobalt and benzimidazolate ligand that were spatially assembled in the metal-organic framework of ZIF-9, creating chemically homogeneous and defined active site for CO<sub>2</sub> reduction.

To further illustrate the importance of the collaboration of ZIF-9 and TiO<sub>2</sub> for the CO<sub>2</sub> reduction reaction in our system, we studied the relationship between the catalytic activity and the adding amount of ZIF-9 and TiO<sub>2</sub>. As is demonstrated in Fig. 28.1, the initial formations of CO and H<sub>2</sub> exhibit a linear dependence on both ZIF-9 and TiO<sub>2</sub> concentrations [63]. The observations firmly indicate that both TiO<sub>2</sub> (the light sensitizer) and ZIF-9 (the redox promoter and CO<sub>2</sub> absorber/activator) are absolutely indispensable for achieving the effective CO<sub>2</sub> conversion photocatalysis in the current chemical system.

It was found that when the sacrificial electron donor TEOA was removed from the system, the production of CO (0.5 μmol) and H<sub>2</sub> (0.9 μmol) was substantially decreased, which reveals the important role of the electron donors played in the reaction. Indeed, the production of CO and H<sub>2</sub> generated from the electron-donor-free system was very small, but it was still a very intriguing finding for establishing artificial photosynthetic systems without sacrificial agents. By inspiration of this attractive finding, the corresponding works are in progress. In the current ZIF-9-promoted

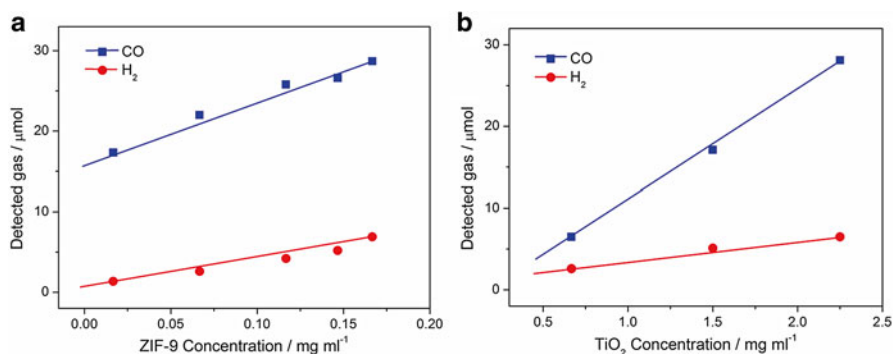


**Fig. 28.1** Initial evolution of CO and H<sub>2</sub> produced from the ZIF-9- and TiO<sub>2</sub>-based CO<sub>2</sub> photoreduction system as a function of ZIF-9 (a) and TiO<sub>2</sub> (b) concentration

**Table 28.2** Effects of electron donors on the catalytic performance of the ZIF-9-enhanced CO<sub>2</sub> photoreduction system<sup>a</sup>

Amine	CO (μmol)	H <sub>2</sub> (μmol)	CO+H <sub>2</sub> (μmol)	Sel. <sub>CO</sub> (%)
TEOA	28.7	6.9	35.6	80.6
TEA <sup>b</sup>	0	0.3	0.3	0
TPA <sup>c</sup>	0	0.2	0.2	0
TBA <sup>d</sup>	0	0.2	0.2	0
DEAIPO <sup>e</sup>	25.5	3.8	29.3	87.0
DEAEO <sup>f</sup>	7.7	0.8	8.5	90.6

<sup>a</sup>Reaction conditions are the same as those in Table 28.1

<sup>b</sup>Triethylamine

<sup>c</sup>Tri-*n*-propylamine

<sup>d</sup>Tri-*n*-butylamine

<sup>e</sup>1-(Diethylamine)-2-propanol

<sup>f</sup>2-(Diethylamino)ethanol

CO<sub>2</sub> fixation system, the electron donor is essential to construct a highly efficient catalytic cascade for CO<sub>2</sub> reduction. Therefore, we applied a series of tertiary amines in the reaction system to further explore the effects of sacrificial agents on the reaction activity and the results were listed in Table 28.2. As shown, once TEOA was replaced by the unhydroxylated alkylamines such as TEA, TPA, or TBA, the chemical system was inactive to produce any detectable CO but with very small amount of H<sub>2</sub>. From the comparison of these results, it is concluded that using the β-hydroxylated amines as the electron donors can significantly enhance the photocatalytic activity of the CO<sub>2</sub> conversion reaction. Thus, two other β-hydroxylated tertiary amines of DEAIPO and DEAEO were further individually employed to replace TEOA for running the CO<sub>2</sub> reduction reactions. It can be found that the productions of CO and H<sub>2</sub> are much higher than those of using unhydroxylated alkylamines, which therefore confirms the conclusion that the β-hydroxylated tertiary amines are favorable for operating the photochemical reduction of CO<sub>2</sub> in

the TiO<sub>2</sub>- and ZIF-9-based catalytic system under the applied conditions. Interestingly, when using DEAIPPO or DEAEAO as the electron donors, the generations of the products are somewhat smaller than those of TEOA, but the selectivity for CO formation is increased apparently. The results imply that, owing to steric hindrance effect, the different adsorption of the sacrificial electron donors may have remarkable impacts on both the catalytic activity and the product selectivity of the CO<sub>2</sub> reduction system.

Results of the negative controlled experiment, which was conducted in N<sub>2</sub> atmosphere, displayed that no CO formation was detected, but a small evolution of H<sub>2</sub> (0.2 μmol). The observations verify that the produced CO is stemmed from the reactant CO<sub>2</sub>. We also carried out the controlled experiments using <sup>12</sup>CO<sub>2</sub> and <sup>13</sup>CO<sub>2</sub>, respectively, to further validate the carbon source of the produced CO. As demonstrated in Fig. 28.2a, when the reaction occurred under <sup>12</sup>CO<sub>2</sub> atmosphere, the results of GC-MS analysis gave a peak of <sup>12</sup>CO at 3.99 min with *m/z*=28. However, under the same reaction conditions, the GC-MS spectra of the produced CO from the <sup>13</sup>C-labelled isotopic experiment presented a peak at 4.11 min with *m/z* value of 29, which is assigned to <sup>13</sup>CO (Fig. 28.2b). From the results of the GC-MS measurements, we confirm that the detected CO is derived from the deoxygenative reduction of CO<sub>2</sub>, but not the organics in the hybrid system, thus defeating any doubt about the carbon source of the CO production.

The formations of CO and H<sub>2</sub> produced from the chemical system as a function of reaction time were investigated by conducting the reaction under different irradiation periods. As displayed in Fig. 28.3, the generation rates of CO and H<sub>2</sub>

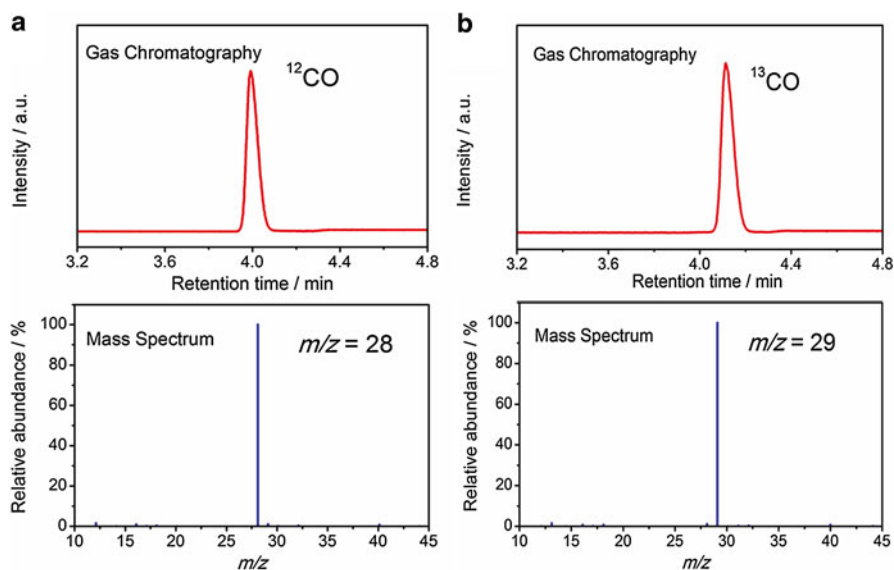
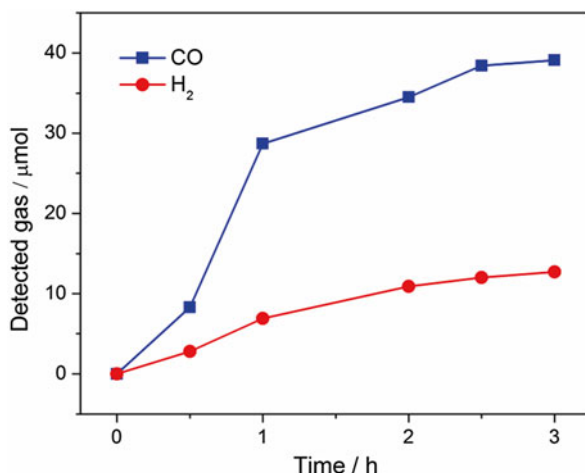


**Fig. 28.2** Results of the GC-MS analysis of the generated CO in the photochemical reduction of <sup>12</sup>CO<sub>2</sub> and <sup>13</sup>CO<sub>2</sub> by the cooperation of ZIF-9 and TiO<sub>2</sub>

**Fig. 28.3** Time-production plot of CO and H<sub>2</sub> generated from the CO<sub>2</sub> photoreduction system under irradiation at mild conditions



increase during the reaction time of 0.5–1 h. When the reaction time was continuing and prolonged till 3 h, the generation rates of the products were gradually diminished, and the accumulated productions of CO and H<sub>2</sub> were 39.1 μmol and 12.7 μmol, respectively, affording a turnover number of *ca.* 13 (in terms of the ZIF-9 cocatalyst). The reason for the decrease in the reaction rate may be attributed to the depletion/degradation of the CO<sub>2</sub> and bpy in the reaction system, but the ZIF-9 cocatalyst is still stable to preserve its intrinsic cocatalytic functions for supporting the photochemical reduction of CO<sub>2</sub> [56–58].

To evaluate the stability of the structure of the ZIF-9 cocatalyst, after photocatalytic reactions, the mixture of ZIF-9 and TiO<sub>2</sub> was filtrated from the reaction mixture, and then was subjected to XRD measurement. As can be seen from Fig. 28.4, there are no noticeable alternations in the XRD patterns of the fresh and used mixture of ZIF-9 and TiO<sub>2</sub>. This study reflects that the ZIF-9 cocatalyst is stable during the procedure of CO<sub>2</sub> reduction catalysis even under ultraviolet irradiations, consistent with our reported work [56–58].

We also explored the effect of reaction temperature on the catalytic performance of the reaction system and the results are showed in Fig. 28.5. In the case of reaction temperature elevated from 10 to 30 °C, the productions of CO and H<sub>2</sub> are gradually increased, presenting nearly a linear dependence on the reaction temperature. However, when the reaction temperature was further increased from 30 to 60 °C, both yields of the products are obviously reduced. This observation is mainly ascribed to the release/desorption of CO<sub>2</sub> for the reaction mixture at relatively high reaction temperatures. Therefore, under the reaction conditions, the optimal temperature for running CO<sub>2</sub> reduction reactions is 30 °C, exhibiting a high CO evolution rate of 28.7 μmol h<sup>-1</sup>.

It is widely acknowledged that reaction activity is largely affected by the reaction surroundings; thus various solvents were utilized in the system to explore a favorite reaction medium for realizing effective CO<sub>2</sub> reduction reactions. As is

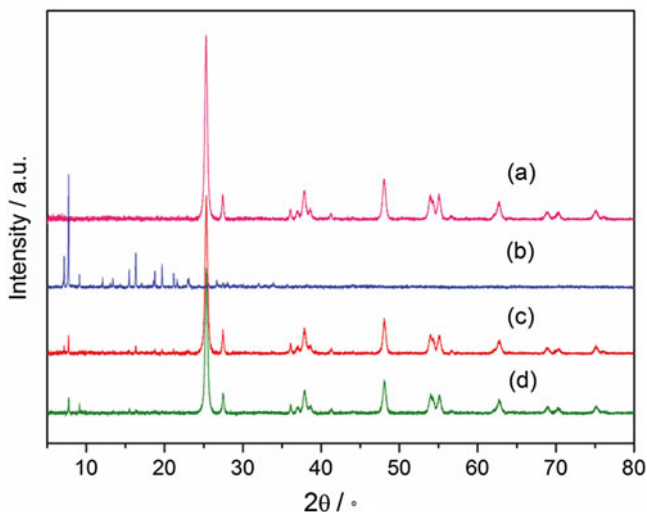


**Fig. 28.4** Powder XRD patterns of (a) TiO<sub>2</sub>, (b) ZIF-9, (c) fresh, and (d) used mixture of ZIF-9 and TiO<sub>2</sub>

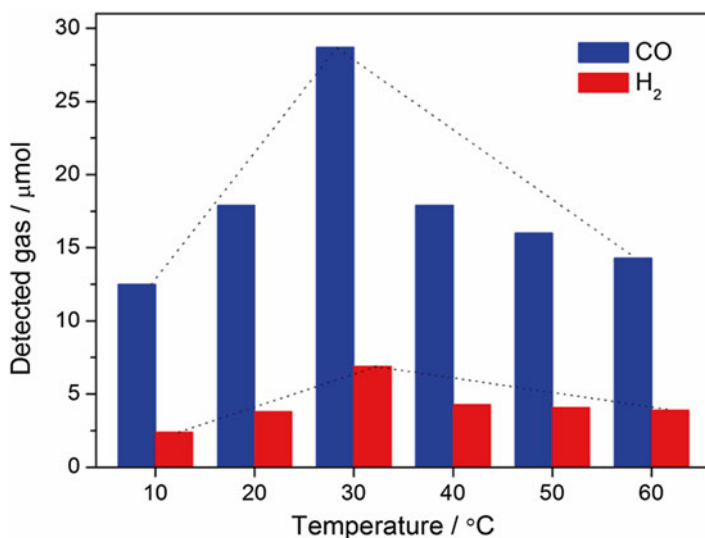


**Fig. 28.5** Evolutions of CO and H<sub>2</sub> produced from the reaction system by light illumination under various reaction temperatures

listed in Table 28.3, when the reaction was carried out in the pure H<sub>2</sub>O environment, the system indeed converted CO<sub>2</sub> into CO, but mainly favored for H<sub>2</sub> evolution, showing a very low selectivity for CO formation. This result is in accordance with the fact that TiO<sub>2</sub> is a prominent water-splitting photocatalyst [64, 65]. While aprotic

**Table 28.3** Studies of the solvent effects on catalytic activity of the chemical system<sup>a</sup>

Solvent	CO ( $\mu\text{mol}$ )	H <sub>2</sub> ( $\mu\text{mol}$ )	CO+H <sub>2</sub> ( $\mu\text{mol}$ )	Sel. <sub>CO</sub> (%)
H <sub>2</sub> O	2.0	21.2	23.2	9.4
MeCN	3.5	0.7	4.2	83.3
DMF	0.9	0.4	1.3	69.2
DMSO <sup>b</sup>	0.8	0.7	1.5	53.3
THF <sup>c</sup>	2.4	0.1	2.5	96.0
DCM	0.3	0.03	0.33	90.9
EA <sup>d</sup>	1.3	0.3	1.6	81.3

<sup>a</sup>Reaction conditions are the same as those in Table 28.1

<sup>b</sup>Dimethyl sulfoxide

<sup>c</sup>Tetrahydrofuran

<sup>d</sup>Ethyl acetate

solvents such as MeCN, DMF, DMSO, THF, DCM, and EA were applied as the reaction medium, all the catalytic systems demonstrate high CO selectivity, but obvious variations in CO production were observed when using different reaction solvents. The main reason responsible for the difference in catalytic performance can be ascribed to the different interactions between the used solvents and CO<sub>2</sub> molecules. It has been proposed that N- and/or O-containing solvents are favored for solubilizing CO<sub>2</sub> due to the Lewis acid-base interaction between these atoms and CO<sub>2</sub> molecule [66, 67]. Thus, when the reactions occurred in MeCN, THF, DMF, DMSO, and EA, the reaction activities were much better than those in DCM that only held a weak chemical affinity toward CO<sub>2</sub> molecule. It is also clearly demonstrated that the evolution of CO produced from the systems in MeCN and THF is much higher than the case of DMF, DMSO, and EA, which may be originated from the steric hindrance effect. Therefore, among the examined solvents under the reaction conditions, MeCN shows the best efficiency for the generation of CO, and THF exhibits the highest performance for CO selectivity.

Based on the findings from the study of reaction solvents, we further used the mixture of H<sub>2</sub>O and MeCN as reaction medium, and inspected the relationship between the reaction activity and the ratio of H<sub>2</sub>O in the solvent, because water addition could in principle promote the reaction kinetics as well as reduce the thermodynamic barrier of CO<sub>2</sub> reduction reactions [68]. As shown in Fig. 28.6, it is obvious that the yield of CO is substantially increased as the H<sub>2</sub>O ratio gradually added till 40 %, and further increasing the amount of water in the reaction medium results in the decrease in CO production. Thus, when the reaction system contains a H<sub>2</sub>O ratio of 40 %, the chemical system exhibits the highest efficiency for CO<sub>2</sub> photoreduction. Unlike the case of CO formation, the yield of H<sub>2</sub> increases exclusively following the H<sub>2</sub>O ratio gradually enlarged. So, the amount of water contained in the reaction medium has remarkable influence on the catalytic performance of the ZIF-9-promoted CO<sub>2</sub> photoreduction system.

Lastly, we investigated the photocurrent generation of the ZIF-9 and TiO<sub>2</sub> cocatalyzed CO<sub>2</sub> conversion system. The photocurrent action spectra of the catalytic

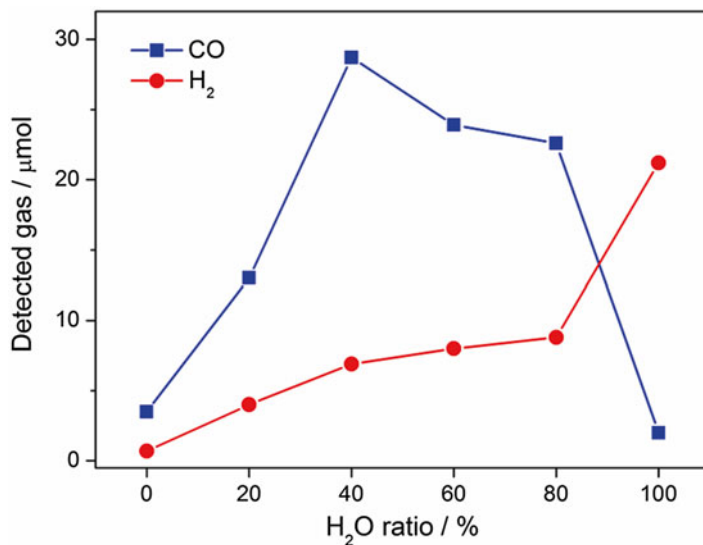


**Fig. 28.6** Dependence of catalytic activity on the amount of water contained in the reaction solvent

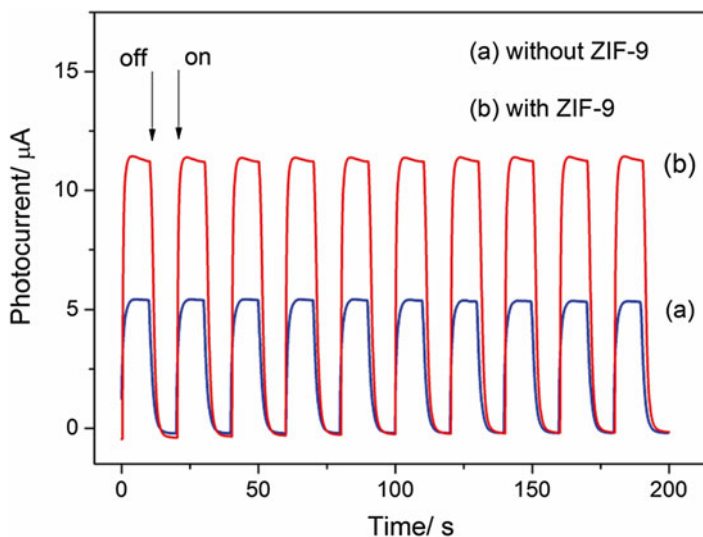


**Fig. 28.7** Transient photocurrent response of the ZIF-9-promoted CO<sub>2</sub> reduction system containing different components under simulated sunlight illumination

system are presented in Fig. 28.7. As shown, once ZIF-9 was employed as a cocatalyst in the system, the photocurrent was remarkably improved compared with that without its presence. Note that when ZIF-9 was added, the photocurrent immediately increases to the maximum as long as the light was switched on and then

rapidly reduces to zero when the light was switched off. It is known that photocurrent is mainly generated by the diffusion of the photoinduced electrons to the back contact, and meanwhile the photogenerated holes are taken up by the hole acceptor [69]. Thus, the improved photocurrent generation of the system indicated that an efficient electron transportation existed when ZIF-9 was served as the cocatalyst. The observations highlight the excellent function of ZIF-9 for promoting electron transfers in the CO<sub>2</sub> photoreduction system.

## 28.4 Conclusions

The cobalt-containing zeolitic imidazolate framework ZIF-9 was further developed as an efficient non-noble-metal cocatalyst for promoting the photocatalytic reduction of CO<sub>2</sub> by the cooperation of titanium oxide as a photocatalyst under simulated sunlight irradiation. This hybrid system effectively catalyzed the CO<sub>2</sub>-to-CO photoreduction catalysis. The <sup>13</sup>C isotopic experiment firmly identified that the produced CO is indeed originated from the deoxygenative reduction of CO<sub>2</sub>. Reaction conditions including the reaction temperatures, the reaction solvents, the characteristics of the electron donors, and the water ratio in the reaction medium were investigated and optimized for operating optimal CO<sub>2</sub> reduction reaction. The stability of ZIF-9 was confirmed by the powder XRD characterization after reactions. Photocurrent testing revealed the function of ZIF-9 for promoting the light-induced electron transfer in the chemical system. Considering the variety of semiconductor photocatalyst, and the flexible engineering in the composition, structure, and functionality of MOFs, we think that this work will bring great opportunities for establishing effective hybrid chemical systems for CO<sub>2</sub> photoreduction catalysis in artificial photosynthesis by the cooperation of MOFs cocatalyst and TiO<sub>2</sub>-based photocatalyst, where using the well-known tools for the visibilization of TiO<sub>2</sub> will establish sustainable CO<sub>2</sub> photoreduction via visible light.

**Acknowledgment** This work is financially supported by the National Basic Research Program of China (2013CB632405), the National Natural Science Foundation of China (21425309), the State Key Laboratory of NBC Protection for Civilian (SKLNBC2013004K), and the Specialized Research Fund for the Doctoral Program of Higher Education (20133514110003).

## References

1. Khodakov AY, Chu W, Fongarland P (2007) Advances in the development of novel cobalt Fischer-Tropsch catalysts for synthesis of long-chain hydrocarbons and clean fuels. *Chem Rev* 107:1692–1744
2. Rofer-DePoorter CK (2012) A comprehensive mechanism for the Fischer-Tropsch synthesis. *Chem Rev* 81:447–474
3. Vennestrøm PNR, Osmundsen CM, Christensen CH, Taarning E (2011) Beyond petrochemicals: the renewable chemicals industry. *Angew Chem Int Ed* 50:10502–10509

- Sunley GJ, Watson DJ (2000) High productivity methanol carbonylation catalysis using iridium: the Cativa™ process for the manufacture of acetic acid. *Catal Today* 58:293–307
- Silvia JS, Cummins CC (2010) Ligand-based reduction of CO<sub>2</sub> to CO mediated by an anionic niobium nitride complex. *J Am Chem Soc* 132:2169–2171
- Porosoff MD, Yang X, Boscoboinik JA, Chen JG (2014) Molybdenum carbide as alternative catalysts to precious metals for highly selective reduction of CO<sub>2</sub> to CO. *Angew Chem Int Ed* 53:6705–6709
- Teramura K, Iguchi S, Mizuno Y, Shishido T, Tanaka T (2012) Photocatalytic conversion of CO<sub>2</sub> in water over layered double hydroxides. *Angew Chem Int Ed* 51:8008–8011
- Morris AJ, Meyer GJ, Fujita E (2009) Molecular approaches to the photocatalytic reduction of carbon dioxide for solar fuels. *Acc Chem Res* 42:1983–1994
- Wen F, Li C (2013) Hybrid artificial photosynthetic systems comprising semiconductors as light harvesters and biomimetic complexes as molecular cocatalysts. *Acc Chem Res* 46:2355–2364
- Lehn JM, Ziessel R (1982) Photochemical generation of carbon monoxide and hydrogen by reduction of carbon dioxide and water under visible light irradiation. *Proc Natl Acad Sci U S A* 79:701–704
- Inoue T, Fujishima A, Konishi S, Honda K (1979) Photoelectrocatalytic reduction of carbon dioxide in aqueous suspensions of semiconductor powders. *Nature* 277:637–638
- Kohno Y, Tanaka T, Funabiki T, Yoshida S (2000) Reaction mechanism in the photoreduction of CO<sub>2</sub> with CH<sub>4</sub> over ZrO<sub>2</sub>. *Phys Chem Chem Phys* 2:5302–5307
- Teramura K, Tanaka T, Ishikawa H, Kohno Y, Funabiki T (2004) Photocatalytic reduction of CO<sub>2</sub> to CO in the presence of H<sub>2</sub> or CH<sub>4</sub> as a reductant over MgO. *J Phys Chem B* 108:346–354
- Liao F, Huang Y, Ge J, Zheng W, Tedsree K, Collier P, Hong X, Tsang SC (2011) Morphology-dependent interactions of ZnO with Cu nanoparticles at the materials' interface in selective hydrogenation of CO<sub>2</sub> to CH<sub>3</sub>OH. *Angew Chem Int Ed* 50:2162–2165
- Yu J, Jin J, Cheng B, Jaroniec M (2014) A noble metal-free reduced graphene oxide–CdS nanorod composite for the enhanced visible-light photocatalytic reduction of CO<sub>2</sub> to solar fuel. *J Mater Chem A* 2:3407–3416
- Wang Y, Li B, Zhang C, Cui L, Kang S, Li X, Zhou L (2013) Ordered mesoporous CeO<sub>2</sub>-TiO<sub>2</sub> composites: highly efficient photocatalysts for the reduction of CO<sub>2</sub> with H<sub>2</sub>O under simulated solar irradiation. *Appl Catal B Environ* 130–131:277–284
- Park H, Choi JH, Choi KM, Lee DK, Kang JK (2012) Highly porous gallium oxide with a high CO<sub>2</sub> affinity for the photocatalytic conversion of carbon dioxide into methane. *J Mater Chem* 22:5304–5307
- Sato S, Morikawa T, Saeki S, Kajino T, Motohiro T (2010) Visible-light-induced selective CO<sub>2</sub> reduction utilizing a ruthenium complex electrocatalyst linked to a p-type nitrogen-doped Ta<sub>2</sub>O<sub>5</sub> semiconductor. *Angew Chem Int Ed* 49:5101–5105
- Li Y, Wang WN, Zhan Z, Woo MH, Wu CY, Biswas P (2010) Photocatalytic reduction of CO<sub>2</sub> with H<sub>2</sub>O on mesoporous silica supported Cu/TiO<sub>2</sub> catalysts. *Appl Catal B Environ* 100:386–392
- Zhang Q, Li Y, Ackerman EA, Gajdardziska-Josifovska M, Li H (2011) Visible light responsive iodine-doped TiO<sub>2</sub> for photocatalytic reduction of CO<sub>2</sub> to fuels. *Appl Catal A Gen* 400:195–202
- Anpo M, Yamashita H, Ichihashi Y, Ehara S (1995) Photocatalytic reduction of CO<sub>2</sub> with H<sub>2</sub>O on various titanium oxide catalysts. *J Electroanal Chem* 396:21–26
- Tseng IH, Chang WC, Wu JCS (2002) Photoreduction of CO<sub>2</sub> using sol-gel derived titania and titania-supported copper catalysts. *Appl Catal B Environ* 37:37–48
- Indrakanti VP, Kubicki JD, Schober HH (2009) Photoinduced activation of CO<sub>2</sub> on Ti-based heterogeneous catalysts: Current state, chemical physics-based insights and outlook. *Energy Environ Sci* 2:745–758
- Zhai Q, Xie S, Fan W, Zhang Q, Wang Y, Deng W, Wang Y (2013) Photocatalytic conversion of carbon dioxide with water into methane: Platinum and copper(I) oxide co-catalysts with a core-shell structure. *Angew Chem Int Ed* 52:5776–5779

25. Boccuzzi F, Chiorino A, Manzoli M, Andreeva D, Tabakova T (1999) FTIR study of the low-temperature water–gas shift reaction on Au/Fe<sub>2</sub>O<sub>3</sub> and Au/TiO<sub>2</sub> catalysts. *J Catal* 188:176–185
26. Sekizawa K, Maeda K, Domen K, Koike K, Ishitani O (2013) Artificial Z-scheme constructed with a supramolecular metal complex and semiconductor for the photocatalytic reduction of CO<sub>2</sub>. *J Am Chem Soc* 135:4596–4599
27. Woolerton TW, Sheard S, Reiser E, Pierce E, Ragsdale SW, Armstrong FA (2010) Efficient and clean photoreduction of CO<sub>2</sub> to CO by enzyme-modified TiO<sub>2</sub> nanoparticles using visible light. *J Am Chem Soc* 132:2132–2133
28. Kohno Y, Hayashi H, Takenaka S, Tanaka T, Funabiki T, Yoshida S (1999) Photo-enhanced reduction of carbon dioxide with hydrogen over Rh/TiO<sub>2</sub>. *J Photochem Photobio A Chem* 126:117–123
29. Maeda K, Sekizawa K, Ishitani O (2013) A polymeric-semiconductor–metal-complex hybrid photocatalyst for visible-light CO<sub>2</sub> reduction. *Chem Commun* 49:10127–10129
30. Wang C, Xie Z, deKrafft KE, Lin W (2011) Doping metal–organic frameworks for water oxidation, carbon dioxide reduction, and organic photocatalysis. *J Am Chem Soc* 133:13445–13454
31. Anpo M, Yamashita H, Ichihashi Y, Fujii Y, Honda M (1997) Photocatalytic reduction of CO<sub>2</sub> with H<sub>2</sub>O on titanium oxides anchored within micropores of zeolites: Effects of the structure of the active sites and the addition of Pt. *J Phys Chem B* 101:2632–2636
32. Zhang QH, Han WD, Hong YJ, Yu JG (2009) Photocatalytic reduction of CO<sub>2</sub> with H<sub>2</sub>O on Pt-loaded TiO<sub>2</sub> catalyst. *Catal Today* 148:335–340
33. Qin Z, Thomas CM, Lee S, Coates GW (2003) Cobalt-based complexes for the copolymerization of propylene oxide and CO<sub>2</sub>: active and selective catalysts for polycarbonate synthesis. *Angew Chem Int Ed* 42:5484–5487
34. Cohen CT, Chu T, Coates GW (2005) Cobalt catalysts for the alternating copolymerization of propylene oxide and carbon dioxide: combining high activity and selectivity. *J Am Chem Soc* 127:10869–10878
35. Louie J, Gibby JE, Farnworth MV, Tekavec TN (2002) Efficient nickel-catalyzed [2 + 2 + 2] cycloaddition of CO<sub>2</sub> and diynes. *J Am Chem Soc* 124:15188–15189
36. Matsuoka S, Yamamoto K, Ogata T, Kusaba M, Nakashima N, Fujita E, Yanagida S (1993) Efficient and selective electron mediation of cobalt complexes with cyclam and related macrocycles in the *p*-terphenyl-catalyzed photoreduction of carbon dioxide. *J Am Chem Soc* 115:601–609
37. Fischer H, Tom GM, Taube H (1976) Intramolecular electron transfer mediated by 4,4'-bipyridine and related bridging groups. *J Am Chem Soc* 98:5512–5517
38. Rillema DP, Allen G, Meyer TJ, Conrad D (1983) Redox properties of ruthenium(II) tris chelate complexes containing the ligands 2,2'-bipyrazine, 2,2'-bipyridine, and 2,2'-bipyrimidine. *Inorg Chem* 22:1617–1622
39. Willner I, Maida R, Mandler D, Duerr H, Doerr G, Zengerle K (1987) Photosensitized reduction of carbon dioxide to methane and hydrogen evolution in the presence of ruthenium and osmium colloids: strategies to design selectivity of products distribution. *J Am Chem Soc* 109:6080–6086
40. Trammell SA, Meyer TJ (1999) Diffusional mediation of surface electron transfer on TiO<sub>2</sub>. *J Phys Chem B* 103:104–107
41. Saji T, Aoyagui S (1975) Electron-transfer kinetics of transition-metal complexes in lower oxidation states: IV<sup>1</sup>. Electrochemical electron-transfer rates of tris(2,2'-bipyridine) complexes of iron, ruthenium, osmium, chromium, titanium, vanadium and molybdenum. *J Electroanal Chem* 63:31–37
42. Rosi NL, Eckert J, Eddaoudi M, Vodak DT, Kim J, O'Keeffe M, Yaghi OM (2003) Hydrogen storage in microporous metal-organic frameworks. *Science* 300:1127–1129
43. Stroppa A, Jain P, Barone P, Marsman M, Perez-Mato JM, Cheetham AK, Kroto HW, Picozzi S (2011) Electric control of magnetization and interplay between orbital ordering and ferroelectricity in a multiferroic metal–organic framework. *Angew Chem Int Ed* 50:5847–5850

44. Cooper AI, Rosseinsky MJ (2009) Metal–organic frameworks: improving pore performance. *Nat Chem* 1:26–27
45. James SL (2003) Metal–organic frameworks. *Chem Soc Rev* 32:276–288
46. Hayashi H, Cote AP, Furukawa H, O’Keeffe M, Yaghi OM (2007) Zeolite a imidazolate frameworks. *Nat Mater* 6:501–506
47. Zhang JP, Zhang YB, Lin JB, Chen XM (2012) Metal azolate frameworks: from crystal engineering to functional materials. *Chem Rev* 112:1001–1033
48. Park KS, Ni Z, Côté AP, Choi JY, Huang R, Uribe-Romo FJ, Chae HK, O’Keeffe M, Yaghi OM (2006) Exceptional chemical and thermal stability of zeolitic imidazolate frameworks. *Proc Natl Acad Sci U S A* 103:10186–10191
49. Liu Q, Low ZX, Li L, Razmjou A, Wang K, Yao J, Wang H (2013) ZIF-8/Zn<sub>2</sub>GeO<sub>4</sub> nanorods with an enhanced CO<sub>2</sub> adsorption property in an aqueous medium for photocatalytic synthesis of liquid fuel. *J Mater Chem A* 1:11563–11569
50. Wang B, Cote AP, Furukawa H, O’Keeffe M, Yaghi OM (2008) Colossal cages in zeolitic imidazolate frameworks as selective carbon dioxide reservoirs. *Nature* 453:207–211
51. Miralda CM, Macias EE, Zhu M, Ratnasamy P, Carreon MA (2011) Zeolitic imidazole framework-8 catalysts in the conversion of CO<sub>2</sub> to chloropropene carbonate. *ACS Catal* 2:180–183
52. Dimitrakakis C, Easton CD, Muir BW, Ladewig BP, Hill MR (2013) Spatial control of zeolitic imidazolate framework growth on flexible substrates. *Cryst Growth Des* 13:4411–4417
53. Aguado S, Bergeret G, Titus MP, Moizan V, Nieto-Draghi C, Bats N, Farrusseng D (2011) Guest-induced gate-opening of a zeolite imidazolate framework. *New J Chem* 35:546–550
54. Reyes SC, Santiesteban JG, Ni Z, Paur CS, Kortunov P, Zengel J, Deckman HW (2009) US 2009/0214407, Accessed 27 Aug 2009
55. Reyes SC, Ni Z, Paur CS, Kortunov P, Zengel J, Deckman HW, Santiesteban JG (2009) US 2009/0211441, Accessed 27 Aug 2009
56. Wang S, Yao W, Lin J, Ding Z, Wang X (2014) Cobalt imidazolate metal–organic frameworks photosplit CO<sub>2</sub> under mild reaction conditions. *Angew Chem Int Ed* 53:1034–1038
57. Wang S, Wang X (2015) Photocatalytic CO<sub>2</sub> reduction by CdS promoted with a zeolitic imidazolate framework. *Appl Catal B Environ* 162:494–500
58. Wang S, Lin J, Wang X (2014) Semiconductor–redox catalysis promoted by metal–organic frameworks for CO<sub>2</sub> reduction. *Phys Chem Chem Phys* 16:14656–14660
59. Wang S, Hou Y, Lin S, Wang X (2014) Water oxidation electrocatalysis by a zeolitic imidazolate framework. *Nanoscale* 6:9930–9934
60. Rosen BA, Salehi-Khojin A, Thorson MR, Zhu W, Whipple DT, Kenis PJA, Masel RI (2011) Ionic liquid–mediated selective conversion of CO<sub>2</sub> to CO at low overpotentials. *Science* 334:643–644
61. Wang C, Luo H, Jiang D, Li H, Dai S (2010) Carbon dioxide capture by superbase-derived protic ionic liquids. *Angew Chem Int Ed* 49:5978–5981
62. Bates ED, Mayton RD, Ntai I, Davis JH (2002) CO<sub>2</sub> capture by a task-specific ionic liquid. *J Am Chem Soc* 124:926–927
63. Wen F, Wang X, Huang L, Ma G, Yang J, Li C (2012) A hybrid photocatalytic system comprising ZnS as light harvester and an [Fe<sub>2</sub>S<sub>2</sub>] hydrogenase mimic as hydrogen evolution catalyst. *ChemSusChem* 5:849–853
64. Xiang Q, Yu J, Jaroniec M (2012) Synergetic effect of MoS<sub>2</sub> and graphene as cocatalysts for enhanced photocatalytic H<sub>2</sub> production activity of TiO<sub>2</sub> nanoparticles. *J Am Chem Soc* 134:6575–6578
65. Kho YK, Iwase A, Teoh WY, Mädler L, Kudo A, Amal R (2010) Photocatalytic H<sub>2</sub> evolution over TiO<sub>2</sub> nanoparticles. The synergistic effect of anatase and rutile. *J Phys Chem C* 114:2821–2829
66. Kazarian SG, Vincent MF, Bright FV, Liotta CL, Eckert CA (1996) Specific intermolecular interaction of carbon dioxide with polymers. *J Am Chem Soc* 118:1729–1736
67. Kim KH, Kim Y (2008) Theoretical studies for Lewis acid–base interactions and C–H...O weak hydrogen bonding in various CO<sub>2</sub> complexes. *J Phys Chem A* 112:1596–1603

68. Schneider J, Jia H, Muckerman JT, Fujita E (2012) Thermodynamics and kinetics of CO<sub>2</sub>, CO, and H<sup>+</sup> binding to the metal centre of CO<sub>2</sub> reduction catalysts. *Chem Soc Rev* 41:2036–2051
69. Soedergren S, Hagfeldt A, Olsson J, Lindquist SE (1994) Theoretical models for the action spectrum and the current-voltage characteristics of microporous semiconductor films in photoelectrochemical cells. *J Phys Chem* 98:5552–5556

# Chapter 29

## Nanometal-Loaded Metal-Organic-Framework Photocatalysts

Meicheng Wen, Yasutaka Kuwahara, Kohsuke Mori, and Hiromi Yamashita

### 29.1 Introduction

Nanostructured metals with the size of 1–100 nm have attracted considerable attention in recent years due to the unique physical–chemical properties as well as potential technological applications especially in the catalytic reaction [1–6]. It is well known that the catalytic performance strongly depends on the shapes and sizes of the nanoparticles. Compared with the bulk form, size-reduced nanomaterials showed the significant improvement in catalytic performance due to the increase of surface-to-volume ratio, high surface energy, enhanced light absorption, and scattering resonances and greatly reduced the transport pathway of photoexcited charge [7–9]. As the unique properties taken by nanoparticles, considerable efforts regarding the synthesis of nanometal with unique physical–chemical properties and developing the catalytic properties in catalytic synthesis have been made to break a major drawback of high cost, allowing effective utilization of expensive catalyst metals.

Photocatalysis, as one of the typical heterogeneous catalyses and highly important technologies for the energy conversion of solar energy to chemical energy, has been widely studied for environment cleaning and energy production [10–12]. In the photocatalytic reaction, the utilization of the nanometal for catalyzed photochemical reactions especially in photocatalytic hydrogen production has received

---

M. Wen

Division of Materials and Manufacturing Science, Graduate School of Engineering,  
Osaka University, 2-1 Yamadaoka, Suita, Osaka 565-0871, Japan

Y. Kuwahara • K. Mori • H. Yamashita (✉)

Division of Materials and Manufacturing Science, Graduate School of Engineering,  
Osaka University, 2-1 Yamadaoka, Suita, Osaka 565-0871, Japan

Elements Strategy Initiative for Catalysts and Batteries Kyoto University, ESICB,  
Kyoto University, Katsura, Kyoto 615-8520, Japan

e-mail: [yamashita@mat.eng.osaka-u.ac.jp](mailto:yamashita@mat.eng.osaka-u.ac.jp)

significant attentions. In the past decades, there have been extensive efforts for synthesis of monodispersed and small-sized nanometal, being introduced as a surface capping agent [13]. However, the problem of deactivation caused by sintering and particle agglomeration during the photocatalytic reaction and the difficulties with product separation and catalyst recycling limited the efficient utilization of the nanometal in future. The general approach to overcoming these limitations is to immobilize metal nanoparticles within the photoactive materials, and hence take advantages of the unique physical and chemical properties [14–16]. The purpose of this immobilization is the physical interaction between the absorbent surface and the nanometal adsorbate that immobilizes the nanometal under certain conditions, preventing the sintering or agglomeration particle during the catalytic reactions. The most convenient method for attaining the immobilization of nanometals is using the support with low synthetic cost and high surface area. Furthermore, not only the intrinsic catalytic property of nanometal affects the activity of chemical reaction but also the surface atomic coordination, porosity, and external and internal environment of supports play vital roles for improving catalytic performance because the supports can greatly affect the light harvesting and the molecular transport of reactants and products [1]. Therefore, selecting the suitable supports for the immobilization of nanometal is very important in optimizing the performance of catalysts.

Among various common photoactive supports such as Ti-substituted silica, Ti-containing zeolites, or inorganic semiconductors, metal organic materials (MOFs), also known as porous coordination polymers (PCPs), have emerged as an attractive class of functional materials employed in photocatalysis because of its large surface area, uniform pore size, and porosity [17, 18]. MOFs are built from inorganic metal ions as connecting centers and organic moieties as linkers. The advantages of MOFs over the classical inorganic porous materials should be that MOFs possess high surface area generally ranging from 1000 to 4000 m<sup>2</sup>/g and tunable pore sizes and topologies, and offer significant new chemical diversity because not only the linker can be systematically modified by functional groups but also the foreigner metal ions can be easily doped within the nodes [19]. The presence of suitable functional groups either in the organic linker or in the nodes can greatly facilitate the controllable synthesis of nanoparticle with precise location and particle size incorporated within MOFs to improve the photocatalytic performances [20, 21]. Moreover, such organic-inorganic composed polymers exhibit distinctive optical properties. The harvested photon energies by the linker of MOFs are transferred through the network and relayed to the inorganic charge-separation centers to give the redox couple, which plays a crucial role in photocatalytic reactions. Therefore, a large number of well-defined MOFs have been designed and applied as catalysts for a number of light-driven organic transformations [22, 23]. It can be expected that the nanometal can be easily deposited on the light-responsive MOFs to form well-controlled metal nanoparticles from the mixture of MOFs in the solution of metal precursors. Compared with the traditional photocatalysts, this nanometal-loaded light-responsive MOF photocatalysts will afford unexpected photocatalytic

performance of various chemical reactions due to the synergic effects between metal nanoparticles and MOFs in enhancing the light absorption, fast molecular transport of reactants and products, efficient photo-generated charge separation, promoting the distribution of metal nanoparticles, and preventing the aggregation of nanoparticle.

In this chapter, we highlight our recent progress in the design and architecture of the nanoparticle-incorporated MOFs using novel techniques and their efficient application in photocatalytic hydrogen generation. Additionally, other MOFs modified during in situ synthesis procedure or post-synthetic modification with function groups for optimizing the nanoparticle loading amount or controlling the nanometal location are also introduced in this chapter. Owing to the bright future of those nanometal-loaded metal organic framework in photocatalysis for environment cleaning and energy production, we sincerely hope that those powerful materials can serve as eco-materials to replace commercially available photocatalysts for practical application.

## **29.2 A Photo-Assisted Deposition Method for Preparation of Supported Metal Nanoparticle Catalysts Using Photoactive MOFs**

In general, the synthesis method starts by impregnation of a metal precursor with a porous solid followed by a reduction of the metal precursor to metal particles, which aggregate to metal nanoparticles [24]. However it is challenging to prevent the diffusion of the precursor from the pores to the surface, and aggregation on the outer surface. Nowadays, the incorporation of metal nanoparticle in the porous materials with precise control of size and location by a photo-deposition method has found to be an efficient and simple approach [25, 26]. Photo-assisted deposition method for immobilization of nanometals within porous materials is to fabricate metal NPs by UV photochemical reaction on photoactive supports. Upon UV light irradiation, electrons and holes in conduction and valence bands are generated by photochemical excitation and can react with electron donors and acceptors adsorbed on the surface of supports. The reduction by the conduction band electrons is initiated by the UV irradiation which precedes the formation of metal NPs. The advantage of this method is that the nucleation and growth of metal NPs can be controlled by the UV irradiation, thus allowing better spatial resolution. A photoactive support is a prerequisite for applying the photocatalytic metallic nanoparticle deposition. General photoactive supports to embed nanometal are those porous inorganic materials with defined pore such as Ti-substituted silica, Ti-containing zeolites, or inorganic semiconductors [8, 27]. In particular, MOFs have been utilized as supports for the stabilization of metal nanoparticles with adjustable size and controllable location at the confined cavities or in well-defined pores [28–30]. The utilization of MOFs as supports for nanometal and its application in photocatalysis have several

advantages over other photoactive inorganic porous materials: (1) Extraordinarily high surface area and well-defined pore structure of MOFs can facilitate the diffusion of the reagent and product molecules through their open channels anchored by the active catalytic sites and can be used for the stabilization of metal nanoparticles. Moreover, the structure features of MOFs, such as the diameter of the cavity and the size of the pore, can be easily controlled by changing the organic ligand with different lengths. (2) Unlike the inorganic porous materials with which only slight amount of functional groups can be introduced into skeleton, the optical properties of MOFs can be easily tailored from UV region to visible region via the linker substitutions with the great amount of organic chromophores in MOF structures or partially replaced by foreign metal ions. (3) The combination of the semiconductor properties and the strong absorption properties of inorganic porous materials within MOFs holds great potentials in many applications. It is possible to deposit nanometal into the photoactive MOFs with high crystallinity by immersion of MOFs in metal salt solution followed by light irradiation in the presence of suitable sacrifice agents. MOF-5, as one of the most studied photoactive MOFs, is built up from terephthalate ligands as linker and zinc ions as center. MOF-5 exhibits zinc oxide quantum dot behavior. It was demonstrated that the MOF-5 behaves as a semiconductor and undergoes the generation of photoexcited electron via a ligand-to-metal charge transfer.

(LMCT) upon UV light irradiation [31]. It was demonstrated that this MOF has a broad absorption band located in low-energy area ranging from 500 to 840 nm due to the delocalized electrons living on the microsecond time scale, and most probably occupying conduction bands. This photoactive MOF was used to photocatalytic degradation of phenol in aqueous solutions in order to demonstrate the behavior of MOF-5 as a microporous semiconductor. As expected, MOF-5 exhibits a remarkable photocatalytic activity, photocatalytic degradation of phenol, because the terephthalate linkers in the organic part of the framework act as antennae and efficient photoexcited electron transferred to the inorganic clusters, resulting in the photocatalytic degradation of phenol. Therefore, the photoexcited electron can also be used for photocatalytic reduction of metal ions to form nanometal-loaded MOF-5. For example, Ag@MOF-5 was prepared by suspended MOF-5 into an ethanol solution containing AgNO<sub>3</sub> followed by UV irradiation; Ag nanoparticles were formed in MOF-5 (Fig. 29.1) [32]. The successful formation of Ag NPs in MOF-5 was visually evidenced by the color change from the initially white powder to dark brown-black. The presence of Ag nanoparticles has no significant influence on homogeneity and crystallinity in the XRD pattern, suggesting that the integrity and crystallinity were preserved. The main advantage of the photochemical deposition of metal nanoparticles is that the nucleation and growth of metal NPs can be controlled by the UV irradiation, thus allowing better spatial resolution and more effective reduction. However, not all of the MOFs can be utilized to support metal nanoparticles by photo-assisted deposition, because this method can only be applied to semiconducting MOFs.

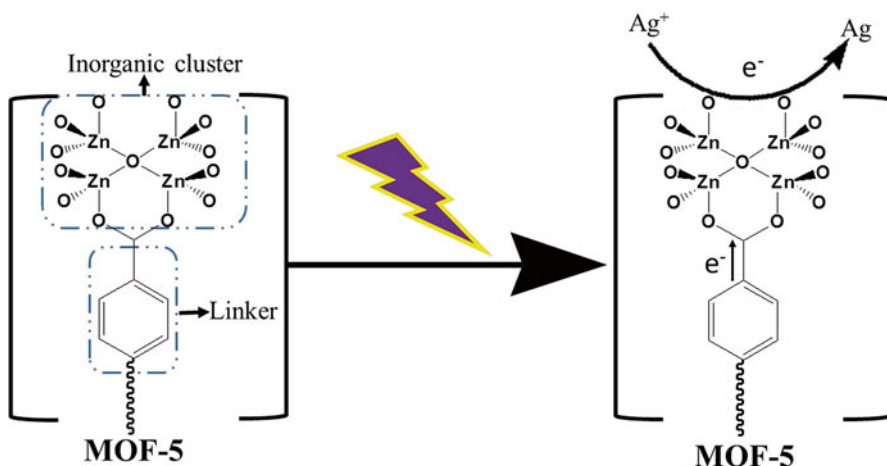


**Fig. 29.1** Formation of charge-transfer excited state in the semiconducting MOF-5 under UV light irradiation and its application for the photocatalytic deposition of Ag nanoparticles

### 29.3 In Situ Synthesis of Amine-Functionalized Semiconducting MOFs for Decrease of Metal Nanoparticle Size

The photo-assisted deposition method is an effective method for producing small and highly dispersed metal nanoparticles within the MOF structure. Herein, we used a photocatalytically active MOF MIL-125 and its amine-functionalized equivalent  $\text{NH}_2$ -MIL-125 to immobilized Pd nanoparticles by photo-assisted deposition methods [33]. MIL-125 was prepared using a method published by Ferey [34] in which 1,4-benzene dicarboxylic acid and titanium isopropoxide were added into a solution containing *N,N*-dimethylformamide (DMF) and methanol followed by hydrothermal treatment. A modified procedure was used for the preparation of the  $\text{NH}_2$ -functionalized MIL-125. Titanium isopropoxide and 2-amino benzene dicarboxylic acid were added to 50 mL of a DMF and  $\text{CH}_3\text{OH}$  (1:1) solution and heated in Teflon-lined stainless steel autoclaves for 16 h at 423 K. Pd NPs were introduced into MIL-125 and  $\text{NH}_2$ -MIL-125 by an aqueous photo-assisted deposition method; MOF-powdered sample was suspended in distilled water and activated by ultrasound inside of a quartz vessel for 30 min. Then, aqueous solution  $\text{PdCl}_2$  (in aqueous solution with HCl) was added, and the vessel was sealed with a rubber septum and bubbled with Ar gas. The vessel was photo-irradiated by a 100 W high-pressure mercury arc for 5 h. For comparison, the ion exchange method was carried out, which was suspended in distilled  $\text{H}_2\text{O}$  and activated by ultrasound for 30 min. Then, aqueous solution  $\text{PdCl}_2$  was added, and the suspension was stirred at ambient temperature for 10 h, and then reduced in  $\text{H}_2$ .

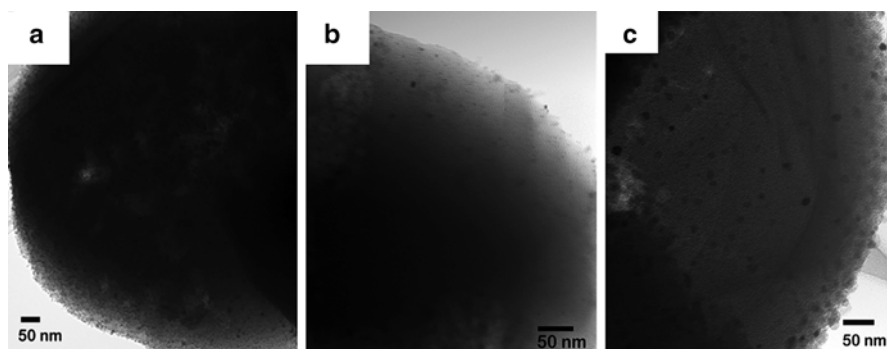


**Fig. 29.2** TEM images of the samples: (a) Pd-MIL-125, (b) Pd-NH<sub>2</sub>-MIL-125, and (c) Pd-NH<sub>2</sub>-MIL-125i

The presence of the NH<sub>2</sub> groups in the organic linkers has been confirmed on evacuated samples by IR spectroscopy. The optical properties of MIL-125 were investigated by UV-Vis as a broad absorption edge to 350 nm. NH<sub>2</sub>-MIL-125 displays an additional absorption edge in the visible region, induced by O-to-Ti charge transfer (ligand-to-metal charge transfer) in the TiO<sub>5</sub>(OH) inorganic cluster. The BET surface area and pore volume of NH<sub>2</sub>-MIL-125 decreased compared to NH<sub>2</sub>-MIL-125 due to the presence of the amine group in the ligand. However, a significant decrease in the BET surface area and pore volume indicates that the internal cavities were occupied or blocked by Pd NPs. In addition, the NH<sub>2</sub>-MIL-125i prepared by the ion exchange method showed a larger decrease in BET in comparison with NH<sub>2</sub>-MIL-125, suggesting the larger Pd nanoparticle size of NH<sub>2</sub>-MIL-125i.

The TEM images (Fig. 29.2) show that the Pd nanoparticles successfully immobilized within the pores of the MOF materials. Pd nanoparticles formed within the Pd-MIL-125 have a mean diameter of 5.5 nm and narrow size distribution. Well-distributed and small NPs are formed within NH<sub>2</sub>-MIL-125 with a mean diameter of 3.1 nm, prepared by the photo-assisted deposition method, but larger nanoparticles with a mean size of 7.6 nm are formed during the ion exchange. Clearly, the preparation method affects the size and dispersion of NPs, and the photo-assisted methods give the best results in terms of controlling the dispersion and size of NPs.

The XRD patterns of the samples after the photo-assisted of Pd nanoparticles suggested that the integrity of the framework was preserved because no visible loss in homogeneity and crystallinity was observed in the XRD. The normalized X-ray absorption near-edge structure (XANES) spectra at the Pd K-edge were measured for Pd foil, Pd-MIL-125, Pd-NH<sub>2</sub>-MIL-125, and Pd-NH<sub>2</sub>-MIL-125i. The shapes of the XANES spectra for Pd-supported NPs resemble those of the Pd foil, suggesting the presence of the Pd(0). TEM images revealed that the size of Pd NPs prepared by photo-assisted deposition within MIL-125 has a mean diameter of 5.5 and 3.1 nm for NH<sub>2</sub>-MIL-125, and larger NPs with a mean size of 7.6 nm are formed during the ion exchange inside NH<sub>2</sub>-MIL-125, and further confirmed that the preparation method affects the size and dispersion of NPs, and the photo-assisted methods show better control of dispersion and size.

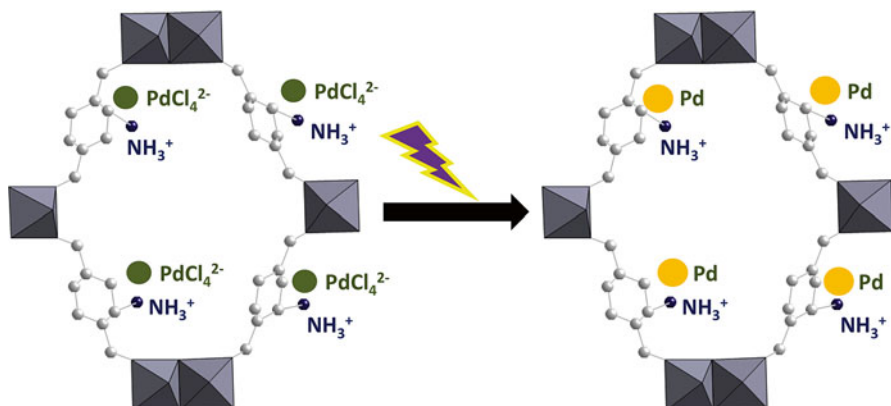


**Fig. 29.3** The effect of amine functional groups within the linker of MOFs on the preparation of Pd nanoparticles

As expected, uniform and small Pd nanoparticles were deposited within the amine-functionalized MIL-125 by the photo-assisted method. Undoubtedly the amine functional groups play an important role on the preparation of well-dispersed Pd nanoparticles with small particle size. A large number of amine groups within MOFs are known as weakly basic groups which can act as proton scavengers, forming  $-\text{H}^+\text{NH}_2$  while exposed to the acid solution including the  $\text{PdCl}_4^{2-}$  as Pd precursor as shown in Fig. 29.3. It is easy to understand that the Pd precursor well attaches with  $-\text{H}^+\text{NH}_2$  via the force of electrostatic attraction, and continuously reduced to metallic Pd nanoparticles by the photoexcited electron generated through a ligand-to-metal charge transfer (LMCT) mechanism upon UV light irradiation. Furthermore, the existence of the unsaturated metal ions within the inorganic nodes of MOFs and extraordinarily high surface area and well-defined pore structure of MOFs are also important factors in attaining small and highly dispersed nanoparticles within the MOF structure. From the above study, it is demonstrated that the photo-assisted deposition method was a more effective method for producing small and highly dispersed NPs within the MOF structure compared with ion exchange method. The amine-functionalized  $\text{NH}_2$ -MIL-125 is beneficial for an increased durability of the MOF in an aqueous environment. The present work shows that functionalization can greatly decrease the metal particle size within MOF materials and can be extended to other metal NPs and functional groups in MOFs.

#### 29.4 Synthetic Modification of Metal-Organic Frameworks: A Rational Route to Design an Integrated Photocatalyst

Energy shortage and environmental pollution are becoming more and more urgent due to continuous consumption of limited fossil fuels, which need to be resolved without any delay. It is interesting to build artificial photosynthetic systems to

harvest solar energy and to enable visible-light-driven chemical reactions because solar energy was considered as the ultimate energy source [35–38]. Photocatalytic hydrogen production from water, in which solar energy is used to break down the water into hydrogen and oxygen over semiconductor in the presence of suitable sacrificial, provides the most alternative and attractive strategy to meet future energy needs. In the past decades, numerous approaches have been devoted to the development of visible-light-driven photocatalysts, for instance, N-TiO<sub>2</sub> [39], metallic doped TiO<sub>2</sub> [40], and other visible-light-responsive semiconductor (CdS, CuInZnS) [41, 42]. Increasing recent efforts have been devoted to exploring molecular systems for energy harvesting, due to the ease of their physical and chemical tuning. Increasing efforts have been made to achieve molecular-based H<sub>2</sub> evolution systems composed of a photosensitizer, a sacrificial reagent, and a non-semiconducting hydrogen-generating catalyst. It is clear that this molecular systems for visible-light-driven H<sub>2</sub> production from water often requires two components: the photosensitizer for harvesting sunlight and the catalysts to act as an active site for producing hydrogen [43]. However, the thermal instability of metal complexes or photobleaching of photosensitizers limits their practical application. The development of visible-light-driven H<sub>2</sub> production system with high stability and activity is still a great challenge. It is well known that a variety of physical properties, such as optical, fluorescence, and guest absorption capacity, integrated within hybrid materials may show synergetic effects for significantly enhancing the performance of many applications. Therefore, integration of the photosensitizer and active site into nanoscale materials has been emerging as a most promising method to construct an integrated photocatalytic hydrogen production system with high photocatalytic activity and stability.

It is clear that MOFs provide a great opportunity for constructing hybrid materials due to the richness of metal-containing center and organic bridging linkers, as well as the controllability of the synthesis, because it is easy to construct MOFs with adjustable optical properties to harvest light, thereby achieving desirable performance for environmental applications and water splitting. Figure 29.4 illustrated the general way to tailor the chemical properties of MOFs and, at the same time, to enrich structural diversity in these materials via ligand modification. The linker of MOFs can be partially or integrally replaced by the metal complexes via the mix-and-match synthetic strategy. The incorporated metal complexes act as a photosensitizer to efficiently harvest the solar light; thus Pt nanoparticles were immobilized into the cavities of MOFs by the photo-generated electron from the photoactive MOFs under light irradiation allowing efficient photocatalytic H<sub>2</sub> production from water. In addition, the cavity of the MOFs can also be tailored by using the elongated metal complex as coordination linker. For instance, Pt NPs were imbedded into the cavities of two phosphorescent UiO MOFs built from Ir-phosphor-derived linear dicarboxylate linkers via photo-assisted deposition method [44]. The photoactive Pt nanoparticle-imbedded MOFs serve as highly efficient photosensitizer and photocatalysts for light harvesting and hydrogen generation. The turnover frequencies and turnover numbers of the Pd/MOFs for hydrogen evolution are higher than those of the homogeneous analogs.

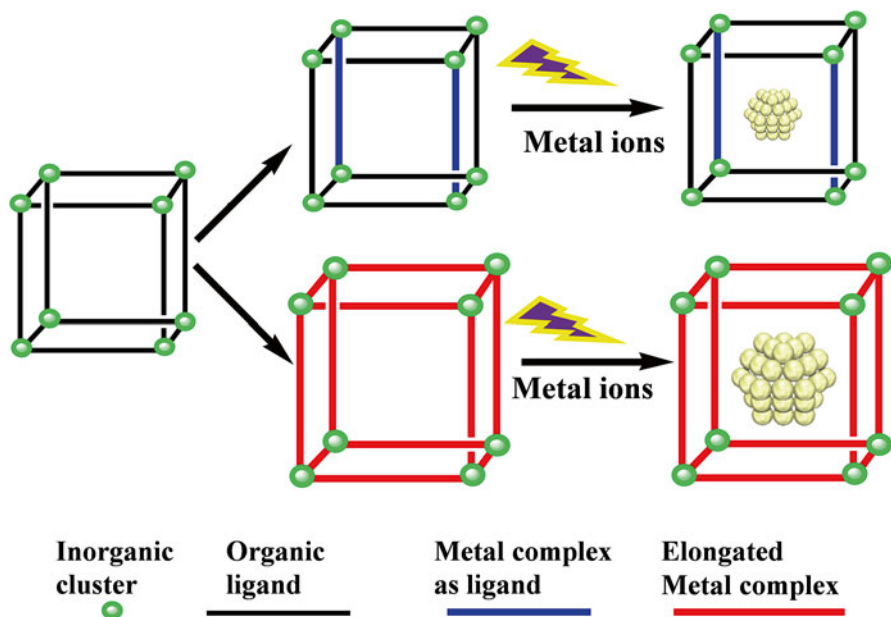


**Fig. 29.4** Ligand elaboration as a strategy for introducing structural and optical diversity in porous metal-organic-framework compounds

## 29.5 Construction of a Durable Photocatalytic Hydrogen Production System Using Pt Nanoparticle-Imbedded MOFs as Photocatalysts

Present photocatalytic  $H_2$  reaction suffered from poor visible light utilization or instability of  $H_2$  production system due to the fascinating physical structure, functional groups, and numerous unsaturated metal sites of MOFs. Up to now, much attention has been paid on exploring the advantages in the application of photocatalysis. A great number of MOFs have been demonstrated to be quite effective in the photocatalytic degradation of organic pollutants. However, there has been limited attention focus on their utilization in photocatalytic hydrogen generation. Herein, we present a new type of  $H_2$  evolution system, in which Pt NPs were loaded on  $NH_2$ -MIL-101(Cr) to act as a catalyst, rhodamine B to act as a chlorophyll to collect sunlight energy, and TEOA to act as a sacrificial reagent. The incorporation of Pt nanoparticles into a highly stable and porous amine-functionalized MIL-101(Cr) was performed for construction of visible-light-driven  $H_2$  evolution system with high activity and strong stability [45].

$NH_2$ -MIL-101(Cr) was prepared using a method published by Chen [46] with a small modification using chromic nitrate hydrate, 2-aminoterephthalic acid, and sodium hydroxide. The synthesized  $NH_2$ -MIL-101(Cr) (0.2 g) was suspended in  $H_2O$  and sonicated for 20 min until it became highly dispersed. Then 3.98 mL

(Pt: 1.5 wt%) of aqueous  $\text{H}_2\text{PtCl}_4$  solution (3.861 mM) was added and stirred at room temperature for 8 h. After the reaction, the products were extracted by centrifugation and washed with water. Finally, the products were dried under vacuum and followed by 1 h  $\text{H}_2$  reduction at 473 K. The XRD patterns of the fresh and Pt-embedded  $\text{NH}_2\text{-MIL-101}$  materials exhibited broad Bragg reflections, indicating the small particle size of  $\text{NH}_2\text{-MIL-101}$ . The presence of Pt NPs had no significant influence on homogeneity and crystallinity in the XRD pattern, suggesting that the integrity and crystallinity were preserved. The absence of the characteristic Pt peak was due to the low Pt loadings. A decrease in BET surface area for Pt/ $\text{NH}_2\text{-MIL-101}$  indicates that the internal cavities are occupied or blocked by Pt NPs formed within the pores of the material.

$\text{MIL-101}(\text{Cr})$  has been widely used as a support in the domains of catalysis due to several unprecedented features such as mesoporous cages, microporous windows, giant cell volume, huge surface area, functional groups, and numerous unsaturated Cr (III) sites. In this study, Pt NPs have successfully encapsulated onto the surface of amine-functionalized  $\text{MIL-101}(\text{Cr})$  by ionic interaction of the positively charged surface ammonium group with anionic  $\text{PtCl}_6^{2-}$ , followed by the reduction with  $\text{H}_2$ . Figure 29.5 presents a TEM image of Pt/ $\text{NH}_2\text{-MIL-101}(\text{Cr})$ . The average particle size of  $\text{NH}_2\text{-MIL-101}(\text{Cr})$  was around 50 nm. The Pt NPs with  $3.75 \pm 0.5$  nm average size can be clearly observed. No significant agglomeration of Pt NPs occurred in the Pt/ $\text{NH}_2\text{-MIL-101}(\text{Cr})$  composites after  $\text{H}_2$  treatment, indicating that Pt NPs were highly distributed on  $\text{NH}_2\text{-MIL-101}(\text{Cr})$ . The average diameter of Pt nanoparticles increased with the increase of the Pt loading weight.

The UV–Vis spectrum shows that both  $\text{NH}_2\text{-MIL-101}$  and 1.5 wt% Pt/ $\text{NH}_2\text{-MIL-101}$  have a clear optical response in the visible light region as shown in Fig. 29.2. The bands in the high-energy region can be assigned to the  $\pi \rightarrow \pi^*$  transition of the linker and in the region around 600 nm can be assigned to  $d \rightarrow d$  transition bands of  $\text{Cr}^{3+}$  (5d) ions. The UV–Vis spectrum of the RhB in TEOA and  $\text{H}_2\text{O}$  solution exhibits intense absorption bands in the low-energy region ( $450 \text{ nm} < \lambda < 600 \text{ nm}$ ). The results demonstrate that our  $\text{H}_2$  evolution system containing RhB solution and Pt/ $\text{NH}_2\text{-MIL-101}$  is a visible-light-absorbing system.

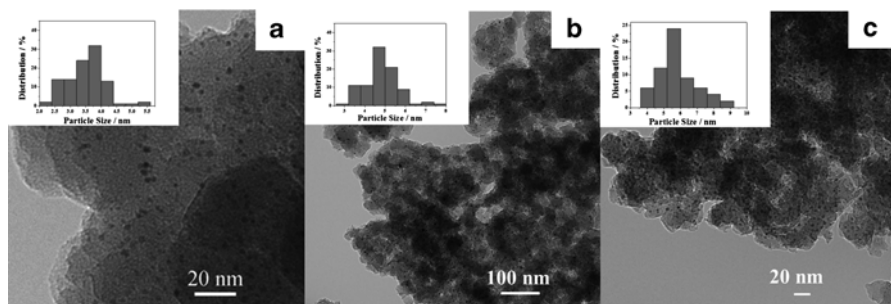


**Fig. 29.5** TEM images of (a) 1.5 wt% Pt NP-embedded  $\text{NH}_2\text{-MIL-101}(\text{Cr})$ , (b) 2.0 wt% Pt NP-embedded  $\text{NH}_2\text{-MIL-101}(\text{Cr})$ , (c) 3.0 wt% Pt NP-embedded  $\text{NH}_2\text{-MIL-101}(\text{Cr})$

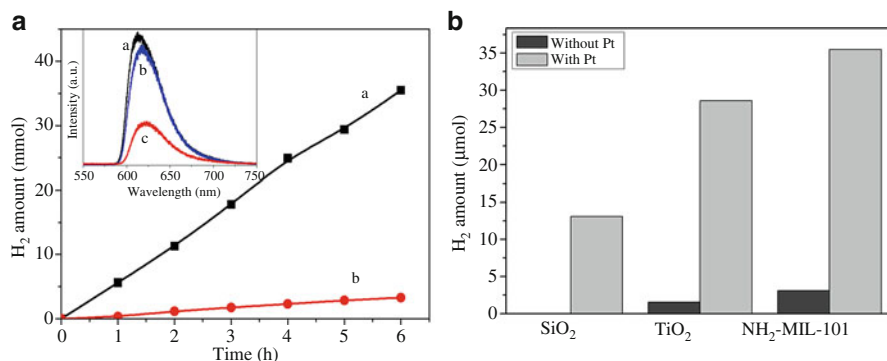


**Fig. 29.6** (A) Photocatalytic H<sub>2</sub> production over (a) 1.5 wt% Pt/NH<sub>2</sub>-MIL-101(Cr), (b) NH<sub>2</sub>-MIL-101(Cr). Inset is photoluminescence spectra of RhB solution (a) without catalyst, (b) with NH<sub>2</sub>-MIL-101(Cr), and (c) with 1.5 wt% Pt/NH<sub>2</sub>-MIL-101(Cr); and (B) influence of different catalysts on the H<sub>2</sub> production

As shown in Fig. 29.6A, the photocatalytic H<sub>2</sub> production was performed under irradiation of visible light. A sample (10 mg) was suspended in H<sub>2</sub>O (4 mL) and TEOA (1 mL) mixture containing 1 mM RhB. Our preliminary tests demonstrated that no significant reaction was observed in the absence of either light irradiation or photocatalyst, suggesting that the H<sub>2</sub> production was mainly driven by photocatalysis. No appreciable H<sub>2</sub> production was detected without RhB molecule. This indicates that the irradiated light is absorbed mainly by RhB photosensitizer. It is noteworthy that the pure NH<sub>2</sub>-MIL-101(Cr) exhibited photocatalytic activity in the presence of RhB and irradiation of visible lights even in the absence of Pt NPs, which indicates that numerous electrophilic unsaturated Cr (III) sites appeared in the MOFs act as reactive site to receive photoelectrons leading to the reduction of proton to H<sub>2</sub>, resulting in reduction of the self-quenching rate of RhB. To our best knowledge, there are no reports examining photocatalytic H<sub>2</sub> production by using pure NH<sub>2</sub>-MIL-101(Cr) as catalyst. Anatase TiO<sub>2</sub>, the most studied semiconductor with remarkable activity for photocatalytic H<sub>2</sub> production and mesoporous material SiO<sub>2</sub>, was selected in this system. Unlike NH<sub>2</sub>-MIL-101(Cr) with unsaturated metal sites, no significant reaction was observed by using SiO<sub>2</sub> as catalyst in our system and very low activity can be observed over TiO<sub>2</sub> with anatase phase due to the photoexcited electron injected from RhB to conduction band of TiO<sub>2</sub>. Platinum nanoparticles have presented superior physical and chemical properties in producing H<sub>2</sub>. After loading with Pt nanoparticles, the Pt/NH<sub>2</sub>-MIL-101(Cr) composite showed much higher photocatalytic activity than pure NH<sub>2</sub>-MIL-101(Cr), Pt/TiO<sub>2</sub>, and Pt/SiO<sub>2</sub> in the identical conditions (Fig. 29.6B). The enhanced photocatalytic activity of Pt-NH<sub>2</sub>-MIL-101(Cr) composite might be attributed to the synergistic effect between Pt NPs and NH<sub>2</sub>-MIL-101(Cr). The inset in Fig. 29.6A shows the photoluminescence spectra of photosensitizer RhB containing TEOA 20 vol.% aqueous solution. The intensity slightly decreased by the addition of the NH<sub>2</sub>-MIL-101, while significant decrease was observed in the presence of the Pt/NH<sub>2</sub>-

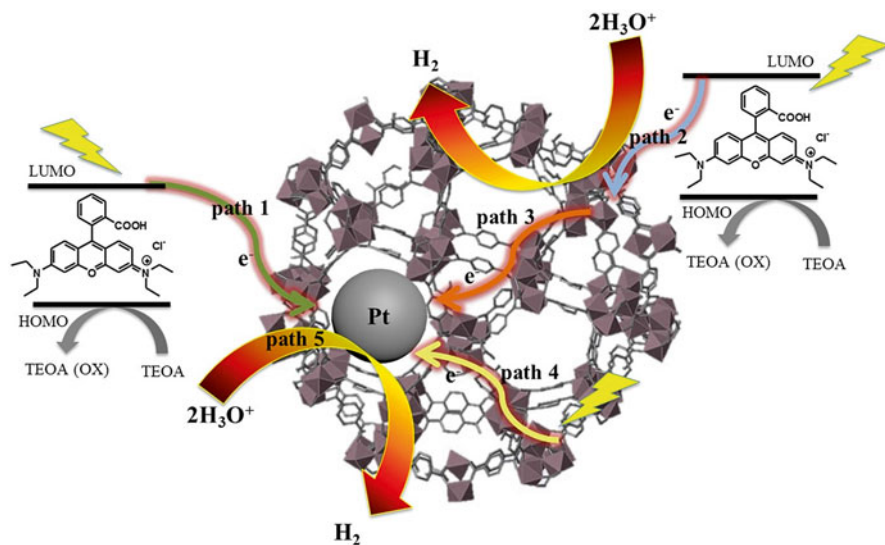


**Fig. 29.7** A plausible mechanism for visible-light-induced photocatalytic  $\text{H}_2$  over Pt/ $\text{NH}_2$ -MIL-101 from RhB solution

MIL-101(Cr). These results suggest that the occurrence of excited electron injection from RhB to  $\text{NH}_2$ -MIL-101(Cr) and the Pt nanoparticles enhances the electron transfer.

The optimum Pt amount for the photoreaction in our system was found to be around 1.5 wt% Pt. The total amount of  $\text{H}_2$  evolved from the system using 0.5 wt% Pt/ $\text{NH}_2$ -MIL-101(Cr) was 28.6  $\mu\text{mol}$ . This corresponds to turnover number (TON) of 110  $\text{mol}_{\text{H}_2} \cdot \text{mol}_{\text{cat}}^{-1}$  (Pt loading 0.5 wt%). The TON for 3 wt% Pt loading sample decreased to 16.5  $\text{mol}_{\text{H}_2} \cdot \text{mol}_{\text{cat}}^{-1}$ . With the increase of Pt loading from 0.50 to 1.5 wt%, the activity enhanced owing to the increased number of active sites. Further increase of Pt loading to 3.0 wt% caused decrease in activity, which can be attributed to the gathering of Pt into large nanoparticles evidenced by Fig. 29.5. Furthermore, the effects of the RhB concentration on  $\text{H}_2$  production were investigated. The optimum RhB concentration for the photocatalytic  $\text{H}_2$  production in this system was found to be around 1 mM. This photocatalytic system can produce  $\text{H}_2$  even irradiation at wavelengths longer than 500 nm, indicating the efficient utilization of visible light. Moreover, this system showed excellent durability and could be used repetitively five times with slight decrease in activity under visible light irradiation. After five consecutive cycles, almost the same concentration of RhB with a maximum absorption at 554 nm accompanied with the shoulder peak at 520 nm was monitored, demonstrating the high chemical stability.

The possible mechanism for  $\text{H}_2$  production from our system was illustrated in Fig. 29.7. After the absorption of visible light by RhB molecule, an excited photoelectron is formed from LUMO state of RhB molecule. The generated photoexcited electron is transferred not only to the Pt NPs (path 1) but also to the unsaturated Cr (III) sites (path 2). The injected electrons to the unsaturated Cr (III) sites are occa-

sionally transferred to the Pt NPs site (path 3). Such electron transfer pathway can be evidenced by the significant decrease of emission intensity of RhB in the presence of  $\text{NH}_2\text{-MIL-101}(\text{Cr})$  with and without Pt. Moreover, the incident visible light absorption by the organic linker of  $\text{NH}_2\text{-MIL-101}(\text{Cr})$  produces the photoexcited electrons, which firstly transfer to chromium-oxo through linker-to-cluster charge-transfer mechanism (LCCT) [47] and then to the Pt NPs (path 4). Finally, the proton which gathered on the surface of  $\text{NH}_2\text{-MIL-101}(\text{Cr})$  by hydrogen bonding is transferred to the Pt NPs or unsaturated Cr(III) sites in  $\text{NH}_2\text{-MIL-101}(\text{Cr})$  by water, and reacts with photoelectron to produce  $\text{H}_2$  (paths 5 and 6). In this case, the porous MOFs not only served as an electric conductor to promote the electron transfer in facilitating the separation of photoelectrons from RhB, but also acted as photo-electron generator to enhance the activity of  $\text{H}_2$  production. Meanwhile, the oxidized RhB molecule then comes back to its ground state by accepting an electron from TEOA.

The present system exhibited high activity and strong durability in visible-light-induced photocatalytic  $\text{H}_2$  production owing to cooperative promoting effects from both the Pt-embedded MOF catalysts and the dye solution in collecting sunlight energy, transporting photoexcited electron, protecting the photosensitizer, reducing the self-quenching of RhB, enhancing light harvest, and forming well-dispersed catalyst nanoparticles on the MOFs. It supplied a platform to design other photosensitizer/MOF-based catalyst systems with strong stability against either destroying or self-quenching of photosensitizer, which may offer more opportunities for photocatalytic applications.

## 29.6 Conclusions

In this chapter, we have focused on the progress in the design and architecture of the nanoparticle-incorporated MOFs using novel techniques allowing effective utilization of expensive catalyst metals and their efficient application in photocatalytic hydrogen generation. It is clear that MOFs have a bright future in photocatalysis due to the fascinated physical structure, functional groups, and numerous unsaturated metal sites of MOFs. However, the disadvantages of MOFs, such as the high cost of organic linker and the thermal/hydrothermal instability, and challenges associated with robust structure and low electric conductivity, hinder the application in photocatalysis. We expect that the design strategy described here can offer a helpful overview to the readers in exploring a cheap, stable, and efficient MOFs served as photocatalysts for solving various global environmental and energy problems.

## References

1. Mori K, Dojo M, Yamashita H (2013) Pd and Pd-Ag nanoparticles within a macroreticular basic resin: an efficient catalyst for hydrogen production from formic acid decomposition. *ACS Catal* 3(6):1114–1119
2. Shown I, Hsu H-C, Chang Y-C, Lin C-H, Roy RK, Ganguly A, Wang C-H, Chang J-K, Wu C-I, Chen L-C, Chen K-H (2014) Highly efficient visible light photocatalytic reduction of  $\text{CO}_2$  to

- hydrocarbon fuels by Cu-nanoparticle decorated graphene oxide. *Nano Lett* 14(11):6097–6103
3. Qian X, Kuwahara Y, Mori K, Yamashita H (2014) Silver nanoparticles supported on CeO<sub>2</sub>-SBA-15 by microwave irradiation possess metal-support interactions and enhanced catalytic activity. *Chem-Eur J* 20(48):15746–15752
  4. Fuku K, Hayashi R, Takakura S, Kamegawa T, Mori K, Yamashita H (2013) The synthesis of size- and color-controlled silver nanoparticles by using microwave heating and their enhanced catalytic activity by Localized surface plasmon resonance. *Angew Chem Int Ed* 52(29):7446–7450
  5. Wen M, Takakura S, Fuku K, Mori K, Yamashita H (2015) Enhancement of Pd-catalyzed Suzuki-Miyaura coupling reaction assisted by localized surface plasmon resonance of Au nanorods. *Catal Today* 242:381–385
  6. Mori K, Kawashima M, Che M, Yamashita H (2010) Enhancement of the photoinduced oxidation activity of a ruthenium(II) complex anchored on silica-coated silver Nanoparticles by localized surface plasmon resonance. *Angew Chem Int Ed* 49(46):8598–8601
  7. Fuku K, Goto M, Sakano T, Kamegawa T, Mori K, Yamashita H (2013) Efficient degradation of CO and acetaldehyde using nano-sized Pt catalysts supported on CeO<sub>2</sub> and CeO<sub>2</sub>/ZSM-5 composite. *Catal Today* 201:57–61
  8. Fuku K, Sakano T, Kamegawa T, Mori K, Yamashita H (2012) Enhanced hydrogenation activity of nano-sized Pd-Ni bimetal particles on Ti-containing mesoporous silica prepared by a photo-assisted deposition method. *J Mater Chem* 22(32):16243–16247
  9. Mori K, Kondo Y, Yamashita H (2009) Synthesis and characterization of FePd magnetic nanoparticles modified with chiral BINAP ligand as a recoverable catalyst vehicle for the asymmetric coupling reaction. *Phys Chem Chem Phys* 11(39):8949–8954
  10. Zhang D, Wen M, Jiang B, Li G, Yu JC (2012) Ionothermal synthesis of hierarchical BiOBr microspheres for water treatment. *J Hazard Mater* 211:104–111
  11. Zhang D, Wen M, Zhang P, Zhu J, Li G, Li H (2012) Microwave-induced synthesis of porous single-crystal-like TiO<sub>2</sub> with excellent lithium storage properties. *Langmuir* 28(9):4543–4547
  12. Zhang D, Wen M, Zhang S, Liu P, Zhu W, Li G, Li X (2014) Au nanoparticles enhanced rutile TiO<sub>2</sub> nanorod bundles with high visible-light photocatalytic performance for NO oxidation. *Appl Catal B Environ* 147:610–616
  13. Mori K, Kumami A, Tomonari M, Yamashita H (2009) A pH-induced size controlled deposition of colloidal Ag nanoparticles on alumina support for catalytic application. *J Phys Chem C* 113(39):16850–16854
  14. Martis M, Wen M, Mori K, Yamashita H (2014) Fabrication of metal nanoparticles in metal organic framework NH<sub>2</sub>-MIL-125 by UV photo-assisted methods for optimized catalytic properties. *Catal Today* 235:98–102
  15. Mori K, Hanafusa A, Che M, Yamashita H (2010) In situ generation of active Pd nanoparticles within a macroreticular acidic resin: efficient catalyst for the direct synthesis of hydrogen peroxide. *J Phys Chem Lett* 1(10):1675–1678
  16. Mori K, Araki T, Shironita S, Sonoda J, Yamashita H (2009) Supported Pd and PdAu nanoparticles on Ti-MCM-41 prepared by a photo-assisted deposition method as Efficient catalysts for direct synthesis of H<sub>2</sub>O<sub>2</sub> from H<sub>2</sub> and O<sub>2</sub>. *Catal Lett* 131(3–4):337–343
  17. Nakatsuka K, Mori K, Okada S, Ikurumi S, Kamegawa T, Yamashita H (2014) Hydrophobic modification of Pd/SiO<sub>2</sub>@single-site mesoporous silicas by triethoxyfluorosilane: enhanced catalytic activity and selectivity for one-pot oxidation. *Chem-Eur J* 20(27):8348–8354
  18. Okada S, Ikurumi S, Kamegawa T, Mori K, Yamashita H (2012) Structural design of Pd/SiO<sub>2</sub>@Ti-containing mesoporous silica core-shell catalyst for efficient one-pot oxidation using in situ produced H<sub>2</sub>O<sub>2</sub>. *J Phys Chem C* 116(27):14360–14367
  19. Zeng M-H, Yin Z, Tan Y-X, Zhang W-X, He Y-P, Kurmoo M (2014) Nanoporous cobalt(II) MOF exhibiting four magnetic ground states and changes in gas sorption upon post-synthetic modification. *J Am Chem Soc* Mar 136(12):4680–4688

20. Gu X, Lu Z-H, Jiang H-L, Akita T, Xu Q (2011) Synergistic catalysis of metal-organic framework-immobilized Au-Pd nanoparticles in dehydrogenation of formic acid for chemical hydrogen storage. *J Am Chem Soc* 133(31):11822–11825
21. Jiang H-L, Akita T, Ishida T, Haruta M, Xu Q (2011) Synergistic catalysis of Au@Ag core-shell nanoparticles stabilized on metal-organic framework. *J Am Chem Soc* 133(5):1304–1306
22. Wang C-C, Li J-R, Lv X-L, Zhang Y-Q, Guo G (2014) Photocatalytic organic pollutants degradation in metal-organic frameworks. *Energy Environ Sci* 7(9):2831–2867
23. Wang J-L, Wang C, Lin W (2012) Metal-organic frameworks for light harvesting and photocatalysis. *ACS Catal* 2(12):2630–2640
24. Mori K, Yoshioka N, Kondo Y, Takeuchi T, Yamashita H (2009) Catalytically active, magnetically separable, and water-soluble FePt nanoparticles modified with cyclodextrin for aqueous hydrogenation reactions. *Green Chem* 11(9):1337–1342
25. Qiao P, Zou S, Xu S, Liu J, Li Y, Ma G, Xiao L, Lou H, Fan J (2014) A general synthesis strategy of multi-metallic nanoparticles within mesoporous titania via in situ photo-deposition. *J Mater Chem A* 2(41):17321–17328
26. Qian X, Fuku K, Kuwahara Y, Kamegawa T, Mori K, Yamashita H (2014) Design and functionalization of photocatalytic systems within mesoporous silica. *ChemSusChem* 7(6):1528–1536
27. Yamashita H, Miura Y, Mori K, Ohmichi T, Sakata M, Mori H (2007) Synthesis of nano-sized Pd metal catalyst on Ti-containing zeolite using a photo-assisted deposition (PAD) method. *Catal Lett* 114(1–2):75–78
28. Pascanu V, Hansen PR, Gomez AB, Platero-Prats AE, Johansson MJ, Pericas MA, Martin-Matute B (2015) Highly functionalized biaryls via suzuki-miyaura cross-coupling catalyzed by Pd@MOF under batch and continuous flow regimes. *ChemSusChem* 8(1):123–130
29. Chen L, Chen H, Li Y (2014) One-pot synthesis of Pd@MOF composites without the addition of stabilizing agents. *Chem Commun* 50(94):14752–14755
30. Moon HR, Lim D-W, Suh MP (2013) Fabrication of metal nanoparticles in metal-organic frameworks. *Chem Soc Rev* 42(4):1807–1824
31. Alvaro M, Carbonell E, Ferrer B, Llabres i Xamena FX, Garcia H (2007) Semiconductor behavior of a metal-organic framework (MOF). *Chem-Eur J* 13(18):5106–5112
32. Ameloot R, Roeffaers MJB, De Cremer G, Vermoortele F, Hofkens J, Sels BF, De Vos DE (2011) Metal-organic framework single crystals as photoactive matrices for the generation of metallic microstructures. *Adv Mater* 23(15):1788–1791
33. Martis M, Mori K, Fujiwara K, Ahn W-S, Yamashita H (2013) Amine-functionalized MIL-125 with imbedded palladium nanoparticles as an efficient catalyst for dehydrogenation of formic acid at ambient temperature. *J Phys Chem C* 117(44):22805–22810
34. Dan-Hardi M, Serre C, Frot T, Rozes L, Maurin G, Sanchez C, Ferey G (2009) A new photoactive crystalline highly porous titanium(IV) dicarboxylate. *J Am Chem Soc* 131(31):10857–10859
35. Mori K, Iwata Y, Yamamoto M, Kimura N, Miyauchi A, Toyoshima T, Yamashita H (2014) An efficient Cu/BaO/La<sub>2</sub>O<sub>3</sub> catalyst for the simultaneous removal of carbon soot and nitrogen oxides from simulated diesel exhaust. *J Phys Chem C* 118(17):9078–9085
36. Mori K, Kawashima M, Yamashita H (2014) Visible-light-enhanced Suzuki-Miyaura coupling reaction by cooperative photocatalysis with an Ru-Pd bimetallic complex. *Chem Commun* 50(93):14501–14503
37. Mori K, Kakudo H, Yamashita H (2014) Creation of nickel-based active species within a macroreticular acidic resin: a noble-metal-free heterogeneous catalyst for visible-light-driven H<sub>2</sub> evolution from water. *ACS Catal* 4(11):4129–4135
38. Kamegawa T, Matsuura S, Seto H, Yamashita H (2013) A visible-light-harvesting assembly with a sulfocalixarene linker between dyes and a Pt-TiO<sub>2</sub> photocatalyst. *Angew Chem Int Ed* 52(3):916–919
39. Huo Y, Bian Z, Zhang X, Jin Y, Zhu J, Li H (2008) Highly active TiO<sub>2-x</sub>N<sub>x</sub> visible photocatalyst prepared by N-doping in Et<sub>3</sub>N/EtOH fluid under supercritical conditions. *J Phys Chem C* 112(16):6546–6550

40. Fuku K, Kamegawa T, Mori K, Yamashita H (2012) Highly dispersed platinum nanoparticles on TiO<sub>2</sub> prepared by using the microwave-assisted deposition method: an efficient photocatalyst for the formation of H<sub>2</sub> and N<sub>2</sub> from aqueous NH<sub>3</sub>. *Chem-Asian J* 7(6):1366–1371
41. Gupta U, Rao BG, Maitra U, Prasad BE, Rao CNR (2014) Visible-light-induced generation of H<sub>2</sub> by nanocomposites of few-layer TiS<sub>2</sub> and TaS<sub>2</sub> with CdS nanoparticles. *Chem-Asian J* 9(5):1311–1315
42. Tang X, Tay Q, Chen Z, Chen Y, Goh GKL, Xue J (2013) CuInZnS-decorated graphene nanosheets for highly efficient visible-light-driven photocatalytic hydrogen production. *J Mater Chem A* 1(21):6359–6365
43. Mori K, Aoyama J, Kawashima M, Yamashita H (2014) Visible-light driven H<sub>2</sub> production utilizing iridium and rhodium complexes intercalated into a zirconium phosphate layered matrix. *Dalton Trans* 43(27):10541–10547
44. Wang C, deKrafft KE, Lin W (2012) Pt Nanoparticles@Photoactive metal-organic frameworks: efficient hydrogen evolution via synergistic photoexcitation and electron injection. *J Am Chem Soc* 134(17):7211–7214
45. Wen M, Mori K, Kamegawa T, Yamashita H (2014) Amine-functionalized MIL-101(Cr) with imbedded platinum nanoparticles as a durable photocatalyst for hydrogen production from water. *Chem Commun* 50(79):11645–11648
46. Lin Y, Kong C, Chen L (2012) Direct synthesis of amine-functionalized MIL-101(Cr) nanoparticles and application for CO<sub>2</sub> capture. *RSC Adv* 2(16):6417–6419
47. Wang D, Huang R, Liu W, Sun D, Li Z (2014) Fe-Based MOFs for photocatalytic CO<sub>2</sub> reduction: role of coordination unsaturated sites and dual excitation pathways. *ACS Catal* 4(12):4254–4260

# Chapter 30

## Metal-Organic Frameworks (MOFs) for Photocatalytic Organic Transformations

Dengrong Sun and Zhaohui Li

### 30.1 Introduction

Metal-organic frameworks (MOFs) are a class of crystalline micro-mesoporous hybrid materials constructed from metal or metal clusters interconnected by organic linkers [1–3]. Their inherent properties including high porosity, uniform but tunable cavities, and versatile structures make them promising for a variety of applications such as gas storage, chemical separation, catalysis, and drug delivery [4–8]. The utilization of MOFs for solar energy harvesting has been demonstrated in recent years and MOFs are emerging as a new type of promising photocatalysts [9–12]. The metal center of MOFs can be regarded as isolated semiconductor quantum dots interconnected by organic linkers, which act as light antenna to activate these quantum dots. Additionally, the highly flexible and tunable structure of MOFs allow for integrating of different functions on the antenna to achieve excellent light-harvesting properties [13–15]. With these advantages, MOFs have been successfully applied in various photocatalytic reactions [16, 17]. In this chapter, we summarized some recent work in using photocatalytic active MOFs for organic transformations, with the focus on our group's work. The incorporations of photocatalytic molecular complex in the MOFs and their application for photocatalytic reactions are not discussed in this chapter since the active species involved in these systems are the molecular compound and have been summarized elsewhere [11, 18, 19].

---

D. Sun • Z. Li (✉)

Research Institute of Photocatalysis, State Key Laboratory of Photocatalysis on Energy and Environment, College of Chemistry, Fuzhou University, Fuzhou 350002, People's Republic of China  
e-mail: [zhaohuili@fzu.edu.cn](mailto:zhaohuili@fzu.edu.cn)

## 30.2 Photocatalytic CO<sub>2</sub> Reduction

The utilization of solar energy to reduce CO<sub>2</sub> to valuable organic compounds is one of the best solutions to solve the problems of global warming and energy shortage. Various kinds of materials including inorganic semiconductors, metal-incorporated zeolites, and molecular complex have been investigated for this reaction [20–22]. Activated by the observations that Ti-incorporated zeolites exhibited superior performance than TiO<sub>2</sub> for photocatalytic CO<sub>2</sub> reduction and considering the analogy between zeolites and MOFs, we believe that Ti-containing MOFs can be promising photocatalyst for CO<sub>2</sub> reduction.

Therefore, a Ti-based MOF material, MIL-125(Ti), was selected to start the photocatalytic CO<sub>2</sub> reduction. MIL-125(Ti) is constructed by TiO<sub>5</sub>(OH) octahedra and 1,4-benzene dicarboxylates (BDC) to form a 3D network [23]. By replacing H<sub>2</sub>BDC with 2-aminoterephthalic acid (H<sub>2</sub>ATA), we have successfully obtained the isostructural amine-functionalized MIL-125(Ti) (NH<sub>2</sub>-MIL-125(Ti)) [24]. The presence of amino group in NH<sub>2</sub>-MIL-125(Ti) introduces an extra absorption in visible light region and improves its adsorption capacity towards CO<sub>2</sub> (Fig. 30.1a, b). Photocatalytic studies showed that NH<sub>2</sub>-MIL-125(Ti) can reduce CO<sub>2</sub> to give HCOO<sup>-</sup> in MeCN with the presence of triethanolamine (TEOA) as sacrificial agent under visible light, with about 8.14 μmol of HCOO<sup>-</sup> produced after reacting for 10 h (Fig. 30.1c). The isotopic <sup>13</sup>CO<sub>2</sub> reaction and a series of control experiments confirmed that the produced HCOO<sup>-</sup> originated truly from the visible light-assisted CO<sub>2</sub> reduction over NH<sub>2</sub>-MIL-125(Ti). NH<sub>2</sub>-MIL-125(Ti) is stable in the reaction as confirmed by the XRD and BET results.

During the reaction, an interesting reversible photochromic phenomenon was observed. The color of the NH<sub>2</sub>-MIL-125(Ti) suspension changed from light yellow to green upon visible light irradiation and recovered the original yellow color when CO<sub>2</sub> was introduced into the reaction system. ESR analyses revealed that the green suspension contains Ti<sup>3+</sup>, suggesting the formation of Ti<sup>3+</sup> and its involvement in the CO<sub>2</sub> reduction. It was proposed that Ti<sup>3+</sup> is produced via an electron transfer from the excited ATA\* to Ti<sup>4+</sup> upon visible light irradiation, which can reduce CO<sub>2</sub> to HCOO<sup>-</sup> (Fig. 30.1d). TEOA acts as both an electron and proton donor and provides an alkaline environment to facilitate the photocatalytic CO<sub>2</sub> reduction. This work gave the first demonstration of CO<sub>2</sub> reduction over MOFs under visible light irradiation, opening new perspectives for the development of photocatalysts for the reduction of CO<sub>2</sub>.

The Ti<sup>3+</sup>-assisted photocatalytic CO<sub>2</sub> reduction over NH<sub>2</sub>-MIL-125(Ti) indicates that MOFs with redox-active metal centers may also be photocatalysts for CO<sub>2</sub> reduction. This inspired us to explore the performance of other MOFs with redox-active metal centers for this reaction. NH<sub>2</sub>-Uio-66(Zr), a Zr-based MOF composed of hexameric Zr<sub>6</sub>O<sub>32</sub> units linked by ATA [25], was selected since it is highly stable in water and we hope that the CO<sub>2</sub> reduction can be performed in water. Unfortunately no reduction of CO<sub>2</sub> was observed over NH<sub>2</sub>-Uio-66(Zr), probably due to the weak electron-donating ability of water. However, NH<sub>2</sub>-Uio-66(Zr) showed activity for photocatalytic CO<sub>2</sub> reduction in MeCN when TEOA was used as a sacrificial agent,

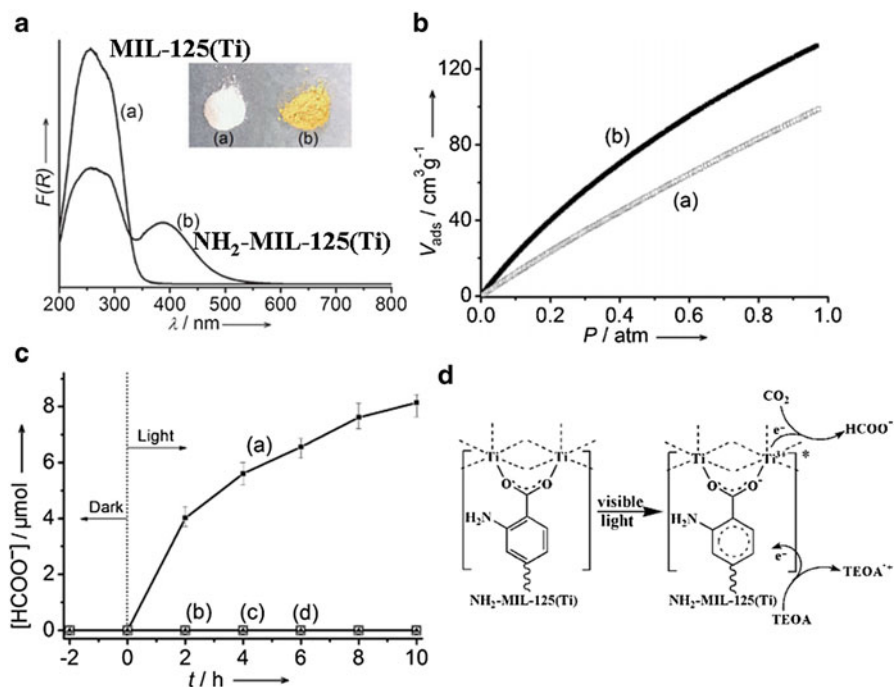


**Fig. 30.1** (a) UV/Vis spectra of MIL-125(Ti) and NH<sub>2</sub>-MIL-125(Ti); (b) CO<sub>2</sub> adsorption isotherms (1 atm, 273 K) of (*open square*) MIL-125(Ti) and (*filled square*) NH<sub>2</sub>-MIL-125(Ti); (c) the amount of HCOO<sup>-</sup> produced as a function of the time of irradiation over (*filled square*) NH<sub>2</sub>-MIL-125(Ti), (*open square*) MIL-125(Ti), (*open circle*) a mixture of TiO<sub>2</sub> and H<sub>2</sub>ATA (19 mg + 32 mg), and (*filled triangle*) visible light irradiation without a sample; (d) proposed mechanism for the photocatalytic CO<sub>2</sub> reduction over NH<sub>2</sub>-MIL-125(Ti) under visible light irradiation. Reproduced with permission from Ref. [24]. Copyright 2012, Wiley-VCH

with about 13.2  $\mu\text{mol}$  of HCOO<sup>-</sup> formed after 10 h of irradiation [26]. This value is higher than that over NH<sub>2</sub>-MIL-125(Ti), probably due to the more negative redox potential of Zr<sup>4+</sup>/Zr<sup>3+</sup> than Ti<sup>4+</sup>/Ti<sup>3+</sup> [27].

For both NH<sub>2</sub>-MIL-125(Ti) and NH<sub>2</sub>-Uio-66(Zr), the reactive species (Ti<sup>3+</sup> and Zr<sup>3+</sup>) are generated by the excited organic linkers in a manner of LMCT. A direct excitation on the metal center of MOFs would be more beneficial to the photocatalysis. Therefore, Fe-based MOFs, including MIL-101(Fe), MIL-53(Fe), and MIL-88B(Fe), were chosen for CO<sub>2</sub> reduction. All three Fe-based MOFs are visible light responsive due to the existence of extensive iron oxo clusters, which makes it possible for a direct excitation of the Fe-O clusters upon visible light irradiation (Fig. 30.2a) [28, 29]. It was found that all three Fe-MOFs showed photocatalytic activity for CO<sub>2</sub> reduction to HCOO<sup>-</sup> under visible light irradiation, among which MIL-101(Fe) exhibited the highest activity with about 59.0  $\mu\text{mol}$  of HCOO<sup>-</sup> produced after reacting for 8 h. Since these three MOFs have similar component, their distinguished structures play a major role on the different catalytic performance. In

situ FT-IR analyses indicated that the presence of coordination unsaturated Fe metal sites (CUSs) in MIL-101(Fe) allows for the direct adsorption of CO<sub>2</sub> onto the Fe center, facilitating the reduction of CO<sub>2</sub> (Fig. 30.2b) [30].

Since amine sites can act as light-absorption chromophore to enhance the visible light absorption of the photocatalysts, we functionalized the above Fe-MOFs with amino group and investigated their performance for photocatalytic CO<sub>2</sub> reduction [30]. As expected, the photocatalytic performance of the amine-functionalization Fe-MOFs is obviously higher than that over un-functionalized ones but with different enhanced degree. The improved photocatalytic performance over amine-functionalized Fe-MOFs can be assigned to the dual excitation of both Fe-O clusters and amino functionality on the organic linker and the synergistic effect between these two pathways under visible light irradiation (Fig. 30.2c). The different degree of the enhancement is probably correlated to the efficiency of the electron transfer from the excited organic linker to the metal center in these three Fe-based MOF materials.

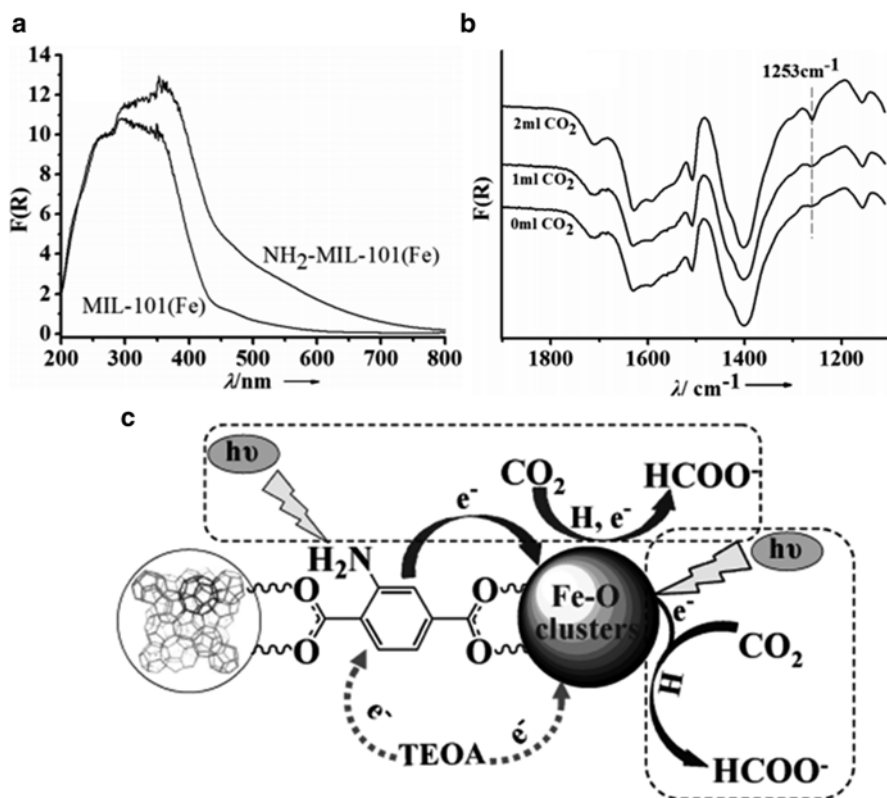


**Fig. 30.2** (a) UV-DRS spectra of MIL-101(Fe) and NH<sub>2</sub>-MIL-101(Fe); (b) in situ FT-IR analyses of CO<sub>2</sub> adsorption over pretreated MIL-101(Fe); (c) dual-excitation pathways over amino-functionalized Fe-based MOFs. Reprinted with permission from Ref. [30]. Copyright 2014, American Chemical Society

### 30.3 Photocatalytic Amine Oxidation

As observed in the photocatalytic CO<sub>2</sub> reduction over NH<sub>2</sub>-MIL-125(Ti), when irradiated with visible light, the yellow NH<sub>2</sub>-MIL-125(Ti) suspension changed to green color [16]. In addition to CO<sub>2</sub>, the green suspension can also be turned back to yellow by introduction of O<sub>2</sub>, indicating that O<sub>2</sub> can react with Ti<sup>3+</sup>. This suggests that NH<sub>2</sub>-MIL-125(Ti) may be used as photocatalyst for aerobic oxidation reactions. The oxidation of amines to imines over NH<sub>2</sub>-MIL-125(Ti) was therefore selected [31]. It was found that over NH<sub>2</sub>-MIL-125(Ti), different amines can be photocatalytically transformed to corresponding imines with medium-to-high conversions and yields under visible light irradiation. Take benzylamine as an example. 73 % of benzylamine can be converted to *N*-benzylidene benzylamine with a high yield of 86 % over NH<sub>2</sub>-MIL-125(Ti) after 12 h of irradiation. This reaction can be applied to a wide range of substrates, including benzylamines with different substituted groups at different substituted positions, secondary amines, and heterocyclic amines with conversion and yield ranging from 41–92 % to 45–93 %, respectively. The photocatalyst can be reused for at least three runs without obvious loss of catalytic activity and indicated that NH<sub>2</sub>-MIL-125(Ti) is stable during the reaction. Mechanism study revealed that the photogenerated Ti<sup>3+</sup> in NH<sub>2</sub>-MIL-125(Ti) can reduce O<sub>2</sub> to form ·O<sub>2</sub><sup>-</sup>. In the meantime, the amine donates an electron and undergoes a de-protonation process to generate carbon-centered radical, which would react with the as-formed ·O<sub>2</sub><sup>-</sup> leading to the formation of aldehydes. The nucleophilic attack on aldehydes by the unreacted amines thus yields the corresponding imines (Fig. 30.3). Since a de-protonation process of amine is involved in the reaction, amines without hydrogen at α-carbon cannot be transformed to imines over NH<sub>2</sub>-MIL-125(Ti). In addition to amine oxidation, NH<sub>2</sub>-MIL-125(Ti) has also been applied in some other photocatalytic oxidation reactions such as benzyl alcohol oxidation and oxidative desulfurization reactions [32, 33]. This work revealed that in addition to reduction reactions such as CO<sub>2</sub> reduction, NH<sub>2</sub>-MIL-125(Ti) also showed potential in photocatalytic aerobic oxidation. This study also highlighted that MOFs are promising as photocatalysts for photocatalytic redox reactions.

### 30.4 Photocatalytic Tandem Reactions

One-pot tandem reaction always requires simultaneous presence of two or more types of active centers in the same vessel. The use of MOFs for sequential one-pot tandem reactions has caught extensive recent attentions since MOFs contain well-differentiated multifunctional catalytic active sites. Actually, some multifunctional MOFs have been successfully applied in one-pot tandem reactions [34–37]. It would be ideal if the tandem reaction can be achieved under light irradiations by combining MOF-based photocatalysis with the multifunctional catalytic sites of MOFs to fulfill some complex organic transformations. Recently, our group reported that

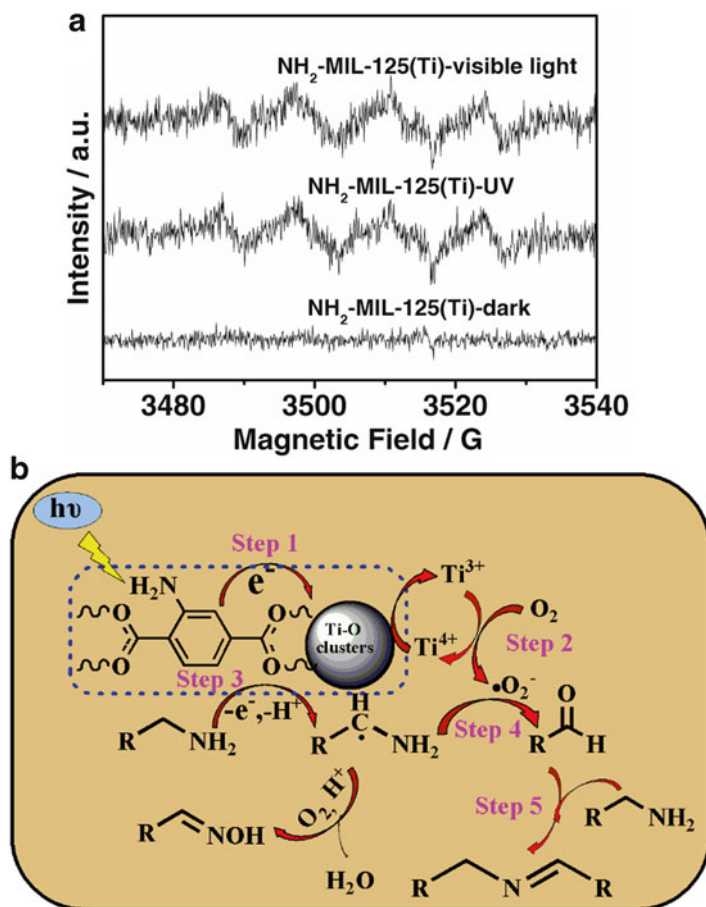


**Fig. 30.3** (a) DMPO spin-trapping ESR spectra of NH<sub>2</sub>-MIL-125(Ti) in methanol dispersion in dark, under UV and visible light irradiations; (b) proposed mechanism of the photocatalytic amine oxidation over NH<sub>2</sub>-MIL-125(Ti). Reprinted with permission from Ref. [31]. Copyright 2015, Elsevier

NH<sub>2</sub>-MIL-101(Fe) can efficiently catalyze a tandem photo-oxidation/Knoevenagel condensation reaction between different aromatic alcohols and active methylene compounds under visible light irradiation [38]. Take the reaction between benzyl alcohols and malononitrile as an example. 88 % of benzyl alcohol was transformed and benzylidene malononitrile was produced as the main product with a yield of 72 % over NH<sub>2</sub>-MIL-101(Fe) after reacting for 40 h. The substrates of this reaction can be further expanded to various alcohol including benzyl alcohol with different functional groups, different substitution positions, and other active methylene compounds with the yield to benzylidene malononitrile ranging from 20 to 76 %. Mechanism study revealed that two steps including alcohol oxidation to form

aldehyde and the Knoevenagel condensation between aldehyde and methylene compounds are involved in this reaction (Fig. 30.4a). The Knoevenagel condensation is the rate-determining step, which involves the deprotonation of the active methylene group with the assistance of basic sites to form a carbanion [39]. Therefore, photocatalysts with high basicity and substrates with high acidity are benefit for the deprotonation process and facilitate this tandem reaction.  $\text{NH}_2\text{-MIL-101(Fe)}$  in the reaction acts as both a photocatalyst to oxidize alcohol to aldehyde and a base to facilitate the condensation between the aldehyde and the active

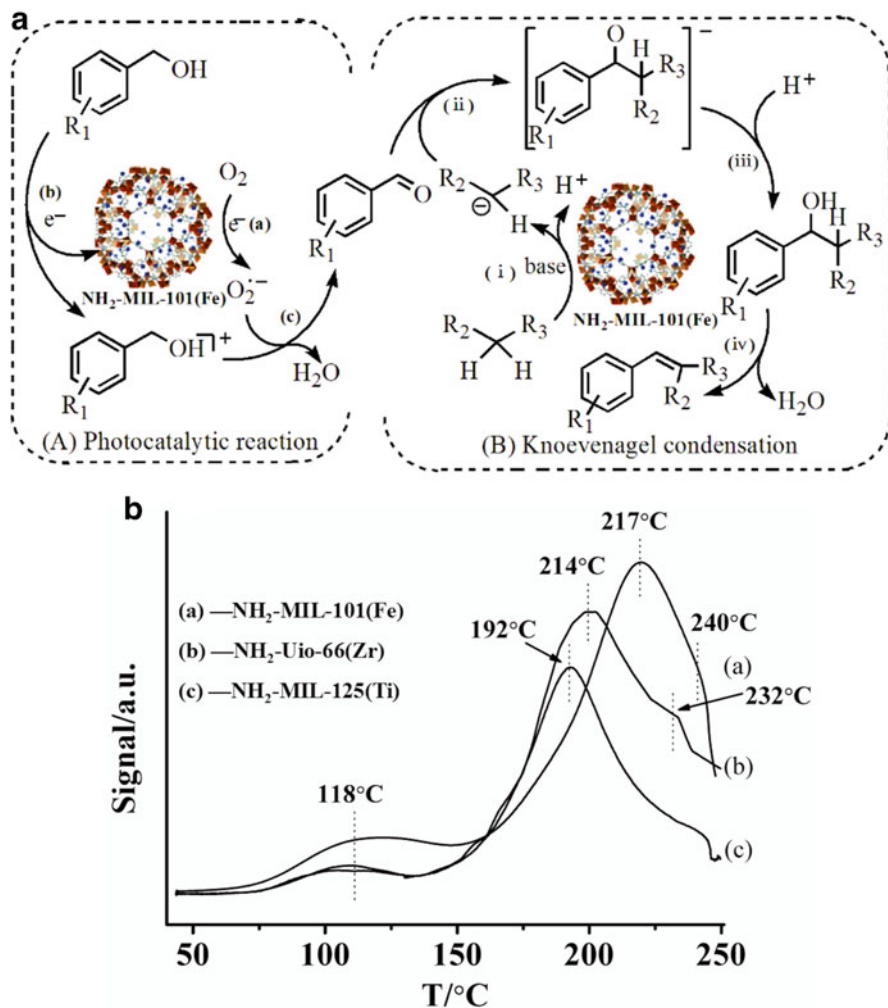


**Fig. 30.4** (a) Proposed mechanism for one-pot tandem photocatalytic oxidation/Knoevenagel condensation over bifunctional  $\text{NH}_2\text{-MIL-101(Fe)}$ ; (b)  $\text{CO}_2\text{-TPD}$  profiles of  $\text{CO}_2$ -adsorbed different MOFs. Reprinted with permission from Ref. [38]. Copyright 2015, the Royal Society of Chemistry

methylene compounds. The higher basicity of  $\text{NH}_2\text{-MIL-101(Fe)}$  as compared with  $\text{NH}_2\text{-UiO-66(Zr)}$  and  $\text{NH}_2\text{-MIL-125(Ti)}$  promotes the deprotonation process in the Knoevenagel condensation and results in higher catalytic activity (Fig. 30.4b). This work showed the great potential of MOFs as multifunctional photocatalysts for various one-pot multistep reactions.

### 30.5 Modifications on MOFs

The highly flexible and tunable structure of MOFs allow for easy designation and functionalization with specific properties. Recently, our group has improved the photocatalytic performance of MOFs following the three strategies below: amine functionalization on organic linkers, postsynthetic metal exchange in the metal center, and doping of noble metal nanoparticles.

### 30.6 Amine Functionalization on Organic Linkers

We partly substituted the ATA in  $\text{NH}_2\text{-UiO-66(Zr)}$  with 2, 5-diaminoterephthalic acid ( $\text{H}_2\text{DTA}$ ) to obtain  $\text{NH}_2\text{-UiO-66(Zr)}$  with mixed ATA and DTA linkers [26]. The mixed  $\text{NH}_2\text{-UiO-66(Zr)}$  showed stronger visible light absorption as compared with  $\text{NH}_2\text{-UiO-66(Zr)}$  (Fig. 30.5a). The photocatalytic  $\text{CO}_2$  reduction over mixed  $\text{NH}_2\text{-UiO-66(Zr)}$  revealed that more than 50 % higher amount of  $\text{HCOO}^-$  was produced over mixed  $\text{NH}_2\text{-UiO-66(Zr)}$  (20.7  $\mu\text{mol}$ ) as compared with  $\text{NH}_2\text{-UiO-66(Zr)}$  (13.2  $\mu\text{mol}$ ) after reacting for 10 h (Fig. 30.5b). Control experiment with irradiation

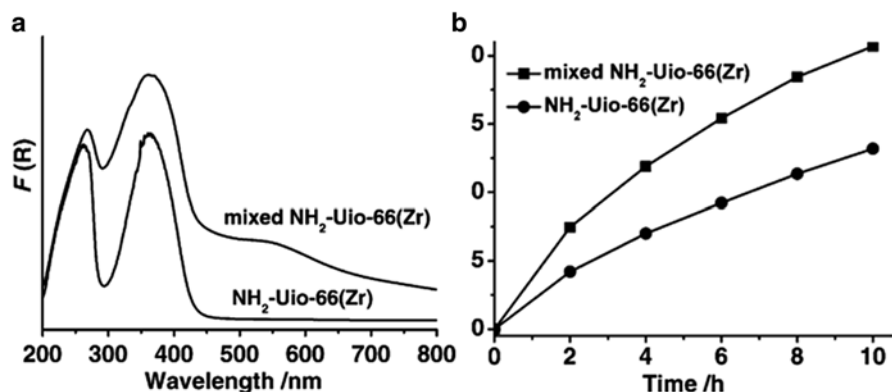


**Fig. 30.5** (a) UV/Vis spectra of  $\text{NH}_2\text{-UiO-66(Zr)}$  and mixed  $\text{NH}_2\text{-UiO-66(Zr)}$ ; (b) amount of  $\text{HCOO}^-$  produced as a function of irradiation time over  $\text{NH}_2\text{-UiO-66(Zr)}$  and mixed  $\text{NH}_2\text{-UiO-66(Zr)}$ . Reproduced with permission from Ref. [26]. Copyright 2013, Wiley-VCH

wavelength larger than 515 nm gave 7.28  $\mu\text{mol}$  of  $\text{HCOO}^-$  over the mixed  $\text{NH}_2\text{-Uio-66(Zr)}$ , while no  $\text{HCOO}^-$  was formed over  $\text{NH}_2\text{-Uio-66(Zr)}$ , indicating that the new absorption induced by the second amino group in the mixed  $\text{NH}_2\text{-Uio-66(Zr)}$  is responsible for the improved activity for  $\text{HCOO}^-$  generation.

### 30.7 Postsynthetic Metal Exchange in the Metal Center

The recent observation of metal ions metathesis in MOFs provided a facile strategy for the functionalization of inorganic part in MOFs, which has been achieved in MOFs including MILs, Uios, and ZIFs [40–43]. By postsynthetic exchange (PSE), we have achieved Ti-substituted  $\text{NH}_2\text{-Uio-66(Zr)}$  (denoted as  $\text{NH}_2\text{-Uio-66(Zr/Ti)}$ ) under mild condition (Fig. 30.6a). Introduction of Ti does not influence the structure

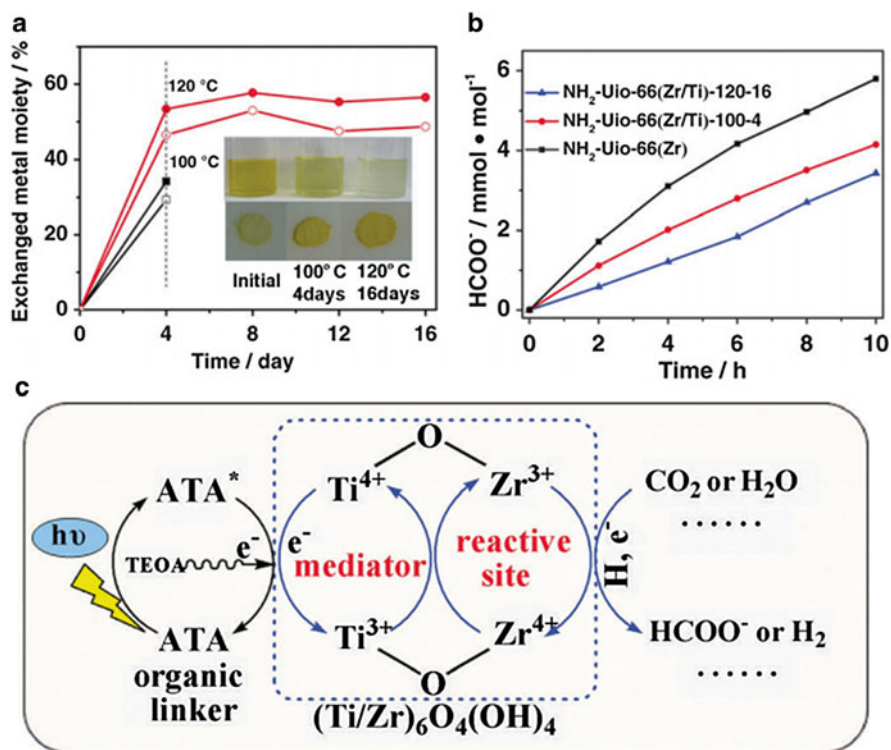


**Fig. 30.6** (a) Change in the amount of the Ti moiety in solids with the incubation period at 120 °C (filled circle) and 100 °C (filled square); change in the amount of the Zr moiety in the solutions with the incubation period at 120 °C (open circle) and 100 °C (open square); (b) amount of  $\text{HCOO}^-$  produced as a function of irradiation time over different samples; (c) proposed enhanced mechanism for the photocatalytic reactions over  $\text{NH}_2\text{-Uio-66(Zr/Ti)}$ . Reprinted with permission from Ref. [44]. Copyright 2015, Royal Society of Chemistry

of  $\text{NH}_2\text{-Uio-66(Zr)}$ . The obtained  $\text{NH}_2\text{-Uio-66(Zr/Ti)}$  showed higher activity for  $\text{CO}_2$  reduction to give  $\text{HCOO}^-$  than  $\text{NH}_2\text{-Uio-66(Zr)}$  under visible light irradiation. About  $5.8 \text{ mmol mol}^{-1}$  of  $\text{HCOO}^-$  was produced over  $\text{NH}_2\text{-Uio-66(Zr/Ti)-120-16}$  after 10 h of irradiation, 1.7 times as that observed over  $\text{NH}_2\text{-Uio-66(Zr)}$  ( $3.4 \text{ mmol mol}^{-1}$ ) under otherwise similar conditions (Fig. 30.6b). ESR analyses and DFT calculations indicated that the incorporated Ti moiety can act as an electron mediator promoting the formation of  $\text{Zr}^{3+}$  and resulted in an enhanced photocatalytic  $\text{CO}_2$  reduction performance (Fig. 30.6c). This work provided a facile and controllable strategy to improve photocatalytic activity over MOFs, which is believed to be a general method to develop highly efficient MOF-based photocatalysts [44].

### 30.8 Doping of Noble Metal Particles

Doping of noble metals like Pt, Pd, and Au onto semiconductor materials is a widely adopted strategy to promote the separation of photogenerated electrons and holes [45–48], but the effect of the noble metals on the photocatalytic performance of MOF-based photocatalysts is largely unexplored. To elucidate the influence of noble metal on MOF-based photocatalysis, we prepared noble metal-doped  $\text{NH}_2\text{-MIL-125(Ti)}$  ( $\text{M/NH}_2\text{-MIL-125(Ti)}$ ,  $\text{M}=\text{Pt}$  or  $\text{Au}$ ) and investigated their photocatalytic performance [49]. M-doped  $\text{NH}_2\text{-MIL-125(Ti)}$  ( $\text{M}=\text{Pt}$  and  $\text{Au}$ ) was prepared by using the wetness impregnation method followed by a treatment with  $\text{H}_2$  flow. The photocatalytic reaction performed in  $\text{CO}_2$ -saturated  $\text{MeCN/TEOA}$  showed that unlike that over pure  $\text{NH}_2\text{-MIL-125(Ti)}$ , in which only  $\text{HCOO}^-$  was produced, both  $\text{H}_2$  and  $\text{HCOO}^-$  were formed over Pt- and Au-loaded  $\text{NH}_2\text{-MIL-125(Ti)}$ , indicating that noble metal doping on  $\text{NH}_2\text{-MIL-125(Ti)}$  promoted the photocatalytic hydrogen evolution (Fig. 30.7a, b). However, Pt and Au have different effects on the photocatalytic performance for  $\text{HCOO}^-$  production. Compared with pure  $\text{NH}_2\text{-MIL-125(Ti)}$  ( $10.75 \text{ }\mu\text{mol}$ ), Pt/ $\text{NH}_2\text{-MIL-125(Ti)}$  showed an enhanced activity for photocatalytic  $\text{HCOO}^-$  formation ( $12.96 \text{ }\mu\text{mol}$ ), whereas Au has a negative effect on this reaction ( $9.06 \text{ }\mu\text{mol}$ ) (Fig. 30.7b). ESR analyses and DFT calculations revealed that the hydrogen formed over Pt/ $\text{NH}_2\text{-MIL-125(Ti)}$  can spill over from noble metal to the metal center and promote the formation of  $\text{Ti}^{3+}$ , facilitating the photocatalytic  $\text{CO}_2$  reduction to form  $\text{HCOO}^-$  (Fig. 30.7c). This work for the first time elucidated the hydrogen spillover mechanism for photocatalytic  $\text{CO}_2$  reduction over MOFs and demonstrated the potential of using noble metal-doped MOFs in photocatalytic reactions involving hydrogen as a reactant, like hydrogenation reactions.

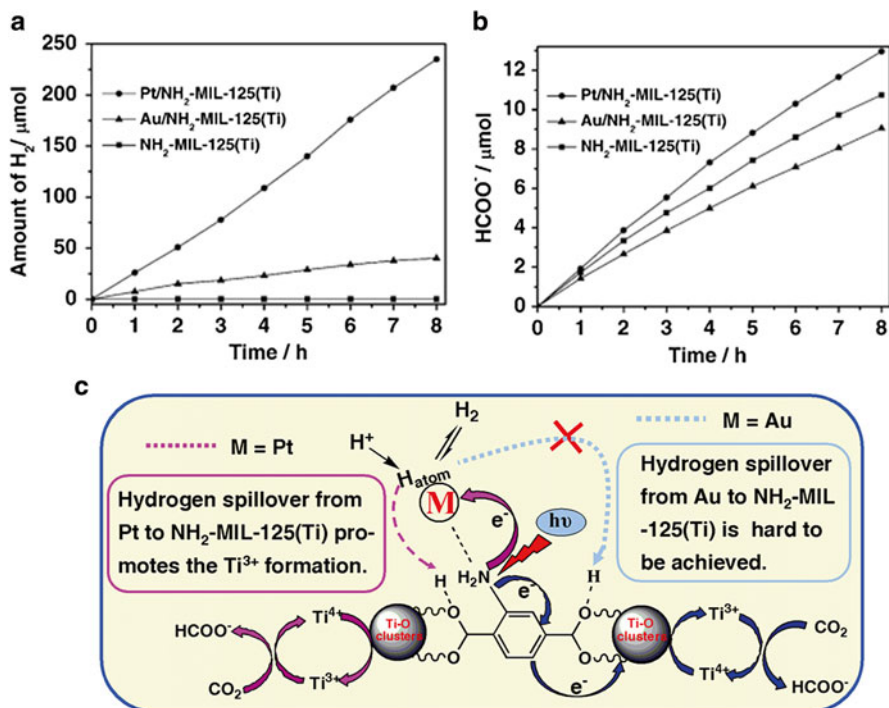


**Fig. 30.7** The amount of the product formed as a function of irradiation time over the as-prepared samples: (a) hydrogen; (b)  $HCOO^-$ ; (c) proposed mechanism for the photocatalytic reactions over  $M/NH_2$ -MIL-125(Ti). Reproduced with permission from Ref. [49]. Copyright 2014, Wiley-VCH

## 30.9 Conclusions and Perspectives

Although in its infancy stage, the use of MOFs as photocatalysts for organic transformations has become the focus of current research. The highly flexible and tunable chemistry of MOFs allow for engineering of MOFs with excellent light absorption property, which is significant for the utilization of solar energy and benefit for photocatalysis.

## References

1. Corma A, García H, Li Xamena FX (2010) Engineering metal organic frameworks for heterogeneous catalysis. *Chem Rev* 110:4606–4655
2. Meek ST, Greathouse JA, Allendorf MD (2011) Metal-organic frameworks: a rapidly growing class of versatile nanoporous materials. *Adv Mater* 23:249–267
3. Férey G (2008) Hybrid porous solids: past, present, future. *Chem Soc Rev* 37:191–214
4. Murray LJ, Dinca M, Long JR (2009) Hydrogen storage in metal-organic frameworks. *Chem Soc Rev* 2009(38):1294–1314

5. Li JR, Sculley J, Zhou HC (2012) Metal-organic frameworks for separations. *Chem Rev* 112:869–932
6. Lee J, Farha OK, Roberts J et al (2009) Metal-organic framework materials as catalysts. *Chem Soc Rev* 38:1450–1459
7. McKinlay AC, Morris RE, Horcajada P et al (2010) Bio-MOFs: metall-organic frameworks for biological and medical applications. *Angew Chem* 122:6400–6406
8. McKinlay AC, Morris RE, Horcajada P et al (2010) Bio-MOFs: metall-organic frameworks for biological and medical applications. *Angew Chem Int Ed* 49:6260–6266
9. Zhang T, Lin W (2014) Metal-organic frameworks for artificial photosynthesis and photocatalysis. *Chem Soc Rev* 43:5982–5993
10. Nasalevich MA, van der Veen M, Kapteijn F et al (2014) *CrystEngComm* 16:4919–4926
11. Wang JL, Wang C, Lin W (2012) Metal-organic frameworks for light harvesting and photocatalysis. *ACS Catal* 2:2630–2640
12. Li SL, Xu Q (2013) Metal-organic frameworks as platform for clean energy. *Energy Environ Sci* 6:1656–1683
13. Cohen SM (2010) Modifying MOFs: new chemistry, new materials. *Chem Sci* 1:32–36
14. Cohen SM (2012) Postsynthetic methods for the functionalization of metal-organic frameworks. *Chem Rev* 112:970–1000
15. Hendon CH, Tiana D, Fontecave M et al (2013) Engineering the optical response of the titanium-MIL-125 metal-organic framework through ligand functionalization. *J Am Chem Soc* 135:10942–10945
16. Silva CG, Luz I, Li Xamena FX et al (2010) Water stable Zr-benzenedicarboxylate metal-organic frameworks as photocatalysts for hydrogen generation. *Chem Eur J* 16:11133–11138
17. Vermoortele F, Ameloot R, Vimont A et al (2011) An amino-modified Zr-terephthalate metal-organic framework as an acid-base catalyst for cross-aldol condensation. *Chem Commun* 47:1521–1523
18. Manna K, Zhang T, Lin W (2014) Postsynthetic metalation of bipyridyl-containing metal-organic frameworks for highly efficient catalytic organic transformations. *J Am Chem Soc* 136:6566–6569
19. Wang C, Xie Z, deKrafft KE et al (2011) Doping metal-organic frameworks for water oxidation, carbon dioxide reduction, and organic photocatalysis. *J Am Chem Soc* 133:13445–13454
20. Inoue T, Fujishima A, Konishi S et al (1979) Photoelectrocatalytic reduction of carbon dioxide in aqueous suspensions of semiconductor powders. *Nature* 277:637–638
21. Lin W, Frei H (2005) Photochemical CO<sub>2</sub> splitting by metal-to-metal charge-transfer excitation in mesoporous ZrCu(I)-MCM-41 silicate sieve. *J Am Chem Soc* 127:1610–1611
22. Appel AM, Bercaw JE, Bocarsly AB et al (2013) Frontiers, opportunities, and challenges in biochemical and chemical catalysis of CO<sub>2</sub> fixation. *Chem Rev* 113:6621–6658
23. Dan-Hardi M, Serre C, Frot T et al (2009) A new photoactive crystalline highly porous titanium(IV) dicarboxylate. *J Am Chem Soc* 131:10857–10859
24. Fu Y, Sun D, Chen Y et al (2012) An amine-functionalized titanium metal-organic framework photocatalyst with visible-light-induced activity for CO<sub>2</sub> reduction. *Angew Chem Int Ed* 51:3364–3367
25. Cavka JH, Jakobsen S, Olsbye U et al (2008) A new zirconium inorganic building brick forming metal organic frameworks with exceptional stability. *J Am Chem Soc* 130:13850–13851
26. Sun D, Fu Y, Liu W et al (2013) Studies on photocatalytic CO<sub>2</sub> reduction over NH<sub>2</sub>-UiO-66(Zr) and its derivatives: towards a better understanding of photocatalysis on metal-organic frameworks. *Chem Eur J* 19:14279–14285
27. Horiuchi Y, Toyao T, Saito M (2012) Visible-light-promoted photocatalytic hydrogen production by using an amino-functionalized Ti(IV) metal-organic framework. *J Phys Chem C* 116:20848–20853
28. Laurier KGM, Vermoortele F, Ameloot R et al (2013) Iron(III)-based metal-organic frameworks as visible light photocatalysts. *J Am Chem Soc* 135:14488–14491

29. Bordiga S, Buzzoni R, Geobaldo F et al (1996) Structure and reactivity of framework and extra framework iron in Fe-silicalite as investigated by spectroscopic and physicochemical methods. *J Catal* 158:486–501
30. Wang D, Huang R, Liu W et al (2014) Fe-based MOFs for photocatalytic CO<sub>2</sub> reduction: role of coordination unsaturated sites and dual excitation pathways. *ACS Catal* 4:4254–4260
31. Sun D, Ye L, Li Z (2015) Visible-light-assisted aerobic photocatalytic oxidation of amines to imines over NH<sub>2</sub>-MIL-125(Ti). *Appl Catal B Environ* 164:428–432
32. McNamara ND, Neumann GT, Masko ET et al (2013) Catalytic performance and stability of (V) MIL-47 and (Ti) MIL-125 in the oxidative desulfurization of heterocyclic aromatic sulfur compounds. *J Catal* 305:217–226
33. Nasalevich MA, Goestena MG, Savenije TJ et al (2013) Enhancing optical absorption of metal-organic frameworks for improved visible light photocatalysis. *Chem Commun* 49:10575–10577
34. Yoon M, Srirambalaji R, Kim K (2012) Homochiral metal-organic frameworks for asymmetric heterogeneous catalysis. *Chem Rev* 112:1196–1231
35. Pintado-Sierra M, Rasero-Almansa AM, Corma A et al (2013) Bifunctional iridium-(2-aminoterephthalate)-Zr-MOF chemoselective catalyst for the synthesis of secondary amines by one-pot three-step cascade reaction. *J Catal* 299:137–145
36. Toyao T, Saito M, Horiuchi Y et al (2014) Development of a novel one-pot reaction system utilizing a bifunctional Zr-based metal-organic framework. *Catal Sci Technol* 2014(4):625–628
37. Gacson J, Corma A, Kapteijn F et al (2013) Metal organic framework catalysis: quo vadis? *ACS Catal* 4:361–378
38. Wang D, Li Z (2015) Bi-functional NH<sub>2</sub>-MIL-10(Fe) for one-pot tandem photo-oxidation/Knoevenagel condensation between aromatic alcohols and active methylene compounds. *Catal Sci Technol* 5:1623–1628
39. Yang Y, Yao HF, Xi FG et al (2014) Amino-functionalized Zr(IV) metal-organic framework as bifunctional acid–base catalyst for Knoevenagel condensation. *J Mol Catal A Chem* 390:198–205
40. Kim M, Cahill JF, Su Y et al (2012) Postsynthetic ligand exchange as a route to functionalization of “inert” metal-organic frameworks. *Chem Sci* 3:126–130
41. Kim M, Cahill JF, Fei H et al (2012) Postsynthetic ligand and cation exchange in robust metal-organic frameworks. *J Am Chem Soc* 134:18082–18088
42. Brozek CK, Dincá M (2013) Ti<sup>3+</sup>-, V<sup>2+/3+</sup>-, Cr<sup>2+/3+</sup>-, Mn<sup>2+</sup>-, and Fe<sup>2+</sup>-Substituted MOF-5 and redox reactivity in Cr- and Fe-MOF-5. *J Am Chem Soc* 135:12886–12891
43. Kim M, Cohen SM (2012) Discovery, development, and functionalization of Zr(IV)-based metal-organic frameworks. *CrystEngComm* 14:4096–4104
44. Sun D, Liu W, Qiu M et al (2015) Introduction of a mediator for enhancing photocatalytic performance via post-synthetic metal exchange in metal-organic frameworks (MOFs). *Chem Commun* 51:2056–2059
45. Ikuma Y, Bessho H (2007) Effect of Pt concentration on the production of hydrogen by a TiO<sub>2</sub> photocatalyst. *Int J Hydrogen Energ* 32:2689–2692
46. Arabatzis IM, Stergiopoulos T, Andreeva D et al (2003) Characterization and photocatalytic activity of Au/TiO<sub>2</sub> thin films for azo-dye degradation. *J Catal* 220:127–135
47. Bae E, Choi W (2003) Highly enhanced photoreductive degradation of perchlorinated compounds on dye-sensitized metal/TiO<sub>2</sub> under visible light. *Environ Sci Technol* 37:147–152
48. Sano T, Kutsuna S, Negishi N et al (2004) Effect of Pd-photodeposition over TiO<sub>2</sub> on product selectivity in photocatalytic degradation of vinyl chloride monomer. *J Mol Catal A* 189:263–270
49. Sun D, Liu W, Fu Y et al (2014) Noble metals can have different effects on photocatalysis over metal-organic frameworks (MOFs): a case study on M/NH<sub>2</sub>-MIL-125(Ti) (M=Pt and Au). *Chem Eur J* 20:4780–4788

# Index

## A

- Ab initio molecular orbital calculation, 181  
Acetaldehyde ( $\text{CH}_3\text{CHO}$ ), 80–82, 85, 89, 91, 92, 94, 95, 191, 229, 249, 265, 266, 359, 392, 393, 397, 400, 434  
Acetic acid ( $\text{CH}_3\text{COOH}$ ), 29, 30, 138, 283, 400, 491  
    deprotonation, 529  
Advanced oxidation processes (AOPs), 125  
Aerobic photooxidation, 475  
Alkali metal, 466–469  
Al-MOF, 486  
 $\text{Al}_2\text{O}_3$ , 243–246, 249, 282  
 $\alpha$ -deprotonation, 213, 219  
 $\alpha$ -S, 305  
Aluminosilicate, 244, 262  
Aminobenzene, 211, 483  
2-Amino benzene dicarboxylic acid, 511  
3-Aminopropyltrimethoxysilane (APS/APTMS), 140, 472  
2-Aminoterephthalic acid, 480  
Ammonia ( $\text{NH}_3$ ), 11, 90, 102, 141, 143, 201–207, 454  
Ammonium chloride ( $\text{NH}_4\text{Cl}$ ), 195  
Anatase, 3, 4, 6, 7, 9, 11, 12, 14, 16, 30, 31, 43, 46, 54, 55, 70, 71, 73–76, 79, 80, 82, 96, 105–108, 110, 111, 125, 137, 157, 174, 178, 187–189, 193, 196, 213, 233, 259, 264, 267–273, 275, 276, 282, 335, 447, 450, 451, 458, 493, 517  
Anionic sulfate surfactant, 34  
Anodization, 156, 157  
Atomic Force Microscope (AFM), 26, 29, 39, 40, 300

## B

- BaTaO<sub>2</sub>N, 452, 454, 455, 459  
B-dopants, 15, 16  
Benzaldehyde, 7, 211, 213, 214, 219, 284, 286, 486  
Benzoic acid (BA), 127, 213  
Benzyl alcohol, 3, 211–222, 284, 286, 485, 486, 527  
Benzylidene malononitrile, 528  
 $\beta$ -hydroxylated amines, 496  
 $\beta$ -rhombohedral B, 307  
BiAg alloy, 308, 309  
Binaphтол, 211  
Bismuth (Bi), 296, 308–309, 343, 347  
     $\text{Bi}_2\text{MoO}_6$ , 375, 392  
     $\text{Bi}_2\text{Mo}_x\text{W}_{1-x}\text{O}_6$ , 375  
     $\text{Bi}_3\text{O}_4\text{Cl}$ , 325, 408–410, 416, 417, 422  
    BiOI, 113, 330  
     $\text{Bi}_5\text{O}_7\text{I}$ , 328, 334  
     $\text{Bi}_4\text{Ti}_3\text{O}_{12}$ , 406  
     $\text{Bi}_x\text{Ti}_{1-x}\text{O}_2$ , 8  
     $\text{Bi}_2\text{W}_2\text{O}_9$ , 392  
    nitrate ( $\text{Bi}(\text{NO}_3)_3$ ), 344, 346, 393–395, 409, 412, 434  
    oxide ( $\text{Bi}_2\text{O}_3$ )<sup>2+</sup>, 325, 328, 337, 341, 348, 352, 360, 392, 394  
    oxybromide (BiOBr), 158, 330, 366  
    oxychloride (BiOCl), 341, 407, 408  
    oxyhalide (BiOX), 113, 158, 325–337  
    tungstate ( $\text{Bi}_2\text{WO}_6$ ), 115–116, 359–386, 391–406  
    tungsten trioxide ( $\text{Bi-WO}_3$ ), 434–436, 441  
    vanadate ( $\text{BiVO}_4$ ), 116, 360, 417, 431, 440, 449  
Bisphenol A (BPA), 132, 133, 234–236, 379

- Boron (B), 111, 296, 307  
 doped graphene, 32, 37, 48, 52  
 Bridge OH, 215, 216  
 Brilliant Red, 155, 193  
 Brookite, 69, 79, 80, 89–96, 105, 137, 188  
 1-Butanol, 75
- C**  
 $C_{60}$ , 376–386  
 $CaBi_2O_4$ , 406  
 Cadmium sulfide (CdS), 37, 56, 57, 133–134, 141, 152, 295, 445, 493, 514  
 Calcium phosphate (CaP), 252–254  
 $Ca_{10}(PO_4)_6(OH)_2$ , 252  
 Carbon dioxide (CO<sub>2</sub>), 314, 500, 502  
 capture, 492, 495  
 photoreduction, 24, 46, 50–52, 337, 492, 495, 502  
 reduction, 51, 52, 297, 301, 332, 480, 524, 527, 530, 532  
 Carbon nitride (C<sub>3</sub>N<sub>4</sub>), 380  
 CdSe, 406  
 CdS-TiO<sub>2</sub>, 16, 36  
 CeO<sub>2</sub>, 282–284, 286, 290, 318, 492  
 Cesium (Cs), 437  
 Cetyltrimethyl ammonium bromide (CTAB), 113, 273, 329  
 CF<sub>3</sub>COOH, 189  
 Chemical oxygen demand (COD), 127, 147, 160  
 4-Chlorophenol (4-CP), 16, 115, 131, 369, 392  
 Chloroplatinic acid, 31  
 Chromium (Cr), 175, 176, 178, 180  
 CrO<sub>3</sub>, 180, 516–518  
 Cr<sub>2</sub>O<sub>3</sub>, 180, 181  
 Cr (VI), 355, 379  
 Cinnamaldehyde, 7  
 Cinnamyl alcohol, 7  
 Clinoptilolite, 275  
 Colloidal Au, 287  
 Colloidal crystal, 230–232  
 Combustion, 36, 100  
 Conduction band (CB), 48, 52, 62, 105, 111, 133, 137, 152, 182, 191, 194, 203, 207, 259, 284, 295, 326, 331, 333, 349, 373, 375, 379, 386, 392, 405, 444, 455  
 CoO<sub>x</sub>, 454, 455  
 Copper (Cu), 161, 242, 281, 431  
 oxide (Cu<sub>2</sub>O), 152, 406  
 Co-precipitation method, 260, 315  
 Coral-like TiO<sub>2</sub>, 157  
 Core-shell, 5, 30, 35, 137–144, 230, 305, 469  
 Co-ZIF, 498  
 Cyclic voltammetry (CV), 483
- D**  
 D-bond, 43  
*d-d* transition, 320  
 Decolorization, 236–238, 396  
 Degradation, 377  
 De-NO<sub>x</sub>, 102, 105, 109, 111, 118, 243  
 Density functional theory (DFT), 303  
 calculation, 111, 212, 213, 217–219, 360, 532  
 Deodorization, 243  
 Deuterium (D<sub>2</sub>), 205  
 oxide (D<sub>2</sub>O), 205  
 2,5-Diaminoterephthalic acid, 530  
 Dichloroacetate (DCA), 193  
 1,2-Dichlorobenzene (DCB), 261, 267–269, 276  
 2,4-Dichlorophenoxyacetic acid (2,4-D), 28, 48, 261  
 Diffuse-reflection spectra (DRS), 377  
 2,3-Dihydroxynaphthalene, 32, 48  
*N,N*-Dimethylformamide (DMF), 30, 480, 485, 493, 500, 511  
 5,5-Dimethyl-1-pyrroline-N-oxide (DMPO), 367  
 Dinitrogen pentoxide (N<sub>2</sub>O<sub>5</sub>), 99  
 Dinitrogen tetroxide (N<sub>2</sub>O<sub>4</sub>), 99  
 Dinitrogen trioxide (N<sub>2</sub>O<sub>3</sub>), 99  
 Dip-coated, 156  
 Doped TiO<sub>2</sub>, 11–17, 48, 74, 95, 175, 180, 368  
 Doping, 16, 17, 74–76, 79, 175, 180, 187, 194–196, 202, 207, 211, 242, 330, 348, 351, 355, 359, 406, 407, 465  
 Dye sensitization, 158, 359
- E**  
 EDX, 81, 83  
 Electrocatalytic (EC), 125  
 Electrochemical impedance spectroscopy (EIS), 45, 46, 377  
 Electrochemical oxidization, 128  
 Electromagnetic field, 469, 471  
 Electron donor, 377, 396, 437, 445, 451, 452, 454, 456, 458, 473, 481, 483, 484, 496, 497, 502, 509  
 Electron-hole recombination, 24, 62, 175, 194, 262, 269, 326, 331, 366  
 Electron-hole separation, 82

- Electron paramagnetic resonance (EPR), 194, 347, 367
- Electron spin resonance (ESR), 116, 180, 181, 192, 202–203, 207, 300, 308, 350, 482, 524, 532
- Electrophotocatalysts, 125–135
- Electrostatic interaction, 31, 107, 188, 246, 253, 261, 262, 272
- Elemental photocatalysts, 295–309
- Emission, 99, 201, 229, 334, 467, 468, 472–475
- Encapsulation, 138, 251, 261, 466–469
- Er<sup>3+</sup>, 334
- Er-doped, 334
- Ethanol, 5, 14, 16, 32, 36, 54, 71, 85, 93, 190, 202, 264, 297, 409, 510
- Ethylenediaminetetraacetic acid (EDTA), 282, 473, 483, 484
- Ethylene glycol (EG), 30, 330, 346
- EXAFS, 181, 273
- F**
- Face-controlled, 79, 80, 89
- Facet, 4, 7, 31, 48, 49, 55, 56, 79, 106–108, 110, 111, 114, 187–190, 196, 242, 309, 327, 329–331, 335, 337, 342–346, 348–355, 364, 407, 437
- {001} Facet, 4, 187–190, 196, 352, 354, 355
- {010} Facet, 107, 343, 346, 349, 350
- FAU, 244, 265
- Fe<sup>2+</sup>, 84–86, 91, 437
- Fe<sup>3+</sup>, 84–89, 91, 93–96, 103, 203, 207, 211, 437, 438
- Fe-doped, 8, 201–207, 333
- Fe(NO<sub>3</sub>)<sub>3</sub>, 84, 93
- Fe<sub>3</sub>O<sub>4</sub>, 318
- Field-emission type scanning electron microscopy (FE-SEM), 134, 394, 397
- Flake-ball, 391–402
- Flower-like, 6, 10, 131, 157, 399
- Fluorinated TiO<sub>2</sub> (F-TiO<sub>2</sub>), 191–195
- Fluorination, 187–194, 196, 197, 371
- Fourier transform infrared (FTIR), 44, 59, 71, 214–216, 264, 316, 317, 355
- G**
- Gallium oxide (Ga<sub>2</sub>O<sub>3</sub>), 492
- GAs, 55, 56, 59–61
- G-bond, 43
- Gibbs–Thomson effect, 395
- Glucose, 55, 56, 59, 60, 140, 351
- Gold (Au), 242, 281
- nanoparticles (NPs), 8, 62, 109, 282, 283, 286, 287, 291, 469, 471
- Gold/titanium dioxide (Au/TiO<sub>2</sub>), 8, 282, 286, 290, 291
- Graphene, 23–63
- Graphene oxide (GO), 24–32, 34–44, 46, 51, 53–55, 57–60, 62
- Graphitic carbon nitride (g-C<sub>3</sub>N<sub>4</sub>), 305, 493
- Green chemistry, 241, 485
- H**
- Harvesting, 443
- H $\beta$ , 263
- H<sub>3</sub>BO<sub>3</sub>, 37
- Heterojunction, 109, 131, 157, 302, 303, 305, 342, 348, 376, 381, 386, 406–408, 414, 417, 422
- Hierarchical macropore, 230, 238
- Hierarchical microsphere, 302, 330
- Hierarchical structure, 17, 114, 158, 327, 332, 394
- Highest occupied molecular orbital (HOMO), 218, 360, 380–381, 455, 483
- High-resolution transmission electron microscopy (HRTEM), 56, 300, 304, 307, 345, 346, 364, 377, 435, 470
- Hollow, 5, 8, 133, 137–144, 192, 194–196, 230, 242, 342, 344, 366, 399, 432, 433
- Host–guest interactions, 466, 472
- HY, 245, 263
- Hybrid photocatalysts, 31, 253, 254, 327, 466, 472
- Hydrazine, 25, 30
- Hydrochloric acid (HCl), 156, 178, 271, 409, 412–414, 472, 511
- Hydrogen (H<sub>2</sub>)
- evolution, 26, 30, 31, 49, 50, 62, 296, 301, 302, 309, 318, 396, 446, 451–459, 473, 499
- generation, 50, 62
- H<sub>2</sub>PtCl<sub>6</sub>, 202, 484, 485
- H<sub>2</sub>WO<sub>4</sub>, 367, 409
- peroxide (H<sub>2</sub>O<sub>2</sub>), 90, 148, 157, 192, 271, 350, 368, 396, 432
- Hydrolysis, 25, 30, 32–34, 50, 57, 188, 190, 264, 315, 341, 343
- Hydrophilic character, 245–247
- Hydrophobic, 243, 245–250, 269
- zeolite, 266

Hydroxyapatite ( $\text{Ca}_{10}(\text{PO}_4)_6(\text{OH})_2$ ), 252  
 Hydroxynaphthalene, 211  
 HZSM-5, 263, 264

## I

$\text{In}_2\text{O}_3$ , 305  
 Inorganic anions, 314  
 Interfacial surface complex (ISC), 211–223  
 Internal electric field (IEF), 328, 334, 337, 342  
 Iodate ( $\text{IO}_3^-$ ), 447–455, 458, 459  
 Iodide ( $\text{I}^-$ ), 447–459  
 Ion beam, 173, 174, 178  
 Ionic liquid, 107, 495  
 Ionized cluster beam (ICB), 173, 178  
 Iridium (Ir), 454, 480  
    $\text{IrO}_x$ , 454

## K

$\text{K}_3[\text{Fe}(\text{CN})_6]$ , 45  
 $\text{K}_4[\text{Fe}(\text{CN})_6]$ , 45  
 $\text{K}_4\text{Nb}_6\text{O}_{17}$ , 475  
 KCl, 45, 321  
 Knoevenagel condensation, 485, 486  
 Kubelka–Munk, 202

## L

Lamellar, 328, 329  
 $\text{La}_2\text{O}_3$ , 15, 16  
 Lattice defect, 37, 105, 110  
 Lauric acid (LA), 71  
 Layer-by-layer, 139  
 Layered double hydroxides (LDHs), 313–321  
 Layered structure, 31, 113, 315, 317, 318, 325,  
   328, 337, 342, 346, 348, 349, 352,  
   355, 360, 361  
 Lewis acid, 487  
 Ligand-to-metal charge transfer (LMCT), 219,  
   513, 525  
 Light harvesting, 5, 8, 10, 105, 133, 150, 196,  
   197, 327, 331, 343, 399–401, 440,  
   479–483, 508, 523  
 Light self-shielding effect, 149, 152  
 Linker, 31, 56, 60, 492, 508, 510, 514, 523,  
   525, 526, 530  
 Liquefied petroleum gas (LPG), 202  
 Liquid crystal (LC), 127  
 L-*N*-propylpipicolinic acid 2,6-xylidide, 141  
 Localized surface plasmon resonance (LSPR),  
   469, 471

Lowest unoccupied molecular orbital  
 (LUMO), 360, 455, 456, 518  
 L-pipicolinic acid (L-PCA), 138, 139, 141–144  
 L-(S)-lysine (L-Lys), 141–144

## M

Macroporous, 127, 157, 230–232, 235, 237,  
   238, 298  
 Manganese (Mn)-doped, 333  
 Manganese dioxide ( $\text{MnO}_2$ ), 6  
 Manganese oxide ( $\text{MnO}_x$ ), 334  
 MCM-41, 32, 33, 48, 103, 246, 250, 267,  
   474, 475  
 Mesoporous, 32, 229–238, 383  
   silica, 48, 183, 230, 231, 243, 244, 246,  
   247, 250–254, 260, 262, 267, 273,  
   465, 466, 471–475  
 Mesostructured, 4  
 Metal complex, 445, 465–475, 514  
 Metal doping, 23, 211, 331, 333  
 Metal ion implantation, 173–183  
 Metal-organic frameworks (MOFs), 479–487,  
   492, 495, 510, 523  
 Metal to ligand charge transfer (MLCT), 465,  
   467–475  
 Methanol, 5, 138, 202, 216, 282, 320, 366,  
   452, 483, 484  
 Methoxybenzaldehyde, 220  
 Methylbenzaldehyde, 220  
 Methylene blue (MB), 12, 15, 24, 26, 47, 48,  
   61, 192, 236–238, 252–254, 261,  
   271, 274, 300, 317, 384  
 Methyl orange (MO), 28, 48, 54, 61, 131, 134,  
   158, 192, 329, 341, 343  
 Methylviologen ( $\text{MV}^{2+}$ ), 473  
 $\text{Mg}^{2+}$  doped, 111  
 MgO, 492  
 Microbial fuel cell (MFC), 152  
 Microemulsion, 261, 330  
 Microflower, 407  
 Microsphere, 5, 6, 8, 113, 117, 157, 187,  
   194–196, 330, 345, 407  
 Microwave, 25, 29, 36–37, 41, 108, 354  
 MIL-53, 525  
 MIL-88B, 525  
 MIL-101, 516, 525  
 MIL-125, 481, 512  
 Mineralization current efficiency (MCE), 130  
 MOF-5, 480, 511  
 Molecular orbital, (MO), 182, 183, 213, 360  
 Molecular sieves, 259–274

- Molybdenum disulfide ( $\text{MoS}_2$ ), 31, 49, 50, 56, 61, 62
- Monochlorobenzene (MCB), 267, 269
- Monoclinic, 299, 411, 414
- Montmorillonite, 273
- Morphology, 5, 6, 17, 34, 38–40, 48, 52, 53, 56, 71, 72, 74, 75, 79–96, 190, 243, 244, 247, 285, 301, 309, 325–334, 337, 362–366
- N**
- $\text{Na}_2\text{CO}_3$ , 315
- N and F Co-doped  $\text{TiO}_2$ , 13
- $\text{Na}_2\text{S}$ , 37, 305
- $\text{Na}_2\text{SO}_4$ , 27, 46
- Na-mordenite, 267
- Nanoarchitecture, 99–118, 343
- Nanobelt, 342, 344, 381, 382
- Nanocomposite, 25, 26, 29–31, 34, 48, 49, 53–55, 57, 60
- Nanocrystal, 3, 4, 16, 26, 30, 31, 49–51, 55, 56, 59, 60, 69–76, 109, 187, 194–196, 351
- Nanocrystalline, 3, 4, 34, 187–197, 329, 439, 440, 457
- Nanofiber, 306, 327, 342, 344
- Nanofilm, 125, 131
- Nanoflake, 369
- Nanoflowers, 342, 344
- Nanographene oxide, 35
- Nanoparticle, 35, 36
- Nanoplate, 330, 341, 347, 362, 364, 366, 374, 391–397, 399–401, 407
- Nanoribbon, 32, 37, 48
- Nanorod, 26, 27, 32, 48, 54, 62, 80–96, 109, 131, 157, 282, 300, 301, 303, 309
- Nanosheet, 31, 32, 38, 49, 50, 52, 56, 60–62, 189, 194, 302, 328, 342, 344–346, 348, 349, 352, 353, 355, 377, 382, 469
- Nanostructure, 5, 133, 235, 335, 336, 342
- Nano-structured silicate, 243
- Nanotube, 6, 24, 50, 133, 156, 260 array, 125
- Nanowires, 297, 342, 344
- $\text{NaY}$ , 246, 267
- $\text{NaZSM-5}$ , 263
- N-doped  $\text{TiO}_2$ , 11, 12, 80, 111, 419, 422
- $\text{NH}_4\text{F}$ , 190, 195
- $\text{NH}_4\text{HF}_2$ , 188, 189
- $\text{NH}_2\text{-MIL-101}$ , 515–517, 519, 528–530
- $\text{NH}_2\text{-MIL-125}$ , 511–513, 524, 530
- $(\text{NH}_4)_2\text{TiF}_6$ , 26, 31
- Nitric acid ( $\text{HNO}_3$ ), 156, 409
- Nitric oxide (NO), 99 decomposition, 175, 176, 183
- Nitrobenzaldehyde, 220
- Nitrobenzene, 282, 482, 483
- Nitrogen dioxide ( $\text{NO}_2$ ), 99
- Nitrogen oxide ( $\text{NO}_x$ ), 99–101, 103, 105, 109
- Nitrosobenzene, 483
- Nitrous acid ( $\text{HNO}_2$ ), 107
- Nitrous oxide ( $\text{N}_2\text{O}$ ), 99, 176, 184
- Noble metal, 8, 31, 50, 109, 110, 242, 320, 492, 532
- N*-(2-aminoethyl)-3-aminopropyltrimethoxysilane (AEAPS), 140
- O**
- One-dimensional (1D), 131, 329, 391 nanofibers, 309 nanostructure, 327
- One-pot, 31, 36, 49, 55, 56, 189, 261, 270, 393, 479, 485, 486, 527
- Organic pollutant, 17, 24, 46–50, 52, 53, 62, 63, 105, 125–135, 148, 152, 162, 178, 191, 192, 194, 197, 242, 243, 249, 254, 259–274, 392, 393, 401, 405–408
- Orthorhombic crystal, 328, 391–392
- Ostwald ripening process, 189, 346, 351, 365, 395, 396
- Oxygen evolution potential (OEP), 128
- Oxygen vacancies, 13, 37, 103, 111, 129, 195, 330–332, 337, 342, 347, 348, 350, 355, 381, 386
- Oxynitride, 295, 446, 452–454
- P**
- P-25, 4, 7
- $\text{PbBi}_2\text{Nb}_2\text{O}_9$ , 406
- $\text{Pb}(\text{NO}_3)_2$ , 81
- $\text{PbO}$ , 325
- $\text{PbO}_2$ , 81, 83, 91
- $\text{PdCl}_4^{2-}$ , 513
- Perovskite, 115, 360, 452
- Peroxotitanium acid (PTA), 71
- Phenol, 6, 48, 72, 74, 178, 192, 194, 211, 234, 250, 251, 263, 264, 268, 270, 332, 368
- Phosphorescence, 466, 470, 472, 473
- Phosphorus (P), 295, 301, 304

- Photocatalyst electrode, 440
- Photocatalytic degradation, 4, 12, 16, 46, 115, 149, 176, 177, 179, 191–194, 234, 243, 245, 249–251, 253, 259, 261, 266, 305, 317, 365, 369, 377, 379, 382, 385, 393, 405, 515
- Photodegradation, 193, 243, 244, 250, 252–254, 259–274
- Photodeposition, 81, 282, 284–288
- Photoelectrocatalytic, 151, 369, 386
- Photoelectrochemical (PEC), 28, 54, 132, 151, 154, 161, 296, 297, 336, 369, 371, 386
- Photoexcited electron, 510
- Photo fuel cell (PFC), 152, 162
- Photoluminescence (PL), 192, 202, 203, 350, 469, 471, 480
- Photooxidation, 29, 197, 332, 373, 466, 468, 469, 472, 473, 475
- Photosensitization, 24, 343, 349, 473
- Photosensitizer, 319, 334, 349, 473, 514, 519
- Phthalocyanine copper (CuPc), 334
- $\pi$ -conjugated, 58, 386
- Pipecolinic acid (PCA), 141
- $\pi$ - $\pi$  interactions, 262
- $\pi$ - $\pi^*$  transition, 467
- Plasmonic photocatalysts, 242, 281–291
- Platinization, 202
- Platinum (Pt), 31, 32, 50, 81, 83, 109, 111, 139, 155, 162, 163, 194, 202–207, 242, 319, 320, 334, 439, 441, 447, 456–458, 472–475, 481, 514–519, 532
- PtO<sub>x</sub>-loaded, 448
- Polyacrylamide (PAM), 53, 60
- Polyethylene glycol, 273
- Polymerization, 139, 247
- Poly(methyl methacrylate) (PMMA), 230–232, 273
- Polyoxometalate anion, 314
- Polyvinyl alcohol (PVA), 89–91, 96
- Poly(vinyl pyrrolidone) (PVP), 89, 90, 393
- Porous coordination polymers (PCPs), 479–487, 508
- Porous silica, 230–238, 248, 254
- 2-Propanol, 48, 176, 179, 245, 249–251, 265, 266, 282, 410
- Pyramid disk, 160
- Q**
- Quantum dots (QDs), 10, 297, 523
- Quantum efficiency, 8, 10–13, 112, 125, 242, 283, 359, 371, 376, 393, 397, 402, 443, 459, 466, 469, 473
- Quantum size effect, 234, 252, 273, 297
- Quantum yield, 149, 151, 161, 163, 217, 454, 481, 485
- Quaternary ammonium hydrate, 71
- R**
- Raman, 26, 27, 41, 43, 54, 469
- Rectangular, 71
- Red P, 296, 301, 302, 309
- Reduced graphene, 36, 37, 318
- Reduced graphene oxide (RGO), 25, 30, 36, 49, 51, 305, 318
- Rehydration, 315, 316
- Reverse micelle methods, 69
- Rhodamine B (RhB), 26, 48, 54, 154, 191, 297, 317, 392, 393
- Rigidchromism, 468
- Rodlike, 71
- Rotating disk, 147–164
- Ru(bpy)<sub>3</sub><sup>2+</sup>, 466–471, 473
- Ru(bpy)<sub>3</sub>Cl<sub>2</sub>, 467
- Ru(tpy)<sub>2</sub>, 483, 484
- RuO<sub>2</sub>, 454
- Russellite, 391
- Rutile, 14, 28, 69, 73, 74, 76, 79–96, 104, 105, 107–109, 111, 137, 157, 188, 193, 194, 196, 203, 207, 259, 264, 268, 269, 275, 282, 448–450, 454, 458, 493
- S**
- Sacrificial electron donor, 318, 437, 445, 452, 473, 481, 483, 484, 495, 497
- Saturated calomel electrode (SCE), 128, 335
- SBA-15, 7, 252–254, 267, 385, 474, 475
- Sb-doped, 126, 127, 129
- Scanning electron microscopy (SEM), 28, 29, 38, 39, 54, 58, 59, 81, 91, 129, 131, 134, 140, 178, 232, 273, 302, 304, 309, 317
- Schottky junction, 385
- S-doped TiO<sub>2</sub>, 12
- Selected area electron diffraction (SAED), 82, 91
- Selective catalytic reduction (SCR), 99, 101
- Selective non-catalytic reduction (SNCR), 99, 101, 102
- Selenium (Se), 295, 299, 300
- Self-doping, 38, 48
- Sensitizer, 80, 334, 407, 408, 422, 493, 495
- SeO<sub>2</sub>, 300
- Shuttle redox mediator, 445, 452, 459
- Silanol group, 244, 247

- Silica-clay (SC), 273  
Siliceous material, 230  
Silicon (Si), 243, 276, 295, 297–299, 303  
  carbide (SiC), 243  
  nitride (Si<sub>3</sub>N<sub>4</sub>), 243  
  SiO<sub>2</sub>/Al<sub>2</sub>O<sub>3</sub>, 244–246, 249  
Silver (Ag), 281, 297, 309, 470  
  AgI, 406  
  AgNO<sub>3</sub>, 194, 196, 318, 354, 359, 510  
  nanoparticles (NPs), 211, 354, 469–471, 510  
Singlet oxygen, 466  
Sn<sup>4+</sup> doped TiO<sub>2</sub>, 73–75  
Sodium borohydride (NaBH<sub>4</sub>), 25, 26, 300  
Sodium chloride (NaCl), 81, 82  
Sodium dodecyl benzene sulfonate (SDBS), 107  
Sodium hydroxide (NaOH), 34, 300, 315, 434–436  
Sodium tungstate (Na<sub>2</sub>WO<sub>4</sub>), 393–395  
Solar cell, 155  
Solar energy, 23, 108, 149, 151, 201, 242, 244, 259, 301, 317, 327, 329, 330, 334, 359, 382, 436–441, 443, 465, 507, 514  
Solar light, 8, 26, 47, 48, 52, 61, 79, 152, 174, 181, 211, 295, 297, 443, 475, 480, 483  
Sol–gel, 33–35, 53, 69, 129, 159, 175, 178, 180  
Solid phase reaction, 34  
Solvothermal, 3–17, 69–71, 76, 330, 343, 345, 480, 481, 485  
Spherical polycrystalline, 393  
Spill over, 532  
Spin-coated, 156  
Square laminar, 362, 393  
Stereoselectivity, 139, 141  
Strontium titanate (SrTiO<sub>3</sub>), 451–452  
Styrene, 470, 472, 473, 475  
Sulfur, 11, 296, 304  
Supercritical fluid, 3–18  
Superoxide anion, 148, 396, 466  
Superoxide radical, 241, 331  
Surface-enhanced Raman scattering (SERS), 281  
Surface hydroxyl group, 259  
Surface plasmonic resonance (SPR), 109, 110, 281–284, 296, 308  
Synergy effect, 62, 495, 508
- T**  
Ta<sub>3</sub>N<sub>5</sub>, 295, 452, 454  
Tantalum oxynitride (TaON), 452–454, 459  
Ta<sub>2</sub>O<sub>5</sub>, 452  
Terephthalate ligand, 510  
Terminal OH, 215, 216, 219  
Tetrabutylorthotitanate (TBOT), 31, 54, 188  
Tetrachloroauric acid (HAuCl<sub>4</sub>), 29, 36, 109, 287  
Tetraethyl orthosilicate (TEOS), 140  
Tetrafluoroborate (BF<sub>4</sub>), 107, 157  
Tetragonal, 74, 407  
Thin film, 163  
  reactor, 151  
Three dimensional (3D), 6, 24, 33, 52–62, 117, 126, 129, 309, 329, 342, 365, 408, 492  
Ti-containing zeolites, 183, 508  
Ti-HMS, 183  
Tin dioxide (SnO<sub>2</sub>), 57, 73, 126–131, 440  
Ti-MOF, 480–485  
Titanium ion (Ti<sup>3+</sup>), 29, 37, 38, 48, 50, 88, 89, 111, 194, 482, 524, 525, 527  
  sulfate (Ti(SO<sub>4</sub>)<sub>2</sub>), 28, 34, 54, 56, 189, 190  
  TiF<sub>4</sub>, 4, 7, 9, 27, 28, 34, 70, 71, 94  
  TiN, 6  
  TiO<sub>2</sub>, 3–17, 23–63, 69–76, 79–96, 103–112, 115, 125–135, 137–144, 148, 152, 156–159, 161, 162, 173–185, 187–197, 201–207, 211–223, 229–238, 241–255, 259–276, 282, 288–291, 295, 297, 306, 317, 318, 330, 333, 335, 336, 350, 367, 368, 371, 381, 382, 397, 398, 400, 405–407, 417, 419–422, 429–432, 438, 443, 447–451, 454, 455, 457–459, 480, 491–502, 514, 517, 524, 525  
  TiOSO<sub>4</sub>, 5, 6, 189  
  TiSn<sub>10</sub>, 73–75  
  TiSn<sub>4</sub>, 74, 75  
  trichloride (TiCl<sub>3</sub>), 27, 28, 34, 81, 111  
  trioxide (Ti<sub>2</sub>O<sub>3</sub>), 406  
Titania, 54, 55, 138–144  
  nanotube, 104  
Titanium bis(ammonium lactate) dihydroxide (TALH), 90  
Transient IR, 400, 401

- Transmission electron microscope (TEM),  
26–29, 38, 39, 54, 56, 58, 59, 81,  
82, 89, 91, 285, 288, 304, 307, 309,  
366, 413, 469, 512, 516
- Triethanolamine (TEOA), 211, 319, 481–485,  
493, 494, 496, 497, 519, 524
- Triethoxyfluorosilane (TEFS), 248–251
- Trifluoroacetic acid (TFA), 194
- Trifluoromethylbenzaldehyde, 220
- Trioctylphosphine oxide, 71
- Tungstate ( $\text{WO}_4^{2-}$ ), 392
- Tungsten ion ( $\text{W}^{6+}$ ), 418
- Tungsten oxide ( $\text{WO}_3$ ), 417, 418, 429,  
431–441, 444, 446–454, 459
- Tungstophosphoric acid (TPA), 271
- Two dimensional (2D), 7, 24, 50, 62, 113, 273,  
313, 328–330, 344, 364, 365, 391,  
393–395, 398–401  
nanosheets, 309, 345
- U**
- Uio-66, 524, 525, 530–532
- Ultrasonic, 32, 57, 115, 329, 362
- UV–Visible diffuse reflectance spectra  
(UV-Vis DRS), 414
- V**
- Valence band (VB), 83, 112, 151, 191, 194,  
195, 207, 259, 295, 326, 331, 373,  
392, 405, 444, 452, 509
- V ion, 174, 176, 183, 184
- Visible-light, 11, 51, 79–96, 108, 133, 149,  
173–185, 187, 191, 202, 211, 242,  
262, 282, 296, 317, 329, 343, 359,  
392, 405, 429, 443, 465, 479, 492,  
514
- Void space, 138–141, 398, 465, 467
- Volatile organic compounds (VOC), 211, 229,  
249, 431
- W**
- Wastewater, 125, 131, 147–164
- Water splitting, 194, 197, 201, 301, 306, 318,  
319, 334, 361, 396, 429–441,  
443–459
- $\text{WO}_6$  octahedral, 360, 392
- X**
- XAFS, 178, 180, 183
- X-ray absorption near-edge structure  
(XANES), 180, 181, 273, 467, 470,  
512
- X-ray diffraction (XRD), 14, 26–29, 41, 43,  
54, 58, 59, 73, 75, 82, 178, 207,  
213–214, 233, 264, 267, 268,  
270–273, 302, 304, 313, 316,  
366–368, 410, 411, 413, 435,  
467, 498, 499, 502, 510, 512,  
516, 524
- X-ray photoelectron spectroscopy (XPS), 12,  
26–29, 41–45, 54, 58, 59, 74, 86,  
175, 178, 180, 214, 371, 374, 418,  
419
- Y**
- Yolk–shell, 5, 8, 138
- $\text{YCl}_3$ , 302, 303
- $\text{YPO}_4$  nanosheet, 302, 303
- Z**
- Zeolite, 102, 183, 230, 243–252, 254,  
262–267, 274–276, 282, 465–469,  
508, 509, 524
- Zeolite Y, 282, 466–469
- Zeolitic imidazolate framework, 492, 502
- ZIF-9, 491–502
- Zinc oxide (ZnO), 492
- $\text{ZnMn}_2\text{O}_4$ , 406
- $\text{ZnWO}_4$ , 371
- $\text{ZrCl}_4$ , 485
- $\text{Zr}(\text{HPO}_4)_2$ , 475
- Zr-MOF, 486
- $\text{ZrO}_2$ , 282, 454, 491
- Z-scheme, 436, 443–459